GAS GEOCHEMISTRY: NEW PROGRESSES AND APPLICATIONS

EDITED BY: Giovanni Martinelli, Francesco Italiano, Yunpeng Wang and Guodong Zheng

PUBLISHED IN: Frontiers in Earth Science



frontiers Research Topics

Frontiers eBook Copyright Statement

The copyright in the text of individual articles in this eBook is the property of their respective authors or their respective institutions or funders. The copyright in graphics and images within each article may be subject to copyright of other parties. In both cases this is subject to a license granted to Frontiers.

The compilation of articles constituting this eBook is the property of Frontiers.

Each article within this eBook, and the eBook itself, are published under the most recent version of the Creative Commons CC-BY licence. The version current at the date of publication of this eBook is CC-BY 4.0. If the CC-BY licence is updated, the licence granted by Frontiers is automatically updated to the new version.

When exercising any right under the CC-BY licence, Frontiers must be attributed as the original publisher of the article or eBook, as applicable.

Authors have the responsibility of ensuring that any graphics or other materials which are the property of others may be included in the CC-BY licence, but this should be checked before relying on the CC-BY licence to reproduce those materials. Any copyright notices relating to those materials must be complied with.

Copyright and source acknowledgement notices may not be removed and must be displayed in any copy, derivative work or partial copy which includes the elements in question.

All copyright, and all rights therein, are protected by national and international copyright laws. The above represents a summary only. For further information please read Frontiers' Conditions for Website Use and Copyright Statement, and the applicable CC-BY licence.

ISSN 1664-8714
ISBN 978-2-88976-496-9
DOI 10.3389/978-2-88976-496-9

About Frontiers

Frontiers is more than just an open-access publisher of scholarly articles: it is a pioneering approach to the world of academia, radically improving the way scholarly research is managed. The grand vision of Frontiers is a world where all people have an equal opportunity to seek, share and generate knowledge. Frontiers provides immediate and permanent online open access to all its publications, but this alone is not enough to realize our grand goals.

Frontiers Journal Series

The Frontiers Journal Series is a multi-tier and interdisciplinary set of open-access, online journals, promising a paradigm shift from the current review, selection and dissemination processes in academic publishing. All Frontiers journals are driven by researchers for researchers; therefore, they constitute a service to the scholarly community. At the same time, the Frontiers Journal Series operates on a revolutionary invention, the tiered publishing system, initially addressing specific communities of scholars, and gradually climbing up to broader public understanding, thus serving the interests of the lay society, too.

Dedication to Quality

Each Frontiers article is a landmark of the highest quality, thanks to genuinely collaborative interactions between authors and review editors, who include some of the world's best academicians. Research must be certified by peers before entering a stream of knowledge that may eventually reach the public - and shape society; therefore, Frontiers only applies the most rigorous and unbiased reviews.
Frontiers revolutionizes research publishing by freely delivering the most outstanding research, evaluated with no bias from both the academic and social point of view. By applying the most advanced information technologies, Frontiers is catapulting scholarly publishing into a new generation.

What are Frontiers Research Topics?

Frontiers Research Topics are very popular trademarks of the Frontiers Journals Series: they are collections of at least ten articles, all centered on a particular subject. With their unique mix of varied contributions from Original Research to Review Articles, Frontiers Research Topics unify the most influential researchers, the latest key findings and historical advances in a hot research area! Find out more on how to host your own Frontiers Research Topic or contribute to one as an author by contacting the Frontiers Editorial Office: frontiersin.org/about/contact

GAS GEOCHEMISTRY: NEW PROGRESSES AND APPLICATIONS

Topic Editors:
Giovanni Martinelli, National Institute of Geophysics and Volcanology, Section of Palermo, Italy
Francesco Italiano, National Institute of Geophysics and Volcanology, Section of Palermo, Italy
Yunpeng Wang, Guangzhou Institute of Geochemistry, Chinese Academy of Sciences (CAS), China
Guodong Zheng, Northwest Institute of Eco-Environment and Resources, Chinese Academy of Sciences (CAS), China

Citation: Martinelli, G., Italiano, F., Wang, Y., Zheng, G., eds. (2022). Gas Geochemistry: New Progresses and Applications. Lausanne: Frontiers Media SA. doi: 10.3389/978-2-88976-496-9

Table of Contents

06 ***Editorial: Gas Geochemistry: New Progresses and Applications***
Giovanni Martinelli, Francesco Italiano, Yunpeng Wang and Guodong Zheng

09 ***The Impact of Atmospheric and Tectonic Constraints on Radon-222 and Carbon Dioxide Flow in Geological Porous Media - A Dozen-Year Research Summary***
Hovav Zafrir, Susana Barbosa, Elad Levintal, Noam Weisbrod, Yochai Ben Horin and Zeev Zalevsky

37 ***Stochastic Models for Radon Daily Time Series: Seasonality, Stationarity, and Long-Range Dependence Detection***
Marianna Siino, Salvatore Scudero and Antonino D'Alessandro

50 ***Groundwater Anomaly Related to CCS-CO_2 Injection and the 2018 Hokkaido Eastern Iburi Earthquake in Japan***
Yuji Sano, Takanori Kagoshima, Naoto Takahata, Kotaro Shirai, Jin-Oh Park, Glen T. Snyder, Tomo Shibata, Junji Yamamoto, Yoshiro Nishio, Ai-Ti Chen, Sheng Xu, Dapeng Zhao and Daniele L. Pinti

60 ***Short-Term Monitoring of Geogenic Soil CO_2 Flux in a Non-Volcanic and Seismically Inactive Emission Site, South Korea***
Chan Yeong Kim, Soonyoung Yu, Yun-Yeong Oh, Gitak Chae, Seong-Taek Yun and Young Jae Shinn

78 ***An Automatic System for Continuous Monitoring and Sampling of Groundwater Geochemistry in Earthquake-Prone Regions of SW Taiwan***
Ching-Chou Fu, Chun-Wei Lai, Tsanyao Frank Yang, David R. Hilton, Cheng-Hong Chen, Vivek Walia, Arvind Kumar and Lou-Chuang Lee

90 ***Catalytic Hydrogenation of Post-Mature Hydrocarbon Source Rocks Under Deep-Derived Fluids: An Example of Early Cambrian Yurtus Formation, Tarim Basin, NW China***
Huang Xiaowei, Jin Zhijun, Liu Quanyou, Meng Qingqiang, Zhu Dongya, Liu Jiayi and Liu Jinzhong

103 ***Soil Degassing From the Xianshuihe–Xiaojiang Fault System at the Eastern Boundary of the Chuan–Dian Rhombic Block, Southwest China***
Yutao Sun, Xiaocheng Zhou, Yucong Yan, Jingchao Li, Wenya Fang, Wanli Wang and Yongmei Liu

115 ***Geochemical Characteristics of Gas and Flowback Water in Lake Facies Shale: A Case Study From the Junggar Basin, China***
Lin Zhang, Dan Liu, Yongjin Gao and Min Zhang

129 ***The Paleoclimate Significance of the $\delta^{13}C$ Composition of Individual Hydrocarbon Compounds in the Maoming Oil Shales, China***
Xinxing Cao, Zhiguang Song, Sibo Wang and Puliang Lyu

142 ***Characteristics of Organic Matter and Biomarkers in Core Sediments From the Offshore Area of Leizhou Peninsula, South China Sea***
Yuan Gao, Jingqian Tan, Jia Xia, Yao-Ping Wang, Sibo Wang, Yongqiang Han, Jiefeng He and Zhiguang Song

156 ***Insight Into Hartoušov Mofette, Czech Republic: Tales by the Fluids***
Kyriaki Daskalopoulou, Heiko Woith, Martin Zimmer, Samuel Niedermann, Johannes A. C. Barth, Alexander H. Frank, Andrea Vieth-Hillebrand, Josef Vlček, Cemile Dilara Bağ and Ralf Bauz

169 ***Geochemical Comparison of the Deep Gases From the Sichuan and Tarim Basins, China***
Yunyan Ni, Limiao Yao, Fengrong Liao, Jianping Chen, Cong Yu and Guangyou Zhu

191 ***Preliminary Experimental Study of Methane Adsorption Capacity in Shale After Brittle Deformation Under Uniaxial Compression***
Mingliang Liang, Zongxiu Wang, Guodong Zheng, Xiaobao Zhang, Hugh Christopher Greenwell, Kaixun Zhang, Xingqiang Feng, Linyan Zhang and Huijun Li

202 ***Factors Controlling Natural Gas Accumulation in the Southern Margin of Junggar Basin and Potential Exploration Targets***
Jianping Chen, Xulong Wang, Yongge Sun, Yunyan Ni, Baoli Xiang and Jiande Liao

220 ***Potential Production of Carbon Gases and Their Responses to Paleoclimate Conditions: An Example From Xiaolongtan Basin, Southeast Tibetan Plateau***
Gen Wang, Yongli Wang, Zhifu Wei, Zepeng Sun, Wei He and Xueyun Ma

233 ***Radioactive Thoron ^{220}Rn Exhalation From Unfired Mud Building Material Into Room Air of Earthen Dwellings***
Nguyệt Thị Ánh Nguyễn, Du'o'ng Nguyễn-Thùy, Hu'ó'ng Nguyễn-Văn, Nam Nguyễn-Hải and Arndt Schimmelmann

246 ***Insights from Fumarole Gas Geochemistry on the Recent Volcanic Unrest of Pico do Fogo, Cape Verde***
Gladys V. Melián, Pedro A. Hernández, Nemesio M. Pérez, María Asensio-Ramos, Eleazar Padrón, Mar Alonso, Germán D. Padilla, José Barrancos, Francesco Sortino, Hirochicka Sumino, Fátima Rodríguez, Cecilia Amonte, Sonia Silva, Nadir Cardoso and José M. Pereira

268 ***Geochemical Features of the Thermal and Mineral Waters From the Apuseni Mountains (Romania)***
Alin-Marius Nicula, Artur Ionescu, Ioan-Cristian Pop, Carmen Roba, Ferenc L. Forray, Iancu Orăşeanu and Călin Baciu

276 ***Black Sea Methane Flares From the Seafloor: Tracking Outgassing by Using Passive Acoustics***
Manfredi Longo, Gianluca Lazzaro, Cinzia Giuseppina Caruso, Vlad Radulescu, Raluca Radulescu, Sergio Simone Sciré Scappuzzo, Dominique Birot and Francesco Italiano

296 ***Inversion Characteristics of Hydrocarbon Gases Carbon Isotopes Varying With Temperature and Implications for Shale Exploration***
Yingqin Wu, Yanhong Liu, Tong Wang, Zhiyu Wang, Longmiao Yuan and Yanqin Xia

304 ***Differences on Geochemical Characteristics and Their Implicating Significances of Nitrogen in Coal-Derived Gas and Oil-typed Gas in China***
Wang Xiaobo, Li Jian, Yang Chunxia, Li Zhisheng, Chen Jianfa, Zheng Yue, Wang Yifeng, Li Jin, Yang Chunlong, Hao Aisheng and Ge Shouguo

316 ***The Characteristics of Organic Carbon in the Offshore Sediments Surrounding the Leizhou Peninsula, China***
Jia Xia, Yongqiang Han, Jingqian Tan, Grace Awinmalsim Abarike and Zhiguang Song

329 ***Genetic Types, Distribution Patterns and Enrichment Mechanisms of Helium in China's Petroliferous Basins***
Shengfei Qin, Dan Xu, Jiyuan Li and Zheng Zhou

frontiers | Frontiers in Earth Science

EDITORIAL
published: 09 June 2022
doi: 10.3389/feart.2022.936733

Editorial: Gas Geochemistry: New Progresses and Applications

Giovanni Martinelli[1,2]*, *Francesco Italiano*[1], *Yunpeng Wang*[3] *and Guodong Zheng*[2,4]

[1]Department of Palermo, INGV Istituto Nazionale di Geofisica e Vulcanologia, Palermo, Italy, [2]Northwest Institute of Eco-Environment and Resources, Chinese Academy of Sciences (CAS), Lanzhou, China, [3]State Key Laboratory of Organic Geochemistry, Guangzhou Institute of Geochemistry, Chinese Academy of Sciences (CAS), Guangzhou, China, [4]School of Environmental Studies, China University of Geosciences at Wuhan, Wuhan, China

Keywords: carbon dioxide, volcanic gases, tectonically derived geofluids, hydrocarbons, noble gases

Editorial on the Research Topic

Gas Geochemistry: New Progresses and Applications

INTRODUCTION

Geosphere is constantly crossed by fluid fluxes of varying flow velocity and chemical composition. The development of gas geochemistry techniques over the last 50 years allowed of gaining a significant understanding of gas accumulations, gas fluxes, and their geological sources. Although gas geochemistry is a relatively recent discipline of geochemistry, advancements over the last 2 decades in sampling, storage and analysis of gas samples have enabled gas geochemistry to emerge as a critical scientific tool for constraining processes occurring in the geosciences. Chemical and isotopic features of various gas species have provided critical information about their origin, source, migration, and accumulation in specific environments, making gas geochemistry a widely used tool in a variety of fields of geosciences, including environmental/climate problems, geohazards, origin and evolution of rocks, as well as biogeochemical processes involving microbial activity. Due to the economic relevance of hydrocarbons and hydrothermal gases, they have been investigated more intensively than other gas types since very early time. Additionally, advances in our understanding of unconventional gases such as shale and tight gas in recent decades, represent new applications for these gas-related approaches. Over the last half-century, scientists in the field of gas geochemistry have exchanged their findings/experiments at major international scientific conferences organized by the International Conference on Gas Geochemistry (ICGG), the Geochemical Society, the American Geophysical Union (AGU), the European Geosciences Union (EGU), the American Association of Petroleum Geologists (AAPG), and the International Association of Volcanology and Chemistry of the Earth's Interior (IAVCEI). Numerous applications of gas geochemistry in geology and the environment have been studied in recent years, and the present trend confirms that Earth and Environmental Sciences are the most promising domains for gas geochemistry applications. It is worth noting that advances in our understanding of noble/rare gas geochemistry are more closely tied to technology achievements than to fundamental geological knowledge. The current Research Topic has been devoted of compiling the most recent and pertinent experiences in the various domains of gas geochemistry. 23 papers presented but not limited in the 2019 ICGG meeting in Sicily have been accepted for publication.

Hereby it is useful to report the list of published papers by date of publications and a keyword at the end in parentheses able to roughly identify the basic field of interest. In particular the paper by:

OPEN ACCESS

Edited and reviewed by:
Martyn Tranter,
Aarhus University, Denmark

***Correspondence:**
Giovanni Martinelli
giovanni.martinelli15@gmail.com

Specialty section:
This article was submitted to Geochemistry, a section of the journal Frontiers in Earth Science

Received: *05 May 2022*
Accepted: *09 May 2022*
Published: *09 June 2022*

Citation:
Martinelli G, Italiano F, Wang Y and Zheng G (2022) Editorial: Gas Geochemistry: New Progresses and Applications. Front. Earth Sci. 10:936733. doi: 10.3389/feart.2022.936733

(1) Qin et al. reported about *Genetic Types, Distribution Patterns and Enrichment Mechanisms of Helium in China's Petroliferous Basins* (raw materials)
(2) Xia et al. reported about *The Characteristics of Organic Carbon in the Offshore Sediments Surrounding the Leizhou Peninsula, China* (hydrocarbons)
(3) Xiaobo et al. reported about *Differences on Geochemical Characteristics and Their Implicating Significances of Nitrogen in Coal-Derived Gas and Oil-typed Gas in China* (hydrocarbons)
(4) Wu et al. reported about *Inversion Characteristics of Hydrocarbon Gases Carbon Isotopes Varying With Temperature and Implications for Shale Exploration* (hydrocarbons)
(5) Longo et al. reported about *Black Sea Methane Flares From the Seafloor: Tracking Outgassing by Using Passive Acoustics* (hydrocarbons)
(6) Nicula et al. reported about *Geochemical Features of the Thermal and Mineral Waters From the Apuseni Mountains* (*Romania*) (geothermics)
(7) Melián et al. reported about *Insights from Fumarole Gas Geochemistry on the Recent Volcanic Unrest of Pico do Fogo, Cape Verde* (volcanic risk)
(8) Nguyễn et al. reported about *Radioactive Thoron ^{220}Rn Exhalation From Unfired Mud Building Material Into Room Air of Earthen Dwellings* (radioprotection in living environment)
(9) Wang et al. reported about *Potential Production of Carbon Gases and Their Responses to Paleoclimate Conditions: An Example From Xiaolongtan Basin, Southeast Tibetan Plateau* (hydrocarbons)
(10) Chen et al. reported about *Factors Controlling Natural Gas Accumulation in the Southern Margin of Junggar Basin and Potential Exploration Targets* (hydrocarbon)
(11) Liang et al. reported about *Preliminary Experimental Study of Methane Adsorption Capacity in Shale After Brittle Deformation Under Uniaxial Compression* (hydrocarbons)
(12) Ni et al. reported about *Geochemical Comparison of the Deep Gases From the Sichuan and Tarim Basins, China* (hydrocarbons)
(13) Daskalopoulou et al. reported about *Insight Into Hartoušov Mofette, Czech Republic: Tales by the Fluids* (tectonophysics)
(14) Gao et al. reported about *Characteristics of Organic Matter and Biomarkers in Core Sediments From the Offshore Area of Leizhou Peninsula, South China Sea* (hydrocarbons)
(15) Cao et al. reported about *The Paleoclimate Significance of the $\delta^{13}C$ Composition of Individual Hydrocarbon Compounds in the Maoming Oil Shales, China* (hydrocarbons)
(16) Zhang et al. reported about *Geochemical Characteristics of Gas and Flowback Water in Lake Facies Shale: A Case Study From the Junggar Basin, China* (hydrocarbons)
(17) Sun et al. reported about *Soil Degassing From the Xianshuihe–Xiaojiang Fault System at the Eastern Boundary of the Chuan–Dian Rhombic Block, Southwest China* (tectonophysics)
(18) Xiaowei et al. reported about *Catalytic Hydrogenation of Post-Mature Hydrocarbon Source Rocks Under Deep-Derived Fluids: An Example of Early Cambrian Yurtus Formation, Tarim Basin, NW China* (hydrocarbons)
(19) Fu et al. reported about *An Automatic System for Continuous Monitoring and Sampling of Groundwater Geochemistry in Earthquake-Prone Regions of SW Taiwan* (tectonophysics)
(20) Kim et al. reported about *Short-Term Monitoring of Geogenic Soil CO_2 Flux in a Non-Volcanic and Seismically Inactive Emission Site, South Korea* (tectonophysics)
(21) Sano et al. reported about *Groundwater Anomaly Related to CCS-CO_2 Injection and the 2018 Hokkaido Eastern Iburi Earthquake in Japan* (carbon capture and storage)
(22) Siino et al. reported about *Stochastic Models for Radon Daily Time Series: Seasonality, Stationarity, and Long-Range Dependence Detection* (data processing)
(23) Zafrir et al. reported about *The Impact of Atmospheric and Tectonic Constraints on Radon-222 and Carbon Dioxide Flow in Geological Porous Media—A Dozen-Year Research Summary* (tectonophysics)

CONCLUSION

52% of published papers is related to the geochemical characterization and to the study of the chemical and isotopic evolution of hydrocarbon gases. 22% of published papers is related to geochemical characterization and monitoring of geofluids in tectonophysics and seismicity-oriented researches. The other 26% of published papers is related to the research of raw materials, geothermal energy, groundwaters, volcanic risk, radioprotection, carbon capture and storage and to data processing of time series of recorded data. Current trends obtained by published papers indicate that Earth, Energy, and Environmental Sciences are the most promising fields for the application of Gas Geochemistry and of Noble/Rare Gas Geochemistry, as they are more concerned with technological advancements than with basic geological knowledge. A close collaboration with geophysical sciences demonstrated to be a winning approach to solve the increasingly difficult problems in Gas Geochemistry.

AUTHOR CONTRIBUTIONS

All authors listed have made a substantial, direct, and intellectual contribution to the work and approved it for publication.

ACKNOWLEDGMENTS

The editors of this Research Topic thank all authors for their contributions, and all reviewers for their constructive comments. Department of Palermo, INGV Istituto Nazionale di Geofisica e Vulcanologia, Italy is acknowledged for organizing ICGG 2019,

which provided an extraodinary platform for communication and initialization of this Research Topic.

Conflict of Interest: The authors declare that the research was conducted in the absence of any commercial or financial relationships that could be construed as a potential conflict of interest.

Publisher's Note: All claims expressed in this article are solely those of the authors and do not necessarily represent those of their affiliated organizations, or those of the publisher, the editors, and the reviewers. Any product that may be evaluated in this article, or claim that may be made by its manufacturer, is not guaranteed or endorsed by the publisher.

Copyright © 2022 Martinelli, Italiano, Wang and Zheng. This is an open-access article distributed under the terms of the Creative Commons Attribution License (CC BY). The use, distribution or reproduction in other forums is permitted, provided the original author(s) and the copyright owner(s) are credited and that the original publication in this journal is cited, in accordance with accepted academic practice. No use, distribution or reproduction is permitted which does not comply with these terms.

frontiers in Earth Science

ORIGINAL RESEARCH
published: 30 October 2020
doi: 10.3389/feart.2020.559298

The Impact of Atmospheric and Tectonic Constraints on Radon-222 and Carbon Dioxide Flow in Geological Porous Media - A Dozen-Year Research Summary

Hovav Zafrir[1,2], Susana Barbosa[3], Elad Levintal[4], Noam Weisbrod[4], Yochai Ben Horin[5] and Zeev Zalevsky[1]*

[1] Faculty of Engineering, Bar Ilan University, Ramat-Gan, Israel, [2] Geological Survey of Israel, Jerusalem, Israel, [3] INESC TEC, Porto, Portugal, [4] The Jacob Blaustein Institutes for Desert Research, Ben Gurion University of the Negev, Midreshet Ben Gurion, Israel, [5] Soreq Nuclear Research Center, Yavne, Israel

OPEN ACCESS

Edited by:
Giovanni Martinelli, National Institute of Geophysics and Volcanology, Section of Palermo, Italy

Reviewed by:
Vivek Walia, National Center for Research on Earthquake Engineering, Taiwan
Heiko Woith, German Research Centre for Geosciences, Helmholtz Centre Potsdam, Germany

***Correspondence:**
Hovav Zafrir
hzafrir@gmail.com

Specialty section:
This article was submitted to Geochemistry, a section of the journal Frontiers in Earth Science

Received: *05 May 2020*
Accepted: *07 September 2020*
Published: *30 October 2020*

Citation:
Zafrir H, Barbosa S, Levintal E, Weisbrod N, Ben Horin Y and Zalevsky Z (2020) The Impact of Atmospheric and Tectonic Constraints on Radon-222 and Carbon Dioxide Flow in Geological Porous Media - A Dozen-Year Research Summary. Front. Earth Sci. 8:559298. doi: 10.3389/feart.2020.559298

Long-term monitoring of Rn-222 and CO_2 at a depth of several dozen meter at the Sde-Eliezer site, located within one of the Dead Sea Fault Zone segments in northern Israel, has led to the discovery of the clear phenomenon that both gases are affected by underground tectonic activity along the Dead Sea Fault Zone. It may relate to pre-seismic processes associated with the accumulation and relaxation of lithospheric stress and strain producing earthquakes. This approach assumes that meteorological influences on physico-chemical parameters are limited at depth since its strength diminishes with the increase of the overlay layer thickness. Hence, the monitoring of natural gases in deep boreholes above the water table enables to reduce the climatic-induced periodic contributions, and thus to identify the specific portion of the radon signals that could be related to regional tectonic pre-seismic activity. The plausible pre-seismic local movement of the two gases at depth - is identified by the appearance of discrete, random, non-cyclical signals, wider in time duration than 20 h and clearly wider than the sum of the width of the periodic diurnal and semidiurnal signals driven by ambient meteorological parameters. These non-cyclical signals may precede, by one day or more, a forthcoming seismic event. Hence, it is plausible to conclude that monitoring of any other natural gas that is present at depth may show a similar broadening signal and may serve as a precursor too. The necessary technical conditions enabling to distinguish between anomalous signals of gases that may be induced locally by pre-seismic processes at depth, and the relatively low periodic signals that are still established at depth related to external climatic conditions, are presented in detail.

Keywords: radon monitoring, thermal flow in porous media, earthquake precursors, borehole monitoring, barometric pumping

INTRODUCTION

Overview

Previous research on radon has been carried out in the last 45 years in various geological environments such as soil (e.g., Akerblom et al., 1984; Schubert and Schultz, 2002; Fujiyoshi et al., 2006; Muga, 2017; Cannelli et al., 2018; Siino et al., 2019), solid rocks (e.g., Vulkan et al., 1992; Steinitz et al., 2007; Barbosa et al., 2010), fans of erosion streams (e.g., Steinitz et al., 1992), subterranean structures such as caves, tunnels and mines (e.g., Hakl et al., 1996; Przylibski, 2001; Muramatsu et al., 2002; Cigna, 2005; Richon et al., 2005; Mentes and Eper-Pápai, 2015; Sahu et al., 2016) and groundwater (e.g., Igarashi et al., 1995; Atkins et al., 2016; Barberio et al., 2018). The main objective of such studies was either to examine the association between radon concentration changes in shallow surface environments and the health risk of radon in augmenting lung cancer, or to investigate the connection between radon and geodynamics (e.g., Mogro-Campero et al., 1977; Fleischer, 1981; Monnin et al., 1993; Trique et al., 1999; Steinitz et al., 2003; Zafrir et al., 2003; Groves-Kirkby et al., 2004; Cicerone et al., 2009; Ghosh et al., 2009; Vaupotič et al., 2010; Oh and Kim, 2015; Riggio et al., 2015; Zafrir et al., 2016; Fu et al., 2017; Singh et al., 2017) and volcanic eruptions (e.g., Eff-Darwich et al., 2002; Martin-Luis et al., 2015; Falsaperla et al., 2017; Torres-Gonzalez et al., 2019).

The available techniques for the measurement of radon and its decay products (RDPs) in sub-ground media are based on the interaction of either alpha particles or gamma-rays with the sensor material. The most common means for the measurement of radon is through the detection of alpha particle emission from the decay of Rn-222 (5.49 MeV), Po-218 (6.00 MeV) and Po-214 (7.69 MeV), or gamma ray radiation from radon decay products (RDPs) mainly Bi-214 and Pb-214 (e.g., Ivanovich and Harmon, 1982). The detection process includes recording of the alpha or gamma radiation for sequential time intervals (seconds to hours). Electronic automatic radon monitoring station are known to be operated in diverse places such as Japan (e.g., Noguchi and Wakita, 1977), China (e.g., King, 1986), and Europe (e.g., Koch and Heinicke, 1994). Most of these stations measure radon in water or soil using either Lucas cells (based on ZnS for detection of alpha particles) or NaI (for gamma detection).

A wide variety of measuring methods are presented in the literature (e.g., Knoll, 2000). For example, for passive detection, activated charcoal that adsorbs radon and its decay products from air (e.g., George, 1984) and alpha-sensitive CR-39 or LR-115 nuclear track films (e.g., Fleischer et al., 1984; Jönsson, 1997; Wertheim et al., 2010). Sealed metal cells covered with scintillator as zinc sulphide (Lucas cells, Lucas, 1957) used to measure pumped radon samples as well as ionization chambers (e.g., Ichitsubo and Yamada, 2004), and silicon photodiodes (e.g., George, 1990). Gamma sensors including Geiger-Mueller counters, scintillation light detection devices (e.g., Vulkan et al., 1995; Walia et al., 2005; Zafrir et al., 2009; Zafrir et al., 2011) and silicon photodiodes (e.g., Pinault and Baubron, 1996), have been exploited during the last 30 years, for radon detection.

In continuous long-term radon measurements, the mandatory essential condition is not to violate the natural thermodynamic equilibrium nor the radon and RDPs secular equilibrium, by pumping and grabbing radon samples from the geological porous media below the surface. The measurement technologies that allow working in passive mode are the alpha-particles sensors based on silicon photodiodes or ionization chambers, and gamma detectors based on various scintillation materials. It enables tracking temporal radon fluctuations under natural stable internal conditions, with a high-resolution sampling rate from once every few seconds up to several minutes.

For radon measurement by alpha detectors, the prime concealed problem is the ability of radon gas to move out from the solid grain to the intergranular space in the bedrock (emanation), and then to flow out to the air space (exhalation) in order to be perceived and measured by the detector. By taking into consideration that less than 32 percent of the radon content in rock emanate from the solid grains to the porous media (Hassan et al., 2009) and that the radon exhalation greatly depends on the features of the investigated media, such as its thickness, the internal structure as well as the moisture content of the solid phase, the amount of the radon gas being exhaled to the air and that may temporally be detected is less than 10%.

In addition, when an alpha detector is set inside a borehole, for example, it has to respond to radon particles that first have to enter by diffusion from the air space into the detector's sensing volume (dozens of cm^3). Then the alpha radiation which is emitted by the Rn-222 and its RDPs, Po-218 and Po-214, has to reach the internal silicon solid state sensor to produce counting signals. This process greatly reduces the efficiency of the measurement.

On the other side, there is an intrinsic distinction between the alpha and the gamma measurement, related to the sensing capabilities. When a gamma detector is installed, inside a borehole, within a geological formation, it responds to the radon existing within a surrounding spherical body of bedrocks of a radius of R + 35 cm (where R is the borehole radii and the 35 cm is the average gamma absorption length). In addition to the three-scale difference in the size of sensing volume, the gamma detection method enables principally the measurement of radon content directly inside the country rock media. Thus, it is the ideal passive method for measuring radon concentration under natural and undisturbed conditions, suitable for resolving small temporal changes provided that the gamma detectors have high detection sensitivity which is essential to distinguish between minor variations in amplitudes and time.

In light of the above, it is possible to summarize in general the important requirements to be taken into account in choosing radon detection systems for long-time monitoring as follows:

- The ability to discern small changes in the intensity of measured signals high resolution capability with high signal to noise ratio
- The ability to discern small changes in the variability of the signals at a high level of time separation, at a measurement rate of at least a few seconds high temporal resolution

- Reliability in measurements over time—a stable measurement capacity for months to years
- Automatic data collection and remote data transmission

The rules listed above rule out the use for long-time radon monitoring of the techniques based on alpha particles detection by nuclear track films or active charcoal, or even radon extraction and grabbing from subsurface soil or rocks into ionization or Lucas cells, since the results are not continuous, the measurement times are too long, and the devices may reach saturation. Radon monitoring ionization chambers and silicon photodiodes-based alpha particle detectors that do not disturbed the local environments, and crystal scintillation-based gamma detectors are the most suitable sensors for passive long-term measurements.

If there is a priority to make measurements deeper than the shallow surface and monitor radon and other natural gases at a depth of tens of meters, it is necessary to adapt the detector to this configuration.

Finally, all studies based on radon monitoring are confronted with identifying the mechanisms that control radon temporal changes produced within the geological subsurface media. The models that were developed are based on the conventional assumptions that concentration and pressure gradients within the air-filled pores within soil porous media are the main guiding-forces for radon flow by diffusion and advection. For this, a time dependent radon transport equation for the air-filled part of the porous media that combines generation, radioactive decay, diffusion, and advection of radon in porous media, was the best model developed so far (Rogers and Nielson, 1991; Van der Spoel et al., 1998).

This radon transport model for the air-filled part of the porous media as formulated by Van der Spoel (1998) is reproduced below:

$$\beta\frac{\partial Ca}{\partial t} = \nabla\cdot(D\nabla Ca) + \frac{k}{\mu}(\nabla p\cdot\nabla Ca) - \beta\lambda Ca + \Phi$$

β is the partition-corrected porosity, Ca is the radon concentrations in the air-phase (Bq/m^3), D is the radon diffusion coefficient in air-filled pores (m^2/s), k is the isotropic air-filled permeability (m^2), μ is the air-filled dynamic viscosity (kg/m^1s^1), p is the air pressure (Pa) λ is the decay constant of radon ($2.1/10^6\ s^1$), $\Phi = \lambda\eta\rho_b C^{Ra}$ is the radon production rate from the immediate parent Ra-226 (Bq/m^3s^1), $\nabla\cdot(D\nabla Ca)$ is the diffusive bulk flux density of radon which is proportional to the bulk radon concentration gradient ∇Ca, $\frac{k}{\mu}(\nabla p\cdot\nabla Ca)$ is the radon advective flux density with velocity u, produced by a local gradient in pressure ∇p (deviation from the aerostatic absolute pressure) calculated from Darcy's law: $\nabla p = -\frac{\mu}{k}u$.

But even though the existing model proved to be quite satisfactory for non-isothermal radon transport, it had one major flaw: physical equations do not include temperature, which is one of the most significant parameters affecting gas thermodynamics.

This work builds the experimental basis for extending the above model in order to include explicitly the connection between the temperature gradient and the radon movement.

The data base of the last dozen years will serve to further model radon variability by eventually determining an additional function F(Ca, ΔT, κ, E_k, T, t) to effectively describe and quantify the radon thermal flux from the surface heated by the Sun, to the subsurface porous rock and vice versa. It will allow to determine the gas flux, its direction and range, as a function of: Ca—the concentration of radon in the porous media airspaces, ΔT—the temperature gradient, κ—the thermal conductivity of the gas, E_k—the transitional kinetic energy of the radon atoms as a function of the temperature T ($E_k = 3/2k_BT$), and t—the time.

The Goals of This Work

In this article we intend to summarize the research and achievements, carried out in 7 phases over the past dozen years, in connection with the following subjects:

The radon and CO_2 temporal periodic variability patterns; Differentiating between the effect of atmospheric temperature and pressure on radon and CO_2 flow through a variety of sub terrains media; Eliminating the climatic-induced periodic contributions in order to identify within the measured time series the portion of the signals that could be associated with the regional geodynamic pre-seismic evolution.

The seven stages of work are described below.

Phase I

Response of subsurface Rn-222 to a 20-ton blast experiment investigated at shallow levels during seismic calibration explosion experiment, simulating a 2.6-M_L earthquake, in order to investigate the influence of the explosive blast and the transitory seismic wave fields on the radon transport in the country rock, adjacent to the focus of the explosion (Zafrir et al., 2009).

Phase II

The analysis of the temporal behavior of radon and environmental parameters measured continuously at the Amram tunnel, near Eilat (Gulf of Aqaba). The analysis of the results over a period of several years shows radon variability at multiple time scales, associated with the air temperature outside the tunnel, specifically the temperature gradient between the external environment and the more stable environment inside the tunnel (Barbosa et al., 2010).

Phase III

Study of the suitability of silicon photodiodes alpha particles detectors, gamma scintillation sensors and ionization chamber detectors, for utilization in long-term radon monitoring in sub terrain geological media. A comparison of the efficiency and sensitivity, the capability to resolve signal to noise, background, stability, and reliability of their long-term measurements was presented (Zafrir et al., 2011).

Phase IV

Long-term high-resolution collection of radon time series carried out in the southern part of Israel. It shows that long-term radon monitoring based on simultaneous alpha and gamma

measurement enables to differentiate between the impact of ambient temperature and pressure on radon transportation within porous media (Zafrir et al., 2013).

Phase V

Concurrent radon measurements by gamma and alpha detection systems in a deep drilling hole served as a proxy for studying radon movement within the shallow and deep subsurface, as well as for analyzing the effect of various environmental and tectonic parameters on the radon transport pattern. The technique enabled measuring, for the first time, the radon vertical velocity in the subsurface geologic media as 25 m/hr, and the recovery of a preseismic radon anomalous signal apparently associated with a regional geodynamic process (Zafrir et al., 2016).

Phase VI

Open deserted drillings and abandoned wells are an interacting interface between the subsurface hydrosphere, lithosphere, and biosphere to the atmosphere above it. The effect of atmospheric conditions, namely atmospheric pressure and temperature, on air, CO_2, and Rn-222 transport across the borehole-ambient atmosphere interface, was investigating inside a 110 m deep by 1 m diameter borehole in northern Israel. The air exchange rate of these features was analyzed and, consequently their contribution as sources for greenhouse gas (GHG) emissions to the atmosphere was quantified (Levintal et al., 2020).

Phase VII

Long-term monitoring method of Rn-222 and CO_2 at a depth of several tens of meters at Sde-Eliezer site, located within one of the Dead Sea Fault Zone (DSFZ) segments in northern Israel, has led to the discovery of the phenomenon that both gases are affected by underground tectonic activity along the DSFZ, possible related to the pre-seismic processes associated with the accumulation and relaxation of lithospheric stress and strain producing earthquakes (Zafrir et al., 2019).

All the technological components used in each of the phases described above included the configuration of a system designed for multi-parametric measurement at a depth of tens of meters, which will be presented in the next section.

EXPERIMENTAL SETTING

Each measurement system installed in the above-mentioned sites included at least two radon gamma detectors and, in some sites, also radon alpha detectors.

Several types of gamma detectors have been adopted: standard (2″ diameter) NaI (Tl) gamma scintillation detectors controlled by total count electronic circuit as single channel analyzer (SCA), from two sources—PM-11 system (of Rotem Industries, Israel) and narrow BGO and NaI (Tl) (1.5″ diameter) scintillation detectors (of Scionix, Holland).

These BGO and NaI detectors were chosen after we ascertained, depending on the rules listed above, that they have high sensitivity, stability and suitability for use in a 2-inch diameter exploration drilling holes to a depth of several dozen meters. We have also re-defined the energy range of the SCA used in the Scionix's gamma detectors to count gamma rays only between 475 and 3,000 keV, cancelling the measurement of gamma radiation in the field of the Compton scattering, between 50 and 475 keV, enabling to improve the ratio of signal to noise by 70% in comparison to the PM-11 detection systems (**Figure 1A**).

The basic principle to choose the SCA for total counting of RDPs gamma rays, is the assumption that radon is the only element within the porous media that can vary in time, under the influence of atmospheric variables or tectonic activity. This fluctuation is observed in addition to the natural gamma radiation from other solid radioactive elements as uranium, thorium and potassium that produce a constant local background (**Figure 1B**). This validates the use of total counting by gamma detection systems equipped with a SCA for monitoring the temporal variation of radon in geological environment. The sensitivity of Scionix's gamma detectors is 0.01–0.02 Bq/m^3 per 1 count/1 hr (see Zafrir et al., 2011, based on the comparative test with a calibrated AlphaGUARD detection system, of Saphymo GmbH, Germany).

For radon detection by alpha sensing, the Barasol, BT45 N (Algade Inc., France) is a suitable instrument since it was designed to be used in difficult environments and the calibration of the sensor enables to calculate the volume activity of the Rn-222 in the measured airspace, under undisturbed natural condition. The sensor is an implanted silicon detector with a 400 mm^2 of sensitive area. It enables the counting of Rn-222 and its daughter alpha products by spectrometry of the alpha particles (with energy between 1.5 and 6 MeV) created in the sensing volume. The sensitivity is about 50 Bq/m^3 per 1 pulse/1 hr.

For CO_2 monitoring, the detectors that were lowered down for measurements at depth, were the GMD-20 and GMP-252 infrared gas analyzers of Vaisala, Finland, with measurement ranges of 0–2,000, 0–3,000, and 0–10,000 ppm according to the borehole depth. CO_2 sensor accuracy varied between ±40 ppm with a drift of ±60 ppm/year for the lower range, to ±2% and drift of ±150 ppm/year, for the 0–10,000 ppm range.

The meteorological variables are measured at each site and with the same high time resolution, as well as complementary parameters such as temperature and relative humidity at depth.

THE RESULTS AND THE ACHIEVEMENTS OF THE CONSECUTIVE STUDIES

Overview

In Israel, the first radon electronic stations were installed in 1995, in the northwestern sector of the Dead Sea. The measurements, with high temporal resolution of 15 min and with adequate sensitivity, showed the presence of a high and temporally fluctuating radon flux in gravel and water (Vulkan et al., 1995).

A research activity based on cooperation between physicists, geophysics, and geologists has begun in Israel, in 2001, aiming to integrate multi-disciplinary scientific methods in Earth sciences

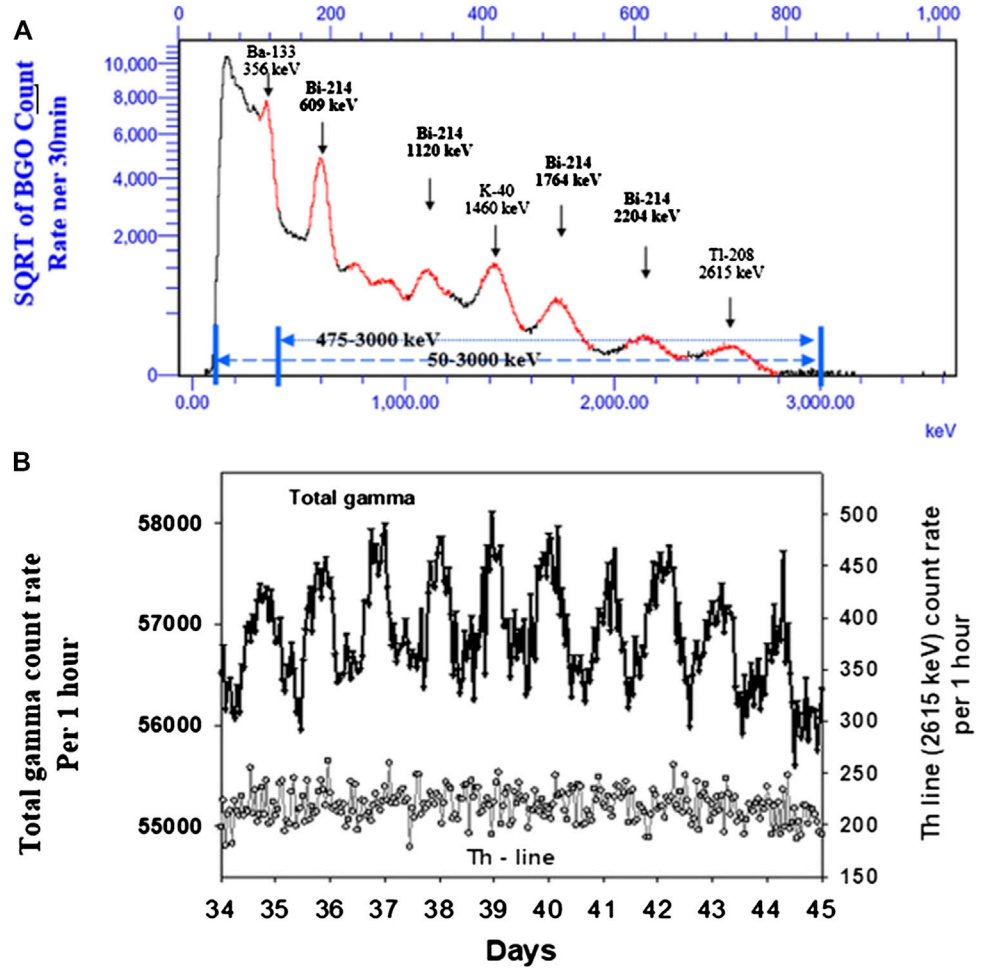


FIGURE 1 | (A) The Gamma spectra of Uranium, Thorium, and Potassium, measured using a 3″ × 3″ NaI scintillator. It displays the Bi-214 energy (RDP) lines of 609, 1,120, 1,764, and 2,204 keV in the gamma-ray spectra from magmatic rocks. The spectrum includes also energy lines of U-238 and Th-232 decay products and the isotope K-40. The Ba-133 line is due to an artificial source added for the stabilization of the electronic amplification of the MCA (Multi Channel Analyzer). **(B)** A 10-days measurement exhibiting the total daily gamma variations due to the RDPs, while the gamma level of the thorium decay products within the rock is stable. This demonstrates the use of total gamma measurement to track temporal variations of radon in a soil or country rock media.

in order to promote the understanding of the processes of earthquake formation and to allow their early prediction (Zafrir et al., 2003).

In the last dozen years, about seven combined and diversified studies have been conducted investigating the impact of temperature, pressure, tectonic and other constrains on radon and CO_2 flow within the subsurface geological media, and they are presented in the following sections.

Phase I: Response of Subsurface Rn-222 to a 20-Ton Seismic Calibration Experiment

An underground 20-ton explosion for the purpose of performing spatial calibration of a seismic systems array in Israel (Gitterman et al., 2005) was utilized to investigate its effect on the radon movement in the shallow geological media, very close to the focal point of the explosion. A network of five radon detectors was set-up, with the radon sensors installed a few meters apart along 150 m from the center of the explosion. All the detectors were lowered to a depth of 2 m, protected by a metal pipe and suitable cushioning (**Figures 2A,B**).

Measurements were initiated 4 days before the explosion and carried on for 9 days after the calibration blast with 15 min integration time (**Figure 2C**). A higher sampling rate of 10 s was inserted in use for few hours before and after the explosion (**Figure 2D**).

Although it was possible to assume that in the center of the explosion there might be local changes in the radon concentration due to the crushing of the surrounding bedrock, there was no significant change in the radon content along the measuring line of 150 m for the duration of the expansion of the blast wave along this distance, of about 200–400 milliseconds, under acceleration of 1,700 cm/s^2 (Zafrir et al., 2009).

The calculations showed that in this short period of less than half a second, even under a stronger explosion that would create an earthquake simulation even more powerful than the measured

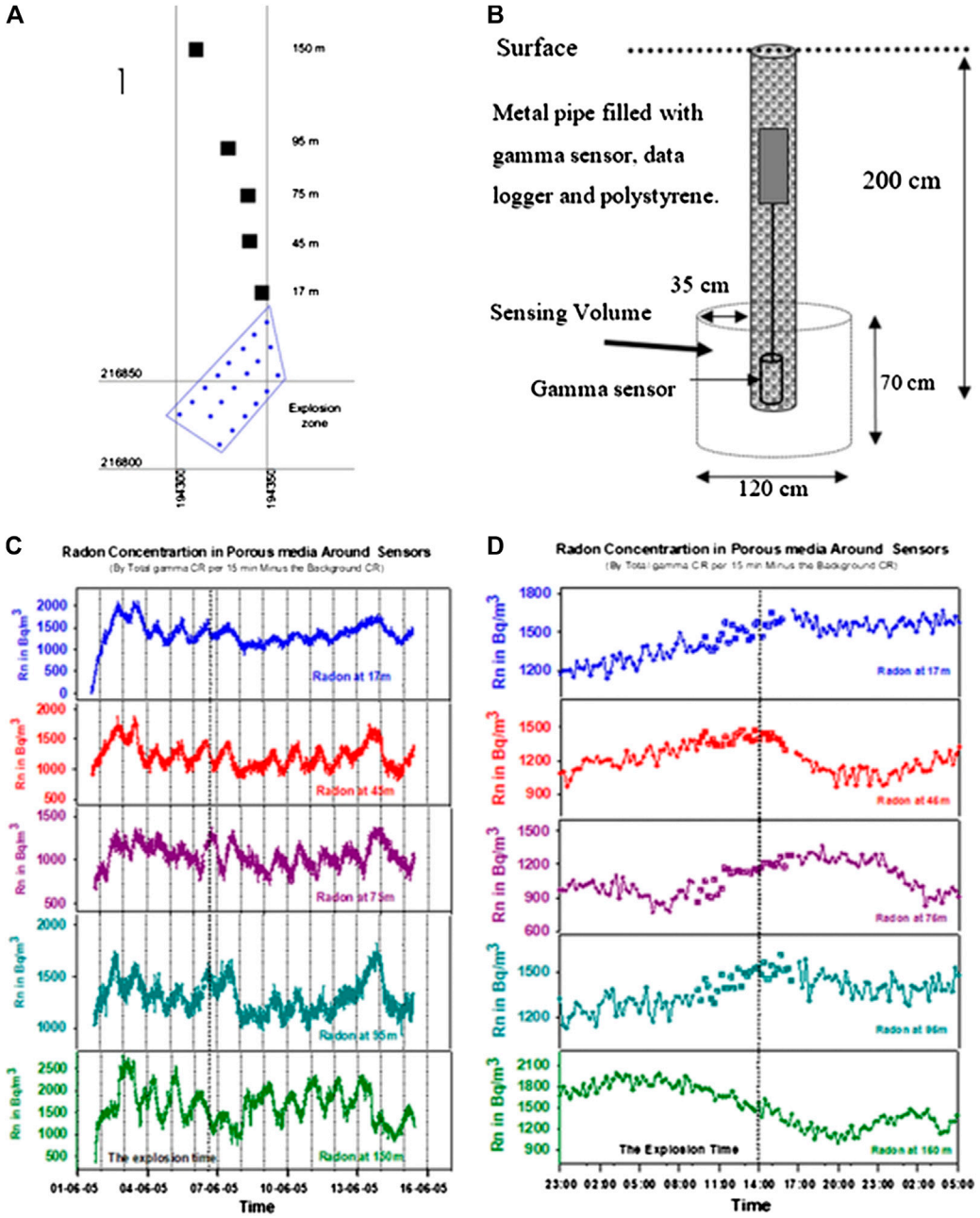


FIGURE 2 | (A) Map (Israel grid) showing relation of radon measurement sites relative to 20-ton explosion zone. **(B)** Radon monitoring was performed at a depth of about 2 m and a "Sensing Volume" of about 0.65 m^3. **(C)** Overview of 15-min resolution time series of five gamma detector systems during the 13-days experiment. It presents the variations in radon concentration in the porous media in Bq/m^3 around sensors (By total gamma counting rate per 15 min minus the background counting rate). The time of the explosion is marked with a vertical line. All sensors show build-up of Radon in the porous media within the "Sensing Volume", and typical daily variations. **(D)** Radon concentration measured 15 h before and after the explosion, including the high resolution 10-s data averaged to 15 min (in squares). Explosion time is indicated.

M = 2.6, the radon could not respond and move more than 10 cm. Therefore, no changes were measured in the radon concentration at each of the five detectors.

The original article from 2009 includes a calculation showing that around the gamma detector which was close to 17 m from an explosion of 20 tons of explosive material, developed a huge pressure of about 5 atm that could move radon up to 0.3 m per s. [In comparison to pressure gradient-controlled variations between 10–100 Pa that were sufficient to constrain advective movement within a sand column—Van der Spoel (1998)]. However, the transition time in the explosion that was used for simulating earthquakes with magnitude of 2.6, was 0.25 s.

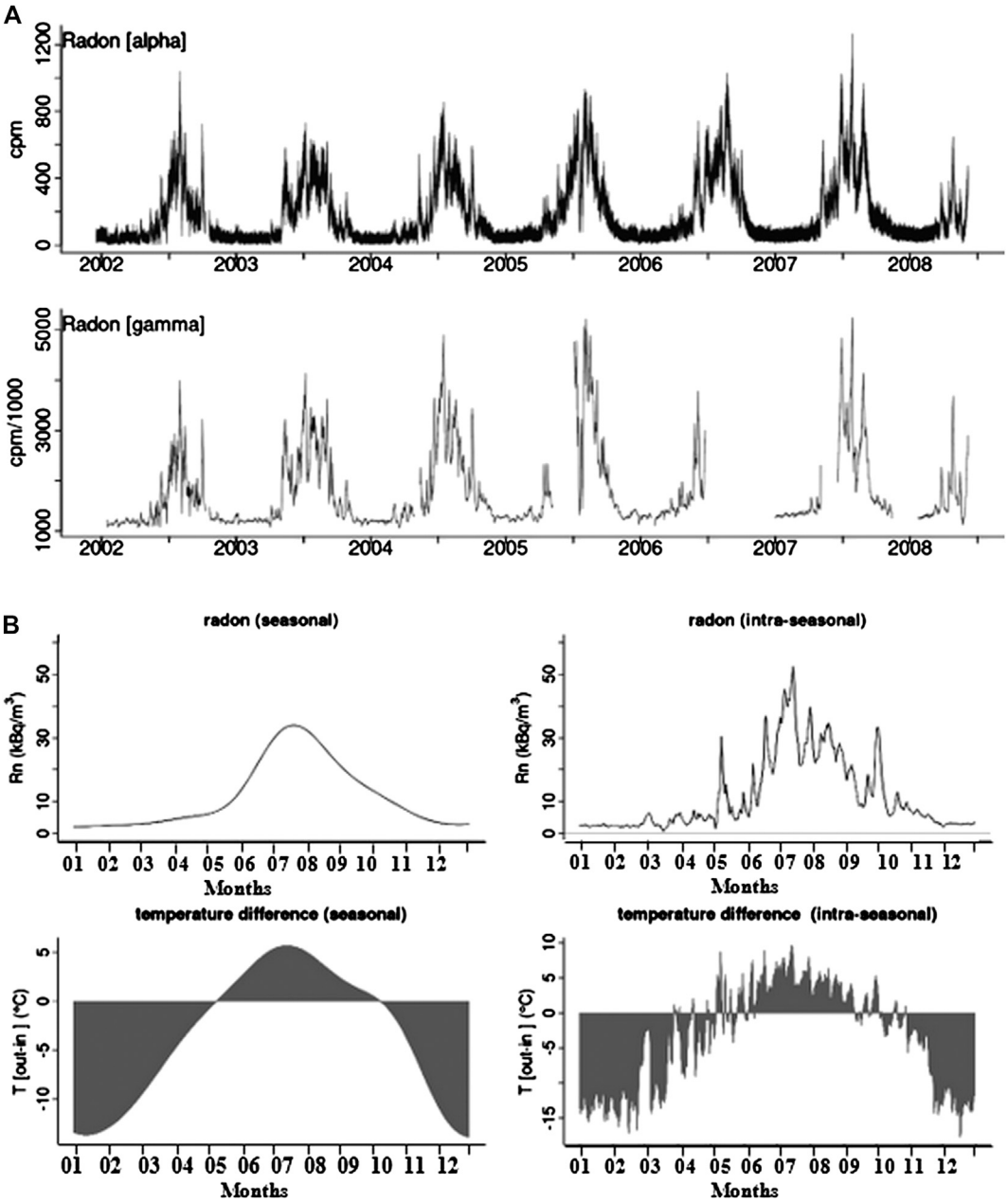


FIGURE 3 | Time-series of measurements at the Amram tunnel (15-min temporal resolution), from top to bottom panels: **(A)** Radon by gamma, and radon by alpha) during 6 years. **(B) (left)** The similarity between the two seasonal patterns becomes evident when considering the difference between the external temperature and the constant temperature inside the tunnel (temperature gradient). **(B) (right)** The intra-seasonal variability is also associated with changes in the temperature gradient between the inner part of the tunnel and the outside environment.

Therefore, the time for the pressure impact on the radon gas, even if the EQ energy would be large in some order of magnitude (M = 4.5), would still be too short to move the radon gas more than a few meters away.

Hence it is possible to conclude from this experiment that the effect in the subsurface radon concentration of a sudden pressure increase associated with an occurring earthquake is very reduced, as a result of the very short distance that radon is able to move in such a short time. This does not contradict the possibility of subsurface radon being affected by a pre-seismic event, as the pressure build-up associated with earthquake preparation processes typically develops over much longer time scales, enabling radon movement over larger distances.

Phase II: The Analysis of the Long-Term Temporal Variability of Radon in Research Tunnel

Continuous radon monitoring using co-located alpha and gamma detectors was performed over a period of more than 10 years at the 170 m research tunnel in Mt. Amram. Radon was measured under stable conditions more than 100 m from the tunnel's entrance and below a rock burden of about 100 m (see **Figure 4**, "Phase III: A Comparative Assessment of Radon Sensing Systems for Long–Term Monitoring in Sub Terrain Geological Media" section, **Figure 5**, and "Phase IV: Impact of Atmospheric Aspects on Radon Transportation Within Porous Media" section). This research tunnel in the Arava valley, which is part of the Negev desert, is particularly suitable for the investigation of the factors inducing radon variability, as some of the effects known to influence radon mobility, such as rainfall and soil moisture, are negligible in such a dry (<20 mm/year) environment. The natural environmental conditions in the tunnel are constant, specifically indoor humidity and temperature are kept stable throughout the year. In addition to the radon and environmental parameters which were measured inside the tunnel, air temperature and barometric pressure were also measured outside the tunnel.

The time series resulting from the continuous radon monitoring by both alpha and gamma systems display corresponding temporal variations (**Figure 3A**). Thus, the simultaneous use of alpha and gamma monitoring systems demonstrated that the detailed signals visible in both time series are genuine signals reflecting radon variability, as they are obtained from different detection systems based on distinct measurement principles.

The temporal variability is characterized by a clear seasonal pattern, with maximum values in summer. As expected, the temperature and atmospheric pressure measured outside the tunnel also exhibit a clear seasonal pattern, in contrast the temperature measured inside the tunnel, at a distance of 140 m from the tunnel's entrance, which is very stable along the year with a value of 28 ± 0.3°C. The humidity is also fairly constant and close to 90%.

The temporal variability displayed by the time series of radon and environmental parameters covers multiple time scales, from less than 1 h to years. The decomposition of the time series using the maximal overlap discrete wavelet transform (Percival, 2008) allows to extract the dominant modes of variability and to isolate seasonal, intra-seasonal, and diurnal time scales. The results show that at all the time scales temperature is the main factor responsible for the observed temporal patterns (Barbosa et al., 2010).

At the seasonal scale the variability of radon and temperature is very similar, with both variables displaying a maximum in summer; however, a detailed analysis shows that the temperature outside the tunnel increases since mid-January, while radon concentrations remain low, only increasing slightly in mid-March and then faster by mid-May. However, the similarity between the two seasonal patterns becomes evident when analyzing in detail the difference between the temperature outside the tunnel and the constant temperature inside the tunnel (hereafter noted as temperature gradient), as displayed in **Figure 3B**, left).

The temporal variability of the temperature gradient also drives intra-seasonal variability. radon anomalies spanning multiple days are only observed when the temperature gradient is positive. This dependence of radon on the temperature gradient is non-linear, as the amplitude of the radon anomaly is not directly related to the amplitude of the temperature gradient, but dependent on the sign of the temperature gradient (**Figure 3B**, right).

As for the case of seasonal and intra-seasonal variability, the daily variations are closely related to the temperature gradient between the internal part of the tunnel and the exterior. Daily variations are absent in the winter, corresponding to a negative temperature gradient. When the external temperature rises and becomes higher than the temperature in the inner part of the tunnel, the radon time series display daily cycles with maximum at night.

Temperature influences natural ventilation as well as radon transport within the porous media. Thus, the mechanisms through which temperature can influence radon variability include temperature-driven air ventilation, through the air medium, and temperature-driven radon migration by thermal gradient dependent function—in the porous media (Nield and Bejam, 2006; Zafrir et al., 2007; Zafrir et al., 2008).

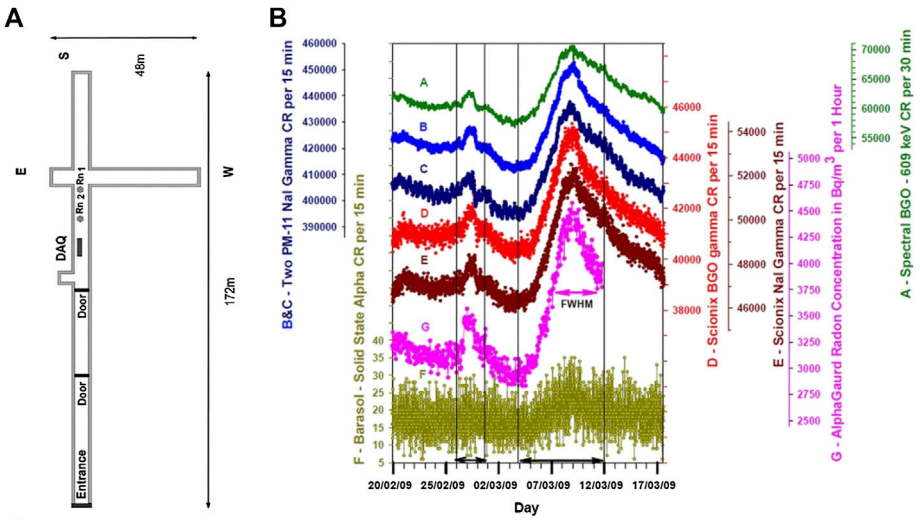
Phase III: A Comparative Assessment of Radon Sensing Systems for Long-Term Monitoring in Sub Terrain Geological Media

A comparative study between alpha particles radon detectors based on silicon photodiode or passive ionization cells, and gamma-rays radon detectors based on scintillation materials, were performed in order to determine their suitability for long-term monitoring in terms of sensitivity, resolution in the parameters of signals intensity and time, as well as long-term operating reliability (Zafrir et al., 2011).

The test system was installed in the research tunnel at Mt. Amram near Eilat, within a closed room at a depth of 140 m (Rn1 and Rn2 in **Figure 4A**). The constant internal temperature of 28 ± 0.3°C in the tunnel's rooms have enabled the comparison of the various radon detectors under the same environmental conditions. The setup included: Five gamma-ray systems with different dimensions (noted **A–E**, Rotem, Israel, and Scionix, Holland), one silicon photodiode alpha detector (noted **F**, Algade, France) and one calibrated ionization chamber (noted **G**, Saphymo, Germany). All the detectors were exposed over several days to the same natural radioactivity levels under undisturbed thermodynamic equilibrium between the air space and the tunnel walls, recording count rates with high time resolution of every 15 or 30 min (**Figure 4B**).

A conversion scale that enable to evaluate the counting rate (CR) per 15 or 30 min of the various detectors sensors (**A–F**) at peaks in Bq/m^3, is included in **Figure 4** (**Figure 4C**).

The main result was that gamma detectors have a high sensitivity between 2 and 4 times in relation to the alpha detectors, enabling the detection of low sub-diurnal radon fluctuations.



C

Detection system	Spectral BGO Gross Counts in 609 keV line /30min (A)	PM-11 (experiment) Counts/15min (B)	PM-11 Tunnel Counts/15min (C)	Scionix BGO Counts/15min (D)	Scionix NaI Counts/15min (E)	Barasol counts/15min (F)	AlphaGuard Bq/m³ (G)
Net counting rate of a signal peak equivalent to 1 Bq/m³	7.3	24.2	25	3	3.8	0.018	1

FIGURE 4 | (A) Radon setup in the Amram tunnel. **(B)** Variations of radon from 20 February to March 18, 2009, as measured simultaneously by seven different radon sensors. *The **AlphaGUARD** system* **(G)**, which stopped measuring on March 12, presents the radon concentration in Bq/m^3 per 60 min measurement cycle time, while the rest present the CR (Counting Rate) per 30 min **(A)**, or per 15 min **(B–F)**. Two radon anomalies occurred: a small (in amplitude) and short (in time) one for almost two days from 26 to 28 February and a predominant one from 4 to March 18, 2009. **(C)** a conversion scale that enable to evaluate the counting rate, CR, per 15 or 30 min of the various detectors sensors **(A–F)** ***at peaks*** in Bq/m^3.

In relation to the alpha detector, it was found that the statistical error during the measurements was higher than 20%, because of the low sensitivity (see **Figure 4B**), even in sampling intervals of 30 min [0.022 counts per 1 h for 1 Bq/m^3 by the Barasol (**F**)]. Therefore, in order to identify variations with a required statistical accuracy of at least 5% (which can be obtained easily with each one of the gamma detectors), it is necessary to take measurements with this alpha detector in time periods of at least 8 h or even more.

There is another advantage of using a gamma detector for the measurement of radon temporal fluctuations within the geologic environment: gamma detectors do not violate environmental thermodynamic conditions or the radon secular equilibrium, as happens when grabbing or pumping radon samples. Therefore, the gamma detectors have the highest priority regarding the alternative detectors that were examined in this work. Furthermore, even mechanically it is also harder to handle and lower ionization chambers to typical depths of narrow exploration boreholes.

Phase IV: Impact of Atmospheric Aspects on Radon Transportation Within Porous Media

Long-term high-resolution Rn-222 time series, were collected in the subsurface of the southern area of Israel, at the Mt. Amram research tunnel near Eilat and in shallow and deep drillings at Gevanim site in Makhtesh Ramon (Steinitz and Piatibratova, 2009; Zafrir et al., 2013).

In general, if the radon measurements are performed at a tightly closed site, as in the Amram tunnel, the radon within the air space will be in undisturbed environmental conditions and will reach temporal thermodynamic equilibrium with the radon in the bedrocks as well as secular equilibrium with its RDPs, as encountered in the previous "Phase III: A Comparative Assessment of Radon Sensing Systems for Long-Term Monitoring in Sub Terrain Geological Media" section, **Figure 4**.

Then, the radon time series in the tunnel, exhibit daily and seasonal radon levels varying periodically and depending on the climatic temperature gradient outside the rock surface, 100 m above the horizontal tunnel (**Figures 3B, 5B, 6A,B**). The Fourier amplitude spectrum of temperature and of the "summer Radon" is greatly similar (**Figures 6C,E**), and the radon diurnal periodical variations are canceled during the winter (**Figure 6F**).

Hence, the tunnel measurement system reveals a radon signal that pushed down via the country rock porous media, by the daily heating of the surface at a height of 100 m above the tunnel. The heating engine is the gradient temperature ΔT_a (down) pointing downward (**Figure 5B**). In a delay of about 10 h after the maximum exterior heating, the radon signal reaches the tunnel (**Figure 6B**). Ten hours is the time it takes for the gas to flow from the surface to the tunnel. When the surface heating is fading with the external temperature, the size of the temperature gradient ΔT_a is reset and its direction turned upward ΔT_a (up). Then also the radon daily signal fades over time.

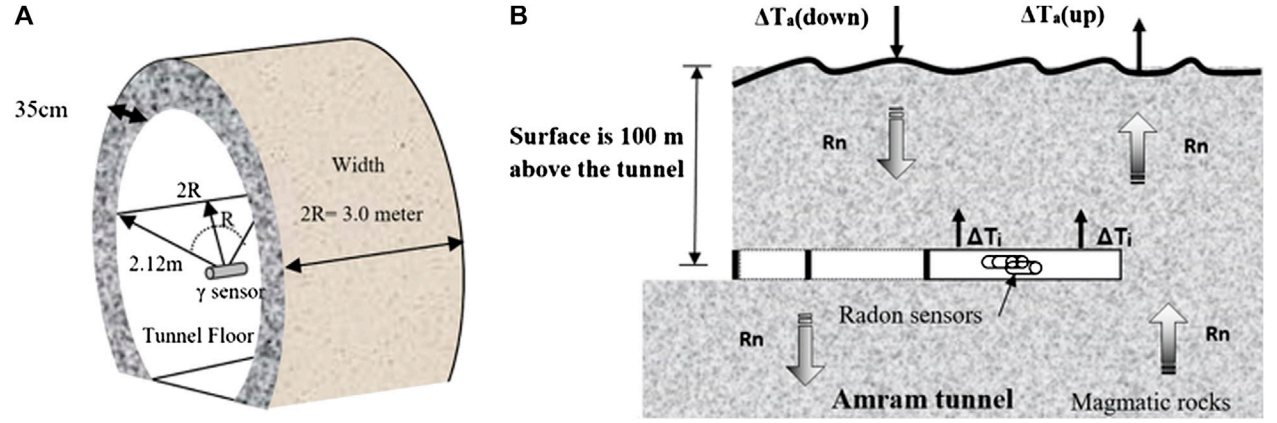


Figure 5 | The Amram tunnel cross-section **(A)** and scheme **(B)**.

In winter, when the temperature inside the tunnel is stable and higher than the surface temperature, the interior temperature gradient ΔT_i is always directed toward the surrounding rock, and inhibits the radon daily flow into the tunnel space (**Figures 3B, 5B**, **6A**).

The temperature gradient is the only geophysical driver available to force the radon via the air-filled space of the surrounding bedrock, as it will be demonstrated also in the next phase ("Phase V: Differentiating Between Radon Anomalies Produced by Climatic Constituent and Pre Seismic Tectonic Activity" section). The alternative mechanism, pressure gradient on the surface, is too weak to compel radon to move along the pore's media within the bedrock to 100 m depth.

In contrast, the radon concentration in open boreholes in Makhtesh Ramon, as measured in the boreholes air space by the alpha particle's detectors at 1.2 and 85 m depth, suggests an association with the diurnal (24 h) and semidiurnal (12 h) periodic components and even with multiday barometric pressure variations (**Figure 7B**). The FFT spectra of the radon signals exhibits a similar component which is different from the temperature periodicity (**Figures 7C, 6E**).

The appearance of double daily signals like the one circled in drawing 7b is analogous to the pressure's half-day cycle S2 and S1 (**Figure 7C**) as presented by Dai and Wang (1999). Those peaks appear locally at 8–10 a.m. and 12–2 night (Steinitz and Piatibratova, 2009), and they demonstrate the connection within the open drilling between the barometric pressure and the radon movement in the inner space (see also "Phase VI: CO_2 and Rn–222 Emissions From an Abandoned Water Well Under the Influence of Climatic Pressure and Temperature" section and "Phase VII: Radon and CO_2 Monitoring Technique in Deep Subsurface, as a Proxy for Investigating Tectonic Pre–seismic Activity" section).

Accordingly, when the semi-daily pressure reaches the minimum (negative pressure in **Figure 7B**, bottom), the radon can flow into the drilling air space in order to achieve equilibrium. On the other side, when the semi-daily increase in pressure occurs (positive pressure gradient) it prevents the migration of radon from the country rock into the borehole air space. This mechanism was demonstrated by Van der Spoel (1998), showing that even pressure gradient controlled variations between 10 and 100 Pa were sufficient to constrain advective movement within a sand column.

At the multiday scale, the barometric pressure variations produce a long multi-day radon signals at a borehole depth of 85 m, with the same time span as in the shallow depth of 1.2 m (**Figure 7B**, top). But the radon daily and half a day periodicity that was observed at 1.2 m air space is concealed at the depth of 85 m most of the time except for few days when the pressure varies around 950 mbar level.

The understandings and knowledge that came out of this study, about utilizing in parallel two different types of radon measurement methods in closed and open-air spaces, led to the idea to operate these combined methods of radon measurement within deep abandoned boreholes as a proxy for underground geodynamic research.

Phase V: Differentiating Between Radon Anomalies Produced by Climatic Constituent and Pre Seismic Tectonic Activity

The combination of long-term, radon measurement by gamma and alpha methods within deep abandoned boreholes enabled to distinguish between radon anomalous signals at depth induced by the periodical climatic parameters (temperature and barometric pressure), and those that may be driven by deep tectonic processes along active seismic faults. The concurrent identification of radon signals in various depths with 50 m between them, allowed for the first time to calculate the radon vertical velocity in the bedrock under the influence of the temperature gradient on the surface. It also revealed a radon anomaly that apparently occurred ahead of a tectonic event, the Nuweiba earthquake, which occurred within the Dead Sea Fault Zone on June 27, 2015, with magnitude of M = 5.5 (Zafrir et al., 2016).

The first deep dedicated combined radon monitoring system was installed in January 2015 at an abandoned water well (110 m

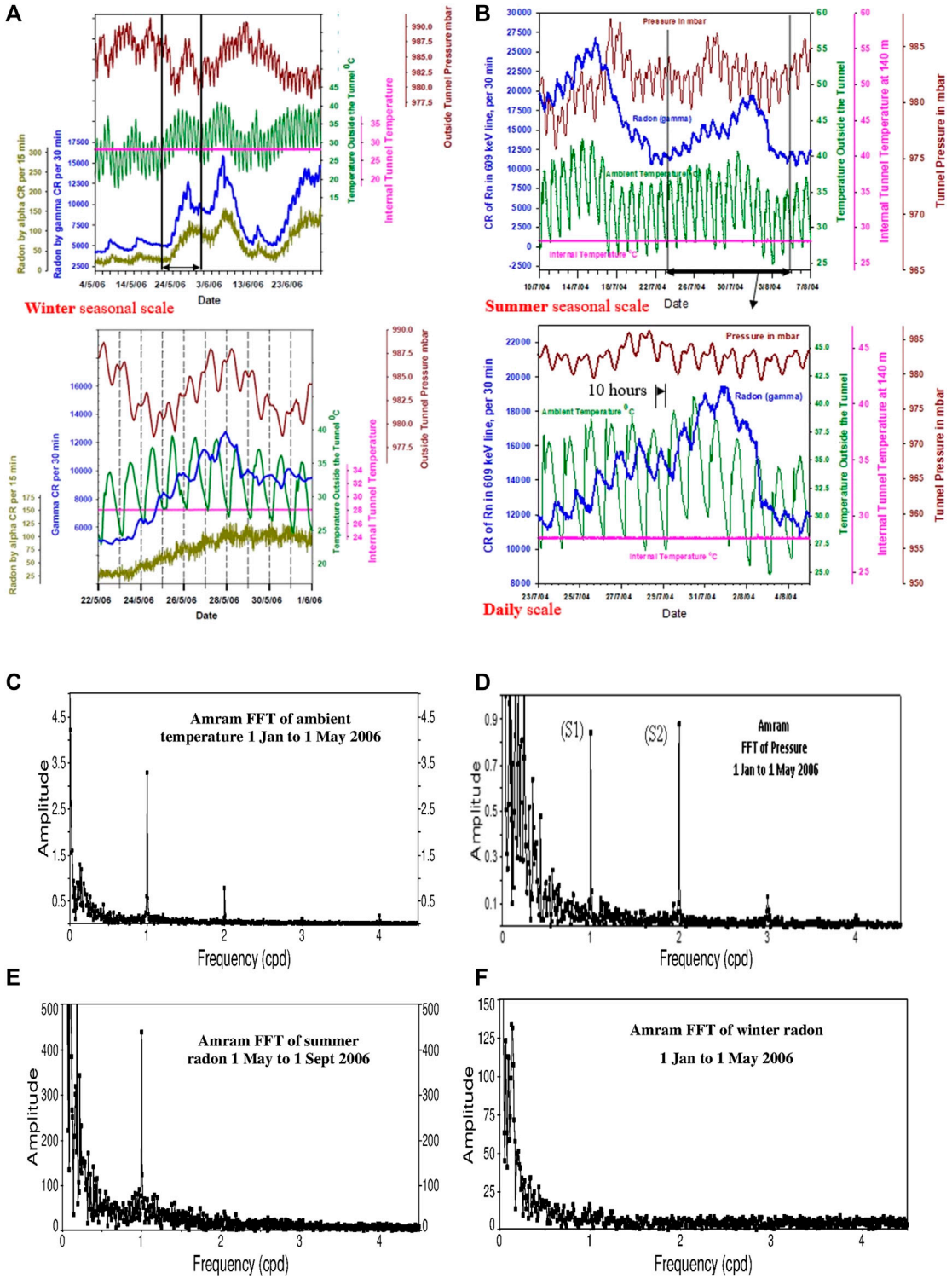


FIGURE 6 | (A) During spring, **only** when the external temperature (**green**) is higher than the tunnel internal temperature (**violet**) the radon diurnal variations wake up (see the winter situation without daily signals at all, in panel **(E)**, while the multi-day and seasonal variations are not affected. **(B)** During summer radon levels within the tunnel (**blue**) consistently follow the summer seasonal and diurnal ambient temperature variations **with a daily delay of about 10 h. (C)** The ambient temperature and the summer radon FFT amplitude spectrum **(D)** display a clear diurnal cycle. **(E)** The Amram radon FFT winter amplitude highlighting the disappearance of the radon diurnal variations in the winter when the tunnel stable internal temperature of 28 ± 0.3°C is higher than the outside temperature. In this figure, 7.3 counts per 30 min of the gamma sensors, are equivalent to concentration of 1 Bq/m^3 within the surrounding country rock, and 0.018 counts per 15 min of the alpha particle detector is equivalent also to 1 Bq/m^3.

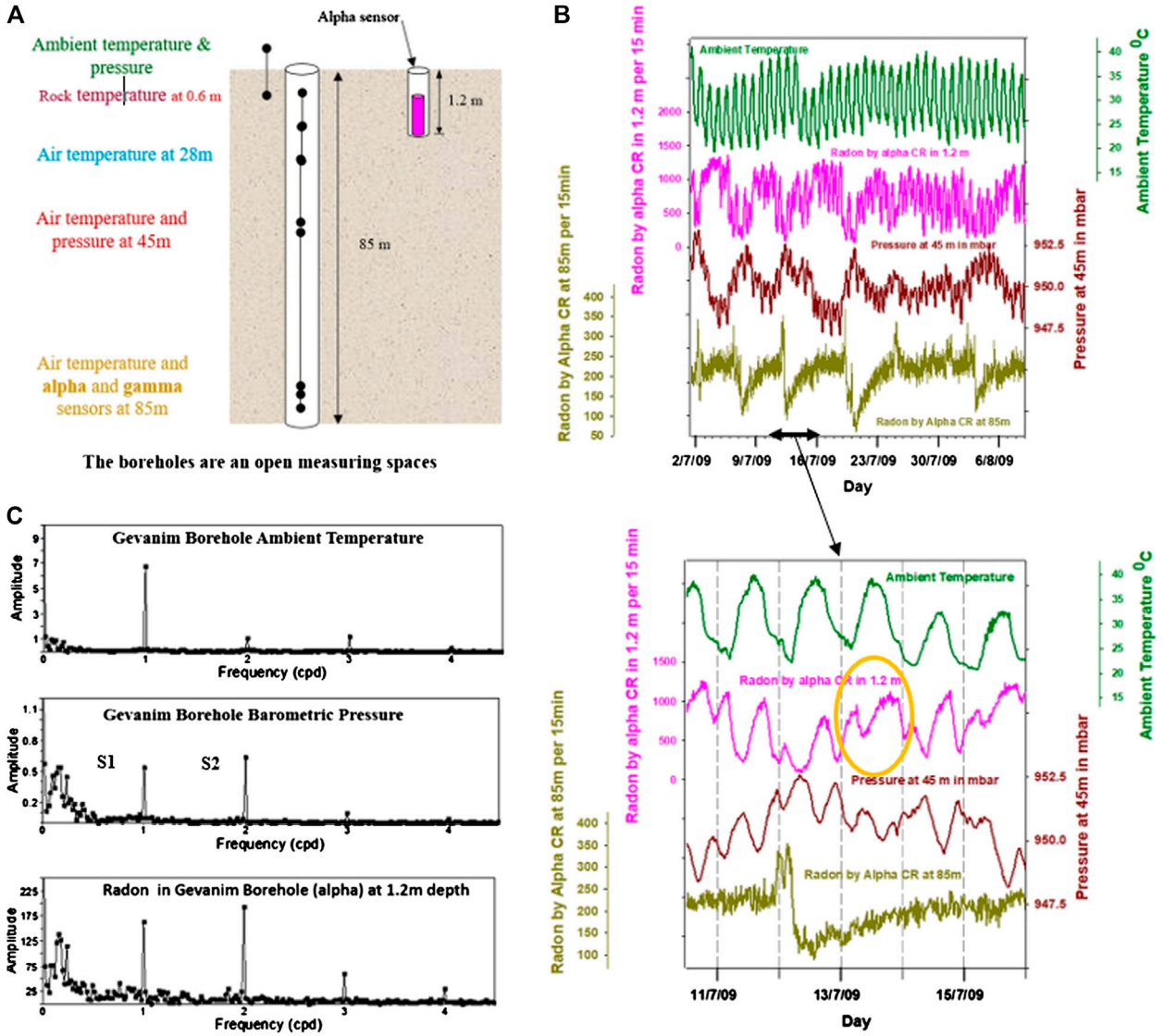


FIGURE 7 | (A) The radon setup in Makhtesh Ramon at Gevanim valley including alpha detectors at 1.2 and 85 m. **(B)** Radon time series as measured by alpha detectors in the boreholes air space near the surface at 1.2 m depth and at depth of 85 m. **(C)** The FFT amplitude spectrum of the ambient pressure and radon temporal concentration changes at the Gevanim Valley, as measured by alpha counting at 1.2 m depth.

depth and about 1 m diameter) at the Sde Eliezer site, which is located within the Hula Valley western border fault (**Figure 8A**).

Lowering simultaneously gamma and alpha radon detectors to different depths within the deep borehole (**Figure 8B**) and monitoring their temporal variations, enabled to differentiate in the radon time series signals, between the daily periodical influence of the ambient temperature (stars in **Figure 9A**) and the semi-daily effects of the barometric pressure (arrows in **Figure 9A**).

The gamma detectors at 10 and 60 m depth at Sde-Eliezer site (**Figures 8B, 9A,B**) are narrow BGO detectors, presented in "Experimental Setting" section and "Phase III: A Comparative Assessment of Radon Sensing Systems for Long–Term Monitoring in Sub Terrain Geological Media" section. These detectors measure contributions from a source volume of 1.5 m^3 of surrounding bed rock (**Figure 8B**).

According to **Figure 9A** the maximum signal in the raw data for the BGO gamma sensor at the depth of 60 m (for example, in blue in 27/4/15), is about 53,000 counts per 15 min minus the background of 4,000 counts per 15 min. It is thus equal to a net rate of 49,000 counts per 15 min, which is equivalent to 16,333 Bq/m^3 according to the above calibration scale (Figure 4c). This peak is reached, with a delay of about 2 h from the peak of the radon in the borehole airspace, as measured by the alpha sensor at 40 m (see **Figure 9C**). This radon peak of 125 counts per 15 min, with a background of five counts, corresponds, according to the stated calibration scale (Barasol sensor) to 120/0.018 = 6,666 Bq/m^3. This fact proves that the concentration of the radon within the sealed iron casing airspace (see **Figure 8B**) corresponds to less than 40% of the radon content that is measured by the gamma detector.

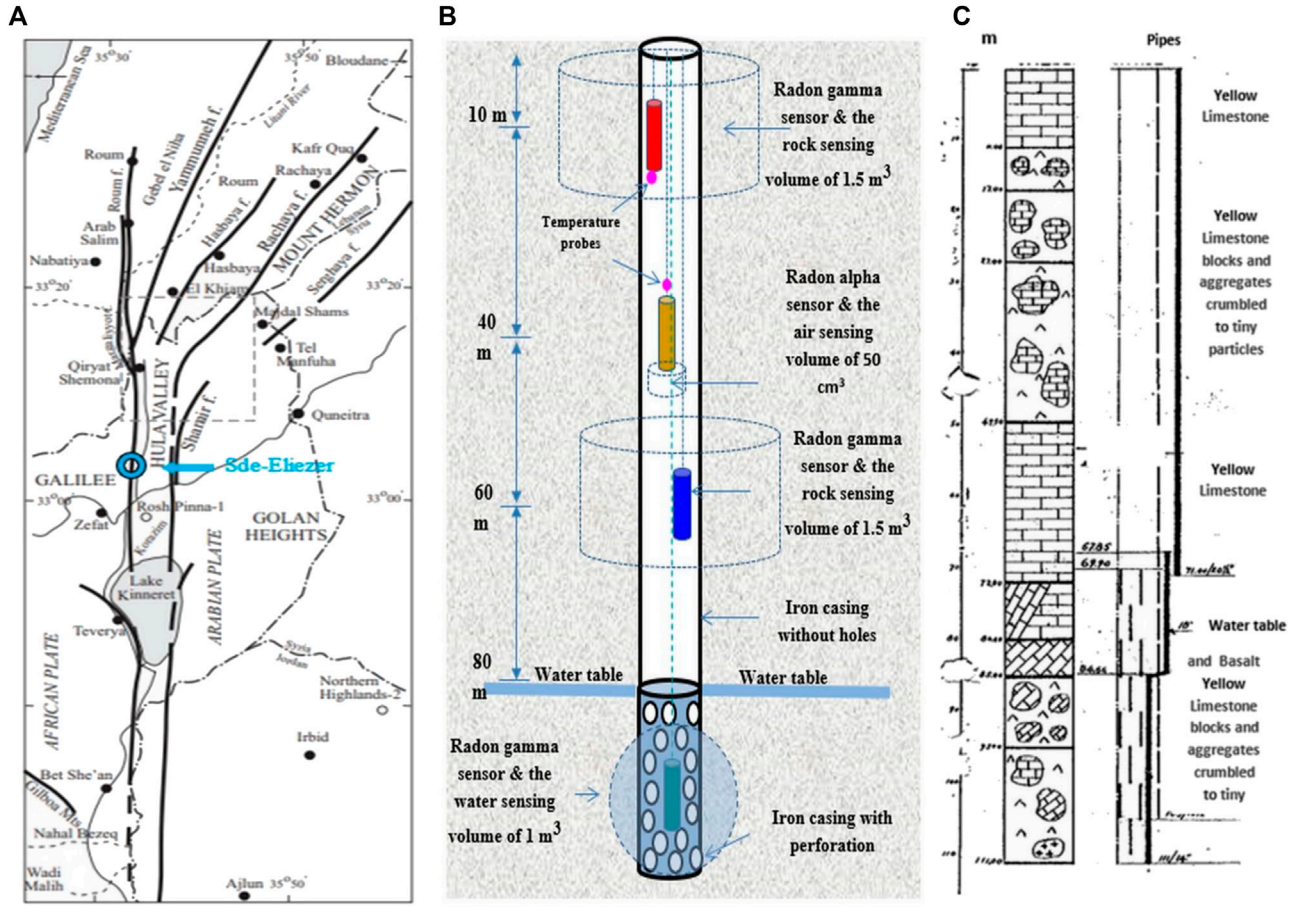


FIGURE 8 | (A) Sde Eliezer site in the Hula basin western border fault—HWBF, and map of the main segments of the Dead Sea Fault Zone (DSFZ) in northern Israel (Weinberger et al., 2009). **(B)** The radon monitoring setup. **(C)** The geological column section.

Thus more than half of the gamma counts result from the contribution of the radon in the surrounding bedrock in the form of a background from the radon that remains stuck within the rock grains, and a variable part from the radon able to move within the rock porous media, mainly driven by the influence of the Sun heating on the surface creating a temperature gradient ("Phase II: The Analysis of the Long-Term Temporal variability of Radon in Research Tunnel" section, and "Phase IV: Impact of Atmospheric Aspects on Radon Transportation Within Porous Media" section). The background portion is a further proof that this contribution originates from outside the iron pipe, as it does not decrease to near zero as the radon signal within the casing airspace does under the effect of the positive barometric pressure gradient (**Figures 9B,C**).

The semi-daily cycle measured by the gamma and alpha detectors (**Figure 9A**) results from the radon which is pumped from the water into the well airspace by the barometric extraction (minima) at early morning, as measured by the alpha detector at 40 m. The secondary peak of the three radon signals appear at around the same hour, 4 a.m. (**Figure 9C**). The contribution from the mobile radon within the surrounding bedrock to the radiation measured by the gamma detectors is very low at that time.

In addition, the pronounced time delays between the radon peeks measured by the three sensors (**Figure 9C**), prove that if all the radon variations would happen in the same borehole airspace then we would have to look for fast streaming from the middle (the first peak at 40 m) upward to 10 m and then back downwards to reach the 60 m level 2 h later. It seems very unlikely as there is a single direction of CO_2 streaming, from 70 m level to 40, 20, and 5 m, and vice versa, as described in "Phase VI: CO_2 and Rn-222 Emissions From an Abandoned Water Well Under the Influence of Climatic Pressure and Temperature" section and in **Figures 10B,D**, with a faster air velocity between 2 and 6 m/min (120–360 m/h).

Now, considering the radon temporal variation in the bedrock around the pipe. From 10 m downward, we would find after about 2 h a similar concentration peak of about several thousand Bq/m^3 at a depth of 60 m, high above the radon concentration within the borehole airspace that reduced at that moment to at least half level (**Figure 9C**). The temperature-driven downward movement of radon outside the sealed casing, brings radon into the saturation zone at 80 m. Since the borehole casing is not perforated down to the water table, radon can only enter the casing from the groundwater. Considering that Ra-226 was not found in the

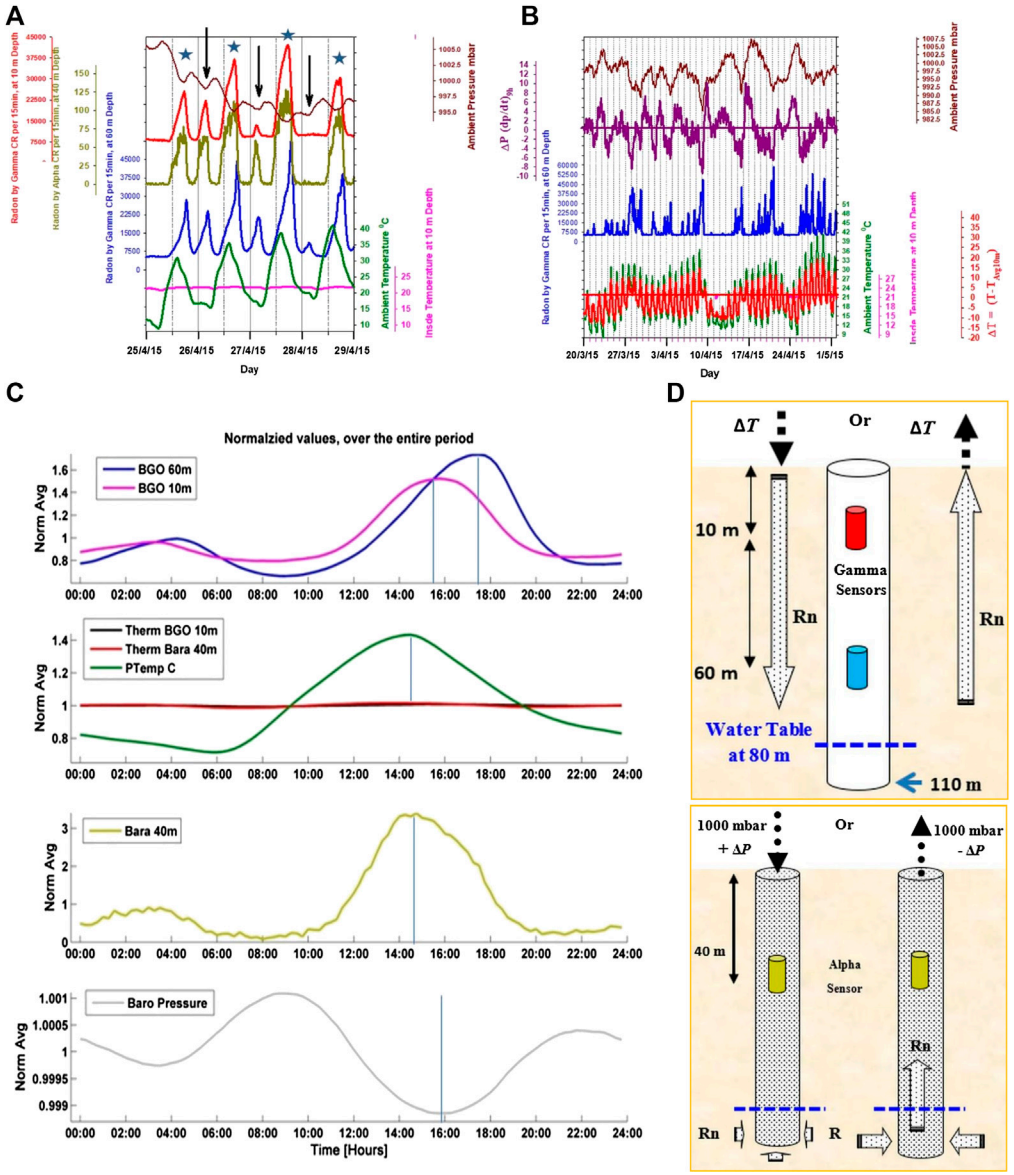


FIGURE 9 | (A) Example of time interval of 4 days in which the radon at different depths consistently follows the daily temperature profile with a variable lag between each other. The dotted lines in the figure mark daily noon and the full lines the midnight. Radon early morning semi-diurnal signals are exhibited by the three radon detectors with anti-correlations to the pressure (see arrows) in addition to their response to the daily temperature periodicity after noon (see stars). The parameters are: **ambient barometric pressure,** radon by gamma detectors (at **10** and **60 m**), radon by alpha detector (**at 40 m**), ambient **temperature** and internal temperature (**at 10 m**). **(B)** The radon time series at **60 m depth** in relation to the gradients of the climatic parameters: pressure (**ΔP, dark purple**) and temperature (**ΔT, red**). **(C)** The daily normalized values of each parameter's (**maximum** for radon **at 10** and **60 m**, **ambient temperature**, **radon at 40 m** and **minimum for barometric pressure**) summarized for a period of 150 days: 16 January to June 14, 2015. **(D)** The basic principles for the behavior of radon movement under the climatic influence. Radon in a rock media (as measured by gamma detector) is driven by the surface temperature gradient **ΔT**. Radon in the open borehole air space (as measured by alpha detector) is driven by the pressure variation **ΔP** (Zafrir et al., 2013). In this figure, three counts per 15 min of the **gamma sensors peaks** at 10, and 60, are equivalent to concentration of 1 Bq/m^3 within the surrounding country rock, and 0.018 counts per 15 min of the **alpha particle detector peak** is equivalent also to 1 Bq/m^3.

Sde Eliezer water, radon streamed downward into the groundwater via the porous rock, driven down by the surface temperature gradient ΔT. It means that the groundwater is the source for supplying radon to the open borehole air space.

In a shallow, open, abandoned wells such as the Sde-Eliezer well, long-term equilibrium between the radon within the porous media and inside the open borehole air space is not necessarily established. Therefore, the radon measured by the gamma and the alpha detectors is different. The negative barometric pressure gradient is the driving force that pumps the radon upward via the open borehole (as named Barometric Pumping in "Phase VI: CO_2 and Rn-222 Emissions From an Abandoned Water Well Under the Influence of Climatic Pressure and Temperature" section).

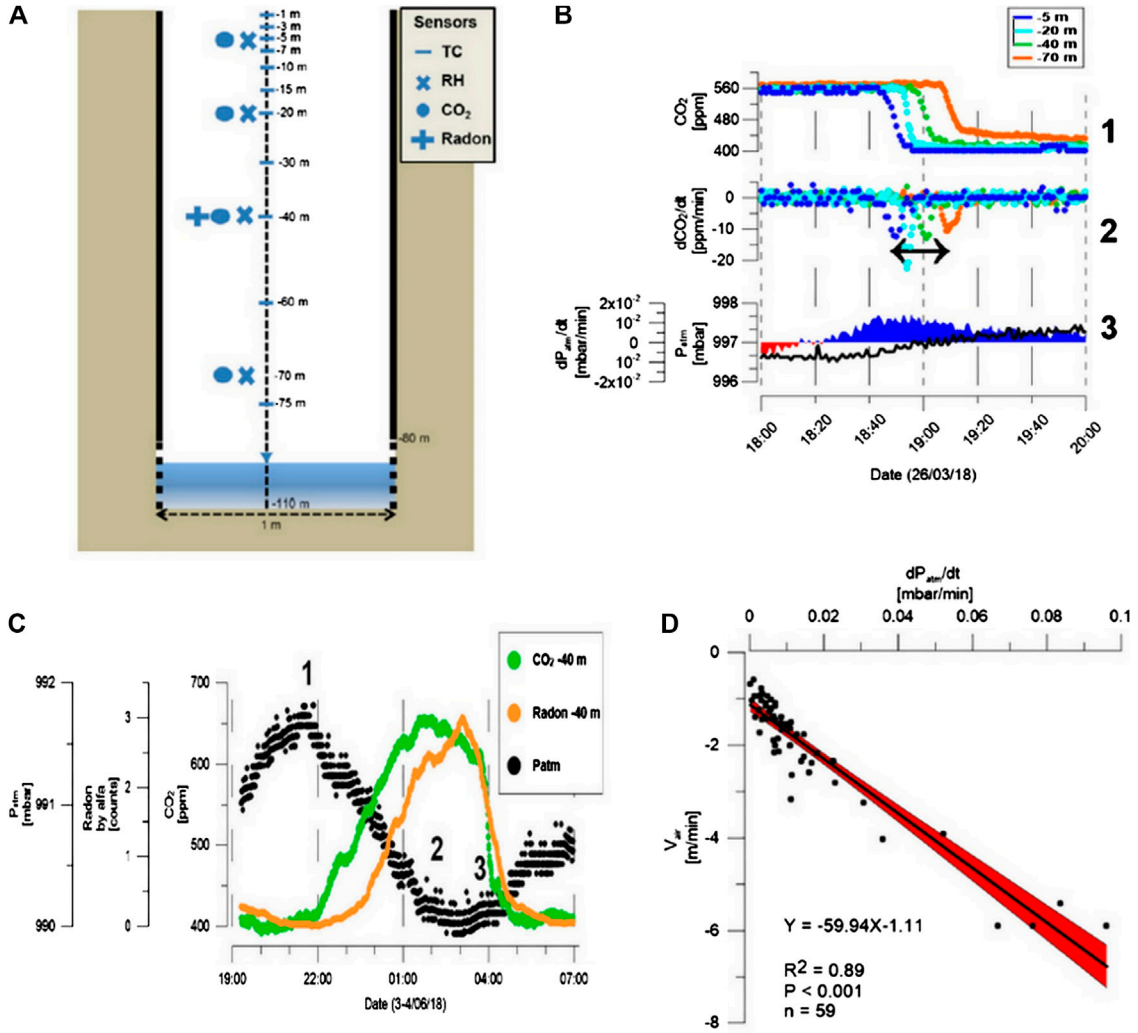


FIGURE 10 | Analysis of the relationship between air velocity (V_{air}) and atmospheric pressure changes (dP_{atm}/dt). **(A)** Experimental setting. **(B)** Demonstrates the method using a single inflow event. **(C)** CO_2 and radon responses to changes in barometric pressure (P_{atm}). Labels 1, 2, and 3 refer to the time when P_{atm} begins to decrease, becomes stable (i.e., between points 2 and 3), and increases, respectively. **(D)** Plot displays V_{air} as a function of dP_{atm}/dt using 59 analyzed inflow events over three months (March-May 2018). Black arrow in **(A)** denotes the time interval between the minimum decrease value of CO_2 (dCO_2/dt) at −5 and −70 m, from which V_{air} was quantified. Red area represents the 95% confidence range according to the calculated linear regression (black line) (Levintal et al., 2020).

The assumption that radon can flow downward via the porous media is also suggested from other measurements at diverse sites, including various time delay measurements (see "Discrimination Between the Influence of Climatic Temperature and Pressure on Radon Flow in Geological Media" section).

Analyzing the time series in detail, (**Figure 9B**) an interesting relationship between the radon signals and the gradients of both temperature and pressure parameters appears: the disappearance of the radon signals at some time intervals, as occurred on 22 March, 30 March, 10–14 April, or 23–24 Aapril. This phenomenon is related to the inversion of the temperature gradient $\Delta T = T - T_{10m}$, from positive to negative (when T_{10m} is the stable temperature in the well at a 10 m depth). This situation happens when the outside temperature becomes lower than the constant temperature of 21.29°C at the 10 m depth (as described in "Phase II: The Analysis of the Long-Term Temporal variability of Radon in Research Tunnel" section and "Phase IV: Impact of Atmospheric Aspects on Radon Transportation Within Porous Media" section). It is also happened when the inversion from negative to positive occurred of the pressure gradient $\Delta P = dP/dt_{9h}$, from negative to positive occurred, leading to the same effect. The disappearance of radon daily signals because of the inversion in the temperature gradient was already observed (Barbosa et al., 2010; Choubey et al., 2011).

The whole process is very clear: the higher the external temperature, the more gas will flow down the bedrock. If more radon gas reaches the water, then more radon is sucked into the well airspace. At noon, because parallel to the rising of the

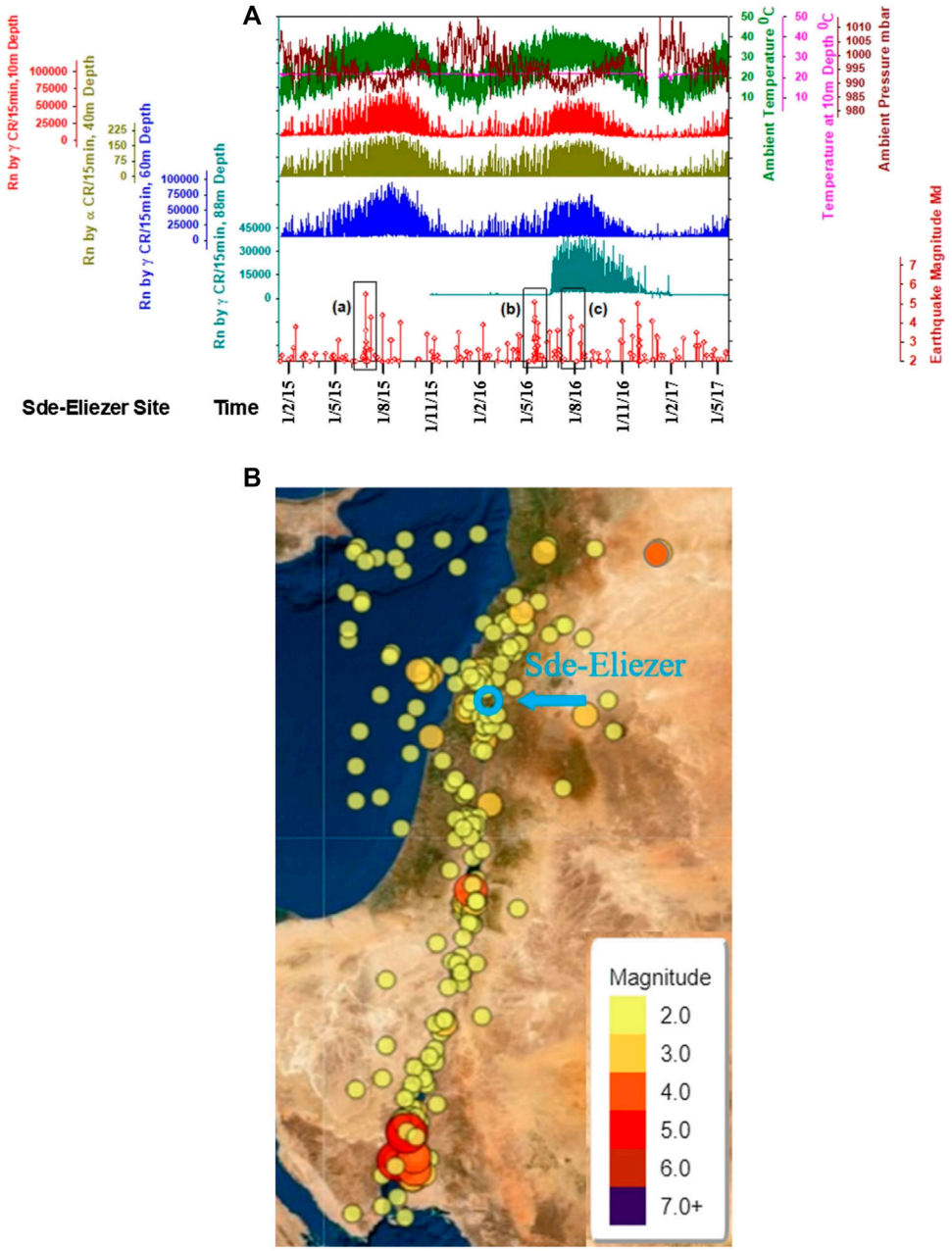


FIGURE 11 | (A) Continuous time series of the measured parameters at the Sde-Eliezer site (with 15-min temporal resolution) collected during the first two and a half years (844 days). The parameters measured including: barometric pressure (**dark red**), ambient temperature (**green**), borehole temperature at **10 m depth** (**pink**), radon within the surrounding rocks **at** 10 m **depth** as measured by gamma rays **(red)**, radon within the borehole air space at **40 m depth** as measured by alpha particles (**dark yellow**), radon within the surrounding rock at **60 m depth** as measured by gamma rays (**blue**), radon within the groundwater at **88 m depth** (since November 2015, **cyan**). **(B)** More than 260 earthquakes with magnitude greater than M = 2) recorded by the Israel Seismic Network of The Geophysical Institute of Israel [http://seis.gii.co.il]. For three time periods marked in letters **a**, **b**, **c**, there were three earthquakes preceded by an unusual radon anomalous signal.

external temperature during the day, the barometric pressure is decreasing accordingly, and the barometric pumping is getting stronger. Then, more radon is measured by the alpha detectors at a depth of 40 m (**Figure 9A**).

The time lag of about 2 h between the maximum values of the two gamma detectors separated vertically by 50 m, defines the radon vertical velocity as 25 m/h in the local subsurface porous media (**Figure 9C**). This is the first determination of the downward radon transportation velocity within porous rock media, by direct field measurement. It also proves that radon in the Amram tunnel moves downwards to the tunnel (100 m depth) in 10 h (**Figure 6B**).

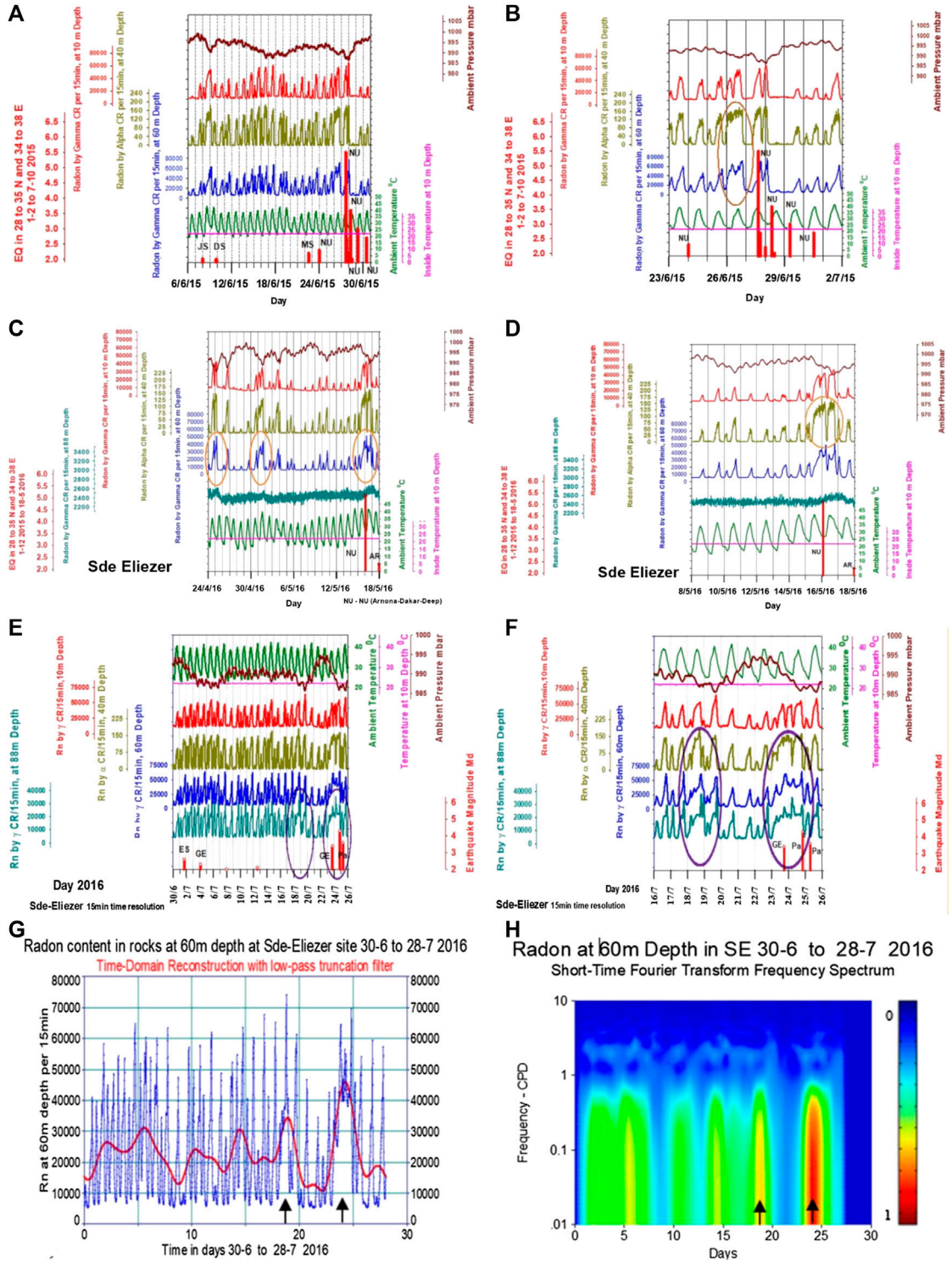


FIGURE 12 | Case a: **(A)**The first-time interval, June 2015, that reveals **anomalous broadened radon signals** while most of the radon signals are recognized as induced by climatic parameters by appearing once or twice a day at specific times, 3–4 A.M. and 4–8 P.M. **(B)** The 26 June radon anomalous signal is different from the radon periodic signals appearing once or twice a day. **Case b**: **(c)** This time interval reveals **anomalous broadened radon signals** on 25 april, 1 and 15 May 2016, preceding by days and hours the Nuweiba, M 5.1 earthquake (NU) of May 16, 2016. **(D)** It happens while most of the radon signals are recognized as induced by climatic parameters, by appearing once or twice a day at specific times. **Case c**: **(E)** and **(F)** These time intervals between 30 June to July 26, 2016**,** reveals **two anomalous broadened radon signals** of at least 20 h each, precede the Palmyra Syria M = 4.5 earthquake (**Pa**) on 25 July. It occurred 300 km northeast of the Hula Valley on one of the branches of the main fracture into Syria called Palmyrides, (Al-Zoubi et al., 2006). The signal from the deepest detector at 88 m depth became the

(*Continued*)

FIGURE 12 | most pronounced since the water table within the borehole of the abundant well, dropped down below 100 m, **by unique event** on June 25, 2016 (see **Figure 11**) as a result of massive pumping in the Hula Valley area, since February 2016, because of a drought. The EQs locations are Palmyra (**Pa**), Gulf of Eilat (**GE**) and East Sinai (**ES**). **(G)** and **(H)** are the FFT low-pass filtering and the reconstruction spectrogram of the radon's 60 m time series in the time interval of 30 June to July 27, 2016, shows the **discrete radon broadened signals** that are marked in the with **black arrows**. The results of the FFT filtering and the time domain reconstruction of the above time intervals **(E)** show that although the procedure does not disable the entire cyclical signature in the original data, it keeps the **seasonal fluctuated background** under 30,000 counts per 15 min at the 60 m radon gamma detector. **(H)** The reconstruction STFT spectrogram of the radon 60 m time series in the same time interval. **The procedure pinpoints the two broadened signals 6 and 2 days before the earthquake on July 25, 2016.** The FFT analysis have done to each one of the above cases. In this figure, three counts per 15 min of the gamma sensors at 10, 60 and 88 m, are equivalent to concentration of 1 Bq/m^3 within the surrounding country rock, and 0.018 counts per 15 min of the alpha particle detector is equivalent also to 1 Bq/m^3.

The most important observation in the study of the radon time series obtained during the first 10 months of 2015 at the Sde Eliezer site, was the discovery of a broadened pre-seismic radon signal (wider than the sum of the expected width of the diurnal and semidiurnal radon signals combined) that have been ahead by one day (**Figure 12** at "Phase VII: Radon and CO_2 Monitoring Technique in Deep Subsurface, as a Proxy for Investigating Tectonic Pre-seismic Activity" section) the Nuweiba M = 5.5, 4 km deep earthquake, which happened on June 27, 2015, near Eilat (GE) about 480 km from Sde-Eliezer site at Hula Valley. It was the first evidence that a pre-seismic earth strain, stress or deformation along an active fault like the DSFZ, may produce a faraway local pressure gradient (Aharonov and Scholtz 2018) to induce, non-periodic, radon anomalies.

Since no experimental method proved or contradicted, the assumption that a long-lasting stress or strain produced during pre-seismic rupture processes can exist and operate along active faults, far away to hundreds of kilometers, we can raise the hypothesis that a pressure gradient in the magnitude of a few pascal (10^{-5} atm) can be produced by pre-seismic tectonic driving forces in the subsurface, and induce radon and CO_2 anomalous flow within the porous media, even for strains below the tidal magnitude of ~10^{-8}. Models to assess the total strain that can develop in geological media before seismic events, to a distance of a few hundred kilometers from the center of the earthquake, as a function of its magnitude, were presented in the literature (Cicerone et al., 2009; Wang and Manga, 2010; Skelton et al., 2015; Woith et al., 2018).

Phase VI: CO_2 and Rn-222 Emissions From an Abandoned Water Well Under the Influence of Climatic Pressure and Temperature

Boreholes and wells are a complex interplaying interface between the subsurface hydrosphere, lithosphere, and biosphere to the atmosphere above it. Quantitative computing the air exchange rate between these features is therefore very relevant, as these are potential sources for greenhouse gas (GHG) emissions to the atmosphere. The influence of atmospheric conditions, including barometric pressure and ambient temperature, on the air, CO_2, and radon transport across the borehole-ambient atmosphere interface and groundwater-borehole bottom interface is studied based on measurements inside a 110 m deep by 1 m diameter borehole in Sde-Eliezer site in northern Israel (Levintal et al., 2020).

For CO_2 monitoring, the detectors that were lowered down to acquired measurements at depths of 5, 20, 40 and 70 m, were the GMD-20 and GMP-252, infrared CO_2 analyzers (Vaisala, Finland), with measurement ranges of 0–2,000, 0–3,000, and 0–10,000 ppm conforming to the borehole depth.

In parallel the setup included thermocouples (T type) and Relative Humidity probes (Humitter ^{50}U, also of Vaisala, Finland) at almost the same depths, and radon alpha-particle detector (Barasol of Algade Inc., France) as described previously ("Experimental setting" section, "Phase III: A Comparative Assessment of Radon Sensing Systems for Long-Term Monitoring in Sub Terrain Geological Media" section, and "Phase IV: Impact of Atmospheric Aspects on Radon Transportation Within Porous Media" section).

- The high resolution of CO_2 measurements enables to determine *in-situ* the air velocities within the borehole. During barometric pumping (BP), when there is inflow of atmospheric air from the top to the bottom direction, the CO_2 measured by the upper sensor (−5 m) is expected to decrease before the CO_2 variation will be measured at the bottom (−70 m). Then the distance of 65 m between the two sensors can be divided by the time interval between sensor responses, in order to get the vertical component of the CO_2 velocity within the borehole (Vair), assuming that CO_2 transport is advective—carried as part of the air mass movement within the borehole. The basic assumption was based on the photographed proof that the borehole casing above the 80 m depth is a sealed iron pipe, and the only CO_2 inlet and outlet are the bottom or the top entries. Therefore, the minimum value of dCO_2/dt provides an easily identifiable signal. The time difference between sensors' minimum value used to calculate the velocity of the atmospheric air pulse between sensors. This analysis is illustrated in **Figures 10B–D**. Preliminary calculations indicated that the average vertical CO_2 velocity inside the borehole equal ~1.3 m/s.

Calculating the air exchange rate at the well from the measured air/CO_2 velocities, using two independent methods as detailed in Levintal et al., 2020, (fluctuating up to ~6 m/min) gave a mass flux rate to the atmosphere of ~5 g-CO_2/min CO_2 emissions, becoming higher during the summer with two daily peaks as presented for example in **Figure 15** at the next "Phase VII: Radon and CO_2 Monitoring Technique in Deep Subsurface, as a Proxy for Investigating Tectonic Pre-seismic Activity" section.

This reveals the time-dependent behavior of boreholes as an additional source of CO_2 emissions. On a yearly scale, the calculated CO_2 emissions from Sde-Eliezer site were similar in magnitude to a wheat field in the range of 100 to 6,000 m^2.

The most notable results are summarized as follow:

- Barometric pressure changes were the governing mechanism for air movement along the well. The thermal internal instability played a minor role.
- CO_2, water vapor, and radon, moved along the air space in a similar manner.
- The transport of gases from the vadose zone to the atmosphere via the borehole airspace depends on two processes: the transport of the pore gas into the borehole lower entry, and the movement of the gas out of the borehole and into the atmosphere.

Phase VII: Radon and CO_2 Monitoring Technique in Deep Subsurface, as a Proxy for Investigating Tectonic Pre-seismic Activity

Overview

Long-term monitoring method of Rn-222 and CO_2 at a depth of several tens of meters at Sde-Eliezer site, located within one of the DSFZ segments in northern Israel (Phase V: Differentiating Between Radon Anomalies Produced by Climatic Constituent and Pre Seismic Tectonic Activity), has led to the discovery of the phenomenon that both gases are affected by underground tectonic activity along the DSFZ, possible related to the pre-seismic processes associated with the accumulation and relaxation of lithospheric stress and strain producing earthquakes (Zafrir et al., 2019).

The Results of the First Period From February 2015 to May 2017

The first period of the long-term radon monitoring carried out at the Sde-Eliezer site lasted for two and a half years (844 days) from February 2015 to May 2017. In parallel, about 260 earthquakes with magnitude M ≥ 2.0, that have been recorded during the 844 days along the DSFZ area, was added to the acquired data (**Figure 11A**). The DSFZ area in **Figure 11B** is defined by the Geophysical Survey of Israel as the region from 27° to 36 N in latitude and longitude from 32° to 38 E (see https://earthquake.co.il/en/earthquake/searchEQS.php).

The largest variations in the radon temporal flux are mostly controlled by the temperature gradient on the surface as can be observed in **Figure 11A** at different depths.

The role of the temperature gradient on radon temporal behavior is probably not linear since the ratio between the radon level in winter to summer varies by a factor of 3–10 (**Figure 11A**), while the temperature varies within 10% span (28° change vs. 285K). In parallel, the pressure effects, according to the existing physical model, arise linearly through the negative pressure gradient term. Therefore, it is impossible to predict so far, the total impact of the temperature and pressure at particular time, by the current contemporary model.

Other climatic variables, such as rain and snow, were found unimportant according to the results between winter and spring (December to end of March) and the long Israeli summer (April to November) during which there are no visible signs of rain or snow.

In addition, three, very pronounced radon signals that were different in shape and preceded earthquakes with magnitude >4.5, appeared during disparate events which occurred during the above-mentioned two-and-a-half-year, and marked by **a**, **b** and **c** in **Figure 11A** as presented in the following section.

The Data Analysis Methods to Identify the Nature of the Gases Anomalies

The procedure to exclude periodical radon signals.

Since the existing radon model and the physical equations for radon transport in the subsurface geologic media do not include temperature, which is one of the most significant parameters affecting gas thermodynamics, it is difficult to predict the radon temporal behavior induced by this parameter as was done for the barometric pressure (Perrier and Girault, 2013). On the other hand, in order to identify the nature of the residual anomalies, their specific contribution must be excluded from the measured time series.

One of the possible methods for isolating the components belonging to the periodic signals produced by the climatic parameters in the measured time series is to apply the Fourier domain filtering and component isolation procedure (AutoSignal™, Systat Software Inc.).

Utilizing these existing algorithms that work in the frequency domain for low pass truncation, frequency components above a chosen ideal cutoff frequency be removed from the original radon time series, leaving the frequencies below it unaltered as well as any non-periodic discrete events.

Choosing a frequency cutoff less the diurnal one (1 cycle per day) excludes all the unwanted diurnal, semi diurnal and higher periodical signals (maybe harmonics) that are induced by the atmospheric parameters.

Another extraction method that relies on the Modulation Spectral Analysis is the spectrogram phase space representation in which one may see simultaneously the temporal as well as the spectral information of a given signal.

The main advantage of using a spectrogram is its capability of being a better visualization tool showing in a more emphasized manner the relevant temporal anomaly.

In any case, we have proved by the two methods, based on FFT low-pass truncation filtering and the time domain reconstruction analysis, that indeed a radon anomaly is identified and that it lasts for more than 20 h.

The Recovery of a Pre-seismic Radon Anomalous Signal Apparently Associated With a Regional Geodynamic Process

These are the three disparate events that occurred during the above-mentioned two-and-a-half-year, in which very pronounced radon signals seem to preceded earthquakes with magnitude >4.5:

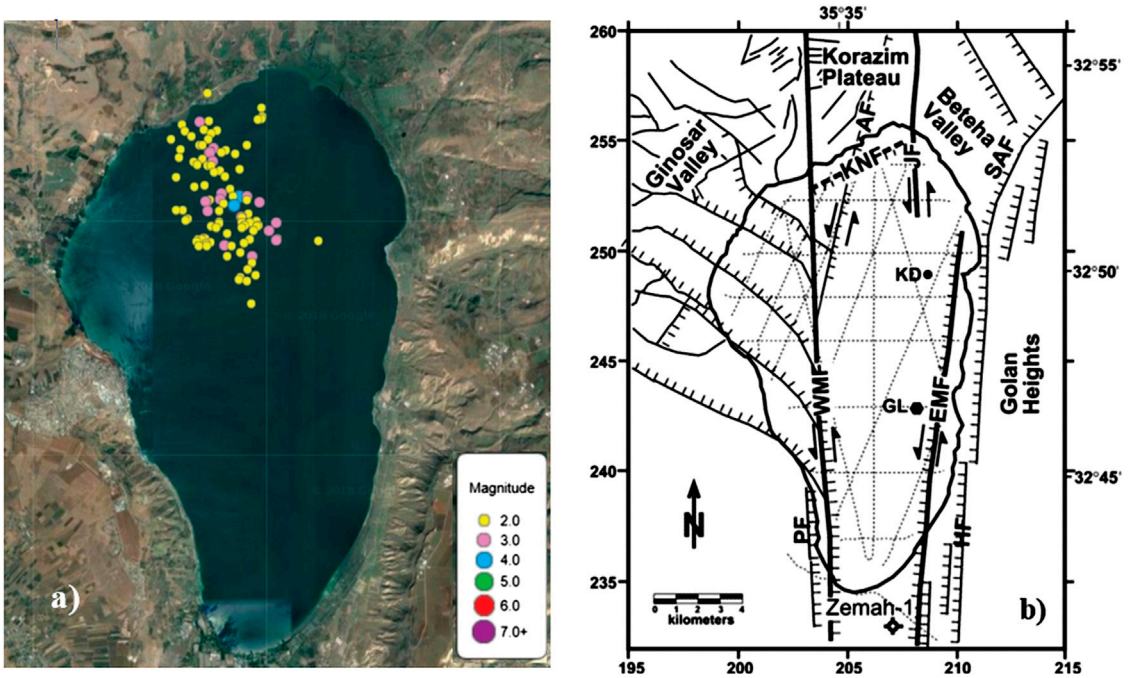


FIGURE 13 | (A) Accumulation of 103 earthquakes in the Dead Sea seismogenic **active faults** at the bottom of Lake Kinneret, which were recorded during the 2018 summer between 4 July and 18 August. **(B)** The tectonic map showing the internal structure of the lake (Hurwitz et al., 2002). EMF and WMF are the eastern and western marginal faults, KNF is the Kfar Nahum fault, and JF and AF are the Jordan and Almagor faults.

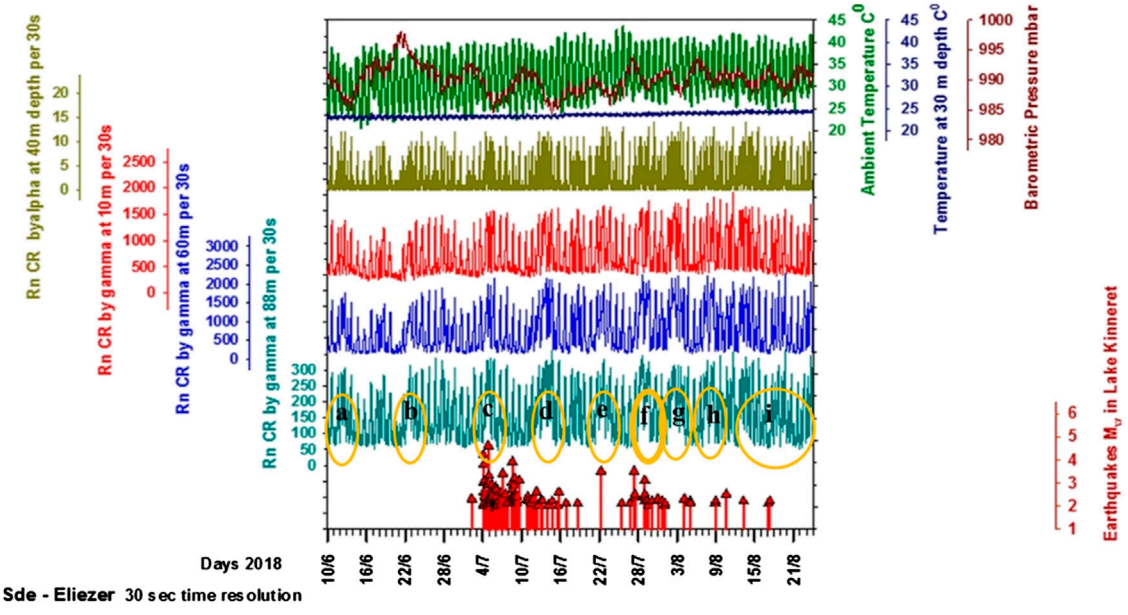


FIGURE 14 | Time series interval of 75 consecutive days at the Sde-Eliezer site. The Sde-Eliezer site is located about 35 km north of Lake Kinneret that was under weak seismic activity during July and August 2018. The **non-periodic, broader than 20 h signals,** on 12 (**a**) and 22 (**b**) June, 4 (**c**), 13 (**d**), 22 (**e**), and 28 & 29 (**f**) July, and 2 (**g**), 7 & 8 (**h**), and 12&13 (**i**) August, may reveal the pre-seismic progression of several weak geodynamic events in depth (details in Figures 24, and 25). In this figure, 0.1 counts per 30 s of the gamma sensors at 10, 60 and 88 m, are equivalent to concentration of 1 Bq/m^3 within the surrounding country rock, and 0.0015 counts per 30 s of the alpha particle detector is equivalent also to 1 Bq/m^3.

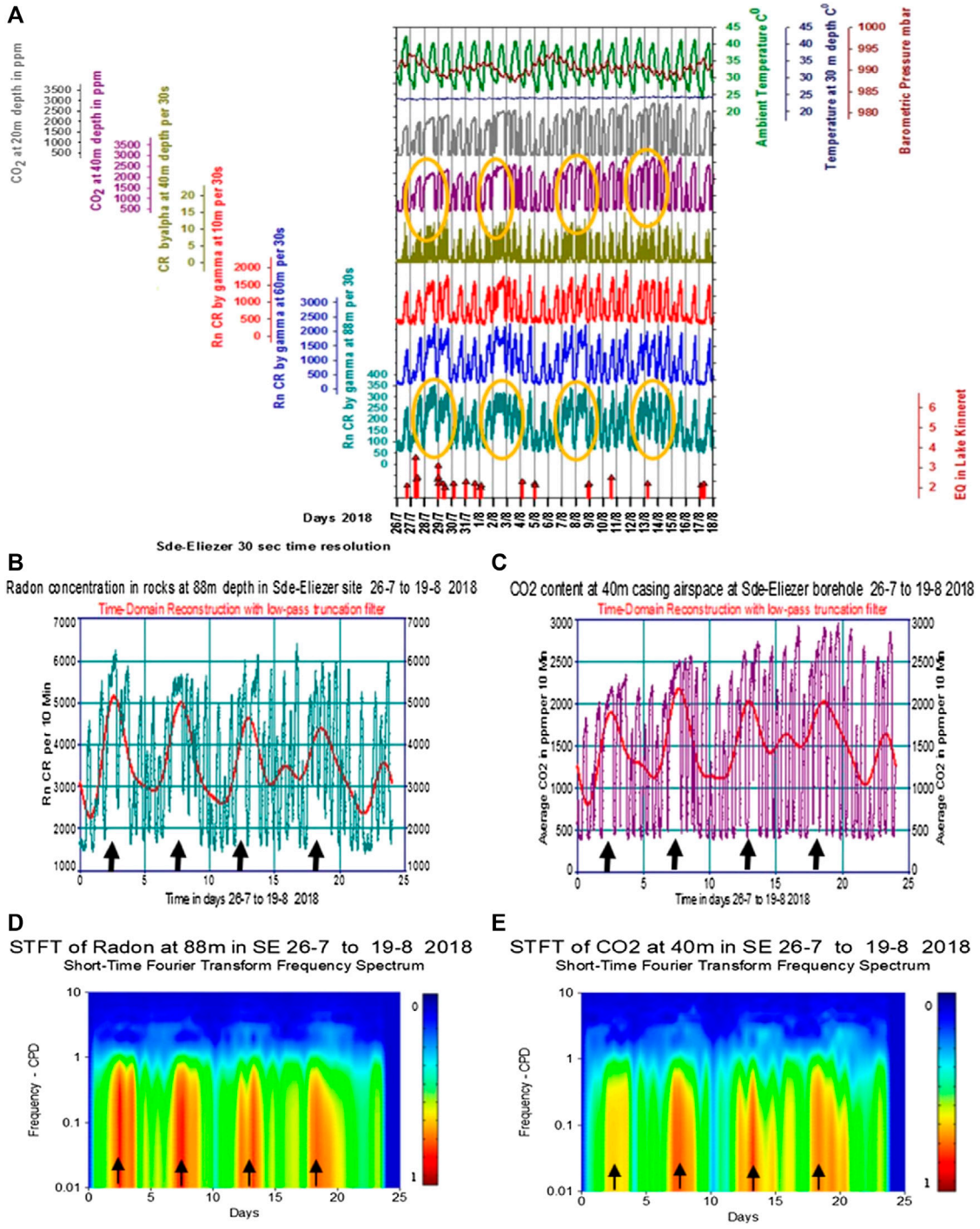


FIGURE 15 | (A) Time series of 24 consecutive days at the Sde-Eliezer site in the time interval of 26 July to August 18, 2018. **(B)** Time domain reconstruction with low-pass truncation filter of the **radon's 88 m,** and **(C)** Time domain reconstruction with low-pass truncation filter of the **CO_2's 40 m time series**. It shows **the same discrete radon and CO_2 broadened signals** on 28 and 29 July, 2, 7, 8 and August 13, 2018, that are marked with **black arrows also** in **(D)** and **(E)**, that are the radon and the CO_2 spectrogram. In this figure, 0.1 counts per 30 s of the gamma sensors at 10, 60 and 88 m, are equivalent to concentration of 1 Bq/m^3 within the surrounding country rock, and 0.0015 counts per 30 s of the alpha particle detector is equivalent also to 1 Bq/m^3.

- **Case a**: happened on June 2015 and it was described in the previous "Phase IV: Impact of Atmospheric Aspects on Radon Transportation Within Porous Media" section and display in **Figures 12A,B**.
- **Case b**: happened on May 16, 2016, a radon anomalous signal preceding by 14 h the Nuweiba, M = 5.1 earthquake as displays in **Figures 12C,D**.
- **case c**: happened on 17 and July 23, 2016, two broadened anomalous radon signals appeared 7 and 2 days before the Palmyra Syria M 4.5 earthquake on 25 July 01:30 AM, as displays in **Figures 12E,F**.

Utilizing an existing algorithm that work in the frequency domain for low-pass truncation, frequency components above a chosen ideal cutoff frequency can be removed from the original radon time series, leaving the frequencies below it unaltered as well as any non-periodic discrete events. Choosing a frequency cutoff less the diurnal one (1 cycle per day) excludes all the unwanted diurnal, semidiurnal, and higher periodical signals (maybe harmonics) that are induced by the atmospheric parameters (e.g., **Figures 12G,H**).

The Second Period From May 2017 to End of 2018—Radon and CO_2 in Depth

Overview

In the middle of 2017, the setup at the Sde-Eliezer site was expanded to study the impact of atmospheric variables, (ambient pressure and temperature) on air flow within the deep dry borehole at the site—110 m deep and 1 m wide (Levintal et al., 2018). Temperature, relative humidity, CO_2 (at 5, 20, 40, and 70 m), and radon detectors (measured by gamma detectors at 10, 60, and 88 m and by alpha at 40 m) were placed along the cased boreholes (**Figures 8B** and **10A**) and barometric pressure probe was installed at the surface. Since then to present, all borehole data has been logged at a high 30 s temporal resolution.

Beyond that initially anticipated, the results show that CO_2 in the open borehole air space, as measured by four CO_2 detectors at different depths, follows the radon (measured by alpha detector at 40 m) as well as the radon temporal variations at the surrounding bedrocks (measured by gamma detectors at 10, 60, and 88 m), and both are driven by the climatic parameters as analyzed for the radon in our previous sections. Therefore, the CO_2 reveals the same daily and semi daily temperature and pressure periodicities in the frequency time domain (Zafrir et al., 2019). Improving the sampling rate by 30 times (from 15 min to high 30 s resolution) and implementing four CO_2 detectors at different depths enabled measuring the CO_2 velocity in the Sde-Eliezer borehole under the influence of barometric pressure that seems to be more effective than temperature within the air space inside the open well (see "Phase VI: CO_2 and Rn-222 Emissions From an Abandoned Water Well Under the Influence of Climatic Pressure and Temperature" section).

Radon, CO_2, and Pre-Seismic Processes—The 2018 Lake Kinneret Scenario

In order to understand whether there is a link between earthquakes in the DSFZ and the gas signal measurements at the depth in the abandoned well, located within the northern part of the fault belonging to the DSFZ (WMF in **Figure 13**), we have chosen to focus on the emergence of 103 seismic events in Lake Kinneret (Sea of Galilee) that occurred in the summer of 2018.

The temporal variations of the radon measurements at Sde-Eliezer site (located on the WMF about 35 km north of Lake Kinneret) and the rest of the environmental parameters, acquired simultaneously with all the earthquakes that occurred in the Lake Kinneret, are presented in **Figure 14**.

Despite the situation that the number of tremors were over 100, only two of them had magnitude of M = 4.2 and M = 4.5, and all the rest had lower magnitude between M = 2 and M = 4. Therefore, there was no early expectation that tectonic activity in the subsurface would be followed by a pre-seismic radon anomalous signals, as occurred before (The Recovery of a Pre-seismic Radon Anomalous Signal Apparently Associated With a Regional Geodynamic Process section). Nonetheless, about nine non-periodic radon signals, broader than 20 h each, have been exposed during 75 consecutive day from 10 June to 20 August (**Figure 14**).

The encircled segments designated as **a, b, c, d, e, f, g, h, i** in **Figure 14**, occurred within the time series in which the signals of radon are exceeding the daily and semi daily periodic effect of atmospheric temperature and pressure as analyzed by the FFT time domain reconstruction with low-pass truncation filter and short time Fourier transform (STFT) methods (for example see **Figure 15**). The results of the FFT filtering and the time domain reconstruction of the time section between 10 June and 12 July pinpointed the two anomalous peaks (**a**)) and (**b**) in **Figure 14**, which started before the first rupture. It shows that two radon, clear, discreet, non-periodic and broadened with time duration that exceeds 20 h, on 12 and 22 June, preceding by 24 and 12 days the more powerful tremors of July 4, 2018, with magnitude M = 4.5.

A selected example in **Figure 15**, shows the analysis of the signals of radon and CO_2 during 24 consecutive days at the Sde-Eliezer site, from 26 July to August 18, 2018 including (**f**), (**g**), (**h**)) and (**i**). The tremors in this time interval, fall below the magnitude of M = 4, and the relations between them and the gases temporal variations become non-diagnostic. There is a mixture of earthquakes on one hand and radon and CO_2 broadening signals, on the other. The broadened signals could probably be related to geodynamic activity as we have shown in the cases of earthquakes with magnitude above 4.5 (**Figures 12A–F**) but it is not possible to associated them to a specific event.

At least, based on our previous investigation on "Response of radon in a seismic calibration explosion" ("Overview" section), we suggest that there will be no an apparent response in the concentration of radon below the surface as a direct effect of short-time transient excess pressure produced by any one of the swarm's earthquake, including the highest one of M = 4.5 on 4 July (**Figure 14**). It is also possible to assume that the phenomenon of dilation in the time of the CO_2 signals that occurs simultaneously with the extension of the radon signals (**Figure 15**), and of course independent with it, is genuine.

In general, any geodynamic process that causes stress or strain release affects subsurface fluids, irrespectively if the process will finally produce an earthquake or not.

SUMMARY AND CONCLUSIONS

In situ Monitoring of Subsurface Radon–Experimental Point of View

The long-term geophysical investigation of radon in shallow and deep boreholes, based on passive measuring systems (no pumping and gas circulation that disturb the local environmental equilibrium) was able to detect radon temporal changes, with very high sensitivity and high time resolution. It enabled the researchers to eliminate climatic-induced periodic contributions from the radon time series, and thus extract the part of the signals that could be correlated with regional geodynamic processes. The various monitoring systems that were found to be suitable for use in a passive way included various types of gamma and alpha detectors.

The basic principle to choose the gamma detection by SCA technique for total counting of RDPs' (radon decay products) gamma rays, is the assumption that radon is the only radioactive element that can vary in terms of its amount in the porous media under the impact of upper climatic or deeper geodynamic activities. These fluctuations are measurable as an additional increment to the measured gamma radiation from natural elements as uranium, thorium and potassium that form a constant background in time. This background also includes the contributions of all the RDPs atoms that remain confined inside the solid material and are not emanated to the porous media neither free to move under the influence of various driving forces.

Therefore, the variable contribution in the measurement of radon by the gamma detector does not actually exceed 10–25% of the total radiation that is measured. Thus, the first test for a system's performance is its capability to recover the daily changes in the temporal radon transport variation within a soil media, while the detector is lowered into ground depth of at least 2–5 m in an open area. It also needs to take into consideration that too lower radon contents do not allow to measure significant temporal variations in the concentration of radon, under the daily periodic behavior. Experimentally, it should be higher than 1 kBq/m^3, few times above 200 Bq/m^3, the average outdoor radon levels.

BGO and NaI gamma detectors were selected after being ascertained that they have high sensitivity, stability and suitability for use in a 2-inch diameter drilling holes to a depth of several dozen meters. We have also re-defined the energy range the SCA of the gamma detectors to count gamma rays between 475 and 3,000 keV, cancelling the measurement of gamma radiation in the field of the Compton scattering, between 50 and 450 keV, enabling to improve the ratio of signal to noise by 70% in comparison to the common detection systems (**Figure 1A**).

The main result was that gamma detectors have a higher sensitivity between 2 and 4 times in relation to the alpha detector, which enables them reveal to detect low sub-diurnal fluctuations. The construction of hermetic and water-protected housing enables the use of these radon gamma radiation detectors in a variety of environments such as soil, country rock, ground and seawater, and any subterranean spaces including drillings.

Discrimination Between the Influence of Climatic Temperature and Pressure on Radon Flow in Geological Media

Combined long-term radon measurement by gamma and alpha methods within deep abandoned boreholes empowered the capability to distinguish between radon anomalous signals at depth induced by temperature and barometric pressure. The main evidences of our research are:

1)The radon present in country rock formations that is measured by gamma radiation detectors is propelled by the surface temperature gradient to at least a proven depth of 100 m. The radon reveals a daily periodicity similar to the one per day cycle of the surface temperature. The gamma detector at each level, presents very sharp, clear and accurate peaks as a result of a high counting rate and low error, with a specific time lag between each other. It was found that the time lag depends on the downward radon velocity within the bedrock type.

The list of results that includes measurement from different monitoring sites is as follows:

- At Sde Eliezer site, Israel, a time lag of 2 h was measured between 10 and 60 m depth, implying a downward radon velocity of 25 m per h (Zafrir et al., 2016).
- At Nachal Mor site, Israel, a time lag of 2 h was measured between 10 and 40 m depth implying a downward radon velocity of 15 m per h (Zafrir et al., 2019).
- At Amram tunnel site, Israel, a time lag of 10 h was measured, between 0 and 100 m depth implying a downward radon velocity of 10 m per h (Zafrir et al., 2013).
- At Bentonite mine, in Makhtesh Ramon, Israel, a time lag of 5 h was measured between 0 and 40 m depth, implying a downward radon velocity of 8 m per h (Zafrir and Malik, 2010).
- At Ghuttu site in Garhwal Himalaya, India, a time lag of 3 h was measured between 0 and 10 m depth, implying a downward radon velocity of 3.3 m per h (Choubey et al., 2011).

In general, from a geophysical point of view, there was no need to find any other gases that would bear radon up or down (e.g. Etiope and Martinelli, 2002; Neri et al., 2016). Once the Sun surface heating provides energy to the radon atoms their ballistic moment (mv) downward is at least 4 times larger than any other natural gas atoms. The same process can lead to the emergence of radon and other gases, close to the surface, under the effects of underground heating associated with volcanic events.

2) The radon concentration within any open underground space, such as an abandoned drilling, as measured by a detector of its alpha particles, is controlled by the negative barometric pressure gradient (in anti-correlation).

3) Most of the radon daily signals that are recognized as induced by climatic parameters, appear once or twice a day at specific times: early morning and afternoon (e.g.,, 4–6 AM and 5–7 PM, in 60 m depth at Sde-Eliezer site, **Figure 9C**).

4) The amplitudes of the radon periodical signals are controlled by the intensity of the climatic driving force, in

linear dependency with the pressure gradient according to the existing physical model, and with largest non-linear variations induced by the ambient temperature gradient, that according to the ratio between the radon level in winter to summer varies by a factor of 3–10 while the temperature varies within 10% span (28 change vs. 285 K).

These phenomenological indications cause difficulties in accepting the results of any statistical analysis that is based on daily, multi-day, seasonal and multi-year averages calculations, of the radon gas levels in any media. Since the half-life of radon is short and constant (3.8 days), and naturally it always tends to be in secular equilibrium, only external driving forces will cause the radon to move within the geological media. Hence, such calculations actually reveal and reflect the temporal variations of the external climatic parameters, the ambient temperature and pressure, which undulate a combined change of the amplitude of the radon signal during daily scale, multi-day variation and significant changes between seasons too. This assumption is undoubtedly correct when the radon gas detector is installed at a shallow depth of a few dozen centimeters.

In addition to the difference in the intensity of the radon signals between the summer and winter, it is also possible to discern in all the above works, the multi day heat waves, mainly in the spring and summer, that are simultaneously producing waves of radon that are prolonging within the same time (e.g.,, **Figures 6A,B**). Over these heat waves there are exposed signals in a daily cycle with a peak that follows the maximum of the daily temperature, with a delay in time depending on the depth of the detector. The same phenomena can be observed with barometric pressure waves lasting few days that also affect the continuous level of the radon under the surface in addition to the semidaily and diurnal signals (**Figure 7B**). It is important to emphasize that the two phenomena with daily and multi-day variations, are not always dependent on each other, as for example, the semi-daily cycle that exists only in the periodicity of barometric pressure, prompted by an atmospheric tide (Zafrir et al., 2013).

Therefore, it is impossible to separate the influence of the climatic driving force by additive arithmetic operations. For example, the subtraction of the moving average of 7 days from the daily average as part of the statistical manipulation to calculate anomalies higher than twice the standard deviation is uncertain and problematic (e.g., Ghosh et al., 2009; Cannelli et al., 2016; Singh et al., 2017; Barkat et al., 2018; Alam et al., 2020). Even the attempt to adapt regression equations to radon time series utilizing every environmental variable and generating a best linear regression model to correlate between radon variations and meteorological parameters, does not enable to resolve and defined the subsurface contribution to the anomalous radon temporal variation (Neri et al., 2016).

5) There can be a number of ways for analyzing, identifying the nature of the anomalies in the measured time series, dismount to various components, and isolating the parameters operating as driving forces for the radon movements beneath the surface. The **convolution** is a mathematical procedure of combining different signals to form an another signal, or isolate components and detect signals with filtering and reconstruction techniques. It is the single and most important technique in Digital Signal Processing (e.g.,, Smith, 2002).

Although, there is no yet explicit mathematical expression for the thermal gradient rule in the radon transportation process, to be insert within the convolution integral, one can use the Fourier analysis to convert signals from their original time domain to a presentation in the frequency domain and vice versa.

We apply the Fourier domain filtering and component isolation procedure (by AutoSignal™ of Systat Software Inc.). Utilization of an existing algorithm that work in the frequency domain for low-pass truncation of frequency components above a chosen ideal cutoff frequency, enabled to remove them from the original radon time series, leaving the frequencies below it unaltered as well as any non-periodic discrete events. Choosing a frequency cutoff less the diurnal (one cycle per day), excludes all the unwanted diurnal, semidiurnal, and higher periodical signals (maybe harmonics) that are induced by the atmospheric parameters and proved that indeed we measured radon anomaly that its emergence lasts for more than 20 h and that these non-cyclical signals may precede by several hours or more a forthcoming seismic events even if they are weak.

It is important to note that according to our ongoing experience, the broad signals associated with tectonic activity almost cannot be revealed even by the measurements of radon temporal variation at 10 m depth. It was easy to observe within the long-time series acquired during the last 4 years, that the entire radon measured signals at the shallow depth of 10 m, used as reference for the deep data acquisition, are mostly radon periodical signals produced under the direct effect of the climatic driving forces on the ground surface.

As long as investigations continue to rely on detectors installed at a depth that does not exceed 10 m, the likelihood of discovering non-cyclical signals associated with tectonic activity in depth remains slim.

Currently, it is clear that there are gaps in our knowledge, including depths, time scale, range and magnitude of the energy release by pre-seismic geophysical processes and the relationship between radon temporal behavior and these various tectonic processes. Moreover, it seems that there is no proof for the assumption that the radon signal induced by seismo-tectonic processes has to appear with an intensity higher than the climatic-induced periodic signal, except in the case of a high-magnitude earthquake and a measuring system that is located near the event, such as occurred in Kobe, Japan (M = 7.2 at 30 km distance, Igarashi et al., 1995).

Radon, CO_2 and Other Natural Gas in Depth as a Proxy for Investigating Tectonic Pre-seismic Activity

As observed in the Sde Eliezer results, radon signals that are induced by the ambient temperature and pressure have diurnal and semidiurnal periodicity and amplitudes which are variable and not uniform. In general, they preserve the multiday profiles of the atmospheric temperature and barometric pressure as well. Monitoring radon at a depth of several dozen meters, substantially attenuates the climatic contribution and increases the possibility of resolving from the radon temporal spectrum the

preseismic radon signals that are not periodic and are independent from the atmospheric driving forces.

In parallel it was observed that CO_2, within the internal airspace of the borehole at Sde Eliezer, within various depth (5, 20, 40, and 70 m) follows the radon (measured by alpha detector at 40 m) as well as the radon temporal variations at the surrounding bedrock (measured by gamma detectors at 10, 60, and 88 m), and both are driven by the climatic parameters as analyzed for radon (e.g., **Figure 15**). Thus, CO_2 reveals the same daily and semi daily temperature and pressure periodicities in the frequency time domain and clearly responds, simultaneously with radon, to the apparently tectonic pre-seismic driving force, with the same rise, fall, and broadening times.

Improving the sampling rate by 30 times (from 15 min to high 30 s resolution) and implementing four CO_2 detectors at different depths enabled measuring the CO_2 velocity in the Sde-Eliezer borehole under the influence of barometric pressure that seems to be more effective than temperature within the air space inside the open well (Levintal et al., 2020).

Similar to radon, the high CO_2 concentration above the atmospheric content (about 400 ppm) and up to 2,800 ppm at Sde-Eliezer site, entered the sealed borehole's iron casing through the perforated lower sections below 80 m, and then degassing into the sealed casing from the water table. The source of the high CO_2 content could be the microbial activity within the vadose zone, or the presence of an organic substance (peat/lignite) trapped in the Hula Valley's bedrock. Hence, it is reasonable to assume the same thermodynamic mechanism supplies CO_2 as well as radon to the groundwater.

The above conclusion means that the two gases, radon and CO_2 are driven down within the geological media by the combined temperature ΔT and pressure ΔP gradients. Therefore, they reveal the same daily and semi-daily periodicity (**Figure 15**).

Now, it is expected that recovering of non-periodic broadening of radon and CO_2 signals, enables eliminating the climatic-induced periodic contributions and extract the residual portion of the radon and CO_2 signals related to the regional tectonic pre-seismic processes, and could be used as earthquake precursors before the main rupture occurs. It is not essential that each one of these geodynamic processes will end as an earthquake.

In order to use the CO_2 temporal variations as a proxy for pre-seismic activity its concentration within the geological media, should be at least twice as high as the atmospheric contents of about 400 ppm. Otherwise, any change will only be a fluctuation of the atmospheric concentration by few tens of ppm under the influence of the barometric pressure, as measured at Nachal Mor site (Zafrir et al., 2019) or even reaching lower levels as 200 ppm in isolated tunnels as in Amram site (Zafrir et al., 2013). The results at Nachal Mor for example, prove that there are no organic materials in rocks and soil around the Dead Sea and they are not the source of radon there either (Kronfeld et al., 1991).

Another important result that emerged is our deep gas monitoring technology. The technology may become a useful tool for the investigation of seismic precursors since similarly to radon and CO_2, the existence of any natural gas such as nitrogen, oxygen, methane, hydrogen sulfide, carbon monoxide and helium within deep subsurface media can serve as a proxy for pre-seismic precursory phenomena.

In general, any geodynamic process that causes stress or strain release affects subsurface fluids, irrespectively if the process will finally produce an earthquake or not.

DATA AVAILABILITY STATEMENT

The raw data supporting the conclusions of this article will be made available by the authors, without undue reservation.

AUTHOR CONTRIBUTIONS

H.Z. Conceptualization, Methodology, Fieldwork, Writing – original draft, Data Analysis, and Presentation. S.B. Conceptualization, Methodology, Writing, Review & editing, and Data analysis. E.L. Conceptualization, Methodology, Fieldwork, Formal analysis. N.W. Supervision, Conceptualization, Methodology, and Review. Y.H. Conceptualization, Methodology, Seismology and Data analysis. Z.Z. Conceptualization, Methodology, Data analysis and Methods, and Review.

ACKNOWLEDGMENTS

The authors would like to thank Dr Heiko Woith and Dr Vivek Walia for the very careful, constructive and throughout review and for the significantly improving the clarity and the quality of this paper. The authors would like to gratefully thank and honor Mr. Haim Hemo who worked for many years at the Geological Survey of Israel (GSI) and passed away in October 2018. He was a tireless worker and a supporting pillar in all of the field work since 2012. The authors acknowledge and honor Dr Gideon Steinitz who also passed away in July 2017 for the cooperation offered to the team, allowing to perform the research, from 2007 to 2012, within the partially supporting funds the Ministry of Energy of Israel (grants 25-017-13, 27-17-058, 28-17- 011, 29-17-004), and for constructive and valuable joint discussions on radon as natural tracer in general, and for cooperating with the publication of the two manuscripts in 2009 and 2011, in particular. Mr. Uri Malik from GSI and Mr. Raz Amir from Ben-Gurion University of the Negev assisted in the data collection and the field work. Many thanks to Dr Yossi Guttman from Mekorot Israel National Water Co., Tel-Aviv, Israel, for the permission to install the research system in the abandoned water well at Sde-Eliezer site in The Hula Valley. The data used in this study were acquired also in the framework of activity supported by the Ministry of Energy, Israel (grant 216-17-010, and 11-17-2012).

REFERENCES

Aharonov, E., and Scholz, C. H. (2018). A physics-based rock friction constitutive law: steady state friction. *J. Geophys. Res. Solid Earth.* 123, 1591–1614. doi:10.1002/2016jb013829

Akerblom, G., Andersson, P., and Clevensjö, B. (1984). Soil gas radon—a source for indoor radon daughters. *Radiat. Protect. Dosim.* 7, 49–54. doi:10.1093/oxfordjournals.rpd.a082961

Alam, A., Wang, N., Zhao, G., and Barkat, A. (2020). Implication of radon monitoring for earthquake surveillance using statistical techniques: a case study of Wenchuan earthquake. *Geofluids* 2020, 14. doi:10.1155/2020/2429165

Al-Zoubi, A. S., Abu-Hamatteh, Z. S. H., and Abdealkaderer, A. (2006). The seismic hazard assessment of the Dead Sea rift, Jordan, *J. Afr. Earth Sci.* 45, 489–501. doi:10.1016/j.jafrearsci.2006.04.007

Atkins, M. L., Santos, I. R., Perkins, A., and Maher, D. T. (2016). Dissolved radon and uranium in groundwater in a potential coal seam gas development region (Richmond River Catchment, Australia). *J. Environ. Radioact.* 154, 83–92. doi:10.1016/j.jenvrad.2016.01.014

Barberio, M., Gori, F., Barbieri, M., Billi, A., Devoti, R., Doglioni, C., et al. (2018). Diurnal and semidiurnal cyclicity of radon (222Rn) in groundwater, giardino spring, central apennines, Italy. *Water* 10, 1276. doi:10.3390/w10091276

Barbosa, S. M., Zafrir, H., Malik, U., and Piatibratova, O. (2010). Multiyear to daily radon variability from continuous monitoring at the Amram tunnel, southern Israel. *Geophys. J. Int.* 182 (2), 829–842. doi:10.1111/j.1365-246x.2010.04660.x

Barkat, A., Ali, A., Hayat, U., Crowley, Q. G., Rehman, K., Siddique, N., et al. (2018). Time series analysis of soil radon in Northern Pakistan: implications for earthquake forecasting. *Appl. Geochem.* 97, 197–208. doi:10.1016/j.apgeochem.2018.08.016

Cannelli, V., Piersanti, A., Galli, G., and Melini, D. (2018). Italian radon monitoring network (IRON): a permanent network for near real-time monitoring of soil radon emission in Italy. *Ann. Geophys.* 61 (4), 444. doi:10.4401/ag-7604

Cannelli, V., Piersanti, A., Spagnuolo, E., and Galli, G. (2016). Preliminary analysis of radon time series before the M=6 Amatrice earthquake: possible implications for fluid migration. *Ann. Geophys.* 59, 1–7. doi:10.4401/ag-7166

Choubey, V. M., Arora, B. R., Barbosa, S. M., Kumar, N., and Kamra, L. (2011). Seasonal and daily variation of radon at 10m depth in borehole, Garhwal Lesser Himalaya, India. *Appl. Radiat. Isot.* 69 (7), 1070–1078. doi:10.1016/j.apradiso.2011.03.027

Cicerone, R. D., Ebel, J. E., and Britton, J. (2009). A systematic compilation of earthquake precursors. *Tectonophysics* 476, 371–396. doi:10.1016/j.tecto.2009.06.008

Cigna, A. (2005). Radon in caves. *Int. J. Speleol.* 34, 1. doi:10.5038/1827-806X.34.1.1.

Dai, A., and Wang, J. (1999). Diurnal and semidiurnal tides in global surface pressure fields. *J. Atmos. Sci.* 56, 3874–3891. doi:10.1175/1520-469(1999)056<3874:DASTIG>2.0.CO;210.1175/1520-0469(1999)056<3874:dastig>2.0.co;2

Eff-Darwich, A., Martín-Luis, C., Quesada, M., de la Nuez, J., and Coello, J. (2002). Variations on the concentration of222Rn in the subsurface of the volcanic island of Tenerife, Canary Islands. *Geophys. Res. Lett.* 29 (22), 26. doi:10.1029/2002GL015387

Etiope, G., and Martinelli, G. (2002). Migration of carrier and trace gases in the geosphere: an overview. *Phys. Earth Planet. Inter.* 129, 185–204. doi:10.1016/S0031-9201(01)00292-8

Falsaperla, S., Neri, M., Di Grazia, G., Langer, H., and Spampinato, S. (2017). What happens to in-soil Radon activity during a long-lasting eruption? Insights from Etna by multidisciplinary data analysis. *G-cubed* 18, 2162. doi:10.1002/2017GC006825

Fleischer, R. L. (1981). Dislocation model for radon response to distant earthquakes. *Geophys. Res. Lett.* 8 (5), 477–480. doi:10.1029/GL008i005p00477

Fleischer, R. L., Turner, L. G., and George, A. C. (1984). Passive measurement of working levels and effective diffusion constants of radon daughters by the nuclear track technique. *Health Phys.* 47 (1), 9–19. doi:10.1097/00004032-198407000-00001

Fu, C.-C., Walia, V., Yang, T. F., Lee, L.-C., Liu, T.-K., Chen, C.-H., et al. (2017). Preseismic anomalies in soil-gas radon associated with 2016 M 6.6 Meinong earthquake, Southern Taiwan. *Terr. Atmos. Ocean Sci.* 28, 787–798. doi:10.3319/TAO.2017.03.22.01

Fujiyoshi, R., Sakamoto, K., Imanishi, T., Sumiyoshi, T., Sawamura, S., Vaupotic, J., et al. (2006). Meteorological parameters contributing to variability in 222Rn activity concentrations in soil gas at a site in Sapporo, Japan. *Sci. Total Environ.* 370, 224–234. doi:10.1016/j.scitotenv.2006.07.007

George, A. C. (1984). Passive, integrated measurement of indoor radon using activated carbon. *Health Phys.* 46 (4), 867–872. doi:10.1097/00004032-198404000-00012

George, A. C. (1990). An overview of instrumentation for measuring environmental radon and radon progeny. *IEEE Trans. Nucl. Sci.* 37, 892–901. doi:10.1109/23.106733

Ghosh, D., Deb, A., and Sengupta, R. (2009). Anomalous radon emission as precursor of earthquake. *J. Appl. Geophys.* 69, 67–81. doi:10.1016/j.jappgeo.2009.06.001

Gitterman, Y., Hofstetter, A., and Pinsky, V. (2005). (GII) Report No. 554/163/05. Beit-alfa calibration experiment. Geophysical Institute of Israel.

Groves-Kirkby, C. J., Denman, A. R., Crockett, R. G. M., and Phillips, P. S. (2004). "Periodicity in domestic radon time series—evidence for earth tides," in 11th International congress of the international radiation protection association (IRPA11-6a27), Madrid, Spain, May 23–28, 2004.

Hakl, J., Csige, I., Hunyadi, I., Várhegyi, A., and Géczy, G. (1996). Radon transport in fractured porous media - experimental study in caves. *Environ. Int.* 22 (1), 433–437. doi:10.1016/S0160-4120(96)00143-2

Hassan, N. M., Hosoda, M., Ishikawa, T., Sorimachi, A., Sahoo, S. K., Tokonami, S., et al. (2009). Radon migration process and its influence factors; review. *Jpn. J. Health Phys.* 44 (2), 218–231. doi:10.5453/jhps.44.218

Hurwitz, S., Garfunkel, Z., Ben-Gai, Y., Reznikov, M., Rotstein, Y., and Gvirtzman, H., (2002). The tectonic framework of a complex pull-apart basin: seismic reflection observations in the Sea of Galilee, Dead Sea transform. *Tectonophysics* 359, 289–306. doi:10.1016/S0040-1951(02)00516-4

Ichitsubo, H., and Yamada, Y. (2004). Effect of a grounded object on radon measurement using AlphaGUARD. *Health Phys.* 87 (1), 79–81. doi:10.1097/00004032-200407000-00010

Igarashi, G., Saeki, S., Takahata, N., Sumikawa, K., Tasaka, S., Sasaki, Y., et al. (1995). Ground-water radon anomaly before the Kobe earthquake in Japan. *Science* 269, 60–61. doi:10.1126/science.269.5220.60

Ivanovich, M., and Harmon, R. S. (Editors) (1982). *Uranium-series disequilibrium: applications to environmental problems*. Oxford, UK: Oxford Science Publications, 1–32.

Jönsson, G. (1997). The nuclear track detector—a tool in radon measurements. *Radiat. Meas.* 28 (6), 695–698. doi:10.1016/S1350-4487(97)00166-2

King, C.-Y. (1986). Gas geochemistry applied to earthquake prediction: an overview. *J. Geophys. Res.* 91, 12269–12281. doi:10.1029/jb091ib12p12269

Knoll, G. F. (2000). *Radiation detection and measurement*. Hoboken, NJ, USA, John Wiley & Sons.

Koch, U., and Heinicke, J. (1996). Radon behavior in mineral spring water of bad brambach (vogtland, Germany) in the temporal vicinity of the 1992 Roermond earthquake, the Netherlands. *Int. J. Rock Mech. Min. Sci. Geomech. Abstr.* 33, 5A. doi:10.1016/0148-9062(96)87376-1

Kockum, S. W. (2002). *Digital signal processing: a practical guide for engineers and scientists*. Oxford, UK: Newnes Publ., ISBN 0-7506-7444-X.

Kronfeld, J., Ilani, S., and Strull, A. (1991). Radium precipitation and extreme 238U-series disequilibrium along the Dead Sea coast, Israel. *Appl. Geochem.* 6, 355–361. doi:10.1016/0883-2927(91)90011-d

Levintal, E., Dragila, M. I., Zafrir, H., and Weisbrod, N. (2020). The role of atmospheric conditions in CO_2 and radon emissions from an abandoned water well. *Sci. Total Environ.* 722, 137857. doi:10.1016/j.scitotenv.2020.137857

Levintal, E., Zafrir, H., Dragila, M. I., and Weisbrod, N. (2018). The role of atmospheric conditions in driving air movement along a deep borehole using radon and CO_2 mutual relation. *Geophys. Res. Abstr.* 20, 6075.

Lucas, H. F. (1957). Improved low-level alpha scintillation counting for radon. *Rev. Sci. Instrum.* 68, 680–683. doi:10.1148/68.2.258

Martin-Luis, M. C., Steinitz, G., Soler, V., Quesada, M. L., and Casillas, R. (2015). 222Rn and CO_2 at las cañadas caldera (Tenerife, Canary islands). *Eur. Phys. J. Spec. Top.* 224 (4), 641–657. doi:10.1140/epjst/e2015-02397-7

Mentes, G., and Eper-Pápai, I. (2015). Investigation of temperature and barometric pressure variation effects on radon concentration in the Sopronbánfalva Geodynamic Observatory, Hungary. *J. Environ. Radioact.* 149, 64–72. doi:10.1016/j.jenvrad.2015.07.015

Mogro-Campero, A., and Fleischer, R. L., (1977). Subterrestrial fluid convection: a hypothesis for long distance migration of radon within the earth. *Earth Planet Sci. Lett.* 34, 321–325. doi:10.1016/0012-821X(77)90017-6.

Monnin, M., Morin, J. P., and Seidel, J. L. (1993). A comprehensive approach of radon measurements for geophysical studies. *Nucl. Tracks Radiat. Meas.* 22(4), 403–411. doi:10.1016/0969-8078(93)90095-l

Muga, J.. (2017). Geochemical assessment for morendat East geothermal prospect, using radon and carbondioxide concentration from soil, Kenya, *J. Geol. Resour. Eng.* 1, 38–47. doi:10.17265/2328-2193/2017.01.004.

Muramatsu, H., Tashiro, Y., Hasegawa, N., Misawa, C., and Minami, M. (2002). Seasonal variations of 222Rn concentrations in the air of a tunnel located in Nagano city. *J. Environ. Radioact.* 60, 263–274. doi:10.1016/s0265-931x(01)00085-6

Neri, M., Ferrera, E., Giammanco, S., Currenti, G., Cirrincione, R., Patanè, G., et al. (2016). Soil radon measurements as a potential tracer of tectonic and volcanic activity. *Sci. Rep.* 6, 24581. doi:10.1038/srep24581

Nield, D. A., and Bejan, A. (2006). *Convection in porous media*. New York: Springer. ISBN 978-1-4614-5541-7.

Noguchi, M., and Wakita, H. (1977). A method for continuous measurement of radon in groundwater for earthquake prediction. *J. Geophys. Res.* 82, 1353–1357. doi:10.1029/jb082i008p01353

Oh, Y., and Kim, G. (2015). A radon-thoron isotope pair as a reliable earthquake precursor. *Sci. Rep.* 5, 13084. doi:10.1038/srep13084.

Percival, D. B. (2008). "Analysis of geophysical time series using discrete wavelet transforms: an overview," in *Lecture notes in Earth Sciences*. Editors R. V. Donner and S. M. Barbosa (Berlin, Germany: Springer), 112, 61–79. ISBN 978-3-540-78937-6.

Perrier, F., and Girault, F. (2013). Harmonic response of soil radon-222 flux and concentration induced by barometric oscillations. *Geophys. J. Int.* 195 (2), 945–971. doi:10.1093/gji/ggt280.

Pinault, J. L., and Baubron, J. C. (1996). Signal processing of diurnal and semidiurnal variations in Radon and atmospheric pressure, moisture, and soil temperature data: a new approach for radon concentration modeling. *J. Geophys. Res.* 101 (B2), 31573171. doi:10.1029/95jb03121

Przylibski, T. A. (2001). Radon and its daughter products behavior in the air of an underground tourist route in the former arsenic and gold mine in zloty stok (Sudety Mountains, SW Poland). *J. Environ. Radioact.* 57 (1), 87–103. doi:10.1016/s0265-931x(01)00012-1

Richon, P., Perrier, F., Sabroux, J.-C., Trique, M., Ferry, C., Voisin, V., et al. (2005). Spatial and time variations of radon-222 concentration in the atmosphere of a dead-end horizontal tunnel. *J. Environ. Radioact.* 78 (2), 179–198. doi:10.1016/j.jenvrad.2004.05.001

Riggio, A., and Santulin, M. (2015). Earthquake forecasting: a review of radon as seismic precursor. *Boll. Geofis. Teorica.* 56 (2), 95–114. doi:10.4430/bgta0148

Rogers, V. C., and Nielson, K. K. (1991). Multiphase radon generation and transport in porous materials. *Health Phys.* 60, 807–815. doi:10.1097/00004032-199106000-00006

Sahu, P., Panigrahi, D. C., and Mishra, D. P. (2016). A comprehensive review on sources of radon and factors affecting radon concentration in underground uranium mines. *Environ. Earth Sci.* 75, 617. doi:10.1007/s12665-016-5433-8

Schubert, M., and Schulz, H. (2002). Diurnal radon variations in the upper soil layers and at the soil-air interface related to meteorological parameters. *Health Phys.* 83 (1), 91–96. doi:10.1097/00004032-200207000-00010

Siino, M., Scudero, S., Cannelli, V., Piersanti, A., and D'Alessandro, A. (2019). Multiple seasonality in soil radon time series. *Sci. Rep.* 9, 8610. doi:10.1038/s41598-019-44875-z

Singh, S., Jaishi, H. P., Tiwari, R. P., and Tiwari, R. C. (2017). Time series analysis of soil radon data using multiple linear regression and artificial neural network in seismic precursory studies. *Pure Appl. Geophys.* 174, 2793–2802. doi:10.1007/s00024-017-1556-4

Skelton, A., Andrén, M., Kristmannsdóttir, H., Stockmann, G., Mörth, C.-M., Sveinbjörnsdóttir, Á., et al. (2014). Changes in groundwater chemistry before two consecutive earthquakes in Iceland, *Nat. Geosci.* 7, 752–756. doi:10.1038/ngeo2250

Steinitz, G., Begin, Z. e. B., and Gazit-Yaari, N. (2003). Statistically significant relation between radon flux and weak earthquakes in the Dead Sea rift valley. *Geol.* 31, 505–508. doi:10.1130/0091-7613(2003)031<0505:ssrbrf>2.0.co;2

Steinitz, G., and Piatibratova, O. (2009). Radon signals in the gavnunim intrusion, Makhtesh Ramon, Israel. *Geophys. J. Int.* 180 651665. doi:10.1111/j.1365- 246X.2009.04450.x.

Steinitz, G., Piatibratova, O., and Barbosa, S. M. (2007). Radon daily signals in the elat granite, southern Arava, Israel, *J. Geophys. Res.* 112, B10211. doi:10.1029/2006JB004817.

Steinitz, G., Vulkan, U., Lang, B., Gilat, A., and Zafrir, H. (1992). Radon emanation along border faults of the rift in the Dead Sea area. *Isr. J. Earth Sci.* 41, 9–20.

Torres-González, P., Moure-García, D., Luengo-Oroz, N., Villasante-Marcos, V., Soler, V., Iribarren, I. E., et al. (2019). Spatial and temporal analysis of temperature and gaseous emission inside a gallery in an active volcanic island (tenerife, canary islands). *Pure Appl. Geophys.* 176, 3467. doi:10.1007/s00024-019-02174-8

Trique, M., Richon, P., Perrier, F., Avouac, J. P., and Sabroux, J. C. (1999). Radon emanation and electric potential variations associated with transient deformation near reservoir lakes. *Nature* 399, 137–141. doi:10.1038/20161

Van der Spoel, W. H. (1998). Radon transport in sand: a laboratory study. PhD thesis. Eindhoven (The Netherlands): Technical University Eindhoven.

Van der Spoel, W. H., Van der Graaf, E. R., and de Meijer, R. J. (1998). Combined diffusive and advective transport of radon in a homogeneous column of dry sand. *Health Phys.* 74, 48–63. doi:10.1097/00004032-199801000-00006

Vaupotič, J., Riggio, A., Santulin, M., Zmazek, B., and Kobal, I. (2010). Radon anomaly in soil gas at Cazzaso, NE Italy, as a precursor of an ML = 5.1 earthquake. *Nukleonika* 55 (4), 507–511.

Vulkan, U., Lang, B., and Steinitz, G. (1995). Electronic monitoring of radon in soil and water at the Northwestern Dead Sea area, first results. Isr. Geol. Surv. Rep. GSI/45/95, and SNRC Rep. ZD/179/95.

Vulkan, U., Steinitz, G., Strull, A., and Zafrir, H. (1992). Long-distance (+100 m) transport of radon in syenitic rocks at Makhtesh Ramon, Israel. *J. Nucl. Geophys.* 6 (2), 261–271. ISSN 0886-0130.

Walia, V., Virk, H. S., Yang, T. F., Mahajan, S., Walia, M., and Bajwa, B. S. (2005). Earthquake prediction studies using radon as a precursor in N-W himalayas, India: a case study. *Terr. Atmos. Ocean Sci.* 16 (4), 775–804. doi:10.3319/tao.2005.16.4.775(gig)

Wang, C.-Y., and Manga, M. (2010). Hydrologic responses to earthquakes and a general metric. *Geofluids* 10, 206–216. doi:10.1111/j.1468-8123.2009.00270.x

Weinberger, R., Gross, M. R., and Sneh, A. (2009). Evolving deformation along a transform plate boundary: example from the Dead Sea Fault in northern Israel. *Tectonics* 28 (5), 1–19. doi:10.1029/2008tc002316

Wertheim, D., Gillmore, G., Brown, L., and Petford, N., (2010). A new method of imaging particle tracks in solid state nuclear track detectors. *J. Microsc.* 237, 1–6. doi:10.1111/j.1365-2818.2009.03314.x.

Woith, H., Petersen, G. M., Hainzl, S., and Dahm, T. (2018). Review: can animals predict earthquakes? *Bull. Seismol. Soc. Am.* 108, (3A), 1031–1045. doi:10.1785/0120170313

Zafrir, H. (2007). "The diurnal, multiday and seasonal evolution of Rn-222 within rocks along the Dead Sea Transform in relevance to earthquakes related phenomena," in Eos Trans. AGU 88 (52), Fall meeting Suppl. Abstract T43A-1080.

Zafrir, H. (2008). The evolution, transportation and variation in time of Rn-222 within rocks in a desert region. *Geophys. Res. Abstr.* 10, , 2008 EGU2008-A-05386.

Zafrir, H., Barbosa, S. M., and Malik, U. (2013). Differentiation between the effect of temperature and pressure on radon within the subsurface geological media. *Radiat. Meas.* 49, 39–56. doi:10.1016/j.radmeas.2012.11.019

Zafrir, H., Ben Horin, Y., Malik, U., Chemo, C., and Zalevsky, Z. (2016). Novel determination of radon-222 velocity in deep subsurface rocks and the feasibility to using radon as an earthquake precursor. *J. Geophys. Res. Solid Earth.* 121, 6346–6364. doi:10.1002/2016JB013033

Zafrir, H., Ginzburg, B., Hrvoic, I., Shirman, B., Gazit-Yaari, N., Steinitz, G., et al. (2003). "Ultra-sensitive monitoring of the geomagnetic field combined with radon emanation as a tool for studying earthquake related phenomena." in AGU, Fall Meeting, April 11, 2003, Available at:https://ui.adsabs.harvard.edu/abs/2003AGUFM.T51E0206Z/abstract.

Zafrir, H., Haquin, G., Malik, U., Barbosa, S. M., Piatibratova, O., and Steinitz, G. (2011). Gamma versus alpha sensors for Rn-222 long-term monitoring in geological environments. *Radiat. Meas.* 46, 611–620. doi:10.1016/j.radmeas.2011.04.027

Zafrir, H., and Malik, U. (2010). "The effect of climatic condition on radon-222 within subsurface media." in The 3rd Ra–Rn international workshop on "The Radium and Radon Isotopes as Environmental Tracers," Jerusalem, Israel, March 14–19, 2010.

Zafrir, H., Malik, U., Levintal, E., Weisbrod, N., Ben Horin, Y., Zalevsky, Z., et al. (2019). "Radon and CO_2 in deep, as a proxy for pre-seismic research," in 15th International conference on gas geochemistry ICGG15, Palermo & Milazzo, 30 September 5 October 2019.

Zafrir, H., Steinitz, G., Malik, U., Haquin, G., and Gazit-Yaari, N. (2009). Response of Radon in a seismic calibration explosion, Israel. *Radiat. Meas.* 44, 193–198. doi:10.1016/j.radmeas.2009.01.002

Conflict of Interest: The authors declare that the research was conducted in the absence of any commercial or financial relationships that could be construed as a potential conflict of interest.

Copyright © 2020 Zafrir, Barbosa, Levintal, Weisbrod, Ben Horin and Zalevsky. This is an open-access article distributed under the terms of the Creative Commons Attribution License (CC BY). The use, distribution or reproduction in other forums is permitted, provided the original author(s) and the copyright owner(s) are credited and that the original publication in this journal is cited, in accordance with accepted academic practice. No use, distribution or reproduction is permitted which does not comply with these terms.

frontiers in Earth Science

ORIGINAL RESEARCH
published: 10 November 2020
doi: 10.3389/feart.2020.575001

Stochastic Models for Radon Daily Time Series: Seasonality, Stationarity, and Long-Range Dependence Detection

Marianna Siino, Salvatore Scudero and Antonino D'Alessandro*

Istituto Nazionale di Geofisica e Vulcanologia, Osservatorio Nazionale Terremoti, Rome, Italy

This study detects the presence of seasonality, stationarity, and long-range memory structures in daily radon measurements from a permanent monitoring station in central Italy. The transient dynamics and the seasonality structure are identified by power spectral analysis based on the continuous wavelet transformation and a clear 1-year periodicity emerges. The stationarity in the data is assessed with the Dickey–Fuller test; the decay of the estimated autocorrelation function and the estimated Hurst exponent indicate the presence of long-range dependence. All the main characteristics of the data have been properly included in a modeling structure. In particular, an autoregressive fractionally integrated moving average (ARFIMA) model is estimated and compared with the classical ARMA and ARIMA models in terms of goodness of fit and, secondarily, of forecast evaluation. An autoregressive model with a noninteger value of the differencing parameter (d = 0.278) resulted to be the most appropriate on the basis of the Akaike Information Criterion, the diagnostic on the residuals, and the root mean squared error. The results suggest that there is statistically significant evidence for not rejecting the presence of long memory in the radon concentration. The radon measurements are better characterized as being stationary, but with long memory and so, the statistical dependence decays more slowly than an exponential decay.

Keywords: autoregressive integrated moving average model, autoregressive fractionally integrated moving average model, continuous wavelet transform, radon, spectral analysis, forecast

OPEN ACCESS

Edited by:
Francesco Italiano, National Institute of Geophysics and Volcanology, Italy

Reviewed by:
Kit Lai, Universiti Brunei Darussalam, Brunei
Dimirios Nikolopoulos, University of West Attica, Greece

****Correspondence:***
Salvatore Scudero
salvatore.scudero@ingv.it

Specialty section:
This article was submitted to Economic Geology, a section of the journal Frontiers in Earth Science

Received: *23 June 2020*
Accepted: *22 September 2020*
Published: *10 November 2020*

Citation:
Siino M, Scudero S and D'Alessandro A (2020) Stochastic Models for Radon Daily Time Series: Seasonality, Stationarity, and Long-Range Dependence Detection. Front. Earth Sci. 8:575001. doi: 10.3389/feart.2020.575001

1. INTRODUCTION

The monitoring of soil radon ($^{222}R_n$) emission is a relevant topic for the risk that this radioactive gas poses to human health but also for its relationship with environmental and geological processes. The radon signals usually present a complex dynamic structure that is directly and indirectly influenced by several factors, such as environmental and climatic conditions of the site and characteristics of the ground soil, tide, and solar effect. (Pinault and Baubron, 1996; Piersanti et al., 2015; Siino et al., 2019b). All these factors have a different effect on the signal, as they can result either in a trend, seasonal, or stochastic component. For instance, climate or tidal forces reflect in a multiple seasonality of the radon time series: hourly, diurnal, multi-day, annual, and even multi-annual cycles have been detected in different studies worldwide (Crockett et al., 2006; Udovičić et al., 2014; Yan et al., 2017; Crockett et al., 2018; Siino et al., 2019b; D'Alessandro et al., 2020). Of particular interest is the role of Rn as a potential earthquake precursor (Barbosa et al.,

2015; Woith, 2015; Baskaran, 2016; Morales-Simfors et al., 2019) because the fracturing processes in the crust could enhance the mobility of Rn toward the surface (Toutain and Baubron, 1999; Woith, 2015). Similarly, anomalies can be the result of weather episodes which cannot be explained by meteorological variables. Whatever the cause, these anomalies can be masked within the signal, and a way to bring them to light would be to de-noise the signal from the trend and/or periodic components (Baykut et al., 2010; Siino et al., 2019b; D'Alessandro et al., 2020). As a matter of fact, it is a challenging task to untangle and properly quantify all of these effects on the radon fluctuations because Rn time series present generally a nonstationary behavior, not constant variability over time and a long-term memory (Donner et al., 2015).

Methodologically, time series analysis techniques are proper statistical tools to extract meaningful characteristics from data. Moreover, because long-term records of environmental variables show often long-range memory, some other tools are usually applied. The fractionally integrated moving average models [ARFIMA (p,d,q)] have been widely used in the literature to describe meteorological variables (Yaya and Fashae, 2015; Bowers and Tung, 2018), pollutants and soil gas (Pan and Chen, 2008; Donner et al., 2015; Belbute and Pereira, 2017; Reisen et al., 2018), and hydrological time series (Montanari et al., 1997; Wang et al., 2007). This class of models is used when the long-term correlations in the data decay more slowly than an exponential form, that is, a typical shape of autocorrelation in the autoregressive moving average [ARMA(p,q)] processes (Box et al., 2015). Furthermore, several studies investigate the predictability of the ARFIMA model assessing multi-step ahead performance with respect to others univariate time series forecasting methods such as a naive method, random walk (with drift), ARMA with trend and seasonality, and the exponential smoothing (Papacharalampous et al., 2018a; Papacharalampous et al., 2018b).

In the literature, the radon data have been described with different methods. Dunn and Henschel (1989) characterize a three-week record at an hourly frequency using simple autoregressive moving-average (ARMA) models. Later, the Box–Jenkins methodology often used in econometrics was applied to describe five-year-long radon time series considering a seasonal integrated, autoregressive moving averages model with exogenous variables (SARIMAX) also adding external covariates such as delayed atmospheric parameters (Stránský and Thinová, 2017). Donner et al. (2015) present complementary methods that have been applied for evaluating the presence of long-range correlations and fractal scaling in environmental radon measurements.

In this study, we analyze a 3-year-long radon concentration signal aiming at the assessment of a model which describes its dynamics with time series methodologies (Shumway and Stoffer, 2017). A comprehensive analysis of the seasonality structure is performed to detect clues about the stationarity and the presence of long-range memory in the data that could be related to geological processes. We estimate some ARFIMA models which explicitly consider simultaneously both the short-term and long-term correlation structures of the series. Moreover, we tested the forecast performance of the obtained models. The novelty of this analysis relies on the simultaneous estimation of seasonality and long-range memory in the estimation of proper ARFIMA stochastic models.

2. MATERIALS AND METHODS

In this section, the time series methods used in the analysis of daily radon measurements are described following Shumway and Stoffer (2017) and Beran (2017). We briefly present some tools useful to check in an observed time series the presence of nonstationarity (in terms of seasonality and trend) and long-range memory behaviors.

The seasonality behavior in the data is studied by power spectral density based on the time-averaged continuous wavelet spectrogram (Daubechies, 1992; Conraria and Soares, 2011). To properly apply the stochastic models, the daily radon time series is examined for the presence of stationarity. The Dickey–Fuller test (Dickey and Fuller, 1979) is used for this purpose to determine the presence of a unit root in an autoregressive model. The presence of long-range memory has been assessed on the data estimating the Hurst exponent (Hurst, 1951) and looking at the shape of the estimated autocorrelation coefficients for several lags. The presence of long-term memory can justify the estimation of the ARFIMA models, and their structure is also explained.

2.1. Spectral Analysis for Seasonal Detection

In this paragraph, we briefly describe the spectral analysis in the time–frequency domain based on continuous wavelet transformation following the notation in Daubechies (1992) and Conraria and Soares (2011).

The space $L^2(\,)$ is the set of square integrable functions satisfying $\int_{-\infty}^{+\infty}|g(t)|^2dt<\infty$ and denoted by the capital letter, G(t) the Fourier transformation of a given function, $G(\omega)=\int_{-\infty}^{+\infty}g(t)e^{(-i\omega t)}dt$. A function $\psi(t)\in L^2(R)$ that satisfies the admissibility condition $\Psi(0)=\int_{-\infty}^{+\infty}\psi(t)dt=0$ is called "mother wavelet," and a doubly indexed family ("wavelet daughters") is generated by scaling and translating $\psi(\cdot)$: $\psi_{\tau,s}(t)=|s|^{-1/2}\psi\left(\frac{t-\tau}{s}\right)$ with $s,\tau\in$ and $s\neq 0$. In this analysis, we use the well-known, quite flexible, and complex-valued Morlet mother wavelet that takes the form $\psi(t)=\pi^{-1/4}e^{i\omega t}e^{-t^2/2}$. The local wavelet power spectrum (WPS) based on the continuous wavelet transformation (CWT) of a given function $g(t)\in L^2(\,)$ with respect to the wavelet family

$$|WPS|_g(\tau,s)=\left|W_{x;\psi}(\tau,s)\right|^2=\left|\int_{-\infty}^{+\infty}g(t)|s|^{-1/2}\psi^*\left(\frac{t-\tau}{s}\right)dt\right|^2 \quad (1)$$

where * represents the complex conjugate operation, s is the scale parameter controlling the wavelet width, and τ controls the wavelet location in the time domain. The wavelet power spectrum **Eq. 1** can be interpreted as the local variance of the time series.

To do a comparison with the classical spectral method, the previous quantity can be averaged over time (τ) obtaining the global wavelet power spectrum,

$$\int_{-\infty}^{+\infty} \left| W_{x;\psi}(\tau, s) \right|^2 d\tau \qquad [2]$$

The peaks in the global power spectral density indicate the prevalent periods in the data. In this study, the wavelet transformation and the computation of the global power spectrum are computed with the *WaveletComp* package (Roesch and Schmidbauer, 2018) in *R* statistical software (Team, 2005).

2.2. Autocorrelation and Partial Autocorrelation Functions

Given a time series $\{y_t\}$, the autocorrelation is the similarity between the observations as a function of the time lag between them. The j^{th} order autocorrelation $\rho(j)$ can be estimated by using the formula

$$\hat{\rho}(j) = \frac{\widehat{Cov}(y_t, y_{t-j})}{\widehat{Var}(y_t)}, \qquad (3)$$

where

$$\widehat{Cov}(y_t, y_{t-j}) = \frac{1}{n-1} \sum_{t=j+1}^{n} (y_t - \bar{y})(y_{t-j} - \bar{y}) \qquad (4)$$

and

$$\widehat{Var}(y_t) = \frac{1}{n-1} \sum_{t=j+1}^{n} (y_t - \bar{y})^2 \qquad (5)$$

In **Eqs. 4 and 5**, $\bar{y}$ is the mean of y_t, and 5 is just the special case of 4 in which $j = 0$. The empirical autocorrelation function (ACF) is $\hat{\rho}(j)$ defined in **Eq. 3**, computed in the data as a function of the lag j.

Moreover, another way to characterize the relationship between $\{y_t\}$ and its lagged values is by the partial autocorrelation function, or PACF. The partial autocorrelation coefficient of order j, $\rho_j^{(j)}$ measures the effect (linear dependence) of y_t on y_{t-j} after removing the effect of $y_{t-1}, y_{t-2}, \ldots y_{t-j-1}$ on both y_t and y_{t-j}. Each partial autocorrelation can be obtained as a series of regressions of the form:

$$y_t = \gamma^{(j)} + \rho_1^{(j)} y_{t-1} + \ldots + \rho_j^{(j)} y_{t-j} + \epsilon_t \qquad (6)$$

The empirical PACF of order J is computed by running 6 for $j = 1, \ldots, J$ and retaining only the estimate $\rho_j^{(j)}$ for each j. The shape of both the sample ACF and PACF provides a way to see which is the pattern of serial dependence, and it may help to suggest which kind of stochastic process would fit well the data.

If $\{y_t\}$ presents long-range memory, the correlation function 3 decays hyperbolically showing a power law distribution (Höll et al., 2019). Clauset et al. (2009) give an overview of the statistical methods that can be used to detect and characterize power law distribution in empirical data.

2.3. The Hurst Coefficient and the Rescaled Range (R/S) Method

The Hurst exponent (H) is an index of long-term memory of time series $\{y_t\}$ originally developed for hydrological data (Hurst, 1950; Hurst et al., 1965). It is defined in asymptotic terms of the rescaled range as $E[R(n)/S(n)] = Cn^H$ as $n \to \infty$, where n is the number of data points in a time series, E is the expected value, C is a constant, $R(n)$ is the range of the first n cumulative deviations from the mean, and $S(n)$ is their standard deviation.

We consider the rescaled range (R/S) method to estimate H (Mandelbrot and Wallis, 1968; Mandelbrot and Wallis, 1969).

Given y_t, the mean is computed ($m = \frac{1}{n}\sum_{i=1}^{n} y_i$) and the mean adjusted series $x_t = y_t - m$ for $t = 1, 2, \ldots, n$. Then, the cumulative series is $z_t = \sum_{i=1}^{t} x_i$, and the range series is $R_t = \max(z_1, z_2, \ldots, z_t) - \min(z_1, z_2, \ldots, z_t)$ for $t = 1, 2, \ldots, n$. A standard deviation series S is computes as $S_t = \sqrt{\frac{1}{t}\sum_{i=1}^{t} (y_i - m(t))^2}$ where m(t) is the mean for the time series values through time t. The following series of the ratio is considered (R_t/S_t) for $t = 1, 2, \ldots, n$.

The Hurst exponent is estimated as the slope of the line between $\log[R_t/S_t]$ and $\log t$. The long memory structure exists when $0 < H < 1$. If $H \geq 1$, the process has infinite variance and is nonstationary. If $0 < H < 0.5$, an antipersistence structure exists; if $0.5 < H < 1$ the series is persistence, instead when $H = 0.5$, the process is a white noise. Other methods have been proposed in the literature to detect the presence of long-range temporal correlations in the presence of nonstationary in the data, that is, the detrended fluctuation analysis (Höll et al., 2019).

2.4. Autoregressive Fractionally Integrated Moving Average Model

Environmental data, and also radon measurements, can exhibit characteristics consistent with long-range memory in time series (Donner et al., 2015). Such characteristics consist in a specific structure of the autocorrelation function of the process.

If $\{y_t\}$ presents long-range memory, correlation function 3 decays hyperbolically, rather than showing the exponential decay that is a characteristic of an ARIMA$(p, 0, q)$ process. A way to characterize long-range dependence in observational data is by fitting autoregressive fractionally integrated moving average (ARFIMA(p, d, q)) models, which are a natural extension of the classic ARIMA(p, d, q) models (Hosking, 1981). The ARFIMA models allow for handling explicitly both the short-term and the long-term correlation structures of a series. Let $\{y_t\}$ be a stationary process, an ARFIMA(p, d, q) process where p and q are integers and d is real, represented as

$$\phi(B)\nabla^d (y_t - x_t\beta) = \theta(B)\epsilon_t \quad t = 1, \ldots, T, \qquad [7]$$

where ∇^d is the fractional differencing operator $\nabla^d = (1-B)^d = \sum_{k=0}^{\infty} \binom{d}{k} (-B)^k$, B is the backward shift operator defined by $By_t = y_{t-1}$, and $\{\epsilon_t\}$ is a white noise with variance σ_ϵ^2. $\phi(B) = 1 - \phi_1 B - \ldots - \phi_p B^p$ and $\theta(B) = 1 - \theta_1 B - \ldots - \theta_q B^q$ are the autoregressive and the moving average operators,

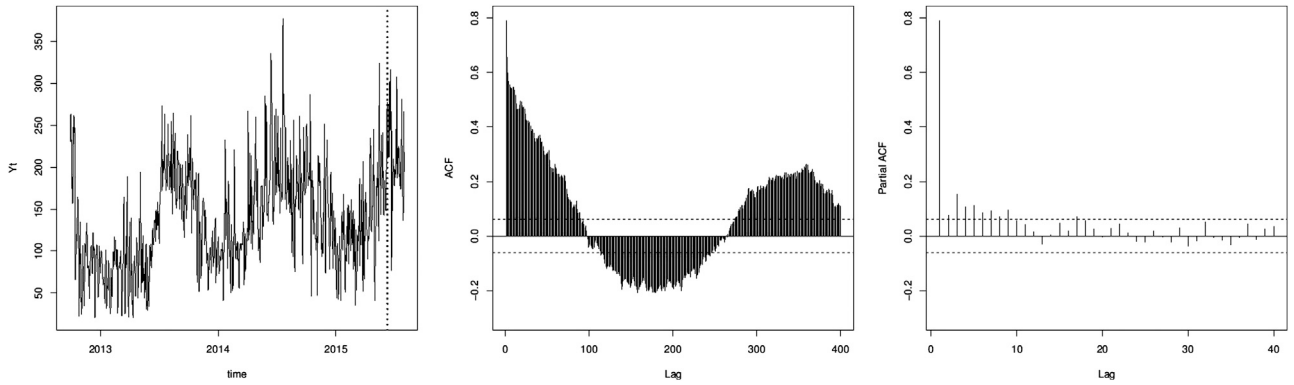


FIGURE 1 | (Left) Data, mean daily radon observations in Bq/m^3 at Pietralunga (Umbria, Italy). The red vertical line separates the training set and the remaining 5% of the test set. **(Central)** Autocorrelation coefficient and **(right)** partial autocorrelation coefficient of the time series.

respectively. Note that the binomial coefficient can be defined for real values of d, $\binom{d}{k}=\frac{d(d-1)(d-2)\ldots(d-k+1)}{k(k-1)(k-2)\ldots1}$ for $k\in\mathbb{N}$ and an arbitrary d.

The row vector x_t contains the exogenous variables, and in our analysis, they are harmonic terms used to describe the seasonality in the radon time series. The parameter d in **Eq. 7** describes the high-lag correlation structure of a time series, while the p and q parameters are chosen to describe the low-lag correlation structure.

An important aspect to assess in a time series is its stationarity; a process is defined as stationary when its mean, variance, or autocorrelation structure remains constant over time. For stationary series, $d \in (-0.5, 0.5)$, and the Hurst exponent associated with the process is given by $H = (2d + 1)/2$. Consequently, long-range memory is present for $d \in (0,\ 0.5)$, while $d \in (-0.5,\ 0)$ indicates antipersistent fluctuations. When $|d| > 0.5$, the process is nonstationary and its variance is infinite. The process exhibits short memory for $d = 0$, corresponding to stationary and invertible ARMA (autoregressive moving average) model. Instead, the arbitrary restriction of d to integer values corresponds to the standard autoregressive integrated moving average (ARIMA) model, and in this case, the variable is $I(d)$, and it becomes stationary after d differences and it is nonstationary after day 1 differences. For instance, an $I(1)$ variable can have a linear trend but no quadratic trend, and it can be transformed into a stationary series with the first-order differences. If a series exhibits long memory, it is neither stationary ($I(0)$) nor it is a unit root process ($I(1)$); it is an $I(d)$ process, with d a real number.

There are statistical tests to check stationarity, named unit root tests. The results are traditionally interpreted as that the effects of one-time shocks to the series are either transitory (if the series is stationary), or permanent (if the series is not stationary). The Dickey–Fuller test (DF) (Dickey and Fuller, 1979) tests the null hypothesis that the series is nonstationary; however, DF only considers the dichotomy between stationarity and nonstationarity. The rejection of the null provides evidence for a stationary series, then the ARMA model can be directly

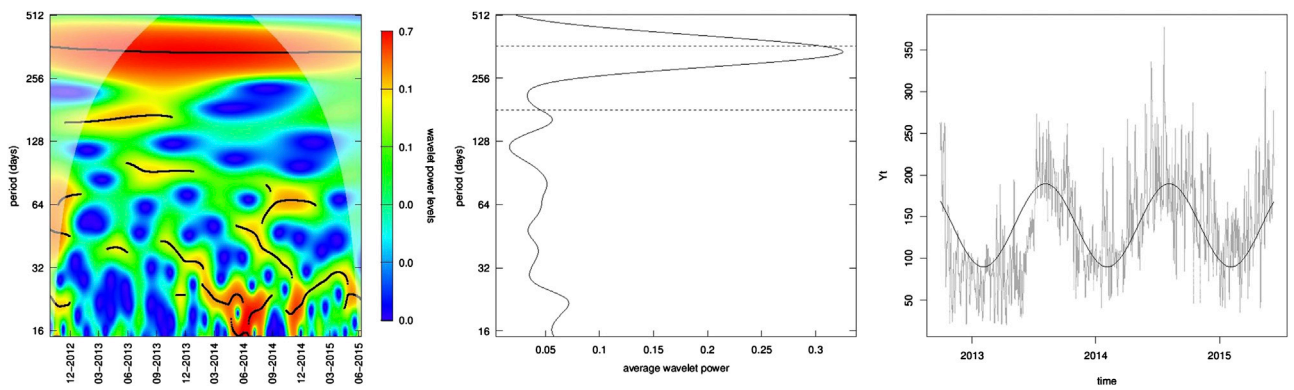


FIGURE 2 | (Left) Wavelet power spectrum of daily radon series in time–frequency domain with the CWT method. The black contour indicates the significant period with 90% confidence level. The lighter shade is the regions influenced by edge effects. **(Central)** The corresponding global power spectrum density marginalizing over time. The horizontal lines are for 180- and 365-day periods. **(Right)** The gray line is the observed time series, and the black curve is the fitted linear regression model with respect to harmonic terms to describe the 1-year periodicity.

TABLE 1 | Estimates of ARFIMA models with different orders where the response variable is the average daily radon measurements in **Figure 1**.

	Models			
	ARFIMA (p,d,q)			
	(0,d,0)	**(1,0,0)**	**(1,d,0)**	**(1,1,0)**
	(a)	**(b)**	**(c)**	**(d)**
ϕ_1	—	0.687*** (0.023)	0.347*** (0.056)	−0.164*** (0.031)
d	0.488*** (0.014)	—	0.278*** (0.045)	—
β_1	−42.570*** (11.336)	−40.101*** (5.007)	−40.966*** (7.293)	−52.456 (82.747)
β_2	34.138*** (11.256)	30.380*** (4.908)	31.942*** (7.183)	33.731 (84.475)
Intercept	139.986 (118.533)	140.042*** (3.519)	141.287*** (11.828)	−0.046 (1.020)
Observations	985	985	985	985
Log likelihood	−3,490.32	−3,484.35	−3,467.65	−3,550.49
AIC	6,990.635	6,978.698	6,947.309	7,110.988
σ^2	1,192.12	1,182.27	1,143.44	1,362.99
Range res	[−127.690; 204.301]	[−108.365; 207.550]	[−104.312; 204.553]	[−135.772; 214.456]
$RMSE_{1lag}$	44.214	44.626	44.511	49.921
$RMSE_{5lag}$	51.719	49.087	49.838	66.994

*Model (a) is a fractional model without autoregressive and moving average terms. Model (b) is an autoregressive model [AR(1)], with d fixed to 0. Model (c) is a fractional autoregressive model. Model (d) is an integrated moving average model with order of integration equals to 1 (d = 1). ϕ_1 is the estimate of the autoregressive coefficient in **Eq. 7**. β_1 and β_2 are associated to the harmonic terms ($\sin(2\pi t\omega)$ and $\cos(2\pi t\omega)$, where t is the time and $\omega = 1/365$) introduced in the model 7 as external variables x_t to describe the observed seasonality at 365-day. The log-likelihood, the Akaike Information Criterion and the range of the model residuals are shown. The root mean square errors (RMSE) for the rolling forecasts at 1- and 5-lag are reported. The significance of the estimates is in terms of p-value.*p < 0.1; **p < 0.05; ***p < 0.01.*

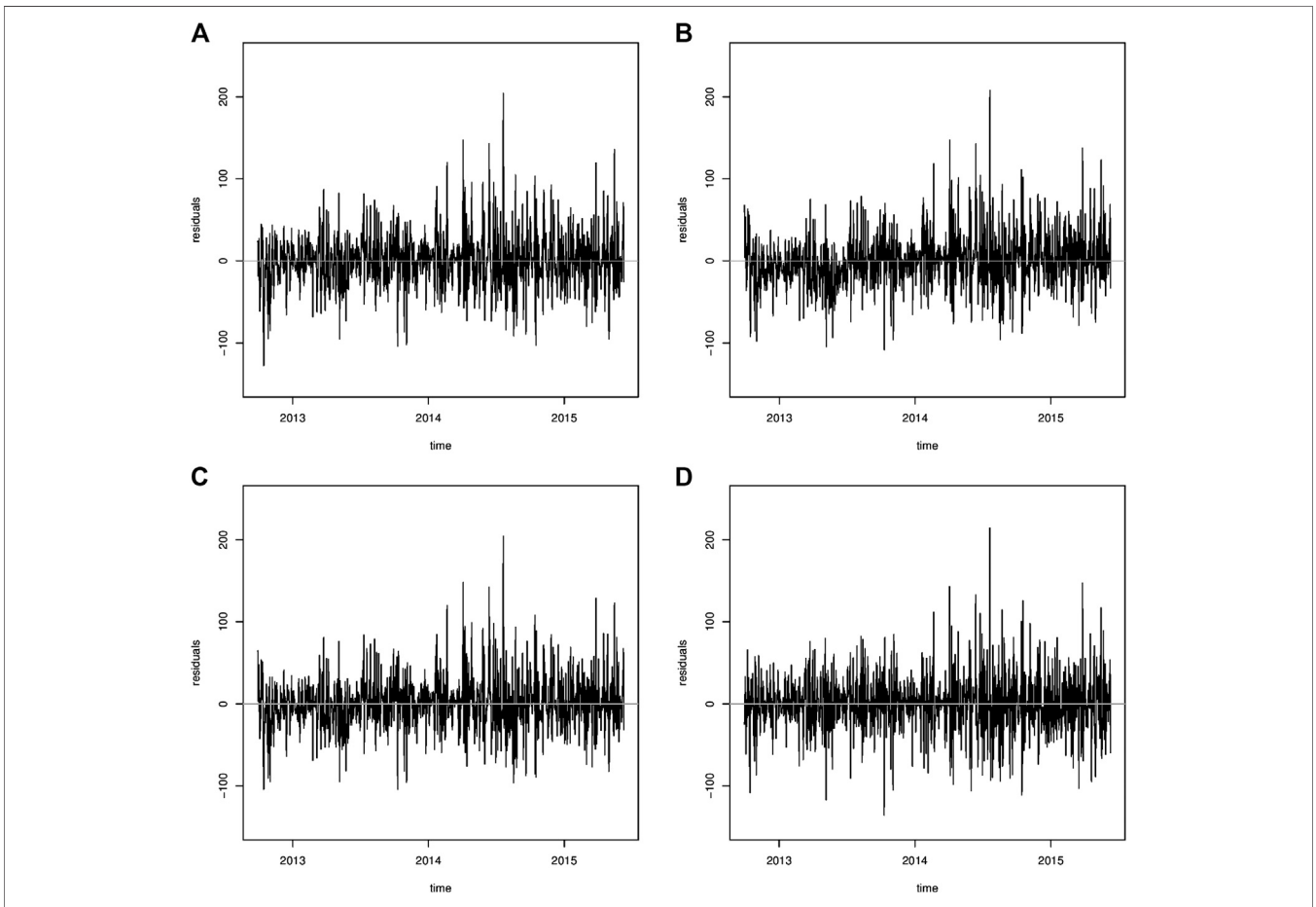


FIGURE 3 | Residual time series for the estimated Models **(A–D)** as labeled in Table 1.

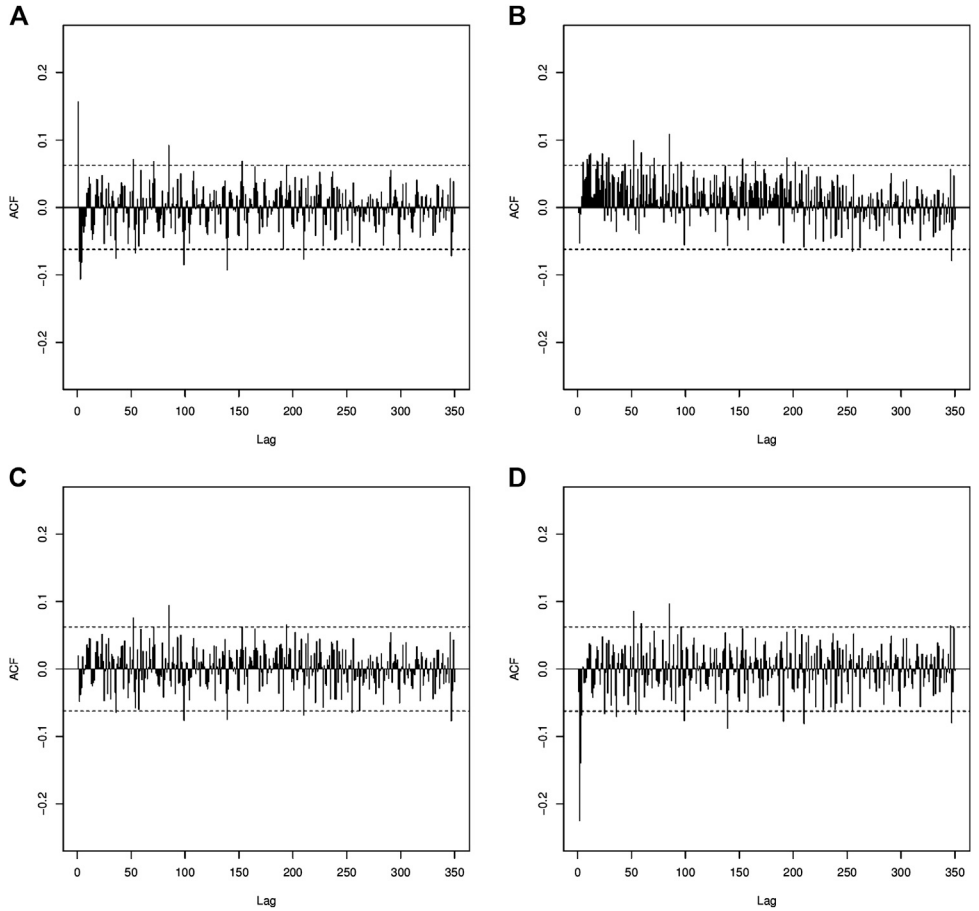


FIGURE 4 | Autocorrelation coefficients of the residuals of the estimated Models **(A–D)** as labeled in **Table 1**. The horizontal lines indicate the confidence interval at 95% for not significant correlation coefficient.

applied. Instead, if the null hypothesis is accepted, the series needs to be made stationary through differencing.

The model in **Eq. 7** is estimated with exact maximum likelihood estimation explained in Veenstra (2013) using *arfima* package of *R* statistical software (Team, 2005). Usually, the model selection is performed evaluating simultaneously the goodness of fit and the forecast performances. The assessment of the goodness of fit can be done using the Akaike Information Criteria, $AIC = 2k - 2ln(L)$, where k is the number of estimated parameters in the model **Eq. 7** and L is the maximized value of the likelihood function for the estimated model, and the model with the smallest AIC value is preferred. Moreover, the assumptions of the model on the random component (ϵ_t) are checked assessing the constant variability, the normality assumption, and the absence of correlation structure in the model residuals ($\widehat{\epsilon_t}$).

The model family in **Eq. 7** is fitted to time series data both to understand the data and to forecast (to predict future points in the series). Forecast evaluation can be done when the observed values are available. Usually, the observed data are divided into training and test samples. The model is fitted to the training sample, and then its k-step ahead forecast performance is evaluated on the test one. The root mean square errors (RMSEs) are used to check the forecast accuracy of the estimated models; it is given by $RMSE = \sqrt{\sum_{i=1}^{n}(y_i - \tilde{y}_i)^2 n^{-1}}$, where y_i is the observed value for the ith observation and $\tilde{y}_i$ is the predicted one.

3. RESULTS

3.1. Data

The analyzed radon time series is recorded at Pietralunga (PTRL, Italy, lat 43.44 N and long 12.44 E) between 28/09/2012 and 01/08/2015 for a total of 1,038 days. The PTRL station is in a framework of near real-time monitoring of soil radon emission to study earthquake preparatory processes, the Italian radon monitoring network (IRON) (Cannelli et al., 2018). The selected station is equipped with a Lucas cell, an alpha scintillation detector with an acquisition window of about 2 h (115 min of data acquisition followed by a 5-min standby time). In detail, the Lucas cell consists of a flask in which the inner surface is coated with silver-activated zinc sulfide (ZnS). It integrates a front-end electronics and measures radon concentration by counting the radon decay signals in the given acquisition window. The radon detector is located in a

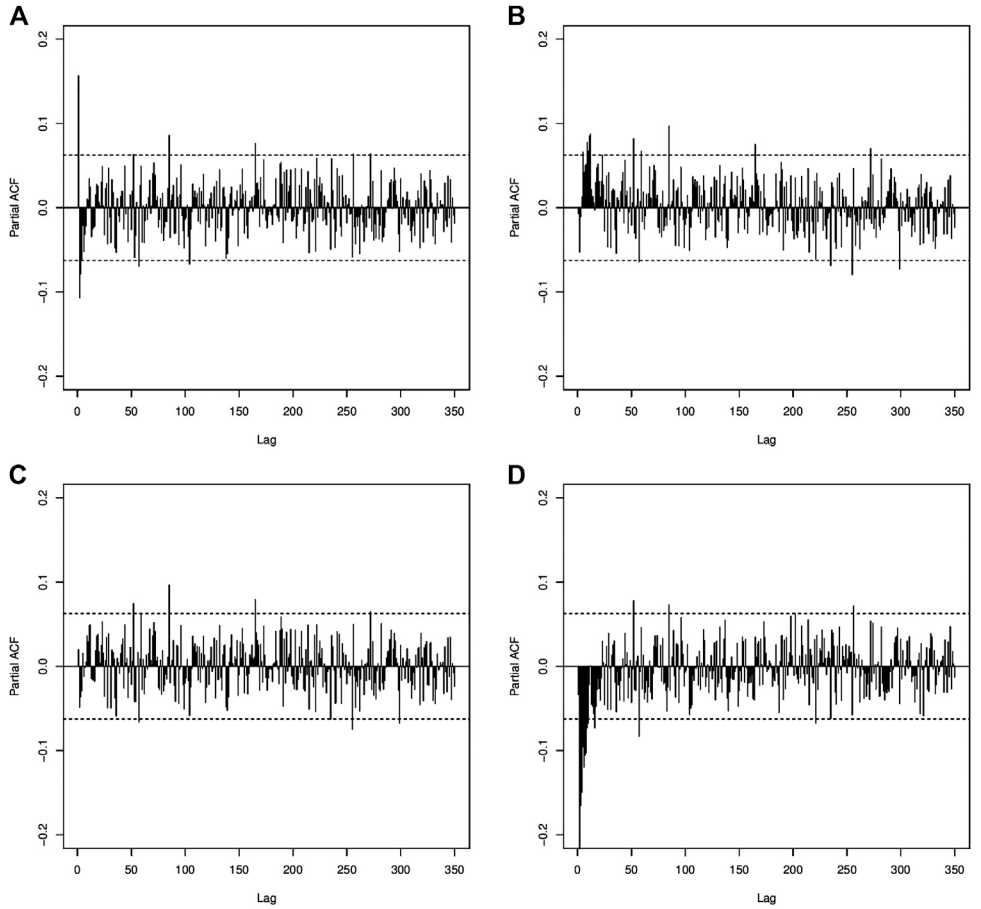


FIGURE 5 | Partial autocorrelation coefficients of the estimated Models **(A–D)** as labeled in **Table 1**. The horizontal lines indicate the 95% confidence bounds for strict white noise.

small room of a school basement, not disturbed by anthropogenic influences and without any kind of opening and/or aeration system. However, the pressure and the temperature could affect the radon measures. The PTRL site is characterized by a contained seasonal variability also if compared with other sites of the same network, even equipped with a borehole probe which should be more immune from such effects (c.f. Figure 2 in Siino et al. (2019b)). The radon concentration is measured in Bq/m^3, becquerel per cubic meter.

The raw time series of the mean daily concentrations is shown in **Figure 1**; the measured values range between 20.35 Bq/m^3 and 377.86 Bq/m^3, and they show a clear seasonal signal connected with the temperature (Cannelli et al., 2018; Siino et al., 2019b), and the higher values are during the summer period.

The 0.87% of the daily data are missing. Generally, it is a challenge to handle missing values, especially for time series data. Two possible ways to deal with the incomplete data can be to omit the entire record that contains information or impute the missing values. However, since a small percentage of the analyzed data presents missing values, they are filled by the weighted moving average method with a semi-adaptive window of 4 days. Weighted moving averages assign a linear weighting to the data points used to perform the imputation.

The data are divided into two subsets: the training set used to do the main analysis and to fit the stochastic models, and the test set (5% of the data identified by a vertical line in **Figure 1**) used to compare the models in terms of forecasts.

3.2. Seasonality, Stationarity, and Long-Memory Detection

We report the main results about the seasonality detection, the autocorrelation, and the long-memory analysis of the observed series. For the study of the dynamical and seasonal behaviors of the observed radon concentrations, we compute the spectral density analysis in the time–frequency domain based on the continuous wavelet transformation. The wavelet power spectrum is shown in **Figure 2** where the period ranges from 16 to 512 days. The time–frequency regions with warm colors are characterized by high power, and the black lines indicate the significant maxima of the undulations of the wavelet power spectrum, and they give an indication of the permanent cycle period. The thick black contour

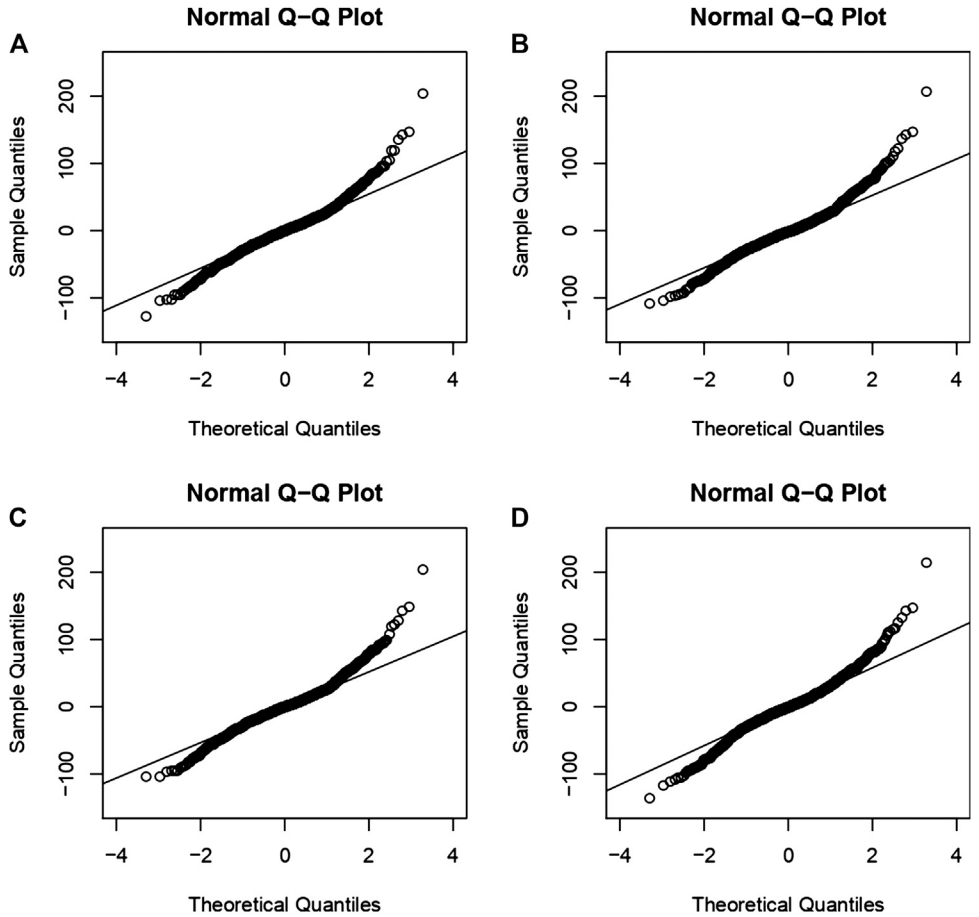


FIGURE 6 | Q-Q norm of the residuals time series for the estimated Models **(A–D)** as labeled in **Table 1** to check the normality assumption.

indicates the 90% confidence level, and the lighter shade indicates regions inside the cone of influence due to the border effect.

Clearly, the series exhibits transient dynamics and the magnitude of the WPS is not constant over time fixing a specific frequency. We can observe a high value of the spectral power density at about 1-year periodicity that is persistently significant. Other high-power periodicities are present, even though not continuous over the entire period. A medium-power, ~180-day cycle is recognizable in the first half of the series, and a ~22-day cycle characterized by high-power appears around summer 2014. These cycles can be also observed in **Figure 2** which shows the global wavelet power spectrum; the horizontal lines provide a reference at 180 and 365 days. The series show a clear 1-year periodicity and subordinate periodicities at about 180 days and three weeks. The longer cycles are probably related to the annual and semiannual cycles of the climatic variables (temperature, pressure, and rainfall), while the ~22-day cycle is likely ascribable to the lunisolar gravitational influence which results in a tide effect on the flux or radon [see Siino et al. (2019b)]. This descriptive analysis is preparatory to decide which seasonality terms include in the model formulation for the explanatory variables (x_t in **Eq. 7**). In particular, we consider harmonic terms to describe the 1-year periodicity that is the only one persistent with a constant power over time. **Figure 2** shows the estimated curves considering a regression linear model fitted on the data with harmonic terms for a 365-day period (with R^2 coefficient equals to 0.34).

The shapes of the correlogram and the partial correlogram provide indication about the properties of the time series and could indicate a plausible structure of the stochastic model in **Eq. 7**. In **Figure 1**, the estimated autocorrelation up to 400 lags seems to decay slower than an exponential one. Also from the autocorrelation, it is clear that the data exhibit a prevalent seasonal cycle which dominates the dependence structure. The partial autocorrelation coefficient is defined as the autocorrelation at each lag after controlling for the autocorrelation due to all preceding lags. It helps determine how many AR terms (i.e., lagged observations as predictors) should be included in **Eq. 7**. If there is a sharp drop in the PACF after p lags, then the previous p-values are responsible for the autocorrelation in the series, and the model should include p autoregressive terms. In our case, the highest and also significant value is at lag 1, with a value of the correlation equals to 0.792, and in the following lags ($p > 1$), the autocorrelation coefficients are close to zero. It indicates that an autocorrelation term ($p = 1$) can be included in the model.

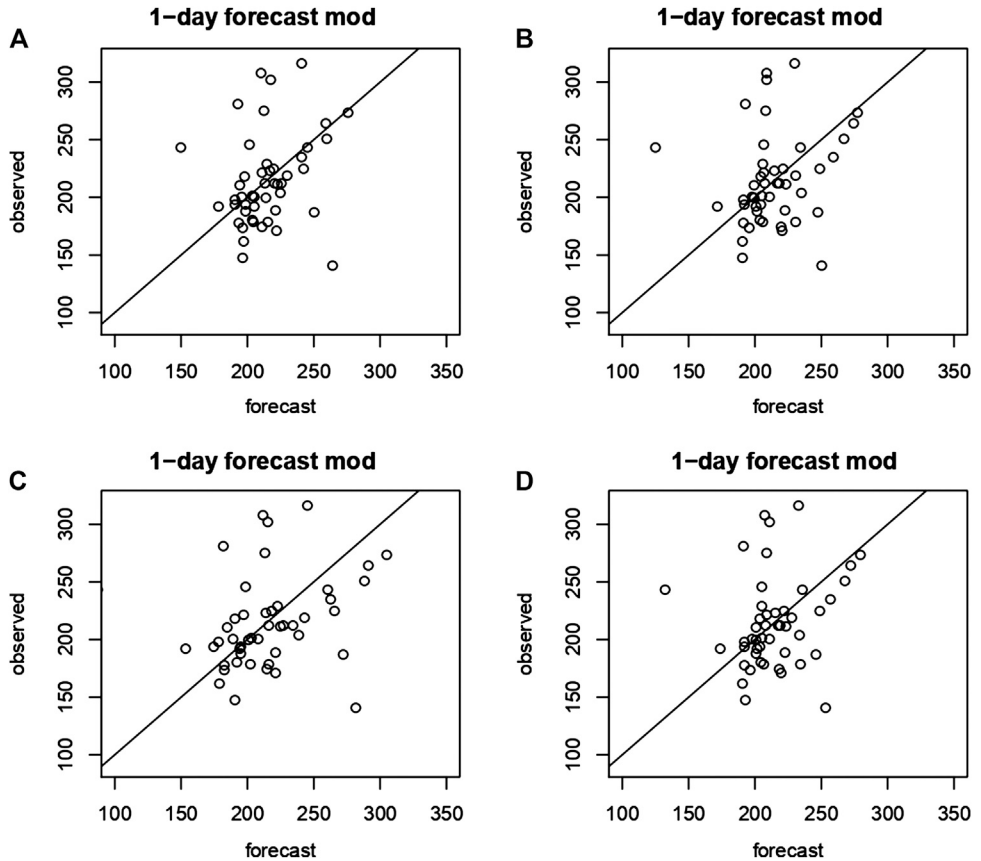


FIGURE 7 | Prediction at 1-lag and observed radon measurements for the estimated Models **(A–D)** as labeled in **Table 1**.

The estimate of the Hurst exponent (H) with the rescaled range analysis (**Section 2.3**) is used to assess the presence of long memory. The obtained value is 0.785 indicating that the mean daily measurements have a persistent long-memory structure since $0.5 < H < 1$. In the literature, there are several results consistent with our analysis. For instance, in Cuculeanu et al. (1996), the determined values of Hurst's coefficient (0.809) highlight a persistent behavior of the gas. Also, Nikolopoulos et al. (2018) compute the rescaled range analysis for several time intervals obtaining a persistent Hurst exponent between 0.7 and 0.9 and in some periods between 0.9 and 1.

The Dickey–Fuller test is used to check the null hypothesis that the series is nonstationary, and thus, the rejection of the null provides evidence for a stationary series. The value of the test on the data in **Figure 1** is −5.285, and the value of the p-value (1.53e−07) is lower than the significant level $\alpha = 0.05$, and we can reject the null hypothesis that the series has a unit root and hence is not stationary. According to this result, for our data, integration (first-order differences) is not necessary.

3.3. Modeling Results

The obtained results indicate that the studied radon concentrations present persistent long-memory structure, 1-year seasonality, and an absence of a trend. Also, according to the PACF, an autoregressive term can be appropriate to describe the short-term correlation.

Starting from these evidences, four models are estimated and compared, and all of them have the harmonic terms $(\sin(2\pi t\omega)$ and $\cos(2\pi t\omega))$ as external covariates to describe the seasonality. Four candidate models are estimated:

- Model (a) is a fractional model with $p = q = 0$, ARIMA$(0, d, 0)$

$$\nabla^d (y_t - x_t\beta) = \epsilon_t \quad t = 1, \ldots, T$$

- Model (b) is an ARMA$(1, 0)$, so it is an autoregressive model of order 1 without differencing (also it can be indicated as an ARIMA (1,0,0) model)

$$(1 - \phi_1 B)(y_t - x_t\beta) = \epsilon_t \quad t = 1, \ldots, T$$

- Model (c) is an ARFIMA$(1, d, 0)$ model

$$(1 - \phi_1 B)\nabla^d (y_t - x_t\beta) = \epsilon_t \quad t = 1, \ldots, T$$

- Model (d) is ARIMA$(1, 1, 0)$ model with order of integration equal to $d = 1$

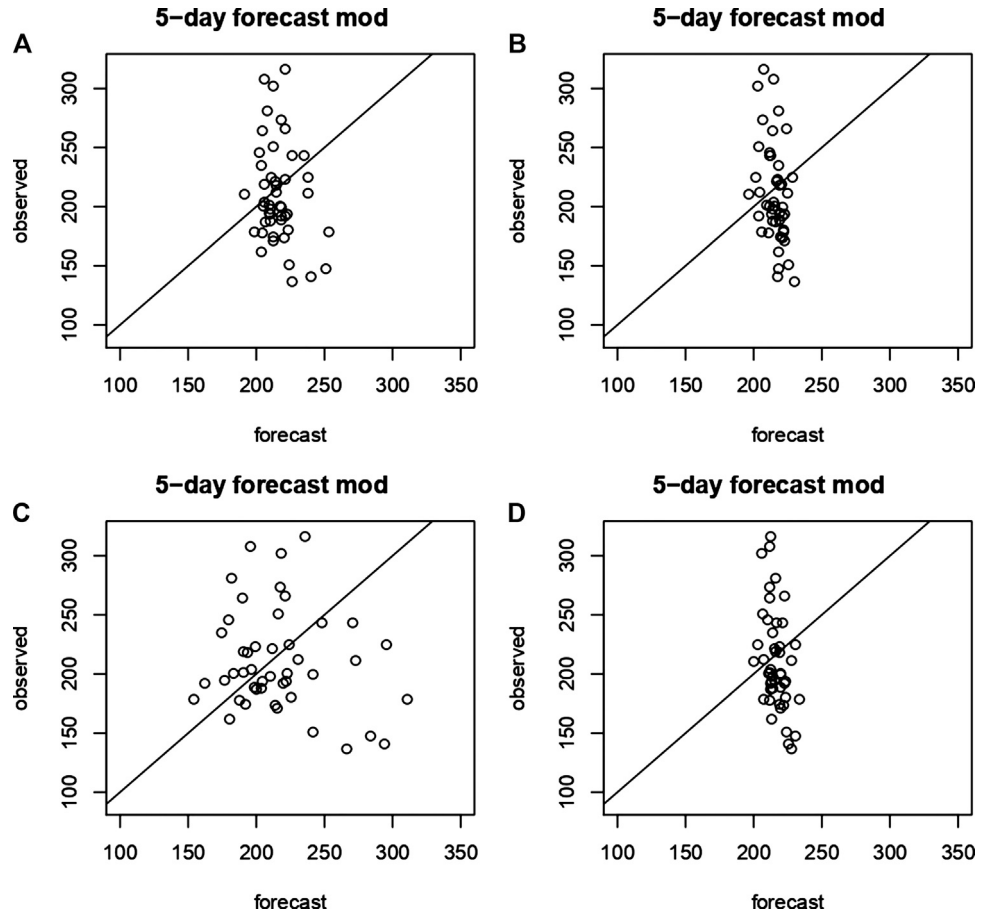


FIGURE 8 | Prediction at 5-lag and observed radon measurements for the estimated Models **(A–D)** as labeled in **Table 1**.

$$(1 - \phi_1 B)\nabla^1 (y_t - x_t\beta) = \epsilon_t \quad t = 1, \ldots, T$$

The Models (b), (c), and (d) have an autoregressive term ($p = 1$) since doing several comparisons, a parsimonious model is obtained without moving average terms ($q = 0$). Only in the Models (a) and (c), the fractional integration parameter is freely estimated. The estimated parameters, their standard errors, and significance are reported in **Table 1**. Also, additional information for each model such as the log-likelihood, the AIC, the range of the residuals, and the RMSE at 1- and 5-lag are shown.

The results of the estimate models suggest that for all of them, the coefficients associated to the harmonic terms are significant, and the comparison with the models without the external covariates are worse (the results are not shown).

Examining the results of Models (a) and (c) where the parameter d is estimated varying in the real values, the fractional parameter for both models is between 0 and 1, thus allowing us to reject both the case of pure stationarity (I = 0) and the unit root model (I = 1). The estimated parameters are statistically significant at the 1% level and lie within the interval (0, 0.5). The confidence intervals for the estimated fractional-integration parameters are relatively narrow and always in the positive range of persistent long-memory.

The results show that Model (c) is the best model in terms of fitting since it has the lowest AIC and the shorter range of the residuals. For the RMSE at 1- and 5-lag forecast, Model (a) performs slightly better than Model (c); however, the fractional model has too simple parametrization, and it is not able to describe the autocorrelation dynamic in the data (see the residuals time series in **Figure 3** and the diagnostics on the residuals **Figures 4**, **5**).

For all the estimated models, the assumption of constant variability along time appears respected (**Figure 3**), and there is not a marked pattern in the residuals, in particular the seasonality behavior in the original data is not present (**Figure 1**). The residual ACF (**Figure 4**) and PACF (**Figure 5**) of the fitted Models (a), (b), and (d) show that there are significant estimated correlation coefficients at short lags; therefore, these models are not adequate. Instead, for the Model (c), the residual ACF and PACF are not significant. The Ljung–Box test from 1 to 10 lags is computed to assess the absence of serial autocorrelation in the residuals. For the model (c), the null hypothesis is not rejected for all the considered lags. The q-q plot of the residuals is used to assess the normality assumption of the considered models. In **Figure 6**, for all the four models, there is a slight departure from the normality in the tails. Finally, the plots of

observed and estimated values obtained with the four model at 1- and 5-lags are shown in **Figures 7**, **8** respectively.

4 DISCUSSION AND CONCLUSIONS

Being sensitive to crustal stress, the soil radon discharge is widely considered as a promising earthquake precursor. Because of the influence of several environmental factors and local geological conditions, pre-seismic radon anomalies cannot be easily detected with conventional statistical methodologies.

The general approach is to model the observation and highlight the anomalies. This study tests a radon concentration time series, covering almost 3 years, for the presence of nonstationarity (seasonality and trend) and long memory. Overall, our results indicate that the radon series are better characterized as being stationary in the trend, but with persistent long-memory and 1-year seasonality. It is widely accepted that the periodic annual component in radon concentration time series is correlated to the climatic variables as temperature, atmospheric pressure, and rainfall (Siino et al., 2019a; Siino et al., 2019b; D'Alessandro et al., 2020).

The class of the ARFIMA model presented here provides a general framework for representing radon time series that display both short- and long-term persistence. The analysis of daily radon shows that the ARFIMA approach provides a better representation of the observed data with respect to the traditional ARMA and ARIMA models. More specifically, according to the model comparison, an ARFIMA model with an autoregressive term has a better fitting to the data. The estimated fractional integration parameters of this ARFIMA model is positive and smaller than 0.5 ($d = 0.278$). It corresponds to a Hurst's coefficient of H=0.778 that is consistent with the results obtained with the rescaled range analysis and in general with other literature results (Cuculeanu et al., 1996; Nikolopoulos et al., 2018). The proposed model has been also assessed in terms of its predictive capacity, however the performances are quite poor especially increasing the lag of prediction (moving from 1-day forecast to 5-day forecast).

The occurrence of long-range correlation in the time series has been also tested by the application of Detrended Fluctuation Analysis (DFA) (Höll et al., 2019). Also, this method indicates that the radon concentration can be considered as coming from a fractional Gaussian noise (fGn).

It is widely recognized that radon time series are strongly controlled by the combination between site-specific factors and large-scale variations (i.e., astronomical cycles) (Schery et al., 1984; Schumann et al., 1988; Aumento, 2002; Piersanti et al., 2015; Crockett et al., 2018). It is note worth that the proposed approach (based only on radon measurements) is able to describe with good reliability the data and also to perform short-term forecasts when accurate radon measurements are taken for a reasonably long time span.

Model residuals could be retrospectively compared with external evidence of transitory phenomena in the study area (seismic, meteorological, etc.). Having available the seismic catalogue of the area, we make an attempt to find the relationship between the found anomalies in the radon time series and the earthquakes. In this case study, there is no evidence between the residuals of the fitted model and the seismicity in the study area. However, it should be considered the absence of any relevant earthquakes during the observation period but only the occurrence of background seismicity. In fact, in spite of the well-known seismicity of the area, the larger recorded event was a $M_w = 3.9$ located at 9.5 km from the radon monitoring site.

In conclusion, our findings on the long-memory nature of radon measurements have important implications that can be useful for further analysis. The long-memory structure is the result of a long-lasting and aperiodic process such as a weather episode and changes in the circulation of geofluids, ground sealing. However, at this stage (i.e., a single time series), it is not possible to propose a comprehensive physical/geological or physical/meteorological mechanism that could account for the long memory in radon concentration time series; moreover, it would also be out of the purpose of this work. The extension of this methodology by applying the ARFIMA models to longer radon time series, or to series with a different measurement range, or recorded in other monitoring sites, could provide the missing hints.

The proposed approach represents an effective tool to analyze radon signals, and in particular to detect long-range memory in the times series, which are the necessary preliminary steps to explore the relationship between radon anomalies and seismic activity. Finally, it would be interesting for further analysis, to compare the forecast of radon observations, or the identification of preseismic anomalies with those obtained with other methods such as the linear regression analysis (Stojanovska et al., 2017), the artificial neural network approach (Pasini and Ameli, 2003), or the decision tree method (Zhang et al., 2020). It would also be interesting to consider other external covariates in the model formulation **Eq. 7**, such as weather variables (Stránský and Thinová, 2017).

DATA AVAILABILITY STATEMENT

The raw data supporting the conclusions of this article will be made available by the authors, without undue reservation.

AUTHOR CONTRIBUTIONS

AD and MS conceived the idea of the analysis approach. Data analyses and comments were made by MS. MS and SS prepared and reviewed the manuscript.

ACKNOWLEDGMENTS

We thank A. Piersanti e V. Cannelli (Istituto Nazionale di Geofisica e Vulcanologia) who provided the data.

REFERENCES

Aumento, F. (2002). Radon tides on an active volcanic island: Terceira, azores. *Geofisc. Int.* 41, 499–505. doi:10.22201/IGEOF.00167169P.2002.41.4.501

Barbosa, S., Donner, R., and Steinitz, G. (2015). Radon applications in geosciences—progress and perspectives. *Eur. Phys. J. Spec. Top.* 224, 597–603. doi:10.1140/epjst/e2015-02393-y

Baskaran, M. (2016). *Radon: a tracer for geological, geophysical and geochemical studies*. New York, NY: Springer.

Baykut, S., Akgül, T., İnan, S., and Seyis, C. (2010). Observation and removal of daily quasi-periodic components in soil radon data. *Radiat. Meas.* 45, 872–879. doi:10.1016/j.radmeas.2010.04.002

Belbute, J. M., and Pereira, A. M. (2017). Do global co_2 emissions from fossil-fuel consumption exhibit long memory? A fractional-integration analysis. *Appl. Econ.* 49, 4055–4070. doi:10.1080/00036846.2016.1273508

Beran, J. (2017). *Statistics for long-memory processes*. Upper Saddle River: Routledge.

Bowers, M. C., and Tung, W.-w. (2018). Variability and confidence intervals for the mean of climate data with short-and long-range dependence. *J. Clim.* 31, 6135–6156. doi:10.1175/JCLI-D-17-0090.1

Box, G. E., Jenkins, G. M., Reinsel, G. C., and Ljung, G. M. (2015). *Time series analysis: forecasting and control*. Hoboken: John Wiley & Sons.

Cannelli, V., Piersanti, A., Galli, G., and Melini, D. (2018). Italian radon monitoring network (iron): a permanent network for near real-time monitoring of soil radon emission in Italy. *Ann. Geophys.* 61, 444. doi:10.4401/ag-7604

Clauset, A., Shalizi, C. R., and Newman, M. E. (2009). Power-law distributions in empirical data. *SIAM Review.* 51, 661–703. doi:10.1137/070710111

Conraria, L. A., and Soares, M. J. (2011). The continuous wavelet transform: a primer. *NIPE Work. Paper.* 16, 1–43. doi:10.1111/joes.12012

Crockett, R. G., Gillmore, G. K., Phillips, P. S., Denman, A. R., and Groves-Kirkby, C. J. (2006). Tidal synchronicity of built-environment radon levels in the UK. *Geophys. Res. Lett.* 33, 1319–1334. doi:10.1029/2005GL024950

Crockett, R. G., Groves-Kirkby, C. J., Denman, A. R., and Phillips, P. S. (2018). Significant annual and sub-annual cycles in indoor radon concentrations: seasonal variation and correction. *Geol. Soc. Lond. Spl. Publ.* 451, 35–47. doi:10.1144/SP451.2

Cuculeanu, V., Lupu, A., and Sütö, E. (1996). Fractal dimensions of the outdoor radon isotopes time series. *Environ. Int.* 22, 171–179. doi:10.3390/environments6030029

D'Alessandro, A., Scudero, S., Siino, M., Alessandro, G., and Mineo, R. (2020). Long-term monitoring and characterization of soil radon emission in a seismically active area. *Geochem. Geophys. Geosyst.* 21, e2020GC009061. doi:10.1029/2020GC009061

Daubechies, I. (1992). *Ten lectures on wavelets*. Philadelphia: SIAM, Vol. 61.

Dickey, D. A., and Fuller, W. A. (1979). Distribution of the estimators for autoregressive time series with a unit root. *J. Am. Stat. Assoc.* 74, 427–431. doi:10.1080/01621459.1979.10482531

Donner, R. V., Potirakis, S. M., Barbosa, S. M., Matos, J. A., Pereira, A. J., and Neves, L. J. (2015). Intrinsic vs. spurious long-range memory in high-frequency records of environmental radioactivity. *Eur. Phys. J. Spec. Top.* 224, 741–762. doi:10.1140/epjst/e2015-02404-1

Dunn, J., and Henschel, B. (1989). Statistical aspects of autoregressive-moving average models in the assessment of radon mitigation. *Environ. Int.* 15, 247–252. doi:10.16966/2576-6430.112

Höll, M., Kiyono, K., and Kantz, H. (2019). Theoretical foundation of detrending methods for fluctuation analysis such as detrended fluctuation analysis and detrending moving average. *Phys. Rev.* 99, 033305. doi:10.1103/PhysRevE.99.033305

Hosking, J. R. M. (1981). Fractional differencing. *Biometrika* 68, 165–176. doi:10.1093/biomet/68.1.165

Hurst, H. (1951). Long-term storage capacity of reservoirs. *Am. Soc. Civil Eng.* 76, 770–799.

Hurst, H., Black, R., and Simaika, Y. (1965). *Long-term storage: an experimental study constable*. London, UK: Constable.

Mandelbrot, B. B., and Wallis, J. R. (1968). Noah, joseph, and operational hydrology. *Water Res. Res.* 4, 909–918. doi:10.1029/WR004i005p00909

Mandelbrot, B. B., and Wallis, J. R. (1969). Robustness of the rescaled range r/s in the measurement of noncyclic long run statistical dependence. *Water Resour. Res.* 5, 967–988. doi:10.1029/WR005i005p00967

Montanari, A., Rosso, R., and Taqqu, M. S. (1997). Fractionally differenced arima models applied to hydrologic time series: identification, estimation, and simulation. *Water Res. Res.* 33, 1035–1044. doi:10.1029/97WR00043

Morales-Simfors, N., Wyss, R. A., and Bundschuh, J. (2019). Recent progress in radon-based monitoring as seismic and volcanic precursor: a critical review. *Crit. Rev. Environ. Sci. Technol.* 50, 1–34. doi:10.1080/10643389.2019.1642833

Nikolopoulos, D., Matsoukas, C., Yannakopoulos, P., Petraki, E., Cantzos, D., and Nomicos, C. (2018). Long-memory and fractal trends in variations of environmental radon in soil: results from measurements in lesvos island in Greece. *J. Earth Sci. Clim. Chang.* 9, 1–11. doi:10.4172/2157-7617.1000465

Pan, J.-N., and Chen, S.-T. (2008). Monitoring long-memory air quality data using arfima model. *Environ. Off. J. Int. Environ. Soc.* 19, 209–219. doi:10.1002/env.882

Papacharalampous, G., Tyralis, H., and Koutsoyiannis, D. (2018a). One-step ahead forecasting of geophysical processes within a purely statistical framework. *Geosci. Lett.* 5, 12. doi:10.1186/s40562-018-0111-1

Papacharalampous, G., Tyralis, H., and Koutsoyiannis, D. (2018b). Predictability of monthly temperature and precipitation using automatic time series forecasting methods. *Acta Geophys.* 66, 807–831. doi:10.1007/s11600-018-0120-7

Pasini, A., and Ameli, F. (2003). Radon short range forecasting through time series preprocessing and neural network modeling. *Geophys. Res. Lett.* 30, 39. doi:10.1029/2002GL016726

Piersanti, A., Cannelli, V., and Galli, G. (2015). Long term continuous radon monitoring in a seismically active area. *Ann. Geophys.* 58, 0437. doi:10.4401/ag-6735

Pinault, J.-L., and Baubron, J.-C. (1996). Signal processing of soil gas radon, atmospheric pressure, moisture, and soil temperature data: a new approach for radon concentration modeling. *J. Geophys. Res.: Solid Earth.* 101, 3157–3171. doi:10.1029/95JB03121

Reisen, V. A., Monte, E. Z., da Conceição Franco, G., Sgrancio, A. M., Molinares, F. A. F., Bondon, P., et al. (2018). Robust estimation of fractional seasonal processes: modeling and forecasting daily average so_2 concentrations. *Math. Comput. Simulat.* 146, 27–43. doi:10.1016/j.matcom.2017.10.004

Roesch, A., and Schmidbauer, H. (2018). WaveletComp: computational wavelet analysis. R package version 1.1.

Schery, S., Gaeddert, D., and Wilkening, M. (1984). Factors affecting exhalation of radon from a gravelly sandy loam. *J. Geophys. Res.: Atmos.* 89, 7299–7309. doi:10.1029/JD089iD05p07299

Schumann, R., Owen, D., and Asher-Bolinder, S. (1988). "Factors affecting soil-gas radon concentrations at a single site in the semiarid western us," in Proceedings of the 1988 EPA symposium on radon and radon reduction technology 2, Citeseer. Washington, DC, September 22–25, 1992.

Shumway, R. H., and Stoffer, D. S. (2017). *Time series analysis and its applications: with R examples*. New York, NY: Springer.

Siino, M., Alessandro, G., Buonmestieri, S., D'Alessandro, A., Mineo, R., and Scudero, S. (2019a). "Radon concentration in the ragusa province (sicily, Italy)," in International scientific conference man and Karst. Silicy, Italy, June 24–26, 2019.

Siino, M., Scudero, S., Cannelli, V., Piersanti, A., and D'Alessandro, A. (2019b). Multiple seasonality in soil radon time series. *Sci. Rep.* 9, 8610. doi:10.1038/s41598-019-44875-z

Stojanovska, Z., Ivanova, K., Bossew, P., Boev, B., Zora, S., Kolar, P., et al. (2017). Prediction of long-term in door radon concentration based on short-term measurements. *Nucl. Technol. Radiat.* 32, 77–84. doi:10.2298/NTRP1701077S

Stránský, V., and Thinová, L. (2017). Radon concentration time series modelling and application discussion. *Radiat. Protect. Dosim.* 177, 155–159. doi:10.1093/rpd/ncx207

Team, R. D. C. (2005). *R: a language and environment for statistical computing*. Vienna, Austria: R Foundation for Statistical Computing.

Toutain, J.-P., and Baubron, J.-C. (1999). Gas geochemistry and seismotectonics: a review. *Tectonophysics* 304, 1–27. doi:10.1016/S0040-1951(98)00295-9

Udovičić, V., Filipović, J., Dragić, A., Banjanac, R., Joković, D., Maletić, D., et al. (2014). Daily and seasonal radon variability in the underground low-

background laboratory in belgrade, Serbia. *Radiat. Protect. Dosim.* 160, 62–64. doi:10.1093/rpd/ncu109

Veenstra, J. Q. (2013). Persistence and anti-persistence: theory and software. PhD thesis. Ontario (Canada): The University of Western Ontario.

Wang, W., Van Gelder, P., Vrijling, J., and Chen, X. (2007). Detecting long-memory: Monte Carlo simulations and application to daily streamflow processes. *Hydrol. Earth Syst. Sci. Discuss.* 11, 851–862. doi:10.5194/hessd-3-1603-2006

Woith, H. (2015). Radon earthquake precursor: a short review. *Eur. Phys. J. Spec. Top.* 224, 611–627. doi:10.1140/epjst/e2015-02395-9

Yan, R., Woith, H., Wang, R., and Wang, G. (2017). Decadal radon cycles in a hot spring. *Sci. Rep.* 7, 12120. doi:10.1038/s41598-017-12441-0

Yaya, O. S., and Fashae, O. A. (2015). Seasonal fractional integrated time series models for rainfall data in Nigeria. *Theor. Appl. Climatol.* 120, 99–108. doi:10.1007/s00704-014-1153-8

Zhang, S., Shi, Z., Wang, G., Yan, R., and Zhang, Z. (2020). Groundwater radon precursor anomalies identification by decision tree method. *Appl. Geochem.* 121, 104696. doi:10.1016/j.apgeochem.2020.104696

Conflict of Interest: The authors declare that the research was conducted in the absence of any commercial or financial relationships that could be construed as a potential conflict of interest.

Copyright © 2020 Siino, Scudero and D'Alessandro. This is an open-access article distributed under the terms of the Creative Commons Attribution License (CC BY). The use, distribution or reproduction in other forums is permitted, provided the original author(s) and the copyright owner(s) are credited and that the original publication in this journal is cited, in accordance with accepted academic practice. No use, distribution or reproduction is permitted which does not comply with these terms.

frontiers in Earth Science

ORIGINAL RESEARCH
published: 10 December 2020
doi: 10.3389/feart.2020.611010

Groundwater Anomaly Related to CCS-CO_2 Injection and the 2018 Hokkaido Eastern Iburi Earthquake in Japan

Yuji Sano[1,2], Takanori Kagoshima[1,3], Naoto Takahata[1], Kotaro Shirai[1], Jin-Oh Park[1], Glen T. Snyder[1,4], Tomo Shibata[5], Junji Yamamoto[6], Yoshiro Nishio[7], Ai-Ti Chen[8], Sheng Xu[2], Dapeng Zhao[9] and Daniele L. Pinti[10]*

[1]Atmosphere and Ocean Research Institute, University of Tokyo, Kashiwa, Japan, [2]Institute of Surface-Earth System Science, Tianjin University, Tianjin, China, [3]Graduate School of Science and Engineering, University of Toyama, Toyama, Japan, [4]Department of Chemistry, Gakushuin University, Tokyo, Japan, [5]Institute for Geothermal Sciences, Kyoto University, Beppu, Japan, [6]University Museum, Hokkaido University, Sapporo, Japan, [7]Faculty of Agriculture and Marine Sciences, Kochi University, Nangoku, Japan, [8]Department of Geosciences, National Taiwan University, Taipei, Taiwan, [9]Department of Geophysics, Tohoku University, Sendai, Japan, [10]Geotop, Research Center on the Dynamics of the Earth System, Université Du Québec à Montréal, Montreal, QC, Canada

OPEN ACCESS

Edited by:
Giovanni Martinelli, National Institute of Geophysics and Volcanology, Italy

Reviewed by:
Tiziano Boschetti, University of Parma, Italy
Walter D'Alessandro, National Institute of Geophysics and Volcanology, Italy

***Correspondence:**
Yuji Sano
yujisano128@g.ecc.u-tokyo.ac.jp

Specialty section:
This article was submitted to Geochemistry, a section of the journal Frontiers in Earth Science

Received: *28 September 2020*
Accepted: *09 November 2020*
Published: *10 December 2020*

Citation:
Sano Y, Kagoshima T, Takahata N, Shirai K, Park J-O, Snyder GT, Shibata T, Yamamoto J, Nishio Y, Chen A-T, Xu S, Zhao D and Pinti DL (2020) Groundwater Anomaly Related to CCS-CO_2 Injection and the 2018 Hokkaido Eastern Iburi Earthquake in Japan. Front. Earth Sci. 8:611010. doi: 10.3389/feart.2020.611010

Carbon capture and storage (CCS) is considered a key technology for reducing CO_2 emissions into the atmosphere. Nonetheless, there are concerns that if injected CO_2 migrates in the crust, it may trigger slip of pre-existing faults. In order to test if this is the case, covariations of carbon, hydrogen, and oxygen isotopes of groundwater measured from Uenae well, southern Hokkaido, Japan are reported. This well is located 13 km away from the injection point of the Tomakomai CCS project and 21 km from the epicenter of September 6th, 2018 Hokkaido Eastern Iburi earthquake (M 6.7). Carbon isotope composition was constant from June 2015 to February 2018, and decreased significantly from April 2018 to November 2019, while total dissolved inorganic carbon (TDIC) content showed a corresponding increase. A decrease in radiocarbon and $\delta^{13}C$ values suggests aquifer contamination by anthropogenic carbon, which could possibly be attributable to CCS-injected CO_2. If such is the case, the CO_2 enriched fluid may have initially migrated through permeable channels, blocking the fluid flow from the source region, increasing pore pressure in the focal region and triggering the natural earthquake where the brittle crust is already critically stressed.

Keywords: Hokkaido earthquake, carbon capture and storage-CO_2 injection, groundwater, carbon isotopes, radiocarbon

INTRODUCTION

There is a global consensus that some form of carbon capture and storage (CCS) technology is necessary to reduce CO_2 emission associated with fossil fuel combustion into the atmosphere (IPCC Special Report, 2005). The majority of research into this technology has focused on securely isolating CO_2 from the Earth's surface and storing it in a reservoir which is sealed by an impermeable cap rock (Johnson et al., 2005; Michael et al., 2011). This strategy should prevent CO_2 from leaking into the closest areas around the injection well but it may promote horizontal flow of CO_2-rich fluids through available permeable horizons. Interactions between injected fluids and high angle faults may result in

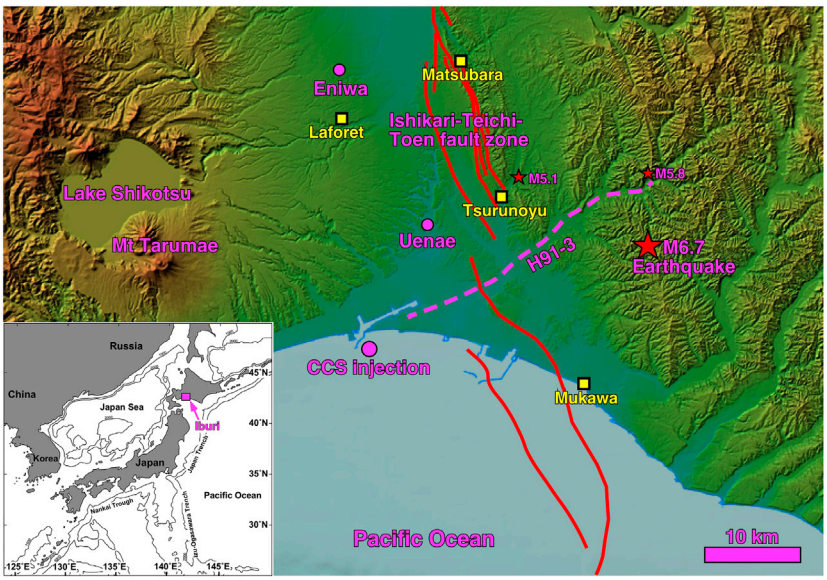


FIGURE 1 | Location of Uenae and Eniwa sampling wells in the Hokkaido Iburi region; the CCS-CO_2 injection point (purple dots); and main shock epicenter (M6.7) of the 2018 Hokkaido Eastern Iburi earthquake (red star). Two additional red stars denote the epicenters of the M5.1 earthquake on July 1st, 2017 and of the largest (M5.8) aftershock on February 21st, 2019. The red lines represent active faults in the Ishikari-Teichi-Toen fault zone (ITTFZ). The purple dashed line denotes the seismic reflection transect H91-3. Yellow squares show hot springs sampled for helium isotopes. The inset map shows the location of the Iburi region in Hokkaido, Japan.

fluid accumulation and increases in pore pressure in the region around the area. This increase in pressure may propagate to much deeper regions where the brittle crust is already critically stressed and perhaps trigger slippage of pre-existing faults (Zoback and Gorelick, 2012). This mechanism is similar to the triggering of anthropogenic seismicity during high-pressure hydraulic injection experiments (Grigoli et al., 2018). However, to date, there are no case studies reported on the possible environmental consequences of CCS-CO_2 injection.

The 2018 Hokkaido Eastern Iburi earthquake (M6.7) occurred on September 6th, 2018 in Northern Japan, close to the major active Ishikari-Teichi-Toen Fault Zone (ITTFZ), with a focal depth of 37 km (Asano and Iwata, 2019). The earthquake triggered large landslides and caused severe damage to the surrounding area with 36 casualties. Uniform strain accumulation was observed in this area from data collected by a global navigation satellite system in very recent years (Ohzono et al., 2019). The large-scale Tomakomai CCS demonstration project, built in the same region, was initially suspected to have indirectly caused the earthquake (KIKO network, 2019). The Japan CCS Co. Ltd.—the company that developed the project - reported that the CO_2 injection point was too far from the epicenter to produce any appreciable amount of strain change or to induce an earthquake (Japan CCS, 2019). However, many concerns still exist regarding the potential relationship between large-scale CO_2 injection and local earthquakes, and given that there is little consensus as to the potential consequences, further study is needed. Deep wells close to the CCS site may provide direct evidence of the CO_2 leakage that can potentially trigger natural earthquakes.

TABLE 1 | Temperature, pH and chemical compositions of groundwater samples in Hokkaido, Japan.

Site	Uenae	Eniwa
Date	2019 May 28th (H18)	2018 October 4th (H6)
Temperature (°C)	9.0	8.2*
pH	6.3	7.3
Na (mmol/L)	1.11	0.42
K (mmol/L)	0.16	0.046
Mg (mmol/L)	0.19	0.13
Ca (mmol/L)	0.61	0.27
Cl (mmol/L)	1.05	0.20
NO_3 (mmol/L)	0.48	0.18
SO_4 (mmol/L)	0.38	0.11

Estimated by annual mean temperature and geothermal gradient in the region.

GROUNDWATER SAMPLES

We collected groundwater samples from wells used for producing commercial bottled mineral water at Uenae and Eniwa sites, located 13 and 29 km from the CCS Tomakomai site, respectively (**Figure 1**). Commercial water has a precise production date and both the chemical compositions and stable isotopic composition are well preserved (Tsunogai and Wakita, 1995; Onda et al., 2018), with the exception of helium because of the high permeability of this gas through PET bottles. We purchased as many bottles as possible covering a period of three years before and a year and half after the M6.7 earthquake. Both wells are 90–100 m deep and tap a volcanic-sedimentary aquifer belonging to the Shiatsu pyroclastic flow, which erupted in the Late Pleistocene (Nakagawa et al., 2018). High-quality drinking

mineral water is available from altered ignimbrite units. Chemical compositions of representative samples from Uenae and Eniwa sites are listed in **Table 1** together with temperature and pH. Twenty-one untreated bottled water samples were analyzed for carbon, hydrogen and oxygen isotopes. The samples cover the period from June 2015 to February 2020, and include the critical period between April 2016 and December 2019, when a total of 300 kilotons of CO_2 were injected, as well as the timing of the M6.7 Hokkaido earthquake event in September 2018.

Carbon, Hydrogen, Oxygen, and Helium Isotopes, and ^{14}C Activity Measurements

We have carefully selected unopened mineral water bottles to avoid contamination by air CO_2, which has a different isotopic composition than dissolved carbonates. Carbon isotopes were measured at the Atmosphere and Ocean Research Institute, University of Tokyo, Japan with a conventional continuous flow mass spectrometer (Delta V plus, Thermo Fisher) after standard decarbonation with phosphoric acid. Experimental details followed the methodology provided in Zhao et al. (2019). The $^{13}C/^{12}C$ ratios were calibrated against our in-house standard, converted to conventional V-PDB units, and expressed as δ values in per mil (‰). Total Dissolved Inorganic Carbon (TDIC) concentrations were estimated by a peak height method with standard samples of known amounts of TDIC. Experimental errors on carbon isotopes and TDIC concentrations were calculated by repeated measurements of standard samples. Hydrogen ($^2H/^1H$) and oxygen ($^{18}O/^{16}O$) isotopes of water were measured with a cavity ring-down spectrometer without any preprocessing at Geotop, Université du Québec à Montréal, Canada, using a Los Gatos LGR-T-LWIA-45-EP, and then verified at the Atmosphere and Ocean Research Institute, University of Tokyo, Japan (Onda et al., 2018) using a L2120-I Analyzer (PICARRO Co. Ltd.). They were calibrated against in-house standards, converted to the conventional V-SMOW units, and expressed as δ values in per mil (‰). Experimental errors on hydrogen and oxygen isotopes were calculated by repeated measurements of standard samples. TDIC was precipitated and purified. It was then reduced into pure amorphous carbon and the $^{14}C/^{12}C$ ratios were measured with a compact AMS system at the Institute of Surface-Earth System Science, Tianjin University, China (Dong et al., 2019). Extracted helium and neon from spring water samples were purified with hot Ti getters and charcoal traps held in liquid nitrogen. The $^4He/^{20}Ne$ ratios were measured by online QMS, and helium was separated from neon by a cryogenic charcoal trap. The $^3He/^4He$ ratios were measured with a noble gas mass spectrometer (Helix SFT, Thermo Fisher). Experimental details are provided in Sano et al. (2008).

Tomakomai Carbon Capture and Storage Demonstration Project

A large-scale CCS demonstration project was undertaken by the Japanese government in the Tomakomai site in Hokkaido, Japan (**Figure 1**). Intensive stakeholder engagement was implemented by the Japan CCS company because the operation was taking place in the port area close to a highly populated city. The CO_2 source was offgas derived from a hydrogen production unit of an oil refinery located in the region. A high purity CO_2 (>99%) was recovered from the offgas by an amine scrubbing process and the gaseous CO_2 was compressed and then injected into two different offshore geological reservoirs (Yamanouchi et al., 2011; Sawada et al., 2018). The host reservoirs are the shallow Moebetsu Formation located at a depth of approximately 1000 m below the seabed and the deep Takinoue Formation with the depth of 2400 m. The former is a Lower Quaternary saline aquifer composed of 200 m thick sandstone, while the latter is a Miocene saline aquifer which consists of volcanic and volcaniclastic rocks with a thickness of 600 m. A schematic diagram of geological section is referred from Tanaka et al. (2017) and reproduced in **Supplementary Figure S1**. The CO_2 injection of the shallow reservoir started in April 2016 and continued until November 2019. A total of 300 kilotons of gaseous CO_2 was injected gradually (**Supplementary Figure S2**). A smaller amount of CO_2, approximately 100 tons, was injected into the deeper reservoir.

DISCUSSION

Temporal Variations of Stable and Radioactive Isotopes in Groundwater

The $\delta^{13}C$ values and the TDIC contents, δ^2H and $\delta^{18}O$ values, and ^{14}C activity were measured in commercially-bottled groundwater as stated above, and are listed in **Table 2**. The $\delta^{13}C$ value of the TDIC in Uenae well groundwater was constant at −17.8 ± 0.2‰ from June 2015 through February 2018, and then decreased to −18.8 ± 0.2‰ with some fluctuation (**Figure 2A**). The TDIC concentration at Uenae was also constant from June 2015 to February 2018, and increased significantly in December 2018, which is the inverse of the observed trend for $\delta^{13}C$ (**Figure 2B**). On the other hand, the $\delta^{13}C$ of TDIC in groundwater from the Eniwa well decreased over time, from −18.5‰ to −20.9‰, except for October 2017, while TDIC concentration remained constant at 0.68 ± 0.03 mmol/L, except for the most recent sample. Injected CO_2 was the by-product of a hydrogen production unit of an oil refinery (Sawada et al., 2018). Its $\delta^{13}C$ value should therefore have been lighter than −25‰ (Hoefs, 2018) and its ^{14}C activity close to zero, because fossil fuels are too old to contain any anthropogenic ^{14}C. Injection began in April 2016 and reached 100 kilotons of CO_2 in November 2017 (**Supplementary Figure S2**), which is approximately one third of the total injected amount (Tanaka et al., 2014; Japan CCS, 2020). There was no heavy rain or flooding in the region during this period. Additionally, there is no large bridge or dam construction close to the observation wells that could have altered the groundwater system and triggered the earthquake (Gupta and Iyer, 1984). The Uenae site is located in non-volcanic frontal arc region, even though it is close to the volcanic front. There is no known cause, and no physical or chemical processes, capable of changing geochemical parameters such as carbon isotopes of groundwater except for oxidation of organic matter.

TABLE 2 | Hydrogen, oxygen and carbon isotopes together with total DIC contents of groundwater samples in Hokkaido, Japan.

Code	Date	δ^2H* (‰)	$\delta^{18}O$* (‰)	δ^{13} (‰)	TDIC* (mmol/L)	C-14 (pMC)
Uenae						
H7	28/06/2015	−59.47	−8.64	−17.69	0.79	
H8	19/09/2016	−60.39	−8.57	−17.78	0.79	101.10
H9	13/02/2018	−60.45	−8.36	−17.93	0.75	100.91
H10	19/04/2018	−61.21	−9.18	−18.17	0.82	
H11	03/07/2018	−60.90	−8.85	−18.50	0.82	
H12	12/07/2018	−60.93	−9.07	−18.11	0.81	
H13	07/08/2018	−61.01	−8.96	−18.33	0.80	
H14	13/09/2018	−60.80	−8.83	−18.04	0.81	100.43
H15	18/10/2018	−62.17	−9.30	−18.63	0.84	100.23
H16	06/12/2018	−61.98	−9.18	−18.22	0.80	
H17	25/12/2018	−62.15	−9.23	−18.76	0.84	100.07
H18	28/05/2019	−61.74	−9.29	−18.46	0.80	100.16
H20	20/09/2019	−60.79	−9.29	−18.32	0.82	
H21	13/11/2019	−60.67	−9.20	−18.43	0.82	
Eniwa						
H1	21/06/2016	−62.79	−9.12	−18.53	0.71	
H2	04/11/2016	−63.25	−9.36	−18.81	0.67	
H3	01/07/2017	−63.57	−9.53	−19.02	0.69	
H4	22/10/2017	−64.29	−9.61	−19.75	0.68	
H5	22/04/2018	−64.37	−9.44	−19.56	0.71	
H6	04/10/2018	−64.68	−9.54	−19.85	0.64	
H19	18/02/2020	−64.55	−9.98	−20.86	0.79	

**Experimental errors of each values are as follows: δ^2H (0.6‰), $\delta^{18}O$ (0.2‰), $\delta^{13}C$ (0.2‰), TDIC (0.2 mmol/L).*

There may be a deep magmatic carbon component in the region close to Uenae (Marumo et al., 1995; Nitta and Inoue, 2011). The $\delta^{13}C$ values of approximately −4‰ in magmatic CO_2 is much heavier than that of present groundwater TDIC. Addition of a magmatic component should increase $\delta^{13}C$ values of our samples. However this is not the case. The observed increase in TDIC contents at Uenae may be attributable to the CO_2 injected at the Tomakomai site, because of the concomitant decrease in $\delta^{13}C$ (**Figure 2A**), which is also observed in the ^{14}C activity of the total carbonate (**Supplementary Figure S3**). It is possible to calculate $\delta^{13}C$ values of CO_2 in the samples under the chemical and isotopic equilibrium of groundwater (Barbieri et al., 2020). When we take into account the mass balance equation of TDIC, Mg^{2+}, Ca^{2+}, SO_4^{2-} using data set of **Table 1** and assuming the $\delta^{13}C$ value of −7‰ in local carbonate rock (Nitta and Inoue, 2011), $\delta^{13}C$ values of hypothetical CO_2 gas in the Uenae sample would become approximately −50‰, much lighter than those of present groundwater TDIC. This may be attributable to the discrepancy between the referred local carbonate and the true $\delta^{13}C$ value of calcite in aquifer system.

At the Uenae site, both δ^2H and $\delta^{18}O$ groundwater values were constant at −60.1 ± 0.5‰ and −8.52 ± 0.15‰, respectively, from June 2015 to February 2018 (**Figures 2C,D**). These values then fluctuated and decreased significantly down to −62.2‰ and −9.3‰, respectively, from April 2018 to December 2018. These variations are similar to those of the carbon isotopes, and may be attributable to groundwater mixing with light δ^2H and $\delta^{18}O$ of summer precipitation in the region (Kawaraya et al., 2016; **Supplementary Figure S4**). At Eniwa, δ^2H values decreased slightly from −62.8‰ to −64.3‰ and consistently from June 2016 to February 2020, while $\delta^{18}O$ values remained constant with the value of −9.43‰ except for the most recent sample of −9.98‰. These oxygen isotope values may be explained by the mixing of local surface meteric water and a deep high temperature water (Nitta and Inoue, 2011).

Potential Triggering Mechanism of the Hokkaido Earthquake

Previous studies have indicated a high probability that earthquakes are triggered by the injection of large volumes of CO_2 into the brittle crust (Zoback and Gorelick, 2012; Nicol et al., 2011). In this case study, the possible link between groundwater geochemical anomalies, the Hokkaido earthquake, and the CCS-CO_2 injection was examined. **Figure 3** shows a schematic vertical cross-section of the studied region before the CCS CO_2 injection of April 2016 (Stage 1), including two features: **Figure 3A** (top) is P-wave velocity (Vp) structure of the crust and uppermost mantle in the region (Kobayashi et al., 2019). A part of this figure (red square) is enlarged in **Figure 3B**, which shows geological structure of the seismic section along H91-3 in **Figure 1** (Yokokura et al., 2014). The CO_2 injected in the Moebetsu and Takinoue Formations are shown by broken curves. ITTFZ and Uenae indicate the major active fault system and the monitoring well, respectively. There may be upward natural fluid flows by buoyancy through a fault system as well as permeable aquifer (black arrows in **Figures 3A,B**) where a deeper flow (**Figure 3A**) was suggested by a seismological study (Hua et al., 2019). The upper boundary of Takinoue Formation is consistent with the active fault in the left side of diagram, but it is discrepant in the right. The branch position is approximately 1 km left side beneath the Uenae site.

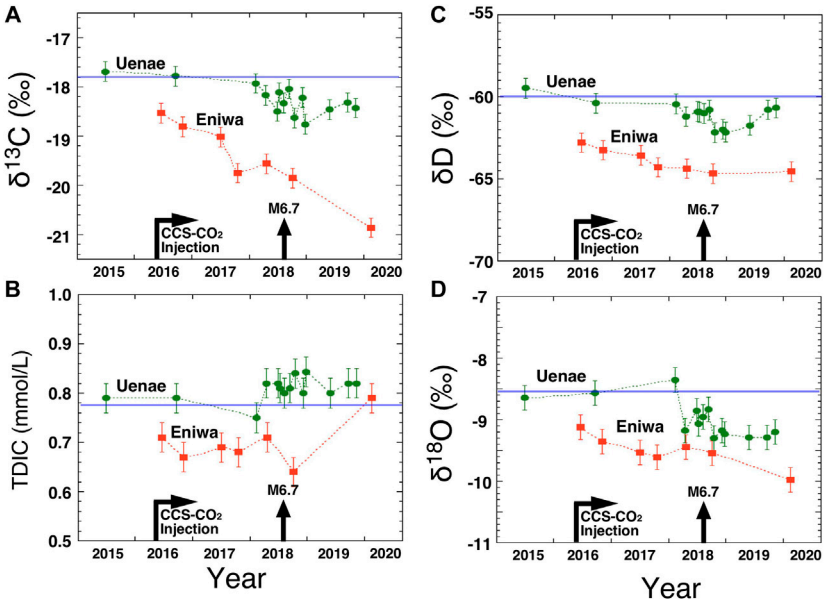


FIGURE 2 | Temporal variations of **(A)** $\delta^{13}C$ values of total carbonate in mineral water **(B)** total dissolved inorganic carbon (TDIC) concentration (mmol/L), **(C)** $\delta^{2}H$, and **(D)** $\delta^{18}O$ values of mineral water. Error bars show 2σ values. Blue lines represent averages of three samples (2015, 2016, and april 2018) from the Uenae well. Start dates of CCS-CO_2 injection and origin time of M6.7 earthquakes (M6.7 in **Figure 1**) are indicated by arrows in **(A)** and **(D)**.

Figure 4 shows the cross-section of two years after the injection of CO_2 (Stage 2), which is also immediately before the M6.7 earthquake. This indicates a geochemical model explaining the possible role of CO_2 in triggering the M6.7 earthquake, together with the distribution of earthquake occurred in the region and the hypothetical CO_2 accumulation zone. A large amount of CO_2, up to the 100 kilotons injected by the Tomakomai CCS project at the time, may have accumulated below the cap rock. Regional CO_2 monitoring indicates no apparent CO_2 leakage immediately above or in the vicinity of the cap rock (Sawada et al., 2018; Japan CCS, 2019). Long before the M6.7 earthquake, a seismic reflection survey was conducted along transect H91-3 by the National Institute of Advanced Industrial Science and Technology, AIST (Yokokura et al., 2014), as illustrated in **Figure 1**. The seismic survey revealed a low-angle fault, starting from the CCS-CO_2 injection area and dipping eastward (orange dotted line in **Figures 3A**,**4A**,**5A**). Generally speaking, a fault plane is a mechanically weak and possibly a more permeable surface than the surrounding region. There was upward natural fluid flow though the low-angle fault and Takinoue Formation (black arrows in **Figure 3B**). Injected CO_2 of Takinoue layer could be dissolved in local saline groundwater and make a high-pressure gas-water mixture, which can not go downward but may have temporally interrupted the fluid flow and the internal pressure could be buildup in the region. The increased pressure may propagate into deeper part, that is reverse direction of natural fluid flow, subject to the trajectory of pink dotted arrows in **Figures 4A,B**. Then dilatation may occur in the fault system (Arrows in circles in **Figure 4B**). The presence of this increase of pore pressure is suggested by the increase of natural earthquakes that took place along the fault in 2017 and 2018, when compared to those in 2016 (see **Supplementary Figure S5**).

The major part of the CO_2 injected in the Moebetsu Formation may be mixed with saline water which subsequently moved along the permeable layer towards the east as indicated by green arrow in **Figures 4A,B**. Most of the CO_2-fluid (gas-water mixture) may arrive at the area beneath the Uenae site, where there is no permeable connection between the Moebetsu Formation and shallow volcanic-sedimentary aquifer. Our sampling well taps the latter aquifer. Some part of CO_2-fluid may travel further eastward and will arrive at the region beneath the ITTFZ. When the high-pressure fluid encountered another high angle fault, which is possibly part of the ITTFZ, the CO_2-fluid may have accumulated in the region (**Figures 4A,B**), building up the pore pressure. There may be a pre-existing fault closer to the seismogenic fault of the M6.7 earthquake, at the western edge of the low-Vp zone (**Figure 4A**). In addition, low Vp/Vs was identified east of the slip area, suggesting the presence of water or fluid (Kobayashi et al., 2019). Before the M6.7 earthquake, there may have been natural upward fluid flow in the region parallel to the seismogenic fault (Hua et al., 2019). When the anthropogenic CO_2-fluid accumulated above this area, natural fracture flow may have been blocked, increasing pore pressure in the region. This increase as well as hydrological perturbations in the Takinoue Formation may have propagated to a much deeper region, and high pressure finally arrived at the focal zone of the M6.7 earthquake, again this is the reverse direction of natural fluid flow (dotted line in **Figure 3A**). It may have induced dilation of fault system and then have triggered the natural slip of pre-existing faults in a region where the brittle crust was already critically stressed.

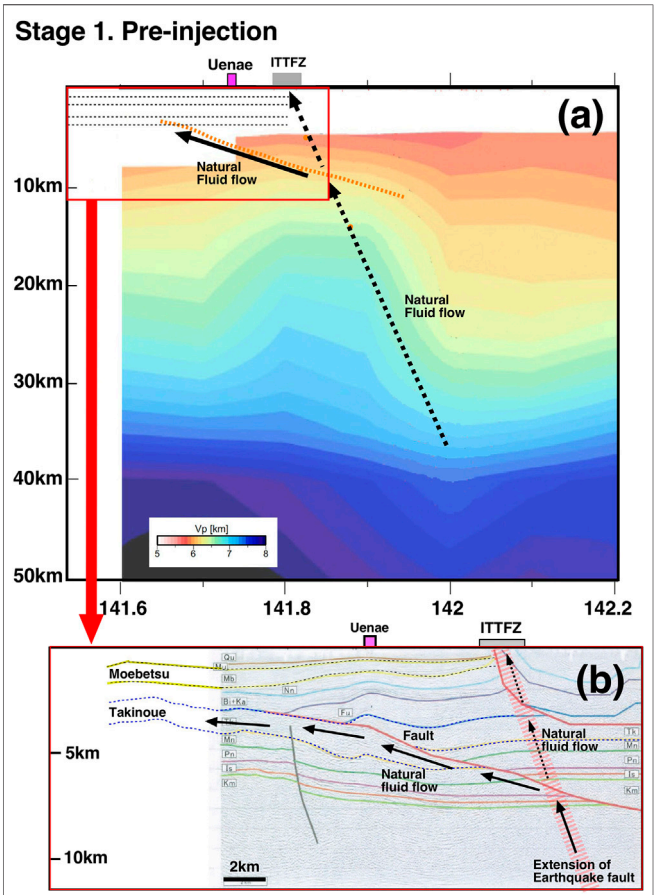


FIGURE 3 | Schematic vertical cross-section of the Hokkaido Iburi region along the H91-3 seismic profile of **Figure 1**, and its extension southwest and northeast before CCS-CO_2 injection **(A)** P-wave velocity (Vp) structure of the crust and uppermantle in the region. The orange dotted curve shows a fault determined by seismic reflection survey, which corresponds to the red solid line in bottom figure. The black solid and dotted arrows show possible natural fluid flows in the region supported by a seismological study. **(B)** Modified subsurface structure of the seismic section along H91-3 in **Figure 1** reported by Yokokura et al. (2014). Red square of top figure is enlarged here. The red solid line is the active fault. Uenae and ITTFZ denote the position of Uenae site and ITTFZ.

Part of CO_2-fluid may have ascended through the ITTFZ fault zone by buoyancy and introduced into the Shiatsu aquifer at a 90–100 m depth, where the Uenae monitoring well draws groundwater (green arrows in **Figures 4A,B**). The increase in TDIC concentration and the concomitant decrease in $\delta^{13}C$ values and ^{14}C activity in the Uenae mineral water would be caused by the injected low-$\delta^{13}C$ and ^{14}C-free CO_2. Concordant with the TDIC concentration and carbon isotopic variation, both $\delta^{2}H$ and $\delta^{18}O$ values also decrease over time (**Figure 2**). Their relationship has a slope of 2.2 in the $\delta^{18}O$-$\delta^{2}H$ diagram (**Supplementary Figure S4**), departing from the Global Meteoritic Water Line, which has a slope of 8. This suggests that the water carrying the injected CO_2 may have a low $\delta^{18}O$ value, and is then mixed with Uenae groundwater, which recharges possibly in the region (**Supplementary Figure S4**).

Figure 5 shows the cross-section after the M6.7 earthquake. The aftershock distribution of the M6.7 event coincides closely with the seismogenic fault. It is worth noting that the extension of the seismogenic fault estimated from the source fault model (Asano and Iwata, 2019) of the M6.7 earthquake (solid red line in **Figure 5A**) connects the epicenter with the ITTFZ at the surface (wide dotted red line; **Figure 5B**). Aftershocks of the M6.7 event terminated at a depth of ~10 km, where the pore pressure was high and the region may be ductile due to the interruption of natural fluid flow by CO_2 injection. After the earthquake, new fluid flow may occur beneath the ITTFZ (**Figures 5A,B**), which will be discussed in the latter section.

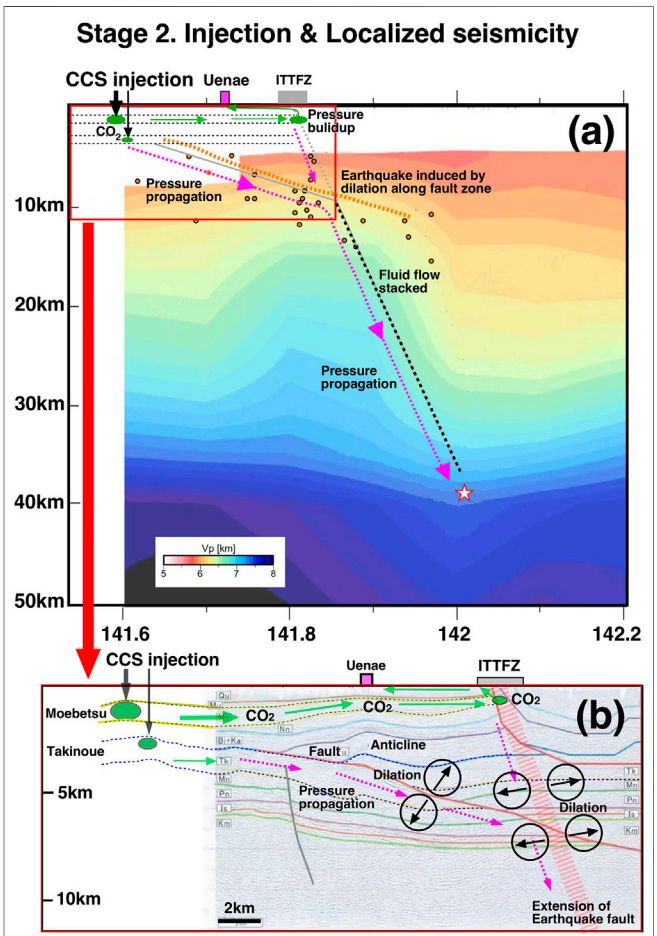


FIGURE 4 | Schematic vertical cross-section of the Hokkaido Iburi region along the H91-3 seismic profile of **Figure 1**, and its extension southwest and northeast in two years after CCS-CO_2 injection and immediately before the M6.7 earthquake **(A)** P-wave velocity (Vp) structure of the crust and upper mantle in the region. The red dotted arrows and gray thin line show possible pressure propagation and a pre-existing fault in the region, respectively. The orange dotted curve denotes a fault found by seismic reflection survey. Orange dots are possibly induced earthquakes by dilation along fault zone. **(B)** Modified subsurface structure of the seismic section along H91-3 in **Figure 1** reported by Yokokura et al. (2014). Red square of top figure is enlarged here. The green solid arrows and red dotted arrows show movement of CO_2 fluid and direction of pressure propagation, respectively. Arrows in circles indicate the dilation due to pore pressure.

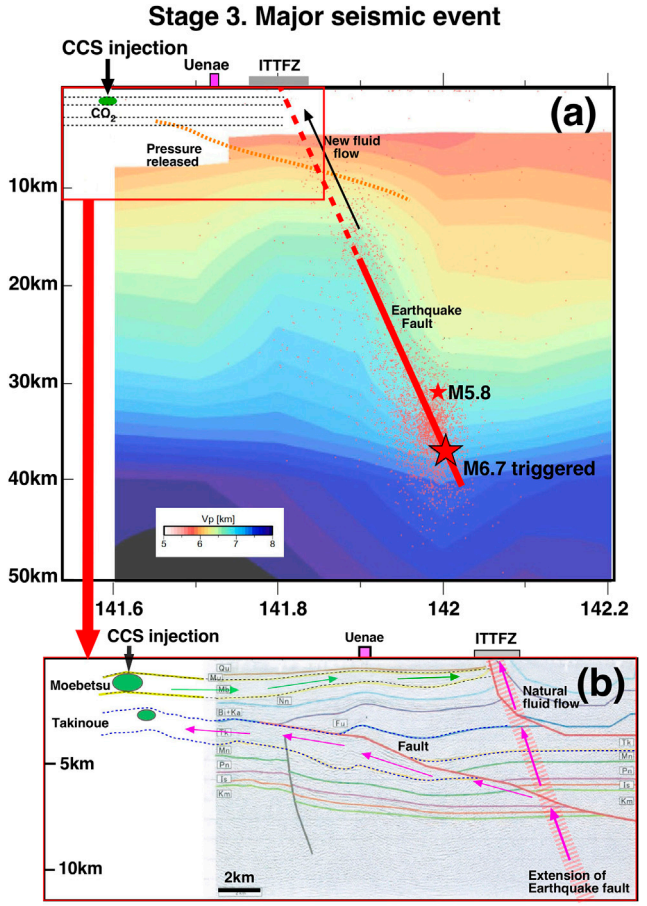


FIGURE 5 | Schematic vertical cross-section of the Hokkaido Iburi region along the H91-3 seismic profile of **Figure 1**, and its extension southwest and northeast soon after the M6.7 earthquake **(A)** P-wave velocity (Vp) structure of the crust and uppermantle in the region. The red solid line and dotted line show earthquake fault and hypothetical new fluid flow, respectively. The orange dotted curve denotes a fault found by seismic reflection survey. Distributions of small red dots are aftershocks. A large red star indicates the position of main shock (M6.7). **(B)** Modified subsurface structure of the seismic section along H91-3 in **Figure 1** reported by Yokokura et al. (2014). Red square of top figure is enlarged here. The red solid arrows and green arrows are direction of CO_2 fluid movement and possible pressure propagation.

Velocity of Anthropogenic Fluid Flow

In the proposed geochemical model, the velocity of the CO_2-fluid flow should correspond with the sequence of events (i.e., the injection of CO_2, the groundwater anomaly, and the M6.7 earthquake) for it to be considered realistic (**Figures 3–5**). In the case of the Uenae well, the carbon anomaly began in April 2018, while CO_2-injection began in April 2016. The total distance from the CCS injection point to Uenae is estimated to be ca. 30 km along the trajectory of movement simulated in the model (green arrows in **Figure 4A**). The average fluid velocity is then calculated to be approximately 40 m/day. This value is higher than the typical confined groundwater velocity of 1 m/day (Shibasaki, 1981), but is consistent with the maximum velocity calculated for Japanese sedimentary basins of 40 m/day (Shibasaki, 1981) and the value > 50 m/day of volcanic CO_2-fluid flow observed at the 1986 eruption of Izu-Oshima volcano in Japan (Sano et al., 1988; Sano et al., 1995). If we assume a velocity of 40 m/day, the first phase of injected CO_2 may have arrived at the build up and accumulation zone (**Figure 4A**) in September 2017, which is one year before the M6.7 earthquake. This may have been a sufficient amount of time for pore pressure to build up in the deep focal region. Considering a high-pressure injected CO_2 and enhanced permeability along the fault plane, one may assume a faster velocity than 40 m/day, similar to the case of above Izu-Oshima volcano. During the great 2011 Tohoku-Oki earthquake (Mw 9.0), a velocity of 4 km/day was estimated for the upward migration of mantle fluids along the fault plane at the subducting plate interface (Sano et al., 2014). This value is two orders of magnitude greater than 40 m/day. If this higher fluid flow rate is applied to our model, the injected CO_2-fluid phase could have reached the accumulation point within 5 days of injection. On the other hand, a groundwater flow rate from ITTFZ to the Uenae well may be slower than 40 m/day. Therefore, either groundwater anomalies might have not yet have appeared in the more distant Eniwa well after the M6.7 earthquake, because the distance between the two wells is ca. 20 km (**Figure 1**), or significant increase of total carbonate in February 2020 (**Figure 2B**) may be due to the CCS-CO_2 injection.

TABLE 3 | Helium isotopes and helium/neon ratios of natural springs after the M6.7 earthquake in Hokkaido, Japan.

Code	Date	$^3He/^4He$ (Ra)	Error 1 σ	$^4He/^{20}Ne$	cor $^3He/^4He$* (Ra)
Matsubara					
H22	22/09/2018	0.50	0.02	1.22	0.36
H23	18/03/2019	0.49	0.04	1.16	0.34
H24	05/11/2019	0.89	0.04	0.40	0.68
Tsurunoyu					
H25	22/09/2018	0.14	0.02	3.29	0.06
H26	04/11/2019	0.42	0.03	0.85	0.15
Laforet					
H27	22/09/2018	0.65	0.04	15.8	0.64
H28	12/12/2018	0.67	0.04	6.41	0.66
H29	18/03/2019	0.68	0.04	2.41	0.64
H30	05/11/2019	0.68	0.04	20.4	0.68
Mukawa					
H31	12/12/2018	0.06	0.05	4.93	0.01
H32	19/03/2019	0.05	0.02	34.0	0.04
H33	04/11/2019	0.09	0.01	36.1	0.09

**ASW correction is following Sano and Fischer (2013).*

Natural Fluid Flow Paralleling the Seismogenic Fault

For the model to be valid, it must be assumed a fluid flow through a pre-existing fault plane (**Figures 3A,B**), before the M6.7 Eastern Iburi earthquake. The fluid in the source zone may have originated from the dehydration of the subducting Pacific slab beneath southern Hokkaido, a phenomenon clearly identified by low-seismic velocity anomalies, high attenuation, and high Poisson's ratio (Hua et al., 2019). Tomography suggests that the fluid from the slab dehydration ascended through the forearc mantle wedge and then entered the seismogenic fault in the crust, triggering the 2018 Eastern Iburi earthquake. The same mechanism also caused the 1995 M7.2 Kobe earthquake (Zhao et al., 1996), as well as the

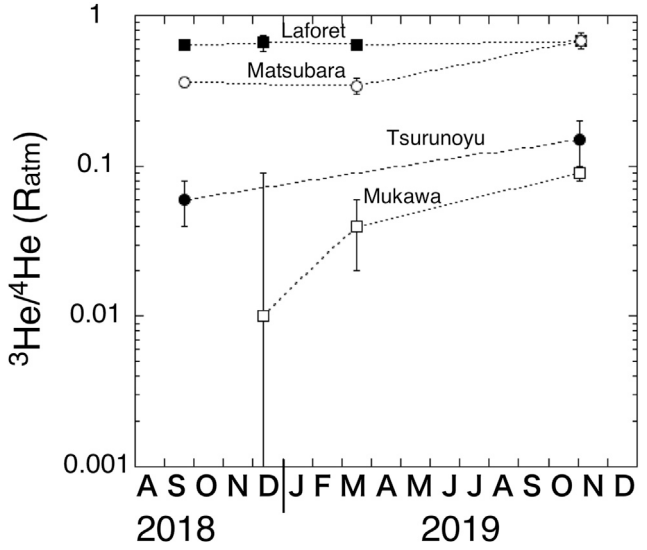


FIGURE 6 | Temporal variations of air-corrected ^{3}He/^{4}He ratios and normalized to the air ratio (Ratm = 1.382×10^{-6}), measured in natural springs after the M6.7 earthquake at Mukawa, Tsurunoyu, Matsubara, and Laforet in Hokkaido, Japan. Error bars are 2σ.

2000 M7.3 western Tottori earthquake and the 2016 M6.6 central Tottori earthquake in southwestern Japan, where the Philippine Sea plate is subducting (Zhao et al., 2018). If this is the case, the deep fluid would have a mantle helium signature with a high ^{3}He/^{4}He ratio (Sano and Fischer, 2013). We collected hot and mineral spring water samples from four sites around the ITTFZ after the M6.7 Eastern Iburi earthquake (**Figure 1**) and measured the ^{3}He/^{4}He and ^{4}He/^{20}Ne ratios at different sampling times (**Table 3**; **Figure 6**). At three sites close to the ITTFZ (Matsubara, Tsurunoyu, and Mukawa), the air-corrected ^{3}He/^{4}He ratios increased significantly after the M6.7 earthquake. In September 2018, the ^{3}He/^{4}He ratio is 0.36 ± 0.03 Ra at Matsubara and 0.06 ± 0.02 Ra at Tsurunoyu. Immediately after the M6.7 earthquake, in November 2019, the ratio increased to 0.68 ± 0.08 Ra at Matsubara and 0.15 ± 0.05 Ra at Tsurunoyu; it was 0.01 ± 0.08 Ra at Mukawa in December 2018, but increased to 0.09 ± 0.01 Ra in November 2019. In contrast, the ratio is almost constant, at 0.66 ± 0.04 Ra, at the Laforet site located far from the ITTFZ (**Figure 1**). These results suggest that a mantle helium component was slightly enriched in the ITTFZ subsurface region fluids after the M6.7 earthquake. Before CCS-CO_2 injection, there may have been steady state fluid flow including a small mantle helium component (**Figures 3A,B**). Immediately before and during the M6.7 event, the natural fluid flow may have been interrupted by high pore pressure caused by CO_2 accumulation (**Figures 4A,B**). Consequently, the surface manifestation of mantle helium may have ceased or have been weakened. After the M6.7 earthquake, new channels may have been created from the deep crust to the ITTFZ subsurface region. The ^{3}He/^{4}He ratios of natural springs then increased significantly because of the connection to the mantle source (**Figure 6**). Therefore, the overall variation of the measured helium isotopes in groundwater supports the proposed geochemical model of the M6.7 Eastern Iburi earthquake triggering.

Relationship Between δ^{13}C and ^{14}C Activity of Groundwater Carbonate

There is a simple correlation between observed δ^{13}C values and ^{14}C activity of total carbonate in groundwater samples from the Uenae well (**Supplementary Figure S6**) with a correlation coefficient, r^2 = 0.85. There may be three independent carbon components in subduction-type region (Sano and Marty, 1995): 1) surface carbon (a mixture of organic and marine carbonate carbon) with intermediate δ^{13}C (−10‰ in surface meteoric water by Nitta and Inoue, 2011) and high ^{14}C; 2) anthropogenic (CCS injection) carbon with low δ^{13}C (−25‰) and low ^{14}C; and 3) deep-seated carbon (possibly derived from the mantle) with high δ^{13}C (−6‰) and low ^{14}C. The correlation between δ^{13}C and ^{14}C may be explained by the binary mixing of the surface and anthropogenic CCS carbon from September 2016 to May 2019. Even though there is an increase of mantle helium component in hot and mineral springs close to the ITTFZ region (**Figure 6**), a substantial amount of deep-seated carbon was not introduced into the Uenae aquifer after the M6.7 earthquake, which should have made the δ^{13}C value higher. This mechanism should be studied more precisely in future work.

CONCLUSION

In conclusion, secular variations of carbonate contents, carbon isotopes (δ^{13}C), and ^{14}C activity in groundwater at the Uenae well, southern Hokkaido, Japan may have some relation to the CO_2 injection from the Tomakomai CCS demonstration project in the area. Considering the position of the pre-existing fault, the natural earthquakes that occurred between 2016 and 2017, and the crustal structure of the region, the injected CO_2 fluid may have interrupted a natural fluid flow in the deep Takinoue Formation and may have increased pore pressure in the area. The injected CO_2 fluid in the shallow Moebetsu Formation, may have flowed into the region just beneath ITTFZ region. The accumulation of CO_2-fluid could have potentially interrupted the natural upward fluid flow, thereby increasing the pore pressure in the focal area, and possibly triggering the 2018 Hokkaido Eastern Iburi earthquake. A part of CO_2-fluid may be incorporated in the aquifer of the Uenae site and may have induced chemical and isotopic variations of the groundwater. Future projects should consider regional sampling of noble gas and stable isotopes to confirm the potential influence of carbon sequestration on seismicity.

DATA AVAILABILITY STATEMENT

The original contributions presented in the study are included in the article/**Supplementary Material**, further inquiries can be directed to the corresponding author.

AUTHOR CONTRIBUTIONS

YS designed the study. YS, TK, TS, and A-TC conducted field trips and sample collection. KS measured carbon isotopes and carbonate

contents in groundwater. NT analyzed groundwater oxygen and hydrogen isotopes. NT, TK, and A-TC measured helium isotopes and helium/neon ratios of hot spring samples. SX analyzed C-14 of carbonate in groundwater. JY and YN provided geological interpretations of the area. J-OP and DZ provided the seismological model and implication. YS, GS and DP wrote the manuscript. All authors contributed to the final manuscript preparation.

FUNDING

This work was partly supported by a research grant from the Japan Society for the Promotion of Science (17H00777).

ACKNOWLEDGMENTS

We gratefully acknowledge the regional mineral water companies for groundwater sampling. We thank KT for reviewing the paper and TM for help with analyzing hydrogen and oxygen isotopes of water samples. J-FH is thanked for hydrogen and oxygen isotopic analyses at Geotop in Montreal, Canada. We thank reviewers for constructive comments.

SUPPLEMENTARY MATERIAL

The Supplementary Material for this article can be found online at: https://www.frontiersin.org/articles/10.3389/feart.2020.611010/full#supplementary-material

REFERENCES

Asano, K., and Iwata, T. (2019). Source rupture process of the 2018 Hokkaido Eastern Iburi earthquake deduced from strong-motion data considering seismic wave propagation in three-dimensional velocity structure. *Earth Planets Space* 71, 101. doi:10.1186/s40623-019-1080-0

Barbieri, M., Boschetti, T., Barberio, M. D., Billi, A., Franchini, S., Iacumin, P., et al. (2020). Tracing deep fluid source contribution to groundwater in an active seismic area (central Italy): a combined geothermometric and isotopic ($\delta^{13}C$) perspective. *J. Hydrol.* 582, 124495. doi:10.1016/j.jhydrol.2019.124495

Dong, K., Lang, Y., and Xu, S. (2019). Progress in XCAMS at Tianjin University. *Rad. Detect. Tech. Meth.* 3, 62. doi:10.1007/s41605-019-0141-z

Grigoli, F., Cesca, S., Rinaldi, A. P., Manconi, A., Lopez-Comino, J. A., Clinton, J. F., et al. (2018). The November 2017Mw5.5 Poyang earthquake: a possible case of induced seismicity in South Korea. *Science* 360, 1003–1006. doi:10.1126/science.aat2010

Gupta, H. K., and Iyer, H. M. (1984). Are reservoir-induced earthquakes of magnitude ≧5.0 at Koyna, India, proceeded by pairs of earthquakes of magnitude ≧4.0?. *Bull. Seismol. Soc. Am.* 74, 863–873.

Hoefs, J. (2018). *Stable isotope geochemistry*. (Berlin, Germany: Springer), 208.

Hua, Y., Zhao, D., Xu, Y., and Wang, Z. (2019). Arc-arc collision caused the 2018 Eastern Iburi earthquake (M 6.7) in Hokkaido, Japan. *Sci. Rep.* 9, 13914. doi:10.1038/s41598-019-50305-x

IPCC Special Report (2005). "Carbon dioxide capture and storage," in *Prepared by working group III of the intergovernmental panel on climate change* (Cambridge, England: Cambridge University Press), 442.

Japan CCS (2019). Report of influence of the 2018 Hokkaido Eastern Iburi earthquake on CO_2 reservoir by CCS project. Available at: https://www.japanccs.com/wp/wp-content/uploads/2019/09/report_re2.pdf. second version.

Japan CCS (2020). Tomakomai CCS demonstration project. Project overview and schedule. Available at: https://www.japanccs.com/en/business/demonstration/overview.php.

Johnson, J. W., Nitao, J. J., and Morris, J. P. (2005). in *Carbon dioxide capture for storage in deep geologic Formations*. Editor S. M. Benson (Amsterdam, Netherlands: Elsevier Science), 787–813.

Kawaraya, H., Abiko, T. and Matsubaya, O. (2016). *Hydrogen and oxygen isotopic ratios of precipitation at Noboribetsu, Hokkaido*. (Akita, Japan: Graduate School of Science and Technology Reports, Akita University Reports) 37, 31–36.

KIKO Network (2019). Risky dreams: carbon capture, utilization and storage (CCUS). Available at: https://www.kikonet.org/eng/publication-en/2019-08-15/paper-on-ccus.Position paper

Kobayashi, K., Hayashi, K., and Yarai, H. (2019). Geodetically estimated location and geometry of the fault plane involved in the 2018 Hokkaido Eastern Iburi earthquake. *Earth Planets Space* 71, 62. doi:10.1186/s40623-019-1042-6

Marumo, K., Longstaffe, F. J., and Matsubaya, O. (1995). Stable isotope geochemistry of clay minerals from fossil and active hydrothermal systems, southwestern Hokkaido, Japan. *Geochem. Cosmochim. Acta* 59, 2545–2559. doi:10.1016/0016-7037(95)00149-2

Nakagawa, M., Miyasaka, M., Miura, D., and Uesa, S. (2018). Tephrostratigraphy in Ishikari Lowland, southwestern Hokkaido. *J. Geol. Soc. Japan* 124, 473–489. doi:10.5575/geosoc.2018.0038

Nicol, A., Carne, R., Gerstenberger, M., and Christophersen, A. (2011). Induced seismicity and its implications for CO_2 storage risk. *Energy Procedia* 4, 3699–3706. doi:10.1016/j.egypro.2011.02.302

Nitta, M., and Inoue, A. (2011). Carbon and oxygen isotope compositions of calcite and rhodochrosite from geothermal exploratory drills TH-4 and TH-6 near the Toyoha deposit, Hokkaido, Japan. *Resour. Geol.* 61, 159–173. doi:10.1111/j.1751-3928.2011.00156.x

Ohzono, M., Takahashi, H., and Ito, C. (2019). Spatiotemporal crustal strain distribution around the Ishikari-Teichi-Toen fault zone estimated from global navigation satellite system data. *Earth Planets Space* 71, 50. doi:10.1186/s40623-019-1024-8

Onda, S., Sano, Y., Takahata, N., Kagoshima, T., Miyajima, T., Shibata, T., et al. (2018). Groundwater oxygen isotope anomaly before the M6.6 Tottori earthquake in Southwest Japan. *Sci. Rep.* 8, 4800. doi:10.1038/s41598-018-23303-8

Sano, Y., and Fischer, T. P. (2013). "The analysis and interpretation of noble gases in modern hydrothermal systems," in *The noble gases as geochemical tracers*. Editor P. Burnard (Berlin, Heidelberg, Germany: Springer), 249–317.

Sano, Y., Gamo, T., Notsu, K., and Wakita, H. (1995). Secular variations of carbon and helium isotopes at Izu-Oshima Volcano, Japan. *J. Volcanol. Geoth. Res.* 64, 83–94. doi:10.1016/0377-0273(94)00041-e

Sano, Y., Hara, T., Takahata, N., Kawagucci, S., Honda, M., Nishio, Y., et al. (2014). Helium anomalies suggest a fluid pathway from mantle to trench during the 2011 Tohoku-Oki earthquake. *Nat. Commun.* 5, 3084. doi:10.1038/ncomms4084

Sano, Y., and Marty, B. (1995). Origin of carbon in fumarolic gas from island arcs. *Chem. Geol.* 119, 265–274. doi:10.1016/0009-2541(94)00097-r

Sano, Y., Nakamura, Y., Notsu, K., and Wakita, H. (1988). Influence of volcanic eruptions on helium isotope ratios in hydrothermal systems induced by volcanic eruptions. *Geochem. Cosmochim. Acta* 52, 1305–1308. doi:10.1016/0016-7037(88)90284-0

Sano, Y., Tokutake, T., and Takahata, N. (2008). Accurate measurement of atmospheric helium isotopes. *Anal. Sci.* 24, 521–525. doi:10.2116/analsci.24.521

Sawada, Y., Tanaka, J., Suzuki, C., Tanase, D., and Tanaka, Y. (2018). Tomakomai CCS demonstration project of Japan, CO_2 injection in progress. *Energy Procedia* 154, 3–8. doi:10.1016/j.egypro.2018.11.002

Shibasaki, T. (1981). *Fluid dynamics in a deep sedimentary basin*. (Tokyo, Japan: Tokai University Press), 356.

Tanaka, Y., Abe, M., Sawada, Y., Tanase, D., Ito, T., and Kasukawa, T. (2014). Tomakomai CCS demonstration project in Japan, 2014 Update. *Energy Procedia* 63, 6111–6119. doi:10.1016/j.egypro.2014.11.643

Tanaka, Y., Sawada, Y., Tanase, D., Tanaka, J., Shiomi, S., and Kasukawa, T. (2017). Tomakomai CCS demonstration project of Japan, CO_2 injection in process. *Energy Procedia* 114, 5836–5846. doi:10.1016/j.egypro.2017.03.1721

Tsunogai, U., and Wakita, H. (1995). Precursory chemical changes in ground water: Kobe earthquake, Japan. *Science* 269, 61–63. doi:10.1126/science.269.5220.61

Yamanouchi, Y., Higashinaka, M., Yoshii, T., and Todaka, N. (2011). Study of geological storage for a candidate CCS demonstration Project in Tomakomai, Hokkaido, Japan. *Energy Procedia* 4, 5677–5684. doi:10.1016/j.egypro.2011.02.561

Yokokura, T. Okada, S., and Yamaguchi, K. (2014). "Subsurface geological structure revealed by seismic reflection surveys around the southern part of the Eastern Boundary Fault Zone of the Ishikari Lowland, Hokkaido, Japan," in *Sea-land seamless geological map, Ishikari-Teichi South Coast.* (Warrendale, PA: AIST).

Zhao, D., Kanamori, H., Negishi, H., and Wiens, D. (1996). Tomography of the source area of the 1995 Kobe earthquake: evidence for fluids at the hypocenter?. *Science* 274, 1891–1894. doi:10.1126/science.274.5294.1891

Zhao, D., Liu, X., and Hua, Y. (2018). Tottori earthquakes and Daisen volcano: effects of fluids, slab melting and hot mantle upwelling. *Earth Planet Sci. Lett.* 485, 121–129. doi:10.1016/j.epsl.2017.12.040

Zhao, L., Zuykov, M., Tanaka, K., Shirai, K., Anderson, J., McKindsey, C. W., et al. (2019). New insight into light-enhanced calcification in mytilid mussels, Mytilus sp., infected with photosynthetic algae Coccomyxa sp.: $\delta^{13}C$ value and metabolic carbon record in shells. *J. Exp. Mar. Biol. Ecol.* 520, 151211. doi:10.1016/j.jembe.2019.151211

Zoback, M. D., and Gorelick, S. M. (2012). Earthquake triggering and large-scale geologic storage of carbon dioxide. *Proc. Natl. Acad. Sci. Unit. States Am.* 109, 10164–10168. doi:10.1073/pnas.1202473109

Conflict of Interest: The authors declare that the research was conducted in the absence of any commercial or financial relationships that could be construed as a potential conflict of interest.

Copyright © 2020 Sano, Kagoshima, Takahata, Shirai, Park, Snyder, Shibata, Yamamoto, Nishio, Chen, Xu, Zhao and Pinti. This is an open-access article distributed under the terms of the Creative Commons Attribution License (CC BY). The use, distribution or reproduction in other forums is permitted, provided the original author(s) and the copyright owner(s) are credited and that the original publication in this journal is cited, in accordance with accepted academic practice. No use, distribution or reproduction is permitted which does not comply with these terms.

frontiers in Earth Science

ORIGINAL RESEARCH
published: 15 January 2021
doi: 10.3389/feart.2020.599388

Short-Term Monitoring of Geogenic Soil CO_2 Flux in a Non-Volcanic and Seismically Inactive Emission Site, South Korea

Chan Yeong Kim[1†], *Soonyoung Yu*[2*], *Yun-Yeong Oh*[2†], *Gitak Chae*[1], *Seong-Taek Yun*[2] *and Young Jae Shinn*[1]

[1]Korea Institute of Geoscience and Mineral Resources (KIGAM), Daejeon, South Korea, [2]Department of Earth and Environmental Sciences and Korea-CO2 Storage Environmental Management (K-COSEM) Research Center, Korea University, Seoul, South Korea

Temporal changes of soil CO_2 flux (FCO_2) and soil CO_2 concentration ($[CO_2]_v$) were surveyed in a natural CO_2 emission site to characterize the factors controlling the short-term temporal variation of geogenic FCO_2 in a non-volcanic and seismically inactive area. Due to a lack of long-term monitoring system, FCO_2 was discontinuously measured for three periods: I, II at a high FCO_2 point (M17) and III about 30 cm away. Whereas $[CO_2]_v$ was investigated at a point (60 cm depth) for all periods. A 2.1 magnitude earthquake occurred 7.8 km away and 20 km deep approximately 12 h before the period II. The negative correlation of FCO_2 with air pressure suggested the non-negligible advective transport of soil CO_2. However, FCO_2 was significantly and positively related with air temperature as well, and $[CO_2]_v$ showed different temporal changes from FCO_2. These results indicate the diffusive transport of soil CO_2 dominant in the vadose zone, while the advection near the surface. Meanwhile $[CO_2]_v$ rapidly decreased while an anomalous FCO_2 peak was observed during the period II, and the CO_2 emission enhanced by the earthquake was discussed as a possible reason for the synchronous decrease in $[CO_2]_v$ and increase in FCO_2. In contrast, $[CO_2]_v$ increased to 56.8% during the period III probably due to low gas diffusion at cold weather. In addition, FCO_2 was low during the period III and showed different correlations with measurements compared to FCO_2 at M17, implying heterogeneous CO_2 transport conditions at the centimeter scale. The abnormal FCO_2 observed after the earthquake in a seismically inactive area implies that the global natural CO_2 emission may be higher than the previous estimation. The study result suggests a permanent FCO_2 monitoring station in tectonically stable regions to confirm the impact of geogenic CO_2 to climate change and its relation with earthquakes.

Keywords: geogenic soil CO_2 flux, temporal changes, controlling factors, non-volcanic and seismically inactive, earthquake

OPEN ACCESS

Edited by:
Guodong Zheng,
Chinese Academy of Sciences (CAS), China

Reviewed by:
Jianguo Du,
China Earthquake Administration, China
Zhi Chen,
China Earthquake Administration, China
Georgy Alekseevich Chelnokov,
Geological Institute (RAS), Russia

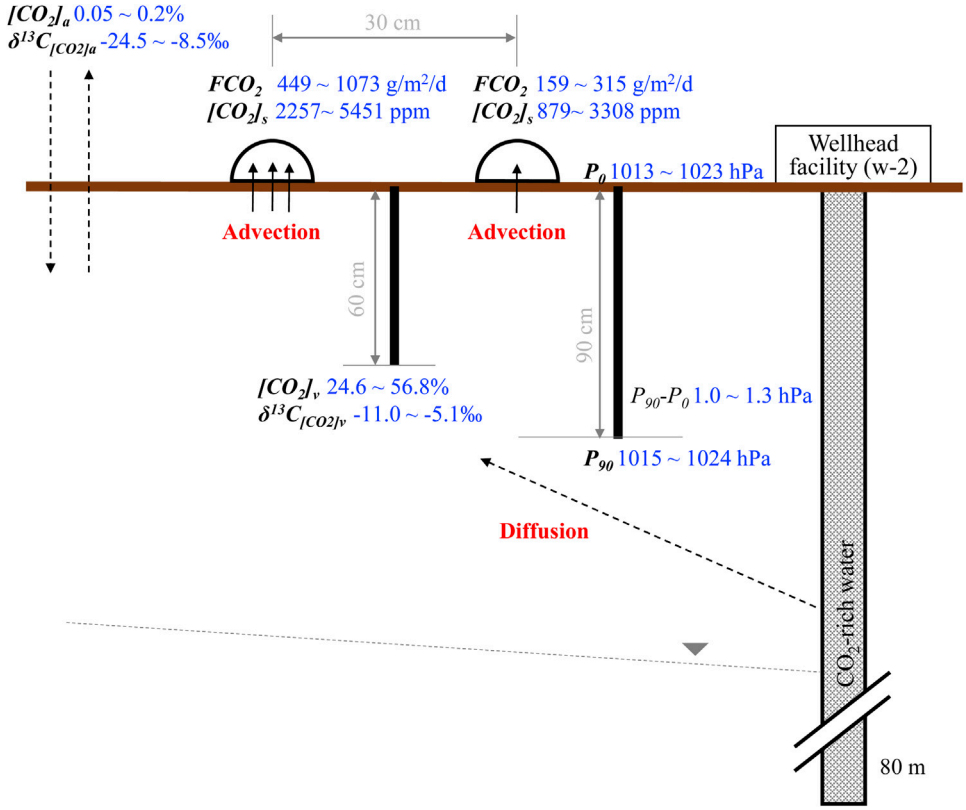
****Correspondence:***
Soonyoung Yu
iamysy@korea.ac.kr

†Present address:
Chan Yeong Kim,
Pohang Accelerator Laboratory, Pohang, South Korea
Yun-Yeong Oh,
Korea National Institute of Environmental Research, Incheon, South Korea

Specialty section:
This article was submitted to Geochemistry, a section of the journal Frontiers in Earth Science

Received: *27 August 2020*
Accepted: *26 November 2020*
Published: *15 January 2021*

Citation:
Kim CY, Yu S, Oh Y-Y, Chae G, Yun S-T and Shinn YJ (2021) Short-Term Monitoring of Geogenic Soil CO_2 Flux in a Non-Volcanic and Seismically Inactive Emission Site, South Korea. Front. Earth Sci. 8:599388. doi: 10.3389/feart.2020.599388



GRAPHICAL ABSTRACT |

INTRODUCTION

Annual CO_2 emission from the Earth was estimated to be approximately 600 million tonnes, with almost half produced from subaerial volcanism and the other half from non-volcanic inorganic degassing such as tectonic activities (Kerrick et al., 1995; Mörner and Etiope, 2002; Chiodini et al., 2005; Burton et al., 2013; Fischer et al., 2019). Lots of studies have been performed on the spatial distributions of geogenic soil CO_2 flux (FCO_2) for various purposes: to identify the extent of anomalous CO_2 outflow and its relation to the structural geology (e.g., Annunziatellis et al., 2008; Ciotoli et al., 2014; Ciotoli et al., 2016; Jung et al., 2014; Ascione et al., 2018; Kim et al., 2019); to calculate the total CO_2 output (e.g., Chiodini et al., 1999; Cardellini et al., 2003; Sun et al., 2018); to investigate the origin of CO_2 (e.g., Schroder et al., 2016; Chen et al., 2020); to assess volcanic (e.g., Chiodini et al., 2001; Hernández et al., 2001; Carapezza et al., 2011; Morita et al., 2019) and seismic hazards (eg, Camarda et al., 2016; Fischer et al., 2017; Sciarra et al., 2017).

Meanwhile, the temporal changes of geogenic FCO_2 and their controlling factors were relatively less studied and mostly in volcanic or seismic areas (e.g., Chiodini et al., 1998; Granieri et al., 2003; Carapezza et al., 2011; Camarda et al., 2016; Camarda et al., 2019; Oliveira et al., 2018; Morita et al., 2019; Chen et al., 2020). Morita et al. (2019) showed that barometric pressure, air temperature, soil temperature and humidity, and wind speed were decisive variables that could explain more than half of the variations in FCO_2 at 1 km southwest of the active crater of Aso volcano, while the residuals were explained using an increase in magmatic CO_2 flux. Repeated measurements by Chiodini et al. (1998) showed that FCO_2 was governed by the change in barometric pressure, while other meteorological parameters such as rain, soil and air temperature, and humidity also influenced FCO_2 in volcanic and geothermal areas. As for seismically active regions, Kerrick and Caldeira (1993), Kerrick and Caldeira (1994), Kerrick and Caldeira (1998), and Kerrick et al. (1995) studied metamorphic CO_2 degassing, including convective hydrothermal CO_2 emission. In addition, Chiodini et al. (1999) suggested the non-volcanic CO_2 derived from mantle degassing and/or metamorphic decarbonation in Central Italy. Lee et al. (2016) estimated 4 Mt/yr of mantle-derived CO_2 released along deep faults in the Magadi–Natron Basin at the border between Kenya and Tanzania. Ascione et al. (2018) introduced anomalously high FCO_2 resulting from the combination of 1) intense CO_2 generation from magmatic bodies causing decarbonation of carbonate rocks; 2) a very thin or absent top seal overlying the carbonate reservoirs; 3) the occurrence of a dense network of active fault segments at the tip of a major crustal fault zone.

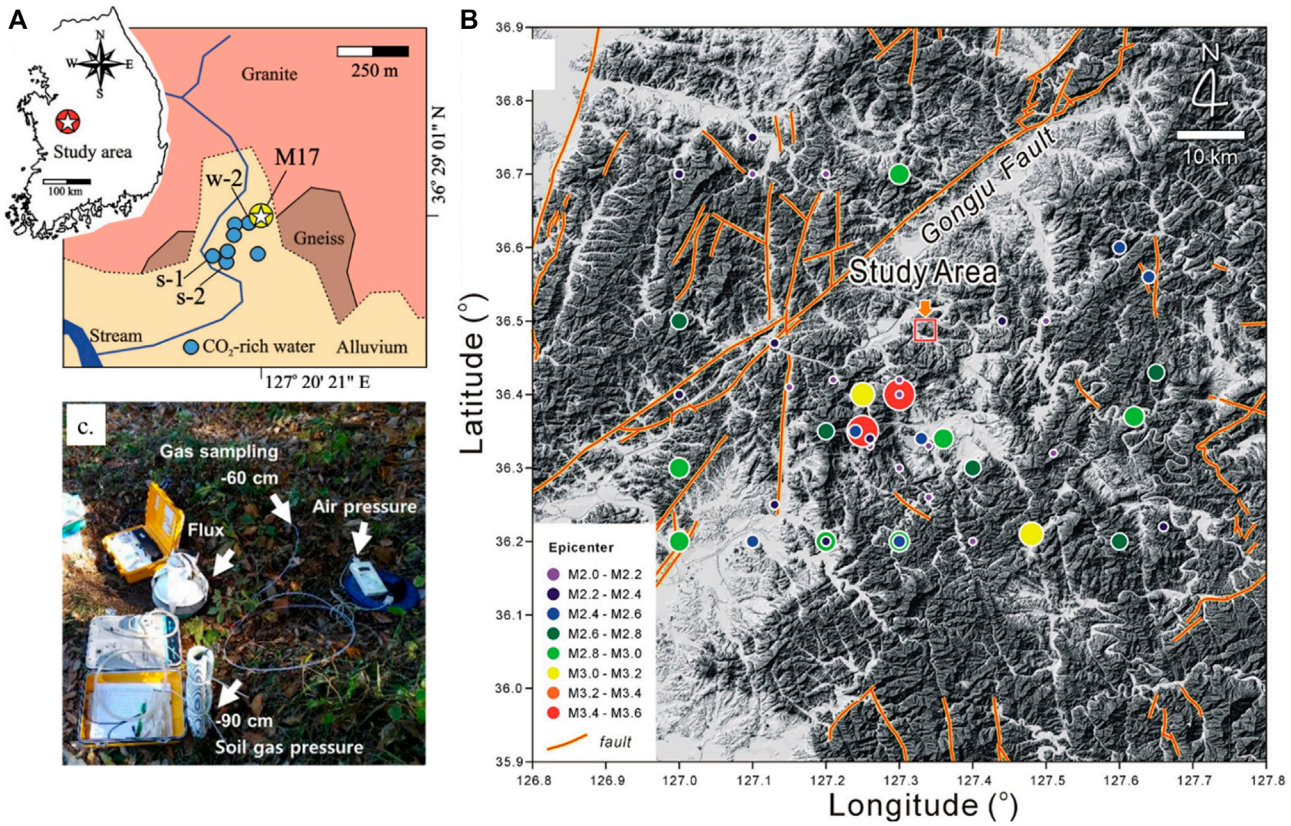


FIGURE 1 | Study area. **(A)** Location of the study point (M17) on the geological map. Five CO_2-rich groundwater wells including w-2 and two springs (s-1 and s-2) are also shown. **(B)** 49 epicenters around the study area in the past 30 years (KMA, 2019) including a recent earthquake (magnitude 2.1 and 20 km depth) occurring on November 19, 2018 at 7.8 km southwest of the study area. The larger circle indicates the larger magnitude. **(C)** Field measurements.

Moreover, seismic activity has been considered as an endogenous cause of the temporal variation of geogenic FCO_2 (Camarda et al., 2016; Camarda et al., 2019; Fischer et al., 2017; Sciarra et al., 2017; Chen et al., 2020). Specifically, Camarda et al. (2019) found that, of the two anomalous FCO_2 periods (A and C), the period A had a seismic swarm (3,471 seismic events in 79 days; Ricci et al., 2015) and thus showed the higher-amplitude anomalies than the period C. Camarda et al. (2016) showed the high spatial and temporal correlation between seismicity and FCO_2 in a district with continuous seismic activity, whereas FCO_2 varied independently in the districts with low and sporadic seismicity. According to Chen et al. (2020), seismic activity also can be responsible for the jumpily temporal variations of CO_2 concentration and flux in soil gas wells. Furthermore, vibro-stimulation was applied to increase the oil production based on the physics that the rate of degassing increases due to vibration energy (Kouznetsov et al., 1998; Kouznetsov et al., 2002).

However, studies have been rarely conducted about either the temporal variation of geogenic FCO_2 or the effect of small seismic events to FCO_2 in a geologically quiescent (e.g., non-volcanic or seismically inactive) environment. As an alternative, CO_2-rich waters have been studied in tectonically stable regions, in particular as a natural analogue study of geologic carbon storage to understand CO_2 leakage (e.g., Chae et al., 2016), because non-volcanic CO_2 is discharged by high-CO_2 groundwater as well as by focused degassing (Chiodini et al., 1999). For instance, in South Korea, which has no active volcanoes and had been relatively safe from seismic activity until the 2016 Gyeongju earthquake (M 5.8) (Woo et al., 2019), CO_2-rich waters have been studied to identify anomalously high soil CO_2 areas, and their origins (e.g., magmatic degassing, metamorphic devolatilization, oxidation of organic matter) and ascending pathways. According to Jeong et al. (2005), the CO_2 gas derived from a deep-seated source moves into the groundwater system along faults or geologic boundaries in South Korea. However, FCO_2 has been rarely studied, which motivated this study.

This study aimed 1) to characterize the temporal variation of FCO_2 in a non-volcanic and seismically inactive site (**Figure 1A**) where soil CO_2 was suggested to have a deep-seated magmatic origin (Kim et al., 2019), and 2) to identify the factors controlling the temporal changes of geogenic FCO_2. The time-variant CO_2 supply and the effect of a small earthquake were discussed. This study contributes to provide a new study direction of long-term FCO_2 monitoring to the atmosphere in tectonically stable regions,

which is important to assess due to the impacts of CO_2 on climate change, whereas many existing studies have focused on volcanic or seismic regions.

STUDY AREA

The study area (Daepyeong; Lat. 36°29′01″N and Long. 127°20′21″E) is located in the central South Korea (**Figure 1A**) and in the middle of a small basin (about 1.1 km^2). The small watershed is surrounded by mountains lower than 270 m above sea level, and the low and flat area of the basin is mostly used for rice cultivation. There are also farmhouses and gardens that cultivate vegetables, fruits, and pine saplings on a small scale.

The bedrock of the study area consists of Precambrian gneiss that was intruded by Jurassic granite (**Figure 1A**). The gneiss and granite are overlain by Quaternary sediments at lower altitudes. It is noticeable that the study area is located at the geologic boundary between gneiss and granite, along which five CO_2-rich groundwater wells and two CO_2-rich springs occur (**Figure 1A**; Jeong et al., 2001; Jeong et al., 2005; Chae et al., 2016). Chae et al. (2016) observed fractures (fissures and/or joints) and CO_2 bubbles from the fractures at a CO_2-rich spring (s-1). Kim et al. (2019) found a high FCO_2 point (M17 in **Figure 1A**) about 1.8 m away from a CO_2-rich groundwater well (w-2) to release geogenic CO_2 through the soil layer among a total of 94 points within 1 km^2. The well (w-2) has a depth of 80 m and a diameter of 150 mm, and CO_2-rich water is irregularly taken at w-2 for domestic usage by countless residents. The contact of gneiss and granite is observed on a slope near the well w-2.

A fault has not been identified in the study area (MCT et al., 2006), whereas there are faults in a regional scale including the closest Gongju Fault approximately 13 km away from the study area (**Figure 1B**). At the regional scale, the study area is located on the southwest of the NE/SW trending Ogcheon Belt (Ogcheon region). The Ogcheon Belt is a fold-and-thrust belt affected by several deformational phases, and the Ogcheon region is mainly composed of metamorphosed clastic and volcanic rocks (Kihm and Kim, 2003). In the Ogcheon region, CO_2-rich waters occur in the NE-SW direction (**Supplementary Figure S1**), parallel to the Gongju Fault and Ogcheon Belt, which implies the relation of CO_2-rich waters to faults or fractures, while no evidence has yet been found.

A total of 49 small earthquakes (≥magnitude 2.0) occurred within 30 km from the study area in the past 30 years (**Figure 1B**; KMA, 2019), including the 2.1 magnitude (M) earthquake occurring on 03:34 November 19, 2018 at 7.8 km southwest of the study area and 20 km deep. The information of focal depths is available only for five earthquakes occurring after 2017 and in the range of 11–20 km. The distribution of earthquake epicenters and their magnitudes indicate that the study area is relatively free from seismic hazards, while there may be unidentified and buried fractures.

The annual average temperature of the study area was 12.2°C, while the annual average relative humidity (*RH*) was 70.8% in 1967–2004 (MCT et al., 2006). The atmospheric temperature (T_{aws}) varied from 2.5 to 17.8°C in the period Ⅰ (**Table 1**; KMA, 2019). There was no rainfall, while it rained a week before the period Ⅰ. The total rainfall amount was 35.3 mm from October 26 to 29, 2018. During the periods Ⅱ and Ⅲ, T_{aws} ranged between −0.9 and 12.7°C and between −10.7 and 9.5°C (**Table 1**), and the total amount of precipitation was 6.5 and 1.0 mm (**Supplementary Figure S2**), respectively.

METHODOLOGY

This study was conducted around the M17 point in **Figure 1A** found by a preliminary study on the spatial variation of FCO_2 around the CO_2-rich wells and springs with 50 –100 m spacing within 1 km^2 (Kim et al., 2019). Among a total of 94 points, M17 was the only point to show geogenic CO_2 outflow through the soil layer. FCO_2 was detected up to 546 g/m^2/d, while the soil CO_2 concentration at a depth of 60 cm ($[CO_2]_v$) and its carbon isotope ($\delta^{13}C_{[CO2]v}$) were 36.0% and -5.7‰, respectively at M17 in summer, 2017 (**Table 1**), which were much higher than the values of biogenic origin (average FCO_2 of 44.9 g/m^2/d, $[CO_2]_v$ of 0.7% and $\delta^{13}C_{[CO2]v}$ of −25.2‰) observed at 79 samples in the study area (Kim et al., 2019).

Three Periods

Field works were conducted through three periods Ⅰ (from November 2 to 5, 2018), Ⅱ (November 19, 2018 to January 30, 2019), and Ⅲ (December 2 to 8, 2019) (**Table 1**; **Supplementary Figure S2**). Monitoring during the periods Ⅰ and Ⅲ was conducted to assess the background level of FCO_2 and CO_2 concentration in soil gas ($[CO_2]_v$), while FCO_2 and $[CO_2]_v$ were investigated during the period Ⅱ to assess the effect of a 2.1 M earthquake nearby (i.e., 7.8 km southwest and 20 km deep) on FCO_2.

Note that there is no long-term automated FCO_2 measurement system in the study area unlike other seismic or volcanic areas (e.g., Chiodini et al., 2001; Camarda et al., 2016; Morita et al., 2019) because FCO_2 is not a big concern. Besides, the study area is a private land. Thus, data were missing between periods, and measurement frequency varied at each period (**Supplementary Figure S2**) depending on the situations in the field (e.g., accessibility, power supply). Specifically, FCO_2 measurement and soil gas sampling were conducted simultaneously every 2 h during the period Ⅰ. Atmospheric air samples were collected in an 8-h interval approximately 1 m above the surface. Two weeks after the period Ⅰ ended, a 2.1 M earthquake occurred. Thus, further investigations for FCO_2 and soil gas were conducted since about 12 h after the earthquake occurred (period Ⅱ). FCO_2 was measured three times a day (at 14:00, 15:00, and 16:00), while soil gas samples were taken once a day (around at 14:00) until November 25. Then FCO_2 and soil gas were monitored once a week between December 26, 2018 and January 30, 2019 (**Table 1**). Lastly, FCO_2 was frequently (every 30 min) measured for a week from 00:30 December 2 to 22:30 December 8, 2019 (period Ⅲ). Soil gas and atmospheric gas samples were collected once at 15:00 on 8 December, 2019 for comparison.

TABLE 1 | Measurement results (mean ± standard deviation and range). '*n*' represents the number of measurements.

Variable[a]	Unit	Period				August, 2017 (Kim et al., 2019)
		I	II until November 25, 2018	II after December 26, 2018[b]	III	
FCO_2	g/m^2/d	564 ± 52 (*n* = 42) (449–674)	727 ± 99 (*n* = 22) (580–1,073)	606 ± 100 (*n* = 18) 449–802	228 ± 25 (*n* = 328) (159–315)	546
T_s	°C	10.1 ± 5.7 (*n* = 42) (2.3–20.7)	10.4 ± 2.5 (*n* = 22) (6.8–14.8)	8.6 ± 2.7 (*n* = 18) 4.1–12.5	0.0 ± 4.7 (*n* = 329) (–9.3–14.9)	25.5
RH_s	%	83 ± 16 (*n* = 43) (25–97)	78 ± 10 (*n* = 22) (59–95)	50 ± 12 (*n* = 18) 38–73	68 ± 17 (*n* = 329) (18–95)	89.0
$[H_2O]_s$	mmol/mol	10.4 ± 2.3 (*n* = 42) (6.9–14.5)	9.9 ± 1.6 (*n* = 22) (7.4–12.4)	5.8 ± 1.7 (*n* = 18) 3.3–8.3	4.3 ± 1.5 (*n* = 329) (1.6–8.4)	29.6
$[CO_2]_s$	ppm	3,271 ± 500 (*n* = 42) (2,457–5,451)	3,504 ± 410 (*n* = 22) (2,697–4,272)	2,926 ± 404 (*n* = 18) (2,257–3,643)	1,423 ± 484 (*n* = 329) (879–3,308)	4,428
P_s	hPa	999 ± 2 (*n* = 42) (996–1,005)	999 ± 2 (*n* = 22) (996–1,003)	999 ± 4 (*n* = 18) 994–1,006	1,002 ± 5 (*n* = 329) (992–1,011)	987
P_{aws}	hPa	1,025 ± 2 (*n* = 43) (1,021–1,030)	1,024 ± 2 (*n* = 22) (1,021–1,028)	1,025 ± 4 (*n* = 18) 1,020–1,033	1,030 ± 5 (*n* = 333) (1,019–1,039)	1,013
T_{aws}	°C	9.7 ± 5.0 (*n* = 43) (2.5–17.8)	8.0 ± 2.9 (*n* = 22) (4.0–12.7)	3.7 ± 3.6 (*n* = 18) –0.9–8.1	–0.3 ± 4.2 (*n* = 333) (–10.7–9.5)	25.1
RH_{aws}	%	65 ± 23 (*n* = 43) (25–96)	48 ± 25 (*n* = 22) (17–94)	28 ± 5 (*n* = 18) 22–37	68 ± 20 (*n* = 333) (23–100)	68
WS_1	m/s	0.7 ± 0.5 (*n* = 43) (0.0–2.3)	1.5 ± 1.0 (*n* = 22) (0.1–4.2)	2.1 ± 0.9 (*n* = 18) 0.6–3.9	1.3 ± 1.1 (*n* = 328) (0.0–7.6)	1
WS_{10}	m/s	0.7 ± 0.4 (*n* = 43) (0.0–1.9)	1.4 ± 0.8 (*n* = 22) (0.4–3.0)	1.9 ± 0.8 (*n* = 18) 0.9–3.5	-	1
P_0	hPa	1,017 ± 2 (*n* = 43) (1,013–1,023)	-	-	-	
P_{90}	hPa	1,018 ± 2 (*n* = 35)[c] (1,015–1,024)	-	-	-	
ΔP	hPa	1.1 ± 0.1 (*n* = 35)[c] (1.0–1.3)	-	-	-	
$[N_2]_v$	%	42.9 ± 1.4 (*n* = 43) (40.0–46.3)	56.1 ± 0.6 (*n* = 7) (55.0–56.8)	51.5 ± 0.9 (*n* = 5) 50.6–52.9	30.3 (*n* = 1)	49.8
$[O_2]_v$	%	11.4 ± 0.3 (*n* = 43) (10.6–12.2)	14.9 ± 0.2 (*n* = 7) (14.7–15.1)	13.6 ± 0.1(*n* = 5) 13.4–13.8	7.8 (*n* = 1)	13.2
$[CO_2]_v$	%	43.8 ± 1.9 (*n* = 43) (39.6–48.9)	26.1 ± 1.0 (*n* = 7) (24.6–27.3)	32.5 ± 0.9 (*n* = 5) 31.0–33.2	56.8 (*n* = 1)	36.0
$[N_2]_a$	%	77.9 ± 0.8 (*n* = 11) (76.9–79.0)	-	-	76.6 (*n* = 1)	20.8
$[O_2]_a$	%	20.6 ± 0.1 (*n* = 11) (20.5–20.7)	-	-	20.4 (*n* = 1)	77.3
$[CO_2]_a$	%	0.11 ± 0.05 (*n* = 9) (0.05–0.19)	-	-	0.2 (*n* = 1)	0.05
$\delta^{13}C_{[CO2]v}$	‰	–7.1 ± 1.2 (*n* = 43) (–10.1 ~ –5.4)	–7.0 ± 1.9 (*n* = 7) (–11.0 ~ –5.1)	–5.9 ± 0.5 (*n* = 5) (–6.4 ~ –5.1)	–6.2 (*n* = 1)	–5.7
$\delta^{13}C_{[CO2]a}$	‰	–19.0 ± 2.8 (*n* = 10) (–24.5 ~ –15.7)			–8.5 (*n* = 1)	–10.6

[a] *See* ***Supplementary Table S1*** *for details.*

[b] *weekly monitored.*

[c] P_{90} *values (thus* $\Delta P = P_{90}$-P_0*) were missing between 8 PM on November 2 and 10 AM on November 3 (see* ***Figure 3****).*

The FCO_2 measurement point during the period III was not exactly the same as M17, and about 30 cm away from M17 (called M17–1 hereafter) because the flux measurement device (i.e., LI-COR) had to be reinstalled in December, 2019 and we did not expect that the small spatial distance (i.e., 30 cm separation) affected the FCO_2 measurement. In contrast, $[CO_2]_v$ was investigated from the same tube (M17v) installed in August 2017 by Kim et al. (2019) for all three periods.

Sampling and Measurement

FCO_2, compositions of soil gas and atmospheric air, and their stable carbon isotopes ($\delta^{13}C_{CO2}$) were monitored. In addition, gas pressures were measured at a depth of 90 cm (P_{90}) and on the surface (P_0) during the period I. Meteorological parameters were obtained from an automatic weather station (AWS) of the Korea Meteorological Administration (KMA) near the study area (about 10 km away). All the measurements and their devices were summarized in **Supplementary Table S1**. FCO_2, P_0, and P_{90} measurements (*CO_2 flux and Gas Pressure Measurement*) and gas sampling and analysis (*Ga Sampling and Analysis*) were detailed below.

CO_2 flux and Gas Pressure Measurement

A PVC collar (height of 11.5 cm and inside diameter of about 20 cm) was implanted into the soil, on which a bottom-opened chamber was placed (**Figure 1C**). Then pressure (P_s; hPa), temperature (T_s; °C), relative humidity (RH_s; %), CO_2 concentration ($[CO_2]_s$; ppm), and water vapor mole fraction ($[H_2O]_s$; mmol/mol) in the soil chamber were measured for 2 min by a built-in infrared gas analyzer using LI-COR 8100A (LI-COR Inc. Lincoln, NE, USA). FCO_2 (g/m^2/d) was calculated by **Equation 1** as Jung et al. (2014):

$$FCO_2 = k\frac{10V\,P\left(1-\frac{[H_2O]}{1000}\right)}{R\cdot S(T+273.15)}\frac{d[CO_2]}{dt} \quad (1)$$

where k is a unit conversion factor (3.80 g·s/μmol/d), R is the universal gas constant (8.31 m^3·Pa/K/mol), S is the soil surface area (herein, 317.8 cm^2 for the about 20 cm diameter chamber), V is the system volume (i.e., the sum of the chamber volume and the extra volume by a offset), P, T, and $[H_2O]$ are the initial P_s, T_s, and $[H_2O]_s$, respectively, and $d[CO_2]/dt$ is the rate of change in $[CO_2]_s$ for the 2-min measurement.

Pore gas pressure (P_{90}) and atmospheric pressure (P_0) were monitored using a pressure transducer (BAT® geosystem). A porous filter tip was connected to the end of a 2.54 cm diameter pipe and then installed to a target depth (i.e., 90 cm). Then the pressure transducer with a needle was poked to the rubber on the top of the filter tip. Pressures were measured at a 1-min interval over the whole survey period I. However, 30-min average values

of P_{90} and P_0 were used when the relationships with other measurements were assessed. In other words, P_{90} and P_0 data (thus $\Delta P = P_{90} - P_0$) were taken for 15 min before and after the FCO_2 measurement, respectively and then averaged for the 30 min.

Ga Sampling and Analysis

Soil gas samples were taken using a Teflon tube which had the outer diameter of 0.64 cm and was embedded down to 60 cm below the surface with the AMS Gas Vapor Probe (AMS, Inc., USA). Atmospheric air samples were collected 1 m above the surface. Soil gas and atmospheric air samples were purged for 5 min using a portable Masterflex E/S peristaltic pump (Cole-Parmer Instruments, USA) and then collected in a 1 L multi-layered Tedlar bag (Restek©, USA). Soil gas duplicates were collected once a day (at 14:00; n = 4) during the period I to double check the results of $\delta^{13}C_{[CO2]v}$ analysis, with connecting the y-shaped adapter at the end of the sampling tube.

The carbon isotope of CO_2 ($\delta^{13}C_{CO2}$) in the gas samples were analyzed by the Picarro G2121-i isotope and gas analyzer (Picarro Inc., USA) at the Korea Institute of Geoscience and Mineral Resources (KIGAM). The Picarro cavity ring-down spectroscopy (CRDS) was calibrated by IAEA standard materials ($\delta^{13}C_{CO2}$ = 2.492, −5.764, −47.321‰) before analyzing samples. All gas samples were purged for 10 min with laboratory air and then analyzed for 15 min to avoid the memory effect. Results were expressed relative to the international V-PDB standard. The soil gas duplicates (n = 4) obtained during the period I and a soil gas sample obtained during the period III were analyzed by Thermo Fisher Delta V™ IRMS (isotope ratio mass spectrometer) at Beta Analytic Inc. (Miami, USA) for comparison.

Gas compositions (N_2, O_2, and CO_2) were determined by the Agilent 490 Micro Gas Chromatograph (GC) at KIGAM. Before the laboratory analysis, two columns in GC (i.e., CP-Molsieve 5A column for N_2 and O_2 and PoraPLOT U column for CO_2) were calibrated by three different standards (CO_2 = 49.98; 5.00; 0.04%: Rigas©, Korea). Each sample was analyzed at least three times, and the coefficient of variation was less than 0.9% for CO_2.

Statistical Analysis and CO_2 Solubility Calculation

Simple statistical analyses were applied for each period because of discontinuous and short-term observations at different intervals. First, Pearson correlation coefficients (r) were calculated to evaluate the effect of environmental parameters to FCO_2, and to find the relation varying depending on a measurement period. According to Camarda et al. (2019), the response of FCO_2 to exogenous parameter variations is dependent on the predominant process of CO_2 transport through the soil. At sites with diffusion-dominated CO_2 transport, FCO_2 was mainly affected by variation in the volumetric water content of the soil and the air temperature, while at sites with high fluxes and non-negligible advective components, FCO_2 was affected solely by variation in the atmospheric pressure (Camarda et al., 2019). The relationship between FCO_2 and exogenous parameters is also influenced by the amount of deep CO_2 supply. Then multiple regression was used to explain the relationship between FCO_2 and highly correlated environmental parameters and to estimate the effect of endogenous parameters. Regression analyses have been widely conducted (Granieri et al., 2003; Vodnik et al., 2009; Carapezza et al., 2011; Camarda et al., 2016; Oliveira et al., 2018; Morita et al., 2019) to distinguish the effect of each factor to the FCO_2 variation, including endogenous (e.g., seismicity) and environmental parameters. It should be noted that we used P_s, T_s, $[CO_2]_s$ and $[H_2O]_s$ in the soil chamber measured for 2 min using LI-COR 8100A as environmental parameters (see **Table 1** and **Supplementary Table S1**) and discussed their usefulness (*Environmental Parameters*), because they represent the mixture of soil efflux from the soil layer for 2 min and the air initially filling the chamber, and are different from the initial values used to calculate FCO_2 in **Equation 1**.

Second, autocorrelation of time series was assessed to find the periodicity for the data obtained during the periods I and III (**Supplementary Figures S3, S4**). Cross-correlation coefficients (R_{xy}) were evaluated for the data obtained during the period I to characterize the lead-lag relationship between input variables (x; measurements in **Table 1**) and output variables (y; mainly FCO_2 in this study) and a time lag (**Supplementary Figure S5**):

$$R_{xy}\left(t_{lag}\right) = \frac{C_{xy}\left(t_{lag}\right)}{\sigma_x\left(t_{lag}\right)\sigma_y\left(t_{lag}\right)} \quad (2)$$

where C_{xy} is the covariance between x and y, while σ_x and σ_y are the standard deviations of x and y in a lag time (t_{lag}), respectively. When t_{lag}= 0, $r = R_{xy}(0)$. R statistical software was used for autocorrelation and cross-correlation analysis (R core team, 2019).

In addition, the amount of CO_2 degassing from a CO_2-rich aquifer was estimated by calculating the variation in CO_2 solubility in groundwater due to the variation in pressure, salinity and temperature based on the method by Duan and Sun (2003).

RESULTS

Background Levels

Measurements during the periods I and III were compared to assess the background levels of FCO_2 and soil gas compositions (**Table 1**) and their relations with environmental variables (**Tables 2**, **3**). **Table 4** showed R_{xy} with a non-zero t_{lag}. The other parameters showed a t_{lag} of zero with FCO_2, and thus R_{xy} = r in **Table 2** when $y = FCO_2$.

CO_2 Flux

The average FCO_2 during the period I was 564 g/m^2/d and ranged from 449 to 674 g/m^2/d, which was similar to 546 g/m^2/d obtained at M17 in August 2017 (**Table 1**) and quite high compared to FCO_2 in the other 93 points (7.5–118 g/m^2/d) in the study area measured by Kim et al. (2019) and in typical normal soil systems (~40 g/m^2/d) suggested in Ascione et al. (2018). Meanwhile, FCO_2 during the period III ranged between 159 and 315 g/m^2/d (average of 228 g/m^2/d), which was higher than those in the 93 points of Kim et al. (2019) and in typical normal soil systems by Ascione et al. (2018), but much lower than

TABLE 2 | Pearson correlation coefficients during the period I. Absolute values ≥0.6 are in bold.

	FCO_2	T_s	RH_s	$[H_2O]s$	$[CO_2]_s$	P_s	P_{awa}	T_{aws}	RH_{aws}	WS_1	WS_{10}	P_0	P_{90}	ΔP	$[N_2]_v$	$[O_2]_v$	$[CO_2]_v$	$[N_2]_a$	$[O_2]_a$	$[CO_2]_a$	$\delta^{13}C_{[CO2]v}$	$\delta^{13}C_{[CO2]a}$
FCO_2	1.0																					
T_s	0.5	1.0																				
RH_s	**–0.6**	**–0.9**	1.0																			
$[H_2O]_s$	0.5	**1.0**	**–0.8**	1.0																		
$[CO_2]_s$	0.3	0.2	–0.1	0.3	1.0																	
P_s	**–0.8**	–0.3	0.3	–0.3	–0.2	1.0																
P_{aws}	**–0.8**	–0.4	0.3	–0.3	–0.2	1.0	1.0															
T_{aws}	0.5	***1.0***	***–0.8***	**1.0**	0.3	–0.3	–0.4	1.0														
RH_{aws}	–0.4	**–0.9**	**0.7**	**–0.9**	–0.2	0.3	0.4	**–0.9**	1.0													
WS_1	0.2	**0.6**	–0.5	0.5	0.0	0.0	–0.1	**0.6**	**–0.6**	1.0												
WS_{10}	0.1	0.5	–0.4	0.5	0.0	0.1	0.1	0.5	**–0.6**	**0.8**	1.0											
P_0	**–0.8**	–0.3	0.3	–0.3	–0.2	**1.0**	**1.0**	–0.4	0.3	–0.1	0.1	1.0										
P_{90}	**–0.6**	–0.1	0.1	–0.1	–0.4	**1.0**	**1.0**	–0.1	0.1	0.2	0.4	**1.0**	1.0									
ΔP	0.4	**0.9**	**–0.8**	**1.0**	0.2	–0.2	–0.2	**0.9**	**–0.8**	0.5	0.4	–0.2	–0.1	1.0								
$[N_2]_v$	0.1	0.3	–0.3	0.3	0.1	0.1	0.0	0.4	–0.5	0.4	0.4	0.0	**0.7**	0.1	1.0							
$[O_2]_v$	0.1	0.3	–0.2	0.3	0.1	0.1	0.0	0.4	–0.5	0.4	0.4	0.0	**0.7**	0.0	**1.0**	1.0						
$[CO_2]_v$	–0.2	–0.4	0.3	–0.4	0.0	0.0	0.1	–0.4	0.5	–0.4	–0.4	0.1	**–0.6**	–0.1	**–0.9**	**–1.0**	1.0					
$[N_2]_a$	**0.6**	0.0	–0.1	–0.1	0.1	–0.5	–0.5	–0.1	0.0	–0.2	0.0	–0.5	–0.4	–0.3	–0.2	–0.3	0.1	1.0				
$[O_2]_a$	**0.9**	0.3	–0.3	0.2	0.2	**–0.8**	**–0.8**	0.3	–0.2	–0.2	–0.3	**–0.8**	**–0.8**	0.0	–0.2	–0.2	0.0	**0.7**	1.0			
$[CO_2]_a$	**–0.8**	0.0	0.0	0.0	0.0	**0.8**	**0.8**	–0.1	0.0	0.2	**0.6**	**0.8**	**0.8**	–0.1	**0.6**	**0.6**	–0.5	–0.1	**–0.7**	1.0		
$\delta^{13}C_{[CO2]v}$	–0.2	0.3	–0.2	0.2	0.0	0.2	0.2	0.3	-0.3	0.1	0.1	0.2	0.1	0.4	0.2	0.2	–0.1	–0.5	–0.5	0.4	1.0	
$\delta^{13}C_{[CO2]a}$	–0.–4	–0.2	0.1	–0.3	0.0	0.4	0.4	–0.2	0.0	–0.1	0.2	0.4	0.2	0.1	–0.2	–0.3	0.3	0.3	–0.3	**0.7**	–0.1	1.0

TABLE 3 | Pearson correlation coefficients during the period III. Absolute values ≥0.6 are in bold.

	FCO_2	T_s	RH_s	$[H_2O]_s$	$[CO_2]_s$	P_s	P_{aws}	T_{aws}	RH_{aws}	WS
FCO_2	1.0									
T_s	**0.6**	1.0								
RH_s	0.0	−0.3	1.0							
$[H_2O]_s$	0.5	**0.6**	0.5	1.0						
$[CO_2]_s$	**0.0**	−0.2	0.4	0.1	1.0					
P_s	**−0.6**	−0.4	−0.3	−0.6	−0.2	1.0				
P_{aws}	**−0.7**	−0.5	−0.3	**−0.7**	−0.2	**1.0**	1.0			
T_{aws}	**0.6**	**0.9**	−0.1	**0.7**	−0.1	−0.5	**−0.6**	1.0		
RH_{aws}	0.1	−0.2	**0.7**	0.4	0.5	−0.4	−0.4	−0.2	1.0	
WS	0.1	0.5	−0.4	0.1	−0.4	0.0	0.0	0.4	−0.5	1.0

TABLE 4 | Cross-correlation coefficients with a non-zero time lag during the period I. See **Supplementary Figure S5** for cross-correlation functions.

X	$Rx_{-,\ FCO2}$	*Time lag (*tlag*; hours)*
$[CO_2]_s$	0.3	22
WS_1	−0.4	−18
WS_{10}	−0.4	−18
ΔP	−0.5	6
$[N_2]_v$	−0.4	−14
$[O_2]_v$	−0.4	−16
$[CO_2]_v$	0.5	−16
$\delta^{13}C_{[CO2]v}$	−0.4	−14
$\delta^{13}C_{[CO2]a}$	−0.5	6

those during the period I in 2018 and that in August, 2017 (**Table 1**). $[H_2O]_s$ and $[CO_2]_s$ were also lower than those during the period I (**Table 1**; **Figure 2**). Besides, during the period I, T_s, 1/RH_s, $[H_2O]_s$, and ΔP increased daytime and decreased at night (**Figures 2**, **3** and **Supplementary Figure S3**), while the diurnal variation of $[H_2O]_s$ was not clear during the period III (**Figure 2D** and **Supplementary Figure S4**), especially until December 6, 2019 when the temperature was lowered down to −10°C and the pressure exceeded 1,010 hPa (**Figures 2B,F**). RH_s ($r = -0.6$) and RH_{aws} ($r = -0.4$) were negatively correlated with FCO_2 during the period I (**Table 2**), but not related with FCO_2 during the period III (**Table 3**).

Despite the different ranges in FCO_2 at each period, FCO_2 had significant correlations with T_s, $[H_2O]_s$, T_{aws}, P_s and P_{aws} at both periods (**Tables 2**, **3**). FCO_2 increased with increasing $[H_2O]_s$, T_s and T_{aws} but decreased with P_s and P_{aws}. In addition, P_0 and P_{90} were negatively correlated with FCO_2 during the period I. The negative relation of FCO_2 with P_{aws} was explained by the fact that a decrease in barometric pressure increases the pressure gradient of the ground, which subsequently enhances the viscous gas flux (Rogie et al., 2001; Granieri et al., 2003; Morita et al., 2019). The positive relation with T_{aws} on the short time scale was explained as the effect of variations in soil gas diffusivity with air temperature as well as surficial biological productivity (Camarda et al., 2016 and references therein). The positive effect of $[H_2O]_s$ can be explained by its positive relationship with T_s and T_{aws} and negative with P_s and P_{aws} in **Tables 2**, **3**, and will be further discussed in *Environmental Parameters* regarding the usefulness of the environmental parameters obtained in the chamber.

Soil Gas and Air

CO_2 concentrations in the soil gas obtained at a depth of 60 cm ($[CO_2]_v$) ranged from 39.6 to 48.9% (average = 43.8%) during the period I (**Figure 4A**), which were slightly higher than that measured in August, 2017 (36.0%) but lower than that during the period III (56.8%) in **Table 1**. $\delta^{13}C_{[CO2]v}$ for the soil gas was between −10.1 and −5.4‰ (average = −7.1‰) during the period I and was −6.2‰ during the period III, which were a little lower than the value (−5.7‰) obtained in August, 2017 (**Figure 4A**; **Table 1**). However, the variations in $\delta^{13}C_{[CO2]v}$ were insignificant and the $\delta^{13}C_{[CO2]v}$ values were relatively high compared to the $\delta^{13}C_{[CO2]v}$ of biogenic origin in the study area between −32.0 and −13.0‰ (average −25.2‰) in Kim et al. (2019).

$[CO_2]_v$ did not show a distinct diurnal variation during the period I (**Figure 4A**) similar to FCO_2 and $[CO_2]_s$ that showed the pattern out of the diurnal variation during both periods I and III unlike T_s, RH_s or $[H_2O]_s$ (**Figure 2**; **Supplementary Figures S3, S4**). $[CO_2]_v$ was not linearly correlated with either FCO_2 ($r = -0.2$) or $\delta^{13}C_{[CO2]v}$ ($r = -0.1$) in **Table 2**, while positively with FCO_2 at the time lag of −16 h ($R_{xy} = 0.5$ in **Table 4**; **Supplementary Figure S5**) and negatively with $\delta^{13}C_{[CO2]v}$ ($R_{xy} = -0.3$) at the time lag of −24 h (**Supplementary Figure S5**). $[CO_2]_v$ was negatively related with P_{90} ($r = -0.6$ in **Table 2**), indicating that the high P_{90} caused $[CO_2]_v$ to decrease. The average N_2 ($[N_2]_v$) and O_2 concentrations ($[O_2]_v$) of soil gas obtained at a depth of 60 cm was different between the two periods: 42.9% (40.0–46.3%) and 11.4% (10.6–12.2%) respectively during the period I, while 30.3% and 7.8% respectively during the period III (**Figure 5**; **Table 1**), probably due to the high proportion of CO_2 during the period III.

It is noticeable that both $[CO_2]_v$ and $[CO_2]_s$ showed a rapid increase during the period I with the time lag of about 12 h. Specifically, $[CO_2]_v$ rapidly increased from 39.8 to 48.9% at 22:00 on November 2 (**Figure 4A**), while $[CO_2]_s$ increased from 0.3 to 0.5% at 10:00 on November 3 (**Figure 2C**). Consistently, the cross-correlation analysis showed that the correlation between $[CO_2]_v$ and $[CO_2]_s$ increased up to 0.55 at the time lag of -12 h in **Supplementary Figure S5** from zero in **Table 2**, and suggested the transport rate of approximately 60 cm/12 h. $[CO_2]_s$ occasionally showed rapid increases during the period III as well, in particular around December 4 (see the red arrow in **Figure 2D**), whereas $[CO_2]_v$ measurements were not available for comparison.

Meanwhile the CO_2 concentrations in the air samples ($[CO_2]_a$) measured during the periods I (0.05–0.19%) and period III (0.20%) in **Figure 4B** and **Table 1** showed high values compared to a reported atmospheric CO_2 composition (0.04%) and the value previously detected in the study site (0.05%). $[CO_2]_a$ was negatively correlated with FCO_2 ($r = -0.8$) and $[CO_2]_v$ ($r = -0.5$), but not with $[CO_2]_s$ ($r = 0.0$) during the period I (**Table 2**). $\delta^{13}C_{[CO2]a}$ for the air samples was different between two periods. The average $\delta^{13}C_{[CO2]a}$ (-19.0 ± 2.8‰; $n = 10$) during the period I was much lower

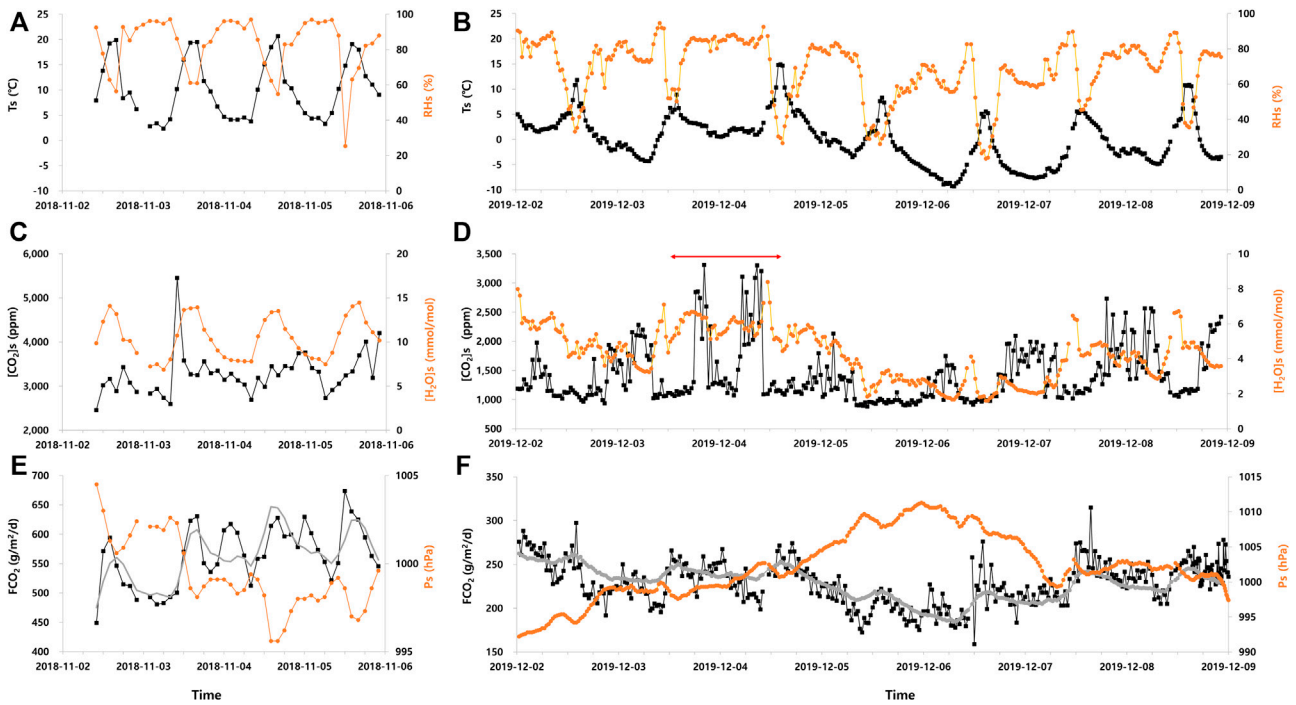


FIGURE 2 | Temporal comparison of temperature (T_s; °C), relative humidity (RH_s; %) in **(A,B)**, CO_2 concentrations ($[CO_2]_s$; ppm), water vapor mole fraction ($[H_2O]_s$; mmol/mol) in **(C,D)**, and pressure (P_s; hPa) in the chamber and calculated CO_2 flux (FCO_2; g/m^2/d) in **(E,F)** during the periods I **(left)** and III **(right)**. In **(E,F)**, the gray line addresses the FCO_2 estimated using T_{aws} and P_{aws} in **Equations 3**, **4**, respectively. Note that $[CO_2]_s$, $[H_2O]_s$, FCO_2, and P_s have different scales between two periods. The red arrow in **(D)** indicates the time of rapid increases in $[CO_2]_s$.

than the values measured during the period III (−8.5‰) and in August 2017 (−10.6‰). The higher $[CO_2]_a$, the higher $\delta^{13}C_{[CO2]a}$ (r = 0.7) during the period I. On the other hand, the air samples showed similar N_2 ($[N_2]_a$) and O_2 ($[O_2]_a$) compositions in both periods: 77.9% N_2 and 20.6% O_2 in average during the period I, while 76.6% N_2 and 20.4% O_2 during the period III. $[N_2]_a$ and $[O_2]_a$ were positively related with FCO_2 unlike $[CO_2]_a$ during the period I (**Table 2**).

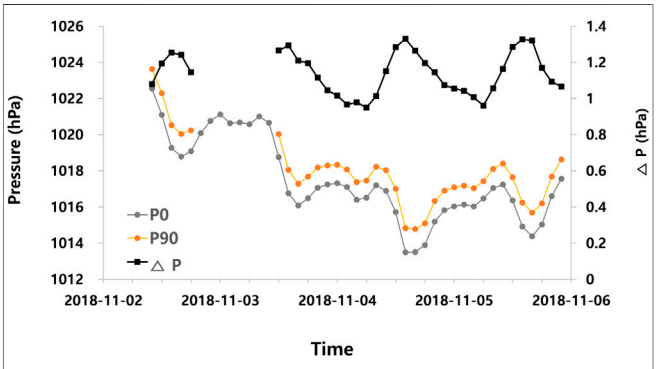


FIGURE 3 | Pressures at surface (P0; hPa) and at a depth of 90 cm (P90; hPa) measured by the BAT® geosystem and the pressure difference between P_0 and P_{90} ($\Delta P = P_{90}-P_0$; hPa) during the period I.

After the Earthquake

FCO_2 increased up to 1,073 g/m^2/d by a factor of two approximately 12 h after the earthquake (**Figure 6** and **Supplementary Figure S2**), which was much higher than the sum of mean (μ) and 2 times standard deviation (2σ) of FCO_2 during the period I (μ + 2σ; 668 g/m^2/d). Besides, relatively high FCO_2 was observed on November 25, 2018 (836 g/m^2/d) and January 23, 2019 (802 g/m^2/d) (**Figure 6**). Those high FCO_2 values were not observed either during the period I or in the previous study at M17 (**Table 1**).

The high FCO_2 seemed to be related with $[CO_2]_s$ (**Figure 7**; r = 0.9 in **Table 5**). Their high correlation was not observed in the other periods. Namely, $[CO_2]_s$ rapidly increased after the earthquake and decreased with FCO_2, and high $[CO_2]_s$ was observed on both November 25, 2018 and January 23, 2019 (**Figure 7**), although the maximum $[CO_2]_s$ (5,451 ppm) was observed during the period I (**Table 1**; **Figure 2C**). Unlike FCO_2 increasing abruptly, however, $[CO_2]_v$ dropped by about half after the earthquake, and then increased back but did not reach the pre-earthquake values until January 30, 2019, although a high value of $[CO_2]_v$ (56.8%) was observed in December, 2019 (**Table 1**). Thus, $[CO_2]_v$ was negatively related with FCO_2 during the period II (r = −0.5 in **Table 5**). The maximum $[CO_2]_s$ observed during the period I and the increasing in $[CO_2]_s$ and FCO_2 but the decreasing in $[CO_2]_v$ after the earthquake will be discussed in relation to the earthquake in *Possible Causes of a High CO_2 Emission During the Period* II.

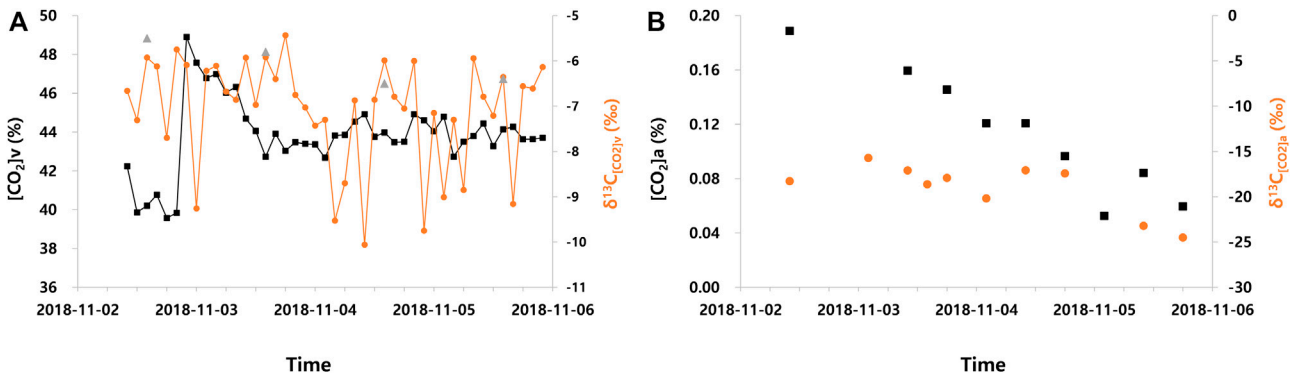


FIGURE 4 | Temporal changes of **(A)** CO_2 concentrations measured at a depth 60 cm ([CO_2]v) and its $\delta13C_{[CO2]v}$; **(B)** CO_2 concentrations in air samples ([CO_2]a) and its $\delta13C_{[CO2]a}$ during the period I. Gray triangles in **(A)** show the $\delta13C_{[CO2]v}$ values determined by the Beta Analytic Inc. (n = 4) for cross-checking.

Besides, it was observed that the relative humidity (RH) in the chamber (RH_s) and from the AWS (RH_{aws}) were positively related with FCO_2 during the period II (r = 0.7 and 0.4 respectively in **Table 5**) unlike the other periods, probably due to the precipitation as well as earthquake (see *Environmental Parameters*).

DISCUSSION

Source of CO_2

Scatter plots of soil gas compositions revealed that the soil gas was the mixture of atmospheric air and geogenic CO_2 (**Figure 5**). Specifically, the CO_2 vs. O_2 was plotted on the air-CO_2 mixing line (**Figure 5A**), while the N_2 vs. CO_2 was not on the biological respiration or CH_4 oxidation (**Figure 5B**). Besides, the consistent $\delta^{13}C_{[CO2]v}$ regardless of the season and the $\delta^{13}C_{[CO2]v}$ ranges (**Figure 5D**) indicated a deep-seated CO_2 source despite the different proportion of CO_2 in soil gas at each period as the $\delta^{13}C_{CO2}$ of geogenic CO_2 is reported to be −6‰ in Baines and Worden (2004) and −9.7 ~ −2.7‰ (−6.5 ± 2.5‰) in Sano and Marty (1995). In contrast, the $\delta^{13}C_{CO2}$ from the microbial decomposition of C3 plants generally ranges between −34 and −23‰ (Faure, 1998) and seasonally changes due to the change in biological activities (White and Corfield, 2006; Zhu et al., 2019). FCO_2 did not show the diurnal variation (**Supplementary Figures S2–S4**), and had a significantly negative relation with barometric pressure (**Tables 2**, **3**, **5**), which also indicates the geogenic CO_2 emission in the study site (Camarda et al., 2019). At the measurement site around M17, the geological FCO_2 seems to exceed the microbial respiratory FCO_2 by several orders of magnitude as in the sites with high CO_2 concentrations in Vodnik et al. (2009).

During the period I, P_{90} was always higher than P_0 (**Figure 3**). The positive ΔP indicates that the atmospheric air did not intrude and dilute $[CO_2]_v$ at the measurement point (M17v). Instead, the mixing with air seemed to be diffusive at M17v due to concentration gradients with depth, which may be affected by the barometric pressure given that P_{90} was synchronized with P_0 (**Figure 3**). Besides, the geogenic CO_2 uprising could be mixed with soil gas influenced by the atmospheric air in the vadose zone. According to Massmann and Farrier (1992) and Chen et al. (2020), the changes in barometric pressure migrate air into the vadose zone. Air intrusion due to the barometric pressure fluctuation depends on soil characteristics, the thickness of vadose zone, and climate (Massmann and Farrier, 1992; Auer et al., 1996).

Meanwhile, $\delta^{13}C_{[CO2]a}$ was widely ranged particularly during the period I (**Figure 4B**) probably due to various sources of CO_2 in the air 1 m above the surface. A CO_2 source in the air seemed to be geogenic given high $[CO_2]_a$ values up to 0.2% (**Table 1**), the positive relation between $[CO_2]_a$ and $\delta^{13}C_{[CO2]a}$ (r = 0.7 in **Table 2**; **Figure 4B**), and the significant relations between air compositions and FCO_2 (**Table 2**).

Factors to Control Geogenic CO_2 Flux

The variation in geogenic FCO_2 depends on soil properties (e.g., air permeability and diffusion coefficient), prevailing mechanisms of CO_2 transport (e.g., advection and diffusion), environmental parameters (e.g., air pressure and temperature), and deep-seated CO_2 supply via endogenous processes (e.g., volcano and tectonic activity). We discussed the factors controlling the temporal variations of FCO_2 in relation to time-variant geogenic CO_2 supply due to exploitation of CO_2-rich water (*Time-Variant Supply of Geogenic CO_2)*, the effect of environmental variables including precipitation (*Environmental Parameters*), and the prevailing mechanisms of CO_2 transport (*Prevailing Mechanisms of CO_2 Transport*). *Besides, the difference between the periods* I *and* III *was discussed with respect to the spatial variability of* FCO_2 (Heterogenous Transport of Geogenic CO_2). Soil properties could not be investigated in this private land.

Time-Variant Supply of Geogenic CO_2

The geogenic CO_2 supply seemed to be variant with time given the irregular increases of $[CO_2]_s$ (i.e., CO_2 concentration in the chamber 2 min after closing the chamber in **Figure 2**) regardless of environmental variables (**Tables 2**, **3**). According to Kim et al. (2019), CO_2 gas in the study area forms by degassing from the water table of a CO_2-rich aquifer

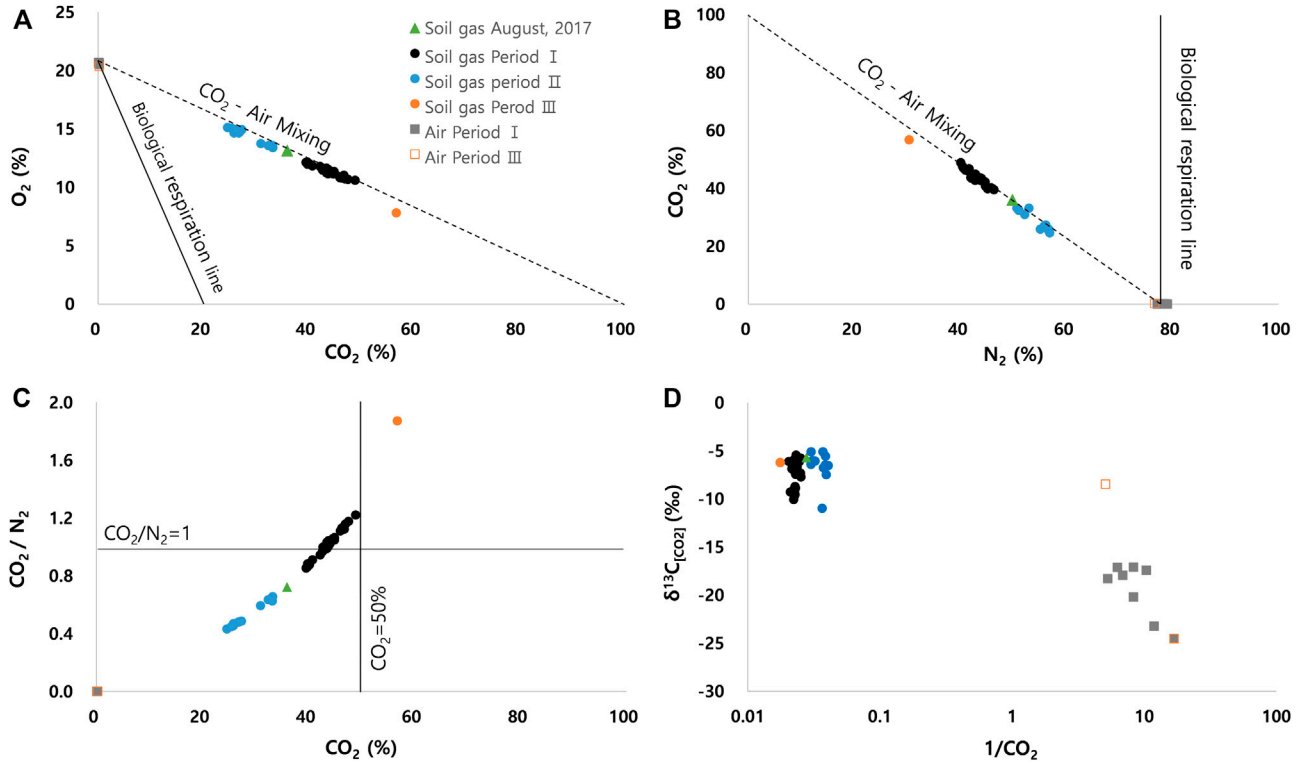


FIGURE 5 | Compositions and stable carbon isotopes ($\delta 13C_{[CO2]}$) of soil gas and atmospheric air. The relationships between CO_2 and O_2 **(A)** and between N_2 and CO_2 **(B)** (after Romanak et al., 2012). Dotted lines represent the mixing between atmospheric air concentrations measured in this study and 100% geogenic CO_2, while solid lines represent the biological respiration in **(A,B)**. **(C)** CO_2/N_2 vs. CO_2; **(D)** $1/CO_2$ vs. $\delta 13C_{[CO2]}$ (after Sun et al., 2018). The soil gas data in August 2017 is from Kim et al. (2019).

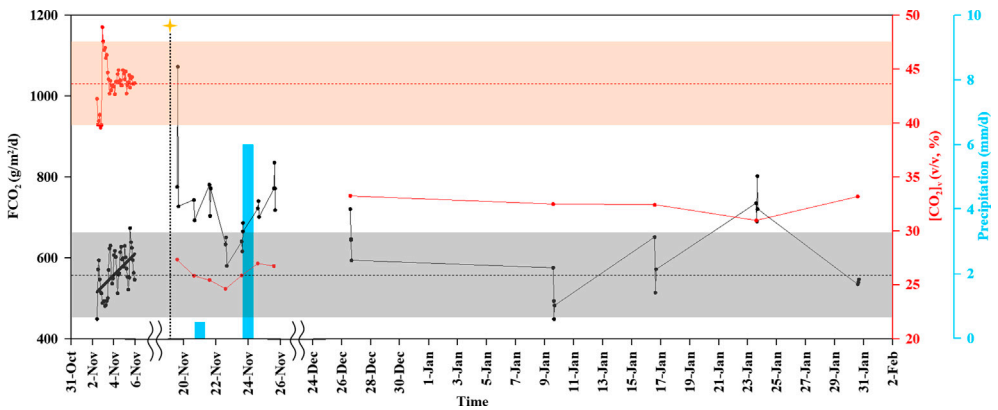


FIGURE 6 | Temporal changes of CO_2 flux (FCO_2) and CO_2 concentrations measured at a depth 60 cm ($[CO_2]v$) before and after the 2.1 M earthquake (yellow star) occurred on November 19, 2018. The shaded areas cover the mean (μ; dotted line) ± two times standard deviation (2σ) of the period Ⅰ (**Table 1**). The solid thick line represents the linear regression (r^2 = 0.3).

and transports toward the M17 site and leaks at M17 via the voids surrounding the well w-2. The amount of CO_2 degassing is expected to be time-variant because the CO_2-rich water is taken from w-2 by countless people, which changes the groundwater level and subsequently the fluid pressure, affecting the amount of CO_2 degassing (Duan and Sun, 2003). The time-variant CO_2 degassing seemed to alter $[CO_2]_v$ and the CO_2 gradient in the subsurface, and subsequently $[CO_2]_s$, for instance with the time lag of −12 h between M17v and M17(**Supplementary Figure S5E**) and consequently FCO_2 with the time lag of −16 h (**Table 4**) during the period Ⅰ.

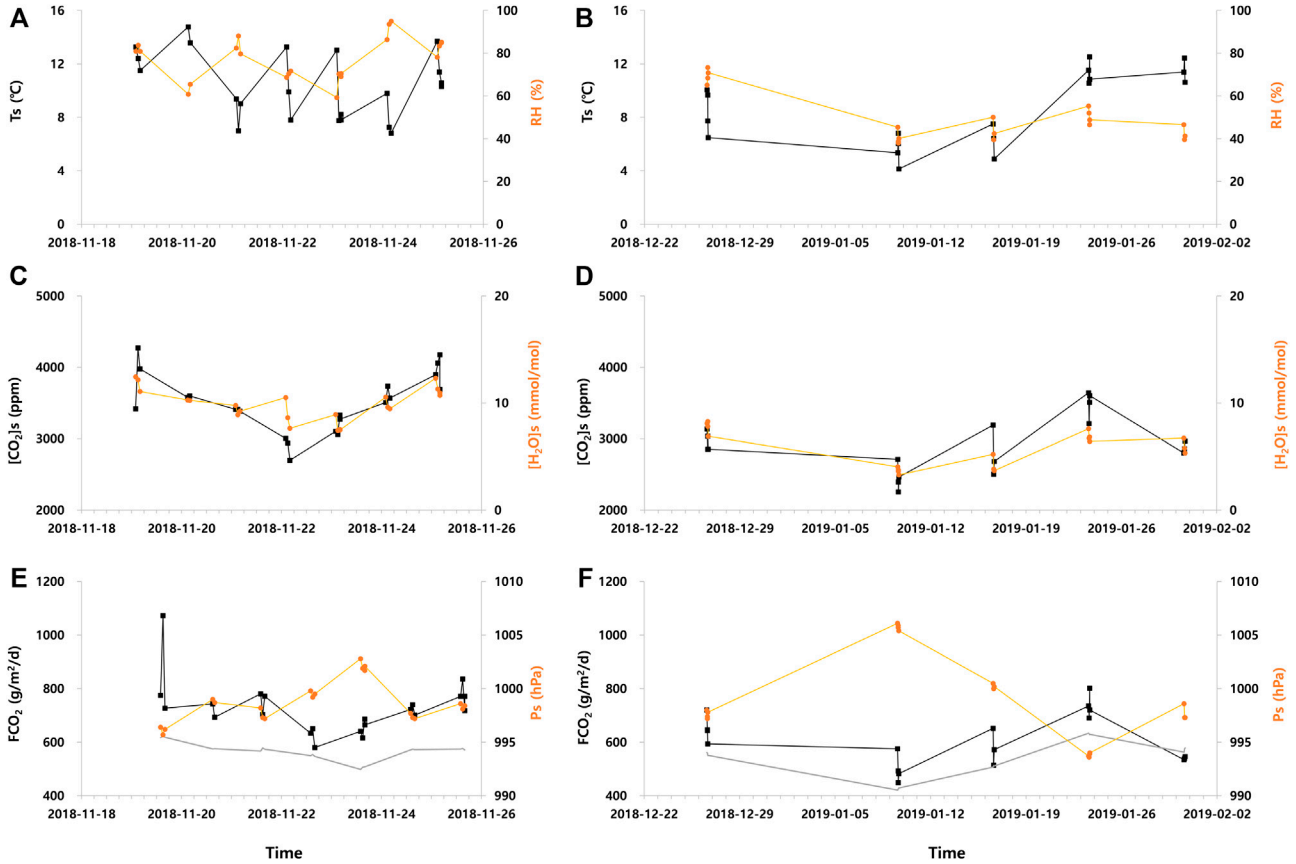


FIGURE 7 | Temporal comparison of temperature (Ts), relative humidity (RHs) in **(A,B)**, CO_2 concentrations ([CO_2]s), water vapor mole fraction ([H_2O]s) In **(C,D)**, and pressure (Ps) in the chamber and calculated CO_2 flux (FCO_2) In **(E,F)** during the period **II**. In **(E,F)** the gray line addresses the FCO_2 estimated using Taws and Paws in **Equation 3**. Note that the left (until November 25, 2018) and right figures (after December 26, 2018) have different scales of the x axis (time).

TABLE 5 | Pearson correlation coefficients during the period **II**. Absolute values ≥0.6 are in bold.

	FCO_2	T_s	RH_s	$[H_2O]_s$	$[CO_2]_s$	P_s	P_{aws}	T_{aws}	RH_{aws}	WS_1	WS_{10}	$[N_2]_v$	$[O_2]_v$	$[CO_2]_v$	$\delta^{13}C_{[CO2]v}$
FCO_2	1.0														
T_s	0.5	1.0													
RH_s	**0.7**	0.2	1.0												
$[H_2O]_s$	**0.8**	**0.7**	**0.8**	1.0											
$[CO_2]_s$	**0.9**	**0.6**	**0.7**	**0.8**	1.0										
P_s	**−0.6**	−0.5	−0.3	−0.5	**−0.6**	1.0									
P_{aws}	**−0.6**	**−0.6**	−0.4	−0.5	**−0.6**	**1.0**	1.0								
T_{aws}	**0.7**	**0.8**	0.4	**0.8**	**0.7**	**−0.6**	**−0.6**	1.0							
RH_{aws}	0.4	−0.1	**0.7**	0.5	0.5	−0.3	−0.3	0.1	1.0						
WS_1	−0.1	0.2	−0.3	−0.1	−0.2	−0.3	−0.3	0.0	−0.4	1.0					
WS_{10}	−0.1	0.0	−0.4	−0.3	−0.3	−0.2	−0.2	−0.1	−0.4	**0.8**	1.0				
$[N_2]_v$	0.4	**0.7**	**0.7**	**0.8**	0.4	−0.2	−0.3	**0.7**	0.4	−0.2	−0.1	1.0			
$[O_2]_v$	0.5	**0.6**	**0.7**	**0.8**	0.4	−0.1	−0.2	**0.6**	0.4	−0.2	−0.1	**1.0**	1.0		
$[CO_2]_v$	−0.5	**−0.6**	**−0.7**	**−0.8**	−0.4	0.1	0.1	**−0.6**	−0.3	0.2	0.1	**−0.9**	**−1.0**	1.0	
$\delta^{13}C_{[CO2]v}$	−0.5	−0.2	−0.4	−0.5	−0.2	0.2	0.3	−0.4	0.0	0.0	0.2	−0.3	−0.4	0.3	1.0

The impact of pressure variation on degassing was quantitatively compared to that of temperature and salinity in **Table 6** because the saline fluid in the deep part can rise temperature and salinity as well as pressure of groundwater. The salinity was assumed to be low (100–150 mg/L) because the CO_2-rich water in the study area was characterized by low pH and electrical conductivity (EC), probably due to short (<35 years) reaction times between water and rocks despite a large amount of CO_2 inflow into the aquifer (Kim et al., 2008; Chae et al., 2016). According to Chae et al. (2016), the

TABLE 6 | Sensitivity analysis of CO_2 degassing from a CO_2-rich water.

Scenario	T(°C)	T (K)	P (bar)	cNaCl (m)	mCO_2(m)
Base case	13	286.15	1	0.002[a]	0.0471
Increase in temperature	15	288.15	1	0.002[a]	0.0442
Increase in pressure	13	286.15	8.14[b]	0.002[a]	0.3692
Increase in salinity	13	286.15	1	0.003[c]	0.0471
Increase in all[d]	15	288.15	8.14[b]	0.003[c]	0.3474

[a]*Corresponding to the total dissolved solids (TDS) of 100 mg/L.*
[b]*At a depth of 80 m (w-2 in Figure 1A).*
[c]*Corresponding to TDS of 150 mg/L.*
[d]*The saline fluid in the deep part can rise temperature, pressure and salinity of groundwater altogether.*

temperature and salinity (EC) of the CO_2-rich water from w-2 varied between 11.6 and 15.8°C and between 108 and 175 μS/cm for 14 months, respectively. **Table 6** shows that the change in CO_2 solubility (i.e., degassing) is more influential by the pressure variation than by the temperature or salinity in the study site.

When the water is pumped and thus the water pressure drops, gas bubbles occurs in CO_2-rich water. Subsequently the gas release ceases and the gas dissolved in the CO_2-rich water is being released as a result of a slow diffusion process (Kouznetsov et al., 2002). The "bubbly" stage may be resumed at shaking (see *Possible Causes of a High CO_2 Emission During the Period* II*).* The changes in the water table also affect FCO_2 in the vadose zone as in Schroder et al. (2017) who found the FCO_2 distribution shifted between two CO_2 release tests due to the changes in groundwater depth in wet and dry season. The low water table in dry season facilitates lateral CO_2 migration, reducing FCO_2 along a wellbore. The quantitative assessment of the effect of pressure variation caused by water usage on the CO_2 degassing (and subsequently on FCO_2) in the study area remains future work due to little information on the water table and the amount of water consumption at w-2.

In addition, Chae et al. (2016) speculated dry CO_2 flowing directly into the aquifer of w-2 (80 m depth) from the magmatic origin, since the study site is located at the geologic boundary between gneiss and granite (**Figure 1A**) and unknown fractures may exist around the study area given the small earthquakes (**Figure 1B**) and CO_2-rich waters (**Supplementary Figure S1**), although none has been reported within 13 km around the study area. According to Kerrick and Caldeira (1998), the plutonic-metamorphic belt can be a source area to emit CO_2 to the atmosphere. In fact, Yu et al. (2015) observed the temporal variation of CO_2 supply to the aquifer for 48 h in a CO_2-rich spring (s-2 in **Figure 1A**), which decreased pH and increased total dissolved inorganic carbon (TDIC) and $\delta^{13}C_{TDIC}$ and might further cause the temporal variation of $[CO_2]_v$, $[CO_2]_s$, or FCO_2.

Environmental Parameters

We found the significant influence of air temperature (T_{aws}, T_s) and pressure (P_{aws}, P_s) to FCO_2 at all periods as the previous studies (Chiodini et al., 1998; Granieri et al., 2003; Carapezza et al., 2011; Camarda et al., 2016; Morita et al., 2019). The temperature was correlated with FCO_2 probably due to the effect of temperature to soil gas diffusivity near the M17 site, and not due to the biological effect in November (late fall during the period I) and December (winter during the period III) in South Korea (Camarda et al., 2016 and references therein). In particular, the high $[CO_2]_v$ at M17v during the period III suggested the accumulation of geogenic CO_2 in the subsurface due to low soil gas diffusion at cold weather.

T_s and P_s were highly related with T_{aws} and P_{aws} respectively ($r \geq 0.8$ at all periods), while RH_s was significantly with RH_{aws} ($r = 0.7$ at all periods) despite the 10 km distance of AWS from the study area. These high correlations between measurements imply the usefulness of the environmental data from the chamber in LI-COR and the AWS data. A multiple regression line using T_{aws} and P_{aws} for FCO_2 during the periods I and III was obtained respectively as:

$$FCO_2_estimated\ for\ the\ period\ I = 2.8 \times T_{aws} - 14.8 \times P_{aws} + 15,752 \quad (3)$$

$$FCO_2_estimated\ for\ the\ period\ III = 2.0 \times T_{aws} - 2.4 \times P_{aws} + 2,676 \quad (4)$$

which had $r^2 = 0.65$ and $p = 0.00$ in **Equation 3** and $r^2 = 0.53$ and $p = 0.00$ in **Equation 4**, supporting the significant effects of T_{aws} and P_{aws} to FCO_2. However, microclimates may greatly affect some environmental parameters. For instance, the wind speed (*WS*) from the AWS did not influence FCO_2 (**Tables 2**, **3**, **5**), probably because *WS*, which is sensitive to topography (Helbig et al., 2016), was not measured near the measurement point. **Table 4** shows the negative correlation of FCO_2 with *WS* at the time lag of −18 h. According to Carapezza et al. (2011), the negative effect of *WS* reflects that the gas is confined underground under strong wind conditions.

In addition to T_s and P_s, $[H_2O]_s$ (i.e., water vapor mole fraction in the chamber 2 min after closing the chamber), showed significant correlations with FCO_2 ($r \geq 0.5$) at all periods, while with $[CO_2]_s$ only during the period II ($r = 0.8$ in **Table 5**). $[H_2O]_s$ increased with T_s and T_{aws} but decreased with P_s and P_{aws} at all periods as FCO_2. Similarly, Schroder et al. (2016), Schroder et al. (2017) found some degree of spatial correlation between FCO_2 and surface H_2O fluxes and suggested that water vapor can be used as a proxy for escaping gas in some leak scenarios. Moreover, Schroder et al. (2016) discussed the possible source of the water, e.g., the same CO_2 reservoir or a function of the CO_2 passage through the water table, and proposed that the water is sourced from the same CO_2 reservoir based on the slightly elevated temperature of the upwelled water compared with surrounding groundwater in the Qinghai research site, whereas the CO_2 efflux transported H_2O from the top of the water table at or marginally above the release well at the Ginninderra controlled release facility, Australia (Schroder et al., 2017). Besides, Zhou et al. (2013) suggested that the released CO_2 not only depletes soil O_2 but also enhances evaporation and reduces the soil moisture.

On the other hand, the relative humidity (*RH*) was positively related with FCO_2 during the period II (e.g., $r = 0.7$ of RH_s and $r = 0.4$ of RH_{aws} in **Table 5**) but negatively with FCO_2 during the period I (**Table 2**), while not related with FCO_2 during the period III (**Table 3**). The different correlation between measurements suggests the different major mechanism for CO_2 transport, e.g., low gas diffusion at cold weather during the period III and the earthquake during the period II (see *Possible Causes of a High CO_2 Emission During the Period* II). Similarly, Zhou et al. (2013) found the opposite relationship between the soil O_2 concentration and soil moisture for the during-release and post-release due to the pumping effect of the released CO_2 gas plume at the interface between the CO_2 plume and the soil liquid water. Besides, the period II had precipitation. The precipitation may cause the CO_2 gas uprising, filling the pore with water (e.g., Lewicki et al., 2010; Johnson and Rostron, 2012; Garcia-Anton et al., 2014), although the opposite effect of precipitation is also possible, dissolving the CO_2 gas in infiltrating water (Annunziatellis et al., 2008) or reducing the gas permeability (e.g., Carapezza et al., 2011; Garcia-Anton et al., 2014).

Prevailing Mechanisms of CO_2 Transport

The high FCO_2 and its high correlation with P_{aws} indicate that the study site has a non-negligible advective component (Hernández et al., 2001; Ascione et al., 2018). Similarly, Kim et al. (2019) showed that the M17 site was located in the high-advection zone using the relationship between FCO_2 and $[CO_2]_s$ suggested by Jung et al. (2014). The negative correlation between P_{90} and $[CO_2]_v$ (**Table 2**) and the positive ΔP (1.0–1.3 hPa in **Table 1**; **Figure 3**) and thus the pressure gradient in the range of 1.1 and 1.4 hPa/m during the period I also suggest the advective flow upward in the unsaturated soil. Takle et al. (2004) showed that pressure differences between −15 and 15 Pa at depths of 0–60 cm caused FCO_2 exceeding diffusional fluxes due to pressure pumping. According to Altevogt and Celia (2004), the leakage rate of 0.1 g/m s to 100 g/m s were reached at a CO_2 source with the vertical pressure gradient of 0.18–49.65 hPa/m adjacent to the source boundary.

However, FCO_2 was affected by air temperature and $[H_2O]_s$ as well as air pressure in **Tables 2**, **3**, **5**, implying that the diffusive transport of CO_2 is also significant in the study site (Camarda et al., 2019). Accordingly, temperature gradient might affect the pressure gradient of 1.1 and 1.4 hPa/m during the period I, while the gradient was not measured. In addition, $[CO_2]_v$ showed different temporal changes from FCO_2 during the period I in **Figures 2E**, **4A** and its correlation with FCO_2 increased at the time lag of −16 h in **Table 4**. Moreover, soil CO_2 seems to mainly form through degassing of a CO_2-rich aquifer and the degassing may vary depending on the pressure variation in the aquifer for w-2 (**Table 6**).

Thus, it can be concluded that the advection is dominant at the near surface, while the transport of geogenic soil CO_2 is diffusive-dominated in the vadose zone by the CO_2 gradient. Similarly, Kim et al. (2018) observed that CO_2 concentrations measured at 15 cm depth were significantly lower than those measured at 60 cm depth, as the CO_2 gas escaped quickly into the atmosphere at the ground surface due to the atmospheric pressure effect at an inject test, for which approximately 1.8 t CO_2 was injected at 2.5 m depth with a CO_2 release rate of 6 L/min. Rillard et al. (2015) showed that the advective flux between an injection point and the surface through a preferential path was the dominant gas transport process during the injection phase because it was difficult to avoid a slight overpressure at the injection point. Altevogt and Celia (2004) determined the diffusive flux as well as the slip and Darcy fluxes associated with natural CO_2 leakage into the vadose zone based on a two-dimensional numerical model, and showed that the mole fraction-driven flux played an important role in the development of the CO_2 plume even in situations where pressure-driven advection was the dominant flux mechanism.

Heterogenous Transport of Geogenic CO_2

FCO_2 was in different ranges (**Table 1**) and had different correlations with measurements during the periods I and III (**Tables 2**, **3**) probably because the measurement points were not exactly the same but at the 30 cm separation between M17 (period I) and M17–1 (period III), implying the spatial variability of FCO_2, as reported by other researchers including Annunziatellis et al. (2008) and Ascione et al. (2018). Similar to this study result, Annunziatellis et al. (2008) mentioned a test showing a change of more than one order of magnitude over only 30 cm. However, the spatial difference in FCO_2 at the centimeter scale was not expected before the study area, and the extreme spatial variability of FCO_2 needs to be further studied in the study area.

Note that the different FCO_2 between November (period I) and December (period III) cannot be explained by the seasonal variation, given the similar FCO_2 between August (summer) in 2017 and November (fall) in 2018 despite distinct climate conditions. We acknowledge that the low FCO_2 might reflect the weather condition given the low temperature (T_s) and high pressure (P_s) during the period III (**Figure 2**) and their positive and negative influence on FCO_2 respectively (**Tables 2**, **3**). However, the different ranges in FCO_2 as well as in $[H_2O]_s$ and $[CO_2]_s$ between the periods I and III in **Figure 2** imply that the effect of heterogeneous CO_2 transport in the vadose zone is stronger than the weather effect. In addition, the FCO_2 estimated using **Equation 3** was much higher than the measured FCO_2 during the period III (**Supplementary Figure S6**).

Possible Causes of a High CO_2 Emission During the Period II

The FCO_2 value of 1,073 g/m^2/d was exceptionally high, exceeding the $\mu + 2\sigma$ of the period I (**Figure 6**). Besides, FCO_2 measurements were much higher than the estimations using **Equation 3**, in particular until November 25, 2018 (**Figures 7E,F**), implying the effect of factors other than T_{aws} and P_{aws}. Meanwhile, $[CO_2]_v$ rapidly decreased after the earthquake. This anomalously high FCO_2 peak and sudden decreases in $[CO_2]_v$ during the period II cannot be explained by the environmental parameters given similar climate conditions (**Table 1**), and imply a high CO_2 emission, causing that FCO_2 was negatively related with $[CO_2]_v$ ($r = -0.5$ in **Table 5**). In addition, $[CO_2]_s$ was highly correlated with FCO_2 ($r = 0.9$), and the residual FCO_2 filtered by T_{aws} and P_{aws} was also well correlated with $[CO_2]_s$

(**Supplementary Figure S7**; r = 0.7). According to Camarda et al. (2019), the relationship between FCO_2 and environmental parameters depends on the amount of deep CO_2 supply as well as the prevalent process of CO_2 transport. **Table 5** shows that the FCO_2 variations brought by $[CO_2]_s$, RH_s and RH_{aws} increased after the earthquake.

Emission Scenario

We suggest that vibrations caused by the earthquake induced the soil gas to transport to the surface, with rapidly decreasing $[CO_2]_v$ and increasing $[CO_2]_s$ and FCO_2 since the study site is located between the geologic boundary (**Figure 1**) and unknown fracture may exist, while CO_2 gas probably forms by degassing of a CO_2-rich aquifer and leaks through the well (w-2) casing in the shallow (<80 m) subsurface given no high flux except M17 near w-2. Earthquake might increase air permeability by a change in site features or modification of the structural parts of the well (w-2) from which the CO_2 originates. Besides, mechanical processes, including vibrations induced by an earthquake, have been known to increase degassing of dissolved gas and to enhance the movement of gas bubbles in fractured aquifers (Kouznetsov et al., 1998; Toutain and Baubron, 1999; Manga et al., 2012), changing the physicochemical parameters of water (e.g., EC, pH, temperature, water level). According to Kouznetsov et al. (1998), degassing is related to local instantaneous ruptures in the formation fluid due to the effect of elastic waves. Nuclei of bubbles are formed in these ruptures, and gas diffusion from fluid into these bubbles takes place (Kouznetsov et al., 1998). Crews and Cooper (2014) also showed that seismic waves initiated bubble nucleation and growth in groundwater, which increased the water level in boreholes, reducing effective stress in critically loaded geologic faults, and consequently induced secondary earthquakes. Fischer et al. (2017) observed the CO_2 bubbles increasing in a CO_2-rich well water 4 days after a 3.5 M earthquake occurring 9 km away. The high CO_2 bubble concentrations lasted for 150 days.

We acknowledge that it is difficult to determine whether the high FCO_2 and low $[CO_2]_v$ were caused by the earthquake because of the short-term and discontinuous data with only a small earthquake. Besides, this observation was opposite to the jumps of both FCO_2 and $[CO_2]_v$ in soil gas wells during the seismic activity in the active fault zones (Chen et al., 2020). We did not observe the CO_2-rich water to support the emission scenario during this study. However, the impact of the small earthquake cannot be excluded for the high FCO_2 during the period II, given that FCO_2 measured immediately after the earthquake was beyond the seasonal and diurnal variation of FCO_2 at M17 (**Table 1**) and much higher than that estimated using T_{aws} and P_{aws} (**Figure 7**). Moreover, it should be noted that we began to measure FCO_2 12 h after the earthquake occurred, and we might miss higher values given a synchronous sharp increase of seismicity and FCO_2 in a seismically active area (Camarda et al., 2016) and the velocity of P (7–8 km/s) and S wave (4–5 km/s).

Suggestion of an Earthquake Precursor

We noted that $[CO_2]_v$ rapidly increased to be 48.9% on 22:00 November 2, 2018, and then the maximum $[C\,O_2]_s$ was observed 12 h later (**Figures 2C**, **4A**), approximately 16 days before the earthquake (**Figure 6**). Besides, FCO_2 had an increasing trend during the period I (r^2 = 0.3 in **Figure 6**), although the average FCO_2 (564 g/m$_2$/d) was similar to 546 g/m^2/d obtained at M17 in August 2017 (**Table 1**). These temporal variations might be a precursor of the earthquake. We acknowledge that many researches have been carried out on the precursors of earthquakes, while there is no general agreement among scientists on the earthquake precursors (Tsunogai and Wakita, 1995; Hernández et al., 2001; Pérez et al., 2008; Ingebritsen and Manga, 2014). Besides, the changes in soil CO_2 have been reported as a result of earthquakes or volcanic activities, rather than an earthquake precursor (Hernández et al., 2001; Troll et al., 2012). Moreover, only one earthquake case was observed in this study (**Supplementary Figure S2**).

However, many studies suggested the soil gas to be one of the most reliable tools to investigate earthquake precursory signals (Walia et al., 2010; Sciarra et al., 2017). For instance, Sciarra et al. (2017) suggested that crustal dilation linked to seismic activity favors the uprising of geogas toward the surface. Walia et al. (2010) showed that the spatial distribution of soil gases was useful in identifying tectonic systems since it showed a clear anomalous trend along the Hsinhua Fault. Chiodini et al. (2004) found in the Apennine that the anomalous FCO_2 suddenly disappeared in a narrow band with the seismicity concentrated, and suggested that the gas accumulates in crustal traps at depth, generating CO_2 overpressurized reservoirs, which induce seismicity.

CONCLUSION

Temporal variations of soil CO_2 flux (FCO_2) and soil CO_2 concentration ($[CO_2]_v$) were investigated for three periods to recognize the factors controlling the temporal variation of geogenic FCO_2 in a non-volcanic and seismically inactive area. The periods I (November 2 to 5, 2018) and III (December 2 to 8, 2019) were to assess the baseline, while the period II (November 19, 2018 to January 30, 2019) was to survey the effect of a small (2.1 M) earthquake occurring 7.8 km away. The correlation coefficients indicated that the air pressure was the most significant controlling factor to FCO_2 regardless of the periods, and the air temperature was also noteworthy.

In contrast, some environmental parameters were significantly related with FCO_2 during one or two periods only, e.g., $[CO_2]_s$ and $[CO_2]_v$ during the period II. In particular, the low $[CO_2]_v$ but high FCO_2 during the period II implied the high emission of soil CO_2 after the small earthquake, which affected the relations between some environmental parameters (e.g., $[CO_2]_s$, RH_s and RH_{aw}) and FCO_2. Meanwhile, the low FCO_2 during the period III suggested the heterogenous subsurface conditions for CO_2 transport at the centimeter scale, while the high $[CO_2]_v$ implied the accumulation of soil CO_2 in the subsurface due to low soil gas diffusion at cold weather. Based on the high FCO_2, its high correlation with air temperature as well as air pressure, and the different temporal changes of $[CO_2]_v$ from FCO_2 including the high $[CO_2]_v$ at cold weather, the study area seemed to have the diffusive transport of soil CO_2 dominant in the vadose zone, while the advection near the surface.

The merit of this study is to present the temporal variation of high FCO_2 of deep CO_2 origin in a non-volcanic and seismically inactive area and to discuss the controlling factors, given few studies on the temporal changes of geogenic CO_2 emissions in a geologically

stable region, although CO_2-rich water discharges. In particular, we found a rapid increase of FCO_2 after the small earthquake, which implies that the global natural CO_2 emission can be larger than the previous estimation. In addition, artificial vibrations (e.g., building construction and transportation vibration) may enhance natural CO_2 emissions, and thus CO_2-rich waters or FCO_2 should be monitored to assess the effect of artificial and natural vibrations to CO_2 emissions. Besides, we provided the usefulness of data in the chamber and AWS data to understand the temporal variation in FCO_2.

We acknowledge however that we only observed a period (II) with respect to an earthquake because the study area has low and sporadic seismicity and no automated FCO_2 monitoring system. It was difficult to determine a cause for the high FCO_2 peak and decreases in $[CO_2]_v$ mostly because of short-term and discontinuous monitoring at different acquisition intervals. Thus our speculation about the effect of the small earthquake to abnormal increases in FCO_2 and the applicability of $[CO_2]_v$ as an earthquake precursor needs to be confirmed through a physics-based numerical modeling work and long-term monitoring data. A process-based understanding for the effects of earthquakes to FCO_2 and $[CO_2]_v$ remains future work. Besides, we could not clearly explain the irregular temporal variations of $[CO_2]_s$ and its high correlation with FCO_2 during the period II. Thus, the carbon isotopic compositions of $[CO_2]_s$ is also needed to be investigated in the next study. With defining end-member properties, the proportion of geogenic CO_2 in $[CO_2]_s$ should be assessed to verify the temporal variation of geogenic CO_2 supply with $[CO_2]_s$. Lastly, the low FCO_2 during the period III implied the high spatial variability of FCO_2. A spatially intensive FCO_2 investigation close to M17 will be conducted in the near future to address the reason for heterogeneity in the centimeter scale.

Based on the temporal changes in FCO_2 in this non-volcanic and seismically inactive study area, we suggest to install an automated FCO_2 monitoring system in natural emission sites to understand temporal increases in natural CO_2 emissions and their causes (e.g., earthquake) in geologically stable regions and consequently the global natural CO_2 emission based on long-term monitoring data. In particular, the FCO_2 monitoring should be complemented with the monitoring of degassing from groundwater to assess the impact of tectonic stresses because endogenous factors affect the physicochemical parameters of water as well, which subsequently changes CO_2 concentrations and FCO_2.

DATA AVAILABILITY STATEMENT

The datasets presented in this study can be found in online repositories. The names of the repository/repositories and accession number(s) can be found below: https://zenodo.org/record/3818108#.X0c3DOR7k6Y.

AUTHOR CONTRIBUTIONS

CK conducted the field work, wrote a first draft, and made figures. SY interpreted the data, wrote the manuscript, and made figures. Y-YO interpreted the temporal data and suggested the cross-correlation analysis. GC designed and initiated the field work, and acquired and interpreted the data. S-TY contributed to the conception and design of the work. YS supervised the field work and sample analysis. All authors contributed to discussions and revisions of the manuscript.

FUNDING

This research was supported by the fundamental research project of KIGAM (Korea Institute of Geoscience and Mineral resources) and was partially supported by the National Research Foundation of Korea (NRF) grant funded by the Korean government (MEST) (No. 2019R1A2C1084297) and the Korea Ministry of Environment (MOE) as K-COSEM (Korea CO_2 Storage Environmental Management) Research Program.

ACKNOWLEDGMENTS

The authors acknowledge diligent field and laboratory works by Inhye Lee, Byeongjun Park, and Gibeom Seok.

SUPPLEMENTARY MATERIAL

The Supplementary Material for this article can be found online at: https://www.frontiersin.org/articles/10.3389/feart.2020.599388/full#supplementary-material.

REFERENCES

Altevogt, A. S., and Celia, M. A. (2004). Numerical modeling of carbon dioxide in unsaturated soils due to deep subsurface leakage. *Water Resour. Res.* 40, W03509. doi:10.1029/2003WR002848

Annunziatellis, A., Beaubien, S. E., Bigi, S., Ciotoli, G., Coltella, M., and Lombardi, S. (2008). Gas migration along fault systems and through the vadose zone in the Latera caldera (central Italy): implication for CO_2 geological storage. *Int. J. Greenhouse Gas Control* 2 (3), 353–372. doi:10.1016/j.ijggc.2008.02.003

Ascione, A., Ciotoli, G., Bigi, S., Buscher, J., Mazzoli, S., Ruggiero, L., et al. (2018). Assessing mantle versus crustal sources for non-volcanic degassing along fault zones in the actively extending southern Apennines mountain belt (Italy). *GSA Bulletin* 130 (9-10), 1697–1722. doi:10.1130/B31869.1

Auer, L. H., Rosenberg, N. D., Birdsell, K. H., and Whitney, E. M. (1996). The effects of barometric pumping on contaminant transport. *J. Contam. Hydrol.* 24 (2), 145–166. doi:10.1016/S0169-7722(96)00010-1

Baines, S. J., and Worden, R. H. (2004). The long-term fate of CO2 in the subsurface: natural analogues for CO2 storage. *Geol. Soc. London Spec. Publ.* 233 (1), 59–85. doi:10.1144/GSL.SP.2004.233.01.06

Burton, M. R., Sawyer, G. M., and Granieri, D. (2013). Deep carbon emissions from volcanoes. *Rev. Mineral. Geochem.* 75 (1), 323–354. doi:10.2138/rmg.2013.75.11

Camarda, M., De Gregorio, S., Di Martino, R. M., and Favara, R. (2016). Temporal and spatial correlations between soil CO_2 flux and crustal stress. *J. Geophys. Res. Solid Earth.* 121 (10), 7071–7085. doi:10.1002/2016JB013297

Camarda, M., De Gregorio, S., Capasso, G., Di Martino, R. M., Gurrieri, S., and Prano, V. (2019). The monitoring of natural soil CO_2 emissions: issues and

perspectives. *Earth Sci. Rev.* 198, 102928. doi:10.1016/j.earscirev.2019.102928

Carapezza, M. L., Barberi, F., Ranaldi, M., Ricci, T., Tarchini, L., Barrancos, J., et al. (2011). Diffuse CO_2 soil degassing and CO_2 and H_2S concentrations in air and related hazards at vulcano island (aeolian arc, italy). *J. Volcanol. Geoth. Res.* 207 (3-4), 130–144. doi:10.1016/j.jvolgeores.2011.06.010

Cardellini, C., Chiodini, G., and Frondini, F. (2003). Application of stochastic simulation to CO2 flux from soil: mapping and quantification of gas release. *J. Geophys. Res. Solid Earth* 108 (B9), 2425. doi:10.1029/2002JB002165

Chae, G., Yu, S., Jo, M., Choi, B. Y., Kim, T., Koh, D. C., et al. (2016). Monitoring of CO_2-rich waters with low pH and low EC: an analogue study of CO_2 leakage into shallow aquifers. *Environ. Earth Sci.* 75 (5), 390. doi:10.1007/s12665-015-5206-9

Chen, Z., Li, Y., Martinelli, G., Liu, Z., Lu, C., and Zhao, Y. (2020). Spatial and temporal variations of CO_2 emissions from the active fault zones in the capital area of china. *Appl. Geochem.* 112, 104489. doi:10.1016/j.apgeochem.2019.104489

Chiodini, G., Cardellini, C., Amato, A., Boschi, E., Caliro, S., Frondini, F., et al. (2004). Carbon dioxide earth degassing and seismogenesis in central and southern italy. *Geophys. Res. Lett.* 31 (7), L07615. doi:10.1029/2004GL019480

Chiodini, G., Cioni, R., Guidi, M., Raco, B., and Marini, L. (1998). Soil CO_2 flux measurements in volcanic and geothermal areas. *Appl. Geochem.* 13 (5), 543–552. doi:10.1016/S0883-2927(97)00076-0

Chiodini, G., Frondini, F., Kerrick, D. M., Rogie, J., Parello, F., Peruzzi, L., et al. (1999). Quantification of deep CO_2 fluxes from Central Italy. Examples of carbon balance for regional aquifers and of soil diffuse degassing. *Chem. Geol.* 159 (1-4), 205–222. doi:10.1016/S0009-2541(99)00030-3

Chiodini, G., Frondini, F., Cardellini, C., Granieri, D., Marini, L., and Ventura, G. (2001). CO_2 degassing and energy release at solfatara volcano, campi flegrei, italy. *J. Geophys. Res. Solid Earth* 106 (B8), 16213–16221. doi:10.1029/2001JB000246

Chiodini, G., Granieri, D., Avino, R., Caliro, S., Costa, A., and Werner, C. (2005). Carbon dioxide diffuse degassing and estimation of heat release from volcanic and hydrothermal systems. *J. Geophys. Res. Solid Earth* 110 (B8), B08204. doi:10.1029/2004JB003542

Ciotoli, G., Bigi, S., Tartarello, C., Sacco, P., Lombardi, S., Ascione, A., et al. (2014). Soil gas distribution in the main coseismic surface rupture zone of the 1980, M_s= 6.9, Irpinia earthquake (southern italy). *J. Geophys. Res. Solid Earth* 119 (3), 2440–2461. doi:10.1002/2013JB010508

Ciotoli, G., Etiope, G., Marra, F., Florindo, F., Giraudi, C., and Ruggiero, L. (2016). Tiber delta CO2-CH4 degassing: a possible hybrid, tectonically active Sediment-Hosted Geothermal system near rome. *J. Geophys. Res. Solid Earth* 121 (1), 48–69. doi:10.1002/2015JB012557

Crews, J. B., and Cooper, C. A. (2014). Experimental evidence for seismically initiated gas bubble nucleation and growth in groundwater as a mechanism for coseismic borehole water level rise and remotely triggered seismicity. *J. Geophys. Res. Solid Earth* 119 (9), 7079–7091. doi:doi.org/10.1002/2014JB011398

Duan, Z., and Sun, R. (2003). An improved model calculating CO_2 solubility in pure water and aqueous NaCl solutions from 273 to 533 K and from 0 to 2000 bar. *Chem. Geol.* 193 (3-4), 257–271. doi:10.1016/S0009-2541(02)00263-2

Faure, G. (1998). *Principles and applications of geochemistry*. Upper Saddle River, New Jersey: Prentice-Hall, Vol. 625.

Fischer, T., Matyska, C., and Heinicke, J. (2017). Earthquake-enhanced permeability–evidence from carbon dioxide release following the ML 3.5 earthquake in West bohemia. *Earth Planet Sci. Lett.* 460, 60–67. doi:10.1016/j.epsl.2016.12.001

Fischer, T. P., Arellano, S., Carn, S., Aiuppa, A., Galle, B., Allard, P., et al. (2019). The emissions of CO_2 and other volatiles from the world's subaerial volcanoes. *Sci. Rep.* 9, 18716. doi:10.1038/s41598-019-54682-1

Garcia-Anton, E., Cuezva, S., Fernandez-Cortes, A., Benavente, D., and Sanchez-Moral, S. (2014). Main drivers of diffusive and advective processes of CO_2-gas exchange between a shallow vadose zone and the atmosphere. *Int. J. Greenh. Gas Con.* 21, 113–129.

Granieri, D., Chiodini, G., Marzocchi, W., and Avino, R. (2003). Continuous monitoring of CO_2 soil diffuse degassing at phlegraean fields (Italy): influence of environmental and volcanic parameters. *Earth Planet Sci. Lett.* 212, 167–179. doi:10.1016/s0012-821x(03)00232-2

Helbig, N., Mott, R., van Herwijnen, A., Winstral, A., and Jonas, T. (2016). Parameterizing surface wind speed over complex topography. *JGR Atmosphere* 122 (2), 651–667. doi:10.1002/2016jd025593

Hernández, P. A., Salazar, J. M., Shimoike, Y., Mori, T., Notsu, K., and Pérez, N. (2001). Diffuse emission of CO2 from miyakejima volcano, japan. *Chem. Geol.* 177 (1-2), 175–185. doi:10.1016/S0009-2541(00)00390-9

Ingebritsen, S. E., and Manga, M. (2014). Earthquakes: hydrogeochemical precursors. *Nat. Geosci.* 7 (10), 697–698. doi:10.1038/ngeo2261

Jeong, C. H., Kim, H. J., and Lee, S. Y. (2005). Hydrochemistry and genesis of CO_2-rich springs from mesozoic granitoids and their adjacent rocks in south korea. *Geochem. J.* 39 (6), 517–530. doi:10.2343/geochemj.39.517

Jeong, C. H., Kim, J. G., and Lee, J. Y. (2001). Occurrence, geochemistry and origin of CO_2-rich water from the chungcheong area, korea. *Econo. Environ. Geol.* 34, 227–241. doi:10.9720/kseg.2016.4.515

Johnson, J. W., and Rostron, B. J. (2012). "Geochemical monitoring," in Best practices for validating CO_2 geological storage: observations and guidance from the IEAGHG Weyburn-Midale CO_2 monitoring and storage project. *Editor B. Hitchon (Alberta, Canada: Geoscience Pub.)* 119–154.

Jung, N. H., Han, W. S., Watson, Z. T., Graham, J. P., and Kim, K. Y. (2014). Fault-controlled CO_2 leakage from natural reservoirs in the colorado plateau, east-central utah. *Earth Planet Sci. Lett.* 403, 358–367. doi:10.1016/j.epsl.2014.07.012

Kerrick, D. M., and Caldeira, K. (1994). Metamorphic CO_2 degassing and early cenozoic paleoclimate. *GSA Today* 4 (3), 57–65.

Kerrick, D. M., and Caldeira, K. (1998). Metamorphic CO_2 degassing from orogenic belts. *Chem. Geol.* 145 (3-4), 213–232. doi:10.1016/S0009-2541(97)00144-7

Kerrick, D. M., and Caldeira, K. (1993). Paleoatmospheric consequences of CO_2 released during early Cenozoic regional metamorphism in the Tethyan orogen. *Chem. Geol.* 108 (1-4), 201–230. doi:10.1016/0009-2541(93)90325-D

Kerrick, D. M., McKibben, M. A., Seward, T. M., and Caldeira, K. (1995). Convective hydrothermal CO_2 emission from high heat flow regions. *Chem. Geol.* 121 (1-4), 285–293. doi:10.1016/0009-2541(94)00148-2

Kihm, Y. H., and Kim, J. H. (2003). Structural characteristics of the central Ogcheon Belt, South Korea: orogen-parallel tectonic transport model. *J. Asian Earth Sci.* 22, 41–57. doi:10.1016/s1367-9120(03)00022-1

Kim, H.-J., Han, S. H., Kim, S., Yun, S.-T., Jun, S.-C., Oh, Y.-Y., et al. (2018). Characterizing the spatial distribution of CO_2 leakage from the shallow CO_2 release experiment in south korea. *Int. J. Greenhouse Gas Control* 72, 152–162.

Kim, J., Yu, S., Yun, S. T., Kim, K. H., Kim, J. H., Shinn, Y. J., et al. (2019). CO_2 leakage detection in the near-surface above natural CO_2-rich water aquifer using soil gas monitoring. *Int. J. Greenhouse Gas Control* 88, 261–271. doi:10.1016/j.ijggc.2019.06.015

Kim, K., Jeong, D. H., Kim, Y., Koh, Y. K., Kim, S. H., and Park, E. (2008). The geochemical evolution of very dilute CO_2-rich water in Chungcheong Province, Korea: processes and pathways. *Geofluids* 8 (1), 3–15. doi:10.1111/j.1468-8123.2007.00200.x

KMA (Korea Meteorological Administration) (2019). Weather information. Available at: https://www.weather.go.kr.

Kouznetsov, O. L., Simkin, E. M., Chilingar, G. V., and Katz, S. A. (1998). Improved oil recovery by application of vibro-energy to waterflooded sandstones. *J. Petrol. Sci. Eng.* 19 (3-4), 191–200. doi:10.1016/S0920-4105(97)00022-3

Kouznetsov, O. L., Simkin, E. M., Chilingar, G. V., Gorfunkel, M. V., and Robertson, J. O. (2002). Seismic techniques of enhanced oil recovery: experimental and field results. *Energy Sources* 24 (9), 877–889. doi:10.1080/00908310290086761

Lewicki, J. L., Hilley, G. E., Dobeck, L., and Spangler, L. (2010). Dynamics of CO2 fluxes and concentrations during a shallow subsurface CO2 release. *Environ. Earth Sci.* 60, 285–297.

Lee, H., Muirhead, J. D., Fischer, T. P., Ebinger, C. J., Kattenhorn, S. A., Sharp, Z. D., et al. (2016). Massive and prolonged deep carbon emissions associated with continental rifting. *Nat. Geosci.* 9, 145–149. doi:10.1038/ngeo2622

Lewicki, J. L., Hilley, G. E., Dobeck, L., and Spangler, L. (2010). Dynamics of CO_2 fluxes and concentrations during a shallow subsurface CO_2 release. *Environ. Earth Sci.* 60, 285–297.

Manga, M., Beresnev, I., Brodsky, E. E., Elkhoury, J. E., Elsworth, D., Ingebritsen, S. E., et al. (2012). Changes in permeability caused by transient stresses: field observations, experiments, and mechanisms. *Rev. Geophys.* 50 (2), RG2004. doi:10.1029/2011RG000382

Massmann, J., and Farrier, D. F. (1992). Effects of atmospheric pressures on gas transport in the vadose zone. *Water Resour. Res.* 28 (3), 777–791. doi:10.1029/91WR02766

MCT (Ministry of Construction and Transportation), KRCC (Korea Rural Community Co.), and K–Water. (2006). Groundwater basic survey in the Yeongi area. No. 11–1500000–01811–01.

Morita, M., Mori, T., Yokoo, A., Ohkura, T., and Morita, Y. (2019). Continuous monitoring of soil CO 2 flux at aso volcano, japan: the influence of environmental parameters on diffuse degassing. *Earth Planets Space* 71 (1), 1. doi:10.1186/s40623-018-0980-8

Mörner, N. A., and Etiope, G. (2002). Carbon degassing from the lithosphere. *Global Planet. Change* 33 (1-2), 185–203. doi:10.1016/S0921-8181(02)00070-X

Oliveira, S., Viveiros, F., Silva, C., and Pacheco, J. E. (2018). Automatic filtering of soil CO2 flux data; different statistical approaches applied to long time series. *Front. Earth Sci.* 6, 208. doi:10.3389/feart.2018.00208

Pérez, N. M., Hernández, P. A., Igarashi, G., Trujillo, I., Nakai, S., Sumino, H., et al. (2008). Searching and detecting earthquake geochemical precursors in CO_2-rich groundwaters from galicia, spain. *Geochem. J.* 42 (1), 75–83. doi:10.2343/geochemj.42.75

R core team (2019). *R: a language and environment for statistical computing*. Vienna, Austria: R Foundation for Statistical Computing.

Ricci, T., Finizola, A., Barde-Cabusson, S., Delcher, E., Alparone, S., Gambino, S., et al. (2015). Hydrothermal fluid flow disruptions evidenced by subsurface changes in heat transfer modality: the la fossa cone of vulcano (Italy) case study. *Geology* 43 (11), 959–962. doi:10.1130/G37015.1

Rillard, J., Loisy, C., Le Roux, O., Cerepi, A., Garcia, B., Noirez, S., et al. (2015). The DEMO-CO2 project: a vadose zone CO2 and tracer leakage field experiment. *Int. J. Greenhouse Gas Control* 39, 302–317. doi:10.1016/j.ijggc.2015.04.012

Rogie, J. D., Kerrick, D. M., and Sorey, M. L. (2001). Dynamics of carbon dioxide emission at mammoth mountain, california. *Earth Planet Sci. Lett.* 188, 535–541. doi:10.1016/s0012-821x(01)00344-2

Romanak, K. D., Bennett, P. C., Yang, C., and Hovorka, S. D. (2012). Process-based approach to CO_2 leakage detection by vadose zone gas monitoring at geologic CO_2 storage sites. *Geophys. Res. Lett.* 39 (15), L15405. doi:10.1029/2012GL052426

Sano, Y., and Marty, B. (1995). Origin of carbon in fumarolic gas from island arcs. *Chem. Geol.* 119 (1–4), 265–274. doi:10.1016/0009-2541(94)00097-R

Schroder, I. F., Zhang, H., Zhang, C., and Feitz, A. J. (2016). The role of soil flux and soil gas monitoring in the characterisation of a CO_2 surface leak: a case study in qinghai, china. *Int. J. Greenhouse Gas Control* 54, 84–95. doi:10.1016/j.ijggc.2016.07.030

Schroder, I. F., Wilson, P., Feitz, A. F., and Ennis-King, J. (2017). Evaluating the performance of soil flux surveys and inversion methods for quantification of CO2 leakage. *Energy Procedia* 114, 3679–3694. doi:10.1016/j.egypro.2017.03.1499

Sciarra, A., Cantucci, B., and Coltorti, M. (2017). Learning from soil gas change and isotopic signatures during 2012 emilia seismic sequence. *Sci. Rep.* 7 (1), 1–7. doi:10.1038/s41598-017-14500-y

Sun, Y., Guo, Z., Liu, J., and Du, J. (2018). CO_2 diffuse emission from maar lake: an example in changbai volcanic field, NE china. *J. Volcanol. Geoth. Res.* 349, 146–162. doi:10.1016/j.jvolgeores.2017.10.012

Takle, E. S., Massman, W. J., Brandle, J. R., Schmidt, R. A., Zhou, X., Litvina, I. V., et al. (2004). Influence of high-frequency ambient pressure pumping on carbon dioxide efflux from soil. *Agric. For. Meteorol.* 124, 193–206. doi:10.1016/j.agrformet.2004.01.014

Toutain, J. P., and Baubron, J. C. (1999). Gas geochemistry and seismotectonics: a review. *Tectonophysics* 304 (1-2), 1–27. doi:10.1016/S0040-1951(98)00295-9

Troll, V. R., Hilton, D. R., Jolis, E. M., Chadwick, J. P., Blythe, L. S., Deegan, F. M., et al. (2012). Crustal CO_2 liberation during the 2006 eruption and earthquake events at Merapi volcano, indonesia. *Geophys. Res. Lett.* 39 (11), L11302. doi:10.1029/2012GL051307

Tsunogai, U., and Wakita, H. (1995). Precursory chemical changes in ground water: kobe earthquake, japan. *Science* 269 (5220), 61–63. doi:10.1126/science.269.5220.61

Vodnik, D., Videmšek, U., Pintar, M., Maček, I., and Pfanz, H. (2009). The characteristics of soil CO_2 fluxes at a site with natural CO_2 enrichment. *Geoderma* 150 (1-2), 32–37. doi:10.1016/j.geoderma.2009.01.005

Walia, V., Lin, S. J., Fu, C. C., Yang, T. F., Hong, W. L., Wen, K. L., et al. (2010). Soil–gas monitoring: a tool for fault delineation studies along hsinhua fault (Tainan), southern taiwan. *Appl. Geochem.* 25 (4), 602–607. doi:10.1016/j.apgeochem.2010.01.017

White, F. M., and Corfield, I. (2006). *Viscous fluid flow*. New York: McGraw-Hill, Vol. 3, 433–434.

Woo, J. U., Rhie, J., Kim, S., Kang, T. S., Kim, K. H., and Kim, Y. (2019). The 2016 Gyeongju earthquake sequence revisited: aftershock interactions within a complex fault system. *Geophys. J. Int.* 217 (1), 58–74. doi:10.1093/gji/ggz009

Yu, S., Chae, G., Jo, M., Kim, J. C., and Yun, S. T. (2015). *Assessment of CO2 discharge in a spring using time-variant stable carbon isotope data as a natural analogue study of CO2 leakage*. Vienna, Austria: EGU general assembly, Vol. 17.

Zhou, X., Apple, M. E., Dobeck, L. M., Cunningham, A. B., and Spanglerc, L. H. (2013). Observed response of soil O_2 concentration to leaked CO_2 from an engineered CO_2 leakage experiment. *Int. J. Greenh. Gas Con.* 16, 116–128.

Zhu, M., Xue, W., Xu, H., Gao, Y., Chen, S., Li, B., et al. (2019). Diurnal and seasonal variations in soil respiration of four plantation forests in an urban park. *Forests* 10 (6), 513. doi:10.3390/f10060513

Conflict of Interest: The authors declare that the research was conducted in the absence of any commercial or financial relationships that could be construed as a potential conflict of interest.

Copyright © 2021 Kim, Yu, Oh, Chae, Yun and Shinn. This is an open-access article distributed under the terms of the Creative Commons Attribution License (CC BY). The use, distribution or reproduction in other forums is permitted, provided the original author(s) and the copyright owner(s) are credited and that the original publication in this journal is cited, in accordance with accepted academic practice. No use, distribution or reproduction is permitted which does not comply with these terms.

frontiers in Earth Science

ORIGINAL RESEARCH
published: 25 February 2021
doi: 10.3389/feart.2021.635913

An Automatic System for Continuous Monitoring and Sampling of Groundwater Geochemistry in Earthquake-Prone Regions of SW Taiwan

Ching-Chou Fu[1], Chun-Wei Lai[2], Tsanyao Frank Yang[2†], David R. Hilton[3†], Cheng-Hong Chen[2], Vivek Walia[4], Arvind Kumar[4] and Lou-Chuang Lee[1]*

[1]Institute of Earth Sciences, Academia Sinica, Taipei, Taiwan, [2]Department of Geosciences, National Taiwan University, Taipei, Taiwan, [3]University of California, San Diego, La Jolla, CA, United States, [4]National Center for Research on Earthquake Engineering, NARL, Taipei, Taiwan

OPEN ACCESS

Edited by:
Guodong Zheng, Chinese Academy of Sciences (CAS), China

Reviewed by:
Tianming Huang, Chinese Academy of Sciences (CAS), China
Ying Li, China Earthquake Administration, China

***Correspondence:**
Ching-Chou Fu
ccfu@earth.sinica.edu.tw

[†]*Deceased*

Specialty section:
This article was submitted to Geochemistry, a section of the journal Frontiers in Earth Science

Received: *30 November 2020*
Accepted: *25 January 2021*
Published: *25 February 2021*

Citation:
Fu C-C, Lai C-W, Yang TF, Hilton DR, Chen C-H, Walia V, Kumar A and Lee L-C (2021) An Automatic System for Continuous Monitoring and Sampling of Groundwater Geochemistry in Earthquake-Prone Regions of SW Taiwan. Front. Earth Sci. 9:635913. doi: 10.3389/feart.2021.635913

Previous studies have revealed that gas compositions of fluid samples collected from southwestern Taiwan, where many hot springs and mud volcanoes are distributed along with tectonic structures, show significant variation before and after some disaster seismic events. Such variations, including radon activity, CH_4/CO_2, and $^3He/^4He$ ratios of gas compositions, are considered precursors of earthquakes in this area. An automatic system for continuous on-line gas monitoring and groundwater sampling was established at Yun-Shui (YS), where an artesian well located at an active fault zone in SW Taiwan, to validate the relationship between fluid compositions and seismicity. It is equipped with a quadrupole mass spectrometer (QMS) and a radon detector for *in-situ* measurement of the dissolved gas composition. Variations of dissolved gas compositions are transmitted to the laboratory through the internet. Furthermore, a syringe pump apparatus for the retrieval and temporal analysis of helium (SPARTAH) is also installed for off-line laboratory analysis for obtaining the detailed time-series records of helium, hydrogen, oxygen, and dissolved inorganic carbon (DIC) isotopic compositions as well as dissolved inorganic carbon and chloride concentration of water samples at this station. After continuous monitoring for several months, two substantial anomalies of multiparameter were observed prior to the significant earthquakes. This automated system has been demonstrated to be feasible for long-term continuous seismo-geochemical research in this area.

Keywords: on-line gas monitoring, syringe pump apparatus for the retrieval and temporal analysis of helium, off-line laboratory analysis, multiparameter, seismo-geochemical research

INTRODUCTION

Since the 1970s, geochemical studies have been carried in the world for earthquake precursors (Sugisaki, 1978; O'Neil and King, 1981; Sugisaki, and Sugiura, 1985; Roeloff, 1988). Precursory anomalies in the radon concentration of groundwater were reported before the Izu–Oshima–kinkai earthquake in 1978 and the Kobe earthquake in 1995 (Wakita et al., 1980; Igarashi et al., 1995).

Hydrogeochemical changes, including stable isotopes and noble gas isotopes, were observed before and after the large earthquakes in Iceland and Japan (Sano et al., 1998; Sano et al., 2016; Skelton et al., 2014; Onda et al., 2018). Preseismic changes in groundwater level and temperature were detected from the well before the 1970 M6.7 Przhevalsk Earthquake and the 2011 Tohoku Earthquake (Sadovsky et al., 1972; Orihara et al., 2014). Change in several water parameters is proposed as the precursory signals, particularly groundwater chemistry, water temperature, water level, and radon concentration, have also been reported before the earthquakes in many geological environments in Taiwan, such as hot/cold springs, mud volcanoes, and groundwater well (Liu et al., 1985; Chia et al., 2001; Wang, C. H. et al., 2001; Wang, C. Y. et al., 2001; Song et al., 2003; Song et al., 2005; Song et al., 2006; Yang et al., 2004; Yang et al., 2006; Kuo et al., 2006; Yuo et al., 2010; Lai et al., 2010; Chen et al., 2013).

It is worthy to note that the distribution of many mud volcanoes and hot springs are along with the tectonic structures in southwestern Taiwan, indicating that the fluids and gases may migrate through the fault zones to provide information regarding the deep sources (Yang et al., 2004; Chao et al., 2010; Chao et al., 2011; Chao et al., 2013; Sun et al., 2010; Sano et al., 2017). Regular sampling of radon in water had been performed for earthquake prediction since 1980 in Taiwan, showing Rn anomalies correlated with earthquakes (Liu et al., 1985). Song et al. (2006) concluded that hydrochemical variations of Cl^- and SO_4^{2-} concentrations at the Kuan–tze–ling (KTL) hot spring increased a few days before the Chi–Chi earthquake through the biweekly sampling. Song et al. (2003) collected commercially bottled groundwater around the epicenter for investigating changes in groundwater composition and found the obvious increase of SO_4^{2-} and NO_3^- concentrations before the Chi–Chi earthquake. Similarly, Sano et al. (2020) reported oxygen isotope anomalies before the Kumamoto earthquake by analyzing groundwater samples from the packaged drinking bottle collected from a deep well located 3 km to the epicenter. Yang et al. (2006) have continuously monitored the gas composition of the Chunglun (CL) mud pool along the Chukou Fault (CKF), and proposed CO_2/CH_4 variations in bubbling gases were sensitive to the earthquake events. The significant temporal changes of the $^3He/^4He$ ratio in bubbling gas were detected before and after the 1999 Chi–Chi earthquake (Fu and Lee, 2018). It suggests that the CL area is very susceptible to seismic activity. However, the biweekly or monthly sampling interval was performed based on on-site manual sampling. Yet, some short-term precursory anomalies may not be caught due to the low sampling frequency.

Due to many years of research and improvement, the real-time analysis of gas compositions has been quite mature for studying and monitoring the earthquake precursors (Yang et al., 2006; Weinlich, 2014; Ono et al., 2020). In contrast, precise measurements of chemical concentrations and isotopic ratios in water are difficult presently, and mass-spectrometers cannot be installed directly on the field to carry out continuous monitoring. Hence, there is a lack of understanding of the fluid's geochemical behaviors to produce consecutively anomalous changes. In this paper, we test an automatic sampling system for water samples, which is named the Syringe Pump Apparatus for the Retrieval and Temporal Analysis of Helium (SPARTAH) designed by Barry et al. (2009). The SPARTAH can continuously and precisely sample the fluids and analyze them in the laboratory later.

Gas compositions are dominated with 75–90% of CO_2 and 5–12% of CH_4 together with the higher $^3He/^4He$ value of 5.9 Ra at CL, suggesting that they might be originated from a deep source with a magmatic signal; meanwhile, major constituents of gases are 82–95% of CH_4 and 2–15% of CO_2 with a lower $^3He/^4He$ value of <0.4 Ra at KTL area, indicating a deep crust source (Yang et al., 2004; Yang, 2008). However, the fluids at the CL and KTL sites are too muddy to perform the SPARTAH system. An artisan well at Yunshui (YS) close to the major fault near the CL site is then selected for this experiment. Dissolved gas samples from the YS site are dominated with CH_4 ~96% and associated with C_2H_6 ~ 0.3%, which is similar to nearby mud volcano gases, which are typical thermogenic gas derived from crustal source with low helium isotopic ratios (<0.4 Ra) (Yang et al., 2004; Yang, 2008). It suggests that the YS site may have opportunities to detect gas and fluid geochemical anomalies related to the generation of earthquakes migrating from crustal source upward subsurface along the fault. Fluids of YS are mixed between two different reservoirs from CL and KTL is also likely to have occurred. This paper aims to describe the characteristics of the on-line monitoring system and off-line laboratory analysis and assess the feasibility of using the SPARTAH system to obtain high resolutions and precise measurements of different geochemical parameters in water for earthquake precursory studies in Taiwan.

GEOLOGICAL BACKGROUND

Taiwan is located on the boundary between the Eurasian plate and Philippine Sea plate with a convergence rate of ~80 mm/yr by the northwestward movement (Yu et al., 1997), a series of subparallel ENE-WSW trending reverse faults and folds developed from east to west in Taiwan (Lin et al., 2000). The target of this study is the Chiayi–Tainan area in southwestern Taiwan (**Figure 1**). There are three major faults, the Muchiliao Fault (MCLF), the Chukou Fault (CKF), and the Lunhou Fault (LHF), cutting through this area in a NE-SW trend based on field geological survey, drilling core, Seismic Reflection profiles, and ground resistivity (Shih et al., 2003; Lin et al., 2007). The MCLF is a reverse-slip fault along the Liushuang (Ls) Formation (brownish-yellow sandstone with thick mudstone) and can be identified on the western border of Chiayi hills. Although it might have been reactivated during the Late Quaternary, there is a lack of outcrops and evidence to support its existence. The CKF is a high-angle thrust ~40–60° with a fault plane dipping to the east, dividing from the Miocene to the Pleistocene in the study area.

Stratigraphy in the vicinity of the study area can be classified into several units from east to west, which are the Miocene Tangenshan Sandstone (Tn) Formation (thick-bedded massive sandstone and muddy sandstone), the Miocene Chunlun (Cl) Formation (shale, sandy shale and mudstone), the Pliocene Niaotsui (Nt) Formation (muddy sandstone, sandy shale and thick-bedded sandstone), the Pliocene Yunshuichi (Ys) Formation (shale and sandy shale and

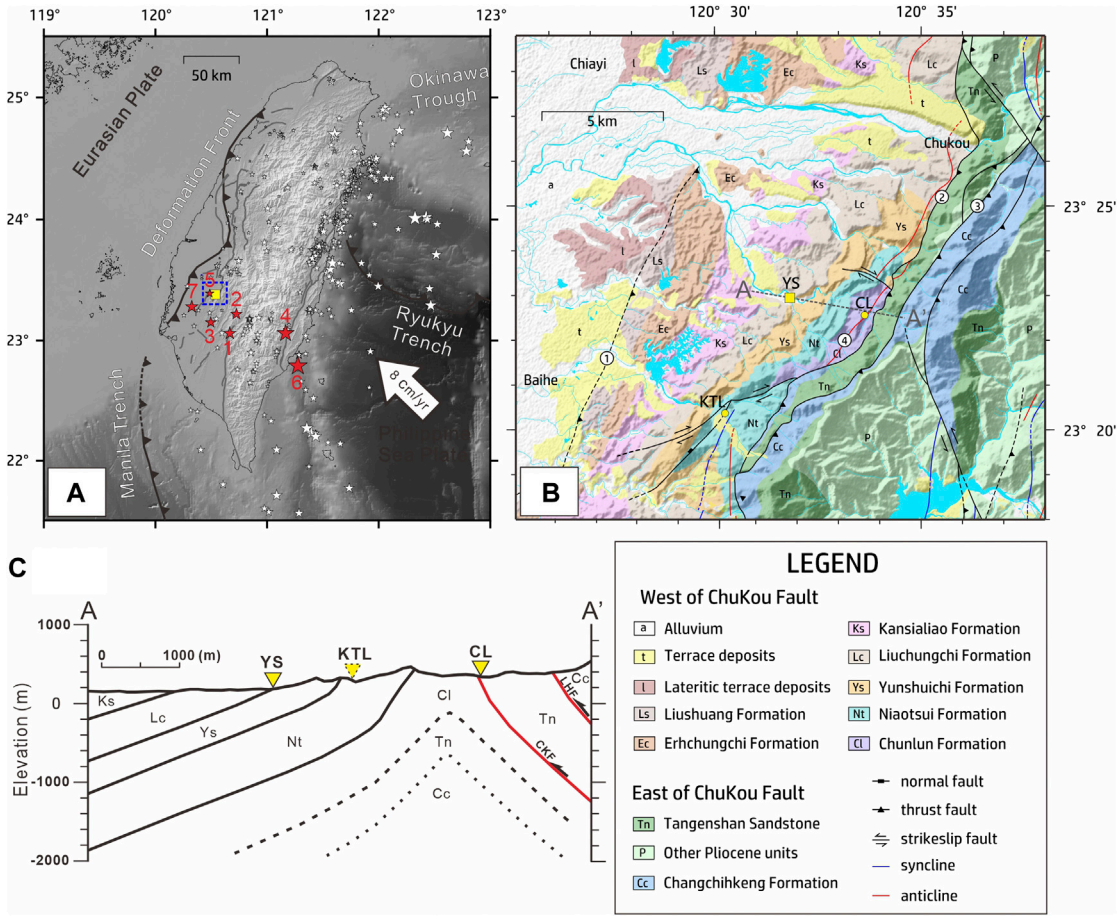


FIGURE 1 | (A) The simplified sketch of the regional map and principal tectonic structures shows the Philippine Sea Plate (PSP) is moving northwest toward Taiwan at a rate of approximately 8 cm/yr (Yu et al., 1997). **(B)** The geological and topographic map of southwestern Taiwan and the relative position of the study area and is marked by the blue dashed rectangle in **Figure 1A**. **(C)** A schematic diagram showing a cross-section along the geological transect (A–A′ in **Figure 1B**) [modified from Hsu and Wey, 1983). The yellow square represents the location of the YS station. The red star symbols represent the related earthquake epicenter with local intensity ≥2 around YS station and are labeled and listed in **Table 1**. Structure lines denote the 1) Muchiliao Fault (MCLF), 2) Chukou Fault (CKF), 3) Lunhou Fault (LHF), and 4) Chunlun Anticline.

mudstone), and the Pleistocene Liuchungchi (Lc) Formation (siltstone with shale, sandy shale or interbedded with muddy sandstone). The LHF is another thrust fault with a strike-slip component dipping to the southeast. It separates the Miocene Changchikeng (Cc) Formation (sandstone, sandstone interbedded with shale) from the Tn Formation. Based on GPS data by Yu and Chen (1998), a significant horizontal velocity of 6.3–13 mm/yr and strain rate of 0.48–2.01 μstrain/yr near the CKF can be observed. Otherwise, the seismicity around the LHF area is not active, but it has a very high horizontal velocity of 14.7 mm/yr (Hung et al., 1999). The CKF–LHF system exhibits an evident creep phenomenon, implying that the crustal stress accumulation is fast in this area and a substantial potential for the generation of the great earthquake.

The observation YS well is approximately 100 m deep. Except for the yellowish-brown weathered soil layer near the surface, the rock core from YS well mainly comprises gray muddy fine sandstone with thin-bedded shale or fine sandstone from 6 to 100 m depth. A more permeable aquifer at a depth of 97–98 m where thick fine sandstone was penetrated to install a screen for monitoring purposes in the Ys Formation. The CL mud pool is located on the culmination of the Chunlun anticline about 3 km east of the YS site, whereas the KTL hot spring locates approximately 7 km south of the YS site in the Nt formation. Fluid materials of CL and KTL might contribute deeper than the Cl formation and the Nt formation, respectively (**Figures 1B,C**).

METHODOLOGY

The monitoring station was set up at YS site to analyze and determine the composition of dissolved gases and geochemistry of water extracted from an artesian well with a low-flow rate of 0.03 L/min. **Figure 2** shows the configuration of the automated monitoring system, which includes on-line monitors and off-line laboratory analysis. Groundwater flows out from a depth of ~100 m, which was introduced into the gas-water separator for on-line monitors, while

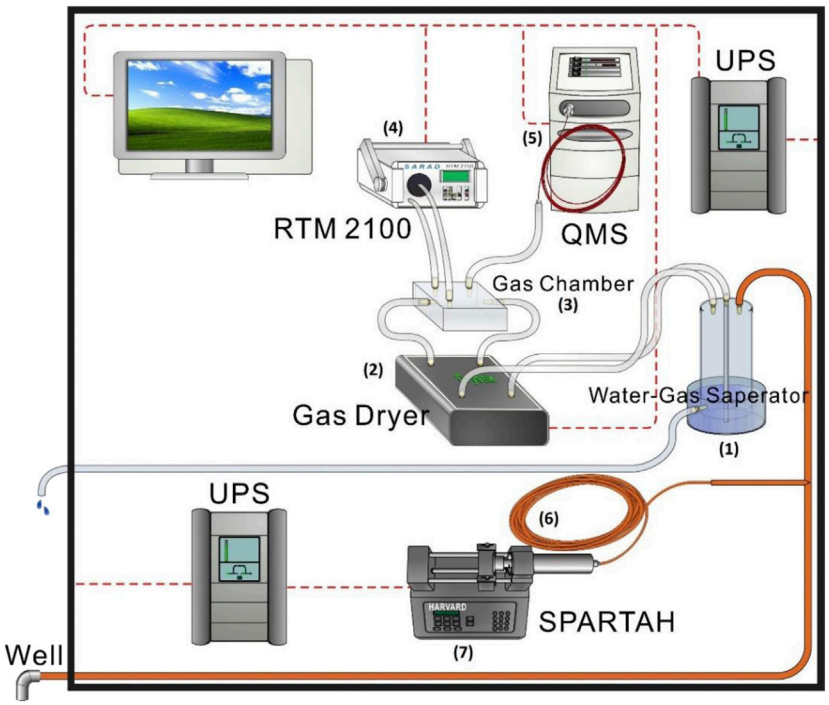


FIGURE 2 | A sketch of the monitoring station, including the dissolved gas analyzer, fluid collection system, and associated equipment.

groundwater was connected via the coils of Cu tubing to a storage device for off-line laboratory analysis. After passing through a condensing water trap and a DRYSTIK (Durridge Co.), the dry dissolved gases are split to (1) quadrupole mass spectrometer (QMS100, Stanford Research Systems, Inc.); and radon counter (RTM 2100, SARAD, Dresden, Germany) from a ~1-L chamber. The dissolved gas compositions were continuously analyzed through the QMS system at the interval of every 2 min, while radon concentration was recorded once every 30 min, then transmitted to the laboratory at the National Taiwan University via the Internet. The accuracy of Rn measurement is better than ±10%, and the analytical limit of detection is ~30 Bq/m^3. The accuracy of QMS is approximately 1–10% according to different gas concentrations in the ranges of a percent (%) to parts per million (ppm), and the analytical limit of detection is less than one ppm. Before gas monitoring at YS station, the QMS has been calibrated for the mass scale (to measure at the peak maximum) and quantified gas concentrations. A similar instrumental setup can be found in Yang et al. (2006).

The sampling and analysis procedure charts of the off-line laboratory are shown in **Figure 3**. The automatic sampling system for water samples is named the Syringe Pump Apparatus for the Retrieval and Temporal Analysis of Helium (SPARTAH) as a storage device for fluids designed by Barry et al. (2009). The system is composed of a syringe pump (model PHD 4400 by Harvard Apparatus) equipped with a 100 ml stainless-steel syringe (the syringe volume can be upgraded) to provide a stable pumping force of up to 91 kg and accurate sampling volume calibration.

The coils of Cu tubing are composed of a length of ~30.3 m and an inner diameter of 2.05 mm is used to connect with the syringe pump, which can be considered as the storage container. The coils of Cu tubing are filled with deionized (DI) water using the refill mode of the syringe pump before connection. The DI water is drawn into the stainless-steel syringe and is replaced by water from the wellhead during operation. The fluid is accurately and smoothly drawn into the syringe at a user-defined rate through the withdrawal mode operating by the syringe pump. To evaluate the feasibility of using the SPARTAH system in Taiwan, we first determine a constant flow rate of 0.0417 ml/h (1 ml/day) to collect groundwater for analyzing the ratio of hydrogen, oxygen, DIC, helium isotopes and the concentration of chloride during the period from January 20 to March 21, 2014 (the first period). The SPARTAH system was further performed for sampling groundwater at a constant flow rate of 0.2085 ml/hr (5 ml/day) for the second period, which mean the coils would have to be replaced approximately twenty days. That is, each batch of Cu coils can hold a total of 100 ml of water samples, and the sample length of each copper tubing is about 30.3 cm for 1 ml of water. Upon return to the laboratory, the batch of copper coils are immediately sectioned into one and five segments per day during the first period and the second period, respectively, using refrigeration clamps and labeled the date. The labeled Cu tubing then can be broken by a torsion to transferred water samples into the Teflon containers for further analysis. In this study, each section of Cu tubing contains 1 ml of the water sample and which used to analyze the concentration of anion (Cl^-) and dissolved inorganic carbon (DIC) in water and the ratio of DIC, hydrogen, oxygen, and helium isotopes. All measurements were analyzed within two weeks after sectioning the Cu tubing, except for helium analysis.

According to the capillary action, the sample in the Cu tubing is affected by 1) fluid diffusion and 2) fluid dispersion during

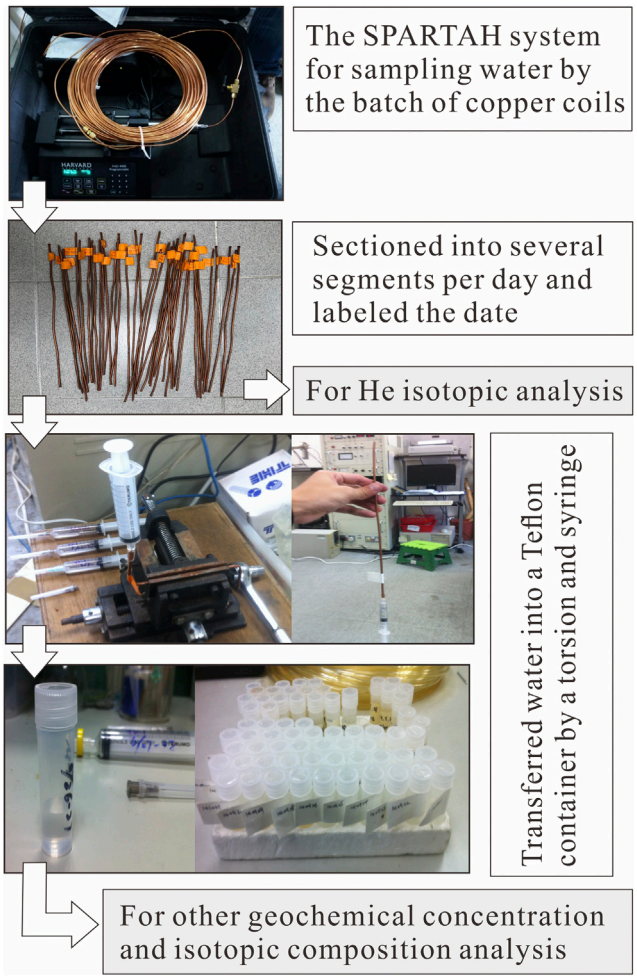


FIGURE 3 | The flowchart of the methodology illustrating the sampling and procedure used for analysis in water samples through the SPARTAH system.

sampling. According to the research experiment with the similar configuration conditions at a low flow rate (Tryon et al., 2001), it showed that after 6 months of copper tubing in storage, those two factors only made a slight impact on water samples. The trend of fluid chemical properties can yet be recognized in time series, even if it may be contaminated with a small perturbation (Barry et al., 2009).

The concentrations of chloride in the water samples were determined using an ion chromatography (Metrohm 882 Personal IC) at the Department of Geosciences, National Taiwan University, with a relative standard deviation of <1.5% and a detection limit of 0.1 ppm in weight.

Helium concentrations and isotopic ratios in water samples were directly analyzed from the Cu tubing sample after the Ultra-high Vacuum (UHV) extraction system and purification in the high-vacuum inlet line of a MAP215E noble gas mass spectrometer at the Scripps Institution of Oceanography, University of California San Diego. The observed $^{3}He/^{4}He$ ratios were calibrated against atmospheric standard gas and were expressed relative to Ra, where Ra is the air $^{3}He/^{4}He$ ratio of 1.39×10^{-6} (Poreda and Craig, 1989). This system can process 1 cm^3 of water for helium isotope analysis at a precision <2%, and experimental details following a similar process were described in detail by Barry et al. (2009).

The concentration and stable carbon isotope composition of dissolved inorganic carbon (DIC) were conducted by an isotopic ratio mass spectrometer (Thermo-Finnigan MAT253, Bremen, Germany) at the Institute of Oceanography, National Taiwan University, equipped with a Kiel carbonate device (Thermo-Finnigan) at which carbonate minerals react with phosphoric acids to at generating CO_2 for downstream isotopic analysis. Observed carbon isotopic ratios were normalized to the Vienna Pee Dee Belemnite (V-PDB) and shown as δ values. The precision of carbon isotopic composition was 0.03‰ at 1σ.

Hydrogen and oxygen isotopes of water samples were analyzed using the Liquid-Water Isotope Analyzer (LWIA) by off-axis integrated-cavity laser spectroscopy (DLT-100, LGR Co. Ltd.) at the Department of Geosciences, National Taiwan University without any chemical preprocessing, following the procedure described in Lis et al. (2008) and Berman et al. (2009). Observed hydrogen and oxygen isotopic ratios were calibrated against five LGR standards (LGR 1A-5A) and converted into the conventional V-SMOW (Vienna Standard Mean Ocean Water) scale, presented as δ values. per mil (‰). According to the manufacturer's specifications (Los Gatos Research Inc., 2008), the precision of $\delta^{18}O$ and δD values were less than 0.6‰ and 0.2‰ at 1σ, respectively. The δ notation is defined as:

$$\delta\,(0/00) \;=\; \left[\left(R_{sample}/R_{standard}\right) - \;1\right] \times 1000$$

where R is the ratio of $^{13}C/^{12}C$, $^{2}H/^{1}H$, or $^{18}O/^{16}O$.

Hourly precipitation is available from a meteorological station of the Central Weather Bureau (CWB) of Taiwan, located at about 3 km from the YS station. Seismic data used in this study are taken from the earthquake catalogs of CWB of Taiwan. The distribution of each earthquake's intensity to present the amount of shaking could also be detected, meanwhile, the local intensity of an earthquake to the YS site then could be known. There were 495 earthquakes with local magnitudes (ML) ranging from 2.0 to 5.9 in the Taiwan area during the deployment period. Only when those earthquakes with local intensity ≥ two around YS station together with, the distance between station and earthquake of the epicenter is ≤30 km for M ≥ 4 or the distance is 30–110 km for M ≥ 5 (**Table 1**), which are considered significant to the monitoring site (e.g., Yang et al., 2005; Fu et al., 2017).

RESULTS AND DISCUSSIONS

Temporal Variation of Geochemical Compositions During the First Deployment

Fourteen helium isotope and concentration results, along with the ratio of hydrogen, oxygen, carbon isotopes, and chloride concentration from the Cu coils during the first deployment from January 20 to March 21, 2014, are presented in **Table 2** and **Figure 4**. The range in $^{3}He/^{4}He$ and $\delta^{13}C$ values of dissolved inorganic carbon (DIC) are observed from 0.42 to 0.56 Ra (1 Ra =

TABLE 1 | Catalog of related earthquakes[a] occurring in Taiwan from January 20 to March 21, 2014, and May 1 to November 30, 2014.

No	Date	Long (°E)	Lat (°N)	Mag (M_L)	Depth (km)	Dist (km)	Intensity[b]	△t[c] (day)	D_t[d] (day)
1	2014/02/16 00:14	120.69	23.07	4.1	17.7	29.5	2	4	5
2	2014/03/05 00:02	120.74	23.19	4.4	5.6	25.5	2	8	10
3	2014/05/16 04:21	120.49	23.16	4.0	20.4	14.3	2	None	None
4	2014/05/25 20:41	121.16	23.06	5.1	7.1	74.2	2	Unknown	Unknown
5	2014/07/22 10:30	121.66	23.79	4.0	11.3	13.2	3	10	Unknown
6	2014/09/25 18:35	121.30	22.74	5.2	17.4	104.1	2	6	12
7	2014/10/29 07:16	120.32	23.28	4.3	20.8	23.3	2	Unknown	Unknown

[a]*There were in total 495 earthquakes recorded in Taiwan during this period (**Figure 1**). Only those earthquakes with local intensity ≥2 and the epicenter distance ≤30 km with M ≥ 4, or the epicenter distance ≤ 110 km with M ≥ 5, are considered significant to the monitoring site.*
[b]*Intensity of each earthquake is presented the amount of shaking around the monitoring station.*
[c]*Time difference between the anomalous peak of geochemical compositions and the earthquake event.*
[d]*Duration of the anomaly.*

atmospheric $^3He/^4He$ value) and −20.01 to −0.07‰, respectively, similar to the previous values of <0.4 Ra for the study area. The He/Ne value (as X has shown in **Table 1**) varies from 7.69 to 512 and ^4He concentration from 24.1 to 1060 cc STP/gH_2O. The δD and $\delta^{18}O$ values range from −11.37 to −5.00‰ and −1.30 to −0.07‰, respectively, and the concentration of chloride range from 12,700 to 13,500 ppm. Temporal variations of all measurements were relatively small. Moreover, we can confirm that the DI water in the coils of Cu tubing was replaced by groundwater from the well based on a low value of $^3He/^4He$ ratio and a very high chloride concentration. Taking together all observations is shown that the SPARTAH system successfully retrieved fluid samples during the first deployment.

The background values were determined using the mean value plus two standard deviations shown by the yellow bar to recognize their background and anomalous value (**Figure 4**). Some substantial but short increase in the $^3He/^4He$, $\delta^{13}C_{DIC}$, and ^4He data can be observed during this deployment period. Changes in those geochemical parameters from February 12 to 16, 2014, may be associated with a local earthquake (M = 4.1), which occurred on February 16, 2014, approximately 29.5 km to YS station. Similar anomalies were observed from February 25 to March 7, 2014, followed by an earthquake, which occurred on March 5, 2014, with a focal depth of 5.6 km, approximately 25.5 km to YS station with magnitude 4.4. As in the case of the first deployment, not only ^4He concentrations but also the isotopic value of $^3He/^4He$ and $\delta^{13}C_{DIC}$ presented the valuable indicators for tracing the possible earthquake precursor. However, Cl^- concentrations, δD, and $\delta^{18}O$ values did not change significantly during this period.

Temporal Variation of Geochemical Compositions During the Second Deployment

Continuous on-line monitoring and off-line laboratory analysis at the YS station started from May 1 to November 30, 2014, for the second period. The concentration and ratio of dissolved gases,

TABLE 2 | Helium isotope and relative abundance characteristics from January 20 to March 21, 2014.

Sample ID	R_m/R_a[a]	X[b]	R_c/R_a[c]	$[^4He]_m$[d] cc STP/g H_2O (×10^{-9})	$[^4He]_c$[d] cc STP/g H_2O (×10^{-9})	$\delta^{13}C_{DIC}$ (‰)
2014/01/27	0.54	7.69	0.47 ± 0.01	67.5	58.8	−16.91
2014/02/09	0.49	11.9	0.44 ± 0.01	62.9	57.6	−14.31
2014/02/12	0.50	14.1	0.46 ± 0.01	195	181	−2.07
2014/02/13	0.55	13.4	0.52 ± 0.01	169	156	−15.84
2014/02/14	0.50	10.1	0.45 ± 0.01	50.9	45.9	−5.84
2014/02/16	0.53	11.4	0.48 ± 0.02	47.8	43.6	−0.07
2014/02/21	0.44	15.2	0.42 ± 0.01	60.5	55.7	−17.37
2014/02/25	0.56	8.90	0.51 ± 0.02	41.1	36.5	−8.82
2014/02/27	0.49	10.7	0.44 ± 0.01	47.1	42.7	−17.89
2014/03/01	0.48	29.4	0.46 ± 0.01	519	501	−3.34
2014/03/05	0.43	512	0.43 ± 0.01	1300	1300	−20.01
2014/03/07	0.41	165	0.44 ± 0.01	2,230	2220	−18.38
2014/03/09	0.44	33.3	0.43 ± 0.01	99.7	96.7	ND
2014/03/15	0.60	11.4	0.56 ± 0.03	55.6	50.8	−12.77

All reported errors are at the 1σ level.
[a]R_m/R_a *is measured* $^3He/^4He$ *ratio divided by the* $^3He/^4He$ *in air* = 1.4×10^{-6}.
[b]$X = (^4He/^{20}Ne)_{measured}/(^4He/^{20}Ne)_{air} \times \beta_{Ne}/\beta_{He}$ *and* β *represents the Bunsen coefficient from (Weiss, 1971) assuming a groundwater recharge temperature of 15°C.*
[c]R_c/R_a *is the air-corrected He isotope ratio* = $[(R_m/R_a \times X)-1]/(X-1)$.
[d]*Dissolved He concentrations are air-corrected where* $[He]_C = ([He]_m \times (X-1))/X$.

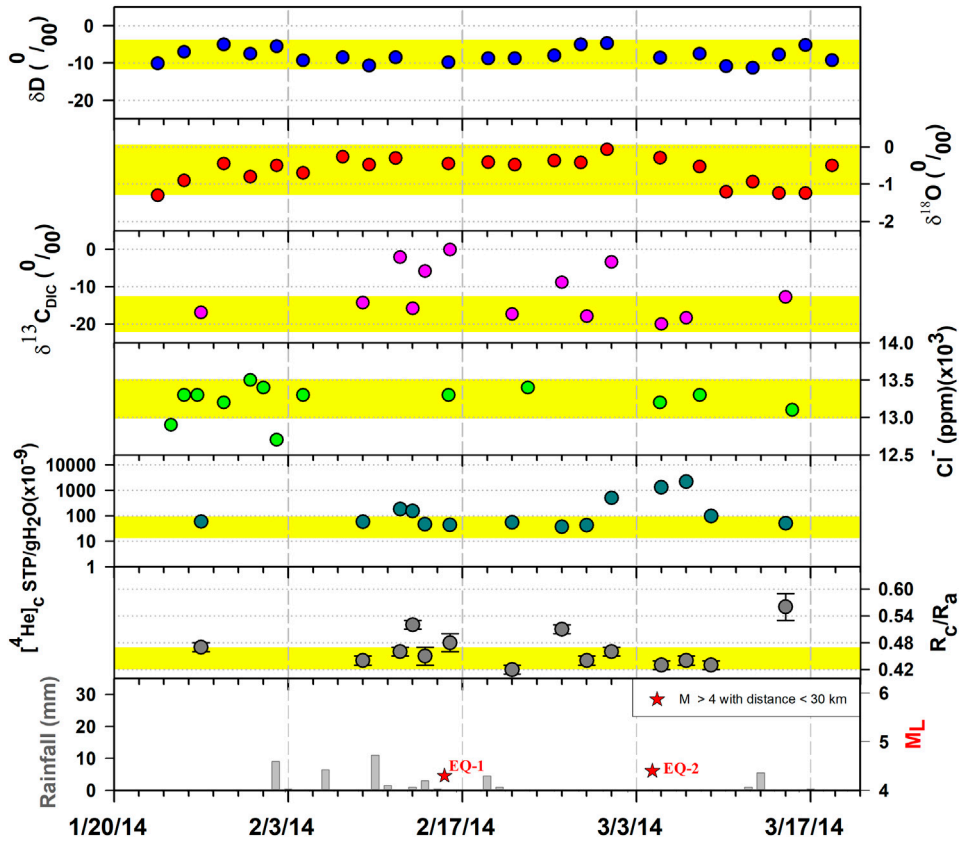


FIGURE 4 | The temporal variations of δD, $\delta^{18}O$, $\delta^{13}C_{DIC}$, and $^{3}He/^{4}He$ values as well as ^{4}He and chloride concentrations from January 20 to March 21, 2014. Horizontal yellow bar indicates two standard deviations from the mean of the observed results. Red dashed line denotes the date of the specific seismic events. The magnitude of related earthquakes with local intensity ≥2 and hourly rainfall data are also included. Red star symbols indicate that the epicenter distance of the earthquake to the station was ≤30 km with a magnitude ≥4.

as well as the isotopic ratio of hydrogen, oxygen, DIC, and the concentration of DIC and chloride, were recorded (**Figure 5**). The hourly average of dissolved gases had chemical compositions of 90.2–96.5% for CH_4, 0.8–2.0% for O_2, 1.7–6.7% for N_2, 0.13–0.25% for CO_2, 0.04–0.11% for Ar, and 748–1391 Bq/m^3 for Rn. The ratio of CH_4/N_2, N_2/CO_2, and CH_4/CO_2 range from 13.5 to 56.9, 9.9 to 41.5, and 375.2 to 689.0. The range in δD, $\delta^{18}O$, and $\delta^{13}C_{DIC}$ values were presented from −11.12 to −4.21‰, −0.90 to 0.52‰, and −19.32 to −8.63‰, respectively. The concentration of 30.5–38.4 mM for DIC and 12,900 to 14,700 ppm for chloride were observed. Two significant but short changes in several observed results can be observed during the second deployment. However, some discrete changes and a loss of the time-series in the monitoring data occasionally are due to manual factor calibration, system servicing, and supply problems. It is noted that there is a lack of helium results during the second deployment because of some technical problems for the arrangement of Cu tubing samples to the Scripps Institution of Oceanography.

Continuous dissolved gas concentrations in CH_4, CO_2, and Ar together with the ration of CH_4/N_2 showed the substantial increase after July 12 until July 21, 2014, with the highest value, while the decrease in dissolved gas concentrations of O_2 and N_2 were observed simultaneously (**Figures 5A,B**). It suggests an evidence that the change was not induced by air contamination. There is a noticeable decrease in gas compositions, followed by a local earthquake with magnitude 4, which occurs on July 22, 2014. The earthquake with a focal depth of 11.3 km is only located at about 13.2 km away from the station. The timing is consistent with the period of the observed $\delta^{18}O$ anomalies on July 18, 2014, the $\delta^{13}C_{DIC}$ changes on July 17, 2014, and higher fluctuation in Cl^- concentrations on July 14 and 18, 2014 (**Figure 5C**).

An abrupt change in dissolved gas concentrations in CH_4 and CH_4/N_2, as well as a slight increase in Rn concentrations were observed from September 19 to October 1, 2014, and September 24 to October 7, 2014, respectively; meanwhile, the significantly decreasing trend in O_2, N_2, Ar, and N_2/CO_2 were found (**Figures 5A,B**). During the observed gas anomalies, there is an earthquake (M = 5.2) occurring on September 25, 2014, with a focal depth of 17.4 km and an epicenter distance of 104.1 km from the station. Similarly, the timing is consistent with the period of the observed $\delta^{13}C_{DIC}$ changes of −9.96 to −8.63‰ on September 22, 23, and 25, 2014, and higher variations in Cl^- concentrations of 1.42–1.47 ppm on September 21 and 28, 2014 (**Figure 5C**).

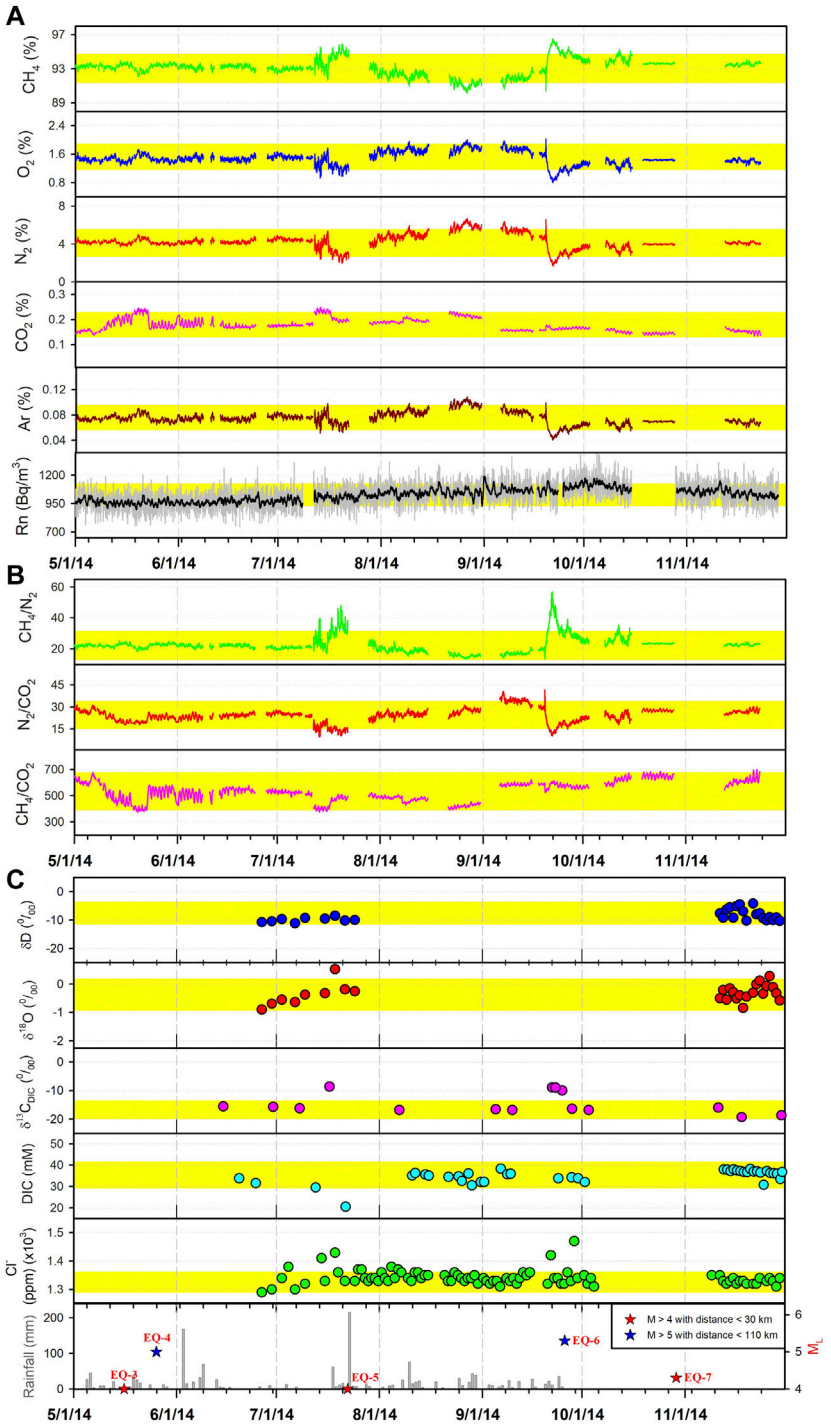


FIGURE 5 | The temporal variations of **(A)** concentration and **(B)** ratio of dissolved gases as well as **(C)** water chemical compositions (δD, $\delta^{18}O$, and $\delta^{13}C_{DIC}$ values along with DIC and chloride concentrations) from May 1 to November 30, 2014. Horizontal yellow bar indicates two standard deviations from the mean of the observed results. The magnitude of related earthquakes with local intensity ≥2 and hourly rainfall data are also included. The star symbols in different colors indicate that the epicenter distance of the earthquake to the station was ≤30 km (red) with a magnitude ≥4 and ≤110 km (blue) with a magnitude ≥5, respectively.

It is noted that a slight fluctuation of gas compositions can be observed from May 17 to 23, 2014, two days prior to the EQ-4 (M = 5.2), which occurs on May 25, 2014, approximately 74.2 km to the station. Furthermore, the hypocenter depth of EQ-4 is only 7.1 km, which may affect pre-stress transfer across due to the complex tectonic structures in the shallow crust. It may be

explained that no substantial anomaly was obviously found before the EQ-4. However, there is no anomaly related to the EQ-3 and EQ-7, which occurred on May 16 and October 29, 2014, with a hypocenter depth greater than 20 km. During the second deployment, all observations have demonstrated that the automatic system of online monitoring and the SPARTA for off-line analysis is feasible for long-term continuous seismo-geochemical research in this area.

The Possible Effect on the SPARTAH System

Tryon et al. (2001) have shown a tracer record from fluid samples through approximately 75 m of Cu tubing for more than two months and pointed out that the diffusion and dispersion of the tracer are slight during more than two months sampling period. Déhais et al. (2016) have reported that the diffusion of helium in the Cu tube through the SPARTAH system was slight during four to six months and recommended a shorter sampling duration of two months to be appropriately deployed on the field for obtaining the reliable preservation of the information. This study operated the SPARTAH system to obtain groundwater samples and replace the Cu coils approximately every two months and twenty days for the first and second deployment, respectively. All groundwater samples analysis was completed within two weeks after taking the Cu coils back from the station, except for helium analysis. The duration of fluid in the Cu coil in the study is similar to the previous studies mentioned above. Several substantial geochemical compositions were found for a short period to provide excellent proofs without any significant contamination by diffusion or dispersion process. Therefore, the effect of diffusion and dispersion on the SPARTAH system can be ignored.

Mechanism for Geochemical Changes

The mechanism for changes in the chemical compositions of subsurface water bodies can be attributed to several processes: 1) water-rock interactions; 2) the mixing of groundwater and formation or pore waters; 3) by the mixing of different reservoirs with different chemical compositions; 4) by the mixing of meteoric waters; 5) artificial pollutants (Igarashi et al., 1995; Song et al., 2006; Reddy et al., 2011; Skelton et al., 2014; Sano et al., 2020). The processes (1) and (2) may gradually cause the hydro-chemical changes during a long period of time, resulting in a shift from an equilibrium between water and rock because of increased exposure of reactive surfaces to the fluid. According to the observed temporal variations of all geochemical anomalies only occurring a few days before the relevant earthquake in a short duration, the processes (1) and (2) then can be ruled out.

Groundwater is mainly derived from meteoric water, including precipitation, and river and lake water (Mizota and Kusakabe, 1994). The origin and evolution of the groundwater can be evaluated by the hydrogen and oxygen isotopes (Claesson et al., 2004; Peng et al., 2010). Their signatures can characterize the groundwater samples in Craig's diagram (Craig, 1961), and their relationship between the δD and $\delta^{18}O$ values of

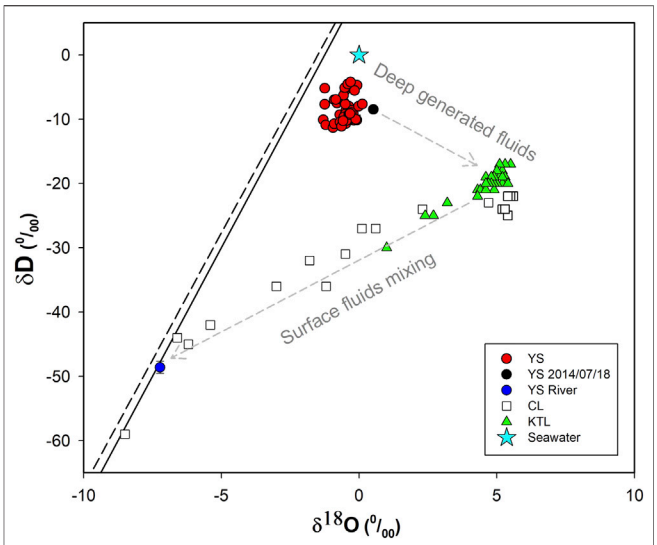


FIGURE 6 | Plot of δD and $\delta^{18}O$ for groundwater samples in this study with literature results of CL and KTL for comparison (Chan, 2001). Seawater composition, local meteoric water line (Wang et al., 2001; solid line), and global meteoric water line (Craig, 1961; dash line) are shown for reference.

groundwater samples from the YS well is presented in **Figure 6**. Those fluids have slightly higher $\delta^{18}O$ values and have lower δD values than seawater, suggesting those were not significantly contributed by surface water. The nearly constant δD and $\delta^{18}O$ composition of YS over time, possibly reflecting the compositions of formation water. Meanwhile, the large δD and $\delta^{18}O$ variations at CL and KTL over time indicated the potential of two end members mixing between formation water and meteoric water (Chan, 2001). The higher oxygen isotopic value of YS was detected on July 18, 2014, four days before the EQ-5, which occurs on July 22, 2014. We proposed that a slight contribution of higher $\delta^{18}O$ was attributed to the mixing of different groundwater types, which may be associated with the deep generated fluids of CL and KTL.

The higher $^3He/^4He$ value with enrichment of CO_2 and the lower $^3He/^4He$ value with enrichment of CH_4 would represent the magmatic and crustal end-member, respectively, as suggested by the data from CL and KTL (Yang et al., 2004; Yang, 2008), which may provide two different potential sources around the studied area for the gas and fluid interacting with the YS well. Since the samples during the first deployment exhibit the lower $^3He/^4He$ ratios as well as a $^4He/^{20}Ne$ variation of 8.9–512, far exceeding the ratio of air (0.318) (Sano and Wakita, 1985), air contamination cannot be the primary process responsible for the observed differences in the $^3He/^4He$ values. As no obvious mantle signal and higher CO_2 concentrations were found in the monitoring results of YS, a contribution of mantle helium associated with higher CO_2 from CL can be excluded. Moreover, Yang et al. (2003) reported that the average Rn concentrations of approximately 16,800 Bq/m^3 at the CL site and proposed Rn exhalation is mainly controlled by the CO_2 carrier gases along the CKF. Similarly, Etiope and Martinelli (2002) suggested that

carrier gases (e.g., CH_4 and CO_2) may play an essential role in controlling the migration and transportation of Rn in the fractured zone toward the surface. Therefore, very slight increases in Rn and CO_2 prior to an impending earthquake suggest that CL may not be the primary contributor to change gas compositions at the YS site. KTL could be the potential source to provide a higher $\delta^{18}O$ fluid but not CL, due to a lower $^3He/^4He$ value at YS without any significant mantle signature. Furthermore, an additional CH_4 inputting was observed from July 12 to July 21, 2014, that may indicate a potential contribution with enrichment of CH_4 around the YS site. It is another evidence to support that KTL can be the candidate for providing a fluid source. Hence, based on those evidences, we deduced that the mechanism for pre-geochemical anomalies was caused by rapid fluids mixing between YS and KTL area as the process (3).

No correlated relationships between the anomalies of Cl^- in the temporal variations and hourly precipitation were found during the monitoring period (**Figure 5**), highly suggesting that the observed temporal variations in the geochemical compositions were not induced by the meteoric water flowing down into the circulation system of the subsurface water system. For a similar reason, artificial pollutants cannot cause hydro-geochemical changes in this study. Therefore, the processes (4) and (5) can be ignored.

We observed continuous dissolved gases together with chemical and isotopic changes in groundwater sampled at YS well near the active CKF, those of anomalies before some specific earthquakes with $M \geq 4$ and ≤ 30 km and $M \geq 5$ and ≤ 110 km away from the station. Those events have induced the local intensity ≥ 2 around the monitoring region. According to those findings and interpretations mentioned above, we proposed pre-seismically induced gas-fluid source mixing, with the connection of different fluids due to the development of microcracks causing changes in rock permeability of the formation below the YS station. The observed compositions returned to background levels within a few days after the duration of the anomaly due to the closing of microfractures reducing the permeability of the rock.

CONCLUSION

In the present study, we applied on-line monitoring for continuous dissolved gas compositions and off-line analysis by the SPARTAH system for automated sampling groundwater samples at YS station, located around the active fault zone in southwestern Taiwan. The major findings of this study are listed below:

(1) The significant changes of dissolved gases (e.g., CH_4, CO_2, Ar, and CH_4/N_2) together with anomalous hydro-geochemical compositions (e.g., $\delta^{18}O$, $\delta^{13}C_{DIC}$, DIC, and Cl^- concentration) may be considered good indicators with high confidence related to the specific earthquake event in this area. Meanwhile, oxygen and nitrogen are relevant indexes for evaluating air-contamination of the observed results.
(2) Our observations demonstrate that this automatic monitoring and sampling system operating at the active fault zone is feasible for long-term continuous seismo-geochemical research in this area. Taking the variations of multi-anomalies can be recognized from a few to several days before an earthquake with local intensity ≥ two, that could be used to have a reliable information about the short-term precursor.
(3) We propose a potential mechanism for geochemical changes, suggesting that those anomalies can be attributed to mixing different fluids (e.g., KTL) from different geochemical signatures caused by strain-induced changes in the permeability of surrounding formation around the YS station.
(4) The SPARTAH system could be a useful technique for collecting any fluids of interest that support within the specified time interval sampling depend on the syringe volume. Therefore, we consider that it could be applied not only to earthquake precursors but also other research purposes, for example, chemical weathering and water pollution.

DATA AVAILABILITY STATEMENT

The raw data supporting the conclusions of this article will be made available by the authors, without undue reservation, to any qualified researcher.

AUTHOR CONTRIBUTIONS

CCF was responsible for the design and organization of the work and writing the manuscript. CWL was responsible for the collection of data and analysis of samples. TFY and DRH provided the writing ideas of the paper. CHC, VW, AK and LCL were involved in the data interpretation.

FUNDING

The research is supported by grants MOST 108-2116-M-002-025, MOST 108-2116-M-001-024, and MOST 109-2628-M-001-002-MY3 through the Ministry of Science and Technology (MOST).

ACKNOWLEDGMENTS

We deeply dedicate this paper to the late Prof. Tsanyao Frank Yang (TFY), who passed away on March 12, 2015 at the age of 54 and the late Prof. David Raymond Hilton (DRH), who passed away on January 7, 2018 at the ages of 59. Prof. Yang had worked as a geochemist at the Department of Geosciences, National Taiwan University (NTU), Taiwan, for more than 20 years and Prof. Hilton was a geochemist at Scripps Institution of Oceanography at the University of California San Diego

(UCSD), for more than 30 years. Their passions for research included setting new standards for relevant measurements, which enables us to present our work here. We thank Mr. K.W. Wu and K.H. Chen for helping in the operation and maintenance of the monitoring station and preliminary data analysis. The TEC contribution number for this article is 00167.

REFERENCES

Barry, P. H., Hilton, D. R., Tryon, M. D., Brown, K. M., and Kulongoski, J. T. (2009). A new syringe pump apparatus for the retrieval and temporal analysis of helium in groundwaters and geothermal fluids. *Geochem. Geophys. Geosyst.* 10 (5), Q05004. doi:10.1029/2009GC002422

Berman, E. S., Gupta, F. M., Gabrielli, C., Garland, T., and McDonnell, J. J. (2009). High-frequency field-deployable isotope analyzer for hydrological applications. *Water Resour. Res.* 45 (10), W10201. doi:10.1029/2009WR008265

Chan, P. S. (2001). $\delta^{18}O$ and δD of spring waters from active structure zones, southern Taiwan. MS thesis. Taipei: Dep. Geosci. Nat. Taiwan Univ., 80 [in Chinese with English abstract].

Chao, H. C., You, C. F., and Sun, C. H. (2010). Gases in Taiwan mud volcanoes: chemical composition, methane carbon isotopes, and gas fluxes. *Appl. Geochem.* 25 (3), 428–436. doi:10.1016/j.apgeochem.2009.12.009

Chao, H. C., You, C. F., Wang, B. S., Chung, C. H., and Huang, K. F. (2011). Boron isotopic composition of mud volcano fluids: implications for fluid migration in shallow subduction zones. *Earth Planet. Sci. Lett.* 305 (1, 2), 32–44. doi:10.1016/j.epsl.2011.02.033

Chao, H. C., You, C. F., Liu, H. C., and Chung, C. H. (2013). The origin and migration of mud volcano fluids in Taiwan: evidence from hydrogen, oxygen, and strontium isotopic compositions. *Geochim. Cosmochim. Acta* 114, 29–51. doi:10.1016/j.gca.2013.03.035

Chen, C. H., Wang, C. H., Wen, S., Yeh, T. K., Lin, C. H., Liu, J. Y., et al. (2013). Anomalous frequency characteristics of groundwater level before major earthquakes in Taiwan. *Hydrol. Earth Syst. Sci.* 17 (5), 1693–1703. doi:10.5194/hess-17-1693-2013

Chia, Y., Wang, Y. S., Chiu, J. J., and Lin, C. W. (2001). Changes of groundwater level due to the 1999 Chi–Chi earthquake in the Choshui River alluvial fan in Taiwan. *Bull. Seismol. Soc. Am.* 91 (5), 1062–1068. doi:10.1785/0120000726

Claesson, L., Skelton, A., Graham, C., Dietl, C., Morth, M., Torssander, P., et al. (2004). Hydrogeochemical changes before and after major Earthquake. *Geology* 32 (8), 641–644. doi:10.1130/g20542.1

Craig, H. (1961). Isotopic variations in meteoric waters. *Science* 133 (3465), 1702–1703. doi:10.1126/science.133.3465.1702

Déhais, T., Burnard, P., Pik, R., Caracausi, A., and Zimmermann, L. (2016). "Experimental determination of helium diffusion in automated sampling apparatus (SPARTAH): implications for preservation of individual peaks signal," in Poster session presented at developments in noble gas understanding and expertise, Vandoeuvre-lès-Nancy, France, April 13–15, 2016. Available at: http://helium.crpg.cnrs-nancy.fr/DINGUE-4/home.html.

Etiope, G., and Martinelli, G. (2002). Migration of carrier and trace gases in the geosphere: an overview. *Phys. Earth Planet. Inter.* 129 (3, 4), 185–204. doi:10.1016/s0031-9201(01)00292-8

Fu, C. C., and Lee, L. C. (2018). "Continuous monitoring of fluid and gas geochemistry for seismic study in Taiwan," in *Pre-earthquake processes: a multidisciplinary approach to earthquake prediction studies*. Editors D. Ouzounov, S. Pulinets, K. Hattori, and P. Taylor (Hoboken, NJ: John Wiley and Sons, Inc. Press), 199–218.

Fu, C. C., Yang, T. F., Chen, C. H., Lee, L. C., Wu, Y. M., Liu, T. K., et al. (2017). Spatial and temporal anomalies of soil gas in northern Taiwan and its tectonic and seismic implications. *J. Asian Earth Sci.* 149, 64–77. doi:10.1016/j.jseaes.2017.02.032

Hsu, C., and Wey, S. (1983). Structural geology in the Chiayi foothills, Taiwan. *Pet. Geology. Taiwan* 19, 17–28.

Hung, J. H., Wiltschko, D. V., Lin, H. C., Hickman, J. B., Fang, P., and Bock, Y. (1999). Structure and motion of the southwestern Taiwan fold and thrust belt. *Terr. Atmos. Ocean. Sci.* 10 (3), 543–568. doi:10.3319/tao.1999.10.3.543(t)

Igarashi, G., Saeki, S., Takahata, N., Sumikawa, K., Tasaka, S., Sasaki, Y., et al. (1995). Ground-water radon anomaly before the Kobe earthquake in Japan. *Science* 269 (5220), 60–61. doi:10.1126/science.269.5220.60

Kuo, M. C. T., Fan, K., Kuochen, H., and Chen, W. (2006). A mechanism for anomalous decline in radon precursory to an earthquake. *Ground Water* 44 (5), 642–647. doi:10.1111/j.1745-6584.2006.00219.x

Kuo, T., Su, C., Chang, C., Lin, C., Cheng, W., Liang, H., et al. (2010). Application of recurrent radon precursors for forecasting large earthquakes (Mw > 6.0) near Antung, Taiwan. *Radiat. Meas.* 45 (9), 1049–1054. doi:10.1016/j.radmeas.2010.08.009

Lai, W. C., Hsu, K. C., Shieh, C. L., Lee, Y. P., Chung, K. C., Koizumi, N., et al. (2010). Evaluation of the effects of ground shaking and static volumetric strain change on earthquake-related groundwater level changes in Taiwan. *Earth Planets Space* 62 (4), 391–400. doi:10.5047/eps.2009.12.008

Lin, C. W., Chang, W. C., Lu, S. T., Shih, T. S., and Huang, W. C. (2000). An introduction to the active faults of Taiwan. *Spec. Publ. Cent. Geol. Surv.* 13, 1–122. 2nd edition.(in Chinese).

Lin, C. W., Lu, S. T., Shih, T. S., Liu, Y. C., Lin, W. H., and Lin, Y. H. (2007). Active faults of southwestern Taiwan: explanatory text for the strip maps of active faults scale: 25000, Meishan fault. *Spec. Publ. Cent. Geol. Surv.* 17, 81–94.(in Chinese).

Lis, G., Wassenaar, L. I., and Hendry, M. J. (2008). High-precision laser spectroscopy D/H and 18O/16O measurements of microliter natural water samples. *Anal. Chem.* 80 (1), 287–293. doi:10.1021/ac701716q

Liu, K. K., Yui, T. F., Yeh, Y. H., Tsai, Y. B., and Teng, T. (1985). Variations of radon content in ground waters and possible correlation with seismic activities in northern Taiwan. *Pure Appl. Geophys.* 122 (2–4), 231–244. doi:10.1007/bf00874596

Los Gatos Research Inc. (2008). Liquid-water isotope analyser, automated injection (Accessed August 18, 2008).

Mizota, C., and Kusakabe, M. (1994). Spatial distribution of δD-$\delta^{18}O$ values of surface and shallow groundwaters from Japan, South Korea and East China. *Geochem. J.* 28 (5), 387–410. doi:10.2343/geochemj.28.387

Onda, S., Sano, Y., Takahata, N., Kagoshima, T., Miyajima, T., Shibata, T., et al. (2018). Groundwater oxygen isotope anomaly before the M6.6 Tottori earthquake in Southwest Japan. *Sci. Rep.* 8 (1), 4800. doi:10.1038/s41598-018-23303-8

Ono, T., Mori, T., and Tsunomori, F. (2020). High-frequency field auto-sampling of volcanic waters discharged near craters of active volcanoes. *Bull. Volcanol.* 82 (2), 16. doi:10.1007/s00445-020-1357-y

Orihara, Y., Kamogawa, M., and Nagao, T. (2014). Preseismic changes of the level and temperature of confined groundwater related to the 2011 Tohoku Earthquake. *Sci. Rep.* 4 (1), 6907. doi:10.1038/srep06907

O'Neil, J. R., and King, C. Y (1981). Variations in stable-isotope ratios of ground waters in seismically active regions of California. *Geophys. Res. Lett.* 8 (5), 429–432. doi:10.1029/gl008i005p00429

Peng, T. R., Wang, C. H., Huang, C. C., Fei, L. Y., Chen, C. T. A., and Hwong, J. L. (2010). Stable isotopic characteristic of Taiwan's precipitation: a case study of western Pacific monsoon region. *Earth Planet. Sci. Lett.* 289 (3, 4), 357–366. doi:10.1016/j.epsl.2009.11.024

Poreda, R., and Craig, H. (1989). Helium isotope ratios in Circum-Pacific volcanic arcs. *Nature* 338 (6215), 473–478. doi:10.1038/338473a0

Reddy, D., Nagabhushanam, P., and Sukhija, B. S. (2011). Earthquake (M5.1) induced hydrogeochemical and $\delta^{18}O$ changes: validation of aquifer breaching-Mixing model in Koyna, India. *Geophys. J. Int.* 184 (1), 359–370. doi:10.1111/j.1365-246X.2010.04838.x

Roeloff, E. (1988). Hydrologic precursors to earthquakes: a review. *Pure Appl. Geophys. PAGEOPH* 126 (2-4), 177–209. doi:10.1007/bf00878996

Sadovsky, M. A., Nersesov, I. L., Nigmatullaev, S. K., Latynina, L. A., Lukk, A. A., Semenov, A. N., et al. (1972). The processes preceding strong earthquakes in some regions of Middle Asia. *Tectonophysics* 14 (3, 4), 295–307. doi:10.1016/0040-1951(72)90078-9

Sano, Y., Takahata, N., Igarishi, G., Koizumi, N., and Sturchio, N. C. (1998). Helium degassing related to the Kobe earthquake. *Chem. Geol.* 150 (1, 2), 171–179. doi:10.1016/S0009-2541(98)00055-2

Sano, Y., Takahata, N., Kagoshima, T., Shibata, T., Onoue, T., and Zhao, D. (2016). Groundwater helium anomaly reflects strain change during the 2016 Kumamoto earthquake in southwest Japan. *Sci. Rep.* 6 (1), 37939. doi:10.1038/srep37939

Sano, Y., Kinoshita, N., Kagoshima, T., Takahata, N., Sakata, S., Toki, T., et al. (2017). Origin of methane-rich natural gas at the West Pacific convergent plate boundary. *Sci. Rep.* 7 (1), 15646. doi:10.1038/s41598-017-15959-5

Sano, Y., Onda, S., Kagoshima, T., Miyajima, T., Takahata, N., Shibata, T., et al. (2020). Groundwater oxygen anomaly related to the 2016 Kumamoto earthquake in Southwest Japan. *Proc. Jpn. Acad. Ser. B Phys. Biol. Sci.* 96 (7), 322–334. doi:10.2183/pjab.96.024

Sano, Y., and Wakita, H. (1985). Geographical distribution of $^3He/^4He$ ratios in Japan: implications for arc tectonics and incipient magmatism. *J. Geophys. Res.* 90 (B10), 8729–8741. doi:10.1029/jb090ib10p08729

Shih, R. C., Chen, P. H., Lu, M. T., and Chen, W. S. (2003). Earthquake geology investigation and the construction of the active faults database. *Geophys. Invest. Projects Active Faults. Ann. Rep., Cent. Geol. Surv., Ministry Econ. Aff. Taipei, Taiwan*, 218, (in Chinese).

Skelton, A., Andren, M., Kristmannsdottir, H., Stockmann, G., Morth, C. M., Sveinbjornsdottir, A., et al. (2014). Changes in groundwater chemistry before two consecutive earthquakes in Iceland. *Nat. Geosci.* 7 (10), 752–756. doi:10.1038/ngeo2250

Song, S. R., Ku, W. Y., Chen, Y. L., Lin, Y. C., Liu, C. M., Kuo, L. W., et al. (2003). Groundwater chemical anomaly before and after the Chi-Chi earthquake in Taiwan. *Terr. Atmos. Oceanic Sci.* 14 (3), 311–320. doi:10.3319/tao.2003.14.3.311(t)

Song, S. R., Chen, Y. L., Liu, C. M., Ku, W. Y., Chen, H. F., Liu, Y. J., et al. (2005). Hydrochemical changes in spring waters in Taiwan: implications for evaluating sites for earthquake precursory monitoring. *Terr. Atmos. Ocean. Sci.* 16 (4), 745–762. doi:10.3319/tao.2005.16.4.745(gig)

Song, S. R., Ku, W. Y., Chen, Y. L., Liu, C. M., Chan, P. S., Chen, Y. G., et al. (2006). Hydrogeochemical anomalies in the springs of the Chiayi area in west-central Taiwan as likely precursors to earthquakes. *Pure Appl. Geophys.* 163, 675–691. doi:10.1007/s00024-006-0046-x

Sugisaki, R., and Sugiura, T. (1985). Geochemical indicator of tectonic stress resulting in an earthquake in central Japan, 1984. *Science* 229 (4719), 1261–1262. doi:10.1126/science.229.4719.1261

Sugisaki, R. (1978). Changing He/Ar and N_2/Ar ratios of fault air may be earthquake precursors. *Nature* 275 (5677), 209–211. doi:10.1038/275209a0

Sun, C. H., Chang, S. C., Kuo, C. L., Wu, J. C., Shao, P. H., and Oung, J. N. (2010). Origins of Taiwan's mud volcanoes: evidence from geochemistry. *J. Asian Earth Sci.* 37 (2), 105–116. doi:10.1016/j.jseaes.2009.02.007

Tryon, M., Brown, K., Dorman, L. R., and Sauter, A. (2001). A new benthic aqueous flux meter for very low to moderate discharge rates. *Deep Sea Res. Part I Oceanogr. Res. Pap.* 48 (9), 2121–2146. doi:10.1016/S0967-0637(01)00002-4

Wakita, H., Nakamura, Y., Notsu, K., Noguchi, M., and Asada, T. (1980). Radon anomaly: a possible precursor of the 1978 izu-oshima-kinkai earthquake. *Science* 207 (4433), 882–883. doi:10.1126/science.207.4433.882

Wang, C. H., Kuo, C. H., Peng, T. R., Chen, W. F., Liu, T. K., Chiang, C. J., et al. (2001). Isotope characteristics of Taiwan groundwaters. *West. Pac. Earth Sci.* 1 (4), 415–428.

Wang, C. Y., Cheng, I. H., Chin, C. V., and Yu, S. B. (2001). Coseismic hydrologic response of an alluvial fan to the 1999 Chi-Chi earthquake, Taiwan. *Geology* 29 (9), 831–834. doi:10.1130/0091-7613(2001)029<0831:CHROAA>2.0.CO;2

Weinlich, F. H. (2014). Carbon dioxide controlled earthquake distribution pattern in the NW Bohemian swarm earthquake region, western Eger Rift, Czech Republic-Gas migration in the crystalline basement. *Geofluids* 14 (2), 143–159. doi:10.1111/gfl.12058

Weiss, R. F. (1971). Solubility of helium and neon in water and seawater. *J. Chem. Eng. Data* 16 (2), 235–241. doi:10.1021/je60049a019

Yang, T. F., Chou, C. Y., Chen, C. H., Chyi, L. L., and Jiang, J. H. (2003). Exhalation of radon and its carrier gases in SW Taiwan. *Radiat. Meas.* 36 (1–6), 425–429. doi:10.1016/s1350-4487(03)00164-1

Yang, T. F., Yeh, G. H., Fu, C. C., Wang, C. C., Lan, T. F., Lee, H. F., et al. (2004). Composition and exhalation flux of gases from mud volcanoes in Taiwan. *Environ. Geol.* 46 (8), 1003–1011. doi:10.1007/s00254-004-1086-0

Yang, T. F., Walia, V., Chyi, L. L., Fu, C. C., Chen, C. H., Liu, T. K., et al. (2005). Variations of soil radon and thoron concentrations in a fault zone and prospective earthquakes in SW Taiwan. *Radiat. Meas.* 40 (2–6), 496–502. doi:10.1016/j.radmeas.2005.05.017

Yang, T. F., Fu, C. C., Walia, V., Chen, C. H., Chyi, L. L., Liu, T. K., et al. (2006). Seismo-geochemical variations in SW Taiwan: multi-parameter automatic gas monitoring results. *Pure Appl. Geophys.* 163 (4), 693–709. doi:10.1007/s00024-006-0040-3

Yang, T. F. (2008). Recent progress in the application of gas geochemistry: examples from Taiwan and the 9th international gas geochemistry conference. *Geofluids* 8 (4), 219–229. doi:10.1111/j.1468-8123.2008.00232.x

Yu, S. B., Chen, H. Y., and Kuo, L. C. (1997). Velocity field of GPS stations in the Taiwan area. *Tectonophysics* 274 (1-3), 41–59. doi:10.1016/s0040-1951(96)00297-1

Yu, S. B., and Chen, H. Y. (1998). Strain accumulation in southwestern Taiwan. *Terr. Atmos. Ocean. Sci.* 9 (1), 31–50. doi:10.3319/TAO.1998.9.1.31

Conflict of Interest: The authors declare that the research was conducted in the absence of any commercial or financial relationships that could be construed as a potential conflict of interest.

Copyright © 2021 Fu, Lai, Yang, Hilton, Chen, Walia, Kumar and Lee. This is an open-access article distributed under the terms of the Creative Commons Attribution License (CC BY). The use, distribution or reproduction in other forums is permitted, provided the original author(s) and the copyright owner(s) are credited and that the original publication in this journal is cited, in accordance with accepted academic practice. No use, distribution or reproduction is permitted which does not comply with these terms.

frontiers in Earth Science

ORIGINAL RESEARCH
published: 01 March 2021
doi: 10.3389/feart.2021.626111

Catalytic Hydrogenation of Post-Mature Hydrocarbon Source Rocks Under Deep-Derived Fluids: An Example of Early Cambrian Yurtus Formation, Tarim Basin, NW China

Huang Xiaowei[1,2], *Jin Zhijun*[2,3,4]*, *Liu Quanyou*[2,3]*, *Meng Qingqiang*[2,3], *Zhu Dongya*[2,3], *Liu Jiayi*[2,3] and *Liu Jinzhong*[5]

[1]School of Energy Resources, China University of Geosciences, Beijing, China, [2]State Key Laboratory of Shale Oil and Gas Enrichment Mechanisms and Effective Development, SINOPEC, Beijing, China, [3]Research Institute of Petroleum Exploration and Production, SINOPEC, Beijing, China, [4]Institute of Energy, Peking University, Beijing, China, [5]State Key Laboratory of Organic Geochemistry, Guangzhou Institute of Geochemistry, Chinese Academy of Sciences, Guangzhou, China

OPEN ACCESS

Edited by:
Guodong Zheng,
Chinese Academy of Sciences, China

Reviewed by:
Алексей Вахин,
Kazan Federal University, Russia
Mohamed El Nady,
Egyptian Petroleum Research Institute, Egypt

***Correspondence:**
Jin Zhijun
jinzj.syky@sinopec.com
Liu Quanyou
liuqy.syky@sinopec.com

Specialty section:
This article was submitted to Geochemistry, a section of the journal Frontiers in Earth Science

Received: 04 November 2020
Accepted: 06 January 2021
Published: 01 March 2021

Citation:
Xiaowei H, Zhijun J, Quanyou L, Qingqiang M, Dongya Z, Jiayi L and Jinzhong L (2021) Catalytic Hydrogenation of Post-Mature Hydrocarbon Source Rocks Under Deep-Derived Fluids: An Example of Early Cambrian Yurtus Formation, Tarim Basin, NW China. Front. Earth Sci. 9:626111. doi: 10.3389/feart.2021.626111

As a link between the internal and external basin, the deep derived fluids play a key role during the processes of hydrocarbon (HC) formation and accumulation in the form of organic-inorganic interaction. Two questions remain to be answered: How do deep-derived fluids affect HC generation in source rocks by carrying a large amount of matter and energy, especially in post-mature source rocks with weak HC generation capability? Can hydrogen and catalysts from deep sources significantly increase the HC generation potential of the source rock? In this study, we selected the post-mature kerogen samples of the early Cambrian Yurtus Formation in the Tarim Basin of China. Under the catalytic environment of $ZnCl_2$ and MoS_2, closed system gold tube thermal simulation experiments were conducted to quantitatively verify the contribution of catalytic hydrogenation to "HC promotion" by adding H_2. The catalytic hydrogenation increased the kerogen HC generation capacity by 1.4–2.1 times. The catalytic hydrogenation intensity reaction increased with temperature. The drying coefficient of the generated gas decreased significantly as the increasing yield of heavy HC gas. In the simulation experiment, alkane $\delta^{13}C$ becomes lighter after the catalytic hydrogenation experiment, while $\delta^{13}C_{CO2}$ becomes heavier. In the process of catalytic hydrogenation, the number of gaseous products catalyzed by $ZnCl_2$ is higher than that catalyzed by MoS_2 under the same conditions, indicating that $ZnCl_2$ is a better catalyst for the generation of gaseous yield. Meanwhile, Fischer-Tropsch synthesis (FFT) reaction was happened in the catalytic hydrogenation process. The simulation experiment demonstrates that hydrogen-rich components and metal elements in deep-derived fluids have significant catalytic hydrogenation effects on organic-rich matter, which improved the HC generation efficiency of post-mature source rocks.

Keywords: yurtus formation, simulation experiment, catalytic hydrogenation, gaseous yield, isotope fractionation

INTRODUCTION

The deep-derived fluids refer to the mantle source volatile fluid below the basement of the sedimentary basin, which is originated from the dehydrating fluid generated in the process of plate subduction or deep metamorphism, and the deep circulating fluid driven by the heat from the mantle or the deep shell source (Jin et al., 2002; Jin et al., 2004; Jin et al., 2007; Liu et al., 2018). A large amount of gas components carried by the deep-derived fluids contain volatile materials, such as H_2, CH_4, H_2S, CO_2, N_2, and He. As one of the main volatile fluids, the distribution of geologic H_2 (molecular hydrogen) is widespread in ocean ridges, active tectonic belts, and the Precambrian or Cenozoic strata distributed on land (Jeffrey and Kaplan, 1998; Allen and Seyfried, 2004; Newell et al., 2007; Tivey, 2007; Bradley and Summons, 2010; Sherwood-Lollar et al., 2014; Meng et al., 2015; Etiope, 2017; Guélard et al., 2017; Etiope and Whiticar, 2019; Bougault et al., 2019; Klein et al., 2019; Klein et al., 2020). H_2 has a variety of genetic types, including the release of deep magma degassing, the serpentinization of ultrabasic-basic rocks (Sherwood-Lollar et al., 2014; Etiope, 2017; Klein et al., 2019; Klein et al., 2020), radiolysis of water due to the presence of radioactive minerals (Sherwood-Lollar et al., 2014; Milesi et al., 2016), mechanical cracking of Si-bearing rock (Hirose et al., 2011; Telling et al., 2015), and the reduction of organic matter by microorganisms (Shuai, et al., 2010). The deep-derived fluids not only carry energy and hydrogen-rich matter, but a large amount of metal catalysts and other elements such as Mg, Fe, Mn, Ni, Zn, Mo, and Cu (Coveney, 1987; Pinto et al., 1999; Tivey, 2007; Proskurowski et al., 2008; Resing et al., 2015). Meanwhile, in sedimentary basins the enrichment of organic matter is normally accompanied by abundant metal elements (e.g., Fe, Mn, Zn, and Mo) (Lv et al., 2018).

The geological kerogen catalytic hydrogenation reaction is a reduction reaction that generates new products and is accompanied by energy conversion. To study the contribution of material conditions in organic-inorganic interactions to hydrocarbon (HC) generation from organic matter, previous studies examined different external hydrogen sources and catalysts (Hawkes, 1972; Jin et al., 2002; Jin et al, 2004). As the energy of the H-H bond is theoretically 436 kJ mol^{-1}, which is less than the H-OH bond energy of 497 kJ mol^{-1} (Luo, 2004), H_2 is easier to hydrogenate organic matter than H_2O under simulated experimental conditions (Jin et al., 2004). Lewan et al. (1979), Lewan, (1997)and Seewald (2003) confirmed that the contribution of exogenous H plays a key role in HC generation and distribution of underground HC components. Mango et al. (1996, 1997) showed in an open system that the reaction of exogenous hydrogen with organic matter promotes the rate of HC generation under the action of transition metals. Meng et al. (2015) confirmed that deep hydrogen-rich fluids can activate and increase the HC regeneration of ancient source rocks through experiments. Liu et al. (2016) showed that there is Fischer-Tropsch-type (FTT) interaction between H_2 and CO_2 produced by the thermal alteration of source rocks in the geological environment to synthesize HCs.

These deep-derived fluids can hydrogenate post-mature kerogen, thereby activating kerogen's ability to regenerate HCs, by activating the original inert carbon in kerogen and generating HCs (Meng et al., 2015). The post-mature kerogen is rich in polycyclic aromatic HC compounds and polymer groups and has a low H/C ratio. H is a hydrocarbon-generating restrictive reactant for high-maturity kerogen. The hydrocracking reaction can hydro-isomerize and crack (including ring-opening) aromatic compounds and macromolecular groups, i.e., break long-chain alkanes into short-chain alkanes, so that aromatic or naphthenic HCs can be opened to form long-chain alkanes. The hydrocracking reaction can further break the chain (Han, 2001) to promote the reactivation of kerogen to generate HCs (Liu et al., 2018; Liu et al., 2019). In order to simulate the geological regularities of catalytic hydrogenation more accurately in a more consistent environment with deep-derived fluids, on the basis of previous studies, we further optimized the hydrogen quantification in the simulation experiment. The main objectives of this work are to examine the potential of HC generation in high-maturity marine I-type kerogen in the quantitative hydrogenation process, which involves different catalysts under closed system conditions. Meanwhile, it provided to understand the characteristics of HC isotope fractionation of alkane gas under the influence of deep-derived fluids; and to provide theoretical support for the evaluation of organic HC generation.

EXPERIMENTAL SAMPLES AND METHODS

Experimental Samples

In this study, kerogen was selected from the argillaceous source rocks of the early Cambrian Yurtus Formation in the Dongergou section of the Tarim Basin. Kerogen (Ker) was type I with the vitrinite reflectance (Ro) of 1.91%. The experimental samples were approximately 200 meshes. Total organic carbon (TOC) content of kerogen is 64.0% with purification, atomic ratio H/C = 0.87, T_{max} = 530°C, pyrolysis parameter S_1 = 1.43 mg HC/g ker, S_2 = 10.95 mg HC/g ker, S_3 = 16.17 mg CO_2/g ker, hydrocarbon index (HI) = 18, oxygen index (OI) = 28. The catalysts used in this study, $ZnCl_2$ and MoS_2, had a particle size of 200 mesh and met the experimental analytical purity requirements. Deionized water was prepared in the laboratory, and H_2 was high-purity hydrogen gas containing 5% internal standard helium (He).

Experimental Method

The simulation experiment was conducted in the State Key Laboratory of Organic Geochemistry, Guangzhou Institute of Geochemistry, Chinese Academy of Sciences in a closed system composed of gold tubes. During the sample loading process, the loading method of solid-liquid samples described in detail by Liu and Tang (1998) was used. In short, we added the weighed kerogen powder, deionized water, and catalyst powder (10:10: 1, wt: wt: wt) into a gold tube (6 mm inner diameter and 70 mm length), which was welded and sealed for cleaning, placed the tube in an argon atmosphere for 25 min to replace the air in the tube, pinched the wall of the gold tube with manual pliers, and sealed the top port with argon arc welding to complete the loading steps. For the hydrogenation sample loading, we made sure precise

quantitative volume H_2 injected into a larger gold tube. The tube (10 mm inner diameter, 120 mm long) was used. The pre-solid and liquid reactant injection method was the same as above: when quantitatively injecting H_2 (containing 5% He as the internal standard gas), temperature control was carried out under room temperature (25°C) with two high-sensitivity pressure gauges connected in series to ensure the amount of H_2 injection using the principle of hydrogen gas replacement to effectively eliminate air interference. The mass of the reactants added to the tube was 40 mg kerogen powder, 40 mg deionized water, 4 mg catalyst powder, and 0.65 mg H_2. Then we pressed the top port of the gold tube with a pressure clamp to seal the hydrogen component inside the gold tube and flattened the port with the pressure clamp after the wall of the gold tube was welded by argon arc welding. Next, the gold tube was placed in hot water (>60°C) without bead-shaped bubbles overflowing to ensure gas tightness in the tube.

After the sample loading of gold tubes was completed, the tubes were placed in the high-temperature reaction kettle set for heating. The temperature was first raised in 2 h to reach each predetermined temperature point, and then constant heating was performed for 72 h. There were five groups of experimental samples with each set at six temperature points, 350°C, 375°C, 400°C, 450°C, 500°C, and 550°C. Group I is kerogen + deionized water, group II is kerogen + deionized water + $ZnCl_2$, group III is kerogen + deionized water + MoS_2, group IV is kerogen + deionized water + $ZnCl_2$+H_2, group V is kerogen + deionized water + MoS_2+H_2. The simulated experimental pressure was constant at 500 bar, and the abnormal pressure change in the kettle did not exceed 1 bar.

Experimental Analysis

Following the research method of Pan et al. (2006) and Jia et al. (2014), the gold tube was removed and carefully placed into a custom-made vacuum glass tube. The vacuum tube was connected to an Agilent 6890 N full-component gas chromatograph (GC), which was modified by Wasson ECE Instrumentation for determination of gas molecular composition. The GC contains three detection channels, one flame ionization detector (FID), and two thermal conductivity detectors (TCD). N_2 was the carrier gases for the organic detection channel (FID) and inorganic channel (TCD1), and He was the carrier gas for hydrogen and helium detection channel (TCD2). The detection column was a Paraplot Q-type capillary column. The vacuum environment of the system was maintained by connecting a vacuum pump in the glass tube and piercing the gold tube inside to release the gas component. There are two valves connected in series to the vacuum tube and the chromatograph, which are used to measure the pressure change of the gas component and release part of the gas into the chromatograph to measure its molecular composition. We determined the type and composition of the gas products through different detection response values and corresponding time points. The method used the peak areas of different detection values of FID and TCD to complete the quantification of different gaseous products generated by the peak area ratio of the known quantitative standard gas (Liu and Tang, 1998).

After the GC detection analysis, a gas-tight syringe was used to extract a small amount of gas was extracted from the vacuum tube using a compact gas sampling needle for the carbon and hydrogen isotope analysis. The ratios of carbon and hydrogen isotopes refer to the Vienna Peedee belemnite standard (VPDB). The carbon isotope ratio detection and analysis were performed using a GV Isoprime IRMS interfaced with an Agilent 6890 N-Isoprime 100 instrument. The detection value of each sample was measured two to three times. If there was no obvious difference between the previous two detection values, the average value was taken as the same position value of the sample. If the difference between the first two test values was large, the third test was required, and the average value of the two adjacent values in three tests was taken as the final sample isotope composition. The carbon isotope analysis accuracy of this equipment was within ±0.4‰. Hydrogen isotope ratio detection was performed using the Thermo Trace GC 1310-Delta V Advantage instrument. The detection method was consistent with the carbon isotope analysis, and the hydrogen isotope accuracy was within ±3‰. During the detection process, the pre-determined $\delta^{13}C$ value calibration gases were periodically analyzed to check the accuracy of the measured value.

RESULTS

Total Gas Yield

The total gas yield of different simulated experimental samples showed an upward trend with increasing temperature (**Table 1**). The total gas yield of group I was measured at the initial temperature of 350°C at 56.6 m^3/t Ker, and the yield increased substantially after 400°C. At the highest temperature of 550°C, the yield reached a maximum value of 241.8 m^3/t Ker. After the catalysts $ZnCl_2$ and MoS_2 were added to groups II and III, the total gas yield increased from the lowest values of 70.0 m^3/t Ker (350°C) and 70.5 m^3/t Ker (350°C), respectively, and began to increase significantly at 400°C. The maximum yields were 513.4 m^3/t Ker and 347.5 m^3/t Ker, which were 2.1 to 1.4 times the maximum value in group I, respectively. The addition of $ZnCl_2$ and MoS_2 significantly promoted the reaction, and the yield increased more by the addition of $ZnCl_2$ than MoS_2, and the gas increase was mainly from CH_4 and CO_2. In groups IV and V, the total gas yields (without accounting for H_2 yield) were 55.7 m^3/t Ker (350°C) and 29.2 m^3/t Ker (350°C), respectively, and then the yield increased greatly at 375°C. The maximum yields were 506.5 m^3/t Ker and 368.4 m^3/t Ker at 550°C, respectively. Compared with groups II and III, the groups IV and V showed little change in the total yield. With the addition of H_2 reaction resulted in the alkane yield increased, but the CO_2 yield decreased, resulting in an insignificant change in the total gas yield overall.

Product Components

In terms of the total yield distribution of gaseous HCs, the $\sum C_{1\text{-}5}$ yield of group I increased continuously with temperature, and the maximum yield was 99.49 m^3/t Ker. After the catalysts $ZnCl_2$ and MoS_2 were added to groups II and III, the maximum yields of $\sum C_{1\text{-}5}$ were 208.22 m^3/t Ker and 137.77 m^3/t Ker, which were

TABLE 1 | Types and concentrations (m^3/t Ker) of gas generated during the catalytic pyrolysis experiments at 350°C/72 h, 375°C/72 h, 400°C/72 h, 450°C/72 h, 500°C/72 h, and 550°C/72 h.

Group	Temp (°C)	CO_2	CH_4	C_2H_6	C_3H_8	iC_4	nC_4	iC_5	nC_5	H_2
		Yield (m^3/t ker)								
I	350	55.57	0.95	0.11	0.00	0.00	0.00	0.00	0.00	0.00
	375	57.97	2.78	0.21	0.00	0.00	0.00	0.00	0.00	0.00
	400	67.72	12.57	0.51	0.00	0.00	0.00	0.00	0.00	0.00
	450	76.45	29.20	0.67	0.00	0.00	0.00	0.00	0.00	0.00
	500	98.08	52.99	0.72	0.02	0.01	0.03	0.02	0.04	0.01
	550	142.25	98.55	0.80	0.07	0.05	0.03	0.00	0.00	0.02
II	350	69.00	0.83	0.10	0.01	0.00	0.00	0.00	0.00	0.03
	375	77.68	4.46	0.34	0.01	0.00	0.00	0.00	0.00	0.16
	400	80.58	12.11	0.68	0.02	0.00	0.00	0.00	0.00	0.45
	450	108.17	44.09	0.93	0.00	0.00	0.00	0.00	0.00	2.57
	500	160.11	99.93	1.16	0.03	0.00	0.00	0.00	0.00	9.03
	550	280.91	207.56	0.65	0.01	0.00	0.00	0.00	0.00	24.27
III	350	69.47	0.86	0.11	0.01	0.00	0.00	0.00	0.00	0.00
	375	79.05	4.23	0.29	0.01	0.00	0.00	0.00	0.00	0.00
	400	80.06	10.08	0.49	0.01	0.00	0.00	0.00	0.00	0.02
	450	91.92	38.31	0.61	0.01	0.00	0.00	0.00	0.00	0.84
	500	126.29	69.88	0.64	0.01	0.00	0.00	0.00	0.00	4.61
	550	192.35	136.89	0.85	0.01	0.00	0.00	0.00	0.00	17.43
IV	350	35.70	11.07	3.20	2.97	0.39	1.62	0.52	0.23	-
	375	38.64	18.09	5.35	5.09	0.73	2.94	0.85	0.38	-
	400	39.60	41.31	14.44	16.91	2.44	7.90	1.79	0.79	-
	450	41.01	117.10	42.49	34.35	4.77	4.57	0.54	0.09	-
	500	54.54	225.51	64.76	0.94	0.02	0.05	0.01	0.00	-
	550	109.11	369.82	5.06	0.04	0.19	0.21	0.00	0.00	-
V	350	15.66	10.55	1.53	0.82	0.08	0.41	0.11	0.08	-
	375	20.92	14.33	3.77	3.45	0.35	1.90	0.50	0.57	-
	400	27.75	31.86	10.57	11.81	1.30	5.99	1.28	0.98	-
	450	29.79	87.35	30.90	21.84	2.19	2.10	0.10	0.13	-
	500	41.24	164.67	42.59	0.44	0.01	0.03	0.01	0.08	-
	550	76.06	283.63	8.61	0.04	0.00	0.00	0.00	0.03	-

increased 2.1 and 1.4 times as much as group I, respectively. It proved that the addition of $ZnCl_2$ and MoS_2 significantly promoted the generation of the gas components. In groups IV and V, the maximum yields of $\sum C_{1-5}$ were 375.34 m^3/t Ker and 292.32 m^3/t Ker, representing 1.8 and 2.1 times increase compared to groups II and III. The catalytic hydrogenation.

The methane (C_1) yield increased with temperature and reached the maximum at 550°C. The maximum C_1 yield in group I was 98.55 m^3/t Ker. When the catalysts $ZnCl_2$ and MoS_2 were added to groups II and III, the maximum yields of C_1 were 207.56 m^3/t Ker and 136.89 m^3/t Ker, which were 2.0 and 1.4 times as much as the yield of group I, respectively. In groups IV and V, the maximum yields of C_1 were 369.82 m^3/t Ker and 283.63 m^3/t Ker, respectively, which were 1.8 and 2.1 times the yields of groups II and III (**Figure 1**).

The change in the ethane (C_2) yield of group I with temperature was very small, and the maximum C_2 yield was 0.8 m^3/t Ker (500°C). After the catalysts $ZnCl_2$ and MoS_2 were added to groups II and III, the maximum C_2 yields were 1.16 m^3/t Ker and 0.85 m^3/t Ker, respectively. The addition of $ZnCl_2$ and MoS_2 did not increase the C_2 yield significantly. In groups IV and V, the maximum yields of C_2 were 64.76 m^3/t Ker and 42.59 m^3/t Ker (both 500°C), which were 80 and 50 times those of groups II and III without H_2, respectively. Exogenous H_2 reacts more easily than H_2O to promote the generation of C_2 (**Figure 2**).

The change in the propane (C_3) yield of group I with temperature was close to 0.0 m^3/t Ker. After adding the catalysts $ZnCl_2$ and MoS_2 to groups II and III, the change in the C_3 yield was still 0.0 m^3/t Ker, indicating that the addition of metal salts did not significantly increase the C_3 yield. In groups IV and V, the maximum yields of C_3 were 34.4 m^3/t Ker and 21.8 m^3/t Ker (450°C), respectively; the addition of external H_2 and catalysts exceedingly improved the C_3 yield (**Figure 3**). The comparison of the results of C_1, C_2, and C_3 shows that the addition of exogenous H_2 increases the HC generation yield, and the peak temperature of HC generation decreases sequentially with the increasing carbon number.

The catalytic addition of the H cracking reaction had a significant effect on the drying coefficient of natural gas ($C_1/\sum C_{1-5}$) (**Table 1**). The $C_1/\sum C_{1-5}$ ratio of group I (kerogen + deionized water) increased with temperature, from a minimum of 0.90 (350°C) to 0.99 (550°C). When the catalysts $ZnCl_2$ and MoS_2 were added to groups II and III, the $C_1/\sum C_{1-5}$ ratio became larger with increasing temperature at the ratios of 0.89–1.00 and 0.87–0.99, respectively. The addition of $ZnCl_2$ and MoS_2 promoted the formation of C_{2+} HCs at relatively low temperatures (≤400°C). After adding H_2 and catalysts $ZnCl_2$ and MoS_2, the addition of exogenous H_2 greatly increased the heavy HC (C_{2+}) components, and the $C_1/\sum C_{1-5}$ ratios at 350°C were 0.55 and 0.78, respectively. The $C_1/\sum C_{1-5}$ ratio gradually decreased with the increasing temperature and dropped to the lowest point at 0.48 and 0.50, respectively, at 400°C. After 400°C, C_1 produced by the hydrocracking of kerogen continued to increase, as well as C_{2+} HCs in the product. The conversion to C_1 significantly increased the C_1 yield, and the natural gas drying coefficient reached the maximum values of 0.99 and 0.97 at 550°C.

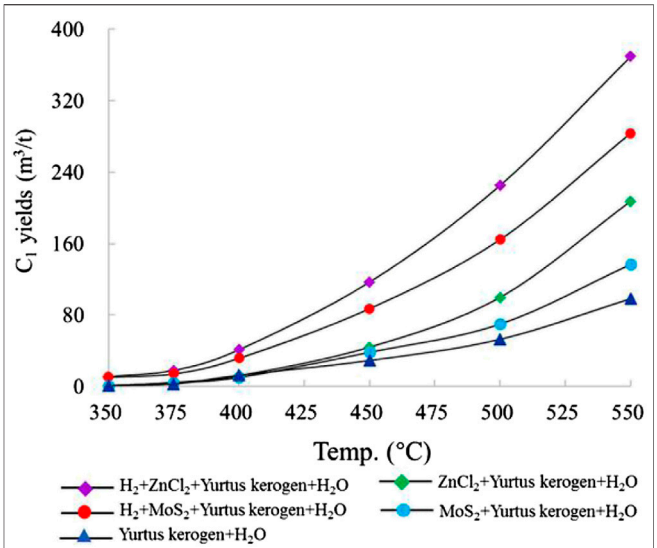


FIGURE 1 | Characteristics of C_1 yield simulated under different catalytic hydrogenation control conditions of the closed system.

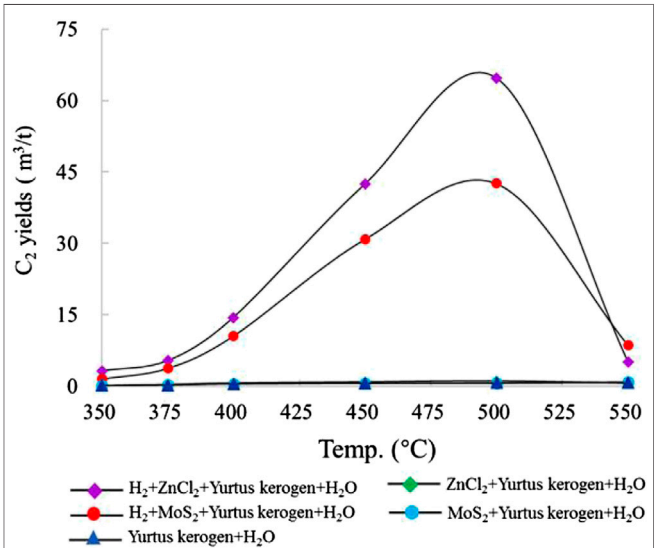


FIGURE 2 | Change in C_2 yield simulated under different catalytic hydrogenation control conditions of the closed system.

The CO_2 yield in each group of experiments increased with increasing temperature and reached the maximum value at 550°C. The CO_2 yield of group I gradually increased with increasing temperature, and the maximum CO_2 yield was 142.25 m^3/t Ker. In groups II and III, with the addition of catalysts $ZnCl_2$ and MoS_2, the maximum yields of CO_2 were 280.91 m^3/t Ker and 192.35 m^3/t Ker, respectively, which are 2.0 and 1.4 times the maximum yield without the addition of the catalysts. The increase in CO_2 and HC components was similar, indicating that the metal ions mainly catalyze the lysis of kerogen itself rather than decomposing the bond between H and O. The CO_2 yields in

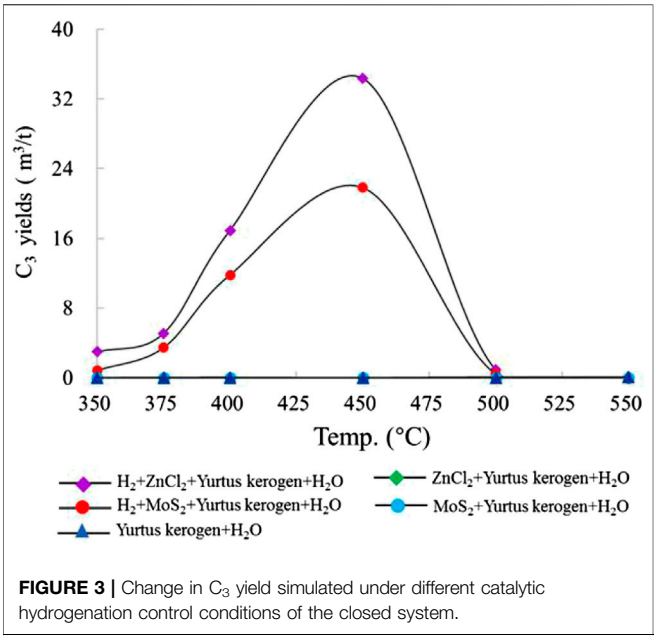


FIGURE 3 | Change in C_3 yield simulated under different catalytic hydrogenation control conditions of the closed system.

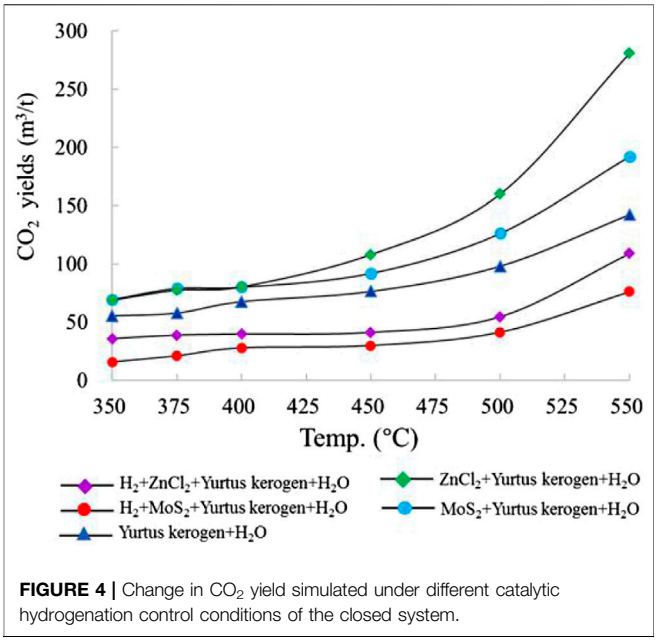


FIGURE 4 | Change in CO_2 yield simulated under different catalytic hydrogenation control conditions of the closed system.

groups IV and V were 0.39–0.40 times those of groups II and III, respectively (**Figure 4**). The significant decrease in the yield of CO_2 resulted from the reaction that occurred with the addition of H_2.

The experimental comparison of groups I, II, and III showed that the H_2 yield did not increase significantly with temperature (the highest is 0.02 m^3/t Ker at 550°C in group I), but the maximum yields after adding $ZnCl_2$ and MoS_2 were 24.27 m^3/t Ker and 17.43 m^3/t Ker at 550°C. The yield increased by one to two orders of magnitude, indicating that the H_2 production was significantly promoted by the addition of catalysts, combined with the C_2 yield. The dominant reason of the H increase is the cracking of organic matter.

Product Component Carbon Isotope Changes

The results show that $\delta^{13}C$ becomes heavier with increasing temperature. Since kerogen of the Yurtus Formation is at a high maturity stage, only C_1, C_2, and CO_2 isotope values can be effectively detected in product components. For the $\delta^{13}C$ value of gaseous HCs under different control conditions at the same temperature point, the $\delta^{13}C$ value of each gaseous HCs increased with the intensity of reaction between catalysis and hydrogen addition (**Table 2**). The $\delta^{13}C_1$ value of group I increased continuously with the increase in temperature from −39.8 to −34.9‰. When $ZnCl_2$ and MoS_2 were added to groups II and III, the $\delta^{13}C_1$ values changed from −44.7 to −36.7‰ and from −43.6 to −36.2‰. In groups IV and V, the $\delta^{13}C_1$ values changed from −45.9 to −40.2‰ and from −52.4 to −43.4‰, showing an increase before the 400°C stage, then a decrease in the 400–450°C interval, and finally becoming heavier with increasing temperature. For the C_1 yield after 400°C, catalytic hydrocracking plays a major role in promoting the disproportionation of small low-carbon molecules. Since the bond energy of ^{12}C–^{12}C is less than the bond energy of ^{12}C–^{13}C, the $\delta^{13}C_1$ fractionation follows; as the intensity of catalytic hydrogenation increases, $\delta^{13}C_1$ becomes lighter (**Figure 5**).

The $\delta^{13}C_2$ value increased sequentially with the increasing temperature. In group I, the value of $\delta^{13}C_2$ changed from −28.2 to −24.4‰ at 350–400°C. After 400°C, the $\delta^{13}C_2$ value only changed from −24.4 to −23.6‰. In groups II and III with catalysts $ZnCl_2$ and MoS_2, the $\delta^{13}C_2$ value was generally stable, similar to group I, changing from −29.9 to −24.0‰ and from −29.1 to −23.7‰, respectively. The addition of $ZnCl_2$ and MoS_2 promoted the reaction and the exchange of C elements to a lesser extent. The $\delta^{13}C_2$ value changed in groups IV and V from −38.4 to −14.1‰ and from −37.6 to −12.1‰, indicating that catalytic hydrogenation significantly increases the formation of C_2 and the exchange of C elements. At 550°C, the $\delta^{13}C_2$ value was the largest because the addition of H_2 promoted the catalytic cracking reaction. When the temperature exceeded the gas generation window (<500°C), a large amount of C_2 cracked to form C_1, resulting in an abnormally large $\delta^{13}C_2$ value (**Figure 6**).

As one of the main reaction products, the CO_2 isotope fractionation value is mainly controlled by its own molecular quality. The comparison of the experimental results between the hydrogenated and unhydrogenated groups showed that the $\delta^{13}C_{CO2}$ value in the hydrogenated group was larger than the unhydrogenated group, which is negatively correlated with the change in the fractional distillation of the $\delta^{13}C$ value of alkanes. The $\delta^{13}C_{CO2}$ value of CO_2 generated by hydrocracking was relatively stable. The $\delta^{13}C_{CO2}$ values of groups I, II, and III were distributed between −35‰ and −33‰. The $\delta^{13}C_{CO2}$ values in groups IV and V showed a decreasing trend first and then an increasing trend. The participation of $ZnCl_2$ catalyst increased the $\delta^{13}C_{CO2}$ value of the product. The joint addition of H_2 and the catalyst further increased the fractionation of the $\delta^{13}C_{CO2}$ value.

TABLE 2 | $\delta^{13}C$ values of gas generated during the catalytic pyrolysis experiments at 350°C/72 h, 375°C/72 h, 400°C/72 h, 450°C/72 h, 500°C/72 h, and 550°C/72 h.

Group	Temp. (°C)	$\delta^{13}C_{CO2}$	$\delta^{13}C_1$ ‰ (VPDB)	$\delta^{13}C_2$
I	350	−34.6	-39.8	−28.2
	375	−34.0	−39.4	−27.3
	400	−33.8	−38.0	−24.4
	450	−33.9	−35.7	−24.3
	500	−34.1	−35.2	−24.9
	550	−34.7	−34.9	−23.6
II	350	−34.0	−44.7	−29.9
	375	−33.9	−42.9	−27.5
	400	−33.7	−42.7	−27.0
	450	−33.2	−40.0	−25.0
	500	−33.4	−37.0	−24.9
	550	−33.5	−36.7	−24.0
III	350	−34.5	−43.6	−29.1
	375	−33.4	−41.6	−27.5
	400	−33.8	−40.8	−25.6
	450	−33.6	−37.4	−25.6
	500	−33.7	−36.2	−25.3
	550	-34.9	−36.2	−23.7
IV	350	−32.7	−45.9	−38.4
	375	−33.1	−45.0	−38.6
	400	−33.3	−43.7	−39.4
	450	−33.4	−44.1	−37.4
	500	−32.4	−43.1	−29.5
	550	−32.1	−40.2	−14.1
V	350	−23.0	−52.4	−37.6
	375	−32.2	−45.4	−38.2
	400	−33.5	−43.9	−39.4
	450	−34.2	−44.6	−36.9
	500	−33.4	−44.0	−28.1
	550	−34.2	−43.4	−12.1

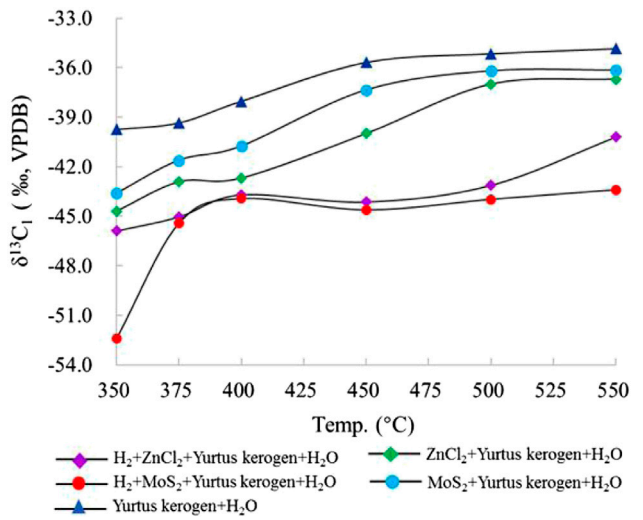


FIGURE 5 | Change in $\delta^{13}C_1$ simulated under different catalytic hydrogenation control conditions of the closed system.

The effect of MoS_2 on the $\delta^{13}C_{CO2}$ value was larger at the early stage of the reaction (**Figure 7**). At the same time, relative to the changes in $\delta^{13}C$ values for C_1 and C_2, the range of carbon isotope

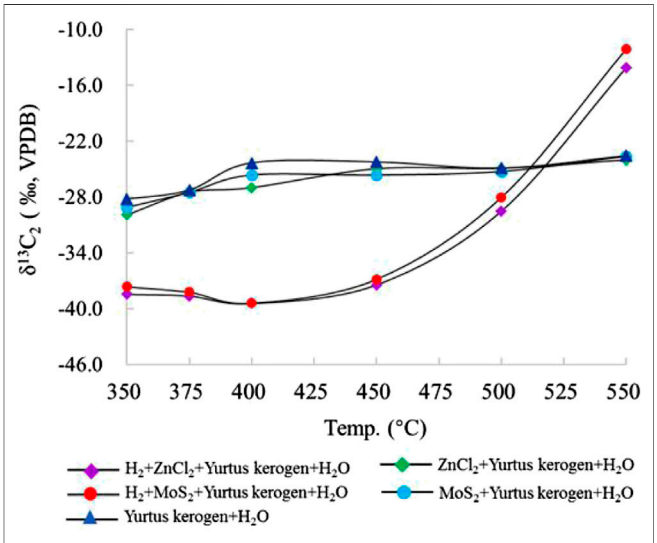


FIGURE 6 | Change in $\delta^{13}C_2$ simulated under different catalytic hydrogenation control conditions of the closed system.

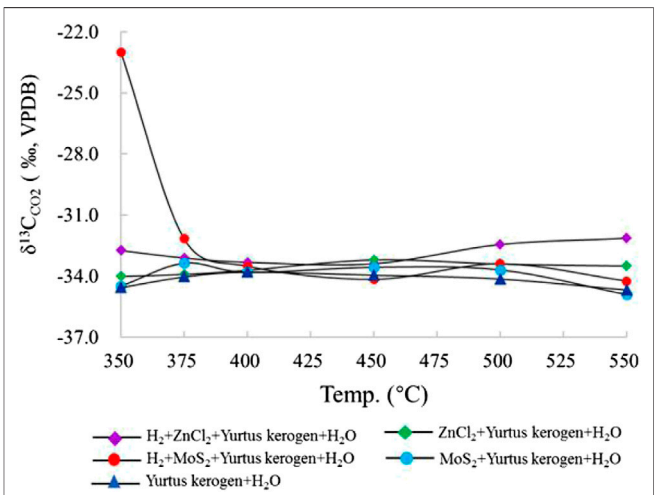


FIGURE 7 | Change in $\delta^{13}CO_2$ simulated under different catalytic hydrogenation control conditions of the closed system.

fractionation of CO_2 was smaller than that of alkanes because of the oxidative decarboxylation of its controlled long-chain HCs, rather than the bond energy difference controlled by the C-C bond leading to preferential cracking (Lu et al., 2010).

DISCUSSION

Catalytic Hydrogenation Mechanism

Catalytic hydrogenation showed that the yield and isotopic value of the gaseous product components changed significantly and were also accompanied by FTT synthesis reaction products. The source supply angle mainly depends on the control influence of H_2 and different metal elements in the reaction environment.

Product Component Comparison

The post-mature kerogen of the Yurtus Formation has very weak pyrolysis and HC generation capacity. With the increase in temperature and the catalysis of hydrogenation by different catalysts, the kerogen HC generation capacity significantly improved. As the most stable HC molecule, C_1 had an increased yield. In addition to the catalytic hydrogenation reaction of kerogen, there were other gaseous HCs produced by catalytic hydrocracking. The yield of different catalysts changed significantly. Under the same hydrogenation conditions, the yield of C_1 under the action of $ZnCl_2$ was greater than that of MoS_2, with a yield ratio of 1.0–1.4 and average of 1.3. The results of the control experiment between the experimental group with added H_2 and catalyst and the experimental group with catalyst only showed that the addition of H_2 delayed the decomposition of heavy HCs such as C_2 and C_3, leading to a higher temperature of HC generation peaks. Meanwhile, the heavy HC group bond energy was smaller than the methyl group energy, which led to the preferential participation of heavy HC groups in hydrocracking and thus to a significant increase in the yield of C_{2+} HCs and a significant reduction in the drying coefficient of the product. The addition of exogenous H_2 greatly changed the kerogen's own cracking mode, and heavy HC component C_{2+} increased significantly. It was well consistent with the results that the drying coefficient of the product gases with the increased intensity of catalytic hydrogenation is significantly lower than that of the ordinary geological environment (Lewan et al., 1979; Mango et al, 1994; Ma et al., 2018).

Change in the i/n-Alkane Ratio

Among gaseous HC components, normal paraffins are formed by free radical reactions, and isoparaffins are derived from free radical cracking on kerogen and asphalt branches under acidic cationic ion reaction (Eisma and Jurg, 1969; Almon and Johns, 1977; Kissin, 1987; Pan et al., 2006). The Yurtus Formation kerogen is high maturity, and the branched chains of its molecular structure is not developed; thus, the main source of isoparaffin is the acidification cation reaction. Thompson and Creath, (1966) showed that in North American industrial HC reservoirs mainly generated by free radical HC generation, the iC_4/nC_4 ratio is around 0.5, generally not greater than 1.0; the iC_5/nC_5 ratio is around 1.0 and generally less than 2.0. In this study, the comparison of the same component at the same temperature showed that the value of iC_n/nC_n under the action of $ZnCl_2$ was larger than MoS_2. For the products of butane (C_4), from the initial temperature of 350°C–400°C, the iC_4/nC_4 value of the products produced by the two catalysts was relatively stable, ranging from 0.241 to 0.309 and 0.184 to 0.217, respectively. The maximum values were 1.045 and 1.042, respectively, at 450°C. For the products of pentane (C_5), the temperature changed greatly from the initial temperature of 350°C–500°C; the range of the iC_5/nC_5 ratio under the action of $ZnCl_2$ was 2.200–6.252 and under the action of MoS_2 was 0.096–1.409 (**Table 1**, **Figure 8**). The results showed that under the action of $ZnCl_2$, more HCs were generated by the cationic reaction, which promoted more formation of the isoparaffins. The higher the temperature is, the more significant changes in the cationic reaction are. The results further reveal that the catalytic effect of $ZnCl_2$ on promoting HC generation by the cation reaction is stronger than that of MoS_2.

Reaction Mechanism

HC generation of catalytic hydrogenation is mainly carried out in the form of H radicals and H ions. There are two modes of catalysis: "Lewis acid" catalysis and "Brønsted acid" catalytic processes (**Figure 9**). When performing Lewis acid site catalytic processes, the main chemical reactions are decarboxylation and C-C bond breaking (Li et al., 2002; He et al., 2011; Ma et al., 2018). Since the Lewis acid site composed of Zn^{2+} or Mo^{2+} is an empty orbital position with high affinity for electrons, when the organic matter is decarboxylated, Zn^{2+} or Mo^{2+} at this position gets an electron from the adsorbed organic molecule, and carboxylic acid loses CO_2. Free radicals further undergo a rearrangement reaction with H radicals, leading to the breakage of the C-C bond and the formation of free HCs with shorter bond lengths. The product of the decarboxylation reaction is mainly CO_2. The breakage of the C-C bond mainly promotes the generation of free HCs. When performing Brønsted acid catalytic processes, through contact with Zn^{2+} and Mo^{2+}, H_2 or water molecule lose an electron to generate H ions, promoting the kerogen unsaturated cycloalkane addition reaction. As the hydrogenation reaction continues, low-molecular-weight saturated chain HCs are eventually formed (Wu et al., 2012; Ma et al., 2018).

The yield results show that Zn^{2+} has a better catalytic effect than Mo^{2+} because Zn^{2+} has a more stable and long-lasting catalytic activity than Mo^{2+}, and it is easier to fully contact the reactants. The chemical properties of Cl^- are extremely stable. Previous studies suggest that Cl^- has a certain inhibitory effect on the catalyzed cracking of kerogen (Li et al., 2002). In the catalytic hydrogenation experiment of H_2, $ZnCl_2$ shows a strong catalytic effect on hydrogen generation. S^{2-}reacts with H_2 to generate part of H_2S, which has a catalytic effect on HC generation (He et al., 2011), but the product test results show that the H_2S content is relatively low, and the catalytic contribution is not significant.

Stable Carbon and Hydrogen Isotope Change Mechanism

$\delta^{13}C_1/\delta^{13}C_2$

For the HC isotope composition of oil and natural gas, relative to its parent material, kerogen is lean in ^{13}C and ^{2}H. This is because the kerogen ^{12}C–^{12}C bond and the C-C bond in ^{1}H-CC-^{1}H are more easily broken than the ^{12}C–^{13}C bond and the ^{2}H-CC-^{1}H CC bond, thereby allowing lighter isotopes to enter HC (Lu et al., 2010).

The change in $\delta^{13}C_1$-$\delta^{13}C_2$ values can reflect the catalytic hydrogenation effects effectively. The data of groups I, II and III showed that $\delta^{13}C_1$-$\delta^{13}C_2$ has a strong linear relationship (**Figure 10**). After adding the catalysts, the change in the $\delta^{13}C_1$-$\delta^{13}C_2$ value was decreased significantly and the range changed widely, but C_2 yield changed little (**Figure 2**). The results showed that C_2 mainly promotes the elemental exchange between carbon isotopes after the catalyst were added and has little effect on the yield reaction equilibrium. The comparison of the experimental results showed that the catalyst addition leads to lighter $\delta^{13}C_1$ and $\delta^{13}C_2$. Meanwhile, the

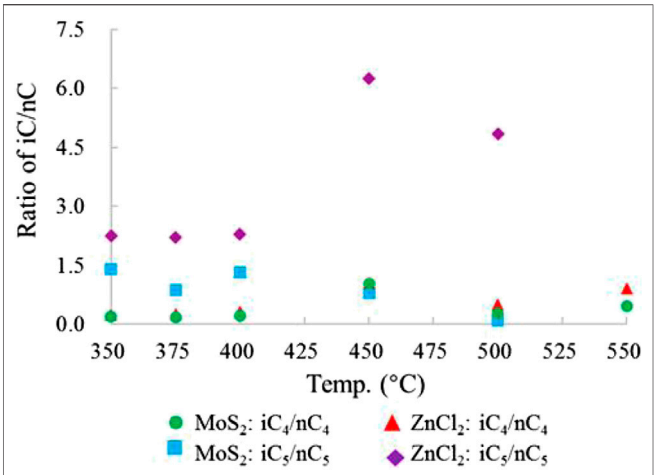


FIGURE 8 | Comparison of the iC_5/nC_5 alkane ratio between butane and pentane under the condition of $ZnCl_2/MoS_2$ of the closed system.

metal ions are involved in enhancing the reaction process and promoting the isotope fractionation level during the reaction. The catalytic hydrogenation extremely promotes the activation of the carbon source in post-mature kerogen. Within a certain temperature range (≤450°C), the distribution of $\delta^{13}C_1$-$\delta^{13}C_2$ is clustered and distributed in a stable lighter interval. At 500°C, the $\delta^{13}C_1/\delta^{13}C_2$ ratio is close to the range with no H_2 added. The C_2 component passed the peak of HC generation because the C_2 component with a smaller $\delta^{13}C$ value starts to crack into C_1, which led to the leaving C_2 with heavier $\delta^{13}C$. At the same time, C_3 cracked completely due to the $\delta^{13}C$ kinetic fractionation to promote the formation of lighter $\delta^{13}C_1$ and heavier $\delta^{13}C_2$. Restricted by high temperature and the amount of carbon material, the heavier carbon content retained in generated C_2 increases at 550°C, resulting in larger change of linear variations. It also implies the $\delta^{13}C_1$-$\delta^{13}C_2$ parameters can provide supplementary verification to evaluate whether the HC generation process of source rocks was affected by catalytic hydrogenation in sedimentary basins.

Relationship Between CO_2 and Alkane $\delta^{13}C$

CO_2 is one of the main by-products of the reaction process. Its $\delta^{13}C$ fractionation change is opposite to that of alkane $\delta^{13}C$. $\delta^{13}C_{CO2}$ increases with the enhancing intensity in the reaction (**Figures 11**, **12**). When the catalytic hydrogenation stage is weak, the kerogen HC generation is mainly carried out by self-cracking; thus, the changes in kerogen $\delta^{13}C$ in the low temperature stage are greatly affected by temperature and the external H_2 participation in the reaction. The $\delta^{13}C_{CO2}$ value became larger accompanied by an increasing intensity of the catalytic reaction. In group I, the $\delta^{13}C_{CO2}$ change from the large to the small was at the 400 °C inflection point. In group II and III, the $\delta^{13}C_{CO2}$ change from large to small was at the 450°C inflection point and the HC generation mode of kerogen was affected distinctly by the catalytic elements during pyrolysis reaction. In group IV and V, the addition of H_2 changed the characteristics of the original kerogen evolution process and promoted isotope exchange in the HC generation. The change in $\delta^{13}C_{CO2}$ from lighter to heavier was mainly controlled by the dynamic fractionation of carbon isotope of CO_2. The maximum $\delta^{13}C_{CO2}$ temperature under the action of $ZnCl_2$ is delayed compared to that under the action of MoS_2. The $\delta^{13}C_2$ value under the action of $ZnCl_2$ is less than that under the action of MoS_2, which demonstrates that the catalytic effect of $ZnCl_2$ under the same conditions is stronger than that of MoS_2.

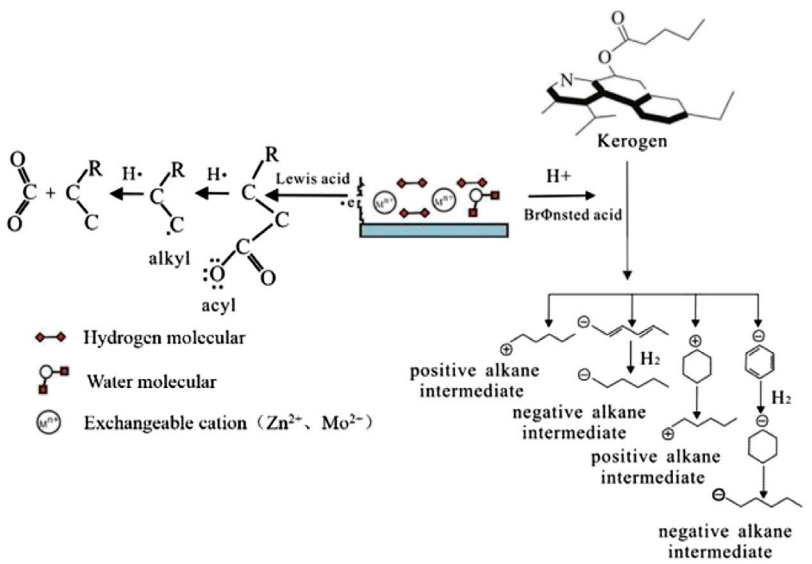


FIGURE 9 | Catalytic mechanism of transition metal based on free radical cracking and H ion reaction (modified according to Johns, 1979; Mango et al, 1994; Mango, 1996; He et al., 2011; Wu et al., 2012; Ma et al., 2018).

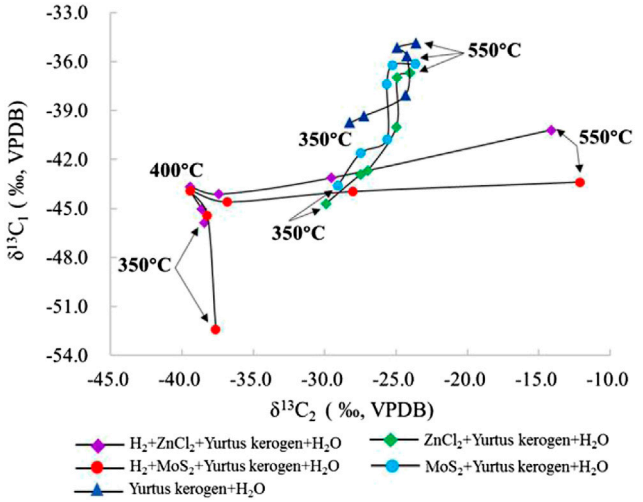


FIGURE 10 | Change in the $\delta^{13}C_1$-$\delta^{13}C_2$ contrast simulated under different catalytic hydrogenation control conditions of the closed system.

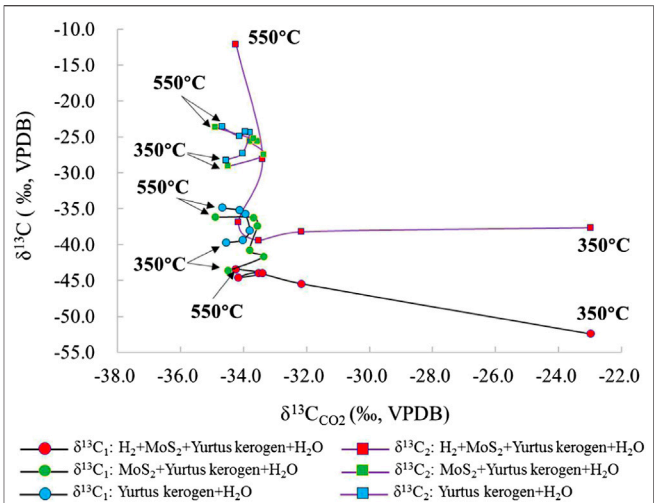


FIGURE 12 | Change in the $\delta^{13}C$ values of different alkanes and CO_2 under the simulated MoS_2 catalyzed hydrogenation control condition of the closed system.

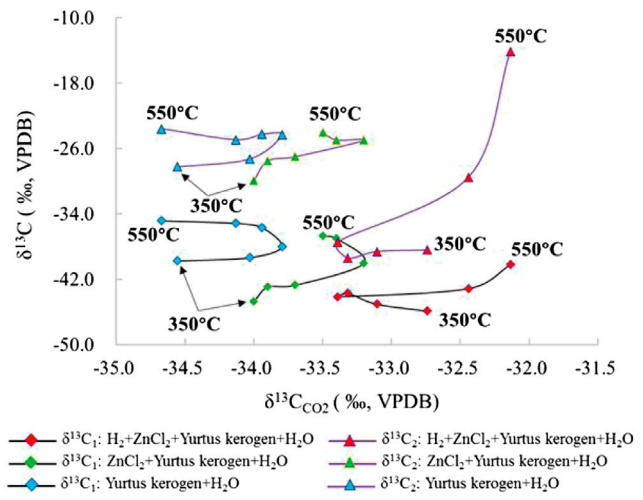


FIGURE 11 | Change in the $\delta^{13}C$ values of different alkanes and CO_2 under the simulated $ZnCl_2$ catalyzed hydrogenation control condition of the closed system.

Accompanying Secondary Reaction—Fischer-Tropsch-Type Synthesis

As one of the main modes of inorganic HC generation, FTT synthesis is well verified in geological discoveries and experiments (Fu et al., 2007; Hosgörmez, 2007; McCollom, 2013; Suda et al., 2014; McCollom, 2016; Etiope, 2017; Liu et al., 2018) and greatly affected by the redox conditions of the environment. The catalytic hydrogenation experiment provides a good reduction environment and source supply conditions. As shown in **Figure 13**, the relationship between CO_2 and CH_4 in the catalytic hydrogenation state of $ZnCl_2$ was y = 1.1359x-17.687, R^2 = 0.9375. Under the catalytic hydrogenation state of MoS_2, the relationship between CO_2 and CH_4 changed to y = 2.1496x-97.873, R^2 = 0.9533. Under the stable reaction at >400°C, the relationship between CO_2 and CH_4 changed to y = 1.9199x-73.472, R^2 = 0.9921, indicating that the decrease in the yield of CO_2 in the hydrogenation reaction showed a strong linear relationship with the increase in C_1. The CO_2 yield decreased rapidly at 375 °C owing to the solubility of water at high temperatures. In the high-temperature stage (≥400°C) under the catalytic state, the activation reaction of hydrogen radicals and carbon molecules was accelerated. In the catalytic hydrogenation reaction of CO_2, a large quantity of HCs and water mainly composed of C_1 are produced in the FTT synthesis reaction accompanying H_2 and CO_2. The change in the slope of the equation shows that the catalytic effect of $ZnCl_2$ on kerogen pyrolysis and HC generation is stronger than that of MoS_2.

With H_2 added to the HC generation reaction, the CO_2 yield decreased significantly. However, the CO_2 yield remained stable after falling to a certain value. The yield was stable under the influence of different temperature points. According to the $\delta^{13}C_{CO2}$ isotope change, a heavier trend in both H_2 added groups implies that ^{12}C is more likely to participate in the catalytic hydrogenation response than ^{13}C. Combined with the experimental results described in **Table 1**, **Figures 4, 13**, the addition of H_2 inhibited the CO_2 generation. The FTT synthesis decreased the generated CO_2 and H_2 yield. The results of the control experiment showed that the final CO_2 conversion rate was a constant under a different reaction environment. The amount of activated C with the H_2 addition reaction indicated that activated C reactants would not react in the geological environment.

The catalysis reaction by the addition of H_2 was carried out in a neutral reduction system, and the FTT synthesis accompanied by CO_2 generated HCs, which had a significant effect on the total HC yield. In geological processes, the FTT synthesis reaction plays an important role as a link between the deep hydrogen-rich fluid and the hydrogen generation of post-mature organic matter.

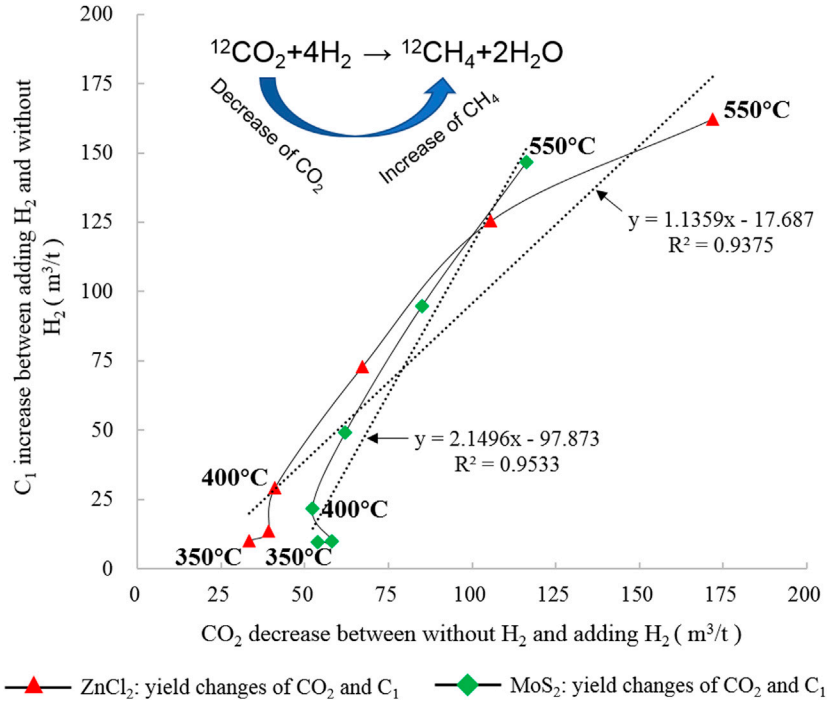


FIGURE 13 | Changes in the characteristics of C_1 and CO_2 under different catalytic hydrogenation control conditions simulated of the closed system.

CONCLUSION

For the ancient source rocks of the Yurtus Formation in the Tarim Basin, the catalytic substances and exogenous hydrogen carried under deep-derived fluids can "secondarily generate HCs" for the activation of source rocks. $ZnCl_2$ and MoS_2 have a strong catalytic effect on the reaction of post-mature kerogen and H_2. Catalytic addition of H_2 promotes the HC generation capacity of kerogen and the increase in HCs by 0.4–1.1 times, significantly reduces the natural gas drying coefficient, and promotes FTT synthesis of secondary reactions. Isotope fractionation mainly follows the laws of kinetics and shows good identification characteristics. By comparing the composition of gaseous products and isotope characteristics, the catalytic effect of $ZnCl_2$ is stronger than MoS_2 under the same conditions. Meanwhile, it implies deep-derived hydrogen fluids containing Zn, Mo and other metal elements can make a remarkable contribution to reactivate the post-mature source rocks for HC generation.

DATA AVAILABILITY STATEMENT

The original contributions presented in the study are included in the article/Supplementary Material, further inquiries can be directed to the corresponding authors.

AUTHOR CONTRIBUTIONS

All authors listed have made a substantial, direct, and intellectual contribution to the work and approved it for publication.

FUNDING

This work was supported by National Key R&D Program of China (Grant No. 2017YFC0603102), National Natural Science Foundation of China (Project No.: 41625009 and 41673066), Strategic Priority Research Program of Chinese Academy of Sciences (Project No.: XDA14010404) and National Oil and Gas Major Project (No. 2017ZX05008-002-050).

ACKNOWLEDGMENTS

We are grateful to Yunpeng Wang, Hong Lu, and Qiang Wang for their experimental supports. The authors also thank Xiaoqi Wu for his critical comments that significantly improved the quality of manuscript.

REFERENCES

Allen, D. E., and Seyfried, W. E., Jr. (2004). Serpentinization and heat generation: constraints from Lost City and Rainbow hydrothermal systems 1 1Associate editor: J. C. Alt. *Geochem. Cosmochim. Acta.* 68 (6), 1347–1354. doi:10.1016/j.gca.2003.09.003

Almon, W. R., and Johns, W. D. (1977). "Petroleum-forming reactions. The mechanism and rate of clay catalyzed fatty acid decarboxylation," in *Advances in organic Geochemistry* Editors R. Campos and J. Goni (Madrid: Enadimsa), 157–172.

Bougault, H., and Dpt, M.G. (2019). Hydrothermal hydrogen and methane: scientific insight a new potential resource? [J]. Mines & carrieres. *Les techniques, 196(hors series),* 73–80.

Bradley, A. S., and Summons, R. E. (2010). Multiple origins of methane at the lost city hydrothermal field. *Earth Planet. Sci. Lett.* 297 (1–2), 34–41. doi:10.1016/j.epsl.2010.05.034

Coveney, R.M.J. (1987). Serpentinization and the origin of hydrogen gas in Kansas[J]. *American Association of Petroleum Geologists Bulletin,* 71 (1), 39–48.

Eisma, E., and Jurg, J. W. (1969). "Fundamental aspects of the generation of petroleum," in *Organic Geochemistry, methods and results*. Editors G. Eglinton and M.T.J. Murphy (Berlin: Springer-Verlag), 675–698.

Etiope, G. (2017). Abiotic methane in continental serpentinization sites: an overview. *Procedia Earth Planet. Sci.* 17, 9–12. doi:10.1016/j.proeps.2016.12.006

Etiope, G., and Whiticar, M. J. (2019). Abiotic methane in continental ultramafic rock systems: towards a genetic model. *Appl. Geochem.* 102, 139–152. doi:10.1016/j.apgeochem.2019.01.012

Fu, Q., Sherwood Lollar, B., Horita, J., Lacrampe-Couloume, G., and Seyfried, W. E. (2007). Abiotic formation of hydrocarbons under hydrothermal conditions: constraints from chemical and isotope data. *Geochem. Cosmochim. Acta.* 71 (8), 1982–1998. doi:10.1016/j.gca.2007.01.022

Guélard, J., Beaumont, V., Rouchon, V., Guyot, F., Pillot, D., Jézéquel, D., et al. (2017). Natural H2in Kansas: deep or shallow origin?. *Geochem. Geophys. Geosyst.* 18 (5), 1841–1865. doi:10.1002/2016gc006544

Hawkes, H. E. (1972). Free hydrogen in genesis of petroleum: Geological notes. *AAPG Bull.* 56 (11), 2268–2270. doi:10.1306/819a4202-16c5-11d7-8645000102c1865d

Han, C. (2001). *Hydrocracking Process and Engineering (in Chinese)*. Beijing: China Petrochemical Press, 224–226.

He, K., Zhang, S., Mi, J., Chen, J., and Cheng, L. (2011). Mechanism of catalytic hydropyrolysis of sedimentary organic matter with MoS2. *Petrol. Sci.* 8 (02), 134–142. doi:10.1007/s12182-011-0126-0

Hirose, T., Kawagucci, S., and Suzuki, K. (2011). Mechanoradical H2 generation during simulated faulting: implications for an earthquake-driven subsurface biosphere. *Geophys. Res. Lett.* 38 (17), L17303. doi:10.1029/2011gl048850

Hosgörmez, H. (2007). Origin of the natural gas seep of Çirali (Chimera), Turkey: site of the first Olympic fire. *J. Asian Earth Sci.* 30 (1), 131–141. doi:10.1016/j.jseaes.2006.08.002

Jeffrey, A. W. A., and Kaplan, I. R. (1988). Hydrocarbons and inorganic gases in the gravberg-1 well, siljan ring, Sweden. *Chem. Geol.* 71 (1–3), 237–255. doi:10.1016/0009-2541(88)90118-0

Jia, W., Wang, Q., Liu, J., Peng, P., Li, B., and Lu, J. (2014). The effect of oil expulsion or retention on further thermal degradation of kerogen at the high maturity stage: a pyrolysis study of type II kerogen from Pingliang shale, China. *Org. Geochem.* 71, 17–29. doi:10.1016/j.orggeochem.2014.03.009

Jin, Z., Zhang, L., and Yang, L. (2002). Preliminary study on geochemical characteristics of fluids in deep sedimentary basins and Hydrocarbon Accumulation Effect. [J]. *Earth Sci.* 27 (6), 659–665. doi:10.3321/j.issn:1000-2383.2002.06.001

Jin, Z., Zhang, L., Yang, L., and Hu, W. (2004). A preliminary study of mantle-derived fluids and their effects on oil/gas generation in sedimentary basins. *J. Petrol. Sci. Eng.* 41 (1–3), 45–55. doi:10.1016/s0920-4105(03)00142-6

Jin, Z., Hu, W., and Zhang, L. (2007). *Deep fluid activity and hydrocarbon accumulation effect [M]*. Beijing: Science Press.

Johns, W. D. (1979). Clay mineral catalysis and petroleum generation. *Annu. Rev. Earth Planet Sci. C.* 7 (1), 183–198. doi:10.1146/annurev.ea.07.050179.001151

Kissin, Y. V. (1987). Catagenesis and composition of petroleum: origin of n-alkanes and isoalkanes in petroleum crudes. *Geochem. Cosmochim. Acta.* 51 (9), 2445–2457. doi:10.1016/0016-7037(87)90296-1

Klein, F., Grozeva, N. G., and Seewald, J. S. (2019). Abiotic methane synthesis and serpentinization in olivine-hosted fluid inclusions. *Proc. Natl. Acad. Sci. U.S.A.* 116 (36), 17666–17672. doi:10.1073/pnas.1907871116

Klein, F., Tarnas, J. D., and Bach, W. (2020). Abiotic sources of molecular hydrogen on Earth. *Elements* 16 (1), 19–24. doi:10.2138/gselements.16.1.19

Lewan, M. D., Winters, J. C., and McDonald, J. H. (1979). Generation of oil-like pyrolyzates from organic-rich shales. *Science* 203 (4383), 897–899. doi:10.1126/science.203.4383.897

Lewan, M. D. (1997). Experiments on the role of water in petroleum formation. *Geochem. Cosmochim. Acta.* 61 (17), 3691–3723. doi:10.1016/s0016-7037(97)00176-2

Li, S., Lin, S., and Guo, S. (2002). Effects of minerals on kerogen pyrolysis hydrocarbon generation. *J. Petrol. Univ. (Nat. Sci.)* 26 (1), 69–74. doi:10.3321/j.issn:1000-5870.2002.01.022

Liu, Q., Dai, J., Jin, Z., Li, J., Wu, X., Meng, Q., et al. (2016). Abnormal carbon and hydrogen isotopes of alkane gases from the Qingshen gas field, Songliao Basin, China, suggesting abiogenic alkanes? *J. Asian Earth Sci.* 115, 285–297. doi:10.1016/j.jseaes.2015.10.005

Liu, Q., Zhu, D., Meng, Q., Liu, J., Wu, X., et al. (2018). The scientific connotation of oil and gas formations under deep fluids and organic-inorganic interaction[J]. *Science China Earth Sciences*. doi:10.1007/s11430-018-9281-2

Liu, J., Liu, Q., Zhu, D., et al. (2019). The function and impact of deep fluid on the organic matter during the hydrogeneration and evolution process[J]. *J. Nat. Gas Geosci.* 4 (4), doi:10.1016/j.jnggs.2019.07.002

Liu, J., and Tang, Y. (1998). Kinetics of early methane generation from Green River shale. *Chin. Sci. Bull.* 43 (22), 1908–1912. doi:10.1007/bf02883470

Liu, Q., Zhu, D., Meng, Q., Liu, J., Wu, X., Zhou, B., et al. (2018). Basic connotation of hydrocarbon Formation under deep fluid and Organic-inorganic interaction. *Sci. China Earth Sci.*, 1–22.

Lu, S., Xue, H., and Li, J. (2010). *Dynamics of isotope fractionation of natural gas and hydrocarbon and its application [M]*. Beijing: Petroleum Industry Press.

Luo, Y. (2004). *Handbook of chemical bond energy data*. Beijing: Science Press, 1–396.

Lv, Y., Liu, S., Wu, H., Hohl, S. V., Chen, S., Li, S., et al. (2018). Zn-Sr isotope records of the Ediacaran Doushantuo Formation in South China: diagenesis assessment and implications[J]. *Geochimica et Cosmochimica Acta*, 239, doi:10.1016/j.gca.2018.08.003

Ma, X., Zheng, G., Sajjad, W., Xu, W., Fan, Q., Zheng, J., et al. (2018). Influence of minerals and iron on natural gases generation during pyrolysis of type-III kerogen. *Mar. Pet. Geol.* 89, 216–224. doi:10.1016/j.marpetgeo.2017.01.012

Mango, F. D. (1996). Transition metal catalysis in the generation of petroleum and natural gas. *Geochem. Cosmochim. Acta*. 56 (1), 553–555. doi:10.1016/0016-7037(92)90153-a

Mango, F. D. (1996). Transition metal catalysis in the generation of natural gas. *Org. Geochem.* 24 (10–11), 977–984. doi:10.1016/s0146-6380(96)00092-7

Mango, F. D., and Hightower, J. (1997). The catalytic decomposition of petroleum into natural gas. *Geochem. Cosmochim. Acta.* 61 (24), 5347–5350. doi:10.1016/s0016-7037(97)00310-4

Mango, F. D., Hightower, J. W., and James, A. T. (1994). Role of transition-metal catalysis in the formation of natural gas. *Nature* 368 (6471), 536–538. doi:10.1038/368536a0

McCollom, T. M. (2013). Laboratory simulations of abiotic hydrocarbon Formation in earth's deep subsurface. *Rev. Mineral. Geochem.* 75 (1), 467–494. doi:10.2138/rmg.2013.75.15

McCollom, T. M. (2016). Abiotic methane formation during experimental serpentinization of olivine. *Proc. Natl. Acad. Sci. U.S.A.* 113 (49), 13965–13970. doi:10.1073/pnas.1611843113

Meng, Q., Sun, Y., Tong, J., Fu, Q., Zhu, J., Zhu, D., et al. (2015). Distribution and geochemical characteristics of hydrogen in natural gas from the Jiyang Depression, Eastern China. *J. Acta Geol. Sin. (Engl. Ed.)* 89 (5), 1616–1624. doi:10.1111/1755-6724.12568

Milesi, V., Mccollom, T. M., and Guyot,, F. (2016). Thermodynamic constraints on the formation of condensed carbon from serpentinization fluids [J]. *Geochimica Et Cosmochimica Acta*. 391–403. doi:10.1016/j.gca.2016.06.006

Newell, K. D., Doveton, J. H., Merriam, D. F., Lollar, B. S., Waggoner, W. M., and Magnuson, L. M. (2007). H2-rich and hydrocarbon gas recovered in a deep precambrian well in northeastern Kansas. *Nat. Resour. Res.* 16 (3), 277–292. doi:10.1007/s11053-007-9052-7

Pan, C., Yu, L., Liu, J., and Fu, J. (2006). Chemical and carbon isotopic fractionations of gaseous hydrocarbons during abiogenic oxidation. *Earth Planet Sci. Lett.* 246 (1–2), 70–89. doi:10.1016/j.epsl.2006.04.013

Pinto, F., Gulyurtlu, I., Lobo, L. S., and Cabrita, I. (1999). The effect of catalysts blending on coal hydropyrolysis. *Fuel* 78 (7), 761–768. doi:10.1016/s0016-2361(98)00212-9

Resing, J. A., Sedwick, P. N., German, C. R., Jenkins, W. J., Moffett, J. W., Sohat, B. M., et al. (2015). Basin-scale transport of hydrothermal dissolved metals across the South Pacific Ocean. *Nature* 523 (7559), 200–203. doi:10.1038/nature14577

Seewald, J. S. (2003). Organic-inorganic interactions in petroleum-producing sedimentary basins. *Nature* 426 (6964), 327–333. doi:10.1038/nature02132

Sherwood Lollar, B., Onstott, T. C., Lacrampe-Couloume, G., and Ballentine, C. J. (2014). The contribution of the Precambrian continental lithosphere to global H2 production. *Nature* 516 (7531), 379–382. doi:10.1038/nature14017

Shuai, Y., Zhang, S., Su, A., et al. (2010). Geochemical evidence for strong ongoing methanogenesis in Sanhu region of Qaidam Basin[J]. *Science in China*, 53 (001): 84–90. doi:10.1007/s11430-009-0081-4

Suda, K., Ueno, Y., Yoshizaki, M., Nakamura, H., Kurokawa, K., Nishiyama, E., et al. (2014). Origin of methane in serpentinite-hosted hydrothermal systems: the CH4-H2-H2O hydrogen isotope systematics of the Hakuba Happo hot spring. *Earth Planet Sci. Lett.* 386, 112–125. doi:10.1016/j.epsl.2013.11.001

Telling, J., Boyd, E. S., Bone, N., Jones, E. L., Tranter, M., MacFarlane, J. W., et al. (2015). Rock comminution as a source of hydrogen for subglacial ecosystems. *Nat. Geosci.* 8 (11), 851–855. doi:10.1038/ngeo2533

Thompson, R. R., and Creath, W. B. (1966). Low molecular weight hydrocarbons in Recent and fossil shells. *Geochem. Cosmochim. Acta.* 30 (11), 1137–1152. doi:10.1016/0016-7037(66)90034-2

Tivey, M. (2007). Generation of seafloor hydrothermal vent fluids and associated mineral deposits. *Oceanogr.* 20 (1), 50–65. doi:10.5670/oceanog.2007.80

Wu, L. M., Zhou, C. H., Keeling, J., Tong, D. S., and Yu, W. H. (2012). Towards an understanding of the role of clay minerals in crude oil formation, migration and accumulation. *Earth Sci. Rev.* 115 (4), 373–386. doi:10.1016/j.earscirev.2012.10.001

Conflict of Interest: Author JZ, LQ, MQ, ZD, and LJ were employed by the company SINOPEC.

The remaining authors declare that the research was conducted in the absence of any commercial or financial relationships that could be construed as a potential conflict of interest.

Copyright © 2021 Xiaowei, Zhijun, Quanyou, Qingqiang, Dongya, Jiayi and Jinzhong. This is an open-access article distributed under the terms of the Creative Commons Attribution License (CC BY). The use, distribution or reproduction in other forums is permitted, provided the original author(s) and the copyright owner(s) are credited and that the original publication in this journal is cited, in accordance with accepted academic practice. No use, distribution or reproduction is permitted which does not comply with these terms.

frontiers in Earth Science

ORIGINAL RESEARCH
published: 18 March 2021
doi: 10.3389/feart.2021.635178

Soil Degassing From the Xianshuihe–Xiaojiang Fault System at the Eastern Boundary of the Chuan–Dian Rhombic Block, Southwest China

Yutao Sun[1,2], Xiaocheng Zhou[3], Yucong Yan[3], Jingchao Li[3], Wenya Fang[3], Wanli Wang[3] and Yongmei Liu[4]*

[1]Hebei Key Laboratory of Strategic Critical Mineral Resources, Hebei GEO University, Shijiazhuang, China, [2]College of Earth Sciences, Heibei GEO University, Hebei Province, Shijiazhuang, China, [3]Institute of Earthquake Forecasting, China Earthquake Administration, Beijing, China, [4]Seismological Bureau of Inner Mongolia Autonomous Region, Hohhot, China

OPEN ACCESS

Edited by:
Francesco Italiano, National Institute of Geophysics and Volcanology, Italy

Reviewed by:
Alessandra Sciarra, Istituto Nazionale di Geofisica e Vulcanologia (INGV), Italy
Galip, Yuce, Hacettepe University, Turkey

***Correspondence:**
Xiaocheng Zhou
zhouxiaocheng188@163.com

Specialty section:
This article was submitted to Structural Geology and Tectonics, a section of the journal Frontiers in Earth Science

Received: *30 November 2020*
Accepted: *21 January 2021*
Published: *18 March 2021*

Citation:
Sun Y, Zhou X, Yan Y, Li J, Fang W, Wang W and Liu Y (2021) Soil Degassing From the Xianshuihe–Xiaojiang Fault System at the Eastern Boundary of the Chuan–Dian Rhombic Block, Southwest China. Front. Earth Sci. 9:635178. doi: 10.3389/feart.2021.635178

The Chuan–Dian region, situated in the middle part of the north-south seismic zone of mainland China in a highly deformed area of the eastern margin of the Tibetan Plateau, is one of the principal areas for monitoring earthquake activities in China. In this study, the geochemical characteristics of soil degassing (of CH_4, H_2, CO_2, Rn, and Hg) and, the relationship between degassing and fault activity, were investigated in the Xianshuihe–Xiaojiang fault system (XXFS) at the eastern boundary of the Chuan–Dian rhombic block. The mean soil-gas concentrations of CH_4, H_2, CO_2, Rn, and Hg in the XXFS were 8.1 ppm, 9.9 ppm, 0.5%, 15.1 kBq/m^3 and 12.9 ng/m^3, respectively. The $\delta^{13}C_{CO2}$ and $\delta^{13}C_{CH4}$ values of the hot-spring gases varied from –11.9‰ to –3.7‰ and –62.5‰ to 17‰, respectively. The He-C isotopic ratios indicate that the carbon in the northern and middle parts of the XXFS may have originated from deep fluids, whereas the carbon in the southern part of the XXFS is of organic origin. The high concentrations of soil gas were distributed near the faults, indicating that the faults could act as channels for gas migration. The distributions of the high soil-gas concentrations in the XXFS coincide with the highest stress and maximum strain rates, indicating that the fault activity enhanced permeability and increased the emission rates of the gases. The results of this study will be helpful for degassing in active fault zones and earthquake monitoring.

Keywords: soil gas, CO_2, CH_4, H_2, Rn, Hg

INTRODUCTION

Degassing (of gases such as Rn, He, CO_2, CH_4, CO, H_2, N_2, and Hg) from the solid Earth to the atmosphere can be enhanced by varying the crustal stress (King, 1986; Toutain and Baubron, 1999; Du et al., 2008; Bohnhoff and Zokack, 2010). Previous studies and field observations have demonstrated that faults and/or fractures are highly permeable pathways for gas migration from gas sources, which retain the signatures of gas sources in the soil cover (e.g. Fu et al., 2005; Ciotoli et al., 2014, 2016; Sciarra et al., 2015, 2017, 2018, 2020; Yuce et al., 2017; Xiang et al., 2020). Gas anomalies are well-correlated with earthquakes (e.g. King, 1986; Du et al., 2008; Einarsson et al.,

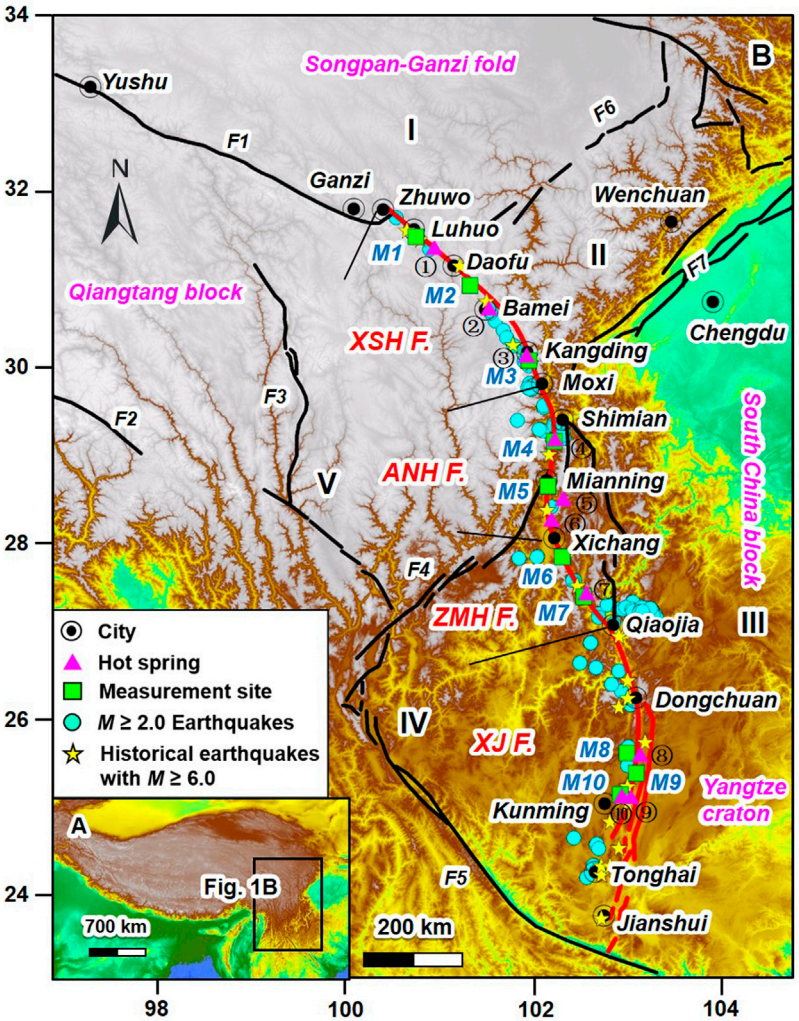


FIGURE 1 | (A) Geological map showing the location of the study area. **(B)** Tectonic and topographic map in the Chuan–Dian rhombic block. I, Ahba block; II, Longmenshan block; III, south China block; IV, the southern subblock of the Chuan–Dian terrace; V, the northern subblock of the Chuan–Dian terrane. F1, Ganzi-Yushu fault; F2, Jiali fault; F3, Jinshajiang fault; F4, Xiaojinhe fault; F5, Red River fault; F6, Longriba fault; F7, Longmenshan fault zone. Modified after Jiang et al. (2014). M1-M10 are the soil-gas measurement sites in this study. Abbreviations of the faults: XSH, Xianshuihe fault; ANH, Anninghe fault; ZMH, Zemuhe fault; XJ, Xiaojiang fault. Numbers ①–⑩ represent the bubbling hot springs distributed along the XXFS (Kama, Guanding, Zimakua, Xide, Hongmo, Liutie, Xundiantang, Yiliang, and Tangchi hot springs, respectively). The $M \geq 2.0$ earthquakes occurred from January 2012 to October 2020 within 50 km of the XXFS. Earthquake data are from China Earthquake Networks Center (CENE, http://www.ceic.ac.cn). Data of the histotical earthquakes are from Wang et al. (2008) and Wen et al. (2011).

2008; Li et al., 2009) and are much more sensitive to stress variations (King, 1986; Einarsson et al., 2008; Toutain and Baubron, 1999). Therefore, soil-gas measurement is an efficient tool for the study of fault activity (e.g. Toutain and Baubron, 1999; Walia et al., 2010; Yang et al., 2011).

Northward subduction of the Indian plate beneath the Tibetan Plateau makes south-eastern Tibet an important domain involved in the convergence and interaction between the Eurasian and Indian plates (**Figure 1A**, Tapponnier et al., 2001). The Chuan–Dian region, in the southern part of the north-south seismic zone of mainland China, is tectonically located in the highly deformed area of the eastern Tibetan Plateau. Enclosed by the Xianshuihe–Xiaojiang fault system (XXFS), the Red River fault, and the Jinshajiang fault (**Figure 1B**), the Chuan–Dian rhombic block is one of the principal areas of earthquake monitoring in China.

The XXFS is located at the eastern boundary of the Chuan–Dian rhombic block (**Figure 1B**) and has a curved left-lateral strike-slip structure extending at least 1,400 km into the eastern margin of the Tibetan Plateau (Allen et al., 1991). Fieldwork confirms that the XXFS is one of the largest and most seismically active fault systems in China. The XXFS has experienced at least 35 earthquakes of $M > 6$ in the last 300 years, and almost all segments of the system have been the locus of major earthquakes within the historical record (BGMRSP, 1993; **Figure 1B**).

Previous studies primarily focused on the soil gas and hot-spring gas at the western boundary of the Chuan–Dian rhombic

block (e.g. Li et al., 2018; Zhou et al., 2020). However, at the eastern boundary of the rhombic block, only the geochemical characteristics of several gas species (CO_2, Rn, and Hg) in the middle part of the XXFS have been reported (Zhang et al., 2019a; Zhange, 2019b). So far, systematic investigation of multi-gas components in soil gases at the eastern boundary of the rhombic block has rarely been reported. In this study, the geochemical characteristics of soil degassing of CH_4, H_2, CO_2, Rn, and Hg and the relationship between degassing and fault activity in the XXFS were reported.

GEOLOGICAL SETTING

The XXFS consists of the Xianshuihe (XSH), Anninghe (ANH), Zemuhe (ZMH), and Xiaojiang (XJ) faults from north to south (**Figure 1B**).

The NW-striking XSH fault is a highly active strike-slip fault in the eastern margin of the Tibetan Plateau that begins in Luding, passes through Kangding and Luhuo, and extends into Qinghai Province (**Figure 1B**). The XSH fault has a long active history. The regional uplift tectonic motion of the Tibetan Plateau in the Neogene produced the XSH NW–NNW striking left-lateral slip fault that cuts through the sialsphere, producing the belts of intensive faults and cleavage. The XSH fault is very active and is accompanied by many destructive earthquakes, such as the M = 7.9 earthquake that occurred in Luhuo in 1973 (**Figure 1B**, BGMRSP, 1993).

The ANH fault starts from the town of Jintang, passes through Mianning, Dechang, and Huili, and extends into Yunnan Province. The ANH fault is multi-segmented. The northern, middle, and southern segments are separated at Shimian and Dechang. In this study, the northern and middle segments of the ANH fault were selected for targeting. The northern segment of the ANH fault is characterized by thrust and ductile shear, whereas the middle segment is characterized by deep faulting. Seismic activities in these segments are severe, with many $M \geq 6$ earthquakes occurring (BGMRSP, 1993).

The ZMH NW-striking fault conjoins with the ANH fault at Xichang and is currently active (BGMRSP, 1993). The basement of the ZMH fault primarily consists of metamorphic rocks derived from granite, rhyolite, and basalt (Ren et al., 2010). Quaternary alluvial sediments, which are primarily composed of sandy gravel, fine sand, silt, and clay, are widely distributed in the study area (Ren et al., 2010).

The XJ fault is a zone of intense seismic activity that starts from Zhaojue in Sichuan Province and terminates in Yunnan Province. The fault divides into two branches south of the city of Dongchuan (**Figure 1B**). A wide crushed zone formed along the fault. The XJ fault is distinctly currently active and is characterized by frequent seismic activities and many hot springs (BGMRSP, 1993).

The field survey showed hot springs widely distributed along the XXFS (Zhou et al., 2015). In this study, the Jinkagu (①), Kama (②), and Guanding (③) hot springs in the XSH fault; the Zimakua (④), Xide (⑤), and Hongmo (⑥) hot springs in the ANH fault; the Liutie (⑦) hot spring in the ZMH fault; and the Xundian (⑧), Yiliang (⑨), and Tangi (⑩) hot springs in the XJ fault (**Figure 1B**) are distributed near the soil-gas measurement sites (**Figure 1B**); bubbling gas from these hot springs was sampled.

MEASUREMENT AND SAMPLING METHOD

Measurement Method of Soil Gas

The soil-gas measurements in the XXFS were conducted on 1–13 March 2019 to minimize the effect of weather factors. Ten

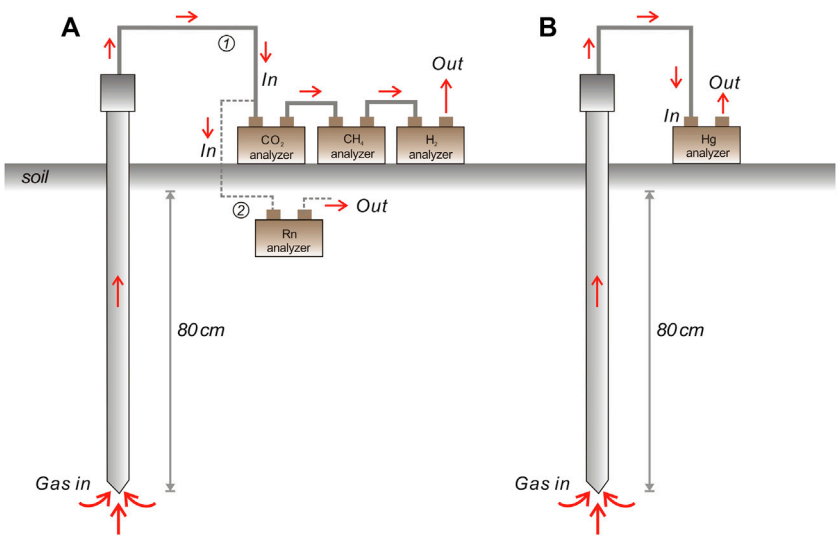


FIGURE 2 | Sketch map showing the measurement method of soil gases in the XXFS. ① and ② represent the first and second steps of the measurement at S1. Details of the measurement method can be found in the text.

TABLE 1 | Soil-gas concentrations at each measurement site in the XXFS.

Measurement site	Fault	CH_4 (ppm)		H_2 (ppm)		CO_2 (%)		Rn (kBq/m^3)		Hg (ng/m^3)	
		Min	Max	Min	Max	Min	Max	Min	Max	Min	Max
M1	XSH	0.8	31.4	0.3	59.1	0.02	2	2.3	258	5	18
M2	XSH	0.5	13.4	0.3	52.9	0.01	2.53	4.2	32.7	7	22
M3	XSH	0	9.2	0.2	43.5	0.03	1.56	1.1	52.6	7	26
M4	ANH	0	25.8	0.2	174.8	0.03	1.14	2.1	15.6	9	21
M5	ANH	0	180	0.2	96.1	0.04	1.05	0.2	43.1	4	50
M6	ZMH	0.8	97.4	0.2	193.3	0.08	1.04	0.9	26.1	7	63
M7	ZMH	0	1,130	0.2	22.7	0.02	0.82	1.1	28.4	4	19
M8	XJ	0	2.9	0.2	1.6	0.05	1.54	2.6	90.8	5	36
M9	XJ	0	7.3	0.2	19	0.18	25	1.1	43.5	4	32
M10	XJ	0	2.5	0.2	2.6	0.26	2.24	0.03	53.8	1	78

measurement sites (M1 to M10 in **Figure 1B**) along the XXFS were selected for measurement. The measurement sites of M1–M3, M4–M5, M6–M7, and M8–M10 were in the XSH, ANH, ZMH, and XJ faults, respectively (**Figure 1B**). M8 and M10 were in the western branch of the XJ fault, whereas M9 was in the eastern branch of the XJ fault (**Figure 1B**).

Four parallel survey lines with an interval of approximately 10 m were laid across the fault at each measurement site. Gas concentrations were measured at 16 points on each survey line; 72 measurement points at M3 were laid out across the XSH fault. The distance between each measurement point was approximately 10 m, whereas those far from the fault were separated by approximately 20–100 m at places that were confined by local conditions. A total of 648 soil-gas measurement points for each gas species were measured in the XXFS.

The measurement method of the soil-gas concentration was the same as that reported by Zhou et al. (2016). Before measurement, two samplers (S1 and S2), 1-m in length and 2.3-cm in diameter, were hammered into the soil at a depth of ~80 cm (**Figure 2**). The concentrations of soil gas at a depth of ~80 cm were measured. The distance between the two samplers was 50 cm. S1 was used to measure CO_2, CH_4, H_2, and Rn concentrations. The CO_2 analyser was connected to S1 to first measure the CO_2 concentration. The CH_4 analyser was connected to the outlet of the CO_2 analyser, and the H_2 analyser was connected to the outlet of the CH_4 analyser (**Figure 2A**). When the measurements of CO_2, CH_4, and H_2 concentrations were finished, the Rn analyser was connected to S1 for the measurement (**Figure 2A**). S2 was only used to measure Hg concentration (**Figure 2B**).

The CO_2 concentration was measured using the non-dispersive infrared gas analyser GXH-3010 with a measuring resolution and accuracy of 0.001% and 4%, respectively (Zhou et al., 2016). The concentration of CH_4 was measured using the Huberg LASER ONE with a measurement resolution and accuracy of 1 ppm and 5%, respectively. The concentration of H_2 in the soil gas was measured using the ATG-300H analyser, which has been widely used for the measurement of fault degassing. The measurement range and resolution of the H_2 analyser were 0–5,000 ppm and 0.1 ppm, respectively. An RAD7 Radon Detector and an RA-915+ Zeeman Mercury Analyser were used to measure Rn and Hg concentrations in soil gas, respectively.

Sampling and Analyzing Methods of Hot-Spring Gas

Ten bubbling hot-spring gas samples were collected from the hot springs of ①–⑩ in the XXFS (**Figure 1B**) in 2017 and 2018 using the water displacing method. The gases were collected in soda-lime glass bottles with a volume of 500 ml. An inverted funnel was submerged and placed on top of the bubbles to collect the hot-spring gas. The collected gas in the funnel flowed into a bottle

TABLE 2 | Threshold values, proportions, mean concentration of each population, and 95% confidence interval of soil gases in the XXFS obtained by statistical approach.

Gas species	Number of measurement point	LAT[a]	UAT[a]	Proportion (%)			Mean gas concentration of each population			Mean gas concentration	95% confidence interval
				A[b]	B[b]	C[b]	A[b]	B[b]	C[b]		
CH_4 (ppm)	648	1.6	8.1	24.4	54.8	20.8	1.1	2.8	72.3	8.1	4.1–12.9
H_2 (ppm)	648	2.0	47.7	30.4	61.3	8.3	0.5	13.5	77.7	9.9	8.3–11.4
CO_2 (%)	648	0.2	0.7	54.0	40.7	5.2	0.1	0.4	1.3	0.5	0.4–0.6
Rn (kBq/m^3)	648	2.3	24.9	2.2	84.9	13.0	1.2	11.8	38.4	15.1	13.9–16.1
Hg (ng/m^3)	648	5.0	29.0	4.9	93.1	2.0	3.2	12.8	42.5	12.9	12.4–13.4

[a]*LAT, lower anomaly threshold; UAT, upper anomaly threshold.*

[b]*The A, B and C are the three populations identified by the thresholds. See details in the text.*

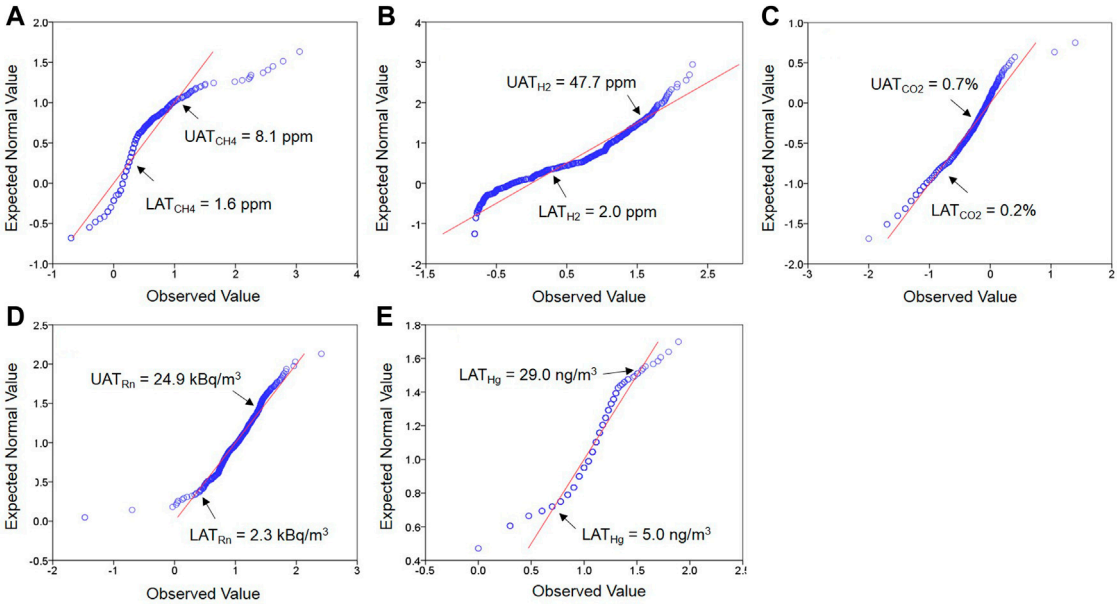


FIGURE 3 | Normal probability plots for: **(A)**, CH_4; **(B)**, H_2; **(C)**, CO_2; **(D)**, Rn; **(E)**, Hg.

filled with hot-spring water and replaced the water in the bottle (Zhou et al., 2015; Zhang et al., 2017). Details of the sampling method can be found in Zhou et al. (2015) and Zhang et al. (2017).

The $\delta^{13}C_{CO2}$ and $\delta^{13}C_{CH4}$ values of the gas samples were analysed at the Key Laboratory of Petroleum Resources Research, Institute of Geology and Geophysics, Chinese Academy of Science. A GC-IRMS analytical system gas chromatograph (Agilent 6890)-stable isotope ratio mass spectrometer (Thermo-Fisher Scientific Delta Plus XP) was used for carbon isotopic ratio analysis. The $\delta^{13}C_{CO2}$ and $\delta^{13}C_{CH4}$ values were reported relative to PDB.

RESULTS AND DISCUSSION

Statistical Results and Spatial Distributions of Soil Gases in the XXFS

The statistical results of the CH_4, H_2, CO_2, Rn, and Hg concentrations at each measurement site are listed in **Table 1**. The concentrations of CH_4, H_2, CO_2, Rn, and Hg in the XXFS range from 0–1,130 ppm, 0.2–193.3 ppm, 0.01–25%, 0.03–258 kBq/m^3, and 1–78 ng/m^3, respectively (**Table 1**).

We used the normal probability method proposed by Sinclair (1991) to objectively identify the threshold, which distinguishes different populations (background, mixing, and anomalous) well (e.g. Sinclair, 1974, 1991; Sciarra et al., 2015, 2017, 2018, 2020; Zhou et al., 2015; Yuce et al., 2017). The background population is related to surface processes, such as soil respiration, air dilution, and biological gas origin. The anomaly population is primarily related to internal processes, such as fault/magma degassing (e.g. Chiodini et al., 2004; Sciarra et al., 2015, 2017, Sciarra, 2018, Sciarra, 2020; Di Martino et al., 2016; Yuce et al., 2017). The mixing population represents soil gas with mixing sources by external and internal processes (e.g. Yuce et al., 2017).

The lower anomaly thresholds (LAT) of CH_4, H_2, CO_2, Rn, and Hg in the XXFS were 1.6 ppm, 2.0 ppm, 0.2%, 2.3 kBq/m^3, and 5.0 ng/m^3, respectively (**Figure 3** and **Table 2**). The upper anomaly thresholds (UAT) of CH_4, H_2, CO_2, Rn, and Hg were 8.1 ppm, 47.7 ppm, 0.7%, 24.9 kBq/m^3, and 29.0 ng/m^3, respectively (**Figure 3** and **Table 2**). Accordingly, the data of each soil-gas species in the XXFS could be divided into the background (A), mixing (B), and anomaly (C) populations. The proportion and mean concentrations of each population of CH_4, H_2, CO_2, Rn, and Hg in the XXFS are listed in **Table 2**. The mean concentration of each gas species was calculated using **Eq. 1** (Sinclair, 1974):

$$P_M = f_A P_A + f_B P_B + f_C P_C \quad (1)$$

where P_M is the mean concentration of each gas species; f_A, f_B and f_C are the proportion of each population, and P_A, P_B, and P_C are

TABLE 3 | The $\delta^{13}C_{CO2}$ and $\delta^{13}C_{CH4}$ values of bubbling hot-spring gases in the XXFS.

No	Hot springs	Fault	Sampling date	Temp (°C)	$\delta^{13}C_{CH4}$ (‰, vs. PDB)	$\delta^{13}C_{CO2}$ (‰, vs. PDB)
①	Jinkagu	XSH	2017-7-17	16.5	n.d	−3.7
②	Kama	XSH	2017-7-13	32.0	−21.0	−5.2
③	Guanding	XSH	2017-7-6	75.8	−27.9	−6.0
④	Zimakua	ANH	2018-6-17	14.0	n.d	−5.9
⑤	Xide	ANH	2015-7-18	39.7	−49.0	−9.7
⑥	Hongmo	ANH	2017-1-7	49.2	17.0	−9.5
⑦	Liutie	ZMH	2017-1-8	57.9	−62.5	−6.7
⑧	Xundiantang	XJ	2017-1-10	58.2	−20.6	−4.1
⑨	Yiliang	XJ	2018-3-11	51.0	n.d	−11.9
⑩	Tangchi	XJ	2018-3-11	72.0	n.d	−6.9

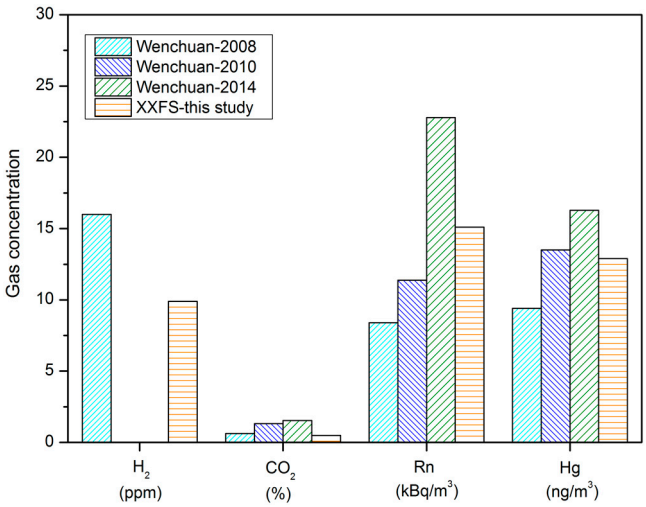


FIGURE 4 | Comparations of H_2, CO_2, Rn, and Hg concentrations in the XXFS and the surface rupture zone produced by the Wenchuan *Ms* 8.0 earthquake. Data sources: Zhou et al. (2010); Zhou et al. (2015); Zhou et al. (2016).

the mean gas concentrations of each population. Therefore, the mean concentrations of CH_4, H_2, CO_2, Rn, and Hg in the XXFS were calculated to be 8.1 ppm, 9.9 ppm, 0.5%, 15.1 kBq/m^3, and 12.9 ng/m^3, respectively (**Table 2**), which were close to the soil-gas concentrations measured in the surface rupture zone produced by the Wenchuan *Ms* 8.0 earthquake in 2008 and 2010 (**Figure 4**, Zhou et al., 2010; Zhou, et al., 2017).

The spatial distributions of soil-gas concentrations at the 10 measurement sites (obtained by using Kriging interpolation) are shown in **Figure 5**. From the spatial distributions of each gas species, high concentrations of soil gas were spatially coincident with the location of the fault and appeared close to the fault (**Figure 5**).

Origin of Carbon in the CO_2 and CH_4

Gas emissions from the fault zones are from multiple sources (e.g. Williams-Jones et al., 2000; Hong et al., 2010). Mantle, metamorphism of carbonate-bearing rocks, decomposition of organic material and surface biological activity are the principal sources of CO_2 in active fault zones (Irwin and Barnes, 1980; Toutain and Baubron, 1999), whereas microbiological and thermogenic genesis are the major processes of CH_4 genesis (e.g. Toutain and Baubron, 1999; Milkov and Etiope, 2018).

In this study, the $\delta^{13}C_{CO2}$ and $\delta^{13}C_{CH4}$ values of the hot-spring gas samples varied from -11.9‰ to -3.7‰ and -62.5‰ to 17‰, respectively (**Table 3**), and are consistent with the $\delta^{13}C_{CO2}$ and $\delta^{13}C_{CH4}$ values reported in previous studies (**Figure 6A**; Zhou et al., 2015; Shen et al., 2007). Combined with the carbon isotopic values reported in previous studies, the $\delta^{13}C_{CO2}$ and $\delta^{13}C_{CH4}$ values in the XXFS varied from -21.37‰ to -2.9‰ and -62.5‰ to 19‰, respectively (**Figure 6A** and **Supplementary Table S1**; Zhou et al., 2015; Shen et al., 2007).

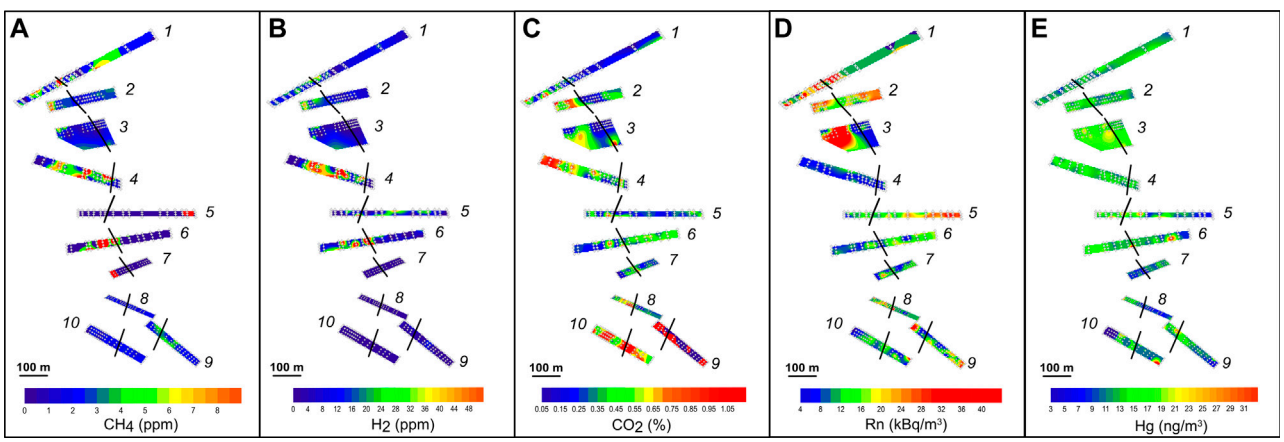


FIGURE 5 | Spatial distribution of soil-gas concentrations from M1–M10 in the XXFS. The white cross shows the distribution of the measurement points.

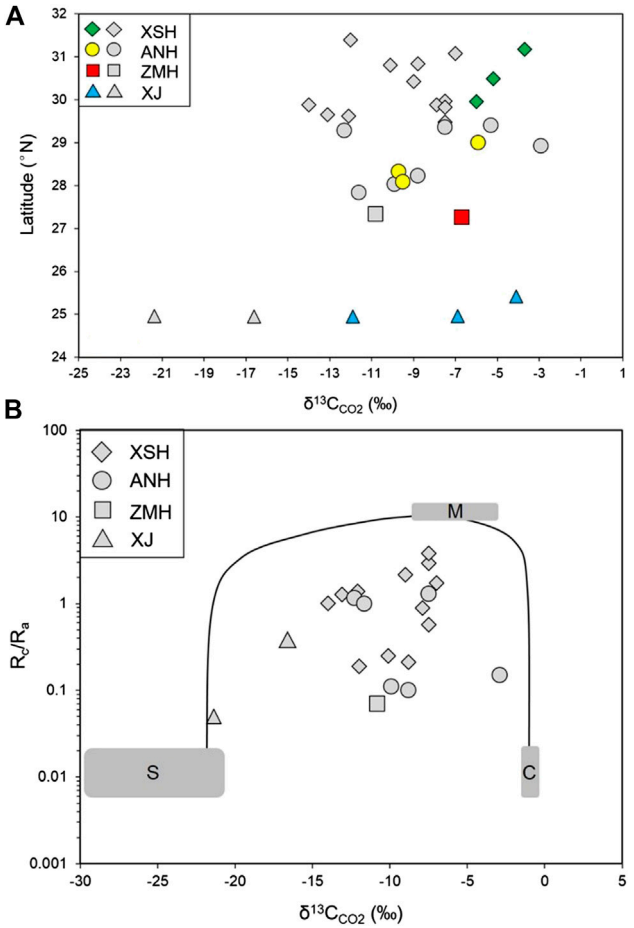


FIGURE 6 | (A) Plot of the $\delta^{13}C_{CO2}$ values from south to north along the XXFS. **(B)** R_c/R_a *vs.* $\delta^{13}C_{CO2}$ plot showing mixing of the end-members of mantle (M), crust (C), and sediment (S) of the bubbling gas samples in the XXFS. The colour symbols are data from bubbling hot-spring gas in this study. The grey symbols are hot-spring gas data reported in Shen et al. (2007) and Zhou et al. (2015). The He-C isotopic data in June 2009 were selected in this study in consideration of the significant influence of earthquake on the variations of He-C isotopic ratios (Zhou et al., 2015).

Previous studies indicated that upper mantle-derived CO_2 has $\delta^{13}C_{CO2}$ values between −3‰ and −9‰ with an average value of −6.5‰ (Javoy et al., 1986; Marty and Jambon, 1987). Soil organic matter derived from C3 and C4 plants have $\delta^{13}C_{CO2}$ values varying from −12‰ to −14‰ and −24‰ to −27‰, respectively (Cheng, 1996). The R_c/R_a-$\delta^{13}C_{CO2}$ plot reveals that the gas samples in the XXFS show characteristics of mixing among the end-members of the mantle, crust, and sediment (**Figure 6B**). However, the He-C isotopic ratios in the XSH and ANH faults showed obvious characteristics of mixing between the end-members of the mantle and crust, whereas those in the ZMH and XJ faults showed greater addition of organic sources (**Figure 6B**). The $\delta^{13}C_{CO2}$ values near M9 and M10 in the XJ fault are −21.37‰ to −6.9‰ (**Table 3** and **Supplementary Table S1**; Shen et al., 2007), with majority of the $\delta^{13}C_{CO2}$ values within the domain of organic carbon source.

The spatial distributions of the CO_2 concentration in the XXFS show that the highest concentrations of CO_2 were found at M9 and M10 in the XJ fault (**Figure 5C**). Therefore it could deduce that the carbon in the XJ fault in southern part of the XXFS has an organic carbon source.

CH_4 of microbial origin usually has $\delta^{13}C_{CH4}$ values < -55‰, whereas $\delta^{13}C_{CH4}$ values of thermogenic origin vary from −30‰ to −50‰ (Milkov and Etiope, 2018 and references therein). Abiotic CH_4 is ^{13}C-enriched with $\delta^{13}C_{CH4}$ values > −20‰ (Milkov and Etiope, 2018 and references therein). The $\delta^{13}C_{CH4}$-$\delta^{13}C_{CO2}$ diagram shows that the majority of the gas samples in the XXFS are plotted within the thermogenic and abiotic domains (**Figure 7**), indicating the mixing sources of CH_4 in the XXFS.

Geophysical studies (e.g. Liu and Wang, 2020) indicate that anomalies of low velocity and high Poisson's ratio are present at the XSH, ANH, and ZMH faults in the XXFS (26.5° N, 28° N, 29.5° N, 31.5° N, **Figure 1B** and Liu and Wang, 2020) and are interpreted as fluid intrusions (partial melt of deep material) from the lower crust and/or uppermost mantle. The $\delta^{13}C_{CO2}$ values in the XSH, ANH, and ZMH faults are higher than those in the XJ fault (**Figure 8A**; **Table 3** and **Supplementary Table S1**). According to previous studies, the $^3He/^4He$ ratios in the XXFS are 0.05–3.8 R_a (where R_a is the air-corrected $^3He/^4He$ ratios, **Supplementary Table S1**; Shen et al., 2007; Zhou et al., 2015), which lie within the typical crust and mantle domains (e.g. Sano and Marty, 1995; Zhang et al., 2017). The $^3He/^4He$ ratios in the XSH, ANH, and ZMH faults range from 0.19 to 3.8 R_a, 0.1–1.3 R_a, and 0.07 R_a, respectively, which are higher than those in the XJ fault (0.05–0.35 R_a) (**Figure 8B** and **Supplementary Table S1**). Analysis of He-C isotopic ratios in the XXFS was used to deduce that the carbon in the XSH, ANH, and ZMH faults might have originated from deep fluids, whereas the carbon in the XJ fault is of organic origin.

Anomaly and Degassing of Rn in the XXFS

Rn is inert and has low mobility in the geological environment (Tanner, 1964; Dubois et al., 1995). The uranium decay and the upward migration of Rn along the fault could represent the two sources of Rn in the fault zone (Toutain and Baubron, 1999; Sciarra et al., 2015; Sciarra et al., 2017; Sciarra et al., 2018; Sciarra et al., 2020). Previous studies indicate that the emanating power of the rock and soil, the permeability of the host rock, and the flow of the carrying gas are the primary factors that influence Rn activity in a diffusive system (e.g. Ball et al., 1991; Morawska and Phillips, 1993). Therefore, we used the formula of Åkerblom (1993) (**Eq. 2**), which is based on the ^{222}Rn activity at equilibrium with parent radionuclides (radium) in the soil, by verifying the anomaly threshold to determine the origin of Rn in the XXFS (Åkerblom, 1993; Sciarra et al., 2018):

$$C_{Rn} = C_{Ra}\varepsilon\rho n^{-1} \quad (2)$$

where C_{Rn} and C_{Ra} are the concentrations of Rn and radium in the soil gas (Bq/m^3) and soil (Bq/kg), respectively. ε is the emanation power coefficient (non-dimensional), ρ is the soil density (kg/m^3), and n is the effective porosity coefficient (non-dimensional).

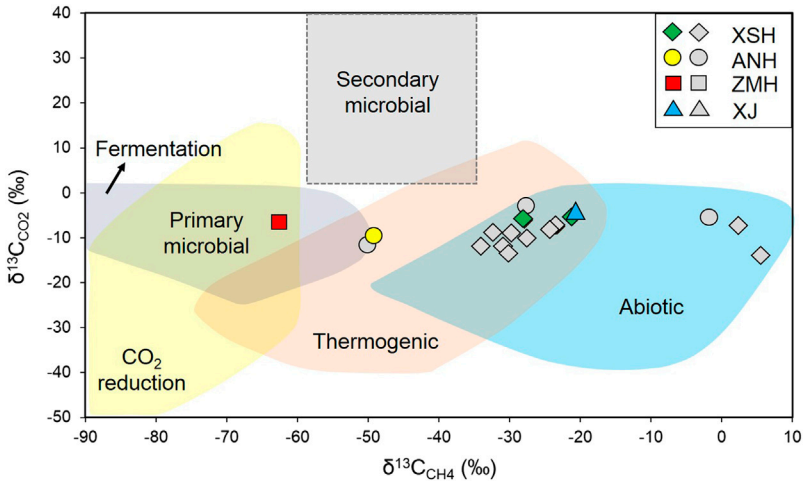


FIGURE 7 | Plot of $\delta^{13}C_{CO2}$ *vs.* $\delta^{13}C_{CH4}$. The colour symbols are data from bubbling hot-spring gas in this study. The grey symbols are hot-spring gas data reported in Shen et al. (2007) and Zhou et al. (2015). Modified after Milkov and Etiope (2018).

Previous studies show that the average content of soil radium-226 in China is 36.5 Bq/kg (e.g. Sun et al., 2004). The ε values are variable in different rock and soil types (e.g. Righi and Bruzzi, 2006; Jobbágy et al., 2009; Qin, 2012; Shen et al., 2012). The surrounding rocks and strata outcrop in the XXFS can be divided into four types: 1) volcanic rocks and acidic intrusions; 2) dolomite, limestone and carbonate; 3) sandstone; and 4) polyterrigenous materials (**Table 4**, BGMRSP, 1993). Therefore, the ε values of the four types of surrounding rocks and strata in the XXFS have values of 0.48 (Qin, 2012), 0.074 (Righi and Bruzzi, 2006; Jobbágy et al., 2009), 0.4 (Qin, 2012), and 0.12 (Shen et al., 2012), respectively (**Table 5**). The values of the soil porosity (n) were calculated using **Eq. (3)**:

$$n = 1 - (\text{subsoil bulk density}/2.65) \quad (3)$$

where 2.65 g/cm^3 is the mean density of soil porosity. The values of subsoil bulk density (kg/m^3) at a depth of 100 cm in the XXFS were selected from the Harmonized World Soil database (HWSD), which is elaborated by the Food and Agriculture Organization (FAO) (FAO/IIASA/ISRIC/ISSCAS/JRC, 2012). Therefore, the calculated Rn concentrations from M1–M10 in the XXFS ranged from 8.5 kBq/m^3 to 61.1 kBq/m^3 (**Table 5**), with mean value of 40.2 kBq/m^3. The calculated Rn concentration in the XXFS was higher than the statistically defined anomaly threshold (24.9 kBq/m^3) (**Table 2**). Therefore, the Rn concentrations that exceeded the calculated value were likely not supported by *in-situ* production.

The measurement sites with high Rn concentrations were spatially consistent with the distributions of the volcanic and acidic intrusions in the XXFS (**Figure 5D** and **Table 4**). The abovementioned analysis concluded that the concentrations of Rn lower than the UAT in the XXFS might originate from *in-situ* production. Rn concentrations higher than the UAT in the XXFS might be related to the upward migration of Rn along the

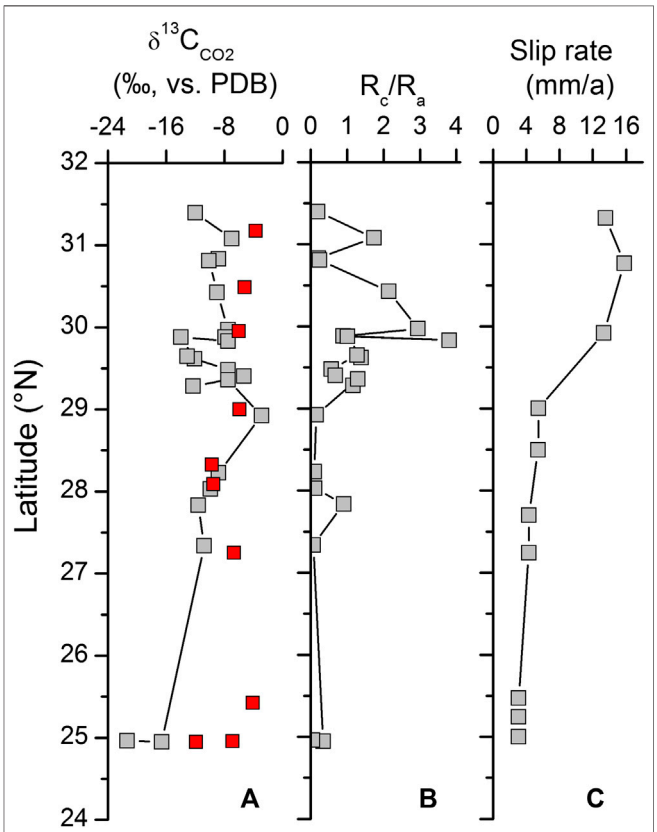


FIGURE 8 | Variations of $\delta^{13}C_{CO2}$ values **(A)**, R_c/R_a ratios **(B)**, and fault slip rates **(C)** from north to south in the XXFS. The colour symbols are data reported in this study. The grey symbols are data reported by previous studies. Data sources: Chen (2006), Shen et al. (2007), Shi et al. (2012), Zhou et al. (2015), and Yue et al. (2017).

TABLE 4 | Strata of the measurement sites in the XXFS.

Measurement site	Strata[a]
M1	Intermediate volcanic rock
M2	Basic volcanic rock
M3	Indosinian intermediate and acidic intrusions
M4	Chengjiangian intermediate and acidic intrusions
M5	(1) yanshanian intermediate and acidic intrusions (2) intermontane depression and fault-subsidence
M6	Multicolored polyterrigenous, red polyterrigenous and molasse formation
M7	Algal-reef carbonate, distal siliceous and endogenous carbonate formation
M8	(1) sandstone, shale and carbonateous shale intercalated with carbonate rock (2) dolomite and limestone intercalated with siltstone and shale
M9	(1) basic volcanic rock (2) dolomite and limestone
M10	Basic volcanic rock

[a]*Data sources: BGMRSP, 1993.*

TABLE 5 | Parameters of radium concentration (C_{Ra}), emanation power coefficient (ε), soil density (ρ), and effective porosity coefficient (n) in the XXFS.

Site	C_{Ra}[a] (Bq/kg)	ε[b]	ρ[c] (kg/m^3)	n[d]	C_{Rn} (kBq/m^3)
M1	36.5	0.48	1,490	0.44	59.3
M2	36.5	0.48	1,140	0.57	35.0
M3	36.5	0.48	1,390	0.48	50.7
M4	36.5	0.48	1,510	0.43	61.5
M5	36.5	0.12	1,350	0.49	12.1
M6	36.5	0.12	1,350	0.49	12.1
M7	36.5	0.074	1,440	0.46	8.5
M8	36.5	0.4	1,500	0.43	50.9
M9	36.5	0.48	1,380	0.48	50.4
M10	36.5	0.48	1,500	0.43	61.1

[a]*Data sources: Sun et al. (2004).*
[b]*Data sources: Righi and Bruzzi (2006); Jobbágy et al. (2009); Qin (2012); Shen et al. (2012).*
[c]*Data sources: the Harmonized World Soil database (HWSD).*
[d]*The soil porosity is calculated by using the formula n = 1-(subsoil bulk density/2.65). The soil density took value of 2.65 g/cm^3, which is the mean density of soil porosity. See details in the text.*

faults. Rn degassing from the fault was also verified by the spatial distributions of Rn concentrations in the XXFS (**Figure 5D**). Additionally, the high concentrations of Rn in M5 (**Figure 5D**) demonstrate the degassing of Rn from the fault according to the field survey.

Relationship Between Soil-Gas Concentration and Fault Activity

In our study, high concentrations of Rn were primarily found at the XSH fault (**Figure 5D** and **Table 1**), which has the highest stress, fault slip rate, and maximum strain rate in the XXFS (**Figure 8C** and Chen., 2006; He and Lu, 2007; Shi et al., 2012; Zhao et al., 2015; Yue et al., 2017; Li et al., 2019). Fault activity can facilitate the transport of fluids due to episodic fracturing events that can release quantities of deep fluids (Evans et al., 1997; Kulongoski et al., 2005; Tanikawa et al., 2010; Zhang et al., 2016).

In our study, granites are well-developed in the XSH fault (BGMRSP, 1993; **Table 4**). In a previous study, the permeability of granites increased by three orders of magnitude as the slip rate increased, indicating that increasing the slip rate could create and maintain elevated fault permeability (Zhang et al., 2017).

From the spatial distributions of soil gases in the XXFS (**Figure 5**), the anomalously high concentrations of CH_4, H_2, CO_2, Rn, and Hg appeared near the fault, which might indicate that the fault slip-rate influenced degassing from the active fault zone. The elevated permeability of the fault facilitates the migration of gases in the active fault zone. The different patterns of soil-gas concentrations across the fault might be influenced by the permeability of the fault zone, such as the porosity of the fault and soil characteristics of the measurement site (e.g. Fu et al., 2005).

CONCLUSION

In this study, the geochemical characteristics of soil gas and the relationship between degassing and fault activity in the XXFS were examined. Summarising:

(1) The mean concentrations of CH_4, H_2, CO_2, Rn, and Hg in the XXFS are 8.1 ppm, 9.9 ppm, 0.5%, 15.1 kBq/m^3, and 12.9 ng/m^3, respectively. Anomalously high concentrations of soil gases primarily appeared near the fault, indicating the degassing of faults in the XXFS.
(2) In the XXFS, the $\delta^{13}C_{CO2}$ and $\delta^{13}C_{CH4}$ values varied from −11.9‰ to -3.7‰ and −62.5‰ to 17‰, respectively. He-C

isotopic analysis indicates that the soil gas in the XSH, ANH, and ZMH faults might have originated from deep fluids, whereas the carbon in the XJ fault is of organic origin. The CH_4 in the XXFS might have thermogenic and abiotic origins.

(3) The concentrations of Rn lower than the UAT in the XXFS might be due to the *in-situ* production. The anomaly of Rn concentrations (higher than the UAT) in the XXFS might be related to the upward migration of Rn along the faults.

(4) The distributions of the high concentrations of soil gases were spatially coincident with the highest stress and the maximum strain rate in the XXFS, which might indicate that the fault activity enhanced permeability and, thus, increased gas emission rates.

DATA AVAILABILITY STATEMENT

The original contributions presented in the study are included in the article/**Supplementary Material**, further inquiries can be directed to the corresponding author.

AUTHOR CONTRIBUTIONS

YS: Methodology, data analysis, conceptualization and writing XZ: Investigation, methodology and conceptualization YY: Investigation JL: Investigation WF: Investigation WW: Investigation YL: Investigation.

FUNDING

This study was supported by the National Key Research and Development Project (2017YFC1500501), the National Natural Science Foundation of China (41673106, 41902312), the Special Fund of the Institute of Earthquake Forecasting, China Earthquake Administration (2017IES010205, 2016IES010304, 2018IES010104, 2020IEF0604, 2020IEF0703) and the Natural Science Foundation of Hebei Province (D2020403050).

ACKNOWLEDGMENTS

The authors are grateful to Fang Du and Hong Fu for their assistance with fieldwork. Two anonymous referees are acknowledged for their extremely constructive reviews of an earlier version of the paper. We thank the journal editor, Francesco Italiano, for his support. Harmonized World Soil Database (HWSD) is thanked for providing the soil data in this research. The CGIAR Consortium for Spatial Information (CGIAR-CSI) provided the STRM data.

SUPPLEMENTARY MATERIAL

The Supplementary Material for this article can be found online at: https://www.frontiersin.org/articles/10.3389/feart.2021.635178/full#supplementary-material.

REFERENCES

Åkerblom, G. (1993). *Ground radon: monitoring procedure in Sweden: lecture at the"JAG" discussion meeting on "radon workshop, Geology, environment, technology"*. London,United Kingdom: Royal Astronomical Society.

Allen, C. R., Luo, Z. L., Qian, H., Wen, X. Z., Zhou, H. W., and Huang, W. S. (1991). Field study of a highly active fault zone: the Xianshuihe fault of southwestern China. *Geol. Soc. Am. Bull.* 103, 1178–1199.

Ball, T. K., Cameron, D. G., Colman, T. B., and Roberts, P. D. (1991). Behaviour of radon in the geological environment: a review. *Q. J. Eng. Geol.y* 24, 169–182.

BGMRSP (1993). *Regional Geology of xizang (Tibet) autonomous region*. Beijing, China: Geological Publishing House.

Bohnhoff, M., and Zoback, M. D. (2010). Oscillation of fluid-filled cracks triggered by degassing of CO_2 due to leakage along wellbores. *J. Geophys. Res.* 115, B11305. doi:10.1029/2010JB000848

Chen, G. (2006). Structural transformation and strain partitioning along the northeast boundary belt of the Sichuan-Yunnan Block. Doctor's Thesis. Beijing (China): Institute of Geology, China Earthquake Administration.

Cheng, W. (1996). Measurement of rhizosphere respiration and organic matter decomposition using natural 13C. *Plant and Soil* 183, 263–268.

Chiodini, G., Cardellini, C., Amato, A., Boschi, E., Caliro, S., Frondini, F., et al. (2004). Carbon dioxide Earth degassing and seismogenesis in central and southern Italy. *Geophys. Res. Lett.* 31, L07615. doi:10.1029/2004GL019480

Ciotoli, G., Bigi, S., Tartarello, C., Sacco, P., Lombardi, S., Ascione, A., et al. (2014). Soil gas distribution in the main coseismic surface rupture zone of the 1980, Ms = 6.9, Irpinia earthquake (southern Italy). *J. Geophys. Res. Solid Earth* 119, 2440–2461. doi:10.1002/2013JB010508

Ciotoli, G., Etiope, G., Marra, F., Florindo, F., Giraudi, C., and Ruggiero, L. (2016). Tiber delta CO_2-CH_4 degassing: a possible hybrid, tectonically active Sediment-Hosted Geothermal System near Rome. *J. Geophys. Res. Solid Earth* 121, 48–69. doi:10.1002/2015JB012557

Di Martino, R. M. R., Capasso, G., and Camarda, M. (2016). Spatial domain analysis of carbon dioxide from soils on Vulcano Island: implications for CO_2 output evaluation. *Chem. Geol.* 444, 59–70. doi:10.1016/j.chemgeo.2016.09.037

Du, J., Si, X., Chen, Y., Fu, H., and Jian, C. (2008). "Geochemical anomalies connected with great earthquakes in China," in *Geochemistry research advances*. Editor Stefánssonó (New York, NY: Nova Science Publishers, 57–92.

Dubois, C., Alvarez Calleja, A., Bassot, S., and Chambaudet, A., (1995). "Modelling the 3-dimensional microfissure network in quartz in a thin section of granite," in *Gas geochemistry*. Editor C. Dubois (Northwood, London: Science Reviews), 357–368.

Einarsson, P., Theodórsson, P., Hjartardóttir, Á. R., and Guðjósson, G. I. (2008). Radon changes associated with the earthquake sequence in June 2000 in the south Iceland seismic zone. *Pure Appl. Geophys.* 1, 63–74. doi:10.1007/s00024-007-0292-6

Evans, J. P., Foster, C. B., and Goddard, J. V. (1997). Permeability of fault-related rocks, and implications for hydraulic structure of fault zones. *J. Struct. Geol.* 19, 1393–1404.

FAO/IIASA/ISRIC/ISSCAS/JRC (2012). *Harmonized World soil Database (version 1.2)*. RomeLaxenburg, Austria: FAO.

Fu, C., Yang, T. F., Walia, V., and Chen, C. (2005). Reconnaissance of soil gas composition over the buried fault and fracture zone in southern Taiwan. *Geochem. J.* 39, 427–439. doi:10.2343/geochemj.39.427

He, J., and Lu, S. (2007). Lower friction of the Xianshuihe–Xiaojiang fault system and its effect on active deformation around the south-eastern Tibetan margin. *Terra Nova* 19, 204–210. doi:10.1111/j.1365-3121.2007.00735.x

Hong, W., Yang, T., Walia, V., Lin, S., Fu, C., Chen, Y., et al. (2010). Nitrogen as the carrier gas for helium emission along an active fault in NW Taiwan. *J. Appl. Geochem.* 25, 593–601. doi:10.1016/j.apgeochem.2010.01.016

Irwin, W. P., and Barnes, I. (1980). Tectonic relations of carbon dioxide discharges and earthquakes. *J. of Geo. Res.* 85, 3115–3121. doi:10.1029/JB085iB06p03115

Javoy, M., Pineau, F., and Delorme, H. (1986). Carbon and nitrogen isotopes in the mantle. *Chem. Geol* 57, 41–62. doi:10.1016/0009-2541(86)90093-8

Jiang, G., Xu, X., Chen, G., Liu, Y., Fukahata, Y., Wang, H., et al. (2014). Geodetic imaging of potential seismogenic asperities on the Xianshuihe-Anninghe-Zemuhe fault system, southwest China, with a new 3-D viscoelastic interseismic coupling model. *J. Geophys. Res. Solid Earth* 120, 1855–1873. doi:10.1002/2014JB011492

Jobbágy, V., Somlai, J., Kovács, J., Szeiler, G., and Kovács, T. (2009). Dependence of radon emanation of red mud bauxite processing wastes on heat treatment. *J. Hazard. Mater* 172, 1258–1263. doi:10.1016/j.jhazmat.2009.07.131

King, C. Y. (1986). Gas geochemistry applied to earthquake prediction: an overview. *J. Geophys. Res. Solid Earth* 91, 12269–12281. doi:10.1029/JB091iB12p12269

Kulongoski, J., Hilton, D., and Izbicki, J. (2005). Source and movement of helium in the eastern Morongo groundwater Basin: the influence of regional tectonics on crustal and mantle helium fluxes. *Geochim. Cosmochim. Acta* 69, 3857–3872. doi:10.1016/j.gca.2005.03.001

Li, Q., Wang, Y., Zhou, Y., and Zhao, C. (2018). Geochemical characteristics of hot spring gases from the Deqing-Zhongdian area, northwestern Yunnan, China. *Bull. Mineral. Petrol. Geochemistry* 37, 645–651. doi:10.19658/j.issn.1007-2802.2018.37.097

Li, Y., Du, J., Wang, F., Zhou, X., Pan, X., and Wei, R. (2009). Geochemical characteristics of soil gas in Yanqing-Huailai basin, North China. *Acta Seismologica Sinica* 31, 82–91.

Li, Y., Liu, M., Li, Y., and Chen, L. (2019). Active crustal deformation in southeastern Tibetan Plateau: the kinematics and dynamics. *Earth Planet. Sci. Lett.* 523, 115708. doi:10.1016/j.epsl.2019.07.010

Liu, G., and Wang, Z. (2020). Correlations of the deep structural characteristics, tidal stress variation and earthquake initiation along the Xianshuihe-Anninghe fault zone. *Chinese J. of Geophy.* 63, 928–943. doi:10.6038/cjg2020N0206

Marty, B., and Jambon, A. (1987). $C/^3He$ in volatile fluxes from the solid Earth: implications for carbon geodynamics. *Earth and Planetary Science Letters* 83, 16–26.

Milkov, A. V., and Etiope, G. (2018). Revised genetic diagrams for natural gases based on a global dataset of >20,000 samples. *Organic Geochemistry* 125, 109–120. doi:10.1016/j.orggeochem.2018.09.002

Morawska, L., and Phillips, C. R. (1993). Dependance of the radon emanation coefficient on radium distribution and internal structure of the material. *Geochimica et Cosmochimica Acta* 57, 1783–1797.

Qin, C. (2012). *Study on distribution and model of soil radon in South China*. Beijing, China: Master degree thesis of China University of Geosciences (Beijing), 1–41.

Ren, Z., Lin, A., and Rao, G. (2010). Late pleistocene–holocene activity of the Zemuhe fault on the southeastern margin of the Tibetan plateau. *Tectonophysics* 495, 324–336. doi:10.1016/j.tecto.2010.09.039

Righi, S., and Bruzzi, L. (2006). Natural radioactivity and radon exhalation in building materials used in Italian dwellings. *J Environ Radioact* 88, 158–170. doi:10.1016/j.jenvrad.2006.01.009

Sano, Y., and Marty, B. (1995). Origin of carbon in fumarolic gas from island arcs. *Chemical Geology* 119, 265–274.

Sciarra, A., Cantucci, B., and Coltorti, M. (2017). Learning from soil gas change and isotopic signatures during 2012 Emilia seismic sequence. *Sci Rep.* 7, 14187. doi:10.1038/s41598-017-14500-y

Sciarra, A., Cantucci, B., Sapia, V., De Ritis, R., Ricci, T., Civico, R., et al. (2020). Geochemical and geoelectrical characterization of the Terre Calde di Medolla (Emilia-Romagna, northern Italy) and relations with 2012 seismic sequence. *J. of Geochemical Exploration* 221, 106688. doi:10.1016/j.gexplo.2020.106678

Sciarra, A., Fascetti, A., Moretti, A., Cantucci, B., Pizzino, L., Lombardi, S., et al. (2015). Geochemical and radiometric profiles through an active fault in the Sila Massif (Calabria, Italy). *J. for Geochemical Exploration* 148, 128–137. doi:10.1016/j.gexplo.2014.08.015

Sciarra, A., Mazzini, A., Inguaggiato, S., Vita, F., Lupi, A., and Hadi, S. (2018). Radon and carbon gas anomalies along the Watukosek fault system and Lusi mud eruption, Indonesia. *Marine and Petroleum Geology* 90, 77–90. doi:10.1016/j.marpetgeo.2017.09.031

Shen, C., Shen, L., Xiao, D., and Tan, Y. (2012). Numerical computation of radon distribution in different soils. *Atomic Energy Science and Technology* 46, 370–374.

Shen, L., Yuan, D., Ding, T., Li, Y., Le, G., and Lin, Y. (2007). Distributing inhomogeneity of helium isotope of CO_2 degasification point and its geotectogenesis in southwest of China. *Acta Geologica Sinica* 81, 475–487.

Shi, F., You, W., and Yun, W. (2012). Recent crustal movement characteristics of Xiaojiang River fault based on the GPS data. *J. of Seismological Research* 35, 207–212.

Sinclair, A. J. (1991). A fundamental approach to threshold estimation in exploration geochemistry: probability plots revisited. *J. of Geochemical Exploration* 41, 1–22. doi:10.1016/0375-6742(91)90071-2

Sinclair, A. J. (1974). Selection of threshold values in geochemical data using probability graphs. *J. Geochem. Explor.* 3, 129–149.

Sun, K., Guo, Q., and Zhuo, W. (2004). Feasibility for mapping radon exhalation rate from soil in China. *J Nucl Sci Technol* 41, 86–90. doi:10.1080/18811248.2004.9715462

Tanikawa, W., Sakaguchi, M., Tadai, O., and Hirose, T. (2010). Influence of fault slip rate on shear-induced permeability. *J. of Geophys. Res.* 115, B07412. doi:10.1029/2009JB007013

Tanner, A. B. (1964). "Radon migration in the ground: a review," in *Natural radiation environment*. Editors J. A. Adams and W. Lowder (Illinois, IL: University of Chicago Press), 161–190.

Tapponnier, P., Zhiqin, X., Roger, F., Meyer, B., Arnaud, N., Wittlinger, G., et al. (2001). Oblique stepwise rise and growth of the Tibet plateau. *Science* 294, 1671–1677. doi:10.1126/science.105978

Toutain, J. P., and Baubron, J. C. (1999). Gas geochemistry and seismotectonics: a review. *Tectonophysics* 304, 1–27.

Walia, V., Lin, S. J., Fu, C. C., Yang, T. F., Hong, W., Wen, H., et al. (2010). Soil–gas monitoring: a tool for fault delineation studies along Hsinhua Fault (Tainan), Southern Taiwan. *J. Appl. Geochem.* 25, 602–607. doi:10.1016/j.apgeochem.2010.01.017

Wang, H., Liu, J., Shi, Y., Zhang, H., and Zhang, G. (2008). Dynamic simulation of interactions between major earthquakes on the Xianshuihe fault zone. *Science in China Series D: Earth Sciences* 51, 1388–1400. doi:10.1007/s11430-008-0110-8

Wen, X., Du, F., Long, F., and Zhu, H. (2011). Tectonic dynamics and correlation of major earthquake sequences of the Xiaojiang and Qujiang-Shiping fault systems, Yunnan, China. *Sci China Earth Sci* 54, 1563–1575. doi:10.1007/s11430-011-4231-0

Williams-Jones, G., Stix, J., Heiligmann, M., Charland, A., Sherwood Lood, B., Arner, N., et al. (2000). A model of diffuse degassing at three subduction-related volcanoes. *Bull. Volcanol.* 62, 130–142. doi:10.1007/S004450000075

Xiang, Y., Sun, X., Liu, D., Yan, L., Wang, B., and Gao, X. (2020). Spatial distribution of Rn, CO_2, Hg, and H_2 concentrations in soil gas across a thrust fault in Xinjiang, China. *Front. Earth Sci.* 8, 554924. doi:10.3389/feart.2020.554924

Yang, T. F., Wen, H., Fu, C., Lee, H., Lan, T., Chen, A., et al. (2011). Soil radon flux and concentrations in hydrothermal area of the tatun volcano group, northern taiwan. *Geochem. J.* 45, 483–490.

Yuce, G., Fu, C. C., D'Alessandro, W., Gulbay, A. H., Lai, C. W., Bellomo, S., et al. (2017). Geochemical characteristics of soil radon and carbon dioxide within the dead sea fault and karasu fault in the mik basin (hatay), Turkey. *Chem. Geol.* 469, 129–146.

Yue, C., Dang, Y., Yang, Q., and Zou, B. (2017). Analysis of the current activity in Sichuan-Yunnan Region and its sub blocks of main faults. *Geod Geodyn.* 37, 176–181.

Zhang, L., Liu, Y., Bao, C., Gao, X., Su, Q., and Fang, Z. (2019b). Characteristics of fault soil gas in Manning of western Sichuan Province, China. *Environmental Chemistry* 38, 777–783. doi:10.7524/j.issn.0254-6108.2018100501

Zhang, L., Liu, Y. W., Bao, C., and Guo, L. S. (2019a). Distribution characteristics of soil mercury in Anninghe fault zone. *Acta Seismologica Sinica* 41, 249–258. doi:10.11939/jass.20180141

Zhang, M., Guo, Z., Zhang, L., Sun, Y., and Cheng, Z. (2017). Geochemical constraints on origin of hydrothermal volatiles from southern Tibet and the Himalayas: understanding the degassing systems in the India-Asia continental subduction zone. *Chemical Geology* 469, 19–33. doi:10.1016/j.chemgeo.2017.02.023

Zhang, W., Du, J., Zhou, X., and Wang, F. (2016). Mantle volatiles in spring gases in the Basin and Range Province on the west of Beijing, China: constraints from

helium and carbon isotopes. *J Volcanol Geotherm Res.* 309, 45–52. doi:10.1016/j.jvolgeores.2015.10.024

Zhao, J., Jiang, Z. S., Niu, A. F., Liu, J., Wu, Y. Q., Wei, W. X., et al. (2015). Study on dynamic characteristics of fault locking and fault slip deficit in the eastern boundary of the Sichuan-Yunnan rhombic block. *Chinese J. of Geophy.* 58, 872–885. doi:10.6038/cjg20150316

Zhou, X., Chen, Z., and Cui, Y. (2016). Environmental impact of CO_2, Rn, Hg degassing from the rupture zones produced by Wenchuan M s 8.0 earthquake in western Sichuan, China. *Environ Geochem Health* 38, 1067. doi:10.1007/s10653-015-9773-1

Zhou, X., Du, J., Chen, Z., Cheng, J., Tang, Y. L., et al. (2010). Geochemistry of soil gas in the seismic fault zone produced by the Wenchuan Ms 8.0 earthquake, southwestern China. *Geochem Trans* 11, 5. doi:10.1186/1467-4866-11-5

Zhou, X. C., Sun, F. X., Chen, Z., Lv, C. J., Li, J., Wu, K. T., et al. (2017). Degassing of CO_2, CH_4, Rn, and Hg in the rupture zones produced by Wenchuan Ms 8.0 earthquake. *Acta Petrologica Sinica* 33, 291–303.

Zhou, X. C., Wang, W. L., Li, L. W., Hou, J. M., Xing, L. T., Li, Z. P., et al. (2020). Geochemical features of hot spring gases in the Jinshajiang-Red River fault zone, Southeast Tibetan Plateau. *Acta Petrologica Sinica* 36, 2197–2214. doi:10.18654/1000-0569/2020.07.18

Zhou, X., Wang, W., Chen, Z., Li, Y., Liu, L., Xie, C., et al. (2015). Hot spring gas geochemistry in western sichuan Province, China after the wenchuan ms 8.0 earthquake. *Terrestrial Atmospheric and Oceanic Sciences* 26, 361–373.

Conflict of Interest: The authors declare that the research was conducted in the absence of any commercial or financial relationships that could be construed as a potential conflict of interest.

Copyright © 2021 Sun, Zhou, Yan, Li, Fang, Wang and Liu. This is an open-access article distributed under the terms of the Creative Commons Attribution License (CC BY). The use, distribution or reproduction in other forums is permitted, provided the original author(s) and the copyright owner(s) are credited and that the original publication in this journal is cited, in accordance with accepted academic practice. No use, distribution or reproduction is permitted which does not comply with these terms.

frontiers in Earth Science

ORIGINAL RESEARCH
published: 26 March 2021
doi: 10.3389/feart.2021.635893

Geochemical Characteristics of Gas and Flowback Water in Lake Facies Shale: A Case Study From the Junggar Basin, China

Lin Zhang[1,2], *Dan Liu*[3,4]*, *Yongjin Gao*[2] *and Min Zhang*[1]

[1]College of Resource and Environment, Yangtze University, Wuhan, China, [2]Oil and Gas Survey, China, Geological Survey, Beijing, China, [3]PetroChina Research Institute of Petroleum Exploration and Development, Beijing, China, [4]Institute of Geology and Geophysics, Chinese Academy of Sciences, Beijing, China

The chemical and isotopic compositions of the natural gas and the co-produced flowback water from the XJC 1 well in Junggar Basin, China, were analyzed to determine the origin of gases in the Permian Lucaogou Formation (P_2l) and the Triassic Karamay Formation (T_2k) in the Bogda Mountain periphery area of the Southern Junggar Basin. The value of carbon isotope composition of the P_2l lacustrine shale gas in the Junggar Basin was between the shale gas in Chang 7 Formation of Triassic (T_1y_7) in the Ordos Basin and that in the Xu 5 Formation of Triassic (T_3x_5) in the Sichuan Basin. The difference in gas carbon isotope is primarily because the parent materials were different. A comparison between compositions in the flowback water reveals that the P_2l water is of $NaHCO_3$ type while the T_2k water is of NaCl type, and the salinity of the latter is higher than the former, indicating a connection between P_2l source rock and the T_2k reservoir. In combination with the structural setting in the study area, the gas filling mode was proposed as follows: the gas generated from the lacustrine source rocks of the Permian Lucaogou Formation is stored in nearby lithological reservoirs from the Permian. Petroleum was also transported along the faults to the shallow layer of the Karamay Formation over long distances before it entered the Triassic reservoir.

Keywords: shale gas, potential, maturity, parent material, exploration and development

OPEN ACCESS

Edited by:
Guodong Zheng,
Chinese Academy of Sciences (CAS), China

Reviewed by:
Wenhui Liu,
Northwest University, China
Quanyou Liu,
SINOPEC Petroleum Exploration and Production Research Institute, China

***Correspondence:**
Dan Liu
liudan86@petrochina.com.cn

Specialty section:
This article was submitted to Geochemistry, a section of the journal Frontiers in Earth Science

Received: *30 November 2020*
Accepted: *15 February 2021*
Published: *26 March 2021*

Citation:
Zhang L, Liu D, Gao Y and Zhang M (2021) Geochemical Characteristics of Gas and Flowback Water in Lake Facies Shale: A Case Study From the Junggar Basin, China. Front. Earth Sci. 9:635893. doi: 10.3389/feart.2021.635893

INTRODUCTION

Shale gas is a growing part of global unconventional energy, and the development of hydraulic fracturing technologies has paved the way for increasing gas production. China possesses the largest shale gas reserves worldwide, with a geological resource volume of 80.45 trillion m^3. In 2019, China's annual shale gas production reached 15.4 billion cubic meters, the second-highest in the world. However, many environmental concerns are associated with hydraulic fracturing for shale gas. Two major geochemical fields related to shale gas are currently focused on: 1) the composition and isotopes of shale gases and the related issues such as the gas origin and generating mechanism (Jenden et al., 1993; Hill et al., 2007; Martini et al., 2008; Burruss and Laughrey, 2010; Strąpoć et al., 2010; Hunt et al., 2012; Zumberge et al., 2012; Hao and Zou, 2013; Tilley and Muehlenbachs, 2013; Dai et al., 2014; Feng et al., 2016); and 2) the geochemistry of water coproduced with the shale gas and related environmental issues (Chapman et al., 2012; Warner et al., 2013, 2014; Vengosh et al., 2014; Vengosh et al., 2017; Lauer et al., 2016; Zheng et al., 2017; Ni et al., 2018; Zou et al., 2018; Liu et al., 2020).

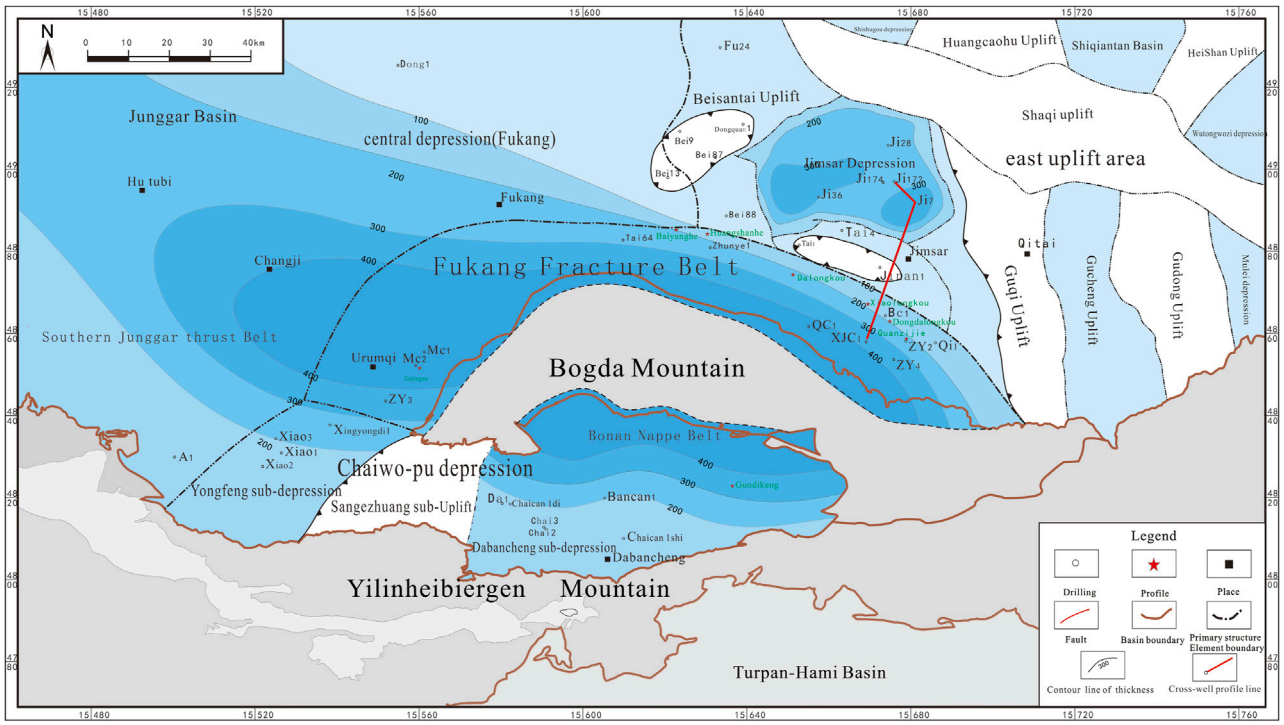


FIGURE 1 | Distribution of source rocks of Lucaogou Formation in the periphery of Bogda Mountain.

Most global gas resources are located in marine shale. As a result, marine shale gas geochemistry has been extensively studied in the United States, Canada (Jenden et al., 1993; Hill et al., 2007; Martini et al., 2008; Burruss and Laughrey, 2010; Strąpoć et al., 2010; Hunt et al., 2012; Zumberge et al., 2012; Tilley and Muehlenbachs, 2013), and the Sichuan Basin of China (Hao and Zou, 2013; Dai et al., 2014; Feng et al., 2016). Moreover, the majority of studies on water geochemistry and the environmental issues related to shale gas exploration are about marine shale (Chapman et al., 2012; Vengosh et al., 2014, 2017; Warner et al., 2014; Ni et al., 2018; Zou et al., 2018; Liu et al., 2020). Few studies have been conducted on the geochemical characteristics of terrestrial shale gas (Dai et al., 2016) and the impact of hydraulic fracturing in terrestrial shale (Zheng et al., 2017).

From the Precambrian to the Neogene, abundant organic-rich shale strata developed in China. The shale formed in three major sedimentary environments, namely marine facies, marine-terrestrial transitional-lacustrine coal facies, and lacustrine facies. The recoverable shale gas generated from continental shale (marine-terrestrial transitional shale and lacustrine shale) reached 4.03 trillion m^3, accounting for 31% of the recoverable shale gas resources in China. The gas geochemistry of the continental shale differs from that of marine shale, and the water chemistry and water-rock reaction process of the two kinds of shale are also quite different. The origin of shale gas and wastewater treatment plans both require further studies.

In 2019, the completion of Well XJC 1 in the Bogda Piedmont of Junggar Basin marked a significant breakthrough (**Figure 1**), with the daily gas production of 1.8 × 104 m^3 and daily oil production of 0.41 t in the Permian Lucaogou Formation. Later, in the same well, gas was detected in the overlying Triassic Karamay Formation. This is the first time that the industrial gas flow of Lucaogou Formation and the Karamay Formation on the southern margin of the Junggar Basin have been obtained, and the result highlights the shale gas exploration potential in the Bogda piedmont of the Junggar Basin. The Lucaogou shale is of lacustrine facies and the continental shale is widely distributed in Western China.

In this work, the composition and isotope of gas in the Lucaogou Formation of Permian (P_2l) was analyzed for well XJC 1. The source rock of the Lucaogou Formation in the periphery of Bogda Mountain was evaluated to establish future areas for shale gas exploration in the study area. The geochemical data of marine shale gas in the Longmaxi Formation and swamp shale gas in the Xu 5 Formation (both situated in the Sichuan Basin), and lake shale gas in the Chang 7 Formation (situated in the Ordos Basin) were obtained from the literature (Dai et al., 2016) to compare with the Lucaogou shale gas. The gas in the Karamay Formation of Triassic (T_2k) could not be obtained; thus, the flowback water from the T_2k reservoir and P_2l shale was compared, in combination with the geological setting, to study the T_2k and P_2l gas origin and the gas filling mode. Additionally, the flowback fluid of unconventional shale reservoirs in the Lucaogou Formation and that of conventional reservoirs in the Karamay Formation were compared to analyze the unconventional flowback water and establish water environmental protection measures that should be

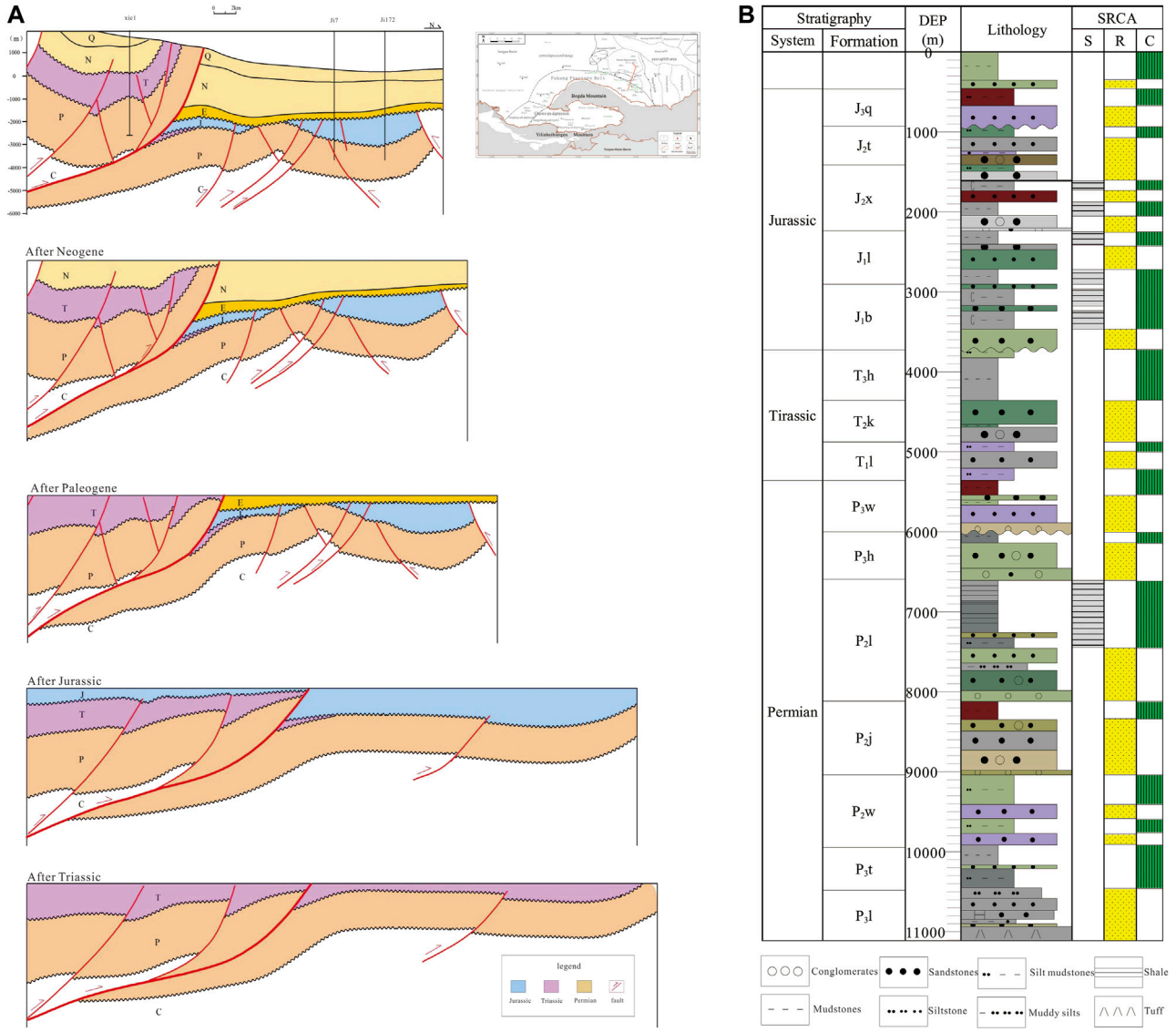


FIGURE 2 | (A) The tectonic evolution of the periphery of the Bogda Mountain; **(B)** Chronostratigraphy of southern Junggar Basin.

implemented during shale gas exploration and development in the area.

GEOLOGICAL CHARACTERISTICS OF THE STUDY AREA

Regional Setting

The Bogda Mountain periphery includes two secondary structural units, the Fukang Fault Zone on the northern margin and the Chaiwopu Sag on the southern margin, located in the eastern part of the southern Junggar thrust belt in the Junggar Basin (**Figure 1**). The Fukang Fault Zone and the Chaiwopu Sag are divided by the uplift of the Bogda Mountains, structural evolution, and hydrocarbon generation. The accumulation area is structurally too complex for oil and gas exploration in northern Xinjiang. Well XJC 1 is located in the Fukang Fault Zone. This area has complex structural deformations, highly developed faults, and diverse trap types. Insufficient research on the source rocks of the Permian Lucaogou Formation limits the evaluation of the oil and gas resource potential for this formation.

Structural Characteristics

The tectonic evolution of the Bogda Mountain periphery is divided into five stages: 1) Early Permian-Middle Permian when the basin was in the extensional rift stage. The whole area experienced the tectonic setting of crustal extension, and the basin was typically a rift or fault basin. 2) Late Permian-Triassic, the compression and flexure stage. In the Late Permian

period, the basin entered the intra-continental evolution stage, the entire Triassic sedimentary depression continued to expand, and the continental deposits developed further in the southern Junggar. During this stage, the sedimentary depression was primarily braided river delta facies and semi-deep lake facies. 3) The Jurassic extension stage, when the early Yanshan movement caused substantial uplift and denudation of a wide range of the Jurassic deposits. These coal-measure strata evolved into the current scattered deposits in the Bogda Mountains and Tianshan Mountains. 4) The foreland stage of the Cretaceous depression. During the Cretaceous sedimentation period, the southern Junggar Basin was generally uplifted in a state of denudation. The basin was in the early Cretaceous compression depression with depositing filling after the late Jurassic denudation. The Late Cretaceous deposit was generally absent in the southern Junggar thrust belt. 5) During the Cenozoic compression foreland stage, the tectonic load generated by the thrust of the orogenic belt into the basin caused the crust of the orogenic belt to sink rapidly, forming the current structure of the basin (**Figure 2A**).

Stratigraphic Characteristics

From bottom to top, the lower Permian includes the Shirenzigou Formation (P_1l) and the Tashikula Formation (P_1t), the Middle Permian includes the Wulabo (P_2w), the Jingjingzigou (P_2j), and the Lucaogou (P_2l) Formation. The upper Permian is composed of the Hongyanchi (P_3h) and Wutonggou (P_3w) Formation. This study focused on the Permian Lucaogou Formation, which is composed of upward blackening mudstone interbedded with gray argillaceous sandstone in the lower section. The upper section of the Lucaogou Formation is dominated by fine-grained sediments, primarily dark gray sandy mudstone, mudstone, gray-black mudstone, and silty mudstone (**Figure 2B**). The Triassic is divided into the Lower Triassic Jiucaiyuan (T_1l), the middle Triassic Karamay Formation (T_2k), and Upper Triassic Huangshanjie Formation (T_3h) from bottom to top. The lithology of the Karamay Formation is mainly gray, gray-green, yellow sandstone, compound sandstone, lithic sandstone, mixed with mudstone and conglomerate (**Figure 2B**).

SAMPLE COLLECTION

Three shale gas samples were collected from well XJC 1 in the Lucaogou Formation. The natural gas composition and carbon isotope characteristics were analyzed at the Xinjiang Oilfield Research Institute. Moreover, geochemical data of marine shale gas in the Longmaxi Formation and swamp shale gas in the Xu 5 Formation (both situated in the Sichuan Basin), and lake shale gas in the Chang 7 Formation (situated in the Ordos Basin) were obtained from the literature for comparison. Flowback water was collected from the well XJC 1 in the Karamay Formation from the first day after hydraulic fracturing. A total of 34 samples were collected during a 66–days period after the hydraulic fracturing of well XJC 1. The fracturing fluid for the Karamay Formation was also collected. The flowback fluid samples from the Lucaogou Formation in well XJC 1 were collected from day 14 to day 20 after fracturing, and a total of five samples were collected. Major element, trace element, and cation analyses of the water samples was conducted at the Beijing Institute of Geology of Nuclear Industry.

EVALUATION OF LUCAOGOU SHALE

Geological Characteristics of Shale in the Lucaogou Formation

According to the comparison results of the drilling strata in the XJC 1, ZY 4, BC 1, MC 2, and CS 1 wells, the Permian source rock of the Lucaogou Formation is a set of deep lake-semi-deep lake deposits on the periphery of the Bogda Mountain (Fukang Fault Zone and Chaiwopu Sag, **Figure 1**). The deposition center is situated close to Bogda Mountain. The lithology is mainly organic-rich black-gray-black shale and mudstone, with silty mudstone and dolomite mudstone, representing a thick set of high-quality lacustrine argillaceous source rocks.

Distribution of Lucaogou Shale

The source rocks of the Lucaogou Formation are distributed throughout the region in the Fukang Fault Zone at the northern foot of the Bogda Mountain, with a thickness of approximately 260–50 m (**Figure 1**). The thicknesses of the Lucaogou Formation's source rocks determined from the XJC 1, BC 1, and ZY 4 wells were 410 m, 330 m, and 270 m, respectively (**Figure 1**). In the Chaiwopu Sag at the southern foot of the Bogda Mountain, five wells, including Xiao1, Da1, and CS 1, revealed varying thicknesses of the Lucaogou Formation (**Figure 1**). Using well Xiao 1 as a representative, the source rock thickness of the Lucaogou Formation revealed is 284 m. From a horizontal perspective, the thickness of the Lucaogou Formation's source rock in the Dahuangshan Piedmont is approximately 376 m and shows a trend of gradually increasing thickness from west to east.

Shale Geochemical Characteristics

The source rock of the Lucaogou Formation is rich in organic matter. Four wells were drilled in the source rock in the Fukang Fault Zone at the northern foot of the Bogda Mountain, namely XJC 1, BC 1, ZY 2, and ZY 4. The total organic carbon (TOC) contour map was drawn based on the TOC data of these wells (**Figure 3**). The average TOC content of the 161 source rock samples from well XJC 1 was 1.03%, and the highest TOC value was 5.45%. (**Figure 4A**). The average content of chloroform bitumen "A" of the 66 samples was 0.05%, and the highest was 0.16% (**Figure 4B**).

Moreover, microscopic kerogen analysis of the Lucaogou Formation indicated that algae and amorphous bodies account for 60–83% of the kerogen composition, with trace concentrations of vitrinite and inertite. Most of the source rocks belong to type I-II_1 kerogen, and their primary parent material was sourced from lower aquatic organisms dominated by algae (**Figure 5**).

The organic matter maturity of the shale in the Lucaogou Formation around the Bogda Mountain varies. The Lucaogou Formation in Quanzijie, where well XJC 1 is located, is deeply

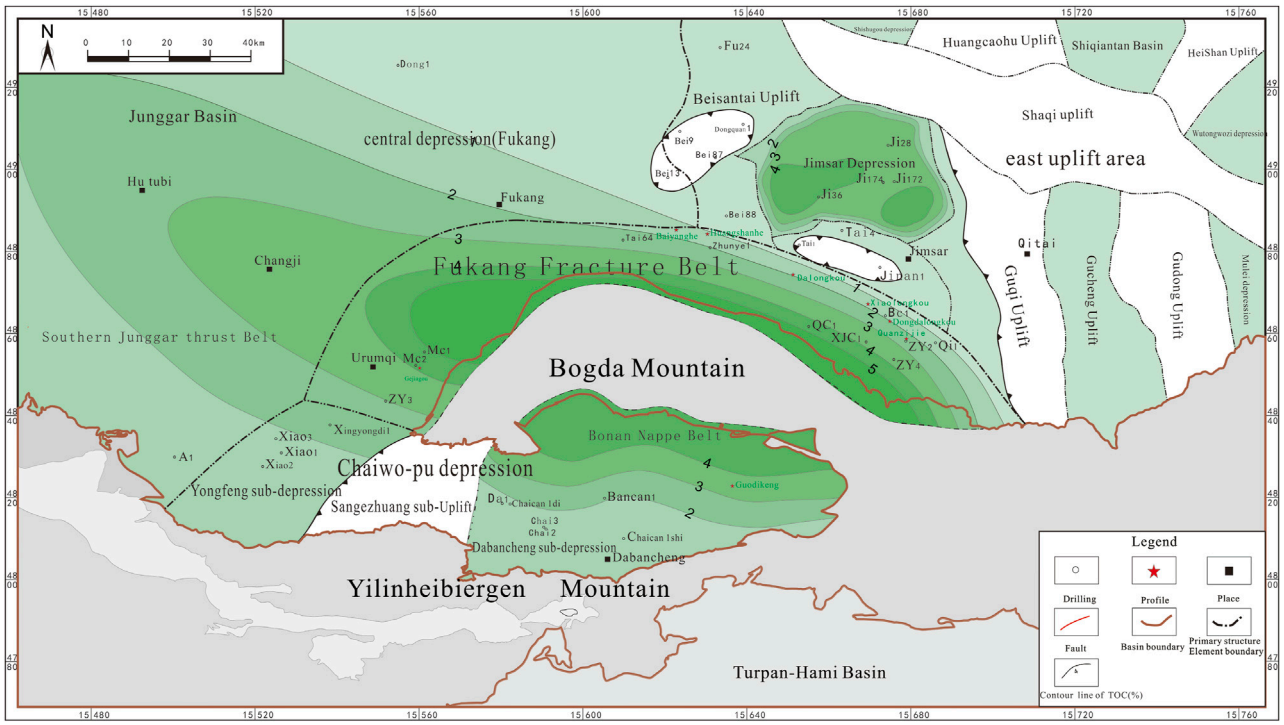


FIGURE 3 | Contour map of organic carbon content in the source rocks of Lucaogou Formation.

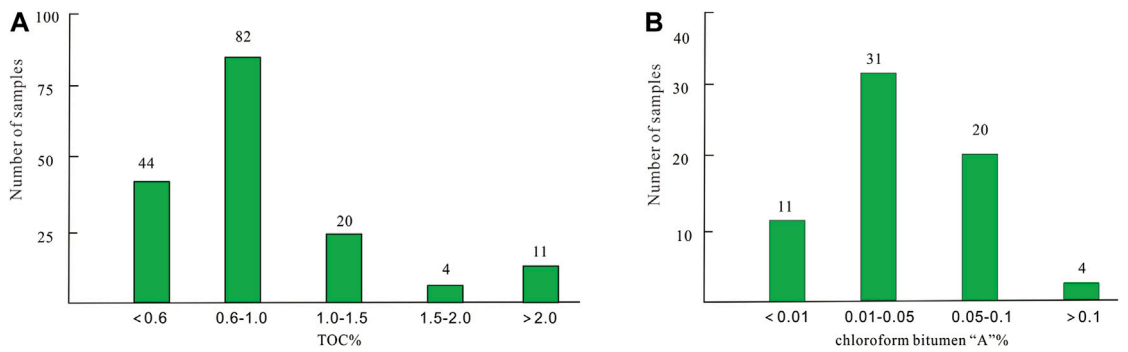


FIGURE 4 | (A) TOC content frequency distribution and **(B)** chloroform bitumen "A"(%) content frequency distribution of source rock of Lucaogou Formation in Well XJC one.

buried and has a high degree of thermal maturity. Light oil and wet gas are mainly produced in this region. The outcrop areas of the Dahuangshan and Fukang faults are shallow-buried and the thermal maturity degree is low. Moreover, significant quantities of oil shale occur in this region. The Chaiwopu and Jimsar sags display a moderate degree of thermal maturity and generate significant oil quantities (**Figure 6**).

The source rock maturity of the Lucaogou Formation encountered in well XJC 1 was generally high. The vitrinite reflectance (Ro) of 13 samples collected from this well ranged from 1.31 to 1.83, with an average of 1.71. Moreover, 12 of the samples exhibited Ro greater than 1.5, indicating that these rocks have entered a high-maturity stage (**Figures 6**, **7**). Therefore, the production of gas instead of oil from well XJC 1 was attributed to the high maturity of the source rocks.

ORIGIN AND FILLING MODE OF THE GASES

In this study, we used analysis data from lacustrine Lucaogou Formation shale gas in the Junggar Basin and data from several

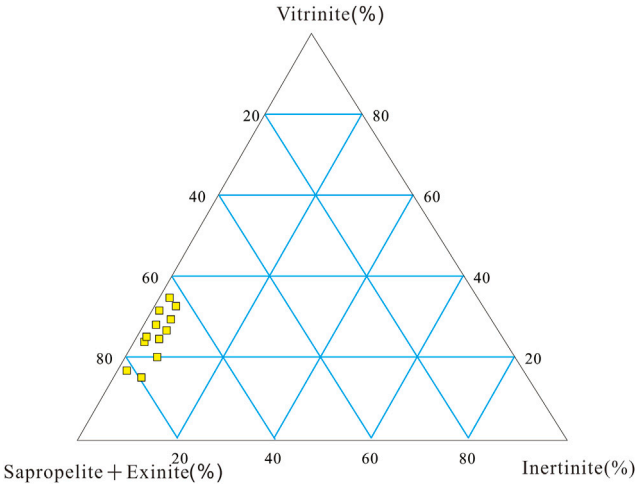


FIGURE 5 | Distribution of kerogen microscopic composition in XJC 1 well.

marine and terrestrial shale gas samples obtained from the literature (Dai et al., 2016; Feng et al., 2016), namely the continental Chang 7 shale gas in the southeastern Ordos Basin, marine Wufeng-Longmaxi shale gas in the southern Sichuan Basin, and swamp Xu 5 shale gas in the Xinchang gas field, to compare the alkane gas components and carbon isotopes in the lacustrine shale gas of the Lucaogou Formation with other marine and terrestrial shale gas samples, and to discuss the origin of the Lucaogou shale gas. Furthermore, we compared the flowback water of the Karamay Formation and the Lucaogou Formation to ascertain the origin and migration pathway of the gases. In combination with the geological setting, the filling mode of Permian and Triassic gas in the periphery of Bogda Mountain of the Junggar Basin was then proposed.

Origin of the Lucaogou Gas

Alkane Gas Composition

The methane, ethane, propane, and butane contents in the shale gas of well XJC 1 ranged from 72.32 to 77.12%, 7.92–8.92%, 2.01–2.21%, and 1.90–2.03%, with average contents of 74.14%, 8.49%, 2.13%, and 1.96%, respectively. Therefore, shale gas from the Lucaogou Formation is characterized by a high content of heavy hydrocarbon gas and is classified as wet gas, similar to that of the mature Ordos Chang 7 shale and the Barnett shale, one of the largest onshore natural gas fields in the United States (**Figure 8**).

The sequence of heavy hydrocarbon gas (C_{2-5}) content in shales from the study area is as follows: Lucaogou shale in the Junggar Basin > gas in the Lower Triassic Chang 7 (T_1y_7) shale of the Ordos Basin > gas in the Upper Triassic Xu 5 (T_3x_5) Shale of the Sichuan Basin. Moreover, the maturity of the Lucaogou Formation shale exceeded that of the other two sets of continental shale, indicating that the Lucaogou shale gas should be drier. Therefore, the variation in the alkane gas composition of these shale gases is predominately affected by the parent source rock and not the maturity of the shale rock. Although the source rocks for the Lucaogou and Chang 7 gases

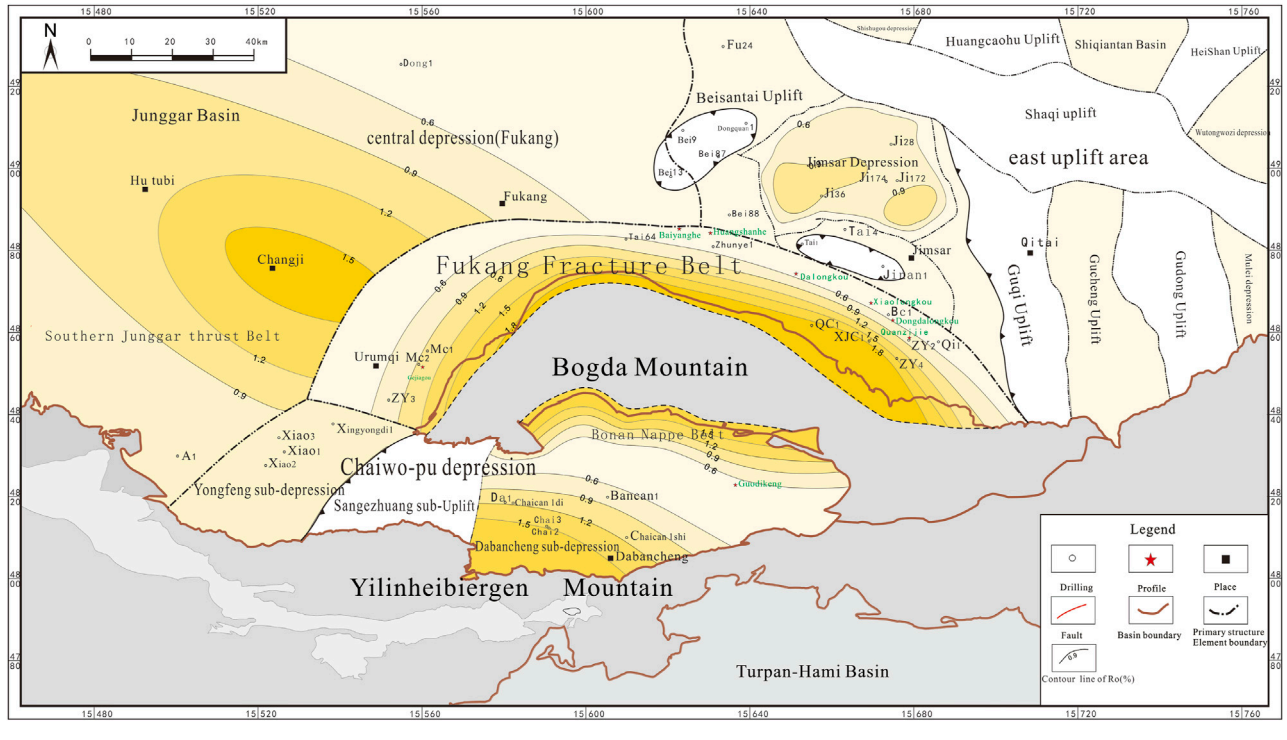


FIGURE 6 | Ro contour map of source rock of Lucaogou Formation.

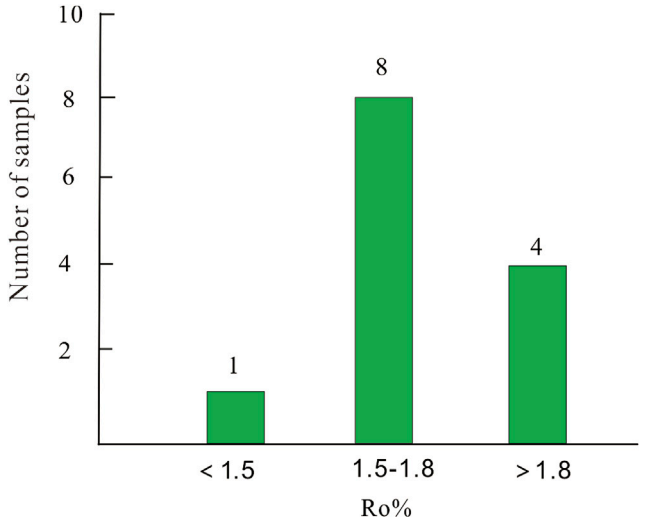


FIGURE 7 | Histogram of Ro distribution of source rock in XJC 1 Well.

are both sapropel shale rocks, the Lucaogou shale contains more saprolite components that are prone to generate heavy hydrocarbons. Conversely, the Chang 7 shale gas, which is derived from humic parent material, is wetter than the Xu 5 shale gas, which is sourced from a sapropel parent material.

As can be seen from **Figure 8**, the marine Wufeng-Longmaxi shale gas has a high methane content, with an average of 98.00%, and a low heavy hydrocarbon gas content, while the continental Lucaogou, Chang 7, and Xu 5 shale gas all have low methane contents and high heavy hydrocarbon gas contents. These variations primarily arise from differences in the source rock maturity.

Carbon Isotopic Composition of Alkane Gas

The $\delta^{13}C_1$ and $\delta^{13}C_2$ compositions of the Lucaogou Formation gas ranged from −41.0‰ to −41.9‰ and 30.7‰ to −31.3‰, with averages of −41.5‰ and −31.1‰, respectively. The $\delta^{13}C_3$ content ranged from −28.1‰ to −29.0‰, with an average of −28.6‰, and a $\delta^{13}C_4$ range of −29.4‰ to −29.5‰ was recorded, with an average of −29.4‰.

Compared to the other continental shale gas samples, the carbon isotope values of shale gas in the Lucaogou Formation was higher than those of the Chang 7 shale gas, with $\delta^{13}C_1$, $\delta^{13}C_2$, $\delta^{13}C_3$, and $\delta^{13}C_4$ averages of −48.7‰, −36.4‰, −31.3‰, and −31.6‰, respectively. Moreover, the carbon isotope values of shale gas in the Lucaogou Formation were lower than those of the Xu 5 (T_3x_5) shale gas, which recorded $\delta^{13}C_1$, $\delta^{13}C_2$, $\delta^{13}C_3$, and $\delta^{13}C_4$ averages of −36.2‰, −25.1‰, −22.9‰, and −22.4‰. A maturity comparison of the three sets of shale revealed that the thermal maturity of the Lucaogou Formation shale exceeded that of the Chang 7 and Xu 5 shales. The higher the maturity, the heavier the carbon isotope composition of the alkane gas. The Luchaogou and Chang 7 shales have a similar parent material type. Therefore, the heavier alkane gas isotopes of the Lucaogou Formation gases are predominately caused by source rock maturity. The Xu 5 shale gas is derived from coal source rocks dominated by swamp facies in the Xujiahe Formation (Dai et al., 2014). The carbon isotopes of methane and the homologs produced by humic source rocks are heavier than those produced by saprophytic source rocks of similar maturity (Stahl and Carey, 1975; Dai and Qi, 1989). Zheng and Chen (2000) pointed out that the $\delta^{13}C_1$ value of methane formed by marine sapropelic source rock is approximately 14‰ lower than that of terrestrial humic source rocks at the same maturity. Therefore, differences between the carbon isotope composition of alkane gas from the Lucaogou and Xu 5 shales can be attributed to different source rocks.

Figure 9 indicates that the continental shale gas from the Lucaogou, Chang 7, and Xu 5 formations displayed a predominately positive carbon isotope series ($\delta^{13}C_1 < \delta^{13}C_2 < \delta^{13}C_3 < \delta^{13}C_4$). Conversely, the Wufeng-Longmaxi Formation shale gas samples recorded a negative carbon isotope series ($\delta^{13}C_1 > \delta^{13}C_2 > \delta^{13}C_3 > \delta^{13}C_4$). The variations in the carbon isotope composition between the continental shale formations and the marine shale formation were attributed to varying degrees of shale maturity. The continental shale gases are in the mature to the high-mature stage, while the Wufeng-Longmaxi Formation marine shale is in the over-mature stage when carbon isotope reversal occurs.

Overall, the geochemical analysis of well XJC 1 indicated that the gas was generated from the mature lacustrine source rock. The anomalous gas production of this well compared to other wells in the vicinity could be attributed to the high maturity of the source rocks. Therefore, future shale gas exploration of the Lucaogou Formation should focus on superimposed areas with high TOC and maturity.

Composition of Reservoir Waters From the XJC1 Well

Both the unconventional shale reservoirs in the Lucaogou Formation and the conventional reservoirs in the Karamay

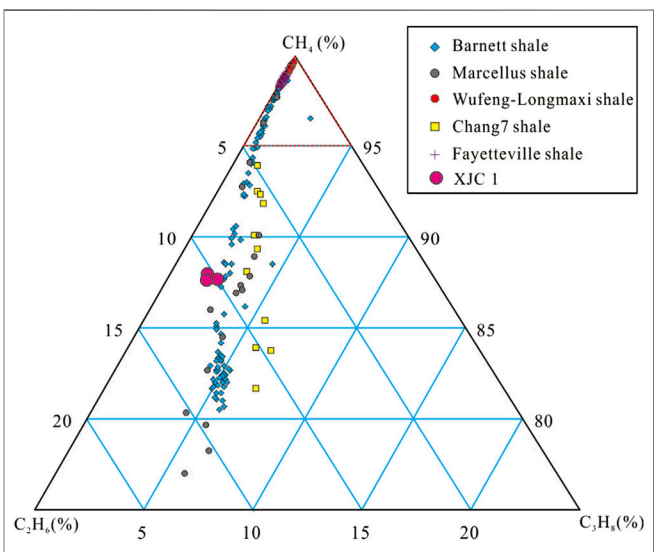


FIGURE 8 | Triangular diagram of CH_4-C_2H_6-C_3H_8 components of major shale gas in China and the United States (modified after Dai et al., 2016).

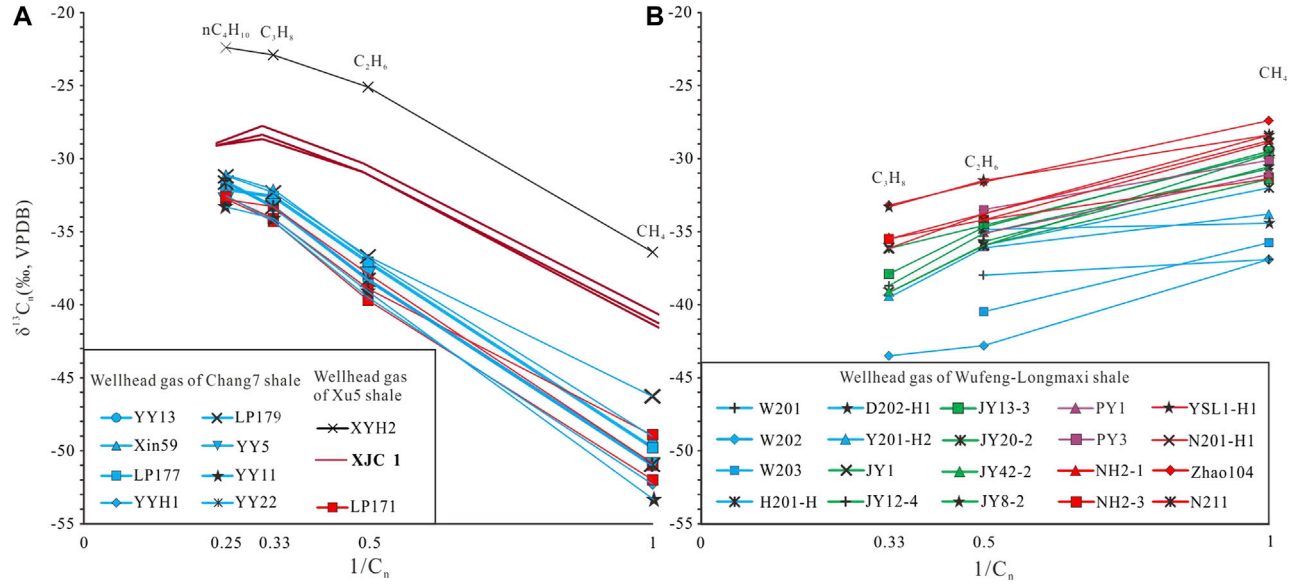


FIGURE 9 | Comparison of carbon isotope series types of alkanes in Chang 7, Xu 5 **(A)** and Wufeng-Longmaxi Formation **(B)** (modified after Dai et al., 2016).

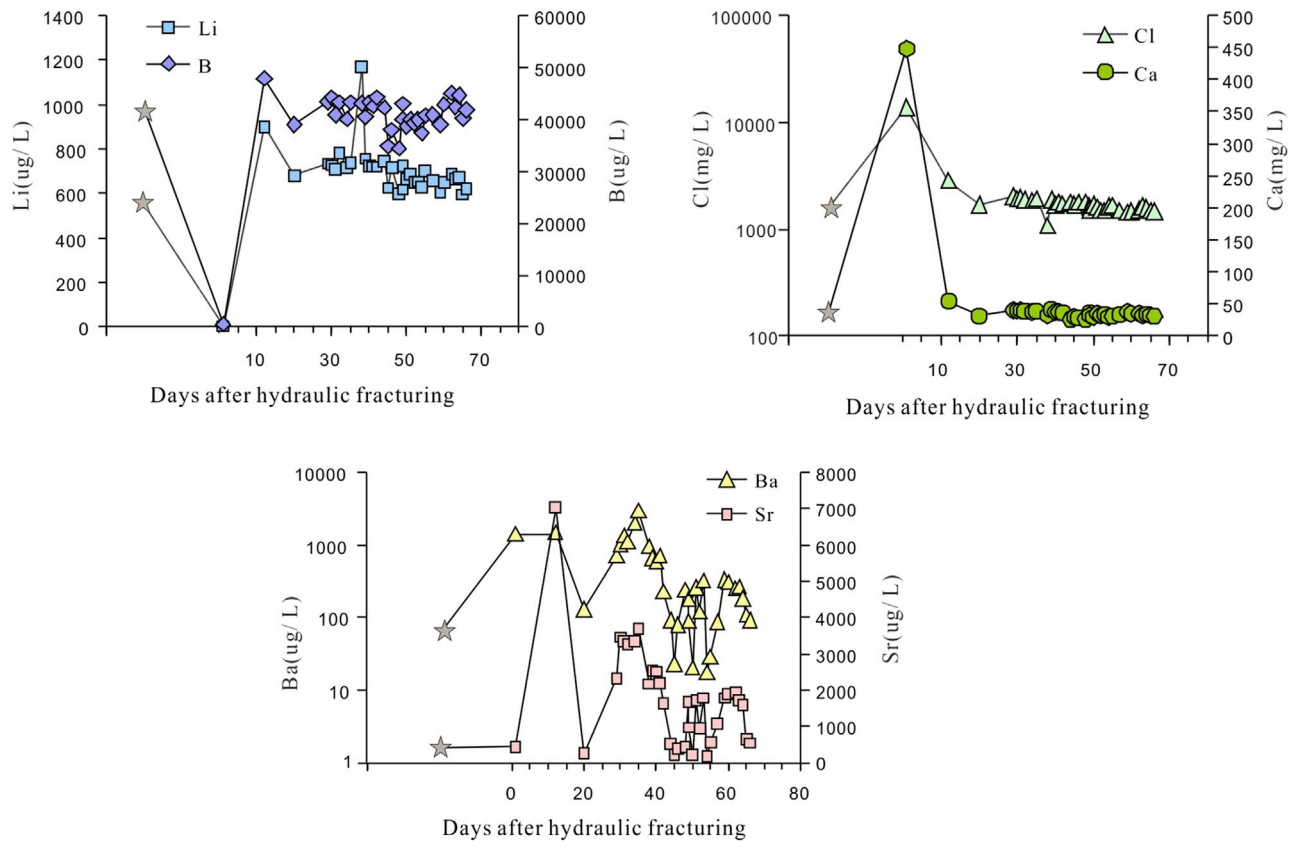


FIGURE 10 | Evolution trend of flowback geochemistry in conventional Karamay Formation (the stars in the diagrams indicate the corresponding characteristics of the fracturing fluid).

Formation have undergone hydraulic fracturing, and both reservoirs have produced flowback fluid. As the T_2k gas was not collected in this study, the gas origin could not be determined directly. We, therefore, used the chemistry of water coproduced with the gas to examine the gas origin. We conducted a comparison of the geochemical characteristics of the flowback fluid for these two reservoirs to analyze the gas migration pathway, the reaction process of the fracturing fluid and formation water, water-rock reactions, and the sources of various elements in the flowback fluid of the different rocks.

Flowback Fluid of Karamay Formation Sandstone

Fracturing fluid samples used in the hydraulic fracturing of the Karamay Formation and flowback fluid from day 1–66 after hydraulic fracturing were collected and analyzed for comparison. A comparison of the results from the flowback fluid, the fracturing fluid, and the evolution trend of the flowback fluid over the production time, revealed several different sources of elements in the flowback fluid. **Figure 10** indicates that the evolution trend of different elements in the flowback fluid can be divided into three types:

1) Type 1: This group comprised Li, B, F, and Br. The concentration of type 1 elements in the fracturing fluid was very high. In the flowback fluid, the type 1 element composition decreased rapidly on the first day after fracturing. However, on the 12th day (or possibly earlier–no samples were collected between days 1–12) the type 1 element concentration in the flowback fluid increased to the same level as the fracturing fluid and remained at a higher level during the later flowback process. In the flowback process, at the beginning of fracturing, the water injected into the formation entered the fracture. On the first day after hydraulic fracturing, most of the flowback fluid was in the target formation. Therefore, the compositions of these elements in the formation water were low. However, after approximately 12 days after fracturing, the proportion of fracturing fluid in the flowback fluid increased until the flowback fluid consisted predominately of fracturing fluid. Therefore, the concentration of type 1 elements in the flowback fluid increased and continued to maintain a level equivalent to that in the fracturing fluid.
2) Type 2: This group comprised Ca, Cl, Mg, K, Na, HCO_3, and SO_4. On the first day after fracturing, the concentration of type 2 elements in the flowback fluid increased rapidly and was significantly higher than in the fracturing fluid. On the 12th day after fracturing, the concentrations of these elements in the flowback fluid gradually decreased to a level equivalent to that of the fracturing fluid. The source of these elements was similar to the type 1 elements, except that the concentrations of these elements were high in the formation water and low in the fracturing fluid. At the start of fracturing, the flowback fluid was dominated by formation water; hence, the contents of these elements in the flowback fluid were higher than in the fracturing fluid. However, in the days following fracturing, the proportion of formation water in the flowback fluid progressively decreased, and the concentration of type 2 elements in the flowback fluid decreased to a level similar to that of the fracturing fluid.
3) Type 3: The third element group contained Mn, Ba, and Sr The concentration of type 3 elements in the fracturing fluid was low. However, during the flowback process, the elemental concentration remained high regardless of the number of days passed since hydraulic fracturing, and the concentration of type 2 elements in the flowback fluid significantly exceeded that of the fracturing fluid. Since type 2 elements could not be derived from the fracturing fluid or the formation water as they maintained a high concentration in the flowback fluid, it was inferred that these elements originated from reservoir rocks. The freshening process caused these elements to be released from the rock, whereby they entered the flowback fluid and returned to the surface.

TABLE 1 | Chemical characteristics of flowback water in the T_2k and P_2l reservoirs.

Well	Strata	Water type	Cl (mg/L)	γNa/γCl
XJC1	T_2k	NaCl	1,092–2,855	1.3–1.7
XJC1	P_21	NaHCO3	635.7–663.0	2.3–2.7

In summary, in conventional flowback fluid, type 1 elements (Li, B, F, and Br) were derived from the fracturing fluid, type 2 elements (Ca, Cl, Mg, K, Na, HCO_3, and SO_4) originated from the formation water, and type 3 elements (Mn, Ba, and Sr) were leached from source rocks. As a result, the contents of Ca, Cl, Mg, K, Na, HCO_3, and SO_4 in the flowback water could represent the characteristics of the Formation water in Karamay Sandstone.

Comparison of Lucaogou and Karamay Formation Flowback Water

The sodium chloride coefficient ($\gamma Na/\gamma Cl$) indicates the degree of concentration metamorphism of formation water. The smaller the value of $\gamma Na/\gamma Cl$, the more concentrated the better sealing of the formation water is. From **Table 1**, the sodium chloride coefficient of T_2k water ($\gamma Na/\gamma Cl$ = 1.3–1.7) is smaller than the P_2l water ($\gamma Na/\gamma Cl$ = 2.3–2.7), indicating that the T_2k water was preserved in a more closed system than the P_2l water. The water samples from the T_2k reservoir have a chloride content of 1,092–2,855 mg/L (mean 1707 mg/L), higher than those from the P_2l reservoirs (Cl = 636–663 mg/L, mean 647 mg/L), also indicating that the T_2k water preserved in a relatively closed system and experienced less mixing from meteoric water. In contrast, the P_2l water was preserved in a relatively open system.

The water samples from the T_2k reservoir are a typical NaCl type. The water samples from the P_2l reservoir are dominated by a $NaHCO_3$ type. The $CaCl_2$ type water reflects deep cycling and closed water environment, while the $NaHCO_3$ type water represents a weak runoff water environment, with a certain hydraulic connection with other formations or surface water (Xu et al., 2000; Li et al., 2005; Tang et al., 2018). It has been proven (Wang and Zhang, 1998) that the $NaHCO_3$ type water with high salinity is related to the latent deep fault in the deep layer. The deep fault can contribute high concentrations of CO_2 to the deep

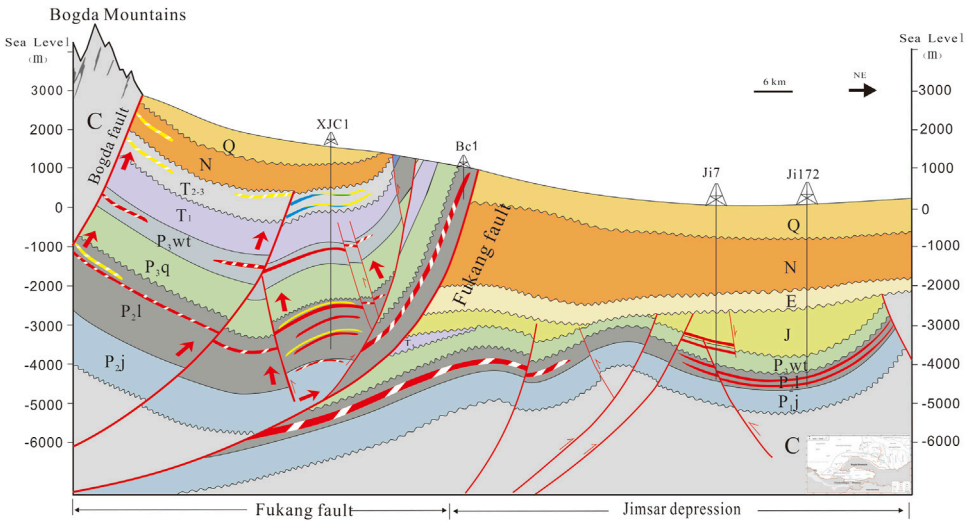


FIGURE 11 | Petroleum accumulation and filling model through well XJC 1 of Fukang fault zone (the cross-well profile line is indicated as the red line in **Figure 1**).

layer, which then enter the formation water, causing the HCO_3^- + CO_2^{3-} concentration in the formation water to be greater than the Cl^- + SO_4^{2-}concentration. While low salinity $NaHCO_3$ type water is caused by leaching and infiltration of surface water, the $NaHCO_3$ type water of the P_2l reservoir indicates the existence of a deep fault connecting the Lucaogou formation and the surface. NaCl type water is produced by mixing $CaCl_2$ type water with high salinity $NaHCO_3$ type water (Chen et al., 2000). The NaCl type water in the T_2k reservoir indicates the existence of fault between the T_2k reservoir and P_2l, which can be a good channel for the migration of oil, gas, and water. The deep P_2l $NaHCO_3$ type water rises along the fault and mixes with the upper $CaCl_2$ type water to form medium and high salinity NaCl type water in the T_2k formation.

Filling Mode

In the study area, the Triassic strata lack a sufficient source rock. The potential source rock in the Karamay Formation of the Triassic shows low TOC. The vitrinite reflectance (Ro) of the 6 samples that are collected from the T_2k reservoir of XJC 1 range from 1.01% to 1.21%, with an average of 1.09%. The Tmax values range from 453 to 458°C, indicating that the T_2k source rock has just entered the mature stage and cannot yet generate gas. Thus, the Lucaogou shale is more likely to be the source of the T_2k gas.

From the structural characteristics of the study area (**Figure 2A**) and the water composition, we can conclude that there is a fault between the Permian Lucaogou shale source rock and the Triassic Karamay reservoir. As a result, the gas filling mode is proposed as follows, below.

The continuously active faults of the Fukang fault zone and the multi-stage unconformity surface and the internal permeability sand bodies of the reservoir, provide channels for the lateral migration of oil and gas. The fault and the unconformity constitute the oil and gas transport system in the Bogda Piedmont. Thus the Permian Lucaogou Formation continental source rock kitchen and Triassic reservoir were connected (**Figure 11**). The oil and gas were generated from the lacustrine source rocks of the Permian Lucaogou Formation reserved in nearby lithological oil and gas reservoirs in the Permian. The petroleum was transported along the faults to the shallow layer over long distances to enter the Triassic reservoir. Within the Triassic formation, the petroleum migrated laterally through the weathering crust of the unconformity and the internal permeability sandstone, and it migrated horizontally upward along the vertical fault to the target area to form oil and gas reservoirs. The deep Permian Lucaogou Formation primarily developed lithologic oil and gas reservoirs with integrated source and reservoir and large area distribution, while the shallow Triassic Karamay Formatio developed structural-type gas reservoirs with fault transport, structural control, and late accumulation.

ENVIRONMENTAL ISSUES ASSOCIATED WITH SHALE GAS DEVELOPMENT IN THE JUNGGAR BASIN

The overall aim of characterizing the geochemical flowback water was to contribute to the environmental protection of the water resources associated with the formations undergoing shale oil and gas exploration and development.

Geochemical Fingerprint of Conventional Vs. Unconventional Oil and Gas Wastewater

One of the issues associated with the environmental effects of shale gas development is the impact of unconventional shale gas exploration and contamination from the operation of

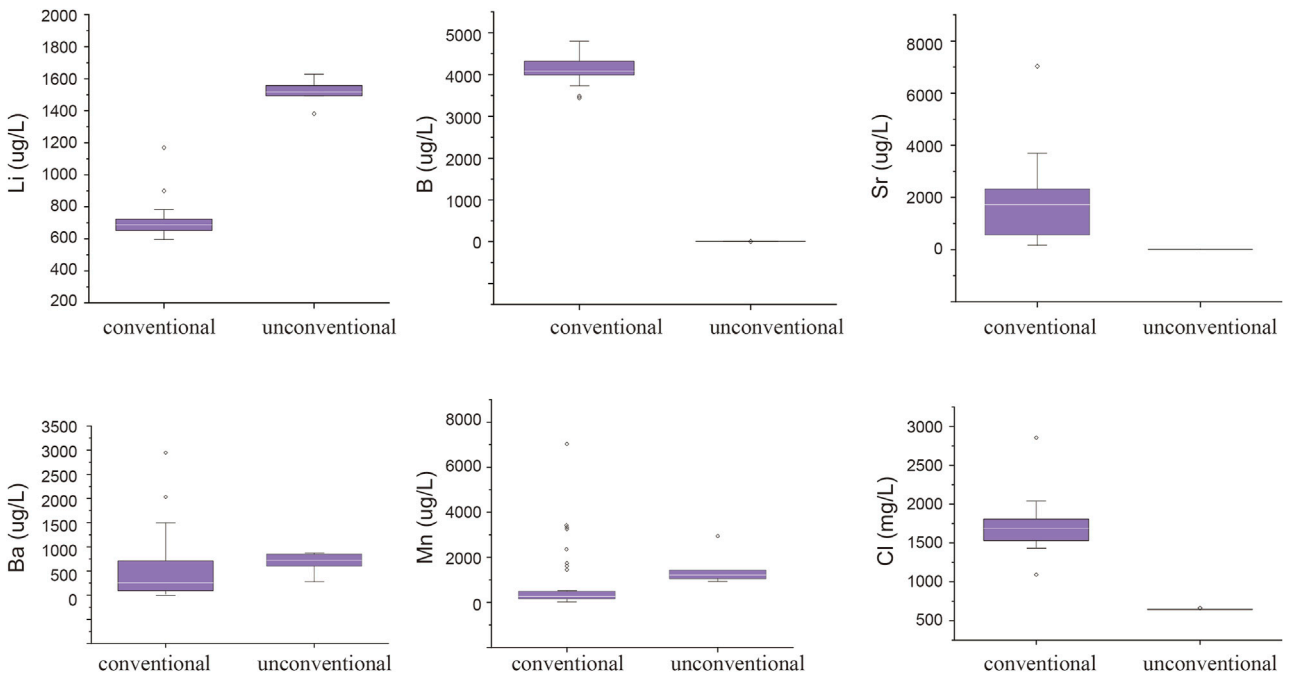


FIGURE 12 | Comparison between conventional and unconventional flowback of Junggar Basin.

conventional oil and gas. Thus, it is important to find the distinct characteristics of the waste water from the unconventional shale reservoir.

The shale strata of the Lucaogou Formation measured a higher Li concentration than that of the conventional Karamay Formation (**Figure 12**). Previous studies on Marcellus shale and Longmaxi shale in the Sichuan Basin have indicated that Li and B in the flowback fluid are predominately derived from clay minerals in shale (Warner et al., 2014; Ni et al., 2018). Because Li and B cannot be sourced from sandstone, the main rock-type in both formations, the concentrations of these elements in the flowback fluid was low. Moreover, a comparison of the conventional and unconventional Li content in the Junggar Basin was consistent with previous research results, indicating that Li in the shale flowback fluid is predominately sourced from the shale layer. However, the B concentration differed from those obtained in previous studies and was attributed to the marine character of the Sichuan and Marcellus shale compared to the continentally derived Junggar shale. The B element is present in high concentrations in marine facies and low concentrations in continental shale, further indicated by the Qaidam Basin in northwest China (Zheng et al., 2017). Therefore, the B content in the flowback fluid of the conventional Karamay Formation was derived from the fracturing fluid, and the significantly high B concentration in the fracturing fluid resulted in a high B concentration in the flowback fluid. Furthermore, the Sr content in the conventional flowback was relatively higher than in the unconventional reservoir. The different properties of the flowback water derived from these two formations result in the unique contrasting characteristics observed in the conventional and unconventional flowback in the Junggar Basin. Similar to B, the Cl content in the conventional formations was significantly higher than in the unconventional flowback fluid, and was attributed to the high Cl content in the conventional fracturing fluid. The contents of Mn, Ba, and Sr in the unconventional flowback fluid were higher than those in the conventional flowback fluid. These elements are mainly derived from rock formations, indicating that the concentrations of these elements in the continental shale layer are higher, or that these elements are more mobile and readily enter the flowback fluid. The above discussion implies that the Li, B, Sr contents could be used as potential indicators for identifying possible migration of wastewater from Lucaogou shale.

Pollutant Concentration in the Flowback Fluid

One of the key environmental issues related to shale gas development is the quality of flowback water coproduced with the shale gas. The ability to reuse and manage the waste water is dependent on the water quantity and quality. Several water quality components in the flowback fluid sampled from the Junggar Basin exceed the three major water quality standards in China: the drinking water quality standard (WQS) (GB 5749–2006), Environmental Quality Standards for Surface Water (EQS) (GB3838–2002), and China's Integrated Wastewater Discharge Standard (IWDS) (GB 8978–1996). Components exceeding these standards include Fe, Ba, Mn, B, Cl, and F (**Table 2**).

TABLE 2 | Concentrations of inorganic chemicals in flowback water of the Junggar Basin. Highlighted rows indicate Mean/WQS ratio >1. WQS is the Water Quality Standards for drinking water from China's sanitary (GB 5749–2006), EQS is the Environmental Quality Standards for Surface Water (GB3838–2002), and IWDS is the Integrated Wastewater discharge standard of China (GB 8978–1996). The cells with dark background represent conventional T_2k flowback, and the corresponding cells represent unconventional P_2l flowback water.

Constituent	Units	WQS	EQS	IWDS	Min	Max	Median	Mean	Mean/WQS
Iron	mg/L	0.3	0.3	-	—	—	—	—	—
					0.43	0.63	0.55	0.54	1.80
Barium	mg/L	0.7	0.7	-	0.02	2.95	0.26	0.54	0.78
					0.28	0.87	0.72	0.67	0.95
Manganese	mg/L	0.1	0.1	2.0	0.03	1.74	0.21	0.34	3.44
					0.94	2.94	1.22	1.52	15.17
Boron	mg/L	0.5	0.5	-	0.57	47.93	40.86	40.05	80.11
					0.04	0.05	0.05	0.05	0.09
Chloride	mg/L	250	250	-	1,092	13,771	1,694	2062	8.25
					636	663	648	647	2.59
Fluoride	mg/L	1.0	1.0	10	1	0.02	24.60	5.15	5.43
					0.0009	0.0014	0.0011	0.0012	0.0012

The ratios of the average value of B, Cl, and F in the conventional flowback fluid to the drinking water quality standards (mean/WQS) reached 80.11, 8.25, and 5.43, respectively, and were considerably higher than those of the unconventional flowback fluid. This was mainly due to the high concentrations of these elements in the unconventional fracturing fluid. Hence, water remediation strategies should focus on the treatment of these elements in the wastewater of conventional wells in the Karamay Formation. In the unconventional Lucaogou Formation, the ratio of Fe and Mn in the flowback fluid to the drinking water quality standards (mean/WQS) peaked at 1.80 and 15.17. These ratios were significantly higher than those recorded in the conventional flowback fluid. The Ba content in the two flowback fluids, however, only slightly exceeded the WQS, and thus its effect on the wastewater was considered negligible.

Compared with the drinking water standard (WQS), the concentrations of B in the conventional flowback fluid and the Mn concentration in the unconventional flowback fluid were significantly high (Mean/WQS values are the highest, **Table 1**), and effective removal strategies are required in the wastewater treatment process.

CONCLUSION

This study aimed to determine the gas origin and filling mode of P_2l and T_2k gases in the Junggar Basin and to propose suggestions for water treatment. Based on our results, the following conclusions were made:

1) The average contents of CH_4, C_2H_6, C_3H_8 of the P_2l lacustrine shale gas are 74.14%, 8.49%, 2.13%, and 1.96%, respectively. Compared with the gas in the Lower Triassic Chang 7 (T_1y_7) continental shale of the Ordos Basin and gas in the Upper Triassic Xu 5 (T_3x_5) continental shale of the Sichuan Basin, the Lucaogou shale gas contains the highest content of heavy hydrocarbon despite its higher maturity. The average values of $\delta^{13}C_1$, $\delta^{13}C_2$, $\delta^{13}C_3$ of P_2l lacustrine shale gas are −41.5‰, −31.1‰, and −28.6‰, respectively, between the T_1y_7 lacustrine shale gas in the Yanchang gas field and the T_3x_5 shale gas in the Xinchang gas field. The alkane composition and isotope of P_2l gas indicate that the gas was generated from continental shale containing more saprolite components that are prone to generate heavy hydrocarbons, which is in accordance with the Lucaogou shale.
2) From the evolution trend of flowback chemistry in the T_2k formation, it can be concluded that the Ca, Cl, Mg, K, Na, HCO_3, and SO_4 in the flowback water are mainly from the formation water and that the content of these chemicals could represent the characteristics of the Formation water. The comparison between compositions in the flowback water reveals that the P_2l water is of $NaHCO_3$ type while the T_2k water is of NaCl type, and the salinity of the latter is higher than the former, indicating a connection between P_2l source rock and the T_2k reservoir. In combination with the structural setting in the study are, the gas filling mode was proposed as follows: the gas generated from the lacustrine source rocks of the Permian Lucaogou Formation reserved in nearby lithological reservoirs in the Permian. The petroleum was transported along the faults to the shallow layer over long distances to enter the Triassic reservoir.
3) The high contents of B, Cl, and F in the flowback fluid of the Karamay Formation were attributed to the high concentration of these elements in the fracturing fluid. Therefore, water remediation strategies should focus on the removal of these elements in the flowback fluid. Moreover, elevated concentrations of Mn and Fe recorded in the Lucaogou Formation should be the focus of research on the sewage treatment process of shale flowback fluid.

The findings of this research could indicate potential targets for shale gas exploration. Moreover, the suggestions for wastewater treatment based on water quality analysis can help mitigate, to some extent, the environmental issues faced during shale gas development.

DATA AVAILABILITY STATEMENT

The original contributions presented in the study are included in the article/Supplementary Material, further inquiries can be directed to the corresponding author.

AUTHOR CONTRIBUTIONS

LZ: data curation, formal analysis. DL: writing, review, and editing the manuscript. YG: writing, review and editing the manuscript. MZ: writing, review and editing the manuscript.

FUNDING

This study was supported by the National Natural Science Foundation for Young Scientists of China (Grant No. 41702161), the International Partnership Program of the Chinese Academy of Sciences (Grant No. 132A11KYSB20180012), the China Geological Survey Program (Grant/Award Numbers DD20160,170, DD20160,203, and DD20190,090), and the China Geological Survey Bureau special project "basic geological survey of oil and gas in Junggar Basin and its surrounding areas" (Grant No. 121201021000150007).

ACKNOWLEDGMENTS

The authors would like to thank the College of Resources and Environment at Yangtze University, the PetroChina Xinjiang Oilfield Company Research Institute of Petroleum Exploration and Development for experimental analysis, and the Oil and Gas Survey of CGS for providing project funding support.

REFERENCES

Burruss, R. C., and Laughrey, C. D. (2010). Carbon and hydrogen isotopic reversals in deep basin gas: evidence for limits to the stability of hydrocarbons. *Org. Geochem.* 41, 1285–1296. doi:10.1016/j.orggeochem.2010.09.008

Chapman, E. C., Capo, R. C., Stewart, B. W., Kirby, C. S., Hammack, R. W., Schroeder, K. T., et al. (2012). Geochemical and strontium isotope characterization of produced waters from Marcellus shale natural gas extraction. *Environ. Sci. Technol.* 46 (6), 3545–3553. doi:10.1021/es204005g

Chen, J. P., Cha, M., and Zhou, Y. Q. (2000). Chemical characteristics of formation water in relation with oil/gas in the northwestern parts of Junggar Basin. *Geology-Geochemistry* 28 (3), 54–58. doi:10.3969/j.issn.1672-9250.2000.03.006

Dai, J., Gong, D., Ni, Y., Huang, S., and Wu, W. (2014). Stable carbon isotopes of coal-derived gases sourced from the Mesozoic coal measures in China. *Org. Geochem.* 74, 123–142. doi:10.1016/j.orggeochem.2014.04.002

Dai, J., and Qi, H. (1989). The relationship between δ13C and Ro in coal- genetic gas. *Chin. Sci. Bull.* 34 (9), 690–692. doi:10.1360/csb1989-34-9-690

Dai, J. X., Zou, C. N., Dong, D. Z., Ni, Y. Y., Wu, W., Gong, D. Y., et al. (2016). Geochemical characteristics of marine and terrestrial shale gas in China. *Mar. Pet. Geol.* 76, 44–463. doi:10.1016/j.marpetgeo.2016.04.027

Feng, Z., Liu, D., Huang, S., Wu, W., Dong, D., Peng, W., et al. (2016). Carbon isotopic composition of shale gas in the silurian Longmaxi Formation of the changning area, Sichuan Basin. *Pet. Exploration Dev.* 43, 769–777. doi:10.1016/s1876-3804(16)30092-1

Hao, F., and Zou, H. (2013). Cause of shale gas geochemical anomalies and mechanisms for gas enrichment and depletion in high-maturity shales. *Mar. Pet. Geology.* 44, 1–12. doi:10.1016/j.marpetgeo.2013.03.005

Hill, R. J., Jarvie, D. M., Zumberge, J., Henry, M., and Pollastro, R. M. (2007). Oil and gas geochemistry and petroleum systems of the Fort Worth Basin. *Bulletin* 91, 445–473. doi:10.1306/11030606014

Hunt, A. G., Darrah, T. H., and Poreda, R. J. (2012). Determining the source and genetic fingerprint of natural gases using noble gas geochemistry: a northern Appalachian Basin case study. *Bulletin* 96 (10), 1785–1811. doi:10.1306/03161211093

Jenden, P. D., Draza, D. J., and Kaplan, I. R. (1993). Mixing of thermogenic natural gas in northern Appalachian basin. *AAPG Bull.* 77 (6), 980–998. doi:10.1306/BDFF8DBC-1718-11D7-8645000102C1865D

Lauer, N. E., Harkness, J. S., and Vengosh, A. (2016). Brine spills associated with unconventional oil development in north Dakota. *Environ. Sci. Technol.* 50 (10), 5389–5397.doi:10.1021/acs.est.5b06349

Li, X. Q., Hou, D. J., Hu, G. Y., and Li, J. (2005). *the Formation fluid characteristics and gas accumulation of central gas fields in the Ordos Basin*. Beijing: Geological Publishing House. (in Chinese).

Liu, Dan., Jian, Li., Zou, Caineng., et al. (2020). Recycling flowback water for hydraulic fracturing in China: implications for gas production and water footprint of flowback water. *Fuel* 272 (15). doi:10.1016/j.fuel.2020.117621

Martini, A. M., Walter, L. M., and McIntosh, J. C. (2008). Identification of microbial and thermogenic gas components from Upper Devonian black shale cores, Illinois and Michigan basins. *Bulletin* 92 (3), 327–339. doi:10.1306/10180706037

Ni, Y., Zou, C., Cui, H., Li, J., Lauer, N., Harkness, J., et al. (2018). Origin of flowback and produced waters from Sichuan Basin, China. *Environ. Sci. Technol.* 52, 14519–14527. doi:10.1021/acs.est.8b04345

Stahl, W. J., and Carey, B. D., Jr (1975). Source-rock identification by isotope analyses of natural gases from fields in the Val Verde and Delaware basins, west Texas. *Chem. Geology.* 16, 257–267. doi:10.1016/0009-2541(75)90065-0

Strąpoć, D., Mastalerz, M., Schimmelmann, A., Drobniak, A., and Hasenmueller, N. R. (2010). Geochemical constraints on the origin and volume of gas in the new albany shale (Devonian–Mississippian), eastern Illinois basin. *AAPG Bull.* 94 (11), 1713–1740. doi:10.1306/06301009197

Tang, S., Tang, D., Li, S., Geng, Y., Xu, H., Tao, S., et al. (2018). Geochemical characteristics and origin of natural gas and gas -filling mode of the Paleozoic in the Yanchuannan gas field, Ordos Basin, China. *J. Nat. Gas Sci. Eng.* 49, 286–297. doi:10.1016/j.jngse.2017.11.013

Tilley, B., and Muehlenbachs, K. (2013). Isotope reversals and universal stages and trends of gas maturation in sealed, self-contained petroleum systems. *Chem. Geology.* 339, 194–204. doi:10.1016/j.chemgeo.2012.08.002

Vengosh, A., Jackson, R. B., Warner, N., Darrah, T. H., and Kondash, A. (2014). A critical review of the risks to water resources from unconventional shale gas development and hydraulic fracturing in the United States. *Environ. Sci. Technol.* 48 (15), 8334–8348.doi:10.1021/es405118y

Vengosh, A., Mitch, W. A., and McKenzie, L. M. (2017). Environmental and human impacts of unconventional energy development. *Environ. Sci. Technol.* 51 (18), 10271–10273. doi:10.1021/acs.est.7b04336

Wang, Z. H., and Zhang, S. J. (1998). The Discovery and characteristics of high salinity sodium bicarbonate type water in Karamay Oilfield, China. *Pet. Geology. Exp.* 20 (1), 39–43. doi:10.11781/sysydz199801039

Warner, N. R., Christie, C. A., Jackson, R. B., and Vengosh, A. (2013). Impacts of shale gas wastewater disposal on water quality in western Pennsylvania. *Environ. Sci. Technol.* 47 (20), 11849–11857.doi:10.1021/es402165b

Warner, N. R., Darrah, T. H., Jackson, R. B., Millot, R., Kloppmann, W., and Vengosh, A. (2014). New tracers identify hydraulic fracturing fluids and accidental releases from oil and gas operations. *Environ. Sci. Technol.* 48 (21), 12552–12560. doi:10.1021/es5032135

Xu, G. S., Song, H. R., and Zhou, W. (2000). Hydrochemical conditions and natural gas accumulation in the middle part gasfield of the Ordos Basin. *Exp. Pet. Geol.* 22, 330–335. doi:10.11781/sysydz200004319

Zheng, Y., and Chen, J. (2000). *Stable isotope geochemistry*. Beijing: Science Press, 196–200. (In Chinese).

Zheng, Z., Zhang, H., Chen, Z., Li, X., Zhu, P., and Cui, X. (2017). Hydrogeochemical and isotopic indicators of hydraulic fracturing flowback fluids in shallow groundwater and stream water, derived from dameigou shale gas extraction in the northern Qaidam Basin. *Environ. Sci. Technol.* 51 (11), 5889–5898. doi:10.1021/acs.est.6b04269

Zou, C., Ni, Y., Li, J., Kondash, A., Coyte, R., Lauer, N., et al. (2018). The water footprint of hydraulic fracturing in Sichuan Basin, China. *Sci. Total Environ.* 630, 349–356. doi:10.1016/j.scitotenv.2018.02.219

Zumberge, J., Ferworn, K., and Brown, S. (2012). Isotopic reversal ('rollover') in shale gases produced from the Mississippian Barnett and Fayetteville formations. *Mar. Pet. Geology.* 31, 43–52. doi:10.1016/j.marpetgeo.2011.06.009

Conflict of Interest: DL was employed by the company PetroChina.

The remaining authors declare that the research was conducted in the absence of any commercial or financial relationships that could be construed as a potential conflict of interest.

Copyright © 2021 Zhang, Liu, Gao and Zhang. This is an open-access article distributed under the terms of the Creative Commons Attribution License (CC BY). The use, distribution or reproduction in other forums is permitted, provided the original author(s) and the copyright owner(s) are credited and that the original publication in this journal is cited, in accordance with accepted academic practice. No use, distribution or reproduction is permitted which does not comply with these terms.

frontiers in Earth Science

ORIGINAL RESEARCH
published: 29 March 2021
doi: 10.3389/feart.2021.648176

The Paleoclimate Significance of the $\delta^{13}C$ Composition of Individual Hydrocarbon Compounds in the Maoming Oil Shales, China

Xinxing Cao[1,2], Zhiguang Song[1], Sibo Wang[1] and Puliang Lyu[2]*

[1] Faculty of Chemical and Environmental Sciences, Guangdong Ocean University, Zhanjiang, China, [2] Key Laboratory of Beibu Gulf Environmental Change and Resources Utilization of Ministry of Education, Nanning Normal University, Nanning, China

Maoming oil shales are typical low-altitude lacustrine sediments that were deposited during the late Paleogene. The hydrocarbon composition and compound-specific stable carbon isotopic composition ($\delta^{13}C$) of organic matter in the profile samples of the oil shales have been analyzed. The results show that algae and aquatic plants are major parent sources of the organic matter in the oil shales associated with a small portion of terrestrial higher plant input. The $\delta^{13}C$ composition of the bulk organic matter and the *n*-alkanes varies greatly on the profile from −26.9 to −15.8‰ and −31.7 to −16.2‰, respectively. While a good positive correlation among the $\delta^{13}C$ composition of individual *n*-alkanes implies that these *n*-alkanes were originated from the similar source input. The $\delta^{13}C$ composition of *n*-alkanes on the profile displays a positive excursion trend from the bottom to the top, and this excursion was likely related to the general decreasing trend of the partial pressure of atmospheric CO_2 (pCO_2) during the late Paleogene. The $\delta^{13}C$ composition of the C_{30}-4-methyl steranes ranges from −11.9 to −6.3‰, which is suggestive of *Dinoflagellates*-related source input. Coincidently, the high abundance C_{33}-botryococcanes were detected in the samples on the top section of the profile and display an extremely positive carbon isotopic composition of −4.5 to −8.4‰, suggesting that the lower partial pressure of atmospheric CO_2 had triggered a bicarbonate consumption mechanism for *Botryococcus braunii B*. Therefore, the $\delta^{13}C$ composition of *n*-alkanes and C_{33}-botryococcanes and their profile variation suggest that a general declining process associated with fluctuation in the partial pressure of atmospheric CO_2 is likely the major reason for the rapid climatic changes toward the end of the late Paleogene.

Keywords: *n*-alkanes, botryococcane, $\delta^{13}C$ of individual compounds, Maoming oil shales, the late Paleogene

OPEN ACCESS

Edited by:
Francesco Italiano, National Institute of Geophysics and Volcanology, Section of Palermo, Italy

Reviewed by:
Dazhen Tang, China University of Geosciences, China
Yongli Wang, Chinese Academy of Sciences, China

***Correspondence:**
Zhiguang Song
zsong@gig.ac.cn

Specialty section:
This article was submitted to Geochemistry, a section of the journal Frontiers in Earth Science

Received: *31 December 2020*
Accepted: *02 March 2021*
Published: *29 March 2021*

Citation:
Cao X, Song Z, Wang S and Lyu P (2021) The Paleoclimate Significance of the $\delta^{13}C$ Composition of Individual Hydrocarbon Compounds in the Maoming Oil Shales, China. Front. Earth Sci. 9:648176. doi: 10.3389/feart.2021.648176

HIGHLIGHTS

- The algae and macrophyte are major source inputs of organic matter in Maoming oil shales.
- The biomarker ratios indicate oxidized condition for early stage of oil shale deposition.
- The $\delta^{13}C$ of source specific biomarkers suggest carbon source shift for specific algae.
- An upward positive excursion of the $\delta^{13}C$ of *n*-alkanes implies a decreasing atmospheric pCO_2.

INTRODUCTION

The paleoclimate had experienced rapidly significant variation during the late Paleogene, as the global climate was switched from the warm "greenhouse" into the "glaciation and interglacial periods" from the Eocene to the Oligocene (Liu et al., 2009; Pearson et al., 2009; Colwyn and Hren, 2019). The evidence of these significant climate changes including the fast formation of the Antarctic ice sheet, the carbonate compensation depth (CCD) rapid deepened and the increase of the oxygen isotope ratio ($\delta^{18}O$) of deep-sea benthic foraminifera (Tripati et al., 2005; Liu et al., 2009; Galeotti et al., 2016; McKay et al., 2016; Passchier et al., 2017). However, the process and the reason for climate change are not well understood yet. The most of previous studies based on marine sediments suggested that the climate change would be connected with the decline of atmospheric carbon dioxide (CO_2) concentration, the switch of ocean current system and the variation of the solar radiation (Coxall et al., 2005; Goldner et al., 2014; Liu et al., 2018; Gallagher et al., 2020). On the other hand, some studies of lacustrine records are not well consistent with marine records and suggested that there was a significant climate cooling with obviously seasonal climate change, and the regional aridification in the middle and high latitude continental areas, while some other studies suggested minor or insignificant climate changes (Stephen et al., 2005; Dupont-Nivet et al., 2007; Pei et al., 2007; Eldrett et al., 2009; Hren et al., 2013; Fang et al., 2019; Ao et al., 2020). Obviously, the systematic research on more terrigenous records, especially the records of the low latitude lacustrine sediments, is much needed to the full understanding of the climate change in the late Paleogene.

The Maoming oil shales are typical low-latitude lacustrine organic-rich sediments. According to the age dating based on the turtle fossils and sporopollen (Chow, 1956; Chow and Yeh, 1962), the Maoming oil shales were widely considered as deposited during the late Eocene to early Oligocene, while a few researchers suggested that the oil shales were deposited in the early and middle Oligocene or the late Eocene (Yu and Wu, 1983; Jin, 2008; Li Y.X. et al., 2016). Therefore, the detailed geochemical research on the Maoming oil shales could provide significant information on the regional paleoclimate change of the late Paleogene in the low-latitude continental region. Previous studies have mainly focused on the source inputs and hydrocarbon composition and distribution of organic matter in Maoming oil shales (Brassell et al., 1986; Meng et al., 2020). For example, Yu et al. (2000) suggested the multi-source inputs of organic matter in Maoming oil shales based on $\delta^{13}C$ of *n*-alkanes in one outcrop sample, while others had analyzed the hydrocarbon compounds and identified a number of the biomarkers such as botryococcanes, 4-methyl steranes and hopanes in some oil shale samples (Fu et al., 1985; Brassell et al., 1986; Liao et al., 2018). Although these researches have provided some useful information on characterizing organic matter in the Maoming oil shales, all these studies are carried out on the casual outcrop samples and there is a lack of the systematic research on the characteristics of organic matter in the oil shales of the whole profile.

Therefore, by studying the composition and distribution of hydrocarbon compounds including biomarkers and their $\delta^{13}C$ composition and profile variations in the oil shale samples symmetrically collected from a full drill core from Maoming Basin, this study aims to correlate organic geochemical profile of the oil shales with the paleoenvironment variation during the geological period of the Maoming oil shale sedimentation, and therefore to provide better understanding of the climate changes of low-latitude continent region during the late Palaeogene.

GEOLOGICAL SETTING AND SAMPLES

The Maoming oil shales are named after the Maoming Basin, which is located in Southwest Guangdong province, China. The geographical and sampling corehole locations associated with geological settings are presented in **Figure 1**. The sediments of Maoming Basin were stratigraphically divided into Tongguling Formation, Shangdong Formation, Youganwo Formation, Huangniuling Formation, Shangcun Formation, Laohuling Formation and Gaopengling Formation from the bottom to the top (Herman et al., 2017). The Youganwo Formation is mainly comprised of organic-rich oil shales with a thickness varying from 2 to 45.5 m and was widely regarded as deposited from the late Eocene to the early Oligocene. The detailed lithology of Youganwo Formation includes brown tight laminar oil shales interlayered with thin clay beds, fine sandstones, carbonaceous shales, lignite, biological debris argillaceous limestone and volcanic tuff (Brassell et al., 1986; Bureau of Geology and Mineral Resources of Guangdong Province, 1996).

The core samples of Maoming oil shales were collected from the "MY-1" borehole, which is located at Shan-ge Town of the Southwestern Maoming Basin (N21°44′20″, E110°57′29″). The drilling depth of the "MY-1" borehole is 860 m and the Youganwo Formation covers the depth from 811 to 857 m, while the depth of the oil shales is from 815 to 854.3 m. The top section of the Youganwo Formation on this borehole is comprised of fine sandstone and carbonaceous shales burying at the depth of 811 to 815 m. And the bottom section of Youganwo Formation is consisted of some lignite layers and some carbonaceous shale layers at the depth of the 854.3 to 857 m. A total of 37 oil shale samples were selected from the core profile at a consistent interval (**Table 1**).

EXPERIMENTAL PROCEDURES

The total organic carbon content (TOC) and pyrolysis data of the core samples was determined using the Rock-Eval 6 pyrolyzer manufactured by French Vinci Technologies (**Table 1** and **Figure 2**), with measurement error of 0.05% for the total organic carbon content (TOC). The sample preparation was to take about 20 mg of oil shale samples and put into a ceramic crucible and then covered up with quartz sand, the sample crucibles were baked at 850°C for 2 h before the pyrolysis measurement.

For soluble organic matter extraction, the oil shale samples were ground to less than 100 meshes and then solvent extracted

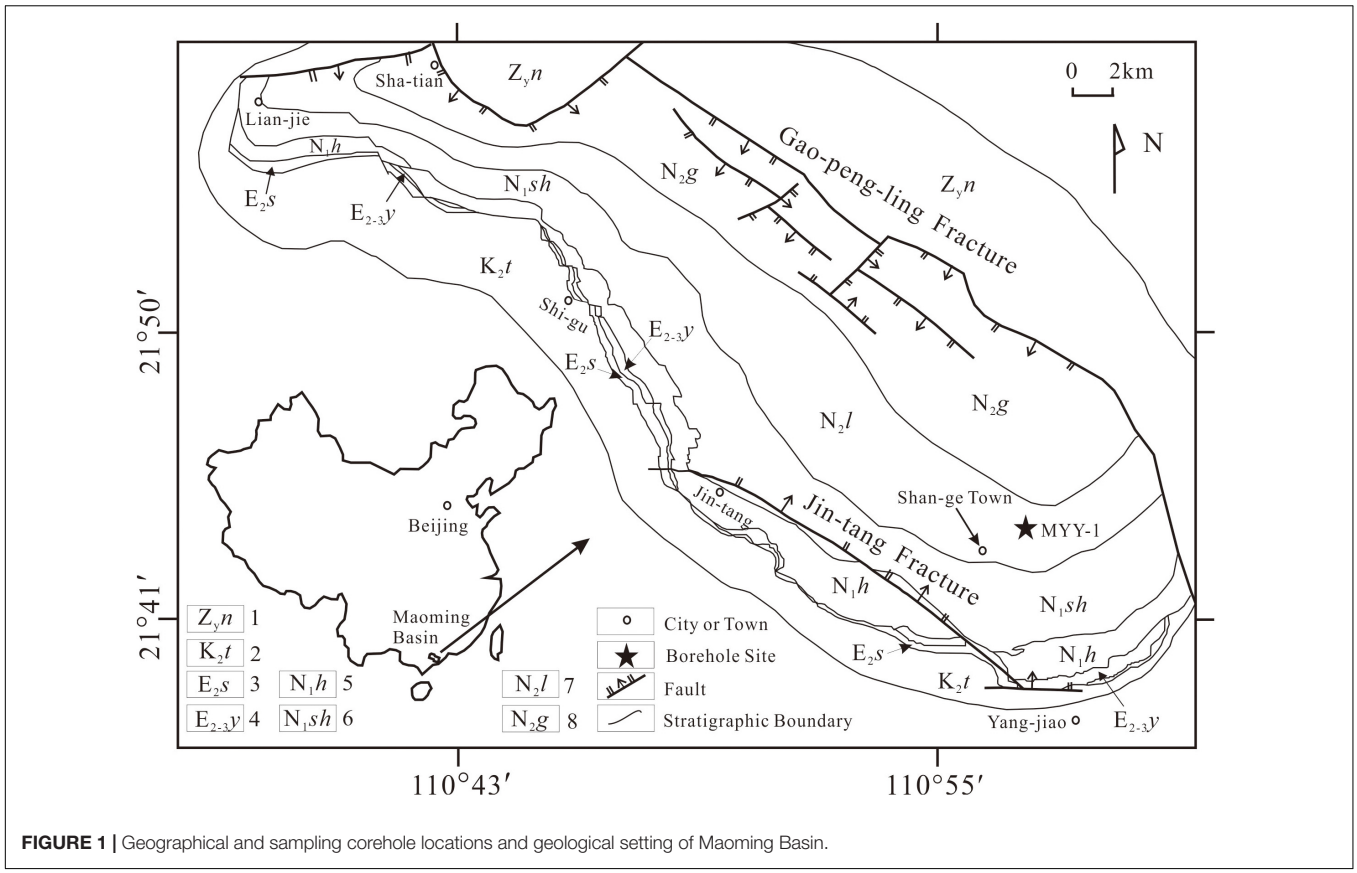


FIGURE 1 | Geographical and sampling corehole locations and geological setting of Maoming Basin.

using Soxhlet-extractor for 72 h. The extracts of soluble organic matter were separated into asphaltene fraction, aliphatic fraction, aromatic fractions and polar compounds, while the aliphatic fraction was further separated into *n*-alkane and branched and cyclic alkane fractions. The detailed experimental procedures and methods can be found in the reference of Li Y. et al. (2016). The aliphatic fractions were subjected to the analysis of the gas chromatograph (GC) and the gas chromatograph-mass spectrometry (GC-MS). The *n*-alkane and branched and cyclic alkane fractions were further analyzed by the GC-MS and the gas chromatograph-isotope ratio mass spectrometry (GC-IRMS).

The gas chromatographic analysis was carried out on an Agilent 7890A GC coupled with a flame ionization detector and the GC-MS was performed using Thermo GC Ultra Trace-DSQ II MS with an electron impact ion source at 70 eV. The capillary column used in GC and GC-MS were a J&W DB-5 fused silica column (30 m × 0.25 mm i.d. × 0.25 μm film thickness), with the injector and detector temperatures were 290 and 300°C, respectively. The samples were injected in splitless mode, and N_2 and helium are the carrier gases for GC and GC-MS, respectively. The oven temperature was initially set at 80°C and held for 2 min, was programmed to 130°C at a rate of 20°C/min, then was programmed to 290°C at 3°C/min and held for 20 min.

The carbon isotopic composition analyses of *n*-alkanes and branched and cyclic (b & c) alkanes were carried out on an Isoprime GC-Isotope Ratio Mass Spectrometer (GC-IRMS). The alkane samples were injected in splitless mode, and the injector temperature was set at 290°C with helium as the carrier gas. A J&W DB-5 silica capillary column (30 m × 0. 25 mm i.d. × 0.25 μm film thickness) was used for the separation elution of *n*-alkane and branched and cyclic alkane compounds. The oven temperature was initially set at 80°C and held for 2 min, and programmed to 130°C at a rate of 20°C/min, and then increased to 290°C at 3°C/min heating rate and held for 20 min. The b & c alkanes were identified based on the retention time of GC-MS chromatograms. The $\delta^{13}C$ composition of all samples was measured at least twice and the average $\delta^{13}C$ values of the individual compounds are reported here. The GC-IRMS was calibrated using the Vienna Peedee Belemnite (VPDB) standard and the isotopic measurement error of parallel analyses was <0.5‰. A standard sample of mixed *n*-alkanes (n-C_{12} ~ n-C_{32}) with known isotopic composition was also measured daily to ensure the reliability of the instrument.

RESULTS AND DISCUSSION

General Characteristics of Organic Matter in Maoming Oil Shales

The total organic carbon content (TOC) of Maoming oil shales ranges from 5.1 to 28.9% (**Table 1**), and the TOC contents in most samples are close to or greater than 10%, except these carbonaceous shale samples from the bottom of the Youganwo Formation. The TOC content also shows significant variation

TABLE 1 | Sampling information and the pyrolytical data of Maoming oil shales.

Sample name	Borehole depth (m)	TOC (%)	Tmax (°C)	S_1 (mg/g)	S_2 (mg/g)	S_3 (mg/g)	HI (mg/gTOC)	OI (mg/gTOC)
MYY-3	815.0	11.1	435	0.88	84.72	0.84	763	8
MYY-4	816.0	9.9	431	0.67	71.06	5.5	716	55
MYY-6	817.3	19.1	432	1.89	164.1	6.2	857	32
MYY-7	817.8	13.1	433	1.32	104.44	2.79	795	21
MYY-8	818.4	13.3	434	0.64	95.97	0.9	719	7
MYY-10	819.6	11.4	434	0.58	91.24	5.18	800	45
MYY-12	821.0	16.4	435	1.28	128.91	1.19	785	7
MYY-13	821.8	11.6	433	0.76	93.47	3.93	808	34
MYY-14	822.3	9.7	430	0.6	74.28	0.83	767	9
MYY-17	824.6	10.7	434	0.44	81.58	0.68	760	6
MYY-20	826.2	9.9	429	0.69	75.57	5.58	764	56
MYY-22	827.5	14.0	434	0.74	115.31	1.16	825	8
MYY-23	828.8	16.4	437	0.65	128.4	2.79	784	17
MYY-24	829.6	13.7	431	0.83	109.82	1.05	804	8
MYY-25	830.4	10.5	433	0.64	82.49	1.13	783	11
MYY-26	830.8	12.8	435	0.53	100.75	0.8	789	6
MYY-27	831.4	18.0	431	1.61	154.6	2.17	860	12
MYY-28	832.0	9.2	434	0.38	71.69	0.38	777	4
MYY-29	832.5	13.8	434	0.79	121.7	1.62	882	12
MYY-31	833.7	13.1	434	0.7	101.29	0.71	771	5
MYY-32	834.5	16.3	435	1.45	146.62	5.2	900	32
MYY-33	835.0	12.1	432	0.62	88.63	0.59	730	5
MYY-34	835.8	17.5	435	1.67	210.82	1.84	901	8
MYY-35	836.5	15.3	432	0.38	110.83	1.07	725	7
MYY-36	837.5	14.3	433	1.01	122.68	1.57	857	11
MYY-37	838.8	12.0	431	0.69	93.79	0.66	782	6
MYY-40	840.2	16.3	434	1.04	124.28	0.95	764	6
MYY-43	841.5	13.5	431	0.95	97.19	4.65	719	34
MYY-45	842.7	28.9	436	1.8	234.79	1.72	813	6
MYY-47	844.2	10.3	425	0.68	58.78	6.01	573	59
MYY-50	845.8	26.7	437	1.3	214.94	1.48	806	6
MYY-53	847.8	13.6	425	1.46	97.56	5.23	717	38
MYY-55	849.0	22.2	429	1.75	167.19	1.48	754	7
MYY-57	850.0	15.3	427	1.44	96.14	7.74	628	51
MYY-59	850.9	20.0	430	1.85	153.93	1.42	768	7
MYY-62	852.7	9.0	427	0.33	53.97	0.66	598	7
MYY-64	853.9	5.1	427	0.36	19.99	3.25	391	64

Hydrogen Indices (HI) are calculated from the ratio of mg HC in S_2/g TOC, and Oxygen Indices (OI) are determined by the ratio of mgCO_2 in S_3/g TOC.

in different section of the profile, as the TOC content of the lower section oil shales on the profile from 840 to 852 m is in the range of 10.3 to 28.9% (with an average of 18.5%), while the TOC content of the upper section oil shales on the profile from 815 to 840 m vary from 9.2 to 19.1% (with an average of 13.3%). Obviously, the organic matter abundance in the lower section oil shales is higher than that of the upper section oil shales on the profile.

The thermal pyrolysis data suggested that these Maoming oil shales are thermally immature or low mature (Peters and Cassa, 1994), as their T_{max} values range from 425 to 437°C and most of them were under 435°C (**Table 1** and **Figure 2**). The free hydrocarbon content (S_1) ranges from 0.33 to 1.89 mg/g (with average of 0.96 mg/g), indicating a high variability of liquid hydrocarbon contents in these shales, and the hydrocarbon content released from the thermal crack of kerogen (S_2) vary from 19.99 to 234.79 mg/g (with an average of 111.99 mg/g). The hydrogen index (HI) and oxygen index (OI) values of Maoming oil shales are in the range of 391–901 mg/gTOC and 4–64 mg/gTOC, respectively (**Table 1**). The $S_1 + S_2$ values varied from 20.35 to 236.59 mg/g (with an average of 112.94 mg/g), and most of them were around 100 mg/g, which illustrate high hydrocarbon generation potential of Maoming oil shales.

The Composition and Distribution of Aliphatic Hydrocarbon Compounds

The composition and distribution of aliphatic hydrocarbon compounds in Maoming oil shales include a series of compounds such as *n*-alkanes, branched and acyclic isoprenoids, hopanes

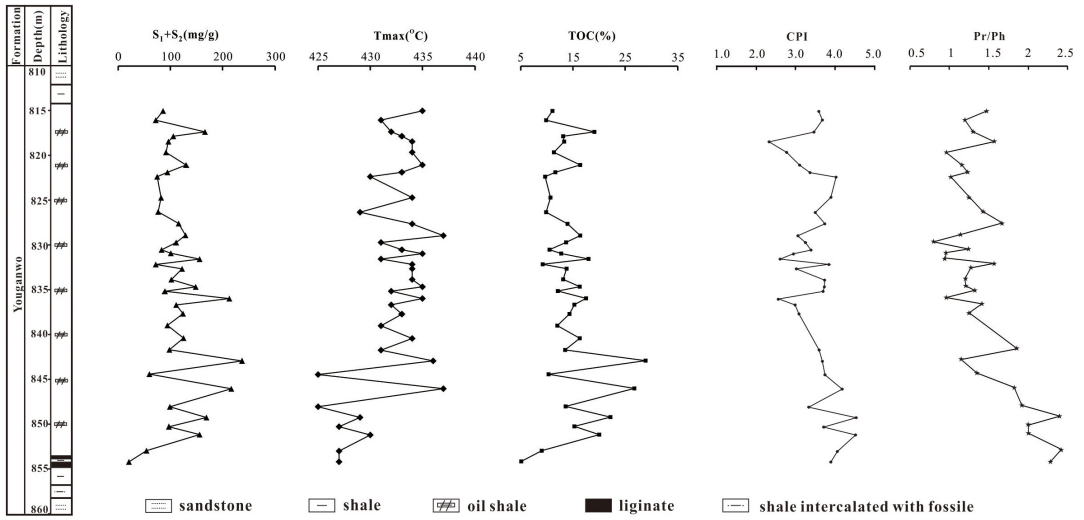


FIGURE 2 | The profile variation of TOC and pyrolytical and aliphatic parameters of Maoming oil shales (S_1: free hydrocarbon content; S_2: hydrocarbon content released from kerogen, CPI = 1/2[(C_{25} + C_{27} + C_{29} + C_{31} + C_{33})/(C_{24} + C_{26} + C_{28} + C_{30} + C_{32}) + (C_{25} + C_{27} + C_{29} + C_{31} + C_{33})/(C_{26} + C_{28} + C_{30} + C_{32} + C_{34})]; Pr = pristine; Ph = phytane). The stratigraphic log is a simplification of the complex sediments and should not be used to infer lithology of the samples.

and steranes, with *n*-alkanes are the dominant components. The chromatograms of aliphatic fraction in representative oil shale samples are displayed in **Figure 3**. The carbon number of the *n*-alkanes is principally distributed in the range of *n*-C_{13} to *n*-C_{33}, while these normal alkanes display a clear bimodal distribution with clear rear peak group dominance as the *n*-C_{27} being the predominance *n*-alkane peak on the chromatograms of all samples on the profile. The front peak group of low carbon number alkanes is dominated by *n*-C_{17} or *n*-C_{15}, while the rear peak group of high carbon number *n*-alkanes is solely dominated by *n*-C_{27}. The high carbon number *n*-alkanes display obviously a carbon number predominance of odd-over-even, as the carbon-preference index (CPI) of *n*-C_{24} to *n*-C_{34} is in the range of 2.33 to 4.54 on the whole profile (**Figure 2**), indicating low maturity or immaturity. Although the overall dominance of rear peak group over the front peak group of *n*-alkanes, the relative abundance of front peak group *vs.* the rear peak group show some variation along with burying depth on the profile, and these variation are likely due to the slightly change in the source inputs of organic matter. The relative abundance of low and medium carbon number alkanes of *n*-C_{13} to *n*-C_{21} and *n*-C_{22} to *n*-C_{26} varies along with bearing depth and the whole profile could be divided into three sections according to the distribution of the *n*-alkanes. The section I ranging from 815 to 828 m and the section III ranging from 840 to 854 m are characterized by relative lower abundance of low and medium carbon number *n*-alkanes, while the section II ranging from 828 to 840 m are characterized by relative higher abundance of low and medium carbon number *n*-alkanes.

Generally, the low carbon number *n*-alkanes (carbon number $\leq$ *n*-C_{19}) are considered as originated from algae and photosynthetic bacteria inputs (Gelpi et al., 1970; Meyers, 2003; Kristen et al., 2010), the medium-chain *n*-alkanes (*n*-C_{20} $\sim$ *n*-C_{26}) often indicate aquatic plant sources (Ficken et al., 2000; Mügler et al., 2008; Aichner et al., 2010; Damsté et al., 2011), while the high carbon number *n*-alkanes (carbon number $\geq$ *n*-C_{27}) with an odd-over-even predominance are widely considered as related with terrestrial higher plant inputs (Eglinton and Hamilton, 1967). Therefore, some samples in section II (for example, MYY-24 at 829.6 m depth) contain high abundance of the medium carbon number *n*-alkanes, which suggested an incremental input of algae and macrophyte (Gelpi et al., 1970).

The main acyclic isoprenoids include the pristane (Pr) and the phytane (Ph) which occur in high abundance in all samples of whole profile. The Pr/Ph ratio (**Figure 2**) vary in the range of 0.80 to 2.42 on the profile and displays profile variation as it is in the range of 0.80 to 1.67 for section I and section II, and 1.15 to 2.42 for section III, respectively. Since the Pr/Ph ratio between 0.80 and 3.5 could not be solely used as depositional redox indicator, the Pr/Ph ratios of these oil shales should be combined with other proxies to reconstruct the paleoenvironment variation.

The Composition and Distribution of Biomarkers

A great number of biomarkers including steroid and hopane compounds are detected in all the oil shale samples (**Figures 4**, **5**).

The steranes identified in Maoming oil shales are mainly included the regular steranes, rearranged steranes (diasteranes), 4-methyl steranes and 4-methyl rearranged sterenes (4-methyl diasterenes). The sedimentary steranes are often transformed from steroids and sterenes that originated from organisms. The composition and distribution of regular steranes (including C_{27}, C_{28}, C_{29} steranes) are consistent in most samples of the whole profile, with the high abundance of C_{27}-cholestanes and C_{29}-cholestanes and the low abundance of C_{28}-cholestanes. The 4-methyl steranes are consisted of a high abundance of the C_{30}-4-methyl steranes, low abundance of C_{29}-4-methyl steranes

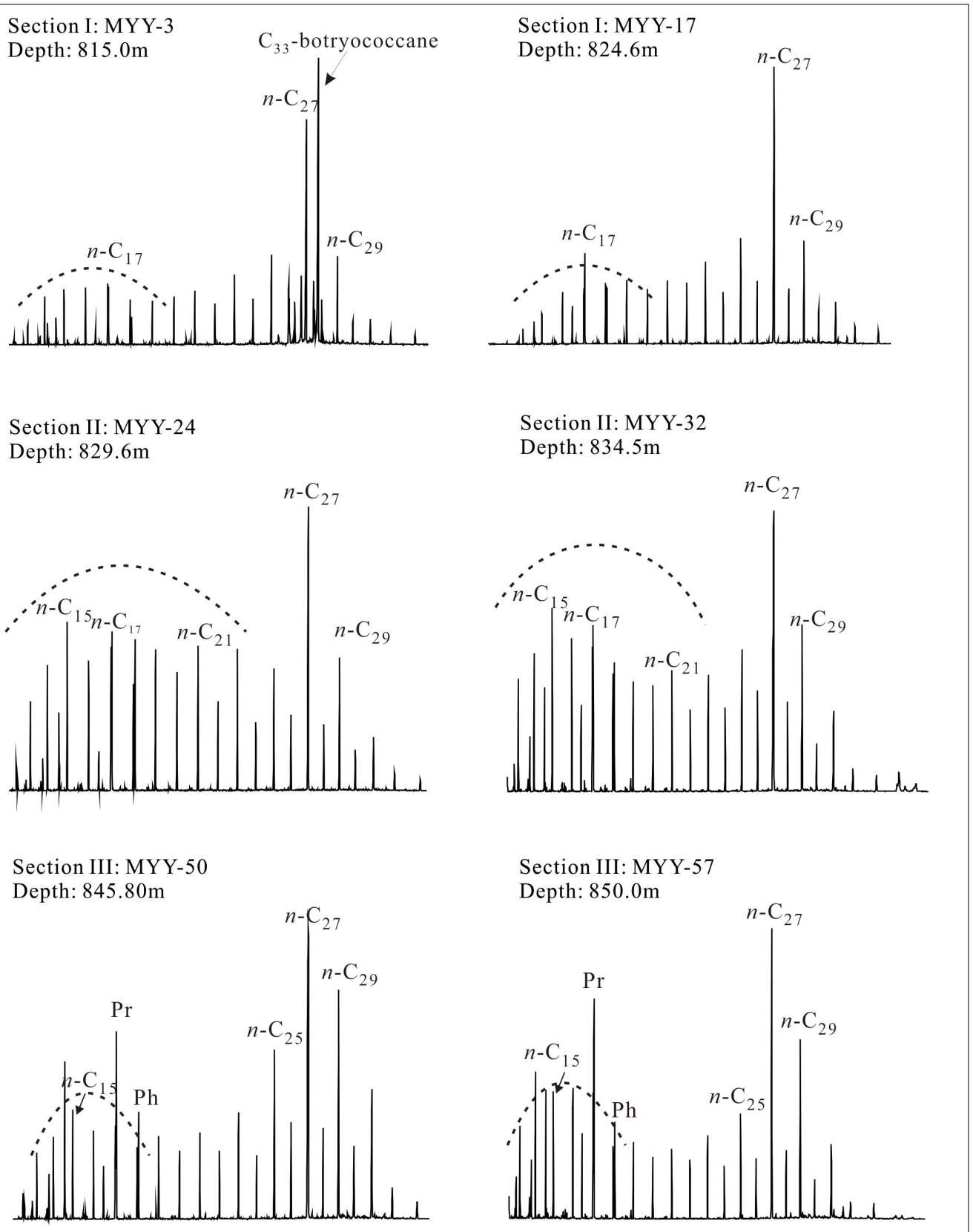


FIGURE 3 | Chromatograms of aliphatic alkane compounds in representative oil shale samples (Pr = pristine; Ph = phytane).

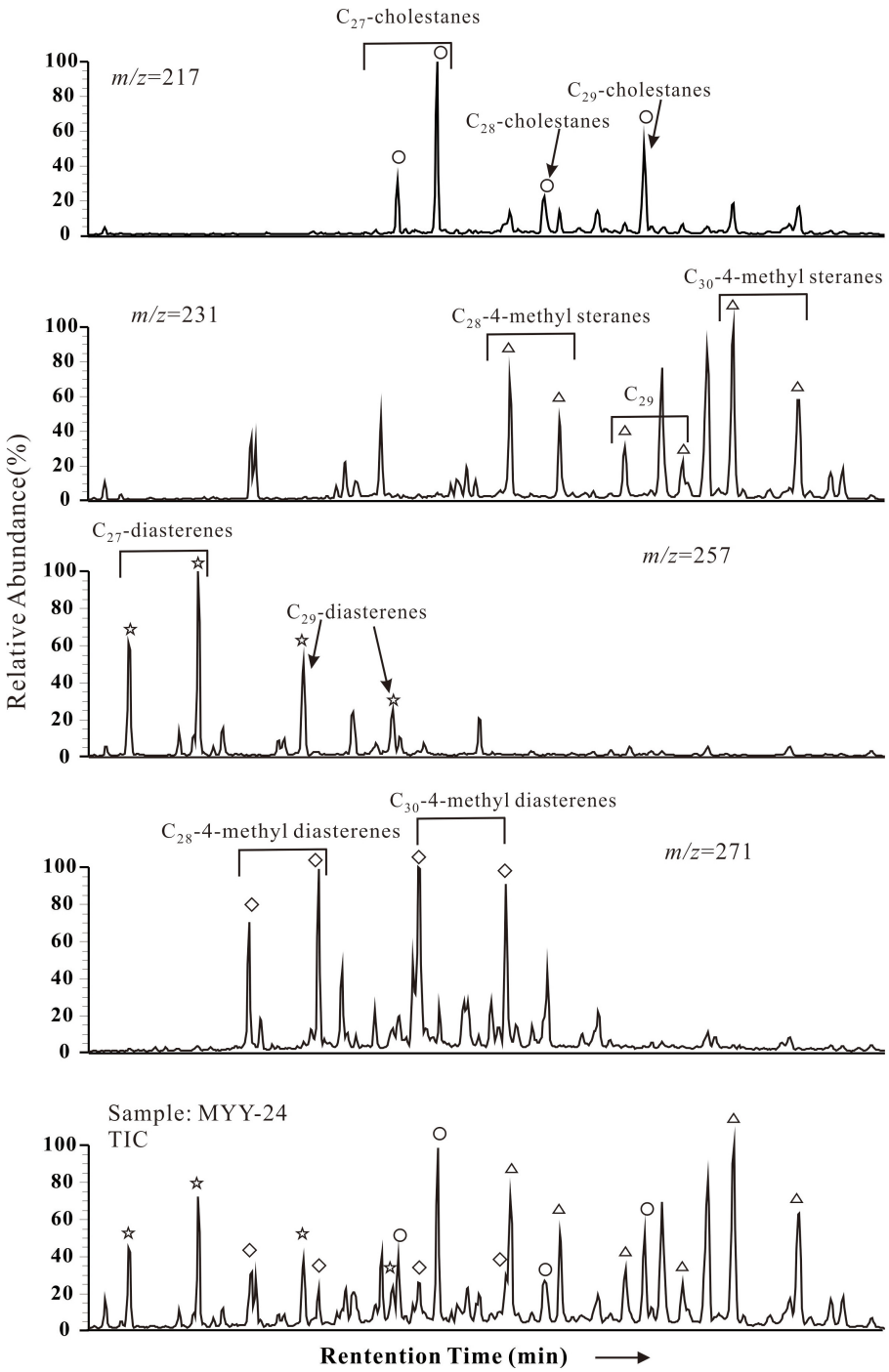


FIGURE 4 | The identification and distribution of steranes in a representative oil shale sample (Note: ○: regular steranes; △: 4-methyl steranes; ⋆: diasterenes; ◇: 4-methyl diasterenes; TIC: total ion chromatogram).

and C_{28}-4-methyl steranes. The rearranged sterenes are mainly consisted of trace amounts of C_{28}-rearranged sterenes, high abundance of the C_{27}-rearranged sterenes and C_{29}-rearranged sterenes. The 4-methyl rearranged sterenes are dominated by a high abundance of the C_{30}-4-methyl rearranged sterenes and a relative high amount of C_{28}-4-methyl rearranged sterenes, while the C_{29}-4-methyl rearranged sterenes are only detected in trace amount of few samples (**Figure 4**).

The hopanes are widely present in high abundance in all samples of the whole profile. The main compounds of hopanes are trisnorhopanes, norhopanes, hopanes, homohopanes, $\Delta^{17(21)}$-hopenes, and $\Delta^{13(18)}$-neohopenes, but the gammacerane

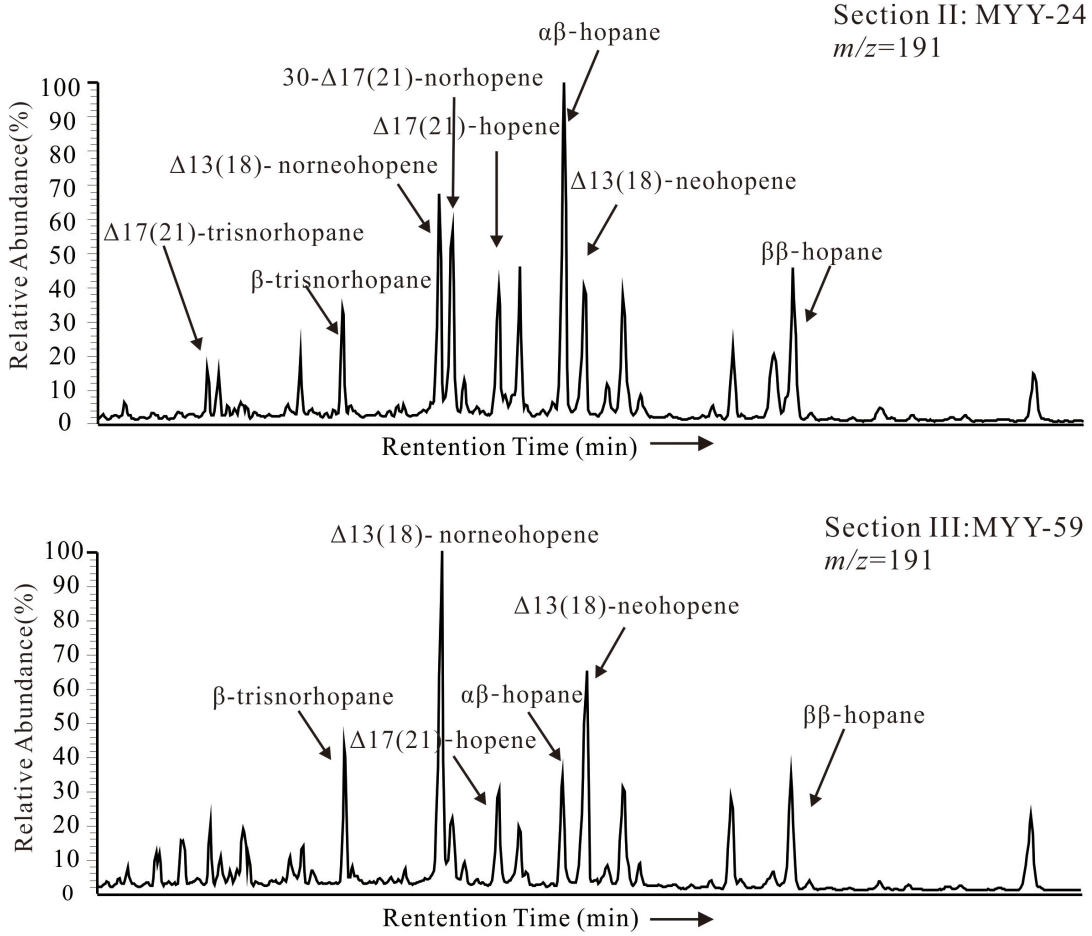


FIGURE 5 | The identification and distribution of hopanes in representative oil shale samples.

is not detected (**Figure 5**). The hopenes are dominant compounds of pentacyclic-terpane as there are abundant of the $\Delta^{17(21)}$-hopenes are detected, which are considered as medium products which the ββ-hopanes transformed to βα-hopanes and αβ-hopanes (Zhou et al., 1998). The occurrence of high abundance of ββ-hopanes, $\Delta^{17(21)}$-hopenes and $\Delta^{13(18)}$-neohopenes in the samples also indicate that these oil shales of Youganwo Formation are of low maturity.

The composition and distribution of the hopanes and the hopenes in these oil shales are generally similar on the whole profile. However, the abundance of the $\Delta^{17(21)}$-hopene compounds are very low as the 30-$\Delta^{17(21)}$-norhopenes and $\Delta^{17(21)}$-trisnorhopenes are absent in section III. On the other hand, the abundance of the $\Delta^{13(18)}$-neohopene and $\Delta^{13(18)}$-norneohopene compounds appear to be significantly increased on the section III. Some previous studies suggested that the $\Delta^{13(18)}$-neohopene is generated from the parent material through molecular bond broke during the late diagenesis; and the others considered that the $\Delta^{13(18)}$-neohopene was transformed from thermodynamically unstable $\Delta^{17(21)}$-hopene as suggested by the $\delta^{13}C$ compositon of the hopenes in the peat samples (Zhou et al., 1998).

Since the maturity of oil shale samples show little change on the profile (**Figure 2**), the lower abundance $\Delta^{17(21)}$-hopene and the higher abundance for both $\Delta^{13(18)}$-norneohopene and $\Delta^{13(18)}$-neohopene in section III than section II might not be related with the diagenesis process, but may be related to the variation in the sedimentary condition. As we have discussed above, the Pr/Ph ratio (**Figure 2**) shows an increasing trend along with the buried depth in section III, this may suggest that the deposition condition of section III could be more oxidized than that of upper sections. Therefore, the $\Delta^{13(18)}$-neohopene would be better preserved or formed than $\Delta^{17(21)}$-hopene under an oxidizing sedimentary condition.

It is worthwhile to point out that C_{33}-botryococcanes and C_{31}-botryococcanes are source-specific biomarkers and has been intermittently detected in high abundance in most samples of the top section at a depth from 815 to 821 m (**Figures 3**, **6**), as the peak height of one C_{33}-botryococcane compound is even higher than that of the dominant *n*-alkane compound of *n*-C_{27}. The botryococcanes are a kind of irregular acyclic isoprenoids and are considered as transformed from botryococcenes, which originated from *Botryococcus braunii* which is a kind of algae living in fresh to brackish water or even estuarine area

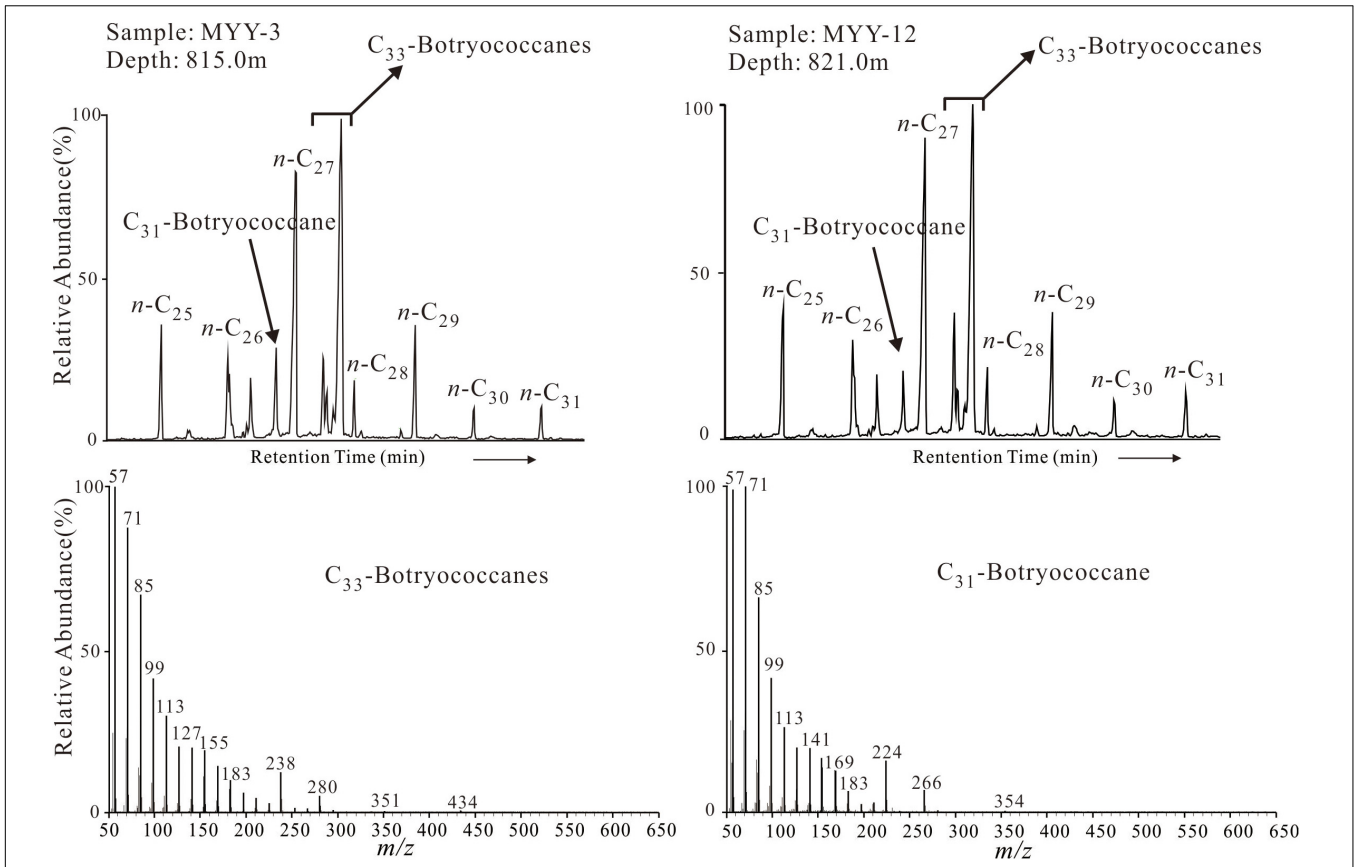


FIGURE 6 | The identification chromatograms of botryococcanes in the oil shale samples.

(Moldowan and Seifert, 1980; McKirdy et al., 1986; Smittenberg et al., 2005; Volkman, 2014). Since the *Botryococcus braunii* is sensitive to the variation of the water condition, the occurrence of botryococcanes in the sediments suggests obvious change in the environmental condition and a decline in the abundance of botryococcanes are often considered as indication of earlier anoxic condition (Smittenberg et al., 2005). The intermittently high abundance presence of the botryococcanes on the top section of the profile indicates that the lake environment was frequently favorable for the thriving of *Botryococcus braunii B.* and therefore there is a significant fluctuation in lake environment during the later stage of sedimentation in the Maoming basin.

The $\delta^{13}C$ Composition of *n*-Alkanes and Individual Biomarkers

The $\delta^{13}C$ composition of *n*-alkanes in representative samples of oil shales varies from −31.7 to −16.2‰ on the profile. The $\delta^{13}C$ composition of *n*-C_{17} and *n*-C_{19}, which are considered as derived from bacteria and algae, range from −26.9 to −19.6‰ and −29.6 to −20.0‰, respectively. The $\delta^{13}C$ of *n*-C_{23} and *n*-C_{25}, which are often considered as originated mainly from aquatic macrophytes (Ficken et al., 2000), range from −30.2 to −18.4‰ and −29.5 to −18.5‰, respectively. While the $\delta^{13}C$ of these *n*-C_{27}, *n*-C_{29}, *n*-C_{31}, and *n*-C_{33}, that are considered as a predominantly contribution from terrigenous plants, range from −28.8 to −16.2‰, −28.9 to −20.5‰, −30.9 to −21.1‰, and −31.7 to −20.1‰, respectively. The $\delta^{13}C$ composition of the same *n*-alkane compounds varies among these samples on the profile (**Figure 7**).

The profile variation trends of the $\delta^{13}C$ composition of the medium odd carbon number *n*-alkanes of *n*-C_{23} and *n*-C_{25} are similar to that of the high odd carbon number *n*-alkanes of *n*-C_{27}, *n*-C_{29}, and *n*-C_{31}. These shows that the $\delta^{13}C$ composition variation of individual hydrocarbon compounds are covariant on the profile and therefore suggests that these changes were caused by similar factors, such as changes in organic matter inputs (the direct carbon source) or of partial pressure (pCO_2) of atmospheric CO_2 (the indirect and the elementary carbon source).

The $\delta^{13}C$ variation trends of individual hydrocarbon compounds are also similar to that of bulk organic matter ($\delta^{13}C_{org}$) in the profile (**Figure 7**). The coefficiency of the $\delta^{13}C$ composition among individual *n*-alkane compounds are analyzed by Pearson correlation methods (level of significance alpha = 0.050). The results show that the $\delta^{13}C$ of *n*-C_{17} has low correlation coefficients with that of *n*-C_{29} (0.388), *n*-C_{31} (0.440), and *n*-C_{33} (0.514), while the $\delta^{13}C$ of *n*-C_{19} also shows low correlation coefficients with that of *n*-C_{29} (0.496), *n*-C_{31}

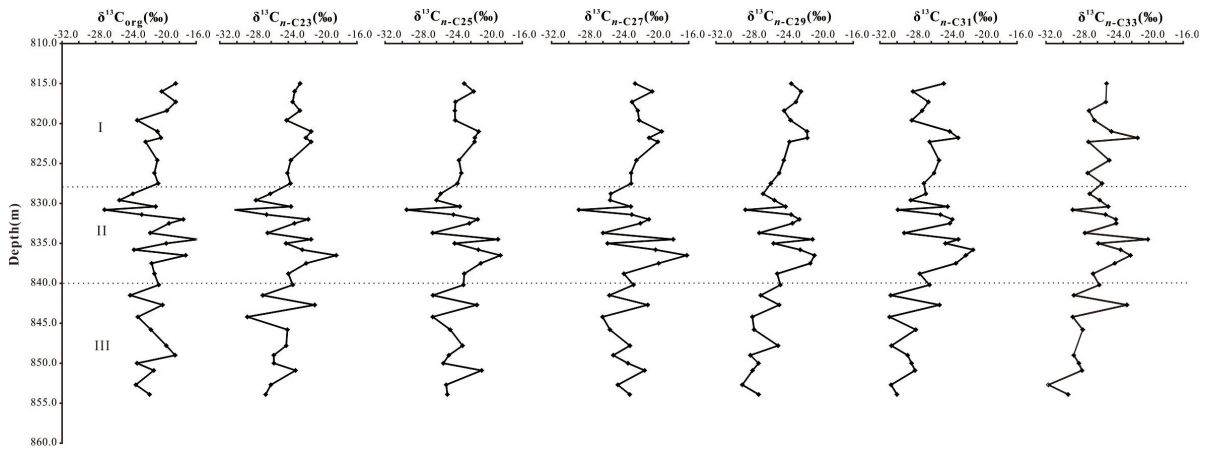


FIGURE 7 | The profile variation of $\delta^{13}C$ composition of the bulk organic matter and individual *n*-alkane compounds.

TABLE 2 | Pearson coefficient of correlation between the $\delta^{13}C$ composition of the bulk organic matter and individual *n*-alkane compounds.

	$\delta^{13}C_{org}$	$\delta^{13}C_{n-C17}$	$\delta^{13}C_{n-C19}$	$\delta^{13}C_{n-C23}$	$\delta^{13}C_{n-C25}$	$\delta^{13}C_{n-C27}$	$\delta^{13}C_{n-C29}$	$\delta^{13}C_{n-C31}$	$\delta^{13}C_{n-C33}$
$\delta^{13}C_{org}$	1	0.481	0.728	0.714	0.701	0.591	0.532	0.488	0.565
$\delta^{13}C_{n-C17}$	0.481	1	0.859	0.736	0.694	0.615	0.388	0.440	0.514
$\delta^{13}C_{n-C19}$	0.728	0.859	1	0.881	0.838	0.731	0.496	0.551	0.531
$\delta^{13}C_{n-C23}$	0.714	0.736	0.881	1	0.929	0.892	0.758	0.746	0.712
$\delta^{13}C_{n-C25}$	0.701	0.694	0.838	0.929	1	0.940	0.765	0.731	0.733
$\delta^{13}C_{n-C27}$	0.591	0.615	0.731	0.892	0.940	1	0.820	0.692	0.707
$\delta^{13}C_{n-C29}$	0.532	0.388	0.496	0.758	0.765	0.820	1	0.800	0.874
$\delta^{13}C_{n-C31}$	0.488	0.440	0.551	0.746	0.731	0.692	0.800	1	0.886
$\delta^{13}C_{n-C33}$	0.565	0.514	0.531	0.712	0.733	0.707	0.874	0.886	1

(0.551), and *n*-C_{33} (0.531), respectively. On the other hand, the $\delta^{13}C$ of *n*-C_{19} are closely correlated with the $\delta^{13}C$ of bulk organic matter, while the $\delta^{13}C$ of *n*-C_{23}, *n*-C_{25}, and *n*-C_{27} are closely correlated with that of the $\delta^{13}C$ of bulk organic matter and the $\delta^{13}C$ of all other *n*-alkane homologs (**Table 2**). So, the primary sources of organic matter in the sediments of Youganwo Formation were mainly composed of aquatic algae and macrophytes, including some of the aquatic (or terrestrial) higher plants input. Since the $\delta^{13}C_{org}$ are highly correlated with the $\delta^{13}C$ of *n*-alkanes (**Table 2**), the $\delta^{13}C$ variation of medium and high carbon number *n*-alkanes on the profile is likely not caused by the changes in the source inputs of organic matter, but possibly correlated with the variation of atmospheric pCO_2 during the late Paleocene. In addition, the $\delta^{13}C$ of all individual *n*-alkane compounds on the profile display a positive excursion trend from the bottom to the top, and the $\delta^{13}C$ of the *n*-alkanes display dramatic changes in the section II of the profile (**Figure 7**). The general upward positive excursion and the dramatic changes of the $\delta^{13}C$ of *n*-alkanes on the profile may correlate with the general decline trend and with the frequent fluctuations in the atmospheric pCO_2 during the late Paleocene (McKay et al., 2016).

Among the steranes, only C_{30}-4-methyl steranes are present in high abundance in all samples of the whole profile. The C_{30}-4-methyl steranes are considered as derived from *Dinoflagellates* or methylotrophic bacteria. The methylotrophic bacteria prefer to consume isotopically lighter methane generated from the methanogens and would consequently result in isotopically lighter lipids (biomarkers) (Games et al., 1978), while the $\delta^{13}C$ composition of C_{30}-4-methyl steranes are in the range of −11.93 to −6.28‰ (**Table 3**) which are very heavier. Therefore, the high abundance of C_{30}-4-methyl steranes was most likely derived from *Dinoflagellates* due to its much heavier $\delta^{13}C$ composition.

TABLE 3 | The $\delta^{13}C$ of source-specific compounds of C_{30}-4-methyl sterane, C_{31}-Botryococcane, and C_{33}-Botryococcane in some representative samples.

Sample name	Borehole depth (m)	$\delta^{13}C_{C30-4-mest}$ (‰)	$\delta^{13}C_{B-C31}$ (‰)	$\delta^{13}C_{B-C33}$ (‰)
MYY-3	815	−10.4	−4.5	−4.6
MYY-7	817.8	−9.8	–	−7.2
MYY-8	818.4	−11.8	n.d.	n.d.
MYY-12	821	n.d.	−7.5	−8.4
MYY-17	824.6	−11.4	n.d.	n.d.
MYY-22	827.5	−11.9	n.d.	n.d.
MYY-35	836.5	−6.3	n.d.	n.d.

$\delta^{13}C_{C30-4-mest}$ for C_{30}-4-methyl sterane; $\delta^{13}C_{B-C31}$) for C_{31}-Botryococcane; $\delta^{13}C_{B-C33}$ for C_{33}-Botryococcane; "n.d." represents not determined.

Meanwhile, the $\delta^{13}C$ composition of the botryococcanes is very heavier and ranges from −4.5 to −8.4‰ (**Table 3**). The exceptional heavier $\delta^{13}C$ of C_{33}-botryococcenes could not be explained by sedimentary conditions alone. Under an aquatic condition of CO_2 (aq) exhaustion, *B. braunii* had to take alternative carbon source by triggering its bicarbonate (HCO_3^-) consumption mechanism (Cepak and Lukavsky, 1994). Since the partial pressure of atmospheric carbon dioxide (pCO_2) during the late Paleocene was significantly lower (Galeotti et al., 2016; Steinthorsdottir et al., 2016) and this could result in low concentration of dissolved CO_2 (aq) in the lake water, and therefore triggered bicarbonate consumption mechanism of the *B. braunii* (Huang et al., 1999). HCO_3^- assimilation by *B. braunii* would cause a significant heavier $\delta^{13}C$ composition of organic matter generated by the *B. braunii* and other algae. Hence, the extreme heavy $\delta^{13}C$ composition of the C_{33}-botryococcanes and the C_{31}-botryococcanes in the samples on the top section of the Youganwo Formation suggests that the atmospheric pCO_2 during the late Paleocene decreased significantly in the low altitude continental region and frequently resulted in lower CO_2(aq) concentration in lake water and therefore would have triggered bicarbonate consumption mechanism of the *B. braunii*.

According to the previous studies, the atmospheric pCO_2 in the late Paleogene displayed a general decreased trend but associated with sharp fluctuations (Pagani et al., 2005; Pearson et al., 2009; Galeotti et al., 2016). So, a general positive excursion associated with significant fluctuation in the $\delta^{13}C$ composition of the *n*-alkanes on the profile of Maoming oil shales, especially the frequently and sharply variation in the section II, could be considered as correlated to the atmospheric pCO_2 variation during the late Paleogene, while the heavier $\delta^{13}C$ composition of some source specific biomarkers would be indication of the lower concentration aquatic CO_2 in the lake water due to the lower atmospheric pCO_2 which caused the bicarbonate consumption mechanism of algae such as *B. braunii*. Therefore, the variation in the $\delta^{13}C$ composition of the *n*-alkanes on the profile and a general positive excursion from the bottom to the top could be considered as responses to the atmosphere pCO_2 decline and variation toward the late Paleogene.

CONCLUSION

The characteristics of organic matter in the Maoming oil shales of Youganwo Formation suggest that the organic matter were mainly derived from the aquatic algae input associated with a small portion of aquatic/terrestrial high plant inputs. The $\delta^{13}C$ composition of the *n*-alkanes, which varied from −31.7 to −16.2‰, display a general upward positive excursion but with frequent and significant fluctuation in the section II of the profile may reflect the regional responses of low altitude continent to the climate change during the late Paleogene. The extreme heavy $\delta^{13}C$ composition of the C_{33}-botryococcanes and C_{31}-botryococcane and C_{30}-4-methyl steranes in some samples in the section I of the upper profile are ranged from −4.5 to −11.9‰, which is the results of carbon source shift when the aquatic CO_2 exhaustion caused by the decline in atmospheric pCO_2 triggered the bicarbonate consumption mechanism of algae such as *Botryococcus braunii*. The upward positive excursion trend and variation in the profile of the $\delta^{13}C$ composition of the individual hydrocarbon compounds in the oil shales of the Youganwo Formation would be obvious evidence for the pCO_2 variation and descent toward the late Paleogene.

DATA AVAILABILITY STATEMENT

The original contributions presented in the study are included in the article/supplementary material, further inquiries can be directed to the corresponding author/s.

AUTHOR CONTRIBUTIONS

XC carried out the field sampling and most of the lab experiments and wrote the draft of this manuscript. ZS organized the project and experimental works and edited and finalized the manuscript. SW and PL carried out some experiments and assisted field sampling and data analysis. All authors contributed to the article and approved the submitted version.

FUNDING

This study was financially supported by the National Science Foundation of China (No. 41773037), the Guangxi Natural Science Foundation (No. 2018GXNSFBA050049), the Open Fund of Key Laboratory of Environment Change and Resources Use in Beibu Gulf, Ministry of Education (GTEU-KLOP-X1803), and the Research Staring Foundation of Nanning Normal University (0819-2018L01).

REFERENCES

Aichner, B., Herzschuh, U., Wilkes, H., Vieth, A., and Böhner, J. (2010). δD values of n-alkanes in Tibetan lake sediments and aquatic macrophytes-A surface sediment study and application to a 16ka record from Lake Koucha. *Organ. Geochem.* 41, 779–790. doi: 10.1016/j.orggeochem.2010.05.010

Ao, H., Dupont-Nivet, G., Rohling, E. J., Peng Zhang, P., Ladant, J. B., Roberts, A. P., et al. (2020). Orbital climate variability on the northeastern Tibetan Plateau across the Eocene-Oligocene transition. *Nat. Commun.* 11:5249.

Brassell, S. C., Eglinton, G., and Fu, J. M. (1986). Biological marker compounds as indicators of the depositional history of the Maoming oil shale. *Organ. Geochem.* 10, 927–941. doi: 10.1016/s0146-6380(86)80030-4

Bureau of Geology and Mineral Resources of Guangdong Province (1996). *Stratigraphy (Lithostratic) of Guangdong Province*. Wuhan: China University of Geosciences Press, 177–178.

Cepak, V., and Lukavsky, J. (1994). The effect of high irradiances on growth, biosynthetic activities and the ultrastructure of the green alga *Botryococcus braunii* strain Droop 1950/807-1. *Algol. Stud.* 72, 115–131.

Chow, M. C. (1956). Supplementary notes on *Anosteira maomingensis*. *Acta Palaeontol. Sin.* 4, 233–237.

Chow, M. C., and Yeh, H. K. (1962). A new emydid from the Eocene of maoming, Kwangtung. *Verteb. Palasiat.* 6, 221–229.

Colwyn, D. A., and Hren, M. T. (2019). An abrupt decrease in Southern Hemisphere terrestrial temperature during the Eocene-Oligocene transition. *Earth Planet. Sci. Lett.* 512, 227–235. doi: 10.1016/j.epsl.2019.01.052

Coxall, H. K., Wilson, P. A., Pälike, H., Lear, H. C., and Backman, J. (2005). Rapid stepwise onset of Antarctic glaciation and deeper calcite compensation in the Pacific Ocean. *Nature* 433, 53–57. doi: 10.1038/nature03135

Damsté, J. S. S., Verschuren, D., Ossebaar, J., Blokker, J., Houten, R. V., Meer, M. T. J., et al. (2011). A 25,000-year record of climate-induced changes in lowland vegetation of eastern equatorial Africa revealed by the stable carbon-isotopic composition of fossil plant leaf waxes. *Earth Planet. Sci. Lett.* 302, 236–246. doi: 10.1016/j.epsl.2010.12.025

Dupont-Nivet, G., Krijgsman, W., Langereis, C. G., Abels, H. A., Dai, S., and Fang, X. (2007). Tibetan plateau aridification linked to global cooling at the Eocene-Oligocene transition. *Nature* 445, 635–638. doi: 10.1038/nature05516

Eglinton, G., and Hamilton, R. J. (1967). Leaf epicuticular waxes. *Science* 156, 1322–1334. doi: 10.1126/science.156.3780.1322

Eldrett, J. S., Greenwood, D. R., Harding, I. C., and Huber, M. (2009). Increased seasonality through the Eocene to oligocene transition in northern high latitudes. *Nature* 459, 969–973. doi: 10.1038/nature08069

Fang, X. M., Galy, A., Yang, Y. B., Zhang, W. L., Ye, C. C., and Song, C. H. (2019). Paleogene global cooling-induced temperature feedback on chemical weathering, as recorded in the northern Tibetan Plateau. *Geology* 47, 992–996. doi: 10.1130/g46422.1

Ficken, K. J., Li, B., Swain, D. L., and Eglinton, G. (2000). An n-alkane proxy for the sedimentary input of submerged/floating freshwater aquatic macrophytes. *Organ. Geochem.* 3, 745–749. doi: 10.1016/s0146-6380(00)00081-4

Fu, J. M., Xu, F. F., Chen, D. Y., Liu, D. H., Hu, C. Y., Jia, R. F., et al. (1985). Biomarker compounds of biological inputs in Maoming oil shale. *Geochemica* 2, 99–114.

Galeotti, S., DeConto, R., Naish, T., Stocchi, P., Florindo, F., Pagani, M., et al. (2016). Antarctic Ice Sheet variability across the Eocene-Oligocene boundary climate transition. *Science* 352, 76–80. doi: 10.1126/science.aab0669

Gallagher, S. J., Wade, B., Li, Q. Y., Holdgate, G. R., Bown, P., Korasidis, V. A., et al. (2020). Eocene to Oligocene high paleolatitude neritic record of Oi-1 glaciation in the Otway Basin southeast Australia. *Glob. Planet. Chang.* 191:103218. doi: 10.1016/j.gloplacha.2020.103218

Games, L. M., HayesRobert, J. M., and Gunsalus, P. (1978). Methane-producing bacteria: natural fractionations of the stable carbon isotopes. *Geochim. Cosmoch. Acta* 42, 1295–1297. doi: 10.1016/0016-7037(78)90123-0

Gelpi, E., Schneider, H., Mann, J., and Oro', J. (1970). Hydrocarbons of geochemical significance in microscopic algae. *Phytochemistry* 9, 603–612. doi: 10.1016/s0031-9422(00)85700-3

Goldner, A., Herold, N., and Huber, M. (2014). Antarctic glaciation caused ocean circulation changes at the Eocene-Oligocene transition. *Nature* 511, 574–577. doi: 10.1038/nature13597

Herman, A. B., Spicer, R. A., Aleksandrova, G. N., Yang, J., Kodrul, T. M., Maslova, N. P., et al. (2017). Eocene-early Oligocene climate and vegetation change in southern China: evidence from the Maoming Basin. *Palaeogeogr. Palaeoclimatol. Palaeoecol.* 479, 126–137. doi: 10.1016/j.palaeo.2017.04.023

Hren, M. T., Sheldon, N. D., Grimes, S. T., Collinson, M. E., Hooker, J. J., Bugler, M., et al. (2013). Terrestrial cooling in Northern Europe during the Eocene-Oligocene transition. *Proc. Natl. Acad. Sci. U.S.A.* 110, 7562–7567. doi: 10.1073/pnas.1210930110

Huang, Y. S., Street-Perrott, F. A., Perrot, R. A., Metzger, P., and Eglinton, G. (1999). Glacial-interglacial environmental changes inferred from molecular and compound-specific δ13C analyses of sediments from Sacred Lake, Mt. Kenya. *Geochim. Cosmochim. Acta* 63, 1383–1404. doi: 10.1016/s0016-7037(99)00074-5

Jin, J. H. (2008). On the age of the You-gan-wo Formation in the Maoming Basin, Guangdong province. *J. Stratigr.* 32, 47–50.

Kristen, I., Wilkes, H., Vieth, A., Zink, K. G., Plessen, B., Thorpe, J., et al. (2010). Biomarker and stable carbon isotope analyses of sedimentary organic matter from Lake Tswaing: evidence for deglacial wetness and early Holocene drought from South Africa. *J. Paleolimnol.* 44, 143–160. doi: 10.1007/s10933-009-9393-9

Li, Y., Song, Z. G., Cao, X. X., and George, S. C. (2016). Sedimentary organic matter record of early cretaceous environmental changes in western Liaoning Province, NE China. *Organ. Geochem.* 98, 54–65. doi: 10.1016/j.orggeochem.2016.05.010

Li, Y. X., Jiao, W. J., Liu, Z. H., Jin, J. H., Wang, D. H., He, Y. X., et al. (2016). Terrestrial responses of low-latitude Asia to the Eocene-oligocene climate transition revealed by integrated chronostratigraphy. *Clim. Past* 12, 255–272. doi: 10.5194/cp-12-255-2016

Liao, J., Lu, H., Feng, Q., Zhou, Y. P., Shi, Q., Peng, P. A., et al. (2018). Two novel decamethylhenicosanes (C31H64) identifified in a Maoming Basin shale, China. *Organ. Geochem.* 125, 212–219. doi: 10.1016/j.orggeochem.2018.09.012

Liu, Z. H., He, Y. X., Jiang, Y. Q., Wang, H. Y., Liu, W. G., Bohaty, S. M., et al. (2018). Transient temperature asymmetry between hemispheres in the Palaeogene Atlantic Ocean. *Nat. Geosci.* 11, 656–660. doi: 10.1038/s41561-018-0182-9

Liu, Z. H., Pagani, M., Zinniker, D. A., Deconto, R., Huber, M., and Brinkhuis, H. (2009). Global cooling during the Eocene-Oligocene climate transition. *Science* 323, 1187–1190. doi: 10.1126/science.1166368

McKay, D. I. A., Tyrrell, T., and Wilson, P. A. (2016). Global carbon cycle perturbation across the Eocene-Oligocene climate transition. *Paleoceanography* 31, 311–329. doi: 10.1002/2015pa002818

McKirdy, D. M., Cox, R. E., Volkman, J. K., and Howell, V. J. (1986). Botryococcane in a new class of Australian non-marine crude oils. *Nature* 320, 57–59. doi: 10.1038/320057a0

Meng, Q. T., Li, J. G., Liu, Z. J., Hu, F., and Xu, C. (2020). Organic geochemical characteristics and depositional environment of oil shale of eocene of paleocene youganwo formation in yangjiao mining area of Maoming Basin. *J. Jilin Univ.* 50, 356–376.

Meyers, P. A. (2003). Applications of organic geochemistry to paleolimnological reconstructions: a summary of examples from the Laurentian Great Lakes. *Organ. Geochem.* 34, 261–289. doi: 10.1016/s0146-6380(02)00168-7

Moldowan, J. M., and Seifert, W. K. (1980). First discovery of botryococcane in petroleum. *J. Chem. Soc. Chem. Commun.* 19, 912–914. doi: 10.1039/c39800000912

Mügler, I., Sachse, D., Werner, M., Xu, B., Wu, G., Yao, T., et al. (2008). Effect of lake evaporation on δD values of lacustrine n-alkanes: a comparison of Nam Co (Tibetan Plateau) and Holzmaar (Germany). *Organ. Geochem.* 39, 711–729. doi: 10.1016/j.orggeochem.2008.02.008

Pagani, M., Zachos, J. C., Freeman, K. H., Tipple, B., and Bohaty, S. (2005). Marked decline in atmospheric carbon dioxide concentrations during the Paleogene. *Science* 309, 600–603. doi: 10.1126/science.1110063

Passchier, S., Ciarletta, D. J., Miriagos, T. E., Bijl, P. K., and Bohaty, S. M. (2017). An Antarctic stratigraphic record of stepwise ice growth through the Eocene-Oligocene transition. *Geo. Soc. Am. Bull.* 129, 318–330. doi: 10.1130/b31482.1

Pearson, P. N., Foster, G. L., and Wade, B. S. (2009). Atmospheric carbon dioxide through the Eocene-Oligocene climate transition. *Nature* 461, 1110–1113. doi: 10.1038/nature08447

Pei, J. L., Sun, Z. M., Zhao, Y., Wang, X. S., and Li, H. B. (2007). Eocene-Oligocene boundary global cooling event recorded in the Qaidam Basin, Qinghai, China. *Geol. Bull. China* 26, 1380–1384.

Peters, K. E., and Cassa, M. R. (1994). "Applied source rock geochemistry," in *The Petroleum System-From Source to Trap*, eds L. B. Magoon and W. G. Dow (Oklahoma: The American Association of petroleum Geologists Tulsa), 93–120. doi: 10.1306/m60585c5

Smittenberg, R. H., Baas, M., Schouten, S., and Damste, J. S. S. (2005). The demise of the alga *Botryococcus braunii* from a Norwegian fjord was due to early eutrophication. *Holocene* 15, 133–140. doi: 10.1191/0959683605hl786rp

Steinthorsdottir, M., Porter, A. S., Holohan, A., Kunzmann, L., Collinson, M., and McElwain, J. C. (2016). Fossil plant stomata indicate decreasing atmospheric CO_2 prior to the Eocene - Oligocene boundary. *Clim. Past* 12, 439–454. doi: 10.5194/cp-12-439-2016

Stephen, T. G., Hooker, J. J., Collinson, M. E., and Mattey, D. P. (2005). Summer temperatures of late Eocene to early Oligocene freshwaters. *Geology* 33, 189–192. doi: 10.1130/g21019.1

Tripati, A., Backman, J., Elderfield, H., and Ferretti, P. (2005). Eocene bipolar glaciation associated with global carbon cycle changes. *Nature* 436, 341–346. doi: 10.1038/nature03874

Volkman, J. K. (2014). Acyclic isoprenoid biomarkers and evolution of biosynthetic pathways in green microalgae of the genus *Botryococcus*. *Organ. Geochem.* 75, 36–47. doi: 10.1016/j.orggeochem.2014.06.005

Yu, J. F., and Wu, Z. J. (1983). Sporopollen assemblage of Mao 5 well of Maoming Basin, Guangdong and its geological age. *J. Stratigr.* 7, 112–118.

Yu, Z. Q., Peng, P. A., Sheng, G. Y., and Fu, J. M. (2000). Biomarker carbon isotopic components of Tertiary oil shales in Maoming and Jianghan Basin. *Sci. Bull.* 45(Suppl.), 2783–2789.

Zhou, Y. P., Shi, J. Y., Xiang, M. J., and Qu, D. C. (1998). Origin study of geohopenes from different depositional environments-stable carbon isotopic evidences. *Acta Sedimentol. Sin.* 16, 14–19.

Conflict of Interest: The authors declare that the research was conducted in the absence of any commercial or financial relationships that could be construed as a potential conflict of interest.

Copyright © 2021 Cao, Song, Wang and Lyu. This is an open-access article distributed under the terms of the Creative Commons Attribution License (CC BY). The use, distribution or reproduction in other forums is permitted, provided the original author(s) and the copyright owner(s) are credited and that the original publication in this journal is cited, in accordance with accepted academic practice. No use, distribution or reproduction is permitted which does not comply with these terms.

frontiers in Earth Science

ORIGINAL RESEARCH
published: 29 March 2021
doi: 10.3389/feart.2021.647062

Characteristics of Organic Matter and Biomarkers in Core Sediments From the Offshore Area of Leizhou Peninsula, South China Sea

Yuan Gao[1,2], Jingqian Tan[1], Jia Xia[1,3], Yao-Ping Wang[1], Sibo Wang[1], Yongqiang Han[1], Jiefeng He[1] and Zhiguang Song[1,2]*

[1]Faculty of Chemistry and Environmental Science, Guangdong Ocean University, Zhanjiang, China, [2]State Key Laboratory of Organic Geochemistry, Guangzhou Institute of Geochemistry, Chinese Academy of Sciences, Guangzhou, China, [3]Southern Marine Science and Engineering Guangdong Laboratory (Zhanjiang), Zhanjiang, China

OPEN ACCESS

Edited by:
Guodong Zheng, Chinese Academy of Sciences (CAS), China

Reviewed by:
Zhifu Wei, Institute of Geology and Geophysics (CAS), China
Mohamed El Nady, Egyptian Petroleum Research Institute, Egypt
Omayma EL-Sayed Ahmed Mousa, Egyptian Petroleum Research Institute, Egypt
Chuanyuan Wang, Chinese Academy of Sciences (CAS), China

***Correspondence:**
Jia Xia
xiaj@gdou.edu.cn

Specialty section:
This article was submitted to Geochemistry, a section of the journal Frontiers in Earth Science

Received: *29 December 2020*
Accepted: *10 February 2021*
Published: *29 March 2021*

Citation:
Gao Y, Tan J, Xia J, Wang Y-P, Wang S, Han Y, He J and Song Z (2021) Characteristics of Organic Matter and Biomarkers in Core Sediments From the Offshore Area of Leizhou Peninsula, South China Sea. Front. Earth Sci. 9:647062. doi: 10.3389/feart.2021.647062

Total organic carbon (TOC), total nitrogen (TN) and multi-biomarker indexes were analyzed for two sediment cores from the eastern coastal area of the Beibu Gulf (core 45, AMS ^{14}C dated) and Qiongzhou Strait (core 29), South China Sea. The results showed that the TOC and TN content of the samples studied were 0.32–0.62% and 0.02–0.07%, respectively. The hydrocarbons in offshore sediments of Leizhou Peninsula were consisted of biogenic hydrocarbons and petrogenic hydrocarbons. The Core 29 sediments contain more terrigenous organic matter than that of sediments in core 45 due to the difference in hydrodynamic conditions. The composition and distribution of various lipid biomarkers indicate the presence of petrogenic hydrocarbons in the sediments of the whole profile of two sediment cores. There are multiple natural sources of hydrocarbons that could potentially contribute to the petroleum background through oil seeps and erosion of carbon-rich rock outcrops or bitumen deposits. Deep sourced hydrocarbon inputs from the submarine hydrocarbon seepage cannot be excluded. Further study is needed to resolve the specific sources for the petrogenic hydrocarbons and may be significant to petroleum exploration in the study area.

Keywords: leizhou peninsula, sediments, organic carbon content, biomarker, beibuwan basin, *n*-alkane

INTRODUCTION

Marine sediments act as the ultimate sink for organic carbon, incorporating organic matter (OM) into the geological carbon cycle (Dickens et al., 2004). Coastal regions are areas where active interaction between land and ocean exists. It plays a significant role in the global carbon cycle since about 80% of the global organic carbon buried in the shallow marine system, even though it only accounts for 7.6% of the total global ocean area (Hedges and Keil, 1995; Tesi et al., 2007). The sedimentary OM in the coastal area is a heterogeneous and complex mixture of organic compounds with different chemical characteristics, originating from various sources. Hydrocarbons from both natural and anthropogenic sources are very common in the marine environment (Bourbonniere and Meyers, 1996). Understanding the sources of hydrocarbons and chemical processes that affect the deposition and preservation of OM is necessary for a comprehensive examination of the global carbon cycle (Tesi et al., 2007).

There are three major hydrocarbon sources in marine sediments: 1) petrogenic hydrocarbons related to fossil organic matter (including hydrocarbons from natural oil seepage, eroded shales and coals, anthropogenic sources) and its refined products; 2) biogenic hydrocarbons generated by biologic or diagenetic process; and 3) pyrogenic hydrocarbons generated by high temperature process, including forest fires and fossil-fuel combustion (Page et al., 1996). These three different hydrocarbons have different biomarker characteristics. Much work has been done using biomarker and hydrocarbon compositional characteristics to discriminate the hydrocarbon sources in marine sediment, especially in the oil spill investigation (Page et al., 1996; Boehm et al., 2001; Yunker et al., 2014).

As one of the most critical subtropical regions of the mangrove ecosystem in China, the Leizhou Peninsula has significant marginal effects on the carbon pool of marine sediments in the offshore area (Yang et al., 2014). The Leizhou Peninsula coast is an active site because of the influence of different water masses, like the Pearl River plume and Red River plume (Bauer et al., 2013). Being the essential low latitude sea and land transition zone, the surrounding offshore region of the Leizhou Peninsula is also a typical region influenced by the East Asia monsoon. Besides, the Beibuwan Basin, located on the west margin of the Leizhou Peninsula, has been paid a lot of attention due to its abundant petroleum resources (Li et al., 2008; Zhou et al., 2019; Gan et al., 2020). The exploration, production, and transportation of crude oil may input oil pollutions into the marginal area in this region. The natural seepages can also be possible sources of the hydrocarbons which need to be taken into consideration.

There are a few studies focused on the geochemical characteristics of the surface sediments in the offshore area of the Leizhou Peninsula (Liu et al., 2012; Bauer et al., 2013; Li et al., 2014; Zhang et al., 2017). Few studies have paid attention to the origin of the OM in the studied area from the vertical perspective of time. Investigation of core sediments provides a useful tool for evaluating sediment composition and geochemistry, as well as providing information on past or ongoing environmental processes and components, both natural and human-induced (Hu et al., 2008; Bigus et al., 2014; Dong et al., 2014; Rothwell and Croudace, 2015; Jafarabadi et al., 2019). In this study, we evaluated the origins of OM using geochemical and biomarker indexes for two sediment cores from the Leizhou Peninsula's coastal zone to explore the temporal changes of sources and sinks of OM in this area.

MATERIALS AND METHODS

Sampling and Age Determination

The sampling sites are shown in **Figure 1**. Two sediment cores were collected in January 2018 on board the O/V Hailong of Guangdong Ocean University at the following stations: the Qiongzhou Strait (station 29; 9.1 m water depth); the eastern margin of the Beibu Gulf (station 45; 17.5 m water depth). Sediment cores were retrieved using a cylindrical box-corer (90 cm length, 60 mm diameter), and sectioned onboard at 5 cm intervals. The overall lithology of two cores is uniform, mainly belonged to clay-silt type. All sediment samples were placed into sterile bags and stored at −20°C until laboratory treatments. A total of twelve sediment samples including ten core sediment samples (20 cm interval) from two shallow cores and two seafloor surface sediments from the site of core samples were subjected for the bulk geochemistry and biomarker analyses in this study (**Table 1**).

Two sediment samples of core 45 was collected for accelerator mass spectrometry (AMS) ^{14}C dating. The sediment sample was washed with standard hydrochloric acid to remove carbonates. Dating of bulk organic carbon sample was done at Beta Analytic Testing Laboratory. The ^{14}C age was calibrated with the IntCal113 curve (Reimer et al., 2009; Reimer et al., 2013; **Table 2**).

Analysis of Total Organic Carbon and Nitrogen

An aliquot of bulk, freeze-dried, and homogenized sediment sample was processed for elemental analyses. After the removal of inorganic carbon with 4 N HCl and being washed with deionized water, the TOC and TN values of dried treated samples were determined in German Elementar Vario MACRO Element Analyzer. Average values were reported. The analysis errors of TOC and TN were ± 0.02% and ±0.005%, respectively.

Analysis of Aliphatic Hydrocarbons

Sediment samples were freeze-dried, grounded to 100 mesh and soxhlet-extracted continuously for 72 h with dichloromethane: methanol (93:7, v/v), with activated copper added to the solvent to remove the elemental sulfur in the samples. After extraction, the solvent was evaporated, and the extract weighed. The extract was deasphalted and separated using silica gel column chromatography into saturates, aromatics, and resins. The saturated fractions were concentrated to 1 ml using a rotary evaporator. $C_{24}D_{50}$ was added to the extract as an internal standard to instrumental analysis. The gas chromatography and mass spectrometry (GC-MS) analysis of aliphatic hydrocarbons was performed using an ISQ 7000 (Thermo Scientific, United States) interfaced to TRACE 1300 gas chromatography (GC) that was fitted with a 30 m DB-5 capillary column (0.25 mm i.d., 0.25 μm film thickness; J&W Scientific, CA, United States). Samples were injected in the splitless mode with an injector temperature of 280°C. For GC analysis, the oven was programmed from 80 to 300°C at 3°C/min with ion source temperature of 300°C. The mass spectrum was operated in the electron ionization (EI) mode (70 eV) with the mass scanning combining selective ion monitoring (SIM) with full-scan detection between m/z 50 and 650 amu. Helium was used as a carrier gas at a constant flow rate of 1 ml/min.

The steranes and terpanes were quantified in the saturated fraction of samples, and their identification was confirmed by GC-MS based on the mass spectral characteristics, peak sequence, and the previous studies.

RESULTS

Chronology

As shown in **Table 2**, the calculated age for core 45 at 45–50 cm depth is ~4.8 cal ka BP, and the age for core 45 at 85–90 cm depth

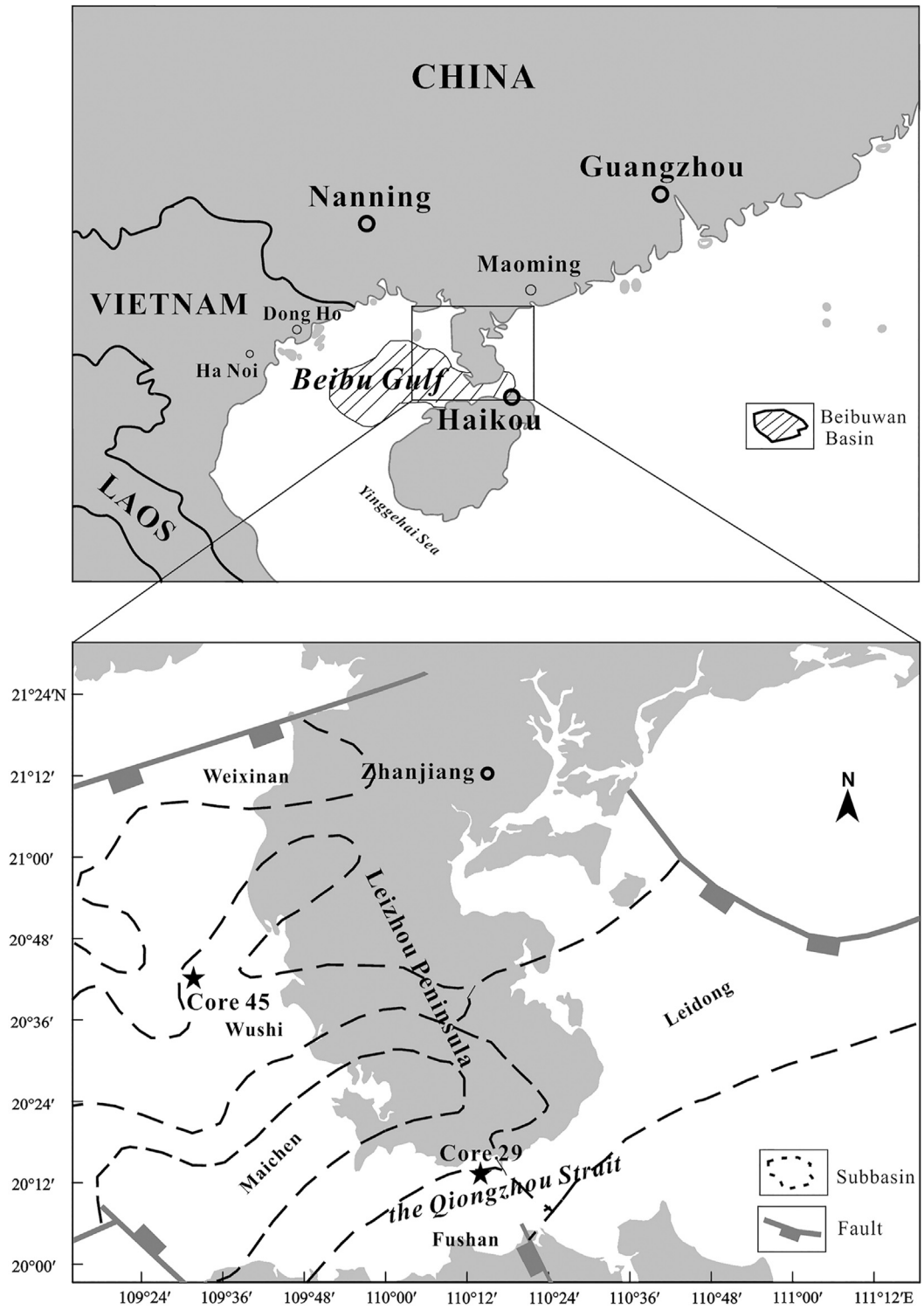


FIGURE 1 | Map of study area and sampling locations (modified after Huang et al., 2017).

is ~9.6 cal ka BP. The AMS ^{14}C dates of core 45 indicated that the sediment record of core 45 covered interval from the early Holocene to the modern time.

TOC and TN

Total organic carbon (TOC) and total nitrogen (TN) data of sediment samples from the two sediment cores are summarized

TABLE 1 | Compositions and parameters of bulk organic matter, concentrations of *n*-alkanes and hydrocarbon parameters for core sediments.

Sampling site	Sample	Depth (cm)	Texture	TOC (%)	TN	Atomic C/N ratio	Σ*n*-alkanes (ug/g dw)	$CPI_{17–21}$	$CPI_{25–35}$	TAR	NAR	Pr/ Ph	Pr/ n-C_{17}	Ph/ n-C_{18}
Core 29	29–1	0–5	Clayed silt	0.45	0.04	11.68	6.03	1.14	1.15	6.58	0.042	0.64	0.52	0.80
	29–2	5–10	Clayed silt	0.5	0.04	13.17	2.65	1.11	1.60	4.48	0.144	0.62	0.77	0.94
	29–6	25–30	Clayed silt	0.51	0.05	11.36	2.50	1.21	1.71	3.08	0.181	0.66	0.73	0.91
	29–10	45–50	Clayed silt	0.45	0.05	11.43	1.54	1.08	1.79	6.05	0.165	0.52	0.69	0.97
	29–14	65–70	Clayed silt	0.32	0.02	15.30	2.09	1.11	1.71	4.77	0.167	0.60	0.77	0.97
	29–18	85–90	Clayed silt	0.39	0.03	15.30	2.60	1.09	1.59	4.70	0.134	0.57	0.71	0.88
Core 45	45–1	0–5	Clayed silt	0.62	0.07	9.92	4.14	1.02	1.34	1.48	0.120	0.70	0.81	0.92
	45–2	5–10	Clayed silt	0.6	0.07	9.57	3.58	1.06	1.51	3.30	0.126	0.52	0.71	0.76
	45–6	25–30	Clayed silt	0.5	0.06	9.77	0.37	0.65	1.39	4.89	0.091	0.53	0.62	0.40
	45–10	45–50	Clayed silt	0.36	0.04	10.65	3.25	0.76	1.28	2.79	0.079	0.60	0.64	0.58
	45–14	65–70	Clayed silt	0.48	0.05	11.37	1.40	1.04	1.41	3.33	0.115	0.59	0.66	0.75
	45–18	85–90	Clayed silt	0.33	0.03	12.09	2.07	0.86	1.25	1.74	0.100	0.67	0.61	0.60

Σn-alkanesv: concentration of total n-alkanes (nC_{14}-nC_{37}).

$CPI_{17–21}$ 30 = (1/2)[(nC_{17} + nC_{19} + nC_{21})/(nC_{18} + nC_{18} + nC_{20})+ (nC_{17} + nC_{19} + nC_{21})/(nC_{18} + nC_{20} + nC_{22}).

$CPI_{25–35}$ = (1/2)[(nC_{25} + nC_{27} + nC_{29} + nC_{31} + nC_{33} + nC_{35})/(nC_{24} + nC_{26} + nC_{28} + nC_{30} + nC_{32} + nC_{34}) + (nC_{25} + nC_{27} + nC_{29} + nC_{31} + nC_{33} + nC_{35})/(nC_{26} + nC_{28} + nC_{30} + nC_{32} + nC_{34} + nC_{36}).

TAR: terrigenous/aquatic ratio = (nC_{27} + nC_{29} + nC_{31})/(nC_{15} + nC_{17} + nC_{19}).

NAR: natural n-*alkane ratio = [$\sum(C_{19}$-$C_{33})$-$2\sum(C_{20}$-$C_{32})_{even}$]/ $\sum(C_{19}$-$C_{32})$.*

TABLE 2 | AMS ^{14}C ages dated on core 45.

Sampling site	Sample	Depth (cm)	Material	AMS^{14}C age (yr BP)	Calendar age (yr BP, 1σ)	Mid-point (cal yr BP)
Core 45	45–10	45–50	Organic sediment	4,120 ± 30	4,829–4,780	4,805
	45–18	85–90	Organic sediment	8,630 ± 30	9,703–9,548	9,626

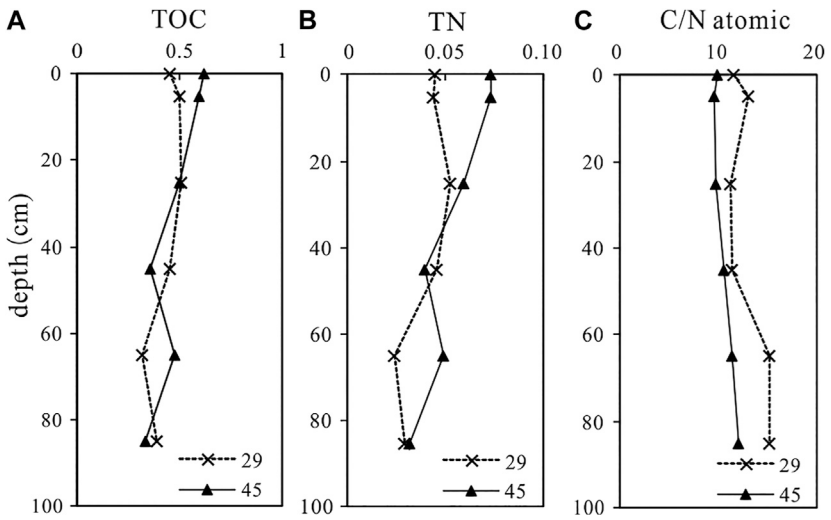


FIGURE 2 | Depth profile of TOC, TN and atomic C/N ratio for core 29 and core 45.

in **Table 1**. The TOC content ranges of the samples of core 29 and core 45 were 0.32–0.51% and 0.33–0.62%, respectively. The mean TOC in core 29 and core 45 samples are 0.44% and 0.48%, respectively. The TN values of core 29 and core 45 varied from 0.02 to 0.05% and between 0.03 to 0.07%, respectively. There was an increasing trend in TOC and TN from the bottom to surface in core 45 and a slight decrease in TOC and TN in core 29 from depth 25–30 cm to surface. The measured atomic C/N ratios of

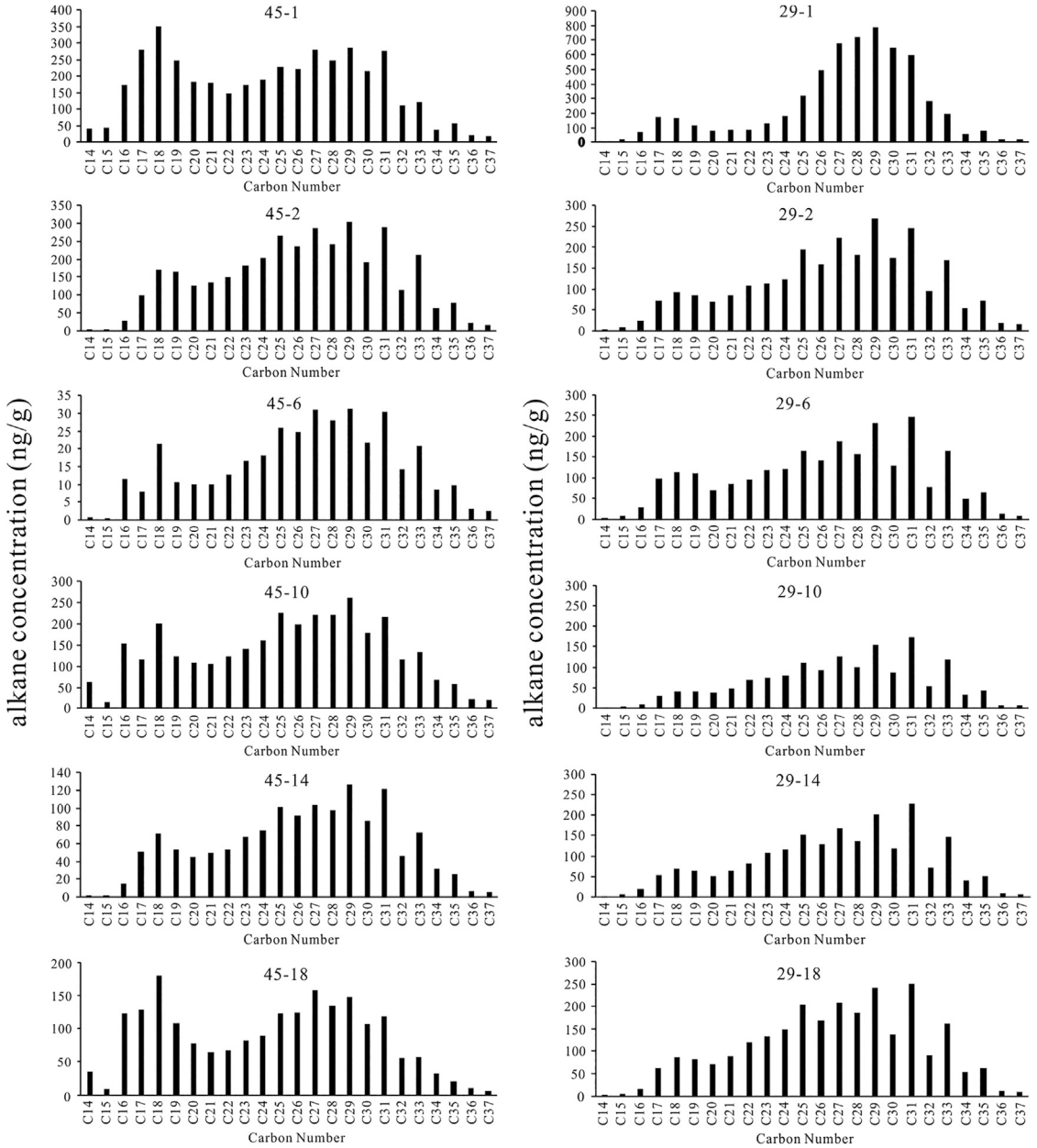


FIGURE 3 | The distribution of *n*-alkanes by carbon number in core sediments.

core 29 and core 45 varied from 11.43 to 15.30 and from 9.57 to 12.09, respectively, showing a downcore trend toward higher values (**Figure 2**).

n-Alkanes and Isoprenoids

The mass of the *n*-alkanes of the samples is shown in **Figure 3** and the relevant parameters are shown in **Table 1**. Generally, *n*-alkanes were in the range of *n*-C_{14}~*n*-C_{37}, showing a bimodal distribution throughout the depositional section. The dominant component in the long-chain *n*-alkanes was mainly *n*-C_{31} for core 29, and *n*-C_{29} for core 45. Concentrations of total *n*-alkanes in sediment cores ranged from 0.37 to 6.03 ug/g dw. Their vertical distribution of total *n*-alkane concentration at two sampling stations is displayed in **Figure 4A** and listed in **Table 1**. The total *n*-alkane concentrations changed little in sediments from two cores, except two sections. The surface sediment in core 29 contained 6.03 ug/g *n*-alkanes, more than twice that found in lower deposits. The *n*-alkane concentration of sediment from core 45 in depth 25–30 cm was relatively low, with 0.37 ug/g.

The CPI_{17-21} values were in the range of 1.08–1.21 and 0.65–1.06 for core 29 and 45, respectively, indicating a weak even-carbon-number predominance of short-chain *n*-alkanes for Core 45 (**Figure 4C**). There was a fluctuation of CPI_{17-21} values for core 45 from the deep to the shallow sediments. The CPI_{25-35}

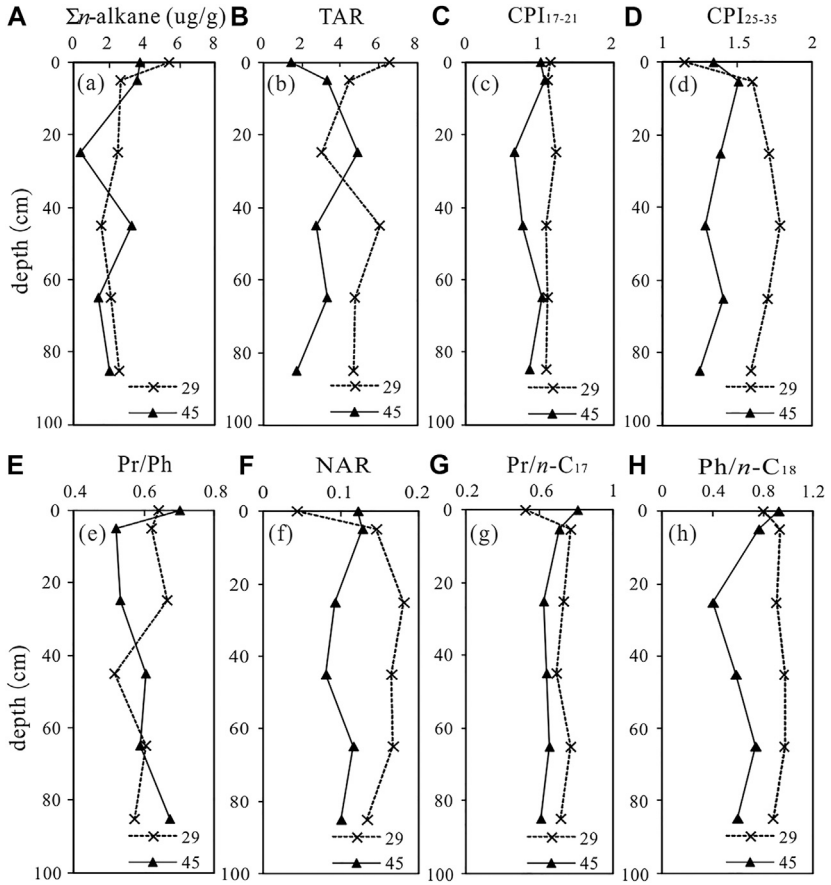


FIGURE 4 | Depth profile of parameters calculated form n-alkanes and isoprenoids in core 29 and core 45. **(A)** total *n*-alkanes concentration, **(B)** TAR, **(C)** $CPI_{17–21}$, **(D)** $CPI_{25–35}$, **(E)** Pr/Ph, **(F)** NAR, **(G)** Pr/*n*-C_{17}, and **(H)** Ph/*n*-C_{18}.

values were in the range of 1.59–1.79 and 1.25–1.51 for core 29 and 45, respectively, showing some odd-carbon-number predominance (**Figure 4D**). No apparent change occurred in $CPI_{25–35}$ value for core 29 and core 45 with depth, except for the decrease in the surface sediment.

The ratio of biogenic terrestrial origins (n-C_{27}, C_{29}, and C_{31}) to aquatic biogenic sources (n-C_{15}, C_{17}, and C_{19}) was defined as TAR (Bourbonniere and Meyers, 1996; Meyers, 2003; Silliman and Schelske, 2003). For core 29 and core 45, the TAR values ranged from 3.08 to 6.58 and 1.74 to 4.89, averaging 4.94 and 2.92, respectively, indicating that higher terrestrial plants were the dominant contributor to the OM for core 29 and 45, with core 45 sediments having more aquatic biogenic material input (**Figure 4B**). As the depth changes, the TAR values changed in the opposite direction for the two sample cores, indicating different OM sources.

The NAR (natural *n*-alkane ratio), defined by Mille et al. (2007), is useful for identifying petrogenic and biological *n*-alkane sources. A high NAR value (close to 1) is considered as a biogenic-related input, while crude oil and petroleum hydrocarbons usually exhibited a low (close to 0) NAR value (Mille et al., 2007; Akhbarizadeh et al., 2016; Wang et al., 2018; Jafarabadi et al., 2019). Herein, the NAR values ranged from 0.042 to 0.181 and 0.120 to 0.126 for core 29 and core 45, respectively (**Figure 4F**). NAR values changed little through the whole core depth, except for the significant decrease in the surface sample of core 29 (**Table 1**). The NAR values revealed that petrogenic hydrocarbon input dominated the *n*-alkane concentration in the core sediments.

As shown in **Table 1** and **Figure 4E**, the ratio of pristine (Pr) to phytane (Ph) in all samples was within the range of 0.52–0.67. On the Pr/*n*-C_{17} vs. Ph/*n*-C_{18} plot (**Figure 5**), the samples lay within the zone of marine OM sources and reducing area. According to previous studies, the increase of Pr/*n*-C_{17} and Ph/*n*-C_{18} suggests the strong microbial activity, and the decrease of the ratios indicates the increasing maturity of the OM (González-Vila et al., 2003). In our study, the ratios of Pr/*n*-C_{17} and Ph/*n*-C_{18} indicated no apparent microbial activity in the studied sediment samples (**Figures 4G,H**, **7**). Core 45 showed lower value of Ph/*n*-C18 than core 29.

Terpanes

The typical m/z 191 mass chromatogram of terpane determined by GC-MS is shown in **Figure 6A** and **Figure 6B**. The terpane parameters of the sediment samples analyzed are reported in **Table 3**.

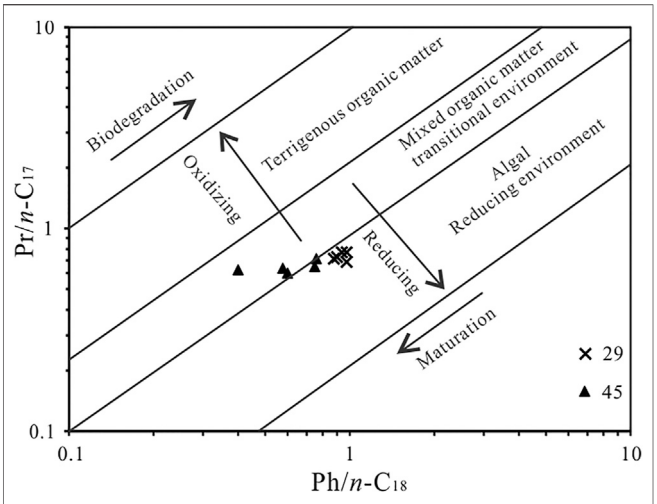


FIGURE 5 | Cross plot of phytane to n-C_{18} alkane (Ph/*n*-C_{18}) vs. pristane to n-C_{17} alkane (Pr/*n*-C_{17}) for core 29 and core 45 (modified after Connan and Cassou, 1980).

A series of hopanes consisting of C_{27} to C_{34} (without C_{28}) were identified in the samples. C_{30} 17α (H)-hopane (C_{30}H) was the dominant triterpane in all samples, with βα hopanes in much lower abundance. In addition to hopanes, tricyclic and tetracyclic terpanes were also observed in m/z 191 mass chromatograms of the marine sediment samples analyzed. The sediment samples had a low content of oleanane. The homohopanes distribution exhibited a decreasing pattern from C_{31} to C_{34} in all the samples.

The ratio of 17β, 21α (H)-moretanes to their corresponding 17α, 21β (H)-hopanes decreases with thermal maturity from ~0.8 in immature bitumens to < 0.15 in mature source rocks and oils to a minimum of 0.05 (Mackenzie et al., 1980; Seifert and Moldowan, 1980). For the sediment samples in our study, the ratio of C_{30}βα (C_{30} moretane)/C_{30}αβ(C_{30} hopane) ranged from 0.15 to 0.23 (**Figure 7B**), suggesting that the hydrocarbons in our marine sediments are in the immature to mature thermal evolution stage, and thus pointing to petrogenic hydrocarbon inputs.

The isomerization ratio of 22S/(22S+22R) for C_{31} homohopane is often used as maturity index in petroleum geochemistry and increases (0 to ~0.6) with thermal maturity, reaching the equilibrium value at 0.57–0.62 (Seifert and Moldowan, 1980; Peters et al., 2005). In this study, this ratio for sediment samples ranged from 0.33 to 0.54 and 0.45–0.52 for core 29 and core 45, respectively (**Figure 7C**).

The ratio of 18α (H)-22,29,30-trisnorhopane (Ts)/17α (H)-22,29,30-trisnorhopane (Tm) is also an index of maturity (Seifert et al., 1978). As shown in **Table 3** and **Figure 7D**, the Ts/Tm ratios ranged from 0.83 to 1.13 and 0.72 to 1.00, respectively, for core 29 and core 45, suggesting the low-mature to mature OM across the whole sediment cores.

The tricyclic terpane series extended from the C_{19} up to C_{29} (**Figures 6A,B**) and were dominated by C_{23} tricyclic terpane (abbreviated C_{23}TT). Samples from core 29 and 45 displayed C_{19}TT/C_{23}TT between 0.06–0.14 and 0.06–0.12, respectively (**Figure 7E**). This indicated the petrogenic hydrocarbon input generated from the marine environment because C_{23}TT is often the dominant homolog in crude oils of saline lacustrine and marine sources (Peters et al., 2005; Tao et al., 2015). The C_{24} Tet (C_{24} tetracyclic terpane)/(C_{24} Tet + C_{26} TT) ratios ranged narrowly from 0.29 to 0.35 and 0.30 to 0.34, respectively for core 29 and core 45. The C_{23} TT/(C_{23} TT + C_{30} H) ratios ranged from 0.37 to 1.57 and 0.80 to 1.50, respectively for core 29 and core 45 (**Figure 8**).

Steranes

The typical sterane (m/z 217) fingerprints of the sediment samples are displayed in **Figures 6C,D**. All samples from section 29 and core 45 possessed similar biomarker compositions and were dominated by regular steranes and pregnane, with a moderate abundance of diasteranes and low content of C_{30} 4-methylsteranes.

The regular C_{27}-C_{29} steranes in the core sediment samples were dominated by the C_{27} series (C_{27} > C_{29} > C_{28}) (**Figures 6C**,D, **7F**). The enhanced occurrence of the C_{27} homolog is a typical characteristic of marine petrogenic hydrocarbons (Huang and Meinschein, 1979; Moldowan et al., 1985; Shanmugam, 1985; Bouloubassi et al., 2001).

For C_{29} steranes, the isomerization ratios S/(S + R) and αββ/(ααα+αββ) are the two most commonly used sterane maturity parameters. Both ratios increase with maturity and reach equilibrium values of approximately 0.55 (equivalent to vitrinite reflectance about 0.8–0.9%) and ~0.70 (equivalent to vitrinite reflectance about 0.90–1.0%), respectively (Mackenzie et al., 1984; Seifert and Moldwan, 1986; Aboul-Kassim and Simoneit, 1996; Peters et al., 2005). Values of ααα C_{29} sterane S/(S + R) ratios in our study ranged from 0.39 to 0.50 and from 0.41 to 0.50, respectively, for core 29 and core 45 (**Figure 7G**). Values of αββ/(ααα+αββ) for C_{29} sterane ranged from 0.40 to 0.49 and from 0.44 to 0.48 for the two core sections, respectively (**Figure 7H**). Both ratios changed little in two cores. The values of both two sterane maturity parameters indicated the maturity stage of early oil generation, suggesting the presence of petrogenic hydrocarbons in all sediment samples.

DISCUSSION

Origins of Organic Matter in Sediments

The C/N ratio is frequently used to identify the biological origins of OM (Meyers, 1994; Meyers, 1997; Jia and Peng, 2003; Hu et al., 2009). It has been reported that marine algae has C/N ratios between 4 to 10 due to richness in protein and cellulose absence. In contrast, vascular plants have atomic C/N ratios >20 due to the abundance of cellulose (Meyers, 1997). TAR value is another index commonly used to identify OM origin. Both C/N ratio and TAR value indicated that both sites' biogenic OM origin included marine phytoplankton and terrestrial higher plants, with the latter dominated.

The dominant peak for long-chain *n*-alkanes was *n*-C_{31} for core 29, whereas, in core 45, *n*-C_{29} dominated (**Figure 3**). This suggested different types of terrestrial plant inputs for two sites,

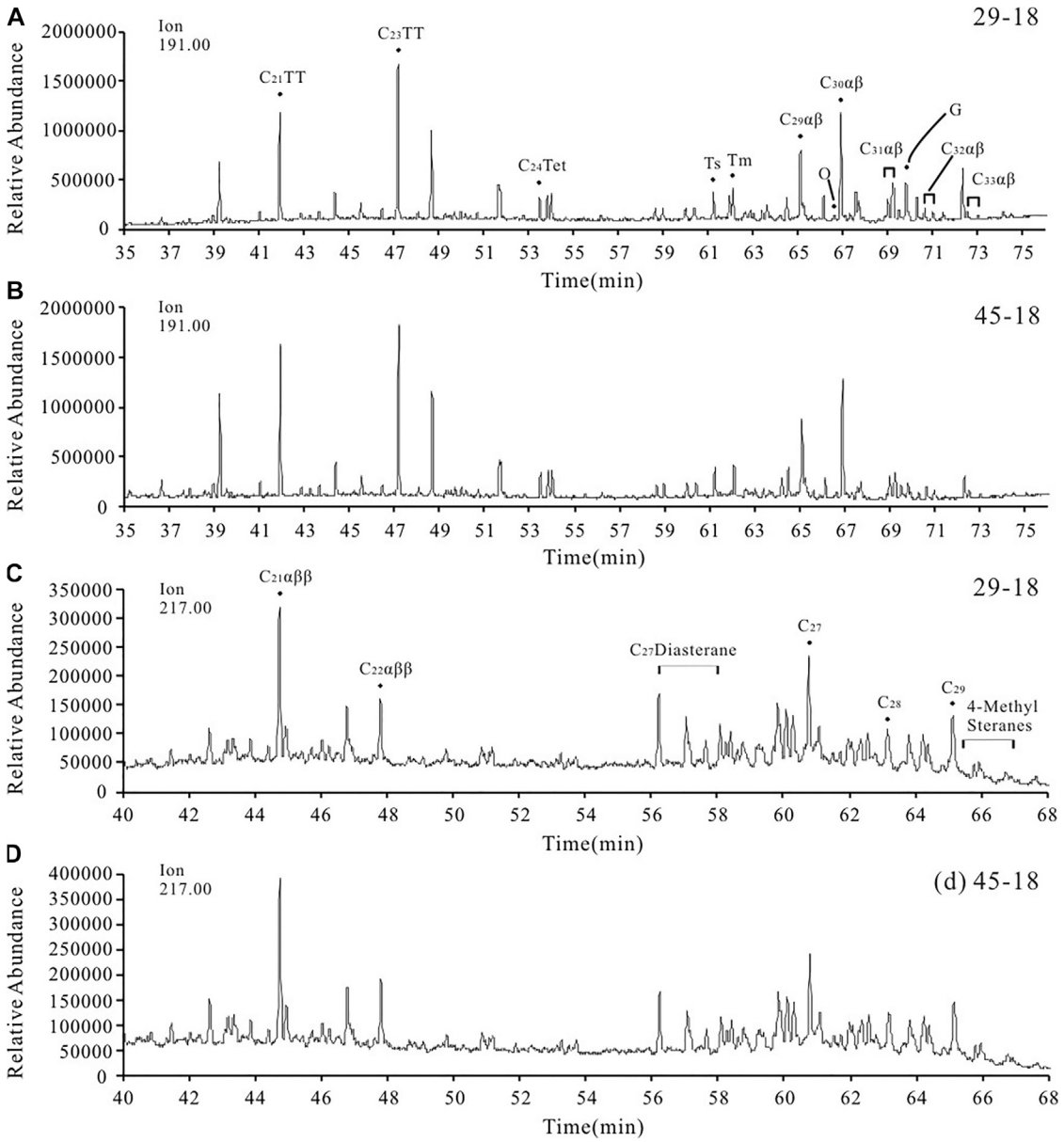


FIGURE 6 | Representative mass chromatogram (m/z 191) for terpane and (m/z 217) for sterane series of organic matter extracted from core sediments. (a): TT = tricyclic terpanes; Tet = tetracyclic terpane; O = oleanane; G = gammacerane; (c):C_{21}αββ - C_{22}αββ = C_{21}αββ - C_{22}αββ pregnane; C_{27} -C_{29} = αααR C_{27}-C_{29} sterane.

consistent with the palynological research of the surface sediment from the Beibu Gulf (Tong et al., 2012). Besides, TAR value was higher in core 29. The value of atomic C/N ratio was also higher in core 29 sediments. This suggested more terrestrial biogenic material input in core 29 than core 45. The TAR values changed in the opposite direction within depth for the two cores. TAR values increased upward in 30 cm upmost sediments in core 29 and decreased upward in 30 cm upmost sediments in core 45 (**Figure 2**), showing that more terrestrial OM deposited in Qiongzhou Strait, whereas more marine algae inputted on the west coast of the Leizhou Peninsula in the latest sedimentation period. Core 45 is farther away from the shore than core 29. Besides, core 29 is located near the port of Haian, an essential passage from the Chinese mainland to Hainan island. In addition to the Leizhou Peninsula's material sources, Hainan Island also contributes to the OM deposits in Qiongzhou Strait through river runoff. As a result, terrestrial OM accumulates more at the site of core 29. In addition to the supply of coastal area, core 29, located in Qiongzhou Strait, can also get the material from the eastern region of Qiongzhou strait or even Taiwan Island, and having more contribution of terrestrial provenance brought by Huanan nearshore current (Zhang

TABLE 3 | Terpane and sterane parameters for core sediments.

Sampling site	Sample	Depth (cm)	$C_{30}\beta\alpha/c_{30}\alpha\beta$	$C_{31}\alpha\beta$ 22S/(22 S + 22 R)	Ts/Tm	$C_{19}TT/C_{23}TT$	$C_{23}TT/C_{30}H$	$C_{24}Tet/(C_{24}Tet + C_{26}TT)$	$C_{23}TT/(C_{23}TT+C_{30}H)$	C_{29}sterane αββ/αββ+ααα	C_{29}sterane ααα20S/(20 S + 20 R)	ααα20RC_{27}/C_{29}
ST29	29–1	0–5	0.18	0.46	1.13	0.14	0.47	0.35	0.32	0.49	0.47	1.28
	29–2	5–10	0.16	0.54	1.08	0.06	0.37	0.31	0.27	0.48	0.49	1.35
	29–6	25–30	0.18	0.51	0.84	0.09	0.75	0.29	0.43	0.47	0.50	0.98
	29–10	45–50	0.22	0.33	0.85	0.06	1.51	0.32	0.60	0.40	0.39	1.81
	29–14	65–70	0.23	0.36	0.83	0.09	1.57	0.34	0.61	0.41	0.41	2.08
	29–18	85–90	0.21	0.37	0.87	0.06	1.48	0.32	0.60	0.42	0.41	1.91
ST45	45–1	0–5	0.16	0.53	0.72	0.11	1.08	0.30	0.52	0.46	0.45	1.59
	45–2	5–10	0.17	0.51	0.93	0.07	0.90	0.30	0.47	0.48	0.50	1.50
	45–6	25–30	0.19	0.45	0.87	0.06	1.50	0.34	0.60	0.45	0.41	1.78
	45–10	45–50	0.15	0.52	0.93	0.07	0.80	0.32	0.44	0.44	0.42	1.90
	45–14	65–70	0.18	0.48	0.98	0.07	0.94	0.32	0.49	0.45	0.43	1.93
	45–18	85–90	0.15	0.45	1.00	0.12	1.43	0.30	0.59	0.45	0.41	1.73

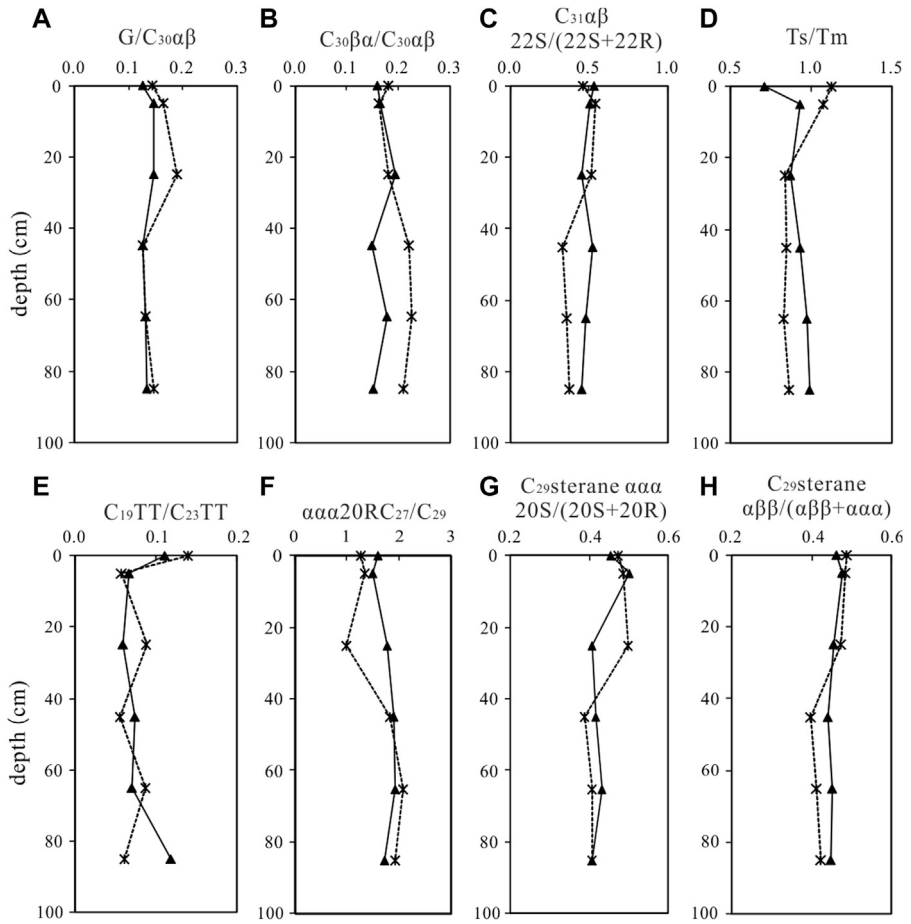


FIGURE 7 | Depth profile of biomarker indexes in core 29 and core 45. **(A)** G/$C_{30}\alpha\beta$, **(B)** $C_{30}\beta\alpha/C_{30}\alpha\beta$, **(C)** $C_{31}\alpha\beta$22S/(22 S + 22 R), **(D)** Ts/Tm, **(E)** $C_{19}TT/C_{23}TT$, **(F)** αααsterane 20RC_{27}/C_{29}, **(G)** C_{29}sterane ααα20S/(20 S + 20 R). amd **(H)** C_{29}sterane αββ/(αββ+ααα).

et al., 2018). Therefore, more higher terrestrial OM in core 29 than core 45 reflects the different hydrodynamic conditions between two sites.

There was a mild odd-even carbon preference in the higher-molecular-weight *n*-alkanes ($n \geq 25$) in the two core samples, and the carbon preference indices $CPI_{25\text{-}35}$ ranged from 1.15 to 1.79.

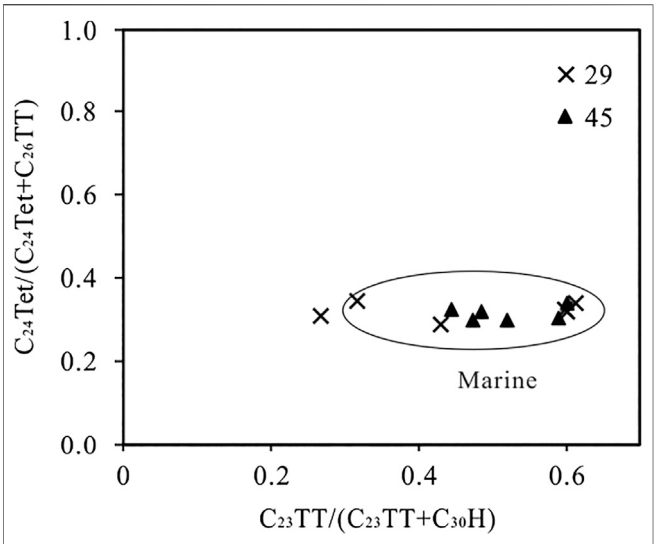


FIGURE 8 | Cross plot of $C_{23}TT/(C_{23}TT + C_{30}H)$ vs $C_{24}Tet/(C_{24}Tet + C_{26}TT)$ for core 29 and core 45 (modified after Hanson et al., 2000).

The CPI value can be influenced by both source input and maturity. According to the previous studies, the *n*-C_{24}~*n*-C_{35} alkanes derived from marine OM tend to have little or no carbon-number preference (Peters et al., 2005). In addition to this, the CPI value decreases with increasing maturity. The high CPI in modern sediment indicates low maturity and land-plant input, and the recent sediments with CPI ~1 may arise from a predominance of marine input and/or petroleum input (Tolosa et al., 2004; Seki et al., 2006). Based on the TAR and C/N value, the origins of OM included marine phytoplankton and terrestrial plants with terrestrial plants dominating. Therefore, the low $CPI_{25\text{-}35}$ in the sediment samples from two core sites indicated the petrogenic hydrocarbon input.

The $CPI_{17\text{–}21}$ ranged from 0.65 to 1.21, and even-to-odd predominance was observed at three depth in core 45. It has been reported that the even carbon number preference in the low molecular weight in sediment mainly indicates microbial activities (Nishimura and baker, 1986; Grimalt and Albaiges, 1987; Wang et al., 2012) or possible petroleum-derived inputs (Harji et al., 2008). The Ph/*n*-C_{18} and Pr/*n*-C_{17} ratio did not indicate obvious biodegradation (**Figure 5**). Given this, the even carbon number preference should be due to petrogenic hydrocarbon input. From the whole section, the $CPI_{17\text{-}21}$ and $CPI_{25\text{-}35}$ of core 45 was lower than core 29, indicating a higher proportion of petrogenic hydrocarbon in core 45 sediment than core 29. **Figure 5** showed that the Ph/*n*-C_{18} of core 45 sediments (sediment 45–6, 45–10, 45–14 and 45–18) was lower than core 29 samples, showing slightly higher maturity. This difference was consistent with the higher values of C_{31} homohopane 22S/(22S+22R) and lower values of C30βα/C30αβ for these four samples than core 29 samples (**Figure 7**). This can be caused by more petrogenic hydrocarbon inputs in core 45 or is simply reflection of variable maturity for the petrogenic hydrocarbon sources.

The isoprenoids pristane and phytane are often found in petroleum products. Pristane is also found biogenically, while phytane rarely occurs in biogenic material (Shaw and Baker, 1978; Venkatesan and Kaplan, 1982; Broman et al., 1987). In addition to indicating a reductive sedimentary environment, pristane/phytane ratio close to or smaller than 1 in our sediment samples can could indicate petrogenic hydrocarbons (Shaw et al., 1985; Broman et al., 1987; Commendatore and Estevesa, 2004).

Hopanes and steranes are derived from bacteria, algae, and vascular plants (biogenic sources) and are also constituents of crude oil and derived products (petrogenic sources) (Huang et al., 1992). The biological ββ-configuration of hopanoids in the organism is unstable and readily convert to βα-(moretane) and αβ-hopane configurations during burial, and αβ-hopane is thermodynamically stable and dominates in petroleum (Seifert et al., 1980; Peters et al., 2005; Huang et al., 2014). The predominance of 17α (H), 21β (H)-hopane, maximizing at C_{30} and C_{29} homologous in all core samples in our study demonstrated a pivotal hydrocarbon contribution from petrogenic sources. No ββ-isomers were identified in core sediment samples, and the contribution of biogenic hopanes can be excluded. Sediment samples in our study were buried less than 1 m, during the very early diagenesis stage of OM evolution. The biomarker ratios, including C_{31} homohopane 22S/(22S+22R), Ts/Tm, $C_{30}βα/C_{30}αβ$, C_{29} sterane αββ/(ααα+αββ) and ααα C_{29} sterane S/(S + R), all suggested that the maturity of OM was in the early oil generation stage. The maturity of the OM indicated the allochthonous petrogenic hydrocarbons.

The NAR value of sediments from both cores were all smaller than 0.2, with a mean of 0.139 and 0.105 for core 29 and core 45, respectively. This low NAR values indicated a predominant petrogenic hydrocarbon input, and a minor role of biogenic hydrocarbons. NAR values lower in core 45 than core 29 indicates more petroleum input in core 45 than core 29, consistent with the CPI indication.

Possible Origin of Petrogenic Hydrocarbons in Sediment Cores

Liquid petroleum and gas are essential industrial materials and necessities of people living in modern society. The worldwide extraction, transportation, and use of petroleum inevitably result in its release to the environment. Most of the spilled oil entering the sea comes from land-based sources and tankers, and so on.

Shaw et al. (1985) investigated the hydrocarbons in the sediments of Ports Valdez, Alaska, after three to five years of oil terminal operation with a routine daily discharge of 170 kg of petroleum residue in an otherwise undeveloped sea. They found the petroleum contamination occurs in the 0–5 cm sediments near the terminal. Jafarabadi et al. (2019) studied the levels and vertical distribution of hydrocarbons in sediment cores from the coral islands of the Persian Gulf. They found that the highest levels recorded at 10–20 cm depth in the industrial sites, and the *n*-alkanes concentration is as high as 5,000 ug/g dw, and down to a tenth of the highest at 40 cm depth. We can conclude from the

above instances that the concentration of *n*-alkanes is highest near the benthic surface and decreases downward in sediment cores polluted by anthropogenic petroleum discharge.

In our study, the concentration of *n*-alkanes ranged from 0.37 to 6.03 ug/g dw, with a mean of 2.68 ug/g dw. The *n*-alkanes concentrations in the core sediment in the coastal region of the Leizhou Peninsula were similar to those in surface sediments and short marine core sediments (50 cm length) from Bohai Sea, where the spilled oil in sediments was identified (Hu et al., 2009; Li et al., 2015; Wang et al., 2018). The concentrations of *n*-alkanes changed little from the surface to the bottom in our study, showing different characteristics with sediment profile contaminated by human. The dating of the sediment core was conducted using the AMS ^{14}C method. The results showed that the age of the bottom sample of core 45 is ~9.6 cal ka BP (**Table 2**). Petroleum has not been large-scaled used until the middle period of the 19th century. The anthropogenic petroleum pollution input is excluded for the petrogenic hydrocarbon input to the sediment samples predate industrial activity in this study.

The identical distribution of terpanes and steranes and similar values of derived parameters in two cores suggested the consistency of sources for the petrogenic hydrocarbon input during different sedimentation period (**Figures 6**, **7**). The tricyclic terpane series are ubiquitous in source rock extracts and petroleum samples (De Grande et al., 1993), and are commonly used to relate oil and source rocks (Peters et al., 2005; Bennett and Olsen., 2007; Hao et al., 2009; Tao et al., 2015). C_{19} or C_{20} tricyclic terpanes are often the dominant homologs in terrigenous petrogenic hydrocarbons, while C_{23} tricyclic terpane is abundant in marine petroleum and source rocks (Peters and Moldowan, 1993; Preston and Edwards, 2000; Volk et al., 2005). Low C_{19}/C_{23} TT ratios of core sediment samples in this study indicated the occurrence of petrogenic hydrocarbons generated from marine OM. The cross plot of C_{24} Tet/(C_{24} Tet + C_{26} TT) vs. C_{23} TT/(C_{23} TT + C_{30} H) ratios have been successfully used to distinguish between marine oils and non-marine oils (Hanson et al., 2000; Duan et al., 2008; Tao et al., 2015). It is clear from **Figure 8** that core 29 and core 45 have the similar marine origins for the petrogenic hydrocarbon input (**Figure 8**).

There are multiple natural sources of hydrocarbons that contribute to the petroleum background in marine area through oil seeps or erosion of carbon-rich rock formations. Residual oil stains, asphaltic sandstones and organic-rich mudstones are present in exposures in Hanoi and Dong Ho, Vietnam. Oil seeps occur onshore and offshore of Vietnam (Traynor and Sladen, 1997). Organic rich mudstones are exposed on island in Beibu Gulf (Nytoft et al., 2020). Oil and gas seepage are also present offshore in the Yinggehai Sea, on the southwest coast of Hainan Island. Oil and bitumen from these sources could be picked up and transported by ocean circulation of Beibu Gulf. Two oil shale horizons outcrop in the vicinity of Maoming in Guangdong Province, some 100 km to the northeast of Leizhou Peninsula (Brassell et al., 1986; **Figure 1**). The weathered and eroded oil shale could be transported by the Huanan nearshore current and the water masses flowing westward through the Qiongzhou Strait into the gulf.

The Beibuwan Basin (**Figure 1**) is a Cenozoic sedimentary basin that includes Paleogene lacustrine and Neogene Quaternary littoral sea-neritic sea facies in the northern South China Sea (Huang et al., 2013). It has been paid a lot of attention due to its petroleum resources since some oil fields and numerous oil-bearing structures have been discovered on Weixinan, Wushi, and Fushan subbasins (**Figure 1**; Huang et al., 2017). Abundant oil and gas have been discovered in the Beibuwan Basin. Wushi and Fushan subbasin are located under the seafloor of core 45 and core 29, respectively. Although no natural oil seepages in the study area have been reported, this source of background petrogenic hydrocarbons could be potentially a very important contributor to Leizhou Peninsula offshore sediment.

The biomarker component characteristics in the core sediments, such as the high ratio of C_{23} tricyclic terpane/hopane ($C_{23}TT/C_{30}H$), low content of oleanane and 4-methyl steranes, and the coexistence of pregnane and diasteranes illustrated that the OM in sediments could be linked to a mixture of sources (Bao et al., 2007; Li et al., 2008; Huang et al., 2011; Huang et al., 2017; Zhou et al., 2019; Gan et al., 2020). Further research is needed to resolve the specific origin of the petrogenic hydrocarbon background in offshore area of Leizhou Peninsula.

The surface sediment in core 29 and core 45 contained more n-alkanes than those found in deeper deposits. Besides, the CPI value of surface sediments from two cores was obviously smaller than the subsurface core sediments. NAR value decreased significantly in the surface sample of core 29. The maturity of the OM in uppermost sediment samples of two cores was higher than deeper sediment samples according to the isomerization of C_{31} homohopane and C_{29} sterane (**Figures 7G,F**). All of these indicated more petrogenic hydrocarbon inputs in the surface sediment for core 29. However, the terpane and sterane indexes showed no obvious difference for the surface sediment with the subsurface core sediments. This suggested a common organic source for all the samples. The increasing input of petrogenic hydrocarbons may be induced by the petroleum exploitation in Beibuwan Basin in the last century.

CONCLUSION

Sedimentary organic matter from two separate sites under different hydrodynamic conditions in the coastal areas of the Leizhou Peninsula are studied in term of atomic C/N ratios, *n*-alkane concentrations, and biomarker indexes. Overall, atomic C/N ratios and TAR values demonstrate a mixed terrestrial and marine source for the sedimented organic matter for the two sites. The lower atomic C/N ratio and TAR value in core 45 imply that aquatic organic matter contributed more to site 45 than site 29. The consistent in the difference of the maximum carbon number of long-chain *n*-alkanes through the whole core length is interpreted to represent different terrestrial vegetation source types between two sites. The NAR value and compositional characteristics of

terpane and sterane revealed major proportion of low mature petrogenic hydrocarbon. The compositional characteristics of terpane and sterane also suggest the occurrence of petroleum hydrocarbons generated from marine organic matter. The anthropogenic petroleum pollution input cannot account for the petroleum input to the deep sediments. The similar biomarker characteristics showed no significant source variation for the petrogenic hydrocarbon in two cores through the whole depth. The biomarker component characteristics in the core sediments also illustrated that the organic matter in sediments indicated mixed petrogenic hydrocarbon sources. Further research is needed to resolve the specific origin of the petrogenic hydrocarbon background in offshore area of Leizhou Peninsula.

DATA AVAILABILITY STATEMENT

The original contributions presented in the study are included in the article/Supplementary Material, further inquiries can be directed to the corresponding author.

AUTHOR CONTRIBUTIONS

YG: Methodology, Investigation, Formal analysis, Conceptualization, Writing - Review and Editing, Funding acquisition JT: Investigation, Visualization JX: Resources, Investigation, Methodology, Software, Conceptualization, Visualization Y-PW: Writing - Review and Editing SW: Project administration YH: Investigation JH: Investigation ZS: Writing - Review and Editing, Fundingacquisition, Methodology.

FUNDING

This work was supported by National Science Foundation of China (Grant No. 41802150), the Doctoral Research Initiation Project of Guangdong Ocean University (Grant No. R19004 and R17001), State Key Laboratory of Organic Geochemistry, GIGGAS (Grant No. SKLOG-201703), Project of Enhancing School with Innovation of Guangdong Ocean University (Grant No. Q18301), and the Fund of Southern Marine Science and Engineering Guangdong Laboratory (Zhanjiang) (Grant No. ZJW-2019-08).

REFERENCES

Aboul-Kassim, T. A. T., and Simoneit, B. R. T. (1996). Lipid geochemistry of surficial sediments from the coastal environment of Egypt I. Aliphatic hydrocarbons - characterization and sources. *Mar. Chem.* 54, 135–158. doi:10.1016/0304-4203(95)00098-4

Akhbarizadeh, R., Moore, F., Keshavarzi, B., and Moeinpour, A. (2016). Aliphatic and polycyclic aromatic hydrocarbons risk assessment in coastal water and sediments of Khark Island, SW Iran. *Mar. Pollut. Bull.* 108, 33–45. doi:10.1016/j.marpolbul.2016.05.004

Bao, J., Zhu, C., and Ni, C. (2007). Distribution and composition of biomarkers in Crude oils from different sags of Beibuwan Basin. *Acta Sedimentologica Sinica* 25, 646–652. (in Chinese with English abstract). CNKI:SUN:CJXB.0.2007-04-022

Bauer, A., Radziejewska, T., Liang, K., Kowalski, N., Dellwig, O., Bosselmann, K., et al. (2013). Regional differences of hydrographical and sedimentological properties in the Beibu gulf, south China sea. *J. Coastal Res.* 66, 49–71. doi:10.2112/si_66_5

Bennett, B., and Olsen, S. D. (2007). The influence of source depositional conditions on the hydrocarbon and nitrogen compounds in petroleum from central Montana, USA. *Org. Geochem.* 38, 935–956. doi:10.1016/j.orggeochem.2007.01.004

Bigus, P., Tobiszewski, M., and Namieśnik, J. (2014). Historical records of organic pollutants in sediment cores. *Mar. Pollut. Bull.* 78, 26–42. doi:10.1016/j.marpolbul.2013.11.008

Boehm, P., Page, D., Burns, W., Bence, A., Mankiewicz, P. J., and Brown, J. S. (2001). Resolving the origin of the petrogenic hydrocarbon background in prince william sound, Alaska. *Environ. Sci. Technol.* 35 (3), 471–479. doi:10.1021/es001421j

Bouloubassi, I., Fillaux, J., and Saliot, A. (2001). Hydrocarbons in surface sediments from the changjiang (yangtze river) estuary, East China sea. *Mar. Pollut. Bull.* 42, 1335–1346. doi:10.1016/s0025-326x(01)00149-7

Bourbonniere, R. A., and Meyers, P. A. (1996). Sedimentary geolipid records of historical changes in the watersheds and productivities of Lakes Ontario and Erie. *Limnol. Oceanogr.* 41, 352–359. doi:10.4319/lo.1996.41.2.0352

Brassell, S. C., Eglinton, G., and Mo, F. J. (1986). Biological marker compounds as indicators of the depositions! history of the Maoming oil shale. *Org. Geochem.* 10, 927–941. doi:10.1016/s0146-6380(86)80030-4

Broman, D., Colmsjö, A., Ganning, B., Näf, C., Zebühr, Y., and Östman, C. (1987). 'Fingerprinting' petroleum hydrocarbons in bottom sediment, plankton, and sediment trap collected seston. *Mar. Pollut. Bull.* 18 (7), 380–388. doi:10.1016/0025-326x(87)90317-1

Commendatore, M. G., and Esteves, J. L. (2004). Natural and anthropogenic hydrocarbons in sediments from the chubut river (patagonia, Argentina). *Mar. Pollut. Bull.* 48, 910–918. doi:10.1016/j.marpolbul.2003.11.015

Connan, J., and Cassou, A. M. (1980). Properties of gases and petroleum liquids derived from terrestrial kerogen at various maturation levels. *Geochimica et Cosmochimica Acta* 44, 1–23. doi:10.1016/0016-7037(80)90173-8

De grande, S. M. B., Aquino Neto, F. R., and Mello, M. R. (1993). Extended tricyclic terpanes in sediments and petroleums. *Org. Geochem.* 20 (7), 1039–1047. doi:10.1016/0146-6380(93)90112-o

Dickens, A. F., Gélinas, Y., Masiello, C. A., Wakeham, S., and Hedges, J. I. (2004). Reburial of fossil organic carbon in marine sediments. *Nature* 427, 336–339. doi:10.1038/nature02299

Dong, C. D., Chen, C. F., and Chen, C. W. (2014). Vertical profile, sources, and equivalent toxicity of polycyclic aromatic hydrocarbons in sediment cores from the river mouths of Kaohsiung Harbor, Taiwan. *Mar. Pollut. Bull.* 85, 665–671. doi:10.1016/j.marpolbul.2013.09.037

Duan, Y., Wang, C. Y., Zheng, C. Y., Wu, B. X., and Zheng, G. D. (2008). Geochemical study of crude oils from the Xifeng oilfield of the Ordos basin, China. *J. Asian Earth Sci.* 31, 341–356. doi:10.1016/j.jseaes.2007.05.003

Gan, H., Wang, H., Shi, Y., Ma, Q., Liu, E., Yan, D., et al. (2020). Geochemical characteristics and genetic origin of crude oil in the Fushan sag, Beibuwan Basin, South China Sea. *Mar. Pet. Geology.* 112, 104–114. doi:10.1016/j.marpetgeo.2019.104114

González-Vila, F. J., Polvillo, O., Boski, T., Moura, D., and de Andrés, J. R. (2003). Biomarker patterns in a time-resolved holocene/terminal Pleistocene sedimentary sequence from the Guadiana river estuarine area (SW Portugal/Spain border). *Org. Geochem.* 34, 1601–1613. doi:10.1016/j.orggeochem.2003.08.006

Grimalt, J., and Albaigés, J. (1987). Sources and occurrence of C12-C22n-alkane distributions with even carbon-number preference in sedimentary environments. *Geochimica et Cosmochimica Acta* 51, 1379–1384. doi:10.1016/0016-7037(87)90322-x

Hanson, A. D., Zhang, S. C., Moldwan, J. M., Liang, D. G., and Zhang, B. M. (2000). Molecular organic geochemistry of the Tarim basin, Northwest China. *AAPG Bull.* 84, 1109–1128. doi:10.1306/A9673C52-1738-11D7-8645000102C1865D

Hao, F., Zhou, X., Zhu, Y., Zou, H., Bao, X., and Kong, Q. (2009). Mechanisms of petroleum accumulation in the Bozhong sub-basin, Bohai Bay Basin, China. Part 1: origin and occurrence of crude oils. *Mar. Pet. Geology.* 26, 1528–1542. doi:10.1016/j.marpetgeo.2008.09.005

Harji, R. R., Yvenat, A., and Bhosle, N. B. (2008). Sources of hydrocarbons in sediments of the Mandovi estuary and the Marmugoa harbour, west coast of India. *Environ. Int.* 34, 959–965. doi:10.1016/j.envint.2008.02.006

Hedges, J. I., and Keil, R. G. (1995). Sedimentary organic matter preservation: an assessment and speculative synthesis. *Mar. Chem.* 49, 81–115. doi:10.1016/0304-4203(95)00008-f

Hu, J., Zhang, G., Li, K., Peng, P. a., and Chivas, A. R. (2008). Increased eutrophication offshore Hong Kong, China during the past 75 years: evidence from high-resolution sedimentary records. *Mar. Chem.* 110, 7–17. doi:10.1016/j.marchem.2008.02.001

Hu, L. M., Guo, Z. G., Feng, J. L., Yang, Z. S., and Fang, M. (2009). Distributions and sources of bulk organic matter and aliphatic hydrocarbons in surface sediments of the Bohai Sea, China. *Mar. Chem.* 113 (3-4), 197–211. doi:10.1016/j.marchem.2009.02.001

Huang, B., Tian, H., Wilkins, R. W. T., Xiao, X., and Li, L. (2013). Geochemical characteristics, palaeoenvironment and formation model of Eocene organic-rich shales in the Beibuwan Basin, South China Sea. *Mar. Pet. Geology.* 48, 77–89. doi:10.1016/j.marpetgeo.2013.07.012

Huang, B., Xiao, X., Cai, D., Wilkins, R. W. T., and Liu, M. (2011). Oil families and their source rocks in the weixinan sub-basin, Beibuwan Basin, south China sea. *Org. Geochem.* 42, 134–145. doi:10.1016/j.orggeochem.2010.12.001

Huang, B., Zhang, Q., and Zhang, Q. (1992). Investigation and origin of oil-gas seepages in the Yinggehai Sea. *China offshore oil & gas (Geology)* 6 (4), 1–7. (in Chinese with English abstract). CNKI:SUN:ZHSD.0.1992-04-004

Huang, B., Zhu, W., Tian, H., Jin, Q., Xiao, X., and Hu, C. (2017). Characterization of Eocene lacustrine source rocks and their oils in the Beibuwan Basin, offshore South China Sea. *Bulletin* 101, 1395–1423. doi:10.1306/10171615161

Huang, L., Chernyak, S. M., and Batterman, S. A. (2014). PAHs (polycyclic aromatic hydrocarbons), nitro-PAHs, and hopane and sterane biomarkers in sediments of southern Lake Michigan, USA. *Sci. Total Environ.* 487, 173–186. doi:10.1016/j.scitotenv.2014.03.131

Huang, W.-Y., and Meinschein, W. G. (1979). Sterols as ecological indicators. *Geochimica et Cosmochimica Acta* 43 (5), 739–745. doi:10.1016/0016-7037(79)90257-6

Jafarabadi, A. R., Dashtbozorg, M., Bakhtiari, A. R., Maisano, M., and Cappello, T. (2019). Geochemical imprints of occurrence, vertical distribution and sources of aliphatic hydrocarbons, aliphatic ketones, hopanes and steranes in sediment cores from ten Iranian Coral Islands, Persian Gulf. *Mar. Pollut. Bull.* 144, 287–298. doi:10.1016/j.marpolbul.2019.05.014

Jia, G., and Peng, P. (2003). Temporal and spatial variations in signatures of sedimented organic matter in Lingding Bay (Pearl estuary), Southern China. *Mar. Chem.* 82 (1-2), 47–54. doi:10.1016/s0304-4203(03)00050-1

Li, F., Lin, J. Q., Liang, Y. Y., Gan, H. Y., Zeng, X. Y., Duan, Z. P., et al. (2014). Coastal surface sediment quality assessment in Leizhou Peninsula (South China Sea) based on SEM-AVS analysis. *Mar. Pollut. Bull.* 84, 424–436. doi:10.1016/j.marpolbul.2014.04.030

Li, M., Wang, T., Liu, L., Zhang, M., Lu, H., Ma, Q., et al. (2008). The occurrence of oleananes in the Beibuwan Basin and its application to the study of maturity and oil-source rock correlation. *Acta Geologica Sinica* 82, 585–595. doi:10.1111/j.1755-6724.2008.tb00609.x

Li, S., Zhang, S., Dong, H., Zhao, Q., and Cao, C. (2015). Presence of aliphatic and polycyclic aromatic hydrocarbons in near-surface sediments of an oil spill area in Bohai Sea. *Mar. Pollut. Bull.* 100, 169–175. doi:10.1016/j.marpolbul.2015.09.009

Liu, J., Yan, W., Chen, Z., and Lu, J. (2012). Sediment sources and their contribution along northern coast of the South China Sea: evidence from clay minerals of surface sediments. *Continental Shelf Res.* 47, 156–164. doi:10.1016/j.csr.2012.07.013

Mackenizie, A. S., Beaumont, C., and Mckenzie, D. P. (1984). Estimation of the kinetics of geochemical reactions with geophysical models of sedimentary basins and applications. *Org. Geochem.* 6, 875–884. doi:10.1016/0198-0254(85)93826-9

Mackenzie, A. S., Patience, R. L., Maxwell, J. R., Vandenbroucke, M., and Durand, B. (1980). Molecular parameters of maturation in the Toarcian shales, Paris Basin, France-I. Changes in the configurations of acyclic isoprenoid alkanes, steranes and triterpanes. *Geochimica et Cosmochimica Acta* 44, 1709–1721. doi:10.1016/0016-7037(80)90222-7

Meyers, P. A. (2003). Applications of organic geochemistry to paleolimnological reconstructions: a summary of examples from the Laurentian Great Lakes. *Org. Geochem.* 34 (2), 261–289. doi:10.1016/s0146-6380(02)00168-7

Meyers, P. A. (1997). Organic geochemical proxies of paleoceanographic, paleolimnologic, and paleoclimatic processes. *Org. Geochem.* 27, 213–250. doi:10.1016/s0146-6380(97)00049-1

Meyers, P. A. (1994). Preservation of elemental and isotopic source identification of sedimentary organic matter. *Chem. Geology.* 114, 289–302. doi:10.1016/0009-2541(94)90059-0

Mille, G., Asia, L., Guiliano, M., Malleret, L., and Doumenq, P. (2007). Hydrocarbons in coastal sediments from the Mediterranean sea (Gulf of Fos area, France). *Mar. Pollut. Bull.* 54, 566–575. doi:10.1016/j.marpolbul.2006.12.009

Moldowan, J. M., Seifert, W. K., and Gallegos, E. J. (1985). Relationship between petroleum composition and depositional environment of petroleum source rock. *AAPG Bull.* 69 (8), 1255–1268. doi:10.1306/AD462BC8-16F7-11D7-8645000102C1865D

Nishimura, M., and Baker, E. W. (1986). Possible origin of with a remarkable even-to-odd predominance in recent marine sediments. *Geochimica et Cosmochimica Acta* 50, 299–305. doi:10.1016/0016-7037(86)90178-x

Nytoft, H. P., Fyhn, M. B. W., Hovikoski, J., Rizzi, M., Abatzis, I., Tuan, H. A., et al. (2020). Biomarkers of Oligocene lacustrine source rocks, Beibuwan-Song Hong basin junction, offshore northern Vietnam. *Mar. Pet. Geology.* 114, 104196. doi:10.1016/j.marpetgeo.2019.104196

Page, D. S., Boehm, P. D., Douglas, G. S., Bence, A. E., Burns, W. A., and Mankiewicz, P. J. (1996). The natural petroleum hydrocarbon background in subtidal sediments of prince william sound, Alaska, USA. *Environ. Toxicol. Chem.* 15 (8), 1266–1281. doi:10.1002/etc.5620150804

Peters, K. E., and Moldowan, J. M. (1993). *The biomarker guide: interpreting molecular fossils in petroleum and ancient sediments*. Englewood Cliffs, New Jersey: Prentice-Hall, 363. doi:10.1016/0146-6380(93)90028-A

Peters, K. E., Walters, C. C., and Moldwan, J. M. (2005). *The biomarker guide. Volume 2: biomakers and isotopes in petroleum exploration and Earth history*. Cambridge: Cambridge University Press, 483–625. doi:10.1017/CBO9781107326040

Preston, J. C., and Edwards, D. S. (2000). The petroleum geochemistry of oils and source rocks from the northern Bonaparte Basin, offshore northern Australia. *APPEA J.* 40, 257–282. doi:10.1071/aj99014

Reimer, P. J., Baillie, M. G. L., Bard, E., Bayliss, A., Beck, J. W., Blackwell, P. G., et al. (2009). IntCal09 and Marine09 radiocarbon age calibration curves, 0-50,000 Years cal BP. *Radiocarbon* 51, 1111–1150. doi:10.1017/s0033822200034202

Reimer, P. J., Bard, E., Bayliss, A., Beck, J. W., Blackwell, P. G., Ramsey, C. B., et al. (2013). IntCal13 and Marine13 radiocarbon age calibration curves 0–50,000 Years cal BP. *Radiocarbon* 55 (4), 1869–1887. doi:10.2458/azu_js_rc.55.16947

Rothwell, R. G., and Croudace, I. W. (2015). "Micro-XRF studies of sediment cores: a perspective on capability and application in the environmental sciences," in *Micro-XRF studies of sediment cores: applications of a nondestructive tool for the environmental Sciences*. Editors I. W. Croudace and R. G. Rothwell (Dordrecht, NL: Springer), 1–21. doi:10.1007/978-94-017-9849-5_1

Seifert, W. K., Moldowan, J. M., and Jones, R. W. (1980). "Application of biological marker chemistry to petroleum exploration," in Proceedings of the tenth world petroleum congress, 9–14 september 1979 (Bucharest, Romania: World Petroleum Congress, SP8).

Seifert, W. K., Moldowan, J. M., Smith, G. W., Whitehead, E. W., and Whitehead, E. V. (1978). First proof of structure of a C28-pentacyclic triterpane in petroleum. *Nature* 271 (5644), 436–437. doi:10.1038/271436a0

Seifert, W. K., and Moldowan, J. M. (1980). The effect of thermal stress on source-rock quality as measured by hopane stereochemistry. *Phys. Chem. Earth* 12, 229–237. doi:10.1016/0079-1946(79)90107-1

Seifert, W. K., and Moldwan, J. M. (1986). "Use of biological markers in petroleum exploration," in *Methods in geochemistry and Geophysics*. Editor R. B. John (Amsterdam: Elsevier), Vol. 24, 261–290.

Seki, O., Yoshikawa, C., Nakatsuka, T., Kawamura, K., and Wakatsuchi, M. (2006). Fluxes, source and transport of organic matter in the western Sea of Okhotsk: stable carbon isotopic ratios of n-alkanes and total organic carbon. *Deep Sea Res. Oceanographic Res. Pap.* 53, 253–270. doi:10.1016/j.dsr.2005.11.004

Shanmugam, G. (1985). Significance of coniferous rain forests and related organic matter in generating commercial quantities of oil, Gippsland Basin, Australia. *AAPG Bull.* 69 (8), 1241–1254. doi:10.1306/AD462BC3-16F7-11D7-8645000102C1865D

Shaw, D. G., and Baker, B. A. (1978). Hydrocarbons in the marine environment of port valdez, Alaska. *Environ. Sci. Technol.* 12 (10), 1200–1205. doi:10.1021/es60146a005

Shaw, D. G., Hogan, T. E., and McIntosh, D. J. (1985). Hydrocarbons in the sediments of Port Valdez, Alaska: consequences of five years' permitted discharge. *Estuarine, Coastal Shelf Sci.* 21, 131–144. doi:10.1016/0272-7714(85)90093-9

Silliman, J. E., and Schelske, C. L. (2003). Saturated hydrocarbons in the sediments of lake apopka, Florida. *Org. Geochem.* 34, 253–260. doi:10.1016/s0146-6380(02)00169-9

Tao, S., Wang, C., Du, J., Liu, L., and Chen, Z. (2015). Geochemical application of tricyclic and tetracyclic terpanes biomarkers in crude oils of NW China. *Mar. Pet. Geology.* 21. 460–467. doi:10.1016/j.marpetgeo.2015.05.030

Tesi, T., Miserocchi, S., Goñi, M. A., Langone, L., Boldrin, A., and Turchetto, M. (2007). Organic matter origin and distribution in suspended particulate materials and surficial sediments from the western Adriatic Sea (Italy). *Estuarine, Coastal Shelf Sci.* 73, 431–446. doi:10.1016/j.ecss.2007.02.008

Tolosa, I., De Mora, S., Sheikholeslami, M. R., Villeneuve, J. P., Bartocci, J., and Cattini, C. (2004). Aliphatic and aromatic hydrocarbons in coastal caspian Sea sediments. *Mar. Pollut. Bull.* 48, 44–60. doi:10.1016/S0025-326X(03)00255-8

Tong, G., Chen, L., Long, J., Li, T., Xiao, X., and Tong, S. (2012). Surface pollen distribution patterns in Beibu Gulf and corresponding sediment dynamics environment. *Chin. Sci. Bull.* 57, 902–911. doi:10.1007/s11434-011-4912-2

Traynor, J. J., and Sladen, C. (1997). Seepage in Vietnam - onshore and offshore examples. *Mar. Pet. Geology.* 14 (4), 345–362. doi:10.1016/s0264-8172(96)00040-2

Venkatesan, M. I., and Kaplan, I. R. (1982). Distribution and transport of hydrocarbons in surface sediments of the alaskan outer continental shelf. *Geochimica et Cosmochimica Acta* 46 (11), 2135–2149. doi:10.1016/0016-7037(82)90190-9

Volk, H., George, S. C., Middleton, H., and Schofield, S. (2005). Geochemical comparison of fluid inclusion and present-day oil accumulations in the Papuan Foreland - evidence for previously unrecognised petroleum source rocks. *Org. Geochem.* 36, 29–51. doi:10.1016/j.orggeochem.2004.07.018

Wang, S., Liu, G., Yuan, Z., and Da, C. (2018). n-Alkanes in sediments from the Yellow River Estuary, China: occurrence, sources and historical sedimentary record. *Ecotoxicol Environ. Saf.* 150, 199–206. doi:10.1016/j.ecoenv.2017.12.016

Wang, Y., Fang, X., Zhang, T., Li, Y., Wu, Y., He, D., et al. (2012). Distribution of biomarkers in lacustrine sediments of the Linxia Basin, NE Tibetan Plateau, NW China: significance for climate change. *Sediment. Geology.* 243-244, 108–116. doi:10.1016/j.sedgeo.2011.10.006

Yang, J., Gao, J., Liu, B., and Zhang, W. (2014). Sediment deposits and organic carbon sequestration along mangrove coasts of the Leizhou Peninsula, southern China. *Estuarine, Coastal Shelf Sci.* 136, 3–10. doi:10.1016/j.ecss.2013.11.020

Yunker, M. B., Mclaughlin, F. A., Fowler, M. G., and Fowler, B. R. (2014). Source apportionment of the hydrocarbon background in sediment cores from Hecate Strait, a pristine sea on the west coast of British Columbia, Canada. *Org. Geochem.* 76, 235–258. doi:10.1016/j.orggeochem.2014.08.010

Zhang, A., Chen, M., Gan, H., Chen, Q., Lan, B., and Fang, Q. (2018). Geochemical characteristics and sediment provenance of core SO-50 sediments in the Beibu Gulf. *Acta Oceanologica Sinica* 40 (5), 107–117. (in Chinese with English abstract). CNKI:SUN:SEAC.0.2018-05-009

Zhang, Z., Chen, L., Wang, W., Li, T., and Zu, T. (2017). The origin, historical variations, and distribution of heavy metals in the Qiongzhou Strait and nearby marine areas. *J. Ocean Univ. China* 16, 262–268. doi:10.1007/s11802-017-2926-3

Zhou, X., Gao, G., Lü, X., Zhao, L., Dong, Y., Xu, X., et al. (2019). Petroleum source and accumulation of WZ12 oils in the Weixi'nan sag, south China sea, China. *J. Pet. Sci. Eng.* 177, 681–698. doi:10.1016/j.petrol.2019.02.078

Conflict of Interest: The authors declare that the research was conducted in the absence of any commercial or financial relationships that could be construed as a potential conflict of interest.

Copyright © 2021 Gao, Tan, Xia, Wang, Wang, Han, He and Song. This is an open-access article distributed under the terms of the Creative Commons Attribution License (CC BY). The use, distribution or reproduction in other forums is permitted, provided the original author(s) and the copyright owner(s) are credited and that the original publication in this journal is cited, in accordance with accepted academic practice. No use, distribution or reproduction is permitted which does not comply with these terms.

frontiers in Earth Science

ORIGINAL RESEARCH
published: 09 April 2021
doi: 10.3389/feart.2021.615766

Insight Into Hartoušov Mofette, Czech Republic: Tales by the Fluids

Kyriaki Daskalopoulou[1], Heiko Woith[1], Martin Zimmer[1], Samuel Niedermann[1], Johannes A. C. Barth[2], Alexander H. Frank[2], Andrea Vieth-Hillebrand[1], Josef Vlček[3], Cemile Dilara Bağ[1,4] and Ralf Bauz[1]*

[1] GFZ German Centre for Geosciences, Potsdam, Germany, [2] GeoZentrum Nordbayern, Schlossgarten 5, Department Geographie und Geowissenschaften, Friedrich-Alexander-Universität Erlangen-Nürnberg, Nürnberg, Germany, [3] Department of Hydrogeology, Engineering Geology and Applied Geophysics, Faculty of Science, Charles University, Prague, Czechia, [4] Department of Geological Engineering, Middle East Technical University, Ankara, Turkey

The Cheb Basin (Czech Republic) is characterized by emanations of magma-derived gases and repeated occurrences of mid-crustal earthquake swarms with small to intermediate magnitudes ($M_L < 4.5$). Associated intense mantle degassing occurs at the Hartoušov Mofette, a representative site for the Cheb Basin. Here, we performed 14 sampling campaigns between June 2019 and March 2020. Gas samples of fluids ascending in two boreholes (F1, ∼28 m depth and F2, ∼108 m depth) and from a nearby natural mofette were analyzed for their chemical (CO_2, N_2, O_2, Ar, He, CH_4, and H_2) and isotope compositions (noble gases and CO_2). CO_2 concentrations were above 99.1% in most samples, while O_2 and N_2 were below 0.6%. He ranged from 19 to 34 μmol/mol and CH_4 was mostly below 12 μmol/mol. Isotope compositions of helium and carbon in CO_2 ranged from 5.39 to 5.86 R_A and from −2.4 to −1.3 ‰ versus VPDB, respectively. Solubility differences of the investigated gases resulted in fluctuations of their chemical compositions. These differences were accompanied by observed changes of gas fluxes in the field and at the monitoring station for F1. Variations in solubilities and fluxes also impacted the chemical concentration of the gases and the $\delta^{13}C$ values that were also likely influenced by Fischer-Tropsch type reactions. The combination of (a) the Bernard ratio, (b) $CH_4/^3He$ distributions, (c) P-T conditions, (d) heat flow, and (e) the sedimentary regime led to the hypothesis that CH_4 may be of mixed biogenic and volcanic/geothermal origin with a noticeable atmospheric contribution. The drilling of a third borehole (F3) with a depth of ∼238 m in August 2019 has been crucial for providing insights into the complex system of Hartoušov Mofette.

Keywords: geogenic degassing, CO_2-rich fluids, solubility, CH_4 origin, gas flow perturbations

OPEN ACCESS

Edited by:
Yunpeng Wang,
Guangzhou Institute of Geochemistry, Chinese Academy of Sciences, China

Reviewed by:
Xianrong Zhang,
Qingdao Institute of Marine Geology(QIMG), China
Galip Yuce,
Hacettepe University, Turkey

****Correspondence:***
Kyriaki Daskalopoulou
kyriaki.daskalopoulou@gfz-potsdam.de;
kikdaskalopoulou@gmail.com

Specialty section:
This article was submitted to Geochemistry, a section of the journal Frontiers in Earth Science

Received: *09 October 2020*
Accepted: *03 March 2021*
Published: *09 April 2021*

Citation:
Daskalopoulou K, Woith H, Zimmer M, Niedermann S, Barth JAC, Frank AH, Vieth-Hillebrand A, Vlček J, Bağ CD and Bauz R (2021) Insight Into Hartoušov Mofette, Czech Republic: Tales by the Fluids. Front. Earth Sci. 9:615766. doi: 10.3389/feart.2021.615766

INTRODUCTION

Gases from various tectonic regions can differ in their geochemical characteristics (Lupton, 1983). Therefore, detailed studies of geothermal gases often contribute to an improved understanding of tectonic and geological settings and their corresponding fluids (Giggenbach, 1992, 1996; Lee et al., 2005). Furthermore, geodynamic settings are often influenced by seismic, volcanic, and geothermal activities and that also plays an essential role in earth degassing (Irwin and Barnes, 1980).

Hydrothermal fluids transport volatiles from the deep crust or mantle to the surface, while their circulation in the crust can also enhance geodynamic processes. The generation and transportation of these fluids are linked to a plethora of faulting processes (including nucleation, propagation, arrest, and recurrence of earthquake ruptures, fault creep or slow earthquakes, and the long-term structural and compositional evolution of fault zones – Hickman et al., 1995). Their study therefore offers a tool for monitoring and better understanding mantle and crustal processes.

Geogenic CO_2 discharges are widespread throughout central Europe (Pearce et al., 2004). Although they occur in diverse geological and geodynamic settings their distribution is principally controlled by the Cenozoic rift systems and associated Tertiary volcanism. The Eger Rift (Czech Republic, **Figure 1A**) is an intraplate region without active volcanism (youngest volcanic activity took place 0.29 Ma ago- Mrlina et al., 2009). However, emanations of magma-derived gases take place in the western part of the Cheb Basin (Weinlich et al., 1999; Geissler et al., 2005). This area associates with earthquake swarms that are likely induced by the ascent of the magmatic fluids (Parotidis et al., 2003). Variations in the gas flow together with chemical and isotope compositions were noticed during periods of seismic activity (Bräuer et al., 2018). For instance, increase in the gas flow was observed at the Hartoušov mofette field (HMF) after a series of earthquakes in 2014 (Fischer et al., 2017). During the same period, the gas flow in the mofette field of Dolní Částkov (Cheb Basin) decreased drastically. Post-seismic shifts in $\delta^{13}C_{CO2}$ and $^{3}He/^{4}He$ after the small swarm on the 4th and 5th of December 1994 were documented by Weise et al. (2001). They estimated the fluid transport velocities in the upper crust at 400 m/d for the Bublák mofette field. Spatial and temporal increase of mantle-derived helium contributions in the eastern Cheb Basin suggested that fluid injection channels reach down to the lithospheric mantle (Bräuer et al., 2005, 2009). It is worth noting that the subcontinental lithospheric mantle (SCLM) contribution at HMF increased from 38% in 1993 to 89% in 2016 (Bräuer et al., 2018), while the isotope ratio of He at the Bublák mofette reached 6.3 R_A before the earthquake swarms in 2000 and 2008. This increase indicated that ascending magma from the SCLM into the crust might have triggered the swarm.

These observations highlight the complexity and uniqueness of the Cheb Basin, and illustrate the need to deepen our knowledge on the system. Especially the relationship between the fluids and the seismic activity demands further research. Toward this goal, this investigation focuses on monitoring fluids encountered at different depths of the HMF (**Figure 1B**). Gases emerging in the mofette (surface expression), as well as in two boreholes (F1 and F2 with depths ∼28 m ∼108 m, respectively) have been sampled regularly over 1 year. Our study aims to identify key processes affecting the gases in the *"micro"*-system of HMF. We also aimed to show first results of gases during the drilling period of a third borehole. This was drilled during the study period, to a depth of ∼238 m. Moreover, our study takes a first step toward the determination of the origin of CH_4.

This work is part of the Mofette Research (MoRe) project, which combines geochemical and geophysical methods to document how fluids can actively act in a non-volcanic rift setting of intraplate seismicity.

STUDY AREA

The Cheb Basin is an asymmetric intracontinental basin that lies within the western part of the Eger Rift close to the Nový Kostel focal zone (NK, Fischer and Horálek, 2003; **Figure 1**). In its eastern part, the basin is defined by the NNW-SSE Mariánské Lázně Fault Zone (MLFZ). Its petrological regime includes rock sequences of Upper Cambrian to Ordovician age and areas characterized by Late Variscan intrusions that are dominated by granites. Its crystalline basement consists of muscovite granites of the Smrčiny/Fichtelgebirge Pluton (Hecht et al., 1997). These combine with crystalline schists of the Saxothuringian Zone of the Variscan Orogen (Fiala and Vejnar, 2004). The basin was formed during the Late Tertiary and Quaternary by the re-activation of Hercynian faults and separated microplates present within the basement (Bankwitz et al., 2003; Babuška and Plomerová, 2008) or either of them. The Cheb Basin was filled with 300 m-thick fluvial and lacustrine deposits (Špičáková et al., 2000; Nickschick et al., 2015). Volcanism in the western part of the Eger Rift was weak and of Quaternary age, and the youngest volcanic activity in the area took place 0.29 Ma ago (Mrlina et al., 2009).

Magma-derived volatiles present in the Cheb Basin consist of CO_2-rich waters, wells, and dry gas vents (Weinlich et al., 1999). The dominant gas species is CO_2 (>98%) with minor amounts of N_2, O_2, Ar, He, and CH_4 (Weinlich et al., 1999; Kämpf et al., 2013; Bräuer et al., 2018). Isotope compositions for both helium and carbon in CO_2 indicate a mantle origin of the fluids (Bräuer et al., 2018). Along with the emanation of magma-derived gases, the recurrence of swarms with small to intermediate magnitudes (M_L < 4.5) is characteristic for the area. Parotidis et al. (2003) hypothesized that the ascent of magmatic fluids triggers most of these anomalous earthquake activities. However, Fischer et al. (2014) suggested that fluids are probably not the only triggering factor of the swarms. It is worth noting that the lack of CO_2 emanations in the epicentral area of the Nový Kostel (NK) focal zone likely results from an impermeable rock formation above the fault zone (Bräuer et al., 2009). Nonetheless, it has produced almost 80% of the earthquake swarms during the past 30 years (Fischer and Michálek, 2008).

In order to investigate relationships between geodynamic processes, CO_2 degassing, and the continental "deep biosphere," three boreholes were drilled in the intensively degassing HMF (Dahm et al., 2013, 26 t/d of diffuse soil degassing; Kämpf et al., 2019). F1 [corresponding to 1H-031 in Bräuer et al. (2018) and VP8303 in Fischer et al. (2020)] was drilled in 2007 down to ∼28 m below ground and taps into a CO_2-saturated, confined aquifer. The F2 borehole [HJB-1 in Bräuer et al. (2018)] has a depth of ∼108 m, and was drilled in spring 2016 to investigate whether the increased fluid and substrate flow can accelerate microbial life in active fault zones

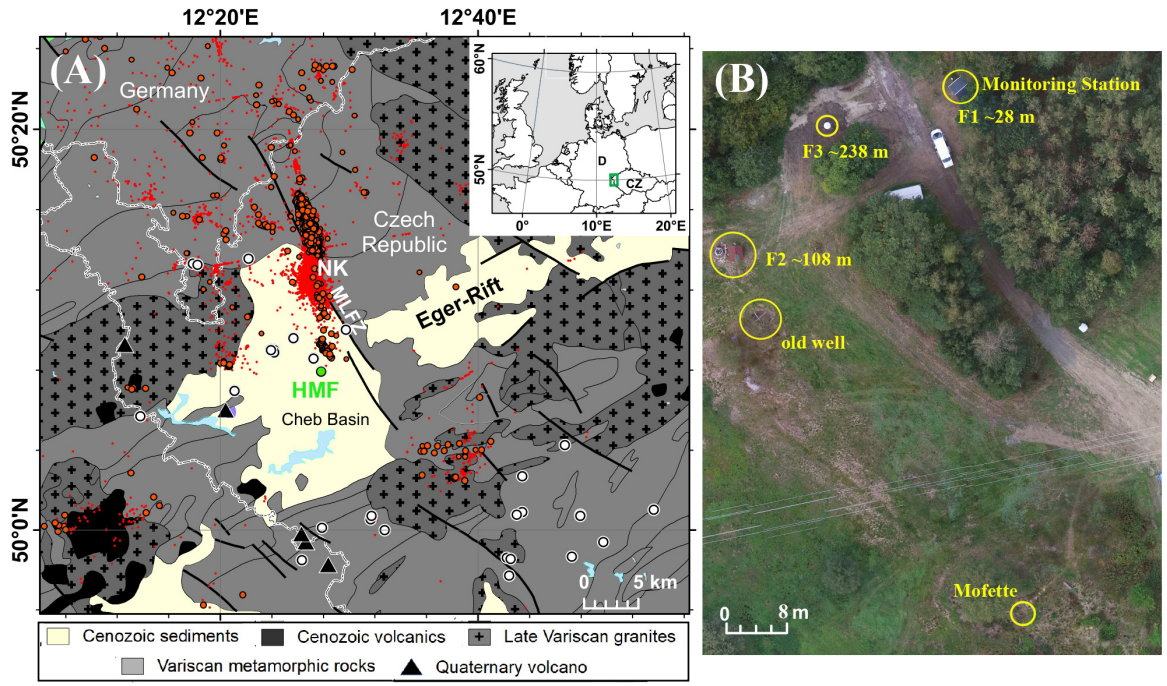


FIGURE 1 | (A) Simplified geological map of the Eger Rift area and its surroundings ["Geological Map of Germany 1:1 000 000 (GK1000)," BGR]. The Hartoušov Mofette Field (HMF) is indicated with a green circle. The white circles correspond to mofettes and springs with CO_2 gas flux >400 l/h, while the red circles portray the seismic activity during the past 30 years. The Mariánské Lázně Fault Zone (MLFZ), as well as the Nový Kostel focal zone (NK), are also shown. **(B)** Orthomosaic image of the HMF, where the positions of the 3 boreholes (F1, F2, and F3) along with their depths, the mofette, and the old well are indicated. A seismological and geochemical monitoring station located at F1 is also marked on the map.

and CO_2 conduits (Bussert et al., 2017). In August 2019, a third borehole (F3) was drilled to a depth of ~238 m. Its principal aim is to investigate the relation between geogenic degassing and earthquake activity by combination of geochemical and geophysical techniques. Further details about the borehole configuration can be found in Woith et al. (2020).

MATERIALS AND METHODS

From June 2019 to March 2020, 14 sampling campaigns took place in the HMF, and 40 gas samples were collected. Samples were obtained from the free gas phase after passage through water. They were collected in Exetainer vials and glass vessels with two vacuum stopcocks. The containers were first filled with water. Subsequently, gas was collected with tubing that was directly connected to the borehole head. Its upward flow replaced the water in the vessel. For mofette samples, the tubing was connected to an inverted funnel, which was immersed in the water. Three samples were collected per sampling site on each sampling day; one of these samples was used to determine the gas composition and the other two for noble gas and carbon isotope analyses of CO_2, respectively.

For analyses of their chemical composition, gases were sampled in 1,000 cm^3 glass vessels. The CO_2 contents were determined volumetrically after absorption in a KOH solution with a precision of 0.1 cm^3. The remaining CO_2-free aliquot was analyzed at a commercial laboratory in the Czech Republic (Labor Union) using gas chromatography. N_2 and O_2 had a relative precision of ± 3%, while the minor components (Ar, He, H_2, CH_4, and light hydrocarbons) were determined at relative precisions of ±10–40%. The detection limit for H_2 and He was <100 μmol/mol of CO_2-free gas, while for CH_4 and other light hydrocarbons it was <1 μmol/mol. This corresponded to 0.5 μmol/mol and 0.005 μmol/mol, respectively, in gas with CO_2 contents of 99.5%. Further details of the method are also available in Weinlich et al. (1998).

$\delta^{13}C$ analyses were performed from the Exetainer vials (12 cm^3) at GFZ Potsdam with a gas chromatograph (GC 6890N, Agilent Technologies, equipped with Plot column) coupled via a combustion device (GC-C/TC III, Thermo Fisher Scientific) to an isotope ratio mass spectrometer (MAT253, Thermo Fisher Scientific). The $\delta^{13}C$ values are reported in ‰ versus Vienna Pee Dee Belemnite (VPDB) standard with a standard deviation of ±0.3‰.

Samples for noble gas analyses were collected in 250 cm^3 glass vessels with two vacuum stopcocks. The isotopic composition of noble gases was determined for selected samples at GFZ Potsdam. For this purpose, aliquots were analyzed for noble gas concentrations and isotopic compositions with a VG 5400 noble gas mass spectrometer after removing the active gas components in a gas purification line. Details of the analytical procedure

can be found in Niedermann et al. (1997). The precision of He isotope measurements generally ranges from ±1.7% to ± 2.4%, with only four samples [(7), (18), (31), and (33)] being above this range (± 4.7% in average). The precision of $^4He/^{20}Ne$ generally ranges from ± 5.5% to ± 16% at 2σ (95% confidence) level. An exception to the latter range is sample (25) (± 84%), because of an extremely low Ne concentration. The measured $^3He/^4He$ ratios were corrected for atmospheric He contributions by assuming that contributions of ^{20}Ne are entirely of atmospheric origin, and by using the $^4He/^{20}Ne$ ratio of air (0.319) according to Craig et al. (1978):

$$(3/4)_c = \frac{[(3/4)_{sample} \times (4/20)_{sample}/(4/20)_{air} - (3/4)_{air}]}{[(4/20)_{sample}/(4/20)_{air} - 1]} \quad (1)$$

where 3/4 and 4/20 are the $^3He/^4He$ and $^4He/^{20}Ne$ ratios. Corrections were <3%, except for sample (1) (∼5%).

TABLE 1 | Analytical results of collected gas samples.

ID	Name	Date	Drilling Depth	CO_2	N_2	O_2	He	H_2	Ar	CH_4	C_2H_4	C_2H_6	C_3H_8
			m		%					μmol/mol			
1	F1	18.06.19		99.72	0.22	0.05	22.2	b.d.l.	46.9	22.8	b.d.l.	0.083	b.d.l.
2	F1	31.07.19		99.79	0.16	0.04	19.1	b.d.l.	37.0	2.38	b.d.l.	0.073	b.d.l.
3	F1	01.08.19	1.9	99.73	0.20	0.06	23.4	b.d.l.	47.5	2.50	b.d.l.	0.090	b.d.l.
4	F1	14.08.19	41.3	99.56	0.31	0.12	27.2	b.d.l.	71.9	8.47	b.d.l.	0.097	b.d.l.
5	F1_AC	23.08.19	70.9	98.70	0.86	0.41	22.6	b.d.l.	264	9.05	0.053	0.093	0.013
6	F1	25.08.19	125.3	99.67	0.27	0.05	25.3	b.d.l.	52.4	22.9	0.013	0.092	b.d.l.
7	F1_AC	29.08.19	197.3	93.23	5.27	1.42	6.81	b.d.l.	756	2.72	b.d.l.	b.d.l.	b.d.l.
8	F1	30.08.19	239.3	99.57	0.34	0.08	26.5	b.d.l.	70.9	2.42	b.d.l.	0.101	b.d.l.
9	F1	04.09.19		99.75	0.20	0.05	25.8	b.d.l.	43.9	4.95	b.d.l.	b.d.l.	b.d.l.
10	F1	06.09.19		99.47	0.39	0.13	26.8	b.d.l.	91	3.53	b.d.l.	b.d.l.	b.d.l.
11	F1	25.09.19		99.58	0.30	0.11	26.1	b.d.l.	69.3	2.61	b.d.l.	0.107	b.d.l.
12	F1	26.11.19		99.74	0.21	0.04	23.2	b.d.l.	40.5	1.74	b.d.l.	0.056	b.d.l.
13	F1	16.01.20		99.36	0.48	0.15	25.0	b.d.l.	93.1	1.41	b.d.l.	0.039	b.d.l.
14	F1	04.03.20		99.60	0.29	0.10	26.4	b.d.l.	59.5	2.66	b.d.l.	0.145	b.d.l.
15	F2_AC	18.06.19		92.45	5.87	1.60	7.6	b.d.l.	835	5.32	b.d.l.	b.d.l.	b.d.l.
16	F2	31.07.19		99.82	0.15	0.02	22.0	b.d.l.	37.6	4.94	b.d.l.	0.086	b.d.l.
17	F2	01.08.19	1.9	99.76	0.17	0.05	23.6	b.d.l.	204	4.64	b.d.l.	0.093	b.d.l.
18	F2	14.08.19	41.3	99.51	0.35	0.13	28.0	b.d.l.	78.7	8.57	b.d.l.	0.084	b.d.l.
19	F2	23.08.19	70.9	99.71	0.21	0.07	26.2	b.d.l.	48.1	2.46	b.d.l.	0.077	b.d.l.
20	F2	25.08.19	125.3	99.86	0.12	0.01	22.7	b.d.l.	26.0	3.76	b.d.l.	0.098	b.d.l.
21	F2	29.08.19	197.3	99.79	0.17	0.03	18.7	b.d.l.	31.4	4.31	b.d.l.	0.078	b.d.l.
22	F2	30.08.19	239.3	99.87	0.12	0.01	31.8	0.27	23.8	6.42	b.d.l.	0.032	b.d.l.
23	F2	03.09.19		99.87	0.11	0.02	24.9	b.d.l.	23.8	5.99	b.d.l.	0.015	b.d.l.
24	F2	25.09.19		99.71	0.22	0.07	24.2	b.d.l.	49.9	5.40	b.d.l.	0.044	b.d.l.
25	F2	26.11.19		99.72	0.23	0.04	33.5	b.d.l.	44.3	4.38	b.d.l.	0.039	b.d.l.
26	F2	15.01.20		99.15	0.56	0.27	28.9	b.d.l.	128	0.54	b.d.l.	0.060	b.d.l.
27	F2	04.03.20		99.63	0.26	0.10	26.4	b.d.l.	62.8	4.13	b.d.l.	0.071	0.030
28	Mofette_AC	18.06.19		98.81	0.91	0.26	43.1	b.d.l.	155	10.1	b.d.l.	0.238	b.d.l.
29	Mofette	31.07.19		99.73	0.20	0.06	23.3	b.d.l.	44.3	6.12	b.d.l.	0.070	b.d.l.
30	Mofette	14.08.19	41.3	99.70	0.22	0.06	24.7	b.d.l.	173	7.64	b.d.l.	0.085	b.d.l.
31	Mofette_AC	23.08.19	70.9	97.70	1.77	0.51	21.1	b.d.l.	250	5.50	b.d.l.	0.069	b.d.l.
32	Mofette	25.08.19	128.3	99.75	0.20	0.04	24.1	b.d.l.	47.0	4.19	b.d.l.	0.079	b.d.l.
33	Mofette_AC	29.08.19	197.3	96.85	2.46	0.64	6.6	b.d.l.	355	6.92	b.d.l.	b.d.l.	b.d.l.
34	Mofette	30.08.19	239.3	99.74	0.22	0.03	25.1	b.d.l.	45.9	6.23	b.d.l.	0.074	b.d.l.
35	Mofette	03.09.19		99.85	0.12	0.02	20.3	b.d.l.	28.1	5.53	b.d.l.	0.060	b.d.l.
36	Mofette	06.09.19		99.75	0.19	0.04	24.6	b.d.l.	46.7	9.02	b.d.l.	b.d.l.	b.d.l.
37	Mofette	25.09.19		99.76	0.19	0.04	29.4	b.d.l.	42.7	6.46	b.d.l.	0.130	b.d.l.
38	Mofette	26.11.19		99.80	0.16	0.03	26.1	b.d.l.	35.9	10.5	b.d.l.	0.075	b.d.l.
39	Mofette	15.01.20		99.73	0.20	0.06	27.7	b.d.l.	43.4	11.1	b.d.l.	0.054	b.d.l.
40	Mofette	04.03.20		99.64	0.26	0.09	29.0	b.d.l.	66.2	3.57	b.d.l.	0.081	b.d.l.

The coordinates of (a) F1 and F2 are 50° 7′ 58.8″ N and 12° 27′ 46.8″ E and (b) the Mofette are 50° 7′ 55.2″ N and 12° 27′ 50.4″ E.
b.d.l. = below detection limit.

RESULTS

Names, sampling dates, chemical concentrations, and isotope values for the collected samples are presented in **Tables 1–3**. **Supplementary Table 1** shows the drilling dates and the bottom depth of F3. The coordinates of the three sites are displayed in the footnote of **Table 1**. Literature data by Bräuer et al. (2018) were considered as background values, and used for comparison. It is worth mentioning that literature data from Weinlich et al. (1999) and Kämpf et al. (2013) were not used in our study, because they were influenced by seismic activity, and may result in misleading conclusions.

CO_2 concentrations exceeded 99 % in most samples, while O_2 and N_2 were mostly below 0.3 and 0.6%, respectively (**Table 1**). Six samples presented lower CO_2 contents (down to 92.5%), most likely due to air contamination during sampling that was manifested in elevated O_2 and N_2 concentrations (up to 1.6 and 5.9%, respectively). These samples are included and presented in the current study, however, they are given in gray color and are signed with "_AC," which stands for Air Contamination.

He in the uncontaminated samples ranged from 18 to 34 μmol/mol, whereas lower concentrations were found in samples with enhanced air component. Ar showed a wide range of concentrations (24 to 835 μmol/mol). Concentrations of CH_4 were generally lower than 12 μmol/mol, while enrichments up to 23 μmol/mol were found in F1 before drilling and during drilling at a core depth of ∼125 m. The lowest CH_4 value (0.5 μmol/mol) was found at F2 in the sample collected after the perforation of the F3 steel casing after the drilling period. H_2 was always below detection limit, apart from one sample collected from F2 when the drilling reached its final depth. C_2H_4 and C_3H_8 were almost always below detection limit apart from three borehole samples [(5) and (6) for C_2H_4 and (5) and (27) for C_3H_8]. C_2H_6 was present in concentrations lower than 0.24 μmol/mol.

Noble gases, as well as carbon isotopes, were measured only in selected samples. The isotope composition of He showed values between 5.37 and 5.86 R_A (where R_A is the atmospheric $^3He/^4He$ ratio of 1.39×10^{-6}). Corresponding $^4He/^{20}Ne$ ratios covered a wide range of values (5.2 to ∼19,000). The samples analyzed for $\delta^{13}C_{CO2}$ were in the range of −2.4 to −1.3‰ vs. VPDB.

Water temperature and gas flow in F1, the wellhead and bottom-hole pressure in F2, and meteorological data were obtained from the monitoring station located at F1 in the HMF (**Figure 1B**). These data were obtained from the CO_2 network (CarbonNet) of Charles University of Prague. Details are provided in the Section of Data Availability Statement.

TABLE 2 | Carbon isotope composition of CO_2.

ID	$\delta^{13}C_{CO2}$ vs. VPDB [‰]
4	−1.3
6	−1.4
9	−1.5
10	−1.9
16	−1.9
20	−1.5
21	−1.7
22	−1.8
23	−2.0
29	−1.8
32	−1.4
34	−1.7
35	−2.4
36	−1.6

DISCUSSION

Processes Affecting the Gases

CO_2 is the dominant gas component emerging from the HMF, with He isotopes and $\delta^{13}C_{CO2}$ showing a mantle origin (Kämpf et al., 2013; Bräuer et al., 2018). In **Figure 2A**, the atmospheric gas component (here represented by N_2) is plotted together with CO_2 and CH_4, which are characteristic of hydrothermal-type components (Giggenbach et al., 1993). This ternary plot aims to identify secondary processes, such as dissolution (Italiano et al., 2014a). As expected, N_2 concentrations are strongly enhanced in the air contaminated samples (gray-colored symbols). Borehole samples (13) and (26), collected after the perforation, as well as samples from F1 collected when F3 arrived at its final depth [(8)] and after the drilling process [(10), (11), and (14)] are also enriched in N_2. This suggests a CO_2 loss that was probably caused by dissolution processes. An increase in CH_4 content is found for two F1 samples [(1) and (6) – **Figure 2A**].

In the He-N_2-Ar ternary diagram (**Figure 2B** – after Giggenbach et al., 1983), the vast majority of the samples are distributed inside the triangle delimited by N_2/Ar ratios of air and air-saturated water (ASW), and the He apex. This distribution shows a two-component mixing relationship between mantle and atmospheric sources. Furthermore, most of the N_2/Ar ratios approach the value of 50 (**Table 1**), the typical value of air-saturated waters (Heaton and Vogel, 1981; Fischer et al., 1998). This suggests that N_2 originates from a mixture of shallow air-saturated fluids and deep circulating groundwaters. Samples (17) and (30), collected when the drilling of F3 arrived at ∼2 m and ∼41 m depth, respectively, revealed an excess of Ar for so far unknown reasons, while samples affected by atmospheric contamination plot close to the air and ASW points.

Enrichments of the geogenic components are evident in the binary plot of He/Ar versus N_2/O_2 (**Figure 3A**), with F2 presenting the most extreme values (**Table 1**). In most cases, samples of HMF have stable CH_4 and He contents (**Figure 3B**). As expected, the variability of CH_4 is somewhat higher in samples not affected by air contamination (**Figure 3B**). The higher He concentration in the F2 samples collected at the end [(22)] and after the F3 drilling [(25)] indicates a CO_2 loss. This loss may have been caused by the strong solubility contrast of these gases in aquatic environments (Reid et al., 1987). This may have been enhanced by the low and non-thermal temperatures of the HMF (up to 15°C for F1 and F2 and up to 20°C for the Mofette during the summer period). D'Alessandro et al. (2014) suggested that

TABLE 3 | Helium concentrations and $^3He/^4He$ and $^4He/^{20}Ne$ ratios from selected samples in the HMF.

ID	^4He	$^3He/^4He$	Error (2σ)	$^4He/^{20}Ne$	Error (2σ)	$(^3He/^4He)_c$	Error (2σ)
	μmol/mol	R_A				R_A	
1	14.9	5.53	±0.13	5.20	±0.37	5.83	±0.14
4	17.4	5.76	±0.09	203	±18	5.77	±0.09
7	17.3	5.77	±0.27	600	±56	5.77	±0.27
12	18.7	5.79	±0.11	725	±61	5.79	±0.11
15	17.9	5.65	±0.13	12.24	±0.67	5.77	±0.13
17	18.7	5.82	±0.10	1660	±260	5.82	±0.10
18	20.7	5.82	±0.28	664	±78	5.82	±0.28
20	16.8	5.71	±0.08	326	±25	5.71	±0.08
21	16.8	5.68	±0.12	116.1	±8.3	5.69	±0.12
22	15.7	5.62	±0.10	18.7	±1.3	5.70	±0.10
25	19.9	5.78	±0.10	19000	±16000	5.78	±0.10
28	18.0	5.68	±0.11	220	±15	5.69	±0.11
30	18.6	5.82	±0.11	690	±100	5.82	±0.11
31	18.3	5.86	±0.26	1040	±100	5.86	±0.26
32	16.5	5.57	±0.09	11.30	±0.80	5.70	±0.09
33	19.2	5.37	±0.26	68.8	±6.0	5.39	±0.26
34	17.3	5.69	±0.09	22.7	±1.6	5.76	±0.09
38	18.5	5.66	±0.10	18.8	±1.3	5.74	±0.10

$(^3He/^4He)_c$ is the air-corrected $^3He/^4He$ ratio (Craig et al., 1978).
^4He concentrations in this table were obtained by relating the He partial pressure determined by noble mass spectrometry to the total pressure in the gas vessel used for the noble gas analyses, assuming that the latter was equal to atmospheric pressure. 2σ uncertainties of these values are estimated at ∼10–15%.

such contrasts may result in strong enrichments in less soluble gases, when a gas mixture rises through unsaturated waters at depleted gas/water ratios.

Enrichment in He content was also noticed in the air-contaminated sample (28) (**Figure 3B** and **Table 1**). However, a different approach in calculating the He concentration yields a much lower value (**Table 3**). This suggests that this difference may result from an analytical problem during gas chromatography. Samples from F1 collected during the 1st campaign [(1)] and when F3 arrived at ∼125 m depth [(6)] exhibit enrichments in CH_4 (**Figure 3B**). This was likely caused by biogenic generation of the gas, a hypothesis promoted by the sedimentary formations (Daskalopoulou et al., 2018), and also supported by the depleted values of the atmospheric components (Goff and Janik, 2002; Easley et al., 2011). It should be noted that CH_4 content changes are common, as the gas can be involved in many production and consumption processes (Rolston et al., 1993). Another possible scenario that may apply to sample (1), collected in June 2019, is that CH_4 was accumulated at the wellhead for the period that the borehole was sealed and due to its low density, it was among the first gases to escape. Consumption by microbial or inorganic oxidation of the gas may explain the depletion in CH_4 that is noticed in the borehole gases collected after the perforation [(13) and (26)]. Indeed, N_2/O_2 ratios of these samples and also of samples (17) and (30) are similar to air. This indicates that the atmospheric component of meteoric water has been modified by redox reactions that took place either in the subsoil or in the aquifer (D'Alessandro et al., 2010).

Relation Between Fluid Parameters and CO_2

Mean bubble fraction and water temperature at F1 are presented in **Figure 4**, along with the wellhead pressure at F2 and the meteorological conditions in the HMF over the drilling period. The mean bubble fraction was calculated according to Fischer et al. (2020), who showed that in boreholes and narrow tube-like mofettes, gas bubble contents in a water-gas mixture can be quantified from the pressure difference over a fixed depth interval. The high gas/water ratio is expressed as an increase in the gas flow and the high bubble fraction. This may also

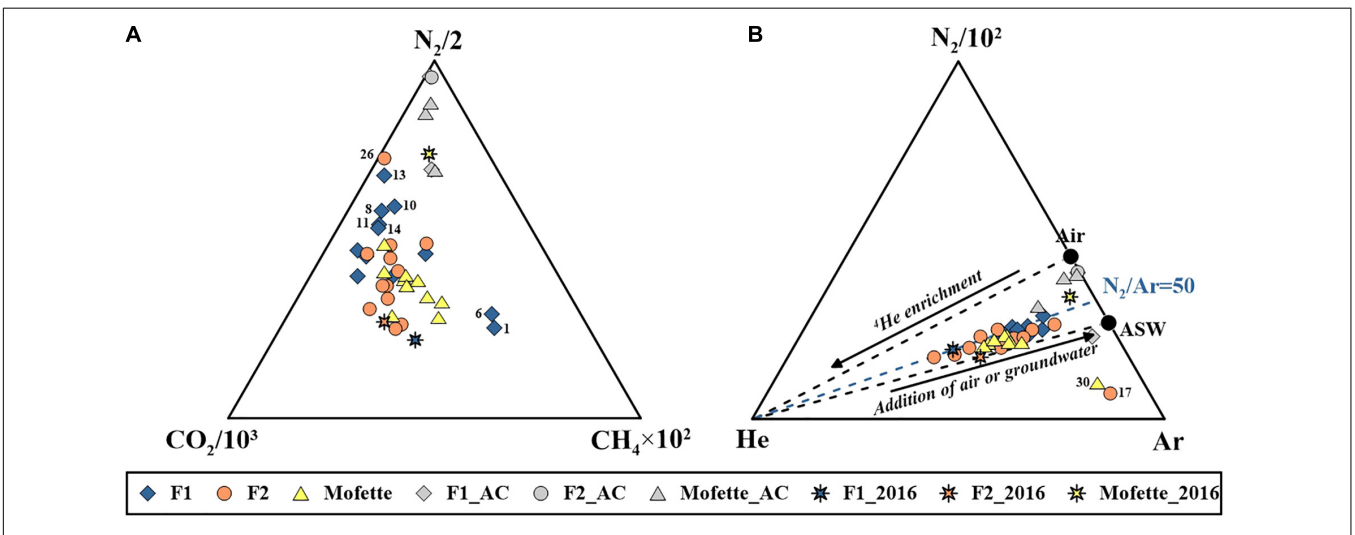


FIGURE 2 | (A) N_2-CO_2-CH_4 ternary diagram after Giggenbach et al. (1993) and **(B)** N_2-He-Ar ternary diagram after Giggenbach et al. (1983) of the gas emitted in the HMF. The abbreviation _AC stands for air contamination, while data of samples collected during 2016 are from Bräuer et al. (2018).

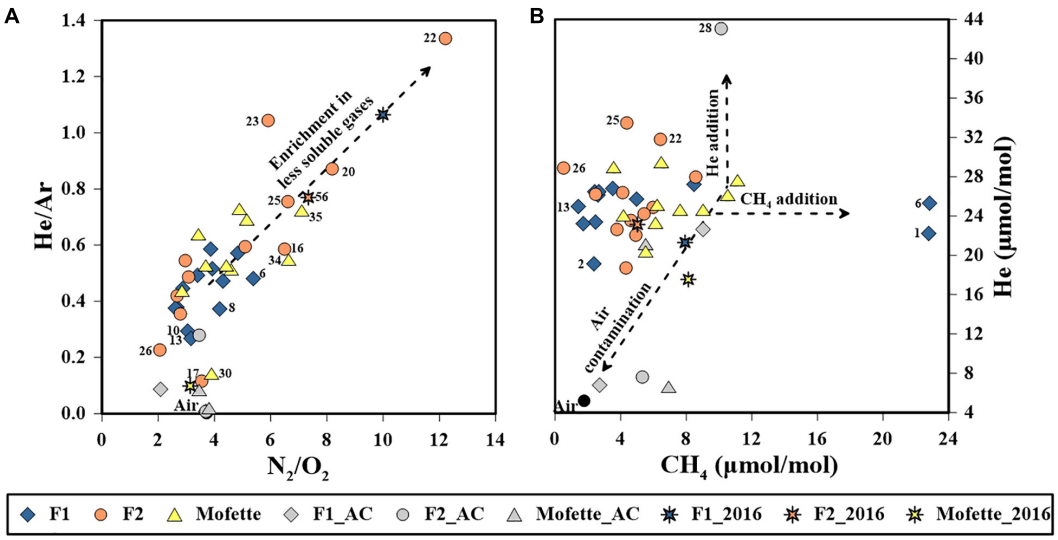


FIGURE 3 | Binary plots of **(A)** He/Ar vs. N_2/O_2 and **(B)** He vs. CH_4. Secondary processes are indicated with dashed arrows. The abbreviation _AC stands for air contamination, while data of samples collected during 2016 are from Bräuer et al. (2018).

cause higher $\delta^{13}C_{CO2}$ values as recognized in samples (4) and (6) (**Figure 5**). It might also be responsible for the depletion of the less soluble gases observed in samples (2) and (10) (**Figures 4A,D**).

Elevated gas flow and bubble fraction values in F1 correspond to depleted atmospheric components in the borehole and *vice versa* (**Figures 4A,D**). Provided that the concentration of atmospheric gases in the groundwater is constant, this observation indicates that mixing with a component of geogenic origin modifies the ratio. Moreover, low gas/water ratios (i.e., less intense bubbling) favor the dissolution, and hence the loss of CO_2 to the water (Reid et al., 1987). At the same time the limited ascent of geogenic gas can be contaminated more easily. The lack of gas flow and bubble fraction data at F2 and the mofette does not allow us to arrive at a similar conclusion for these locations.

Perturbations on the bubble fraction and the gas flow (F1) and on the wellhead pressure (F2) were observed when F3 was at a depth of ∼38 m (**Figure 4D**) and ∼110 m (**Figure 4B**), respectively. This indicates a hydraulic connection between the boreholes. This hypothesis was also supported by Woith et al. (2020), who documented a decrease in the gas flow and bubble fraction (**Figure 4D**) on the 30th of August. At the same time, the Rn concentration of the F3 drill mud reached its maximum. It is worth mentioning that a similar observation to the hydraulic connectivity, though on a larger scale, was made by Kämpf et al. (2013). They identified two connected conduit systems (Bublák and Hartoušov) that were interpreted as highly permeable substructures inside the Počatky–Plesná Fault Zone (PPZ). This observation was further studied by Nickschick et al. (2015), who hypothesized the existence of pull-apart basin-like structures inside the PPZ, and it was tested by Kämpf et al. (2019), who instead identified en-echelon faults, which act as fluid channels to depth.

Barometric pressures (note inverted scale in **Figure 4E**) are negatively correlated to the gas flow and bubble fraction at F1 (Woith et al., 2020). Fischer et al. (2020) explained this by proposing that elevated barometric pressures contribute to the dissolution of CO_2 that in turn hampers degassing. Even though the water temperature seems to be mostly constant, its perturbations are negatively correlated to the gas flow and bubble fraction (note inverted scale in **Figure 4C**). Despite its minor importance, it should be mentioned that the fractionation of C isotopes increases with decreasing temperature (Bottinga, 1968).

The relation between gases of different solubilities and $\delta^{13}C_{CO2}$ observed during the sampling period is presented in **Figure 5**. Gases collected when F3 reached a depth of ∼41 m [F1 (4)] and ∼125 m [F1 (6)] show a shift toward ^{13}C-enriched isotope values that may indicate fractionation due to preferential $^{12}C_{CO2}$ loss caused by phase separation. These phenomena have been observed for dissolved gases from the Apennines (Italy; Chiodini et al., 2000, 2013), the Southern Volcanic Zone of Chile (Ray et al., 2009), the Amik Basin (Turkey; Yuce et al., 2014), eastern Australia (Italiano et al., 2014b; Ring et al., 2016), and the Eastern Carpathians-Transylvanian Basin (Romania; Italiano et al., 2017). Moreover, the vigorous bubbling visible in the field and enhanced flow at F1 (Fischer et al., 2020; cf. **Figure 4**), suggest extensive degassing. This process promotes intense gas separation that subsequently causes isotope fractionation related to water-gas interactions.

Another possible explanation for elevated CH_4 contents and associated $\delta^{13}C_{CO2}$ values are Fischer-Tropsch type (FTT) reactions, during which gaseous CO_2 becomes reduced to produce abiogenic CH_4 (Berndt et al., 1996; Horita and Berndt, 1999; Foustoukos and Seyfried, 2004). Details on FTT reactions and abiogenic CH_4 are provided in the Section "Potential Origins of CH_4."

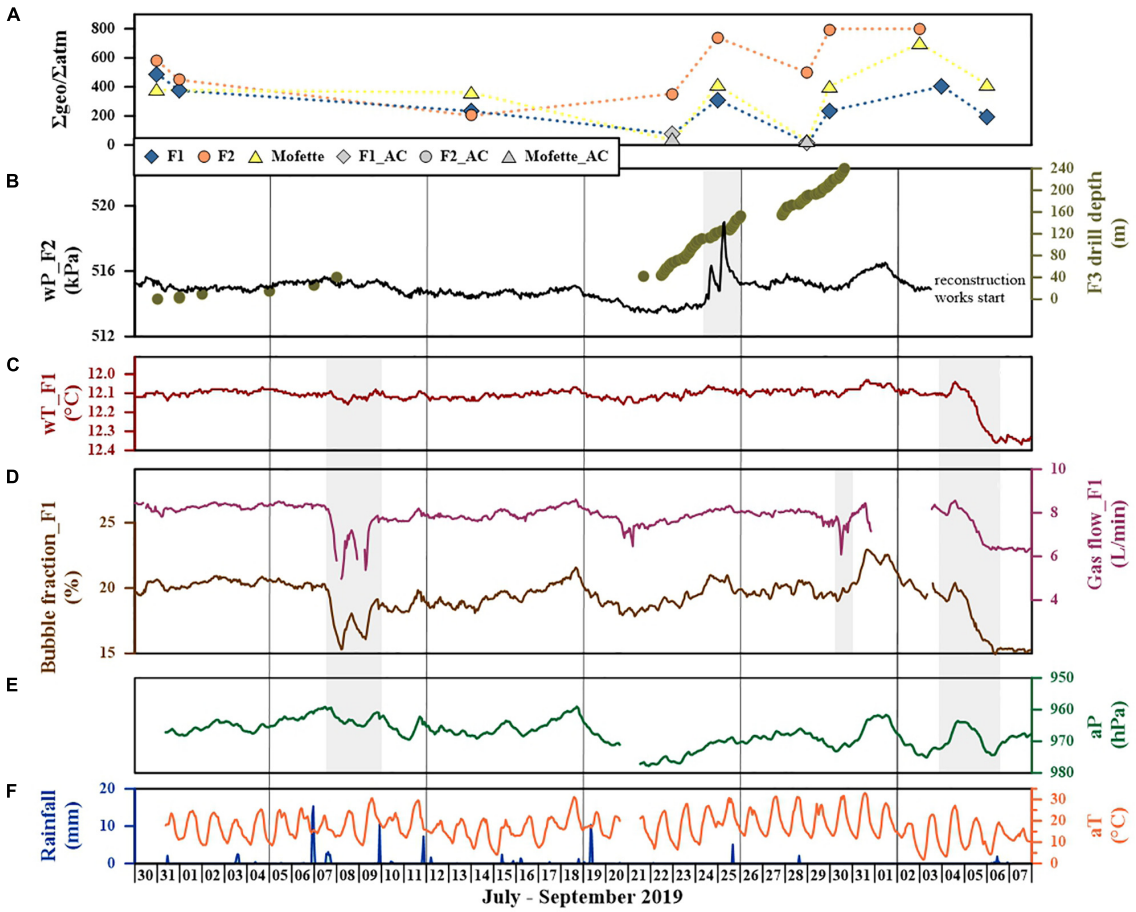


FIGURE 4 | Time series plot for the period 30th of July-7th of September 2019 showing **(A)** Σgeo/Σatm ratio in the two boreholes and the mofette, where Σgeo = CO_2+He+H_2+C_xH_y and Σatm = N_2+O_2+Ar, **(B)** the wellhead pressure (wP) of F2 and the drilling depth of F3 (Woith et al., 2020), **(C)** the water temperature (wT) in F1, **(D)** the calculated bubble fraction and the measured gas flow in F1, **(E)** the barometric pressure (aP) and **(F)** the meteorological conditions represented by the precipitation and the air temperature (aT). The axes of water temperature and barometric pressure are inverted. The vertical gray lines indicate the beginning of a new week, while the gray areas correspond to anomalies discussed in the text. Data of the gas flow and the temperature monitoring at Hartoušov are available at web.natur.cuni.cz/uhigug/carbonnet/en_index.html.

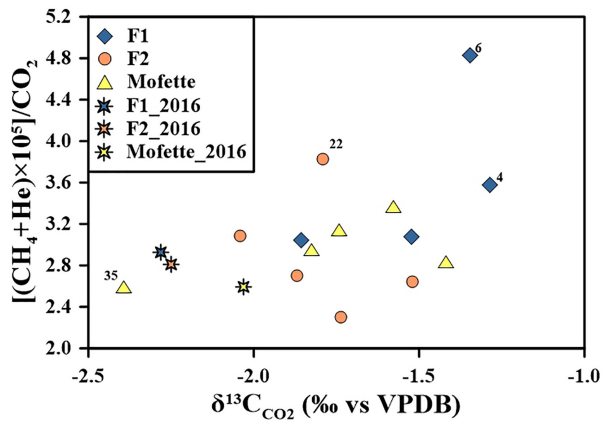


FIGURE 5 | Binary plot of (He+CH_4) /CO_2 vs. $\delta^{13}C_{CO2}$ for the gases of Hartoušov. Data of samples collected during 2016 are from Bräuer et al. (2018).

Sample (35) presents a shift toward more negative $\delta^{13}C$ values that may be related to a decrease in flow observed in the field. It should be also taken into consideration that the dissolution of CO_2 in the water results in CO_2 loss and lower $\delta^{13}C_{CO2}$ values. Moreover, if the hydraulic connection is real, then the mixing of gases ascending from different depths may have had an impact on the $\delta^{13}C$ and chemical composition. Overall the atmospheric components should decrease with increasing depth, while the geogenic components should increase. However, due to the limited amount of data and the standard deviation of the $\delta^{13}C_{CO2}$ values, no conclusions regarding the isotopic changes can be reached in the present work.

Potential Origins of CH_4

In geothermal and volcanic systems, the $CH_4/^3He$ ratio may differentiate possible methane sources (e.g., Welhan and Craig, 1983; Poreda et al., 1988); ^3He is mantle-derived, and the

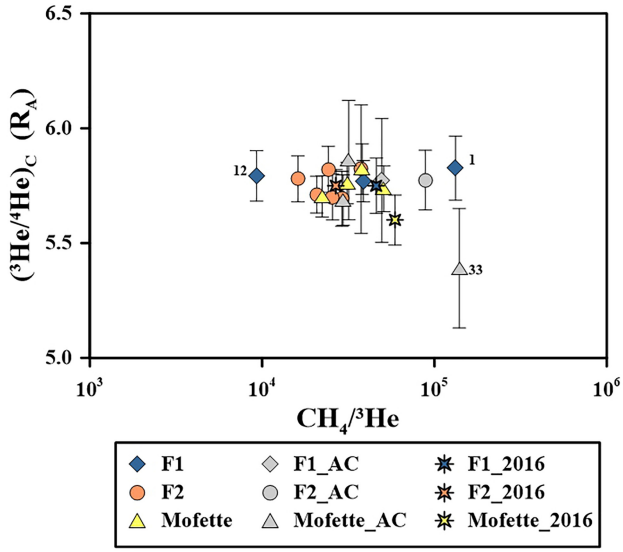


FIGURE 6 | Air-corrected $(^3He/^4He)_c$ vs. $CH_4/^3He$ diagram (cf. Poreda et al., 1988). The abbreviation _AC stands for air contamination, while data of samples collected during 2016 are from Bräuer et al. (2018).

$CH_4/^3He$ ratio may reflect the proportions of crustal and mantle-derived methane (Poreda et al., 1992). In **Figure 6**, the $(^3He/^4He)_c$ ratios are plotted against the $CH_4/^3He$ ratios of the samples collected in the HMF. The values of CH_4 should be considered as minimum estimates, because this gas can be involved in various post-genetic processes, and can also be consumed by methanotrophic bacteria (Murrell and Jetten, 2009; Kip et al., 2012; Gagliano et al., 2020). The $CH_4/^3He$ values range from 1.6×10^4 to 8.9×10^4, with two samples [(1), (33)] that reach up to 1.4×10^5, and one sample [(12)] with only 9.3×10^3. It should be noted that the highest [sample (1)] and the lowest [sample (12)] $CH_4/^3He$ ratios are observed for samples with elevated and depleted CH_4 contents. Likewise, $^3He/^4He$ ratios were relatively constant apart from one sample collected in the mofette during the drilling period [(33), F3 was at ∼197 m depth]. This sample presented a lower isotope ratio, which was most probably due to a higher contribution of crustal He. Except for this single occurrence, no correlation between the $^3He/^4He$ ratios and the drilling depth of F3 was evident.

According to Poreda et al. (1988) and Sakata (1991), low CH_4 contents correspond to low $CH_4/^3He$ ratios in CO_2-rich magmatic gases. This suggests the common origin of CH_4 and He. Mantle-derived fluids typically have $CH_4/^3He$ ratios between 10^5 and 10^8, while those of crust-derived fluids are much higher, and range from 10^8 to 10^{11} (Welhan and Craig, 1979; Giggenbach et al., 1993; Dai et al., 2005). The $CH_4/^3He$ ratios for most of the gases collected in the HMF are lower than 10^5 (**Figure 6**). This indicates that CH_4 may be of volcanic/geothermal origin (Etiope, 2015). If this is the case, CH_4 may have been generated from mantle- and limestone-derived CO_2 or from either of them, according to chemical reactions like Fischer-Tropsch type (FTT) reactions:

$$nCO + (2n + 1)H_2 = C_nH_{2n+2} + nH_2O \quad (2)$$

(Craig, 1953; Berndt et al., 1996; Horita and Berndt, 1999; McCollom and Seewald, 2001), and in the presence of Fe-bearing phase catalysts:

$$CO_2 + 8(FeO) + 2H_2O = CH_4 + 8(FeO_{1.5}) \quad (3)$$

Here FeO and $FeO_{1.5}$ represent iron in the two oxidation states that are generally present in minerals of crustal rocks (Giggenbach, 1987). Both the FTT reactions and the presence of Fe-bearing phase catalysts are fundamental conditions for the chemical and isotope exchange between CO_2 and CH_4 and the establishment of an equilibrium.

In an attempt to determine the P-T conditions under which the gases were formed, the CO_2/Ar and CH_4/Ar ratios were used as geoindicators (**Figure 7**). **Figure 7** was constructed assuming fugacities of H_2O and CO_2 as described in Chiodini et al. (2007). Redox conditions were defined according to D'Amore and Panichi (1980). Excluding the samples affected by air contamination, most samples cluster at T from ∼100 to ∼120^{o}C and P_{CO2} from ∼30 to ∼70 bar. These values can be considered as medium to low P-T conditions that promote the generation of thermogenic CH_4 (Hunt, 1996). Some samples [10), (13), (17), (26), (30), (54)] are characterized by even lower P-T conditions, indicating that the impact of the atmospheric end-member is not negligible in this case. The elevated heat flow values (70–80 mW/m^2, locally as high as 90 mW/m^2; Čermák, 1994) recognized in the area may have contributed to the depleted light hydrocarbon content. It is worth noting that

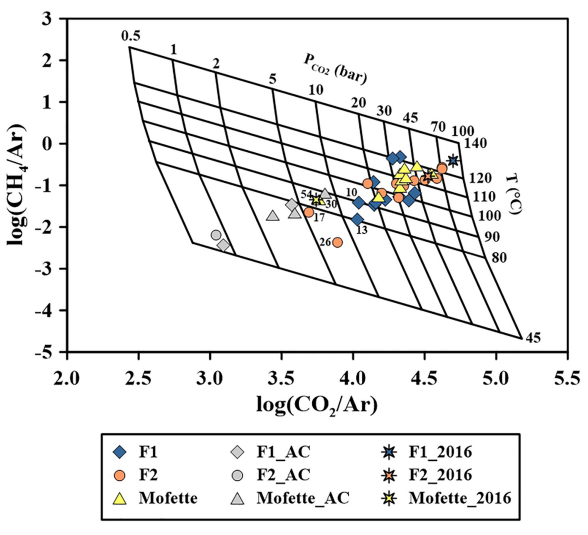


FIGURE 7 | Plot of log(CH_4/Ar) vs. log(CO_2/Ar) after Chiodini et al. (2007). The theoretical P_{CO2}-T grids assume that the redox conditions are fixed by the D'Amore and Panichi (1980) buffer. The abbreviation _AC stands for air contamination, while data of samples collected during 2016 are from Bräuer et al. (2018).

the majority of the gases have values of $CH_4/(C_2H_6+C_3H_8)$ (Bernard ratio; Bernard et al., 1978) in the range of 9 to 93. According to Bernard et al. (1978), these ratios characterize gases of thermogenic origin that are produced by decay of organic matter. If this applies to the gases of the HMF, samples (1), (6), (18), (22), (23), (24), (25), (38), and (39) with Bernard ratios between 100 and 1,000 may reflect secondary processes that stem from inorganic or organic oxidation of CH_4 or mixing of microbial and thermogenic CH_4. Methanogenic archaea detected in various mofette waters in the Cheb Basin (Krauze et al., 2017) may support a biogenic origin of at least parts of the CH_4 present. Moreover, Liu et al. (2018) suggested that the anaerobic and acidophilic taxa identified in soils and sediments collected from two 3-m cores in the HMF may perform methanogenesis under reducing conditions.

Both scenarios seem plausible, however, we cannot confirm or dismiss either of them because the rather low CH_4 concentrations (**Table 1**) did not allow the determination of $\delta^{13}C_{CH4}$ and $\delta^{2}H_{CH4}$ values. Thus, any conclusion on the origin of the gas may be misleading. However, the extraordinary low $CH_4/^3He$ ratios may point to a limited presence of organic matter in the overall process of CH_4 formation. Together with the medium to low P-T conditions, it can be hypothesized that CH_4 in the HMF originates from mixing of volcanic/geothermal and biogenic CH_4 with a non-negligible atmospheric contribution. This hypothesis seems plausible based on the sedimentary formations that characterize the HMF, together with its elevated heat flow values (Čermák, 1994), and the mantle-derived He and CO_2 (Weinlich et al., 1999; Kämpf et al., 2013; Bräuer et al., 2018; this study **Tables 2**, **3**). Procesi et al. (2019) summarized that these are some of the criteria that describe sediment-hosted geothermal systems. Such hybrid geological systems exhibit both volcano-hydrothermal and sedimentary features, in which geothermal and sedimentary domains interact and yield mixtures of inorganic and biogenic gases.

CONCLUSION

The present study investigated processes that affected gases of the HMF in a period when a third borehole was drilled, and no seismic event took place. Changes in CO_2 concentrations are mainly attributed to different solubilities of the gases. This was combined with dilution caused by an enhanced content of atmospheric components. Perturbations on the gas flows, dissolution, and likely FTT reactions had effects on the isotope compositions of CO_2. Moreover, data from the wellhead pressure of F2 as well as from the gas flow of F1 support the assumption that the boreholes are hydraulically connected.

Variations in CH_4 contents indicated generation and consumption of this gas. Despite the lack of CH_4 isotope data, we suggest that CH_4 may be of mixed biogenic and volcanic/geothermal origin. In any case, it derives from sediments characterized by medium to low P-T conditions. It is unclear if it is solely derived from the mantle or also influenced by limestone-derived CO_2 under conditions in which FTT reactions and Fe catalysts are present. The drilling of the third borehole highlighted the complexity of the HMF in a seismically quiescent period. It opens the opportunity for further geochemical investigations in the area.

DATA AVAILABILITY STATEMENT

The original contributions presented in the study are included in the article/**Supplementary Materials**, further inquiries can be directed to the corresponding author.

AUTHOR CONTRIBUTIONS

HW, MZ, SN, and JB developed the conception and design of the MoRe project. KD was responsible for the gas sampling, while all the authors assisted in the field campaigns. AV-H was responsible for the $\delta^{13}C_{CO2}$ analyses, while SN was responsible for the noble gas analyses. JV was responsible for the gas flow, pressure, and temperature measurements. KD wrote the first draft of the manuscript. All authors contributed to manuscript revision, read and approved the submitted version.

FUNDING

This research was a part of the MoRe – "Mofette Research" project, which is included in the International Continental Scientific Drilling Program (ICDP) project "Drilling the Eger Rift: Magmatic fluids driving the earthquake swarms and the deep biosphere." This work was funded by the Deutsche Forschungsgemeinschaft (DFG, German Research Foundation) – 419880416.

ACKNOWLEDGMENTS

We would like to thank Walter D'Alessandro and Artur Ionescu for the fruitful discussions during the preparation of this manuscript. We are indebted to all the laboratory technicians for performing the various analyses: Enzio Schnabel (noble gas measurements), Doreen Noack (carbon isotopes), and Jiři Tesař (chemical composition). We also thank Pouria Marzban for sharing the orthomosaic image presented in **Figure 1**. We are also grateful for the insightful comments of the two reviewers and of the editor YW that helped us to significantly improve the manuscript.

SUPPLEMENTARY MATERIAL

The Supplementary Material for this article can be found online at: https://www.frontiersin.org/articles/10.3389/feart.2021.615766/full#supplementary-material

REFERENCES

Babuška, V., and Plomerová, J. (2008). Control of paths of quaternary volcanic products in western bohemian massif by rejuvenated variscan triple junction of ancient microplates. *Stud. Geophys. Geod.* 52, 607–629. doi: 10.1007/s11200-008-0040-0

Bankwitz, P., Schneider, G., Kämpf, H., and Bankwitz, E. (2003). Structural characteristics of epicentral areas in Central Europe: study case cheb basin (Czech Republic). *J. Geodyn.* 35, 5–32. doi: 10.1016/s0264-3707(02)00051-0

Bernard, B. B., Brooks, J. M., and Sackett, W. M. (1978). *A Geochemical Model for Characterization of Hydrocarbon gas Sources in Marine Sediments*. Houston, TX: Offshore Technology Conference, 435–438.

Berndt, M. E., Allen, D. E., and Seyfried, W. E. (1996). Reduction of CO_2 during serpentinization of olivine at 300°C and 500 bar. *Geology* 24, 351–354. doi: 10.1130/0091-7613(1996)024<0351:rocdso>2.3.co;2

Bottinga, Y. (1968). Calculation of fractionation factors for carbon and oxygen isotopic exchange in the system calcite–carbon dioxide–water. *J. Phys. Chem.* 72, 800–808. doi: 10.1021/j100849a008

Bräuer, K., Kämpf, H., Niedermann, S., and Strauch, G. (2005). Evidence for ascending upper mantle-derived melt beneath the Cheb basin, Central Europe. *Geophys. Res. Lett.* 32:L08303. doi: 10.1029/2004GL022205

Bräuer, K., Kämpf, H., Niedermann, S., and Strauch, G. (2018). Monitoring of helium and carbon isotopes in the western Eger Rift area (Czech Republic): relationships with the 2014 seismic activity and indications for recent (2000–2016) magmatic unrest. *Chem. Geol.* 482, 131–145. doi: 10.1016/j.chemgeo.2018.02.017

Bräuer, K., Kämpf, H., and Strauch, G. (2009). Earthquake swarms in non-volcanic regions: what fluids have to say. *Geophys. Res. Lett.* 36:L17309. doi: 10.1029/2009GL039615

Bussert, R., Kämpf, H., Flechsig, C., Hesse, K., Nickschick, T., Liu, Q., et al. (2017). Drilling into an active mofette: pilot-hole study of the impact of CO_2-rich mantle-derived fluids on the geo–bio interaction in the western Eger Rift (Czech Republic). *Sci. Dril.* 23, 13–27. doi: 10.5194/sd-23-13-2017

Čermák, V. (1994). "Results of heat flow studies in Czechoslovakia, in crustal structure of the bohemian massif and the west carpathians," in *Exploration of the Deep Continental Crust*, eds V. Bucha and M. Blížkovs.ký (Berlin: Springer-Verlag), 85–120. doi: 10.1007/978-3-642-78995-3_4

Chiodini, G., Baldini, A., Barberi, F., Carapezza, M. L., Cardellini, C., Frondini, F., et al. (2007). Carbon dioxide degassing at Latera caldera (Italy): evidence of geothermal reservoir and evaluation of its potential energy. *J. Geophys. Res.* 112:B12204. doi: 10.1029/2006JB004896

Chiodini, G., Cardellini, C., Caliro, S., Chiarabba, C., and Frondini, F. (2013). Advective heat transport associated with regional earth degassing incentral apennine (Italy). *Earth Planet. Sci. Lett.* 373, 65–74. doi: 10.1016/j.epsl.2013.04.009

Chiodini, G., Frondini, F., Cardellini, C., Parello, F., and Peruzzi, L. (2000). Rate of diffuse carbon dioxide earth degassing estimated from carbon balance of regional aquifers: the case of central Apennine, Italy. *J. Geophys. Res.* 105, 8423–8434. doi: 10.1029/1999jb900355

Craig, H. (1953). The geochemistry of the stable carbon isotopes. *Geochim. Cosmochim. Acta.* 3, 53–92. doi: 10.1016/0016-7037(53)90001-5

Craig, H., Lupton, J. E., and Horribe, Y. (1978). A mantle helium component in Circum-Pacific Rise volcanic gases: hakone, the Marianas, and Mt Lassen. *Terr. Rare Gases* 3, 3–16. doi: 10.1007/978-94-010-9828-1_1

Dahm, T., Hrubcová, P., Fischer, T., Horálek, J., Korn, M., Buske, S., et al. (2013). Eger Rift ICDP: an observatory for study of non-volcanic, mid-crustal earthquake swarms and accompanying phenomena. *Sci. Dril.* 16, 93–99. doi: 10.5194/sd-16-93-2013

Dai, J. X., Yang, S. F., Chen, H. L., and Shen, X. H. (2005). Geochemistry and occurrence of inorganic gas accumulations in Chinese sedimentary basins. *Org. Geochem.* 36, 1664–1688. doi: 10.1016/j.orggeochem.2005.08.007

D'Alessandro, W., Brusca, L., Kyriakopoulos, K., Bellomo, S., and Calabrese, S. (2014). A geochemical traverse along the "Sperchios Basin — Evoikos Gulf" Graben (Central Greece): origin and evolution of the emitted fluids. *Mar. Pet. Geol.* 55, 295–308. doi: 10.1016/j.marpetgeo.2013.12.011

D'Alessandro, W., Brusca, L., Martelli, M., Rizzo, A., and Kyriakopoulos, K. (2010). Geochemical characterization of natural gas manifestations in Greece. *Bull. Geol. Soc. Gr.* 43, 2327–2337. doi: 10.12681/bgsg.11633

D'Amore, F., and Panichi, C. (1980). Evaluation of deep temperatures of hydrothermal systems by a new gas geothermometer. *Geochim. Cosmochim. Acta* 44, 549–556. doi: 10.1016/0016-7037(80)90051-4

Daskalopoulou, K., Calabrese, S., Grassa, F., Kyriakopoulos, K., Parello, F., Tassi, F., et al. (2018). Origin of methane and light hydrocarbons in natural fluid emissions: a key study from Greece. *Chem. Geol.* 479, 286–301. doi: 10.1016/j.chemgeo.2018.01.027

Easley, E., Garchar, L., Bennett, M., Morgan, P., and Wendlandt, R. F. (2011). A geochemical and isotopic study of two geothermal prospects in the Rio Grande Rift, Colorado and New Mexico. *Mt. Geol.* 48, 95–106.

Etiope, G. (2015). *Natural Gas Seepage: The Earth's Hydrocarbon Degassing*. Berlin: Springer, 141. doi: 10.1007/978-3-319-14601-0

Fiala, J., and Vejnar, Z. (2004). The lithology, geochemistry, and metamorphic gradation of the crystalline basement of the Cheb (Eger) Tertiary Basin, Saxothuringian Unit. *Bull. Geosci.* 79, 41–52.

Fischer, T., and Horálek, J. (2003). Space-time distribution of earthquake swarms in the principal focal zone of the NW-Bohemian/Vogtland seismoactive region: period 1985-2001. *J. Geodyn.* 35, 125–144. doi: 10.1016/S0264-3707(02)00058-3

Fischer, T., Horálek, J., Hrubcová, P., Vavryčuk, V., Bräuer, K., and Kämpf, H. (2014). Intra-continental earthquake swarms in West-Bohemia and Vogtland: a review. *Tectonophysics* 611, 1–27. doi: 10.1016/j.tecto.2013.11.001

Fischer, T., and Michálek, J. (2008). Post 2000-swarm microearthquake activity in the principal focal zone of West Bohemia/Vogtland: space-time distribution and waveform similarity analysis. *Stud. Geophys. Geod.* 52, 493–511. doi: 10.1007/s11200-008-0034-y

Fischer, T., Matyskac, C., and Heinicke, J. (2017). Earthquake-enhanced permeability – evidence from carbon dioxide release following the M_L 3.5 earthquake in West Bohemia, Earth Planet. *Sc. Lett.* 460, 60–67. doi: 10.1016/j.epsl.2016.12.001

Fischer, T., Vlček, J., and Lanzendörfer, M. (2020). Monitoring crustal CO_2 flow: methods and their applications to the mofettes in West Bohemia. *Solid Earth* 11, 983–998. doi: 10.5194/se-11-983-2020

Fischer, T. P., Giggenbach, W. F., Sano, Y., and Williams, S. N. (1998). Fluxes and sources of volatiles discharged from Kudryavy, a subduction zone volcano, Kurile Islands. *Earth Planet Sci Lett* 160, 81–96. doi: 10.1016/s0012-821x(98)00086-7

Foustoukos, D. I., and Seyfried, W. E. (2004). Hydrocarbons in hydrothermal vent fluids: the role of chromium-bearing catalysts. *Science* 304, 1002–1004. doi: 10.1126/science.1096033

Gagliano, A. L., Calabrese, S., Daskalopoulou, K., Kyriakopoulos, K., Tagliavia, M., and D'Alessandro, W. (2020). Methanotrophy in geothermal soils, an overlooked process: the example of Nisyros island (Greece). *Chem. Geol.* 539:119546. doi: 10.1016/j.chemgeo.2020.119546

Geissler, W. H., Kämpf, H., Kind, R., Klinge, K., Plenefisch, T., Horálek, J., et al. (2005). Seismic structure and location of a CO_2 source in the upper mantle of the western Eger (Ohře) Rift, Central Europe. *Tectonics* 24:TC5001. doi: 10.1029/2004TC001672

Giggenbach, W. F. (1987). Redox processes governing the chemistry of fumarolic gas discharges from White Island, New Zealand. *Appl. Geochem.* 2, 143–161. doi: 10.1016/0883-2927(87)90030-8

Giggenbach, W. F. (1992). The composition of gases in geothermal and volcanic systems as a function of tectonic setting. *Water Rock Interact.* 2, 873–878.

Giggenbach, W. F. (1996). "Chemical composition of volcanic gases," in *Monitoring and Mitigation of Volcano Hazards*, eds R. Scarpa and R. I. Tilling (Berlin: Springer), 221–256. doi: 10.1007/978-3-642-80087-0_7

Giggenbach, W. F., Gonfianti, R., Jangi, B. L., and Truesdell, A. H. (1983). Isotopic and chemical composition of Parbati Valley geothermal discharges, North-West Himalaya, India. *Geothermics* 12, 199–222. doi: 10.1016/0375-6505(83)90030-5

Giggenbach, W. F., Sano, Y., and Wakita, H. (1993). Isotopic composition of helium, and CO_2 and CH_4 contents in gases produced along the New Zealand part of a convergent plate boundary. *Geochim. Cosmochim. Acta* 57, 3427–3455. doi: 10.1016/0016-7037(93)90549-c

Goff, F., and Janik, C. J. (2002). Gas geochemistry of the Valles caldera region, New Mexico and comparisons with gases at Yellowstone, Long Valley and other geothermal systems. *J. Volcanol. Geotherm. Res.* 116, 299–323. doi: 10.1016/s0377-0273(02)00222-6

Heaton, T. H. E., and Vogel, J. C. (1981). Excess air in groundwater. *J. Hydrol.* 50, 201–208. doi: 10.1016/0022-1694(81)90070-6

Hecht, L., Vigneresse, J., and Morteani, G. (1997). Constraints on the origin of zonation of the granite complexes in the Fichtelgebirge (Germany and Czech Republic): evidence from a gravity and geochemical study. *Geol. Rundsch.* 86, S93–S109.

Hickman, S., Sibson, R., and Bruhn, R. (1995). Introduction to special section: mechanical involvement of fluids in faulting. *J. Geophys. Res.* 100, 12831–12840. doi: 10.1029/95jb01121

Horita, J., and Berndt, M. E. (1999). Abiogenic methane formation and isotopic fractionation under hydrothermal conditions. *Science* 285, 1055–1057. doi: 10.1126/science.285.5430.1055

Hunt, J. M. (1996). *Petroleum Geochemistry and Geology*. New York, NY: W.H. Freeman and Co, 743.

Irwin, W. P., and Barnes, I. (1980). Tectonic relations of carbon dioxide discharges and earthquakes. *J. Geophys. Res.* 85, 3115–3121. doi: 10.1029/jb085ib06p03115

Italiano, F., De Santis, A., Favali, P., Rainone, M. L., Ruisi, S., and Signanini, S. (2014a). The marsili volcanic seamount (Southern Tyrrhenian Sea): a potential offshore geothermal resource. *Energies* 7, 4068–4086. doi: 10.3390/en7074068

Italiano, F., Kis, B. M., Baciu, C., Ionescu, A., Harangi, S., and Palcsu, L. (2017). Geochemistry of dissolved gases from the eastern carpathians – transylvanian basin boundary. *Chem. Geol.* 469, 117–128. doi: 10.1016/j.chemgeo.2016.12.019

Italiano, F., Yuce, G., Uysal, I. T., Gasparon, M., and Morelli, G. (2014b). Insights into mantle type volatiles contribution from the dissolved gases in artesian waters of the Great Artesian Basin, Australia. *Chem. Geol.* 378-379, 75–88. doi: 10.1016/j.chemgeo.2014.04.013

Kämpf, H., Bräuer, K., Schumann, J., Hahne, K., and Strauch, G. (2013). CO_2 discharge in an active, non-volcanic continental rift area (Czech Republic): characterisation ($\delta^{13}C$, $^3He/^4He$) and quantification of diffuse and vent CO_2 emissions. *Chem. Geol.* 339, 71–83. doi: 10.1016/j.chemgeo.2012.08.005

Kämpf, H., Broge, A. S., Marzban, P., Allahbakhshi, M., and Nickschick, T. (2019). Nonvolcanic carbon dioxide emission at continental rifts: the bublak mofette area, western eger rift, czech republic. *Geofluids* 2019:4852706. doi: 10.1155/2019/4852706

Kip, N., Fritz, C., Langelaan, E. S., Pan, Y., Bodrossy, L., Pancotto, V., et al. (2012). Methanotrophic activity and diversity in different *Sphagnum magellanicum* dominated habitats in the southernmost peat bogs of Patagonia. *Biogeosciences* 9, 47–55. doi: 10.5194/bg-9-47-2012

Krauze, P., Kämpf, H., Horn, F., Liu, Q., Voropaev, A., Wagner, D., et al. (2017). Microbiological and geochemical survey of CO_2-dominated mofette and mineral waters of the Cheb Basin, Czech Republic. *Front. Microbiol.* 8:2446. doi: 10.3389/fmicb.2017.02446

Lee, H., Yang, T. F., Lan, T. F., Song, S., and Tsao, S. (2005). Fumarolic gas composition of the Tatun Volcano Group, northern Taiwan. *Terr. Atmos. Ocean Sci.* 16, 843–864. doi: 10.3319/tao.2005.16.4.843(gig)

Liu, Q., Kämpf, H., Bussert, R., Krauze, P., Horn, F., Nickschick, T., et al. (2018). Influence of CO_2 degassing on the microbial community in a dry mofette field in Hartoušov, Czech Republic (Western Eger Rift). *Front. Microbiol.* 9:2787. doi: 10.3389/fmicb.2018.02787

Lupton, J. E. (1983). Terrestrial inert gases: isotope tracer studies and clues to primordial components in the mantle. *Annu. Rev. Earth Planet. Sci.* 11, 371–414. doi: 10.1146/annurev.ea.11.050183.002103

McCollom, T. M., and Seewald, J. S. (2001). A reassessment of the potential for reduction of dissolved CO_2 to hydrocarbons during serpentinization of olivine. *Geochim. Cosmochim. Acta.* 65, 3769–3778. doi: 10.1016/s0016-7037(01)00655-x

Mrlina, J., Kämpf, H., Kroner, C., Mingram, J., Stebich, M., Brauer, A., et al. (2009). Discovery of the first quaternary maar in the Bohemian Massif, central Europe, based on combined geophysical and geological surveys. *J. Volcanol. Geotherm. Res.* 182, 97–112. doi: 10.1016/j.jvolgeores.2009.01.027

Murrell, C. J., and Jetten, M. S. M. (2009). The microbial methane cycle. *Environ. Microbiol. Reports* 1, 279–284. doi: 10.1111/j.1758-2229.2009.00089.x

Nickschick, T., Kämpf, H., Flechsig, C., Mrlina, J., and Heinicke, J. (2015). CO_2 degassing in the Hartoušov mofette area, western Eger Rift, imaged by CO_2 mapping and geoelectrical and gravity surveys. *Int. J. Earth Sci.* 104, 2107–2129. doi: 10.1007/s00531-014-1140-4

Niedermann, S., Bach, W., and Erzinger, J. (1997). Noble gas evidence for a lower mantle component in MORBs from the southern East Pacific rise: decoupling of helium and neon isotope systematics. *Geochim. Cosmochim. Acta* 61, 2697–2715. doi: 10.1016/s0016-7037(97)00102-6

Parotidis, M., Rothert, R., and Shapiro, S. A. (2003). Pore-pressure diffusion: a possible triggering mechanism for the earthquake swarms 2000 in the Vogtland/NW Bohemia, central Europe. *Geophys. Res. Lett.* 30, 2075. doi: 10.1029/2003GL018110

Pearce, J. M., Czernichowski-Lauriol, I., Lombardi, S., Brune, S., Mador, A., Baker, J., et al. (2004). "A review of natural CO_2 accumulations in Europe as analogues for geological sequestration," in *Geological Storage of Carbon Dioxide*, Vol. 233, eds S. Baines and R.H. Worden (London: Geological Society of London), 29–42. doi: 10.1144/GSL.SP.2004.233.01.04

Poreda, R. J., Craig, H., Arnórsson, S., and Welhan, J. A. (1992). Helium isotopes in Icelandic geothermal systems: I. ^3He, gas chemistry, and ^{13}C relations. *Geochim. Cosmochim. Acta* 56, 4221–4228. doi: 10.1016/0016-7037(92)90262-H

Poreda, R. J., Jeffrey, A. W., Kaplan, I. R., and Craig, H. (1988). Magmatic helium in subduction zone natural gases. *Chem. Geol.* 71, 198–210.

Procesi, M., Ciotoli, G., Mazzini, A., and Etiope, G. (2019). Sediment-hosted geothermal systems: review and first global mapping. *Earth Sci. Rev.* 192, 529–544. doi: 10.1016/j.earscirev.2019.03.020

Ray, M. C., Hilton, D. R., Munoz, J., Fischer, T. P., and Shaw, A. M. (2009). The effects of volatile recycling, degassing and crustal contamination on helium and carbon geochemistry of hydrothermal fluids from the Southern Volcanic Zone of Chile. *Chem. Geol.* 266, 38–49. doi: 10.1016/j.chemgeo.2008.12.026

Reid, R. C., Prausnitz, J. M, and Poling, B. E. (1987). *The Properties of Gases and Liquids*. New York, NY: McGraw-Hill, Inc.

Ring, U., Uysal, I. T., Yüce, G., Ünal-Ýmer, E., Italiano, F., Ýmer, A., et al. (2016). Recent mantle degassing recorded in carbonic spring deposits along sinistral strike-slip faults, south central Australia. *Earth Planet. Sci. Lett.* 454, 304–318. doi: 10.1016/j.epsl.2016.09.017

Rolston, D. E., Duxbury, J. M., Harper, L. A., Mosier, A. R., and Knowles, R. (1993). *Methane: Processes of Production and Consumption. ASA Special Publication*. Madison, WI: American Society of Agronomy, doi: 10.2134/asaspecpub55.c10

Sakata, S. (1991). Carbon isotope geochemistry of natural gases from the Green Tuff Basin, Japan. *Geochim. Cosmochim. Acta* 55, 1395–1405. doi: 10.1016/0016-7037(91)90316-w

Špičáková, L., Uličný, D., and Koudelková, G. (2000). Tectonosedimentary evolution of the Cheb Basin (NW Bohemia, Czech Republic) between Late Oligocene and Pliocene: a preliminary note. *Stud. Geophys. Geod.* 44, 556–580.

Weinlich, F. H., Bräuer, K., Kämpf, H., Strauch, G., Tesař, J., and Weise, S. M. (1999). An active subcontinental mantle volatile system in the western Eger rift, Central Europe: Gas flux, isotopic (He, C, and N) and compositional fingerprints. *Geochim. Cosmochim. Acta* 63, 3653–3671. doi: 10.1016/s0016-7037(99)00187-8

Weinlich, F. H., Tesař, J., Weise, S. M., Bräuer, K., and Kämpf, H. (1998). Gas flux distribution in mineral springs and tectonic structure in the western Eger Rift. *J. Czech Geol. Soc.* 43, 91–110.

Weise, S. M., Bräuer, K., Kämpf, H., Strauch, G., and Koch, U. (2001). Transport of mantle volatiles through the crust traced by seismically released fluids: a natural experiment in the earthquake swarm area Vogtland/NW Bohemia, central Europe. *Tectonophysics* 336, 137–150. doi: 10.1016/s0040-1951(01)00098-1

Welhan, J. A., and Craig, H. (1979). Methane and hydrogen in East Pacific rise hydrothermal fluids. *Geophys. Res. Lett.* 6, 829–832. doi: 10.1029/gl006i011p00829

Welhan, J. A., and Craig, H. (1983). "Methane, hydrogen and helium in hydrothermal fluids," in *Hydrothermal Processes at Seafloor Spreading Centers*, Vol. 12, eds P. A. Rona, K. Boström, L. Laubier, and K. L. Smith (Boston, MA: Plenum Press), 39l–409l.

Woith, H., Daskalopoulou, K., Zimmer, M., Fischer, T., Vlček, J., Trubač, J., et al. (2020). Multi-level gas monitoring: a new approach in earthquake research. *Front. Earth Sci.* 8:585733. doi: 10.3389/feart.2020.585733

Yuce, G., Italiano, F., D'Alessandro, W., Yalcin, T. H., Yasin, D. U., Gulbay, A. H., et al. (2014). Origin and interactions of fluids circulating over the Amik Basin (Hatay-Turkey) and relationships with the hydrologic, geologic and tectonic settings. *Chem. Geol.* 388, 23–39. doi: 10.1016/j.chemgeo.2014.09.006

Conflict of Interest: The authors declare that the research was conducted in the absence of any commercial or financial relationships that could be construed as a potential conflict of interest.

Copyright © 2021 Daskalopoulou, Woith, Zimmer, Niedermann, Barth, Frank, Vieth-Hillebrand, Vlček, Bağ and Bauz. This is an open-access article distributed under the terms of the Creative Commons Attribution License (CC BY). The use, distribution or reproduction in other forums is permitted, provided the original author(s) and the copyright owner(s) are credited and that the original publication in this journal is cited, in accordance with accepted academic practice. No use, distribution or reproduction is permitted which does not comply with these terms.

frontiers in Earth Science

ORIGINAL RESEARCH
published: 15 April 2021
doi: 10.3389/feart.2021.634921

Geochemical Comparison of the Deep Gases From the Sichuan and Tarim Basins, China

Yunyan Ni, Limiao Yao, Fengrong Liao, Jianping Chen, Cong Yu and Guangyou Zhu*

Research Institute of Petroleum Exploration and Development, PetroChina, Beijing, China

In order to have a better understanding of the geochemical characteristics of gases from deep depths, gases from the clastic sandstone reservoirs in the Dabei and Keshen gas fields in the Kuqa depression, Tarim Basin, and gases from the marine carbonate reservoirs (Ordovician and Cambrian) in the craton area of Tarim Basin and Sichuan Basin (Yuanba, Longgang, Puguang gas fields) are investigated based on the molecular composition, stable carbon and hydrogen isotopes. Deep gas, either from the clastic sandstone reservoirs or from the marine carbonate reservoirs, is dominated by alkane gas. Gases from Kuqa depression and Sichuan Basin are dry gas, with high gas dryness coefficient, 0.976 and 0.999, respectively. Deep gas from the craton area in Tarim Basin includes both dry and wet gases. N_2 and CO_2 are the common non-hydrocarbon components in the deep gas. Gases from the continental sandstone reservoirs have no H_2S, while gases from the marine carbonate reservoirs often have H_2S. The relatively high $\delta^{13}C_2$ value in the Kuqa depression indicates the gas was generated from humic type III kerogen, while the relatively low $\delta^{13}C_2$ value in the craton area of Tarim Basin indicates most of the gas was generated from the marine sapropelic organic matter. Deep gas in Sichuan Basin, which has medium $\delta^{13}C_2$ value, was generated from both humic type III and sapropelic type II organic matter. Carbon isotopic anomaly such as partial carbon isotopic reversal or relatively heavy carbon isotope is common in the deep gas, which is caused by secondary alteration. Gases from the Dabei gas field have a mean δ^2H_1 value of –156‰, while gases from the craton area of Tarim Basin, and Yuanba and Puguang gas fields in Sichuan Basin have relatively heavier δ^2H_1 value, i.e., average at −130 and −122‰, respectively. The abnormally heavier δ^2H_1 value in Dabei gas field is due to the high thermal maturity and possible saline depositional environment of the source rocks. This study performed a comprehensive comparison of the geochemical characteristics of the deep gases with different origins, which may provide a hint for future exploration of deep gas in the world.

Keywords: deep gas, ultra-deep gas, tight gas, hydrogen isotope, carbon isotope, Sichuan Basin, Tarim Basin

OPEN ACCESS

Edited by:
Yunpeng Wang,
Chinese Academy of Sciences, China

Reviewed by:
Se Gong,
Commonwealth Scientific and Industrial Research Organisation (CSIRO), Australia
Xiangchun Chang,
Shandong University of Science and Technology, China

****Correspondence:***
Yunyan Ni
niyy@petrochina.com.cn

Specialty section:
This article was submitted to Geochemistry, a section of the journal Frontiers in Earth Science

Received: *29 November 2020*
Accepted: *03 March 2021*
Published: *15 April 2021*

Citation:
Ni Y, Yao L, Liao F, Chen J, Yu C and Zhu G (2021) Geochemical Comparison of the Deep Gases From the Sichuan and Tarim Basins, China. Front. Earth Sci. 9:634921. doi: 10.3389/feart.2021.634921

INTRODUCTION

After massive exploitation of conventional oil and gas, exploration has been increasingly difficult and more attention has been paid to the deep and ultra-deep resources, especially in the mature exploration area, deep and ultra-deep area has been a significant target. Debates exist in the definition of exact burial depth of the deep and ultra-deep resources. From a geological perspective,

"deep gas" is generally referred to the gas with reservoir depth greater than 4,500 m and "ultra-deep gas" is generally referred to the gas with reservoir depth greater than 6,000 m (He et al., 2016; Li, 2016; Sun et al., 2017; Dai et al., 2018). It is also proposed that definition of the exact reservoir depth of the deep and ultra-deep oil and gas resources should consider the influence of geothermal gradient of the basin (Dai et al., 2004a; Chinese Petroleum Society, 2016). For example, the geothermal gradient is 2.26°C/100 m (Feng et al., 2009) and 2.28°C/100 m (Xu et al., 2011) in the Tarim and Sichuan basins, respectively, so in these two basins, deep gas is referred to the gas with reservoir depth greater than 4,500 m and ultra-deep gas is referred to the gas with reservoir depth greater than 6,000 m (Dai et al., 2018). While in eastern China, due to the relatively high geothermal gradient (i.e., 3.58°C/100 m in the North China Basin) (Chen, 1988), "deep" is referred to reservoir depth greater than 3,500 m and "ultra-deep" is referred to reservoir depth greater than 4,500 m (Chinese Petroleum Society, 2016).

To date, a number of countries have carried out deep gas exploration and great breakthrough has been achieved (Tuo, 2002). During 2008–2018, the global proven oil and gas reserves in the deep and ultra-deep strata with burial depth >4,000 m were around 14×10^9 t and 9.1×10^9 t (oil equivalent), respectively, accounting for 66 and 61% of the total increased oil and gas proven reserves, respectively (Zhao, 2019). In China, most exploration has focused on the shallow-middle depths and few exploration has been carried out on the deep oil and gas resources, so the exploration degree of deep resources is low. However, the deep oil and gas resources in China have great potential. The geological oil and gas reserves of China's deep and ultra-deep depths are 26.6×10^9 t and 49.7×10^{12} m^3, respectively, which account for 21 and 55% of the total oil and gas geological reserves in China, respectively (Strategic Research Center of Oil and Gas Resources, 2017). The exploration degree is only 13 and 10% for the deep and ultra-deep oil and gas, respectively (Strategic Research Center of Oil and Gas Resources, 2017). Recently, significant discoveries have been made in the exploration of deep gas in the Tarim and Sichuan basins in China. For example, a number of marine carbonate oil/gas zones have been discovered, such as Lunnan-Tahe, Tazhong, and Halahatang in the Tarim Basin and Puguang, Longgang and Yuanba in the Sichuan Basin, and terrestrial clastic gas fields such as Dabei and Keshen in the Kuqa depression in Tarim Basin (Sun et al., 2013). In China, the deepest gas field is the Keshen gas field in Tarim Basin with reservoir depth over 8,000 m (Well Keshen 902, 8,038 m).

With increasing improvements in the technological development and theoretical understanding, exploration of deep gas will become more and more practical. Moreover, natural gas may form in the deep parts of the sedimentary basin and migrate upward and accumulate in the shallow layers. A full understanding of the origin of deep gas will shed light for the research of natural gas in both shallow and deep basins. However, knowledge about the deep gas in many sedimentary basins is still poor and geochemical information about the deep gas is limited. Previous study has indicated that a number of factors contribute to the origin of deep gas such as the type of organic matter, thermal maturity, oil stability, the influences of minerals, water, non-hydrocarbon gas, etc. (Dyman et al., 2003). This makes the study of the origin and source of deep gas very difficult. Dai et al. (2018) carried out a geochemical study of the ultra-deep gas in the Sichuan Basin and proposed that most of these deep gases were sourced from humic organic matter. In order to have a better understanding of the origin and distribution of deep gas, this study performed a comprehensive comparative investigation of the geochemical characteristics of the deep gases from different types of reservoirs in China. First of all, gases from the clastic sandstone reservoirs in the Dabei gas field in Kuqa depression, Tarim Basin were emphatically investigated (**Figure 1A**). Dabei gas field is one of the 15 large tight gas fields in China, which is also the only large tight gas field in Tarim Basin (Dai et al., 2014). It is also the one with largest burial depth and most complex structures among the continental large gas fields that have ever been found. The sandstone reservoir under the salts in the Dabei gas field generally has depth more than 5,300 m, porosity of 1∼8%, and permeability of 0.01×10^{-15}∼1.0×10^{-15} m^2, which belongs to typical deep tight gas field (Dai et al., 2014). For comparison, literature data of deep gases from the sandstone reservoir in Keshen gas field in the same depression, and deep gases from the marine carbonate reservoirs in the craton area of Tarim Basin (**Figure 1B**) and Sichuan Basin (Yuanba, Longgang, Puguang gas fields) (**Figure 2**) are also investigated. A detailed comparative geochemical research about the deep gases with different origins from different basins may deepen our understanding of the origin and accumulation of deep gas and shed a light on the future exploration of deep gas in the world.

GEOCHEMISTRY OF SOURCE ROCKS

Tarim Basin

Tarim Basin is located in northwest China and has an area of 560,000 km^2. A series of giant gas fields have been discovered in this basin, which made it one of the most important gas basins in China. Tarim Basin is a large superimposed and composite basin, and it consists of a Paleozoic cratonic basin in the south (**Figure 1B**) and a Mesozoic–Cenozoic foreland basin in the north (**Figure 1A**). The basin was deposited with sediments from Sinian to Quaternary with maximum thickness up to 15,000 m. The main gas-bearing reservoirs include the strata of Ordovician, Carboniferous, Triassic, Jurassic, Cretaceous, and Tertiary. Potential source rocks include the Cambrian–Ordovician highly mature–over mature marine carbonates, Carboniferous–Permian marine–terrestrial transitional highly mature–middle mature carbonates and mudstones, and the Triassic–Jurassic low mature–middle mature lacustrine mudstones and lacustrine-swamp coal measures.

In the Kuqa depression, the widely distributed Middle-Lower Jurassic coal measures deposited in the lacustrine-swamp environment have been regarded as the main source rocks for the coal-derived gases (Liang et al., 2003b; Qin et al., 2007). The thickness of coal bed usually ranges from 6 to 29 m. The Middle-Lower Jurassic source rocks are dominated by type III kerogen and have $\delta^{13}C$ values −22∼−26‰ (Liang et al., 2003a;

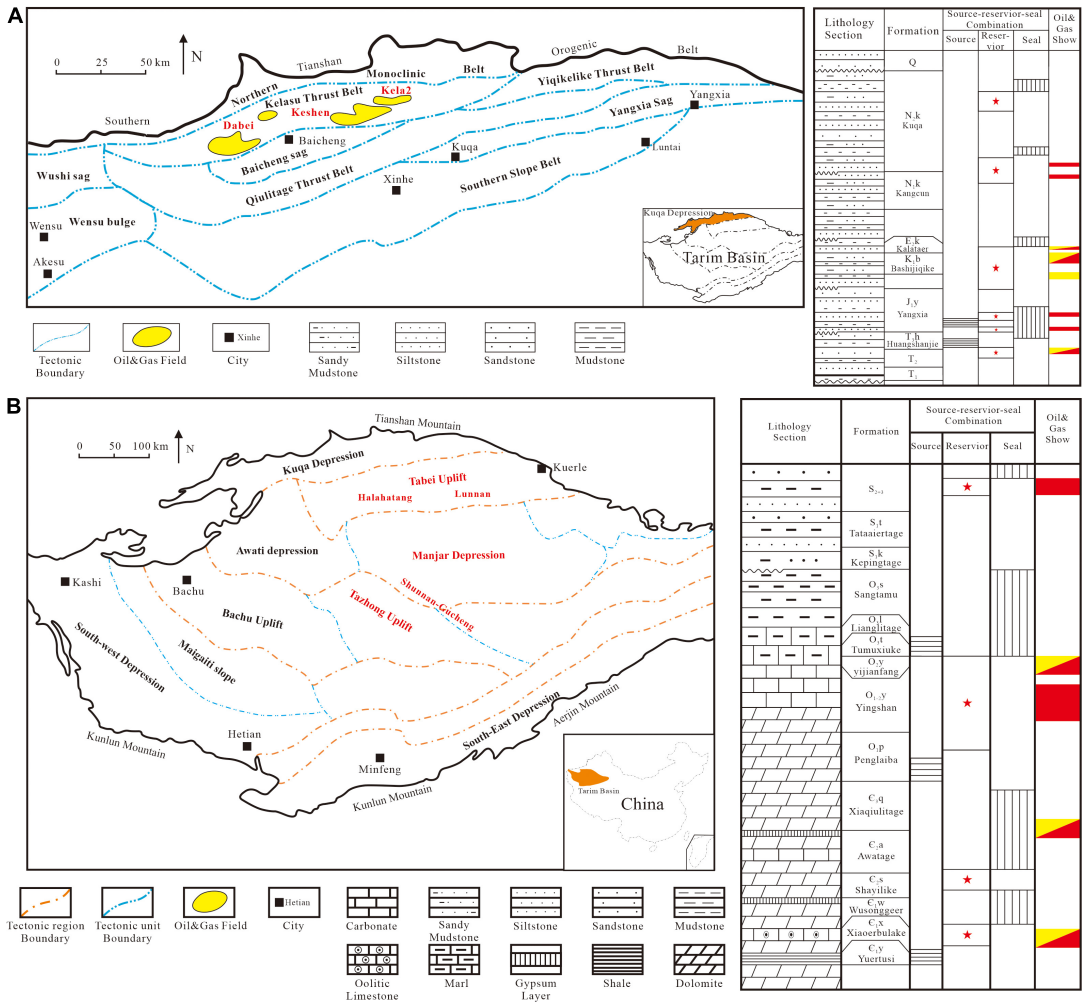


FIGURE 1 | (A) Location map of the Dabei, Keshen, and Kela2 gas fields in the Kuqa depression, Tarim Basin and the stratigraphic column of the Kuqa depression (Wang J. et al., 2018; Zhao et al., 2018). **(B)** Location map of the cratonic Tarim basin and the corresponding stratigraphic column (Ni et al., 2013; Zhu et al., 2019b).

Wang et al., 2005). Thermal maturity of the source rocks in the depression is generally greater than 0.6%, and in the Baicheng sag, thermal maturity of the source rocks is very high, i.e., 1.5∼3.5% (Dai, 2016).

The Cambrian-Lower Ordovician carbonates have been considered as the main source rocks of the oil-derived gases in the Paleozoic cratonic Tarim Basin (Liang et al., 2002). The Cambrian-Lower Ordovician source rocks are deposited in a sub-compensation and evaporating lagoon environment and the water medium is saline water. It is dominated by type I kerogen and it has total organic carbon of 0.27∼5.52%. The carbon isotope value of kerogen is −32.5∼−27.0‰ (Chen et al., 2000, 2001). The source rocks are at high to over mature stage and the vitrinite reflectance value (Ro%) is 1.8∼3.0% (Wang et al., 2002; Zhang Z. et al., 2006).

Sichuan Basin

The Sichuan Basin is located in eastern Sichuan and has an area of 18 × 10^4 km^2 (**Figure 2**). A number of giant gas fields have been discovered in this basin and recent exploration success of the deep gases with reservoir depth more than 4,500 m has made Sichuan Basin one of the most important gas producing basins in China. The Sichuan Basin is a tectonic superimposed basin, where the late Mesozoic–Cenozoic foreland basin overlying on a Sinian–Middle Mesozoic passive margin (Ma et al., 2007). It has deposited super-thick Sinian-Middle Triassic marine carbonates (4∼7 km), the early stage of Late Triassic marine-continental transitional deposition (300∼400 m) and the middle stage of Late Triassic-Eocene terrestrial clastic rocks (2∼5 km) (Ma et al., 2010).

In the Sichuan Basin, Permian is an important strata developing two sets of source rocks including Middle Permian carbonates and Upper Permian coal measures with Upper Permian Dalong Formation marine mudstone source rocks in local areas (Chen et al., 2018b). Among them, the Upper Permian Longtan Formation has been considered to make main contribution to the gas source of Puguang, Yuanba and Longgang gas fields (Ma, 2008; Ma et al., 2008; Wu et al., 2015a;

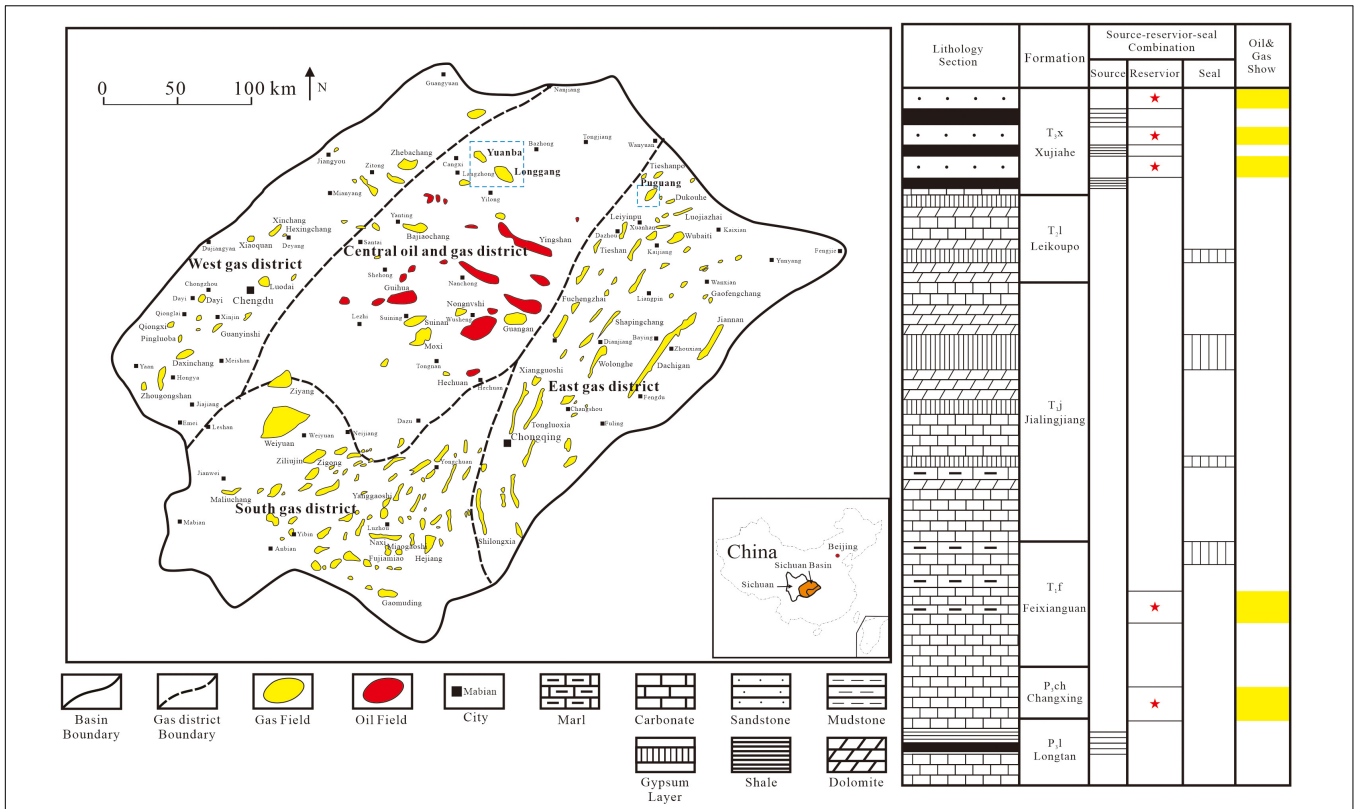


FIGURE 2 | Location map of the Puguang, Yuanba and Longgang gas fields in the Sichuan Basin, the stratigraphic column and source-reservoir-seal combination (Dai et al., 2012a; Qin et al., 2016). Reservoir layer is marked as "*".

Qin et al., 2016; Guo, 2011; Zhao et al., 2011). The marine-continental transitional coal-bearing deposits of the Upper Permian Longtan Formation include mudstone, carbonaceous mudstone, coal and carbonates. The Longtan mudstone source rocks are widely distributed in the whole basin and the coal bed has thickness of 2∼5 m in the northeastern Sichuan Basin, 5∼15 m in the central and southeastern Sichuan Basin, and less than 1 m in the north and southwestern Sichuan Basin (Chen et al., 2018b). According to the analysis of 372 samples, the TOC of Longtan source rocks has an average value of 2.83% (Chen et al., 2018a). In the southwestern part of eastern Sichuan Basin, the Longtan coal measure source rocks have TOC up to 7.47% with an average of 2.91%, $\delta^{13}C$ of kerogen of −24.0∼−23.5‰, thermal maturity (Ro%) of 1.89∼2.63% (Yang et al., 2002).

SAMPLES AND METHODS

276 gas samples with reservoir depth more than 4,500 m from Sichuan and Tarim basins were analyzed in this study, including 11 gas samples collected from the Dabei gas field in the Kuqa depression, Tarim Basin and 265 samples from published literature (see **Table 1** for the natural gas from Dabei gas field). All the gases were called as deep gas, which includes both deep gas and ultra-deep gas. Among the 276 samples, 53 samples were from the Kelasu thrust belt in the Kuqa depression, i.e., 47 samples from the Dabei gas field (Li et al., 2005; Zhang et al., 2011; Dai, 2016; Wei et al., 2019; Zhu et al., 2019a), and 6 samples from the Keshen gas field (Wei et al., 2019), marked as Kuqa-Dabei and Kuqa-Keshen, respectively in all figures; 153 gas samples were from the Tabei and Tazhong uplifts in the Tarim Basin (Wang, 2005; Ni et al., 2013; Wang et al., 2014; Wu et al., 2014; Zhu et al., 2014, 2015; Wang Y. et al., 2018; Zhou et al., 2019), marked as Tarim-craton in all figures; and 70 samples were from Longgang, Yuanba, and Puguang gas fields in Sichuan Basin (Li et al., 2015, 2016; Wang et al., 2015; Wu et al., 2015b; Qin et al., 2016; Dai et al., 2018), marked as Sichuan in all figures.

The 11 gas samples were analysed in the PetroChina Research Institute of Petroleum Exploration and Development (RIPED). Gas molecular composition was conducted on a two-channel Wasson-Agilent 7890 gas chromatograph, equipped with one auxiliary oven, two capillary and six packed analytical columns, one flame ionization detector (FID) and two thermal conductivity detectors (TCD). The carrier gas was high-pure N_2 for FID and He for TCD. GC oven temperature was initially set at 68°C for 7 min, and then increased to 90°C at 10°C/min, held at 90°C for 1.5 min, ramped to 175°C at 15°C/min and held at this temperature for 5 min.

Compound specific stable carbon isotopic composition was determined on a Thermo Delta V mass spectrometer interfaced with a Thermo Trace GC ultra-gas chromatograph (GC). Individual hydrocarbon gas components (C_1-C_5) and CO_2 were

separated by using a fused silica capillary column (PLOT Q 27.5 m × 0.32 mm × 10 μm) on a gas chromatograph with He as the carrier gas, then converted into CO_2 in a combustion interface and introduced into the mass spectrometer. The GC oven temperature was increased from 33 to 80°C at 8°C/min, then to 250°C at 5°C/min, and maintained at this temperature for 10 min. All analyses were analysed in triplicate, and the stable carbon isotopic values were reported in the δ-notation in per mil (‰) relative to VPDB. The analytical precision was estimated to be ± 0.3‰.

Compound specific stable hydrogen isotopic composition was measured on a MAT253 isotope ratio mass spectrometer interfaced with a Trace GC ultra-gas chromatograph (GC) and a micropyrolysis furnace (1,450°C). Gas components were separated on a HP-PLOT Q column (30 m × 0.32 mm × 20 μm). The carrier gas was helium with flow rate of 1.2 ml/min. A split injection sample introduction mode with split ratio of 1:10 was used for methane and a non-split injection mode was used for ethane and propane. The GC oven temperature program was the same as that for the carbon isotope. Natural gas was separated into individual gas components via the gas chromatograph and then transformed into C and H_2 in the micropyrolysis furnace at 1,450°C. H_2 went into the mass spectrometer and was determined for δ^2H. The stable hydrogen isotope value (δ^2H) was reported in the δ-notation in per mil (‰) relative to VSMOW and the analytical precision was expected to be ± 3‰.

The laboratory working standard was a coal-derived hydrocarbon gas which was obtained from the Ordos basin in China. An international laboratory standard comparison has been conducted for the working standard, for which two-point calibrations were performed with international measurement standards for both carbon isotope ratios (NBS19 and L-SVEC CO_2) and hydrogen isotope ratios (VSMOW and SLAP) (Dai et al., 2012b).

GEOCHEMICAL CHARACTERISTICS OF DEEP GASES

Molecular Composition

Methane is the dominant gas component of the gases, 1.39∼99.34% with an average of 83.80% (n = 269) (**Figure 3**). Among them, 236 gas samples have methane content more than 70%, and 110 gas samples have methane more than 90%, accounting for 87.73 and 40.89% of the total, respectively. C_{2+} heavy hydrocarbons range between 0.01 and 36.26% with an average of 4.06% (n = 266). 209 out of 266 samples have C_{2+} heavy hydrocarbons less than 5%, accounting for 78.57%. In general, samples from the Kelasu thrust belt in the Kuqa depression have relatively high content of methane (average 95.76%, n = 49), with average gas dryness coefficient of 0.976 (n = 49), indicative of dry gas. While samples from the craton area of Tarim Basin have average methane content of 81.98% (n = 153) and C_{2+} heavy hydrocarbons of 6.24% (n = 153). The gas dryness coefficient varies greatly, except for sample from Well LN44 in the Tabei uplift which has gas dryness coefficient of 0.238, the gas dryness coefficient mainly ranges between 0.594 and 0.999, indicating the existence of both dry gas and wet gas. Among the gases from the craton area of Tarim Basin, gas in the Shunnan-Gucheng area has relatively very low C_{2+} heavy hydrocarbon (average 0.69%, n = 19) and high gas dryness coefficient (average 0.992, n = 19), belonging to dry gas; while gas from Halahatang area has relatively very high content of C_{2+} heavy hydrocarbons (average 25.50%, n = 9) and low gas dryness coefficient (average 0.713, n = 9), belonging to wet gas. Gases from Puguang, Yuanba and Longgang gas fields in the Sichuan Basin have very low C_{2+} heavy hydrocarbons (0.01∼0.78% with average value of 0.11%, n = 66) and high gas dryness coefficient (average 0.999, n = 66).

Non-hydrocarbon gas has an average content of 11.56% (n = 260). 162 out of 260 samples have non-hydrocarbon gas less than 10%, 82 out of 260 samples have non-hydrocarbon gas of 10∼30%, and only 16 samples have non-hydrocarbon gas more than 30%. N_2 and CO_2 are common non-hydrocarbon gas, and nearly exist in all samples. 215 out of 258 samples have N_2 less than 5%, 31 out of 258 samples have N_2 of 5∼10%; 171 out of 252 samples have CO_2 less than 5%, 61 out of 252 samples have CO_2 of 5∼15% and 20 out of 252 samples have CO_2 more than 15% (**Figure 3**). H_2S only presents in the gases with marine carbonates as reservoirs, such as gases from Sichuan Basin and the craton area of Tarim Basin. In those gases from Kelasu thrust belt which has sandstone as reservoirs, there is no sign of the presence of H_2S. 76 out of 115 samples have H_2S less than 5%, 28 out of 115 samples have H_2S of 5∼15%, 9 out of 115 samples have H_2S of 15∼30% and two samples from Puguang gas field in the Sichuan Basin have H_2S even more than 45%. In general, gases from the Dabei gas field have the lowest content of non-hydrocarbon gas, i.e., 0.01∼2.94% with an average value of 1.37% (n = 34). Followed by the gas from Keshen gas field, which has non-hydrocarbon gas of 3.50% (average, n = 6). Then followed by the gas from the craton area of Tarim Basin (average 11.17%, n = 153) and Sichuan Basin (average 18.39%, n = 67).

Carbon Isotope

The stable carbon isotopes of methane, ethane and propane vary greatly for gases from different areas. In total, $\delta^{13}C_1$ varies from –26.5 to –54.9‰ with an average of –35.4‰ (n = 253), and $\delta^{13}C_2$ varies from –16.1 to –41.1‰ with an average of –29.7‰ (n = 226). Among them, gas from Dabei and Keshen gas fields in the Kuqa depression has $\delta^{13}C_1$ of –26.5∼–33.1‰ (average –29.7‰, n = 50), $\delta^{13}C_2$ of –16.1∼–24.2‰ (average –21.1‰, n = 49) and $\delta^{13}C_3$ of –18.9∼–25.7‰ (average –21.0‰, n = 38). A small number of samples from the Dabei gas field have slight carbon isotopic reversal between ethane and propane. Except one sample has carbon isotopic reversal magnitude up to 5.9‰, most samples have reversal magnitude less than 2.2‰. While most gases from the Keshen gas field have carbon isotopic reversal between ethane and propane and the reversal magnitude can be up to 3.6‰. Gas from the craton area of Tarim Basin has much lower carbon isotopes, i.e., $\delta^{13}C_1$ of −30.2∼−54.9‰ (average −40.5‰, n = 133), and $\delta^{13}C_2$ of −26.2∼−41.1‰ (average −34.2‰, n = 125). Most samples have normal carbon isotopic distribution among C_1∼C_3 alkane gases, i.e., methane and its homologues become more and more enriched in ^{13}C with increasing carbon

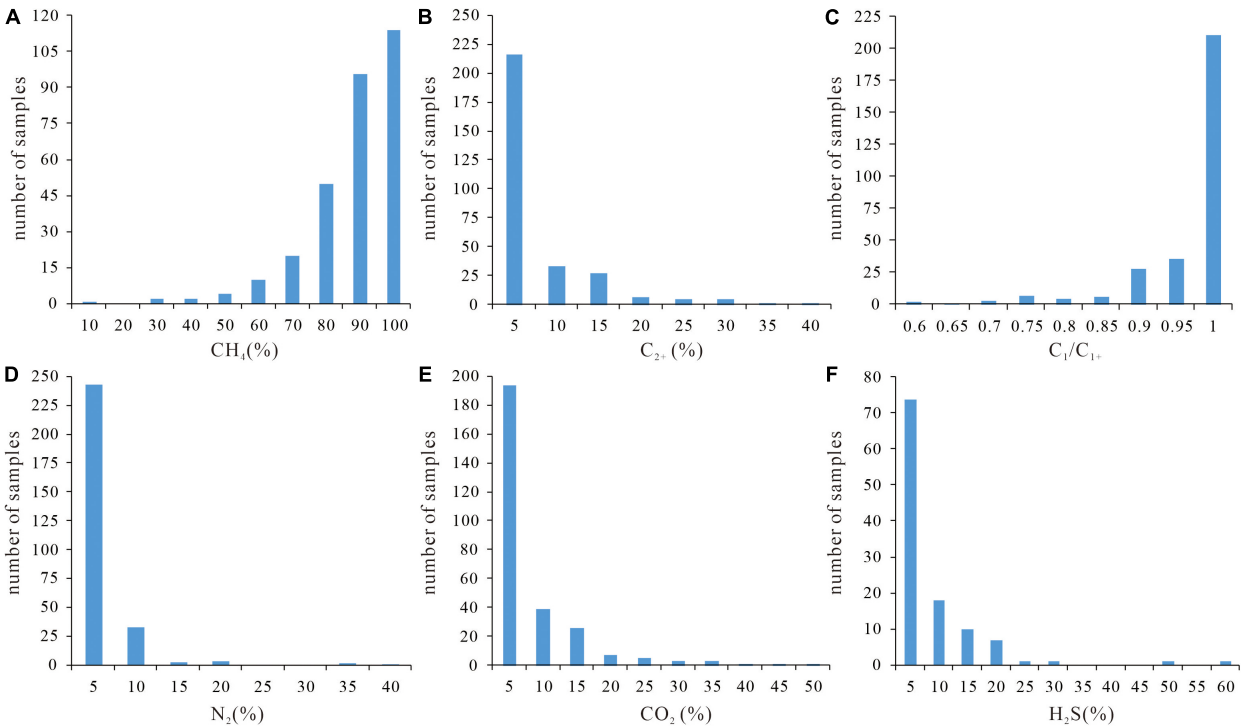


FIGURE 3 | Histogram of the content of CH_4 **(A)**, C_{2+} **(B)**, C_1/C_{1+} **(C)**, N_2 **(D)**, CO_2 **(E),** and H_2S **(F)** of the deep gases from Tarim and Sichuan basins. Data source see section "Samples and Methods" in the text.

number ($\delta^{13}C_1 < \delta^{13}C_2 < \delta^{13}C_3$). Samples from Sichuan Basin have $\delta^{13}C_1$ of −27.4∼−33.7‰ (average −29.9‰, n = 70), and $\delta^{13}C_2$ of −21.0∼−32.2‰ (average −27.0‰, n = 52). The average C_{2+} heavy hydrocarbon content is only 0.11% (n = 66), so only 4 samples have $\delta^{13}C_3$ values with average of −28.0‰.

The $\delta^{13}C$ of CO_2 varies greatly, i.e., −2.8∼−31.0‰ with an average of −6.0‰ (n = 110). Gas from the Dabei and Keshen gas fields has $\delta^{13}C_{CO2}$ values of −3.6∼−31.0‰ (average −15.1‰, n = 19). Among them, one sample has $\delta^{13}C_{CO2}$ value of −3.6‰, 3 samples have $\delta^{13}C_{CO2}$ values of −8.5∼−9.7‰, and all other 15 samples have $\delta^{13}C_{CO2}$ values lower than −10‰. Gas from the craton area of Tarim Basin has $\delta^{13}C_{CO2}$ values of −25.0∼0.6‰ (average −7.1‰, n = 41). Among them, 27 samples have $\delta^{13}C_{CO2}$ values greater than −8‰, 5 samples have $\delta^{13}C_{CO2}$ values of −8.8∼−9.8‰ and 9 samples have $\delta^{13}C_{CO2}$ values lower than −10‰.

Hydrogen Isotope

The stable hydrogen isotopic values vary between −111∼−158‰ with an average of −134‰ (n = 44) for methane, between −94∼−145‰ with an average of −124‰ (n = 29) for ethane and between −91∼−130‰ with an average of −111‰ (n = 18) for propane. Gas from the Dabei gas field has relatively very high δ^2H value, δ^2H value ranges −153 to −158‰ with an average of −156‰ (n = 11) for methane and from −115 to −122‰ with an average of −119‰ (n = 11) for ethane. Gas from the craton area of Tarim Basin has δ^2H_1 value of −121∼−140‰ (average −130‰, n = 18) and δ^2H_2 value of −94∼−145‰ (average −126, n = 18). Due to the relatively small amount of C_{2+} heavy hydrocarbons in the samples from Sichuan Basin but relatively large required sample amount for the hydrogen isotopic analysis, gas from Sichuan Basin only has hydrogen isotopic values for methane, which ranges from −111 to −156‰ with an average of −122% (n = 15). All the samples have normal hydrogen isotopic distribution pattern among C_1∼C_3 alkane gases, i.e., methane and its homologues become more enriched in D with increasing carbon numbers ($\delta^2H_1 < \delta^2H_2 < \delta^2H_3$).

ORIGIN OF DEEP GASES

Type and Origin of Deep Gas

Natural gas in nature can be divided into biotic and abiotic origin, and the biotic gas can be divided into microbial gas and thermogenic gas. According to the type of organic matter, thermogenic gas can be further divided into oil-related gas in sapropelic origin (including oil-associated gas and oil-cracked gas) and coal-derived gas in humic origin. The oil-related gas is produced by the thermal decomposition of sapropelic kerogen or the thermal cracking of oil which was generated from sapropelic kerogen. The coal-derived gas is generated from the thermal degradation of humic kerogen or the thermal cracking of heavy hydrocarbons generated from humic organic matter (Dai et al., 1992). Since natural gas is composed of a few simple small molecules, gas origin studies are mainly dependent on its molecular composition, stable carbon and hydrogen isotopes.

A number of studies using molecular composition, carbon and hydrogen isotopes have been performed to investigate the gas origin (Bernard et al., 1976; James, 1983; Clayton, 1991; Dai, 1993; Prinzhofer and Huc, 1995; Lorant et al., 1998; Whiticar, 1999; Tang et al., 2000; Dai et al., 2005a, 2012a, 2016a; Milkov and Etiope, 2018).

The $C_1/(C_2 + C_3)$ vs. $\delta^{13}C_1$ diagram has been widely used to investigate the gas origin (Bernard et al., 1976; Whiticar, 1999; Milkov and Etiope, 2018). In this diagram (**Figure 4**), all the deep gas samples fall in the field of thermogenic gas and far away from the field of primary microbial gas. This indicates there is no mixing with primary microbial gas. Some gas samples from the craton area of Tarim Basin fall in the oil-associated gas field, but most of the samples are more toward the field of late mature thermogenic gas, especially the gas from Sichuan Basin, which shows particularly low content of C_{2+} heavy hydrocarbons and the $C_1/(C_2 + C_3)$ ratio can be up to 4689 (Well Y123 in Yuanba gas field). Though there is significant overlap of thermogenic, primary microbial and abiotic gases in the $\delta^{13}C_1$ vs. $\delta^{13}C_{CO2}$ diagram (**Figure 5**), this diagram is very useful for distinguishing secondary microbial gas. As seen in **Figure 5**, all gas samples are away from the field of secondary microbial gas. This further indicates that all the deep gas has no mixing with neither primary microbial gas or secondary microbial gas. This agrees well with the geological conditions. The burial depth of the produced layer of all gas samples was more than 4,500 m, microbial activities are unlikely to be active at such depth.

With the increase of thermal evolution degree of the organic matter, natural gas become more and more enriched in ^{13}C, plot of $\delta^{13}C_1$ vs. $\delta^{13}C_2$ has been widely used as a gas maturity trend and classification diagram for natural gas origin (Jenden et al., 1988; Dai and Qi, 1989; Rooney et al., 1995; Berner and Faber, 1996; Huang et al., 1996; Tang et al., 2000). A theoretical slope value of 2.4 was calculated for the correlation line between $\delta^{13}C_1$ and $\delta^{13}C_2$ (Xia and Gao, 2017). Different source rocks, secondary alteration or different gas generation mechanism may cause deviation from the theoretical linear trend. As shown in **Figure 6**, gases from the continental sandstone reservoirs (Dabei and Keshen gas fields) in the Kuqa depression have $\delta^{13}C_2$ values far greater than −28‰, and all fall in the up-left area in the $\delta^{13}C_1$ vs. $\delta^{13}C_2$ diagram for gases generated from type III kerogen (Jenden et al., 1988; Dai and Qi, 1989; Rooney et al., 1995; Berner and Faber, 1996). Compared to the gases generated from type III kerogen, gases from Dabei gas field were the most similar to the gases generated from type III kerogen in Niger Delta (Rooney et al., 1995), but still much heavier carbon isotope of ethane, which result in the fact that only two gas samples from the Dabei gas field obey the evolution trend of gas generated from type III kerogen in Niger Delta and all other gas samples fall above the gas maturity trend (**Figure 6**). Gases from the Keshen gas field have even heavier carbon isotope of ethane (up to −16.1‰ of $\delta^{13}C_2$) and fall far above the evolution trend of gas generated from type III kerogen in Niger Delta of type III kerogen (Rooney et al., 1995). Gases with reservoir depth shallower than 4,500 m from Kela2 gas field in Kuqa depression were also shown for comparison. In general, gases from Kela2 gas field have the heaviest carbon isotope of methane (−25.1∼−30.8‰,

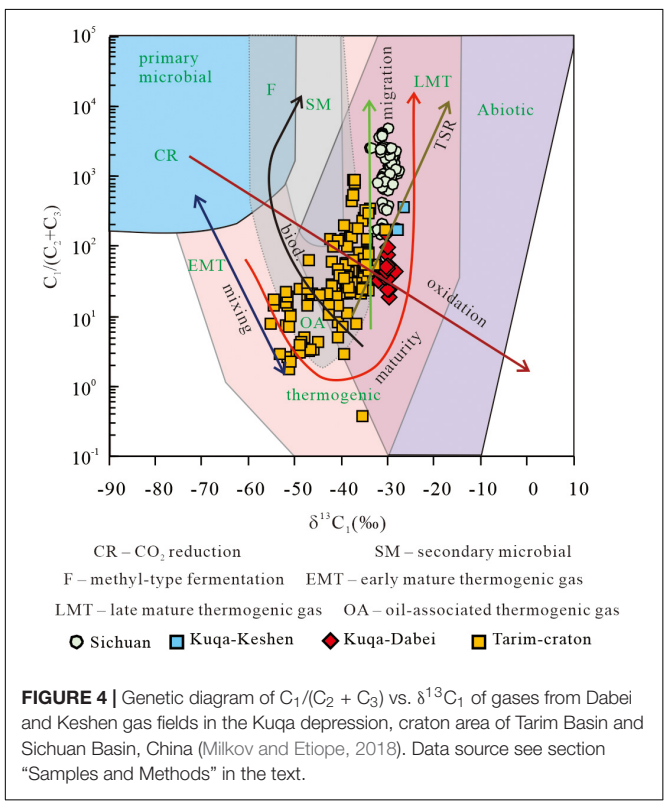


FIGURE 4 | Genetic diagram of $C_1/(C_2 + C_3)$ vs. $\delta^{13}C_1$ of gases from Dabei and Keshen gas fields in the Kuqa depression, craton area of Tarim Basin and Sichuan Basin, China (Milkov and Etiope, 2018). Data source see section "Samples and Methods" in the text.

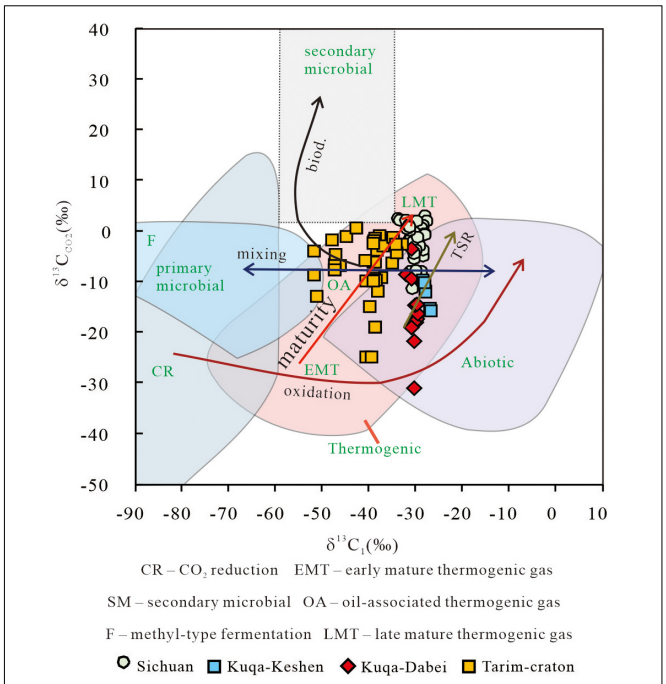


FIGURE 5 | Genetic diagram of $\delta^{13}C_{CO2}$ vs. $\delta^{13}C_1$ of gases from Dabei and Keshen gas fields in the Kuqa depression, craton area of Tarim Basin and Sichuan Basin, China (Milkov and Etiope, 2018). Data source see section "Samples and Methods" in the text.

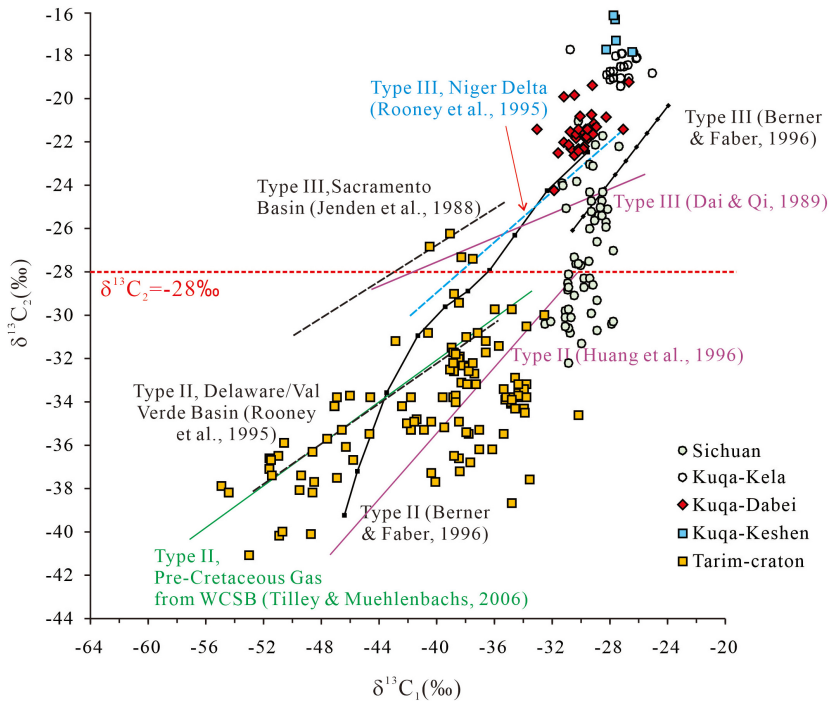


FIGURE 6 | $\delta^{13}C_1$ vs. $\delta^{13}C_2$ cross-plot of gases from Dabei, Keshen and Kela2 gas fields in the Kuqa depression, craton area of Tarim Basin, and Sichuan Basin. Also shown are published maturity trends of type II kerogen (Rooney et al., 1995; Huang et al., 1996; Tilley and Muehlenbachs, 2006) and type III kerogen (Jenden et al., 1988; Dai and Qi, 1989; Rooney et al., 1995; Berner and Faber, 1996). Data source see section "Samples and Methods" in the text.

average −27.4‰, n = 24), gases from the Keshen gas field have the heaviest carbon isotope of ethane (−16.1∼−17.8‰, average −17.0‰, n = 5) and gases from the Dabei gas field have the lightest carbon isotope of methane and ethane. All these characteristics indicate that gases from the continental sandstone reservoirs (Dabei and Keshen gas fields) in the Kuqa depression were generated from higher plant-derived type III kerogen. Gases from Sichuan Basin can be divided into two groups, the first group falls in the region of gases generated from type III kerogen (Dai and Qi, 1989; Rooney et al., 1995; Berner and Faber, 1996), and the second group falls in the region of gases generated from type II kerogen (Huang et al., 1996). Gases in the first group were generated from the humic type III kerogen and gases in the second group were produced from the sapropelic organic matter. Most gas samples from the craton area of Tarim Basin have $\delta^{13}C_2$ values lower than −28‰ and match better with the evolution trend of gas generated from type II kerogen (Rooney et al., 1995; Berner and Faber, 1996; Huang et al., 1996; Tilley and Muehlenbachs, 2006), and only several samples have $\delta^{13}C_2$ values greater than −28‰ and follow the evolution trend of gases generated from the type III kerogen (Jenden et al., 1988; Rooney et al., 1995; **Figure 6**). This indicates that most gases from the craton area of Tarim Basin were generated from the sapropelic organic matter. Compared to the deep gases from the continental sandstone reservoirs in the Kuqa depression and marine carbonate reservoirs in the craton area of Tarim Basin, gases from Sichuan Basin have relatively medium values of carbon isotope of ethane. For the comparison of gases generated from type III kerogen, several samples from the Longgang gas field in Sichuan Basin have $\delta^{13}C_2$ values greater than −25‰, which is close to the $\delta^{13}C_2$ values of gases from Dabei gas field (−19.2∼−24.2‰, average −21.6‰, n = 47). Except these gases, all other coal-derived gases from the marine carbonate reservoirs in Sichuan Basin have lower $\delta^{13}C_2$ values than that of the gases from the continental sandstone reservoirs. However, for the comparison of gases generated from type II kerogen, most gases from Sichuan Basin have greater $\delta^{13}C_2$ values than that of the gases from the craton area of Tarim Basin.

Humic organic matter is dominated by aromatic structures which is enriched in ^{13}C, while sapropelic organic matter is dominated by aliphatic structures which is enriched in ^{12}C. During the decomposition process of kerogen, carbon isotope of methane is more inclined to the influences of thermal maturity while carbon isotope of ethane can better reflect the features of its precursor. Therefore, gas sourced from humic organic matter generally has heavier carbon isotope of ethane compared to that from sapropelic organic matter at similar thermal maturity. A number of cut-off values of $\delta^{13}C_2$ have been proposed for the distinguishing of gas origin in sapropelic or humic according to numerous empirical studies in the Chinese sedimentary basins (Wang, 1994; Gang et al., 1997; Liang et al., 2002; Dai et al., 2005b; Xiao et al., 2008). According to the detailed gas study in the Kuqa depression by Liang et al. (2002), a cut-off value of −28‰ of $\delta^{13}C$ for ethane was proposed to distinguish the gas sources (sapropelic vs. humic). Based on the study of the Sinian-Jurassic gases in the Sichuan Basin, Wang (1994) suggested a

cut-off value of −29‰ of $\delta^{13}C$ for ethane to distinguish the gas origin. Dai et al. (2005b) proposed a $\delta^{13}C_2 > -27.5$‰ for gases sourced from humic organic matter and a $\delta^{13}C_2 < -29$‰ for gases sourced from sapropelic organic matter according to a comprehensive study on the natural gas in China, and Dai et al. (2012a) suggested a cut-off value of $\delta^{13}C_2 > -28$‰ for gases sourced from humic organic matter in the Sichuan Basin. Taking −28‰ of $\delta^{13}C_2$ as a cut-off value, combined with the $\delta^{13}C_1$ vs. $\delta^{13}C_2$ diagram (**Figure 6**), gas from the continental sandstone reservoirs in the Dabei and Keshen gas fields in the Kelasu thrust belt in the Kuqa depression were generated from the type III kerogen and belong to coal-derived gas (Zhang et al., 2011; Dai et al., 2014; Wang, 2014; Wei et al., 2019), gases from the marine carbonate reservoirs (Ordovician and Cambrian) in the craton area in the Tarim Basin are mostly sourced from the sapropelic organic matter and belong to oil-related gas (Wang et al., 2014; Zhu et al., 2014; Chen F. et al., 2018). Gases from the marine carbonate reservoirs (Permian Changxing Formation and Triassic Feixianguan Formation) from the Longgang, Yuanba and Puguang gas fields in Sichuan Basin were complicated (Yang et al., 2002; Zhu et al., 2005; Hao et al., 2008; Ma, 2008; Zhao et al., 2011; Hu et al., 2014; Qin et al., 2016; Dai et al., 2018). Gases from the Longgang gas field were mainly generated from the coal measure of Permian Longtan Formation (Zhao et al., 2011; Qin et al., 2016; Dai et al., 2018), or with minor contribution of oil cracked gas derived from the Upper Permian carbonaceous source rocks (Deng et al., 2018). Different opinions exist for the origin of gases from Yuanba gas field. Some scholars proposed that gases from Yuanba gas field were mainly coal-derived gas or with minor contribution from oil-related gas, which were sourced from the coal measure of Permian Longtan Formation and/or organic matter in Permian Dalong Formation (Hu et al., 2014; Dai, 2016; Dai et al., 2018). However, some scholars proposed that gases from Yuanba gas field were mainly oil cracked gas from oil cracking which was generated from the Permian source rocks (Guo, 2011; Guo et al., 2014; Li et al., 2015; Wu et al., 2015b). Gases from Yuanba gas field were also interpreted as oil cracked gas sourced from the sapropelic organic matter in Sinian/Lower Cambrian Qiongzhusi Formation (Wu et al., 2017). Gases from the Puguang gas field were mainly sourced from the marine sapropelic organic matter with minor contribution from the humic organic matter in Permian Longtan Formation (Hao et al., 2008; Ma, 2008). There is also study indicating that gases in the Puguang gas field were generated from multiple sources such as Permian, Silurian and Cambrian (Zhao et al., 2011). The gas origin distinguishing can be further evidenced in the $\delta^{13}C_1 \sim \delta^{13}C_2 \sim \delta^{13}C_3$ genetic diagram (**Figure 7**). In **Figure 7**, gas from the Keshen gas field has very heavy carbon isotope of ethane, which is also clearly reflected in **Figure 6**. Gas from the craton area of Tarim Basin has relatively heavy carbon isotope of propane and some samples even fall in the area of coal-derived origin.

Carbon Isotope Anomaly of the Deep Gas

Partial carbon isotopic reversal is common in the deep gas. The coal-derived tight gas from the Kuqa depression shows partial carbon isotopic reversal between ethane and propane, especially gas from the Keshen gas field, where 4 out of 5 samples have partial carbon isotopic reversal between ethane and propane ($\delta^{13}C_1 < \delta^{13}C_2 > \delta^{13}C_3$). A few samples from the marine

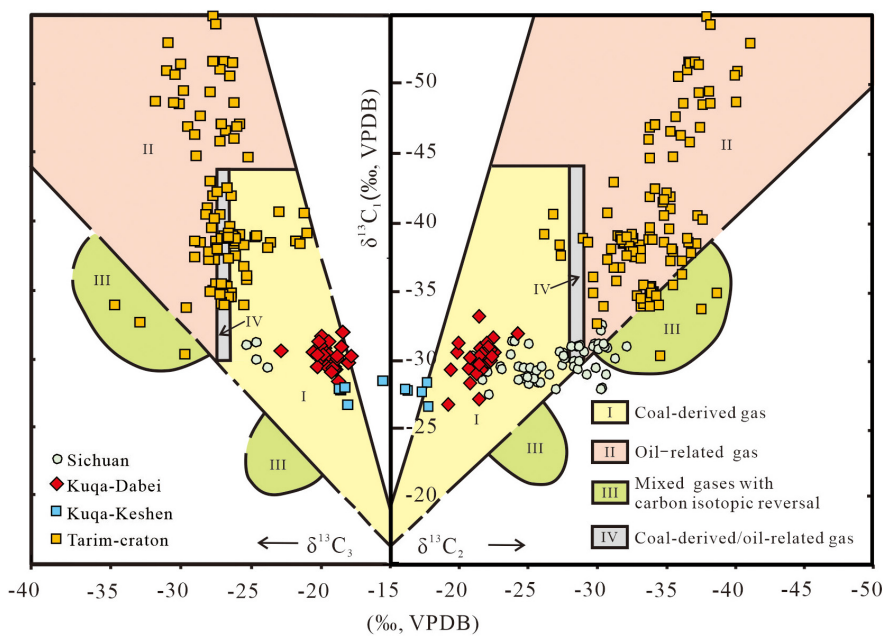


FIGURE 7 | Plot of $\delta^{13}C_1$ vs. $\delta^{13}C_2$ vs. $\delta^{13}C_3$ of gases from Dabei and Keshen gas fields in the Kuqa depression, craton area in the Tarim Basin, and Sichuan Basin (Dai et al., 1992). Data source see section "Samples and Methods" in the text.

carbonate reservoirs either in the craton area of Tarim Basin ($\delta^{13}C_1 < \delta^{13}C_2 > \delta^{13}C_3$) or Sichuan Basin ($\delta^{13}C_1 > \delta^{13}C_2$) also have partial carbon isotopic reversal.

Partial carbon isotopic reversal among $C_1 \sim C_3$ alkane gases are usually interpreted as a result from the mixing of gases generated from different types of organic matter or at different thermal maturity (biotic vs. abiotic, thermogenic vs. microbial, humic vs. sapropelic, gases with different maturities), bacterial oxidation, high thermal maturity, thermochemical sulfate reduction (Dai et al., 2004b; Hao et al., 2008). Some gas samples from the Keshen and Dabei gas fields have partial carbon isotopic reversal between ethane and propane, i.e., $\delta^{13}C_1 < \delta^{13}C_2 > \delta^{13}C_3$. Due to the limited amount for C_{3+} heavy hydrocarbon gas, hydrogen isotopic distribution pattern between ethane and propane is not available. Such partial carbon isotopic reversal has also been reported for gases from other wells with burial depth either more than 4,500 m or less than 4,500 m in the Kelasu-Yiqikelike thrust belt and South Slope Belt (Liu et al., 2007). The partial carbon isotopic reversal between ethane and propane of gases from the Kuqa depression has been explained as abiotic gas (Zhou, 1998; Zhang, 2002). The $\delta^{13}C_1$ vs. $\delta^{2}H_1$ diagram (**Figure 8**) can better interpret the abiotic methane. As shown in **Figure 8**, gas from the craton area of Tarim Basin and Sichuan Basin falls in the area of thermogenic gas, while gas from the Dabei gas field falls in the overlapped area of abiotic gas and thermogenic gas. However, counterview existed according to the helium isotope. Researches found that natural gas in the Kuqa depression has R/Ra values of 0.03∼0.108 with an average of 0.05 (Qin, 1999) or $^3He/^4He$ values of $n \times 10^{-8}$ (Liu et al., 2007), indicating

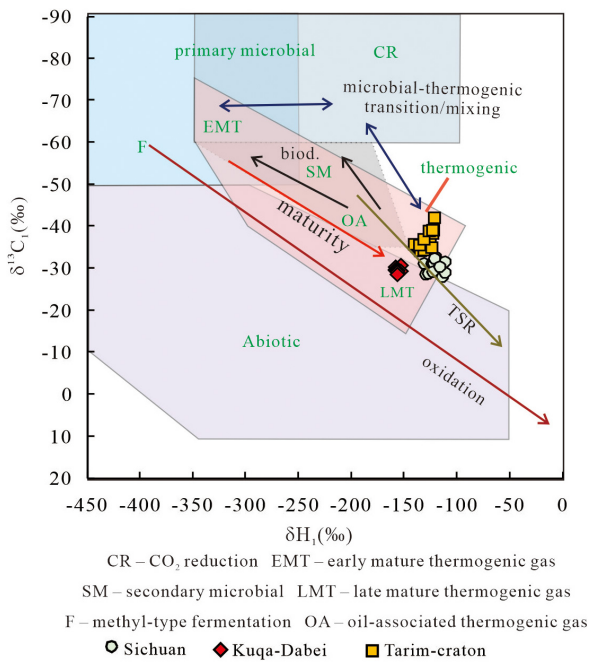


FIGURE 8 | Plot of $\delta^{2}H_1$ vs. $\delta^{13}C_1$ of gases from Dabei gas field in the Kuqa depression, craton area of Tarim basin and Sichuan basin (Milkov and Etiope, 2018). Data source see section "Samples and Methods" in the text.

the absence of mantle-derived helium, hence proposed that the partial carbon isotopic reversal was not caused by the mixing between biotic and abiotic gases. Mixing of gases generated from different sources or generated at different thermal maturity levels have been advocated to interpret the partial carbon isotopic reversal. Zhang et al. (2011) proposed that the partial carbon isotopic reversal of gases from Dabei gas field were caused by the mixing between coal-derived gas sourced from the Jurassic coal measures and oil-related gas that was sourced from the Triassic lacustrine source rocks. Dai et al. (2014) indicated that the partial carbon isotopic reversal of gases from Dabei gas field was due to the mixing of gases with the same origin but different maturity levels. Isotopic fractionation caused by gas leakage has also been proposed to interpret the partial carbon isotopic reversal of gases from the Kuqa depression (Qin, 1999). Except these single factor, multi-factor analysis has also been carried out. For example, Liu et al. (2007) proposed that the partial carbon isotopic reversal of gases from the Kuqa depression was caused by the mixing with gas of the same origin but different maturity or resulting from the high temperature, high pressure, multistage hydrocarbon accumulation and diffusion. A recent study proposed that the partial carbon isotopic reversal was due to the mixing between gases of the same origin but different sources or mixing between oil-related and coal-derived gases or high temperature and high pressure (Wei et al., 2019).

Partial carbon isotopic reversal between methane and ethane also exists in the deep gases from marine carbonate reservoirs in the Sichuan Basin (Wang, 1994; Zhu et al., 2006; Hao et al., 2008). Mixing of gases from different sources/maturity levels has been advocated to interpret the partial carbon isotopic reversal found in the gases from marine carbonate reservoirs (Wang, 1994; Hao et al., 2008; Ma, 2008; Deng et al., 2018). For example, partial carbon isotopic reversal between methane and ethane was found in the gases from Puguang gas field, which has been interpreted as mixing of oil cracked gases with different sources, mixing between secondary-cracking and primary cracking gases, in-reservoir mixing of oil cracked gases with different thermal maturities (Hao et al., 2008), or mixing of gases generated from different sources (Wang, 1994; Ma, 2008). In the Longgang gas field, partial carbon isotopic reversal between methane and ethane has been interpreted as a result from the isotopic fractionation during the migration of coal-derived gas (Dai et al., 2018), or mixing of gases generated from humic organic matter and gases generated from the cracking of oil (Deng et al., 2018).

One biggest difference between the gases from continental sandstone reservoirs and marine carbonate reservoirs is the content of H_2S. Gases from the continental sandstone reservoirs have no H_2S, while gases from marine carbonate reservoirs have varying content of H_2S. In the Puguang gas field in Sichuan Basin, the content of H_2S can be up to 58.34%. In most cases, the high content of H_2S in deeply buried gas reservoirs are due to the thermochemical sulfate reduction (TSR). A number of studies have demonstrated the existence of TSR in gases from the craton area of Tarim Basin and northeastern Sichuan Basin (Cai et al., 2001, 2007, 2009, 2013; Zhu et al., 2005, 2006, 2019b; Hao et al., 2008; Liu et al., 2013). Previous studies found that TSR may affect the carbon isotopic composition of hydrocarbon gases

(Krouse et al., 1988; Worden and Smalley, 1996; Cai et al., 2004; Hao et al., 2008; Pan et al., 2006; Zhu et al., 2006). After the liquid hydrocarbon are exhausted, C_2∼C_5 heavy hydrocarbon gases become the dominant reactants for TSR, then there will be a significant increase of CO_2 and H_2S content (Hao et al., 2008). At this stage, due to the kinetic isotopic fractionation, ^{12}C-^{12}C bond will break faster than ^{12}C-^{13}C bond, resulting in the preferentially loss of C_{2+} heavy hydrocarbon gases enriched in ^{12}C (Worden and Smalley, 1996; Krouse et al., 1988). Methane is the least reactive compound and its involvement in TSR as a reductive reactant has long been in dispute. Therefore, during the stage with C_2∼C_5 heavy hydrocarbon gases as the dominant reactants for TSR, the increasing extent of TSR will cause the increase of $\delta^{13}C_2$ values but not affect the $\delta^{13}C_1$ values, which will change the partial carbon isotopic reversal between methane and ethane into normal trend (Hao et al., 2008). A gas souring index [GSI = $H_2S/(H_2S + \Sigma Cn)$] has been used to show the extent of TSR (Worden et al., 1995). During this stage, CO_2 should positively correlate with H_2S, GSI should positively correlate with gas dryness coefficient (C_1/C_{1+}), $\delta^{13}C_2$ values correlate negatively with $\delta^{13}C_1$-$\delta^{13}C_2$ values. As seen in **Figure 9**, the relatively high content of CO_2 and H_2S in the gases from Sichuan Basin (H_2S: 9.78%, n = 51; CO_2: 8.93%, n = 67) and the craton area of Tarim Basin (H_2S: 2.2%, n = 64; CO_2: 5.38%, n = 152) indicates the existence of TSR. In general, high H_2S content accompanied with high CO_2 content, however, such correlation between H_2S and CO_2 is not very strong (**Figure 9**). The correlation between GSI and C_1/C_{1+}, GSI and $\delta^{13}C_2$, GSI and $\delta^{13}C_1-\delta^{13}C_2$ values is also not very apparent. This has been explained as that TSR has not affected the hydrocarbon gas (Puguang gas field) (Hu et al., 2010), or differences in the depositional environment and thermal maturity of source rocks in different gas fields (Wu et al., 2015a). Previous study in the Puguang gas field proposed that hydrocarbon gas was generated from the oil cracking and altered by TSR, and the transformation from a C_{2+} heavy hydrocarbon dominated TSR stage to a methane dominated stage caused different effects on the $\delta^{13}C$ of different hydrocarbon gas (Hao et al., 2008).

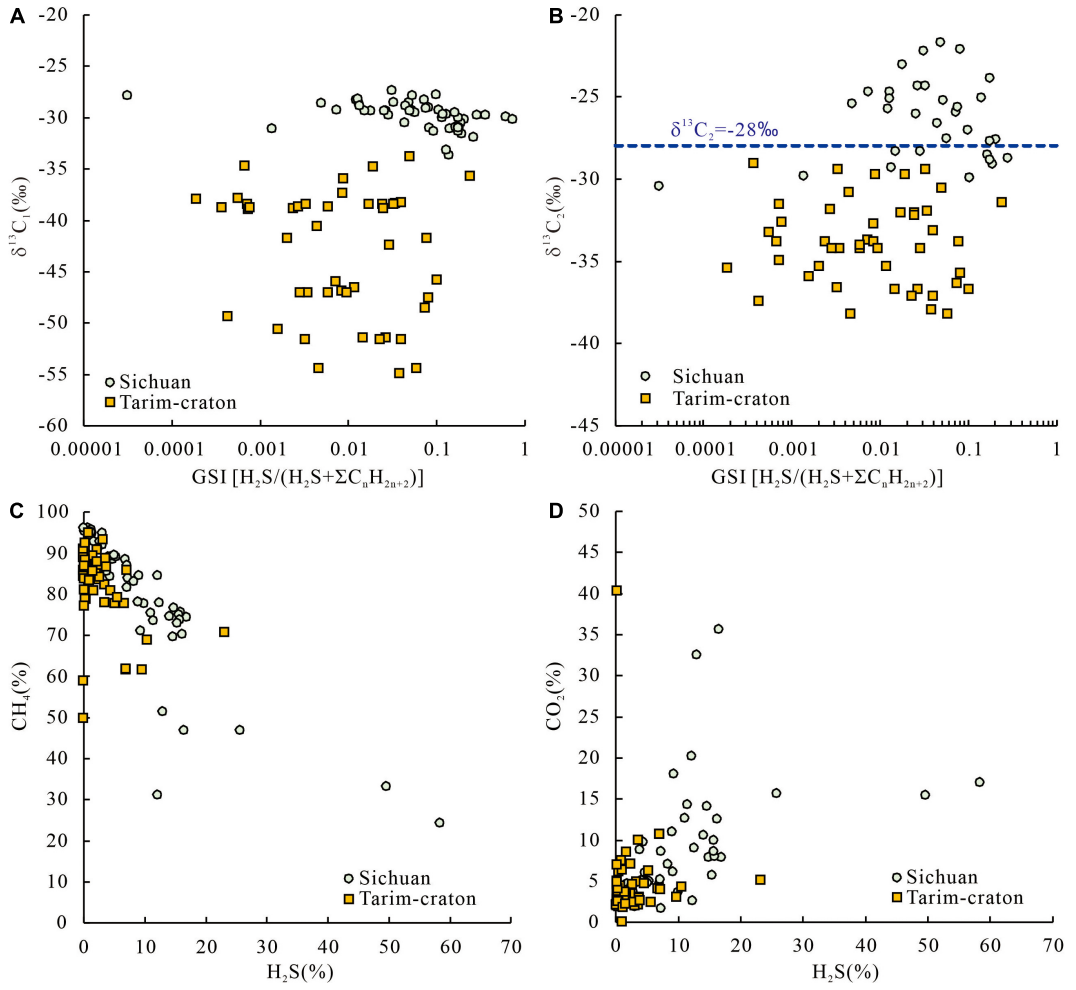


FIGURE 9 | Plot of $\delta^{13}C_1$ vs. GSI [$H_2S/(H_2S + \Sigma C_nH_{2n+2})$] **(A)**, $\delta^{13}C_2$ vs. GSI [$H_2S/(H_2S + \Sigma C_nH_{2n+2})$] **(B)**, CH_4 vs. H_2S **(C)**, and CO_2 vs. H_2S **(D)** of gases from the craton area of Tarim Basin and Sichuan Basin. Data source see section "Samples and Methods" in the text.

Considering the geological background, extremely high thermal maturity of source rocks might play a key role. The present burial depth of these marine carbonates is of 4,775∼7,150 m and the present thermal maturity is between 2.0 and 3.0% (Hao et al., 2008; Qin et al., 2016). However, the compression from the movement of the Pacific plate resulted in the entire uplift of Sichuan Basin during the Himalayan orogeny and the uplift amplitude reached 2,400 m (Liu et al., 2008; Deng et al., 2009). Before the uplift, the marine carbonate reservoir (Changxing and Feixianguan formations) in the Puguang gas field reached a maximum burial depth of 7,000 m with temperature up to 220°C (Hao et al., 2008). The maximum burial depth in the Longgang gas field is also estimated to be over 7,000 m and the present thermal maturity is 2.81% (Ro%) for the reservoir bitumen in the Changxing Formation with burial depth of 6118.81∼6119.89 m (Qin et al., 2016). The deep gases from Sichuan Basin all show extremely high gas dryness coefficient (average 0.999, $n = 67$) and the average content of C_{2+} heavy hydrocarbon is only 0.11%. Both molecular and isotopic compositions of hydrocarbon gases are affected by the thermal evolution degree of source rocks, especially with such high gas dryness coefficient, it is hard to determine the effects from thermal maturity or TSR.

TSR will cause the increase of carbon isotope of hydrocarbon gases, which may contribute to the relatively heavy carbon isotopic values of ethane in the gases from Sichuan Basin (**Figure 6**). As methane can be the dominant reducing reactant for TSR after most C_{2+} heavy hydrocarbons are exhausted at elevated temperature (Hao et al., 2008), in this case, TSR will result in the increase of carbon isotope of methane. However, great care has to be paid to the explanation of the carbon isotope of methane since other processes also exert influences on the $\delta^{13}C_1$ values. For example, the relatively heavy carbon isotope of methane in the Longgang gas field in Sichuan Basin was interpreted as a result of high thermal maturity of the source rocks and the mixing of gas degassed from water (Qin et al., 2016).

Origin of Non-hydrocarbon Gas CO_2

Milkov and Etiope (2018) found that there is significant overlap of $\delta^{13}C_{CO2}$ values for the primary microbial gas, thermogenic gas and abiotic gas in the $\delta^{13}C_{CO2}-CO_2$ plot (**Figure 5**). According to the carbon isotopic studies of 390 CO_2 gas samples from different sedimentary basins in China, Dai et al. (1996) suggested a distinguishing criterion for CO_2, i.e., CO_2 of biotic origin (including thermogenic and microbial): CO_2 content <15% and $\delta^{13}C_{CO2}$ <−10‰; CO_2 of abiotic origin: CO_2 content >60% or $\delta^{13}C_{CO2}$ >−8‰ (**Figure 10**). CO_2 in the deep gas has wide variation of carbon isotope (**Figures 5**, **10**). It is clear that contributions from microbial effects can be ignored (**Figure 5**). In general, samples from the continental sandstone reservoirs have relatively light carbon isotope of CO_2 (average −15.1‰, $n = 19$), indicative of the thermogenic origin (**Figure 10**). Gases from the Sichuan Basin have $\delta^{13}C$ value of −1.77‰ ($n = 50$) for CO_2, indicating that most CO_2 gases are of abiotic origin. As shown in **Figure 10**, most deep gases from Sichuan Basin fall in the region of abiotic CO_2. The content of CO_2 in the deep gas from Sichuan Basin has a peak range of 5∼10%. The $\delta^{13}C$ values of CO_2 have an average of −1.8‰ ($n = 50$) and a peak range of −5‰ ∼ + 3‰, which is close to the $\delta^{13}C$ value of marine carbonate reservoir (0.9∼3.7‰) (Hu et al., 2010). A number of studies have demonstrated the abiotic CO_2 was generated from the dissolution of marine carbonates through acid fluid (Hao et al., 2008, 2015; Huang et al., 2010; Liu et al., 2014). Dai et al. (2018) proposed that the CO_2 was generated from the decomposition of marine carbonates during the over mature thermal evolution stage.

THERMAL MATURITY OF DEEP GASES

Gas Dryness and Gas Wetness

Due to the decomposition of heavy hydrocarbons at elevated temperature, with increasing thermal maturity of source rocks, the relative content of methane of hydrocarbon gases will increase and the content of C_{2+} heavy hydrocarbon gases decrease. Gas dryness coefficient [$D = C_1/(C_1\text{-}C_5)$] or gas wetness coefficient [$W = (C_2\text{-}C_5)/(C_1\text{-}C_5)$] has been used to evaluate the gas maturity. According to compositional study of the natural gases from Ordos, Sichuan, Bohaibay, Qiongdongnan, Junggar, and Turpan-Hami basins in China, a negative correlation between gas wetness and gas maturity was established for the coal-derived gases sourced from the humic organic matter ($Ro\% = -0.419\ln W + 1.908$) (Dai et al., 2016b). In general, gases with gas dryness coefficient (D) greater than 0.95 is defined to be dry gas and gases with gas dryness coefficient (D) lower than 0.95 is wet gas. Gas generation during the thermal stage with vitrinite reflectance greater than 2.0% is usually dominated by methane and the produced gas is commonly dry gas. According to the delineation of dry gas via gas dryness coefficient, deep gases from Dabei and Keshen in the Kelasu thrust belt in Kuqa depression, Longgang, Yuanba and Puguang gas fields in Sichuan Basin are dry gas, while gases from the craton area of Tarim Basin are composed of both dry gas and wet gas. For example, gases from Shunnan-Gucheng area are mostly dry gas, while gases from Halahatang are mostly wet gas.

Theoretically, with increasing burial depth of source rocks, the geothermal temperature will increase and the thermal maturity of source rocks will increase as well. Therefore, gas dryness coefficient commonly increases with increasing burial depth. However, processes such as migration, leakage and TSR may affect the molecular composition of natural gases, thus result in the changes of gas dryness coefficient. Therefore, great care has to be paid to the researches of natural gases with gas dryness coefficient. **Figure 11A** shows the changes of gas dryness coefficient with burial depth of the coal-derived deep gases from Dabei and Keshen gas fields in the Kuqa depression. Gases with different burial depth of reservoirs from Dawanqi oil field (Zhou and Bao, 2011; Wang et al., 2012) and Kela2 gas field (Qin et al., 2007) in the Kelasu thrust belt were shown for comparison. According to previous studies, due to the barrier of the gypsum-salt layer with massive thickness between the Jurassic-Triassic source rocks and the Neogene Kangcun Formation reservoirs, gases generated from the Jurassic-Triassic source rocks could migrate into the Kangcun Formation reservoirs through the Tuzimaza large fault and form the Dawanqi oil field, while it

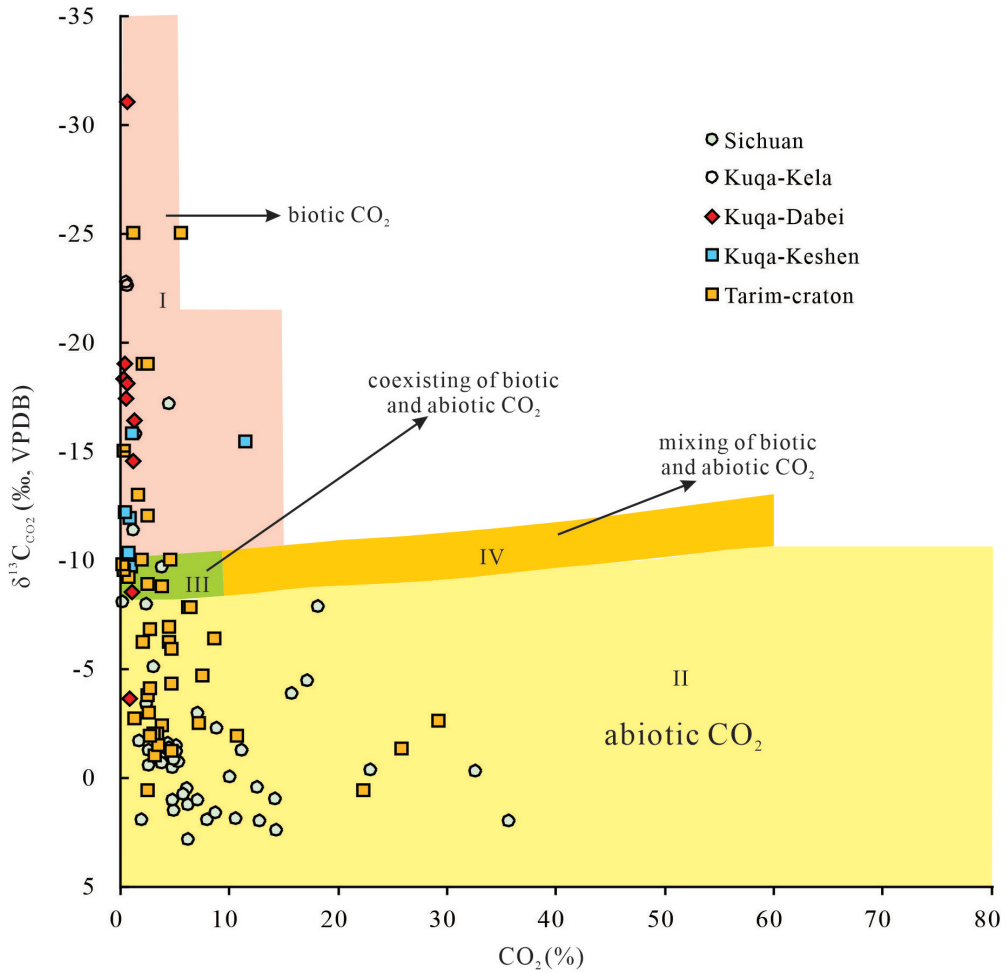


FIGURE 10 | Plot of $\delta^{13}C_{CO2}$ vs. CO_2 of gases from Dabei, Keshen and Kela2 gas fields in the Kuqa depression, craton area of Tarim Basin and Sichuan Basin, distinguishing the origin of CO_2 (Dai et al., 1992). Data source see section "Samples and Methods" in the text.

formed the highly mature-over mature Dabei gas field under the gypsum-salt layer (Liu et al., 2005). Because of the influences of fault and erosion of cap layer, leakage of hydrocarbon gases occurred for the shallow gas, which result in the gas distribution with wet gas in the top and dry gas in the bottom vertically (Tian et al., 2001; Zhou and Bao, 2011). As shown in **Figure 11**, gases from the Dawanqi gas field have relatively low $C_1/(C_1\text{-}C_5)$ ratios and shallower burial depth, while with increasing burial depth, gases from Kela2, Dabei and Keshen gas fields have much higher $C_1/(C_1\text{-}C_5)$ ratios. Actually, gases from Dawanqi oil field have relatively heavy carbon isotope of methane (−28∼−33‰) and the $\delta^{13}C_1$ gets lighter with increasing burial depth (Zhao, 2003), so the apparently low dryness coefficient of gases from Dawanqi oil field is mainly caused by the leakage of light composition in the shallow layers. The deep gases from Dabei and Keshen gas fields demonstrate a slight increasing trend of gas dryness coefficient with increasing burial depth, indicating the influences from thermal maturity.

TSR commonly occurred in the northeastern Sichuan Basin (Cai et al., 2003, 2013; Zhu et al., 2005, 2006; Hao et al., 2008). Since TSR consumed liquid hydrocarbon in the first, followed by C_{2+} heavy hydrocarbon and then methane (Hao et al., 2008), the extremely high gas dryness coefficient in the Longgang, Yuanba and Puguang gas fields not only reflects the high thermal maturity of source rocks to some extent. **Figure 11B** shows the natural gases from Xujiahe, Leikoupo, and Changxing-Feixianguan formations in the Yuanba gas field in Sichuan Basin. In general, all gases in the Yuanba gas field belong to dry gas and have very high dryness coefficient, indicating the high thermal maturity. Gases from Changxing-Feixianguan formations have relatively higher dryness coefficient values (nearly 1) than those from Xujiahe and Leikoupo formations, however, the difference is usually not more than 0.02. Therefore, it is hard to tell the exact contribution of thermal maturity or TSR to the high dryness coefficient of gases from Changxing-Feixianguan formations.

Logarithmic Linear Correlation Between $\delta^{13}C_1$ and Ro%

Due to the kinetic isotopic fractionation effect during the hydrocarbon generation process, a logarithmic linear relation

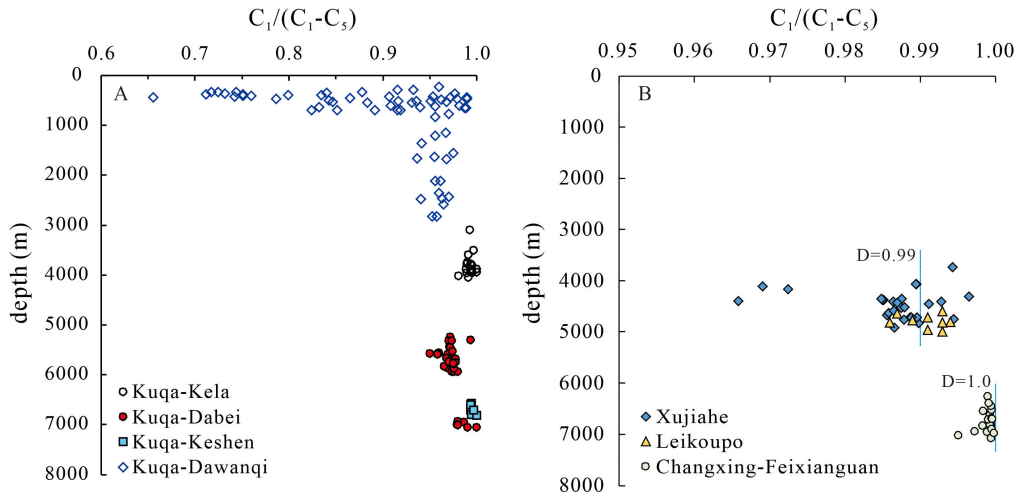


FIGURE 11 | (A) Plot of $C_1/(C_1\text{-}C_5)$ vs. burial depth of natural gases from the Dabei, Keshen, Kela2 and Dawanqi gas fields in the Kuqa Depression, Tarim Basin. **(B)** Plot of $C_1/(C_1\text{-}C_5)$ vs. burial depth of natural gases from the Xujiahe, Leikoupo and Changxing-Feixianguan formations of Yuanba gas field in Sichuan Basin. Data of Kela2 gas field were from Qin et al. (2007), data of Dawanqi oil field were from Zhou and Bao (2011) and Wang et al. (2012), data of Yuanba gas field were from Dai et al. (2013), Yin et al. (2013), Huang (2014), Wu et al. (2015b) and Li et al. (2016).

exists between $\delta^{13}C_1$ and Ro% (Stahl and Carey, 1975; Schoell, 1980). A ^{12}C-^{12}C bond is easier to break than a ^{12}C-^{13}C bond, which makes the residual precursors and late gaseous products more enriched in ^{13}C (Berner and Faber, 1996; Cramer et al., 1998; Tang et al., 2000). Different $\delta^{13}C_1$–Ro% models have been developed for gases derived from different types of organic matters (Stahl and Carey, 1975; Schoell, 1980; Dai and Qi, 1989). So based on the relation between carbon isotope of methane and the thermal maturity of gas source rocks, one can obtain the thermal maturity level of gas source rocks by using the measured $\delta^{13}C$ values of methane. Recently new equations of $\delta^{13}C_1$–Ro% [$\delta^{13}C_1 = 25\lg(Ro)-37.5$ for gases sourced from the humic organic matter; $\delta^{13}C_1 = 25\lg(Ro)-42.5$ for gases sourced from the sapropelic organic matter] have been established for primary gases which have not undergone secondary alteration according to abundant measured carbon isotopic values of methane in China (Chen et al., 2020). According to the $\delta^{13}C_1$–Ro% equation for gases from humic organic matter, deep gas from the Kuqa depression was calculated based on its carbon isotopic values of methane. The gas maturity is estimated to be 1.50∼2.75% with an average of 2.06%. This is consistent with the local geological background. In the Kuqa depression, thermal maturity is higher in the east than that in the west, and in the deposition centre such as Baicheng sag, thermal maturity of source rocks (Ro%) is 1.5∼3.5% (Dai, 2016). The gas dryness coefficient of 0.974 also implies the relatively high thermal maturation.

According to the calculation with the above $\delta^{13}C_1$–Ro% equations, deep gases from the Yuanba, Longgang and Puguang gas fields in the Sichuan Basin also have high gas maturity around 2.0% Ro%. However, methane in these gas fields might be altered by secondary processes such as TSR, water dissolution, resulting in the changes of $\delta^{13}C$ values of methane. Therefore, errors may exist for the gas maturity calculation based on the $\delta^{13}C$ values of methane for these gases.

HYDROGEN ISOTOPES

Carbon isotope of natural gas is mainly affected by the type of organic matter and the level of thermal maturity of source rocks. However, unlike the carbon isotope, the gas hydrogen isotope is highly dependent on the thermal maturity of source rocks and salinity of the water medium of the formation environment of the source organic matters (Schoell, 1980; Dai, 1993; Ni et al., 2015; Wang et al., 2015). Influences from the type of organic matter on the gas hydrogen isotope is weak, which will be easily masked by the influences from the water salinity of the depositional environment of the source organic matter (Ni et al., 2019).

In the Tarim Basin, a boundary δ^2H_1 value of −150‰ has been found between the gases sourced from the Middle-Lower Jurassic humic organic matter in the Kuqa depression (<−150‰) and the oil-cracked gases sourced from Cambrian-Lower Ordovician marine sapropelic organic matter in the Lunnan low uplift and the Ordovician oil-cracked gases in the Tazhong low uplift (>−150‰) (Ni et al., 2013). As shown in **Figure 12**, such boundary value also exists between the deep gases from the Dabei gas field in the Kuqa depression and those from the craton area of Tarim Basin. The deep gases from the Dabei gas field have δ^2H value of methane of −153∼−158‰ with an average value of −156‰, while the deep gases from the craton area of Tarim Basin have relatively heavier hydrogen isotope of methane, with an average value of −130‰. Deep gases from the Yuanba and Puguang gas fields have even heavier δ^2H_1 value, with an average of −122‰. According to previous studies, bacterial methane sourced from the marine and saline-water lacustrine organic matter (δ^2H > −190 or −200‰) has heavier hydrogen isotope compared to those from continental freshwater source rocks (δ^2H < −190 or −200‰) (Schoell, 1980; Shen, 1995). Apparently deep gases from the Dabei gas field have δ^2H_1 value much heavier than

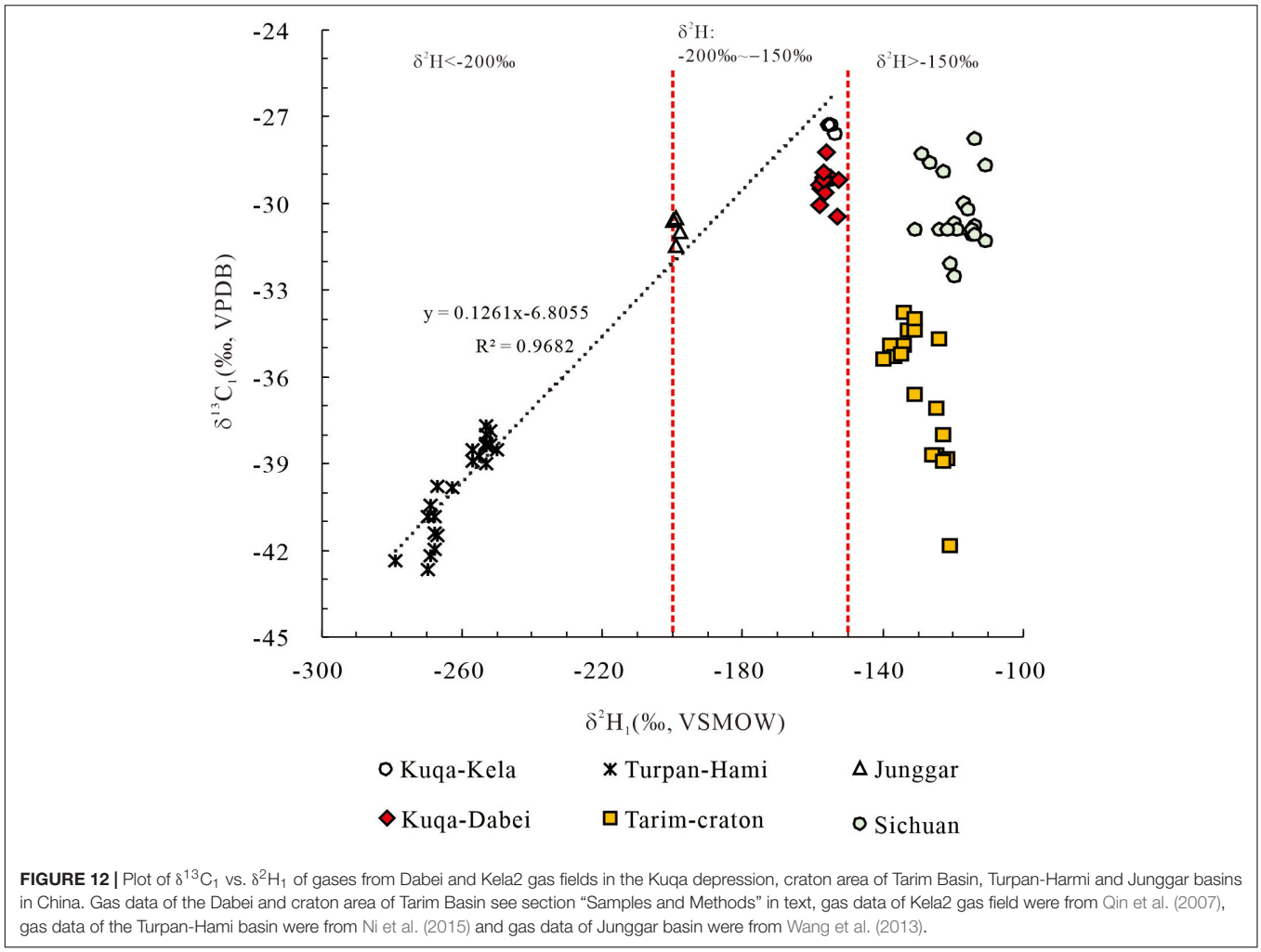


FIGURE 12 | Plot of $\delta^{13}C_1$ vs. δ^2H_1 of gases from Dabei and Kela2 gas fields in the Kuqa depression, craton area of Tarim Basin, Turpan-Harmi and Junggar basins in China. Gas data of the Dabei and craton area of Tarim Basin see section "Samples and Methods" in text, gas data of Kela2 gas field were from Qin et al. (2007), gas data of the Turpan-Hami basin were from Ni et al. (2015) and gas data of Junggar basin were from Wang et al. (2013).

this determining value for gases sourced from the continental freshwater organic matter.

The deuterium concentration in methane was found to increase with increasing thermal maturity (Schoell, 1980; Ni et al., 2011), methane in the Dabei gas field was expected to have relatively higher δ^2H values due to the high thermal maturity of their source rocks (Ro%: 1.5∼3.5%). Because gas hydrogen isotope was mainly dependent on the thermal maturity and the water salinity of depositional environment of source organic matters, if one wants to investigate any influences from the thermal maturity or the water medium of depositional environment, a comparison has to be made with one fixed influencing factor. So gas samples with different thermal maturity but similar depositional environment from various locations in China were compared here (**Figure 12**).

Deep gases in the Dabei gas field are considered mainly sourced from the Middle-Lower Jurassic coal measures deposited in the lacustrine-swamp environment with freshwater medium (Zhang et al., 2011; Guo et al., 2016). Coal resources are widely distributed in the northwestern China and it is mainly accumulated in the Middle-Lower Jurassic formations. Actually in China the Early Middle Jurassic was one of the four major coal forming periods among the 14 coal forming periods in the geological history. The Middle-Lower Jurassic coal-bearing strata which was formed during the Early Middle coal forming period were widely distributed in the Tarim, Junggar, Turpan-Hami, Qaidam basins in northwestern China with similar depositional environment. Gases from the Turpan-Hami Basin (Ni et al., 2015), Junggar Basin (Wang et al., 2013) and Kela 2 gas field in the Kuqa depression in Tarim basin (Dai, 2016) are coal-derived gas sourced from the Jurassic coal measures. Under similar depositional environment, the differences in deuterium concentration of gases from Kela 2 gas field, Junggar and Turpan-Hami basins are mainly due to the differences in the level of thermal maturity of their source organic matters. There is a very good correlation between hydrogen and carbon isotopic compositions of methane ($y = 0.1261\times-6.8055$, $R^2 = 0.9682$). This may indicate a possible influence of thermal maturity on gas isotopes since organic matter $^2H/^1H$ and $^{13}C/^{12}C$ ratios increase systematically throughout the thermal maturation (Schoell, 1980; Dai, 1993; Li et al., 2001).

Compared to the gases from Kela 2 gas field, Turpan-Hami and Junggar basins, considering the influences from thermal maturity of source rocks, the Dabei gases are relatively much

more enriched in D at similar thermal maturity level and show remarkable offset toward the maturity trend (**Figure 12**). However, gases from these four areas demonstrate consistently quite good correlation between $\delta^{13}C_1$ and $\delta^{13}C_2$ (R^2 = 0.9007), δ^2H_1 and δ^2H_2 (R^2 = 0.9975) (**Figure 13**). This implies that the carbon isotope is affected by one type of factor while the hydrogen isotope is affected by another type of factor. Therefore, under one type of influencing factor, the correlation can be linear between methane and ethane for both carbon and hydrogen isotopes. If the carbon isotope was plotted vs. hydrogen isotope, then offset will occur (**Figure 12**).

Considering the heavy carbon isotopes of methane (average: –30.0‰) and ethane (average: –21.7‰), it is unlikely that the heavy hydrogen isotope is due to the mixing with oil-cracked gases. Gas derived from marine source rocks normally has much heavier hydrogen isotope due to the saline water depositional environment, for example, gases from the Lunnan and Tazhong areas in the Tarim basin are gases sourced from the Cambrian-Lower Ordovician marine sapropelic organic matter with saline water depositional environment, so they are more enriched in D but depleted in ^{13}C (**Figure 12**; Ni et al., 2013). Oil-cracked gas normally has much heavier carbon isotope of ethane compared to the oil-associated gas but normally still less than –28‰, and it also contains trace amount of ethane, i.e., the oil-cracked gas from the Sinian strata in the Weiyuan gas field (Dai et al., 2003). The carbon isotopic distribution pattern among methane and its homologues is normal in general and only a few samples have carbon isotopic reversal between ethane and propane of the deep gases from Dabei gas field (**Table 1**). To some extent, mixing of gases with different origins often causes a partial reversed carbon isotopic distribution pattern among methane and its homologues (Dai et al., 2004b). However, mixing with gases from sapropelic organic matter from deeper strata is unlikely. Though potential mixing with gases from the marine sapropelic organic matter will cause the enrichment of D, but it will also cause the depletion of ^{13}C, especially for ethane, which is not consistent with the heavy carbon isotope of the deep gases in the Dabei gas field.

Except the thermal maturity, one other potential cause for the relatively heavy hydrogen isotope is the saline depositional environment. The Kela 2 gases are on the maturity trend, while the gases from Dabei gas field have a big offset (**Figure 12**), which indicates that differences exist in the depositional environment of their source rocks. Based on the studies of paleontological fossil, mineralogy and petrology, and geochemistry (biomarkers, trace elements and carbon/hydrogen isotopes), a number of studies have demonstrated that marine transgressive happened several times during the Triassic-Jurassic period in the Kuqa depression (Chen, 1995; Zhou et al., 1999; Zhang B. et al., 2006). For example, based on the research of paleontological fossils and trace elements, Zhang B. et al. (2006) proposed that there were three big transgressive during the Triassic-Jurassic period in the Kuqa depression. According to the research based on stromatolite and trace elements, Chen (1995) thought that marine transgressive existed during the Middle Jurassic in the Tarim Basin. The author calculated the paleosalinity to be 33.4‰ according to the boron content, which is very similar to the modern seawater salinity. Extensive transgressive-regressive cycles during the Jurassic have been reported in the worldwide since Jurassic sea-level curves were first proposed several decades ago (Hallam, 1978, 2001). Major episodes of eustatic rise occurred in the Early Hettangian, Early Sinemurian, Early Pliensbachian, Early Toarcian, Early and Late Bajocian, Middle Callovian and Late Oxfordian to Kimmeridgian, among them, the Early Bajocian transgessive/deepening event can be recognised widely across the world (Hallam, 2001). Therefore, the relatively heavy hydrogen isotope in the Dabei gases may result from a possible saline depositional environment. Compared to the gases from Kela 2 gas field, the deep gases from Dabei gas field are more inclined to the influences from the transgressive, which caused the apparent enrichment in D in the deep gases in the Dabei gas field.

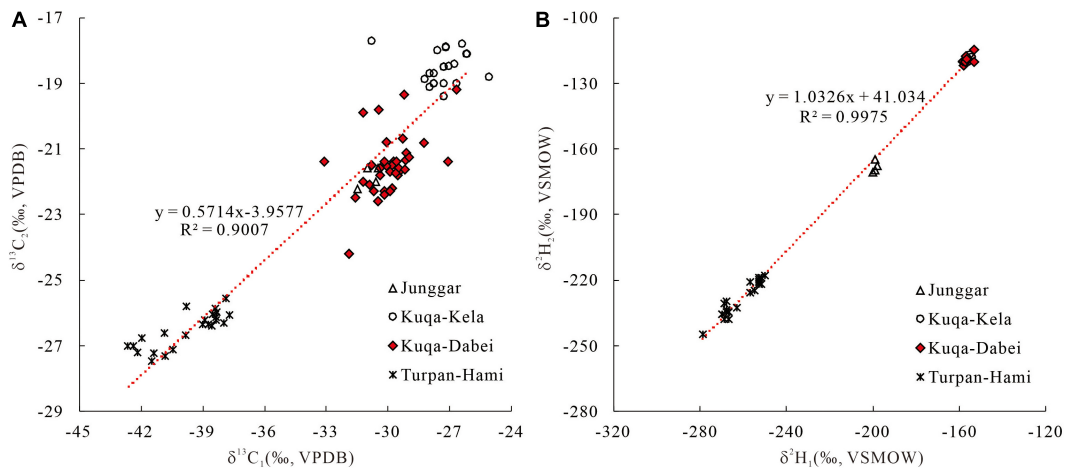


FIGURE 13 | Plots of $\delta^{13}C_1$ vs. $\delta^{13}C_2$ **(A)** and δ^2H_1 vs. δ^2H_2 **(B)** of gases from Dabei and Kela2 gas fields in the Kuqa depression in Tarim Basin, also from the Turpan-Harmi and Junggar basins in China. Gas data of Kela2 gas field were from Qin et al. (2007), gas data of the Turpan-Hami Basin were from Ni et al. (2015) and gas data of Junggar Basin were from Wang et al. (2013).

TABLE 1 | Molecular composition and stable carbon and hydrogen isotopic values of deep gas from Dabei gas field, Kuqa depression, Tarim basin.

Well	Strata	Depth (m)	Main composition (%)								$\delta^{13}C$ (‰,VPDB)					$\delta^{2}H$ (‰, VSMOW)		C_1/C_{1+}	Ro%[a]	References
			CH_4	C_2H_6	C_3H_8	C_4H_{10}	C_5H_{12}	N_2	CO_2	H_2S	CH_4	C_2H_6	C_3H_8	C_4H_{10}	CO_2	CH_4	C_2H_6			
DB1	K_1bs	5,552–5,586	94.50	3.45	0.22	0.28	0.05	1.08	0.42									0.959		Li et al., 2005
Dabei-1	K	5568.0–5620	91.87			4.84					−29.7	−21.4	−20.8					0.950	2.05	Zhang et al., 2011
DB1	E	5568.08–5,620									−29.7	−21.4	−20.8	−21.9	−18.0					Li et al., 2005
Dabei-1	K	5,576–5,586	95.04			3.96					−29.8	−21.5	−21.8					0.960	2.03	Zhang et al., 2011
Dabei-1	K	5,576–5,586	93.57			3.90					−29.9	−21.7	−21.8					0.960	2.01	Zhang et al., 2011
DB1	K_1bs	5,584–5,586	95.28	3.56	0.31	0.20	0.06	0.22	0.37									0.958		Li et al., 2005
DB1	K_1bs	5,586	94.80	2.30	0.36	0.35		1.12	0.44		−33.1	−21.4						0.969	1.50	Zhu et al., 2019a
DB1	K_1bs	5,865–5,872	94.13	3.00	0.03			2.85										0.969		Li et al., 2005
DB101-1	K_1bs	5,248–5,384 5,379–5,384	96.43	2.19	0.39	0.19	0.08	0.38	0.35	0.00	−30.1	−21.5	−21.3			−158	−121	0.971	1.98	This study
DB101-1	K_1bs	5,730	96.10	2.24	0.37	0.31		0.33	0.54		−31.6	−22.5	−21.7	−22.6				0.971	1.72	Zhu et al., 2019a
DB101-2	K_1bs	5,314–5,435,	96.14	2.25	0.41	0.19	0.07	0.46	0.47	0.00	−29.5	−21.8	−20.8			−158	−122	0.970	2.09	This study
DB101-3	K_1bs	5,302–5,380	99.34	0.64	0.02	0.00	0.00			0.00	−30.5	−19.8	−25.7			−153	−115	0.993	1.91	This study
DB101-5	K_1bs	5,438–5,540	96.54	2.19	0.41	0.20	0.09	0.57		0.00	−29.4	−21.7	−20.5			−158	−120	0.971	2.11	This study
DB101-5	K_1bs	5,744	95.10	2.11	0.45	0.36		0.92	0.62		−29.3	−20.7	−22.1	−20.6				0.970	2.13	Zhu et al., 2019a
DB101	K_1bs	5,725	95.70	2.22	0.40	0.29		1.20	0.22		−30.5	−22.6	−21.8	−22.8	−18.3			0.970	1.91	Dai, 2016
DB102	K_1bs	5,315	96.01	2.08	0.38	0.18		0.91	0.44		−29.5	−21.6	−21.0	−22.6	−17.4			0.973	2.09	Wei et al., 2019
DB102	K_1bs	5,451–5,479	96.24	2.17	0.39	0.19	0.07	0.52	0.42	0.00	−29.6	−21.7				−157	−120	0.972	2.06	This study
DB102	K_1bs	5,451	95.30	2.22	0.28	0.25		1.29	0.71		−30.7	−22.3	−21.5	−25.8	−3.6			0.972	1.87	Dai, 2016
Dabei-103	K	5,677–5,687	94.30			2.92					−31.9	−24.2	−19.7					0.970	1.67	Zhang et al., 2011
DB103	K_1bs	5,677	95.67	2.21	0.43	0.21		0.95	0.53		−30.2	−22.3	−21.1	−22.5	−18.1			0.971	1.96	Wei et al., 2019
DB103	K_1bs	5,832	94.30	2.45	0.51	0.45		1.27	0.99		−31.9	−24.2	−19.7		−8.5			0.965	1.67	Dai, 2016
DB104	K_1bs	5,922–5949									−27.1	−21.4							2.61	Dai, 2016
DB104	K_1bs	5,981–5,985									−26.7	−19.2							2.70	Dai, 2016
DB2	K_1bs	5,658–5,669	95.26	2.25	0.38	0.53		1.19	0.39		−30.8	−21.5	−19.8					0.968	1.85	Dai, 2016
DB2	K	5,658–5669.5	96.11	2.18	0.38	0.19	0.14	0.62	0.38		−30.8	−21.5	−19.8		−9.5			0.971	1.85	Li et al., 2005
DB201	K_1bs	5,658	95.26	2.25	0.38	0.53		1.27	0.31		−30.8	−21.5	−19.8		−19.0			0.968	1.85	Wei et al., 2019
DB201	K_1bs	5,932–6,010	96.10	1.98	0.37	0.31		0.64	0.54		−31.2	−22.0	−21.0					0.973	1.79	Dai, 2016
DB201	K_1bs	5,932–6,112	95.80	1.90	0.27	0.18		1.42	0.44		−30.9	−22.1	−21.9					0.976	1.84	Dai, 2016
Dabei-201	K	5932.45–6,145	96.10			1.96					−31.2	−19.9	−22.0					0.980	1.79	Zhang et al., 2011
DB201-1	K_1bs	5,876–5,976	97.13	1.89	0.33	0.16	0.06	0.43		0.00	−29.1	−21.1	−20.3			−155	−120	0.976	2.16	This study
DB202	K_1bs	5,711–5,845	97.59	1.84	0.33	0.17	0.07	0.01		0.00	−29.2	−21.3	−20.5			−157	−119	0.976	2.16	This study
DB202	K_1bs	5,711–5,845	94.80	1.57	0.36	0.30		1.27	1.67		−30.4	−21.8	−22.5					0.977	1.92	Dai, 2016
DB202	K_1bs	5,711	95.10	1.93	0.45	0.36		0.92	1.19		−29.3	-20.7	−22.1	−19.6	−16.4			0.972	2.13	Wei et al., 2019
DB202	K_1bs	5,763	94.80	2.16	0.36	0.30		1.27	0.45		−30.4	−21.6	−22.5	−21.4				0.971	1.92	Zhu et al., 2019a
DB205	K_1bs	5787.5–5,941	97.10	1.89	0.33	0.16	0.06	0.46		0.00	−29.2	−21.6	−21.0			−153	−120	0.975	2.15	This study

(Continued)

TABLE 1 | Continued

Well	Strata	Depth (m)	Main composition (%)							$\delta^{13}C$ (‰,VPDB)				$\delta^{2}H$ (‰, VSMOW)		C_1/C_{1+}	Ro%[a]	References
			CH_4	C_2H_6	C_3H_8	C_4H_{10}	C_5H_{12}	N_2	CO_2	H_2S	CH_4	C_2H_6	C_3H_8	C_4H_{10}	CO_2	CH_4	C_2H_6			
DB207	K_1bs	5,527	95.80	2.20	0.17		0.17	0.64	0.51		−29.8	−22.2						0.974	2.03	Zhu et al., 2019a
DB207	K_1bs	5,746–5,888	96.62	2.08	0.47	0.27	0.14	0.43		0.00	−29.2	−19.4	−20.6			−157	−118	0.970	2.14	This study
DB208	K_1bs	5,681	96.50	2.22	0.01		0.01	0.51	0.59		−30.2	−21.4	−21.6					0.977	1.96	Zhu et al., 2019a
DB208	K_1bs	5,755–5,830	96.80	1.73	0.30	0.15	0.07	0.44	0.51	0.00	−29.0	−21.3	−20.8			−157	−120	0.977	2.19	This study
DB209	K_1bs	5,776–5,878	97.09	1.91	0.33	0.16	0.07	0.44		0.00	−28.3	−20.8	−20.1			−156	−119	0.975	2.34	This study
DB3	E_{1-2}km	6,950	97.20	1.23	0.09	0.03					−29.9	−22.3	−20.3		−14.7			0.986	2.01	Wei et al., 2019
DB3	E_{1-2}km	7,058	96.70					0.71	1.08		−29.6	−21.4	−19.2	−20.1	−14.5			1.000	2.07	Wei et al., 2019
DB3	K_1bs	7,058–7,090									−29.6	−21.4	−19.2						2.07	Dai, 2016
Dabei-3	E	7,058–7090.88	96.90			0.98					−30.1	−20.8	−18.9					0.990	1.98	Zhang et al., 2011
DB301	K_1bs	6,930–7,012	96.20	1.66	0.17	0.17		1.26	0.51		−29.9	−22.3						0.980	2.01	Dai, 2016
DB301	E_{1-2}km	7,000	92.50	1.66	0.24	0.06					−30.1	−20.8	−20.3	−20.3	−21.7			0.979	1.98	Wei et al., 2019
DB301	E_{1-2}km	7,012	96.20	1.69	0.17	0.17		1.26	0.51		−30.2	−22.4	−22.1	−21.2	−31.0			0.979	1.96	Wei et al., 2019

[a]*Ro% values were calculated according to the formula by Chen et al. (2020),* $\delta^{13}C_1 = 25lg(Ro) - 37.5$.

CONCLUSION

With increasing improvements in technological development and theoretical understanding, deep and ultra-deep areas have become more and more important, especially in the mature exploration area. A comprehensive knowledge about the geochemical characteristics of deep gas from continental sandstone reservoirs and marine carbonate reservoirs may improve our understanding of the origin and accumulation of deep gas. This study carried out a detailed comparison of the molecular composition, stable carbon and hydrogen isotopes of deep gases from the clastic sandstone reservoirs in the Dabei and Keshen gas fields in the Kuqa depression, Tarim basin, and deep gases from the marine carbonate reservoirs in the craton area of Tarim Basin and Sichuan Basin (Yuanba, Longgang, Puguang gas fields). The following conclusions were obtained.

(1) Deep gas, either from the continental sandstone reservoirs of Dabei and Keshen gas fields in the Kuqa depression, Tarim Basin or from the marine carbonate reservoirs of the craton area of Tarim Basin and Puguang, Yuanba and Longgang gas fields in the Sichuan Basin, is dominated by alkane gas. The average content of methane is about 83.80%. Deep gas from the Kuqa depression in Tarim Basin has gas dryness coefficient of 0.976, while gas from the Sichuan Basin has even higher gas dryness coefficient of 0.999, indicative of dry gas. Deep gas from the craton area of Tarim Basin has various gas dryness coefficient, mainly 0.594∼0.999, indicating the existence of both dry gas and wet gas. N_2 and CO_2 are the common non-hydrocarbon gases in the deep gas. One important difference between the deep gas from sandstone reservoirs and that from carbonate reservoirs is the content of H_2S. Deep gas from the continental sandstone reservoirs have no H_2S, while deep gases from the marine carbonate reservoirs often have H_2S, which can be even higher than 45%.

(2) Deep gas from the continental sandstone reservoirs in Dabei and Keshen gas fields in the Kuqa depression has $\delta^{13}C_2$ values much higher than −28‰, and has $\delta^{13}C_1$∼$\delta^{13}C_2$ maturity trend similar to the gases generated from type III kerogen, indicative of coal-derived origin. Most gas samples from the craton area of Tarim Basin have $\delta^{13}C_2$ values lower than −28‰ and match better with the evolution trend of gas generated from type II kerogen. Deep gases from the Sichuan Basin include two types: gases generated from humic type III kerogen, and gases generated from sapropelic type II kerogen. Carbon isotopic anomaly such as relatively heavy carbon isotope of methane or/and ethane and carbon isotopic reversal is common in the deep gas. Carbon isotopic reversal between ethane and propane exists in the deep gas from Kuqa depression, and carbon isotopic reversal between methane and ethane is often found in the deep gas from Sichuan Basin. Secondary alteration such as mixing, TSR, diffusion, high temperature may have important contribution to such carbon isotopic anomaly.

(3) A boundary δ^2H_1 value of −150‰ is found between the deep gases from the continental sandstone reservoirs in the Kuqa depression (<−150‰) and the deep gases from the marine carbonate reservoirs in the craton area of Tarim Basin and Sichuan Basin (>−150‰). The deep gas from Kuqa depression has average δ^2H value of methane of −156‰, while the deep gas from the craton area of Tarim Basin has average δ^2H value of methane of −130‰ and the deep gas from Yuanba and Puguang gas fields has even heavier δ^2H_1 value of −122‰. The extremely high hydrogen isotope of methane in Dabei gas field is due to the high thermal maturity and possible saline depositional environment of the source rocks.

DATA AVAILABILITY STATEMENT

The original contributions presented in the study are included in the article/supplementary material, further inquiries can be directed to the corresponding author/s.

AUTHOR CONTRIBUTIONS

YN: manuscript writing. LY, FL, and JC: manuscript discussion. CY: experimental analyses. GZ: assistance in sample collection. All authors contributed to the article and approved the submitted version.

FUNDING

This work was funded by Petrochina Project (2017D-5008-08 and 2019A-0209) and China National Major S&T Projects (2016ZX05007-01).

ACKNOWLEDGMENTS

We thank Prof. Jinxing Dai from the PetroChina Research Institute of Petroleum Exploration and Development for long-standing helpful and open discussion on an earlier version of this study.

REFERENCES

Bernard, B. B., Brooks, J. M., and Sackett, W. M. (1976). Natural gas seepage in the Gulf of Mexico. *Earth Planet. Sci. Lett.* 31, 48–54. doi: 10.1016/0012-821x(76)90095-9

Berner, U., and Faber, E. (1996). Empirical carbon isotope/maturity relationships for gases from algal kerogens and terrigenous organic matter, based on dry, open-system pyrolysis. *Org. Geochem.* 24, 947–955. doi: 10.1016/s0146-6380(96)00090-3

Cai, C., Hu, W., and Worden, R. H. (2001). Thermochemical sulphate reduction in Cambro–Ordovician carbonates in Central Tarim. *Mar. Petrol. Geol.* 18, 729–741. doi: 10.1016/s0264-8172(01)00028-9

Cai, C., Worden, R. H., Bottrell, S. H., Wang, L., and Yang, C. (2003). Thermochemical sulphate reduction and the generation of hydrogen sulphide and thiols (mercaptans)in Triassic carbonate reservoirs from the Sichuan Basin. *China Chem. Geol.* 202, 39–57. doi: 10.1016/s0009-2541(03)00209-2

Cai, C., Wu, G., Li, K., Chen, L., Li, M., and Li, H. (2007). Thermochemical sulfate reduction and origin of sulfur in crude oils in Palaeozoic carbonates. *Bull. Min. Petrol. Geochem.* 26, 44–48.

Cai, C., Xie, Z., Worden, R. H., Hu, G., Wang, L., and He, H. (2004). Methane-dominated thermochemical sulphate reduction in the Triassic Feixianguan Formation East Sichuan Basin, China: towards prediction of fatal H2S concentrations. *Mar. Petrol. Geol.* 21, 1265–1279. doi: 10.1016/j.marpetgeo.2004.09.003

Cai, C., Zhang, C., Cai, L., Wu, G., Jiang, L., Xu, Z., et al. (2009). Origins of Palaeozoic oils in the tarim basin: evidence from sulfur isotopes and biomarkers. *Chem. Geol.* 268, 197–210. doi: 10.1016/j.chemgeo.2009.08.012

Cai, C., Zhang, C., He, H., and Tang, Y. (2013). Carbon isotope fractionation during methane-dominated TSR in East Sichuan Basin gasfields, China: a review. *Mar. Petrol. Geol.* 48, 100–110. doi: 10.1016/j.marpetgeo.2013.08.006

Chen, F., Zhang, Y., Zhu, G., Zhang, B., Lu, Y., and Zhang, Z. (2018). Geochemistry and accumulation process of deep natural gas in the platform-basin region, Tarim Basin. *Nat. Gas. Geosci.* 29, 880–891.

Chen, J., Li, W., Ni, Y., Dai, X., Liang, D., Deng, C., et al. (2018a). The Permian source rocks in the Sichuan Basin and its natural gas exploration potential (Part 2): geochemical characteristics of source rocks and latent capacity of natural gas resources. *Nat. Gas. Ind.* 38, 33–45.

Chen, J., Li, W., Ni, Y., Liang, D., Deng, C., and Bian, L. (2018b). The Permian source rocks in the Sichuan Basin and its natural gas exploration potential (Part 1): spatial distribution of source rocks. *Nat. Gas. Ind.* 38, 1–16.

Chen, J., Wang, X., Chen, J., Ni, Y., Xiang, B., He, W., et al. (2020). New formula to decipher the relationship between carbon isotope composition of methane and maturity of natural gas source rocks. *Sci. China* 64, 470–493.

Chen, J., Xu, Y., and Huang, D. (2000). Geochemical characteristics and origin of natural gas in Tarim basin, China. *AAPG Bull.* 84, 591–606.

Chen, J., Xu, Y., and Huang, D. (2001). Geochemical characteristics and origin of natural gas in east portion of Tarim basin (II). *Acta Sedimentol. Sin.* 19, 141–144.

Chen, M. (1988). *Geothermal in North China*. Beijing: Science Press.

Chen, R. (1995). Once more discussion on the Middle Jurassic marine-flooding event deposition of the Tarim Basin. *Exp. Petrol. Geol.* 17, 311–315.

Chinese Petroleum Society (2016). *Report on Advances in Deep Petroleum Geology Discipline*. Beijing: Science and Technology of China Press.

Clayton, C. (1991). Carbon isotope fractionation during natural gas generation from kerogen. *Mar. Petrol. Geol.* 8, 232–240. doi: 10.1016/0264-8172(91)90010-x

Cramer, B., Krooss, B. M., and Littke, R. (1998). Modelling isotope fractionation during primary cracking of natural gas: a reaction kinetic approach. *Chem. Geol.* 149, 235–250. doi: 10.1016/s0009-2541(98)00042-4

Dai, J. (1993). Characteristics of carbon and hydrogen isotopes of natural gases and their discriminations. *Nat. Gas. Geosci.* 4, 1–40.

Dai, J. (2016). *Giant Coal-Derived Gas Fields and Their Gas Sources in China*. Beijing: Science Press.

Dai, J., Chen, J., Zhong, N., Pang, X., and Qin, S. (2003). *Giant Gas Fields and Its Sources in China*. Beijing: Science Press.

Dai, J., Ding, W., Hou, L., and Mi, J. (2004a). "Deep gas exploration and research in Songliao Basin," in *Proceedings of Symposium on Deep Gas Exploration in Songliao Basin*, ed. C. Jia (Beijing: Petroleum Industry Press), 27–44.

Dai, J., Li, J., Luo, X., Zhang, W., Hu, G., Ma, C., et al. (2005a). Stable carbon isotope compositions and source rock geochemistry of the giant gas accumulations in the Ordos Basin, China. *Org. Geochem.* 36, 1617–1635. doi: 10.1016/j.orggeochem.2005.08.017

Dai, J., Liao, F., and Ni, Y. (2013). Discussions on the gas source of the Triassic Xujiahe Formation tight sandstone gas reservoirs in Yuanba and Tongnanba, Sichuan Basin: an answer to Yinfeng et al. *Petrol. Explor. Develop.* 40, 250–256.

Dai, J., Ni, Y., and Zou, C. (2012a). Stable carbon and hydrogen isotopes of natural gases sourced from the Xujiahe Formation in the Sichuan Basin, China. *Org. Geochem.* 43, 103–111. doi: 10.1016/j.orggeochem.2011.10.006

Dai, J., Ni, Y., Hu, G., Huang, S., Liao, F., Yu, C., et al. (2014). Stable carbon and hydrogen isotopes of gases from the large tight gas fields in China. *Sci. China* 44, 563–578.

Dai, J., Ni, Y., Huang, S., Gong, D., Liu, D., Feng, Z., et al. (2016a). Origins of secondary negative carbon isotopic series in natural gas. *Nat. Gas. Geosci.* 27, 1–7. doi: 10.1016/j.jnggs.2016.02.002

Dai, J., Ni, Y., Qin, S., Huang, S., Peng, W., and Han, W. (2018). Geochemical characteristics of ultra-deep natural gas in the Sichuan Basin, SW China. *Petrol. Explor. Develop.* 45, 619–628. doi: 10.1016/s1876-3804(18)30067-3

Dai, J., Ni, Y., Zhang, W., Huang, S., Gong, D., Liu, D., et al. (2016b). Relationships between wetness and maturity of coal-derived gas in China. *Petrol. Explor. Develop.* 43, 737–740. doi: 10.1016/s1876-3804(16)30088-x

Dai, J., Pei, X., and Qi, H. (1992). *Natural Gas Geology in China (Volume I)*. Beijing: Petroleum Industry Press.

Dai, J., and Qi, H. (1989). Relationship of δ13C-Ro of coal-derived gas in China. *Chin. Sci. Bull.* 34, 690–692.

Dai, J., Qin, S., Tao, S., Zhu, G., and Mi, J. (2005b). Development trends of natural gas industry and the significant progress on natural gas geological theories in China. *Nat. Gas. Geosci.* 16, 127–142.

Dai, J., Song, Y., Dai, C., and Wang, D. (1996). Geochemistry and accumulation of carbon dioxide gases in China. *AAPG Bull.* 80, 1615–1626.

Dai, J., Xia, X., Li, Z., Coleman, D. D., Dias, R. F., Gao, L., et al. (2012b). Inter-laboratory calibration of natural gas round robins for δ2H and δ13C using off-line and on-line techniques. *Chem. Geol.* 31, 49–55. doi: 10.1016/j.chemgeo.2012.03.008

Dai, J., Xia, X., Qin, S., and Zhao, J. (2004b). Origins of partially reversed alkane δ13C values for biogenic gases in China. *Org. Geochem.* 35, 405–411. doi: 10.1016/j.orggeochem.2004.01.006

Deng, B., Liu, S., Liu, S., Li, Z., and Zhao, J. (2009). Restoration of exhumation thickness and its significance in Sichuan basin, China. *J. Chengdu Univ. Technol.* 36, 675–686.

Deng, Y., Hu, G., and Zhao, C. (2018). Geochemical characteristics and origin of natural gas in Changxing-Feixianguan formations from Longgang gasfield in the Sichuan basin, China. *Nat. Gas. Geosci.* 29, 892–907.

Dyman, T. S., Wyman, R. E., Kuuskraa, V. A., Lewan, M. D., and Cook, T. A. (2003). Deep natural gas resources. *Nat. Resour. Res.* 12, 41–56.

Feng, C., Liu, S., Wang, L., and Li, C. (2009). Present-day geothermal regime in Tarim Basin, northwest China. *Chin. J. Geophys.* 52, 2752–2762.

Gang, W., Gao, G., Hao, S., Huang, Z., and Zhu, L. (1997). Carbon isotope of ethane applied in the analyses of genetic types of natural gas. *Exp. Petrol. Geol.* 19, 164–167.

Guo, T. (2011). Basic characteristics of deep reef bank reservoirs and major controlling factors of gas pools in the Yuanba gas field. *Nat. Gas. Ind.* 31, 12–16.

Guo, X., Huang, R., Fu, X., and Duan, J. (2014). Gas accumulation and exploration direction of the Permian and Triassic reservoirs of reef-bank facies in Sichuan Basin. *Oil Gas Geol.* 35, 295–302.

Guo, X., Liu, K., Jia, C., Song, Y., Zhao, M., Zhuo, Q., et al. (2016). Fluid evolution in the Dabei Gas Field of the Kuqa Depression, Tarim Basin, NW China: implications for fault-related fluid flow. *Mar. Petrol. Geol.* 78, 1–16. doi: 10.1016/j.marpetgeo.2016.08.024

Hallam, A. (1978). Eustatic cycles in the Jurassic. *Palaeogeogr. Palaeoclimatol. Palaeoecol.* 23, 1–32. doi: 10.1016/0031-0182(78)90079-2

Hallam, A. (2001). A review of the broad pattern of Jurassic sea-level changes and their possible causes in the light of current knowledge. *Palaeogeogr. Palaeoclimatol. Palaeoecol.* 167, 23–37. doi: 10.1016/s0031-0182(00)00229-7

Hao, F., Guo, T., Zhu, Y., Cai, X., Zou, H., and Li, P. (2008). Evidence for multiple stages of oil cracking and thermochemical sulfate reduction in the Puguang gas field, Sichuan Basin, China. *AAPG Bull.* 92, 611–637. doi: 10.1306/01210807090

Hao, F., Zhang, X., Wang, C., Li, P., Guo, T., Zou, H., et al. (2015). The fate of CO2 derived from thermochemical sulfate reduction (TSR) and effect of TSR on carbonate porosity and permeability, Sichuan Basin, China. *Earth-Sci. Rev.* 141, 154–177. doi: 10.1016/j.earscirev.2014.12.001

He, Z., Jin, X., Wo, Y., Li, H., Bai, Z., Jiao, C., et al. (2016). Hydrocarbon accumulation characteristics and exploration domains of ultra-deep marine carbonates in China. *China Petrol. Explor.* 21, 3–14.

Hu, A., Li, M., Yang, C., Dai, J., Ma, Y., and Guo, T. (2010). Characteristics of reservoir bitumen in Puguang and Maoba gas fields with high H2S content in north-eastern Sichuan basin. *Acta Petrol. Sin.* 31, 231–236.

Hu, G., Yu, C., Gong, D., and Tian, X. (2014). The origin of natural gas and influence on hydrogen isotope of methane by TSR in the Upper Permian Changxing and the Lower Triassic Feixianguan formations in northern Sichuan Basin, SW China. *Energ. Explor. Exploit.* 32, 139–158. doi: 10.1260/0144-5987.32.1.139

Huang, D., Liu, B., Wang, T., Xu, Y., Chen, S., and Zhao, M. (1996). Genetic types of natural gases and their maturity discrimination in the east of Tarim Basin. *Sci. China* 39, 101–111.

Huang, R. (2014). Source and Accumulation of Natural Gas in Leikoupo Formation, Yuanba Area, Eastern-Northern Sichuan Basin. *Geoscience* 28, 412–418.

Huang, S., Huang, K., Tong, H., Liu, L., Sun, W., and Zhong, Q. (2010). Origin of CO2 in natural gas from the Triassic Feixianguan Formation of Northeast Sichuan Basin. *Sci. China* 53, 642–648. doi: 10.1007/s11430-010-0046-7

James, A. T. (1983). Correlation of natural gas by use of carbon isotopic distribution between hydrocarbon components. *AAPG Bull.* 67, 1176–1191.

Jenden, P. D., Newell, K. D., Kaplan, I. R., and Watney, W. L. (1988). Composition of stable-isotope geochemistry of natural gases from Kansas, mid-continent, USA. *Chem. Geol.* 71, 117–147. doi: 10.1016/0009-2541(88)90110-6

Krouse, H. R., Viau, C. A., Eliuk, L. S., Ueda, A., and Halas, S. (1988). Chemical and isotopic evidence of thermochemical sulphate reduction by light hydrocarbon gases in deep carbonate reservoirs. *Nature* 333, 415–419. doi: 10.1038/333415a0

Li, M., Huang, Y., Obermajer, M., Jiang, C., Snowdon, L. R., and Fowler, M. G. (2001). Hydrogen isotopic compositions of individual alkanes as a new approach to petroleum correlation: case studies from the Western Canada Sedimentary Basin. *Org. Geochem.* 32, 1387–1399. doi: 10.1016/s0146-6380(01)00116-4

Li, P., Hao, F., Guo, X., Zou, H., Yu, X., and Wang, G. (2015). Processes involved in the origin and accumulation of hydrocarbon gases in the Yuanba gas field, Sichuan Basin, southwest China. *Mar. Petrol. Geol.* 59, 150–165. doi: 10.1016/j.marpetgeo.2014.08.003

Li, P., Hao, F., Guo, X., Zou, H., Zhu, Y., Yu, X., et al. (2016). Origin and distribution of hydrogen sulfide in the Yuanba gas field, Sichuan Basin, Southwest China. *Mar. Petrol. Geol.* 75, 220–239. doi: 10.1016/j.marpetgeo.2016.04.021

Li, X., Xiao, Z., Hu, G., Tian, H., and Zhou, Q. (2005). Origin and geochemistry of natural gas in Kuqa depression, Tarim Basin. *Xinjiang Petrol. Geol.* 26, 489–492.

Li, Z. (2016). Research frontiers of fluid-rock interaction and oil-gas formation in deep-buried basins. *Bull. Min. Petrol. Geochem.* 35, 807–816.

Liang, D., Chen, J., Zhang, B., Zhang, S., Wang, F., and Zhao, M. (2003a). *Terrestrial Oil and Gas Generation in the Kuqa Depression, Tarim Basin*. Beijing: Oil Industry Press.

Liang, D., Zhang, S., Chen, J., Wang, F., and Wang, P. (2003b). Organic geochemistry of oil and gas in the Kuqa depression, Tarim Basin, NW China. *Org. Geochem.* 34, 873–888. doi: 10.1016/s0146-6380(03)00029-9

Liang, D., Zhang, S., Zhao, M., and Wang, F. (2002). Hydrocarbon sources and stages of reservoir formation in Kuqa depression,Tarim basin. *Chin. Sci. Bull. Suppl.* 1, 62–70. doi: 10.1007/bf02902820

Liu, Q., Jin, Z., Wu, X., Liu, W., Gao, B., Zhang, D., et al. (2014). Origin and carbon isotope fractionation of CO2 in marine sour gas reservoirs in the Eastern Sichuan Basin. *Org. Geochem.* 74, 22–32. doi: 10.1016/j.orggeochem.2014.01.012

Liu, Q., Qin, S., Li, J., Liu, W., Zhang, D., Zhou, Q., et al. (2007). Natural gas geochemistry and its origins in Kuqa depression. *Sci. China* 51, 174–182. doi: 10.1007/s11430-008-5003-3

Liu, Q. Y., Worden, R. H., Jin, Z. J., Liu, W. H., Li, J., Gao, B., et al. (2013). TSR versus non-TSR processes and their impact on gas geochemistry and carbon stable isotopes in Carboniferous, Permian and Lower Triassic marine carbonate gas reservoirs in the Eastern Sichuan Basin, China. *Geochim. Cosmochim. Acta* 100, 96–115. doi: 10.1016/j.gca.2012.09.039

Liu, S., Sun, W., Li, Z., Deng, B., and Liu, S. (2008). Tectonic uplifting and gas pool formation since Late Cretaceous epoch, Sichuan basin. *Nat. Gas. Geosci.* 19, 293–300.

Liu, W., Zhang, D., Zheng, J., Chen, M., Wang, X., and Gao, B. (2005). A preliminary discussion on geochemical dynamic tracing of oil/gas reservoiring process. *Oil Gas Geol.* 26, 717–723.

Lorant, F., Prinzhofer, A., Behar, F., and Huc, A. (1998). Carbon isotopic and molecular constraints on the formation and the expulsion of thermogenic

hydrocarbon gases. *Chem. Geol.* 147, 249–264. doi: 10.1016/s0009-2541(98)00017-5

Ma, Y. (2008). Geochemical characteristics and origin of natural gases from Puguang gas field on eastern Sichuan basin. *Nat. Gas. Geosci.* 19, 1–7. doi: 10.1016/j.coal.2016.12.003

Ma, Y., Cai, X., Zhao, P., Luo, Y., and Zhang, X. (2010). Distribution and further exploration of the large-medium sized gas fields in Sichuan Basin. *Acta Petrol. Sin.* 31, 347–354.

Ma, Y., Guo, X., Guo, T., Huang, R., Cai, X., and Li, G. (2007). The Puguang gas field: new giant discovery in the mature Sichuan Basin, southwest China. *AAPG Bull.* 91, 627–643. doi: 10.1306/11030606062

Ma, Y., Zhang, S., Guo, T., Zhu, G., Cai, X., and Li, M. (2008). Petroleum geology of the Puguang sour gas field in the Sichuan Basin, SW China. *Mar. Petrol. Geol.* 25, 371–386. doi: 10.1016/j.marpetgeo.2008.01.009

Milkov, A. V., and Etiope, G. (2018). Revised genetic diagrams for natural gases based on a global dataset of >20,000 samples. *Org. Geochem.* 125, 109–120. doi: 10.1016/j.orggeochem.2018.09.002

Ni, Y., Dai, J., Zhu, G., Zhang, S., Zhang, D., Su, J., et al. (2013). Stable hydrogen and carbon isotopic ratios of coal-derived and oil-derived gases: a case study in the Tarim basin, NW China. *Int. J. Coal Geol.* 116–117, 302–313. doi: 10.1016/j.coal.2013.06.006

Ni, Y., Liao, F., Gao, J., Chen, J., Yao, L., and Zhang, D. (2019). Hydrogen isotopes of hydrocarbon gases from different organic facies of the Zhongba gas field, Sichuan Basin, China. *J. Pet. Sci. Eng.* 179, 776–786. doi: 10.1016/j.petrol.2019.04.102

Ni, Y., Ma, Q., Ellis, G. S., Dai, J., Katz, B., Zhang, S., et al. (2011). Fundamental studies on kinetic isotope effect (KIE) of hydrogen isotope fractionation in natural gas systems. *Geochim. Cosmochim. Acta* 75, 2696–2707. doi: 10.1016/j.gca.2011.02.016

Ni, Y., Zhang, D., Liao, F., Gong, D., Xue, P., Yu, F., et al. (2015). Stable hydrogen and carbon isotopic ratios of coal-derived gases from the Turpan-Hami Basin, NW China. *Int. J. Coal Geol.* 152, 144–155. doi: 10.1016/j.coal.2015.07.003

Pan, C. C., Yu, L. P., Liu, J. Z., and Fu, J. M. (2006). Chemical and carbon isotopic fractionations of gaseous hydrocarbons during abiogenic oxidation. *Earth Planet. Sci. Lett.* 246, 70–89. doi: 10.1016/j.epsl.2006.04.013

Prinzhofer, A., and Huc, A. (1995). Genetic and post-genetic molecular and isotopic fractinations in natural gases. *Chem. Geol.* 126, 281–290. doi: 10.1016/0009-2541(95)00123-9

Qin, S. (1999). Origin of abnormal natural gas in Kuqa Depression of Tarim Basin. *Petrol. Exploration.* 4, 21–23.

Qin, S., Dai, J., and Liu, X. (2007). The controlling factors of oil and gas generation from coal in the Kuqa Depression of Tarim Basin, China. *Int. J. Coal Geol.* 70, 255–263. doi: 10.1016/j.coal.2006.04.011

Qin, S., Yang, Y., Lv, F., Zhou, H., and Li, Y. (2016). The origin of gas in the Changxing–Feixianguan gas pools in the Longgang gas field in the Sichuan Basin, China. *J. Nat. Gas. Geosci.* 1, 327–334. doi: 10.1016/j.jnggs.2016.11.002

Rooney, M. A., Claypool, G. E., and Chung, H. M. (1995). Modeling thermogenic gas generation using carbon isotope ratios of natural gas hydrocarbons. *Chem. Geol.* 126, 219–232. doi: 10.1016/0009-2541(95)00119-0

Schoell, M. (1980). The hydrogen and carbon isotopic composition of methane from natural gases of various origins Geochim. *Cosmochim. Acta* 44, 649–661. doi: 10.1016/0016-7037(80)90155-6

Shen, P. (1995). Characteristics of carbon and hydrogen isotopic compositions of light hydrocarbons. *Sci. China* 38, 211–220.

Stahl, W. J., and Carey, B. D. (1975). Source-rock identification by isotope analyses of natural gases from fields in the Val Verde and Delaware basins, West Texas. *Chem. Geol.* 16, 257–267. doi: 10.1016/0009-2541(75)90065-0

Strategic Research Center of Oil and Gas Resources (2017). *National Petroleum Resource Assessment*. Beijing: China Land Press.

Sun, L., Zou, C., Zhu, R., Zhang, Y., Zhang, S., Zhang, B., et al. (2013). Formation, distribution and potential of deep hydrocarbon resources in China. *Petrol. Explor. Dev.* 40, 687–695. doi: 10.1016/s1876-3804(13)60093-2

Sun, W., Liu, S., Cao, J., Deng, B., Song, J., Wang, G., et al. (2017). Analysis on the formation conditions of large-scale marine deep and super-deep strata gas fields in the middle-nothern segments of western Sichuan Superimposed Basin, China. *Acta Petrol. Sin.* 33, 1171–1188.

Tang, Y., Perry, J. K., Jenden, P. D., and Schoell, M. (2000). Mathematical modeling of stable carbon isotope ratios in natural gases. *Geochim. Cosmochim. Acta* 64, 2673–2687. doi: 10.1016/s0016-7037(00)00377-x

Tian, Z., Zhang, G., Zou, H., Li, Q., and Pi, X. (2001). The major controlling factors and pool-forming pattern of oil and gas reservoirs in Kuqa petroleum system, Tarim basin. *Petrol. Explor. Dev.* 28, 12–16.

Tilley, B., and Muehlenbachs, K. (2006). Gas maturity and alteration systematics across the estern Canada Sedimentary Basin from four mud gas isotope depth profiles. *Org. Geochem.* 37, 1857–1868. doi: 10.1016/j.orggeochem.2006.08.010

Tuo, J. (2002). Research status and advances in deep oil and gas exploration. *Adv. Earth Sci.* 17, 565–571.

Wang, F., Liu, C., Zhu, L., Zhang, S., Zhang, B., and Liang, D. (2002). Thermal maturity of the Cambrian source rocks in the platform in Tarim basin Xinjiang Petrol. *Geology* 23, 372–375.

Wang, G. (2005). *Analysis of Natural Gas Accumulation Conditions in the Cratonic Area of Tarim Basin*. Ph.D thesis, Southwest Petroleum University, Chengdu.

Wang, J., Zhang, H., Zhang, R., Yang, X., Zeng, Q., Chen, X., et al. (2018). Enhancement of ultra-deep tight sandstone reservoir quality by fractures: a case study of Keshen gas field in Kuqa depression, Tarim Basin. *Oil Gas Geol.* 39, 77–88.

Wang, Y., Chen, J., Pang, X., Zhang, B., Chen, Z., Zhang, G., et al. (2018). Origin of deep sour natural gas in the Ordovician carbonate reservoir of the Tazhong Uplift, Tarim Basin, northwest China: insights from gas geochemistry and formation water. *Mar. Petrol. Geol.* 91, 532–549. doi: 10.1016/j.marpetgeo.2018.01.029

Wang, Q., Bao, J., Xie, Z., and Wang, S. (2012). Geochemical characteristics and origin of the natural gas in the Dabei-Dawanqi. *J. Yangtze Univ. Sci. & Eng.* 9, 28–31. doi: 10.1016/s0140-6701(02)80284-3

Wang, S. (1994). Geochemical characteristics of natural gases from the Jurassic-Sinian formations in the Sichuan basin. *Nat. Gas. Ind.* 14, 1–5.

Wang, T., Song, D., Li, M., Yang, C., Ni, Z., Li, H., et al. (2014). Natural gas source and deep gas exploration potential of the *Ordovician yingshan* formation in the shunnan-gucheng region,tarim basin. *Oil Gas Geol.* 35:602.

Wang, X., Liu, W., Shi, B., Zhang, Z., Xu, Y., and Zheng, J. (2015). Hydrogen isotope characteristics of thermogenic methane in Chinese sedimentary basins. *Org. Geochem.* 8, 178–189. doi: 10.1016/j.orggeochem.2015.03.010

Wang, X., Zhi, D., Wang, Y., Chen, J., Qin, Z., Liu, D., et al. (2013). *Source Rocks and Oil-Gas Geochemistry in Junggar Basin*. Beijing: Oil Industry Press.

Wang, Z. (2014). Formation mechanism and enrichment regularities of Kelasu subsalt deep large gas field in Kuqa depression, Tarim basin. *Nat. Gas. Geosci.* 25, 153–166.

Wang, Z., Wang, G., Xiao, Z., Li, X., Lu, Y., and Zhang, Q. (2005). *Kinetics on Natural Gas Generation in the Kuqa Foreland Basin*. Beijing: Science Press.

Wei, Q., Li, X., Liang, W., Sun, K., Xie, Z., Li, J., et al. (2019). Geochemical characteristics and genesis of deep tight sandstone gas in the Dabei-Keshen Zone, Kuqa Depression. *Bull. Min. Petrol. Geochem.* 38, 418–427.

Whiticar, M. J. (1999). Carbon and hydrogen isotope systematics of bacterial formation and oxidation of methane. *Chem. Geol.* 161, 291–314. doi: 10.1016/s0009-2541(99)00092-3

Worden, R. H., and Smalley, P. C. (1996). H2S-producing reactions in deep carbonate gas reservoirs: Khuff Formation, Abu Dhabi. *Chem. Geol.* 133, 157–171. doi: 10.1016/s0009-2541(96)00074-5

Worden, R. H., Smalley, P. C., and Oxtoby, N. H. (1995). *Gas Souring by Thermochemical Sulfate Reduction at 140oC*. New York, NY: Office of Scientific and Technical Information.

Wu, X., Liu, G., Liu, Q., Liu, J., and Yuan, X. (2015a). Geochemical characteristics and genetic types of natural gas in the Changxing-Feixianguan formations from Yuanba gasfield in the Sichuan basin. *Nat. Gas. Geosci.* 26, 2155–2165.

Wu, X., Liu, G., Liu, Q., Liu, J., and Yuan, X. (2015b). Geochemical characteristics and genetic types of natural gas in the Changxing-Feixianguan Formations from the Yuanba Gas Field in the Sichuan Basin, China. *J. Nat. Gas. Geosci.* 1, 267–275. doi: 10.1016/j.jnggs.2016.09.003

Wu, X., Tao, X., and Liu, J. (2014). Geochemical characteristics and genetic types of natural gas from Lunnan area in Tarim Basin. *Nat. Gas. Geosci.* 25, 53–61.

Wu, Z., Liu, X., Li, X., Wang, X., and Zheng, J. (2017). The application of noble gas isotope in gas-source correlation of Yuanba reservoir, Sichuan basin. *Nat. Gas. Geosci.* 28, 1072–1077.

Xia, X., and Gao, Y. (2017). Mechanism of linear covariations between isotopic compositions of natural gaseous hydrocarbons. *Org. Geochem.* 113, 115–123. doi: 10.1016/j.orggeochem.2017.07.003

Xiao, Z., Xie, Z., Li, Z., and Ma, C. (2008). Isotopic characteristics of natural gas of Xujiahe Formation in southern and middle of Sichuan basin. *Geochimica* 37, 245–250.

Xu, M., Zhu, C., Tian, Y., Rao, S., and Hu, S. (2011). Borehole temperature logging and characteristics of subsurface temperature in the Sichuan Basin. *Chin. J. Geophys.* 54, 1052–1060.

Yang, J., Wang, Y., Wang, L., Wen, Y., Liu, H., and Zhou, G. (2002). The origin of natural gases and geochemistry characters of Changxing reef and Feixianguan oolitic beach gas reservoirs in eastern Sichuan Basin. *Acta Sedimentol. Sin.* 20, 349–353.

Yin, F., Liu, R., Wang, W., Zhang, Y., and Pan, L. (2013). Geochemical characters of the tight sandstone gas from Xujiahe Formation in Yuanba gas field and its gas source. *Nat. Gas. Geosci.* 24, 621–627.

Zhang, B., Chen, J., Bian, L., and Zhang, S. (2006). Rediscussion on the sea-slooding events during Triassic to Jurassic of Kuqa Depression in Tarim Basin. *Acta Geol. Sin.* 80, 236–313.

Zhang, J. (2002). Discussion on the origin of the Kela2 gas field. *Xinjiang Petrol. Geol.* 23:65.

Zhang, S., Zhang, B., Zhu, G., Wang, H., and Li, Z. (2011). Geochemical evidence for coal-derived hydrocarbons and their charge history in the Dabei Gas Field, Kuqa Thrust Belt, Tarim Basin, NW China. *Mar. Petrol. Geol.* 28, 1364–1375. doi: 10.1016/j.marpetgeo.2011.02.006

Zhang, Z., Liu, W., Zheng, J., Wang, Q., and Chen, G. (2006). Carbon isotopic reversed distribution of the soluble organic components for the Cambrian and Ordovician carbonate rocks in Tabei and Tazhong areas. *J. Mineral. Petrol.* 26, 69–74.

Zhao, J. (2003). *Theory and Application of Natural Gas Accumulation in Foreland Basin*. Beijing: Oil Industry Press.

Zhao, L., Zhang, T., Yang, X., Guo, X., and Rao, H. (2018). Gas-water distribution characteristics and formation mechanism in deep tight sandstone gas reservoirs of Keshen block, Kuqa Depression, Tarim Basin. *Nat. Gas. Geosci.* 29, 500–509.

Zhao, W., Xu, C., Wang, T., Wang, H., Wang, Z., Bian, C., et al. (2011). Comparative study of gas accumulations in the Permian Changxing reefs and Triassic Feixianguan oolitic reservoirs between Longgang and Luojiazhai-Puguang in the Sichuan Basin. *Chin. Sci. Bull.* 56, 3310–3320.

Zhao, Z. (2019). Analysis of global oil and gas exploration characteristics during the past decade. *Oil Forum* 38, 58–64.

Zhou, S., Li, Y., Zhang, Z., Luo, B., Yuan, J., and Duan, Y. (1999). Influence on organic matter cauced by Mesozoic transgressive events in the Kuqa Depression, Tarim Basin. *Acta Sedimentol.* 17, 106–111.

Zhou, X. (1998). Traces of plutonic inorganic gas were found in the Tarim Basin. *Nat. Gas. Geosci.* 9, 40–41.

Zhou, X., and Bao, J. (2011). Geochemical characteristics and genesis type of natural gas in the Kuqa Depression Petrol. *Geol. Eng.* 25, 9–12.

Zhou, X., Lü, X., Zhu, G., Cao, Y., Yan, L., and Zhang, Z. (2019). Origin and formation of deep and superdeep strata gas from Gucheng-Shunnan block of the Tarim Basin, NW China. *J. Pet. Sci. Eng.* 177, 361–373. doi: 10.1016/j.petrol.2019.02.059

Zhu, G., Chi, L., Zhang, Z., Li, T., Yang, H., Chen, W., et al. (2019a). Composition and origin of molecular compounds in the condensate oils of the Dabei gas field, Tarim Basin, NW China. *Petrol. Explor. Dev.* 46, 482–495.

Zhu, G., Zhang, Z., Zhou, X., Li, T., Han, J., and Sun, C. (2019b). The complexity, secondary geochemical process, genetic mechanism and distribution prediction of deep marine oil and gas in the Tarim Basin, China. *Earth Sci. Rev.* 198:102930. doi: 10.1016/j.earscirev.2019.102930

Zhu, G., Huang, H., and Wang, H. (2015). Geochemical significance of discovery in cambrian reservoirs at Well ZS1 of the Tarim Basin, Northwest China. *Energy Fuels* 29, 1332–1344. doi: 10.1021/ef502345n

Zhu, G., Zhang, B., Yang, H., Su, J., and Han, J. (2014). Origin of deep strata gas of Tazhong in Tarim Basin, China. *Org. Geochem.* 74, 85–97. doi: 10.1016/j.orggeochem.2014.03.003

Zhu, G., Zhang, S., Liang, Y., Dai, J., and Li, J. (2005). Isotopic evidence of TSR origin for natural gas bearing high H2S contents within the Feixianguan Formation of the northeastern Sichuan Basin, southwestern China. *Sci. China* 48, 1960–1971. doi: 10.1360/082004-147

Zhu, G., Zhang, S., Liang, Y., Ma, Y., Dai, J., Li, J., et al. (2006). The characteristics of natural gas in Sichuan basin and its sources. *Earth Sci. Front.* 13, 234–248.

Conflict of Interest: All authors are affiliated with the company institution Research Institute of Petroleum Exploration and Development, PetroChina.

Copyright © 2021 Ni, Yao, Liao, Chen, Yu and Zhu. This is an open-access article distributed under the terms of the Creative Commons Attribution License (CC BY). The use, distribution or reproduction in other forums is permitted, provided the original author(s) and the copyright owner(s) are credited and that the original publication in this journal is cited, in accordance with accepted academic practice. No use, distribution or reproduction is permitted which does not comply with these terms.

frontiers in Earth Science

ORIGINAL RESEARCH
published: 22 April 2021
doi: 10.3389/feart.2021.542912

Preliminary Experimental Study of Methane Adsorption Capacity in Shale After Brittle Deformation Under Uniaxial Compression

Mingliang Liang[1,2,3], Zongxiu Wang[1,2]*, Guodong Zheng[4], Xiaobao Zhang[4], Hugh Christopher Greenwell[3], Kaixun Zhang[1,2], Xingqiang Feng[1,2], Linyan Zhang[1,2] and Huijun Li[1,2]*

[1] Institute of Geomechanics, Chinese Academy of Geological Sciences, Beijing, China, [2] Key Laboratory of Petroleum Geomechanics, China Geological Survey, Beijing, China, [3] Department of Earth Sciences, Durham University, Durham, United Kingdom, [4] Key Laboratory of Petroleum Resources, Gansu Province, Northwest Institute of Eco-Environment and Resources, Chinese Academy of Sciences, Lanzhou, China

OPEN ACCESS

Edited by:
Giovanni Martinelli,
National Institute of Geophysics and Volcanology, Section of Palermo, Italy

Reviewed by:
Xianglu Tang,
China University of Petroleum, China
Vikram Vishal,
Indian Institute of Technology Bombay, India

***Correspondence:**
Mingliang Liang
liangmingl09@mails.ucas.ac.cn
Zongxiu Wang
wangzongxiu@sohu.com

Specialty section:
This article was submitted to Geochemistry, a section of the journal Frontiers in Earth Science

Received: 14 March 2020
Accepted: 29 March 2021
Published: 22 April 2021

Citation:
Liang M, Wang Z, Zheng G, Zhang X, Greenwell HC, Zhang K, Feng X, Zhang L and Li H (2021) Preliminary Experimental Study of Methane Adsorption Capacity in Shale After Brittle Deformation Under Uniaxial Compression. Front. Earth Sci. 9:542912. doi: 10.3389/feart.2021.542912

This paper presents a preliminary experimental study on methane adsorption capacity in shales before and after artificial deformation. The experimental results are based on uniaxial compression and methane isothermal adsorption tests on different shale samples from the Silurian Longmaxi Formation, Daozhen County, South China. Two sets of similar cylindrical samples were drilled from the each same bulk sample, one set was subjected to a uniaxial compressive simulation test and then crushed as artificial deformed shale sample, the other set was directly crushed as the original undeformed shale sample. And then we conducted a comparative experimental study of the methane adsorption capacity of original undeformed and artificially deformed shales. The uniaxial compression simulation results show that the failure mode of all samples displayed brittle deformation. The methane isothermal adsorption results show that the organic matter content is the main controlling factor of shale methane adsorption capacity. However, the comparative results also show that the compression and deformation have an effect on methane adsorption capacity, with shale methane adsorption capacity decreasing by about 4.26–8.48% after uniaxial compression deformation for the all shale samples in this study.

Keywords: methane adsorption capacity, Longmaxi Shale, uniaxial compressive, brittle deformation, TOC

INTRODUCTION

The adsorbed gas accounts for a large proportion of the total shale gas content and has a significant impact on shale gas resource potential (Ross and Bustin, 2009; Zhang et al., 2012; Wu et al., 2014; Vishal et al., 2019). For example, in the Devonian shale in the Appalachian basin, United States, the adsorbed gas content has been shown to be higher than 50% of the total gas in place (Lu et al., 1995). Ross and Bustin (2009), indicated that the adsorbed gas accounts for 20–85% of total gas for the Antrim, Ohio, New Albany, Barnett, and Lewis shale gas plays. In non-USA based shale systems, based on the raw data from the Changning and Jiaoshiba gas fields, we could calculated that the adsorbed gas accounts for 20–40% of total gas content of the Longmaxi shale (Wang et al., 2016).

In order to determine the amount of adsorbed methane (CH_4) on shale samples, previous studies have performed CH_4 sorption capacity measurements (Ross and Bustin, 2007, 2008, 2009; Chalmers and Bustin, 2008a,b; Zhang et al., 2012; Tan et al., 2014; Psarras et al., 2017; He et al., 2019; Wei et al., 2019). The CH_4 adsorption capacity in shale samples has been widely recognized as varying significantly depending upon the composition (organic matter and clay mineral type and amount) of the shales, as well as the physical porosity and pore properties (Hill et al., 2007; Javadpour et al., 2007; Ross and Bustin, 2007, 2008, 2009; Chalmers and Bustin, 2008a,b; Jenkins and Boyer, 2008; Zhang et al., 2012; Hou et al., 2014; Tan et al., 2014; He et al., 2019; Tang et al., 2019; Jiang et al., 2020). Thus, an understanding of the relationships between organic matter (type, maturity and content), clay mineral (type and content), porosity (microporous structural framework) and methane sorption capacity in shale is crucial for assessing the shale reservoir.

The organic matter (OM) content is the first key factor that determines the gas adsorption capacity of shale (Hill et al., 2007; Mastalerz et al., 2012). Positive correlations are reported between methane sorption capacity and both total organic carbon (TOC) and micropore (<2 nm) volume in shale, indicating micropores associated with the OM are a significant factor controlling gas adsorption (Chalmers and Bustin, 2007; Ross and Bustin, 2007, 2009; Tan et al., 2014). Guo et al. (2017) studied samples from the Mesozoic shales in the Tarim Basin, observing that the CH_4 adsorption capacity increased with increasing TOC content. By studying the relationship between CH_4 sorption capacity and pore characteristics of shales from the Baltic Basin, Poland, Topór et al. (2017) found that CH_4 adsorption in was predominantly controlled by the OM micropore structure. Comparative experiments of methane adsorption on both original shale samples and isolated kerogen were conducted by Zhang et al. (2012), with the total amount of methane adsorbed directly proportional to the TOC content and an average maximum CH_4 sorption of 1.36 $mmol.g^{-1}$ TOC. Yang et al. (2016) found that CH_4 sorption capacity increased with the TOC content, surface area and micropore volume, suggesting OM provided abundant adsorption surfaces, as well as pore space, and enhanced the CH_4 sorption capacity. Moreover, the type of OM and its thermal maturity (usually defined by Ro%) are also known to influence the CH_4 sorption capacity of shales (Lu et al., 1995; Hill et al., 2004; Zhang et al., 2012). Based on CH_4 adsorption experiments of shale samples with different Ro%, Zhang et al. (2012) found that those kerogen types with a greater degree of aromatization have higher gas adsorbing capacity than those with aliphatic structures, leading to Langmuir pressure (P_L) changes according to kerogen type in the sequence of Type I > Type II > Type III. However, compared to the Longmaxi Shale, and other shales, that display Ro% less than 3.0%, Li et al. (2017) argued that the Niutitang shales, with Ro% higher than 4.0% have lower methane adsorption capacity. Similarly, Topór et al. (2017) also observed that CH_4 adsorption potential decreases in micropores with increasing maturity of shales from the Baltic Basin, Poland.

Clay minerals also influence the methane adsorption capacity of shale, especially for organic-lean shale deposits, with low TOC. Cheng and Huang (2004) pointed out that many clay minerals consist of porous aggregates and structures, providing larger surface areas and more potential adsorption sites than other minerals. Ji et al. (2012) observed that methane adsorption capacity showed significant differences with different clay minerals, as CH_4 sorption capacity decreases in the order montmorillonite > I–S mixed layer > kaolinite > chlorite > illite. To try and understand adsorption at mixed mineral-OM interfaces, a study of gas adsorption in organic-inorganic pores made in graphene – montmorillonite composites, as a model shale matrix, by Chen et al. (2020) found that the graphene (OM) surface shows a significantly stronger adsorption capacity than the graphene – montmorillonite, though this decreased with increasing pressure.

As well as shale composition affecting the CH_4 adsorption, there are also environmental effects. Considerable *in situ* and experimental work has been performed on understanding the gas adsorption capacity of shale with environmental factors including the effect of moisture (Zou et al., 2018), high pressure (Li et al., 2016) and particle size (Gao et al., 2018), contributing to the wider understanding of the adsorption characteristics of shales. While the adsorption of CH_4 at nanopores and their associated surface area in shale is controlled by shale matrix composition (OM and mineral content) and geological environmental conditions, it is also affected by tectonic stress and structural deformation (Ma et al., 2015; Liang et al., 2017; He et al., 2018; Wang, 2020; Zhu et al., 2020). Aplin et al. (2006) reported that the microstructure and pore properties of Mexican mudstones changed due to mechanical compaction. Based on uniaxial and/or triaxial compression experiments, several studies have been conducted on the deformational behavior, microstructure and pore/fracture evolution of shale (Arora and Mishra, 2015; Mishra and Verma, 2015; Minaeian et al., 2017; Wang and Li, 2017; Wang et al., 2018; Bakhshian and Hosseini, 2019; Liu et al., 2019; Tan et al., 2019), with microstructure, pore properties and permeability all influenced by compression and deformation. Using artificial compaction to make pellets of Wyoming montmorillonite powder, (Kuila and Prasad, 2013) found that compaction could results in decrease in pore volume and reduction of macropores of the clays. However, to our knowledge, hitherto the effect of compressive deformation on the CH_4 adsorption capacity of shale has received little attention.

With the progress of shale gas research in tectonically deformed areas in southern China, studies have been conducted using natural deformation shale (Ma et al., 2015, 2020; Liang et al., 2017; Zhu et al., 2020) and numerical simulation (Wei et al., 2019). Researchers have recognized that stress deformation has effect on shale adsorption capacity, but whether the relationship between stress deformation and adsorption capacity is promoting (Ma et al., 2015, 2020) or depressing (Wei et al., 2019; Zhu et al., 2020) is still unclear. In this paper we present an experimental study of uniaxial compression induced brittle deformation and its influence on the methane adsorption capacity of shale. The main purpose of the study was to investigate whether or not compression impacted CH_4 adsorption capacity of shale and, if so, quantify the scale of the change in adsorption capacity.

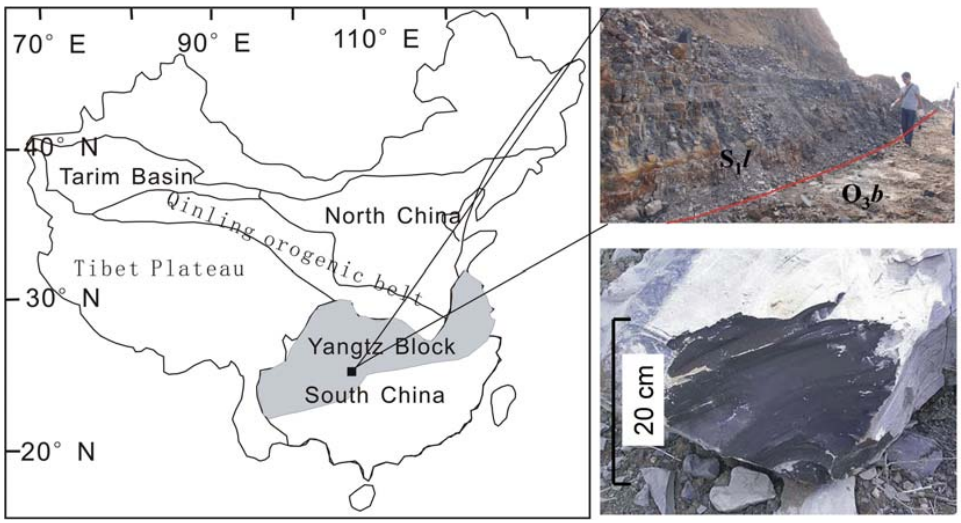


FIGURE 1 | Map showing the location and outcrop photograph of study area in Daozhen, Guizhou province, Southern China. S_1l- Lower Silurian Longmaxi Formation, O_3b- Upper Ordovician Baota Formation.

MATERIALS AND METHODS

Shale Samples and Sample Preparation

Five bulk shale samples were collected from outcrops of the Longmaxi formation. For research purposes, the shale samples are undeformed shale, and no fractures or vein are observed on the hand scale. The sampling site in Daozhen County is located in the North of Guizhou province, which belongs to the edge of the Upper Yangtze Block (28°53′46″N, 107°31′48″E; **Figure 1**). Two similar cylindrical samples of about 25 mm diameter and 20–50 mm length were obtained from each bulk sample, of which one was used in a uniaxial compressive simulation experiment and denoted as the artificial deformed shale sample (D), the other was denoted as the original shale sample (O). And then we got 10 shale samples for methane adsorption capacity tests. All samples were crushed into 0.25 mm (60 mesh) size samples as per the GB/T 19560–2004 testing standard (China National Standard), prepared for methane adsorption capacity measurements. The remaining material from 5 bulk samples were collected and powdered to 200 mesh particle sizes for geochemical (TOC) and mineralogical composition analysis using X-ray diffraction (XRD) analysis. The TOC content was measured with a Leco C/S-344 analyzer after samples were treated with 10% hydrochloric acid to remove carbonate. The mineral composition was measured using a D/Max-III analyzer for X-ray diffraction (XRD) analysis. All the data were obtained under the same sample preparation, analytical models and calculation models for both artificial brittle deformed and original samples, except whether it has experienced uniaxial compression and brittle deformation.

Uniaxial Compressive and Deformation

Uniaxial compression and deformation processes were measured with a TAW 2000 testing machine. The tests were carried out at room temperature. A constant loading rate of 0.2 MPa/s was applied, with the loading controlled by computer. The compression process stopped as soon as rock failure occurred (**Figure 2**).

Methane Isothermal Adsorption

Methane sorption isotherms were measured for all original (O) and compressive deformed (D) core samples in a pressure range of 0–15 MPa at 30°C. The high-pressure methane sorption measurements were conducted on an ISO 300 isothermal adsorption apparatus under moisture equilibrated conditions, adopting the GB/T 19560-2004 (China National Standard GB) testing standard, which uses a volumetric method as described in detail in a series of publications (Ji et al., 2012, 2014). The moisture equilibrium conditions were accomplished in an evacuated dryer with relative humidity controlled using saturated solutions of K_2SO_4. The shale sample was weighed every 24 h until constant. The moisture content of the shale samples was eventually stabilized between 1.26 and 1.68%. On the assumption that gas absorption in organic rich shales follows monolayer adsorbents theory, CH_4 adsorption observed in our experiments was modeled by the Langmuir equation. The temperature and pressure accuracies kept within 0.1°C and 0.1 psi, and variation of temperature and pressure was monitored and recorded by computer. By measuring the pressure before and after expansion, the molar number of the gas at different stages were calculated using an appropriate equation of state, and the amount of gas adsorbed at one pressure level could be determined. The isotherm was obtained by repeating these procedures until the measurement at the highest desired pressure was achieved. Assuming that gas absorption in organic rich shales follows the monolayer adsorbents theory, CH_4 adsorption observed in our experiments can be expressed by the Langmuir equation. Base on the measured CH_4 sorption parameters, we used the

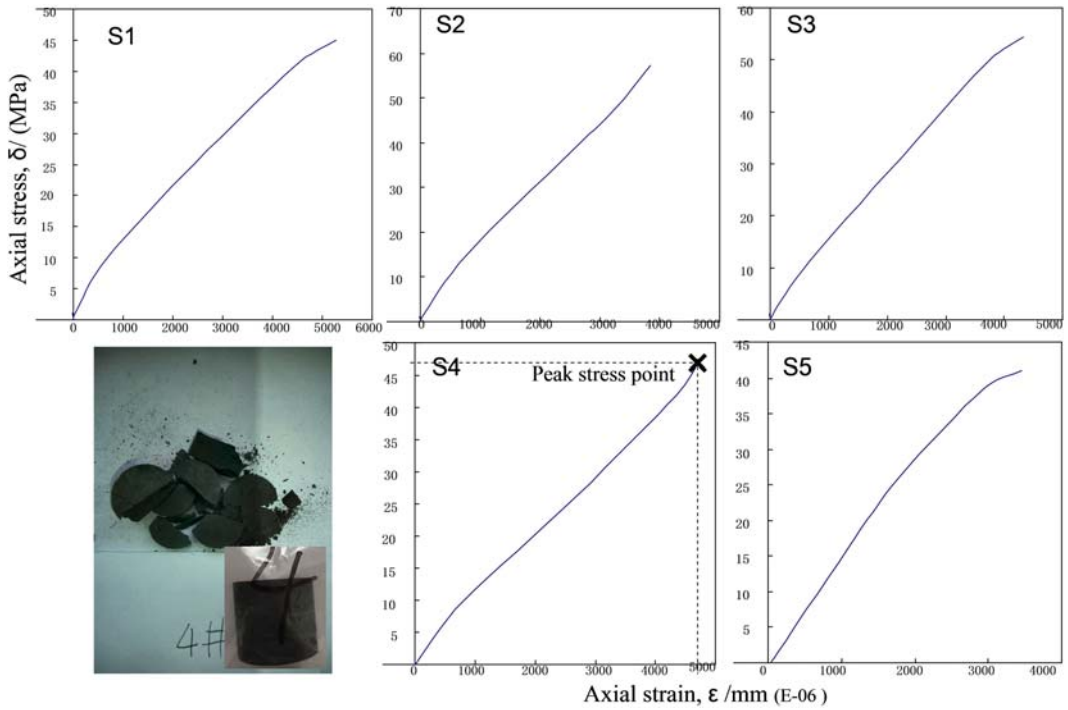


FIGURE 2 | Relationships of axial stress-axial strain for all shale samples. All the curves for represents loading to failure. A typical sample of a Longmaxi shale sample S4 and after failure, abundant graptolite fossils can be observed in the fracture plane (bottom left).

Langmuir equation to describe methane sorption isotherms due to its simplicity and good applicability in fitting the measured data:

$$V = V_L * P/(P_L + P)$$

where V is gas sorption volume per unit weight of shale sample in equilibrium at distinct pressure, V_L is the Langmuir volume (based on monolayer adsorption), which represents the maximum gas sorption capacity at complete surface coverage, P is the gas pressure and P_L is the Langmuir constant, represents the pressure at which total absorbed gas equals to one half of the maximum gas adsorption capacity of Langmuir volume.

RESULTS AND DISCUSSION

Shale Composition, Geochemistry and Mineralogy

All samples were either black or dark gray shale, which deposited in deep sea and shallow sea environments (Chen et al., 2011; Liang et al., 2012). The shale composition characteristics of the samples are shown in **Table 1**. Total organic-matter content (TOC%) of the shale samples ranged from 0.17 to 3.05%, while the organic-lean sample has the lowest TOC (0.17%) is a dark gray shale from the upper Longmaxi Formation. The samples are dominated by quartz and clay minerals, accounting for 84–91% of the mass. The clay mineral compositions were mainly the illite/smectite mixed layer and illite (**Table 1**). The shale of the organic-lean sample has the highest clay mineral content (high illite), but slightly lower quartz content and significant lower TOC than the other samples. However, in general, all shale samples studied were siliceous, with a high brittle mineral content, and the average brittleness index (BRI) was 47.81%.

Mechanical and Deformation Testing

Ideally, samples for compression experiments should be a perfect cylinder having a length-to-diameter (L/D) ratio of 2.0–2.5 (Brown et al., 1981; ASTM D4543-08, 2008; Fjaer et al., 2008; Dudley et al., 2016). However, it is not always easy to obtain sufficient samples with an L/D ratio exceeding 2, as coring soft shale is frequently difficult, and only 10–20% of the required length may be obtained (Agustawijaya, 2001). In this present study, most of the samples had a L/D ratio of less than 2, which is smaller than the minimum suggested in ISRM guidance (Ulusay and Hudson, 2007). Therefore, the mechanical parameters of uniaxial compressive strength (UCS), Young's modulus (E) or Poisson's ratio (μ) in this article will need to be considered with the above caveat in mind. The mechanical characteristics of the Longmaxi shale are related to its properties of lithology, kerogen and porosity (Zhang et al., 2016). However, as the purpose of this paper is to study changes in methane adsorption capacity before and after compressive deformation, and not the comparative mechanical properties of the Longmaxi shale, we list the mechanical parameters of the samples without further discussion (**Table 2**).

TABLE 1 | Geochemical and mineralogical data of the Longmaxi shale samples in this study.

Sample	Strata	TOC (wt%)	Clay minerals (%)			Minerals (%)					BRI (%)
			C	I	I/S	Clay	Quartz	Carbonate	Feldspar	Pyrite	
S1	S_1l	0.17	18	82	nd	58	32	nd	9	nd	35.56
S2	S_1l	0.93	1	38	61	38	55	nd	7	nd	59.14
S3	S_1l	0.60	15	80	5	47	44	nd	8	nd	48.35
S4	S_1l	3.05	7	39	54	37	49	4	6	4	54.44
S5	S_1l	0.51	9	36	55	47	37	5	9	2	41.57

S_1l – Longmaxi formation, Lower Silurian; TOC – total organic carbon (%); C – Chlorite; I – Illite; I/S – mixed-layer illite/montmorillonite; nd – not detected; BRI – brittleness index, BRI = Quartz/(Quartz + Carbonate + Clay) × 100% (Jarvie et al., 2007).

TABLE 2 | Mechanical properties data of shale obtained from uniaxial compressive experiments.

Sample	Compressive load/P (kN)	Uniaxial compressive strength/σc (MPa)	Elastic modulus/E (GPa)	Poisson's ratio/μ	Comments
S1	25.02	45.00	9.39	0.18	The loading and compressive process stop when the failure happens, and brittle deformation is formed by sudden failure.
S2	31.80	57.20	15.19	0.21	
S3	31.80	57.20	15.19	0.21	
S4	26.07	46.90	19.94	0.23	
S5	22.79	41.00	13.10	0.18	

Rock failure occurs when loading creates compressive stresses in the sample that exceed the UCS. The failure modes might exhibit brittle or ductile deformation of rock, depending on the brittleness properties of the shale and experimental conditions, such as temperature and pressure. Previous studies have suggested that the Longmaxi formation shale has high brittleness, and thus is suitable for hydraulic fracturing and should readily form complex crack networks (Zhang et al., 2018). Brittle deformation is characterized by sudden failure. **Figure 2** shows a typical sample (θ = 90°) of a Longmaxi shale sample, before and after failure. Abundant graptolite fossils were observed in the fracture plane. **Figure 2** also displays the uniaxial compressive stress-strain diagrams for all 5 shale samples. From these, the approximately linear relationship can be observed before peak stress-strain, with no obvious compaction visible at the initial stage. The linear elastic stage is long, and typical of the brittle characteristics of Longmaxi shale (Zhang et al., 2018). Generally, the failure mode of all 5 samples displayed brittle deformation (**Figure 2**). Similar results have been found in previous studies (Zhang et al., 2018), the brittle mineral content of Longmaxi Formation shale was found to be as high as 72.58% in their report samples, suggested brittle deformation behaviors are closely related to the mineral composition and high brittleness index of the Longmaxi shale sample.

Methane Adsorption Capacity Measurements

Both the original and artificial deformed shale samples were measured at a temperature of 30°C and pressure up to 15 MPa, under moisture equilibrated condition. Methane sorption capacity varied in the different shale samples. The CH_4 sorption capacity is affected by the organic content of the shale. **Figure 3** shows that the measurement adsorption volume of the two highest TOC% shale samples (S4 = 3.05% and S2 = 0.93%) were always higher than that of other organic-poor shale samples (TOC < 0.6%), regardless of compression and deformation, and under all pressure conditions (**Figure 3** and **Table 3**). For the three organic-poor samples, the effect of TOC on CH_4 adsorption capacity was not obvious. Sample S1, with the lowest organic matter content (TOC = 0.17%), has a larger adsorption capacity than the other two samples S3 and S5 (0.60 and 0.51% TOC, respectively), which may be related to Sample S1 having the highest clay mineral content (58%), indicating that the clay minerals also contribute toward methane adsorption (Ji et al., 2012; Zhang et al., 2012).

Measured methane sorption isotherms at different pressure can be fitted to a Langmuir function (**Figure 3** and **Table 4**). The overlap between the Langmuir fit curves and the experimental measurements is good (**Figure 3**). **Table 4** shows that the Langmuir maximum CH_4 adsorption capacity varies in the different shale samples, obviously affected by the TOC content. Langmuir maximum CH_4 adsorption for the two highest TOC% shale samples (S4 = 3.05% and S2 = 0.93%) were higher than 0.14 mmol/g, while the other three organic-lean shale samples were always less than 0.095 mmol/g, with both original and deformed samples (**Table 4**).

Effect of Compression and Deformation on Methane Gas Adsorption

Measured CH_4 sorption capacity is clearly influenced by uniaxial compression and deformation. As shown in **Figure 3**, the CH_4 adsorption capacity of all deformed samples was less than of the corresponding original samples, regardless of TOC content and under all CH_4 pressures. It shows that compression and the resulting brittle deformation have an effect on the methane adsorption capacity of shale, and the effect is to

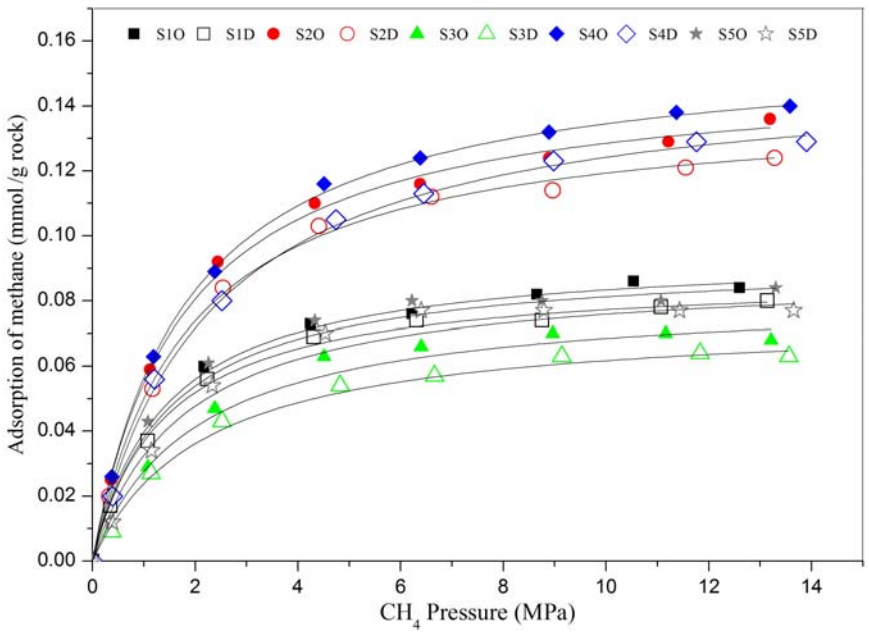


FIGURE 3 | Comparison of methane sorption capacity for original shale samples (O) and artificial compressive deformed shale samples (D). Points are experimentally measured results and lines are Langmuir fitting results.

TABLE 3 | Measured methane sorption capacity for both original shale samples and deformed samples which after uniaxial compressive experiments.

S1O		S2O		S3O		S4O		S5O	
P (MPa)	CH4 (mmol/g rock)	P (MPa)	CH4 (mmol/g rock)	P (MPa)	CH4 (mmol/g rock)	P (MPa)	CH4 (mmol/g rock)	P (MPa)	CH4 (mmol/g rock)
0.00	0.000	0.00	0.000	0.00	0.000	0.00	0.000	0.00	0.000
0.34	0.019	0.36	0.025	0.35	0.009	0.38	0.026	0.34	0.012
1.05	0.037	1.12	0.059	1.08	0.029	1.19	0.063	1.08	0.043
2.17	0.060	2.44	0.092	2.38	0.047	2.38	0.089	2.26	0.061
4.24	0.073	4.33	0.110	4.51	0.063	4.51	0.116	4.33	0.074
6.22	0.076	6.38	0.116	6.40	0.066	6.38	0.124	6.22	0.080
8.65	0.082	8.89	0.124	8.96	0.070	8.89	0.132	8.75	0.080
10.53	0.086	11.21	0.129	11.16	0.070	11.37	0.138	11.07	0.080
12.60	0.084	13.19	0.136	13.21	0.068	13.58	0.140	13.30	0.084
S1D		**S2D**		**S3D**		**S4D**		**S5D**	
0.00	0.000	0.00	0.000	0.00	0.000	0.00	0.000	0.00	0.000
0.35	0.017	0.33	0.020	0.38	0.009	0.39	0.020	0.39	0.012
1.08	0.037	1.17	0.053	1.14	0.027	1.21	0.056	1.15	0.034
2.24	0.056	2.54	0.084	2.52	0.043	2.52	0.080	2.33	0.054
4.31	0.069	4.41	0.103	4.82	0.054	4.74	0.105	4.53	0.070
6.31	0.074	6.60	0.112	6.66	0.057	6.45	0.113	6.40	0.077
8.76	0.074	8.96	0.114	9.14	0.063	8.98	0.123	8.79	0.077
11.07	0.078	11.55	0.121	11.83	0.064	11.76	0.129	11.43	0.077
13.14	0.080	13.28	0.124	13.56	0.063	13.90	0.129	13.65	0.077

Unit conversion factor: 1 mmol/g = 711.24 scf/ton; S4O – shale sample of S4 in Original structure; S4D – shale sample of S4 after compressive.

reduce the shale adsorption capacity (**Figure 3** and **Table 3**). Similar effects have been found in previous studies of natural geologically deformed shale samples (Zhu et al., 2020). As has been discussed in previous studies, adsorbed methane capacity positively correlates with the TOC content and clay minerals (Ji et al., 2012, 2014; Zhang et al., 2012). Zhu et al. (2020) conducted

TABLE 4 | Langmuir fitting results for methane adsorption for both original shale samples and deformed samples.

	S1		S2		S3		S4		S5	
	Original	**Deformed**	**Original**	**Deformed**	**Original**	**Deformed**	**Original**	**Deformed**	**Original**	**Deformed**
Langmuir maximum (mmol/g rock)	0.095	0.088	0.151	0.141	0.082	0.075	0.159	0.152	0.093	0.089
Langmuir constant (1/MPa)	1.40	1.39	1.75	1.82	1.97	2.15	1.82	2.24	1.45	1.73
Reduced volume (mmol/g rock)	0.006		0.010		0.007		0.007		0.004	
Reduced rate (%)	6.81		6.91		8.48		4.67		4.26	

Unit conversion factor: 1 mmol/g = 711.24 scf/ton.

CH_4 adsorption measurements for naturally deformed shale samples of both the Lower Silurian Longmaxi Formation and the Lower Cambrian Lujiaping Formation from Chongqing, South China, finding a significant decrease in adsorption capacity for samples that had experienced deformation conditions, ranging from 0.65 to 1.65 m^3/t, while those of undeformed samples ranged from 1.44 to 4.56 m^3/t. For Longmaxi shale, CH_4 adsorption capacity was 0.65 to 1.65 m^3/t for naturally deformed samples, while $>$ 2.5 m^3/t for undeformed samples, under a CH_4 equilibrium pressure of up to 12 MPa (Zhu et al., 2020). This significant decrease ($>$34%) in the methane adsorption capacity of the naturally deformed Longmaxi shale is much larger than the slight decrease (4.26–8.48%) observed in our present experimental results. This may be due to that there are greater differences in the organic matter and mineral composition between the natural undeformed and deformed samples. On the other hand, it may also be related to the fact that some of the naturally deformed samples in the literature (Zhu et al., 2020) are ductile deformed shale samples, while the influence of ductile deformation on shale pore structure and CH_4 adsorption capacity is more significant. These prior studies inferred that volumes of adsorbed methane in the sample suite declined as a result of changes arising during structural deformation.

In the experimental results presented here, the methane adsorption capacity of all deformed samples was less than the corresponding original samples for both the measured results and Langmuir fitted data. The reduced volume amount and reduce rate of the Langmuir maximum adsorption are 0.004–0.010 mmol/g and 4.26–8.48%, respectively. Compared with the dominant effect of TOC on the shale CH_4 adsorption capacity, compression and deformation will reduce the adsorption capacity of shale, and the Langmuir maximum adsorption capacity (Qmax) in the samples tested here was reduced from 4.26 to 8.48%. **Figure 4A** shows that compared to clay minerals, the methane sorption capacity of shale has a better positive correlation with TOC, regardless of compression and deformation with both the original (O) samples and deformed (D) samples showing increased Q_{max} with increased TOC. The effect of clay mineral content on Q_{max} is shown in **Figure 4B**. As **Figure 4B** shows, Q_{max} CH_4 decreases as the clay content increases, suggesting that clay mineral content is in part responsible for controlling CH_4 adsorption. Our results suggest that TOC content is the major controlling factor for CH_4 adsorption capacity, agreeing with previous studies (Ross and Bustin, 2007, 2009; Chalmers and Bustin, 2008a; Zhang et al., 2012).

Mechanism for Methane Adsorption Reduction in Deformed Samples

The original samples are characterized by well-preserved organic matter pores, interlayer of clay-organic nanocomposites, which may be the possible reason for the higher CH_4 adsorption contents (Ma et al., 2020; Zhu et al., 2020). Compressive stress and structure deformation may change the structure of organic matter, the structure of clay minerals (Ma et al., 2020; Zhu et al., 2020), leading to deformation in the microstructure and pore space of the shale matrix (Aplin et al., 2006; Liang et al., 2017; Wang, 2020). Both the previous research on natural deformation samples (Zhu et al., 2020) and the research on artificial compression deformation samples in the present study have shown that compression and structure deformation reduce methane adsorption capacity. The reduction arises from the applied compressive stress and appears related to shale composition, which acts as a higher order control on the amount of CH_4 adsorption.

In order to relate the reduction in shale CH_4 adsorption capacity to its composition such as TOC and mineral content, the relevant data are plotted in **Figure 5**. Interestingly, unlike the Langmuir Q_{max} value, which is controlled by TOC, the change in Q_{max} for CH_4 adsorption has no correlation with either TOC or clay mineral content. In contrast, the reduction in Q_{max} is positively related to the aggregated total of brittle mineral (quartz), OM and clay content (R^2 = 0.8748). It suggests that the evolution in pore space and adsorption capacity during compression and deformation are the result of the combined influence of brittle minerals (quartz) and pore providers (OM-clay).

Previous research shows that the pore type in shale is mainly comprised of organic matter pores, intergranular mineral pores, intraparticle mineral pores and microfractures (Loucks et al., 2012). The methane adsorption sites are mainly provided by the surfaces of pores within organic matter, and the surfaces of certain clay minerals (Loucks et al., 2009; Curtis et al., 2012; Ji et al., 2012, 2014; Zhang et al., 2012). Furthermore, the organic matter, clay minerals and quartz all have contact surfaces within the shale matrix. In the original samples, the developed and well-preserved organic

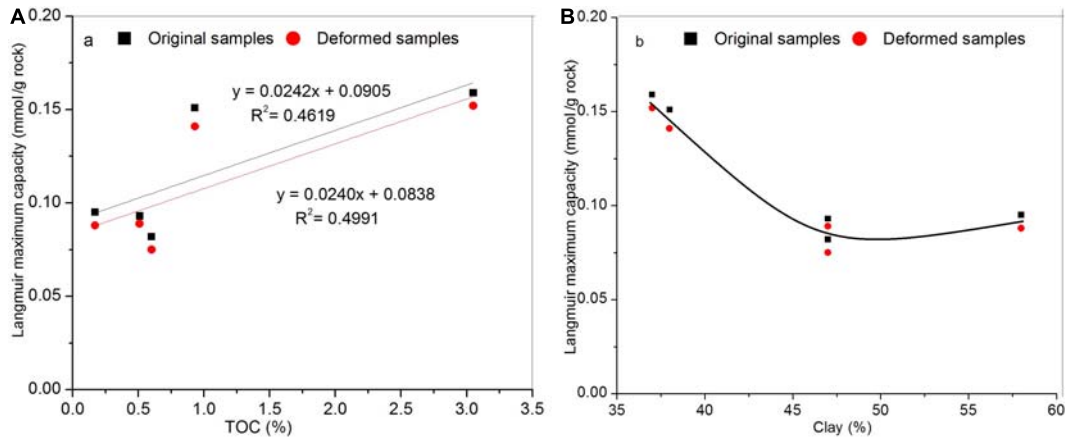


FIGURE 4 | (A) Relationship between Langmuir maximum sorption capacity and TOC%, **(B)** relationship between Langmuir maximum sorption capacity and Clay%.

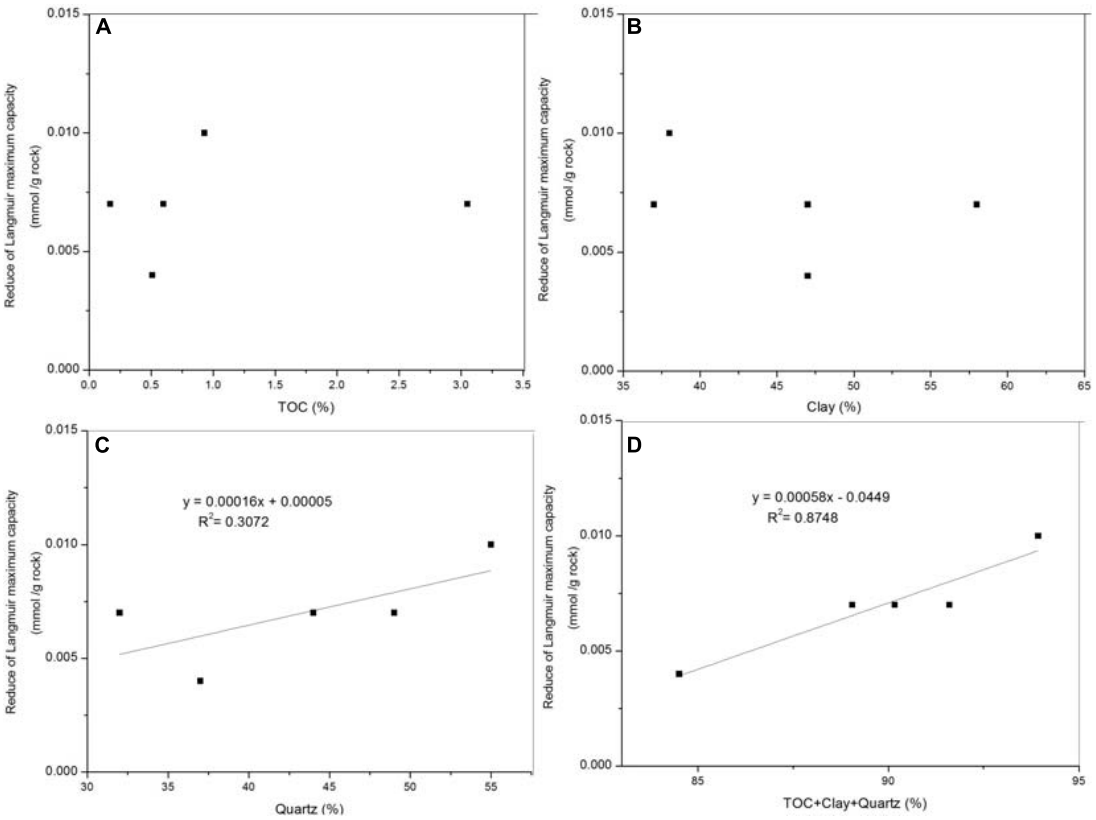


FIGURE 5 | Relationship between reduced volume of Langmuir maximum sorption capacity and **(A)** TOC%, **(B)** clay%, **(C)** quartz and **(D)** amount content of (TOC + Clay + Quartz)%.

matter pores, along with the interlayer of clay pores may be the reason for the higher CH_4 adsorption contents. Under uniaxial compressive condition, brittle minerals of quartz act as stress transmitters, compressing the OM pores and may cause deformation of OM pores (Wang, 2020), changing the pore geometries of organic matter. However, due to the high brittleness characteristics of the Longmaxi Formation shale, the stress transmission will not be applied indefinitely. When the compressive stress exceeds the UCS of the sample, the compression effect will ending with damage and brittle deformation of shale, thereby retaining parts of OM pores (Wang, 2020). Methane adsorption of shale is related to the specific surface area of the pores (Javadpour et al., 2007; Ross and Bustin, 2009), we also obtained the BET specific surface area

and the external surface area of three shale samples before and after compressive tests using the N_2 adsorption method and CT method (**Table 5**). The results show that the external surface area of the damaged shale increases while the internal pore surface area decreases. This may be a reason for the decrease in methane adsorption for deformed shale samples. Unfortunately, when designing the experiments, we did not aimed to determine the pore structure and specific surface area evolution with compressive stress deformation but relationships between compressive deformation and methane adsorption. Therefore, we did not obtain more parameters of the pore structures than the bulk surface area of the limited samples. However, the objective of this present study is still achieved. Overall, the result is that compression will reduce the methane adsorption capacity of the shale, but the impact is slight as shown by the reduction in Q_{max} ranging between 4.26 and 8.48% in this present study.

Implication of Compression and Deformation Affecting Methane Adsorption

Generally, shale gas is mainly stored as free gas in the meso- to macro-pores and micro-cracks, and as adsorbed gas at the surfaces of nanopores associated with organic matters and clay minerals (Javadpour et al., 2007; Ross and Bustin, 2009). Previous studies indicated that adsorbed gas represents a significant percentage, reaching 20–85% of total gas, which cannot be ignored when evaluating the resource potential (Lu et al., 1995; Ross and Bustin, 2009; Zhang et al., 2012; Wang et al., 2016). The organic matter content is a high level control on determining the gas adsorption capacity of shale, due to CH_4 gas primarily being adsorbed within the OM nanopores in shale (Hill et al., 2007; Mastalerz et al., 2012). Unlike North America, the geological conditions of shale reservoirs in South China are highly complicated due to multi-tectonic movement and, as a result, tectonic stress compression. Recently, the effect of tectonic and structural deformation on reservoir characters has attracted more attention (Ma et al., 2015; Liang et al., 2017; He et al., 2018; Zhu et al., 2020). It has been confirmed that the deformation can affect the nanopores in Longmaxi shale (Liang et al., 2017; He et al., 2018), and even reduced the adsorption capacity of deformed shale (Zhu et al., 2020). Whether and how the structural deformation plays an important role in the adsorbed gas capacity in the deformed shale is still unclear. In this study, we present an experimental study of uniaxial compression induced brittle deformation and its influence on methane adsorption capacity of shale. The remaining OM-pores surface after compression, provides a significant surface area for adsorbed gas, causing slight impairment of adsorbed gas in artificial deformed samples, which is strongly suggested by the good correlation between Langmuir Q_{max} and TOC (**Figure 4A**). Using cold pressing techniques, (Kuila and Prasad, 2013) conducted artificial compaction experiments of Wyoming montmorillonite powder, suggested that compaction could only results in reduction of macropores of the clays while the micropores were not affected by compression. Brittle minerals change the shape of kerogen but not its specific surface area under compressive stress (Wang, 2020). Meanwhile, high brittle minerals content interrupt the compression process by failure and deformation of shale. Thus, this prevents shale OM pores from disappearing under compressive stress, even though the shales which strongly tectonically deformation as mylonite, micropores still develop in the Cambrian shale, South China (Ma et al., 2015). Furthermore, well-preserved OM pores generated in compressive deformed shale result in good adsorbed gas capacity, suggesting that there may still be good gas potential in the tectonic deformation and siliceous shale distribution zones in South China. However, it should be noted when considering the uniaxial compression test, without confining pressure, this is different from the real geologic conditions, and the present study still has limitations. Further artificial compression deformation experiments closer to geologic temperature and pressure conditions such as high temperature and high pressure triaxial compression experiments are warranted.

TABLE 5 | BET surface area and External surface area of samples before and after uniaxial compressive tests.

ID	BET surface area (m^2/g)	External surface area (m^2)
S1O	26.7992	0.002707
S2O	28.9569	0.002818
S3O	30.3752	0.002833
S1D	12.2955	0.003852
S2D	17.349	0.004641
S3D	16.4364	0.003624

CONCLUSION

Comparative analysis of methane adsorption capacity of both original shale samples from the Longmaxi formation, and artificially deformed shale after uniaxial compression and deformation was conducted in this study. The main conclusions are as follows:

(1) Compression deformation does affect the CH_4 adsorption capacity of shale. The CH_4 sorption capacity of deformed shale samples is reduced after uniaxial compression and brittle deformation, across all 5 shale samples and at each pressure point tested.
(2) The effect of brittle deformation on the CH_4 sorption capacity of shale was limited. The methane adsorption capacity of shale is slight reduced by 4.26–8.48% after brittle deformation under uniaxial compressive.

DATA AVAILABILITY STATEMENT

The original contributions presented in the study are included in the article/supplementary material, further inquiries can be directed to the corresponding author.

AUTHOR CONTRIBUTIONS

ML and ZW conceived of the presented idea. ML wrote the manuscript with support from GZ and HG. XZ, HL, LZ, XF, and KZ helped supervise the projects. All authors discussed the results and contributed to the final manuscript.

FUNDING

This work was supported by the National Natural Science Foundation of China (NSFC, 41802158), the China Geological Survey (CGS, DD20160183, DD20190085), and the Major State Research Development Program of China (2016YFC0600202), Fundamental Research Funds for Chinese Academy of Geological Sciences (Grant No. JYYWF20181201), and the CGS-CSC Scholarship Fund (No. 201908575013).

ACKNOWLEDGMENTS

We thank the Frontiers in Earth Science editors and reviewers for their thoughtful and constructive comments on earlier versions of our manuscript, which helped us a lot in the paper's revision and enhanced the quality of the article.

REFERENCES

Agustawijaya, D. S. (2001). *The Development of Design Criteria for Underground Excavations in Coober Pedy Arid Soft Rocks*. Ph D. thesis. Australia: University of South Australia.

Aplin, A. C., Matenaar, I. F., McCarty, D. K., and Van Der Pluijm, A. (2006). Influence of mechanical compaction and clay mineral diagenesis on the microfabric and pore-scale properties of deep-water Gulf of Mexico mudstones. *Clays Clay Miner.* 54, 500–514. doi: 10.1346/CCMN.2006.0540411

Arora, S., and Mishra, B. (2015). Investigation of the failure mode of shale rocks in biaxial and triaxial compression tests. *Int. J. Rock Mech. Min. Sci.* 79, 109–123. doi: 10.1016/j.ijrmms.2015.08.014

ASTM D4543-08. (2008). *Standard Practices For Preparing Rock Core As Cylindrical Test Specimens And Verifying Conformance To Dimensional And Shape Tolerances*. West Conshohocken, PA: American Society for Testing and Materials.

Bakhshian, S., and Hosseini, S. A. (2019). Prediction of CO2 adsorption-induced deformation in shale nanopores. *Fuel* 241, 767–776. doi: 10.1016/J.FUEL.2018.12.095

Brown, E. T., International Society for Rock Mechanics (ISRM)., and Commission on Testing Methods. (1981). *Rock Characterization, Testing and Monitoring, ISRM Suggested Methods*. Oxford: Pergamon Press.

Chalmers, G. R. L., and Bustin, R. M. (2007). The Organic Matter Distribution and Methane Capacity of the Lower Cretaceous Strata of Northeastern British Columbia, Canada. *Int. J. Coal Geol.* 70, 223–239. doi: 10.1016/j.coal.2006.05.001

Chalmers, G. R. L., and Bustin, R. M. (2008a). Lower Cretaceous Gas Shales in Northeastern British Columbia, Part I: geological Controls on Methane Sorption Capacity. *Bull. Can. Pet. Geol.* 56, 1–21. doi: 10.2113/gscpgbull.56.1.1

Chalmers, G. R. L., and Bustin, R. M. (2008b). Lower Cretaceous Gas Shales in Northeastern British Columbia, Part II: evaluation of Regional Potential Gas Resources. *Bull. Can. Pet. Geol.* 56, 22–61. doi: 10.2113/gscpgbull.56.1.22

Chen, C., Sun, J., Zhang, Y., Mu, J., Li, W., and Song, Y. (2020). Adsorption characteristics of CH4 and CO2 in organic-inorganic slit pores. *Fuel* 265:116969. doi: 10.1016/j.fuel.2019.116969

Chen, S., Zhu, Y., Wang, H., Liu, H., Wei, W., and Fang, J. (2011). Characteristics and significance of mineral compositions of Lower Silurian Longmaxi Formation shale gas reservoir in the southern margin of Sichuan Basin. *Acta Pet. Sin.* 32, 775–782.

Cheng, A. L., and Huang, W. L. (2004). Selective Adsorption of Hydrocarbon Gases on Clays and Organic Matter. *Org. Geochem.* 35, 413–423. doi: 10.1016/j.orggeochem.2004.01.007

Curtis, M. E., Sondergeld, C. H., Ambrose, R., and Rai, C. (2012). Microstructural investigation of gas shales in two and three dimensions using nanometer-scale resolution imaging. *AAPG Bull.* 96, 665–677. doi: 10.1306/08151110188

Dudley, J. W., Brignoli, M., Crawford, B. R., Ewy, R. T., Love, D. K., McLennan, J. D., et al. (2016). ISRM Suggested Method for Uniaxial-Strain Compressibility Testing for Reservoir Geomechanics. *Rock Mech. Rock Eng.* 49, 4153–4178. doi: 10.1007/s00603-016-1055-4

Fjaer, E., Holt, R. M., Horsrud, P., Raaen, A. M., and Risnes, R. (2008). *Petroleum Related Rock Mechanics, 2nd Edn*. Boston: Elsevier.

Gao, L., Wang, Z., Liang, M., Yu, Y., and Zhou, L. (2018). Experimental Study of the Relationship Between Particle Size and Methane Sorption Capacity in Shale. *J. Vis. Exp.* 138:57705. doi: 10.3791/57705

Guo, S., Lu, X., Song, X., and Liu, Y. (2017). Methane adsorption characteristics and influence factors of Mesozoic shales in the Kuqa Depression, Tarim Basin, China. *J. Pet. Sci. Eng.* 157, 187–195. doi: 10.1016/j.petrol.2017.07.020

He, J., Wang, J., Yu, Q., Liu, W., Ge, X., Yang, P., et al. (2018). Pore structure of shale and its effects on gas storage and transmission capacity in well HD-1 eastern Sichuan Basin, China. *Fuel* 226, 709–720. doi: 10.1016/j.fuel.2018.04.072

He, Q., Dong, T., He, S., and Zhai, G. (2019). Methane adsorption capacity of marine-continental transitional facies shales: the case study of the Upper Permian Longtan Formation, northern Guizhou Province, Southwest China. *J. Pet. Sci. Eng.* 183:106406. doi: 10.1016/j.petrol.2019.106406

Hill, D. G., Lombardi, T. E., and Martin, J. P. (2004). Fractured Shale Gas Potential in New York. *Northeast. Geol. Environ. Sci.* 26, 57–78.

Hill, R. J., Zhang, E. T., Katz, B. J., and Tang, Y. (2007). Modeling of Gas Generation from the Barnett Shale, Fort Worth Basin, Texas. *AAPG Bull.* 91, 501–521. doi: 10.1306/12060606063

Hou, Y., He, S., Yi, J., Zhang, B., Chen, X., Wang, Y., et al. (2014). Effect of pore structure on methane sorption potential of shales. *Pet. Explor. Dev.* 41, 272–281.

Jarvie, D. M., Hill, R. J., Ruble, T. E., and Pollastro, R. M. (2007). Unconventional shale-gas systems: the Mississippian Barnett Shale of north-central Texas as one model for thermogenic shale-gas assessment. *AAPG Bull.* 91, 475–499.

Javadpour, F., Fisher, D., and Unsworth, M. (2007). Nanoscale Gas Flow in Shale Gas Sediments. *J. Can. Pet. Technol.* 46, 55–61. doi: 10.2118/07-10-06

Jenkins, C., and Boyer, C. I. I. (2008). Coalbed- and Shale-Gas Reservoirs. *J. Pet. Technol.* 60, 92–99. doi: 10.2118/103514-ms

Ji, L. M., Zhang, T. W., Milliken, K. L., Qu, J., and Zhang, X. (2012). Experimental Investigation of Main Controls to Methane Adsorption in Clay-Rich Rocks. *Appl. Geochem.* 27, 2533–2545. doi: 10.1016/j.apgeochem.2012.08.027

Ji, W., Song, Y., Jiang, Z., Wang, X., Bai, Y., and Xing, J. (2014). Geological controls and estimation algorithms of lacustrine shale gas adsorption capacity: a case study of the Triassic strata in the southeastern Ordos Basin, China. *Int. J. Coal Geol.* 134, 61–73. doi: 10.1016/j.coal.2014.09.005

Jiang, Z., Song, Y., Tang, X., Li, Z., Wang, X., Wang, G., et al. (2020). Controlling factors of marine shale gas differential enrichment in southern China. *Pet. Explor. Dev.* 47, 661–673.

Kuila, U., and Prasad, M. (2013). Specific surface area and pore-size distribution in clays and shales. *Geophys. Prospect.* 61, 341–362.

Li, J., Zhou, S., Li, Y., Ma, Y., Yang, Y., and Li, C. (2016). Effect of organic matter on pore structure of mature lacustrine organic-rich shale: a case study of the Triassic Yanchang shale. Ordos Basin, China. *Fuel* 185, 421–431. doi: 10.1016/j.fuel.2016.07.100

Li, T., Tian, H., Xiao, X., Cheng, P., Zhou, Q., and Wei, Q. (2017). Geochemical characterization and methane adsorption capacity of overmature organic-rich Lower Cambrian shales in northeast Guizhou region, southwest China. *Mar. Pet. Geol.* 86, 858–873. doi: 10.1016/j.marpetgeo.2017.06.043

Liang, C., Jiang, Z., Yang, Y., and Wei, X. (2012). Characteristics of shale lithofacies and reservoir space of the Wufeng–Longmaxi Formation, Sichuan Basin. *Pet. Explor. Dev.* 39, 691–698.

Liang, M., Wang, Z., Gao, L., Li, C., and Li, H. (2017). Evolution of pore structure in gas shale related to structural deformation. *Fuel* 197, 310–319. doi: 10.1016/j.fuel.2017.02.035

Liu, C., Yin, G., Li, M., Deng, B., Song, Z., Liu, Y., et al. (2019). Shale permeability model considering bedding effect under true triaxial stress conditions. *J. Nat Gas Sci. Eng.* 68:102908. doi: 10.1016/j.jngse.2019.102908

Loucks, R. G., Reed, R. M., Ruppel, S. C., and Hammes, U. (2012). Spectrum of pore types and networks in mudrocks and a descriptive classification for matrix-related mudrock pores. *AAPG Bull.* 96, 1071–1098. doi: 10.1306/08171111061

Loucks, R. G., Reed, R. M., Ruppel, S. C., and Jarvie, D. M. (2009). Morphology, genesis, and distribution of nanometer-scale pores in siliceous mudstones of the Mississippian Barnett Shale. *J. Sediment. Res.* 79, 848–861. doi: 10.2110/jsr.2009092

Lu, X.-C., Li, F.-C., and Watson, A. T. (1995). Adsorption Measurements in Devonian Shales. *Fuel* 74, 599–603. doi: 10.1016/0016-2361(95)98364-k

Ma, Y., Ardakani, O. H., Zhong, N., Liu, H., Huang, H., Larter, S., et al. (2020). Possible pore structure deformation effects on the shale gas enrichment: an example from the Lower Cambrian shales of the Eastern Upper Yangtze Platform, South China. *Int. J. Coal Geol.* 217:103349.

Ma, Y., Zhong, N., Li, D., Pan, Z., Cheng, L., and Liu, K. (2015). Organic matter/clay mineral intergranular pores in the Lower Cambrian Lujiaping Shale in the north-eastern part of the upper Yangtze area, China: a possible microscopic mechanism for gas preservation. *Int. J. Coal Geol.* 137, 38–54. doi: 10.1016/j.coal.2014.11.001

Mastalerz, M., Schimmelmann, A., Lis, G. P., Drobniak, A., and Stankiewicz, A. (2012). Influence of Maceral Composition on Geochemical Characteristics of Immature Shale Kerogen: insight from Density Fraction Analysis. *Int. J. Coal Geol.* 103, 60–69. doi: 10.1016/j.coal.2012.07.011

Minaeian, V., Dewhurst, D., and Rasouli, V. (2017). Deformational behaviour of a clay-rich shale with variable water saturation under true triaxial stress conditions. *Geomech. Energy Environ.* 11, 1–13. doi: 10.1016/j.gete.2017.04.001

Mishra, B., and Verma, P. (2015). Uniaxial and triaxial single and multistage creep tests on coal-measure shale rocks. *Int. J. Coal Geol.* 137, 55–65. doi: 10.1016/j.coal.2014.11.005

Psarras, P., Holmes, R., Vishal, V., and Wilcox, J. (2017). Methane and CO2 Adsorption Capacities of Kerogen in the Eagle Ford Shale from Molecular Simulation. *Acc. Chem. Res.* 50, 1818–1828. doi: 10.1021/ACS.ACCOUNTS.7B00003

Ross, D. J. K., and Bustin, R. M. (2007). Shale Gas Potential of the Lower Jurassic Gordondale Member, Northeastern British Columbia, Canada. *Bull. Can. Pet. Geol.* 55, 51–75. doi: 10.2113/gscpgbull.55.1.51

Ross, D. J. K., and Bustin, R. M. (2008). Characterizing the Shale Gas Resource Potential of Devonian-Mississippian Strata in the Western Canada Sedimentary Basin: application of an Integrated Formation Evaluation. *AAPG Bull.* 92, 87–125. doi: 10.1306/09040707048

Ross, D. J. K., and Bustin, R. M. (2009). The Importance of Shale Composition and Pore Structure upon Gas Storage Potential of Shale Gas Reservoirs. *Mar. Pet. Geol.* 26, 916–927. doi: 10.1016/j.marpetgeo.2008.06.004

Tan, J., Hu, C., Lyu, Q., Dick, J. M., Ranjith, P. G., Li, L., et al. (2019). Multi-fractal analysis for the AE energy dissipation of CO2 and CO2+ brine/water treated low-clay shales under uniaxial compressive tests. *Fuel* 246, 330–339. doi: 10.1016/j.fuel.2019.03.008

Tan, J., Weniger, P., Krooss, B., Merkel, A., Horsfield, B., Zhang, J., et al. (2014). Shale Gas Potential of the Major Marine Shale Formations in the Upper Yangtze Platform, South China, Part II: methane Sorption Capacity. *Fuel* 129, 204–218. doi: 10.1016/j.fuel.2014.03.064

Tang, X., Jiang, S., Jiang, Z., Li, Z., He, Z., Long, S., et al. (2019). Heterogeneity of Paleozoic Wufeng-Longmaxi formation shale and its effects on the shale gas accumulation in the Upper Yangtze Region, China. *Fuel* 239, 387–402.

Topór, T., Derkowski, A., Ziemiański, P., Szczurowski, J., and McCarty, D. K. (2017). The effect of organic matter maturation and porosity evolution on methane storage potential in the Baltic Basin (Poland) shale-gas reservoir. *Int. J. Coal Geol.* 180, 46–56. doi: 10.1016/j.coal.2017.07.005

Ulusay, R., and Hudson, J. A. (eds) (2007). *The Complete Isrm Suggested Methods For Rock Characterization, Testing And Monitoring: 1974-2006*. Ankara: International Society of Rock Mechanics.

Vishal, V., Chandra, D., Bahadur, J., Sen, D., Hazra, B., Mahanta, B., et al. (2019). Interpreting Pore Dimensions in Gas Shales Using a Combination of SEM Imaging, Small-Angle Neutron Scattering, and Low-Pressure Gas Adsorption. *Energy Fuels* 33, 4835–4848. doi: 10.1021/acs.energyfuels.9b00442

Wang, G. (2020). Deformation of organic matter and its effect on pores in mud rocks. *AAPG Bull.* 104, 21–36. doi: 10.1306/04241918098

Wang, Y., Huang, J., Wang, S., Dong, D., Zhang, C., and Guan, Q. (2016). Dissection of two calibrated areas of the Silurian Longmaxi Formation, Changning and Jiaoshiba,Sichuan Basin. *Nat. Gas Geosci.* 27, 423–432.

Wang, Y., and Li, C. (2017). Investigation of the P-and S-wave velocity anisotropy of a Longmaxi formation shale by real-time ultrasonic and mechanical experiments unde uniaxial deformation. *J. Pet. Sci. Eng.* 158, 253–267. doi: 10.1016/j.petrol.2017.08.054

Wang, Y., Li, C., Hao, J., and Zhou, R. (2018). X-ray micro-tomography for investigation of meso-structural changes and crack evolution in Longmaxi formation shale during compressive deformation. *J. Pet. Sci. Eng.* 164, 278–288. doi: 10.1016/j.petrol.2018.01.079

Wei, M., Liu, Y., Liu, J., Elsworth, D., and Zhou, F. (2019). Micro-scale investigation on coupling of gas diffusion and mechanical deformation of shale. *J. Pet. Sci. Eng.* 175, 961–970. doi: 10.1016/J.PETROL.2019.01.039

Wu, Y., Li, J., Ding, D., Wang, C., and Di, Y. (2014). A generalized framework model for the simulation of gas production in unconventional gas reservoirs. *SPE J.* 19, 845–857.

Yang, R., He, S., Hu, Q., Hu, D., Zhang, S., and Yi, J. (2016). Pore characterization and methane sorption capacity of over-mature organic-rich Wufeng and Longmaxi shales in the southeast Sichuan Basin, China. *Mar. Pet. Geol.* 77, 247–261. doi: 10.1016/j.marpetgeo.2016.06.001

Zhang, P., Yang, C., Wang, H., Guo, Y., Xu, F., and Hou, Z. (2018). Stress-strain characteristics and anisotropy energy of shale under uniaxial compression. *Rock Soil Mech.* 39, 2106–2114. doi: 10.16285/j.rsm.2016.1824

Zhang, T., Ellis, G. S., Ruppel, S. C., Milliken, K., and Yang, R. (2012). Effect of OrganicMatter Type and Thermal Maturity on Methane Adsorption in ShaleGas Systems. *Org. Geochem.* 47, 120–131. doi: 10.1016/j.orggeochem.2012.03.012

Zhang, W. H., Fu, L. Y., Zhang, Y., and Jin, W. J. (2016). Computation of elastic properties of 3D digital cores from the Longmaxi shale. *Appl. Geophys.* 13, 364–374. doi: 10.1007/s11770-016-0542-4

Zhu, H., Ju, Y., Huang, C., Chen, F., Chen, B., and Yu, K. (2020). Microcosmic gas adsorption mechanism on clay-organic nanocomposites in a marine shale. *Energy* 197:117256. doi: 10.1016/j.energy.2020.11725

Zou, J., Rezaee, R., Xie, Q., You, L., Liu, K., and Saeedi, A. (2018). Investigation of moisture effect on methane adsorption capacity of shale samples. *Fuel* 232, 323–332. doi: 10.1016/j.fuel.2018.05.167

Conflict of Interest: The authors declare that the research was conducted in the absence of any commercial or financial relationships that could be construed as a potential conflict of interest.

The handling editor is currently organizing a Research Topic with one of the authors (GZ).

Copyright © 2021 Liang, Wang, Zheng, Zhang, Greenwell, Zhang, Feng, Zhang and Li. This is an open-access article distributed under the terms of the Creative Commons Attribution License (CC BY). The use, distribution or reproduction in other forums is permitted, provided the original author(s) and the copyright owner(s) are credited and that the original publication in this journal is cited, in accordance with accepted academic practice. No use, distribution or reproduction is permitted which does not comply with these terms.

frontiers in Earth Science

ORIGINAL RESEARCH
published: 22 April 2021
doi: 10.3389/feart.2021.635230

Factors Controlling Natural Gas Accumulation in the Southern Margin of Junggar Basin and Potential Exploration Targets

Jianping Chen[1], Xulong Wang[2], Yongge Sun[3], Yunyan Ni[1], Baoli Xiang[2] and Jiande Liao[2]*

[1]PetroChina Research Institute of Petroleum Exploration and Development, Beijing, China, [2]PetroChina Xinjiang Oilfield Company, Karamay, China, [3]School of Earth Sciences, Zhejiang University, Hangzhou, China

In this paper, factors controlling natural gas accumulation in the southern margin of Junggar Basin were mainly discussed by a comparison with natural gas generation and accumulation in the Kuqa Depression of Tarim Basin. The southern margin of Junggar Basin and the Kuqa Depression of Tarim Basin are located on the north and south sides of the Tianshan Mountains respectively, and they share the similar sedimentary stratigraphy and tectonic evolution history. In recent several decades, many large gas fields have been found in the Kuqa Depression of Tarim Basin, but no great breakthrough in the southern margin of Junggar Basin. Our results suggest that natural gas in the southern margin of Junggar Basin is mainly thermogenic wet gas, and can be divided into three types as coal-derived gas, mixed gas and oil-associated gas, of which the former two types are dominated. The Jurassic coal measures are the main source rocks of natural gas, and the main gas generation time from this set of source rocks matched well with the formation time of the anticline structures, resulting in favorable conditions for natural gas accumulation. In the western part of the southern margin in the Junggar Basin, the Permian lacustrine and the Upper Triassic lacustrine-swamp source rocks could be important sources of natural gas, and the main gas generation time also matched well with the formation time of traps. Compared with the Kuqa Depression of Tarim Basin, natural gas sources are better in the southern margin of Junggar Basin, and the geologic conditions are favorable for the formation of large oil and gas fields in the southern margin of Junggar Basin. The deep Permian-Jurassic-Cretaceous petroleum system is the most favorable petroleum system for natural gas exploration in the southern margin of Junggar Basin. The western part and the central part of the southern margin in the Junggar Basin could be the first targets for the discovery of the Jurassic coal-derived oil and gas reservoirs. The shallow Cretaceous-Neogene petroleum system is the second target for natural gas exploration.

Keywords: southern margin of Junggar Basin, natural gas, genetic type of natural gas, Jurassic coal measures, natural gas accumulation, favorable exploration target, Kuqa depression

OPEN ACCESS

Edited by:
Guodong Zheng, Chinese Academy of Sciences (CAS), China

Reviewed by:
Changchun Pan, Chinese Academy of Sciences, China
Quanyou Liu, SINOPEC Petroleum Exploration and Production Research Institute, China

****Correspondence:***
Jianping Chen
chenjp@petrochina.com.cn

Specialty section:
This article was submitted to Geochemistry, a section of the journal Frontiers in Earth Science

Received: *30 November 2020*
Accepted: *09 February 2021*
Published: *22 April 2021*

Citation:
Chen J, Wang X, Sun Y, Ni Y, Xiang B and Liao J (2021) Factors Controlling Natural Gas Accumulation in the Southern Margin of Junggar Basin and Potential Exploration Targets. Front. Earth Sci. 9:635230. doi: 10.3389/feart.2021.635230

INTRODUCTION

The southern margin of Junggar Basin mainly includes the southern depression zone in the Junggar Basin (**Figure 1**), with an area of 2.1 × 10^4 km^2 and a maximum strata thickness of 15 km. In the southern margin of Junggar Basin, five sets of possible source rocks were identified in the Permian, Triassic, Jurassic, Cretaceous, and Paleogene, respectively (Wang et al., 2013; Chen et al., 2015a), and many structural traps were well developed, where different types of oils and gases have been found (Wang et al., 2013; Chen et al., 2015b; Chen et al., 2016a; Chen et al., 2016b; Chen et al., 2016c; Chen et al., 2016d; Chen et al.,2016e). Therefore, the southern margin of Junggar Basin has long been considered as the most potential area for natural gas exploration (He et al., 2004; Wu et al., 2007; Lei et al., 2012). However, no great breakthrough occurred in last several decades in terms of oil and gas exploration in this area. On the other hand, the southern margin of Junggar Basin and the Kuqa Depression of Tarim Basin, located on the north and south sides of the Tianshan Mountains respectively, share very similar sedimentary stratigraphy and tectonic evolution history (Fang et al., 2005; Fang et al., 2007; He et al., 2009; Wang, 2014). A breakthrough of natural gas exploration in the Kuqa Depression of Tarim Basin has been achieved in last 3 decades, including the discovery of large gas fields KL-2, Dabei, Dina, Keshen, and others (Wang, 2014). The natural gas in the Kuqa Depression was derived mainly from the Jurassic coal-measures, and probably minor from the Upper Triassic Taliqike coal measures (Liang et al., 2002; Zhao et al., 2002; Liang et al., 2003; Liang et al., 2004; Liu et al., 2007; Qin et al., 2007). In the southern margin of Junggar Basin, coal-measures in the Middle-Lower Jurassic strata, the Upper Triassic Huangshanjie Formation and Haojiagou Formation were also well-developed. More important is that the Permian, Cretaceous and Paleogene source rocks were found in the southern margin of Junggar Basin. Furthermore, the multiple sets of source rocks in the southern margin of Junggar Basin are at highly to over mature stages, and large amounts of natural gas could be theoretically generated (Wang et al., 2013; Chen et al., 2015a, Chen et al., 2016c). For example, theoretical calculation suggested that the gas generation intensity of the Jurassic coal-measures can be 3–8 × 10^9 m^3/km^2, and even up to 10 × 10^9 m^3/km^2 in some areas (Wu et al., 2007), which is basically equivalent to that of the Jurassic coal measures from the Kuqa Depression (Du et al., 2006). This result indicates that the gas generation intensity is not the limited factor to control the formation of large gas fields. Although previous studies have clearly concluded that the natural gas discovered in the southern margin of Junggar Basin is mainly from the Jurassic coal-measures (Li et al., 2004; Liao et al., 2011; Dai et al., 2012; Wang et al., 2013; Chen et al., 2016d; Liu et al., 2016), only two commercial gas fields were discovered to date, namely the Hutubi gas field in the Hutubi anticline and the Mahe gas field in the Manas anticline in the central part of the southern margin in the Junggar Basin, with a total proved geological gas reserve of

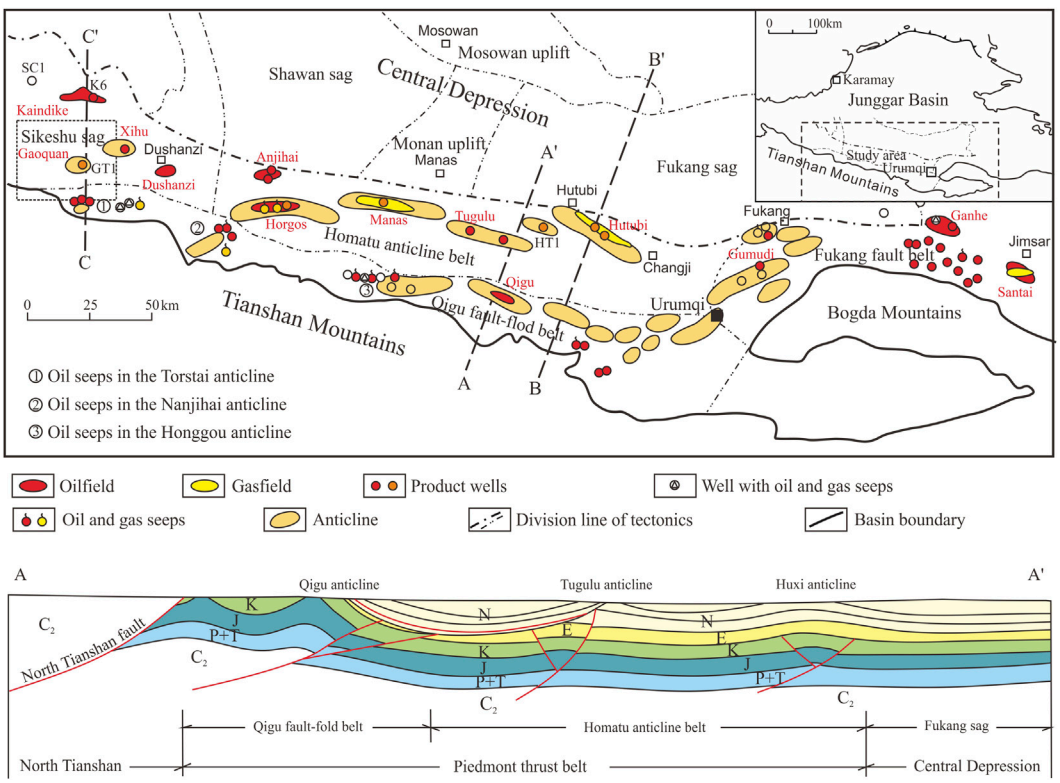


FIGURE 1 | Distribution of structural traps and of oil and gas fields in the southern margin of Junggar Basin.

32.96×10^9 m^3 (Du et al., 2019). The scale of natural gas reserve discovered to date in the southern margin of Junggar Basin is unexpected and much smaller than that in the Kuqa Depression. Previous study by Kuang and Liu (2001) indicated that, in the southern margin of Junggar Basin, there are sufficient gas sources, numerous fold anticlines and effective regional cap rocks, but no faults to connect the deep Jurassic gas source with the upper traps, while in the Kuqa Depression of Tarim Basin, there are not only abundant gas sources, but also high quality reservoir rocks, well-developed faults, and good preservation conditions (gypsum-salt cap rocks), and all together result in natural gas accumulation. Thereafter, a general view is that the gas accumulation conditions in the southern margin of Junggar Basin are not as good as those in the Kuqa Depression.

In the southern margin of Junggar Basin, petroleum geologists and prospectors got confused by many problems for a long time. For examples, is there any possibility for the discovery of large gas fields in the southern margin of Junggar Basin? Where are the favorable exploration areas and targets? What are the factors to induce the great difference in natural gas discovery between the southern margin of Junggar Basin and the Kuqa Depression of Tarim Basin which are located at the north and south depressions of the Tianshan Mountain?

In January 2019, high-product oil and gas flow were obtained from Well GT1 in the Gaoquan anticline of the Sikeshu sag, west part of the southern margin in the Junggar Basin, with 1,213 m^3/d oil and 321.7×10^3 m^3/d natural gas from the deep Cretaceous strata (Chen et al., 2019; Du et al., 2019; Zhang et al., 2020). The daily oil and gas production from this well is the highest in the Junggar Basin so far. In December 2020, once again, high-product oil and gas flow were obtained from the Well HT1 at the depth of 7,367 to 7,382 m in the Huxi anticline (**Figure 1**) in the middle part of the southern margin in the Junggar Basin, with 610×10^3 m^3/d natural gas and 106 m^3/d oil. The great breakthrough in these two wells showed a great potential of oil and gas exploration in the southern margin of Junggar Basin.

In this study, based on our previous results about the genetic type of natural gas and its sources in the southern margin of Junggar Basin (Chen et al., 2019), we investigated the geological and geochemical conditions for natural gas generation and accumulation in the southern margin of Junggar Basin, and conducted a comparative study between the southern margin of Junggar Basin and the Kuqa Depression of Tarim Basin in terms of factors controlling the natural gas accumulation. Also, the favorable natural gas exploration areas and targets were discussed for strategy-making reference.

GEOLOGICAL BACKGROUND

Structural Characters

The southern margin of Junggar Basin starts from the Fukang fault zone in the east, extending to the Sikeshu sag in the west, and connects with the Shawan sag, Monan uplift and Fukang sag in the north, and with the north Tianshan Mountain in the south. It is 500 km in length from east to west, 40–60 km in width from south to north, and 21×10^3 km^2 in area. In terms of regional tectonic background, the southern margin of Junggar Basin belongs to the piedmont thrust belt of the north Tianshan Mountain (**Figure 1**), and is the youngest and most complex fold belt in the Junggar Basin. Also, it is a secondary tectonic unit developed during the Late Hercynian, Indosinian-Yanshanian, and Himalayan periods (Yang et al., 2004; Kuang and Jia, 2005; Kuang and Qi, 2006; Chen et al., 2007). Based on the structural styles and their formation mechanisms, the southern margin of Junggar Basin can be further divided into four sub-tectonic units as the Sikeshu sag, the Homatu structural belt, the Qigu fault fold belt and the Fukang fault zone (Yang et al., 2004; **Figure 1**). From the Qigu fault fold belt to the Homatu structural belt, three rows of anticlines were developed from south to north. The first row includes the Torstai, Nananjihai, Honggou, Qingshuihe, and Qigu anticlines, etc., the second row is the Horgos, Manas and Tugulu anticlines, and the third row has the Anjihai, Huxi, and Hutubi anticlines, etc. In terms of geographic background, the southern margin of Junggar Basin can be divided into three parts as the west, the central and the east (**Figure 1**).

Sedimentary Strata

Six sets of sedimentary strata occur in the southern margin of Junggar Basin, including the Permian, Triassic, Jurassic, Cretaceous, Paleogene, and Neogene (**Figure 2**). In the central part, the gross thickness of sedimentary strata is up to 15 km, and relatively thin in the west and east parts, generally 8–12 km (Wang et al., 2013; Chen et al., 2015a; Chen et al., 2016c). Previous studies showed that the Permian source rock was one of the most important source rocks in the Junggar Basin. In the southern margin of Junggar Basin, the Middle Permian source rock deposited in the semi-deep to deep lacustrine facies, with a thickness of 600–1,600 m. Oil shale deposit in the east part of the southern margin was well-developed in the Lucaogou Formation in the Middle Permian (Graham et al., 1990; Carroll et al., 1992; Gao et al., 2016; Bai et al., 2017; Cao et al., 2017). The Upper Permian strata were mainly deposited in the fluvial-swamp to semi-deep lacustrine facies. The Middle-Lower Triassic strata are mainly composed of fluvial-shallow lacustrine coarse clastic deposits, while the Upper Triassic strata deposited in the shore-shallow to semi-deep lacustrine facies with a thickness of 300–800 m, interbedded with thin carbonaceous mudstone and coal seam of swamp facies. The Badaowan, Sangonghe, Xishanyao, and Toutunhe formations of Middle-Lower Jurassic strata are mainly coal-bearing deposits of fluvial and limnetic facies, which are widely distributed in the Junggar Basin, with a maximum thickness of 3,000 m in the southern margin, and generally 1,000–2,000 m. This set of coal measures is the main oil and gas source rocks in the southern margin of Junggar Basin (Wang et al., 2013; Chen et al., 2015a; Chen et al., 2016c). The Upper Jurassic strata include the Qigu Formation and the Karaza Formation, and it is a set of red coarse clastic deposits, which is widely distributed in the southern margin with a thickness of more than 600 m. The Lower Cretaceous strata are a set of semi-deep to shallow lacustrine deposits, which is widely distributed in the whole basin with the thickness of 1,594 m in the southern margin of Junggar Basin. It is relatively well-developed in the central part of the southern margin in respect to oil and gas

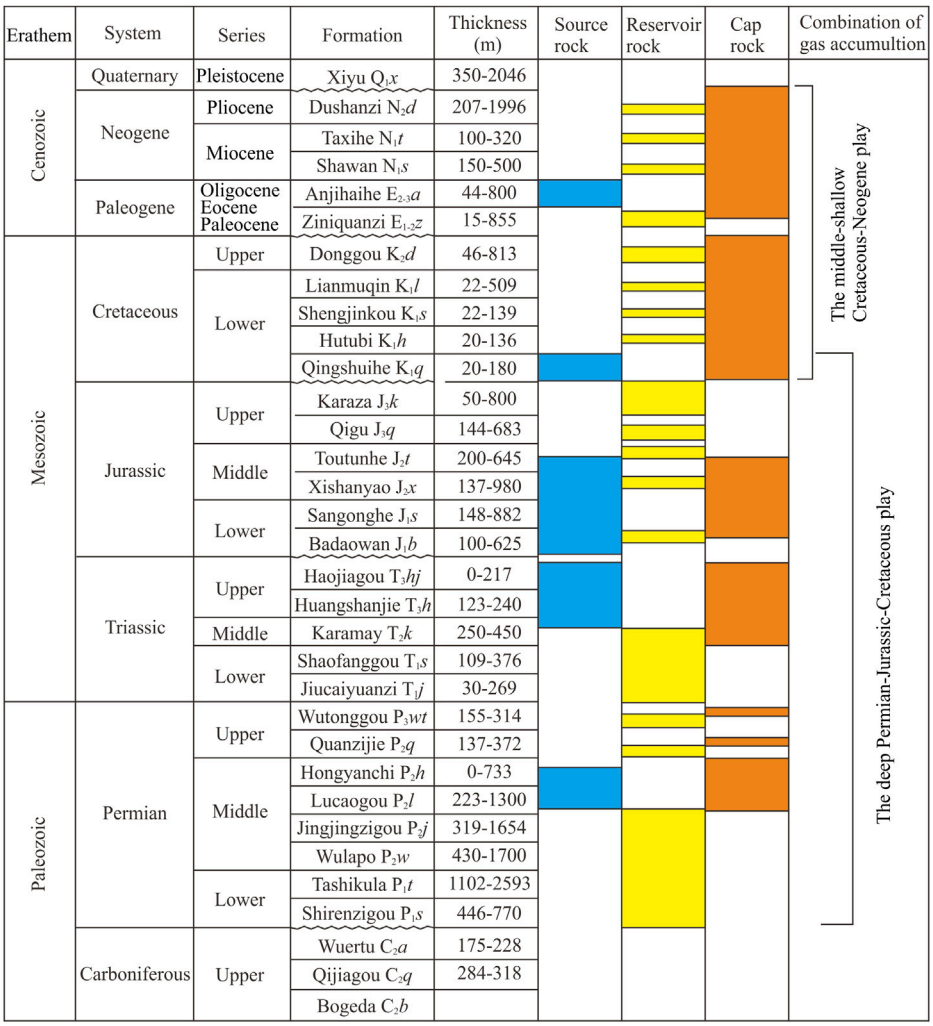


FIGURE 2 | Sedimentary strata as well as combination of source rock, reservoir rock, and cap rock in the southern margin of the Junggar Basin.

generation potential (Wang et al., 2013; Chen et al., 2015a; Chen et al., 2016c). The Upper Cretaceous strata are mainly composed of fluvial coarse clastic deposits, with a thickness of 46–813 m, and generally 300–600 ms. The Paleocene-Eocene strata are fluvial-shallow lacustrine deposits, with a thickness of 15–855 m, and generally >450 m. The Eocene-Oligocene Anjihaihe Formation is mainly composed of deep-semi, deep-shallow lacustrine facies, with a thickness of 44–800 m and generally 350–650 m. Dark mudstone is relatively well developed in the west part of the southern margin. The Oligocene-Pliocene strata are mainly dominated by shallow lacustrine and fluvial deposits, with a thickness of 2,000–2,300 m. The Quaternary Xiyu Formation is composed of piedmont proluvial-alluvial fan-fluvial conglomerate and glutenite deposits, which is widely distributed in the southern margin of Junggar Basin, with a thickness of 350–2046 m, and generally >1,300 m. The thickness of the Quaternary Xiyu Formation in the west part is greater than that in the central and east parts.

DISTRIBUTION AND SOURCES OF NATURAL GAS

Distribution of Natural Gas

Although many oil and gas seeps occur in the southern margin of Junggar Basin, and natural gas shows have also been found in lots of exploration wells (Wang et al., 2013; Chen et al., 2016b; Liu et al., 2016; Zheng et al., 2017), only two commercial gas fields have been discovered in the Hutubi anticline (the Hutubi gas field) and in the Manas Anticline (the Mahe gas field) in the central part (**Figure 1**). The natural gas fields discovered in other structures are mainly small-scale gas reservoirs or associated gas of oil reservoirs revealed by individual well drilling, including the Mazhuang gas field in the Santai, east part.

In these gas fields or gas-bearing structures, the natural gas reservoirs in the Hutubi, Tugulu, Manas, Horgos, and Anjihai anticlines in the central part are mainly located in the Paleogene Ziniquanzi and Anjihaihe formations, and minor in the Neogene

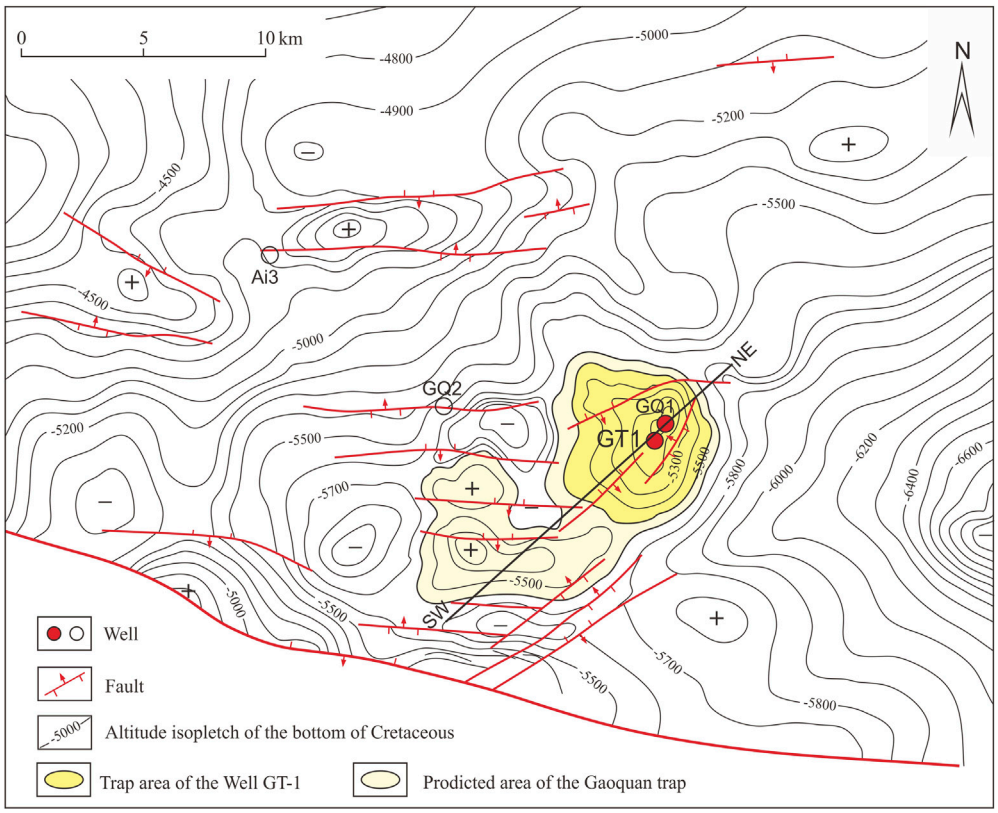


FIGURE 3 | Structural map of Gaoquan anticline and adjacent Cretaceous bottom boundary in west of southern margin.

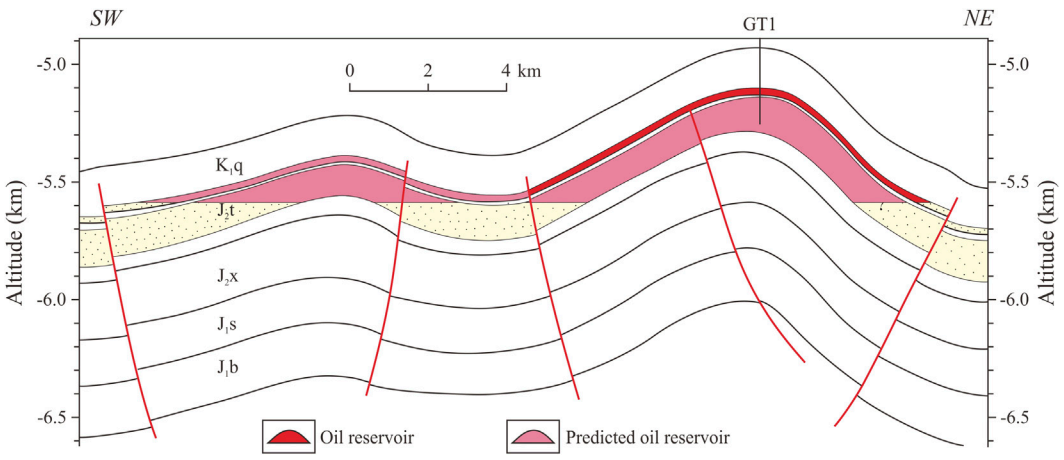


FIGURE 4 | Predicted reservoir profile (through Well GT1) of Gaoquan anticline in west of southern margin (Its location is indicaten in **Figure 3**).

Shawan Formation and the Upper Cretaceous Donggou Formation. The natural gas reservoirs in the Nananjihai structure are distributed in the Jurassic Badaowan Formation, while the natural gas reservoirs from the Qigu oilfield mainly distributed in the Triassic and Jurassic strata.

The oil and gas reservoirs in the Dushanzi anticline, located in the west part of the southern margin, are mainly distributed in the Neogene Shawan Formation and Taxihe Formation. Two condensate gas layers in the Neogene Shawan Formation have been penetrated in Well Du1 and

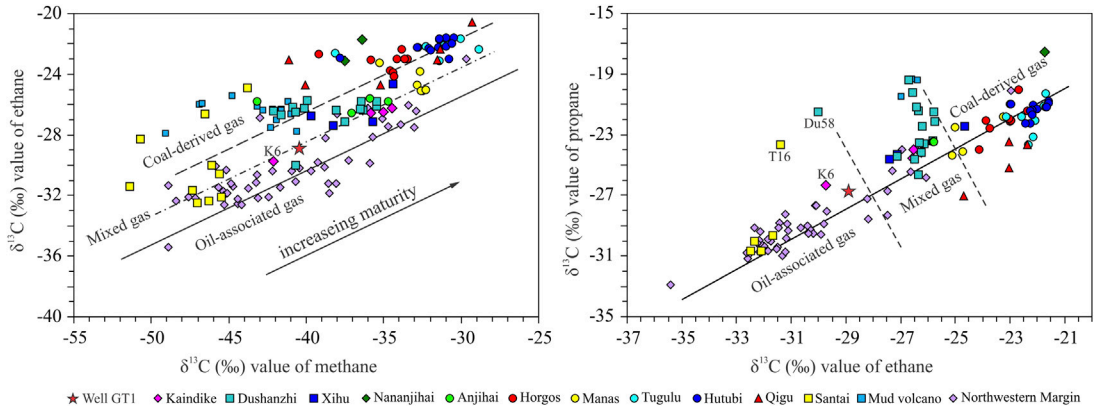


FIGURE 5 | Carbon isotopic composition and types of natural gas in southern margin (Modified from Chen et al., 2019. The data regarding mud volcano are cited from Dai et al., 2012, and the data for the Northwestern margin is provided by the Research Institute of Xinjiang Oilfield Company).

Well XC2. The oil and gas reservoirs in the Kaindick, Xihu, and Gaoquan anticlines in the west part are mainly distributed in the Jurassic Qigu Formation and the bottom of the Lower Cretaceous Qingshuihe Formation. The natural gas reservoirs in the Mazhuang gas field in the east part are mainly in the Upper Jurassic strata. Vertically, oil and gas discovered in the central part are mainly in the middle-shallow Upper Cretaceous-Neogene, while oil and gas discovered in the west part are much deeper, mainly in the Upper Jurassic-Lower Cretaceous.

Recently, high-product oil and gas flow was discovered in Well GT1 in the Gaoquan anticline of the Sikeshu sag (**Figure 1**), west part of the southern margin in the Junggar Basin (Chen et al., 2019; Du et al., 2019), and the oil and gas reservoirs are located in the Toutunhe Formation of Middle Jurassic (**Figures 3**, **4**). Although it is difficult at moment to determine the boundary and scale of oil and gas reservoirs, it was predicted that the structural high trap area of the Gaoquan anticline is about 69 km^2 with the closure height is 450 m, and the Cretaceous structural high trap area where Well GT1 was drilled is about 28 km^2. Thereafter, large oil and gas field is being expected in Gaoquan anticline. More recently, a high-product commercial oil and gas field was discovered in Well HT1 at the depth of 7,367–7,382 m in the Huxi anticline in the middle part of the southern margin (**Figure 1**). It was estimated to be 100 billion cubic meters of natural gas reserve.

Genetic Types and Sources of Natural Gas

The stable carbon and hydrogen isotopic compositions of gasoline hydrocarbons is considered to be closely related to the sedimentary environments, organic matter types and thermal maturity, and can be widely used to determine the genetic types and sources of natural gas (Stahl, 1974; Schoell, 1980; Schoell, 1983; Bernard et al., 1977; James, 1983; James, 1990; Whiticar, 1994; Whiticar, 1996; Whiticar, 1999). Previously, a large body of publications have been focused on the geochemical characters and sources of natural gas discovered in the southern margin of Junggar Basin (Wang et al., 2009; Hu et al., 2010; Wang et al., 2013; Liu et al., 2016; Zheng et al., 2017; Chen et al., 2019), and it is now generally accepted that natural gas discovered in the southern margin of Junggar Basin is thermogenic gas (Chen et al., 2019).

In respect to genetic types and sources of natural gas in the southern margin of Junggar Basin, previous studies by Wang et al. (2009), Hu et al. (2010), Wang et al. (2013), and Liu et al. (2016) suggested that it is mainly coal-derived gas from the Jurassic coal-measures. However, Chen et al. (2019) recently conducted a systematic comparative study on the components and the stable carbon isotopic compositions of natural gas from different anticline structures in the southern margin, and found that the geochemical characters of natural gas from different structures in the southern margin of Junggar Basin were quite different. They can be divided into three types as coal-derived gas, mixed gas and oil-associated gas, of which coal-derived gas and mixed gas are dominated (**Figure 5**). The main genetic types of natural gas are coal-derived gas and mixed gas in the Kaindick, Xihu, and Dushanzi anticlines in the west part of the southern margin, while mixed gas in Well GT1 at the Gaoquan anticline. In the central part, the coal-derived gas is dominated in the Anjihai, Horgos, Manas, Tugulu, and Hutubi anticlines, and mixed gas and coal-derived gas are dominated in the Qigu anticline, while the oil-associated gas in the Nananjihai Anticline. In the Mazhuang gas field from the Santai, Fukang fault fold belt in the east part of the southern margin, the oil-associated gas is the main genetic type.

Gas-source correlation results suggested that natural gas from the Kaindick, Xihu, and Dushanzi anticlines in the west part of the southern margin was derived mainly from the Jurassic coal-measures, and minor from the Permian lacustrine source rocks (Chen et al., 2019). The natural gas from Well GT1 was sourced from the Jurassic coal measures and the Permian lacustrine source rocks. The natural gas from the second and third row anticlines in the Homatu anticline belt in the central part of the southern margin was derived mainly from the Jurassic coal-measures, while the natural gas from the first row anticlines in the Qigu fault fold belt was sourced mainly from the Permian

lacustrine source rocks and the Jurassic coal-measures, minor from the Upper Triassic lacustrine-limnetic source rocks. In the Mazhuang gas field in the Santai, Fukang fault fold belt in the east part of the southern margin, the natural gas was derived mainly from the Permian lacustrine source rocks, and minor from biogenetic gas due to biodegradation of crude oil generated from the Permian source rocks. The results clearly showed that in the southern margin of Junggar Basin, the Jurassic coal-measures is the most important source rock of natural gas, and the Permian lacustrine source rock is the second one. The Triassic lacustrine-limnetic source rock may also be regionally important gas source rocks.

GEOCHEMICAL CONSTRAINTS ON NATURAL GAS GENERATION

Bulk Characters of Source Rocks

Five sets of source rocks from the Permian, Triassic, Jurassic, Cretaceous, and Paleogene strata occurred in the southern margin of Junggar Basin, and the thickness of source rocks mainly depends on its location. In the central part of the southern margin, there are 5 sets of source rocks, while 2-4 sets in east and west parts (Wang et al., 2013; Chen et al., 2015a; Chen et al., 2016c).

The Middle Permian Lucaogou Formation lacustrine source rocks are mainly distributed in the areas from the east part to the central part of the southern margin, with a thickness of 50–250 m, and the maximum thickness up to >700 m in the east part (Carroll, 1998; Wang et al., 2013). The organic carbon content of source rocks ranges from 0.50 to 34.27%, with an average of 6.60%. The average hydrocarbon generation potential (S_1+S_2) is 36.99 mg/g.rock. The organic matters are dominated by sapropelic type (type I) and humic-sapropelic type (type II_A). The Middle Permian Lucaogou Formation lacustrine source rock is now at the low-mature stage at the outcrops in the east part of the southern margin (Wang et al., 2013; Hou et al., 2021). In the sags of the Homatu anticline belt, the Permian source rock is buried greater than 10 km and reached the highly to over mature stage, and was considered to be an effective gas source rock (Wang et al., 2013; Chen et al., 2015a). Crude oils from the Permian source rocks have been previously found in the Dushanzi anticline (Wang et al., 2013; Chen et al., 2016a; Chen et al., 2016b). In Well GT1 and Well K6, half of the natural gas with lighter carbon isotope composition was derived from the Permian source rocks (Chen et al., 2019). These results suggested that the Permian lacustrine source rocks could be an important source rock in the west part of the southern margin. Therefore, further study using seismic and drilling data to determine the distribution and scale of the Permian lacustrine source rocks is needed.

The lacustrine source rock in the Upper Triassic Huangshanjie Formation is also widely distributed in the southern margin of Junggar Basin (Chen et al., 2003; Kang et al., 2012; Wang et al., 2013; Chen et al., 2015a; Chen et al., 2016c), with a thickness of 50–300 m. The total organic carbon is lower than that of the Permian Lucaogou Formation, with an average TOC of 2.89%. The organic matters are mainly type II and type III. The burial depth of the Huangshanjie Formation is now up to >9 km in the central sag, and reaches highly to over mature stage, resulting in an effective source rock. This set of source rock is relatively well developed and is an important candidate as natural gas source rock in the central part of the southern margin and the Fukang sag in the east part.

The Middle-Lower Jurassic source rock is widely distributed in the southern margin of Junggar Basin. In Badaowan Formation of the Lower Jurassic, the dark mudstone, carbonaceous mudstone, and coal seam are generally 200–300 m, 1–10 m, and 5–50 m in thickness, respectively. The thickness of dark mudstone ranges from 50 m to 300 m in the Sangonghe Formation. The thickness of dark mudstone, carbonaceous mudstone and coal seam in the Xishanyao Formation is 75–150 m, 2–15 m and 5–30 m, respectively. The total organic carbon of dark mudstone from the Middle-Lower Jurassic strata ranges from 0.5 to 6.0%, with an average of 1–2% in different Formations. The average TOC of carbonaceous mudstone is about 20%, and ~50–60% for coal seam. The organic matters of the Middle-Lower Jurassic source rocks are mainly type II_B and type III, with type II_A limited. Although the vitrinite reflectance of organic matter from the Jurassic outcrop source rocks ranges from 0.5 to 0.7%, it reaches highly to over mature stage in the depression due to burial depth of >8 km (**Figure 6**). Previous studies concluded it was the most important source rock in the southern margin (Wang et al., 2013; Chen et al., 2015a; Chen et al., 2016c).

The Qingshuihe Formation of Lower Cretaceous lacustrine source rock is widely distributed in the southern margin, but the most developed in the central part of the southern margin with a thickness of 150–200 m, compared to a general thickness of 50–150 m in other parts of the southern margin. The TOC of mudstone ranges from 0.06 to 1.81% with an average of 0.92%. The organic matters are dominated by type I and type II_A. Although organic matter in outcrop samples showed low mature stage, it reaches peak to late oil generation stage in the depression due to burial depth of up to 6–8 km. In the central part of the southern margin, the crude oil was mainly derived from the Qingshuihe source rock (Liao et al., 2006; Wang et al., 2013; Chen et al., 2016b; Chen et al., 2016d; Chen et al., 2016e).

The Paleogene Anjihaihe Formation lacustrine source rock is mainly distributed in the central and west parts of the southern margin, with a thickness of 50 m–200 m. The average TOC is 1.03%, but shows a great change depending on location. Organic carbon content of source rocks from the Sikeshu sag in the west part is much higher, with an average TOC of 1.41%, and the hydrocarbon generation potential is 5.02 mg/g. rock. The organic matter is dominated by type II. In the central and east parts, organic carbon content of dark mudstone is relatively low, and the organic matter is dominated by type III. Organic matter from the outcrop dark mudstone is now at immature stage. However, the thermal maturity of organic matter in source rocks from the Sikeshu Sag to the central part reaches low mature-mature stage in respect to its depth of 5,000–6,500 m. The crude oil in the Paleogene-Neogene reservoirs is sourced from this set of source rock in the Dushanzi, Kaindick, Xihu and Gaoquan anticlines in the west part (Wang et al., 2013; Chen et al., 2016b; Chen et al.,

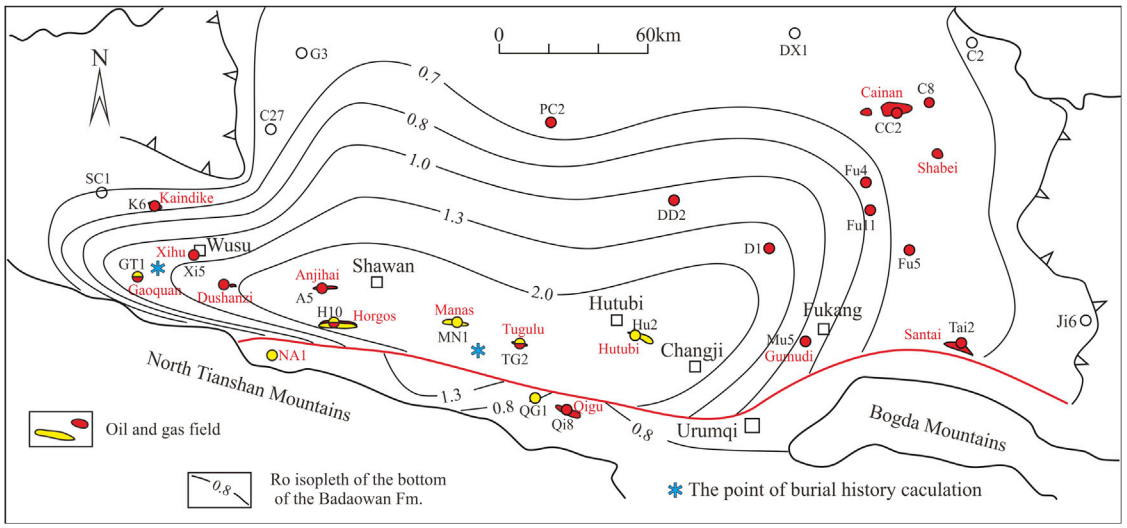


FIGURE 6 | Maturity of source rocks at the bottom of Jurassic and the distribution map of main oil and gas fields (wells) from Jurassic in southern margin of Junggar Basin.

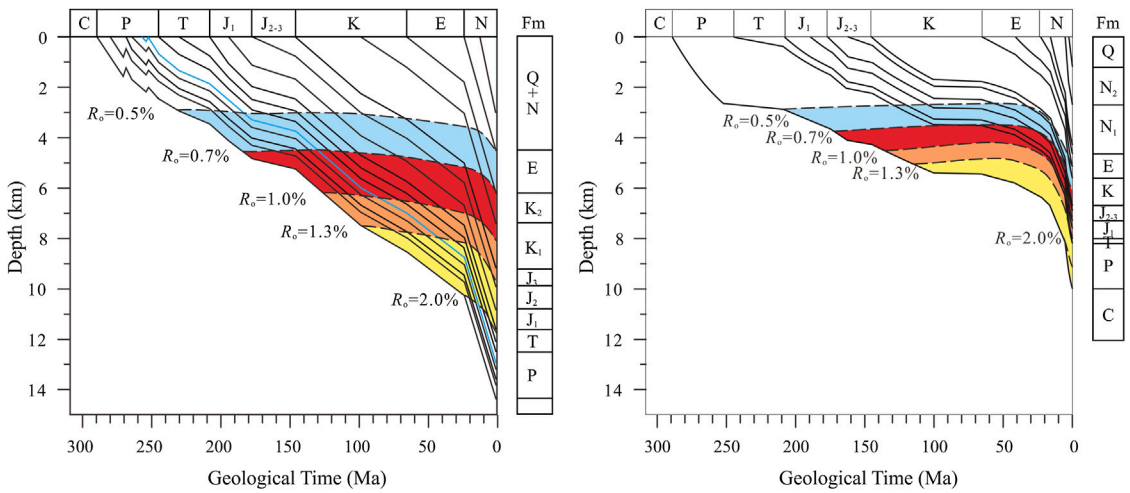


FIGURE 7 | Burial evolution and hydrocarbon generation history of source rocks in the middle and western parts of southern margin. **(A)** Middle part of sedimentary sag in the middle of southern margin (see **Figure 6** for location); **(B)** Middle and west parts of Sikeshu Sag in the west of southern margin (see **Figure 6** for location).

2016d). Therefore, it is an effective oil source rock, with little gas potential.

Conclusively, the effective source rocks for natural gas generation in the southern margin of Junggar Basin are mainly the Middle-Lower Jurassic coal measures, the Upper Triassic limnetic and the Permian lacustrine source rocks.

Thermal Evolution and Hydrocarbon Generation History

Previous studies suggested that the paleo-geothermal field in the southern margin of Junggar Basin experienced a gradual cooling process as revealed by the geothermal gradient from 32.0–36.6°C/km in Permian to 18–22°C/km at present (Wang et al., 2000; Qiu et al., 2001). Within the constraint of measured vitrinite reflectance of drilled source rocks, the thermal evolution and hydrocarbon generation history of source rocks from the sags in the central and west parts were calculated by basin modeling software (**Figure 7**). In the central part, the burial depths of the Permian, Triassic and Jurassic source rocks are much deeper (**Figure 8**), and the hydrocarbon generation occurred relatively early. In the southern sag of the Manas anticline in Homatu structural belt, the main oil generation period of the Middle Permian source rock was in Cretaceous (150–60 Ma), and the main gas generation period was in Paleogene-Oligocene (60–20 Ma; **Figure 7A**). The source rock from the Upper

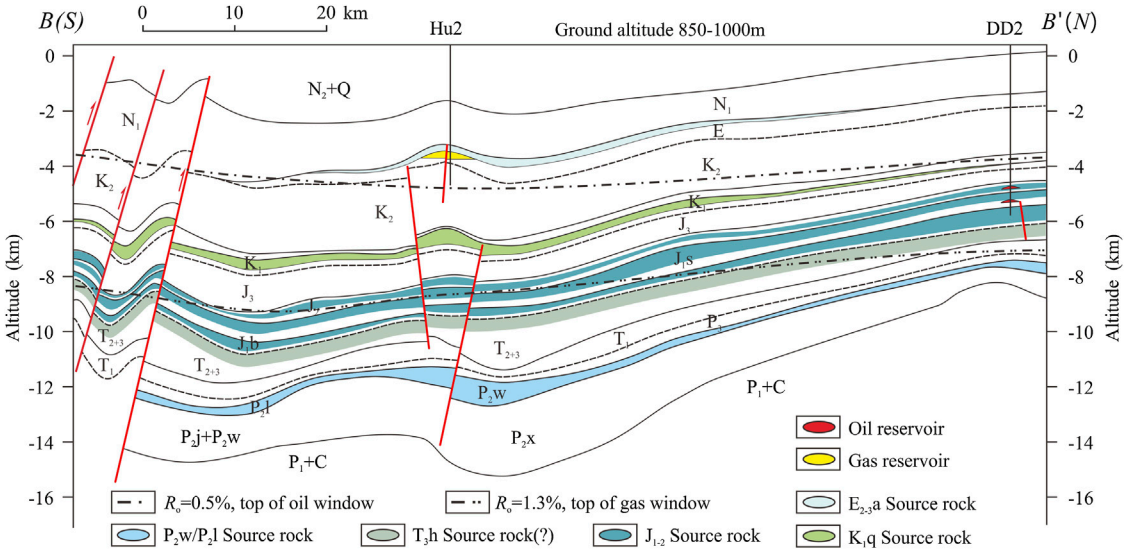


FIGURE 8 | Sketch diagram of structure, source rock burial evolution and hydrocarbon migration and accumulation section in the middle of southern margin.

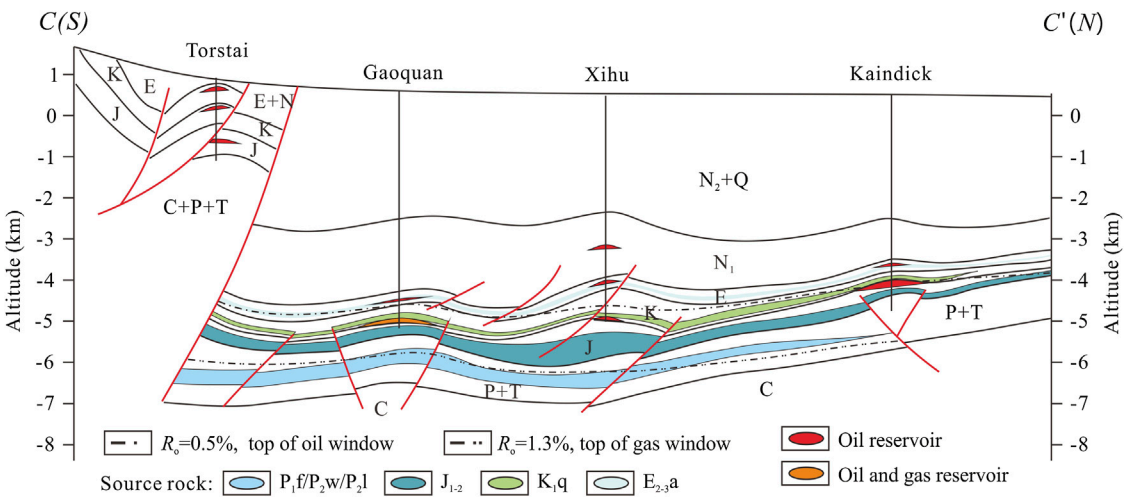


FIGURE 9 | Sketch diagram of structure, source rock burial evolution and hydrocarbon migration and accumulation section in the west of southern margin.

Triassic strata mainly generated oil at the end of Early Cretaceous to Paleogene (110–30 Ma), and the main gas generation period at Miocene (20–5 Ma). The main oil generation period of the Middle-Lower Jurassic source rocks occurred at the Late Cretaceous to Oligocene (100–20 Ma), and the peak oil about 90–25 Ma from the Late Cretaceous to Eocene. Gas generation from kerogen-cracking (R_o = 1.0%) started at the beginning of Eocene (40 Ma), and currently reaches peak gas generation stage. The Lower Cretaceous source rock is now mainly at the peak and late oil generation stage.

It is still unclear to date about the distribution of the Permian-Triassic source rocks in the west part of the southern margin in Junggar Basin. According to seismic interpretation, the Permian-Triassic strata are about 1800–2,300 m in thickness, and are 6–8 km in burial depth in the mid-west of the Sikeshu sag (**Figure 9**), much shallower than that in the central part. Therefore, the main hydrocarbon generation time in the mid-west of the Sikeshu sag could be much later than that in the central part. The Lower Permian source rock (equivalent to the Fengcheng Formation) mainly generated oil during the Late Jurassic to Early Cretaceous (160–100 Ma), and the main gas generation period started from the Late Cretaceous and continues to present (**Figure 7B**). Because the Cretaceous and Paleogene strata in the Sikeshu sag are much thinner than that in the central part, the hydrocarbon generation period of the Jurassic coal-measures in the Sikeshu sag should be later than that in the

central part. The main oil generation stage started from Eocene and continues to present, and it is still at the peak oil to late stage oil generation. The Lower Cretaceous source rock generated oil much later, which was mainly at the mature stage of oil generation. The Paleogene source rock is at immature to early mature stage of oil generation, and basically has no potential for natural gas generation.

COMPARISON ON GAS ACCUMULATION CONDITIONS BETWEEN THE SOUTHERN MARGIN OF JUNGGAR BASIN AND THE KUQA DEPRESSION

The Kuqa Depression of Tarim Basin and the southern margin of Junggar Basin are located on south and north sides of the Tianshan Mountains, respectively, with similar sedimentary cap rocks and tectonic evolution history in respect to petroleum geological background (Hendrix et al., 1994; Li et al., 2000; Kuang and Liu, 2001; Liang et al., 2002; Liang et al., 2004; Fang et al., 2005; Kuang and Jia, 2005; Kuang and Qi, 2006; Fang et al., 2007; He et al., 2009). Many large gas fields have been discovered to date in the Kuqa Depression, such as KL-2, Dabei, Keshen and Dina gas fields (Wang, 2014). However, in the southern margin of Junggar Basin, only two medium-sized gas fields have been found in the Hutubi and Manas anticlines. The main factors leading to the exploration differences between the Kuqa Depression and the southern margin of Junggar Basin were investigated for a long time and are still unclear to date. Kuang and Liu (2001) made a comprehensive comparison on the hydrocarbon accumulation conditions between the two regions, and concluded that both were excellent gas source, fold anticlines, and effective regional cap rocks. The main difference is that in the Kuqa Depression, the quality of the reservoir rock is much better and faults connected source rocks with reservoirs were well developed. Also, the preservation is better in the Kuqa Depression than that in the southern margin of Junggar Basin. Thereafter, it was considered that natural gas accumulation conditions in the southern margin of Junggar Basin are worse than those in the Kuqa Depression. However, recent discovery of high-product oil and gas flow in the Well GT1 and Well HT1 suggested that gas accumulation conditions in the southern margin are probably not worse than expected previously, and need a deep insight on the factors controlling gas generation and accumulation in the southern margin of Junggar Basin.

Difference in Source Rock Development

It is now generally accepted that the Middle-Lower Jurassic coal-measures are main source rocks in the Kuqa Depression and the southern margin of Junggar Basin, followed by the Upper Triassic lacustrine-limnetic source rocks (Du et al., 2006; Qin et al., 2007; Wang et al., 2013; Chen et al., 2015a; Chen et al., 2016c). In the Kuqa Depression, the cumulative thickness of Middle-Lower Jurassic limnetic mudstone and carbonaceous mudstone is 100–600 m, and the cumulative thickness of coal seams is generally 5–30 m (Liang et al., 2004). The mudstone in the Yangxia and Kizilonur Formations of Lower Jurassic is generally 50–500 m in thickness, and the coal seams can reach a maximum thickness of 52 m. The thickness of mudstone in the Chakemak Formation generally ranges from 50 to 150 m. The dark mudstone and carbonaceous mudstone in the Upper Triassic Taliqike Formation are generally 50–150 m in thickness, and the coal seams are generally 0.5–7 m, with a maximum thickness of 12 m.

In the southern margin of Junggar Basin, the cumulative thickness of the Middle-Lower Jurassic limnetic dark mudstone and carbonaceous mudstone is 200–700 m, and the cumulative thickness of coal seams is 10–50 m with a maximum thickness of 60 m (Wang et al., 2013; Chen et al., 2015a; Chen et al., 2016c). The mudstone in the Badaowan Formation of Lower Jurassic is generally 200–300 m in thickness, and the cumulative thickness of coal seams is generally 5–20 m (up to 50 m). The mudstone of the Sangonghe Formation is generally 50–300 m in thickness; the mudstone of the Xishanyao Formation of Middle Jurassic is generally 75–150 m, and the cumulative thickness of coal seams is 5–30 m with a maximum thickness of >40 m. The lacustrine and limnetic source rocks from the Upper Triassic Huangshanjie and Haojiagou Formations are generally 50–300 in thickness, which is similar to those in the Kuqa Depression, but the distribution of coal-measures in the Haojiagou Formation is not as stable as that in Kuqa Depression. As discussed in *Bulk Characters of Source Rocks*, three sets of source rocks occurred in the southern margin of Junggar Basin, including the Lower Permian/Middle Permian, the Lower Cretaceous and Paleogene source rocks, which were not developed in the Kuqa Depression, suggesting multiple sets of source rocks in the southern margin of Junggar Basin, and even the Middle-Lower Jurassic coal-measures were developed better than those in the Kuqa Depression (**Table 1**). However, the Upper Triassic lacustrine and limnetic source rocks in the southern margin of Junggar Basin are basically equivalent to or slightly worse than those in the Kuqa Depression.

Difference in Hydrocarbon Generation Potential of Source Rocks

As showed in **Table 1**, at low-medium maturity, hydrocarbon generation potential of Jurassic dark mudstone, carbonaceous mudstone and coals from the southern margin of Junggar Basin is higher than those of the Jurassic coal measures from the Kuqa Depression (Liang et al., 2004; Wang et al., 2013; Chen et al., 2015a). This is mainly due to the relatively low content of hydrogen-enriched liptinites in coal measures from the Kuqa Depression. The relative percentage of inertinites in mudstone and carbonaceous mudstone from the Kuqa Depression is about 25–50%, and 40–70% vitrinite as well as 3–8% liptinites. However, the relative percentage of inertinites in mudstone and carbonaceous mudstone from the southern margin of Junggar Basin is only 8–10%, and 56–68% vitrinite as well as 25–33% liptinite. This is the same case in coal seams. The relative percentage of inertinites reaches up to 28%, vitrinite to 70%, and liptinites to 2% in coals from the Kuqa Depression. While the

TABLE 1 | Comparison of source rocks between southern margin and Kuqa Depression[a].

Time	Source rock type	Southern margin					Kuqa depression				
		Thickness (m)	TOC (%)	HC generation potential (mg/g)	HI (mg/gTOC)	R_o (%)	Thickness (m)	TOC (%)	HC generation potential (mg/g)	HI (mg/gTOC)	R_o (%)
E	Mud	50–200	1.41	5.02	387	0.4–0.8					
K	Mud	150–250	0.92	1.74	189	0.4–1.3					
J	Mud	200–700	1.70	2.41	142		100–600	2.20	2.18	99	
	Coal	10–50	54.22	109.44	210	0.5–2.2	5–30	55.75	89.49	167	0.5–2.5
T_3	Mud	50–300	2.89			0.8–2.5	50–150	1.85			0.6–2.8
	Coal	<5					0.5–7	64.99			0.6–2.8
P	Mud	50–250	6.60			>1.3					

[a]*The data in the table are mainly based on the statistics of Liang et al. (2004) and Wang et al. (2013). The abundance of organic matter and hydrocarbon generation potential of Jurassic are the average values of source rocks in low to medium maturity stage.*

relative percentage of inertinites is only 16%, and 64% vitrinite as well as up to 20% liptinites in coals from the southern margin of Junggar Basin (Liang et al., 2004; Qin et al., 2007; Wang et al., 2013). In addition, the average TOC of dark mudstones from the Upper Triassic Huangshanjie and Taliqike Formations in the Kuqa Depression is 1.09 and 1.81%, respectively. However, the average TOC of Upper Triassic mudstone and carbonaceous mudstone is 2.89% in the southern margin of Junggar Basin, higher than that in the Kuqa Depression. Therefore, the hydrocarbon sources in the southern margin of Junggar Basin are better than those in the Kuqa Depression.

The maturity of organic matter in Jurassic coal-measures from the Kuqa Depression is higher than that in the southern margin of Junggar Basin. At present, the maturity of organic matter in Jurassic coal measures from the Kuqa Depression ranges from 0.8 to 2.5% as revealed by vitrinite reflectance, showing an increasing trend from east to west with the highest of 2.8% (Wang et al., 1999; Liang et al., 2004). In the eastern region, the Jurassic coal-measures is mainly at the peak oil to late oil stages, while in the central and west parts, source rocks are mainly at highly to over mature stage (equivalent to wet gas-dry gas stages). However, the maturity of organic matter in Jurassic coal measures from the southern margin of Junggar Basin ranges from 0.7 to 2.2% as revealed by vitrinite reflectance, showing an increasing trend from west to east. The Jurassic coal-measures is mainly at peak oil stage in the west part, but mainly at high-mature wet-gas stage in the central part. No source rock reaches at dry gas stage. Therefore, the maturity of organic matter in source rocks from the Kuqa Depression is much higher than that in the southern margin of Junggar Basin, which may be one of the main factors controlling gas generation and accumulation in the Kuqa Depression.

Basin modeling results showed that the total generated hydrocarbon amount from Jurassic source rocks in the southern margin of Junggar Basin is about 397.3×10^9 t (Du et al., 2019), and the total expelled hydrocarbon amount is about 140.3×10^9 t (including the total expelled oil amount of 38.9×10^9 t, and total expelled gas amount of 127×10^{12} m^3). The average intensity of hydrocarbon generation, hydrocarbon expulsion and gas expulsion were 18.92×10^6 t/km^2, 6.68×10^6 t/km^2 and 6×10^9 m^3/km^2, respectively. Also, the Permian and the Upper Triassic source rocks can contribute hydrocarbon resources, which was not included here. Therefore, the southern margin of Junggar Basin has rich sources for hydrocarbon accumulation.

Difference in Physical Properties of Reservoir Rock

Both the Jurassic and Cretaceous sandstones as reservoir rocks in the Kuqa Depression showed high quality (Kuang and Liu, 2001). The porosity and permeability of Jurassic sandstones are 6–21% and 0.1×10^{-3}–300×10^{-3} μm^2, respectively. While the porosity and permeability of Cretaceous Basjiqike Formation sandstone reaches 8.7–19.2% and 87×10^{-3}–696×10^{-3} μm^2, respectively, typical characters of medium porosity and medium permeability reservoir rocks. Furthermore, the Cretaceous Formation sandstone was widely distributed in the Kuqa Depression with huge thickness of 90–500 m (Wang and Hu, 2002). However, compared to the Kuqa Depression, the Jurassic, Cretaceous and Tertiary reservoir rocks are generally poor in quality in the southern margin of Junggar Basin (Kuang and Liu, 2001). In fact, the deep buried reservoirs showed extremely low porosity and ultra-low permeability in the Kuqa Depression, with a porosity of 3–9% (averaging 5.4%) and a matrix permeability of 0.35×10^{-3} to 0.5×10^{-3} μm^2 (Wang, 2014).

Sandstones from the Upper Jurassic Qigu Formation and the Karaza Formation are the effective reservoir rocks in the southern margin of Junggar Basin. The sandstone from the Jurassic Qigu Formation mainly deposited in the braided delta front with an area of >15,000 km^2, resulting in changing physical properties, and thereafter leading to low porosity and low permeability. In the west part of the southern margin, the sandstone from the Jurassic Qigu Formation is relatively thin, with thickness of 100–236 m. The porosity ranges from 3 to 25%, with an average of 10–21%; the permeability ranges from 0.1×10^{-3} to $1{,}640 \times 10^{-3}$ μm^2, with an average of 4×10^{-3}–162×10^{-3} μm^2 (Zhang et al., 2012). In the central part of the southern margin, sandstone from the Jurassic Qigu Formation is much thicker, with a thickness of 60–384 m. The porosity ranges from 9.27 to 14.38%, with an average of 11.5%, and the permeability ranges from 0.16×10^{-3} μm^2 to 17.68×10^{-3} μm^2. Therefore, sandstone from the Jurassic Qigu Formation has medium porosity and low permeability (Wu et al., 1994). The Jurassic Karaza Formation is

mainly distributed in the central and east parts of the southern margin, with relatively limited potentials. Large alluvial fan and braided river delta were well developed, resulting in the formation of a set of very thick massive conglomerate and sandstone. In outcrop area, the thickness of glutenite is usually >150 m, with a maximum thickness up to 860 m in the Karaza area (Du et al., 2019). The exploration results revealed that sandstone from the Jurassic Karaza Formation was 210–450 m in thickness, with an area of 10,000 km^2, and showing mainly medium-low porosity and medium-low permeability. Regionally, high-quality Jurassic Karaza reservoir rocks were well developed, with an average porosity of 16–19%, and permeability of 100×10^{-3}–260×10^{-3} μm^2 (Han et al., 2012; Lei et al., 2012; Du et al., 2019).

The Cretaceous reservoir rock is mainly composed of glutenite and sandstone at the bottom of the Qingshuihe Formation of Lower Cretaceous in the southern margin of Junggar Basin. Previous study by Fang et al. (2006) suggested that this set of reservoir rock was low quality with thin deposit (10–30 m), and was mainly distributed at the basin edge and low uplifts in the central part. However, recent study indicated that the Cretaceous sandstones developed mainly from braided river delta and fan delta front at the bottom of the Qingshuihe Formation, with a thickness of 20–100 m and an area of 15,000 km^2 (Du et al., 2019). The sandstone shows good in the physical properties, with porosity of 9.0–18.6% (averaging 15–18%), permeability of 97.75×10^{-3}–186.00×10^{-3} μm^2. It can be defined as medium-low porosity and medium-high permeability. The main pore type in sandstone from the Qingshuihe Formation is primary residual intergranular pores, with good connectivity. For example, the porosity of sandstone from the Qingshuihe Formation in Well GT1 ranges from 13.4 to 18.4% at the interval of 5767.5–5774.7 m on the basis of well logging interpretation. High-product oil and gas flow confirmed that sandstone from the Cretaceous Qingshuihe Formation also is the excellent reservoir rocks.

Sandstones from the Paleogene Ziniquanzi Formation and the Neogene Shawan Formation are also the effective reservoir rocks in the southern margin of Junggar Basin, with a thickness generally ranging from 10 to 80 m (Lei et al., 2008; Xiao et al., 2011; Bai et al., 2013a). Sandstone from the Ziniquanzi Formation in Homatu structural belt showed medium-high porosity and medium-high permeability, with a porosity of 1.8–34% (mainly 21–26%, averaging 18.94%). The permeability ranges from 0.06×10^{-3} to 1000×10^{-3} μm^2, and mainly 4×10^{-3} to 640×10^{-3} μm^2, with an average of 197×10^{-3} μm^2. Sandstones from the Ziniquanzi Formation and Shawan Formation in the Sikeshu sag are relatively poor in quality as reservoir rock, with porosity of 9–16% and permeability of 10×10^{-3}–127×10^{-3} μm^2. Therefore, reservoir rocks distributed in the Jurassic to Neogene were relatively well-developed in the southern margin of Junggar Basin, and their quality is similar to those in the Kuqa Depression.

Difference in Migration Pathways and Traps

The strong thrust and compression during Himalayan orogeny in the Kuqa Depression resulted in the development of structures in rows and belts, which can be divided into upper and lower structural layers. Natural gas discovered to date was mainly accumulated in the lower structural layer. The thrust faults directly connected source rocks with the lower structural layer, being good vertical migration pathways (Kuang and Liu, 2001; He et al., 2009; Wang, 2014). In the southern margin of Junggar Basin, structural traps were also well developed (Li et al., 2003; Kuang and Jia, 2005; Kuang and Qi, 2006; Lei et al., 2012), which were not only in the shallow structural layer, but also in the deep structural layer. Total 45 traps have been identified to date in the middle-shallow structural layers of the piedmont thrust belt (Li et al., 2003), and 40–46 traps have been preliminarily identified in the deep layer (Lei et al., 2012; Du et al., 2019), of which 21 traps in the deep layer were confirmed, with a total trap area of 2,486 km^2. Most of these traps are anticlines that were formed during the Neogene period (Hendrix et al., 1994; Deng et al., 1999; Fang et al., 2005; Hu et al., 2005; Guo et al., 2006; Du and Wang, 2007; Fang et al., 2007) and are similar to those in the Kuqa Depression. The trap formation time in the southern margin of Junggar Basin matched well with the time of gas generation from the Jurassic coal-measures, which is also similar to that in the Kuqa Depression.

Previously, Kuang and Liu (2001) argued that no fault system connected deep source rocks with the upper anticline traps in the southern margin of Junggar Basin. However, recent study clearly showed faults connecting deep source rocks with the shallow structural traps in the southern margin of Junggar Basin (**Figures 4**, **8**, **9**). This was evidenced by oil and gas shows in outcrops and drilled wells in the southern margin of Junggar Basin, and commercial natural gas fields were also discovered in the shallow Paleogene and Neogene reservoirs from the Manas and Hutubi anticlines. Natural gas was sourced mainly from the deep Jurassic coal-measures, and migrated into shallow layers through fault systems (Wang et al., 2013; Chen et al., 2015b; Chen et al., 2016c; Chen et al., 2017). The results suggested that the fault systems connecting the deep source kitchen with the upper traps were well developed in the southern margin of Junggar Basin, that were favor for the upward migration of deep oil and gas.

Difference in Cap Rocks and Sealing Capability

Two sets of regional cap rocks mainly occurred in the Kuqa Depression. The first one is the Paleogene gypsum-salt rock and gypsum-mudstone cap rock, and the second is the Lower Cretaceous Shushanhe Formation-Jurassic Qigu Formation mudstone. The deposits of cap rocks in the Kuqa Depression were widely distributed with excellent sealing capability, especially for the Paleogene gypsum-mudstone salt rock (Kuang and Liu, 2001; Wang and Hu, 2002). There are also two sets of regional cap rocks developed widely in the southern margin of Junggar Basin. One is the mudstone from the Qingshuihe Formation-Hutubi Formation of Lower Cretaceous, and another is lacustrine mudstone from the Paleogene Anjihaihe Formation. Basically, the quality of the cap rock in the Kuqa Depression is better than that in the southern margin of Junggar Basin in terms of rock characters.

The Qingshuihe Formation in the southern composed of gray and grayish green mudstone, interbedded with thin argillaceous siltstone. A set of thick basal conglomerate is well developed at the bottom of Qingshuihe Formation, with ratio of mudstones to strata of 0.5–1.0. The total thickness of mudstone drilled is 188 m, and the maximum thickness of individual layer is 78 m. The Hutubi Formation is mainly composed of grayish green and brownish red mudstone, with a thickness of 300–700 m, and a maximum thickness of individual layer up to 138 m (Du et al., 2019). The lacustrine mudstone in the Anjihaihe Formation of Paleogene is generally 50–200 m in thickness. Although no gypsum-mud salt rock developed in the Cretaceous and Paleogene strata in the southern margin of Junggar Basin, overpressure occurred in the mudstones of the Middle-Lower Jurassic, Lower Cretaceous, and Paleogene Anjihaihe Formation (Kuang, 1993; Wu et al., 2000; Zha et al., 2000; Wang et al., 2003; Luo et al., 2004; Wu et al., 2006; Luo et al., 2006; Luo et al., 2007). The pressure coefficient ranges from 1.3 to 2.0 with a maximum up to 2.43, and most of them >1.8. Regionally, mudstone system in the west of the southern margin showed high overpressure, while low overpressure in the east. For example, a repeat formation test (RFT) showed pressure coefficients of 2.2 and 2.4 (with an excess pressure of approximately 40–44 MPa) in the lower part of the Cretaceous Qingshuihe Formation and the Anjihaihe Formation from the Gaoquan and Anjihai anticlines in the west, respectively (Luo et al., 2007; Du et al., 2019). The excess pressure in the lower part of the Anjihaihe Formation from the Manas and Tugulu anticlines is approximately 20 MPa, whereas on the Hutubi anticline to the east, the pressure in the same formation and the underlying strata is close to hydrostatic pressure (Luo et al., 2007). The widespread occurrence of overpressure indicates that mudstone system can be good sealing capability in the southern margin of Junggar Basin.

In fact, oil and gas discovered in the Jurassic reservoirs in Kaindick oilfield demonstrated a good sealing capability of mudstones in the Cretaceous Qingshuihe Formation in the southern margin of Junggar Basin. Also, the Dushanzi oil field, Mahe gas field and Hutubi gas field showed good Paleogene and Neogene reservoir–cap rock combination. The exploration facts strongly suggest that the mudstone systems in the southern margin of Junggar Basin can act as good cap rocks for large and medium oil and gas accumulation.

NATURAL GAS ACCUMULATION AND EXPLORATION TARGETS PREDICTED IN THE SOUTHERN MARGIN OF JUNGGAR BASIN

Although source rocks in the Permian, Triassic, Middle-Lower Jurassic, Lower Cretaceous Qingshuihe Formation, and the Lower Tertiary Anjihaihe Formation have been proved to be effective source rocks in the southern margin of Junggar Basin, the main oil and gas generation periods of source rocks are quite different, which strongly depend on the location of source rocks. The relationship between hydrocarbon generation time and the formation time of structural traps is a key factor controlling the formation of large oil and gas reservoirs.

Regionally Tectonic Evolution and Natural Gas Accumulation

The southern margin of Junggar Basin started to uplift greatly since Miocene (25 Ma). Therefore, the anticline structures in this area were developed very late (Fang et al., 2005; Hu et al., 2005; Guo et al., 2006; Du and Wang, 2007; Fang et al., 2007). The Qigu anticline and other anticlines in the first row were formed before ~10–7 Ma; the Horgos anticline and other anticlines in the second row were formed before 3–1.5 Ma; the Anjihai anticline and other anticlines in the third row were formed before 1 Ma, while the Hutubi and Xihu anticlines etc. were formed much later. Therefore, the structures in the first row can only capture the oil and gas formed since ~10 Ma, the structures in the second row can capture oil and gas since ~3 Ma, and the structures in the third row can capture oil and gas since 1 Ma. By comparing the relationship between the oil and gas generation time from five sets of source rocks and the formation time of the anticlines in the southern margin of Junggar Basin, natural gas charging and accumulation process can be deciphered in these anticline structures, and can also interpret the differences in geochemical properties of natural gas from different anticline structures perfectly.

The anticline structures with oil and gas discovery had not formed during the main oil generation stage from the Permian, Triassic and Jurassic source rocks in the central part of the southern margin. Except for the anticlines located at the edge of southern margin where the Permian and Triassic source rock depositions were shallow and can correlated to the initial formation stage of paleo-structures, for most anticline structures in the central part of the southern margin, it is impossible to be charged by crude oil generated from the Permian, Triassic and Jurassic source rocks. Even the main gas generation stage from the Middle Permian and Upper Triassic source rocks, these traps were still not formed, leading to its less possibility to form large gas reservoirs with natural gas from the Permian and Triassic source rocks. Therefore, only a small amount of dry gas generated by the Permian-Triassic source rocks at over mature stage could be captured very late. However, organic matter of the Middle-Lower Jurassic coal-measures began to generate gas (R_o = 1.0%) at the beginning of Eocene (40 Ma), and entered main gas window at 20 Ma. It is now still at the large amount of gas generation stage, suggesting that it matched well with the formation time of the anticlines in the central part. Therefore, the anticline traps in the central part of the southern margin can capture the natural gas generated from the Middle-Lower Jurassic coal-measures. Since the burial depth of Jurassic coal measures is much shallower in the west part, resulting in lower maturity compared to that in the central part (**Figure 7**), and thereafter, the beginning of a large amount of gas generation was later in the west part. Conclusively, the Jurassic coal measures are now still at the stage of crude oil-condensate -wet gas generation, and the central part at the stage of wet gas generation. The natural gas captured by the traps in the

central part shows a gradually drying trend from west to east and an increased trend of maturity. Because the anticline structures in the second and third rows such as the Tugulu and Hutubi anticlines were formed very late, they mainly captured natural gas generated from the Jurassic coal-measures at a highly to over mature stage, leading to much heavier carbon isotopes than those of the Anjihai anticline.

On the other hand, faults were well developed in the thrust-fault zone of the southern margin (Kuang and Qi, 2006; Chen et al., 2007; Lei et al., 2012). These faults connected the multiple deep source kitchens with the upper reservoirs (**Figures 4**, **8**, **9**), resulting in the formation of upward migration channels for oil and gas, and finally in the multiple charging and oil and gas accumulation. Fluid inclusions in sandstones from reservoirs in the Manas anticline and its fluorescence spectrum characteristics suggested that two stages of oil and gas charging occurred in these anticline structures (Bai et al., 2013b). The first stage (11 Ma) was oil charging and accumulation, followed by the second stage (3 Ma) with natural gas charging and accumulation. Other anticline structures in the central part of the southern margin have almost the same structural development background and oil and gas charging history as the Manas anticline The early charged oil in the anticlines from the central part of the southern margin was derived mainly from lacustrine source rocks in the Lower Cretaceous Qingshuihe Formation (Kang et al., 2008; Wang et al., 2013; Chen et al., 2016b; Chen et al., 2016c; Chen et al., 2016d). The late charged natural gas was derived mainly from the Jurassic coal-measures (Wang et al., 2009; Hu et al., 2010; Wang et al., 2013; Liu et al., 2016; Chen et al., 2019). Condensates discovered could be formed by gas charging and secondary reformation of a large amount of Jurassic-derived natural gas to Cretaceous-derived crude oil (Chen et al., 2017).

If the Lower Permian source rocks occurred in the Sikeshu sag in the west part of the southern margin, the main oil generation period started from the Late Jurassic to Early Cretaceous (**Figure 7**). If the Middle Permian source rocks occurred, the main oil generation period started from the Late Cretaceous to Paleogene. Whatever the occurrence of Lower and Middle Permian source rocks, the anticlines such as the Dushanzi, Xihu, and Gaoquan in the west part of the southern margin had not formed. Therefore, it is impossible for these anticlines to capture the crude oil generated from the Permian lacustrine source rocks. One exclusive is that the Permian source rocks buried in relatively shallow areas might still generate a certain amount of crude oil since Neogene, and then form small-scale hydrocarbon accumulation, such as the crude oil reservoir in Well Du68 in the Dushanzi anticline (Wang et al., 2013; Chen et al., 2016b). However, the main gas generation period of the Permian source rocks started from the Late Cretaceous and continued to present. This matched well with the formation time of anticlines in the west part of the southern margin. Therefore, the natural gas generated from these source rocks can be captured and form oil and gas reservoirs. On the other hand, the Jurassic coal-measures in the Sikeshu sag is still at a large amount of oil generation stage or peak oil generation stage. For example, crude oil from the Qigu and Qingshuihe reservoirs in the Kaindick Oilfield and the Xihu anticline was sourced from the Jurassic coal-measures (Wang et al., 2013; Chen et al., 2016b; Chen et al., 2016d). Also, a large amount of natural gas associated with crude oil could be expected. Therefore, the western anticlines in the southern margin might be charged with oil-associated gas from the Permian source rocks or coal-derived gas from the Jurassic coal measures, or mixed. The natural gases produced from Well GT1 in the Qingshuihe Formation reservoir in the Gaoquan anticline might be the mixture of the gases derived from the Jurassic coal-measures and the Permian lacustrine source rocks (Chen et al., 2019).

Exploration Targets for Natural Gas

Although many structural traps were well developed in the shallow and deep layers in the southern margin of Junggar Basin, (Li et al., 2003; Kuang and Jia, 2005; Kuang and Qi, 2006; Lei et al., 2012; Du et al., 2019), the exploration targets in the southern margin mainly focused on the middle-shallow layers for long time, and the natural gas discovered to date is mainly in the shallow Paleogene and Neogene anticlinal traps. Commercial natural gas fields were only found in the Hutubi anticline and Manas anticline in the central part of southern margin. Recently, the Well GT1 in the Gaoquan anticline in the west part and the Well HT1 in the Huxi anticline in the central part revealed high-product oil and gas flow in the sandstone reservoirs at the bottom of the Qingshuihe Formation of Lower Cretaceous, showing a good prospect for oil and gas exploration in the deep layers in the southern margin of Junggar Basin.

The middle and shallow oil and gas plays discovered to date in the southern margin of Junggar Basin were defined as the Cretaceous-Neogene plays, which were mainly generated from the Cretaceous source rocks in the central part of the southern margin and source rocks from the Paleogene Anjihaihe Formation in the Wusu-Dushanzi area in the west of the southern margin. However, the scales and hydrocarbon generation potentials of these two sets of source rocks are relatively small due to its currently low to medium maturity, and it cannot be the main contributors for the formation of large scale of natural gas reservoirs. The deep-buried Jurassic coal-measures could be the main candidate for large scale natural gas reservoirs. The Hutubi gas field and Mahe gas field, which were discovered recently, are located in the middle-shallow depth, in which the crude oil was derived from the Cretaceous source rocks, and the natural gas from the deep Jurassic coal measures. On the other hand, the anticline traps in shallow depth is relatively small, and the sealing capability of cap rocks was partly destroyed due to complex fault systems in the southern margin, resulting in loss of large amounts of oil and gas. Furthermore, these shallow anticline traps were formed very late, especially the anticlines in the central part, leading to a capture of late stage of gas generation from the highly to over mature Jurassic coal-measures, then limiting the scale of oil and gas accumulations.

On the contrary, the deep buried Permian and the Upper Triassic source rocks and Jurassic coal-measures can be the main contributors for the formation of large scale oil and gas fields in the deep Permian-Jurassic-Cretaceous plays in the southern margin of Junggar Basin. Here the reservoirs were well developed within the Jurassic strata and at the bottom of the

Lower Cretaceous, while mudstone within the Jurassic strata and the Cretaceous Qingshuihe Formation is good cap rocks. The overlying thick strata further increased the sealing capability of the cap rocks. Meanwhile, a large number of large-scale structural traps were formed during the Late Yanshanian movement and the Himalayan movement. According to the results of Lei et al. (2012), Du et al. (2019), nearly 40–46 traps have been identified and confirmed in this play, with a total area of 2140–2486 km^2, of which 21 are structural traps with an area greater than 30 km^2, with a total trap area of 1840 km^2. The most important is that the formation period of these structural traps was earlier than gas generation time from the Jurassic coal-measures, and is favor for the large-scale oil and gas accumulation.

Well GT1 drilled recently has confirmed that the oil and gas reservoir in the Cretaceous Qingshuihe Formation in the Gaoquan anticline was typical deep hydrocarbon accumulation pool (**Figures 3**, **4**). Half of the natural gas was derived from the Jurassic coal measures and another half from the Permian lacustrine source rocks (Chen et al., 2019). The reservoir was composed of gravel rock at the bottom of Cretaceous Qingshuihe Formation, and the cap rock is mudstone of the Qingshuihe Formation. In addition, sandstones within the Jurassic strata were also well developed. Therefore, large scale gas reservoirs from the lithologic traps and/or structural-lithologic traps could be one of the main targets in the future exploration. Although deep-buried reservoirs in the Permian-Jurassic-Cretaceous plays resulted in relatively low quality of rock physical properties, the discovery of high-product oil and gas reservoirs at the deep-buried Well GT1 in the Gaoquan anticline and Well HT1 in the Huxi anticline indicated that good reservoirs can be developed in the deep plays for natural gas accumulation.

The oil and gas accumulation conditions and exploration practice and results suggest that the deep Permian-Jurassic-Cretaceous plays in the southern margin are the most favorable gas exploration target. Regionally, the deep play in the west part of the southern margin of Junggar Basin is favorable for discovery of oil and gas reservoirs from the Jurassic coal measures. There is also the possibility to discover gas reservoirs from the Permian lacustrine source rocks. While in the central part, the deep play is favorable for discovery of gas reservoirs from the Jurassic coal measures. The deep play in the east part of the southern margin of Junggar Basin is favorable for discovery of gas reservoirs from the Jurassic coal measures and Permian lacustrine source rocks. The middle-shallow Cretaceous-Neogene play in the central and west parts of the southern margin may be the secondary target for natural gas exploration.

CONCLUSION

(1) Three sets of effective gas source rocks were developed in the southern margin of Junggar Basin. The widely distributed Jurassic coal-measures are the most important oil and gas source rocks, and the Permian and Upper Triassic lacustrine source rocks are important gas source rocks in some area of the southern margin.

(2) In the southern margin of Junggar Basin, the Jurassic coal-measures is mainly at mature to highly mature stage, indicating a main gas generation stage. It matched well with the formation time of anticlines, resulting in the best source-kitchen and trap combination. A series of thrust faults and secondary faults connected the deep source kitchen with the middle-upper traps. All together it made favorable conditions for multiple hydrocarbon migration and accumulation.

(3) Compared studies showed that source rocks in the southern margin of Junggar Basin, were better than those in the Kuqa Depression. Although the maturity of source organic matter, the scale of reservoirs and caps, and sealing capability in the southern margin were slightly lower than those in the Kuqa Depression, the southern margin of Junggar Basin still has good hydrocarbon accumulation conditions, due to multiple source rocks, well-developed faults and traps, good quality reservoirs and sealing conditions.

(4) In the southern margin of Junggar Basin, the deep Permian-Jurassic-Cretaceous play is the most favorable target for natural gas exploration. The middle-shallow Cretaceous-Neogene play is the secondary target for natural gas exploration, with possibility to discover a certain scale natural gas reservoirs under the supply of deep Jurassic gas sources.

DATA AVAILABILITY STATEMENT

Publicly available datasets were analyzed in this study. This data can be found here: see references.

AUTHOR CONTRIBUTIONS

CJ, article writing; WX, reservoir avaluation; XB, geological background; LJ, natural gas analyses; NY and SY, natural gas geochemistry.

FUNDING

This work was supported by the scientific research and technology development project of PetroChina (Grant Nos.: 2019A-0209).

ACKNOWLEDGMENTS

We would like to thank PetroChina for permission to publish this work. Liang Digang reviewed the early version of this article and made suggestions.

REFERENCES

Bai, Z., Jiang, Z., Song, Y., Zhao, M., Fang, S., and Zhang, J. (2013a). Dynamic hydrocarbon accumulation process in Manasi anticline in the southern Junggar foreland basin. *Nat. Gas Industry* 33 (4), 37–42. [in Chinese with English abstract].

Bai, Z., Jiang, Z., Song, Y., Zhao, M., Fang, S., and Zhang, J. (2013b). The reservoir characteristics and its main controlling factor discussion in Ziniquanzi Formation of Homatu tectonic zone, Southern Junggar fold-thrust belt. *Nat. Gas Geosci.* 24, 273–281. [in Chinese with English abstract].

Bai, H., Pang, X., Kuang, L., Pang, H., Wang, X., Jia, X., et al. (2017). Hydrocarbon expulsion potential of source rocks and its influence on the distribution of lacustrine tight oil reservoir, Middle Permian Lucaogou Formation, Jimsar Sag, Junggar Basin, Northwest China. *J. Pet. Sci. Eng.* 149, 740–755. doi:10.1016/j.petrol.2016.09.053

Bernard, B. B., Brooks, J. M., and Sackett, W. M. (1977). "A geochemical model for characterization of hydrocarbon gas sources in marine sediments," in Proceedings of the ninth annual offshore technology conference, OTC 2934, Houston, May 2–5, 1977. Houston, Texas, USA: Offshore Technology Conference, 435–438.

Cao, Z., Liu, G., Xiang, B., Wang, P., Niu, G., Niu, Z., et al. (2017). Geochemical characteristics of crude oil from a tight oil reservoir in the Lucaogou Formation, Jimusar sag, Junggar Basin. *Bulletin* 101 (01), 39–72. doi:10.1306/05241614182

Carroll, A. R., Brassell, S. C., and Graham, S. A. (1992). Upper permian lacustrine oil shales, southern Junggar Basin, northwest China. *AAPG Bull.* 76 (12), 1874–1902. doi:10.1306/bdff8b0a-1718-11d7-8645000102c1865d

Carroll, A. R. (1998). Upper permian lacustrine organic facies evolution, southern Junggar Basin, NW China. *Org. Geochem.* 28 (11), 649–667. doi:10.1016/s0146-6380(98)00040-0

Chen, J., Liang, D., Wang, X., Deng, C., Jin, T., Xiang, S., et al. (2003). The discovery and significance of the crude oils derived from Triassic source rocks in the Junggar Basin. *Geochimica* 32, 582–590. [in Chinese with English abstract].

Chen, S., Wang, X., Abulimit, I., and LiWang, Y. L. (2004). Geochemical study of forming gas reservoir in Hutubi field in Zhungeer basin. *Nat. Gas Industry* 24 , 16–18. [in Chinese with English abstract].

Chen, S., Qi, J., Yu, F., and Yang, Q. (2007). Deformation characteristics in the southern margin of Junggar Basin and their controlling factors. *Acta Geol. Sin.* 81, 151–157. [in Chinese with English abstract].

Chen, J., Wang, X., Deng, C., Zhao, Z., Ni, Y., SunYang, Y. H., et al. (2015a). Geochemical features of source rocks in the southern margin, Junggar Basin, Northwestern China. *Acta Petrolei Sin.* 36, 767–780. [in Chinese with English abstract].

Chen, J., Wang, X., Deng, C., Zhao, Z., Ni, Y., SunYang, Y. H., et al. (2015b). Geochemical features and classification of crude oils in the southern margin, Junggar Basin, northwest China. *Acta Petrolei Sin.* 36, 1315–1331. [in Chinese with English abstract].

Chen, J., Wang, X., Deng, C., Zhao, Z., Ni, Y., SunYang, Y. H., et al. (2016a). Oil-source correlation of typical crude oil in the southern margin, Junggar Basin, Northwestern China. *Acta Petrolei Sin.* 37, 160–171. [in Chinese with English abstract].

Chen, J., Wang, X., Deng, C., Zhao, Z., Ni, Y., SunYang, Y. H., et al. (2016b). Investigation of typical reservoirs and occurrence regularity of crude oil in the southern margin of Junggar Basin, Northwestern China. *Acta Petrolei Sin.* 37, 415–429. [in Chinese with English abstract].

Chen, J., Wang, X., Deng, C., Liang, D., Zhang, Y., Zhao, Z., et al. (2016c). Geochemical features of source rock and crude oil in the Junggar Basin, Northwest China. *Acta Geol. Sin.* 90, 37–67. [in Chinese with English abstract].

Chen, J., Wang, X., Deng, C., Liang, D., Zhang, Y., Zhao, Z., et al. (2016d). Oil and gas source, occurrence and petroleum system in the Junggar Basin, Northwest China. *Acta Geol. Sin.* 90, 421–450. [in Chinese with English abstract]. doi:10.1111/1755-6724.13039

Chen, J., Deng, C., Wang, X., Ni, Y., Sun, Y., Zhao, Z., et al. (2016e). Source of condensate oil in the middle of southern margin, Junggar Basin, NW China. *Pet. Explor. Dev.* 43 (5), 902–913. doi:10.1016/s1876-3804(16)30108-2

Chen, J., Deng, C., Wang, X., Ni, Y., Sun, Y., Zhao, Z., et al. (2017). Formation mechanism of condensates, waxy and heavy oils in the southern margin of Junggar Basin, NW China. *Sci. China Earth Sci.* 60 (5), 972–991. doi:10.1007/s11430-016-9027-3

Chen, J., Wang, X., Ni, Y., Xiang, B., Liao, F., Liao, J., et al. (2019). Genetic type and source of natural gas in the southern margin of Junggar Basin, NW China. *Pet. Explor. Dev.* 46 (3), 482–495. doi:10.1016/s1876-3804(19)60029-7

Dai, J., Wu, X., Ni, Y., Wang, Z., Zhao, C., Wang, Z., et al. (2012). Geochemical characteristics of natural gas from mud volcanoes in the southern Junggar Basin. *Sci. China Earth Sci.* 55 (3), 355–367. doi:10.1007/s11430-012-4363-x

Deng, Q., Feng, X., Zhang, P., Yang, X., Xu, X., Peng, S., et al. (1999). Reverse fault and fold zone in the Urumqi range-front depression of the Northern Tianshan and its genetic mechanism. *Earth Sci. Front.* 6 (4), 191–200.

Du, Z., and Wang, Q. (2007). Mesozoic and Cenozoic uplifting history of the Tianshan Region: insight from apatite fission track. *Acta Geol. Sin.* 81, 1081–1101. [in Chinese with English abstract].

Du, Z., Wang, F., Zhang, S., Zhang, B., and Liang, D. (2006). Gas generation history of mesozoic hydrocarbon kitchen in Kuqa depression, Tarim Basin. *Geochemica* 35, 419–431. [in Chinese with English abstract].

Du, J., Zhi, D., Li, J., Yang, D., Tang, Y., Qi, X., et al. (2019). Major breakthrough of Well Gaotan 1 and exploration prospects of lower assemblage in southern margin of Junggar Basin, NW China. *Pet. Explor. Dev.* 46 (2), 216–227. doi:10.1016/s1876-3804(19)60003-0

Fang, S., Jia, C., Guo, Z., Song, Y., and Zhang, Z. (2005). Preliminary determination of the forming time of foreland thrust belt in the Southern Margin of Junggar Basin. *Earth Sci. Front.* 12 (3), 66, 2005 [in Chinese with English abstract].

Fang, S., Song, Y., Jia, C., Xu, H., Liu, L., and Zhang, J. (2006). Relationship between Cretaceous basal conglomerate and oil/gas reservoiring in the Junggar Basin. *Nutural Gas Industry* 26 (5), 13–16. [in Chinese with English abstract].

Fang, S., Song, Y., Jia, C., Guo, Z., Zhang, Z., and Liu, L. (2007). Timing of cenozoic intense deformation and its implications for petroleum accumulation, northern margin of tianshan orogenic belt, northwest China. *Earth Sci. Front.* 14 (2), 205–214. doi:10.1016/s1872-5791(07)60018-9

Gao, G., Zhang, W., Xiang, B., Liu, G., and Ren, J. (2016). Geochemistry characteristics and hydrocarbon-generating potential of lacustrine source rock in Lucaogou Formation of the jimusaer sag, Junggar Basin. *J. Pet. Sci. Eng.* 145, 168–182. doi:10.1016/j.petrol.2016.03.023

Graham, S. A., Brassell, S., Carroll, A. R., Xiao, X., Demaison, G., McKnight, C. L., et al. (1990). Characteristics of selected petroleum source rocks, Xinjiang uygur autonomous region, northwest China. *AAPG Bull.* 74, 493–512. doi:10.1306/0c9b233f-1710-11d7-8645000102c1865d

Guo, Z., Zhang, Z., Wu, C., Fang, S., and Zhang, R. (2006). The mesozoic and cenozoic exhumation history of tianshan and comparative studies to the junggar and altai Mountains. *Acta Geol. Sin.* 80 (1), 1–15. [in Chinese with English abstract]. doi:10.1201/9781420004106.ch0

Han, S., Li, X., Chen, N., Shen, J., and Xu, Y. (2012). Hydrocarbon reservoirs and their controlling factors in the lower associations of the middle part of southern Junggar Basin, Xinjiang. *Sediment. Geol. Tethyan Geol.* 32 (4), 52–58. [in Chinese with English abstract].

He, D., Zhang, Y., Jia, J., and Shi, X. (2004). Plays for giant oil field in Junggar. *Xinjiang Pet. Geol.* 25 (2), 117–121. [in Chinese with English abstract].

He, D., Zhou, X., Yang, H., Lei, G., and Ma, Y. (2009). Geological structure and its controls on giant oil and gas fields in Kuqa Depression, Tarim Basin: a clue from new shot seismic data. *Geotetonica et Metallogenia* 33, 19–32. [in Chinese with English abstract].

Hendrix, M. S., Dumitru, T. A., and Graham, S. A. (1994). Late Oligocene-Early Miocene unroofing in the Chinese Tian Shan: an early effect of the India-Asia collision. *Geology* 22 (6), 487–490. doi:10.1130/0091-7613(1994)022<0487:loemui>2.3.co;2

Hou, L., Ma, W., Luo, X., Liu, J., Liu, S., and Zhao, Z. (2021). Hydrocarbon generation-retention-expulsion mechanism and shale oil producibility of the permian lucaogou shale in the Junggar Basin as simulated by semi-open pyrolysis experiments. *Mar. Pet. Geol.* 125, 104880. doi:10.1016/j.marpetgeo.2020.104880

Hu, L., He, D., and Hu, D. (2005). Electron spin resonance dating of the late Cenozoic deformation of the Huoerguosi-Manas-Tugulu reverse faults along southern edge of Junggar Basin. *Acta Geoscientica Sinica* 26, 121–126. [in Chinese with English abstract].

Hu, G., Zhang, S., Li, J., Li, J., and Han, Z. (2010). The origin of natural gas in the Hutubi gas field, Southern Junggar Foreland Sub-basin, NW China. *Int. J. Coal Geol.* 84 (3-4), 301–310. doi:10.1016/j.coal.2010.10.009

James, A. T. (1983). Correlation of natural gas by use of carbon isotopic distribution between hydrocarbon components. *AAPG Bull.* 67, 1176–1191. doi:10.1306/03b5b722-16d1-11d7-8645000102c1865d

James, A. T. (1990). Correlation of reservoired gases using the carbon isotopic compositions of wet gas components. *AAPG Bull.* 74, 1441–1458. doi:10.1306/0c9b24f7-1710-11d7-8645000102c1865d

Kang, S., Wang, X., Liao, J., Zhou, N., and Luo, L. (2008). Oil and gas characteristics and charging priority in Huo'erguosi Oilfield of Junggar Basin. *Spec. Oil Gas Reservoirs* 15 (4), 20–23. [in Chinese with English abstract].

Kang, S., Xiang, B., Liao, J., Ablimiti, I., and Sun, P. (2012). Organic geochemistry of Triassic source rock in the southern Junggar Basin. *J. Southwest Pet. Univ. (Sci. Tech. Edition)* 34 (2), 43–53. [in Chinese with English abstract].

Kuang, J., and Jia, X. (2005). Relationship between himalayan movement and hydrocarbon accumulation in southern margin of Junggar Basin. *Xinjiang Pet. Geol.* 26 (2), 129–133. [in Chinese with English abstract].

Kuang, J., and Liu, D. (2001). Comparative analysis on natural gas reservoir formed conditions between Southern Margin of Junggar Basin and Kuche depression of Tarim Basin. *Xinjiang Pet. Geol.* 22 (4), 287–290. [in Chinese with English abstract].

Kuang, J., and Qi, X. (2006). The Structural characteristics and oil-gas explorative direction in Junggar foreland basin. *Xinjiang Pet. Geol.* 27 (1), 5–9. [in Chinese with English abstract].

Kuang, J. (1993). The supperpressure mud seams in the southern margin of Junggar Basin and their significance in structural geology. *Exp. Pet. Geol.* 15, 168–172. [in Chinese with English abstract].

Lei, D., Tang, Y., and Chang, Q. (2008). The deep and relatively high-quality clastic reservoir bodies and favorable exploration areas in southern margin of Junggar Basin. *Xinjiang Pet. Geol.* 29 (4), 435–438. [in Chinese with English abstract].

Lei, D., Zhang, J., Chen, N., and Xiang, B. (2012). Conditions for gas pooling in the lower assemblage in the southern margin of Junggar Basin and the exploration prospect of large hydrocarbon fields. *Nat. Gas Industry* 32 (2), 16–22. [in Chinese with English abstract].

Li, W., Wang, C., Gao, Z., and Peng, D. (2000). Sedimentary evolution of mesozoic ear in kuqhe depression, Tarim Basin. *Acta Sedimentol. Sin.* 18, 543–548. [in Chinese with English abstract].

Li, X., Shao, Yu., and Li, T. (2003). Three oil-reservoir combinations in southern marginal of Junggar Basin, Northwest China. *Pet. Explor. Dev.* 30 (6), 32–34. [in Chinese with English abstract].

Li, Y., Wang, T., Zhang, Y., Chen, S., and Wang, X. (2004). Natural gas genesis and formation of gas pools in the Southern margin of Junggar Basin. *Acta Sedimentol. Sin.* 22, 529–534. [in Chinese with English abstract].

Liang, D., Zhang, S., Zhao, M., and Wang, F. (2002). Hydrocarbon sources and stages of reservoir Formation in Kuqa depression, Tarim Basin. *Chin. Sci. Bull.* 47 (S1), 62–70. doi:10.1007/bf02902820

Liang, D., Zhang, S., Chen, J., Wang, F., and Wang, P. (2003). Organic geochemistry of oil and gas in the Kuqa depression, Tarim Basin, NW China. *Org. Geochem.* 34 (7), 873–888. doi:10.1016/s0146-6380(03)00029-9

Liang, D., Chen, J., Zhang, B., Zhang, S., Wang, F., and Zhao, M. (2004). *Formation of continental oil and gas in Kuqa Depression, Tarim Basin*. Beijing: Petroleum Industry Press [in Chinese].

Liao, J., Wu, Y., Zhao, Z., Jing, W., and Dilidaer (2006). Genesis study of Horgos region, Junggar Basin. *Nat. Gas Explor. Dev.* 29 (1), 21–23. [in Chinese with English abstract].

Liao, J., Zhao, Z., Ma, W., Guo, Y., Shen, N., and Zhou, Ni. (2011). Analysis on oil-gas origin and accumulation hydrocarbons in Hutubi gas field, Junggar Basin. *Xinjiang Geology.* 29, 453–456. [in Chinese with English abstract].

Liu, Q., Qin, S., Li, J., Liu, W., Zhang, D., Zhou, Q., et al. (2007). Natural gas geochemistry and its origins in Kuqa Depression. *Sci. China Ser. D-Earth Sci.* 51 (S1), 174–182.

Liu, J., Zhang, W., Gao, C., Ni, Q., and Yuan, H. (2016). Genetic type and source of the natural gas in Huo-Ma-Tuo articline zone in the Southern Junggar Basin. *Mar. Geol. Quat. Geol.* 26 (3), 135–141. [in Chinese with English abstract].

Luo, X., Xiao, L., Li, X., Zhang, L., Zeng, Z., and Wang, Z. (2004). Overpressure distribution and affecting factors in southern margin of Junggar Basin. *Earth Sci. J. Chin. Univ. Geosci.* 29, 404–412. [in Chinese with English abstract].

Luo, X., Liu, L., and Li, X. (2006). Overpressure distribution and pressuring mechanism on the southern margin of the Junggar Basin, Northwestern China. *Chin. Sci Bull* 51 (19), 2383–2390. doi:10.1007/s11434-006-2126-9

Luo, X., Wang, Z., Zhang, L., Yang, W., and Liu, L. (2007). Overpressure generation and evolution in a compressional tectonic setting, the southern margin of Junggar Basin, northwestern China. *Bulletin* 91 (8), 1123–1139. doi:10.1306/02260706035

Qin, S., Dai, J., and Liu, X. (2007). The controlling factors of oil and gas generation from coal in the Kuqa Depression of Tarim Basin, China. *Int. J. Coal Geol.* 70 (1-3), 255–263. doi:10.1016/j.coal.2006.04.011

Qiu, N., Wang, X., Yang, H., and Xiang, Y. (2001). The characteristics of temperature distribution in the Junggar Basin. *Chin. J. Geol.* 36 (3), 350–358. [in Chinese with English abstract].

Schoell, M. (1980). The hydrogen and carbon isotopic composition of methane from natural gases of various origins. *Geochim. Cosmochim. Acta* 44 (5), 649–661. doi:10.1016/0016-7037(80)90155-6

Schoell, M. (1983). Genetic characterization of natural gases. *AAPG Bull.* 67 (12), 2225–2238. doi:10.1306/AD46094A-16F7-11D7-8645000102C1865D

Stahl, W. (1974). Carbon isotope fractionations in natural gases. *Nature* 251 (5471), 134–135. doi:10.1038/251134a0

Wang, H., and Hu, J. (2002). Cretaceous petroleum system and high pressure gas reservoir formation in Kuche Depression. *Nat. Gas Industry* 22 (1), 5–8. [in Chinese with English abstract].

Wang, F., Zhang, S., Zhang, B., and Zhao, M. (1999). Organic maturity of mesozoic source rocks in Kuqa depression, Tarim Basin. *Xinjiang Pet. Geol.* 20, 221–224. [in Chinese with English abstract].

Wang, S., Hu, S., and Wang, J. (2000). The characteristics of heat flow and geothermal fields in Junggar Basin. *Chin. J. Geophys.* 43, 771–779. [in Chinese with English abstract]. doi:10.1002/cjg2.98

Wang, Z., Sun, M., Geng, P., Song, Y., and Li, Y. (2003). The development features and formation mechanisms of abnormal high formation pressure in southern Junggar region. *Pet. Explor. Dev.* 30 (1), 32–34. [in Chinese with English abstract].

Wang, H., Zhou, N., Zhou, X., Luo, L., and Xie, G. (2009). Petroleum origin in Manas area, Junggar Basin. *Nat. Explor. Dev.* 32 (2), 4–9. [in Chinese with English abstract].

Wang, X., Zhi, D., Wang, Y., Chen, J., Qin, Z., Liu, D., et al. (2013). *Geochemistry of source rock and petroleum in the Junggar Basin*. Beijing: Petroleum Industry Press. [in Chinese].

Wang, Z. (2014). Formation mechanism and enrichment regularities of Kelasu subsalt deep large gas field in Kuqa Depression, Tarim Basin. *Nat. Gas Geosci.* 25, 153–166. [in Chinese with English abstract].

Whiticar, M. J. (1994). "Correlation of natural gases with their sources," in *The petroleum system — from source to trap*. Editors L. Magoon and W. Dow (Tulsa, OK, United States: AAPG Memoir). 60, 261–284. doi:10.1306/m60585c16

Whiticar, M. J. (1996). Stable isotope geochemistry of coals, humic kerogens and related natural gases. *Int. J. Coal Geol.* 32 (1-4), 191–215. doi:10.1016/s0166-5162(96)00042-0

Whiticar, M. J. (1999). Carbon and hydrogen isotope systematics of bacterial formation and oxidation of methane. *Chem. Geol.* 161 (1-3), 291–314. doi:10.1016/s0009-2541(99)00092-3

Wu, X., Wang, L., and Xu, C. (1994). The stracture characteristics and prospect for hydrocarbon exploration in Qigu-Xiaoquzhi area in southern margin of Junggar Basin. *Pet. Explor. Dev.* 21 (1), 1–7. [in Chinese with English abstract].

Wu, X., Wang, L., and Song, Z. (2000). The relations between structural stress field and hydrocarbon migration and accumulation in Southern Margin of Junggar Basin. *Xinjing Pet. Geol.* 21 (2), 97–100. [in Chinese with English abstract].

Wu, K., Zha, M., and Zhong, J. (2006). Distribution and evolution of overpressure system in the Junggar Basin. *Chin. J. Geol.* 41, 636–647. [in Chinese with English abstract].

Wu, X., Liu, D., Abulimiti, I., and Ding, J. (2007). Potential and field of exploration for natural gas in Junggar Bain. *China Pet. Explor.* 12 (2), 1–6. [in Chinese with English abstract].

Xiao, L., Chen, N., Zhang, J., Shen, J., and Zhang, S. (2011). Sedimentary systems of Paleogene Ziniquanzi Formation, south edge of Junggar Basin. *Nat. Gas Geosci.* 22, 426–431. [in Chinese with English abstract].

Yang, H., Chen, L., and Kong, Y. (2004). A novel classification of structural units in Junggar Basin. *Xinjiang Pet. Geol.* 25, 686–688. [in Chinese with English abstract].

Zha, M., Zhang, W., and Qu, J. (2000). The character and origin of overpressure and its explorational significance in Junggar Basin. *Pet. Explor. Dev.* 27 (2), 31–35. [in Chinese with English abstract].

Zhang, J., Li, T., Han, S., Li, X., and Xia, Y. (2012). The development characteristics and distribution of reservoir in jurassic and cretaceous in western part of southern margin of Junggar Basin. *Xinjiang Geol.* 30 (1), 62–66. [in Chinese with English abstract].

Zhang, Z., Zhu, G., Chi, L., Wang, P., Zhou, L., Li, J., et al. (2020). Discovery of the high-yield well GT1 in the deep strata of the southern margin of the Junggar Basin, China: implications for liquid petroleum potential in deep assemblage. *J. Pet. Sci. Eng.* 191, 107178. doi:10.1016/j10.1016/j.petrol.2020.107178

Zhao, M., Lu, S., and Li, J. (2002). The geochemical features of natural gas in Kuqa Depression and the discussion on the gas source. *Pet. Explor. Dev.* 29 (6), 4–7. [in Chinese with English abstract].

Zheng, G., Ma, X., Guo, Z., Hilton, D. R., Xu, W., Liang, S., et al. (2017). Gas geochemistry and methane emission from Dushanzi mud volcanoes in the southern Junggar Basin, NW China. *J. Asian Earth Sci.* 149, 184–190. doi:10.1016/j.jseaes.2017.08.023

Conflict of Interest: Author CJ was employed by the Research Institute of Petroleum Exploration and Development, PetroChina and declare that this study received funding from PetroChina.

The remaining authors declare that the research was conducted in the absence of any commercial or financial relationships that could be construed as a potential conflict of interest.

Copyright © 2021 Chen, Wang, Sun, Ni, Xiang and Liao. This is an open-access article distributed under the terms of the Creative Commons Attribution License (CC BY). The use, distribution or reproduction in other forums is permitted, provided the original author(s) and the copyright owner(s) are credited and that the original publication in this journal is cited, in accordance with accepted academic practice. No use, distribution or reproduction is permitted which does not comply with these terms.

frontiers in Earth Science

ORIGINAL RESEARCH
published: 29 April 2021
doi: 10.3389/feart.2021.582062

Potential Production of Carbon Gases and Their Responses to Paleoclimate Conditions: An Example From Xiaolongtan Basin, Southeast Tibetan Plateau

Gen Wang[1,2], Yongli Wang[3,4], Zhifu Wei[1,2]*, Zepeng Sun[5], Wei He[1,6] and Xueyun Ma[1,6]*

[1] Northwest Institute of Eco-Environment and Resources, Chinese Academy of Sciences, Lanzhou, China, [2] Key Laboratory of Petroleum Resources, Gansu Province, Lanzhou, China, [3] Key Laboratory of Cenozoic Geology and Geophysics, Chinese Academy of Sciences, Beijing, China, [4] CAS Center for Excellence in Life and Paleoenvironment, Beijing, China, [5] College of Resources and Environment, Shanxi Agricultural University, Jinzhong, China, [6] College of Earth and Planetary Sciences, University of Chinese Academy of Sciences, Beijing, China

OPEN ACCESS

Edited by:
Francesco Italiano, National Institute of Geophysics and Volcanology, Italy

Reviewed by:
Jens Kallmeyer, Helmholtz Centre Potsdam, Germany
Weiguo Liu, Chinese Academy of Sciences, China
Xianyu Huang, China University of Geosciences, China
Zhang Chengjun, Lanzhou University, China

***Correspondence:**
Yongli Wang
ylwang@mail.iggcas.ac.cn
Zhifu Wei
weizf@lzb.ac.cn

Specialty section:
This article was submitted to Biogeoscience, a section of the journal Frontiers in Earth Science

Received: *10 July 2020*
Accepted: *08 April 2021*
Published: *29 April 2021*

Citation:
Wang G, Wang Y, Wei Z, Sun Z, He W and Ma X (2021) Potential Production of Carbon Gases and Their Responses to Paleoclimate Conditions: An Example From Xiaolongtan Basin, Southeast Tibetan Plateau. Front. Earth Sci. 9:582062. doi: 10.3389/feart.2021.582062

Uplift of the Tibetan Plateau plays a significant and lasting role in the variations of climate conditions and global carbon cycle. However, our knowledge is limited due to the lack of long-sequence records revealing rates of CO_2 and CH_4 production, hampering our understanding of the relationship between paleoclimatic conditions, carbon cycling and greenhouse gas flux. Here, we present a combination of paleoclimate records and low-temperature thermal simulation results from sediments of the Xiaolongtan Basin at the southeastern margin of the Qinghai-Tibetan Plateau, spanning the late Miocene (14.1 ∼ 11.6 Ma). The *n*-alkane-derived proxies suggested that the sources of organic matter were obviously different: a mixed source including lower organisms and terrestrial higher plants for the Dongshengqiao Formation from 14.1 to 12.6 Ma, and a predominant contribution from terrestrial higher plants for Xiaolongtan Formation between 12.6 and 11.6 Ma. The paleoclimate was generally warm and humid as reflected by the lipid biomarkers, consistent with previous studies. In addition, the carbon gases (including CO_2 and hydrocarbon gases) generated by the low-temperature thermal simulation experiments indicated a production rate of CO_2 and CH_4 were as high as 88,000 ml/kg rock and 4,000 ml/kg rock, respectively, implying there were certain amounts of carbon gases generated and released into the atmosphere during their shallow burial stage. Besides, the calculated production rate of carbon gases and the estimated burial flux of organic carbon varied in response to the variations of paleoclimate conditions. Based on these observations, we propose that the climate conditions predominantly controlled the formation and accumulation of organic matter, which consequently affected the production of carbon gases and burial flux of organic carbon. The results presented here may provide a significant insight into the carbon cycle in the southeast of the Tibetan Plateau.

Keywords: lipid biomarker, low-temperature thermal simulation, carbon cycle, burial rates of organic carbon, late Miocene

INTRODUCTION

In recent years, increasing attention was paid to global warming and greenhouse effects. The carbon cycle in relevant terrestrial ecosystem, especially the organic carbon inventory, has been becoming a focus and hotspot in the field of global climate research (Heimann and Reichstein, 2008; Fang et al., 2018). The production rates of CO_2 and CH_4 released from sediments caused by thermal maturation during their shallow burial stage are critical to improve our understanding about carbon cycling and greenhouse gas flux in terrestrial ecosystems (Wilson et al., 2019). Organic carbon storage can be significantly influenced by anthropogenic activities and/or climate variations, such as air temperatures, atmospheric CO_2 concentrations, precipitation patterns (Smoak et al., 2013; Ruiz-Fernández et al., 2018). Knowledge about how the organic carbon inventory responds to the shifts of climate conditions will definitely enhance our understanding of its variations under the background of global warming and increased human activities. Related studies mainly focused on marshes (Ruiz-Fernández et al., 2018), lake sediments (Xu et al., 2013; Yu et al., 2015; Zhang et al., 2018), coastal wetlands (Choi and Wang, 2004), marine sediments (Shao et al., 2016; Wang K. et al., 2019) reaching back only a few hundred years, with only a few records discussing the relationship over long time scales (Owens et al., 2018; Gao et al., 2019).

The Qinghai-Tibetan Plateau is a globally important terrestrial ecosystem, owing to its special location and continuous uplift during the Cenozoic, it exerts significant influence on the regional and even global climate. Located in the southeastern margin of the Tibetan Plateau, the Xiaolongtan Basin accumulated continuous strata of Cenozoic sediments (Wang et al., 1998), which can provide important information about the evolution of Indian monsoon and southeastward extension of the Tibetan Plateau (Tapponnier et al., 2001; Huang et al., 2016). However, studies about the variations of paleoclimate conditions and organic carbon inventory and their interactions were limited, resulted in patchy understanding of the environmental and uplift history as well as the organic carbon cycle in the southeastern margin of the Tibetan Plateau. Li S.H. et al. (2015) and Zhang et al. (2019) established the chronology for the Xiaolongtan Basin sequence, but the paleoclimate history had not been well documented. As a consequence, in the present study, we analyzed the lipid biomarkers, total organic carbon concentrations, and carried out low temperature thermal simulation experiments of the sediments from Xiaolongtan Basin, in order to gain insights into the evolution of paleoclimate conditions, and its influences on carbon gases (including CO_2 and CH_4) emissions and organic carbon burial rates in the southeastern Tibetan Plateau.

GEOLOGICAL SETTINGS

The Xiaolongtan Basin, located in the Honghe Hani and Yi Autonomous Prefecture, southeastern part of the Yunnan Province (**Figure 1**), is a typical pull-apart basin controlled by the Qujing fault to the east and the Xianshuihe–Xiaojiang fault to the west (Li S.H. et al., 2015), and has accumulated a thick sequence of sediments deposited in swamp-fluviolacustrine environment. The oldest Chinese hominoid fossils have been found in this sequence (Woo, 1987; Ji et al., 2013; Li S.H. et al., 2015). The average elevations of Xiaolongtan Basin and its surrounding mountains are about 1,000–1,150 m a.s.l. and 1,300–1,800 m a.s.l., respectively. At present, the Xiaolongtan Basin is characterized by a subtropical monsoon climate. The mean annual precipitation is about 770 mm, with an amount of 460 mm falling during the summer season. The mean annual temperature is about 20.1°C, with mean monthly temperatures of 24.5°C in July and 13.5°C in January (**Figure 1C**). The vegetation distributed around the basin is mainly composed of subtropical broad-leaved evergreen forest.

The Cenozoic stratigraphy of Xiaolongtan Basin can be divided into four formations according to its lithofacies and paleontology, including Dongshengqiao Formation, Xiaolongtan Formation, Buzhaoba Formation and Hetou Formation, from the bottom to the top (Dong, 2001). The lithology of Dongshengqiao Formation is light-gray clay in its middle-upper parts, above mudstone, sandstone and conglomerate. The Xiaolongtan Formation comprises black lignite and the Buzhaoba Formation is characterized by gray–white marl (Zhang et al., 2019). And the Hetou Formation is attributed to the Quaternary sediments, owing to the observation of fossil mammals in its sediments (Dong, 2001). The hominoid fauna in the Xiaolongtan Formation have been determined spanning the middle-late Miocene (Dong, 2001).

CHRONOLOGY

Li S.H. et al. (2015) reported a magnetostratigraphic study on the Xiaolongtan Formation in the Xiaolongtan Basin, and suggested the Xiaolongtan Formation sedimentary sequence spanned from Chron C5Ar.1r to Chron C5n.2n, ranging from 12.7 to ∼10 Ma. Recently, in combination with previous work, Zhang et al. (2019) carried out high-resolution magnetostratigraphy to the entire late Neogene fluvio-lacustrine sedimentary sequence in order to acquire the whole dates for the start and finish of sedimentation in the Xiaolongtan Basin. Their results revealed 11 reversed and 11 normal zones, covering Chron 5n.2n to Chron 5ACr, indicating that the whole stratigraphic sequence in the Xiaolongtan Basin ranges from ∼14.1 to ∼10.0 Ma. Specifically, the Dongshengqiao Formation was deposited between 14.1 and 12.6 Ma, and the Xiaolongtan Formation was accumulated from 12.6 to 11.6 Ma.

SAMPLING AND METHODS

Sampling

In the present study, we collected outcrop samples from the same sections described by Zhang et al. (2019), including sections Xiaolongtan-I (XLT-I) and Xiaolongtan-II (XLT-II). The XLT-I section, identified as Dongshengqiao Formation, is located in the Buzhaoba open-cast coal mine in the southern Xiaolongtan Basin, and accumulated strata of 198 m. The overall lithology

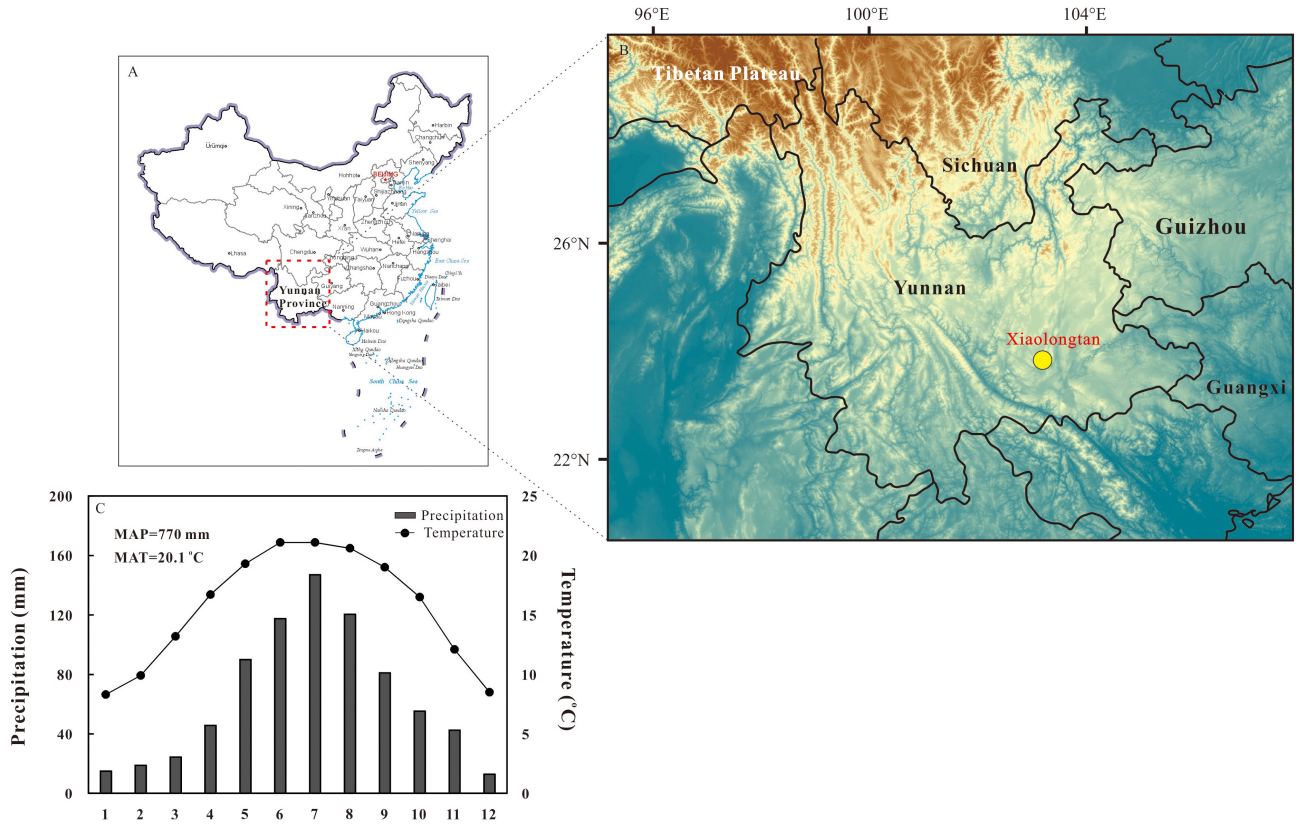


FIGURE 1 | (A) Location of Yunnan Province; **(B)** location of Xiaolongtan Basin in the Yunnan region at the southeast margin of the Tibetan Plateau; **(C)** mean monthly temperature and precipitation from Kaiyuan meteorological station from 1981 to 2010.

of this section mainly consists of brownish yellow and gray–white fine clay and sandstone, containing several thin layers of black coal. The XLT-II section, identified as Xiaolongtan Formation, is 161 m in thickness and exposed in the northern Xiaolongtan Basin. It is characterized by black lignite interbedded with several layers of mudstones. For further information please refer to Zhang et al. (2019).

MATERIALS AND METHODS

Total Organic Carbon (TOC) and Vitrinite Reflectance (Ro%)

An aliquot of each sample was acidified with HCl to remove carbonates before analysis. Then, samples were washed with deionized water until a neutral pH value was reached. Next, samples were dried in an oven at 90°C. Afterward, the treated samples were combusted using a CS-I analyzer (Eltra, Germany) in the Northwest Institute of Eco-Environment and Resources, Chinese Academy of Sciences. Before and during the analysis, standard samples (Carbon and Sulfur in Steel, produced by LECO CORPORATION, Carbon percent 0.881 ± 0.008; Sulfur percent 0.0155 ± 0.009) were applied to calibrate and monitor the accuracy of the CS-I analyzer. Precision was better than 0.03%.

The vitrinite reflectance measurements were conducted on a Leica DM2500P microscope equipped with MPM600 microphotometer following the standard SY/T 5124-2012. Appropriate reflectance standards in including cubic zirconia (3.13% Ro), N-LASF46A glass (1.31% Ro) and Yttrium-aluminum-garnet (0.91% Ro) were used for calibration.

Lipid Biomarkers

In order to avoid contamination during the organic matter extraction, all glassware was washed sequentially with detergent, chromic acid, tap water, distilled water and finally annealed at 450°C for 12 h in the muffle furnace. After air-drying and grinding the samples to about 150 μm, about 20 g were extracted continuously for 72 h with chloroform in a Soxhlet extractor. The solvent was purified by distillation. Afterward, the extracted organic matter was condensed and weighed. Aliphatic fractions were eluted using silica gel-alumina column chromatography with *n*-hexane.

GC-MS analyses for aliphatic fractions were carried out at the Key Laboratory of Petroleum Resources Research, Northwest Institute of Eco-Environment Resources, Chinese Academy of Sciences. The GC-MS analysis was performed using an HP 5973 MSD (Aglient Technologies, Wilmington, DE, United States) interfaced to an HP 6890 gas chromatograph that was fitted with a 30 m × 0.25 mm fused silica capillary column coated with a

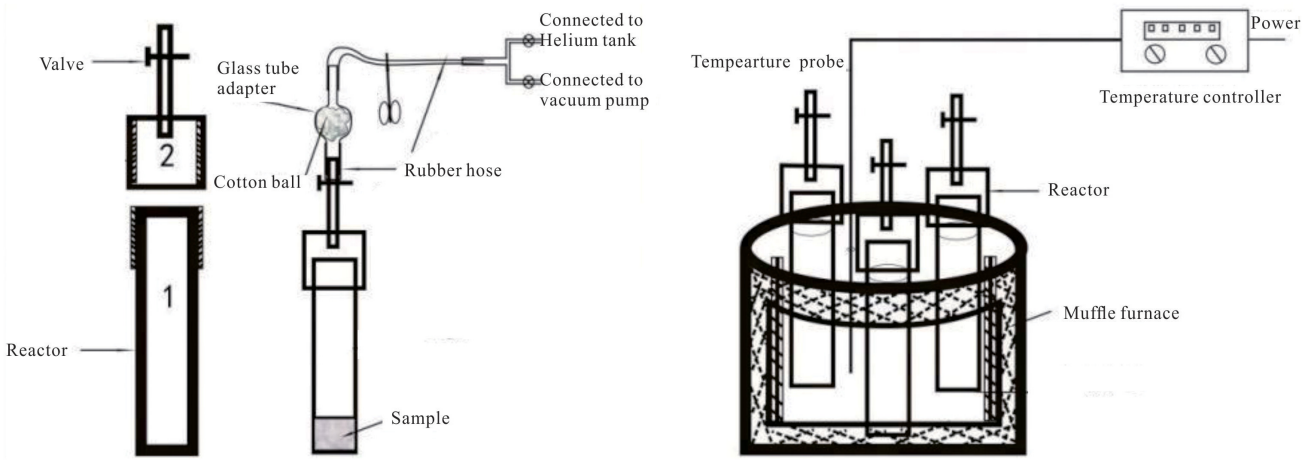


FIGURE 2 | Schematic diagram of the low-temperature thermal simulation experimental apparatus.

film (0.25 μm) of 5% phenyl-methyl. For routine GC analysis, the oven temperature was programmed to increase from 80 to 300°C at a rate of 3°C/min with a final hold time of 20 min. Helium was used as carrier gas at a linear velocity of 32 cm/s, with the injector operating at a constant flow of 0.9 ml/min. The MS was operated with an ionization energy of 70 eV, a source temperature of 230°C and an electron multiplier voltage of 1,900 V over the range of 35–550 Da. Prior to analyses, the GC-MS was tuned using perfluorotributylamine (PFTBA) and blank samples were applied to check the background.

Low Temperature Thermal Simulation Experiments and Analyses of Gas Composition and Compound-Specific Carbon Isotopes

The experiment was conducted in a self-designed simulation instrument. As shown in **Figure 2**, the device is comprised of a reactor with a volume of 300 ml, a ceramic fiber muffle furnace, and a high precision temperature controller (±1°C). Jiang and Song (1992) established the relationship between the simulated temperature and sediment vitrinite reflectance (Ro%) based on the thermal simulation experiments on immature source rocks from Junggar Basin, and indicated that the sediment samples were still in the immature-low mature stage, when the thermal simulation temperature was lower than 350°C. Additionally, previous studies by Zhang et al. (2001) and Xie et al. (2002) suggested that the peak amount of carbon gases generally produced between 300–400°C. Consequently, in the present study, the experiment temperature was set as 350°C, and experiment time was set for 72 h.

The generated gases were analyzed using the MAT 271 mass spectrometer (Finnigan AG) and Gas Chromatography (GC) 5890C (Agilent Technologies). Basically, the non-hydrocarbon gases and the hydrocarbon gases (C_1–C_3) were measured by MAT 271 and GC 5890C equipped with a capillary column (HT-PLOT Al_2O_3, 50 m × 0.53 mm × 25 μm), respectively. A flame ionization detector (FID) and thermal conductivity detector (TCD) were connected to the column using Helium as the carrier gas. The GC 5890C oven temperature was initially set to 50°C for 5 min, and then increased to 200°C at a rate of 6°C/min, finally maintained for 10 min.

The compound-specific carbon isotope values of CO_2 and hydrocarbon gases (C_1–C_3) were performed on a VG Isochrom II isotope ratio mass spectrometer (IRMS) interfaced with an HP 5890 GC, fitted with a Poraplot Q column (30 m × 0.32 mm). Helium was used as the carrier gas. The column head pressure was 0.58 bar. The GC oven temperature was initially held at 40°C for 3 min, ramped from 40 to 180°C at 20°C/min, and held at 180°C for 5 min. Carbon isotope ratios for individual gaseous hydrocarbon compounds were measured using CO_2 as a reference gas, which was automatically introduced into the IRMS at the beginning and end of each analysis. The carbon isotope value of the CO_2 reference gas was calibrated against NBS-22 oil. In addition, a standard mixture (NG3) of gaseous hydrocarbons (C_1–C_3), with known isotope compositions calibrated by our laboratory (**Table 2**, Dai et al., 2012), was used daily to check the performance of the instrument. The standard deviation for replicate analyses of this mixture is better than 0.3‰ for each compound.

RESULTS

Ro, TOC Contents and *n*-Alkane Distribution Patterns of Xiaolongtan Sediments

The Ro values of representative XLT-I and XLT-II sediments varied between 0.29% and 0.32, 0.36, and 0.39%, respectively, suggesting the sediments were in the stage of immature.

The TOC concentration for sediments of XLT-I section fluctuated from 0.05 to 28.56%, with an average of 4.61%. For the upper XLT-II section, the TOC was between 0.24 and 52.34%, with an average value of 24.42%.

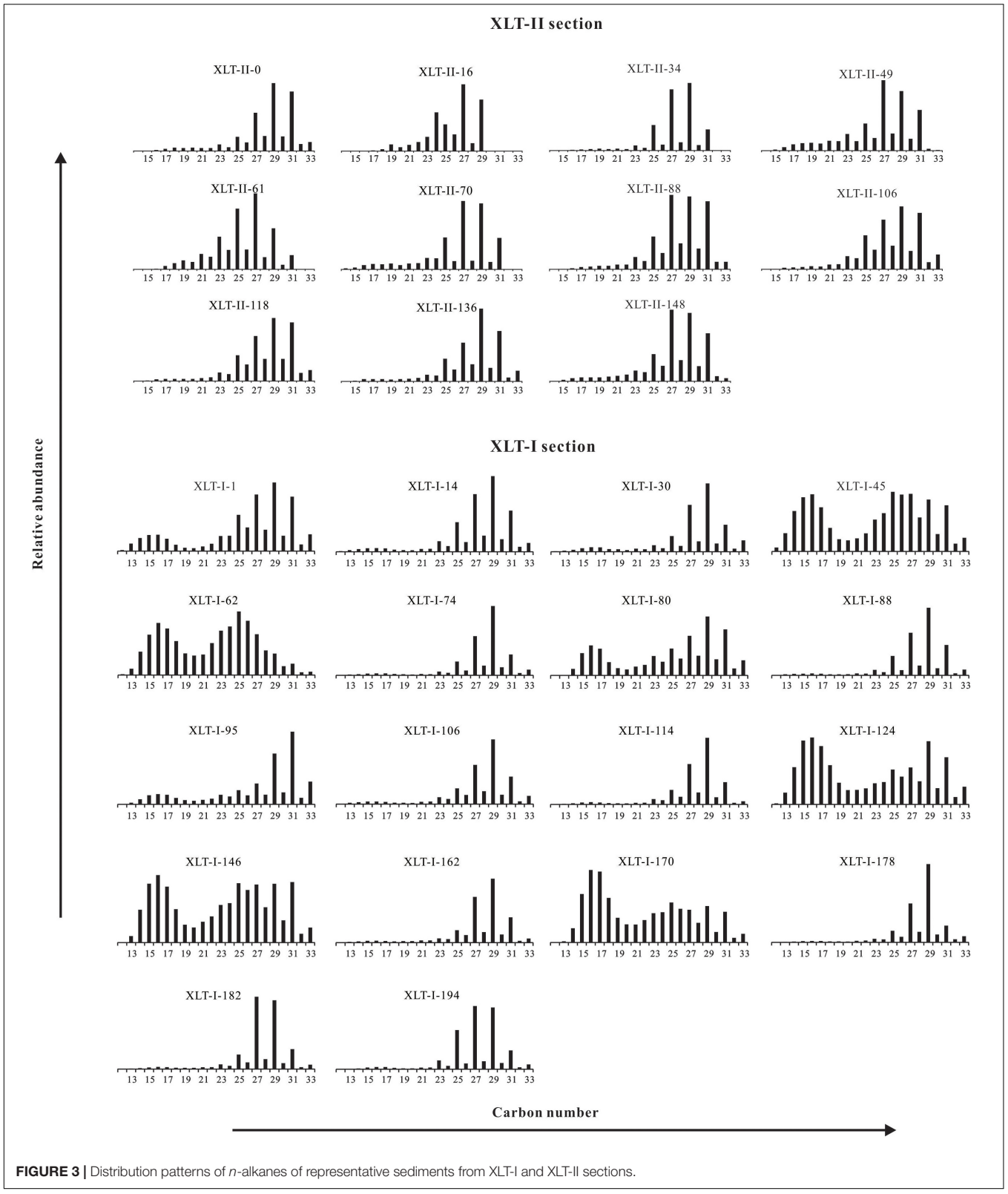


FIGURE 3 | Distribution patterns of *n*-alkanes of representative sediments from XLT-I and XLT-II sections.

The *n*-alkanes of the XLT-I section sediments ranged from nC_{12} to nC_{33}, with either a unimodal or bimodal distribution. The bimodal distribution of *n*-alkanes was centered on nC_{29}/nC_{31} and nC_{16}, generally. Whereas, the characteristic unimodal distribution of *n*-alkanes had a maximum carbon number at nC_{29}/nC_{31} (**Figure 3**). As for the *n*-alkane distribution

pattern of sediments from XLT-II section, it displayed a predominant back modal, ranging from nC_{14} to nC_{33}, with maxima at nC_{27}/nC_{29} (**Figure 3**). For the long-chain *n*-alkanes, a distinct odd-over-even predominance was observed throughout the sequence.

Production Rates of Generated Gases

The main components of the generated gases contained the non-hydrocarbon gases including CO_2, N_2 and H_2, accounting for the 89.0 ∼ 99.7% of the total gases, and the hydrocarbon gases including CH_4, C_2H_6 and C_3H_8, among which the CO_2 was the most abundant fraction ranging from 21.4 to 94.4% (**Table 1**). In terms of the hydrocarbon gases, the CH_4 was the most abundant.

Generally, the total gas production rate was estimated between 2,920 and 88,310 ml/kg rock, with an average value of 36,900 ml/kg rock. As for the carbon gases, the production rate was between 1,150 and 75,140 ml/kg rock for CO_2, 10 and 4,010 ml/kg rock for CH_4, and 20 and 5,890 ml/kg rock for total hydrocarbon gases (including CH_4, C_2H_6, and C_3H_8), with an average value of 31,910 ml/kg rock, 1,290 ml/kg rock and 1,940 ml/kg rock, respectively.

TABLE 1 | Contents of the CO_2, CH_4, and hydrocarbon gases (C_1–C_3) from the low temperature thermal simulation experiments.

Sample	Contents (%)		
	CO_2	CH_4	Hydrocarbon gases
XLT-I-148	90.7	3.0	4.3
XLT-I-136	87.4	3.2	4.9
XLT-I-118	77.2	5.1	7.3
XLT-I-106	88.0	2.9	5.4
XLT-I-88	88.7	3.2	4.9
XLT-I-70	85.7	3.9	5.5
XLT-I-49	87.0	4.2	5.9
XLT-I-34	83.7	4.2	6.2
XLT-I-16	85.1	3.2	4.9
XLT-I-0	82.1	5.4	7.9
XLT-II-194	93.6	2.7	3.9
XLT-II-182	94.4	2.4	3.1
XLT-II-178	92.1	3.4	4.7
XLT-II-170	90.1	0.4	0.6
XLT-II-162	88.6	0.3	0.5
XLT-II-146	75.4	5.3	11.0
XLT-II-124	94.1	0.2	0.3
XLT-II-114	86.2	2.9	5.7
XLT-II-106	61.9	4.2	8.3
XLT-II-95	21.4	1.2	2.2
XLT-II-88	73.2	5.5	9.3
XLT-II-80	90.7	0.7	1.2
XLT-II-74	87.0	4.8	6.6
XLT-II-62	78.4	0.2	0.3
XLT-II-45	46.8	0.6	0.9
XLT-II-30	94.3	1.8	3.0
XLT-II-14	83.1	4.6	9.6
XLT-II-1	79.5	0.7	1.7

Compound-Specific Carbon Isotopes of Carbon Gases

As listed in **Table 2**, the $\delta^{13}C$ values of CO_2 ranged from −24.8 to −16.0‰, with a mean value of −20.9‰. As for the hydrocarbon gases, the $\delta^{13}C$ values of CH_4, C_2H_6, and C_3H_8 fluctuated between −43.8 and −37.2‰, −34.2 and −32.1‰, −33.4 and −30.6‰, with an average of −40.2 −33.3, and −31.9‰, respectively. To be more specific, the $\delta^{13}C$ values of CH_4, C_2H_6, and C_3H_8 were characterized by normal isotope ordering, displaying $\delta^{13}C_{CH4} < \delta^{13}C_{C2H6} < \delta^{13}C_{C3H8}$.

DISCUSSION

Sources of Organic Matter and Paleoclimate Interpretation

In lacustrine environments, organic matter contains a wide range of lipid compounds contributed from autochthonous and/or heterochthonous organisms. Difference in lipid composition can directly reflect different types of biota (Pearson et al., 2007). Previous studies indicated that the short-chain *n*-alkanes ranging from C_{14} to C_{21} and dominated by C_{16} or C_{18}, are derived from lower organisms including algae, cyanobacteria, fungi, and microbes (Cranwell et al., 1987; Meyers and Ishiwatari, 1993). The middle-chain *n*-alkanes with carbon numbers in the range of C_{23} to C_{25} are thought to be from submerged/floating macrophytes (Ficken et al., 2000). By contrast, the long-chain *n*-alkanes ranging from C_{27} to C_{33}, showing an obvious odd-over-even predominance and dominated by C_{27}, C_{29}, C_{31} or C_{33}, are considered to come from terrestrial higher plants (Eglinton and Hamilton, 1967; Ficken et al., 2000).

TABLE 2 | Compound-specific carbon isotopes of the CH_4, C_2H_6, C_3H_8, and CO_2 of generated carbon gases from XLT-I and XLT-II sections.

Sample	$\delta^{13}C$ (‰)			
	CH_4	C_2H_6	C_3H_8	CO_2
XLT-I-148	−37.8	−33.4	−31.7	−21.7
XLT-I-118	−39.1	−32.9	−32.8	−21.2
XLT-I-88	−39.0	−33.6	−32.7	−23.3
XLT-I-34	−38.8	−32.6	−31.5	−20.8
XLT-I-0	−42.6	−33.2	−30.6	−21.5
XLT-II-182	−37.2	−32.8	−31.9	−23.5
XLT-II-170	–	–	–	−18.0
XLT-II-146	−42.1	−34.1	−31.5	−23.5
XLT-II-114	−40.0	−34.2	−32.8	−21.9
XLT-II-95	−40.9	−32.1	−30.8	−17.1
XLT-II-80	−43.6	−33.6	−33.4	−16.6
XLT-II-62	−43.8	–	–	−16.0
XLT-II-30	−39.8	−33.4	−30.9	−24.8
XLT-II-14	−37.7	−34.1	−32.4	−22.7
Standard sample	−43.6	−40.2	−33.8	–

"–" indicate the concentration of the corresponding gas component is too low to be measured, and the $\delta^{13}C$ values of CH_4, C_2H_6, and C_3H_8 of the standard sample (NG3) are from Dai et al. (2012).

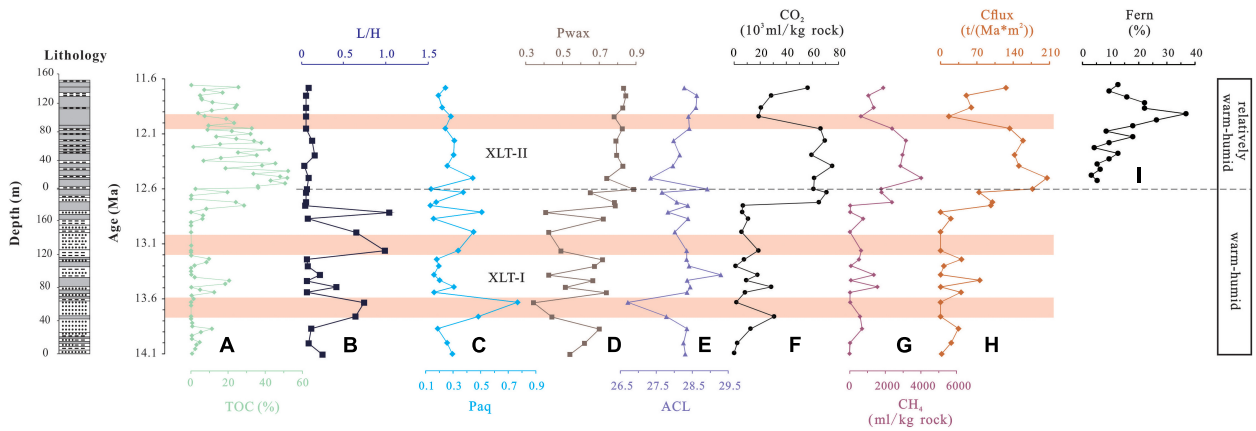


FIGURE 4 | Variations though time in various paleoenvironmental indicators for the Xiaolongtan Basin: **(A)** TOC contents, **(B)** L/H ratios, **(C)** Paq values, **(D)** Pwax values, **(E)** ACL values, **(F)** estimated production rate of CO_2, **(G)** estimated production rate of CH_4, **(H)** burial rate of organic carbon and **(I)** percentage of ferns in the Xiaolongtan Formation. Bars in this figure indicate three episodes of enhanced humidity inferred from lipid biomarkers and pollen concentrations.

The *n*-alkanes of XLT-I sediments were characterized by both bimodal and unimodal distribution patterns (**Figure 3**), indicating mixed sources of organic matter from lower organisms and terrestrial higher plants. With decreasing burial depths, the sources of organic matter shifted from mixed sources to terrestrial higher plants. Throughout the XLT-II section, all the *n*-alkanes displayed unimodal distribution centered at C_{27}, C_{29}, or C_{31} with a strong odd-over-even predominance (**Figure 3**), suggesting a primary contribution from terrestrial plants. The abundance of middle chain *n*-alkanes remained rather low, implying a very limited source from submerged/floating marcrophytes. Previous studies suggested that sediments with Pr/C_{17} and Ph/C_{18} ratios lower than 1, may go through weak microbial degradation (Grimalt et al., 1988; Gonzalez-Vilia et al., 2003; Wang et al., 2012). In most of our samples, the Pr/C_{17} and Ph/C_{18} ratios were lower than 1, implying that the middle chain *n*-alkanes were probably not affected by the microbial degradation (Grimalt et al., 1988; Gonzalez-Vilia et al., 2003; Wang et al., 2012). Thus, it is not likely that the long-chain *n*-alkanes were produced by emergent and submerged aquatic plants, although there are reports pointing out a few emergent and submerged plants can produce C_{27} or C_{29} *n*-alkanes (Aichner et al., 2010; Liu and Liu, 2016; Liu et al., 2016). In addition, the L/H ratio (calculated as $\Sigma nC_{21}^{-}/\Sigma nC_{22}^{+}$), which has been used to reflect the relative abundance of low molecular *n*-alkanes to high molecular homologs (Bai et al., 2006), ranged from 0.04 to 1.05, with an average value of 0.23 (**Figure 4B**), implying a significant contribution of terrestrial higher plants to the organic matter in the XLT-I and XLT-II sediments.

In addition, the XLT-I section is dominated by sandstone and clay intercalated with thin coal and marl layers, which may indicate delta plain and braided river facies (Zhang et al., 2019). Our results showed that the sedimentary organic matter was contributed by lower organisms and terrestrial higher plants, in accordance with the sedimentary environments. Furthermore, as indicated above, the *n*-alkane distribution patterns of XLT-II samples revealed a terrestrial plant contribution to the organic matter. The evidence from lithology and pollen assemblages implied the sedimentary environment of XLT-II section was interpreted as swamp face and the vegetation was dominated by angiosperms (Li S.F. et al., 2015; Zhang et al., 2019). Our *n*-alkane results were consistent with previous claims. Both the source of organic matter and the sedimentary environment favored the formation of lignite in this section.

Previous studies have indicated that the Paq [calculated as $(C_{23} + C_{25})/(C_{23} + C_{25} + C_{27} + C_{29})$] and Pwax [calculated as $(C_{27} + C_{29} + C_{31})/(C_{23} + C_{25} + C_{27} + C_{29} + C_{31})$] proxy can be applied to reflect the relative abundance of non-emergent aquatic marcophytes and input of emergent aquatic and terrestrial plants, and its corresponding paleoclimate conditions (Ficken et al., 2000; Zheng et al., 2007; Pu et al., 2011; Wang G. et al., 2019). A high Pwax value represents a high input of terrestrial plants from herbs and trees, which may indicate a warm climate with low precipitation, corresponding to a low Paq values (Zheng et al., 2007; Pu et al., 2011). Besides, the ACL [average chain length, calculated as $(25^{*}C_{25} + 27^{*}C_{27} + 29^{*}C_{29} + 31^{*}C_{31})/(C_{25} + C_{27} + C_{29} + C_{31})$] values of *n*-alkanes was proposed to be an effective index for evaluating the temperature variation (Poynter et al., 1989), which have been successfully applied in paleoclimate reconstruction in loess/paleosol and lake sediments (Zhang et al., 2006; Pu et al., 2011; Chu et al., 2014). Recent studies have revealed that vegetation types, effective precipitation, as well as biologic function of plant waxes also influence the ACL values (Schefuß et al., 2003; Bush and McInerney, 2015). Thus, the ACL values may represent a combined signal of these factors mentioned above. In our study, the ACL values displayed similar variation trends with the Pwax values and opposite changes with the Paq values, indicating that the ACL proxy contained the same paleoclimatic implications with Pwax, with higher values corresponding to warm and dry climate conditions.

For the XLT-I section between 14.1 and 12.6 Ma, the Pwax and Paq values remained relatively unstable, indicating the source

of organic matter varied accordingly. The relatively low Paq and high ACL values implied that this stage was generally characterized by a warm and humid but unstable climate (**Figure 4**). Based on the lithology with coal representing swamps with dense trees or grasses and marl denoting shallow lakes with evaporative carbonates, Zhang et al. (2019) inferred that the XLT-I sediments can be indicators of forest steppe in a subtropical warm and humid monsoon climate from 14.1 to 12.6 Ma. Previous studies indicated that the significant tectonic activity of the entire Tibetan Plateau at ∼14 Ma was responsible for the differences in aridity in the southeastern Tibetan Plateau during the middle-late Miocene, which was characterized with dry conditions in the western high-elevation regions and relatively humid environment in the eastern low-elevation areas under the background of equal supply of moisture from the Indian monsoon (Jacques et al., 2011), and the differences of flora in the north-south transition displaying evergreen broad-leaved forest in the subtropical areas and taxa in the tropical regions in the late Miocene (Jacques et al., 2014). These observations lead to the argument that the climate during the period between 14.1 and 12.6 Ma was strongly affected by both the evolution of the Indian monsoon and the uplift of the southeaster Tibetan Plateau (Wang et al., 1998; Huang et al., 2007; Zhang et al., 2019). Interestingly, the Pwax values displayed a sharp decrease in the episodes at around 13.8–13.5 Ma and 13.1–12.9 Ma, and the Paq values exhibited the opposite variation, suggesting an enhanced input of aquatic macrophytes during these two intervals, probably in response to the increased precipitation/runoff. During these two intervals, the climate became more humid than before, in concert with the sediment environment shifting from delta plain toward braided river (Zhang et al., 2019). Variations in the hydrodynamic forces may cause changes in the transportation and the later accumulation and deposition of organic matter. This was further corroborated by the varying and low TOC contents (**Figure 4A**).

For the XLT-II section between 12.6 and 11.6 Ma, the *n*-alkane distribution patterns indicated a constant contribution from terrestrial plants, which was further supported by the high Pwax and low Paq proxies (**Figure 4**), implying this interval was characterized by warm but less wet climate conditions. The ACL values displayed an overall increasing trend, suggesting a slight increase of aridity. The results were consistent with the sedimentary facies changing to swamp, and the ecological environment shifting from forest steppe to forest (Zhang et al., 2019). The pollen assemblages found in the XLT-II section were dominated by angiosperms which represent the evergreen broad-leaved forests, such as *Cupuliferoipollenites, Cyrillaceaepollenites, Liquidambarpollenites, Caryapollenites, Salixipollenites, Ilexpollenites, Rutaceoipollis, Juglanspollenites, Talisiipites, Platycaryapollenites* (Wang, 1996; Li S.F. et al., 2015). Moreover, the mammal fossils of arboreal primate hominoids and forest elephants in the Xiaolongtan Basin also indicated a warm and relatively humid climate suitable for the survival of these mammals (Dong, 1987, 2001). During this stage, the warm and less humid climate and stable sedimentary environment benefited the formation, accumulation and deposition of organic matter, leading to the high TOC concentrations of the XLT-II section sediments. Overall, slight increases in arid conditions between 12.6 and 11.6 Ma were superimposed on long-term warm and humid climate.

Carbon Gas Behaviors Associated With Paleoclimate Conditions

The production rate of CO_2 and CH_4 displayed significantly positive correlation with the TOC contents of sediment, with r^2 values of 0.85 and 0.91, respectively (**Figures 5A,B**), indicating the carbon gases were mainly generated from the organic matter. Additionally, the $\delta^{13}C$ values of CH_4, C_2H_6, and C_3H_8 exhibited a normal isotope ordering (**Figure 5E**), and the $\delta^{13}C$ values of CO_2 were lower than $-10‰$, suggesting organic origin of the generated carbon gases (Dai et al., 1996, 2005). Consequently, it is reasonable to infer that the CO_2 and hydrocarbon gases including CH_4, C_2H_6, and C_3H_8 were produced by thermal effect of sedimentary organic matters during their shallow burial process.

Basically, the production rate of carbon gases was primarily controlled by the sedimentary TOC content, showing high production rates of both CO_2 and hydrocarbon gases in response to high sediment TOC concentration. In the XLT-I sediments, the production rate of carbon gases was lower than that of the XLT-II sediments, mainly due to the significant differences of TOC contents of sediments from the two sections. In addition, both the CO_2 and CH_4 (and hydrocarbon gases) production rate displayed weak positive correlations with the Pwax values (**Figures 5C,D**), with r^2 values of 0.48 and 0.52, respectively, indicating that warm and dry climate conditions may be favorable of the formation of carbon gases. Our results suggested that the paleoclimate conditions played an important role in the generation of carbon gases. Particularly, in the XLT-I section, the production rate of carbon gases showed an obvious decrease when the climate shifted toward more humid conditions at around 13.8 ∼ 13.5 Ma and 13.1 ∼ 12.9 Ma. Thereafter, under the background of long-term warm and humid climate conditions, with the increase of aridity, both the CO_2 and hydrocarbon gases production rate rose correspondingly. In the XLT-II section, the sedimentary environment changed to swamp (Zhang et al., 2019), which favored formation, accumulation and deposition of organic matter, resulting in high sedimentary TOC concentrations. The warm and relatively dry climate also benefited the generation of carbon gases during that time. Generally, the average production rate of CO_2 and CH_4 was 2 ∼ 3 times larger than that of the XLT-I section. The pollen records indicated this interval was warm and humid. However, the abundance of ferns and angiosperms exhibited variations, implying variations in humidity and temperature. The production rate of CO_2 and CH_4 showed a negative correlation with the abundance of fern (**Figure 4**), exhibiting high production rates corresponding to low abundance of ferns. Both the CO_2 and CH_4 production rate increased and stayed high from 12.6 to 12.0 Ma, in line with the low fern percentage. However, the gas production rate decreased after 12.0 Ma, in accordance with the sharp rise in the abundance of ferns. Interestingly, a slight increase of Paq value and corresponding decrease of Pwax value at around 12.0 Ma indicated an increase in humidity. In addition, the gradual

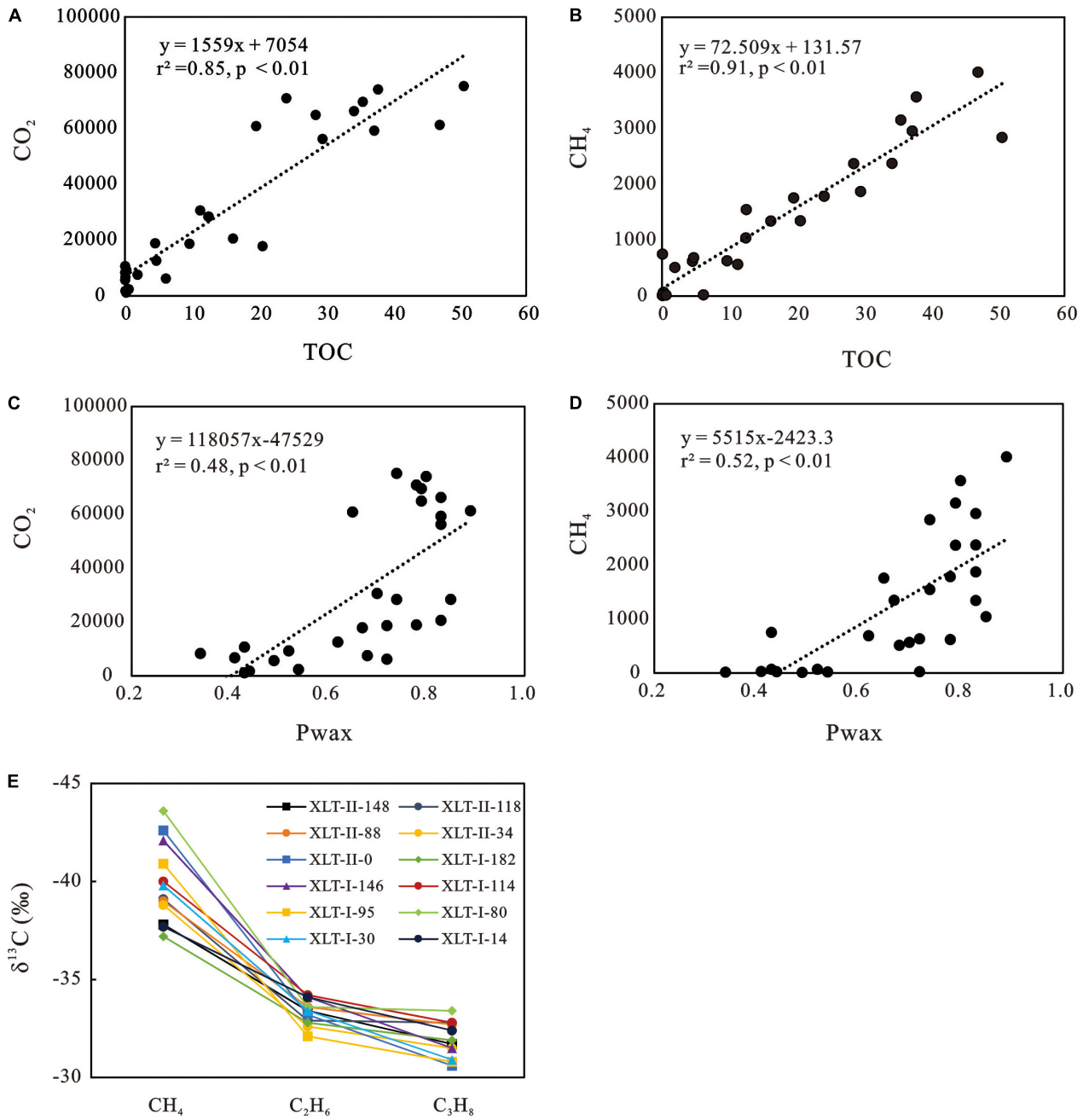


FIGURE 5 | Correlations between TOC contents and production rate of CO_2 and CH_4 **(A,B)**, and Pwax values and production rate of CO_2 and CH_4 **(C,D)**, and compound-specific carbon isotopes of CH_4, C_2H_6 and C_3H_8, respectively **(E)**.

changes of sedimentary facies to shallow lakes at the upper part of XLT-II section as a result of compressive uplift (Dong, 2001; Zhang et al., 2019), also implied that the increase in humidity was probably related to enhanced precipitation, leading to unstable hydrodynamic environment for accumulation and deposition of organic matter, and consequent low carbon gas production rate.

In summary, our results indicated that the carbon gases can be produced during the shallow burial process when the sediments reached appropriate conditions of pressure and temperature. From 14.1 to 11.6 Ma, the production rate of carbon gases displayed significant variations in response to the fluctuations of paleoclimate conditions, which was regulated by the variations of the Indian monsoon and the uplift of the Tibetan Plateau. Generally, warm and less humid climate was conducive to the formation, accumulation and deposition of organic matter, which acted as the material basis for the generation of carbon gases. The low gas production rate corresponded with increased humidity,

indicating that warm and less humid (arid) climate contributed to the thermal effects of organic matter to transform to carbon gases.

Original Organic Carbon Burial Rates

The low-temperature thermal simulation experiments showed that when reaching appropriate temperature and pressure, the organic matter would go through the thermodynamic effect to produce carbon gases during their shallow burial process, resulting in changes of the TOC contents of sediments. Therefore, in order to achieve the original signal of organic carbon concentration, it is important to restore the sediment TOC. Combining the efforts of geologic observation, experimental simulation and numerical modeling, Zhong et al. (2004) proposed a method to evaluate variations of sediment TOC contents during their geological history, and established an equation to estimate the loss of TOC when undergoing thermal maturation.

For the XLT-1 and XLT-II section simulated sediments, the TOC contents varied between 0.05 and 50.70% (**Table 3**). The TOC contents of the samples after thermal simulation experiments (expressed as TOC*) fluctuated from 0.07 to 44.20%. The overall trend exhibited that the TOC contents of sediment decreased after experiments. The loss ratio of TOC (expressed as DTOC) varied in the range from −0.83 to 0.34, and the corresponding calculated recovery coefficients (k) fluctuated between 0.55 and 1.51. The restored TOC (expressed as TOC°) representing the original TOC varied between 0.03 and 58.16% (**Table 3**), further confirming that most of the original sedimentary TOC decreased after the burial process.

It should be pointed out that some of the sediments characterized by low TOC concentrations especially for the XLT-I section (such as samples XLT-I-45, XLT-I-62, XLT-I-80, XLT-I-95, XLT-I-124, XLT-146, and XLT-I-170) displayed a "carbon addition" phenomenon, which revealed during the sediment thermal maturation process, little carbon gases were produced by the organic matter and a certain amount of inorganic sediments consumed. So after restoration, the original TOC (TOC°) displayed slightly higher values than that of the present sediments. By contrast, the rest part of the sediments with high TOC contents were characterized by "carbon reduction," indicating a certain amount of organic matter was transformed to carbon gases.

Based on the restoration of TOC, we estimated the original organic carbon burial rate (expressed as C_{flux}) in the study area. Previous studies indicated that the organic carbon burial rate can be calculated using the following equation, expressed as C_{flux} = TOC × ν × ρ, where ν represents the sedimentation rate, and ρ represents the dry density of the sediments (Xu et al., 2013; Ruiz-Fernández et al., 2018). Generally, the organic carbon burial rate varied from 0.1 to 205.1 t/(m^2·Ma), with an average value of 60.0 t/(m^2·Ma), characterized by far more larger values in the XLT-II section sediments than that of the XLT-I sediments (**Figure 4G**). Generally, under the background of persistent warm and humid climate conditions, our estimated burial rate of organic carbon was mainly controlled by the primary production, which regulated the input of organic matter. Besides, the higher sedimentation rates in the XLT-II sediments also elevated the burial efficiency and preservation of organic matter (Makled et al., 2019). Similar with the estimations of gas production rate, the burial rate of organic carbon corresponded well with the paleoclimate conditions as indicated by the lipid biomarkers, pollen assemblages and lithology (Zhang et al., 2019), showing decreasing trend when climate became wetter.

Quantification of carbon burial of Qinghai Lake sediments by Xu et al. (2013) indicated that TOC flux was higher during the warm and wet periods than in the cold and dry episodes. Besides, based on the studies of 42 lakes across China, Zhang et al. (2013) claimed that the burial rate of organic carbon during the Holocene climatic optimum was higher than in modern times, due to the warm and humid climate, enhanced input of organic matter and high primary productivity in lakes. In the present study, the warm and humid climate and the generally reducing sedimentary environment as reflected by the Pr/Ph proxy (ranging from 0.31 to 1.40, average 0.98) favored the formation, deposition, and preservation of organic matter, resulting in

TABLE 3 | Total organic carbon (TOC) restoration parameters of Xiaolongtan Basin sediments.

Sample	TOC (%)	TOC* (%)	DTOC	*k*	TOC° (%)
XLT-II-148	29.60	24.50	0.17	1.21	35.76
XLT-II-136	12.50	11.10	0.11	1.13	14.08
XLT-II-118	16.20	15.60	0.04	1.04	16.82
XLT-II-106	4.50	4.40	0.02	1.02	4.60
XLT-II-88	34.30	31.10	0.09	1.10	37.83
XLT-II-70	35.60	28.10	0.21	1.27	45.10
XLT-II-49	37.90	35.50	0.06	1.07	40.46
XLT-II-34	37.30	32.50	0.13	1.15	42.81
XLT-II-16	50.70	44.20	0.13	1.15	58.16
XLT-II-0	47.10	44.20	0.06	1.07	50.19
XLT-I-194	19.64	15.00	0.24	1.31	25.72
XLT-I-182	24.18	16.90	0.30	1.43	34.60
XLT-I-178	28.56	24.30	0.15	1.18	33.57
XLT-I-170	0.08	0.14	−0.75	0.57	0.05
XLT-I-162	6.15	5.49	0.11	1.12	6.89
XLT-I-146	0.05	0.07	−0.40	0.71	0.04
XLT-I-124	0.07	0.11	−0.57	0.64	0.04
XLT-I-114	9.67	6.67	0.31	1.45	14.02
XLT-I-106	1.90	1.58	0.17	1.20	2.28
XLT-I-95	0.20	0.33	−0.65	0.61	0.12
XLT-I-88	20.61	16.25	0.21	1.27	26.14
XLT-I-80	0.24	0.34	−0.42	0.71	0.17
XLT-I-74	12.55	11.50	0.08	1.09	13.70
XLT-I-62	0.06	0.11	−0.83	0.55	0.03
XLT-I-45	0.08	0.12	−0.50	0.67	0.05
XLT-I-30	11.29	10.70	0.05	1.06	11.91
XLT-I-14	4.72	3.13	0.34	1.51	7.12
XLT-I-1	0.59	0.46	0.22	1.28	0.76

TOC refers to the TOC contents of present sediments; TOC refers to the TOC contents of samples after thermal simulation experiments; DTOC refers to the loss factor of organic carbon; k refers to the recovery coefficient; TOC° refers to the original TOC contents of the sediments after the restoration estimated according to the method proposed by Zhong et al. (2004).*

DTOC = (TOC − TOC)/TOC*; k = 1/(1 − DTOC); TOC° = TOC × 1/(1 − DTOC).*

relatively high sediment TOC concentrations, and consequently high organic carbon burial rate. Particularly, the low burial rates acted in response to the sharp increase of humidity. For example, during the period of 13.8–13.5 Ma and 13.1–12.9 Ma, the climate was wetter than before. And correspondingly, the burial rate of organic carbon was extremely low, ranging from 0.09 to 0.14 t/(m^2·Ma). Furthermore, the minimum value of organic carbon burial rate at around 12.0 Ma in the XLT-II section also corresponded to the climate becoming wetter.

Generally, the average burial rate of organic carbon in the XLT-I and XLT-II sections was estimated to be 60.0 t/(m^2·Ma), which is larger than 43.2 and 36.4 g/(m^2·a) from the lake sediments in the East China, 50.9 and 22.1 g/(m^2·a) from the lakes in the Inner Mongolia and Xinjiang, 33.5 and 19.7 g/(m^2·a) from the lake records in the Qinghai-Tibetan Plateau, and 22.0 and 16.6 g/(m^2·a) from the lake sediments in the Yunnan–Guizhou Plateau during the Holocene climatic optimum and modern times (Zhang et al., 2013). Our results indicated that the Xiaolongtan Basin might have been a sink for organic carbon between 14.1 and 11.6 Ma. After the sequestration of organic carbon, this carbon pool probably acted as a source for the carbon gases produced by thermal effects during the shallow burial process.

CONCLUSION

Based on the precise chronological framework, analyses of lipid biomarkers and low temperature thermal simulation experiments were carried out from the Xiaolongtan Basin in the southeastern part of the Tibetan Plateau. The preliminary conclusions drawn from this study were listed below:

(1) According to the characteristics of *n*-alkanes and its derived proxies (including Paq and Pwax), it is indicated that the organic matter of the XLT-I sediments was mainly derived from mixed sources including lower organisms and terrestrial higher plants, and terrestrial higher plants primarily contributed to the XLT-II sediments.
(2) As reflected by the lipid biomarkers and pollen records, the climate between 14.1 and 12.6 Ma was warm and humid, and humidity slightly decreased between 12.6 and 11.6 Ma. And the climate was under the influence of both the evolution of Indian monsoon and the uplift of the southeastern Tibetan Plateau.
(3) The low temperature thermal simulation experiments showed that a certain amount of carbon gases (CO_2 and CH_4) can be produced and released into atmosphere owing to thermodynamic effects of organic matter during the shallow burial process. Original accumulation, deposition and preservation of organic matter primarily influenced the production rate of carbon gases and burial rate of organic carbon. Besides, the estimated production rate of carbon gases and burial rate of organic carbon displayed similar variation trends throughout the sequence, generally exhibiting decreasing trends in accordance with strengthened humidity, which was further controlled by the paleoclimate variations forced by the changes of Indian monsoon and the uplift of the Tibetan Plateau.

DATA AVAILABILITY STATEMENT

The original contributions generated for this study are included in the article/supplementary material, further inquiries can be directed to the corresponding author.

AUTHOR CONTRIBUTIONS

GW, YW, and ZW contributed conception and design of the study. GW and ZS executed the thermal simulation experiments. WH and XM carried out chemical analysis. GW wrote the first draft of the manuscript. All authors contributed to the article and approved the submitted version.

FUNDING

This work was financially supported by the National Natural Science Foundation of China (Grant Nos. 41831176, 41902028, and 41972030), the Second Tibetan Plateau Scientific Expedition and Research (STEP) Program (Grant No. 2019QZKK0707), the Chinese Academy of Sciences Key Project (Grant No. XDB26020302), the CAS 'Light of West China' Program, the Youth Innovation Promotion Association CAS (No. 2021425), and the Key Laboratory Project of Gansu (Grant No. 1309RTSA041).

ACKNOWLEDGMENTS

The authors show special thanks to the reviewers for their constructive comments and improvements of the language.

REFERENCES

Aichner, B., Herzschuh, U., and Wilkes, H. (2010). Influence of aquatic macrophytes on the stable carbon isotopic signatures of sedimentary organic matter in lakes on the Tibetan Plateau. *Org. Geochem.* 41, 706–718. doi: 10.1016/j.orggeochem.2010.02.002

Bai, Y., Fang, X. M., Wang, Y. L., Fabien, K., Chen, X. L., and Wang, Y. X. (2006). Branched alkanes with quaternary carbon atoms in Chinese soils: potential environmental implications. *Sci. Bull.* 51, 1115–1122. doi: 10.1007/s11434-006-1115-3

Bush, R. T., and McInerney, F. A. (2015). Influence of temperature and C4 abundance on n-alkane chain length distributions across the central USA. *Org. Geochem.* 79, 65–73. doi: 10.1016/j.orggeochem.2014.12.003

Choi, Y., and Wang, Y. (2004). Dynamics of carbon sequestration in a coastal wetland using radiocarbon measurements, global biogeochem. *Cycles* 18:GB4016.

Chu, G. Q., Sun, Q., Xie, M. M., Lin, Y., Shang, W. Y., and Zhu, Q. Z. (2014). Holocene cyclic climatic variations and the role of the Pacific Ocean as recorded in varved sediments from northeastern China. *Quat. Sci. Rev.* 102, 85–95. doi: 10.1016/j.quascirev.2014.08.008

Cranwell, P. A., Eglinton, G., and Robinson, N. (1987). Lipids of aquatic organisms as potential contributors to lacustrine sediments—II. *Org. Geochem.* 11, 513–527. doi: 10.1016/0146-6380(87)90007-6

Dai, J., Chen, H., and Shen, X. (2005). Geochemistry and occurrence of inorganic gas accumulations in Chinese sedimentary basins. *Org. Geochem.* 36, 1664–1688. doi: 10.1016/j.orggeochem.2005.08.007

Dai, J., Song, Y., Dai, C., and Wang, D. (1996). Geochemistry and accumulation of carbon dioxide gases in China. *AAPG Bull.* 10, 1615–1626.

Dai, J., Xia, X. Y., Li, Z. S., Coleman, D. D., Dias, R. F., Gao, L., et al. (2012). Inter-laboratory calibration of natural gas round robins for δ2H and δ13C using off-line and on-line techniques. *Chem. Geol.* 310-311, 49–55. doi: 10.1016/j.chemgeo.2012.03.008

Dong, W. (1987). Further investigations upon the age and characteristics of the Xiaolongtan fauna, Kaiyuan Co., Yunnan Province. *Vertebrata PalAsiatica* 25, 116–123.

Dong, W. (2001). "Upper Cenozoic stratigraphy and paleoenvironment of Xiaolongtan Basin, Kaiyuan, Yunnan Province," in *Proceedings of the Eighth Annual Meeting of the Chinese Society of Vertebrate Paleontology*, eds T. Deng and Y. Wang (Beijing: China Ocean Press).

Eglinton, G., and Hamilton, R. J. (1967). Leaf epicuticular waxes. *Science* 156, 1322–1335. doi: 10.1126/science.156.3780.1322

Fang, J. Y., Yu, G. R., Liu, L. L., Hu, S. J., and Stuart Chapin, F. (2018). Climate change, human impacts, and carbon sequestration in China. *Proc. Natl. Acad. Sci. USA* 115, 4015–4020.

Ficken, K. J., Li, B., Swain, D. L., and Eglinton, G. (2000). An n-alkane proxy for the sedimentary input of submerged/floating freshwater aquatic macrophytes. *Org. Geochem.* 31, 745–749. doi: 10.1016/s0146-6380(00)00081-4

Gao, Y., Huang, H., Tao, H. F., Carroll, A. R., Qin, J. M., Chen, J. Q., et al. (2019). Paleoenvironmental setting, mechanism and consequence of massive organic carbon burial in the Permian Junggar Basin, NW China. *J. Asian Earth Sci.* 194:104222. doi: 10.1016/j.jseaes.2019.104222

Gonzalez-Vilia, F. J., Polvillo, O., Boski, T., Moura, D., and de Andres, J. R. (2003). Biomarker patterns in a time-resolved holocene/terminal Pleistocene sedimentary sequence from the Guadiana river estuarine area (SW Portugal/Spain border). *Org. Geochem.* 34, 1601–1613. doi: 10.1016/j.orggeochem.2003.08.006

Grimalt, J. O., Torras, E., and Albaiges, J. (1988). Bacterial reworking of sedimentary lipids during sample storage. *Org. Geochem.* 13, 741–746. doi: 10.1016/0146-6380(88)90096-4

Heimann, M., and Reichstein, M. (2008). Terrestrial ecosystem carbon dynamics and climate feedbacks. *Nature* 451, 289–292. doi: 10.1038/nature06591

Huang, Y. J., Jia, L. B., Wang, Q., Mosbrugger, V., Utescher, T., Su, T., et al. (2016). Cenozoic plant diversity of Yunnan: a review. *Plant Diversity* 38, 271–282. doi: 10.1016/j.pld.2016.11.004

Huang, Y. S., Clemens, S. C., Liu, W. G., Wang, Y., and Prell, W. L. (2007). Large-scale hydrological change drove the late Miocene C4 plant expansion in the Himalayan foreland and Arabian Peninsula. *Geology* 6, 531–534. doi: 10.1130/g23666a.1

Jacques, F., Guo, S. X., Su, T., Xing, Y. W., Huang, Y. J., Liu, Y. S., et al. (2011). Quantitative reconstruction of the Late Miocene monsoon climates of southwest China: a case study of the Lincang flora from Yunnan Province. *Palaeogeogr. Palaeoclimatol. Palaeoecol.* 304, 318–327. doi: 10.1016/j.palaeo.2010.04.014

Jacques, F., Su, T., Spicer, R. A., Xing, Y. W., Huang, Y. J., and Zhou, Z. K. (2014). Late Miocene southwestern Chinese floristic diversity shaped by the southeastern uplift of the Tibetan Plateau. *Palaeogeogr. Palaeoclimatol. Palaeoecol.* 411, 208–215. doi: 10.1016/j.palaeo.2014.05.041

Ji, X. P., Jablonski, N. G., Su, D. F., Deng, C. L., Flynn, L. J., You, Y., et al. (2013). Juvenile hominoid cranium from the terminal Miocene of Yunnan, China. *Chin. Sci. Bull.* 58, 3771–3779. doi: 10.1007/s11434-013-6021-x

Jiang, S. B., and Song, Z. Y. (1992). Thermal modelling and gas yield potential analysis of gas source rocks in Junggar Basin. *Xinjiang Petroleum Geol.* 13, 86–93.

Li, S. F., Mao, L. M., Spicer, R. A., Lebreton-Anberrée, J., Su, T., Sun, M., et al. (2015). Late Miocene vegetation dynamics under monsoonal climate in southwestern China. *Palaeogeogr. Palaeoclimatol. Palaeoecol.* 425, 14–40. doi: 10.1016/j.palaeo.2015.02.030

Li, S. H., Deng, C. L., Dong, W., Sun, L., Liu, S. Z., Qin, H. F., et al. (2015). Magnetostratigraphy of the Xiaolongtan formation bearing *Lufengpithecus keiyuanensis* in Yunnan, southwestern China: constraint on the initiation time of the southern segment of the Xianshuihe–Xiaojiang fault. *Tectonophysics* 655, 213–226. doi: 10.1016/j.tecto.2015.06.002

Liu, H., and Liu, W. G. (2016). n-Alkane distributions and concentrations in algae, submerged plants and terrestrial plants from the Qinghai-Tibetan Plateau. *Org. Geochem.* 99, 10–22. doi: 10.1016/j.orggeochem.2016.06.003

Liu, W. G., Yang, H., Wang, H. Y., Yao, Y., Wang, Z., and Cao, Y. N. (2016). Influence of aquatic plants on the hydrogen isotope composition of sedimentary long-chain n-alkanes in the Lake Qinghai region, Qinghai-Tibetan Plateau. *Sci. China Earth Sci.* 59, 1368–1377. doi: 10.1007/s11430-016-5263-2

Makled, W. A., Abd, El Ghany, A. A., and Soliman, S. I. (2019). Tracking the key parameters stimulating organic carbon productivity, accumulation rate and preservation based on foraminiferal proxies in the subsurface Miocene sediments in north Sinai. *Egypt. Mar. Petrol. Geol.* 110, 218–239. doi: 10.1016/j.marpetgeo.2019.07.010

Meyers, P. A., and Ishiwatari, R. (1993). Lacustrine organic geochemistry - an overview of indicators of organic matter sources and diagenesis in lake sediments. *Org. Geochem.* 20, 867–900. doi: 10.1016/0146-6380(93)90100-p

Owens, J. D., Lyons, T. W., and Lowery, C. M. (2018). Quantifying the missing sink for global organic carbon burial during a cretaceous oceanic anoxic event. *Earth Planet. Sci. Lett.* 499, 83–94. doi: 10.1016/j.epsl.2018.07.021

Pearson, E. J., Farrimond, P., and Juggins, S. (2007). Lipid geochemistry of lake sediments from semi-arid Spain: relationships with source inputs and environmental factors. *Org. Geochem.* 38, 1169–1195. doi: 10.1016/j.orggeochem.2007.02.007

Poynter, J., Farrimond, P., Robinson, N., and Eglinton, G. (1989). *Aeolian-Derived Higher Plant Lipids in the Marine Sedimentary Record: Links with Palaeoclimate, Paleoclimatology and Paleometeorology: Modern and Past Patterns of Global Atmospheric Transport*. Berlin: Springer, 435–462.

Pu, Y., Zhang, H. C., Wang, Y. L., Lei, G. L., Nace, T., and Zhang, S. P. (2011). Climatic and environmental implications from n-alkanes in glacially eroded lake sediments in Tibetan Plateau: an example from Ximen Co. *Chin. Sci. Bull.* 56, 1503–1510. doi: 10.1007/s11434-011-4454-7

Ruiz-Fernández, A. C., Carnero-Bravo, V., Sanchez-Cabeza, J. A., Pérez-Bernal, L. H., Amaya-Monterrosa, O. A., Bojórquez-Sánchez, S., et al. (2018). Carbon burial and storage in tropical salt marshes under the influence of sea level rise. *Sci. Total Environ.* 630, 1628–1640. doi: 10.1016/j.scitotenv.2018.02.246

Schefuß, E., Ratmeyer, V., Stuut, J. B. W., Janse, J. H. F., and Damste, J. S. S. (2003). Carbon isotope analyses of n-alkanes in dust from the lower atmosphere over the central eastern Atlantic. *Geochim. Cosmochim. Acta* 67, 1757–1767. doi: 10.1016/s0016-7037(02)01414-x

Shao, H. B., Yang, S. Y., Cai, F., Li, C., Liang, J., Li, Q., et al. (2016). Sources and burial of organic carbon in the middle Okinawa trough during late quaternary paleoenvironmental change. *Deep Sea Res. 1 Oceanogr. Res. Papers* 118, 46–56. doi: 10.1016/j.dsr.2016.10.005

Smoak, J. M., Breithaupt, J. L., Smith, T. J., and Sanders, C. J. (2013). Sediment accretion and organic carbon burial relative to sea-level rise and storm events in two mangrove forests in everglades national park. *Catena* 104, 58–66. doi: 10.1016/j.catena.2012.10.009

Tapponnier, P., Xu, Z. Q., Roger, F., Meyer, B., Arnaud, N., Wittlinger, G., et al. (2001). Oblique stepwise rise and growth of the Tibet plateau. *Science* 294, 1671–1677. doi: 10.1126/science.105978

Wang, E., Burchfiel, B. C., Royden, L. H., Chen, L. Z., Chen, J. S., Li, W. X., et al. (1998). Late cenozoic xianshuihe-xiaojiang, red river, and dali fault systems of southwestern sichuan and central yunnan. *China Geol. Soc. Am. Bull.* 327, 1–108.

Wang, G., Wang, Y. L., Wei, Z. F., He, W., Ma, X. Y., Sun, Z. P., et al. (2019). Paleoclimate changes of the past 30 cal ka BP inferred from lipid biomarkers and geochemical records from Qionghai Lake, southwest China. *J. Asian Earth Sci.* 172, 346–358. doi: 10.1016/j.jseaes.2018.09.019

Wang, K., Zhang, H. S., Han, X. B., and Qiu, W. X. (2019). Sources and burial fluxes of sedimentary organic carbon in the northern Bering sea and the northern Chukchi sea in response to global warming. *Sci. Total Environ.* 679, 97–105. doi: 10.1016/j.scitotenv.2019.04.374

Wang, W. M. (1996). A palynological survey of neogene strara in xiaolongtan basin, yunnan province of south China. *Acta Geol. Sin.* 38, 743–748.

Wang, Y. L., Fang, X. M., Zhang, T. W., Li, Y. M., Wu, Y. Q., He, D. X., et al. (2012). Distribution of biomarkers in lacustrine sediments of the Linxia Basin, NE Tibetan Plateau, NW China: significance for climate change. *Seiment. Geol.* 243-244, 108–116. doi: 10.1016/j.sedgeo.2011.10.006

Wilson, R. M., Neumann, R. B., Crossen, K. B., Raab, N. M., Hodgkins, S. B., Saleska, S. R., et al. (2019). Microbial community analyses inform geochemical reaction network models for predicting pathways of greenhouse gas production. *Front. Earth Sci.* 7:59.

Woo, J. K. (1987). A revision of the classification of the Lufeng great ape. *Acta Anthropol. Sinica* 6, 265–271.

Xie, Z. Y., Jiang, Z. S., Zhang, Y., Li, J., Hu, G. Y., Wang, C. Y., et al. (2002). Novel method of whole rock pyrolysis and application to the evaluation of source rock. *Acta Sedimentologica Sinica* 20, 510–514.

Xu, H., Lan, J. H., Liu, B., Sheng, E. G., and Yeager, K. M. (2013). Modern carbon burial in lake qinghai, China. *Appl. Geochem.* 39, 150–155. doi: 10.1016/j.apgeochem.2013.04.004

Yu, Z. T., Wang, X. J., Zhao, C. Y., and Lan, H. Y. (2015). Carbon burial in Bosten Lake over the past century: impacts of climate change and human activity. *Chem. Geol.* 419, 132–141. doi: 10.1016/j.chemgeo.2015.10.037

Zhang, C. J., Sun, B. N., and Cui, Y. L. (2001). Thermolysis production of lake carbonatite organic matter and its carbon isotope composition characteristic. *J. Lanzhou Univer.* 37, 87–92.

Zhang, F. J., Xue, B., Yao, S. C., and Gui, Z. F. (2013). The organic carbon burial rates in Chinese lake sediments during Holocene Megathermal. *Quat. Sci.* 33, 401–402.

Zhang, F. J., Xue, B., Yao, S. C., and Gui, Z. F. (2018). Organic carbon burial from multi-core records in Hulun lake, the largest lake in northern China. *Quatern. Int.* 475, 80–90. doi: 10.1016/j.quaint.2017.12.005

Zhang, W. L., Yan, M. D., Fang, X. M., Zhang, D. W., Zhang, T., Zan, J. B., et al. (2019). High-resolution paleomagnetic constraint on the oldest hominoid- fossilbearing sequence in the Xiaolongtan Basin, southeast margin of the Tibetan Plateau and its geologic implications. *Global Planet. Change* 182:103001. doi: 10.1016/j.gloplacha.2019.103001

Zhang, Z. H., Zhao, M. X., Eglinton, G., Lu, H. Y., and Huang, C. Y. (2006). Leaf wax lipids as paleovegetational and paleoenvironmental proxies for the Chinese loess Plateauover the last 170 kyr. *Quat. Sci. Rev.* 25, 575–594. doi: 10.1016/j.quascirev.2005.03.009

Zheng, Y. H., Zhou, W. J., Meyers, P. A., and Xie, S. C. (2007). Lipid biomarkers in the Zoigê-Hongyuan peat deposit: indicators of holocene climate changes in West China. *Org. Geochem.* 38, 1927–1940. doi: 10.1016/j.orggeochem.2007.06.012

Zhong, N. N., Lu, S. F., Huang, Z. L., Zhang, Y. S., Xue, H. T., and Pan, C. C. (2004). Evolution of TOC of source rocks during the hydrocarbon generation process and its controlling factors. *Sci. China Earth Sci.* 34, 120–126.

Conflict of Interest: The authors declare that the research was conducted in the absence of any commercial or financial relationships that could be construed as a potential conflict of interest.

Copyright © 2021 Wang, Wang, Wei, Sun, He and Ma. This is an open-access article distributed under the terms of the Creative Commons Attribution License (CC BY). The use, distribution or reproduction in other forums is permitted, provided the original author(s) and the copyright owner(s) are credited and that the original publication in this journal is cited, in accordance with accepted academic practice. No use, distribution or reproduction is permitted which does not comply with these terms.

frontiers in Earth Science

ORIGINAL RESEARCH
published: 30 April 2021
doi: 10.3389/feart.2021.629241

Radioactive Thoron ^{220}Rn Exhalation From Unfired Mud Building Material Into Room Air of Earthen Dwellings

Nguyệt Thị Ánh Nguyễn[1†], Dương Nguyễn-Thùy[1†], Hướng Nguyễn-Văn[1†], Nam Nguyễn-Hải[1†] and Arndt Schimmelmann[2†]*

[1] Faculty of Geology, University of Science, Vietnam National University, Hanoi, Hanoi, Vietnam, [2] Department of Earth and Atmospheric Sciences, Indiana University Bloomington, Bloomington, IN, United States

Thoron (^{220}Rn), an isotope of radon with a strong α-decay energy, and its short-lived metallic progeny can pose an elevated lung cancer hazard in room air when unfired-soil derived building materials are used in earthen dwellings. Changes in moisture content and density influencing the thoron exhalation rate from earthen materials into room air were studied in the laboratory with terra rossa from a village on the Đồng Văn Karst Plateau Geopark, Việt Nam, where ethnic minorities construct traditional dwellings with unfired terra rossa walls and floors. Our results show that the thoron exhalation rate from mud surfaces depends on (i) the content of radioactive parental nuclides in mineral components; (ii) the moisture content of mud where ∼5–10 weight % water maximizes the ^{220}Rn exhalation rate; and (iii) the density of dry mud as primarily controlled by internal macroscopic voids, fractures, and porosity. Additional time-series of ^{220}Rn exhalation data from an interior mud wall of a terra rossa-built house under different seasonal and weather conditions show that the temperature is influencing thoron exhalation *via* the water vapor pressure deficit (VPD) in air and the associated amount of atmospheric moisture adsorbed onto indoor mud surfaces. Our data suggest that occupants of "mud house" earthen dwellings in northern Việt Nam are exposed to an increased thoron geohazard during cooler weather, low VPD, and high relative humidity in air. Detailed studies are needed to evaluate the thoron geohazard for inhabitants of mud-built dwellings in other climates and geological terrains.

Keywords: earthen dwelling, inhalation hazard, radioactivity, mud house, radon isotope, room air, soil brick, thoron

OPEN ACCESS

Edited by:
Francesco Italiano, National Institute of Geophysics and Volcanology, Section of Palermo, Italy

Reviewed by:
Rakesh C. Ramola, Hemwati Nandan Bahuguna Garhwal University, India
Giovanni Martinelli, National Institute of Geophysics and Volcanology, Section of Palermo, Italy

****Correspondence:***
Hướng Nguyễn-Văn
huongtectonics@vnu.edu.vn

†ORCID:
Nguyệt Thị Ánh Nguyễn
orcid.org/0000-0002-3627-1692
Dương Nguyễn-Thùy
orcid.org/0000-0001-8899-6233
Hướng Nguyễn-Văn
orcid.org/0000-0003-1523-5921
Nam Nguyễn-Hải
orcid.org/0000-0002-1705-0106
Arndt Schimmelmann
orcid.org/0000-0003-4648-5253

Specialty section:
This article was submitted to Geochemistry, a section of the journal Frontiers in Earth Science

Received: *13 November 2020*
Accepted: *16 March 2021*
Published: *30 April 2021*

Citation:
Nguyễn NTA, Nguyễn-Thùy D, Nguyễn-Văn H, Nguyễn-Hải N and Schimmelmann A (2021) Radioactive Thoron ^{220}Rn Exhalation From Unfired Mud Building Material Into Room Air of Earthen Dwellings. Front. Earth Sci. 9:629241. doi: 10.3389/feart.2021.629241

INTRODUCTION

Most radioactivity in room air of buildings is typically caused by radon isotopes and their radioactive metallic progeny after exhalation of radon isotopes from building materials, soil, sediment, and rock containing parental radionuclides. Over half of the natural environmental radiation dosage in room air originates from radon-emitting building materials (Meisenberg and Tschiersch, 2010; Cevik et al., 2011; Trevisi et al., 2013). An abundance of studies is available about the radiation geohazard from the radon isotope ^{222}Rn with a comparatively long half-life

of 3.84 days (Samuelsson and Petterson, 1984; Sahoo et al., 2007). In fact, the name of the element radon is often used uncritically and synonymously for the isotope ^{222}Rn (Faheem and Matiullah, 2008; Chen et al., 2010; Sakoda et al., 2010; Hassan et al., 2011; Bavarnegin et al., 2013; Yang et al., 2019), whereas few studies are concerned with the exhalation of the radon isotope ^{220}Rn called thoron with a half-life of only 55.6 s (Tuccimei et al., 2006; Hosoda et al., 2007; Ujić et al., 2008, 2010; Kanse et al., 2013). The relatively short half-life of ^{220}Rn and its limited transport distance *via* diffusion and convection from solid sources into room air often results in the common misconception that thoron exhalation and its radiation geohazard from building materials are negligible. As a consequence, thoron and its progeny have not been considered in official safety thresholds of indoor radiation exposure (Nazaroff and Nero, 1988; Urosević et al., 2008; Meisenberg and Tschiersch, 2010; Ujić et al., 2010). Moreover, thoron is rarely measured individually because the detection of short-lived thoron requires specialized equipment that can discriminate between different α-decay energies, thus often side-lining thoron quantification in radon studies (e.g., Steinhäusler, 1996). In light of the World Health Organization (WHO) (2009) efforts to reduce radiation from radon, proper recognition of the thoron radiation geohazard is important, especially for inhabitants of unfired soil-derived dwellings with significant concentrations of thoron in room air (Meisenberg and Tschiersch, 2011; Meisenberg et al., 2017).

Exhalation rates of radon isotopes from minerals and their subsequent transport into room air depend on the concentration and distribution of parental radionuclides in soil/rock-derived building materials, on the size and shape of grains, porosity, moisture content, temperature, and meteorological conditions (Balek and Beckman, 2005; Hassan et al., 2009; Sakoda et al., 2010, 2011; International Atomic Energy Agency (IAEA), 2013). This study addresses the thoron geohazard from terra rossa that is typically utilized by economically disadvantaged ethnic minorities for the construction of traditional earthen dwellings (i.e., mud houses) in mountainous regions of northern Việt Nam. Such mud houses are constructed by compacting moist, local terra rossa to gradually build up walls (**Figures 1A–C**) with a thickness of ∼60 cm. A typical family of six to eight people, encompassing three generations, lives in a mud house with bare earthen walls and floor. Surveys of indoor air proved that the radiation geohazard of ^{220}Rn substantially exceeds the average environmental background thoron concentration in outdoor air, especially at close distances to earthen walls and floor (Nguyễn-Thùy et al., 2019), while thoron and its progeny account for > 80 % of the combined average effective dose and represent the predominant radioactive inhalation hazard for residents of mud houses (Nguyễn-Văn et al., 2020).

Gypsum-based plaster covering on mud walls and ceramic tiles on floors can provide effective diffusion barriers for radon, yet such modern home improvements are not affordable for most inhabitants of mud houses. Bare earthen walls and floors are able to exchange moisture with ambient room air that is seasonally providing high levels of humidity. The objective of this study is to reproducibly determine and compare the ^{220}Rn exhalation rates from unfired terra rossa building material (i.e., representing typical mud walls in traditional earthen dwellings) under various weather conditions. The results of this study are guiding us toward devising economically affordable and culturally acceptable surface treatment options in mud houses to remediate the thoron geohazard in room air.

MATERIALS AND METHODS

Origin of Mud, and Preparation of Experimental Mud Bricks

Clay-rich terra rossa was collected in December 2016 in the Đồng Văn Karst Plateau Geopark, Hà Giang Province (23°11′ N, 105°03′ E) at a location where villagers traditionally collect material for the construction of their earthen dwellings (i.e., mud houses) (**Figures 1A,D,F**). After removing surface litter, ∼100 kg of moist terra rossa was transferred from a depth interval of ∼20 to ∼100 cm into polyethylene bags and transported to Việt Nam National University (VNU) in Hà Nội where the terra rossa was air-dried for 1 month, powdered, and sieved to a grain size of ∼2 mm to eliminate pebbles, leaves, and roots.

Kilogram aliquots of powdered terra rossa were moistened by addition of 0.2 L of water, kneaded to achieve homogeneity, and manually pressed into a square wooden mold with an interior dimension of 11 × 11 × 7.5 cm to produce 22 standard-sized mud bricks (**Figure 1E**) varying in wet weight from 1.2 to 2.0 kg. The variance was mainly caused by the inclusion of air bubbles when limited pressure was applied by hand during compaction. After their release from the mold, the mud bricks were air-dried for 1 week and re-weighed. Further moisture and volume losses were monitored from first stage measurements on January 9, 2017, until final measurements on December 6, 2017, to document the bricks' surface area, weight, and bulk density. We started with 22 original mud bricks in the first stage, but that number decreased for later stages because some of the original bricks received various surface coverings to evaluate the effect on exhalation of radon isotopes. The water content of mud bricks during the first stage of measurements was determined for ∼2-g brick fragments (i.e., <0.1 wt. % of a total brick) in wt. % *via* their weight loss after 24 h of heating to 105 °C, whereas the moisture contents of bricks during the second and third stages of measurements were determined gravimetrically for whole bricks after prolonged drying at room temperature between measurement stages.

Grain Size

Three randomly chosen samples of collected terra rossa were used for analyses of their grain size distribution. Prior to laser diffraction of wet samples with a Horiba LA 950 Grain Size Analyzer (HORIBA, Ltd., Kyoto, Japan) at VNU, organic matter was removed according to Mikutta et al. (2005). Three milliliters of 6 wt. % aqueous hydrogen peroxide (H_2O_2) was used to treat organic matter in approximately 10 g of terra rossa over 1 h at room temperature, followed by fivefold rinsing with deionized water, centrifugation, and disposal of the supernatant water.



FIGURE 1 | (A) Local mining of terra rossa for the construction of **(B)** Mud houses in the Đồng Văn Karst Plateau Geopark, Hà Giang Province, northern Việt Nam. **(C)** Closeup view of the exterior wall of a mud house. The scale on the left is in cm. **(D)** Collecting terra rossa in Yên Minh District for manufacturing of **(E)** Mud bricks in the laboratory to measure ^{220}Rn exhalation rates. **(F)** The black rectangle on the map of Việt Nam indicates the location of the Yên Minh District where terra rossa was mined for mud houses and mud bricks. Pictures of quarry **(A)** and mud house **(B)** courtesy of Jian Liu, Indiana University.

Metallic Radionuclides in Terra Rossa

The metallic radionuclide occurrence in terra rossa was evaluated by randomly selecting two samples of dried terra rossa from the total collected material. Additional sieving yielded ∼15-g aliquots (equivalent to a volume of ∼10 cm^3) of the 1-mm grain size fractions. After oven-drying at 105 °C for 12 h, the two samples were analyzed for activities of metallic radionuclides ^{226}Ra, ^{232}Th, and ^{40}K at the Analytical Center for Multi-Elemental and Isotope Research, Siberian Branch of the Russian Academy of Sciences, Novosibirsk, Russia (SB, RAS) *via* high-resolution semiconductor γ-spectrometry (Melgunov et al., 2003; Gavshin et al., 2005). Low concentrations of radionuclides required an extended counting time from 12 to 48 h. The accuracy and reproducibility of the analyses were controlled by parallel measurements of Russian National Geological Reference Materials, including samples of SG-1A, SG-3, SG-2, DVG, DVT, ZUK-1, BIL-1, and ST-1A (Govindaraju, 1994). The overall statistical error in the determination due to the random process of decay was < 5 % for all analytical γ lines. Detection limits for ^{226}Ra and ^{232}Th in the measured samples were ∼0.04 Bq, while the limit for ^{40}K was 0.3 Bq.

The combined activity concentrations of radionuclides ^{226}Ra, ^{232}Th, and ^{40}K in terra rossa samples are expressed as the radium equivalent activity (Ra_{eq}) that is calculated *via* the algebraic expression in Eq. 1 (OECD Nuclear Energy Agency (NEA-OECD), 1979; United Nations Scientific Committee on the Effects of Atomic Radiation (UNSCEAR), 1982, 2000; Tufail, 2012):

$$Ra_{eq} = C_{226-Ra} + 1.43C_{232-Th} + 0.077C_{40-K} \quad (1)$$

where Ra_{eq} is the radium equivalent γ-activity (Bq kg^{-1}), and C_{226-Ra}, C_{232-Th}, and C_{40-K} are the activity concentrations of ^{226}Ra, ^{232}Th, and ^{40}K in Bq kg^{-1}, respectively.

Exhalation Rate of ^{220}Rn From Mud Bricks

The thoron exhalation rate from mud bricks was repeatedly measured in 2017 under standard conditions in turbulent air from a chamber (**Figure 2**) in three stages on January 9, January 18, and December 6 with increasing dryness of the mud bricks. A single mud brick was placed into an airtight high-density polyethylene chamber where all brick surfaces were exposed to turbulent air. Forced convection was achieved by a small fan (**Figure 2**). The interior dimension of the chamber measured 28 × 18 × 14 cm with a wall thickness of 2 mm. Air from the chamber rapidly streamed at a flow rate of 1 L min^{-1} in closed-circuit mode through laboratory vinyl tubing, a 1.0-μm air filter, and a SARAD® RTM 2200 α-spectrometer (SARAD GmbH, Dresden, Germany) with an internal membrane pump. The concentration of ^{220}Rn was measured in 10-min intervals for at least 0.5 h. The ^{220}Rn exhalation rate is based on Eq. 2:

$$E_{Tn} = \frac{C_{Tn} V \lambda_{Tn}}{A} \quad (2)$$

where E_{Tn} is the ^{220}Rn exhalation rate (Bq m^{-2} h^{-1}; Tuccimei et al., 2006; Kanse et al., 2013); C_{Tn} is the equilibrium concentration of ^{220}Rn in the air of the chamber (Bq m^{-3}); V is the volume of air surrounding the brick in the chamber (m^3); A is the geometric surface area of the mud brick (m^2); and λ_{Tn} is the ^{220}Rn decay constant (0.0126 s^{-1}).

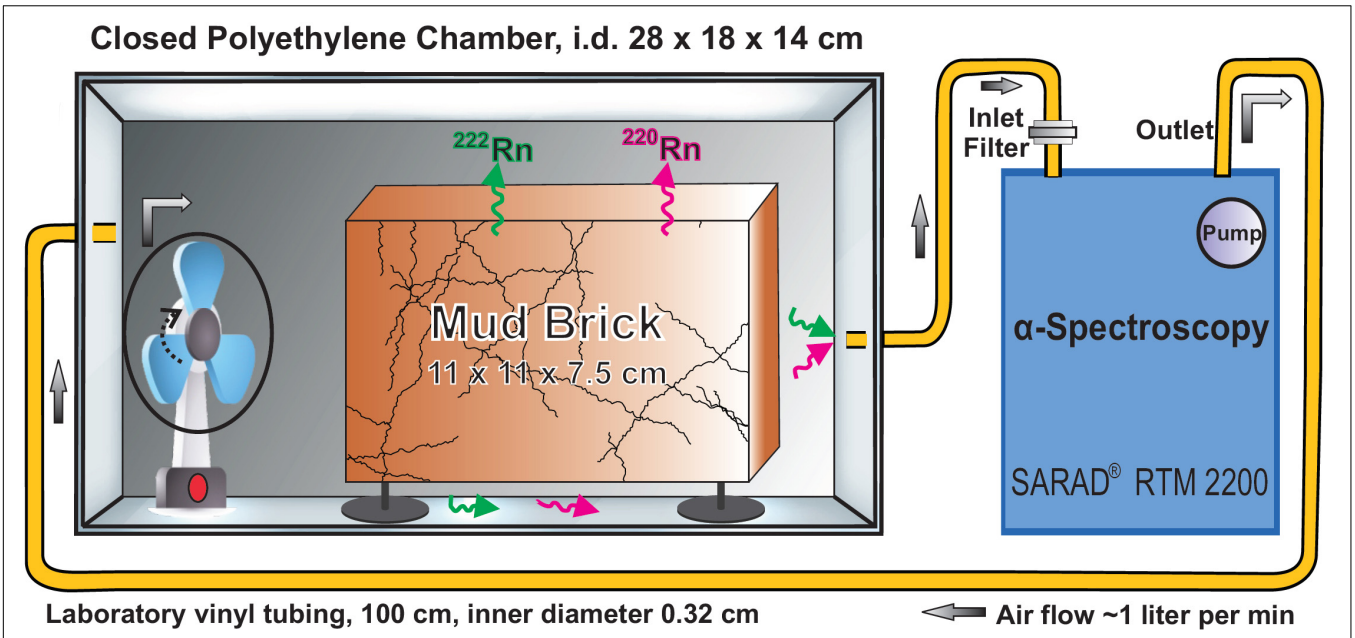


FIGURE 2 | Schematic for the reproducible measurement of ^{220}Rn exhalation rates from mud bricks. A mud brick is placed into a high-density polyethylene chamber exposing all brick surfaces to turbulent air. Air from the chamber rapidly circulates through tubing and an α-spectrometer. Image of fan courtesy of Freepik.

^{220}Rn Exhalation in a Mud House

A full-sized mud house was constructed near Hà Nội (**Figure 3A**) with original moist terra rossa building material from Hà Giang Province, northern Việt Nam, to monitor the long-term ^{220}Rn exhalation from mud walls throughout drying and under changing weather conditions. After completion of the construction in November 2017, a portable SARAD® Thoron Scout (SARAD GmbH, Dresden, Germany) was placed at a distance of 20 cm from an interior mud wall and 50 cm above the mud floor (**Figures 3C–E**). A computer fan drew air from the space between the mud wall and a wooden board through a central hole in the board into a perforated polyethylene enclosure that contained the SARAD® Thoron Scout. Although the Thoron Scout is a passive thoron detection device without an internal pump, the active air flow from an external fan makes its thoron data compatible with those from the SARAD® RTM 2200 with an internal pump (Schimmelmann et al., 2018). Hourly average ^{220}Rn isotope concentrations in room air were automatically logged by the Thoron Scout from November 8, 2017 until January 14, 2018, with a small hiatus in early January. Measurements resumed from June 2 until August 18, 2018.

Meteorological time-series of daily mean air temperature and relative humidity were recorded at the Hà Nội–Nội Bài International Airport ∼40 km north of the mud house location (Weather Underground[1]). A regional precipitation time-series covering the entire 2018 monsoon season in Hà Nội was obtained from Meteoblue®[2]. The water vapor pressure deficit (VPD) corresponds to the difference between the actual amount of water vapor in the air and the theoretical amount of water vapor at 100 % relative humidity. VPD is primarily dependent on temperature, and to a lesser extent on barometric pressure. A higher VPD indicates more intense drying of moist surfaces. To determine the VPD for outdoor air, we first calculated the actual vapor pressure at dew point temperature and the saturation vapor pressure at air temperature using Tetens' formula (Monteith and Unsworth, 2013). Dew point temperature was calculated with coefficients A = 237.3 and B = 17.269 (Weiss, 1977). In addition to ^{220}Rn concentrations, the SARAD® Thoron Scout instrument recorded temperature, barometric pressure, and relative humidity of the air inside the mud house as input for VPD calculation. Outdoor temperature and humidity data next to the mud house near Hà Nội were recorded in 30-min intervals by an Elitech GSP-6 temperature and relative humidity logger (Elitech, London, United Kingdom).

Adsorption of Atmospheric Moisture on Terra Rossa Mud

The initial moisture contents of five terra rossa fragments (∼1.5 g each) of a brick and seven fragments (10–70 g each) from the interior wall of a mud house (**Figure 3A**) were gravimetrically determined *via* weight loss in weight % (wt. %) after heating at 105 °C for 24 h. Three dried fragments from brick and seven dried fragments from the mud wall were placed next to water-soaked sponges in a hermetically closed chamber 40 × 60 × 6 cm, without any direct contact between liquid water and terra rossa samples. The chamber with close to 100 % relative humidity in air was kept at 25 °C in the laboratory. The fragments were re-weighed daily for 14 days to monitor any weight changes owing to adsorption of moisture.

[1]https://www.wunderground.com/
[2]https://www.meteoblue.com

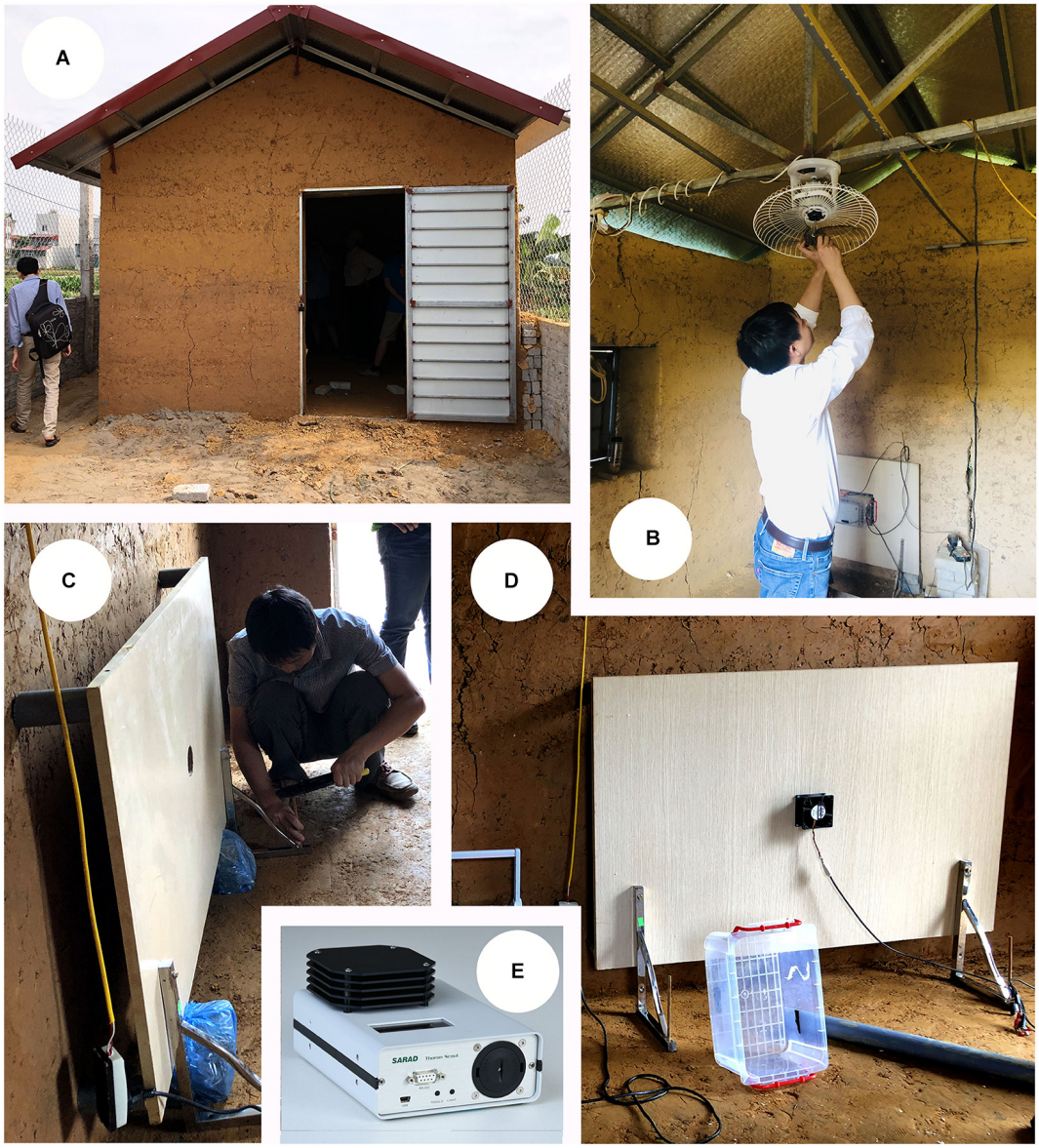


FIGURE 3 | (A) Mud house near Hà Nội that was constructed with terra rossa from Hà Giang Province and was completed in November 2017. **(B)** An oscillatory ceiling fan provides optional turbulence for room air. The background shows the SARAD® Thoron Scout assembly in position ∼50 cm above the floor. **(C)** White board with central hole to draw air from close to the mud wall. **(D)** White board with fan attached. The perforated translucent polyethylene container will house the **(E)** Thoron Scout when attached against the white board.

RESULTS

Physical Properties of Terra Rossa Samples

Terra rossa represents a silty clay loam according to the classification of the U.S. Department of Agriculture (Garcìa-Gaines and Frankenstein, 2015). The sand, silt, and clay size fractions within terra rossa's grain size range from 0.1 to 150 μm are 12.8, 36.9, and 50.2 wt. % on a dry basis, respectively.

The surface area and density of mud bricks were calculated according to measured changes in brick size and weight along slow drying (**Table 1**). The water content of bricks decreased through the three stages of measurements, whereas the bulk density and surface area decreased slightly (**Table 1**).

Adsorption of Atmospheric Moisture on Terra Rossa

Fragments of terra rossa from the interior side of the ∼60-cm thick wall of a mud house near Hà Nội 3 years after its construction (consisting of similar terra rossa as used for the manufacture of mud bricks) averaged 4.2 (±1.1) wt. % moisture. In the 5 days prior to sampling of fragments during October

TABLE 1 | Surface area (cm^2), bulk density (g cm^{-3}), and water content (wt. %) of cuboid-shaped mud bricks after air-drying through three experimental stages, and ^{220}Rn (thoron) concentrations (Conc.) and surface exhalation rates (Surface exh.) of mud bricks in the polyethylene chamber.

Stages of measurements		Parameters of mud bricks			^{220}Rn (thoron)	
		Surface area (cm^2)	Density (g cm^{-3})	Water (wt. %)	Conc. (Bq m^{-3})	Surface exh. (kBq m^{-2} h^{-1})
First stage (January 9, 2017) *n* = 19	Min	519	1.4	20.1	344	1.75
	Max	611	1.9	23.0	1832	9.31
	Aver.	**559**	**1.6**	**21.5**	**1200**	**6.01**
	SD	25.8	0.1	1.0	389	1.88
Second stage (January 18, 2017) *n* = 12	Min	472	1.3	6.3	1288	7.63
	Max	606	1.8	14.3	2419	12.27
	Aver.	**541**	**1.5**	**9.8**	**1964**	**10.01**
	SD	32.8	0.1	2.5	290	1.16
Third stage (December 6, 2017) *n* = 18	Min	472	1.3	0.6	713	4.09
	Max	571	1.7	5.5	1288	6.31
	Aver.	**522**	**1.5**	**2.6**	**970**	**5.30**
	SD	30.7	0.1	1.3	123.3	0.63

The surface area is the sum of the areas of all faces of a brick. Aver., average; SD, standard deviation; n, the number of measured mud bricks.

2020, the outdoor temperature and outdoor relative humidity in the mud house averaged ∼24 °C and ∼75 %, respectively. After exposure of the dried fragments for about 2 weeks to laboratory air at 25 °C and about 100 % relative humidity, the terra rossa samples had gained on average more than 5 wt. % of moisture (**Figure 4**).

Concentrations of ^{226}Ra, ^{232}Th, ^{40}K, and Their Radium Equivalent in Terra Rossa

The concentrations of metal radionuclides ^{226}Ra, ^{232}Th, and ^{40}K in two terra rossa samples DYM and SYM were measured by semiconductor γ-spectrometry (**Table 2**). The two terra rossa samples show similar respective concentrations with averages of 52.0 Bq kg^{-1} for ^{226}Ra, 68.5 (±2.1) Bq kg^{-1} for ^{232}Th, and 259.0 (±1.0) Bq kg^{-1} for ^{40}K.

^{220}Rn Exhalation Rate From Experimental Mud Bricks

Measured concentrations of ^{220}Rn in chamber air surrounding mud bricks and calculated ^{220}Rn exhalation rates (**Table 1**) encompassed large ranges during the first stage of measurements when bricks still contained ≥ 20 wt. % moisture. Values became more stable in the second and third stages (**Figure 5**). Maximum ^{220}Rn exhalation rates were observed during the second stage with a mean value of 10.01 (±1.16) kBq m^{-2} h^{-1} in comparison to the first stage at 6.01 (±1.88) kBq m^{-2} h^{-1} and the third stage at 5.30 (±0.63) kBq m^{-2} h^{-1}.

^{220}Rn Exhalation Rate From Interior Mud Wall in Mud House

Time-series of the ^{220}Rn concentration in air close to the inside wall of a mud house near Hà Nội are compared to meteorological time-series of outdoor Hà Nội air in **Figure 6**. The ^{220}Rn concentration started low in November of 2017 when the ∼60-cm thick mud walls were still glistening wet from recent construction. Over the following months, the mud walls gradually dried and the ^{220}Rn exhalation increased until June of 2018. Drying was most intense by the end of June when high summer temperatures increased the outdoor air VPD. Continued drying during falling temperatures in the later part of the monsoon season witnessed decreasing ^{220}Rn concentrations.

A 9-day time-series of ^{220}Rn concentration in indoor air of the mud house near Hà Nội with ventilation controlled by an optional oscillating ceiling fan (**Figure 3B**) in October 2020 is represented in **Figure 7** together with temperature and VPD of indoor and outdoor air. The large variability of hourly mean ^{220}Rn concentrations suggests dramatic changes in air flow and air residence time between the white board and the mud wall in the single-room mud house (**Figures 3B–D**). No discernible correlation with temperature or VPD is apparent over the 9 days of measurements when the moisture content of the thick mud wall was essentially constant. Air turbulence introduced in the first part of the time-series by the oscillatory fan limited the thoron concentration in air that was admitted to the Thoron Scout by the computer fan blowing air from behind the white wall into the perforated polyethylene enclosure. Turning the ceiling fan off during the fifth day of measurements almost doubled the average thoron concentration in the polyethylene enclosure from 202 to 382 Bq m^{-3} (**Figure 7**).

DISCUSSION

Sources of Radioactivity in Terra Rossa

Radioactive nuclides like ^{238}U of uranium, ^{226}Ra of radium, ^{232}Th of thorium, and ^{40}K of potassium occur naturally in bedrock and soils, as well as in mineral-containing construction materials. While ^{222}Rn is a product from the decay of ^{238}U *via* ^{226}Ra, ^{220}Rn (thoron) is produced along the ^{232}Th decay chain. The measured concentrations for ^{226}Ra (mean value of 52 Bq kg^{-1}) and ^{232}Th (mean value of 68.5 Bq kg^{-1}) in terra

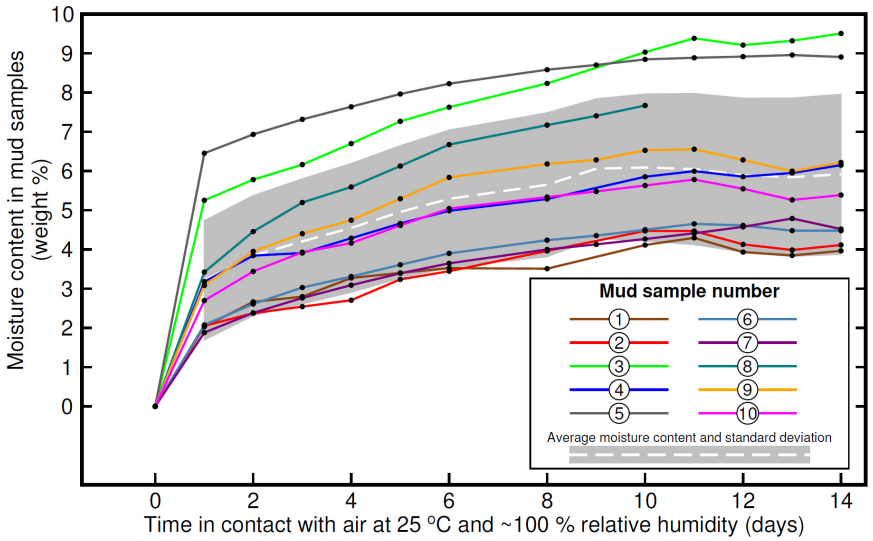


FIGURE 4 | Time-series of adsorption of water to pre-dried (at 105 °C) mud fragments from the inner wall of a mud house while exposed to air with ~100 % relative humidity at 25 °C. The running average and its standard deviation are shown by a white dashed line and a gray band, respectively.

rossa samples are above their corresponding worldwide average concentrations in natural soils (i.e., 35 Bq kg^{-1} for ^{226}Ra and 30 Bq kg^{-1} for ^{232}Th), whereas the concentrations of ^{40}K in terra rossa samples fall below the worldwide average concentration of 400 Bq kg^{-1} for ^{40}K in soils (United Nations Scientific Committee on the Effects of Atomic Radiation (UNSCEAR), 1982, 2000). Elevated activities of ^{226}Ra and ^{232}Th in terra rossa foster the exhalation of radon isotopes from exposed mud surfaces into indoor air.

The radiological hazard from ^{226}Ra, ^{232}Th, and ^{40}K activities in terra rossa was calculated *via* the radium equivalent activity, Ra_{eq} (OECD Nuclear Energy Agency (NEA-OECD), 1979; United Nations Scientific Committee on the Effects of Atomic Radiation (UNSCEAR), 1982, 2000). The calculated average radium equivalent activity of the two terra rossa samples DYM and SYM of 169.9 (±3.1) Bq kg^{-1} is lower than the criterion limit of 370 Bq kg^{-1} (OECD Nuclear Energy Agency (NEA-OECD), 1979; Ravisankar et al., 2014), which makes an annual dose of 1.5 mGy equal to the maximum permissible annual effective dose of 1 mSv for the general public as recommended by the International Commission on Radiological Protection (ICRP) (1991).

With regard to Ra_{eq} alone, terra rossa would be a safe building material for mud houses in the studied area. However, it would be misleading to only take γ-radiation into account and ignore α-radiation. Thoron is an intermittent nuclide along the thorium decay chain, which originates from primordial ^{232}Th. Thoron's transport distance in indoor air is limited owing to the short half-life of 55.6 s. As a consequence, thoron's spatial distribution in room air is inhomogeneous (Meisenberg and Tschiersch, 2011). Building materials are recognized as one of the main sources of radon isotopes in indoor air. The concentration of thoron in indoor air declines with increasing distance from mud walls and floors toward the center of the room. High concentrations of α-emitting thoron and progenies in indoor air of mud houses in the center of rooms (> 100 Bq m^{-3}) and especially near bare mud walls (> 350 Bq m^{-3}) are responsible for > 80 % of the average effective dosage affecting inhabitants (Nguyễn-Thùy et al., 2019; Nguyễn-Văn et al., 2020). Severely elevated concentrations of thoron up to 1500 Bq m^{-3} close to bare mud walls of traditional dwellings were also found in China (Shang et al., 2008) and in an experimental room constructed with unfired mud bricks in a laboratory at the Helmholtz Zentrum in Munich, Germany (Meisenberg and Tschiersch, 2011), although in both cases ^{232}Th in the mud building material only produced γ-radiation with an average activity concentration of 40–50 Bq kg^{-1}. Thoron concentrations in room air adjacent to surfaces of unfired mud are directly linked to the content of ^{232}Th in the building material. Thus, the combined α- and γ-radiation geohazards of the studied terra rossa call into question the safety of unfired terra rossa as a building material.

TABLE 2 | Activity concentrations of ^{226}Ra, ^{232}Th, and ^{40}K (Bq kg^{-1}) together with their radium equivalent activity (Ra_{eq}, Bq kg^{-1}) in two terra rossa samples.

Terra rossa sample	Activity concentration (Bq kg^{-1})			Ra_{eq} (Bq kg^{-1})
	^{226}Ra	^{232}Th	^{40}K	
DYM	52	70	260	172.1
SYM	52	67	258	167.7

Influence of Terra Rossa Bulk Density

The bulk density of experimental mud bricks was primarily influenced by the inclusion of air bubbles when pressing wet terra rossa into a mold to shape bricks, and later decreased *via* drying as water in pore spaces was replaced by air (**Table 1**). During the first stage of measurements, when the

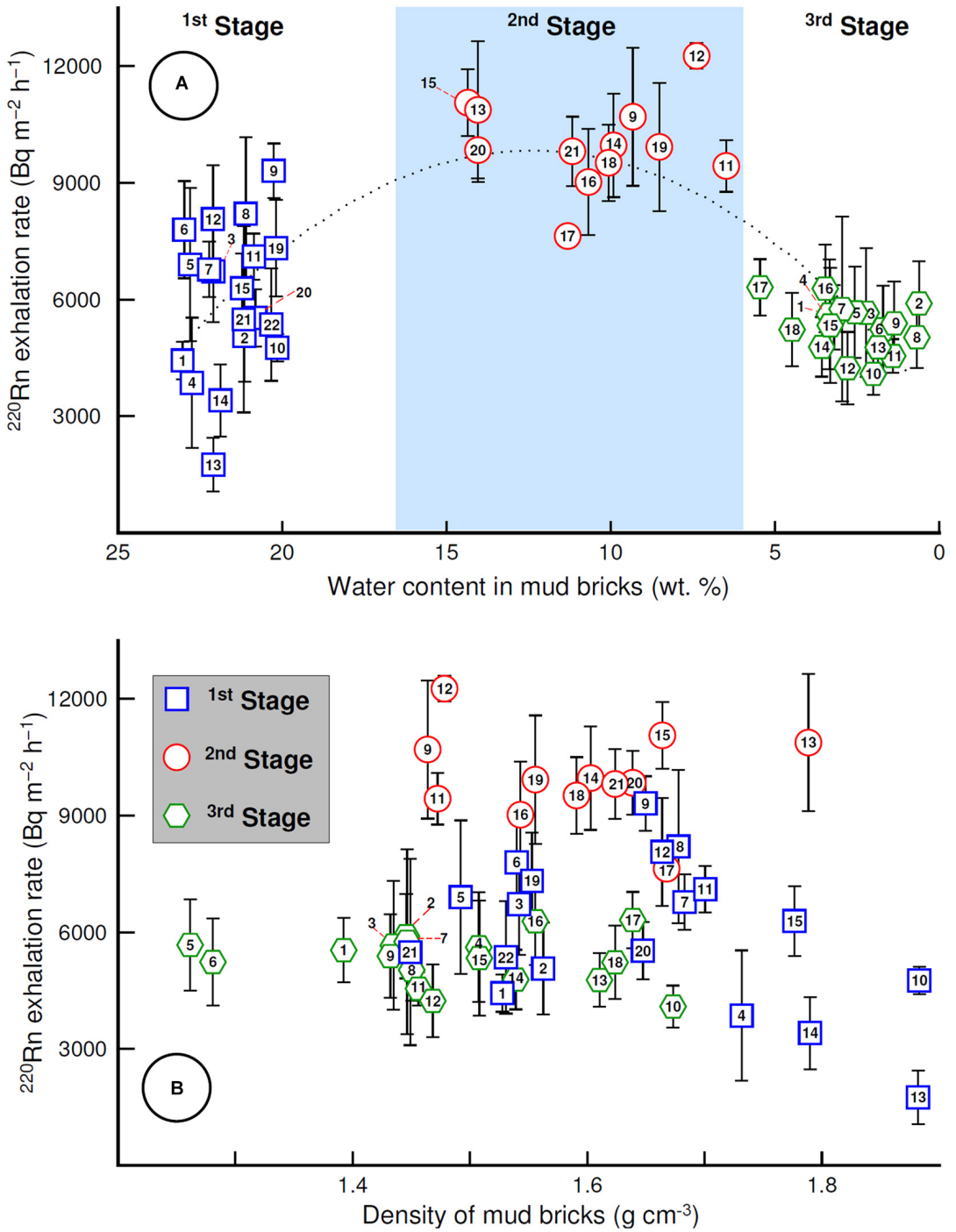


FIGURE 5 | (A) ^{220}Rn exhalation rates from mud bricks (numbered from 1 to 22) with different moisture contents along three consecutive measurement stages (on January 9, January 18, and December 6, 2017) along slow drying. The dotted line was drawn to guide the eye. **(B)** ^{220}Rn exhalation rates from mud bricks *versus* bulk density. Not all bricks were measured during all stages of measurements.

mud bricks were still relatively wet with $\geq$ 20 wt. % water, the high bulk density from 1.5 to 1.9 g cm^{-3} primarily meant fewer air-filled bubbles and partially water-filled pores in the bricks. Scarcity of air-filled passages to outside air slowed the diffusion and suppressed the exhalation of ^{220}Rn. High bulk density in the presence of liquid water decreased the exhalation rate of ^{220}Rn because radon atoms recoiling out of the mineral grains were predominantly retained in water-filled pore space (Rogers and Nielson, 1991; Faheem and Matiullah, 2008) (**Figure 5B**).

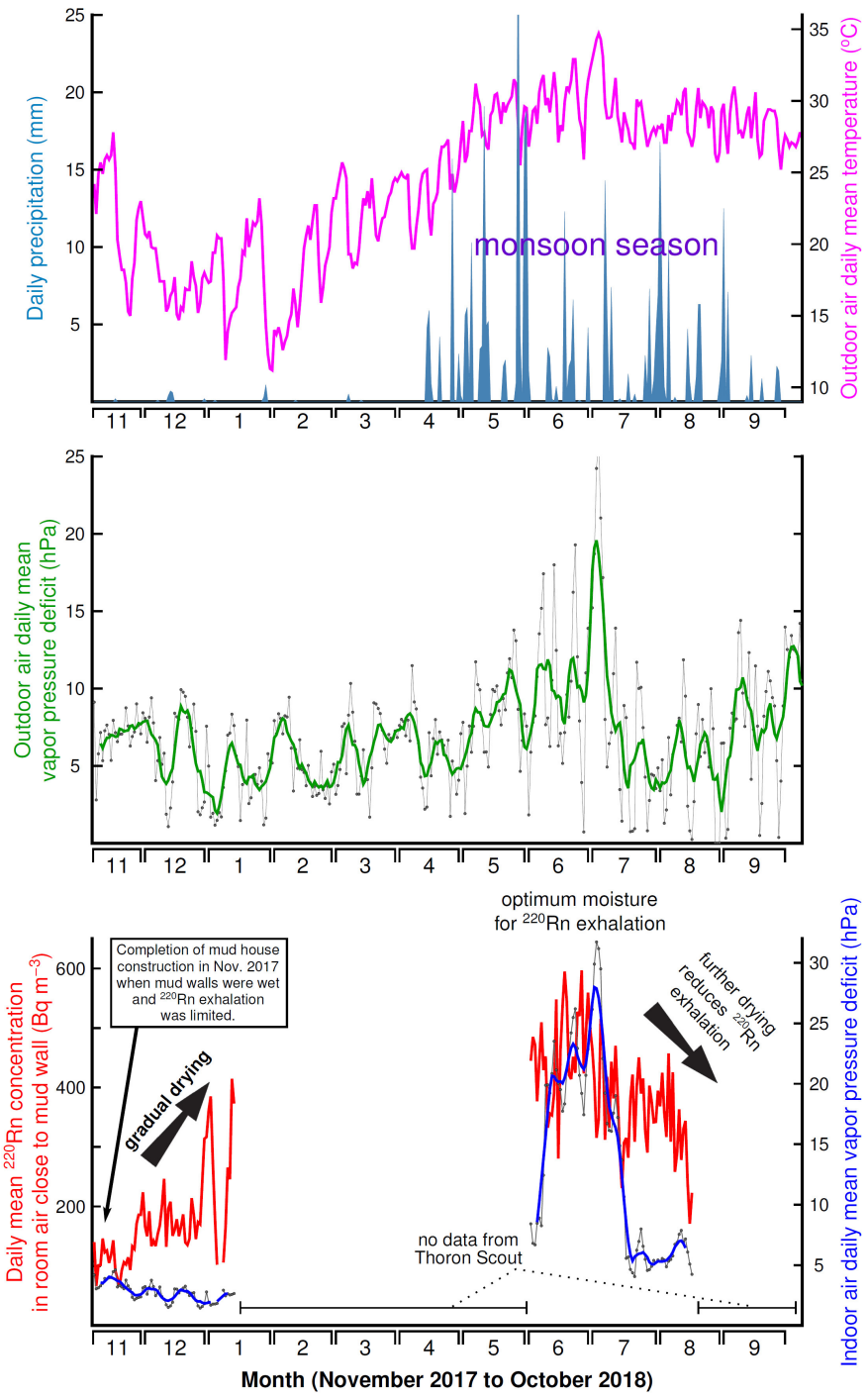


FIGURE 6 | Time-series of daily averages of ^{220}Rn concentration in room air of a mud house near Hà Nội based on measurements with a SARAD® Thoron Scout, in comparison with meteorological time-series of Hà Nội outdoor air (measured at Hà Nội–Nội Bài International Airport) and mud house indoor air (measured by Thoron Scout).

Shrinkage of drying mud bricks caused the formation of open cracks that likely connected internal voids in the bricks to outside air. During the second stage of measurements with reduced moisture content, the strongly turbulent air in the chamber also forced convection and air flow into macroscopic cracks, and thus assisted in the exhalation of ^{220}Rn (**Figure 5B**). During the third stage of measurements with low moisture contents of < 5 wt. %, the bulk density had strongly decreased in comparison with the first and second stages (**Table 1**). The decreased moisture content in

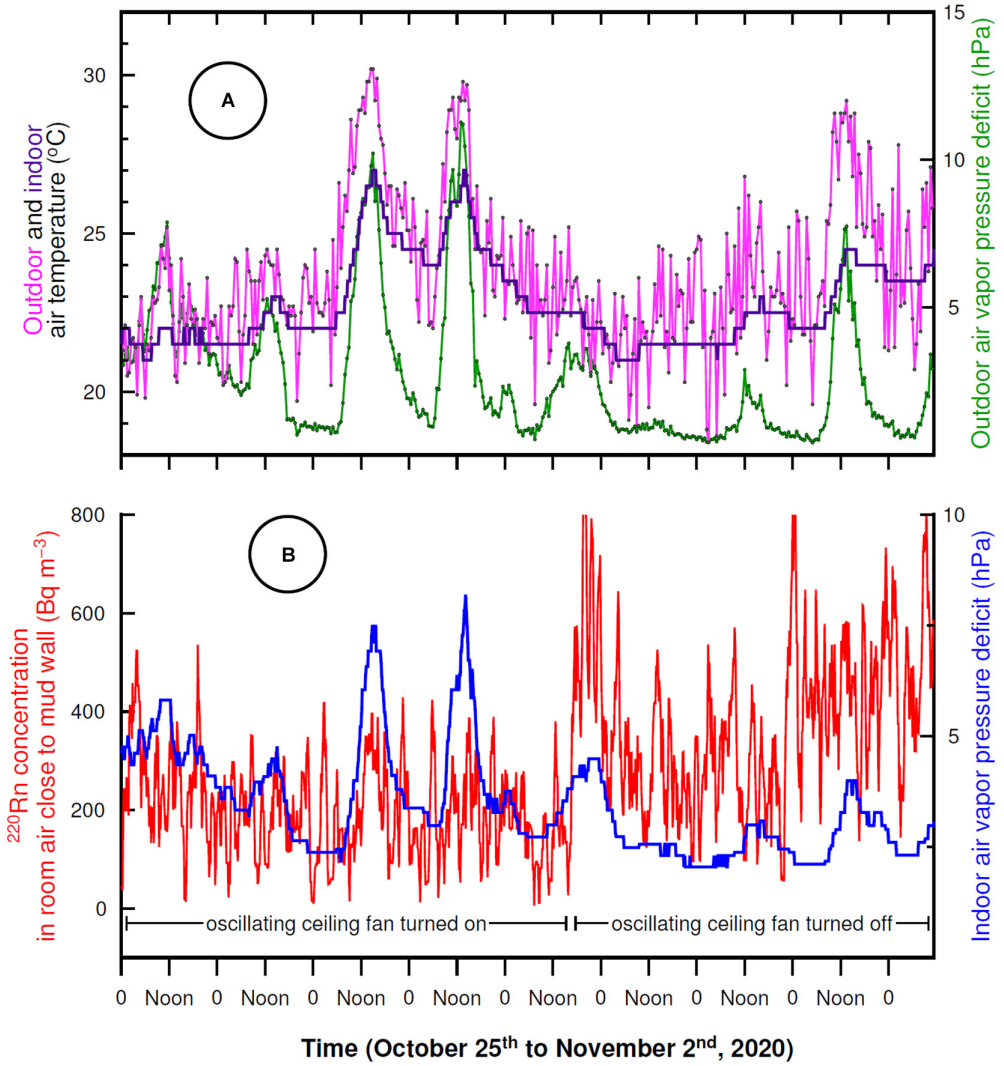


FIGURE 7 | Time-series from a mud house near Hà Nội over 9 days documenting hourly moving average values of **(A)** outdoor and indoor air temperatures, water vapor pressure deficit (VPD) in outdoor air and **(B)** indoor VPD, and ^{220}Rn concentrations in room air near the surface of a mud wall (**Figure 3**) based on data recorded in 10-min intervals by a SARAD® Thoron Scout in October 2020.

mud bricks filled pore spaces and cracks almost completely with air and provided diffusion pathways for radon (Faheem and Matiullah, 2008), but fewer recoiling ^{220}Rn atoms slowed down enough to remain in open pore space and become available for exhalation.

The Role of Residual Moisture for Thoron Exhalation From Terra Rossa

Our results from progressive drying of mud bricks across three stages of measurements emphasize the importance of moisture content (**Figure 5A** and **Table 1**) and indicate highest ^{220}Rn exhalation rates of up to 12.27 kBq m^{-2} h^{-1} with a mean of 10.01 (±1.16) kBq m^{-2} h^{-1} during the second stage at an intermediate moisture content of 9.8 (±2.5) wt. %. The observed residual moisture content in mud bricks during the second stage falls into the range of typical values of 8–13 wt. % moisture in soil that was reported to maximize radon exhalation (Hosoda et al., 2007; Faheem and Matiullah, 2008; Yang et al., 2019).

The principle of maximized exhalation of ^{220}Rn from mud surfaces with an intermediate moisture content of between 5 and 10 wt. % was confirmed by time-series of measurements in the room of a research mud house near Hà Nội (**Figure 6**) where the mean moisture content on the inside of the ∼60-cm thick wall of the mud house was still 4.2 (±1.1) wt. % almost 3 years after construction, at the tail end of the summer monsoon season in mid-October of 2020. Laboratory experiments with fragments of terra rossa samples from the interior wall of the mud house indicated a weight gain commensurate with a moisture content between ∼4 and ∼9 wt. % upon prolonged exposure to air with high humidity (**Figure 4**). A dry interior wall or mud floor of a mud house will adsorb moisture from the air

until it reaches a dynamic equilibrium between adsorption and drying. The ∼60 cm thick walls of traditional mud houses can store a substantial amount of moisture that acts as a reservoir and not only prevents rapid drying over hours to days, but also buffers against fast accumulation of adsorbed moisture close to interior mud surfaces on days when the relative humidity in air is high and the water VPD is low. In effect, diurnal and short-term weather changes cannot rapidly affect the thoron exhalation from interior mud surfaces (**Figure 7**). However, longer-term to seasonal changes in VPD significantly influence the residual moisture in terra rossa and the thoron exhalation.

Practical Considerations for Mud House Inhabitants

The moisture loading in northern Việt Nam's (sub)tropical ambient air is highly variable throughout the year, which is mostly due to the large temperature difference between summer and winter (**Figure 6**). The temperature range across seasons at higher altitude in Hà Giang Province is even larger than in Hà Nội. Low temperatures in mountainous Hà Giang Province combined with low clouds, fog, and high relative humidity in winter decrease VPD in air, increase adsorption of moisture into exposed mud to possibly reach ∼10 wt. %, and temporarily increase the exhalation of radon isotopes from mud into indoor air of mud houses. Occupied mud houses traditionally use open wood fires for cooking and have no chimney. Over time, ash from cooking fires, fingerprints, animal droppings, and aerosols may deposit hygroscopic salts on interior mud surfaces increasing the potential for adsorption of moisture and enhanced ^{220}Rn exhalation.

Paradoxically, although the moisture loading in air is higher during the warm summer monsoon months, the higher summer temperatures greatly increase VPD, which dries mud surfaces inside of mud houses and limits the exhalation of ^{220}Rn from mud into room air (**Figure 6**). The observed high concentrations of ^{220}Rn in the mud house in June can be explained by residual moisture that derived from the compaction of wet terra rossa earlier in November 2017 (**Figure 6**) when the house was newly constructed.

Forced turbulence of room air in a mud house by an oscillating ceiling fan reduced the residence time of ^{210}Rn-laden air close to mud surfaces, mixed the air from near walls and floors with overall room air on the order of seconds, and thus effectively diluted the ^{210}Rn near mud surfaces (**Figure 7**). Without forced turbulence, the air flow close to mud surfaces tends to be laminar and better retains exhaled ^{220}Rn near mud surfaces. The large short-term variability of ^{210}Rn concentrations near a mud wall that was observed regardless of forced turbulence may be due to the convective flow of room air as influenced by meteorological parameters, such as temperature gradients between mud surfaces and outdoor and/or indoor air, as well as wind forcing air through cracks into the room. Forced turbulence of room air by electrical fans is not useful for remediation of the thoron geohazard in room air because (i) it merely dilutes thoron in air near mud surfaces with overall room air and (ii) it does not diminish the health hazard from inhaling metallic radioactive progeny of radon isotopes from room air. Exhalation of radon isotopes from porous earthen substrates can only be stopped by impermeable surface treatments that need to be economically and socially acceptable. Additional research is needed for different types of earthen dwellings in different climates to devise suitable mitigation strategies.

CONCLUSION

Thoron exhalation rates from terra rossa bricks with different densities and moisture contents in conjunction with concentrations of prominent γ-emitting radionuclides call into question the radiological safety of terra rossa and possibly other unfired earthen materials for uses as building material. The average ^{226}Ra and ^{232}Th activities of the studied terra rossa samples are 52.0 and 68.5 Bq kg^{-1}, respectively, which are above the average values of 35 Bq kg^{-1} for ^{226}Ra and 30 Bq kg^{-1} for ^{232}Th in average soil around the world (United Nations Scientific Committee on the Effects of Atomic Radiation (UNSCEAR), 1982, 2000). The relatively high activities of ^{226}Ra and ^{232}Th radionuclides in terra rossa explain the significant exhalation of radon from terra rossa and the associated α-radiation health hazard in indoor air when terra rossa is used for the construction of earthen dwellings. Exhalation of radon isotopes from interior mud walls and mud floors into room air of mud houses is controlled by multiple characteristics of earthen materials and meteorological parameters, i.e., the mineralogical composition of mud, residual moisture, porosity, permeability, temperature, and water VPD in room air. Especially the moisture content of terra rossa mud is strongly affecting ^{220}Rn exhalation rates. Starting from a low exhalation rate in waterlogged terra rossa from northern Việt Nam, subsequent drying gradually increases the ^{220}Rn exhalation rate until peaking at ∼10 kBq m^{-2} h^{-1} at an intermediate moisture content of ∼5–10 wt. %, followed by a decline of the exhalation rate toward dryer mud surfaces. Lowered density and associated macroporosity as a result of cracks in drying bricks effectively add surface area for exhalation and increase the thoron exhalation rate. Seasonal variations of temperature and moisture content in ambient air influence the VPD of air and the potential of mud surfaces to adsorb/desorb moisture. Adsorption of moisture into interior mud walls and floors from air at lower temperature and higher relative humidity can temporarily increase the thoron exhalation rate. The present knowledge of the physical and meteorological parameters affecting the exposure of inhabitants of earthen buildings in northern Việt Nam to radiation makes it unlikely that mud houses can be structurally modified to eliminate the radiation geohazard. Our ongoing efforts focus on affordable treatment of mud surfaces to at least limit the transport of exhaled ^{220}Rn from mud walls into room air.

DATA AVAILABILITY STATEMENT

The raw data supporting the conclusions of this article will be made available by the authors, without undue reservation.

AUTHOR CONTRIBUTIONS

NN: investigation, design of the study, data curation, and writing. DN-T and HN-V: conceptualization, investigation, design of the study, data curation, writing, review, and editing. NN-H: data curation and writing. AS: conceptualization, investigation, design of the study, writing, review, and editing. All authors contributed to the article and approved the submitted version.

FUNDING

This work was funded by Vingroup Joint Stock Company and supported by the Domestic Master/Ph.D. Scholarship Program of Vingroup Innovation Foundation (VINIF), Vingroup Big Data Institute (VINBIGDATA) grant number VINIF.2020.TS.64 (NN). This contribution received support from the Indiana University Open Access Article Publishing Fund. Measurements with the SARAD® RTM 2200 in Vietnam were made possible by the U.S. Department of Energy, Office of Science, Office of Basic Energy Sciences, Chemical Sciences, Geosciences, and Biosciences Division under Award Number DE-SC0006978.

ACKNOWLEDGMENTS

We are grateful to M. S. Melgunov, Director of the Analytical Center for Multi-Elemental and Isotope Research SB RAS, for analyzing the natural γ-radiation of radionuclides in terra rossa. Nùng Văn Minh collected terra rossa samples. Jian Liu from Indiana University contributed images from field work. Minh Ngọc Schimmelmann served as a cultural liaison and facilitated logistics of research. We thank the reviewers for their constructive comments and suggestions.

REFERENCES

Balek, V., and Beckman, I. N. (2005). Theory of emanation thermal analysis XII. Modelling of radon diffusion release from disordered solids on heating. *J. Therm. Anal. Calorim.* 82, 755–759. doi: 10.1007/s10973-005-0960-7

Bavarnegin, E., Fathabadi, N., Moghaddam, M. V., Farahani, M. V., Moradi, M., and Babakhni, A. (2013). Radon exhalation rate and natural radionuclide content in building materials of high background areas of Ramsar, Iran. *J. Environ. Radioact.* 117, 36–40. doi: 10.1016/j.jenvrad.2011.12.022

Cevik, U., Kara, A., Celik, N., Karabidak, M., and Celik, A. (2011). Radon survey and exposure assessment in Karaca and Çal Caves, Turkey. *Water Air Soil Pollut.* 214, 461–469. doi: 10.1007/s11270-010-0437-6

Chen, J., Rahman, N. M., and Atiya, I. A. (2010). Radon exhalation from building materials for decorative use. *J. Environ. Radioact.* 101, 317–322. doi: 10.1016/j.jenvrad.2010.01.005

Faheem, M., and Matiullah, M. (2008). Radon exhalation and its dependence on moisture content from samples of soil and building materials. *Radiat. Meas.* 43, 1458–1462. doi: 10.1016/j.radmeas.2008.02.023

Garcìa-Gaines, R. A., and Frankenstein, S. (2015). *USCS and the USDA Soil Classification System: Development of a Mapping Scheme*. Vicksburg, MS: U.S. Army Engineer Research and Development Center, Cold Regions Research and Engineering Laboratory.

Gavshin, V. M., Melgunov, M. S., Sukhorukov, F. V., Bobrov, V. A., Kalugin, I. A., and Klerkx, J. (2005). Disequilibrium between uranium and its progeny in the lake Issyk-Kul system (Kyrgyzstan) under a combined effect of natural and manmade processes. *J. Environ. Radioact.* 83, 61–74. doi: 10.1016/j.jenvrad.2005.02.012

Govindaraju, K. (1994). Compilation of working values and sample description for 383 geostandards. *Geostand. Newslett.* 18, 1–158. doi: 10.1046/j.1365-2494.1998.53202081.x-i1

Hassan, N. M., Hosoda, M., Ishikawa, T., Sorimachi, A., Sahoo, S. K., Tokonami, S., et al. (2009). Radon migration process and its influence factors; review. *Jpn. J. Health Phys.* 44, 218–231. doi: 10.5453/jhps.44.218

Hassan, N. M., Ishikawa, T., Hosoda, M., Iwaoka, K., Sorimachi, A., Sahoo, S. K., et al. (2011). The effect of water content on the radon emanation coefficient for some building materials used in Japan. *Radiat. Meas.* 46, 232–237. doi: 10.1016/j.radmeas.2010.11.006

Hosoda, M., Shimo, M., Sugino, M., Furukawa, M., and Fukushi, M. (2007). Effect of soil moisture content on radon and thoron exhalation. *J. Nucl. Sci. Technol.* 44, 664–672. doi: 10.1080/18811248.2007.9711855

International Atomic Energy Agency (IAEA) (2013). *Measurement and Calculation of Radon Releases from NORM Residues.* Technical Reports Series No. 474. Vienna: International Atomic Energy Agency (IAEA).

International Commission on Radiological Protection (ICRP) (1991). *1990 Recommendations of the International Commission on Radiological Protection*, Vol. 21. Stockholm: International Commission on Radiological Protection.

Kanse, S. D., Sahoo, B. K., Sapra, B. K., Gawarea, J. J., and Mayya, Y. S. (2013). Powder sandwich technique: a novel method for determining the thoron emanation potential of powders bearing high ^{224}Ra content. *Radiat. Meas.* 48, 82–87. doi: 10.1016/j.radmeas.2012.10.014

Meisenberg, O., Mishra, R., Joshi, M., Gierl, S., Rout, R., Guo, L., et al. (2017). Radon and thoron inhalation doses in dwellings with earthen architecture: comparison of measurement methods. *Sci. Total Environ.* 579, 1855–1862. doi: 10.1016/j.scitotenv.2016.11.170

Meisenberg, O., and Tschiersch, J. (2010). Specific properties of a model of thoron and its decay products in indoor atmospheres. *Nukleonika* 55, 463–469.

Meisenberg, O., and Tschiersch, J. (2011). Thoron in indoor air: modeling for a better exposure estimate. *Indoor Air* 21, 240–252. doi: 10.1111/j.1600-0668.2010.00697.x

Melgunov, M. S., Gavshin, V. M., Sukhorukov, F. V., Kalugin, I. A., Bobrov, V. A., and Klerkx, J. (2003). Anomalies of radioactivity on the southern bank of the Ysyk-Köl Lake (Kyrgyzstan). *Chem. Sustain. Dev.* 11, 859–870.

Mikutta, R., Kleber, M., Kaiser, K., and Jahn, R. (2005). Review: organic matter removal from soils using hydrogen peroxide, sodium hypochlorite, and disodium peroxodisulfate. *Soil Sci. Soc. Am. J.* 69, 120–135. doi: 10.2136/sssaj2005.0120

Monteith, J., and Unsworth, M. (2013). "Chapter 17 – Micrometeorology: (ii) interpretation of flux measurements," in *Principles of Environmental Physics*, eds J. Monteith, and M. Unsworth (Amsterdam: Academic Press), 321–349. doi: 10.1016/B978-0-12-386910-4.00017-2

Nazaroff, W. W., and Nero, A. V. J. (eds) (1988). "Radon and its decay products in indoor air," in *Environmental Science and Technology: A Wiley-Interscience Series of Texts and Monographs*, (New York, NY: John Wiley and Sons, Inc). Available online at: https://www.amazon.com/Products-Indoor-Environmental-Science-Technology/dp/0471628107

Nguyễn-Thùy, D., Nguyễn-Văn, H., Schimmelmann, J. P., Nguyễn, T. A. N., Doiron, K., and Schimmelmann, A. (2019). ^{220}Rn (thoron) geohazard in room air of earthen dwellings in Vietnam. *Geofluids* 4, 1–11. doi: 10.1155/2019/7202616

Nguyễn-Văn, H., Nguyễn-Thùy, D., Nguyễn, N. T. A., Streil, T., Schimmelmann, J., Doiron, K., et al. (2020). Excessive radon-based radiation in indoor air caused by soil building materials in traditional homes on Đồng Văn karst plateau, northern Vietnam. *Chemosphere* 257:127119. doi: 10.1016/j.chemosphere.2020.127119

OECD Nuclear Energy Agency (NEA-OECD) (1979). *Exposure to Radiation from Natural Radioactivity in Building Materials*. Paris: OECD.

Ravisankar, R., Vanasundari, K., Suganya, M., Raghu, Y., Rajalakshmi, A., Chandrasekaran, A., et al. (2014). Multivariate statistical analysis of radiological data of building materials used in Tiruvannamalai, Tamilnadu, India. *Appl. Radiat. Isot.* 85, 114–127. doi: 10.1016/j.apradiso.2013.12.005

Rogers, V. C., and Nielson, K. K. (1991). Multiphase radon generation and transport in porous materials. *Health Phys.* 60, 807–815. doi: 10.1097/00004032-199106000-00006

Sahoo, B. K., Nathwani, D., Eappen, K. P., Ramachandran, T. V., Gaware, J. J., and Mayya, Y. S. (2007). Estimation of radon emanation factor in Indian building materials. *Radiat. Meas.* 42, 1422–1425. doi: 10.1016/j.radmeas.2007.04.002

Sakoda, A., Ishimori, Y., Hanamoto, K., Kataoka, T., Kawabe, A., and Yamaoka, K. (2010). Experimental and modeling studies of grain size and moisture content effects on radon emanation. *Radiat. Meas.* 45, 204–210. doi: 10.1016/j.radmeas.2010.01.010

Sakoda, A., Ishimori, Y., and Yamaoka, K. (2011). A comprehensive review of radon emanation measurements for mineral, rock, soil, mill tailing and fly ash. *Appl. Radiat. Isot.* 69, 1422–1435. doi: 10.1016/j.apradiso.2011.06.009

Samuelsson, C., and Petterson, H. (1984). Exhalation of ^{222}Rn from porous materials. *Radiat. Prot. Dosim.* 7, 95–100. doi: 10.1093/oxfordjournals.rpd.a082971

Schimmelmann, A., Fernandez Cortes, A., Cuezva, S., Streil, T., and Lennon, J. T. (2018). Radiolysis *via* radioactivity is not responsible for rapid methane oxidation in subterranean air. *PLoS One* 13:e0206506. doi: 10.1371/journal.pone.0206506

Shang, B., Tschiersch, J., Cui, H., and Xia, Y. (2008). Radon survey in dwellings of Gansu, China: the influence of thoron and an attempt for correction. *Radiat. Environ. Biophys.* 47, 367–373. doi: 10.1007/s00411-008-0163-2

Steinhäusler, F. (1996). Environmental ^{220}Rn: a review. *Environ. Int.* 22, 1111–1123. doi: 10.1016/S0160-4120(96)00227-9

Trevisi, R., Nuccetelli, C., and Risica, S. (2013). Screening tools to limit the use of building materials with enhanced/elevated levels of natural radioactivity: analysis and application of index criteria. *Constr. Build Mater.* 49, 448–454. doi: 10.1016/j.conbuildmat.2013.08.059

Tuccimei, P., Moroni, M., and Norcia, D. (2006). Simultaneous determination of ^{222}Rn and ^{220}Rn exhalation rates from building materials used in Central Italy with accumulation chambers and a continuous solid state alpha detector: influence of particle size, humidity and precursors concentration. *Appl. Radiat. Isot.* 64, 254–263. doi: 10.1016/j.apradiso.2005.07.016

Tufail, M. (2012). Radium equivalent activity in the light of UNSCEAR report. *Environ. Monit. Assess.* 184, 5663–5667. doi: 10.1007/s10661-011-2370-6

Ujić, P., Čeliković, I., Kandić, A., Vukanac, I., Đurašević, M., Dragosavac, D., et al. (2010). Internal exposure from building materials exhaling ^{222}Rn and ^{220}Rn as compared to external exposure due to their natural radioactivity content. *Appl. Radiat. Isot.* 68, 201–206. doi: 10.1016/j.apradiso.2009.10.003

Ujić, P., Čeliković, I., Kandić, A., and Žunić, Z. (2008). Standardization and difficulties of the thoron exhalation rate measurements using an accumulation chamber. *Radiat. Meas.* 43, 1396–1401. doi: 10.1016/j.radmeas.2008.03.003

United Nations Scientific Committee on the Effects of Atomic Radiation (UNSCEAR) (1982). *Ionizing Radiation: Sources and Biological Effects*. New York, NY: United Nations.

United Nations Scientific Committee on the Effects of Atomic Radiation (UNSCEAR) (2000). *Sources, Effects and Risks of Ionizing Radiation*. New York, NY: United Nations.

Urosević, V., Nikezić, D., and Vulović, S. (2008). A theoretical approach to indoor radon and thoron distribution. *J. Environ. Radioact.* 99, 1829–1833. doi: 10.1016/j.jenvrad.2008.07.010

Weiss, A. (1977). Algorithms for the calculation of moist air properties on hands calculator. *Trans. ASAE* 20, 1133–1136. doi: 10.13031/2013.35716

World Health Organization (WHO) (2009). *WHO Handbook on Indoor Radon: A Public Health Perspective*. Geneva: WHO.

Yang, J., Busen, H., Scherb, H., Hürkamp, K., Guo, Q., and Tschiersch, J. (2019). Modeling of radon exhalation from soil influenced by environmental parameters. *Sci. Total Environ.* 656, 1304–1311. doi: 10.1016/j.scitotenv.2018.11.464

Conflict of Interest: The authors declare that the research was conducted in the absence of any commercial or financial relationships that could be construed as a potential conflict of interest.

Copyright © 2021 Nguyễn, Nguyễn-Thùy, Nguyễn-Văn, Nguyễn-Hải and Schimmelmann. This is an open-access article distributed under the terms of the Creative Commons Attribution License (CC BY). The use, distribution or reproduction in other forums is permitted, provided the original author(s) and the copyright owner(s) are credited and that the original publication in this journal is cited, in accordance with accepted academic practice. No use, distribution or reproduction is permitted which does not comply with these terms.

frontiers in Earth Science

ORIGINAL RESEARCH
published: 15 July 2021
doi: 10.3389/feart.2021.631190

Insights from Fumarole Gas Geochemistry on the Recent Volcanic Unrest of Pico do Fogo, Cape Verde

Gladys V. Melián[1,2,3], Pedro A. Hernández[1,2,3], Nemesio M. Pérez[1,2,3], María Asensio-Ramos[1], Eleazar Padrón[1,2,3], Mar Alonso[1,2], Germán D. Padilla[1,2], José Barrancos[1,2], Francesco Sortino[4], Hirochicka Sumino[5], Fátima Rodríguez[1], Cecilia Amonte[1], Sonia Silva[6], Nadir Cardoso[6] and José M. Pereira[7]*

[1]Instituto Volcanológico de Canarias (INVOLCAN), La Laguna, Spain, [2]Instituto Tecnológico y de Energías Renovables (ITER), Granadilla de Abona, Spain, [3]Agencia Insular de la Energía de Tenerife (AIET), Granadilla de Abona, Spain, [4]Istituto Nazionale di Geofisica e Vulcanologia - Sezione Roma 2, Roma, Italy, [5]Department of General Systems Studies, Graduate School of Arts and Sciences, The University of Tokyo, Komaba, Meguro-ku, Japan, [6]Universidade de Cabo Verde (UNICV), Praia, Cape Verde, [7]Laboratório de Engenharia Civil of Cape Verde (LEC) Tira - Chapéu, Praia, Cape Verde

OPEN ACCESS

Edited by:
Francesco Italiano, National Institute of Geophysics and Volcanology, Italy

Reviewed by:
Pierpaolo Zuddas, Sorbonne Universités, France
Andrea Di Muro, UMR7154 Institut de Physique du Globe de Paris (IPGP), France

***Correspondence:**
Gladys V. Melián
gladys@iter.es

Specialty section:
This article was submitted to Geochemistry, a section of the journal Frontiers in Earth Science

Received: *19 November 2020*
Accepted: *02 July 2021*
Published: *15 July 2021*

Citation:
Melián GV, Hernández PA, Pérez NM, Asensio-Ramos M, Padrón E, Alonso M, Padilla GD, Barrancos J, Sortino F, Sumino H, Rodríguez F, Amonte C, Silva S, Cardoso N and Pereira JM (2021) Insights from Fumarole Gas Geochemistry on the Recent Volcanic Unrest of Pico do Fogo, Cape Verde. Front. Earth Sci. 9:631190. doi: 10.3389/feart.2021.631190

We report the results of the geochemical monitoring of the fumarolic discharges at the Pico do Fogo volcano in Cape Verde from 2007 to 2016. During this period Pico do Fogo experienced a volcanic eruption (November 23, 2014) that lasted 77 days, from a new vent ~2.5 km from the fumaroles. Two fumaroles were sampled, a low (F1~100°C) and a medium (F2~300°C) temperature. The variations observed in the $\delta^{18}O$ and $\delta^{2}H$ in F1 and F2 suggest different fluid source contributions and/or fractionation processes. Although no significant changes were observed in the outlet fumarole temperatures, two clear increases were observed in the vapor fraction of fumarolic discharges during the periods November 2008–2010 and 2013–2014. Also, two sharp peaks were observed in CO_2/CH_4 ratios at both fumaroles, in November 2008 and November 2013. This confirms that gases with a strong magmatic component rose towards the surface within the Pico do Fogo system during 2008 and 2013. Further, F2 showed two CO_2/S_{total} peaks, the first in late 2010 and the second after eruption onset, suggesting the occurrence of magmatic pulses into the volcanic system. Time series of He/CO_2, H_2/CO_2 and CO/CO_2 ratios are low in 2008–2009, and high in 2013–2014 period, supporting the hypothesis of fluid input from a deeper magmatic source. Regarding to the isotopic composition, increases in air-corrected $^{3}He/^{4}He$ ratios are observed in both fumaroles; F1 showed a peak in 2010 from a minimum in 2009 during the first magmatic reactivation onset and another in late 2013, while F2 displayed a slower rise to its maximum in late 2013. The suite of geochemical species analyzed have considerably different reactivities, hence these integrated geochemical time-series can be used to detect the timing of magmatic arrivals to the base of the system, and importantly, indicate the typical time lags between gas release periods at depth and their arrival at the surface. The high $^{3}He/^{4}He$ ratios in both fumaroles in the range observed for mid-ocean ridge basalts, indicating that He is predominantly of upper mantle origin. This work supports that monitoring of the chemical and isotopic composition of the fumaroles of the Pico do Fogo volcano is a very important

tool to understand the processes that take place in the magmatic-hydrothermal system and to be able to predict future episodes of volcanic unrest and to mitigate volcanic risk.

Keywords: geochemistry, volcanic gases, fumarolic emission, precursory signals, Pico do Fogo volcano

INTRODUCTION

Volcanoes are the main degassing windows of the planet, even, in a state of quiescence, are able to degas continuously. Volcanic gases are emitted to the atmosphere both as diffuse degassing (Chiodini et al., 1996; Hernández et al., 2001; Pérez et al., 2011; Melián et al., 2014, 2019; Cardellini et al., 2017; Padrón et al., 2021) and visible emanations (e.g., fumaroles, plumes; Giggenbach, 1975; Fisher et al., 1996; Hilton et al., 2002; Melián et al., 2012; Gresse et al., 2018). The composition of the fluids discharged by volcanoes are a reflection of 1) deep processes such as the injection of new magma, degassing of deep mafic magma in the lower crust etc. and 2) secondary processes, as for example gas re-equilibrium, interaction with meteoric water-fed, water-rock interaction etc. (Giggenbach, 1980, 1984, 1987, 1993; Chiodini and Marini 1998; Taran and Giggenbach, 2003; Oppenheimer et al., 2012). Increases of the volatile content in magma plays a fundamental role in pre-eruptive pressurization of volcanic systems (Wallace, 2001). Indeed, dissolved gases in magma are the driving force behind eruptions (Symonds et al., 1994).

Direct *in situ* sampling of fumaroles has been the commonly used technique for determining the chemical and isotopic composition of volcanic gases (Giggenbach 1975), due to its reliability and the possibility to extensively investigate the main, minor, trace and ultra-trace compounds to isotopic investigation (e.g., Symond et al., 1994; Giggenbach, 1992, Hilton et al., 2002; Chiodini, 2009; Melián et al., 2014). The main disadvantage of this sampling method is that continuous real-time monitoring is not yet feasible. Nevertheless, it is a valuable geochemical tool for evaluating the volcanic activity of those systems where there is no real-time monitoring, or remote sensing observation, of visible volcanic gas emissions (Giggenbach, 1987; Fischer et al., 1996; Melián et al., 2012; Padrón et al., 2012; Caliro et al., 2015). Variations in the relative content of magmatic fluids from fumarole discharges provide us with valuable information about processes that are affecting the volcanic-hydrothermal system at depths (Giggenbach, 1987; Fischer et al., 1996; Taran et al., 1998; Hilton et al., 2010). Likewise, the study of magmatic-hydrothermal fluids is crucial to understand and compare the origin and evolution of volcanoes worldwide (Javoy et al., 1986; Hilton et al., 2002; Aiuppa et al., 2005a, 2005b; Zelenski and Taran, 2011; Chiodini et al., 2012; Melián et al., 2014). The early detection of changes in volcanic activity are fundamental when establishing the necessary criteria to activate early warning protocols for civil protection (Tilling, 1995).

Pico do Fogo (2829 m a.s.l.), which is located on the island of Fogo, is the only currently active stratovolcano in Cabo Verde archipelago. The summit crater of Pico do Fogo is characterized by a wide field of active fumaroles and high emission rates of volcanic gases (Dionis et al., 2015a, 2015b; Aiuppa et al., 2020). During recent years, several volcanic gas studies have been carried out in Pico do Fogo volcano, mainly focused on the diffuse degassing of carbon dioxide (CO_2), hydrogen sulphide (H_2S), and on thermal energy release (Dionis et al., 2015a, 2015b). More recently, Alonso et al. (2021) estimated the diffuse helium (He) degassing and thermal energy from the summit crater of Pico do Fogo during 2007–2018 period observed. Alonso et al. (2021) observes significant increases in $^3He/^4He$ isotopic ratio, ^3He, mantle ^4He emission rates and thermal energy in 2010 and 2013, and drawsa relationship between magmatic intrusions 4 years and 1 year before the eruptive period 2014–2015. However, very few studies of Fogo volcano fumarolic geochemistry have been reported. Recently, Aiuppa et al. (2020) estimated the emission of volatiles from Pico do Fogo fumaroles by combining measurements of the fumarole composition (direct sample and portable Multi-GAS) and SO_2 flux (near-vent UV Camera recording). Aiuppa et al. (2020) showed that the CO_2 emitted from fumarolic vents of Fogo volcano (1,060 ± 340 $t \cdot d^{-1}$) is larger than current diffuse CO_2 degassing (828 ± 5 $t \cdot d^{-1}$; Dionis et al., 2015a) of Fogo Island, evidencing the continuous contribution of deep magmatic gases to the system.

This work presents the first study of the temporal evolution (2007–2016) of fumarole chemistry from Pico do Fogo volcano, and describes the observed changes in the chemical and isotopic composition fumarolic discharges as geochemical precursory signals of the effusive volcanic eruption that commenced on 23 November 2014.

GEOLOGICAL AND GEOGRAPHICAL BACKGROUND OF FOGO ISLAND

The Cape Verde islands are located about 800 km west of Senegal, at 14–17° latitude and 21–25° longitude. The archipelago consists of a volcanic chain of 10 major islands and eight minor islands (**Figure 1A**). The Cape Verde islands are located over Mesozoic oceanic crust and their origin is related to the existence of a mantle plume (Courtney and White, 1986). Volcanic activity is driven by the existence of a hot spot beneath the oceanic crust (Fonseca et al., 2003). Pico do Fogo volcano is the most active volcano of the Cabo Verde Island, with approximately 30 recorded volcanic eruptions since 1500 A.D. (Day et al., 1999). During the 20th century, two eruptions occurred, one in 1951 and the other in 1995, while the last and most recent eruption commenced in late 2014. One of the most striking features of Fogo island is the Cha das Caldeiras (**Figure 1B**), a caldera with a diameter of ~9 km, and surrounded by a wall (Bordeira) that reaches 1000 m in height at some points. The caldera opens towards the sea on its eastern side, caused by a massive flank collapse at ~73 ka (Day et al., 1999; Ramalho et al., 2015). Pico do Fogo volcano is located in the center of the caldera, which gave rise to several eruptions from its summit between 1500 and 1750 A.D. (Torres et al., 1997). Magmatism is dominated by silica-undersaturated alkaline melts of basanitic through phonolitic

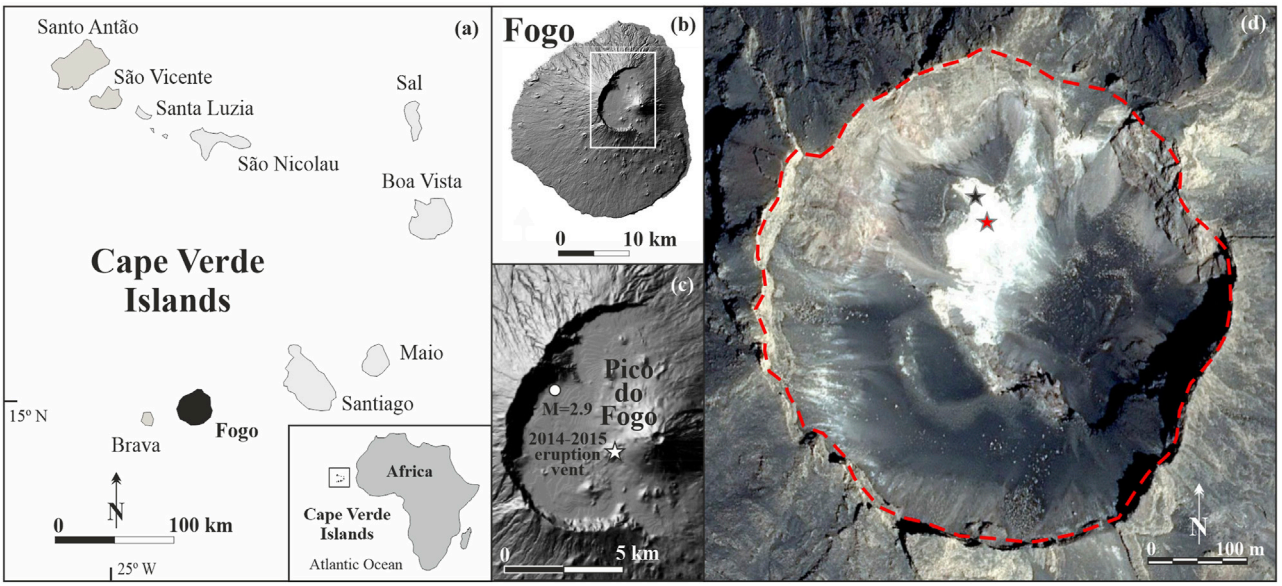


FIGURE 1 | (A) Geographical location of Fogo Island in Cape Verde. **(B)** Shaded relief map of Fogo Island with the location of Cha das Caldeiras (white square). **(C)** Shaded relief map of Cha das Caldeiras showing Pico do Fogo volcano. The white star indicates the location of the main vent of the 2014–2015 eruption. The white circle indicates the location of the earthquake (M = 2.9) occurred on April 12, 2012 (Pérez et al., 2015). **(D)** Aerial view of Pico do Fogo crater with the location of F1 (black star) and F2 (red star) fumaroles.

composition with the occurrence of carbonatites (Jørgensen and Holm 2002; Hildner et al., 2011; Mourão et al., 2012; Klügel et al., 2020). Escrig et al. (2005) reported that erupted lavas span a compositional spectrum from basanites to tephrites and nephelinites, with the 1995 eruption producing cogenetic basanites and phonotephrites (Hildner et al., 2011). The petrological study of lavas during the 2014–2015 volcanic eruption, showed somewhat evolved an alkaline composition ranging from tephrites to phonotephrites (Mata et al., 2017).

Fogo Island generally only experiences minor seismic activity (Leva et al., 2019). The Volcanological Institute of Cape Verde (OVCV), within the framework of the MAKAVOL research project in collaboration with Spanish institutions (INVOLCAN, ITER and University of Granada) and Cape Verdean institutions (University of Cape Verde, Civil Protection Service and Civil Engineering Laboratory), installed a seismic network on the island in April 2012 (Carrion et al., 2012). This seismic network was operational for 2 months and registered a significant seismic event of magnitude 2.9 on April 12, 2012 (**Figure 1C**; Pérez et al., 2015). The epicenter was located within Cha das Caldeira and was felt by the inhabitants of the island. Seismic activity is also recorded by the Fogo seismic network of the Cape Verde National Institute of Meteorology and Geophysics (INMG), who also alerted Civil Protection authorities one day before the start of the eruption (Cape Verde Civil Protection, personal communication).

Cape Verde archipelago has semi-arid climatic conditions, with the southern region being drier. Due to its geographical location, close to the equator, and thermal mass of the surrounding ocean, the average annual temperature of Fogo Island is about 25°C, with variation of the average daily temperature only 5°C in the year (Heilweil et al., 2009). However, the temperature can decrease to 0°C in Chã das Caldeiras (Mota Gomes, 2006). Rainfall varies throughout the year, with long dry spells, concentrating mainly between July and October (equatorial monsoon; Vailleux and Bourguet 1974), and ranging from 550 $mm \cdot y^{-1}$ for the northern regions to 150 $mm \cdot y^{-1}$ for the southern regions, being extremely variable from one year to another. As in other volcanic oceanic island, precipitation is lost primarily through evapotranspiration and runoff to the sea, as a consequence of warm weather, the thickness and type of soil cover, and steep topographic gradients (Langworthy and Finan, 1997). In general, most of infiltration and groundwater recharge occurs in the higher-altitude areas of the island, where precipitation rates are highest, high-permeability basalts, and closed-basin calderas are combined (Barmen et al., 1984; Kallrén and Schreiber 1988; Barmen et al., 1990; Heilweil et al., 2009). In contrast to other active oceanic hotspots, environmental tracers show that deep geothermal circulation does not strongly affect groundwater of Fogo Island (Heilweil et al., 2009). However, there are no comprehensive geochemical studies available in the literature for this hydrothermal system.

The 2014–2015 Volcanic Eruption

On November 23, 2014, a volcanic eruption began at the west flank of Pico do Fogo (González et al., 2015; Cappello et al., 2016; Richter et al., 2016; Calvari et al., 2018; Klügel et al., 2020). The eruption started from a fissure which opened along the southwest flank of the volcano, very close to the site of the previous 1995 eruptive fissure (white star in **Figure 1C**). The 2014 lava flows caused the evacuation of ~1000 residents living in the vicinity of the volcano, and the closure of a local airport. The 2014 event is well documented by a variety of field observations

TABLE 1 | Outlet temperatures (in degree Celsius) and chemical composition (dry gas fraction in mmol/mol total gas) of fumarolic gases from Pico do Fogo volcano.

Fumarole	Sample code	Date	Temp	CO_2	HCl	$S_{total}(SO_4)$	H_2O	He	H_2	O_2	N_2	CH_4	CO
			(°C)	(mmol/mol total gas)									
F1	1	April 30, 2007	113.0	443.4	0.0024	5.824	541.6	0.0066	0.8336	0.0842	8.216	0.0000938	0.007604
F1	2	November 06, 2008	140.0	134.3	0.0718	0.758	863.8	0.0001	0.0052	0.1982	0.874	0.0000025	0.000217
F1	3	February 21, 2010	68.6	455.5	0.0246	4.784	538.4	0.0034	0.3876	0.0563	0.856	0.0000087	0.000043
F1	4	February 24, 2012	62.4	450.6	0.6046	0.752	544.6	0.0061	0.6083	0.1500	2.537	0.0001387	0.005356
F1	5	April 27, 2013	89.6	115.3	0.0773	1.527	881.1	0.0021	0.2587	0.0273	1.656	0.0000535	0.001537
F1	6	November 06, 2013	87.3	161.5	0.0691	1.468	830.2	0.0066	0.8334	0.8683	4.960	0.0000025	0.002648
F1	7	March 22, 2014	77.1	123.6	0.0749	1.262	874.1	0.0021	0.2363	0.1387	0.501	0.0000486	0.001463
F2	1	November 06, 2008	344.0	167.3	0.380	2.381	828.6	0.0004	0.0391	0.2294	1.069	0.0000098	0.002000
F2	2	December 08, 2010	344.0	283.0	0.075	1.229	715.1	0.0030	0.4545	0.0082	0.175	0.0000684	0.012672
F2	3	November 06, 2013	317.9	115.6	0.113	1.619	882.6	0.0030	0.6098	0.1803	1.671	0.0000098	0.011084
F2	4	March 22, 2014	266.0	95.0	0.151	1.177	902.6	0.0032	0.3894	0.1181	0.595	0.0000723	0.009940
F2	5	January 03, 2015	306.2	388.5	0.170	2.384	606.2	0.0464	0.3318	0.0972	2.160	0.0001474	0.002920
F2	6	February 16, 2015	331.6	483.7	0.178	2.190	511.3	0.0094	0.2473	0.0930	2.218	0.0001241	0.009202
F2	7	October 30, 2016	354.0	380.6	0.109	1.638	614.7	0.0031	0.3999	0.2714	1.223	0.0000601	0.038168

(Gonzalez et al., 2015; Cappello et al., 2016; Richter et al., 2016; Klügel et al., 2020). After 77 days of activity, the eruption ended on February 8, 2015.

Several studies have been published that characterize the 2014–2015 volcanic eruption. Mata et al. (2017) carried out a petrological study of lavas to investigate the magma plumbing system, reporting somewhat evolved alkaline compositions ranging from tephrites to phonotephrites. The lavas transported clinopyroxene and kaersutite phenocrysts and megacrysts to the surface, suggesting the main stages of magma evolution took place possibly at mantle depth (25.6 ± 5.5 km b.s.l.). The presence of kaersutite that has been extensively replacement by rhönite indicates that, assuming these crystals are phenocrystic, magma stalled at a shallower depth (<1.5 km b.s.l.) for at least a month prior eruption (Mata et al., 2017). Should these crystals be related to older, more evolved, pockets of phonotephrite magma that were intersected by the tephrite (Klügel et al., 2020) stalling at these depths may not be a salient feature of the principle magmatic pathway. Clinopyroxene and olivine crystals have been examined (Klügel et al., 2020) and feature ubiquitous 10–50 μm wide rims on clinopyroxene crystals, implying they grew in a few days or weeks during the ongoing eruption at upper mantle pressures ~600 MPa (21 km depth), as a consequence of H_2O loss from the melt. According to those authors, the effect of the loss of H_2O could be due to magma degassing after its movement towards more superficial levels, or the exsolution of CO_2 at depth. Ultimately, they concluded that rim zonation of olivine phenocrysts are indicative of magma rising to the surface in less than half a day after leaving this deep stall zone.

The eruption gave rise to a three-branch lava flow of rapid expansion that almost entirely destroyed the Portela and Bangeira villages within the Cha das Caldeiras (Calvari et al., 2018). Bagnardi et al. (2016) used high-resolution tri-stereo optical imagery acquired by the Pleiades-1 satellite constellation to generate a 1 m resolution DEM to quantify topographic changes associated with the 2014–2015 eruption at Fogo. They obtained a lava flow volume of 45.83 ± 0.02 × 106 m^3, emplaced over an area of 4.8 km^2 at a mean rate of 6.8 $m^3 \cdot s^{-1}$. Cappello et al. (2016) used the HOTSAT satellite thermal monitoring system and the MAGFLOW lava flow emplacement model to forecast lava flow hazards during the 2014–2015 Fogo eruption. González et al. (2015) observed deformation at the summit of Fogo Island associated with the last eruption occurred in Pico do Fogo by means of Bayesian inversion of Sentinel-1 TOPS interferometry.

METHODOLOGY

Sample Collection

Direct gas sampling was performed at two fumarole vents located in the northwest sector inside the summit crater of Pico do Fogo (F1 and F2; stars in **Figure 1D**). Fumarole gas samples were collected during the period 2007–2016, over 14 (F1) and 8 (F2) field surveys (**Figure 1D**). F1 fumarole was characterized by a lower outlet temperature (62–140°C) during the period 2007–2014, whereas the F2 fumarole was characterized by a higher outlet temperature (266–354°C) during the entire sampling period (2008–2016). After 2014, the gas flow rate from fumarole F1 decreased significantly.

During sampling, a glass funnel was introduced into the fumarolic vent and buried to prevent atmospheric air entering into the sampling system. Fumarolic gas was collected in a vacuum pre-evacuated glass flask filled with 50 ml of a 4N KOH solution (Giggenbach and Gougel, 1989a, 1989b). The H_2O vapour condenses, and the acidic gases (CO_2, H_2S, SO_2, HCl) are absorbed into the alkaline solution, while the non-condensable gases (N_2, O_2, He, H_2, CH_4, CO) are concentrated in the gas phase of the sampling flask. Different aliquots of the discharging of gases were also collected in separate high-vacuum

TABLE 2 | $\delta^{18}O$ and $\delta^{2}H$ isotope ratios (‰ vs.VSMOW) in fumarole condensates, air-corrected $^{3}He/^{4}He$ and $^{4}He/^{20}Ne$ ratios, and fraction of He source (air, magma and crust) in fumarole gas samples. $\delta^{13}C\text{-}CO_2$ (‰ vs.VPDB), $CO_2/^{3}He$ ratios and fraction of C source (L = limestone, S = organic sediment and M = mantle sources) in fumarole gas samples. M/(L + S) refers to the fraction of components of Pico do Fogo fumaroles are also present.

Fumarole	Date	$\delta^{18}O$	δD	He sources					CO_2 sources					
				$(^{3}He/^{4}He)_{corr}R/R_A$[a]	$^{4}He/^{20}Ne$	Magma He (%)	Crust He (%)	Air He (%)	$\delta^{13}C\text{–}CO_2$ (‰ vs PDB)	$CO_2/^{3}He$ ($\times10^{-9}$)	Mantle (M) (%)	Limestone (L) (%)	Sediment (S) (%)	M/(L+S) (%)
		(‰ vs VSMOW)	(‰ vs VSMOW)											
F1	April 30, 2007	n.m.	n.m.	8.09[a] ± 0.08	123[a]	91.6	8.2	0.2	n.m.	10.2[b]	n.m.	n.m.	n.m.	n.m.
F1	November 06, 2008	n.m.	n.m.	8.22[a] ± 0.09	362[a]	93.2	6.7	0.1	n.m.	7.9	n.m.	n.m.	n.m.	n.m.
F1	May 10, 2009	n.m.	n.m.	7.81[a] ± 0.09	23[a]	87.4	11.3	1.3	n.m.	11.5[b]	n.m.	n.m.	n.m.	n.m.
F1	February 21, 2010	–5.2 ± 0.0	–22 ± 3	8.53[a] ± 0.09	228[a]	96.7	3.2	0.1	–4.07 ± 0.01	10.3	15	80	5	0.17
F1	December 08, 2010	n.m.	n.m.	8.23[a] ± 0.07	94[a]	93.1	6.6	0.3	–4.22 ± 0.01	10.7[b]	14	80	6	0.16
F1	February 24, 2011	–9.6 ± 0.1	–25 ± 3	8.23[a] ± 0.15	42[a]	92.7	6.6	0.7	–4.10 ± 0.01	10.6	14	81	5	0.16
F1	February 24, 2012	–8.7 ± 0.1	–34 ± 2	7.93[a] ± 0.12	194[a]	89.8	10.1	0.1	–4.26 ± 0.01	12.7	12	82	6	0.13
F1	April 27, 2013	–8.0 ± 0.1	–40 ± 2	8.20[a] ± 0.09	18[a]	91.4	6.8	1.8	–4.48 ± 0.02	11.9	13	80	7	0.14
F1	November 06, 2013	–6.0 ± 0.1	–24 ± 1	8.63[a] ± 0.10	406[a]	97.9	2.0	0.1	–4.37 ± 0.02	9.0	17	77	6	0.20
F1	March 22, 2014	–8.3 ± 0.1	–33 ± 6	8.37[a] ± 0.09	110[a]	94.8	4.9	0.3	–4.62 ± 0.02	12.7	12	80	8	0.15
F1	January 03, 2015	–9.0 ± 0.1	–32 ± 3	n.m.	n.m.	n.m.	n.m.	n.m.	–3.61 ± 0.02	n.m.	n.m.	n.m.	n.m.	n.m.
F1	February 16, 2015	–11.8 ± 0.1	–30 ± 4	8.33[a] ± 0.08	36[a]	93.7	5.4	0.9	–3.88 ± 0.05	10.7	14	81	5	0.16
F1	November 22, 2015	n.m.	n.m.	n.m.	n.m.	n.m.	n.m.	n.m.	–4.62 ± 0.02	n.m.	n.m.	n.m.	n.m.	n.m.
F1	October 30, 2016	n.m.	n.m.	7.66[a] ± 0.02	106[a]	86.7	13.0	0.3	–4.29 ± 0.02	7.8[b]	19	76	5	0.24
F2	May 10, 2009	n.m.	n.m.	7.73 ± 0.23	2	71.0	10.0	19.1	n.m.					
F2	December 08, 2010	n.m.	n.m.	8.33 ± 0.12	519	94.5	5.5	0.0	–.20 ± 0.02	10.5	14	80	6	0.17
F2	April 27, 2013	–1.1 ± 0.1	–26 ± 4	8.28 ± 0.57	1	60.7	3.9	35.4	–4.28 ± 0.03					
F2	November 06, 2013	–1.7 ± 0.1	–24 ± 3	8.82 ± 0.09	481	100.0	0.0	0.0	–4.06 ± 0.04	8.9	17	78	5	0.20
F2	March 22, 2014	–0.7 ± 0.1	–23 ± 2	8.36 ± 0.08	167	94.7	5.1	0.2	–4.54 ± 0.07	12.0	13	80	7	0.14
F2	January 03, 2015	–3.1 ± 0.1	–30 ± 5	n.m.	n.m.	n.m.	n.m.	n.m.	–3.78 ± 0.01	n.m.	n.m.	n.m.	n.m.	n.m.
F2	February 16, 2015	–3.1 ± 0.1	–18 ± 3	8.33 ± 0.08	36	93.7	5.4	0.9	–3.90 ± 0.04	10.7	14	81	5	0.16
F2	November 22, 2015	n.m.	n.m.	n.m.	n.m.	n.m.	n.m.	n.m.	–4.44 ± 0.03	n.m.	n.m.	n.m.	n.m.	n.m.

n.m.: not measured.

[a]*Data from Alonso et al. (2021).*

[b]*Measured in sample for $\delta^{13}C\text{–}CO_2$ analysis.*

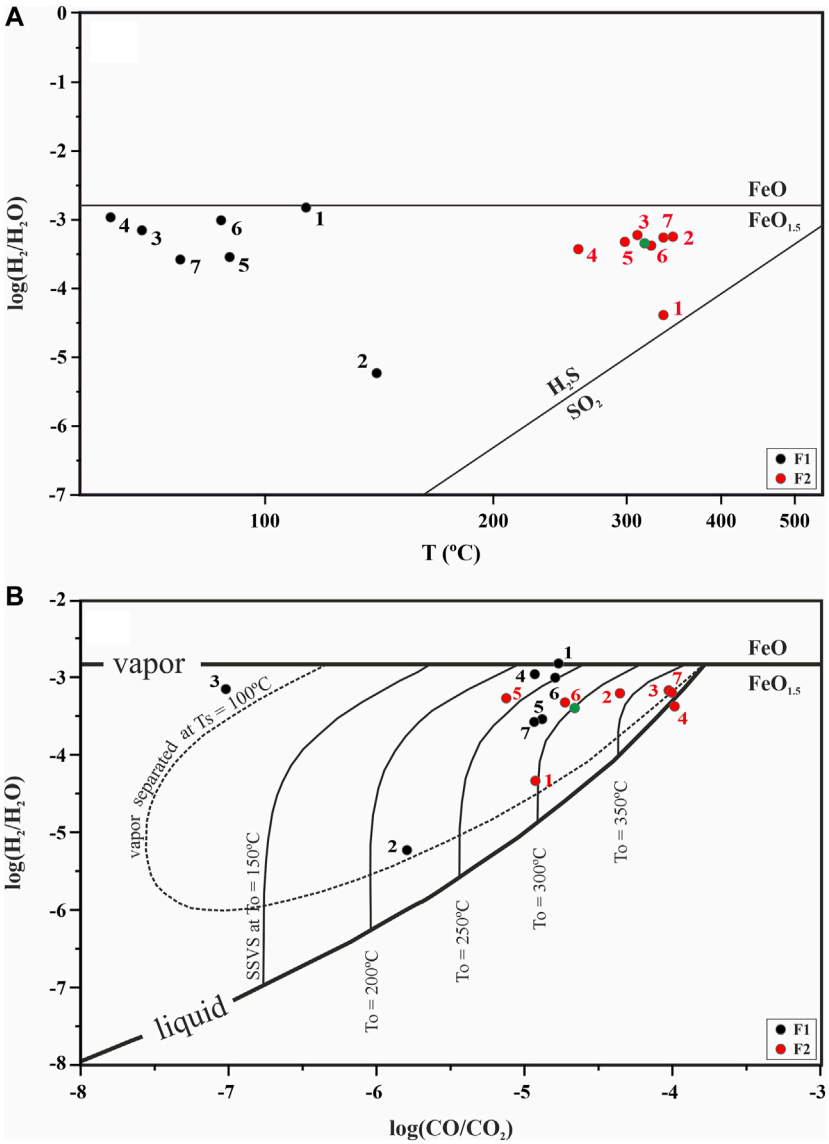


FIGURE 2 | (A) $R_H = \log(X_{H2}/X_{H2O})$ (where X is the mole fraction) vs. outlet fumarole temperatures from Pico do Fogo volcano. Buffer lines from Giggenbach (1987). **(B)** $\log(X_{H2}/X_{H2O})$ vs. $\log(X_{CO}/X_{CO2})$ for different redox conditions (Giggenbach, 1987). Compositions of the vapor phase separated in a single-step (SSVS) at different temperatures from a liquid phase initially at T_o = 150, 200, 250, 300 and 350°C are also shown (thin solid lines), as well as the compositions resulting from single-step vapor separation at 100°C starting from any initial temperature (dashed lines). Acronyms as used by Chiodini and Marini (1998). Green dots represent data from Aiuppa et al. (2020). Codes from **Table 1**.

Pb glass containers for the analysis of C and He isotopes and a sample of the vapor condensate was collected with an ice-cooled condenser in order to analyze O and H isotopes.

Analytical Techniques

The non-condensable gases were analyzed by a Varian 3800 gas-chromatograph equipped with a thermal conductivity detector (TCD) for the analysis of N_2, O_2, He and H_2, and a flame ionization detector (FID) for the analysis of CH_4 and CO (converted to CH_4 at 400°C with a methanizer). Separation was carried out in a 20 m Molecular Sieve 5A packed column using argon as the carrier gas. Analytical error was estimated as <5% for the main gas components and <10% for minor gas compounds.

An aliquot of the alkaline liquid phase was oxidized with H_2O_2 for the determination of CO_2, total sulfur (S_{total}) and HCl. The determination of CO_2 was accomplished through the analysis of CO_3^{-2} performed by titration with diluted HCl using an automatic titration system (Metrohm 716 DMS Titrino, Metrohm). S_{total} and HCl content were determined through the analysis of SO_4^{2-} and Cl^-, respectively, by means of ion chromatography coupled to a conductivity detector (Dionex DX-500 system).

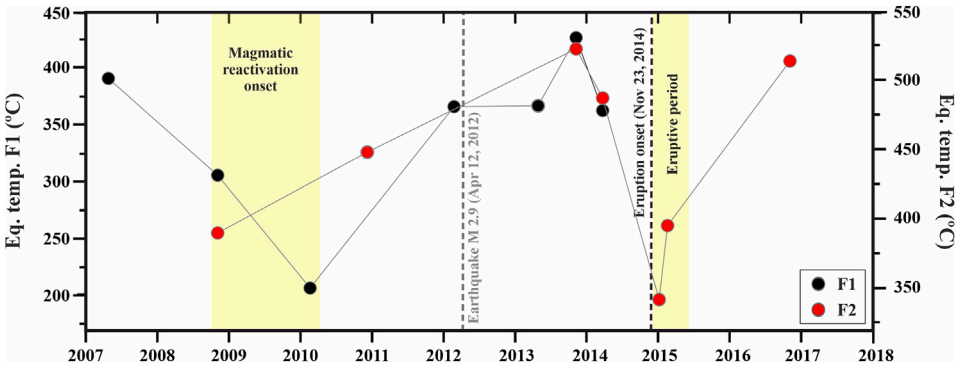


FIGURE 3 | Temporal evolution of the temperature evaluated in the equilibrium conditions CH_4, CO–CO_2 (Giggenbach, 1987) of the Pico do Fogo volcano hydrothermal system.

The isotopic signature of C in CO_2 ($\delta^{13}C$-CO_2) from fumarolic gas was determined with an isotope-ratio mass spectrometer (IRMS) (Finnigan MAT 253, Thermo Fisher Scientific) equipped with a dual inlet system. The results are reported in δ units per mil vs. Vienna Pee Dee Belemnite standard (VPDB). The analytical error for $\delta^{13}C$-CO_2 in the fumarolic gases was estimated in ±0.01‰.

Helium concentration and $^3He/^4He$ ratios were analyzed with a high-precision noble gas mass spectrometer (VG Isotech modified VG-5400) using the method described by Sumino et al. (2001). The analytical error for $^3He/^4He$ determination was <2%. The correction factor for the He isotope ratio was determined by measurements of inter-laboratory He standard named HESJ, with a recommended $^3He/^4He$ value of 20.63 ± 0.10 R_A (Matsuda et al., 2002). The measured $^3He/^4He$ ratios were corrected for the addition of air on the basis of the $^4He/^{20}Ne$ ratios measured by mass spectrometry, assuming that Ne has an atmospheric origin (Craig and Lupton, 1976). The error in the reported $^4He/^{20}Ne$ ratios is 14%, which is estimated from stability of sensitivity of the mass spectrometer during repeated measurements of the air standard.

The isotopic signatures of hydrogen ($^2H/^1H$, δ^2H) and oxygen ($^{18}O/^{16}O$, $\delta^{18}O$) in the fumarole condensate were determined using an IRMS (Finnigan MAT 253, Thermo Fisher Scientific) after a certain time of isotopic equilibrium with helium containing a known concentration of H_2 and CO_2, respectively, at 25°C (Epstein and Mayeda, 1953). In the case of $^2H/^1H$ ratio the use of platinum was necessary to catalyse the reaction (Coplen and Wildman, 1991). The results are reported in δ units per mil vs. Vienna standard mean ocean water (VSMOW) with a precision of ±0.1 and ±1‰ for $\delta^{18}O$ and δ^2H, respectively.

RESULTS

The complete chemical composition of Pico do Fogo sampled fumaroles is reported in **Table 1**. Two groups of fumaroles, F1 and F2, can be distinguished on the basis of measured outlet temperatures and gas contents. F1 fumarolic gases show low (<150°C) outlet temperatures, whereas F2 shows intermediate higher temperatures (>300°C up to 354°C), suggesting active magmatic degassing at the time of this study, and potentially more oxidizing conditions. Both fumaroles are water-dominated, with compositions ranging from 538.4 to 881.1 mmol/mol for F1 and 511.3–902.6 mmol/mol for F2. In the F1 fumarole, the concentration of CO_2 in the total gas reaches 455.5 mmol/mol, followed by N_2 (0.50–8.22 mmol/mol), H_2 (0.01–0.83 mmol/mol) and HCl (0.60 mmol/mol). The concentration of O_2, He, CO and CH_4 reached 0.86, 0.007, 0.007 and 1.4 × 10^{-4} mmol/mol, respectively. For the F2 fumarole, CO_2 concentration in the total gas reaches 483.7 mmol/mol, again followed by N_2 (0.18–2.22 mmol/mol), H_2 (0.04–0.61 mmol/mol) and HCl (0.38 mmol/mol) The concentration of O_2, He, CO and CH_4 concentrations are 0.27, 0.05, 0.038 and 1.5 × 10^{-4} mmol/mol, respectively.

Table 2 reports the oxygen and hydrogen isotopic composition of fumarole condensates, as well as carbon and helium isotopic composition of fumarole gas samples. The values obtained for water stable isotopes (δ units per mil vs. VSMOW) show much heavier $\delta^{18}O$ values at the F2 fumarole (−3.1 to −1.1‰; average −1.9‰) compared to fumarole F1 (−11.8 to −5.2‰; average −8.2‰). F1 fumarole presents a range of δ^2H values from −40 to −22‰, with an average value of −30‰, while F2 fumarole δ^2H values range from −30 to −18‰ with an average of −24‰. The carbon isotopic composition of Pico do Fogo fumarolic CO_2 ($\delta^{13}C$ vs. VPDB) varies from −4.62 ± 0.02 to −3.61 ± 0.02‰ (average −4.23‰) at the F1 fumarole, and from −4.54 ± 0.07 to −3.78 ± 0.01‰ (average −4.17‰) at the F2 fumarole.

The $^3He/^4He$ isotopic ratios of the fumarolic gases were measured for all samples collected in the study period. The air-corrected $^3He/^4He$ $(R/R_A)_{corr}$ ranged from 7.66 to 8.63 (Alonso et al., 2021) and from 7.73 to 8.82 for F1 and F2, respectively. Based on three-component mixture of magmatic He (8.82 ± 0.09 R_A), crust He (0.01 R_A; Sano et al., 1985) and air He (1 R_A), the proportion of magmatic He at Pico do Fogo varies between 86.7 and 97.9% for F1 and 71.0 and 100%, for F2 (**Table 2**).

The relative contents of CO_2 and He (given as $CO_2/^3He$ in **Table 2**) are in the range 7.8–12.7 × 10^9 and 8.9–12.0 × 10^9 for F1 and F2, respectively, which are higher than mid-ocean ridge basalt (MORB) source mantle (~2 × 10^9; Marty and Jambon, 1987). Based on a mass balance calculation proposed by Sano and Marty

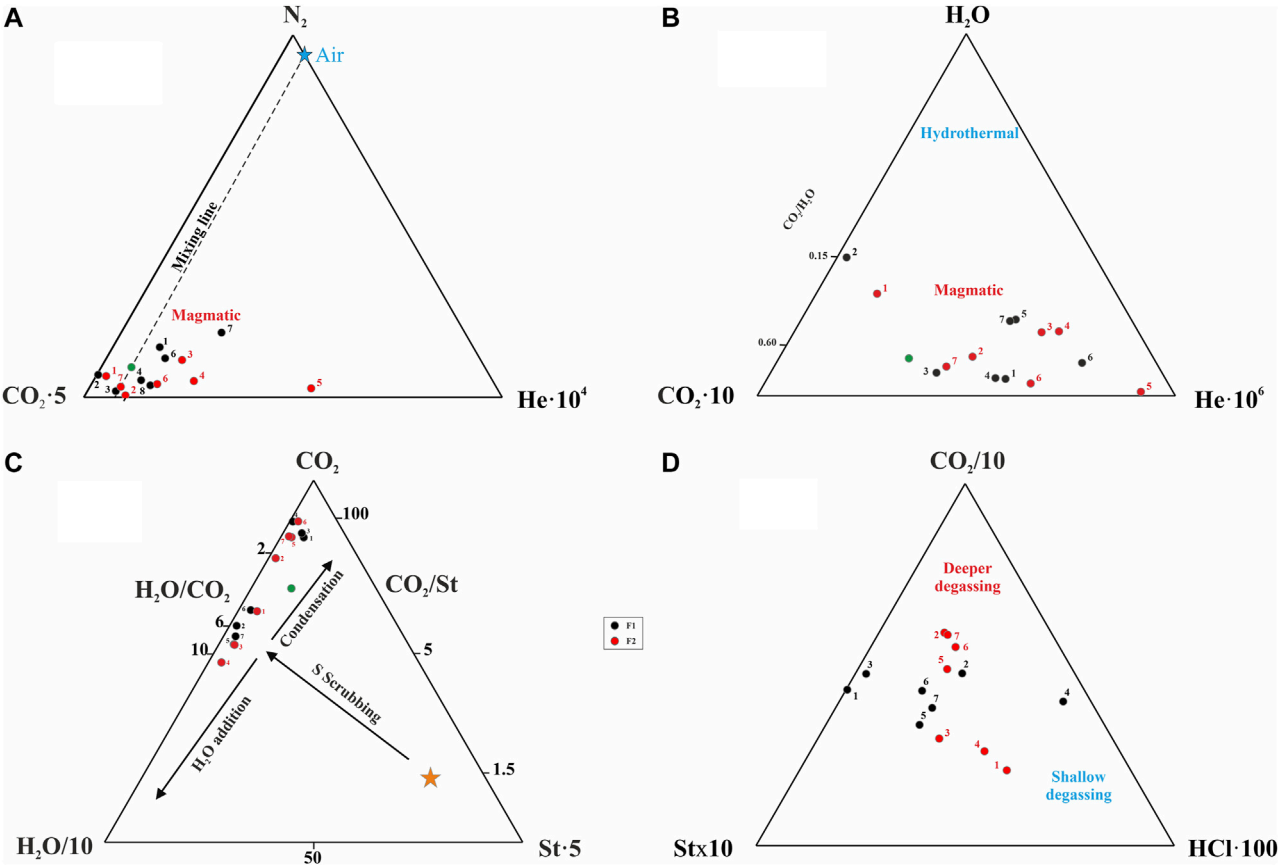


FIGURE 4 | Ternary chemical composition diagrams for Pico do Fogo fumarole samples: **(A)** CO_2-N_2-He, **(B)** CO_2-H_2O-He, **(C)** CO_2-H_2O-St and **(D)** CO_2-St-HCl. The green circle shows the mean values of composition summit fumaroles of Pico do Fogo from Aiuppa et al. (2020). The orange star indicates composition of the 2014–2015 Fogo eruptive plume from Hernández et al. (2015). Codes from **Table 1**.

(1995), a significant contribution of mantle carbon (12–19% for F1, 12–17% for F2) can be estimated for Pico do Fogo volcano.

DISCUSSION

Fumarolic Fluid Geochemistry and Equilibrium Considerations

The fumarolic samples collected during this study provide important insights into the magmatic composition of gas discharge. In this section we focus on the major gaseous species, H_2O, CO_2, and other minority species such as CO and H_2, which are essential to understand the thermodynamic processes occurring within the magmatic-hydrothermal system of the volcano. Two fumaroles with different characteristics were sampled, low temperature (F1) representing a hydrothermal end-member and a medium temperature (F2) representing a magmatic member (higher CO_2/St, H_2/H_2O ratios and lower St/Cl ratios), giving rise to the possibility that equilibrium conditions of the hydrothermal gas in the H_2O-H_2-CO_2-CO-CH_4 system might not be the same in both cases. In **Figure 2A**, F1 gas samples (except sample 2F1) plot close to the rock buffer, indicating that the H_2–H_2O–H_2S–SO_2–CO–CO_2 system at Fogo is controlled by reactions involving the rock buffer and not the H_2S/SO_2 gas buffer. The separate position of sample 2F1 may be due to the extra addition of H_2O which results in more negative R_H factor [$R_H = \log(f_{H2}/f_{H2O}) \sim \log(X_{H2}/X_{H2O})$; Giggenbach, 1987]. However, the samples from the F2 fumarole, although close to the rock buffer line (H_2–H_2O–H_2S–SO_2–CO–CO_2 system is controlled by reaction involving the rock buffer), are also close to the SO_2–H_2S buffer, which involves contribution of elemental sulfur and SO_2. Among the samples analyzed, 2F1 and 1F2 have the lowest R_H, implying more oxidizing conditions (Giggenbach, 1987). These samples were collected in 2008, when the first magmatic intrusion of the period studied is assumed to have occurred. Therefore, the chemical composition of the majority of the gases in the fumarole discharges of the Pico do Fogo volcano are dominantly controlled by the rock buffer (FeO–$FeO_{1.5}$) at 50°C<T<100°C, with a possible influence of gas phase reactions involving sulfur species at higher (>200°C) temperatures. These indices underscore that this system is characterized by extensive exchange of reactive chemical species between phases within the hydrothermal system,

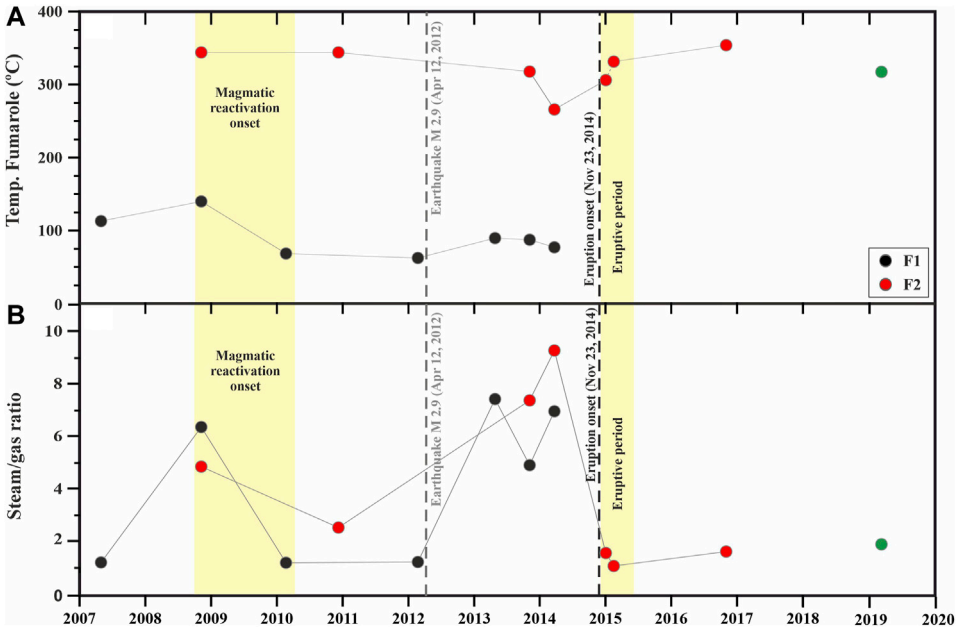


FIGURE 5 | Temporal evolution of **(A)** fumarole temperatures (°C) and **(B)** steam/gas ratios measured in the Pico do Fogo fumaroles discharges. Green dots represent data from Aiuppa et al. (2020).

and so strongly implies that deep changes in the system will be detected at the surface after some delay.

As in **Figure 2A** and **Figure 2B** shows the redox conditions in the gas equilibration zone are controlled by the $FeO–FeO_{1.5}$ hydrothermal buffer (Giggenbach, 1987) at relatively high H_2/H_2O ratios. Except for samples 3F1 and 4F2, all values plot between the vapor line and the composition resulting from single-step vapor separation at two fixed Ts temperatures (100 and 200°C) starting from an initial temperature (dashed lines in **Figure 2B**), indicating the vapours are generated through a single-step steam separation from boiling liquids of different initial temperatures (Chiodini and Marini, 1998). The position of the points along the single-step vapor separation (SSVS) lines is indicative of the extent of the boiling process. Values located near the vapor line have relatively high separation temperatures and low fractions of separated vapor, whereas values close to the 100°C Ts line are related to more energetic boiling processes, i.e., higher fractions of separated vapor (Chiodini and Marini, 1998). Sample 3F1 can be considered representative of equilibrated vapors, while sample 4F2 represents a pure equilibrated liquid phase. In general terms, there are significant variations in equilibrium temperatures between samples and they plot along different SSVS lines. F2 samples in particular have a wide range of separation temperatures indicative of changes in the physico-chemical conditions e.g., changes in the emission rates of magmatic fluids from the magmatic reservoir.

Estimated equilibrium temperatures for Pico do Fogo fumaroles based on the slow-reaction CH_4, $CO-CO_2$ (**Figure 3**; Giggenbach, 1987) thermometer show a range from 205 to 428°C at F1, and from 341 to 524°C at F2 in agree with temperatures estimated in **Figure 2B**. Two maximum values in F1 are observed: the first in 2007 and the second sustained over time (since 2010) and reaching its maximum value in November 2013, one year before the start of the most recent eruption. No data were estimated after 2014 for F1 fumarole. F2 fumarole, measured for the first time in 2009, records a constant increase in the equilibrium temperature until also reaching its maximum value in November 2013, before decreasing rapidly until January 2015, when equilibrium temperatures began increasing again. The changes observed in the equilibrium temperatures of F1 and F2 were likely due to an increase of volatile pressure in the magmatic-hydrothermal system of Pico do Fogo volcano, as is suggested by other geochemical and geophysical signals observed during the same period (González et al., 2015; Cappello et al., 2016; Richter et al., 2016; Calvari et al., 2018; Klügel et al., 2020; Alonso et al., 2021). Temporal variations of equilibria temperature estimated during the period of study showed similar behavior than CO/CO_2 ratio, with a decreasing trend towards the magmatic reactivation onset of 2009–2010, and an increasing trend towards the volcanic eruption onset. Injections of deep-seated CO_2 into the Fogo magmatic-hydrothermal system might have caused the observed variations in the fumarole CO/CO_2 ratio. Magma ascended, decompression caused exsolution of vapor and magmatic gases, which were subsequently injected into the hydrothermal system, producing the observed increase in the temperature and He flux, and later the CO_2 flux (Alonso et al., 2021), of the system.

The Pico do Fogo Fumaroles present, in general, compositions that are less hydrous than the fumaroles of others volcanic systems of the Macaranosia (Aippa et al., 2020). This can be explained be the long periods without significant rainfall at Fogo

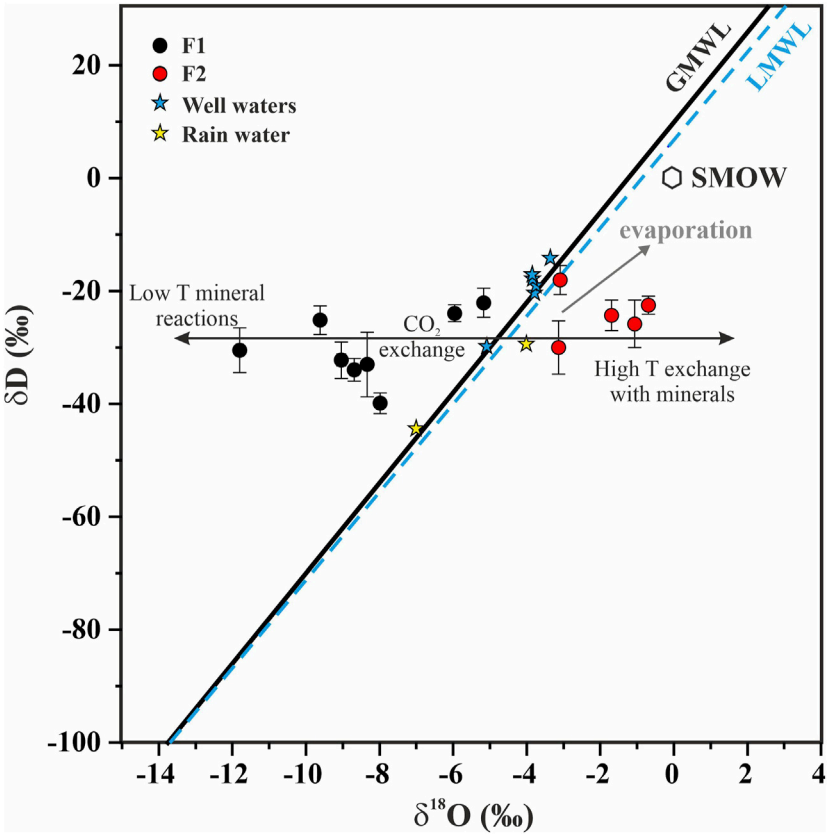


FIGURE 6 | δ^2H -H_2O vs. δ^{18}O-H_2O for condensates collected in F1 and F2 fumaroles at Pico do Fogo volcano. The Global Meteoric Water Line (GMWL; Craig, 1961) and the Local Meteoric Water Line (LMWL; Sacchi et al., 1995) are shown. Blue and yellow stars correspond to ground waters collected from wells, and rain water, respectively (Mosteiros Basin, Fogo Island; Heilweil et al., 2009). Black arrows adapted from D'Amore and Panichi (1987).

Island, and rainfall can be said to not play an important role in fumarole gas chemistry of Pico do Fogo (Vailleux and Bourguet 1974). This matches the observably weaker hydrothermal system of Pico do Fogo Volcano weak when compared to those present on geologically comparable, yet wetter, volcanic islands.

Figure 4 presents the main volatile compositions (CO_2, He, N_2, HCl, S_{total} and H_2O) measured in the F1 and F2 fumaroles. A CO_2–N_2–He ternary diagram (**Figure 4A**) shows that fumarolic gas samples are dominated by a magmatic component rich in CO_2, except for one sample (5F2), which falls between the CO_2 and He end-member. The CO_2–H_2O–He ternary diagram (**Figure 4B**) is used to distinguish between the magmatic and hydrothermal components of volcanic gases, corroborating the above interpretation by showing a strong magmatic component for most fumarolic samples. **Figure 4C** (CO_2–H_2O–St) and **Figure 4D** (CO_2–St–HCl) provide further information about the chemical compositions of volcanic gases. **Figure 4C** evidences an extensive steam condensation process, probably reflecting the relatively low temperature conditions of the fumaroles' conduits (Aiuppa et al., 2020) and/or a relatively weak hydrothermal system present at Pico do Fogo volcano (discussed above). The condensation process favors the scrubbing of S_{total} and HCl as the magmatic gases rise to the surface as are observed in **Figures 4C,D**. The similar trends observed in the C:S:Cl ratios suggest that the sources for the major constituents and processes affecting their concentrations are similar. We note that F2 values seems to have a shallower component in 2008 during the first magmatic reactivation onset, and in 2013–2014, one year before the volcanic eruption onset.

Although only minor changes were observed in the outlet fumarole temperatures (**Figure 5A**), two clear increases were observed in the vapor fraction of fumarolic discharges during the periods 2008–2010 and 2013–2014 (**Figure 5B**). The increase in one order of magnitude in the steam/gas ratio supports two hypotheses: increasing temperature of the hydrothermal aquifer due to the input of magmatic gases and/or exolution of gases from the volcanic hydrothermal system as a consequence of depressurization of the system.

The steam/gas increases were accompanied by increases in concentrations of gas species that are poorly soluble in magma, such as He (see below), and are supported by the temporal evolution of equilibrium temperatures of the hydrothermal system (**Figure 3**), with two clearly differentiated peaks coinciding with the magmatic reactivation and pre-eruptive periods. An increase of

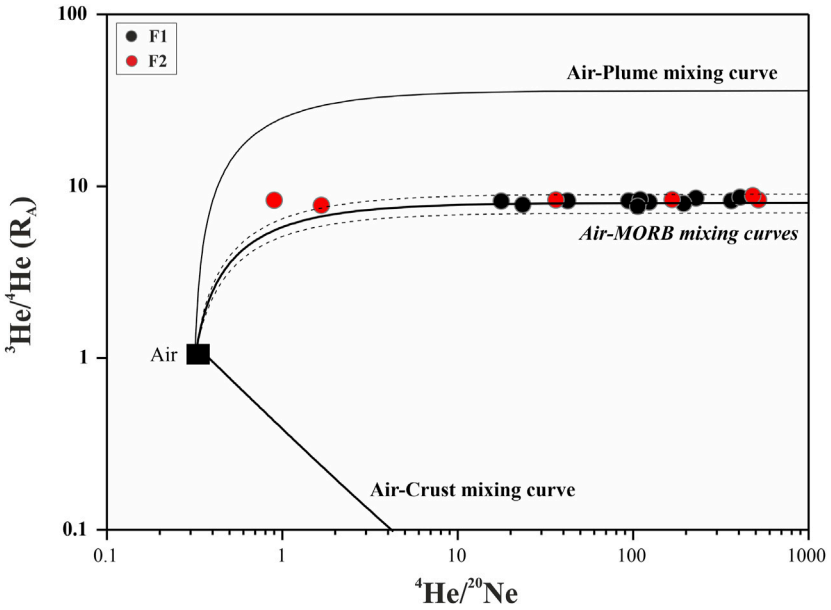


FIGURE 7 | $^4He/^{20}Ne$ ratios and $^3He/^4He$ (R_A) ratios observed in Pico do Fogo fumarole samples. Air has $^3He/^4He$ of 1xR_A and $^4He/^{20}Ne$ ratios of 0.318 (Ozima and Podosek, 2002). Curves represent theoretical mixing lines between air and other end-members.

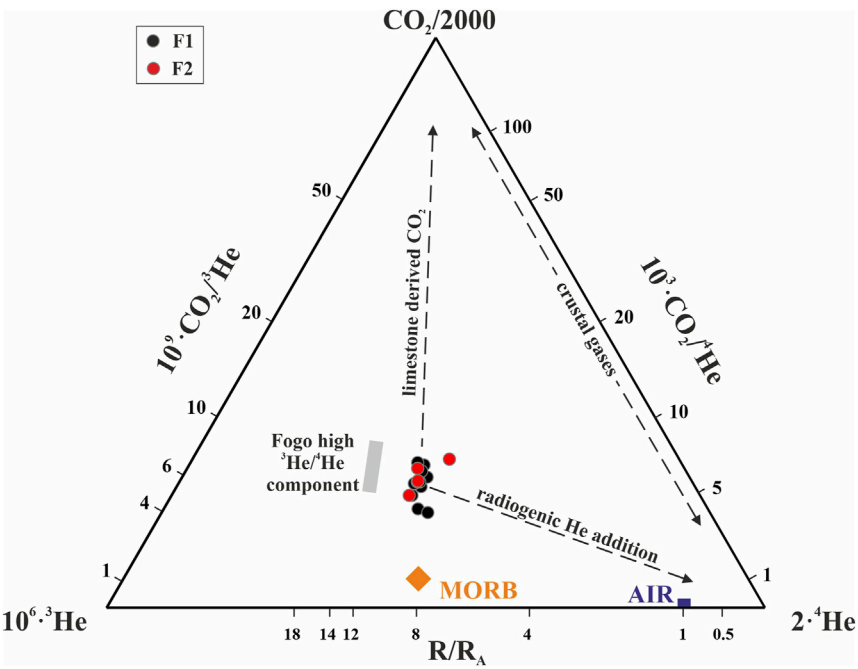


FIGURE 8 | CO_2, ^3He and ^4He relative compositions of the fumarolic samples from Fogo volcano (Giggenbach et al., 1993; Barry et al., 2013). MORB (8 ± 1 R_A, Graham, 2002; $CO_2/^3He$ = 2 ± 1×10^9, Marty and Jambon, 1987) and Air (1 R_A, Graham, 2002; $CO_2/^3He$ = 1×10^9, Marty and Jambon, 1987) are also reported. Gray rectangle represents the Fogo high $^3He/^4He$ component.

equilibrium temperature at depth (see **Figure 3**) may cause a decrease in the coefficients of vapor-liquid gas distribution, and consequently an increase in the steam fraction of the fluids leaving the hydrothermal system (Cioni et al., 1984). The relative low values of the steam/gas ratio in the fumarolic discharges at the Pico do Fogo volcano compared to

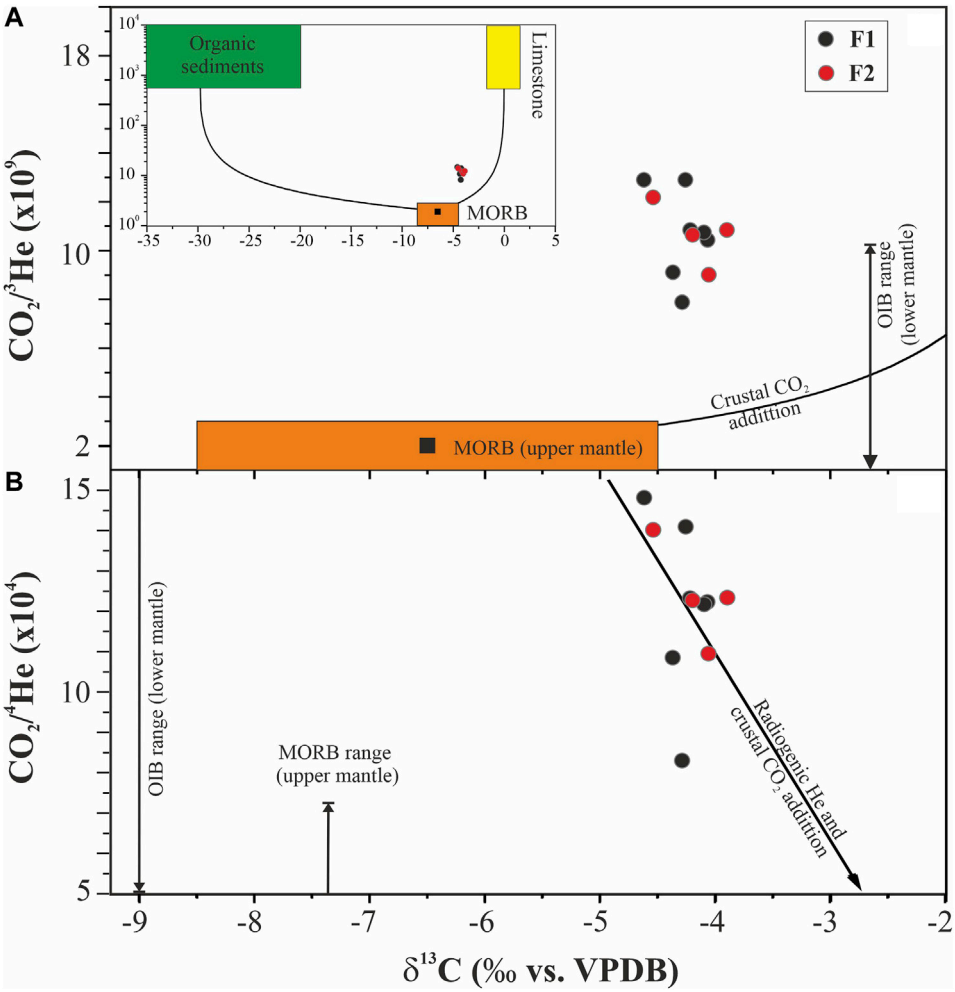


FIGURE 9 | (A) $CO_2/^3He$ ratio vs. $\delta^{13}C$–CO_2 values for F1 and F2 fumarole samples. MORB, organic sediments and marine limestone end-members are shown. Solid lines represent binary mixing curves for mantle-organic sediments, and mantle-marine limestone. Endmembers: MORB $\delta^{13}C$–CO_2 = −6.5 ± 2‰ and $CO_2/^3He$ = 2 × 10^9; organic sediments $\delta^{13}C$–CO_2 −30 ± 10‰ and $CO_2/^3He$ 1 × 10^{13}; marine limestone (including slab carbonates): $\delta^{13}C$–CO_2 0 ± 2‰ and 1 × 10^{13} (Marty et al., 1989; Sano and Marty, 1995; Sano and Williams, 1996). **(B)** $CO_2/^4He$ vs. $\delta^{13}C$–CO_2 for F1 and F2 fumarole samples [modified from Caliro et al. (2015)].

those observed in other volcanic systems in Macaronesia (Caliro et al., 2015; Ferreira et al., 2005; Melián et al., 2012) suggest poor shallow boiling hydrothermal aquifer underneath Fogo summit and therefore a greater magmatic signature evidence with a lower CO_2/S_{total} ratios and higher SO_2/H_2S ratios (Aiuppa et al., 2020). The equilibrium temperatures estimated for Pico do Fogo magmatic-hydrothermal system reached their highest values during the initial magmatic reactivation episode and then prior to eruption (**Figure 3**). Following this hypothesis would suggest that the relatively lower steam/gas ratios observed in 2008–2010 suggest that at that time, fumaroles were fed by a deeper and non-degassed magma source.

The increase of steam/gas ratio in Pico do Fogo volcano could be explained as a consequence of increase of permeability at depth due to increased fracturing, leading to more efficient gas escape and hence decompression. Both processes could have occurred in the Pico do Fogo hydrothermal volcanic system in the study period. The presence of a weak hydrothermal system and agreement between thermal and thermally sensitive geochemical indices suggests that the degree of magmatic contribution is the factor that better explains the observed variations. The steam/gas ratio therefore may be an effective parameter for the detection of changes in heat flow at depth at Fogo.

δ^2H–H_2O, $\delta^{18}O$–H_2O, $\delta^{13}C$–CO_2 and $^3He/^4He$ in Fumarole Discharge

Oxygen and hydrogen isotopic ratios in fumarole condensates, together with carbon and helium isotopic ratios are given in **Table 2**. **Figure 6** reports δ^2H and $\delta^{18}O$ values, the Local Meteoric Water Line (LMWL; $\delta^2H = 7.8 \times \delta^{18}O + 6.8$; Sacchi et al., 1995), which is slightly lower than the Global Meteoric Water Line (GMWL; $\delta^2H = 8 \times \delta^{18}O + 10$; Craig, 1961). Condensates have a wider range of δ^2H isotopic values

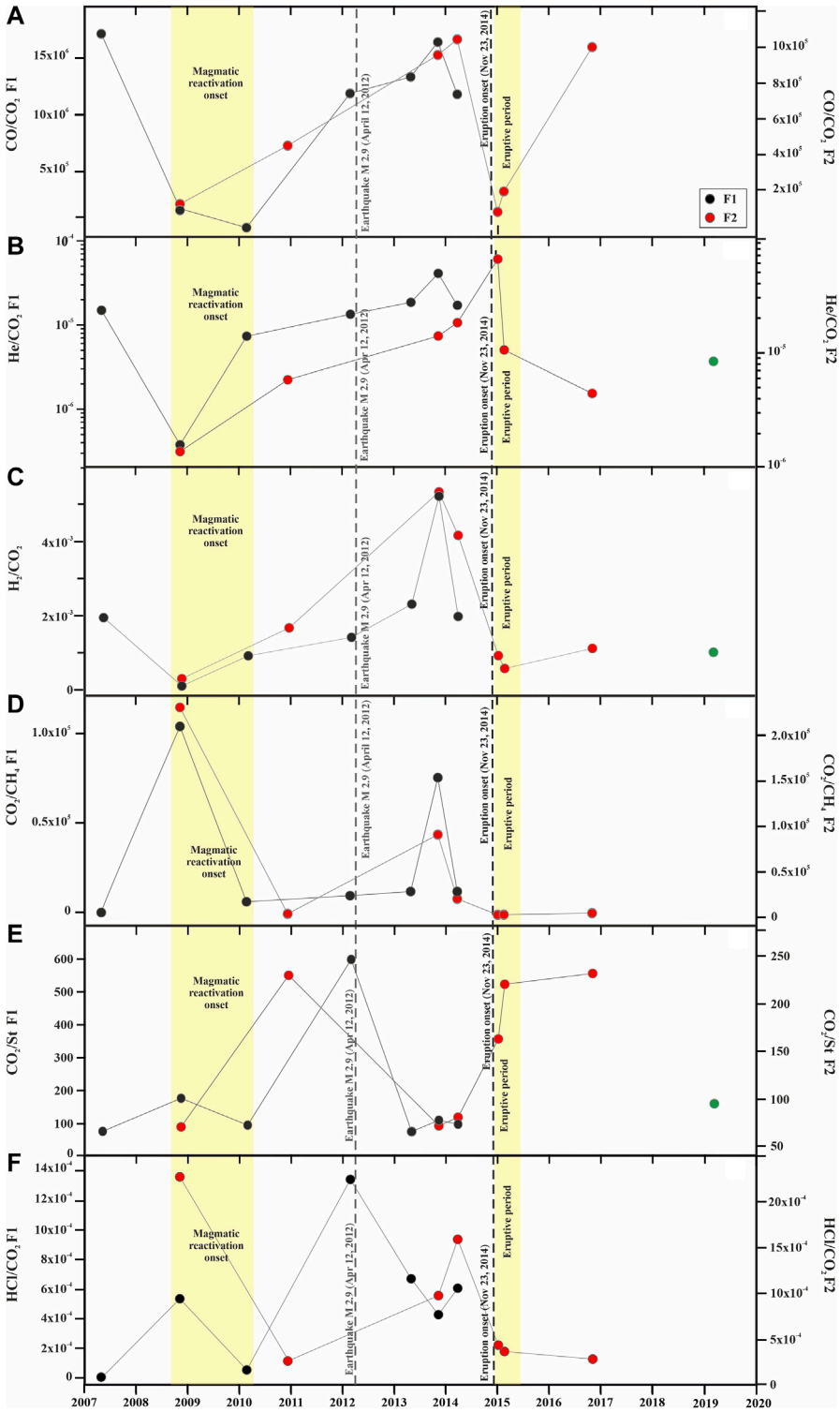


FIGURE 10 | Temporal evolution of **(A)** CO/CO_2, **(B)** He/CO_2, **(C)** H_2/CO_2, **(D)** CO_2/CH_4, **(E)** CO_2/S_{total} **(F)** HCl/CO_2, ratios measured in the Pico do Fogo F1 and F2 fumarole discharges. The green dot represents data from Aiuppa et al. (2020).

(F1 from −40 to −22‰ and F2 from −30 to −18‰) than $\delta^{18}O$ (F1 from −11.8 to −5.2‰ and F2 from −3.1 to −1.1‰). F1 samples are depleted in $\delta^{18}O$ relative to the LMWL by up to −7‰, whereas F2 samples are enriched by up to +3.5‰. All samples are depleted in $\delta^{2}H$ relative to SMOW. Rainfall and well waters from Fogo Island (Heilweil et al., 2009) have a $\delta^{2}H$ range similar to that of fumarole condensates, but a much narrower range of $\delta^{18}O$ values (**Figure 6**).

Depletion/enrichment in $\delta^{18}O$ relative to the meteorological LMWL, without changes in $\delta^{2}H$, are caused by the isotopic exchange of oxygen with CO_2 and bedrock minerals at low and high temperature (black arrows in **Figure 6**; Karolyte et al., 2017), or by the separation of water and steam under geothermal conditions (Giggenbach, 1992). In natural fluids where the vapor phase coexists with abundant CO_2, the exchange of $\delta^{18}O$ between H_2O and CO_2 can be significant as long as the isotopic exchange rate and/or the residence time of the fluids are sufficiently long (Chiodini et al., 2000). The variations observed between F1 and F2 fumaroles suggest their fluid source contributions and/or fractionation processes are different. Samples plotting close to the LMWL probably have a stronger component of heated local water. F2 gas condensates are shifted towards heavier $\delta^{18}O$ isotope values, indicating water-rock interaction and/or mixing with volcanic fluids. $\delta^{18}O$ exchange between steam and CO_2, the principal components of volcanic–hydrothermal vapors, can be mainly considered for fumarole F1 (Chiodini et al., 2000; Heilweil et al., 2009), since $\delta^{18}O$ exchange between both components have a significant bearing on the interpretation of $\delta^{18}O$ data (Chiodini et al., 2000).

The $^3He/^4He$ ratios are normalized to that in the atmosphere ($R_A = 1.4 \times 10^{-6}$; Ozima and Podosek 2002). $^3He/^4He$ and $^4He/^{20}Ne$ ratios are displayed in **Figure 7** and listed in **Table 2**. The air-corrected $^3He/^4He$ ratios at Pico do Fogo volcano (**Table 2**) range from 7.66 to 8.63 R_A in Fumarole F1, and between 7.73 and 8.82 R_A for F2, while $^4He/^{20}Ne$ ratios fluctuate significantly, ranging from 18 to 406 at F1 and 1 to 519 at F2. Fumarole F1 measurements are in agreement with those previously reported by Dionis et al. (2015b). All fumarolic samples fall on or close to a single mixing line between Air and MORB, with relatively constant $^3He/^4He$ indicating that variation in the $^3He/^4He$ ratios is dominated by the level of atmospheric contamination of the magmatic component (**Figure 7**) and indicating that magmatic He is predominantly of MORB-source like, upper mantle origin.

Based on **Figure 7**, mixing between three sources of He has been considered: magmatic, atmospheric, and crustal endmembers. We assume $^3He/^4He$ value of the magmatic endmember to be 8.82 R_A based on the highest air-corrected $^3He/^4He$ ratio observed in this study. Although this value is slightly higher than average $^3He/^4He$ ratio (8.5 ± 0.2 R_A) of olivine phenocrysts in 126 ka ankaramite lava from Fogo Island (Foeken et al., 2012), they are similarly in the range of MORBs (8 ± 1 R_A, Graham, 2002), indicating almost negligible contribution of a plume-type endmember associated with higher $^3He/^4He$ ratio than the MORB range. The He contribution from the crust is required, since some air-corrected $^3He/^4He$ data are significantly lower than the magmatic $^3He/^4He$ value. The proportion of these three reservoirs considered can be calculated using the following equations:

$$(^3He/^4He)_i = (^3He/^4He)_a \times A + (^3He/^4He)_m \times M + (^3He/^4He)_c \times C \quad (1)$$

$$1/(^4He/^{20}Ne)_i = A/(^4He/^{20}Ne)_a + M/(^4He/^{20}Ne)_m + C/(^4He/^{20}Ne)_C \quad (2)$$

$$A + M + C = 1 \quad (3)$$

where subscripts "a", "m" and "c" indicate atmospheric, magmatic and crustal sources respectively, and A, M and C are the fraction of helium from atmospheric, magmatic and crustal respectively (Sano et al., 1985; Sano and Wakita, 1985). Using the following values: $(^3He/^4He)_a$ = 1 R_A, $(^4He/^{20}Ne)_a$ = 0.318, $(^3He/^4He)_m$ = 8.82 R_A, $(^4He/^{20}Ne)_m$ = 1000, $(^3He/^4He)_c$ = 0.01 R_A, $(^4He/^{20}Ne)_c$ = 1000, the fraction of atmospheric, magmatic and crustal components can be calculated (Sano and Wakita, 1985), and are given in **Table 2**. Fumarole F1 contains a magmatic component between 86.7 and 97.9%, while the atmospheric component ranges from 0.1 to 1.8%, and the crust component from 2.0 to 13.0%. Fumarole F2 has a magmatic component between 71.0 and 100%, and atmospheric and crust components from 0 to 35.4% and 0–10.0% respectively. The atmospheric contamination is significant in the F2 samples of May 2009 and April 2013 that present a low $^4He/^{20}Ne$ ratio (19 and 35%, respectively).

In order to further explore potential sources for the fumarole gases, relationships among CO_2, ^3He and ^4He were investigated (**Figure 8**). F1 and F2 samples form a cluster of points, with a MORB-like composition due to high $^3He/^4He$ ratios (7.66–8.82 R_A, air-corrected) and $CO_2/^3He$ ratios (7.76–14.9 × 10^9). The sample cluster shows a slightly linear trend, extending towards the CO_2 vertex, with an average $^3He/^4He$ ratio of 8.2 R_A. Two samples show a slightly higher contribution of crustal-derived ^4He with respect to the main sample cluster.

Fumarole fluid contributions can be further differentiated using isotopic He, C, and CO_2 gas (**Figure 9**). F1 and F2 have $\delta^{13}C$–CO_2 ranging from −4.62 ± 0.02 to −3.61 ± 0.02‰ (vs. VPDB) and $CO_2/^3He$ ratios between 7.8 and 12.7 × 10^9, indicating a strong limestone contribution, as can be expected based on the previous studies (Jørgensen and Holm, 2002), but with different mantle contribution in the range 12–19%. The variation in $CO_2/^3He$ is likely linked to the addition of ^3He-poor, CO_2-rich gases (i.e., limestone-derived CO_2), and radiogenic He (**Figure 9**). **Figure 9A** confirms this interpretation that Pico do Fogo fumarole samples are a mixture of a mantle-derived (MORB-like) component and a crustal component enriched in ^{13}C, with high $CO_2/^3He$ (addition of limestone-derived CO_2), and lower $CO_2/^4He$ at the same $CO_2/^3He$ ratio (because of the addition of crust-derived, radiogenic He; **Figure 9B**). F1 and F2 samples show a trend towards more positive $\delta^{13}C$–CO_2 values and lower $CO_2/^4He$ ratios (**Figure 9B**), confirming an

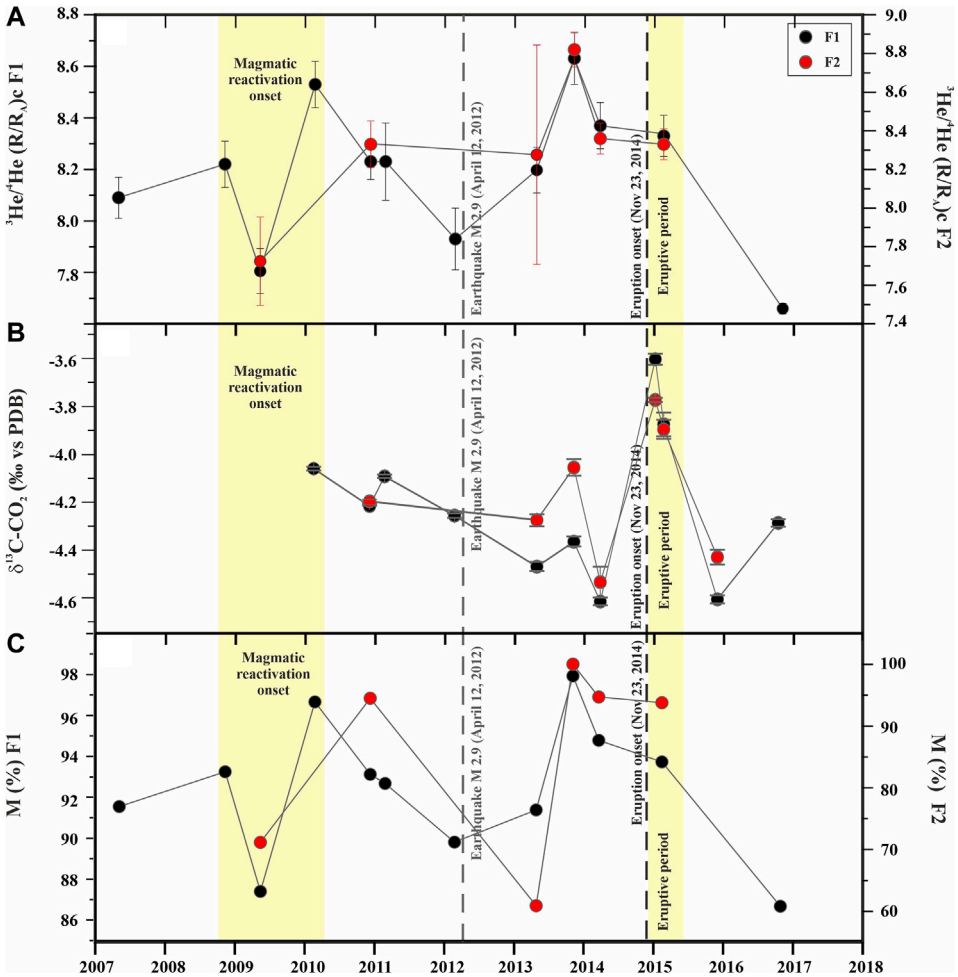


FIGURE 11 | Temporal evolution of **(A)** $^3He/^4He$ $(R/R_A)_{corr}$, **(B)** $\delta^{13}C$–CO_2 (‰ vs. VPDB) and **(C)** magmatic He contribution (M), measured in the Pico do Fogo fumaroles discharges.

increase in radiogenic ^4He and CO_2 due to the addition of fluids of crustal origin.

Temporal Variations in Fumarolic Gas Compositions

Temporal variations recorded in the chemical and isotopic composition of the fumarolic discharges of the Pico do Fogo volcano can be used to understand the relationship between the magmatic-hydrothermal system, and the volcanic activity observed during the study period. The reactive species CH_4 and CO are excellent indicators of T-P redox conditions (Chiodini et al., 1993). **Figure 10A** shows the temporal evolution of CO/CO_2 ratios (a robust proxy for temperature variations at depth; Chiodini, 2009) measured in the Pico do Fogo fumarole discharges. A gradual increase in CO/CO_2 is observed starting in 2010, before the large earthquake on April 12, 2012, and continuing to increase up until the onset of the eruption on November 23, 2014.

Relative abundances of gases with a magmatic origin, such as He, increase during magmatic intrusion episodes. Helium is chemically inert, non-biogenic, highly mobile, and relatively insoluble in water (the opposite behavior to CO_2). H_2 is a well-known geochemical tracer in volcanic systems. H_2 plays a role in key redox reactions that occur in magmatic gases, because of its relationship to fO_2 via the water dissociation reaction (e.g., Giggenbach 1987; Oppenheimer et al., 2012). Time series of He/CO_2 and H_2/CO_2 for the Pico do Fogo fumaroles are given in **Figures 10B,C**. Both ratios are low in the period 2008–2009, and high in the 2013–2014 period. The geochemical anomalies reported here in the chemical composition of the fumarolic gases in 2009 indicate fluid input from a deeper magmatic intrusion, and so an increase in the emission of He (and therefore He/CO_2) is expected at that time. However, He/CO_2 and H_2/CO_2 ratios were higher in 2007, before the magmatic reactivation period of 2009. A similar pattern is seen in the CO/CO_2 ratio (**Figure 10A**). He degassed from new, volatile-rich magma ascends easily to the surface, giving rise to the observed increase (Padrón et al., 2013) before other geochemical markers

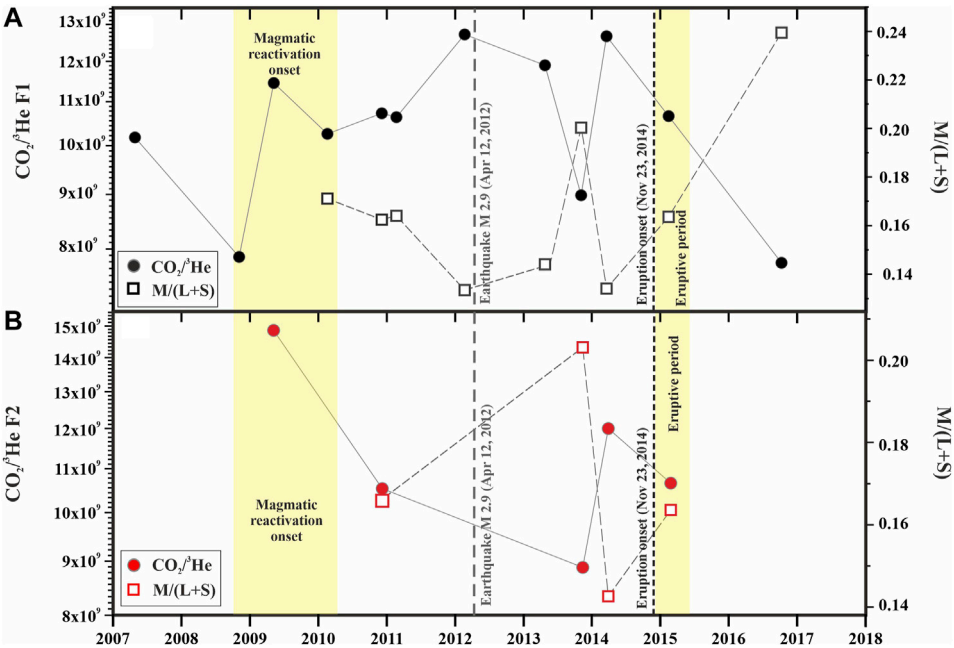


FIGURE 12 | Temporal evolution of $CO_2/^3He$ and M/(L + S) ratio (L = limestone, S = organic sediment and M = mantle sources) for F1 **(A)** and F2 **(B)** fumarole emissions.

of magmatic reactivation in the system. This fact is confirmed by an obvious contribution of mantle-derived gases before 2009, for example $^3He/^4He$ (see following paragraph). The peaks observed in H_2/CO_2 are likely due to the relative increase of H_2 emission because water-rock reactions are enhanced once magma enters the Pico do Fogo volcanic system.

CH_4 is an excellent indicator of T-P redox conditions (Chiodini et al., 1993) and it is widely accepted that an injection of magmatic fluids to a hydrothermal system causes an increase in the CO_2/CH_4 of fumarolic discharges (Chiodini, 2009), albeit with some time delay due to aforementioned interactions and exchanges. The CO_2 concentration in magmatic fluids is much higher than the concentration of CH_4, which in turn is more abundant in hydrothermal fluids than in magmatic fluids. The exsolution of volcanic gases with a strong magmatic component rich in SO_2 (due to higher oxidizing conditions) can dilute the CH_4 content, increasing the CO_2/CH_4 ratio. **Figure 10D** shows the temporal evolution of CH_4/CO_2 ratios measured in the Pico do Fogo fumarole discharges. Pulses in the CO_2/CH_4 ratio are indicative of punctual of injection of magmatic fluids of deep origin (Chiodini, 2009). Two sharp peaks occur in CO_2/CH_4 ratios at both fumaroles, in November 2008 and November 2013.

The temporal evolution of the CO_2/S_{total} ratio in Fumaroles F1 and F2 of Pico do Fogo volcano is shown in **Figure 10E**. CO_2/S_{total} is commonly used to study variations in volcanic activity because CO_2 and S have different solubilities in magma (Carroll and Webster, 1994; Holloway and Blank, 1994). When magma rises towards the surface, the least soluble gases (i.e., CO_2) are first exsolved, producing an increase in the CO_2/S_t. The measured CO_2/S_{total} ratio in the fumarolic discharges at Pico do Fogo volcano are in general higher than the observed in other intraplate volcanoes (Aiuppa, 2015) and from gases emitted in the 2014 eruption (Hernández et al., 2015), suggesting intense scrubbing in the deep S compound (Aiuppa et al., 2020). At Fumarole F1, a peak in the CO_2/S_t ratio was observed 48 days before the 2.9 earthquake on April 12, 2012. In Fumarole F2, two clear peaks are observed in CO_2/St, the first in late 2010 and the second after eruption onset.

During the ascent of magma to shallower levels, the solubility of volatiles in the magma marks the chemical composition of the magmatic fluid, the exsolution of the most insoluble gases occurs in the initial depressurisation phases (CO_2 and He), followed by the most soluble (HCl, HF and H_2O; Gerlach, 1986; Aiuppa et al., 2007; Burton et al., 2007; López et al., 2013). The HCl/CO_2 ratio for the F1 and F2 fumarole for the period 2013–2016 is shown in **Figure 10E**. At Fumarole F1, a peak in the HCl/CO_2 ratio was observed 48 days before the 2.9 earthquake on April 12, 2012. In Fumarole F2, a sharp increase in HCl/CO_2 was observed in March 2014, which correlates with both the increase in CO/CO_2 (**Figure 10A**) and the maximum value of the steam/gas ratio (heat flux; **Figure 5B**). This peak in HCl/CO_2 corresponds to minima in the CO_2/S_{total} measured ratio (**Figure 10D**). The subsequent increase in the HCl/CO_2 ratio in 2014 supports the exsolution of magmatic HCl rich gases in the magmatic plumbing system of Pico do Fogo volcano.

In general, the CO/CO_2, He/CO_2 and H_2/CO_2 ratios showed the best correlation with the variations in magmatic activity, with increases before the magmatic intrusion occurred in 2010 and the onset of the volcanic eruption in November 2014. The CH_4/CO_2, St/CO_2 and HCl/CO_2 ratios showed different temporal variabilities, although they generally increased prior to the volcanic eruption.

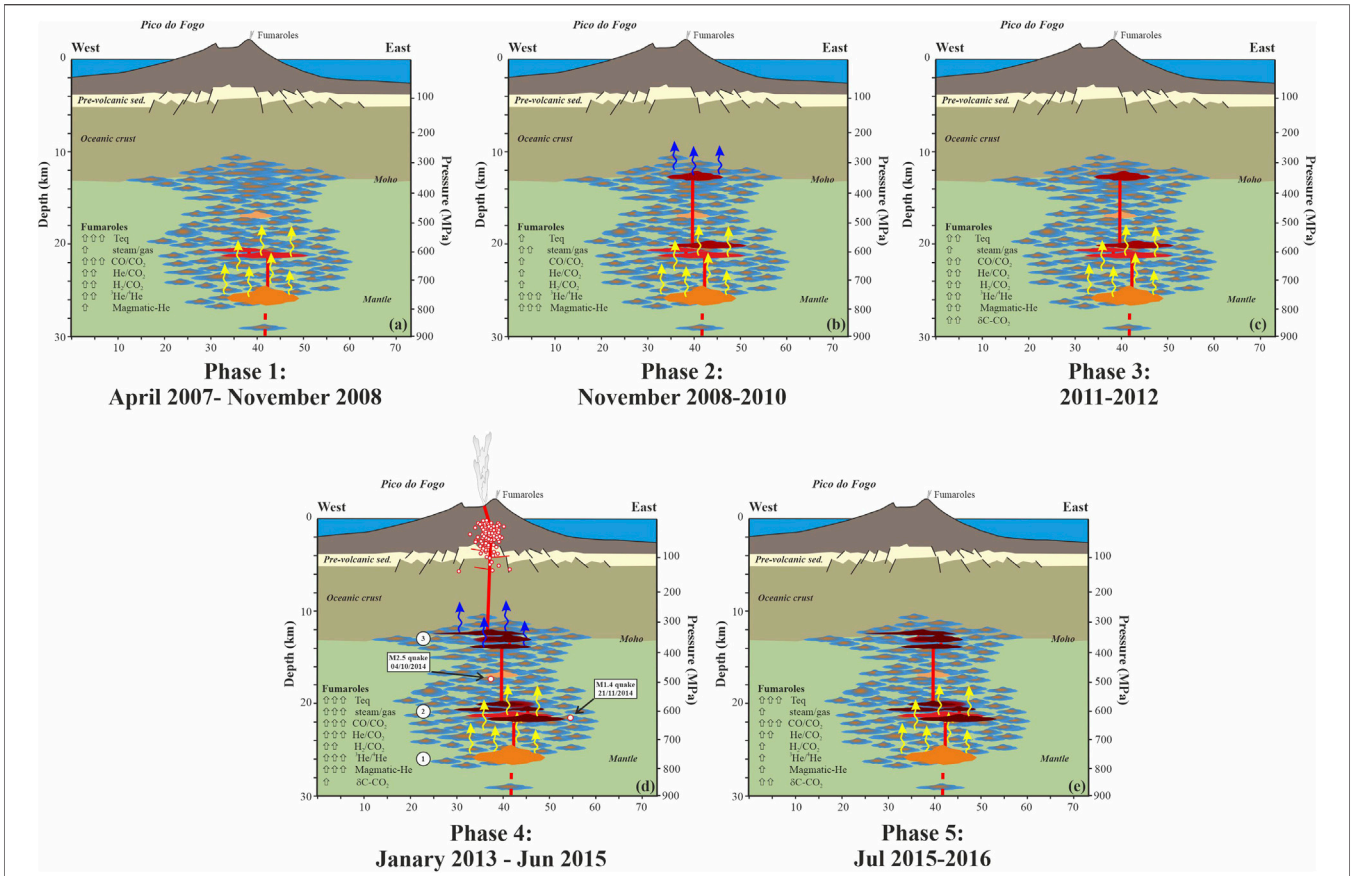


FIGURE 13 | Schematic model for the Pico do Fogo volcano fumarolic gas discharge during the period 2007–2016 [modified from Klügel et al. (2020)].

Peaks in the air-corrected $^3He/^4He$ ratios are a strong indicator for the contribution of magmatic He from a deep magmatic system (Barry et al., 2013). The temporal evolution of air-corrected $^3He/^4He$ ratios in both F1 and F2 fumaroles is illustrated in **Figure 11A**. Clear increases in air-corrected $^3He/^4He$ ratios are visible in both fumaroles: F1 shows a peak in 2010, from a minimum in 2009 during the magmatic reactivation onset (2008–2009) and another in late 2013, while F2 displays a slower rise to its maximum in late 2013, one year before the eruption.

The temporal evolution of the isotopic composition of CO_2 (expressed as $\delta^{13}C–CO_2$‰ vs. VPDB, **Figure 11B**) shows a decreasing trend towards lighter values from 2010 to 2014, with heavier ($^{13}C/^{12}C$) $\delta^{13}C–CO_2$ values measured just after the eruption (–4.62‰ and –4.54‰ vs. VPDB for F1 and F2, respectively). Once the eruption finished, $\delta^{13}C–CO_2$ returned to lighter values. The temporal evolution indicates enrichment in carbon from a deeper source during the eruption onset, due to the volatile rich-magma associated to the extruded eruptive magma.

Observed variations in the air-corrected $^3He/^4He$ ratios at both fumaroles are in general well accompanied by coeval increases in $CO_2/^3He$ (**Figure 12**), with a peak in 2012. The observed changes in the $CO_2/^3He$ ratio coupled with variations in the isotopic composition of CO_2, as well as variations in the $^3He/^4He$ ratio, are consistent with injections of magmatic fluids from depth. **Figure 11C** show the temporal evolution of magmatic He fraction (M) calculated based on the model proposed by Sano et al. (1985). The magmatic He fraction presents a similar behavior for F1 and F2 fumaroles with values of M slightly lower for F1 fumaroles than for F2 fumarole. The maximum M values were observed in 2010 and 2013–2014, when the first magmatic reactivation onset occurred and 1 year before of volcanic eruptions onset, respectively. These peaks are coincident with pulses in H_2/CO_2, He/CO_2, CO_2/S_{total} and CO/CO_2 ratios. These temporal variations of magmatic He fractions are indicative of the occurrence of magmatic fluid pulses from magma.

To estimate carbon sources for the Pico do Fogo fumaroles, the following mixing calculations are used (Sano and Marty, 1995):

$$\delta^{13}C_{obs} = Lim\,\delta^{13}C_L + Morb\,\delta^{13}C_M + Sed\,\delta^{13}C_S \quad (4)$$

$$1/(CO_2/^3He)_{obs} = Lim/(CO_2/^3He)_L + Morb/(CO_2/^3He)_M + Sed/(CO_2/^3He)_S \quad (5)$$

$$M + S + L = 1 \quad (6)$$

where obs, L, M, and S refer to the observed value, marine Limestone (L), MORB (M), and organic Sediments (S), respectively. Fumarole F1 shows: limestone 76–82%, organic Sediments 5–8% and MORB 12–19%; Fumarole F2 displays a

limestone contribution of 78–80%, organic Sediments 5–7% and MORB 12–19% (**Table 2**). The temporal variations of the M/(L + S) ratio are displayed in **Figure 12**. From the first measurement in 2009, fumarole F1 decreases until 2013, followed by a sharp peak at the end of 2013 before falling. F2 also peaks at the end of 2013 and diminishes thereafter. The peaks reflect an increase in the relative proportion of mantle-derived CO_2. The temporal agreement between $^3He/^4He$ ratios and the proportion of CO_2 of mantle derivation is consistent with release of volatiles from a mantle-derived component during the periods 2008–2009 and 2013–2014.

Proposed Conceptual Model

Several authors have reported that magmas from the 1951, 1995 and 2014–2015 eruptions of Pico do Fogo were stored prior to eruption within the uppermost mantle at 15–30 km depth and stalled during ascent within the lower crust at 8–13 km depth (Munhá et al., 1997; Hildner et al., 2011, 2012; Mata et al., 2017; Klügel et al., 2020). No evidence was reported for a very shallow crustal magma reservoir during these eruptions. Klügel et al. (2020) proposed a model for the storage and transport of magma erupted during the 2014–2015 eruption of Pico do Fogo volcano. The main magma storage reservoir was within the uppermost mantle, at ~24–30 km depth. The arrival of fresh and volatile-rich magma to this zone probably occurred during the onset of the first magmatic reactivation observed in 2008–2009 (Alonso et al., 2021). Around one year before the 2014 eruption, magma ascended to a shallower (~21 km) complex storage region with an interconnected network of magma pockets and dyke/sills (Klügel et al., 2020), and was stored along this zone in the lowermost crust.

Based on the present work and other previous findings (Aiuppa et al., 2020; Klügel et al., 2020) we reconstruct the evolution of the fluids at Pico do Fogo volcano from 2007 to 2016 in a conceptual model of five phases (**Figure 13**):

- Phase 1: April 2007–November 2008 (**Figure 13A**). This period corresponds to an inter-eruptive period. Fumarolic discharges were characterized by moderate ratios in the main volcanic gases, as well as a low steam/gas ratio and a relatively high magmatic He component. In general, the composition of Pico do Fogo fumarolic gas discharges were CO_2-richer with lower H_2O contents. This coincidence is supports the hypothesis that CO_2 flushing is responsible of H_2O loss in different magma pockets (Klüger et al., 2020). The source of magmatic gas at Pico do Fogo is located in the magma reservoir at the uppermost mantle at 24–30 km depth (Klüger et al., 2020).
- Phase 2: November 2008–2010 (**Figure 13B**). During this period, the chemical and isotopic composition of fumarolic discharges showed significant changes. In November 2008, the deep magmatic environment became slightly more oxidizing and a decrease in the equilibrium temperature with a minimum in 2010 was observed. This was probably due to injections of magmatic CO_2 into the Fogo magmatic-hydrothermal system that caused decreases in the fumarole CO/CO_2 ratio. In this period, a significant increase of $^3He/^4He$ occurred with a maximum value registered for F1 in 2010. Maximum values of magmatic He component were also observed for F1 and F2 fumarolic discharges. These changes were likely due to an increase of volatile pressure in the magmatic-hydrothermal system. The geochemical data suggest the occurrence of a first magmatic reactivation due possibly to a deep magma intrusion with temporary stalling in a zone of magma accumulation at ~12–13 km depth, near the Moho, which is described by Klügel et al. (2015), such as the magma accumulation zone.
- Phase 3: 2011–2012 (**Figure 13C**). During this period, geochemical parameters generally returned to levels of Phase 1, which suggests that the intrusion of magma of Phase 2 ended. 48 days before a seismic event of magnitude 2.9 occurred in April 2012 (Pérez et al., 2015) an increase in the HCl/CO_2 and CO_2/S_{total} ratios were observed.
- Phase 4: 2014–June 2015 (**Figure 13D**). During this period, significant changes were recorded in the chemical and isotopic composition of the fumarolic discharges. Maximum values of H_2/CO_2, He/CO_2, CO_2/S_{total} and CO/CO_2 ratios were observed in 2013–2014. These peaks are coincident with maximum values of $^3He/^4He$ and magmatic He component in both fumaroles. These changes were likely due to an increase of volatile pressure in the magmatic-hydrothermal system of Pico do Fogo volcano. The composition of Pico do Fogo fumarolic gas discharges were again CO_2-richer with lower H_2O contents. These changes were likely due to a new magmatic volatile injection and heat transfer in the magmatic-hydrothermal system as is suggested by other geochemical and geophysical signals observed during the same period (González et al., 2015; Cappello et al., 2016; Richter et al., 2016; Calvari et al., 2018; Klügel et al., 2020; Alonso et al., 2021). During the rise of magma to the surface, the flowing magma passed through a complex storage region characterized by an interconnected network of dikes/sills, where part of the magma passed through and part was stored (Klügel et al., 2020). The magma was again accumulated in the area near the Moho (~12–13 km depth). After breaking through the storage region, the magma rose rapidly through the crust and reached the surface on November 23, 2014 (Klügel et al., 2020). The presumably thin conduit and distance of ~2.5 km between the vent and the geochemical sample sites explains why close temporal trends are not observed during the magma's final ascent (days-weeks), and geochemical indices. Those indices are reflecting the broader scale and longer-term influences upon the hydrothermal-magmatic system as a whole rather than pre- or syn-eruptive release of gas closer to the eruption site.
- Phase 5: After the eruptive period and from July 2015 (**Figure 13E**), the situation seems to have reset. The steam/gas ratio, CH_4/CO_2, H_2/CO_2, He/CO_2 ratios, $\delta C\text{-}CO_2$, $^3He/^4He$ and magmatic He fraction decreased quite dramatically. These drastic changes are attributed to efficient degassing of the magma responsible for the eruption.

CONCLUSION

The changes recorded in the chemical and isotopic composition of the fumarolic discharges of the Pico do Fogo volcano during the period 2007–2016 provide information of great value to understand

the dynamics of this volcano and the relationship between these changes and the eruptive activity. The injection of hot magmatic fluids from rich-gas magma into the volcanic-hydrothermal system is reflected in the CO_2, CH_4, He, CO and H_2 contents, as well as the He and C isotopic magmatic signatures, exiting from the fumaroles.

The close relationship observed between the geochemical parameters studied in visible emissions (fumaroles) demonstrates the convenience of enhancing the geochemical program for volcanic monitoring of fumaroles as an important complement to understanding the evolution of volcanic activity in Pico do Fogo. Increasing the sampling frequency, at least every six months, would be of great importance to improve the surveillance of this volcano.

DATA AVAILABILITY STATEMENT

The raw data supporting the conclusions of this article will be made available by the authors, without undue reservation.

AUTHOR CONTRIBUTIONS

GM participated in sampling, chemical and isotopic analysis of samples, treatment of data and manuscript writing. PH, EP, and NP participated in sampling, treatment of data and manuscript writing. HS performed isotopic analysis of samples, treatment of data and manuscript writing. MA-R and CA contributed chemical and isotopic analysis of samples. MA, GP, JB, FR, SS, JP, FS, and NC participated in the collection of gas samples. MA and FS also participated in the chemical analysis of samples.

FUNDING

This research was supported by the projects (i) MAKAVOL (MAC/3/C161), financed by the European Union Transnational Cooperation Programme MAC 2007-2013, (ii) CABOVERDE (08-CAP2-1208), financed by the Spanish Agency for International Cooperation & Development, AECID, (iii) VOLRISKMAC (MAC/3.5b/124) and VOLRISKMAC II (MAC2/3.5b/328) financed by the Program INTERREG V A Spain-Portugal MAC 2014-2020 of the European Comission and (iv) TFassistance, financed by the ProgramTFinnova Program of the Cabildo Insular de Tenerife. MA was supported by a grant of the Doctorados Industriales Program (DI-16- 08974) financed by Spanish National Plan for Scientific and Technical Research and Innovation 2013–2016.

ACKNOWLEDGMENTS

Special thanks are given for logistical support from the residents of Cha das Caldeira in Fogo Island. We would also like to thank Samara Dionis, Paolo Fernandes and Vera Alfama for their help during this study and Beverley Coldwell and Matthew James Pankhurst for their revision of written English and constructive comments that greatly improved the quality of paper.

REFERENCES

Aiuppa, A., Federico, C., Giudice, G., and Gurrieri, S. (2005a). Chemical Mapping of a Fumarolic Field: La Fossa Crater, Vulcano Island (Aeolian Islands, Italy). *Geophys. Res. Lett.* 32, 13. doi:10.1029/2005GL023207

Aiuppa, A., Inguaggiato, S., McGonigle, A. J. S., O'Dwyer, M., Oppenheimer, C., Padgett, M. J., et al. (2005b). H2S Fluxes from Mt. Etna, Stromboli, and Vulcano (Italy) and Implications for the Sulfur Budget at Volcanoes. *Geochimica et Cosmochimica Acta* 69, 1861–1871. doi:10.1016/j.gca.2004.09.018

Aiuppa, A., Moretti, R., Federico, C., Giudice, G., Gurrieri, S., Liuzzo, M., et al. (2007). Forecasting Etna Eruptions by Real-Time Observation of Volcanic Gas Composition. *Geol* 35 (12), 1115–1118. doi:10.1130/g24149a.1

Aiuppa, A., Ronchi, A., Bitetto, M., Rizzo, A. L., Viveiros, F., Allard, P., et al. (2020). The Fumarolic CO2 Output from Pico Do Fogo Volcano (Cape Verde). *Ijg* 139, 325–340. doi:10.3301/IJG.2020.03

Aiuppa, A. (2015). "Volcanic-gas Monitoring," in *Volcanism and Global Environmental Change*. Editors A. Schmidt, F. Kirtsen, and L. Elkins-Tanton (Cambridge University Press), 81–96. doi:10.1017/CBO9781107415683.009

Alonso, M., Pérez, N. M., Padrón, E., Hernández, P. A., Melián, G. V., Sumino, H., et al. (2021). Changes in the thermal Energy and the Diffuse 3He and 4He Degassing Prior to the 2014-2015 Eruption of Pico Do Fogo Volcano, Cape Verde. *J. Volcanology Geothermal Res.* 416, 107271. doi:10.1016/j.jvolgeores.2021.107271

Bagnardi, M., Gonzàlez, P. J., and Hooper, A. (2016). High-resolution Digital Elevation Model from Tri-stereo Pleiades-1 Satellite Imagery for Lava Flow Volume Estimates at Fogo Volcano: Tristereo Pleiades DEM of Fogo Volcano. *Geophys. Res. Lett.* 43. doi:10.1002/2016GL0694510.1002/2016gl069457

Barmen, G., Carvalho, V., and Querido, A. (1990). "Groundwater-related Geological and Isotopic Investigations on the Island of Fogo: an Overview,". Report LUTVDG/TVTG-90/3027 (Lund, Sweden: Lund Institute of Technology), 72.

Barmen, G., Joseffson, G., Magnusson, M., and Wernersson, H. (1984). "A Hydrogeological Investigation on Santiago, Cape Verde Islands,". Report TVTG-5009 (Lund, Sweden: Lund Institute of Technology), 43.

Barry, P. H., Hilton, D. R., Fischer, T. P., de Moor, J. M., Mangasini, F., and Ramirez, C. (2013). Helium and Carbon Isotope Systematics of Cold "Mazuku" CO2 Vents and Hydrothermal Gases and Fluids from Rungwe Volcanic Province, Southern Tanzania. *Chem. Geology.* 339, 141–156. doi:10.1016/j.chemgeo.2012.07.003

Burton, M., Allard, P., Mure, F., and La Spina, A. (2007). Magmatic Gas Composition Reveals the Source Depth of Slug-Driven Strombolian Explosive Activity. *Science* 317, 227–230. doi:10.1126/science.1141900

Caliro, S., Viveiros, F., Chiodini, G., and Ferreira, T. (2015). Gas Geochemistry of Hydrothermal Fluids of the S. Miguel and Terceira Islands, Azores. *Geochimica et Cosmochimica Acta* 168, 43–57. doi:10.1016/j.gca.2015.07.009

Calvari, S., Ganci, G., Victória, S., Hernandez, P., Perez, N., Barrancos, J., et al. (2018). Satellite and Ground Remote Sensing Techniques to Trace the Hidden Growth of a Lava Flow Field: The 2014-2015 Effusive Eruption at Fogo Volcano (Cape Verde). *Remote Sensing* 10, 1115. doi:10.3390/rs10071115

Cappello, A., Ganci, G., Calvari, S., Pérez, N. M., Hernández, P. A., Silva, S. V., et al. (2016). Lava Flow hazard Modeling during the 2014-2015 Fogo Eruption, Cape Verde. *J. Geophys. Res. Solid Earth* 121, 2290–2303. doi:10.1002/2015jb012666

Cardellini, C., Chiodini, G., Frondini, F., Avino, R., Bagnato, E., Caliro, S., et al. (2017). Monitoring Diffuse Volcanic Degassing during Volcanic Unrests: the Case of Campi Flegrei (Italy). *Sci. Rep.* 7, 6757. doi:10.1038/s41598-017-06941-2

Carrion, F., Diaz Moreno, A., Martin, B. J., Moreno, J., Prudencio, J., García Yeguas, A., Ibañez, J. M., Barrancos, J., Pérez, N., Barros, I., Bandomo, Z., and Gonçalves, A. (2012). "The New Seismic Network for Seismo-Volcanic Monitoring of Fogo Island (Cape Verde): Evidences of a Seismically Active Volcano," in MAKAVOL 2012 El Hierro, El Hierro, 20.

Carroll, M. R., and Webster, J. D. (1994). "Solubilitiies of Sulfur, noble Gases, Nitrogen, Chlorine, and Fluorine in Magmas," in *Volatiles in Magmas. Reviews in Mineralogy. Min. Soc. Am.* Editors M. R. Carroll and J. R. Holloway (Fredericksburg, VA), 232–279.

Chiodin, G., Cioni, R., Leonis, C., Marini, L., and Raco, B. (1993). Fluid Geochemistry of Nisyros Island, Dodecanese, Greece. *J. Volcanol. Geotherm. Res.* 56, 95–112.

Chiodini, G., Allard, P., Caliro, S., and Parello, F. (2000). 18O Exchange between Steam and Carbon Dioxide in Volcanic and Hydrothermal Gases: Implications for the Source of Water. *Geochimica et Cosmochimica Acta* 64 (14), 2479–2488. doi:10.1016/s0016-7037(99)00445-7

Chiodini, G., Caliro, S., De Martino, P., Avino, R., and Gherardi, F. (2012). Early Signals of New Volcanic Unrest at Campi Flegrei Caldera? Insights from Geochemical Data and Physical Simulations. *Geology* 40, 943–946. doi:10.1130/g33251.1

Chiodini, G. (2009). CO2/CH4ratio in Fumaroles a Powerful Tool to Detect Magma Degassing Episodes at Quiescent Volcanoes. *Geophys. Res. Lett.* 36, a–n. doi:10.1029/2008GL036347

Chiodini, G., Frondini, F., and Raco, B. (1996). Diffuse Emission of CO 2 from the Fossa Crater, Vulcano Island (Italy). *Bull. Volcanology* 58, 41–50. doi:10.1007/s004450050124

Chiodini, G., and Marini, L. (1998). Hydrothermal Gas Equilibria: the H2O-H2-CO2-CO-CH4 System. *Geochimica et Cosmochimica Acta* 62, 2673–2687. doi:10.1016/s0016-7037(98)00181-1

Cioni, R., Corazza, E., and Marini, L. (1984). The Gas/steam Ratio as Indicator of Heat Transfer at the Solfatara Fumaroles, Phlegraean Fields (Italy). *Bull. Volcanol* 47, 295–302. doi:10.1007/bf01961560

Coplen, T. B., Wildman, J. D., and Chen, J. (1991). Improvements in the Gaseous Hydrogen-Water Equilibration Technique for Hydrogen Isotope-Ratio Analysis. *Anal. Chem.* 63, 910–912. doi:10.1021/ac00009a014

Courtney, R. C., and White, R. S. (1986). Anomalous Heat Flow and Geoid across the Cape Verde Rise: Evidence for Dynamic Support from a thermal Plume in the Mantle. *Geophys. J. Int.* 87, 815–867. doi:10.1111/j.1365-246x.1986.tb01973.x

Craig, H. (1961). Isotopic Variations in Meteoric Waters. *Science* 133, 1702–1703. doi:10.1126/science.133.3465.1702

Craig, H., and Lupton, J. E. (1976). Primordial Neon, Helium, and Hydrogen in Oceanic Basalts. *Earth Planet. Sci. Lett.* 31, 369–385. doi:10.1016/0012-821x(76)90118-7

D'Amore, F., and Panichi, C. (1987). Geochemistry in Geothermal Exploration. *Appl. Geotherm.* 9, 69e89.

Day, S. J., Heleno da Silva, S. I. N., and Fonseca, J. F. B. D. (1999). A Past Giant Lateral Collapse and Present-Day Flank Instability of Fogo, Cape Verde Islands. *J. Volcanology Geothermal Res.* 94, 191–218. doi:10.1038/s41467-017-01256-2

Dionis, S. M., Melián, G., Rodríguez, F., Hernández, P. A., Padrón, E., Pérez, N. M., et al. (2015b). Diffuse Volcanic Gas Emission and thermal Energy Release from the summit Crater of Pico Do Fogo, Cape Verde. *Bull. Volcanol.* 77. doi:10.1007/s00445-014-0897-4

Dionis, S. M., Pérez, N. M., Hernández, P. A., Melián, G., Rodríguez, F., Padrón, E., et al. (2015a). Diffuse CO2 Degassing and Volcanic Activity at Cape Verde Islands, West Africa. *Earth Planet. Sp* 67. doi:10.1186/s40623-015-0219-x

Epstein, S., and Mayeda, T. (1953). Variation of O18 Content of Waters from Natural Sources. *Geochimica et Cosmochimica Acta* 4, 213–224. doi:10.1016/0016-7037(53)90051-9

Escrig, S., Doucelance, R., Moreira, M., and Allègre, C. J. (2005). Os Isotope Systematics in Fogo Island: Evidence for Lower continental Crust Fragments under the Cape Verde Southern Islands. *Chem. Geology.* 219, 93–113. doi:10.1016/j.chemgeo.2005.02.011

Ferreira, T., Gaspar, J. L., Viveiros, F., Marcos, M., Faria, C., and Sousa, F. (2005). Monitoring of Fumarole Discharge and CO_2 Soil Degassing in the Azores: Contribution to Volcanic Surveillance and Public Health Risk Assessment. *Ann. Geophys.* 48, 787–796. doi:10.4401/ag-3234

Fischer, T. P., Arehart, G. B., Sturchio, N. C., and Williams, S. N. (1996). The Relationship between Fumarole Gas Composition and Eruptive Activity at Galeras Volcano, Colombia. *Geol* 24, 531–534. doi:10.1130/0091-7613(1996)024<0531:trbfgc>2.3.co;2

Foeken, J. P. T., Stuart, F. M., and Mark, D. F. (2012). Long-term Low Latitude Cosmogenic 3He Production Rate Determined from a 126ka basalt from Fogo, Cape Verdes. *Earth Planet. Sci. Lett.* 359-360, 14–25. doi:10.1016/j.epsl.2012.10.005

Fonseca, J. F. B. D., Faria, B. V. E., Lima, N. P., Heleno, S. I. N., Lazaro, C., d'Oreye, N. F., et al. (2003). Multiparameter Monitoring of Fogo Island, Cape Verde, for Volcanic Risk Mitigation. *J. Volcanology Geothermal Res.* 125 (1–2), 39–56. doi:10.1016/s0377-0273(03)00088-x

Gerlach, T. (1986). Exsolution of H_2O, CO_2, and S during Eruptive Episodes at Kilauea Volcano, Hawaii. *J. Geophys. Res.* 91 (B12), 112177–112185. doi:10.1029/jb091ib12p12177

Giggenbach, W. F. (1975). A Simple Method for the Collection and Analysis of Volcanic Gas Samples. *Bull. Volcanol.* 39, 132–145. doi:10.1007/bf02596953

Giggenbach, W. F. (1980). Geothermal Gas Equilibria. *Geochimica et Cosmochimica Acta* 44, 2021–2032. doi:10.1016/0016-7037(80)90200-8

Giggenbach, W. F., and Goguel, R. L. (1989a). *Collection and Analysis of Geothermal and Volcanic Water and Gas Discharges, Unpublished Report, Chemistry Division*. New Zealand: DSIR-Petone.

Giggenbach, W. F., and Goguel, R. L. (1989b). *Methods for the Collection and Analysis of Geothermal and Volcanic Water and Gas samples CD 2387*. New Zealand: Department of Scientific and Industrial Research, Chemistry Division.

Giggenbach, W. F. (1992). Isotopic Shifts in Waters from Geothermal and Volcanic Systems along Convergent Plate Boundaries and Their Origin. *Earth Planet. Sci. Lett.* 113 (4), 495–510. doi:10.1016/0012-821x(92)90127-h

Giggenbach, W. F. (1984). Mass Transfer in Hydrothermal Alteration Systems-A Conceptual Approach. *Geochimica et Cosmochimica Acta* 48, 2693–2711. doi:10.1016/0016-7037(84)90317-x

Giggenbach, W. F. (1993). Redox Control of Gas Compositions in Philippine Volcanic-Hydrothermal Systems. *Geothermics* 22, 575–587. doi:10.1016/0375-6505(93)90037-n

Giggenbach, W. F. (1987). Redox Processes Governing the Chemistry of Fumarolic Gas Discharges from White Island, New Zealand. *Appl. Geochem.* 2, 141–161. doi:10.1016/0883-2927(87)90030-8

González, P. J., Bagnardi, M., Hooper, A. J. Y., Larsen, Y., Marinkovic, P., Samsonov, S. V., et al. (2015). The 2014-2015 Eruption of Fogo Volcano: Geodetic Modeling of Sentinel-1 TOPS Interferometry. *Geophys. Res. Lett.* 42, 9239–9246. doi:10.1002/2015GL066003

Graham, D. W. (2002). "8. Noble Gas Isotope Geochemistry of Mid-ocean Ridge and Ocean Island Basalts: Characterization of Mantle Source Reservoirs," in *Noble Gases in Geochemistry and Cosmochemistry*. Editors D. Porcelli, R. Wieler, and C. J. Ballentine (Washington, D.C: Mineral. Soc. Amer.), 247–318. doi:10.1515/9781501509056-010

Gresse, M., Vandemeulebrouck, J., Byrdina, S., Chiodini, G., Roux, P., Rinaldi, A. P., et al. (2018). Anatomy of a Fumarolic System Inferred from a Multiphysics Approach. *Sci. Rep.* 8, 7580. doi:10.1038/s41598-018-25448-y

Heilweil, V. M., Solomon, D. K., Gingerich, S. B., and Verstraeten, I. M. (2009). Oxygen, Hydrogen, and Helium Isotopes for Investigating Groundwater Systems of the Cape Verde Islands, West Africa. *Hydrogeol. J.* 17 (5), 1157–1174. doi:10.1007/s10040-009-0434-2

Hernández, P. A., Melián, G. V., Dionis, S., Barrancos, J., Padilla, G., Padrón, E., et al. (2015). Chemical Composition of Volcanic Gases Emitted during the 2014-15 Fogo Eruption, Cape Verde. *Geophys. Res. Abstr.* 17, EGU2015–9577. 2015, EGU General Assembly 2015.

Hernández, P. A., Notsu, K., Salazar, J. M., Mori, T., Natale, G., Okada, H., et al. (2001). Carbon Dioxide Degassing by Advective Flow from Usu Volcano, Japan. *Science* 292, 83–86. doi:10.1126/science.1058450

Hildner, E., Klügel, A., and Hansteen, T. H. (2012). Barometry of Lavas from the 1951 Eruption of Fogo, Cape Verde Islands: Implications for Historic and Prehistoric Magma Plumbing Systems. *J. Volcanology Geothermal Res.* 217-218, 73–90. doi:10.1016/j.jvolgeores.2011.12.014

Hildner, E., Klügel, A., and Hauff, F. (2011). Magma Storage and Ascent during the 1995 Eruption of Fogo, Cape Verde Archipelago. *Contrib. Mineral. Petrol.* 162, 751–772. doi:10.1007/s00410-011-0623-6

Hilton, D. R., Fischer, T. P., and Marty, B. (2002). Noble Gases and Volatile Recycling at Subduction Zones. *Rev. Mineralogy Geochem.* 47, 319–370. doi:10.2138/rmg.2002.47.9

Hilton, D. R., Ramirez, C. J., Mora-Amador, R., Fischer, T. P., Furi, E., Barry, P. H., et al. (2010). Monitoring of Temporal and Spatial Variations in Fumarole Helium and Carbon Dioxide Characteristics at Poāacute;s and Turrialba Volcanoes, Costa Rica (2001-2009). *Geochem. J.* 44, 431–440. doi:10.2343/geochemj.1.0085

Holloway, J. R., and Blank, J. G. (1994). "Chapter 6. APPLICATION of EXPERIMENTAL RESULTS to C-O-H SPECIES IN NATURAL MELTS,"

in *Volatiles in Magmas. Reviews in Mineralogy*. Editor M. R. C. J. R. Holloway (Fredericksburg, VA: Mineralogical Society of America), 187–230. doi:10.1515/9781501509674-012

Javoy, M., Pineau, F., and Delorme, H. (1986). Carbon and Nitrogen Isotopes in the Mantle. *Chem. Geology.* 57, 41–62. doi:10.1016/0009-2541(86)90093-8

Jørgensen, J. Ø., and Holm, P. M. (2002). Temporal Variation and Carbonatite Contamination in Primitive Ocean Island Volcanics from São Vicente, Cape Verde Islands. *Chem. Geol.* 192, 249–267.

Kallrén, L., and Schreiber, I. (1988). *Groundwater Survey on Western Fogo, Cape Verde. Report TVTG-5019*. Lund, Sweden: Lund Institute of Technology, 83.

Karolyte, R., Serno, S., Johnson, G., and Gilfillan, S. M. V. (2017). The Influence of Oxygen Isotope Exchange between CO_2 and H_2O in Natural CO_2-rich spring Waters: Implications for Geothermometry. *J. Appl. Geochem.* 84, 173–186.

Klügel, A., Day, S., Schmid, M., and Faria, B. (2020). Magma Plumbing during the 2014-2015 Eruption of Fogo (Cape Verde Islands). *Front. Earth Sci.* 8, 157. doi:10.3389/feart.2020.00157

Klügel, A., Longpré, M.-A., García-Cañada, L., and Stix, J. (2015). Deep Intrusions, Lateral Magma Transport and Related Uplift at Ocean Island Volcanoes. *Earth Planet. Sci. Lett.* 431, 140–149. doi:10.1016/j.epsl.2015.09.031

Langworthy, M., and Finan, T. J. (1997). *Waiting for Rain: Agriculture and Ecological Imbalance in Cape Verde*. Boulder, CO: Rienner, 212.

López, T., Ushakov, S., Izbekov, P., Tassi, F., Cahill, C., Neill, O., et al. (2013). Constraints on Magma Processes, Subsurface Conditions, and Total Volatile Flux at Bezymianny Volcano in 2007-2010 from Direct and Remote Volcanic Gas Measurements. *J. Volcanology Geothermal Res.* 263, 92–107. doi:10.1016/j.volgores.2012.0.015

Leva, C., Rümpker, G., Link, F., and Wölbern, I. (2019). Mantle Earthquakes Beneath Fogo Volcano, Cape Verde: Evidence for Subcrustal Fracturing Induced by Magmatic Injection. *J. Volcanol. Geother. Res.* 386, doi:10.1016/j.jvolgeores.2019.106672

Marty, B., and Jambon, A. (1987). C3He in Volatile Fluxes from the Solid Earth: Implications for Carbon Geodynamics. *Earth Planet. Sci. Lett.* 83, 16–26. doi:10.1016/0012-821x(87)90047-1

Marty, B., Jambon, A., and Sano, Y. (1989). Helium Isotopes and CO_2 in Volcanic Gases of Japan. *Chem. Geol.* 76 (1-2), 25–40. doi:10.1016/0009-2541(89)90125-3

Mata, J., Martins, S., Mattielli, N., Madeira, J., Faria, B., Ramalho, R. S., et al. (2017). The 2014-15 Eruption and the Short-Term Geochemical Evolution of the Fogo Volcano (Cape Verde): Evidence for Small-Scale Mantle Heterogeneity. *Lithos* 288-289, 91–107. doi:10.1016/j.lithos.2017.07.001

Matsuda, J., Matsumoto, T., Sumino, H., Nagao, K., Yamamoto, J., Miura, Y., et al. (2002). The 3He/4He Ratio of the New Internal He Standard of Japan (HESJ). *Geochem. J.* 36, 191–195. doi:10.2343/geochemj.36.191

Melián, G., Hernández, P. A., Padrón, E., Pérez, N. M., Barrancos, J., Padilla, G., et al. (2014). Spatial and Temporal Variations of Diffuse CO2 degassing at El Hierro Volcanic System: Relation to the 2011-2012 Submarine Eruption. *J. Geophys. Res. Solid Earth* 119 (9), 6976–6991. doi:10.1002/2014JB011013

Melián, G., Tassi, F., Pérez, N., Hernández, P., SortinoVaselli, F. O., Vaselli, O., et al. (2012). A Magmatic Source for Fumaroles and Diffuse Degassing from the summit Crater of Teide Volcano (Tenerife, Canary Islands): a Geochemical Evidence for the 2004-2005 Seismic-Volcanic Crisis. *Bull. Volcanol* 74, 1465–1483. doi:10.1007/s00445-012-0613-1

Melián, G. V., Pérez, N. M., Mora Amador, R. A., Hernández, P. A., Ramírez, C., Sumino, H., et al. (2019). "Diffuse CO2 Degassing and Thermal Energy Release from Poás Volcano, Costa Rica," in *Poás Volcano, Active Volcanoes of the World*. Editors F. Tassi, et al. (Springer Nature Switzerland AG 2019), 135–154. doi:10.1007/978-3-319-02156-0_6

Mota Gomes, A. (2006). *A problemática da Geologia e dos Recursos Hídricos na Ilha do Fogo*. Praia, Cabo Verde: Relatório inédito.

Mourão, C., Mata, J., Doucelance, R., Madeira, J., Millet, M.-A., and Moreira, M. (2012). Geochemical Temporal Evolution of Brava Island Magmatism: Constraints on the Variability of Cape Verde Mantle Sources and on Carbonatite-Silicate Magma Link. *Chem. Geology.* 334, 44–61. doi:10.1016/j.chemgeo.2012.09.031

Munhá, J. M., Mendes, M. H., Palácios, T., Silva, L. C., and Torres, P. C. (1997). "Petrologia e geoquímica da erupção de 1995 e de outras lavas históricas na Ilha Do Fogo, Cabo Verde," in *A Erupção Vulcanica de 1995 Na Ilha Do Fogo, Cabo Verde*. Editor A. Réffega (Lisbon: Instituto de Investigação Científica e Tropical), 171–186.

Oppenheimer, C., Fischer, T. P., and Scaillet, B. (2012). "Volcanic Degassing: Process and Impact," in *Treatise on Geochemistry*. Second Edition (Elsevier), 111–179. doi:10.1016/B978-0-08-095975-7.00304-1

Ozima, M., and Podosek, F. A. (2002). *Noble Gas Geochemistry*. 2nd ed. Cambridge: Cambridge University Press, 287.

Padrón, E., Hernández, P. A., Pérez, N. M., Toulkeridis, T., Melián, G., Barrancos, J., et al. (2012). Fumarole/plume and Diffuse CO2 Emission from Sierra Negra Caldera, Galapagos Archipelago. *Bull. Volcanol* 74, 1509–1519. doi:10.1007/s00445-012-0610-4

Padrón, E., Pérez, N. M., Hernández, P. A., Melián, G., Asensio-Ramos, M., D'Auria, L., et al. (2021). Changes in Diffuse Degassing from the Summit Crater of Teide Volcano (Tenerife, Canary Islands) Prior to the 2016 Tenerife Long-Period Seismic Swarm. *J. Geophys. Res. Solid Earth* 126, e2020JB020318. doi:10.1029/2020JB020318

Padrón, E., Pérez, N. M., Hernández, P. A., Sumino, H., Melián, G. V., Barrancos, J., et al. (2013). Diffusive Helium Emissions as a Precursory Sign of Volcanic Unrest. *Geology* 41 (5), 539–542. doi:10.1130/g34027.1

Pérez, N. M., Dionis, S., Fernandes, P., Barrancos, J., Rodríguez, F., Bandomo, Z., et al. (2015). *Precursory Signals of the 2014-15 Fogo Eruption (Cape Verde) Detected by Surface CO_2 Emission and Heat Flow Observations*. Vienna: EGU General Assembly.

Pérez, N. M., Hernández, P. A., Padilla, G., Nolasco, D., Barrancos, J., Melián, G., et al. (2011). Global CO2 Emission from Volcanic Lakes. *Geology* 39, 235–238. doi:10.1130/G31586.1

Ramalho, R. S., Winckler, G., Madeira, J., Helffrich, G. R., Hipólito, A., Quartau, R., et al. (2015). Hazard Potential of Volcanic Flank Collapses Raised by New Megatsunami Evidence. *Sci. Adv.* 1, e1500456. doi:10.1126/sciadv.1500456

Richter, N., Favalli, M., de Zeeuw-van Dalfsen, E., Fornaciai, A., da Silva Fernandes, R. M., Pérez, N. M., et al. (2016). Lava Flow hazard at Fogo Volcano, Cabo Verde, before and after the 2014-2015 Eruption. *Nat. Hazards Earth Syst. Sci.* 16, 1925–1951. doi:10.5194/nhess-2016-81

Sacchi, E., Cossio, R., Dray, M., Petrucci, B., and Zuppi, G. M. (1995). "Present Recharge and Groundwater Circulation in Ilha Do Sal (Cape Verde Islands). Application of Tracers in Arid Zone Hydrology," in Proceedings of the Vienna Symposium, Vienna, August 1994 (IAHS Publ), 232.

Sano, Y., and Marty, B. (1995). Origin of Carbon in Fumarolic Gas from Island Arcs. *Chem. Geology.* 119 (1–4), 265–274. doi:10.1016/0009-2541(94)00097-r

Sano, Y., Urabe, A., WakitaChiba, H. H., Chiba, H., and Sakai, H. (1985). Chemical and Isotopic Compositions of Gases in Geothermal Fluids in Iceland. *Geochem. J.* 19, 135–148. doi:10.2343/geochemj.19.135

Sano, Y., and Wakita, H. (1985). Geographical Distribution of 3He/4 He Ratios in Japan: Implications for Arc Tectonics and Incipient Magmatism. *J. Geophys. Res.* 90, 8729–8741. doi:10.1029/jb090ib10p08729

Sano, Y., and Williams, S. N. (1996). Fluxes of Mantle and Subducted Carbon along Convergent Plate Boundaries. *Geophys. Res. Lett.* 23 (20), 2749–2752. doi:10.1029/96gl02260

Sumino, H., Nagao, K., and Notsu, K. (2001). Highly Sensitive and Precise Measurement of Helium Isotopes Using a Mass Spectrometer with Double Collector System. *J. Mass. Spectrom. Soc. Jpn.* 49, 61–68. doi:10.5702/massspec.49.61

Symonds, R. B., Rose, W. I., Bluth, G. J. S., and Gerlach, T. M. (1994). Chapter 1. VOLCANIC-GAS STUDIES: METHODS, RESULTS, and APPLICATIONS. *Rev. Mineral.* 30, 1–66. doi:10.1515/9781501509674-007

Taran, Y. A., and Giggenbach, W. F. (2003). "Geochemistry of Light Hydrocarbons in Subduction-Related Volcanic and Hydrothermal Fluids," in *Volcanic, Geothermal, and Ore-Forming Fluids: Rulers and Witnesses of Processes within the Earths*. Editors S. F. Simmons and I. Graham (Littleton, Colo: Soc. Econ. Geol.), 61–74.

Taran, Y., Fischer, T. P., Pokrovsky, B., Sano, Y., Armienta, M. A., and Macias, J. L. (1998). Geochemistry of the Volcano-Hydrothermal System of El Chichón Volcano, Chiapas, Mexico. *Bull. Volcanology* 59, 436–449. doi:10.1007/s004450050202

Tilling, R. I. (1995). "The Role of Monitoring in Forecasting Volcanic Events," in *Monitoring Active Volcanoes: Strategies, Procedures, and Techniques, Chapter 14.* Editors W. J. McGuire, C. R. J. Kilburn, and J. B. Murray (London: UCL Press), 369–402.

Torres, P., Madeira, J., Silva, L., Brum da Silveira, A., Serralheiro, A., and Mota Gomes, A. (1997). Carta Geológica das Erupções Históricas da Ilha Do Fogo (Cabo Verde): revisão e actualização. *Comun. Instit. Geol. Mine.* 84, A193–A196.

Vailleux, Y., and Bourguet, L. (1974). "La mise en valeur des eaux souterraines dans l'archipel du Cap Vert [The development of groundwater in the archipelago of Cape Verde]," Final Mission Report 140. (Paris: BURGEAP, Ministerio da Coordenacão Interterritorial, Brigada de Aguas Subterraneas do Cabo Verde), 291.

Wallace, P. J. (2001). Volcanic SO 2 Emissions and the Abundance and Distribution of Exsolved Gas in Magma Bodies. *J. Volcanology Geothermal Res.* 108, 85–106. doi:10.1016/s0377-0273(00)00279-1

Zelenski, M., and Taran, Y. (2011). Geochemistry of Volcanic and Hydrothermal Gases of Mutnovsky Volcano, Kamchatka: Evidence for Mantle, Slab and Atmosphere Contributions to Fluids of a Typical Arc Volcano. *Bull. Volcanol.* 73, 373–394. doi:10.1007/s00445-011-0449-0

Conflict of Interest: The authors declare that the research was conducted in the absence of any commercial or financial relationships that could be construed as a potential conflict of interest.

Copyright © 2021 Melián, Hernández, Pérez, Asensio-Ramos, Padrón, Alonso, Padilla, Barrancos, Sortino, Sumino, Rodríguez, Amonte, Silva, Cardoso and Pereira. This is an open-access article distributed under the terms of the Creative Commons Attribution License (CC BY). The use, distribution or reproduction in other forums is permitted, provided the original author(s) and the copyright owner(s) are credited and that the original publication in this journal is cited, in accordance with accepted academic practice. No use, distribution or reproduction is permitted which does not comply with these terms.

frontiers in Earth Science

BRIEF RESEARCH REPORT
published: 17 August 2021
doi: 10.3389/feart.2021.648179

Geochemical Features of the Thermal and Mineral Waters From the Apuseni Mountains (Romania)

*Alin-Marius Nicula[1], Artur Ionescu[1,2], Ioan-Cristian Pop[1], Carmen Roba[1], Ferenc L. Forray[3], Iancu Orăşeanu[4] and Călin Baciu[1]**

[1]Faculty of Environmental Science and Engineering, Babes-Bolyai University, Cluj-Napoca, Romania, [2]Department of Physics and Geology, University of Perugia, Perugia, Italy, [3]Department of Geology, Babeş-Bolyai University, Cluj-Napoca, Romania, [4]Romanian Association of Hydrogeologists, Bucuresti, Romania

The Apuseni Mountains are located between the large geothermal area of the Pannonian Basin and the low thermal flux Transylvanian Basin. Thermal and mineral waters have been sampled from 42 points along a NW-SE transect. The general chemistry and the water isotope (deuterium and oxygen-18) composition were analyzed. Most of the thermal aquifers are located in carbonate reservoirs. The waters mainly belong to the Ca-HCO_3 hydrochemical type, excepting the western side, towards the Pannonian Basin, where the Na-HCO_3 type may occur. The isotope composition indicates aquifer recharge from precipitation. The geochemical characteristics and the structural position of the study area suggest two distinct geothermal contexts. The Southern Apuseni area geothermal features are likely connected to the Neogene—Early Quaternary magmatic activity from the Mureş Valley and Zarand Depression. The geothermal manifestations in the north-western part of the study area, at the border between the Northern Apuseni and the Pannonian Depression, share features of the latter one.

Keywords: geothermal, mineral water, hydrogeochemistry, water isotopes, geothermometer, Apuseni Mts, Romania

OPEN ACCESS

Edited by:
Giovanni Martinelli, National Institute of Geophysics and Volcanology, Italy

Reviewed by:
Giovanni Vespasiano, University of Calabria, Italy
Tamara Marković, Croatian Geological Survey, Croatia
Nina Rman, Geological Survey Ljubljana, Slovenia

****Correspondence:***
Călin Baciu
calin.baciu@ubbcluj.ro

Specialty section:
This article was submitted to Geochemistry, a section of the journal Frontiers in Earth Science

Received: *31 December 2020*
Accepted: *05 August 2021*
Published: *17 August 2021*

Citation:
Nicula A-M, Ionescu A, Pop I-C, Roba C, Forray FL, Orăşeanu I and Baciu C (2021) Geochemical Features of the Thermal and Mineral Waters From the Apuseni Mountains (Romania). Front. Earth Sci. 9:648179. doi: 10.3389/feart.2021.648179

INTRODUCTION

The mineral and thermal waters from the Apuseni Mountains have been less studied by respect to other areas in Romania, although their resources are not negligible. Some of the thermal sources, as Geoagiu (Germisara) and Călan (Ad Aquas), are known since the Roman times (Fodorean, 2012). However, the geochemical information able to deepen our understanding on the geothermal potential and the genesis of the thermal and mineral waters in the Apuseni area are scarce.

The Apuseni Mountains are bordered towards the west by the Romanian part of the Pannonian Basin, an extensive unit well known for its rich geothermal resources (e.g.,: Horvath et al., 2006; Szocs et al., 2018; Rman et al., 2019). On the opposite side, the Transylvanian Basin is recognized as having low heat flow compared to the Pannonian Basin, but comparable values to other European areas (Demetrescu and Andreescu, 1994; Tiliță et al., 2018).

Information about the mineral and thermal waters from the Apuseni Mts. is available in general works regarding the Romanian mineral waters (e.g.,: Institutul de Balneologie și Fizioterapie (IBF), 1970; Pricajan, 1972; Pricăjan and Airinei, 1981). Groundwater with temperatures higher than 20°C is generally considered as thermal water. A series of relevant contributions to the hydrogeological description of the Apuseni Mts., especially of the karst areas, were authored by Orășeanu, here

including also mineral and thermal waters (e.g., Orăşeanu, 1987; Orăşeanu and Mather, 2000), and synthesized by Orăşeanu (2016, 2020). The thermal waters are used or have been used for bathing purposes in resorts as Băile Felix, Geoagiu, Moneasa, Vaţa, Călan. Carbonated waters are bottled in Boholt, Băcâia, and Chimindia.

The present contribution aims to extend the current knowledge on the occurrence and characteristics of the mineral and thermal waters in the Apuseni Mts. area, by adding a set of hydrogeochemical data that includes chemical and isotopic analyses. These results will help in better constraining the thermal features of the study region. Water samples from 42 locations along a NW-SE transect were collected. Groundwater sources with temperatures between 10 and 20°C, although not corresponding to the definition of thermal water, were included in this study as indicators of the geothermal influence. The analytical results are interpreted by geochemical methods, and an assessment of the origin and geothermal context of the investigated waters is presented, correlated with the geological setting of the study area.

GEOLOGICAL SETTING

The Apuseni Mountains represent a segment of the Carpathian orogen, with an inner position relative to the main ridge. They are located between two connected Neogene sedimentary basins, the Pannonian Basin to the west, and the Transylvanian Basin to the east. Although the Apuseni Mts. have the appearance of an island, their structure continues beneath the sediments of the two basins.

The basement of the Pannonian Basin consists of two entities with different origin and evolution, the ALCAPA and Tisza/Tisia mega-units, separated by the Mid Hungarian fault zone (Schmid et al., 2020). The ALCAPA block, originated from the Adria realm, comprises the Austroalpine unit of the Alps and internal units of the Western Carpathians. A significant part of it, representing the basement of the north-western part of the Pannonian Basin, is covered by Neogene sediments. Tisza mega-unit is a Europe-derived block, which forms the basement of the south-eastern side of the Pannonian Basin, being visible in the Mecsek Mts. in Hungary, or the Slavonian Hills in Croatia. The largest outcropping area of the Tisia block corresponds to the Northern Apuseni Mts. (Inner Dacides, after Săndulescu, 1984), where the upper two units of this block, the Bihor and Codru nappe systems are exposed. These units generally consist of an Early Proterozoic—Variscan basement, basement-cover and pre-Alpine cover nappes (Seghedi, 2004).

The Bihor unit consists of medium-grade crystalline rocks, with granitic intrusions, covered by Permian—Mesozoic detrital and carbonate sedimentary formations (Săndulescu, 1984). The lithologic composition of the Codru unit is dominated by Permian—Mesozoic sedimentary formations, with Permian volcanics and few low- or medium-grade metamorphic elements underlying some of the nappes.

A north-vergent thrusting shear zone, corresponding to the Biharia unit, separates the North and South Apuseni Mts. (Seghedi, 2004). It mainly consists of medium-grade metamorphic rocks. The Biharia nappe system belongs to the Dacia mega-unit, as an equivalent of the Supragetic nappe system from the Southern Carpathians (Schmid et al., 2008, 2020), and overthrusts the Bihor and Codru units.

The South Apuseni segment is the remnant of a branch of Neotethys, the Eastern Vardar mobile area. It mainly consists of ophiolitic units, placed over the margin of the Dacia block during the Upper Jurassic (Schmid et al., 2008). They are the result of an intra-oceanic back-arc basin that persisted a very short period, between the Middle Jurassic and Late Kimmeridgian to Tithonian. The closure of the basin is marked by the obduction of the ophiolitic units on the Biharia nappe system (Schmid et al., 2020). The ophiolitc complex is represented by Middle Jurassic tholeites and Late Jurassic to Early Cretaceous calc-alkaline magmatic rocks (Mutihac, 1990). An intensive Late Jurassic to Late Cretaceous sedimentation has accompanied and followed the ophiolitic magmatism. Two types of sediments dominate: the reef limestone (Malm to Lower Cretaceous), and flysch-type detrital units.

THE STUDY AREA

Two distinct areas have been considered within the study region, which show different geological, hydrogeological, and structural features. The southern area corresponds to the depression between the Apuseni Mts. and the Southern Carpathians, filled with Neogene-Quaternary deposits along the Mureş and Strei Rivers, and to the southern part of the Apuseni Mountains. The northern area corresponds to the Northern Apuseni structural units, including also the Neogene depressions on the western side of the mountain range (**Figure 1**).

Within the southern area (A), two distinct subareas have been investigated. Rapolt subarea corresponds to the crystalline isolated massif of Rapolt and its surroundings, extending southward along Strei River. Its southern part is represented by a flat area filled with Neogene-Quaternary sediments. The northern part includes the Rapolt crystalline body, the Măgura Uroiului shoshonitic body (Seghedi et al., 2011), and the surrounding sedimentary areas that host geothermal sources. The following sources have been investigated within this subarea: Călan, Chimindia, Banpotoc, Rapolţel, Feredee, Rovina, Nătău, Geoagiu.

Zarand subarea (B) corresponds to a NW-SE oriented depression along Crişul Alb River, within the Southern Apuseni Mts, narrower in the SE (Brad area), and extending gradually to the Pannonian Basin. This intramountainous area is filled with Neogene sediments penetrated by Neogene magmatic bodies (Pécskay et al., 1995; Roşu et al., 1997; Roşu et al., 2004; Seghedi and Downes, 2011). The investigated sources in Zarand subarea are Vaţa and Dezna.

Within the Northern Apuseni, four subareas have been separated. Moneasa (C), although geographically located very close to the northern edge of Zarand depression, shows features that confirm its belonging to the Northern Apuseni. Beiuş subarea (D) is a NW-SE oriented depression, filled with Neogene sediments, and extending along Crişul Negru River,

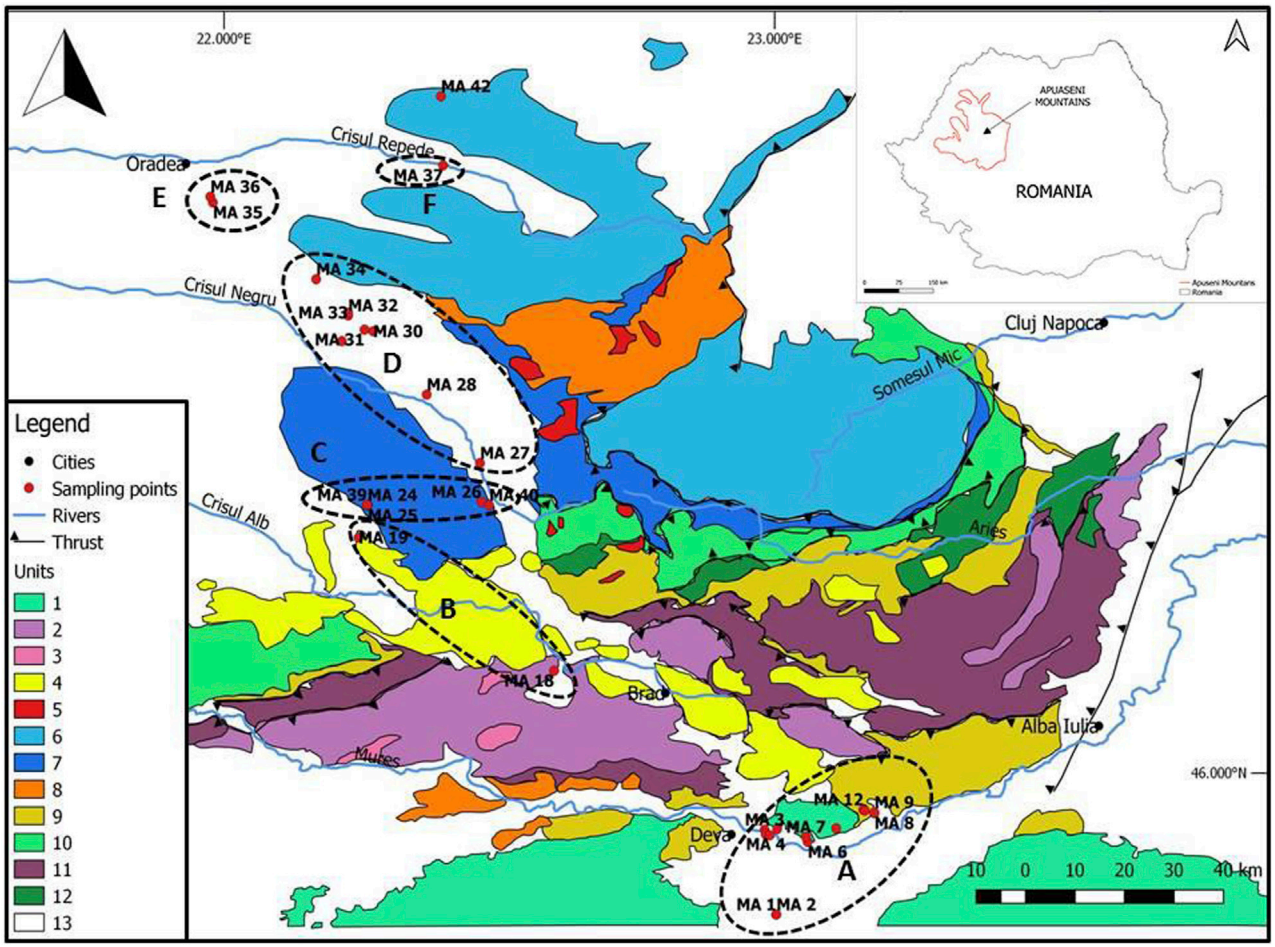


FIGURE 1 | The general geological structure of the Apuseni Mts. and distribution of the investigated areas (map modified after Kounov and Schmid, 2013; Gallhofer et al., 2017). 1. Supragetic, getic nappes; 2. Ophiolites (mainly Jurassic); 3. Jurassic granitoids; 4. Neogene magmatic rocks; 5. Late Cretaceous intrusions; 6. Bihor nappe; 7. Codru nappe system; 8. Late Cretaceous volcanics; 9. Gosau-type sediments; 10. Highiş-Poiana, Biharia, Muncel-Lupşa nappes; 11. Early Cretaceous flysch; 12. Baia de Arieş nappe; 13. Paleogene to recent sedimentary units; A—Mureş area; B—Zarand basin; C—Moneasa-Vaşcău; D—Beiuş Depression; E—Felix area; F—Vad-Borod Depression.

widely opening to the Pannonian Depression. The following localities have been investigated: Ştei, Beiuş, Răbăgani, Coşdeni, Albeşti, Rotăreşti and Ceica. A similar but smaller depression occurs along Crişul Repede River, where Aleşd well was sampled (F). Baile Felix is located on a westward extension of the Mesozoic carbonate units to the Pannonian Depression (E). The northernmost investigated source is Pădurea Neagră (MA 42), laying on the northern edge of the Apuseni metamorphic units (Plopis Mts.).

MATERIAL AND METHODS

Three field campaigns for site investigation and sample collection were conducted—the southern area in October 2018, the northern area in February 2019, and samples 38 to 42 in November 2019 (**Supplementary Table S1**—Supplementary material). A total of 42 sampling points has been selected, 20 of them being located in the southern area, and 22 in the northern one (**Figure 1**). The coordinates and elevation of the sampling points are inserted in **Supplementary Table S1**. A GoogleEarth map showing the position of the sampling points is available as **Supplementary Figure S1** in Supplementary material. The sampling sites were selected based on the water temperature at the outlet, considering that temperatures higher than 10°C may reveal a potential geothermal influence. The background information was mainly extracted from the works of Orăşeanu (2016, 2020) and Pricăjan (1972). The investigated physico-chemical parameters (temperature—T°C, pH, redox potential—Eh, and electrical conductivity—EC) were measured *in situ*, using a portable multiparameter instrument (WTW Multi 350i), which was previously calibrated using standard solutions. For the determination of alkalinity on site as HCO_3, the titrimetric method with methylorange was applied, using a microdosimeter. The flow rate

(**Supplementary Table S1**) was determined where possible as an average of more measurements, by measuring the filling time in calibrated vessels (Nicula et al., 2019).

Water samples for ion analysis have been collected in 250-ml pre-cleaned polyethylene bottles. The samples were filtered in the field by using a syringe and 0.45 μm Millipore™ filters, and then transported in cool boxes to the laboratory, where they have been stored at 4°C in the refrigerator.

Chemical analyses were performed in the Laboratories of the Faculty of Environmental Science and Engineering, Babeș-Bolyai University. A Dionex 1500 IC ion chromatography system was used for the dissolved ion analysis (F^-, Cl^-, Br^-, NO_2^-, NO_3^-, SO_4^{2-}, PO_4^{3-}, Li^+, Na^+, K^+, NH_4^+, Mg^{2+}, and Ca^{2+}).

The quantifications were performed based on the external standard method, using the calibration curves plotted for six standard solutions prepared by serial dilutions of the stock solutions: Dionex™ Combined Seven Anion Standard II/ 057590 and Dionex™ Combined Six Cation Standard-II/ 046070. The method proved to have a good linearity (R^2 > 0.999) and low detection limits. The limits of detection (LoD) were: 10.3 μg/L (Li^+), 12.2 μg/L (Na^+), 11.9 μg/L (NH_4^+), 12.7 μg/L (K^+), 11.8 μg/L (Mg^{2+}), 17.1 μg/L (Ca^{2+}), 10.1 μg/L (F^-), 21.2 μg/L (Cl^-), 12.4 μg/L (Br^-), 11.4 μg/L (NO_2^-), 12.0 μg/L (NO_3^-), 15.8 μg/L (PO_4^{3-}), and 12.7 μg/L (SO_4^{2-}).

In order to quantify the amount of dissolved H_2S as HS^- ions, 10 ml of water were collected in falcon tubes containing 2 ml of ammonia-cadmium solution. For preparing the ammonia-cadmium solution, 0.5 mol of $Cd(CH_3COO)_2$ was dissolved in 225 ml of 30%v/v NH_3 solution in 1 L of ultrapure (Milli-Q quality) water. At the final stage, the samples are prepared based on the methodology developed by Montegrossi et al. (2006), and measured by ion-chromatography as sulfate ions.

Distinct samples were collected for measuring the metal content. The samples were filtered in the field, using 0.45 μm syringe filters, and acidified to pH = 2 with HNO_3 65% (Merck). The analyses were performed by atomic absorption spectrometry (AAS), by using a ZEEnit 700 system (Analytik Jena) equipped with air—acetylene burner and a specific hollow-cathode lamp for each metal. The calibration curves were plotted for six standard solutions prepared by serial dilutions of an ICP multi-element standard solution (1,000 mg/L, standard IV/ 111355, Merck). The method proved to have good linearity (R^2 > 0.999). The detection limits for flame atomization were 12 μg/L (Fe and Cd), 35.0 μg/L (Cr), 38 μg/L (Ni), 13 μg/L (Zn), 83 μg/L (Pb), and 36 μg/L (Cu).

Mineral saturation indices (SI) for carbonates [calcite and aragonite—$CaCO_3$, dolomite—$CaMg(CO_3)_2$ and siderite ($FeCO_3$)], sulfates [gypsum—$CaSO_4{\cdot}2H_2O$, anhydrite $CaSO_4$, K-jarosite—$KFe_3\ 3(OH)_6(SO_4)_2$ and melanterite—$FeSO_4{\cdot}7H_2O$], halides (fluorite—CaF_2, halite—NaCl and sylvite—KCl) and iron oxides [goethite—α-FeO(OH), hematite—α-Fe_2O_3] minerals were used to predict the tendency for precipitation or dissolution of those minerals. A saturation index of 0 indicates thermodynamic equilibrium, while SI > 0 indicates oversaturation, and SI < 0 indicates undersaturation. Mineral saturation indices of waters from the study area were calculated at the *in situ* measured spring temperatures and pH using the PHREEQC computer program, with the default PHREEQC database (version 3, USGS, Denver, CO, United States). The most representative samples for each subarea have been selected.

For measuring the stable isotopes of water, the samples have been collected in 4-ml glass vials, and analyzed at the Babeș-Bolyai University Stable Isotope Laboratory using a Picarro L2130i cavity ring-down spectroscopy system. Detail on the method, calibration and errors are provided elsewhere (Wassenaar et al., 2013; Dumitru et al., 2017). The isotopic data are expressed using the standard notation, as δ (‰) = ($R_{sample}/R_{standard}$ −1) × 1,000. Internal laboratory standards calibrated with international standards VSMOW2 and VSLAP2 were used for data calibration. The measurement spectra were analysed for spectral contamination (organic interferences) using the ChemCorrect software after each measurement. None of the samples showed spectral contamination that can affect the isotopic measurement.

RESULTS AND DISCUSSION

Physicochemical Features

The physicochemical parameters measured in the field are listed in **Supplementary Table S1**. The pH of the waters ranges between 6.16 (MA 42—Pădurea Neagră) and 8.80 (MA 18—Vața Băi 2). The waters collected from the southern area generally show lower pH than the samples from the northern area, reflecting the presence of CO_2 in free and dissolved forms, in most of the samples. The main exception to this general trend is Pădurea Neagră, which shows the lowest pH, although located in the northern area, due to the CO_2 content.

Many of the investigated water sources show temperature at the outlet between 20 and 30°C (19 out of 42 sources). This is the case of the sources from the areas of Călan, Rapolt (Banpotoc, Rapolțel, Rovina, and Nătău), Geoagiu, Moneasa, Răbăgani, and La Feredee (subarea A). Higher temperatures, between 30 and 40°C, were measured in six sources, at Geoagiu (one source), Dezna, Vața, Felix, and Aleșd. Temperatures above 40°C were recorded in only two deep wells (subarea D), from Ștei (44.5°C) and Beiuș (79.8°C). Fifteen of the investigated sources show temperatures between 11 and 20°C, however they were taken into account, as compared to the background temperatures, a geothermal influence is visible. Low electrical conductivities, below 500 μS/cm, were recorded in Moneasa area and in the sources located close to the Pannonian Basin, as Felix, Dezna, and Beiuș Basin. The temperature and electrical conductivity of the water released by drilled wells is generally higher than in the case of springs. The springs are likely influenced by the shallow infiltration water.

Water Chemistry and Isotopic Composition

The concentration of the main cations (Na^+, K^+, Li^+, NH_4^+, Ca^{2+}, and Mg^{2+}) and anions (Cl^-, F^-, NO_3^-, HCO_3^-, and SO_4^{2-}) are listed in **Supplementary Table S2**—Supplementary material. As revealed by the Piper diagram (**Figure 2**), the HCO_3 water-type is dominant for most of the sampled waters. The cation

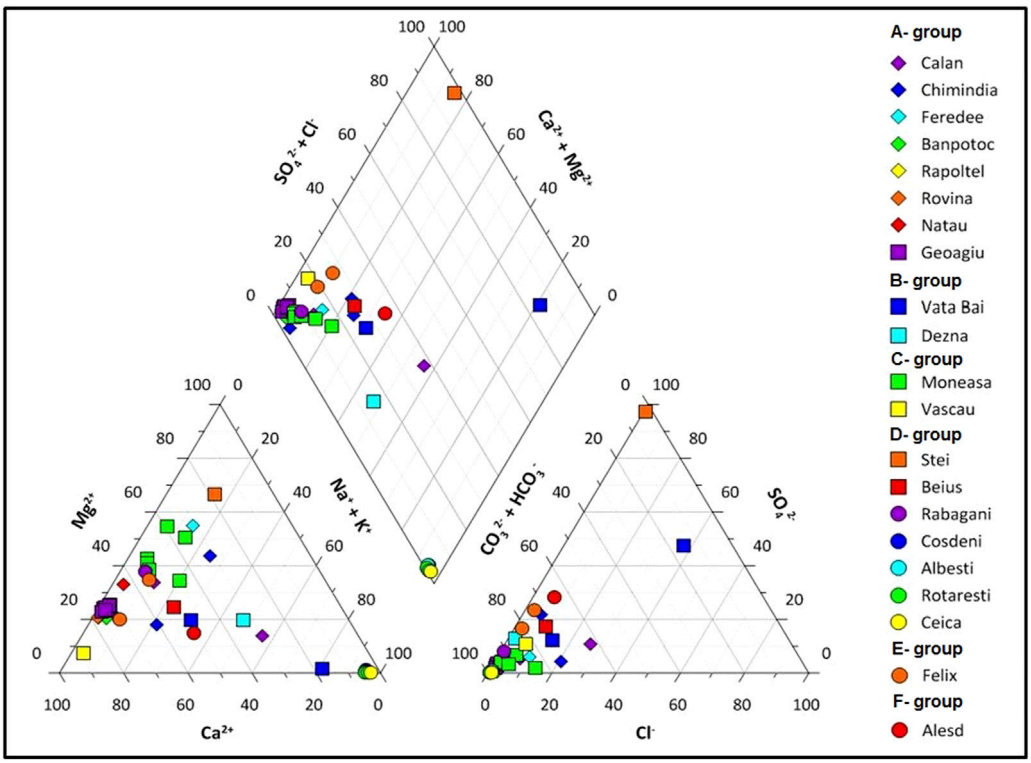


FIGURE 2 | Piper plot showing the hydrochemical type of the investigated waters.

composition is more variable, generally in the range of the Ca-Mg type. The Ca (Mg)—HCO_3 water type is also dominant in the surface water and cold aquifers in the area. This situation is expected, taking into account that most of the aquifers are confined in carbonate reservoirs. Particular features show the waters from the western part of the investigated area, with affinities with the Pannonian Basin (Ceica, Rotărești, Coșdeni, and Albești), with a very peculiar Na-HCO_3 type. This particular water type is common in the Pannonian Basin and it is generally explained by cation exchange and dissolution of minerals such as mica and feldspars (Rowland et al., 2011 and references therein). Different hydrochemical features by respect to the general trend are noticed in the case of the Mg-SO_4 water from Ștei well (MA 27), and Na-SO_4-Cl water from Vața Băi (MA 18). The total ionic salinity (TIS) plot (**Supplementary Figure S2** Supplementary material) indicates relatively low salinities for most of the samples, mainly determined by the HCO_3^--Cl^- ion pair. It is visible the exception in the case of SO_4^{2-}-rich MA 27 water. The MA 34 Ceica and MA 41 Chimindia samples, with high HCO_3+Cl contents (55.06 and 34.10 meq/L, respectively), and low SO_4 content, fall outside the plot. The AAS analysis has revealed metal concentrations (Cu, Cr, Ni, Pb, Zn, and Cd) below the detection limit in all the samples. The only metal with high concentrations is iron, that is detectable in all samples, and shows higher contents in the CO_2-rich, sparkling waters, also revealed by the Fe-hydroxide yellow deposits around the source. The concentrations of iron were between 0.013 and 4.97 mg/L.

Lithium (Li^+) was found in only two samples: MA 34 (1.06 mg/L) and MA 35 (0.01 mg/L). The sodium (Na^+) concentrations were between 1.1 and 794.23 mg/L (standard deviation σ = 155.68). Potassium (K^+) has shown concentrations between 0.02 and 55.59 mg/L (σ = 14.98). Calcium (Ca^{2+}) and magnesium (Mg^{2+}) are generally abundant in the analyzed waters, with concentrations between 4.02 and 649 mg/L (σ = 132.55) for calcium, and 0.22–545.33 mg/L (σ = 84.34) for magnesium. Ammonium (NH_4^+) was not identified in the analyzed samples (LoD = 11.9 µg/L NH_4^+).

The chloride (Cl^-) and sulphate (SO_4^{2-}) anions were identified in all the analyzed water samples, with concentrations between 1.31 and 260.38 mg/L for chloride (σ = 50.74), and sulphate concentrations between 0.37 and 875.17 mg/L (σ = 144.50). The fluoride (F^-) concentrations were between 0.02 and 2.78 mg/L. Nitrate (NO_3^-) concentration has shown values between 0.04 and 160 mg/L, while nitrite (NO_2^-) was found in a single sample (0.61 mg/L in MA 17). Bromide (Br^-) and phosphate (PO_4^{3-}) concentrations were below the detection limit in all the investigated samples. Alkalinity measured as HCO_3^- varied in the range of 115.9 mg/L to 2,754.15 mg/L (σ = 766.87).

Some of the investigated sources contain gases in free or dissolved form. Orășeanu (2020) reports the occurrence of gases in thermal and non-thermal waters in different units of the Apuseni Mts: Beiuș Basin—Vașcău, Moneasa, Rapolt area, Călan, Bihor Mts., Pădurea Craiului Mts. In most of the cases, the composition of the gas mixtures is dominated by nitrogen, and the N_2-O_2 ratio suggests their atmospheric origin. Most of the

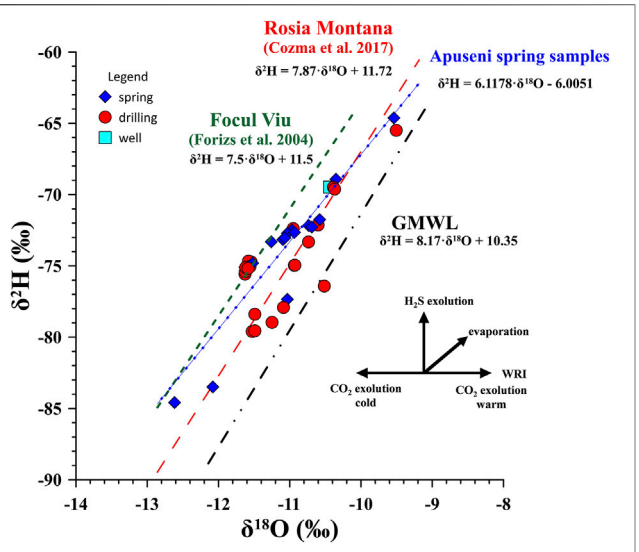


FIGURE 3 | Water stable isotope composition of the sampled sources. Symbols as in **Figure 2**.

sampling locations in the southern area (Călan, La Feredee, Geoagiu, and Chimindia), and some sites from the western part of the study area (Felix, Ceica, Beius), as well as Pădurea Neagră in the north, contain various proportions of CO_2. High concentrations of methane were found on the western side, as free gas at Ceica, or dissolved with much lower concentrations at Chimindia, Geoagiu, Albeşti, and Rotăreşti. The presence of hydrocarbons in water in this area was also reported by Rowland et al. (2011), Ionescu et al. (2017) and Baciu et al. (2018).

Most of the samples contain small amounts of dissolved H_2S. The highest amount was found in the Southern Apuseni area, and in some cases in the western part of Beiuş Depression, with the highest concentration in Ştei borehole (109.07 mg/L).

The saturation indices (SI) generally show slight oversaturation in aragonite, calcite and dolomite (**Supplementary Table S3**—Supplementary material). In the areas of Călan, Banpotoc, Rapolţel, and Geoagiu (Group A), where CO_2 emissions are also present, this is also indicated by the presence of thick travertine deposits. Same tendency can be observed at Vaţa, Dezna, and in Beiuş and Vad-Borod depressions, but without travertine deposition. Undersaturation by respect to the carbonates has been found in Stei and Pădurea Neagră sites. Most of the samples show oversaturation in iron minerals goethite and hematite. Undersaturation by respect to sulphate minerals is the common case in the study area. The highest SI for sulphate minerals was found in Ştei well.

The stable isotope values, as presented in **Figure 3**, confirm the meteoric origin for all the investigated sources. In most of the cases, the values plot along the LMWL drawn by Cozma et al. (2017) for Roşia Montană, while another part are located on the LMWL drawn by Forizs et al. (2004) based on the isotopic composition of samples from Focul Viu ice cave. The correlation line intersects all three water lines (GMWL, Focul Viu, and Roşia Montană), indicating the possibility that the samples fall along this theoretical "mixing" line. Based on this we infer that the samples intersecting the Focul Viu line could be of a deeper circulation, "older water", while the ones intersecting Roşia Montană LMWL could have a shallower, more rapid circulation. However, further analyses are needed to demonstrate this. The range of elevations of the sampling points is relatively narrow, spanning over 226 m (from 139 to 365 m. a.s.l.), thus the effect of elevation on the isotopic composition is expected to be less significant.

Based on GNIP precipitation data from IAEA (Nucleus server) for Romania, the average $\delta^{18}O$ and $\delta^{2}H$ is –8.91 and –63.08‰, respectively. These values are not significantly different from GNIR surface water data from IAEA (Nucleus server) for Romania (–9.90‰ and –70.60‰). The average of the $\delta^{18}O$ and $\delta^{2}H$ values in the case of the springs we investigated is –11.62‰ and –75.87‰, respectively. The limited number of samples and the lack of drilled wells water ages prevents us from further advancing in the interpretation of the isotopic data.

Within the same area, significant differences in the position of points along the LMWL may be observed, supporting the variability of the residence time for the concerned aquifers and the influence of other factors, as exsolution of CO_2 from water exposed to atmospheric temperature and pressure, in the southern area (e.g., Geoagiu). Evaporation may also influence the results when the samples have been collected from open pools, as in the case of La Feredee and Călan, or when the water path through pipelines from the source to the sampling outlet is long, and contact with atmospheric air is possible.

The content and ratio of some indicative chemical compounds from geothermal waters may be indicative for the reservoir temperature. In the case of our particular study area, the Giggenbach ternary plot and several cation geothermometers have been used. In the Giggenbach ternary diagram (**Figure 4**), most of the points fall in the Immature waters field, also suggesting shallow circulation. The samples from Beiuş Depression plot in the partial equilibration field. They contain different amounts of hydrocarbons, as reported by Ionescu et al. (2017). The inferred equilibrium temperature based on the Giggenbach diagram is around 60°C for Beiuş Depression, excepting Ceica, which shows the highest amount of methane in solution but also as free gas, with an equilibrium temperature around 160°C.

CONCLUSION

In the Apuseni Mountains and the adjacent southern and western areas, the geothermal potential is revealed by several thermal water sources and localized emissions of CO_2. The temperature of the investigated sources is low (hypothermal, between 20 and 30°C) in most of the cases, with the exception of the deep wells (2000 m deep), that may rise up to 80°C.

Chemical and isotopic analyses were performed on samples collected from 42 locations. The dominant hydrochemical type is

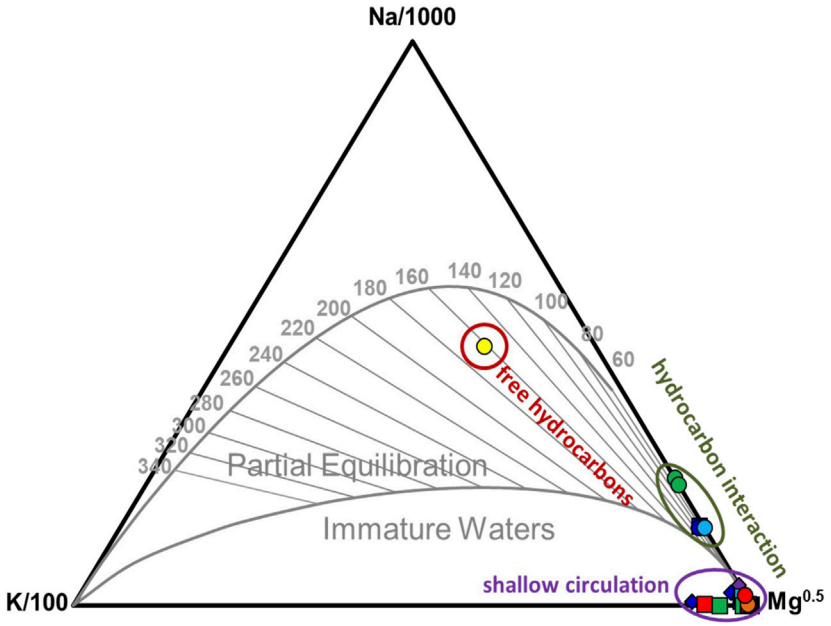


FIGURE 4 | Position of the sampled waters in the Giggenbach plot.

Ca-HCO_3. Only in the northern part of the study area (Beiuș Depression), at some points, the waters exhibit Na-HCO_3 type. The isotopic measurements indicate recharging of the aquifers with meteoric water and a predominantly shallow circulation. The short time of water residence in the aquifer limits the processes of water-rock interaction. The geochemical features and the structural setting of the study area suggest two main heat sources for the thermal aquifers in the Apuseni Mts. The Southern Apuseni area hosts large volumes of Neogene igneous rocks, with the last episode of magmatic activity during the Early Pleistocene. Strong CO_2 emissions occur in the area, possibly related to carbonate metamorphism. A more detailed geochemical investigation, currently in progress, will likely increase our understanding on the occurrence and nature of the heat sources in the investigated area.

The western part of the study area corresponds to the limit between the Apuseni Mts. and the Pannonian Depression, with its demonstrated high heat flux. The geochemical features of the investigated waters from this area suggest their affinity with the Pannonian geothermal region, expressed by the Na-HCO_3 hydrochemical type, occurrence of dissolved hydrocarbons, and relatively high temperatures.

This study represents a preliminary approach of the hydrogeochemical and geothermal features of the Apuseni Mountains, an area that has the potential to yield further interesting results. Additional isotopic data are needed in order to better understand these thermal and mineral water systems. A geothermal model of the Apuseni Mts. region would greatly benefit from the geochemical data, based on compositional and isotopic analysis of fluids (water and gas), and accurate geothermometers.

DATA AVAILABILITY STATEMENT

The original contributions presented in the study are included in the article/**Supplementary Material**, further inquiries can be directed to the corresponding author.

AUTHOR CONTRIBUTIONS

A-MN, AI, and CB contributed to the conception and design of this study, writing the manuscript and field work; I-CP contributed to the sampling and fieldwork; CR contributed to the laboratory analyses; FLF contributed to the laboratory analyses and isotope data interpretation; and IO contributed to the fieldwork and literature data analysis. All authors contributed to manuscript revision, read and approved the submitted version.

ACKNOWLEDGMENTS

The authors acknowledge support from the Deep Energy and Reservoir and Fluxes communities of the Deep Carbon Observatory. We also thank the Editor of this special volume, and three reviewers, whose comments and suggestions greatly helped improve and clarify this manuscript.

SUPPLEMENTARY MATERIAL

The Supplementary Material for this article can be found online at: https://www.frontiersin.org/articles/10.3389/feart.2021.648179/full#supplementary-material

REFERENCES

Baciu, C., Ionescu, A., and Etiope, G. (2018). Hydrocarbon Seeps in Romania: Gas Origin and Release to the Atmosphere. *Mar. Pet. Geology.* 89 (1), 130–143. doi:10.1016/j.marpetgeo.2017.06.015

Cozma, A., Baciu, C., Papp, D., Roşian, G., and Pop, C. (2017). Isotopic Composition of Precipitation in Western Transylvania (Romania) Reflected by Two Local Meteoric Water Lines. *Carpathian J. Earth Environ. Sci.* 12, 357–364.

Demetrescu, C., and Andreescu, M. (1994). On the Thermal Regime of Some Tectonic Units in a continental Collision Environment in Romania. *Tectonophysics* 230, 265–276. doi:10.1016/0040-1951(94)90140-6

Dumitru, O. A., Forray, F. L., Fornós, J. J., Ersek, V., and Onac, B. P. (2017). Water Isotopic Variability in Mallorca: A Path to Understanding Past Changes in Hydroclimate. *Hydrol. Process.* 31, 104–116. doi:10.1002/hyp.10978

Fodorean, F. (2012). "Spa" Vignettes in Tabula Peutingeriana. Travelling Ad Aquas: thermal Water Resources in Roman Dacia. *Ephemeris Napocensis* 22, 211–221.

Forizs, I., Kern, Z., Szanto, Z., Nagy, B., Palcsu, L., and Molnar, M. (2004). Environmental Isotopes Study on Perennial Ice in the Focul Viu Ice Cave, Bihor Mountains, Romania. *Theor. Appl. Karstology* 17, 61–69.

Gallhofer, D., von Quadt, A., Schmid, S. M., Guillong, M., Peytcheva, I., and Seghedi, I. (2017). Magmatic and Tectonic History of Jurassic Ophiolites and Associated Granitoids from the South Apuseni Mountains (Romania). *Swiss J. Geosci.* 110, 699–719. doi:10.1007/s00015-016-0231-6

Horváth, F., Bada, G., Szafián, P., Tari, G., Ádám, A., and Cloetingh, S. (2006). Formation and Deformation of the Pannonian Basin: Constraints from Observational Data. *Geol. Soc. Lond. Mem.* 32, 191–206. doi:10.1144/gsl.mem.2006.032.01.11

Institutul de Balneologie şi Fizioterapie (IBF) (1970). *Apele Minerale Şi Namolurile Terapeutice Din Republica Populară Romînă (Mineral Waters and Therapeutic Muds from Romania)*, Vols. I–IV. Bucharest: Edit. Medic. in Romanian.

Ionescu, A., Baciu, C., Kis, B.-M., and Sauer, P. E. (2017). Evaluation of Dissolved Light Hydrocarbons in Different Geological Settings in Romania. *Chem. Geology.* 469, 230–245. doi:10.1016/j.chemgeo.2017.04.017

Kounov, A., and Schmid, S. M. (2013). Fission-track Constraints on the thermal and Tectonic Evolution of the Apuseni Mountains (Romania). *Int. J. Earth Sci.* 102, 07–233. doi:10.1007/s00531-012-0800-5

Montegrossi, G., Tassi, F., Vaselli, O., Bidini, E., and Minissale, A. (2006). A New, Rapid and Reliable Method for the Determination of Reduced sulphur (S2−) Species in Natural Water Discharges. *Appl. Geochem.* 21, 849–857. doi:10.1016/j.apgeochem.2006.02.007

Mutihac, V. (1990). *Structura Geologică a Teritoriului României (The Geological Structure of Romania)*. Bucharest: Edit. Tehn., 418. in Romanian.

Nicula, A. M., Ionescu, A., Pop, I. C., Orăşeanu, I., and Baciu, C. (2019). Preliminary Considerations Regarding the Geothermal Potential in the Apuseni Mountains Area. *Studia UBB Ambientum* 64 (2), 45–56. doi:10.24193/subbambientum.2019.2.04

Orăşeanu, I. (2016). *Hidrogeologia Carstului Din Munţii Apuseni (Karst Hydrogeology from Apuseni Mts.)*. Oradea: Edit. Belvedere, 300. in Romanian.

Orăşeanu, I. (2020). *Hidrogeologia Carstului Din Munţii Apuseni (Karst Hydrogeology from Apuseni Mts.*. 2nd ed. Oradea: Edit. Belvedere, 349. (in Romanian).

Orăşeanu, I. (1987). Hydrogeological Study of Moneasa Area (Codru Moma Mountains). *Theor. Appl. Karstology* 3, 175–199.

Orăşeanu, I., and Mather, J. (2000). Karst Hydrogeology and Origin of thermal Waters in the Codru Moma Mountains, Romania. *Hydrogeology J.* 8, 379–389. doi:10.1007/s100400000080

Pécskay, Z., Edelstein, O., Seghedi, I., Szakács, A., Kovács, M., Crihon, M., et al. (1995). K-Ar Datings of Neogene-Quaternary Calcalkaline Volcanic Rocks in Romania. *Acta Vulcanologica* 7 (2), 53–61.

Pricăjan, A. (1972). *Apele minerale si termale din Romania (Mineral and thermal waters from Romania)*. Bucharest: Tehn., 206. in Romanian.

Pricăjan, A., and Airinei, S. (1981). *Bogatia Hidrotermala Balneara Din Romania (The Hydrothermal Wealth of Romania)*. Bucharest: Stiintifica si Enciclopedica, 134. in Romanian.

Rman, N., Bălan, L.-L., Bobovečki, I., Gál, N., Jolović, B., Lapanje, A., et al. (2019). Geothermal Sources and Utilization Practice in Six Countries along the Southern Part of the Pannonian basin. *Environ. Earth Sci.* 79, 1. doi:10.1007/s12665-019-8746-6

Rowland, H. A. L., Omoregie, E. O., Millot, R., Jimenez, C., Mertens, J., Baciu, C., et al. (2011). Geochemistry and Arsenic Behaviour in Groundwater Resources of the Pannonian Basin (Hungary and Romania). *Appl. Geochem.* 26, 1–17. doi:10.1016/j.apgeochem.2010.10.006

Roşu, E., Pécskay, Z., Ştefan, A., Popescu, G., Panaiotu, C., and Panaiotu, C. E. (1997). The Evolution of the Neogene Volcanism in the Apuseni Mountains (Romania): Constraints from New K-Ar Data. *Geologica Carpathica* 48 (6), 353–359.

Roşu, E., Seghedi, I., Downes, H., Alderton, D. H. M., Szakács, A., Pécskay, Z., et al. (2004). Extension-related Miocene Calc-Alkaline Magmatism in the Apuseni Mountains, Romania: Origin of Magmas. *Schweizerische Mineralogische und Petrographische Mitteilungen* 84, 153–172.

Schmid, S. M., Bernoulli, D., Fügenschuh, B., Matenco, L., Schefer, S., Schuster, R., et al. (2008). The Alpine-Carpathian-Dinaridic Orogenic System: Correlation and Evolution of Tectonic Units. *Swiss J. Geosci.* 101, 139–183. doi:10.1007/s00015-008-1247-3

Schmid, S. M., Fügenschuh, B., Kounov, A., Maţenco, L., Nievergelt, P., Oberhänsli, R., et al. (2020). Tectonic Units of the Alpine Collision Zone between Eastern Alps and Western Turkey. *Gondwana Res.* 78, 308–374. doi:10.1016/j.gr.2019.07.005

Seghedi, I. (2004). "Geological Evolution of the Apuseni Mountains with Emphasis on the Neogene Magmatism – a Review," in *Au-Ag-telluride Deposits of the Golden Quadrilateral, Apuseni Mts., Romania, Guidebook of the International Field Workshop of IGCP Project 486, IAGOD Guidebook Series*. Editors N.J. Cook and C.L. Ciobanu, 11, 5–23.

Seghedi, I., and Downes, H. (2011). Geochemistry and Tectonic Development of Cenozoic Magmatism in the Carpathian-Pannonian Region. *Gondwana Res.* 20 (4), 655–672. doi:10.1016/j.gr.2011.06.009

Seghedi, I., Maţenco, L., Downes, H., Mason, P. R. D., Szakács, A., and Pécskay, Z. (2011). Tectonic Significance of Changes in post-subduction Pliocene-Quaternary Magmatism in the South East Part of the Carpathian-Pannonian Region. *Tectonophysics* 502, 146–157. doi:10.1016/j.tecto.2009.12.003

Szocs, T., Rman, N., Rotár-Szalkai, Á., Tóth, G., Lapanje, A., Černák, R., et al. (2018). The Upper Pannonian thermal Aquifer: Cross Border Cooperation as an Essential Step to Transboundary Groundwater Management. *J. Hydrol. Reg. Stud.* 20, 128–144. doi:10.1016/j.ejrh.2018.02.004

Săndulescu, M. (1984). *Geotectonica Romaniei (Geotectonics of Romania)*. Bucuresti: Editura Academiei Romane, 336. in Romanian.

Tiliţă, M., Lenkey, L., Maţenco, L., Horvath, F., Suranyi, G., and Cloetingh, S. (2018). Heat Flow Modelling in the Transylvanian basin: Implications for the Evolution of the Intra Carpathian Area. *Glob. Planet. Change* 171, 148–166. doi:10.1016/j.gloplacha.2018.07.007

Wassenaar, L. I., Coplen, T. B., and Aggarwal, P. K. (2013). Approaches for Achieving Long-Term Accuracy and Precision of δ18O and δ2H for Waters Analyzed Using Laser Absorption Spectrometers. *Environ. Sci. Technol.* 48, 1123–1131. doi:10.1021/es403354n

Conflict of Interest: The authors declare that the research was conducted in the absence of any commercial or financial relationships that could be construed as a potential conflict of interest.

Publisher's Note: All claims expressed in this article are solely those of the authors and do not necessarily represent those of their affiliated organizations, or those of the publisher, the editors and the reviewers. Any product that may be evaluated in this article, or claim that may be made by its manufacturer, is not guaranteed or endorsed by the publisher.

Copyright © 2021 Nicula, Ionescu, Pop, Roba, Forray, Orăşeanu and Baciu. This is an open-access article distributed under the terms of the Creative Commons Attribution License (CC BY). The use, distribution or reproduction in other forums is permitted, provided the original author(s) and the copyright owner(s) are credited and that the original publication in this journal is cited, in accordance with accepted academic practice. No use, distribution or reproduction is permitted which does not comply with these terms.

frontiers in Earth Science

ORIGINAL RESEARCH
published: 23 August 2021
doi: 10.3389/feart.2021.678834

Black Sea Methane Flares From the Seafloor: Tracking Outgassing by Using Passive Acoustics

Manfredi Longo[1], Gianluca Lazzaro[1], Cinzia Giuseppina Caruso[1], Vlad Radulescu[2], Raluca Radulescu[2], Sergio Simone Sciré Scappuzzo[1], Dominique Birot[3] and Francesco Italiano[1]*

[1]Istituto Nazionale di Geofisica e Vulcanologia, INGV, Palermo, Italy, [2]Institutul National de Cercetare - Dezvoltare pentru Geologie si Geoecologie Marina, GeoEcoMar, Constanta, Romania, [3]Département Ressources physiques et Ecosystèmes de fond de Mer (REM), Unité des Géosciences Marines, IFREMER, Brest, France

The Black Sea bottom is well known to be earth's largest anaerobic methane source, hosting a huge amount of cold seeps releasing significant volumes of methane of both thermogenic and biogenic origin. Taking into account the well-known effects of methane concerning global warming, including the warming up of the oceans, an effective monitoring of its output from the Black Sea is nowadays an essential target for interdisciplinary studies. We discuss the results achieved during monitoring campaigns aimed to detect and track methane flares from the seafloor of the Romanian sector of the Black Sea, in order to better constrain the possible mechanisms responsible for its injection from the marine sediments, through the water column, into the atmosphere. In the mainframe of the ENVRI-Plus project, we deployed a multidisciplinary seafloor observatory for short, mid and long time monitoring and collected samples of the water column. The multidisciplinary seafloor observatory was equipped with probes for passive acoustic signals, dissolved CH_4 and chemical-physical parameters. The collected data showed a high concentration of dissolved methane up to values of 5.8 micromol/L. Passive acoustics data in the frequencies range 40–2,500 Hz allow us to discriminate different degassing mechanisms and degassing styles. The acoustic energy associated with gas bubbling is interpreted as a consequence of the gas dynamics along the water column while the acoustic range 2–20 Hz reveals vibration mechanisms generated by gas dynamic's along the cracks and inside the sediments.

Keywords: methane, greenhouse gas, passive acoustics, bubbles, multidisciplinary submarine observatory

OPEN ACCESS

Edited by:
Zhilei Sun,
Qingdao Institute of Marine Geology (QIMG), China

Reviewed by:
Cuiling Xu,
Qingdao Institute of Marine Geology (QIMG), China
Jianghui Li,
University of Southampton, United Kingdom

****Correspondence:***
Manfredi Longo
manfredi.longo@ingv.it

Specialty section:
This article was submitted to Geochemistry, a section of the journal Frontiers in Earth Science

Received: *10 March 2021*
Accepted: *10 August 2021*
Published: *23 August 2021*

Citation:
Longo M, Lazzaro G, Caruso CG, Radulescu V, Radulescu R, Sciré Scappuzzo SS, Birot D and Italiano F (2021) Black Sea Methane Flares From the Seafloor: Tracking Outgassing by Using Passive Acoustics. Front. Earth Sci. 9:678834. doi: 10.3389/feart.2021.678834

INTRODUCTION

Methane is the second major contributor to the greenhouse effect after carbon dioxide (Shindell et al., 2009). On a 100 years time scale, it holds a global warming potential that is 20–40 times higher than CO_2 (Gentz et al., 2013). Methane is generated in sediments and sedimentary rocks by the natural destruction or microbial mediated degradation of pre-existing organic matter, (Judd et al., 2002; Judd 2003). The generation of thermogenic methane occurs when complex (long-chain organic) molecules are broken down by high-temperature and high-pressure conditions, at depths typically exceeding 1 km (Schoell 1988; Whiticar 1990; Floodgate and Judd 1992). Once generated, methane migrates towards the surface (land or seabed), although some becomes

trapped to form natural gas accumulations, and some other is sequestered by the formation of gas hydrates, ice-like mixtures of water and gas. Gas hydrate molecules are trapped within a cage-like framework of hydrogen-bonded water molecules, formed under very specific temperature and pressure conditions where sediments contain both water and an adequate supply of gas. These conditions are found within seabed sediments, where the water depth exceeds 300–500 m and the water temperature is less than 5°C (Ginsburg and Soloviev 1998; Ainslie and McColm, 1998, 1999). Gas hydrates may represent the largest methane reservoir of the planet. However, the majority of this gas is safely "locked" within the hydrates, and will remain there unless there is a change in the temperature/pressure conditions critical to hydrate stability. There is a growing concern that much higher atmospheric methane concentrations may result in the future, if a substantial amount of the huge methane pools stored in the ocean (Milkov 2004) and lake/reservoir sediments will be released (Buffett 2000). Gas seeps are known to be associated with leakage from gas reservoirs, shallow gas accumulations and from gas hydrates. However, the majority of methane escaping from deep-water hydrates is likely to dissolve in the water column rather than enter the atmosphere. As bubbles rise from the seabed, a portion of methane is lost to the hydrosphere by solution and microbial oxidation. The ability of methane bubbles to survive after crossing the water column is dependent upon the bubble size, the rise velocity and the presence of surfactants on the bubble surface (Leifer and Patro 2002). Surfacing bubble plumes are most likely to be found in shallow water (Hornafius et al., 1999). Judd (2000) suggested that a total of 0.4–12.2 Tg [CH_4]/year is emitted to the atmosphere from natural seabed seeps world-wide. Methane transfer from the seafloor to the atmosphere may become an important issue affecting global climate change (Hovland et al., 1993; Etiope and Klusman, 2002; Judd, 2004; Etiope and Milkov, 2004). Moreover, methane injection into the water column may contribute to the ocean acidification due to its oxidation although in shallow shelf areas, like the Black Sea, the CH_4 release from the seafloor has a greater potential to enter the atmosphere. The Black Sea represents an ideal site for investigating the fate of marine methane as methane flares are widespread recognized from the continental shelf to the deepest part of the basin, where cold seeps (mostly biogenic as a consequence of chemosynthetic communities at the seafloor) are continuously vented into the water column. During 2019, in the mainframe of ENVRIplus, a Horizon 2020 project bringing together Environmental and Earth System Research Infrastructures, we carried out three oceanographic cruises over the Romanian sector of the Black Sea with the aim to better constrain the possible mechanisms of methane injection into the atmosphere by detecting methane flares at the seafloor and tracking them across the water column.

By the cooperation of three European Research Institutions (INGV, GeoEcoMar, IFREMER) a multidisciplinary submarine observatory (EMSO-MedIT 001) was deployed at the depth of 120 m for a short, 5 days-long, period (D1) in an area already identified by previous active acoustic surveys and characterized by the presence of a pockmark and widespread methane flares. The Observatory was then recovered, the data downloaded and then re-deployed a few hundred meters away from the first site, for a 2 months-long monitoring period (D2). Once again, the Observatory was deployed for a 4 months–long acquisition period (D3) over an area close to the D1 site, in order to obtain a clear and long frame of that exhalative site, in the absence of any anthropic noise or external disturbance. The multidisciplinary seafloor observatory, able to operate in extreme environments up to the depth of 4,000 m, has been equipped with probes for passive acoustic signals, dissolved methane, temperature, hydrostatic pressure, conductivity, pH and turbidity. All the recorded data are stored in an internal mass storage and downloaded for analysis after each recovery.

During the first cruise, the water column was also sampled by Niskin bottles allowing us to improve the knowledge of its geochemical features. This paper accounts for the information gained by the passive acoustics coupled with the geochemical features of the dissolved gases. The results show the power of multidisciplinary submarine observatories in continuous monitoring of the gases discharges as well as the chemical-physical features of submarine environments, including the temporal changes due to anthropic and natural-induced processes. In particular, this paper poses the accent in passive acoustics as a tool to track gases escaping from seafloor focusing in mechanisms, detectable by hydrophone, generating noises and seismic vibrations, related to gas dynamics inside the sediment and along the water column.

Study Area

The study area is the NW sector of the Black Sea (**Figure 1**) where the composite Danube and Dnieper deep sea fans constitute a prominent morphological feature. These paleo-fans extend from the shelf-break, at about 200 m water depth, down to the abyssal plain of over 2000 m and were fed by rivers that drained into this area, notably the Danube, the Dnieper, the Dniester and the Bug (Wong et al., 1997). Nowadays, those rivers discharge an average annual total sediment of 65×10^6 t, 81% of which (52×10^6 t) is delivered by the Danube (Popa 1993). Such a huge deposition of organic-rich sediments especially at the shelf-edge deltas and the anoxic conditions below approximately 150 m that caused microbial degradation, led to the formation of shallow gas in the sub-bottom and therefore prolific gas seepage into the water column (Pape et al., 2008; Römer et al., 2020). Anoxic conditions below 150 m come from a persistently stratified water column due to the combination of the high freshwater supply from the numerous rivers and the inflow of highly saline Mediterranean waters via the Bosporus (Özsoy and Ünlüata, 1997). The sediments below the anoxic interface are the methane source for the Black Sea water column. Marine methane derives from biogenic and thermogenic processes occurring within those sediments and enters the water column by various pathways (Judd 2003). The gas discharge occurred as a dissolved methane flare or non-dissolved gaseous amounts of methane, escaping from sediments at the sea-bottom methane is therefore transferred to the water column either dissolved in the vented fluids or, in case of over-saturation, as gas bubbles (Dziak et al., 2018). When the gas discharge is persistent and vigorous, it leads

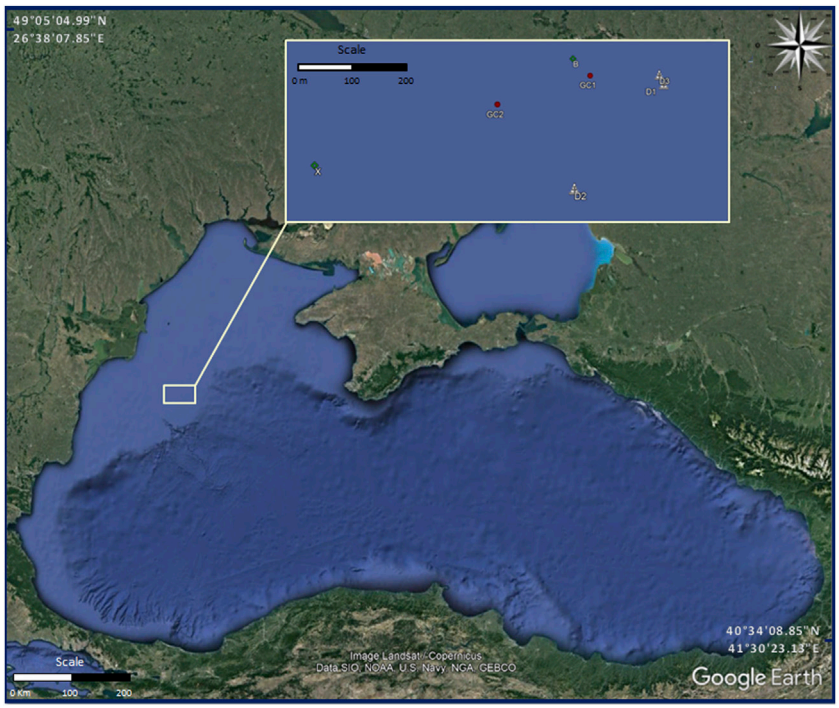


FIGURE 1 | Location map of the study area extracted from Google Earth. In the insert figure: D1 - 1st deployment; D2 - 2nd deployment; D3 - 3rd deployment; X and B - vertical cast; GC1 - 1st gravity core; GC2 - 2nd gravity core.

to the formation of large dissolved methane plumes. Common degassing style consists in an intermittent low-flux emanation of sub-millimetric bubble plumes, while under specific conditions the gas could be suddenly released generating almost continuous high flux emissions, characterized by even centimetric bubbles plumes (Leifer and Boles 2005; Leifer 2010; Leifer and Culling 2010). The dissolved methane is diluted by mixing with the surrounding ocean water and it is further oxidized by aerobic methanotrophs bacteria. Only in cases where dissolved methane reaches the surface-mixed layer in concentrations above saturation, it can be transferred to the atmosphere via sea-air gas exchange (Cynar and Yayanos, 1993; Mau et al., 2017).

The selected area shown in **Figure 1** (the Romanian sector of the Black Sea), hosts a large number of sites of methane-rich gases, from the continental shelf to the deepest part of the basin. It is consequently a good candidate for investigating the fate of marine methane, from the sedimentary layers throughout the water column to the atmosphere.

METHODS

Multidisciplinary Seafloor Observatory

The multidisciplinary seafloor observatory (built in the mainframe of the EMSO-Medit project) is a versatile underwater system, able to operate in extreme environments up to the depth of 4,000 m. It is able to automatically record and store a large spectrum of long-term data, coming from acoustic and chemical-physical sensors, using an open hardware architecture that allows to integrate any commercial underwater instrument. The observatory is composed of three hard anodized aluminum vessels, hosting electronic boards and batteries, connected together by underwater high-pressure type cables and connectors (**Figure 2**). Vessels and sensors are hosted on the nylon-made, main frame structure (1 m × 1 m x 1.6 m). The set of sensors used during these cruises is composed by:

- Hydrophone: HTI 94-SSQ
- Temperature: SeaBird SBE 3F
- Conductivity: SeaBird SBE 4C
- Depth (Pressure): SeaBird SBE 29
- pH: SeaBird SBE 18
- Turbidity: STM11
- Methane: Franatech K-METS, S/N:K4

Many efforts were made in order to have a modular and fully customizable hardware and software system architecture, allowing to easily set up the data collection configuration of the multidisciplinary observatory, e.g. to adapt the acquisition rate and the power consumption to the battery capacity and sensors needs.

The electronic system was designed to be able to acquire from both analog and digital signals. It consists of eight analog synchronous channels with configurable front-end (current, voltage or high impedance input), each channel can accept wide band signals (0.1 Hz–52 kHz) with 24-bit resolution. Digital inputs can communicate by serial protocols or Ethernet. The modular system also includes a dedicated power

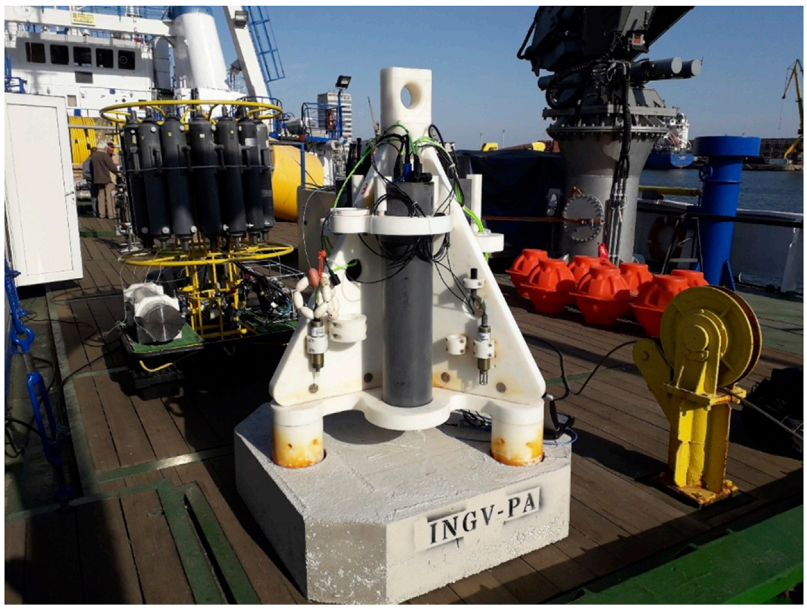


FIGURE 2 | Multidisciplinary seafloor observatory EMSO MedIT-001.

management board, allowing to selectively power each sensor or all sensors together. The special HW/SW design allows extremely low power consumption, thus obtaining extended autonomy, even with constrained battery volume resources. It is therefore possible to properly configure period and acquisition time to schedule sequences lasting even more than 1 year. Methane gas concentration was measured using Franatech K-METS, S/N: K4 sensor, calibrated to operate in the range from 100 nmol/L to 10 µmol/L. Following datasheet specifications in order to collect good quality data, prior to each acquisition the observatory electronics management software was configured to execute a preliminary 20 min warm-up, to stabilize its electronics response at the deployment conditions. It is reasonable to presume that there was no need for such a long warm-up period, since the sensor was submerged constantly during the three deployments and the relative humidity of the detector is supposed to be in a full stable condition.

The main data set used for this study was acquired during three oceanographic campaigns in 2019.

Deployment has been done by free fall from the research vessel, using a 1 ton concrete dead weight, while recovery has been guaranteed by acoustic releaser using the buoyancy effects of seven benthospheres.

The observatory was deployed and recovered three times, each time varying the distance from the flares area and the length of the observation period. The first and third deployment sites were indeed a few meters away each other, close to flares and surrounded by several gas emissions, while the second deployment site was at a distance of 275 m from the main emission area:

D1: Deployed on 3rd April 2019 at 120 m depth - Recovered on 07th April 2019;

D2: Deployed on 7th April 2019 at 117 m depth - Recovered on 04th June 2019;

D3: Deployed on 5th June 2019 at 121 m depth - Recovered on 26th September 2019.

Acoustic Records

Spectral Data Extrapolation

Hydrophone audio records along the three deployments revealed a variety of sounds, produced by different mechanisms that characterize distinct bands in the frequency spectrum analysis. Acoustic signals were sampled at 105 kHz with a 24-bit resolution A/D converter. The used hydrophone, based on a piezo-ceramic sensor element, was HTI-94-SSQ with a -198 dB re 1 V/µPa omnidirectional response sensitivity within 2 Hz–30 kHz frequency band, connected to a 40 dB fixed gain input channel. In order to perform long-term acquisition with a limited amount of storage capacity, audio recordings were bounded to segments of short duration. Segment length and data acquisition frequency were varied at each deployment (a total amount of 72 records of 10 s each were gathered per day during D2, while 12 daily records of 40 s each were acquired for D3). After a pre-processing down-sampling technique, that included anti-aliasing filtering for each record, two main approaches were used in order to inspect audio frames: at first, daily spectrograms of the resulting merged audio records were visually inspected in order to detect spectral signatures of the degassing process; then, each file was transformed to pressure signals, evaluating both manufacturer specified hydrophone sensitivity and the overall system gain; each acoustic record was then processed using spectral analysis, to extract power magnitude time-series for different acoustic frequencies bands of interest. Every acoustic record was down-sampled, in order to exclude high frequency induced noise, then low-pass filters were

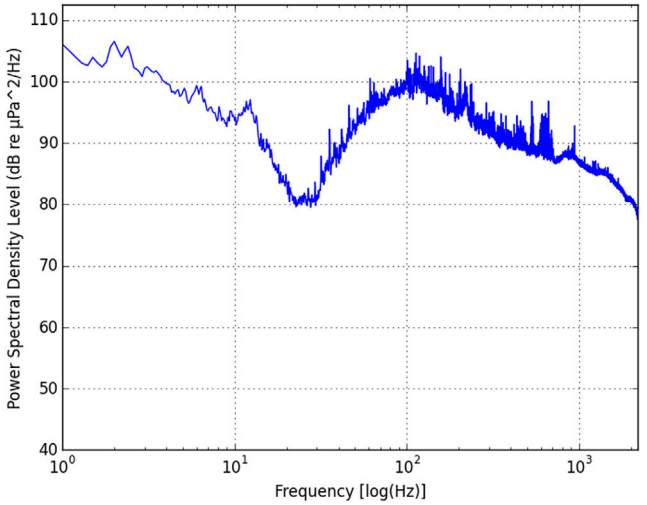


FIGURE 3 | Monthly averaged Power Spectrum Density (PSD) of June 2019, depicting the typical envelope of the ambient noise background of the area D3. Most energetic spikes in the range 30–1,000 Hz are related to intermittent ship traffic and wind noise. Infrasonic frequencies highlight the seismic events related to methane seep release. Single, less energetic spots above 1,000 Hz are likely related to bubble streams.

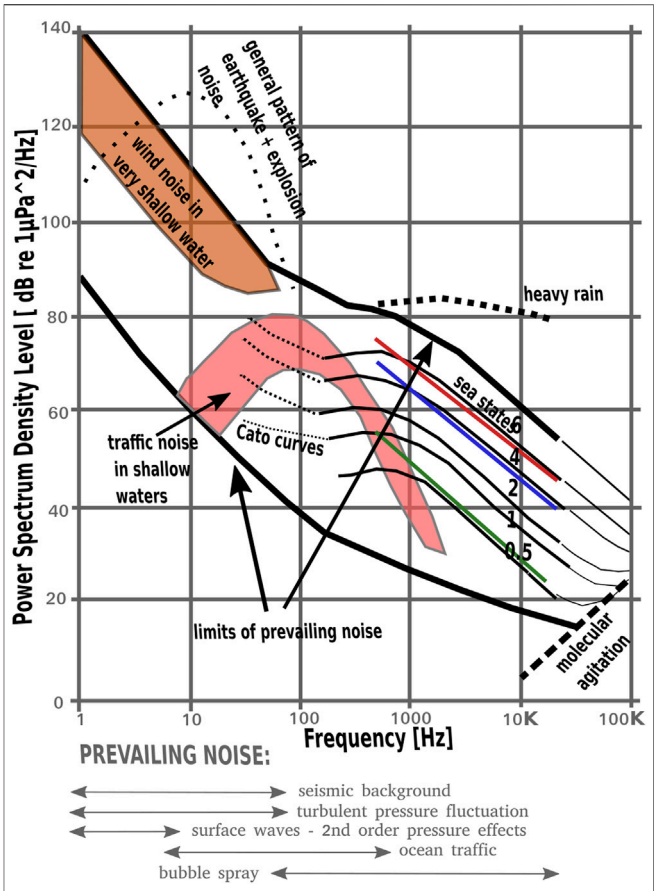


FIGURE 4 | Typical spectra and frequency distribution of underwater sound sources (Erbe, 2008, adapted from; Wenz (1962)). Black arrows indicate the frequency range covered by the sounds emitted from various sources. Thick black lines indicate limits of prevailing ambient noise. Sea states unit describe different wave heights (e.g. wind at Beaufort 4 = approx. sea state 3).

applied to remove inducted aliasing effects. Power Spectral Density (PSD) was then estimated for each band applying Welch's method (Gupta and Mehra 2013), on a 10 s long segment window with 50% overlapping factor, multiplied by Hanning window, together with a 6-pole band-pass Butterworth filter to selectively analyze each band. Acoustic average pressure (intensity magnitude) modulation, and frequency bin peaks values were then extracted from every selected frequency range. Chronological metadata series were used to analyze the magnitude modulation along time and thus provide a relative estimation of the flares flow rate changes. For weaker and intermittent or impulsive energy events, once visually recognized, the relative segments were analyzed using a short-time Fourier transform and a threshold algorithm was implemented following Peregrine, 1994 and Li et al., 2021 in order to identify and count bubbles events, obtaining a bubble size distribution for each deployment.

The power spectrum analysis, performed on the acoustic records, revealed that the areas surrounding the observatory deployment sites radiated significant acoustic energy at a wide frequency band, apart from the ones of the typical ambient noise, as depicted by **Figure 3**, where PSD representative of the entire month of June is shown. Nevertheless, ambient noise energy levels often overcome weaker seep-related signals, representing a challenge in using this methodology to fully track the release process behaviour over time.

Indeed, in a typical shallow underwater environment, ambient noise intensity regularly decreases from low frequencies with a slope varying from −8 to −10 dB/dec, notwithstanding that both the intensity and signature of spectral curves undergo variability in the presence of meteorological, biological and anthropogenic intermittent sources, especially in shallow sites (Wenz 1962; Wilcock et al., 2014). This represents the major difficulty of passive acoustic sources detection. A multiplicity of studies has been carried out to understand sources of underwater ambient noise that can be grouped in four representative frequency bands, each one related to different source mechanisms (Wenz 1962).

The low frequency band from 0.01 to 5 Hz is dominated by microseisms (seismic noise created by the nonlinear interaction of ocean waves) and represents the most energetic band. Spectral noise ranging from 5 to 200 Hz has a predominant anthropogenic source, produced mainly by shipping. Ships radiate a distinctive signature containing multiple harmonics, relative to the rotary machinery involved in the propulsion system (Wilcock et al., 2014 and references therein). In this band also wind induced noise can play a significant role in shallow sites. The central frequency, from 100 to 10,000 Hz, is therefore influenced by sea state and wind condition, where noise can be induced by rain droplets, shoaling gravity and breaking waves. Finally, spectral power above 10 kHz is produced by thermal agitation of water molecules. Also biological sources can be part of ambient noise;

dolphins for example, can generate intense short-duration sounds from 100 Hz to 50 kHz.

Most of the spectral energy received by the observatory during the three deployments lies within the 40–2,500 Hz interval (**Figure 4**). The power spectral signature, composed of narrow and broadband components, testify the existence of different mechanisms responsible for sound production in this submarine system. In the first site, due to the proximity of the module to the methane flares, we assumed that the contribution of the bubbles vibration could represent part of the spectral signature, apart from the high anthropic noise due to the oceanographic operations that fully blanks the signals in some cases. In this study, we focused our analysis on frequencies up to 2,500 Hz and separately analyzed the audible frequency range (400–2,500 Hz) and the infrasonic frequency range (2–20 Hz), as the corresponding sound waves are reasonably produced by different physical mechanisms.

Audible "Bubbles" Frequency Band

As mentioned above, in a submarine environment most of the energetic radiated noise could be produced by gas bubbles, due to the volume oscillation motion of the 'bubbles' wall after their formation at the vents. As demonstrated by Minnaert (1933) and Strasberg (1956), the fundamental peak frequency (the zeroth oscillatory mode) f depends on its equivalent radius r and ambient pressure P and can be analytically expressed by the equation:

$$f = \frac{1}{2\pi r}\sqrt{\left(\frac{3P\gamma}{\rho}\right)} \quad (1)$$

where [γ] is the ratio of gas specific heat, at constant pressure and volume, and ρ is the water density. Comparisons of Minnaert's simple expression with experimental values and with theoretical expressions, which take into account the effects of viscosity, surface tension and thermal conductivity (Devin 1959), demonstrate that for a bubble radius greater than 0.001 cm this simple expression is valid within 5%, for the bubble fundamental frequency (also known as breathing mode).

Considering that the bubbling gas is mainly composed of CH_4, using **Eq. (1)** we can assume $\gamma = 1.32$, $\rho = 1{,}030$ kg/m^3, attaining a product frequency by radius of fr ≈ 11.33 Hz m. Thus, for radius spanning from 0.47 to 5.6 cm, as reported in several studies based on active acoustics surveys, conducted in the same area even if at shallower depth (McGinnis et al., 2006), the 'breathing-mode' of bubbles should be in the range 2,400–200 Hz ± 5%. Coherently, our data revealed that the most energetic peaks emerging from the spectral analysis covered this range, rising even higher frequencies. The presence of peaks at lower frequencies, bounded between 60 and 400 Hz, may also be ascribed to bubble clouds, as bubbles together act as coupled oscillators and the resulting gas-water mixture region behaves with its own 'breathing-mode' frequency (Lu et al., 1990) mimicking bigger bubbles oscillation mode. As reported in several optical and passive acoustics studies, there could be three different types of bubbles plumes depending on flux: minor plumes characterized by low flow rate and bubble size strictly dependent on flux, major plume characterized by high flow rate showing broad bubble size distribution with small and large bubbles as well and intermediate plumes that show characteristics of both minor and major plumes. Depth and type of sediments (mud covered by centimetric sandy layer, as retrieved by gravity core performed during the cruise and also reported in letterature Commission on the Protection of the Black Sea Against Pollution/State of the Environment of the Black Sea (2001)) play also a fundamental role in bubbles formation mechanisms, release style and bubbles dimension (Leifer and Boles, 2005; Leifer 2010; Leifer and Culling, 2010).

Turbulent jet stream can generate a shift of the bubble frequencies due to overlapping of bubbles of various sizes (Vazquez et al., 2005; Leifer and Tang 2007; Wiggins et al., 2015).

Visual inspection of the spectrograms related to the collected data within 40–2,500 Hz confirmed the existence of pulsating sounds, having bandwidth in the same range of the one analytically assumed, likely related to bubbling oscillatory mechanism, mimicking the gas outflow behaviour over time. As the bubble stream bandwidth overlap the ambient noise one, this represented a concrete obstacle to extract clear bubble signals (Li et al., 2020). Since sea roughness could represent a relevant noise source, in order to evaluate this effect upon acoustic intensity level, we looked for any correlation between wind speed, also intended as a proxy of sea roughness variation, and bubbling related signatures, with the aim to exclude any mismatches. A weak or no correlation was found in the first site, while a clear wind-effect was found in the second and third deployment.

Acoustical Bubble Identification and Thresholding Algorithm

At low flow rates, the signal of bubble emission is not stationary and distinct transient events can be recognised. A time-frequency approach to discriminate between bubble sound emission and noise can be implemented. We took into account what was already proposed and successfully used by Li et al. (2021) and implemented a single bubble identification method based upon bubble characteristics recognition, that includes pulsation time interval, frequency bandwidth and energy strength. As the signature of a bubble is a transient event with an exponentially decaying coda, each discrete time series of the acquired acoustic record was firstly divided into 75% overlapping segments, where the length of each one was chosen in order to approximately match the average duration of the bubble signature and simultaneously guarantee a suitable frequency resolution. On each segment, a windowing Hanning function is applied before the use of Short Time Fourier Transform, in order to get spectral characteristics of the investigated segment. Once achieved the spectral computation, the algorithm was instructed to consider both the energy threshold and the frequency bandwidth threshold for identifying the bubble sounds. The damping sinusoid duration of a bubble, its dependence with frequency, gas composition within the bubble's wall and depth, has been firstly studied by Devin (Devin, 1959) and further refined by Ainslie & Leigthon (Ainslie and Leighton, 2011). Experimental test taken by

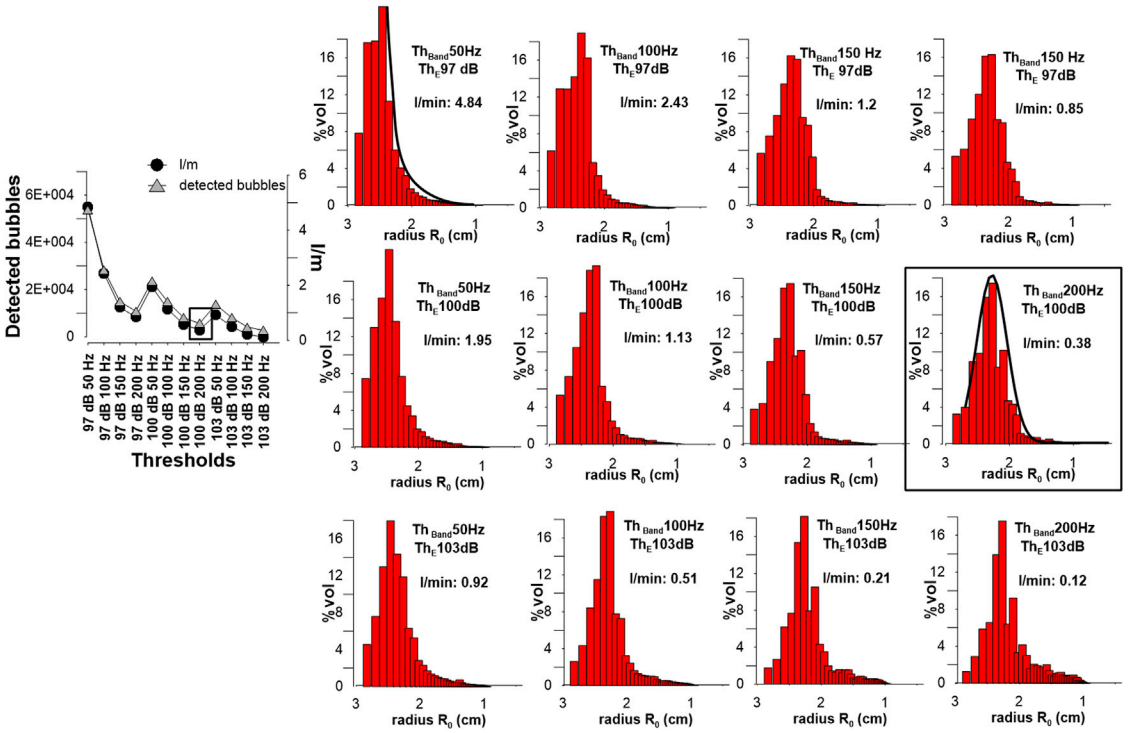


FIGURE 5 | Bubble size distribution matrix at increasing Th_E [97–103 dB] and TH_{Band} [50–200 Hz] relative to April 2019. Each barchart plot shows, once Th_E and Th_{Band} fixed, the evolution of %vol related to detected "bubble" events vs radius size as a function of frequency. Barchart plot in the black box represents the chosen thresholds where the gaussian function describes the distribution at the best. First Barchart plot on the top right indicates a distribution described by a power law function giving an idea of not optimized threshold choices. Line plot on the right shows Number of detected bubbles and relative computed l/m vs increasing thresholds. Black square inside the line plot hilights the best agreement between false positive and bubble detection

Walton et al., 2005 demonstrates that the calculated exponential decay of methane bubbles was characterised by a quality factor Q = 24 at atmospheric pressure. As a rough generalization, the value holds up to within about 50% of its surface value down to a depth of about 100 m. Having Q expressed, it is possible to roughly estimate the typical duration in ~5ms for methane bubbles having resonance frequency centered at 1 kHz at a depth of 120 m. Thus, once Fourier parameters were determined, the thresholding technique was applied in order to identify spectral peaks above a certain energy threshold Th_E. After the peaks have been identified, all adjacent peaks were collected in a vector, and the difference between the minimum and the maximum frequency constituting the vector were compared with a bandwidth threshold Th_{band} (detailed algorithm conceptualization can be found in Li et al., 2021). If the resulting difference exceeds the bandwidth threshold, the sound event is recognised as a bubble signal, excluded otherwise. Such thresholding technique improves bubble signature recognition, as it eliminates isolated noise peaks. From Leighton (Peregrine, 1994. The Acoustic Bubble), the predicted bandwidth of a bubble signature, calculated upon the quality factor Q = 12 is 66 Hz for a bubble peaked at 800 Hz, rising up to 200 Hz for bubbles peaked at 2,400 Hz. However, as evidenced by Walton (Walton et al., 2005), a certain percentage of difference between calculated quality factor and measured quality factor of 3.5–40% place this value as a lower limit, It is worth mentioning that setting low thresholds, notwithstanding the increase of the probability to detect the majority of bubble events, will mostly affect the detection of false events, as many noise pulses may be identified as bubbles. Setting high thresholds prevents false alarms, but may filter too much, producing a dataset with reduced detection.

In this section we discuss the steps carried out to refine the algorithm thresholding techniques and the obtained results. The implemented algorithm has to be refined and "tuned" using experimental criteria in order to suppress the noise background from bubble events, paying attention to not exclude bubbles together with the noise. Therefore several threshold bandwidths (Th_{band}) have been investigated, moving by steps of 50 Hz, starting to 50 Hz (chosen as lower limit, due to the concepts discussed before) up to 200 Hz. In the same way, several energy Thresholds (Th_E) were examined by steps of 3 dB (corresponding to a doubling in energy). choosing a specific energy depending upon the deployment site and the degassing style. (see sections below). The **Figure 5** describes the distribution matrix of the events detected along the whole period of acoustic records acquired in April during D2, and how it evolves as the bandwidth threshold increases. Increasing both bandwidth and energy thresholds produce a distribution of bubbles size that move from a power law distribution and become even more assimilable to a gaussian distribution that represents the best agreement between detection of bubbles events and false positive counting due to background noise. On the other hand, choosing higher energy and bandwidth thresholds could result in a misreading

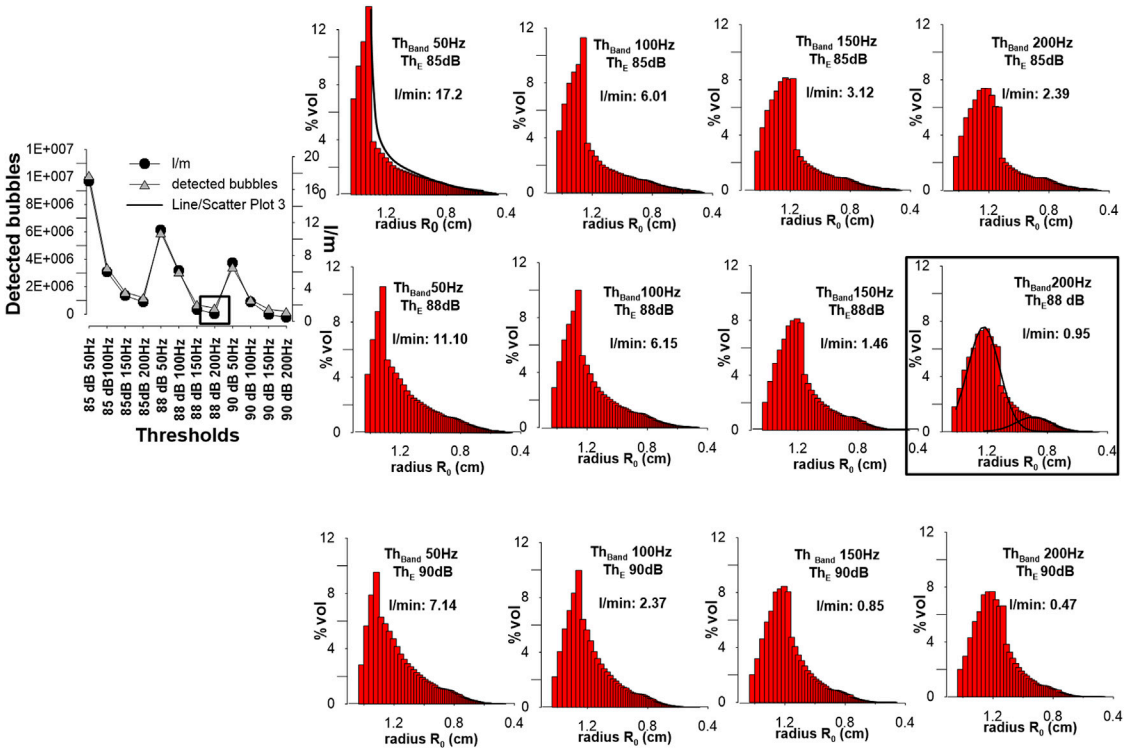


FIGURE 6 | Bubble size distribution matrix at increasing ThE 85–90 dB] and THBand [50–200 Hz] relative to the entire D3. Each barchart plot shows, once ThE and ThBand fixed, the evolution of %vol related to detected "bubble" events vs radius size as a function of frequency. Barchart plot in the black box represents the chosen thresholds where the gaussian function describes the distribution at the best. First Barchart plot on the top right indicates a distribution described by a power law function giving an idea of not optimized threshold choices. Line plot on the right shows Number of detected bubbles and relative computed l/m vs increasing thresholds. Black square inside the line plot hilights the best agreement between false positive and bubble detection

of detection at higher frequency, thus underestimating bubbles count and, as a consequence, the amount of released gas over time. Looking at the distribution, it becomes clear that the shape is insensitive with respect to the choice of the energy threshold, while it changes as the bandwidth threshold increases. The figure shows also how a higher energy threshold represents a good filter, but at the same threshold, setting a good bandwidth threshold improves discrimanationn of bubble events. Some bubble events could however be excluded, thus, in order to choose the right thresholds, it is necessary to investigate how the distribution for all pulses is affected by noise other than bubbles. For each deployment period, we generated a distribution matrix where each row represents the investigation of bandwidth threshold, considering the same energy threshold. **Figure 6** describes distribution matrix of the events detected along the whole period of acoustic records acquired during D3

The **Figure 7** highlights how the filtering technique helps step by step to improve the detection of the "bubbles" events with respect to noise. Fixing the optimal energy threshold, the resulting spectrograms depict the improvement of the performance of the detection as the bandwidth threshold increases.

Infrasonic Frequency Band: 2–20 Hz

Over the three deployment periods analyzed in this paper, low acoustic frequencies within the range 2–20 Hz were investigated as well in order to detect and follow the vibrational signals evolution. Such "vibrational" signals depend on a totally different acoustics mechanism with respect to the one generating bubbling noise, being the conversion into acoustic waves at the solid-liquid interfaces of seismic energy (Wilcock et al., 2014 and references therein) generated below the seafloor by dynamics of ascending fluids along cracks (Dziak and Fox Christopher, 2002, 2004; Tolstoy et al., 2002; Ohminato 2006; Dziak and Haxel, 2008, 2012; Alparone et al., 2010; Milluzzo et al., 2010; Longo et al., 2021). Searching for acoustics sources from these kinds of mechanisms results from the assumption that if there is gas in the water column producing bubbles noise (named bubbling, whose oscillatory mode is acoustically detected at higher frequencies within 200 and 2,500 Hz), there necessarily should be a gas flowing inside the sediments along a network of pathways that links the gas source area with the sea bottom. Gas flow dynamic itself makes the pathways vibrating and produces a seismic signal converted in infrasonic frequency acoustic energy at the solid-liquid interface just at the seafloor.

Vertical Casts

During the first cruise we performed vertical casts along the water column using a Rosette with 16 Niskin sampling bottles. We collected water samples at various depths in two localities (named B and X) nearby the deployment site (**Figure 1** and **Table 1**). The results allowed us to define the geochemical

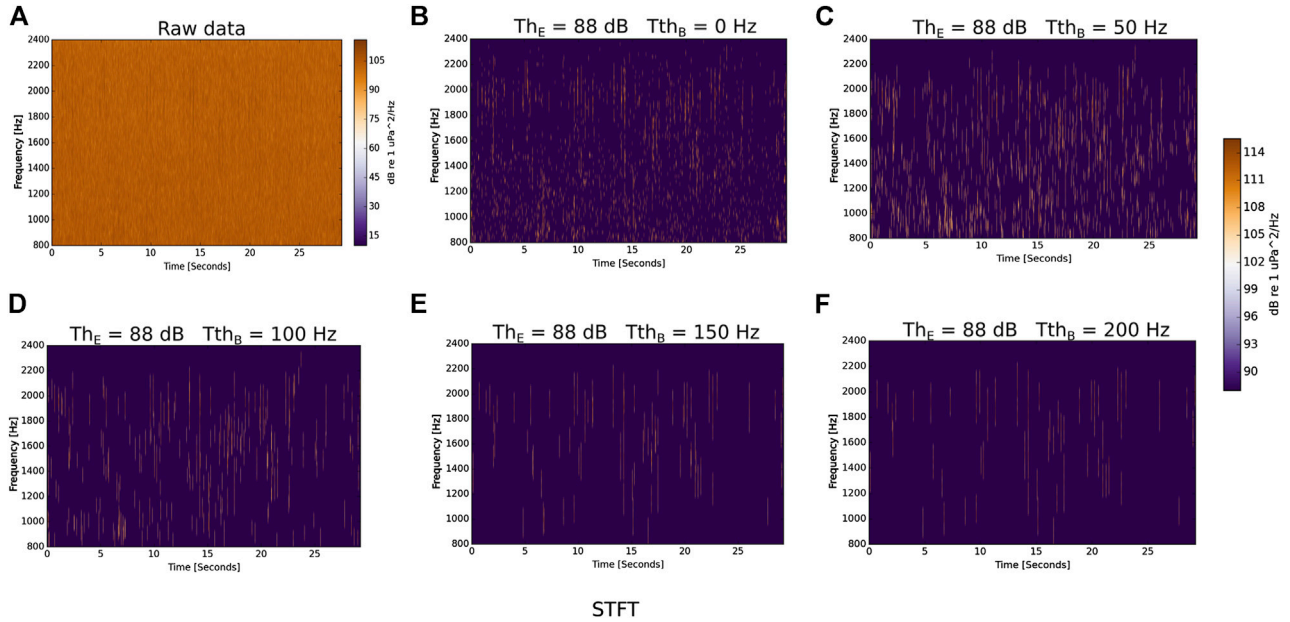


FIGURE 7 | Spectrogram matrix using short-time Fourier transform, where different thresholds are applied; **(A)** Spectrogram of raw data recorded; **(B)** data filtered applying Th_E = 88 dB, without bandwidth thresholding **(C)** data filtered applying Th_E = 88 dB, Th_B = 50 Hz, from which is possible to note the coexistence of bubbles and noise events; **(D)** data filtered with Th_E = 88 dB, Th_B = 100 Hz, the resulting data present still false positives; **(E)** Th_E = 88 dB, Th_B = 150 Hz, identified "bubbles" are clearly shown as orange dots dominantly at frequency interval 800–2,200 Hz; **(F)** defined Th_{eng} = 88 dB, Th_{Band} = 200 Hz as best couple of values from the distribution matrix, identified single "bubbles" are easily identified from the spectrogram.

TABLE 1 | List of sites for: deployment multidisciplinary seafloor observatory (D1 - D2 - D3); sampling gravity cores (GC-01 - GC-02) and sampling seawater columns (B - X) during the first surveys.

Site	Depth (m)	Longitude E (WGS84)	Latitude N (WGS84)
multidisciplinary seafloor observatory			
D1	110	30°43′56.8620″	44°13′28.3440″
D2	117	30°43′46.7340″	44°13′23.2560″
D3	110	30°43′56.88″	44°13′29,04″
seawater column sampling			
B	110	30°43′50.1″	44°13′31.38″
X	108	30°43′27.96″	44°13′27.48″
gravity cores			
GC-01		30°43′51.0600″	44°13′29.9820″
GC-02		30°43′42.6300″	44°13′29.1780″

features of the water column and its dissolved gases up to the sea bottom. The samples, specifically collected for the extraction of the whole gas phase for chemical and isotopic analyses, were stored into 240 ml Pyrex bottles, sealed onboard using rubber or Teflon septa and purpose-built pliers, and analyzed within 2 weeks. Details on the sampling methodology are reported in Italiano et al. (2009, 2014). During the cruise, the sampled bottles were stored upside down, keeping the necks with the rubber septa submerged in seawater until they were transferred to the laboratory. The collected seawater samples underwent laboratory procedures for chemical (concentration of dissolved gas species) determinations. In the laboratory, the dissolved gases were extracted after equilibrium was reached at constant temperature with a host gas (high-purity argon) injected in the sample bottle (see Capasso and Inguaggiato, 1998, Inguaggiato and Rizzo, 2004 and Italiano et al., 2009, 2014, for further details). The chemical analyses of O_2, N_2, CH_4 and CO_2 were carried out by gas chromatography (Agilent 7800B equipped with a double thermal conductivity detector–flame ionization detector; TCD–FID) using argon as a carrier gas. Typical analytical uncertainties were within 5%.

RESULTS AND DISCUSSION

Geochemical Features of Seawater Columns

The chemical-physical features and the analytical results in terms of dissolved gases composition of the water samples collected at various depths are listed in **Table 2**.

The seawater samples collected along the water column show a chemical composition similar to the ASSW (Air Saturated Sea Water) up to a depth of 60 m. From 60 m to the bottom, the dissolved methane concentration started to increase, reaching the highest concentration in the range of 0.2 micromol/L close to the bottom at a depth between 100 and 110 m. The pH values decreased up to 7.8 value, lower than normal seawater. The dissolved carbon dioxide shows an increased concentration as well, reaching values around 0.08 millimol/L. The rise of carbon dioxide content was coherent with the pH decrease and could be related to methane oxidation processes. The Eh values exhibited values around 0 or negative close to the sea bottom accounting for enhanced anoxic conditions (**Figure 8**).

TABLE 2 | Chemical-physical features and dissolved gas composition of the seawater columns from the studied localities in the Black Sea (B, X). T. BDL: below detection limit, na: not analyzed.

Site	Date	Depth (m)	T°C	pH	Conductivity mS/cm^2	Eh mV	H_2 (mmol/L)	O_2 (mmol/L)	N_2 (mmol/L)	CO (mmol/L)	CH_4 (mmol/L)	CO_2 (mmol/L)
B	04/04/2019	−110	7.8	7.78	39.9	−40	9.60E-05	0.038	0.245	1.05E-06	1.07E-04	0.047
	04/04/2019	−100	7.1	7.77	43.9	108.4	3.92E-05	0.029	0.353	8.42E-07	5.09E-05	0.055
	04/04/2019	−80	7.4	8.31	39.6	84	5.82E-05	0.161	0.371	2.58E-06	4.69E-05	0.022
	04/04/2019	−60	7.2	8.33	40.1	81	2.47E-04	0.176	0.345	*bdl*	3.95E-05	0.019
	04/04/2019	−30	7.9	8.39	38.7	84	1.00E-05	0.176	0.323	1.29E-06	6.67E-06	0.017
	04/04/2019	−10	7.5	8.39	38.5	86.7	7.62E-05	0.193	0.356	3.44E-06	6.92E-06	0.016
X	04/04/2019	−108	8.2	7.76	*na*	40	9.56E-05	0.051	0.242	8.22E-07	4.98E-05	0.052
	04/04/2019	−100	7.7	7.73	*na*	41	3.17E-05	0.078	0.375	1.61E-06	1.25E-04	0.060
	04/04/2019	−89	7.9	7.7	*na*	57	4.78E-05	0.062	0.364	1..44E-06	8.53E-05	0.055
	04/04/2019	−70	7.9	7.74	*na*	55	9.79E-06	0.076	0.376	1.47E-06	3.14E-05	0.057
	04/04/2019	−60	7.4	7.81	*na*	61	6.50E-05	0.057	0.233	1.03E-06	7.82E-06	0.039
	04/04/2019	−50	7.7	8.24	*na*	37	2.81E-05	0.111	0.220	2.58E-06	2.96E-06	0.017
	04/04/2019	−40	8	8.26	*na*	31	6.57E-05	0.195	0.383	2.64E-06	4.27E-06	0.020
	04/04/2019	−30	8.4	8.28	*na*	35	6.65E-05	0.149	0.298	3.21E-06	3.65E-06	0.016
	04/04/2019	−20	8	8.21	*na*	60	3.43E-05	0.164	0.299	2.52E-06	2.60E-06	0.016

Chemical-Physical Parameters

The continuous recording of chemical-physical parameters (temperature, conductivity, pH, hydrostatic pressure), performed by the observatory over the three deployment periods (**Figure 8**), showed how the main features of the bottom water did not suffer significant variations over the time. Conductivity being not T-compensated shows the same modulation over time with respect to the temperature that changes in the narrow range of 8.5 ± 0.1°C. Regarding the pH value, it ranges from 7.6 to 8, mostly persisting on lower values (7.8) with respect to the normal seawater, in agreement with the values recorded near the sea-bottom during cast profiles (**Figure 9**).

First Deployment (D1)

Investigating the acoustic energy either as a gas detecting tool or as a proxy of gas flow is the main goal of the passive acoustic measurements. Methane bubbles coming from flares radiate significant broadband and narrowband acoustic pressure waves. In addition, dissolved methane results in chemical anomalies detectable by the methane sensor. The first 4 days-long deployment (D1) allowed us to verify the acoustic response of an abrupt methane injection into the water column. For D1, the observatory was set up to promptly start acquisition, recording all parameters every 20 min, once reached the sea-bottom. The very first data of dissolved methane, turbidity and acoustic energy in the typical bubbling frequency range as predicted by the Minneart equation (400–2500 Hz) have shown low values that we could consider as the local background.

All those three parameters kept low values until the first planned gravity core (GC-01) was performed less than 200 m away from the site of the observatory deployment (**Figure 1**). After GC-01, all the measured parameters suddenly increased. The gravity core activity likely induced the stripping of gas trapped in the shallower sediments. As a secondary effect, turbidity, produced by sediments moved by gas jets and/or bubbles clouds, grew up. Dissolved methane within 24 h reached higher values around 3.5 micromol/L. The increasing trend of dissolved methane values was exactly matched with the trend of turbidity ones. The acoustic energy levels followed the trends of both turbidity and methane as well, as the enhanced high gas flow likely produced turbulent gas-jets and plumes of bubbles characterized by different sizes (from millimetric up to even centimetric) which oscillation, increased the acoustic intensity (**Figure10**). Spectral short-time Fourier transform analysis was performed over 512 points, corresponding to 9.7 ms observing window size, followed by a threshold denoising algorithm. This allowed us to discriminate, during loud less periods (e.s. records acquired overnight, when the survey activities were stopped), bubbles streams, as shown in **Figure 11**. Moreover, acoustic energy levels in infrasonic frequency ranges (2–20 Hz) showed variations due to ascending methane through the pathways inside the sediments below the seafloor. From the beginning of April 5th all parameters showed a synchronous decreasing trend. On the same day at 05: 15 (UTC) the second planned gravity core (GC-02) was performed more than 400 m away from the observatory. After the GC-02, only acoustics data recorded a weak simultaneous variation related to the gravity core activity. In fact, due to both effective double distances of GC-02 from the observatory with respect the previous (GC-01) and the likely weak presence of methane still trapped in the sediments, only a little and delayed increase was recorded by acoustics and turbidity, while dissolved methane concentration showed a slight increase up to 1.9 micromol/L. All parameters went back to their initial values at the end of April 6th.

Due to coring activity D1 is therefore characterized by high flow and plume of bubbles that produce a stationary acoustic signal. Identification bubbles could be performed using the acoustic inversion method proposed by Leighton and White, 2011 but, considering the concurring high level of anthropic noise that often superimposes over the spectral bandwidth related to bubble streams, it is hard to apply. Despite all, it was however possible to track and extract the parameters described above, that

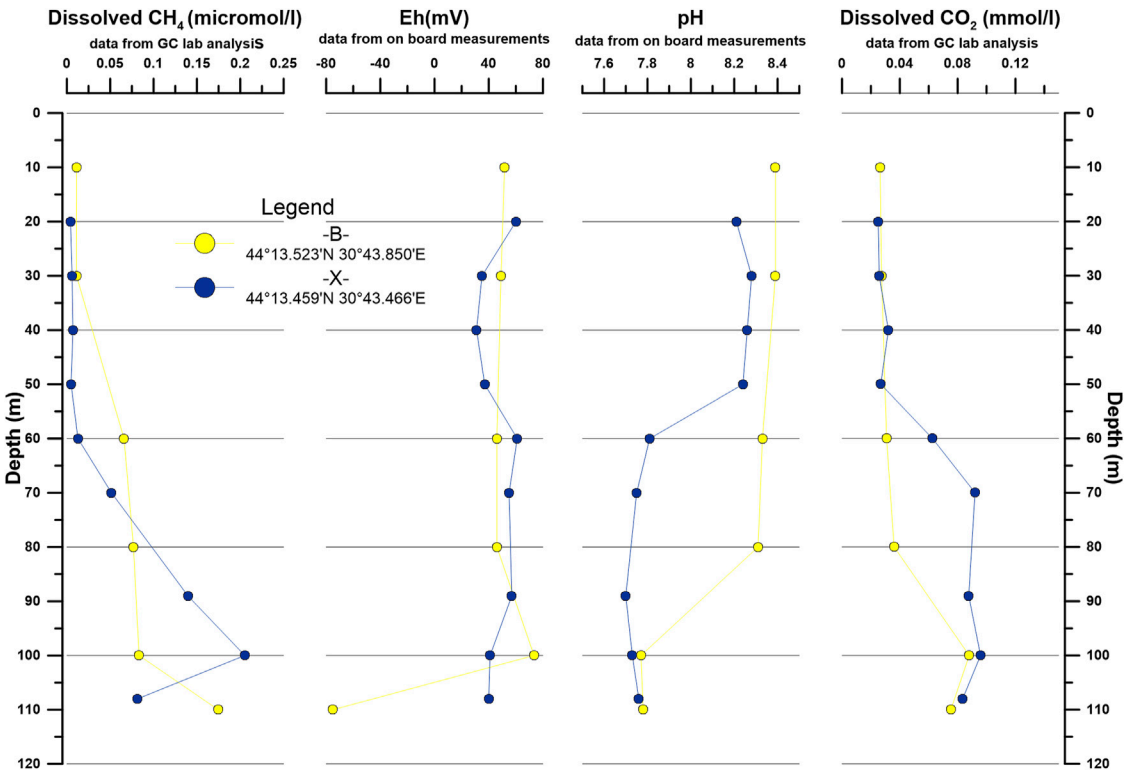


FIGURE 8 | Cast profiles obtained by discrete sampling from niskin bottles collected at different depths. Data highlight increasing dissolved methane concentrations from the depth of 60 m to the bottom with the highest values ranging about 0.2 micromol per liter, negative values of Eh and pH about 7.78 at 110 m water depth. Yellow marker represents cast profile data from site B, blu marker represents cast profile data from site X (see **Figure 1** for locations of both B and X sites).

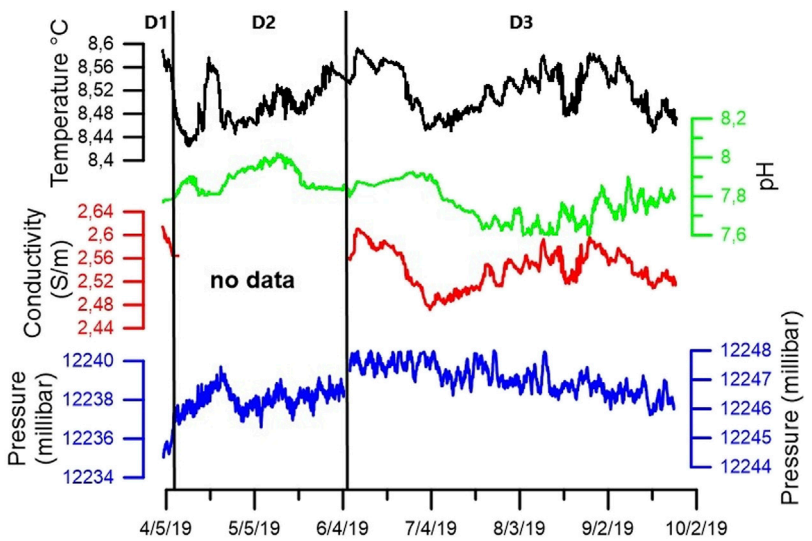


FIGURE 9 | Chemical-physical parameters recorded by seafloor observatory from April 2019 to September 2019. The diagram shows, from the top to the bottom, variation over time of temperature (black line), pH (green line), electric conductivity (red line), hydrostatic pressure (dark blue line). D1, D2, D3 vertical black bars separate the three different deployments in the three different sites.

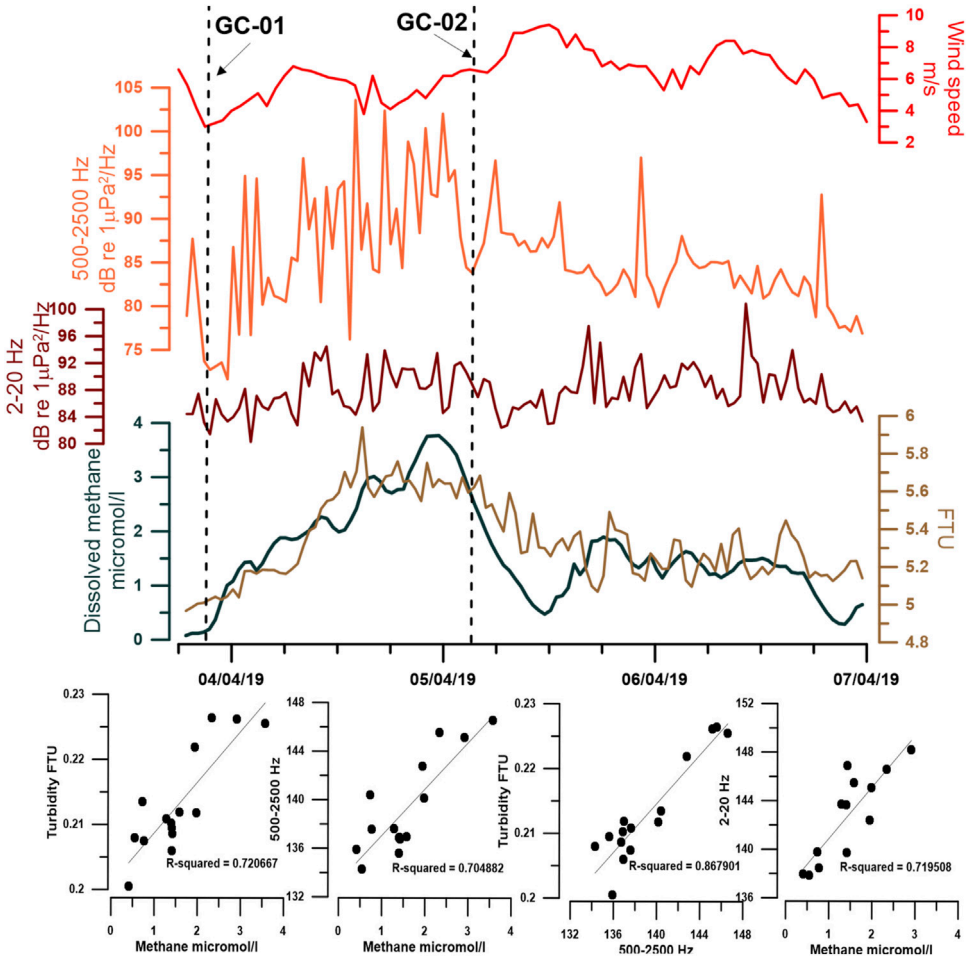


FIGURE 10 | Evolution over 5 days of the parameter recorded by the seafloor observatory during D1 from the bottom variation over time of dissolved methane (dark green line), turbidity (brown line), low acoustic energy levels 2–20 Hz (dark red line), acoustic energy level 500–2,500 Hz (orange line), wind speed (red line). Dashed black vertical lines mark the time of gravity core activity (GC-01 and GC02). On the bottom, from left to right, correlation plots of Turbidity vs Dissolved methane, 500–2,500 Hz vs Dissolved methane, Turbidity vs 500–2,500 Hz and 2–20 Hz vs Dissolved methane

showed high correlation, round-crossing all parameters one with each other, with R^2 factor spanning from 0.7 up to 0.86 as shown in the correlations plots of **Figure 10**, therefore revealing a strict dependence among the physical phenomena observed.

Second Deployment (D2)

On April 7th the seafloor observatory was recovered, and after data downloading and battery recharging operations, was again deployed at the second site (D2), 275 m to the SW of the first site. In order to collect data for a longer period the observatory was set to acquire every 40 min and record 10 seconds-long audio segments each time, obtaining a total of 72 audio records per day. Data acquisition of this deployment lasted for 2 months and showed pulsating variation of dissolved methane at the sea bottom that never reached values higher than 1.5 micromol/L. Pulsating behavior suggested a cyclic, although not-regular, disappearance of the methane emissions. This is coherent with the observations reported by other authors (Judd, 2003 and references therein, Dziak et al., 2018) that described, for similar areas, an exhalation style characterized by cyclic accumulation inside the sediment followed by low-flux methane release. With respect to D1, in which turbulent high flow gas release has been induced by anthropic activity (Gravity Core activities), in D2 gas release likely occurred every time the sediments were not able to retain pressure induced by gas accumulation (**Figure 12**).

In such conditions, during a month long period starting from the second week of April and the beginning of May, we observed an increasing stage of energetic burst-like and intermittent broadband events, that slowly decreased until totally disappearing from May 9th on. From both visual and acoustical inspection, we are confident that such events are likely related to methane bubbles streams, as shown in **Figure 13A**, accounting for a sudden release of variously sized, even centimetric, bubbles. In order to investigate the bubble size distribution of the events, the thresholding analysis was performed for all the records in the mentioned period, using the thresholding algorithm described in section 3.2.3 above. As

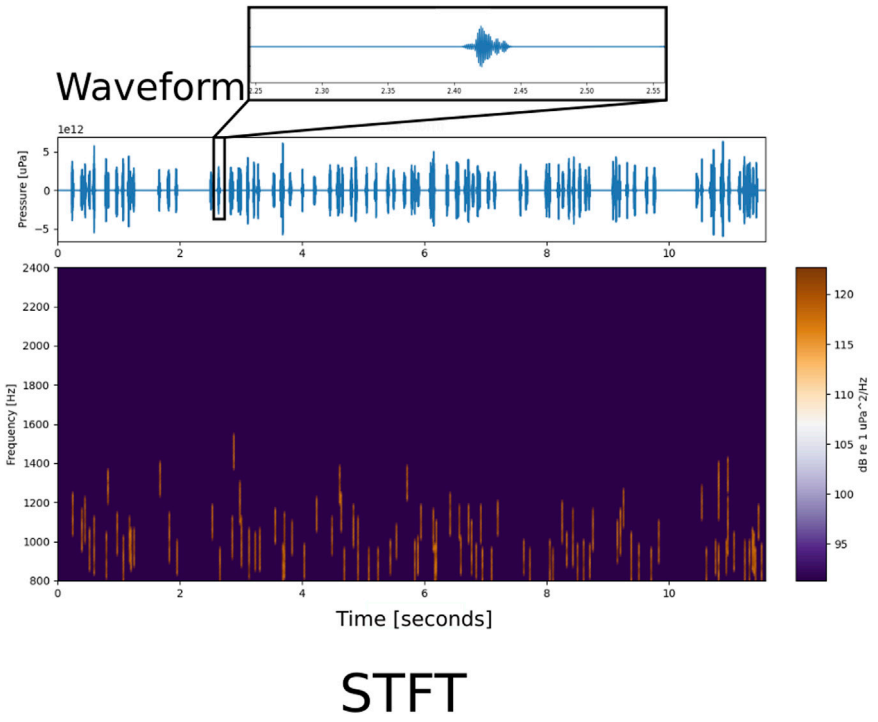


FIGURE 11 | Detailed short-time Fourier transform (STFT) and waveform relative to a single 10-second-long audio segment acquired on 5th April, where diffuse bubble streams are recorded. STFT was calculated over 120 points, 75% overlapping factor, corresponding to 20 ms window size.

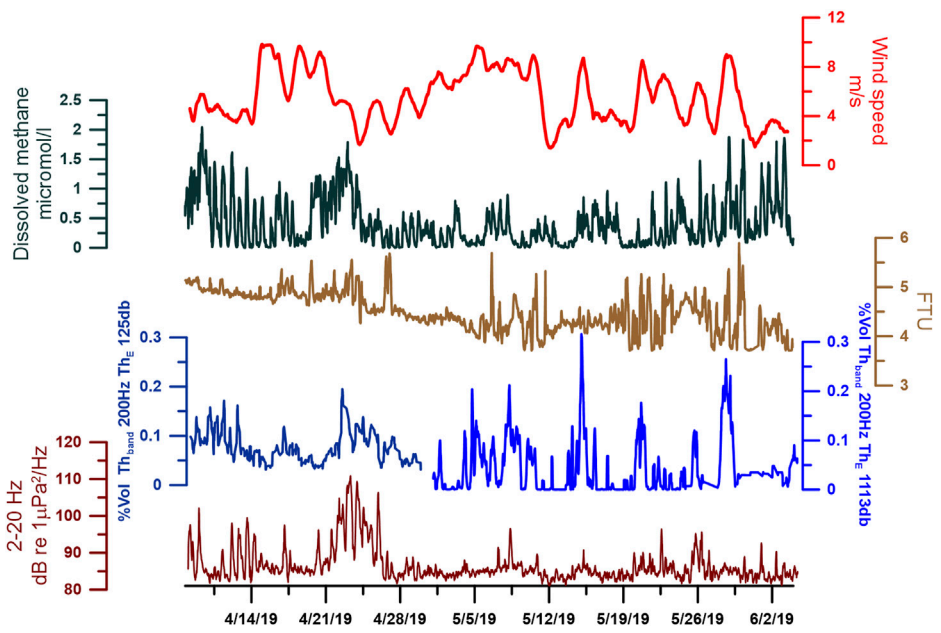


FIGURE 12 | Evolution over 2 months of the parameter recorded by the seafloor observatory during D2 from the bottom variation over time of low acoustic energy levels 2–20 Hz (dark red line),, %vol released during April (dark-blue line) and %vol released during May (light-blue line), turbidity (brown line), dissolved methane (dark green line),and wind speed (red line).

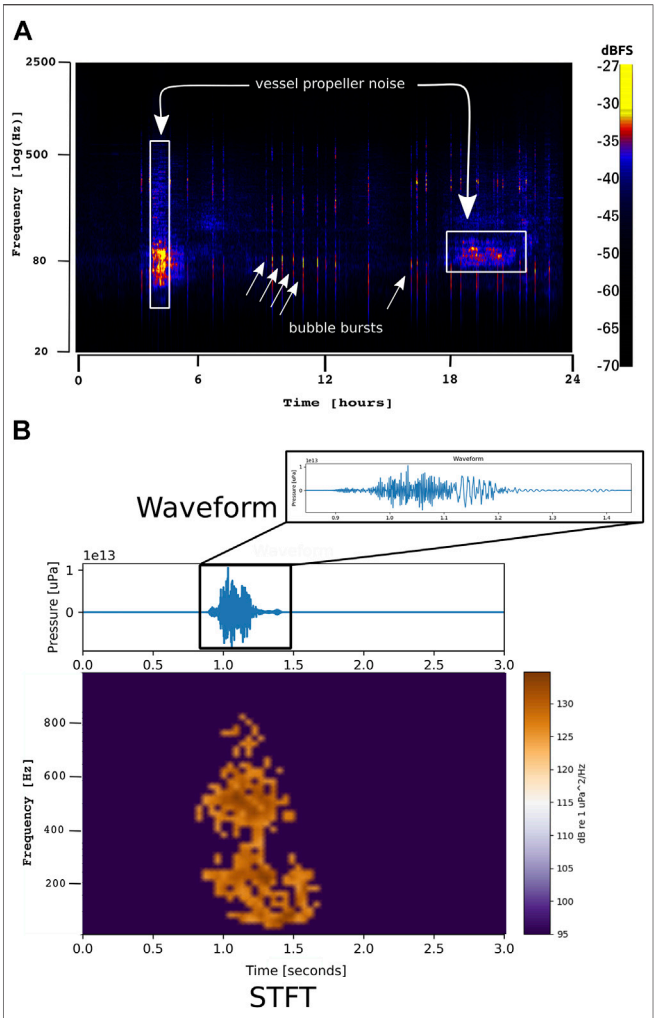


FIGURE 13 | (A) Daily resulting spectrogram, calculated on 2048 point-sized window (38.6 ms), of merged 10 seconds-long audio records, recorded on 26th of April; the bandwidth shown is bounded to the inspected 20–2,500 Hz band, where energetic bubble bursts signals emerge, together with ship related noise. **(B)** Detailed short-time Fourier transform (STFT) and waveform of a single burst event recorded. STFT was calculated over 120 points, 75% overlapping factor, corresponding to 20 ms window size.

the visual inspection of the spectrogram returned energetic broadband signals, we investigated frequency windows within 400 and 1,200 Hz. The algorithm was instructed to better analyze frequency content and retrieve several distribution histograms, by the inspection of different energy thresholds Th_E, in the range [97–103] dB, by step of 3 dB, corresponding to a doubled energy. For each fixed Th_E, different frequency bandwidths were inspected, from 50 to 200 Hz. **Figure 5** shows the resulting bubble size distribution matrix, highlighting how the peaks centered on frequency 500 Hz, corresponding to radius 2.2 cm, persist even though the increase of threshold values. Looking at the distribution matrix, it is possible to observe how the application of high threshold values may produce an overfiltering, excluding bubbles from the distribution dataset, especially the ones less energetic with higher frequency, while the distribution shape doesn't change significantly. On the other hand, setting a low Th_{Band}, such as 50 Hz, retrieves false positive detections. Infact, as can be seen from the insert graph in **Figure 12**, setting low Th_{Band} threshold produces a local peak of detection. The investigation of energy thresholds suggests that, from the 100 dB, the slope of the curve smoothly decreases, suggesting that the detected events preserve a consistent bandwidth and are thus assimilable to bubble events. Moving forward from this point on, may result in an excessive filtering of bubbles events. Therefore, the best agreement between bubble detection and false positives is reached choosing Th_E = 100 dB, Th_B = 200 Hz, corresponding to the distribution highlighted by the solid-black square in the matrix. Once selected the best suited histogram to express bubble size distribution, the related evolution of volume percentage were compared to wind speed (as proxy of sea roughness), low frequency averaged spectral energy and chemical-physical time series of **Figure 11**, revealing a high coherence over time. t The correct tuning of the algorithm made therefore possible to acoustically track the energy signature related to the bubbles' walls motion, just nearby the time corresponding with the higher values reached by dissolved methane (**Figure 13B**). The waveform of the reconstructed signal further highlights the chronological succession of the signals, suggesting a foregoing release of millimetric and sub-centrimetic bubbles followed by larger ones. Lower frequency content is likely produced by the oscillatory mode of the bubble cloud that surrogate a larger bubble oscillatory motion, as previously mentioned (Lu et al., 1990) or even the frequency shift produced by coalescing effect of small chained bubbles (**Figure 10B**) (Vazquez et al., 2005; Leifer and Tang 2007; Wiggins et al., 2015). At the same time, infrasonic signal levels, acting in pulsating mode as well, synchronously reached high intensity levels, revealing the best agreement over time with dissolved CH_4 in the water column. Also turbidity showed variation over time correlated to methane, somehow testifying the suspension of sediments due to bubbles rise dynamic (**Figure 12**). Comparisons of infrasonic frequency with wind time series (as a proxy of sea state) exclude any correlation. It is therefore plausible to exclude the contribution of microseismicity induced by sea roughness. It is a matter of fact that the infrasonic level rise (which energetic intensities gained the highest values of the entire period) is exactly in accordance with the bursts increase, testifying that the two parameters describe consequential mechanisms. Such anomalous events of gas release slowly exhausted until totally disappearing on May 10th, following a rather quiescent period. Since the beginning of May, a new gas emission style was recorded by the hydrophone, following seismic and methane concentration changes as well. Bubble size distribution performed on the entire D2 period (**Figure 14**) confirmed the change in gas release style. After a visual inspection of acoustic records, the threshold algorithm has been tuned to analyze a frequency window within 800 and 2,400 Hz, looking for, by Equation (**1**), oscillatory bubbles' mode likely sourced by bubbles which radii laid in the range 0.4–1.5 cm. Therefore, applying Th_E by steps of 3 dB from 85 to 90 dB and Th_{Band} from 50 to 200Hz, the resulting matrix

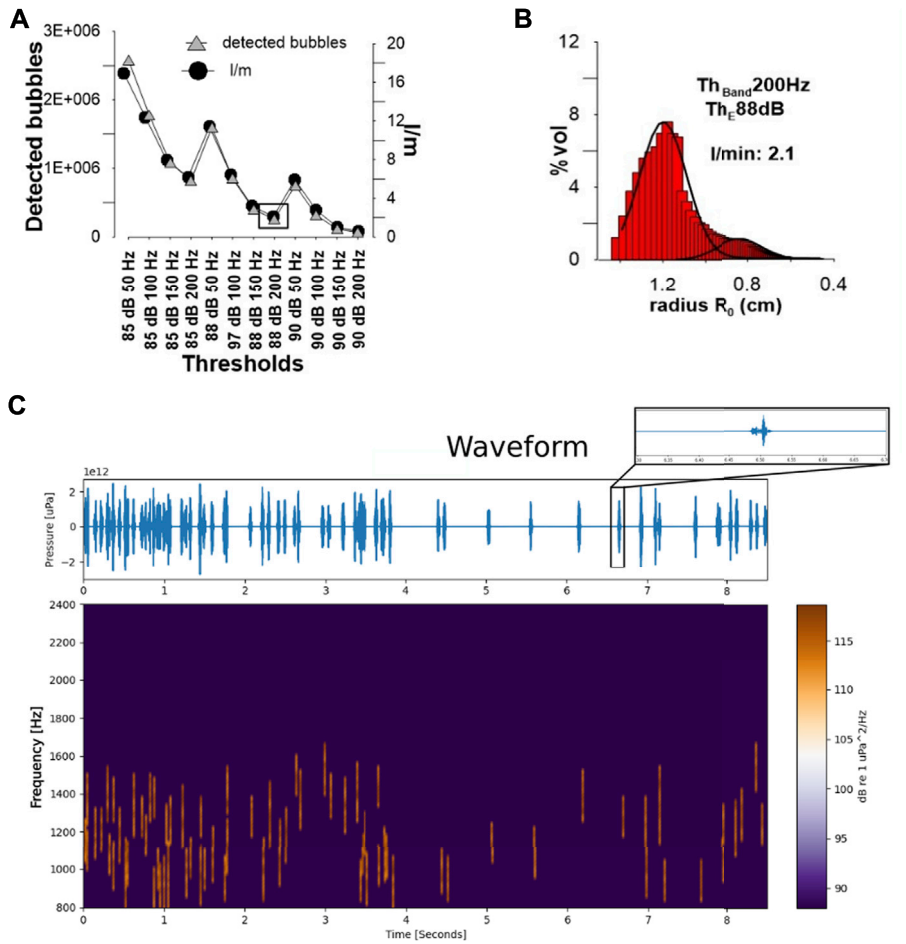


FIGURE 14 | Graphs describing the D2 features resulting from the investigation. **(A)** Line plot describing "Number of events" and related l/min vs. threshold. **(B)** Bar chart plot showing the distribution chosen after the thresholds investigation. **(C)** Detailed short-time Fourier transform (STFT) spectrogram and waveform (Th_E = 88 dB, Th_{Band} = 200 Hz) relative to a single record acquired on May 15th.

highlights how the most confident distribution is obtained choosing Th_E 88 dB and Th_{Band} 200 Hz (**Figure 14**). Once again plotting the relative Volume percentage over time we obtained the evolution of bubbles released with a high degree of coherence with respect to dissolved methane and infrasonic energy levels. The recorded bubble release process was definitely different from the previous one, being characterized by a single smaller bubble emission, whose rate slowly increased until rising its maximum during the period May 30th–June 2nd.

Third Deployment (D3)

The third deployment site was 20 m away from the first site, already described as an extensive exhalative area. This was the longest monitoring period thus, in order to further reduce power consumption, the observatory was configured to acquire every 2 hours, obtaining a total of 12 samples per day. Audio records were set to acquire 30 s-long segments. Data recording lasted 4 months and revealed, as expected, a significant and almost continuous methane release with dissolved concentrations that in certain periods reached values up to 5.8 micromol/L (**Figure 13**). Higher dissolved methane values were somehow preceded by an increase of the acoustic energy in infrasonic frequencies levels with a synchronous increase of the bubbles emission rate. Bubble size distribution (**Figure 6**) obtained through the application of the threshold algorithm in the frequency range [800–2,400] Hz returned similar characteristics with respect to D2, with the best distribution obtained using Th_{Band} 200 Hz and Th_E 88 dB. The investigation process revealed the existence of two gaussian distributions, the main one peaked at 1.2 cm, while the second one characterized by a moda at 0.9 cm. Such evidence likely suggests the detection of almost two different degassing features, characterized by small bubbles gently released. **Figure 15** shows the evolution over 4 months of volume percentage, obtained plotting the time series of the number of detected events, using the threshold values that gave the best distribution. The series is compared with dissolved methane, wind speed and infrasonic energy levels. Looking at the figure it is possible to note a temporal shift among acoustics data and methane concentration, suggesting that the deployment site is quite distant from the seeps, differently with respect to D1 and D2,

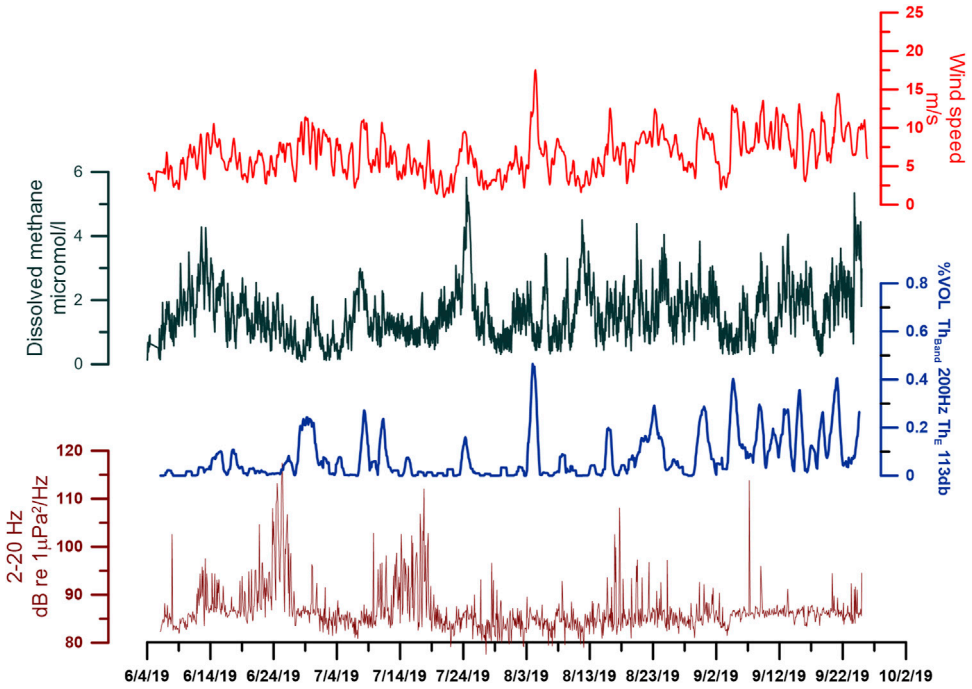


FIGURE 15 | Evolution over 4 months of the parameter recorded by the seafloor observatory during D3 from the bottom variation over time of low acoustic energy levels 2–20 Hz (dark red line), %vol released over the entire D3 (blu line), dissolved methane (dark green line). and wind speed (red line)

and resulting in a sort of hysteresis in the chemical response on the water column. In light of this scenario, choosing a lower energy threshold might retrieve a more realistic quantification of volume of gas released, but might also include too much noise, resulting in a higher percentage of false detection as the longer distance attenuates less intense seeps. Our hypothesis could be further confirmed if we take into account the energetic levels received: the burst-like events generated in D2 april raised 120 dB, while the sound of bubble detachment never overcame 107 dB. Acoustic record signatures describe a natural and gentle exhalation style, characterized by an almost continuous release of small (millimetric) bubbles, centered in the 900–1,000 Hz range, as shown in **Figure 16**. During the increasing stages, the presence of larger, but still subcentimetric bubbles (peaked in the frequency range 700–900 Hz) was detected as well. The overall acoustic results describe a general low emission rate.

Bubbles Volume and Rate Estimation

Bubble size distribution method proposed by Leighton allows to obtain a quantification of bubbles detection versus frequency bands. Using the Minneart equation, each frequency band corresponds to a bubble radius. Under the assumption of spherical bubble shape, it is therefore possible to convert events detected to volume of gas if we simply consider the volume corresponding to a spherical bubble with the detected radius. Hence, using each distribution, it is possible to estimate the degassing volume emitted per day. Looking at the distribution matrix of D3 **Figure 6**), obtained by the cumulative detected bubbles over 4 month of observation, it returns major events peaking at radius equals to 1.2 cm, corresponding to bubbles of about 7cc. Hence, if we consider the entire distribution of radii and their corresponding volume per number of detected bubbles, under the assumption of steady degassing rate we obtain the total averaged gas emitted during the D3 period. Thus, D3 bubble size distribution gives back about 0.7 L/min, which results to a total degassing volume of 1,368 L/day corresponding to 771 mol/day. In the same way we can compute the outgassing values relative to D2 (**Figure 14**). As already described in section 4.4, D2 is characterized by a general degassing stage, similar to the one observed in D3 during 4-month long deployment. During D2, within some limited period, particularly during April, burst style degassing events were observed. Analyzing the bubble size distribution of the entire D2 it is worth to note that, despite the shorter length of the observation temporal window (2 months long), a greater overall averaged volume of gas per day was observed, estimated at 3,054 L/day corresponding to 1721 mol/day. Moreover, analyzing the size distribution relative to burst events of April (**Figures 5**, **13**), characterized by bubbles radii of about 2.3 cm, we obtain a further outgas value per day equals to 547 L/day corresponding to 308 mol/day. Adding this estimation to the previous value, a total value of 3,601 L/day equals to a 2030 mol/day is obtained, about three times greater than the estimation retrieved from D3. The comparison between the obtained volume estimations and the different mean concentration of the dissolved methane in both the areas, allows us to assume that, even though D3 shows a gentle

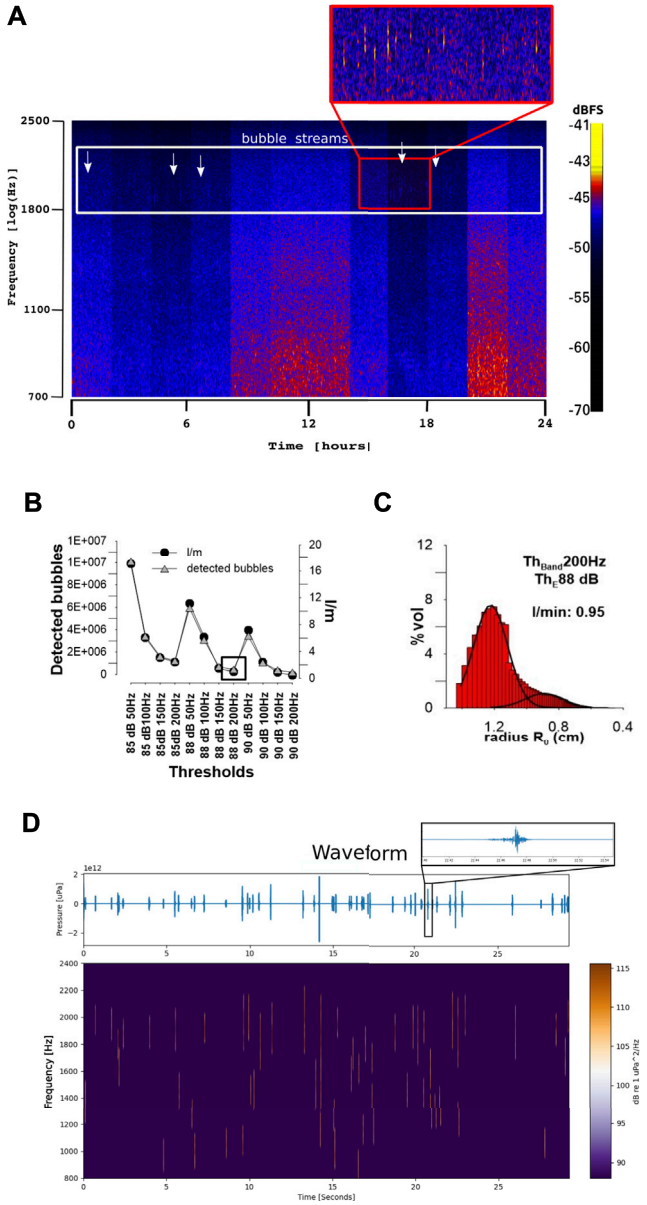


FIGURE 16 | (A) Example of raw daily resulting spectrogram, calculated on 2048 point-sized window (38.6 ms), of merged 30-second-long audio records, recorded on 24th of June; the bandwidth shown is bounded to 700–2,500 Hz band; white rectangular highlight single bubbles' oscillatory signals; red rectangle details a specific bubble stream. **(B)** Line plot (relative to D3 investigation) describing "Number of events" and related l/min vs. threshold. **(C)** Bar chart plot showing the distribution chosen after the investigation made on D3 thresholds investigation. **(D)** Detailed short-time Fourier transform (STFT) spectrogram and waveform (Th_EE = 88 dB, Th_{Band} = 200 Hz) relative to a single record acquired on August 26^{thc} during D3.

emission style and released small size bubbles, albeit continuously, it shows the highest concentration values (5.8 micromol/L). Such evidence is likely due to the position of the observatory with respect to the flares emitting methane. Specifically, it may be located downstream with respect to the direction of the currents that possibly transport the gas just in the direction of the chemical sensor. Differently, despite the two combinated degassing style, continuously diffused and punctual burst-like release, D2 could be likely sited upstream with respect to the dominant currents. Hence, while acoustic records could detect bubble signatures, chemical sensor acquisitions may gain less concentration of dissolved methane (1.5 micromol/L). The lack of a current meter in our equipment represents a limit in the robustness of the above assumptions.

CONCLUSION

Coupling the geochemical features of the water column with the temporal changes recorded by a sea-floor multidisciplinary observatory and the spectra analysis of acoustic records we gained further information useful to better constrain the processes and the interactions governing the injection of methane from the sea bottom sediments to the water column in the Black Sea.

The Romanian sector of the Black sea, hosting a huge amount of methane of various origin, has been a perfect study area where we deployed a multidisciplinary submarine observatory (EMSO-MEDIT_001) in the main frame of the ENVRI-Plus activities. The geochemical features of the dissolved gases along the water column show a methane content which increases in the deep water layers besides lowering of pH down to 7.8 or negative Eh values.

The data of the continuous monitoring of temperature, pH, EC, turbidity, dissolved methane collected by the sea-floor observatory during short, mid and long-term deployments, depicted temporal changes induced by anthropic disturbances (coring) as well as by natural forces (e.g. wind, sea waves) and natural events (e.g. earthquakes). The information from passive acoustics allowed us to detect and describe several mechanisms related to the gas release inside the sediments and along the water column. Albeit the short duration of every single acoustic record, it was yet possible to identify different frequency ranges (within the 200–2400 Hz range) related to the energy produced by the motion of methane bubble's walls of various sizes.

As this feature is a consequence of the emission style, we discriminated sudden and impulsive gas bursts from continuous gentle gas emission. Moreover we d roughly estimated volume of the released gas, based on bubble size distribution and the bubbles acoustic signature in the different areas. We estimated a methane flow rate in the range of 771-2030 mol/day. The acoustic technique is thus capable of identifying single bubbles in noisy environments and determining bubble size distribution and gas flux. The implemented single bubble identification technique can be performed automatically for any length of acoustic signals. This allows long-term underwater acoustic detection and quantification of different gas releases over a variety of marine environments in the world-wide ocean seafloor. The technique is applicable when bubbles are generated as a single stream or multiple streams. However, when the bubbles are generated as plumes or clouds rather than single stream, it is difficult for the technique to identify single bubbles, which may make the estimate results inaccurate and an alternative way would be the acoustic inversion method (Leighton and White, 2011).

The use of multiple hydrophones in an array configuration may however improve the detection performance, especially in noisy environments, and even extend the range of observation. Furthermore, equipping the submarine observatories with bottom-currents measurement devices could result in a more complete and exhaustive information concerning the water column features. The hydro-acoustic data gathered allowed also to detect the "vibrations" of the pathways network induced by the escaping gas dynamics through the sediments below the sea bottom (in the infrasonic band 1–20 Hz), providing an additional perspective to better bind the mechanisms responsible for the generation of methane degassing.

As the methane release in the submarine environment is a cause of growing concern worldwide, due to the effects related to global warming and ocean acidification, the results we gained provide new tools to better constrain and quantify the acceleration of production and release in marine environments.

DATA AVAILABILITY STATEMENT

The raw data supporting the conclusions of this article will be made available by the authors, without undue reservation.

AUTHOR CONTRIBUTIONS

ML and GL contributed to conception and design of the study. CC organized the database. ML and GL wrote the first draft of the manuscript. CC, SS, VR, RR, FI and DB wrote sections of the manuscript. All authors contributed to article revision, read, and approved the submitted version.

ACKNOWLEDGMENTS

The authors are grateful to all crew members of R/V MareNigrum, for their precious help and professionality. All the valuable results couldn't have been possible without the financial support of the "European Multidisciplinary Seafloor and water column Observatory" consortium (EMSO), which under EMSO-Medit and EMSO-Miur projects enabled infrastructure maintenance and data analysis. The authors would also like to tank the reviewers Cuiling Xu, Jianghui Li and the third anonimous reviewer for their precious suggestions and comments that made possible a significant improvement of the manuscript.

REFERENCES

Ainslie, M. A., and Leighton, T. G. (2011). Review of Scattering and Extinction Cross-Sections, Damping Factors, and Resonance Frequencies of a Spherical Gas Bubble. *The J. Acoust. Soc. America.* 130, 3184–3208. doi:10.1121/1.3628321

Ainslie, M. A., and McColm, J. G. (1998). A Simplified Formula for Viscous and Chemical Absorption in Sea Water. *J. Acoust. Soc. America.* 103, 1671–1672. doi:10.1121/1.421258

Alparone, S., Cannata, A., Gambino, S., Gresta, S., Milluzzo, V., and Montalto, P. (2010). Time-Space Variation of Volcano-Seismic Events at La Fossa (Vulcano, Aeolian Islands, Italy): New Insights into Seismic Sources in a Hydrothermal System. *Bull. Volcanol.* 72, 803–816. doi:10.1007/s00445-010-0367-6

Buffett, B. A. (2000). Clathrate Hydrates. *Annu. Rev. Earth Planet. Sci.* 28, 477–507. doi:10.1146/annurev.earth.28.1.477

Capasso, G., and Inguaggiato, S. (1998). A Simple Method for the Determination of Dissolved Gases in Natural Waters. An Application to thermal Waters from Vulcano Island. *Appl. Geochem.* 13, 631–642. doi:10.1016/s0883-2927(97)00109-1

Commission on the Protection of the Black Sea Against Pollution/State of the Environment of the Black Sea (2001). Available at: http://www.blacksea-commission.org/_publ-SOE2009.asp#_Toc225838294.

Cynar, F. J., and Yayanos, A. A. (1993). *Biogeochemistry of Global Change: Radiatively Active Trace Gases*. Editor R. S. Oremland (Menlo Park, CA: Chapman & Hall), 551–573.

Devin, C. (1959). Survey of thermal, Radiation, and Viscous Damping of Pulsating Air Bubbles in Water. *J. Acoust. Soc. America.* 31, 1654–1667. doi:10.1121/1.1907675

Dziak, J. J., Nahum-Shani, I., and Collins, L. M. (2012). Multilevel Factorial Experiments for Developing Behavioral Interventions: Power, Sample Size, and Resource Considerations. *Psychol. Methods.* 17 (2), 153–175. doi:10.1037/a0026972

Dziak, R. P., and Fox Christopher, G. (2002). Evidence of Harmonic Tremor From a Submarine Volcano Detected across the Pacific Ocean basin. *JGR Solid Earth.* 107, ESE 1-1–ESE 1-11. doi:10.1029/2001jb000177

Dziak, R. P., and Haxel, J. H. (2008). Observations of Regional Seismicity and Local Harmonic Tremor at Brothers Volcano, South Kermadec Arc, Using an Ocean Bottom Hydrophone Array. *J. Geophys. Res. Solid Earth.* 113, B08S04. doi:10.1029/2007jb005533

Dziak, R. P., Matsumoto, H., Embley, R. W., Merle, S. G., Lau, T.-K., Baumberger, T., et al. (2018). Passive Acoustic Records of Seafloor Methane Bubble Streams on the Oregon continental Margin. *Deep Sea Res. Part Topical Stud. Oceanography.* 150, 210–217. doi:10.1016/j.dsr2.2018.04.001

Dziak, R. P., Smith, D. K., Bohnenstiehl, D. R., Fox, C. G., Desbruyeres, D., Matsumoto, H., et al. (2004). Evidence of a Recent Magma Dike Intrusion at the Slow Spreading Lucky Strike Segment, Mid-Atlantic Ridge. *J. Geophys. Res.* 109, B12102. doi:10.1029/2004JB003141

Erbe, C. (2008). Critical Ratios of Beluga Whales (*Delphinapterus leucas*) and Masked Signal Duration. *J. Acoust. Soc. America.* 124, 2216–2223. doi:10.1121/1.2970094

Etiope, G., and Klusman, R. W. (2002). Geologic Emissions of Methane to the Atmosphere. *Chemosphere.* 49 (8), 777–789. doi:10.1016/s0045-6535(02)00380-6

Etiope, G., and Milkov, A. V. (2004). A New Estimate of Global Methane Flux From Onshore and Shallow Submarine Mud Volcanoes to the Atmosphere. *Env Geol.* 46 (8), 997–1002. doi:10.1007/s00254-004-1085-1

Floodgate, G. D., and Judd, A. G. (1992). The Origins of Shallow Gas. *Continental Shelf Res.* 12 (Issue 10), 1145–1156. doi:10.1016/0278-4343(92)90075-u

Gentz, T., Damm, E., Schneider von Deimling, J., Mau, S., McGinnis, D. F., and Schlüter, M. (2014). A Water Column Study of Methane Around Gas Flares Located at the West Spitsbergen continental Margin. *Continental Shelf Res.* 72 (1 January 2014), 107–118. doi:10.1016/j.csr.2013.07.013

Ginsburg, G. D., and Soloviev, V. A. (1998). *Submarine Gas Hydrates*. Russia/Statoil, Stavanger, Norway: VNII Okeanologia, St. Petersburg, 216

Gupta, H. R., and Mehra, R. (2013). Power Spectrum Estimation Using Welch Method for Various Window Techniques. *Int. J. Scientific Res. Eng. Technology (Ijsret).* 2 (6), 389–392. ISSN 2278 - 0882

Hornafius, J. S., Quigley, D., and Luyendyk, B. P. (1999). The World's Most Spectacular Marine Hydrocarbon Seeps (Coal Oil Point, Santa Barbara Channel, California): Quantification of Emissions. *J. Geophys. Res.* 104, 20703–20711. doi:10.1029/1999jc900148

Hovland, M., Judd, A. G., and Burke, R. A. (1993). The Global Flux of Methane From Shallow Submarine Sediments. *Chemospher.* 26 (1-4), 559–578. doi:10.1016/0045-6535(93)90442-8

Inguaggiato, S., and Rizzo, A. (2004). Dissolved Helium Isotope Ratios in Ground-Waters: a New Technique Based on Gas-Water Re-equilibration and its

Application to Stromboli Volcanic System. *Appl. Geochem.* 19, 665–673. doi:10.1016/j.apgeochem.2003.10.009

Italiano, F., Bonfanti, P., Ditta, M., Petrini, R., and Slejko, F. (2009). Helium and Carbon Isotopes in the Dissolved Gases of Friuli Region (NE Italy): Geochemical Evidence of CO2 Production and Degassing Over a Seismically Active Area. *Chem. Geology.* 266, 76–85. doi:10.1016/j.chemgeo.2009.05.022

Italiano, F., Yuce, G., Uysal, I. T., Gasparon, M., and Morelli, G. (2014). Insights Into Mantle-type Volatiles Contribution from Dissolved Gases in Artesian Waters of the Great Artesian Basin, Australia. *Chem. Geology.* 2014, 75–88. doi:10.1016/j.chemgeo.2014.04.013

Judd, A. G. (2000). "Geological Sources of Methane," in *Atmos. Methane.*. Editors M. A. K. Khalil (Berlin, Heidelberg: Springer, 280–303. doi:10.1007/978-3-662-04145-1_15

Judd, A. G. (2003). The Global Importance and Context of Methane Escape from the Seabed. *Geo-mar. Lett.* 23, 147. doi:10.1007/s00367-003-0136-z

Judd, A. G. (2004). Natural Seabed Gas Seeps as Sources of Atmospheric Methane. *Env Geol.* 46, 988–996. doi:10.1007/s00254-004-1083-3

Judd, A. G., Hovland, M., Dimitrov, L. I., García Gil, S., and Jukes, V. (2002). The Geological Methane Budget at Continental Margins and its Influence on Climate Change. *Geofluids.* 2 (2), 109–126. doi:10.1046/j.1468-8123.2002.00027.x

Konstantinou, K. I. (2015). Tornillos Modeled as Self-Oscillations of Fluid Filling a Cavity: Application to the 1992-1993 Activity at Galeras Volcano, Colombia. *Phys. Earth Planet. Interiors.* 238, 23–33. doi:10.1016/j.pepi.2014.10.014

Kvenvolden, K. A. (1999). Potential Effects of Gas Hydrate on Human Welfare. *Proc. Natl. Acad. Sci.* 96 (7), 3420–3426. doi:10.1073/pnas.96.7.3420

Leifer, I., and Boles, J. (2005). Measurement of marine Hydrocarbon Seep Flow through Rock and Unconsolidated Sediment. *J. Mar. Petrol. Geol.* 22 (4), 551–568. doi:10.1016/j.marpetgeo.2004.10.026

Leifer, I. (2010). Characteristics and Scaling of Bubble Plumes from marine Hydrocarbon Seepage in the Coal Oil Point Seep Field. *J. Geophys. Res.* 115, C11014. doi:10.1029/2009JC005844

Leifer, I., and Culling, D. (2010). Formation of Seep Bubble Plumes in the Coal Oil point Field. *Geo-mar. Lett.* 30 (3–4), 339–353. doi:10.1007/s00367-010-0187-x

Leifer, I., and Patro, R. K. (2002). The Bubble Mechanism for Methane Transport From the Shallow Sea Bed to the Surface: A Review and Sensitivity Study. *Continental Shelf Res.* 22 (16), 2409–2428. doi:10.1016/S0278-4343(02)00065-1

Leifer, I., and Tang, D. (2007). The Acoustic Signature of Marine Seep Bubbles. *J. Acous. Soc.* doi:10.1121/1.2401227

Leighton, T. G., and White, P. R. (2011). Quantification of Undersea Gas Leaks From Carbon Capture and Storage Facilities, from Pipelines and From Methane Seeps, by Their Acoustic Emissions. *Proc. R. Soc. A.* 468, 485–510. doi:10.1098/rspa.2011.0221

Li, J., Roche, B., Bull, J. M., White, P. R., Davis, J. W., Deponte, M., et al. (2020). Passive Acoustic Monitoring of a Natural CO2 Seep Site - Implications for Carbon Capture and Storage. *Int. J. Greenhouse Gas Control.* 93, 102899. doi:10.1016/j.ijggc.2019.102899

Li, J., White, P. R., Roche, B., Bull, J. M., Leighton, T. G., Davis, J. W., et al. (2021). Acoustic and Optical Determination of Bubble Size Distributions - Quantification of Seabed Gas Emissions. *Int. J. Greenhouse Gas Control.* 108, 103313. doi:10.1016/j.ijggc.2021.103313

Longo, M., Lazzaro, G., Caruso, C. G., Corbo, A., Sciré Scappuzzo, S., Italiano, F., et al. (2021). "Hydro-acoustic Signals From the Panarea Shallow Hydrothermal Field: New Inferences of a Direct Link With Stromboli, Geological Society, London, Special Publications. From," in *Volcanic Island: From Hazard Assessment to Risk Mitigation*. Editors E. Marotta, L. D'Auria, F. Zaniboni, and R. Nave (London, UK: Geological Society, London, Special Publications), 519, SP519–2020. doi:10.1144/SP519-2020-184

Lu, N. Q., Prosperetti, A., and Yoon, S. W. (1990). Underwater Noise Emissions from Bubble Clouds. *IEEE J. Oceanic Eng.* 15, 275–281. doi:10.1109/48.103521

Mau, S., Römer, M., Torres, M. E., Bussmann, I., Pape, T., Damm, E., et al. (2017). Widespread Methane Seepage Along the Continental Margin off Svalbard - from Bjørnøya to Kongsfjorden. *Sci. Rep.* 7, 42997. doi:10.1038/srep42997

McGinnis, D. F., Greinert, J., Artemov, Y., Beaubien, S. E., and Wüest, A. (2006). Fate of Rising Methane Bubbles in Stratified Waters: How Much Methane Reaches the Atmosphere?. *J. Geophys. Res.* 111, C09007. doi:10.1029/2005jc003183

Milkov, A. V. (2004). Global Estimates of Hydrate-Bound Gas in Marine Sediments: How Much Is Really Out There?. *Earth-Science Rev.* 66, 183–197. doi:10.1016/j.earscirev.2003.11.002

Milluzzo, V., Cannata, A., Alparone, S., Gambino, S., Hellweg, M., Montalto, P., et al. (2010). Tornillos at Vulcano: Clues to the Dynamics of the Hydrothermal System. *J. Volcanology Geothermal Res.* 198, 377–393. doi:10.1016/j.jvolgeores.2010.09.022

Minnaert, M. (1933). XVI.On Musical Air-Bubbles and the Sounds of Running Water. *Lond. Edinb. Dublin Philosophical Mag. J. Sci.* 16, 235–248. doi:10.1080/14786443309462277

Ohminato, T. (2006). Characteristics and Source Modeling of Broadband Seismic Signals Associated With the Hydrothermal System at Satsuma-Iwojima Volcano, Japan. *J. Volcanology Geothermal Res.* 158, 467–490. doi:10.1016/j.jvolgeores.2006.08.004

Özsoy, E., and Ünlüata, Ü. (1997). Oceanography of the Black Sea: A Review of Some Recent Results. *Earth-Science Rev.* 42 (4), 231–272. doi:10.1016/s0012-8252(97)81859-4

Pape, T., Blumenberg, M., Seifert, R., Bohrmann, G., and Michaelis, W. (2008). *Marine Methane Biogeochemistry of the Black Sea: A Review, Links between Geological Processes, Microbial Activities & Evolution of Life: Microbes and Geology*. Dordrecht: Springer Netherlands, 281–311.

Peregrine, D. H. (1994). The Acoustic Bubble. By T. G. Leighton. Academic Press, 1994. 613 Pp. £95. ISBN 0-12-441920-8. The Acoustic Bubble. From Peregrine, D. H. Academic Press Pp 613. ISBN 0-12-441920-8. *J. Fluid Mech.* 272, 407–408. doi:10.1017/s0022112094214519

Popa, A. (1993). Liquid and Sediment Inputs of the Danube River Into the Northwestern Black Sea. *Mitt. Geol.-Palaont. Inst. Univ. Hamburg.* 74, 137–149.

Römer, M., Sahling, H., dos Santos Ferreira, C., and Bohrmann, G. (2020). Methane Gas Emissions of the Black Sea-Mapping From the Crimean continental Margin to the Kerch Peninsula Slope. *Geo-mar Lett.* 40, 467–480. doi:10.1007/s00367-019-00611-0

Sano, Y., and Wakita, H. (1988). Precise Measurement of Helium Isotopes in Terrestrial Gases. *Bcsj.* 61, 1153–1157. doi:10.1246/bcsj.61.1153

Schmale, O., Greinert, J., and Rehder, G. (2005). Methane Emission From High-Intensity Marine Gas Seeps in the Black Sea into the Atmosphere. *Geophys. Res. Lett.* 32, a–n. doi:10.1029/2004GL021138

Schoell, M. (1988). Multiple Origins of Methane in the Earth. *Chem. Geology.* 71, 1–10. doi:10.1016/0009-2541(88)90101-5

Shindell, D. T., Faluvegi, G., Koch, D. M., Schmidt, G. A., Unger, N., and Bauer, S. E. (2009). Improved Attribution of Climate Forcing to Emissions. *Science.* 326 (5953), 716–718. doi:10.1126/science.1174760

Stadnitskaia, A., Ivanov, M. K., Poludetkina, E. N., Kreulen, R., and van Weering, T. C. E. (2008). Sources of Hydrocarbon Gases in Mud Volcanoes From the Sorokin Trough, NE Black Sea, Based on Molecular and Carbon Isotopic Compositions. *Mar. Pet. Geology.* 25 (10), 1040–1057. doi:10.1016/j.marpetgeo.2007.08.001

Strasberg, M. (1956). Gas Bubbles as Sources of Sound in Liquids. *J. Acoust. Soc. America.* 28, 20–26. doi:10.1121/1.1908212

Tolstoy, M., Vernon, F. L., Orcutt, J. A., and Wyatt, F. K. (2002). Breathing of the Seafloor: Tidal Correlations of Seismicity at Axial Volcano. *Geol.* 30, 503–506. doi:10.1130/0091-7613(2002)030<0503:botstc>2.0.co;2

Vazquez, A., Sanchez, R. M., Salinas-Rodríguez, E., Soria, A., and Manasseh, R. (2005). A Look at Three Measurement Techniques for Bubble Size Determination. *Exp. Therm. Fluid Sci.* 30, 49–57. doi:10.1016/j.expthermflusci.2005.03.018

Walton, A. J., Gunn, M. G., and Reynolds, G. T. (2005). The Quality Factor of Oscillating Bubbles as an Indication of Gas Content With Particular Reference to Methane. *IEEE J. Oceanic Eng.* 30, 924–926. doi:10.1109/joe.2004.834171

Wenz, G. M. (1962). Acoustic Ambient Noise in the Ocean: Spectra and Sources. *J. Acoust. Soc. America.* 34, 1936–1956. doi:10.1121/1.1909155

Whiticar, M. J. (1990). A Geochemical Perspective of Natural Gas and Atmospheric Methane. *Org. Geochem.* 16 (Issues 1–3), 531–547. doi:10.1016/0146-6380(90)90068-B

Wiggins, S. M., Leifer, I., Linke, P., and Hildebrand, J. A. (2015). Long-Term Acoustic Monitoring at North Sea Well Site 22/4b. *Mar. Pet. Geology.* 68, 776–788. doi:10.1016/j.marpetgeo.2015.02.011

Wilcock, W. S. D., Stafford, K. M., Andrew, R. K., and Odom, R. I. (2014). Sounds in the Ocean at 1-100 Hz. *Annu. Rev. Mar. Sci.* 6, 117–140. doi:10.1146/annurev-marine-121211-172423

Wong, H. K., Winguth, C., Panin, N., Dinu, C., Wollschläger, M., Ungureanu, G., et al. (1997). The Danube and Dniepr Fans: Morphostructure and Evolution". *GeoEcoMarina.* 2, 77–102. doi:10.5724/gcs.12.32.0701

Conflict of Interest: The authors declare that the research was conducted in the absence of any commercial or financial relationships that could be construed as a potential conflict of interest.

Publisher's Note: All claims expressed in this article are solely those of the authors and do not necessarily represent those of their affiliated organizations, or those of the publisher, the editors and the reviewers. Any product that may be evaluated in this article, or claim that may be made by its manufacturer, is not guaranteed or endorsed by the publisher.

Copyright © 2021 Longo, Lazzaro, Caruso, Radulescu, Radulescu, Sciré Scappuzzo, Birot and Italiano. This is an open-access article distributed under the terms of the Creative Commons Attribution License (CC BY). The use, distribution or reproduction in other forums is permitted, provided the original author(s) and the copyright owner(s) are credited and that the original publication in this journal is cited, in accordance with accepted academic practice. No use, distribution or reproduction is permitted which does not comply with these terms.

frontiers in Earth Science

ORIGINAL RESEARCH
published: 17 September 2021
doi: 10.3389/feart.2021.620161

Inversion Characteristics of Hydrocarbon Gases Carbon Isotopes Varying With Temperature and Implications for Shale Exploration

Yingqin Wu[1]†, Yanhong Liu[1†], Tong Wang[2], Zhiyu Wang[1,3], Longmiao Yuan[1,3] and Yanqin Xia[1]*

[1]Key Laboratory of Petroleum Resources, Gansu Province/Northwest Institute of Eco-Environment and Resources, Chinese Academy of Sciences, Lanzhou, China, [2]School of Engineering, Newcastle University, Newcastle, United Kingdom, [3]University of Chinese Academy of Sciences, Beijing, China

In order to understand the influence of source rock types and maturity on hydrocarbon gases carbon isotope change more objectively, a closed-system pyrolysis experiment was carried out on six samples from 250 to 550°C. The values of $\delta^{13}C_1$, $\delta^{13}C_2$, and $\delta^{13}C_3$ were ranged from −73.3 to −29.8%, from −36.3 to −9.5%, and from −38.5 to −12.4%, respectively. The range of $\delta^{13}C_1$ was the largest, reaching a top value of 43.5%. The results showed that the temperature has an effect on the carbon isotope value of pyrolysis gas. With the increase of the degree of thermal evolution, the carbon isotope value of methane in all samples, except for huangxian gangue, had a change trend from heavy to light firstly, then got heavier. In addition, the carbon isotope values of methane, ethane and propane had the features of $\delta^{13}C_1 < \delta^{13}C_2 < \delta^{13}C_3$ when the temperatures were under 550°C, which were made up of a series of positive carbon isotopes. However, when the temperature increased above 550°C, there was an inversion of the simulated gas carbon isotope values in Huangxian coal gangue, Minqin oil shale and Huaan carbonaceous shale, i.e., $\delta^{13}C_2 > \delta^{13}C_3$ and $\delta^{13}C_2 > \delta^{1}3C_1$. It indicates that the secondary cracking has occurred at high maturity or over maturity stage.

Keywords: pyrolysis, hydrocarbon source rocks, organic matter types, gas carbon isotope, isotope inversion

OPEN ACCESS

Edited by:
Giovanni Martinelli, National Institute of Geophysics and Volcanology, Section of Palermo, Italy

Reviewed by:
Ksenija Stojanovic, University of Belgrade, Serbia
Yunpeng Wang, Guangzhou Institute of Geochemistry, Chinese Academy of Sciences, China

***Correspondence:**
Yingqin Wu
yingqinwu@lzb.ac.cn

†These authors have contributed equally to this work and share first authorship

Specialty section:
This article was submitted to Geochemistry, a section of the journal Frontiers in Earth Science

Received: *22 October 2020*
Accepted: *23 July 2021*
Published: *17 September 2021*

Citation:
Wu Y, Liu Y, Wang T, Wang Z, Yuan L and Xia Y (2021) Inversion Characteristics of Hydrocarbon Gases Carbon Isotopes Varying With Temperature and Implications for Shale Exploration. Front. Earth Sci. 9:620161. doi: 10.3389/feart.2021.620161

INTRODUCTION

The distribution and evolution of stable carbon isotopes contain important information of natural gas. As a result, carbon stable isotope has an important role in the study of natural gas genesis, oil and gas filling history, migration and oil source correlation (Cramer, 2004; Duan et al., 2011; Tian et al., 2012; Hao and Zou, 2013; Wu et al., 2015; Han et al., 2018). The most widely used and technically mature index is the stable carbon isotopes of methane and ethane in the previous studies (Peter, 2020; Hill et al., 2007; Li et al., 2013; Wu et al., 2017). As an important means to understand the natural evolution of geochemical characteristics, hydrothermal pyrolysis simulation experiment makes multi-parameter analysis of the controlled system possible, and the analysis results can be applied to practical production. In order to meet the needs of oil and gas exploration, many scholars have studied the relationship between methane stable carbon isotopes and temperature and maturity by simulating hydrocarbon generation in immature and low-mature sediments (Dieckmann et al., 2006; Lewan and Roy, 2011; Duan et al., 2011; Li et al., 2018). Thus, the

TABLE 1 | Characterstics and data for TOC, Rock-Eval pyrolysis values, and Ro for the studied samples.

Sample	Basin	Formation	Kerogen type	TOC (%)	Tmax (°C)	S_1 (mg/g)	S_2 (mg/g)	HI (mg S_2/g)	Ro (%)
Green River Shale	Green River Basin	Green River Formation	I	23.63	438	4.54	215.83	913	0.24[a]
Pine Needle	Yellow River Valley Basin	Ten years old higher plant	–	–	–	–	–	–	–
Minqin Oil Shale	Ordos Basin	Guodikeng Formation	I–II		435	1.1	54.84	559	0.43
Cangcan 1# Shale	Bohai Bay Basin	Yuertusi Formation	II	4.65	443	1.35	10.60	228	0.53
Huaan Carbonaceous Shale	Huaan Basin	Jijuntun Formation	III	70.13	438	3.74	82.05	117	0.49
Huangxian Coal Gangue	Huangxian Basin	Lijiaya Formation	III	30.25	437	1.86	16.94	56	0.48

TOC = total organic carbon; T_{max} = temperature with maximum hydrocarbon generation; S_1 = free hydrocarbons; S_2 = pyrolytic hydrocarbon yield; HI= hydrogen index (HI = (S_2/TOC) ×100, mg S_2/g TOC)

[a]*Represents asphalt reflectivity*

thermal evolution of methane stable carbon isotopes was been quantitatively calibrated. Previous studies showed that the stable carbon isotopes of methane decrease first and then increase with the increase of thermal evolution under thermal simulation conditions. Besides, the relationship between the stable carbon isotopes of methane and the maturity of corresponding parent rocks was established, and it was proved with a linear correlation. Obviously, the variation trend of methane carbon isotope was different from that of thermal simulation results. Furthermore, there were still many differences in the thermal evolution of methane stable carbon isotopes under experimental conditions.

Most researchers have used methane, ethane, and propane from global natural gas reserves to derive a normal sequence of carbon isotopes, such as $\delta^{13}C$ methane (C_1) < $\delta^{13}C$ ethane (C_2) < $\delta^{13}C$ propane (C_3) (Clayton 1991; Pan et al., 2010). However, in the study of unconventional shale gas, it was found that the change of carbon isotope in natural gas was reversed and had two characteristics: partially reversed ($\delta^{13}C_1 > \delta^{13}C_2 < \delta^{13}C_3$) and completely reversed ($\delta^{13}C_1 > \delta^{13}C_2 > \delta^{13}C_3$) (Tilley and Muehlenbachs, 2013; Cheng et al., 2020; Milkov and Eriope, 2018, 2020). The Wufeng Formation of the Upper Ordovician to the Longmaxi Formation of the Lower Silurian in Sichuan Basin is the only strata in China that have realized commercial shale gas development at present, but there are still some differences on the origin of shale gas, mainly due to the lack of direct experimental evidence. However, the lack of these early understandings had restricted the evaluation of natural gas accumulation and the deployment of natural gas exploration strategies. Thus, the purpose of this study is to analyze the composition of natural gas and carbon isotope composition characteristics, and further to improve the understanding of gas-source correlation. In addition, the effects of temperature and kerogen types on light hydrocarbon isotopes were also poorly understood. In this paper, the composition and evolution of carbon isotopes of hydrocarbon gases were studied by the hydrous pyrolysis of several immature organic sources under the condition of continuous heating at 250–550°C. Furthermore, the evolution and inversion of gas stable carbon isotopes at different temperatures were systematically studied. These results have an important contribution to the exploration of shale gas.

SAMPLING AND METHODS

Sampling

The six samples used in this study included different types source rocks and a higher plant sample. The samples were all thermally immature, and the geochemical data were shown in **Table 1**. I) Green River shale, from the Green River Basin in US, was collected from the Eocene Green River Formation containing Type-I kerogen; II) Minqin oil shale, from the Ordos Basin in Northwest China, was from the Triassic Guodikeng Formation containing Type-I-II kerogen; It is deposited in a deep-semi-deep lake environment, the Minqin Oasis is located in the western part of the Gansu Province, northwestern China. III) Huaan carbonaceous shale, from the Huaan Basin in Northwest China, was mainly collected from the Eocene-Oligocene Jijuntun Formation with Type-III kerogen; IV) Cangcan 1# shale from the Bohai Bay Basin in Northeast China, was formed in the Cenozoic Eocene epoch with Type-II kerogen; V) Huangxian coal gangue, from the Tertiary humus coals, was collected from the Lijiaya Formation of the Huangxian Basin in the eastern of China's Shandong peninsula with Type-III kerogen. VI) Pine needle, from higher plant, was collected from a 10 years old pine tree of Lanzhou, China. The characterstics and data for TOC, Rock-Eval pyrolysis values, and Ro for the studied samples were showed in **Table 1**.

METHODS

Closed-System Pyrolysis Experiments

The hydrolysis experiment was carried out in a stainless steel reactor. The samples were crushed into powder ≤100 mesh and dried at 50°C for 24 h. The weighed sample and distilled water are first placed in a reactor (details are provided in **Supplementary Data Sheet 1**). The reactor (with an internal volume of 0.27 L) loaded with sample was vacuumized and replaced with He gas for 3 times, then heated in a furnace with a temperature controller. Isothermal pyrolysis was then heated from room temperature to the final temperature (250, 300, 350, 400, 450, 500, and 550°C) for 72 h, with a heating rate of 20°C/min. During experiments, the accuracy of temperature measurements was better than ±0.5°C. The pressure during the heating was equal to the vapor pressure of water and gas at each temperature level.

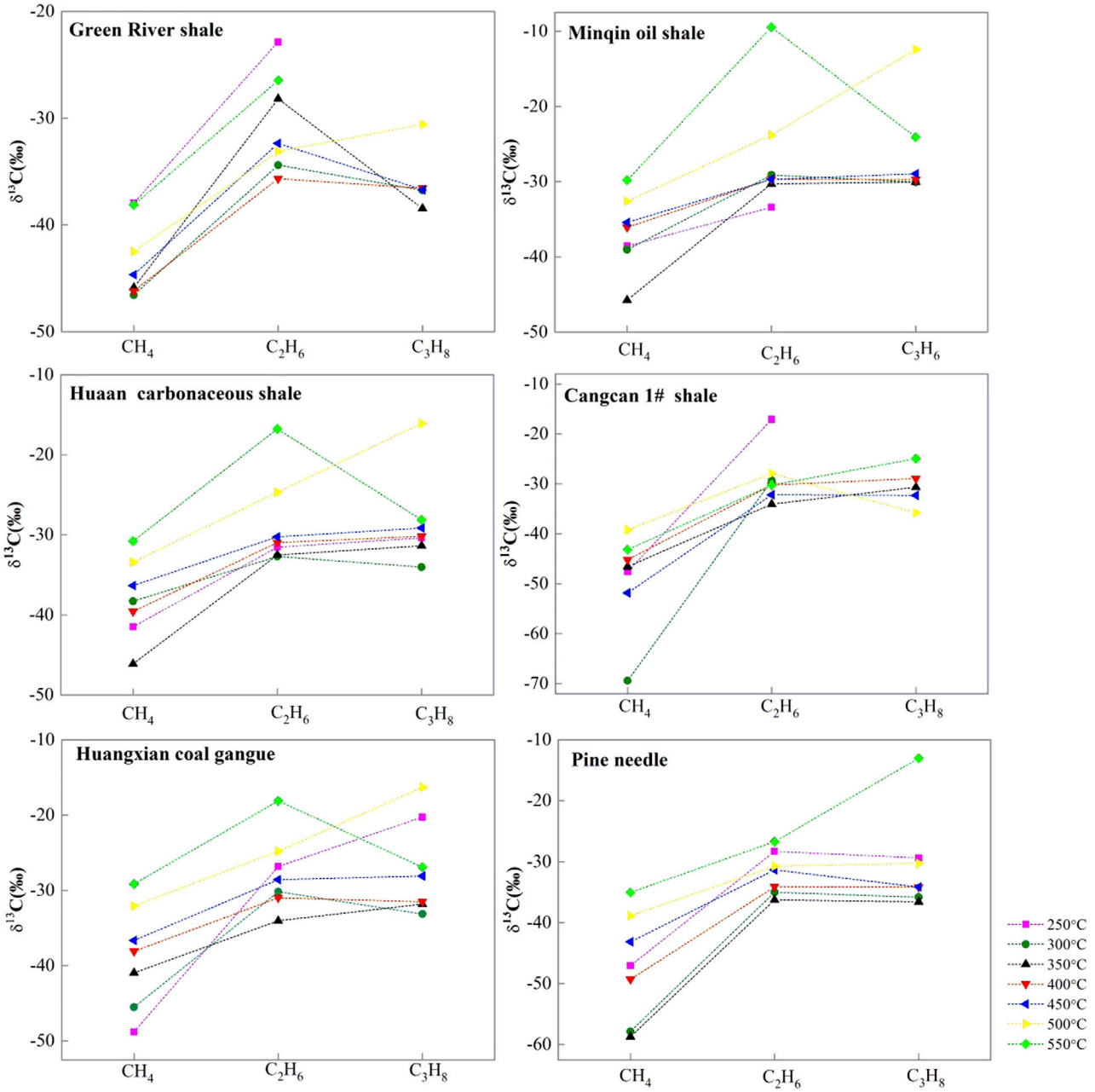


FIGURE 1 | Evolution characteristics of gas carbon isotope in thermal simulation.

Isotopic Analysis

Stable carbon isotope analysis was performed with a MAT 253 (Thermo Fisher Scientific Corp., Bremen, Germany) gas chromatographic isotope ratio mass spectrometer (GC-IRMS). The Gas chromatography (GC) was equipped with an HP-5 fused silica column (100 m × 0.32 mm × 0.25 μm, Agilent, United States), helium as carrier gas, fixed at 1.1 ml/min. In splitless mode, the GC inlet temperature was maintained at 280°C. The oven temperature was started at 80°C (held 2 min), and increased to 300°C at 4°C/min (held 30 min). The temperature of combustion furnace was 800°C, and CuO and Pt wires were loaded as oxidant and catalyst, respectively.

Samples was injected at an initial temperature of 50°C (maintained for 3 min), then the sample was heated at a rate of 15°C/min to 190°C, 5°C/min to 250°C, and kept for 15 min. To ensure the standard deviation was less than ±0.3%, each sample was analyzed continuously for at least 3 times, and a known standard sample (5°C/min) was also measured every day to monitor the analysis accuracy.

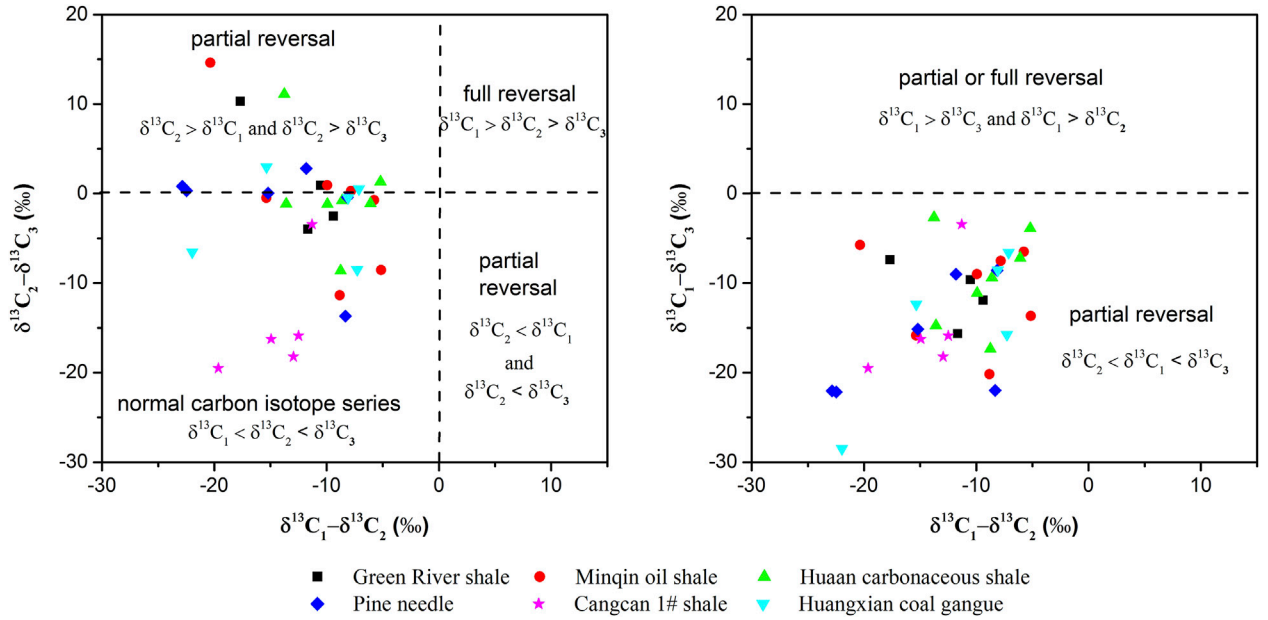


FIGURE 2 | Reversal distribution mode of carbon isotopic composition of shale gas (Modified from References (Rodriguez and Philp, 2010; Tilley and Muehlenbachs, 2013).

RESULTS AND DISCUSSIONS

Distribution Mode of $\delta^{13}C_1$, $\delta^{13}C_2$, and $\delta^{13}C_3$

In general, the carbon isotopic composition ($\delta^{13}C$) indicated the stability of gaseous hydrocarbons in geochemical reactions (Deines 2002; Zhou et al., 2014). In the present study, the carbon isotope values of methane, ethane, and propane showed two trends. Early in the pyrolysis process, methane, ethane and propane were enriched in ^{12}C. After reaching a ^{13}C minimum, methane and ethane become enriched in ^{13}C as temperature increases other than propane of the samples contained Type-III kerogen, which shift to ^{13}C enrichment at 550°C (**Figure 1**). The phenomenon was similar to the previously reported hydrous pyrolysis experiments (Liu et al., 2012). The

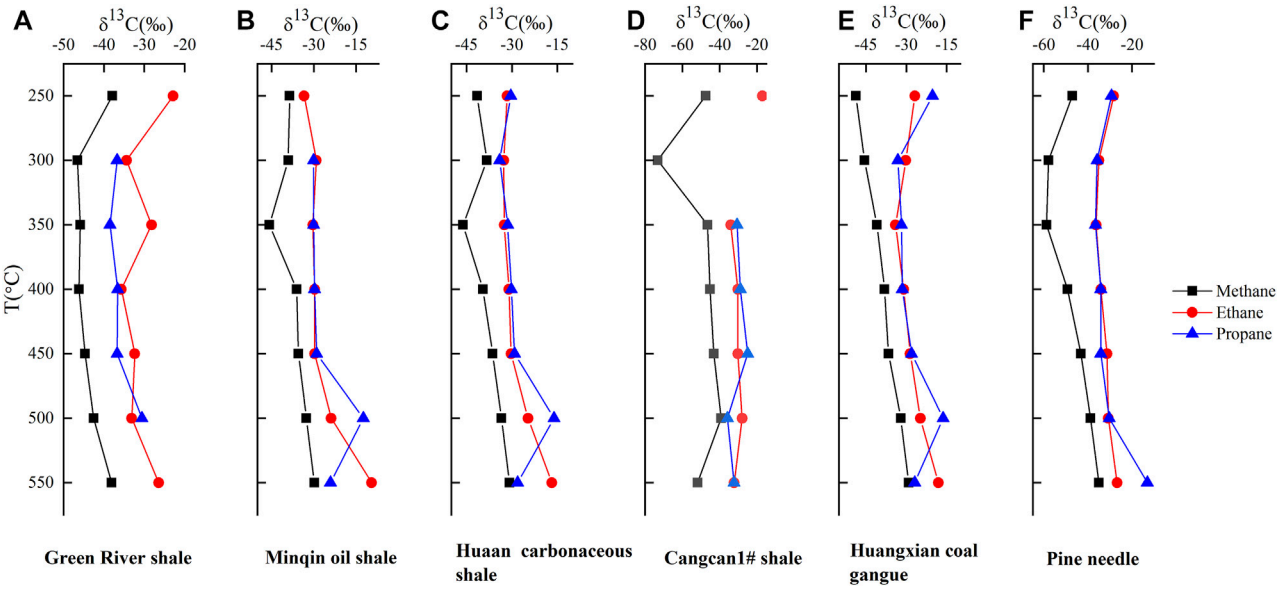


FIGURE 3 | Evolution characteristics of the isotopes of methane, ethane, and propane with temperature.

TABLE 2 | Geochemical composition and stable carbon isotopic of gas in different temperatures.

Sample	T (°C)	Total productivity of gas (ml/g)	Carbon isotopic composition (%)		
			$\delta^{13}C_1$	$\delta^{13}C_2$	$\delta^{13}C_3$
Green River Shale	250	16.0	−37.9	−22.9	–
	300	29.3	−46.6	−34.4	−36.7
	350	43.1	−45.9	−28.2	−38.5
	400	56.2	−46.2	−35.7	−36.6
	450	82.5	−44.7	−32.4	−36.7
	500	115.5	−42.5	−33.1	−30.6
	550	154.1	−38.1	−26.5	–
Minqin Oil Shale	250	11.0	−38.6	−33.4	–
	300	5.2	−39.1	−29.1	−30.1
	350	26.1	−45.7	−29.3	−28.8
	400	33.3	-36.1	−29.7	−29.7
	450	86.2	−35.4	−29.7	−29.0
	500	90.0	−32.6	−23.8	−12.4
	550	128.2	−29.8	−9.5	−24.1
	250	1.3	−41.5	−31.6	−30.4
Huaan Carbonaceous Shale	300	9.1	−38.3	−32.7	−34.0
	350	8.0	−46.1	−32.5	−31.4
	400	20.1	−39.6	−31.0	−30.2
	450	50.0	−36.3	−30.3	−29.2
	500	78.2	−33.4	−24.7	−16.1
	550	74.5	−30.8	−16.8	−28.1
	250	4.8	−48.8	−26.8	−20.3
Huangxian Coal gangue	300	5.2	−45.5	−30.2	−33.1
	350	5.6	−40.9	−34.0	–
	400	9.2	−38.1	−31.0	−31.5
	450	8.3	−36.6	−28.6	−28.1
	500	8.1	−32.1	−24.8	−16.3
	550	11.3	−29.1	−18.1	−25.9
	250	58.8	−47.1	−28.3	N
Pine Needle	300	82.5	−57.8	−35.0	−35.8
	350	118.3	−58.7	−36.3	−36.6
	400	133.3	−49.3	−34.1	−34.1
	450	281.7	−43.1	−31.3	−34.1
	500	275.0	−38.9	−30.7	−30.3
	550	366.2	−35.0	−26.7	−13.0
	250	6.5	−47.6	−17.1	–
Cangcan 1# Shale	300	6.5	−73.3	–	–
	350	9.1	−46.6	−34.1	−30.7
	400	11.3	−45.2	−30.3	−28.9
	450	14.0	−43.2	−30.2	−25.0
	500	4.3	−39.2	−27.9	−35.8
	550	10.7	−51.8	−32.2	−32.3

most negative ^{13}C value was observed approximately at 300 or 350 C for each gas.

In **Figure 2**, the difference and relationship between the "normal" and "reversed" distributions can be clearly observed in plots of $\delta^{13}C$ vs. carbon-number reciprocal. Type-I kerogen at 250–450°C, Type-II kerogen at 500°C and Type-III kerogen at 300, 550°C respectively showed the "reversed" isotope distribution patterns. Compared with methane and propane, the $\delta^{13}C$ values of ethane produced from the hydrous pyrolysis were more positive, showing an obvious significant "dogleg" trend. As the temperature increased from 250 to 350°C, the isotopes reverse trend was also increased significantly in all Type-I, II and III kerogen samples, then the phenomenon was weakened or even disappeared when the temperature was rised from 350 to 500°C. However, as the temperature was increased from 500 to 550°C, the change in carbon isotopic compositions became more and more obvious. There were showed more significant reversal phenomenon for Huangxian coal gangue, Huaan carbonaceous shale (Type III kerogen), Minqin oil shale (Type I-II kerogen) at 550°C (**Figure 3**). This was typical coal-formed gas characteristics. In general, the degree of ethane enriching ^{13}C was far more than methane and propane in all samples other than Pine needle and Green River shale. They showed positive sequences in Pine needle and Green River shale, where propane enriched at ^{13}C far outweighed methane and ethane. This phenomenon may be also applied to the Type-I kerogen samples. With the increase of temperature, the trend of isotope inversion was gradually appeared for Cangcan 1# shale between 350 and 500°C and the carbon sequence was positive at 550°C. The isotopic variation of ethane was obviously different from that of methane and propane, which leads to the evolution of this carbon isotope.

As shown in **Figure 3**, when the temperature reached 300°C, the heavier carbon isotope of ethane appeared. That was, the value of $\delta^{13}C_2$ was heavier than that of $\delta^{13}C_1$ and $\delta^{13}C_3$ respectively, which was especially prominent in the Green River shale (**Figure 3A**; Type I). It was not obvious in Type II (**Figures 3B,D**) and Type III kerogen (**Figures 3C,E**) and Pine needle (**Figure 3F**). After 300°C, kerogen began to produce hydrocarbons. The reason why the carbon isotopic of methane from crude pyrolysis gas was lighter was that carbon isotopic fractionation had occurred to a certain extent during the conversion from kerogen to oil. At the same time, since most of the methane came from the cracking of ethane and other heavy hydrocarbons, and the carbon isotopic value of ethane and other heavy hydrocarbons at the cracking stage was lower than that of crude oil, the carbon isotopic value of the methane generated by ethane must be low (Xiong et al., 2016). This was because that ethane cracking first cracks the ^{12}C–^{12}C bond, and more remaining ^{12}C–^{13}C bond made the $\delta^{13}C_2$ heavier. When the evolution degree was very high, oil and even light hydrocarbon ran out, and finally ethane, propane and other moisture could no longer be formed, and a large number of pyrolysis started. Under the influence of activation energy, the less ethane content was, the heavier the isotope value of ethane. In the Rayleigh Distill stage, no new ethane and propane were generated, but the synchronous cracking of both continued to meet the similar isotopic fractionation model. The isotopic values of ethane and propane increased together, but ethane increased faster, and soon showed the phenomenon that $\delta^{13}C_2$ was heavier than $\delta^{13}C_3$. The increase rate of the isotopic values of ethane and propane was determined by the isotope fractionation factor during pyrolysis. Tang et al. (2000) had already proved that the isotope fractionation factor of ethane during pyrolysis was greater than that of propane. So that's why the carbon isotopes of ethane in Green River shale (Type I) showed heavier than the carbon isotopes of methane and propane in the whole process. This phenomenon was unknown in Type II and Type-III kerogen, and the cause remained to be studied.

Influence of Temperature on Methane Carbon Isotopes

The carbon isotopic compositions of methane from the pyrolysis of the six samples are compared in **Figures 1**, **3**. The methane carbon isotopes generated from pyrolysis experiment in the Green River shale, Minqin oli shale, Huaan carbonaceous shale, Huangxian coal gangue, Pine needle and Cangcan 1# shale were changed in a range of −46.6% to −37.9%, −45.7% to −29.8%, −46.1% to −30.8%, −48.8% to −29.1%, −58.7% to −335.0% and −73.3% to −39.2%, respectively (**Table.2**). In general, methane from the Cangcan 1# shale was more enriched in $^{12}C_1$ than other samples at the same thermal maturity levels. For example, the methane carbon isotopic value for the Huaan carbonaceous shale was as heavy as −38.3% whereas the value for the Cangcan 1# shale was as light as −73.3% at 300°C, with a difference as high as −35.0%. The environment of deposition, tectonic activity and evolutionary sequence determined chemical property and methane carbon isotopes, resulting in significant difference in the influence of kerogen type on methane carbon isotopes.

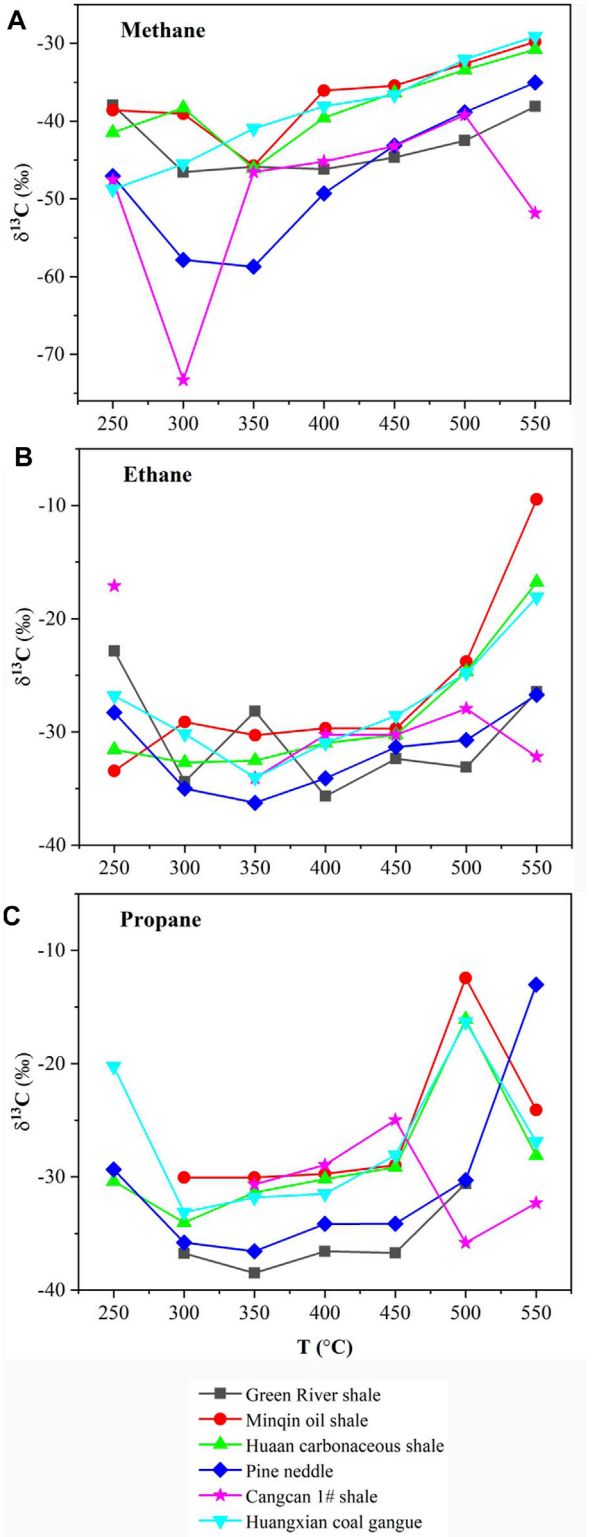


FIGURE 4 | Evolution law of gas carbon isotopic of alkane simulated products from different hydrocarbon sources.

As can be seen from **Figure 3**, with the increase of thermal evolution degree, the carbon isotope values of methane in each sample, except for Huangxian coal gangue (**Figure 3E**), showed a trend of becoming lighter firstly and then becoming heavier with increasing thermal simulation temperature. The reason may be that cracked gas in high-temperature causes methane carbon isotope to heavy between 350 and 400°C. This indicated that methyl radicals increase significantly during the pyrolysis of organic matter between 350 and 400°C, which was likely to generate more methane with heavy isotope composition after exchanging with inorganic carbon during the pyrolysis process.

According to the research results from Lorant et al. (1998) and Tang et al. (2000), the ^{12}C–^{12}C bond is more reactive than ^{12}C–^{13}C bond, which is more likely to be broken than ^{12}C–^{13}C bond because it has a slightly higher bond energy than ^{12}C–^{12}C bond. Therefore, after reaching the oil window, the ^{12}C–^{12}C bond was firstly enriched in methane molecules, this makes the methane isotope lighter. But as the temperature continued to rise, the ^{12}C–^{13}C bond also began to break, making the carbon isotope of methane heavier and heavier.

Another phenomenon can be seen in **Figure 4**. There was a dramatic increase in the carbon isotope values of methane (**Figure 4A**), ethane (**Figure 4B**), and propane (**Figure 4C**) in all samples when the temperature reaches 500°C, which was caused by Rayleigh Distill at the high over-maturity stage. The hydrocarbon generation of source rocks is divided into three stages: primary generation, secondary cracking and Rayleigh Distill, and the principles in different stages are different (James, 1983; Xiong et al., 2016). During the Rayleigh Distill phase, the isotopes became much heavier with the deepening of cracking and exceeded the commonly used identification basis. Thus, the carbon isotopic value of methane is no longer suitable for identification of hydrocarbon source relationship in the high-over mature stage. Therefore, in the future exploration of deep gas fields, the type of natural gas parent material cannot be judged by heavy hydrocarbon isotopic composition only, but should be judged comprehensively by combining with other indicators.

CONCLUSIONS

The methane carbon isotope value from different types of hydrocarbon source products were first light and then heavy with the increase of thermal simulation temperature, and an inflection point occurred after reaching the oil window.

At low temperature, there was a linear negative correlation between methane carbon isotope and simulated temperature. However, in the high temperature evolution phase, the simulated temperature was positively correlated with the carbon isotopes of methane.

In the process of hydrocarbon generation by different types of source rocks, the carbon isotope composition of their parent source had a little degree of fractionation, and which was mainly controlled by the type of parent material, with strong inheritance effect and good tracer significance. This conclusion can be used for oil source comparison and hydrocarbon source tracer research.

The evolution characteristics of gas $\delta^{13}C$ values may be caused by the combination of organic matter type and thermal maturation under the experimental conditions. This research would provide more insights into the distribution of "reverse" isotopes of natural gases.

DATA AVAILABILITY STATEMENT

The original contributions presented in the study are included in the article/Supplementary Material, further inquiries can be directed to the corresponding author.

AUTHOR CONTRIBUTIONS

YW, YX, and YL contributed ideas and design to the study and executed the thermal simulation experiments. TW, ZW, and LY performed chemical analysis and data processing. YW wrote the first draft of the manuscript.

FUNDING

Financial support from the National Science Foundation (Grant Nos. 42072180; 41772147; 41272147; 41831176), the National Key R&D Program of China (Grant No. 2017YFA0604803) and the Chinese Academy of Sciences Instrument Equipment Function Development Technology Innovation Project (Grant No. E0280101). We are also particularly grateful to the anonymous reviewers for their constructive comments for the manuscript.

SUPPLEMENTARY MATERIAL

The Supplementary Material for this article can be found online at: https://www.frontiersin.org/articles/10.3389/feart.2021.620161/full#supplementary-material

REFERENCES

Cheng, B., Xu, J., Deng, Q., Liao, Z., Wang, Y., Faboya, O. L., et al. (2020). Methane Cracking within Shale Rocks: A New Explanation for Carbon Isotope Reversal of Shale Gas. *Mar. Pet. Geology.* 121, 104591. doi:10.1016/j10.1016/j.marpetgeo.2020.104591

Clayton, C. (1991). Carbon Isotope Fractionation during Natural Gas Generation from Kerogen. *Mar. Pet. Geology.* 8, 232–240. doi:10.1016/0264-8172(91)90010-X

Cramer, B. (2004). Methane Generation from Coal during Open System Pyrolysis Investigated by Isotope Specific, Gaussian Distributed Reaction Kinetics. *Org. Geochem.* 35, 379–392. doi:10.1016/j.orggeochem.2004.01.004

Deines, P. (2002). The carbon isotope geochemistry of mantle xenoliths. *Earth-Sci. Rev.* 58, 247–278. doi:10.1016/j.lithos.2020.105774

Dieckmann, V., Ondrak, R., Cramer, B., and Horsfield, B. (2006). Deep basin Gas: New Insights from Kinetic Modelling and Isotopic Fractionation in Deep-Formed Gas Precursors. *Mar. Pet. Geology.* 23, 183–199. doi:10.1016/j.marpetgeo.2005.08.002

Duan, Y., Wu, B., He, J., and Sun, T. (2011). Characterization of Gases and Solid Residues from Closed System Pyrolysis of Peat and Coals at Two Heating Rates. *Fuel* 90, 974–979. doi:10.1016/j.fuel.2010.10.039

Han, W., Ma, W., Tao, S., Huang, S., Hou, L., and Yao, J. (2018). Carbon Isotope Reversal and its Relationship with Natural Gas Origins in the Jingbian Gas Field, Ordos Basin, China. *Int. J. Coal Geology.* 196, 260–273. doi:10.1016/j.coal.2018.06.024

Hao, F., and Zou, H. (2013). Cause of Shale Gas Geochemical Anomalies and Mechanisms for Gas Enrichment and Depletion in High-Maturity Shales. *Mar. Pet. Geology.* 44, 1–12. doi:10.1016/j.marpetgeo.2013.03.005

Hill, R. J., Zhang, E., Katz, B. J., and Tang, Y. (2007). Modeling of Gas Generation from the Barnett Shale, Fort Worth Basin, Texas. *Bulletin* 91, 501–521. doi:10.1306/12060606063

James, A. T. (1983). Correlation of Nature Gas by Use of Carbon Isotopic Distribution between Hydrocarbon Components. *AAPG Bull.* 67 (7), 1176–1191. doi:10.1306/03B5B722-16D1-11D7-8645000102C1865D

Lewan, M. D., and Roy, S. (2011). Role of Water in Hydrocarbon Generation from Type-I Kerogen in Mahogany Oil Shale of the Green River Formation. *Org. Geochem.* 42, 31–41. doi:10.1016/j.orggeochem.2010.10.004

Li, E., Pan, C., Yu, S., Jin, X., and Liu, J. (2013). Hydrocarbon Generation from Coal, Extracted Coal and Bitumen Rich Coal in Confined Pyrolysis Experiments. *Org. Geochem.* 64, 58–75. doi:10.1016/j.orggeochem.2013.09.004

Li, W., Zhu, Y.-M., and Liu, Y. (2018). Gas Evolution and Isotopic Fractionations during Pyrolysis on Coals of Different Ranks. *Int. J. Coal Geology.* 188, 136–144. doi:10.1016/j.coal.2018.02.009

Liu, W., Wang, J., Tenger, G. E., Qin, J., and Zheng, L. (2012). Stable Carbon Isotopes of Gaseous Alkanes as Genetic Indicators Inferred from Laboratory Pyrolysis Experiments of Various marine Hydrocarbon Source Materials from Southern China. *Sci. China Earth Sci.* 55, 966–974. (in Chinese). doi:10.1007/s11430-012-4392-5

Lorant, F., Prinzhofer, A., Behar, F., and Huc, A.-Y. (1998). Carbon Isotopic and Molecular Constraints on the Formation and the Expulsion of Thermogenic Hydrocarbon Gases. *Chem. Geology.* 147, 249–264. doi:10.1016/S0009-2541(98)00017-5

Milkov, A. V., and Etiope, G. (2018). Revised Genetic Diagrams for Natural Gases Based on a Global Dataset of >20,000 Samples. *Org. Geochem.* 125, 109–120. doi:10.1016/j.orggeochem.2018.09.002

Milkov, A. V., Faiz, M., and Etiope, G. (2020). Geochemistry of Shale Gases from Around the World: Composition, Origins, Isotope Reversals and Rollovers, and Implications for the Exploration of Shale Plays. *Org. Geochem.* 143, 103997. doi:10.1016/j.orggeochem.2020.103997

Pan, C., Jiang, L., Liu, J., Zhang, S., and Zhu, G. (2010). The Effects of Calcite and Montmorillonite on Oil Cracking in Confined Pyrolysis Experiments. *Org. Geochem.* 41, 611–626. doi:10.1016/j.orggeochem.2010.04.011

Peter, D. (2002). The Carbon Isotope Geochemistry of Mantle Xenoliths. *Earth-Science Rev.* 58, 247–278. doi:10.1016/s0012-8252(02)00064-8

Rodriguez, N. D., and Philp, R. P. (2010). Geochemical Characterization of Gases from the Mississippian Barnett Shale, Fort Worth Basin, Texas. *Bulletin* 94, 1641–1656. doi:10.1306/04061009119

Tang, Y., Perry, J. K., Jenden, P. D., and Schoell, M. (2000). Mathematical modeling of stable carbon isotope ratios in natural gases. *Geochim. Cosmochim. Acta* 64, 2673-2687. doi:10.1016/S0016-7037(00)00377-X

Tian, H., Xiao, X., Wilkins, R. W. T., and Tang, Y. (2012). An Experimental Comparison of Gas Generation from Three Oil Fractions: Implications for the Chemical and Stable Carbon Isotopic Signatures of Oil Cracking Gas. *Org. Geochem.* 46, 96–112. doi:10.1016/j.orggeochem.2012.01.013

Tilley, B., and Muehlenbachs, K. (2013). Isotope Reversals and Universal Stages and Trends of Gas Maturation in Sealed, Self-Contained Petroleum Systems. *Chem. Geology.* 339, 194–204. doi:10.1016/j.chemgeo.2012.08.002

Wu, W., Fang, C. C., Dong, D. Z., and Liu, D. (2015). Shale Gas Geochemical Anomalies and Gas Source Identification. *Acta Petrolei Sinica* 36, 1332–1340. doi:10.7623/syxb201511002

Wu, X., Liu, Q., Zhu, J., Li, K., Liu, G., Chen, Y., et al. (2017). Geochemical Characteristics of Tight Gas and Gas-Source Correlation in the Daniudi Gas Field, the Ordos Basin, China. *Mar. Pet. Geology.* 79, 412–425. doi:10.1016/j.marpetgeo.2016.10.022

Xiong, Y. Q., Zhang, L., Chen, Y., Wang, X. T., Li, Y., Wei, M. M., et al. (2016). The Origin and Evolution of Thermogenic Gases in Organic-Rich marine Shales. *J. Pet. Sci. Eng.* 143, 8–13. doi:10.1016/j.marpetgeo.2014.04.001

Zhou, Q., Xiao, X., Tian, H., and Pan, L. (2014). Modeling Free Gas Content of the Lower Paleozoic Shales in the Weiyuan Area of the Sichuan Basin, China. *Mar. Pet. Geology.* 56, 87–96. doi:10.1016/j.marpetgeo.2014.04.001

Conflict of Interest: The authors declare that the research was conducted in the absence of any commercial or financial relationships that could be construed as a potential conflict of interest.

Publisher's Note: All claims expressed in this article are solely those of the authors and do not necessarily represent those of their affiliated organizations, or those of the publisher, the editors and the reviewers. Any product that may be evaluated in this article, or claim that may be made by its manufacturer, is not guaranteed or endorsed by the publisher.

Copyright © 2021 Wu, Liu, Wang, Wang, Yuan and Xia. This is an open-access article distributed under the terms of the Creative Commons Attribution License (CC BY). The use, distribution or reproduction in other forums is permitted, provided the original author(s) and the copyright owner(s) are credited and that the original publication in this journal is cited, in accordance with accepted academic practice. No use, distribution or reproduction is permitted which does not comply with these terms.

frontiers in Earth Science

ORIGINAL RESEARCH
published: 14 October 2021
doi: 10.3389/feart.2021.636193

Differences on Geochemical Characteristics and Their Implicating Significances of Nitrogen in Coal-Derived Gas and Oil-typed Gas in China

Wang Xiaobo[1,2], Li Jian[1,2]*, Yang Chunxia[1]*, Li Zhisheng[1,2], Chen Jianfa[3], Zheng Yue[4]*, Wang Yifeng[1,2], Li Jin[1,2], Yang Chunlong[1,2], Hao Aisheng[1,2] and Ge Shouguo[3]*

[1]PetroChina Research Institute of Exploration and Development, Beijing,, China, [2]Key Laboratory of Gas Reservoir Formation and Development of CNPC, Langfang, China, [3]State Key Laboratory of Petroleum Resources and Prospecting, China University of Petroleum, Beijing, China, [4]University of Chinese Academy of Sciences, Beijing, China

OPEN ACCESS

Edited by:
Giovanni Martinelli,
National Institute of Geophysics and Volcanology, Italy

Reviewed by:
Weijiao Ma,
China University of Petroleum (Huadong), China
Haiping Huang,
China University of Geosciences, China
Weilong Peng,
SINOPEC Petroleum Exploration and Production Research Institute, China
Alexandra Hakala,
National Energy Technology Laboratory (DOE), United States

***Correspondence:**
Wang Xiaobo
wangxb69@petrochina.com.cn
Li Jian
lijian69@petrochina.com.cn
Yang Chunxia
yangcx83@petrochina.com.cn
Zheng Yue
zhengyue@mail.iggcas

Specialty section:
This article was submitted to Geochemistry, a section of the journal Frontiers in Earth Science

Received: 01 December 2020
Accepted: 13 September 2021
Published: 14 October 2021

Citation:
Xiaobo W, Jian L, Chunxia Y, Zhisheng L, Jianfa C, Yue Z, Yifeng W, Jin L, Chunlong Y, Aisheng H and Shouguo G (2021) Differences on Geochemical Characteristics and Their Implicating Significances of Nitrogen in Coal-Derived Gas and Oil-typed Gas in China. Front. Earth Sci. 9:636193. doi: 10.3389/feart.2021.636193

Natural gases in China are mainly coal-derived gas, with assistance from oil-typed gas. At present, many genetic identification methods, from hydrocarbon composition and isotope to light hydrocarbon and biomarker indexes, have been formed, but combined methods from non-hydrocarbon gases are lacking. Based on compositions and isotopes geochemical characteristics and the differences of non-hydrocarbon nitrogen gas in coal-derived gas and oil-typed gas, and combining the isotopic geochemical characteristics of non-hydrocarbon helium, the comprehensive identification methods of coal-derived gas and oil-typed gas for hydrocarbon gases according to the associated non-hydrocarbon gases of nitrogen and helium are established and the preliminary applications have been engaged. The main recognitions are as follows:1)Coal-derived gas generally has relatively lower nitrogen abundance, mainly distributed from 0 to 31.2% with main frequency from 0 to 2%. Oil-typed gas, on the other hand, usually has relatively higher nitrogen abundance, mainly distributed from 1.1 to 57.1% with main frequency from 2 to 16%. 2) Coal-derived gas generally has relatively heavier nitrogen isotope values, mainly distributed from -8 to 19.3‰ with main frequency from -8 to 8‰.Oil-typed gas usually has relatively lower nitrogen isotope values, mainly distributed from -10.6 to 4.6‰ with main frequency from -8 to 4‰.3)The geochemical characteristic differences of coal-derived gas and oil-typed gas are mainly due to the fact that the sapropel parent material is relatively rich in nitrogen element and rich in light $\delta^{14}N$, while the humic parent material is relatively poor in nitrogen element and rich in heavy $\delta^{15}N$. The differences on thermal maturity of source rocks, the redox conditions of source rock sedimentary environment, and the salinity of water body are also important effective factors.4)Differences on nitrogen abundances and isotopes in coal-derived gas and oil-typed gas have great significance in genetic identification. The genetic identification chart of R/Ra-$\delta^{15}N$ for organic and inorganic nitrogen in natural gas and the comprehensive joint identification charts of R/Ra-$\delta^{15}N$-N_2 of nitrogen and helium for coal-derived gas and oil-typed gas have been

established, and are of great reference in investigating the origins and sources of natural gas and guiding natural gas exploration in China.

Keywords: comprehensive identification, oil-typed gas, coal-derived gas, helium, nitrogen, geochemical characteristics differences

INTRODUCTION

Natural gas is an environmentally friendly, low-carbon, effective, and clean energy. It occupies an important position in the world's energy structure and is one of three important sources and targets in future energy development (natural gas, unconventional oil and gas, and new energy). The present proportion of natural gas in China's energy structure (only about 8%) is lower than the world average (about 25%).

Natural gas is usually composed of more hydrocarbon gases such as CH_4 (methane), C_2H_6 (ethane), C_3H_8 (propane), and C_4H_{10} (butane), with lower or trace amounts of non-hydrocarbon gases such as CO_2 (carbon dioxide), N_2 (nitrogen), He (helium), Ne (neon), Ar (argon), Kr (krypton), and Xe (xeon). Non-hydrocarbon gases are very important components of natural gases, and usually have a close relation to hydrocarbon gases. Nitrogen, as a very important and common non-hydrocarbon gas component in natural gas, has closer physical properties with hydrocarbon gases than other non-hydrocarbon gas components, and has similar reservoir forming conditions with hydrocarbon gas reservoir. Therefore, studying the geochemical characteristics and origin of nitrogen in natural gases is helpful to find out the origin of formation, preservation, and enrichment of hydrocarbon gases. Nitrogen has two stable isotopes, ^{14}N and ^{15}N, with atmospheric abundances of 99.633 and 0.366% respectively (Rosman and Taylor, 1998). The atmosphere is the largest nitrogen reservoir on the earth. The origins of nitrogen in gas reservoirs are diverse. The total variation range of $\delta^{15}N$ is 100‰, from about -50‰ to + 50‰, and most of them fall in the range of -10‰ to + 20‰(Hoefs, 1972; Heaton, 1986; Owens, 1987; Peterson and Fry, 1987; Kendall, 1998). As the nitrogen isotope value in natural gas is similar to or overlaps with the isotope value of many kinds of nitrogen-bearing materials in nature, it is difficult to identify the origin and source of nitrogen in natural gas only by using nitrogen isotope value and nitrogen content. The isotope value of associated helium is an important indirect indicator for assisted identification of the organic and inorganic origin of nitrogen in natural gas. There are also reports on the use of associated helium to determine the origin of mantle-derived magma nitrogen globally. So, a comprehensive judging method including nitrogen isotope of $\delta^{15}N$ and other possible isotope indexes for effectively identifying organic and inorganic nitrogen needs to be established.

In China, natural gases are mainly coal-derived gas with assistance from oil-typed gas. Coal-derived gas contributes more to the gas reserves and production (Dai et al., 2014), and plays a pivotal role in promoting the development of China's natural gas industry. The identification of oil-typed gas and coal-derived gas is of great significance for clarifying the origin and source of natural gas, guiding the exploration of natural gas, and promoting the rapid development of the natural gas industry. At present, three methods involving 28 comprehensive indicators and charts for identifying the origin of natural gas, especially for coal-derived gas and oil-typed gas, have been developed, such as carbon isotopes and compositions, light hydrocarbons, and biomarkers (Dai et al., 1988; Dai et al., 1992; Dai et al., 1993; Dai et al., 1994; Dai et al., 1995; Dai et al., 1996; Dai et al., 1999; Dai et al., 2005; Dai et al., 2008; Dai et al., 2009; Dai et al., 2014; Dai and Qi, 1989; Li Jian et al., 2001; Li Jian et al., 2005; Hu Guoyi et al., 2007). However, there are few comprehensive identification methods for coal-derived gas and oil-typed gas by jointly using the non-hydrocarbon gases. The compositions and isotopes of the non-hydrocarbon gases of helium and nitrogen contain rich geological information, which play an important tracing and indicative role in identifying the origin and source of hydrocarbon gases of natural gases. So it is necessary and meaningful to promote and advance the comprehensive identification index system for coal-derived gas and oil-typed gas from an non-hydrocarbon gas point of view. Based on geochemical characteristics of compositions and isotopes and their differences of non-hydrocarbon nitrogen gas in coal-derived gas and oil-typed gas, and combining the isotope geochemical characteristics of non-hydrocarbon helium, the comprehensive identification methods of coal-derived gas and oil-typed gas according to the associated non-hydrocarbon gases of nitrogen and helium need to be established.

In this study, the geochemical characteristics of non-hydrocarbon nitrogen gas and their differences in coal-derived gas and oil-typed gas are clarified first. Then the genesis of nitrogen in natural gases is identified and the reasons for the different geochemical characteristics of nitrogen are discussed. Finally, based on the difference of nitrogen content and $\delta^{15}N$ value in coal-formed gas and oil-typed gas, combined with the R/Ra value of helium isotope, the genetic identification chart of R/Ra-$\delta^{15}N$ for organic and inorganic nitrogen in natural gas and the comprehensive joint identification charts of R/Ra-$\delta^{15}N$-N_2 of nitrogen and helium for identifying oil-typed gas and coal-derived gas jointly by nitrogen and helium are established and applied in the selected typical gas-bearing basins. The research results are of great significance for clarifying the origins and sources of natural gas and guiding natural gas exploration.

RESEARCH SITUATIONS

Studies on nitrogen of natural gas overseas have been carried out as early as the 1950s. Hoering and Moore (1958) first studied the changes of nitrogen isotope during the migration of the gas in the Permian gas reservoirs in the Republic of Germany and

Groningen in the Netherlands. Jenden et al. (1988) summarized the data of 12,000 natural gas samples and found that the average content of N_2 in natural gas is 3%, of which 10% of the gas samples have $N_2 \geq 25\%$, 3.5% of gas samples have $N_2 \geq 50\%$, and 1% of gas samples have $N_2 \geq 90\%$. Studies on non-hydrocarbon gases of natural gas in China started in the 1980s. Zhang (1988) first analyzed the distribution and sources of nitrogen and the geochemical characteristics of nitrogen isotope in natural gas reservoirs in China and foreign countries, and concluded that nitrogen in gas reservoirs mainly came from the decomposition of organic matter, production of rock degassing, and atmospheric gas. Dai et al. (1992) calculated the analysis results of more than 1,000 gas samples in China and found that $N_2 \leq 4\%$ accounted for 76% and $N_2 \leq 8\%$ accounted for 86%. Since the 1990s, many domestic and foreign scholars have carried out a large number of studies on nitrogen composition, distribution, forming mechanism, origin and source, migration, accumulation, isotope analytical technique, nitrogen generation thermal simulation experiment, sedimentary environment, gas composition forecasting, and exploration risk reduction (Prisolov et al., 1991; Du, 1992; Zhu, 1994; Zhu and Shi, 1998; Krooss et al., 1995; Littke et al., 1995; Dai et al., 1995; Du et al., 1996; Zhu, 1999; He et al., 2001, 2011; Zeng, 2002; Shi et al., 2003; Chen et al., 2003; Chen, 2004; Liu et al., 2005; Liu et al., 2006; Qin et al., 2007; Zhang et al., 2008; Li et al., 2013; Xu et al., 2017; Chen et al., 2018), promoting rapid development of research into nitrogen in natural gases.

RESEARCH AREAS AND EXPERIMENTAL METHODS

China's natural gas is dominated by coal-derived gas, generally originating from coal-series source rocks, which are mainly distributed in the upper Paleozoic of the Ordos Basin, Upper Cretaceous in Kuche Depression of the Tarim Basin, and the Xujiahe formation of Upper Triassic in Sichuan Basin,. Coal-derived gas plays a pivotal role in natural gas reserves and production increases and promotes the rapid development of China's natural gas industry. Oil-typed gas in China is mostly distributed in marine sediment strata in the three biggest marine basins: the Tarim, Sichuan, and Ordos Basin. Oil-typed gases also have an important position in China's natural gas development, having encouraged many great exploration discoveries in deep and ancient strata, especially in recent years. Non-hydrocarbon nitrogen and helium gases are important components of natural gases, and have rich geological information in indirectly tracing and identifying the origin and source of associated hydrocarbon gases in natural gases. For the purpose of conducting deep studies on geochemical characteristic differences and their significance in nitrogen in coal-derived gas and oil-typed gas in China, typical coal-derived gases from the Tarim and Ordos Basin and typical oil-typed gases from the Tarim Basin are especially selected. Considering the importance and representativeness of typical coal-derived gas and oil-typed gas basins and gas fields, as well as gas samples sampling accessibility, the research areas of typical coal-derived gas fields referred to are Kela 2, Dabei, Dina 2, Akemomu, Kekeya, and Yaha gas fields in the Tarim Basin and the Sulige gas field in the Ordos Basin; the research areas of oil-typed gas fields referred to are Tazhong I, Hetianhe, Donghetang, Lunnan, and Hadexun oil and gas fields in the Tarim Basin. In order to make comprehensive and comparative studies, the nitrogen geochemical data from previous research on the Dongfang gas field in the YingQiong Basin are also selected (He et al., 2001,2011).

In order to minimize the impact of air pollution and sampling process on the accuracy of data measurement, samples should be collected as follows: 1) Use a stainless steel cylinder with double valves to collect natural gas samples in the study area to be tested, and the stainless steel cylinder should be vacuumed by a mechanical or molecular pump for more than 15 min, or to be below 10^{-2} Pa before collecting the sample; 2) connect the stainless steel cylinder to the valve of the natural gas well through a relief valve, then collect the mid-stage gas flow until the gas pressure in the stainless steel cylinder is 3–6 MPa after using the wellhead high-pressure natural gas to repeatedly flush the cylinder more than 6 times and for more than 15 min; and 3) Gas sample analysis and testing must be carried out within 1 week after sample collection.

In this paper, the typical coal-derived gases were sampled from the Kela 2, Dabei, Dina 2, Akemomu, Kekeya, and Yaha gas fields in the Tarim Basin, and Sulige gas field in the Ordos Basin. The typical oil-typed gases were sampled from the Tazhong I, Hetianhe, Lunnan, and Hadexun oil and gas fields in the Tarim Basin (**Figure 1**). The analysis of nitrogen component and isotope in natural gas was completed in the Key Laboratory of Gas Reservoir Formation and Development of China National Petroleum Corporation. The nitrogen composition was analyzed on an Agilent 6890 N gas chromatograph (GC) equipped with a thermal conductivity detector (TCD), using helium as the carrier gas. It was separated using a capillary column with 30 m × 0.32 mm × 20 μm PLOT Q. The gas chromatograph oven temperature was initially set at 30°C for 10 min, and programed at 10°C/min to 180°C and then isothermal at 180°C for 10 min. The precision of the nitrogen composition is estimated to be ±0.07%. The nitrogen isotopic compositions of natural gases were determined on the MAT 253 (GC/IRMS) isotopic mass spectrometer equipped with an Agilent 6890N Gas Chromatography with a 30 × 0.32 mm × 20 μm capillary column of HP Plot molesieve 5 Å molecular sieves. Helium was used as the carrier gas. Compositions of CO, N_2, O_2, CH_4, and C_2H_6 can be completely separated by the above capillary column and the separated nitrogen is directly detected by MAT 253 isotopic mass spectrometer. The temperature of the GC oven was initially set at 30°C and maintained at such for 8 min, and then raised to 280°C at 10°C/min. The atmospheric nitrogen was selected as the standard material for nitrogen isotopic analysis. The nitrogen isotopic values of samples are reported in conventional δ notation in per mil (‰) relative to atmospheric nitrogen as the standard. The international atmospheric nitrogen isotope value of $\delta^{15}N/^{14}N = 0.00361$ is defined as $\delta^{15}N = 0‰$. The nitrogen isotope of the gas sample was calculated based on atmospheric nitrogen as the standard according to the formula of $\delta^{15}N=(R_{sample}/R_{standard} -1) \times 1000‰$. In order to check the reliability of the instrument in the long-term detection process, air standard and a natural gas sample are selected for nitrogen isotope repeatability test at a

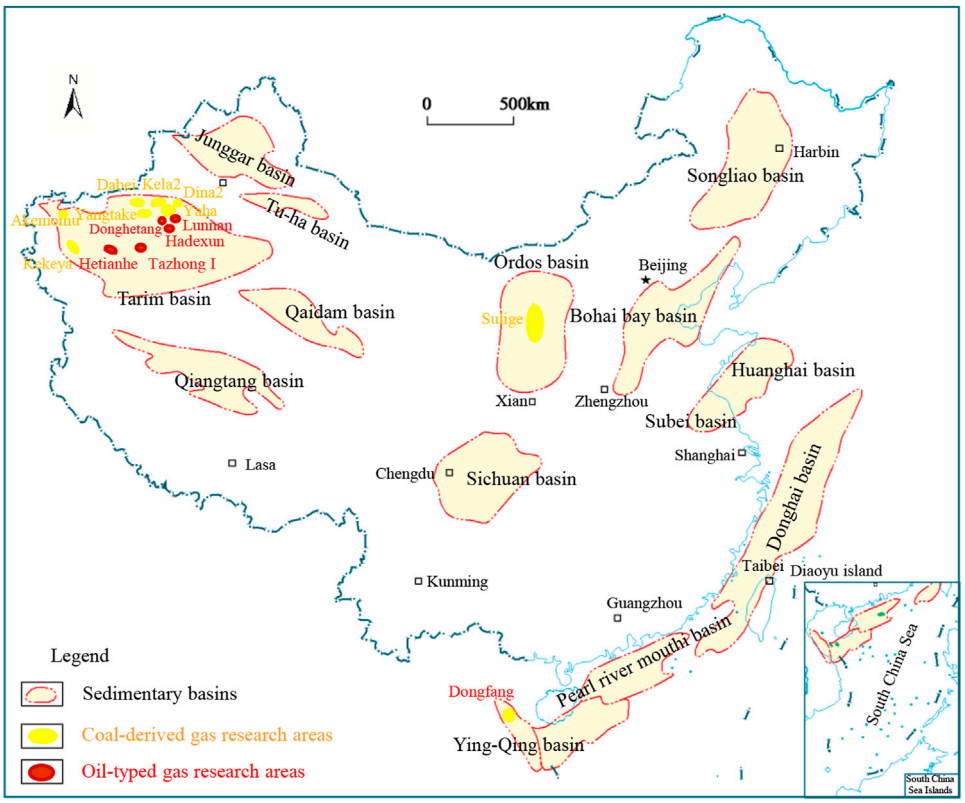


FIGURE 1 | Research areas of coal-derived gas and oil-typed gas on gas-bearing basins in China.

relatively fixed time interval. The air standard was tested 5 times; the detected average nitrogen isotope value of $\delta^{15}N$ for atmospheric nitrogen was −0.0065‰ and the standard deviation was 0.047‰. The gas sample was tested 7 times; the detected average nitrogen isotope of $\delta^{15}N$ for gas sample was 4.6‰, and the standard deviation was 0.135‰. The tested results indicated that the repeatability of the test system was good and the stability of the instrument was reliable. In order to systematically study nitrogen in coal-derived gas and oil-typed gas, some previous research was collected and referenced (Du et al., 1996; He et al., 2001, 2011; Chen et al., 2001; Chen and Zhu, 2003; Liu and Xia, 2005; Liu et al., 2007; Li et al., 2013). Based on the experimental analysis and previous researcher's data statistics, the geochemical characteristics of nitrogen component and isotope of coal-derived gas and oil-typed gas in China were systematically studied and discussed.

RESULTS AND DISCUSSIONS

Differences on Geochemical Characteristics of Nitrogen in Coal-Derived Gas and Oil-typed Gas in China

According to the comparative analysis of nitrogen components of 109 coal-derived gas samples and 47 oil-typed gas samples in the nitrogen content distribution histogram of coal-derived gas and oil-typed gas in China (**table 1**), it can be seen that the content of nitrogen in coal-derived gas is mainly distributed from 0 to 31.2%, with main frequency from 0 to 2%; the content of nitrogen in oil-typed gas, meanwhile, is mainly distributed from 1.1 to 57.1%, and with main frequency from 2 to 16% (**Figure 2**). From **Figure 2**, it can also be seen that the nitrogen component content of coal-formed gas and oil-typed gas can be obviously divided by 2% in the dominant frequency distribution.

From the relationship between nitrogen content and ethane isotope $\delta^{13}C_2$ of coal-derived gas and oil-typed gas in China, it can be obviously seen that oil-typed gas has a relatively high nitrogen content with most ethane isotope $\delta^{13}C_2$ generally from −41.5‰ to −30‰, while coal-derived gas has a relatively low nitrogen content with most ethane isotope $\delta^{13}C_2$, generally from −26.5‰ to −16‰ (**Figure 3**). From **Figure 3**, it can be seen that the nitrogen content of coal-derived gas and oil-typed gas is significantly different and distinct in total distributed range, and the overlapped areas of nitrogen content is mostly less than 10% in low-content areas.

From the histogram depicting nitrogen isotope distribution of coal-derived gas and oil-typed gas in China, it can be concluded that the value of the nitrogen isotope ($\delta^{15}N$) of 41 coal-derived gas samples is totally distributed from −8 to 19.3‰ with main frequency from −8 to 8‰, while the value of the nitrogen isotopes of 40 oil-typed gas samples is generally distributed from −10.6 to 4.6‰ with main frequency from −8 to 4‰(**Figure 4**). From **Figure 4**, it can be seen that the nitrogen isotopic composition

TABLE 1 | Composition and isotope data of non-hydrocarbon gases of nitrogen and helium in some typical coal-derived gas and oil-typed gas in China.

Gas type	Basin	Gas field or gas bearing structure	Well	Gas production strata	N_2 (%)	$\delta^{15}N$(‰)	R/Ra	Reference
Coal-derived gas	Tarim	Kela 2	kela 2-7	K_{1bs},E	0.69	−0.62	0.028	This paper
			Kela 2-10	K_{1bs},E	0.56	−1.03	0.061	
			Kela 2-4	K_{1bs},E	0.36	−0.78	0.048	
		Dabei	DB201	K_{1bs},E	0.54	0.43	0.045	
			DB302	K_{1bs},E	0.58	0.39	0.062	
		Dina 2	DN2	E	1.41	11.57	0.025	
			DN2-24	E	1.58	11.89	0.024	
		Akemomu	AK1	K	8.40	−3.01	0.597	
			AK1-2	K	7.80	−2.89	0.592	
		Kekeya	K2	N_1	3.91	−0.98	0.052	
			K241	N_1	3.45	−0.70	0.051	
			K8002	N	1.97	−1.6	—	Li et al. (2013)
		Yaha	YH23-1-18	E + K	3.74	17.20	0.025	This paper
			YH3	E	3.87	16.60	0.023	
			YH1-6	E	3.85	19.3	—	Li et al. (2013)
	Ordos	Sulige	S47-44-37	P	6.72	−4.81	0.052	This paper
			S11-18-36	P	0.92	−4.29	0.048	
			S54-24-65	P	1.45	−4.13	0.032	
	Yiong-Qiong	Dongfang	DF1-1-4	Ny1	27.55	−9.0	0.126	He et al. (2001), (2011)
			DF1-1-8	Ny1	18.63	−1.0	0.081	
			DF29-1-2	Ny1	23.70	−3.0	0.132	
Oil-typed gas	Tarim	Tazhong 1	TZ117	S	12.89	−4.42	0.027	This paper
			ZG162	OI	6.65	−8.39	0.025	
			TZ101-1	C_{III}	9.17	−6.52	0.029	
			TZ16	C_{III}	57.1	2.53	—	Chen and Mei. (2001)
			TZ30	O	55.3	3.51	—	
		Hetianhe	MA4-H1	C	12.31	−3.62	0.066	This paper
			MA5-1	O	9.15	−3.48	0.074	
			MA401	O	14.0	1.51	—	Chen and Mei. (2001)
		donghetang	DH23	O	5.1	4.08	—	
			—	O, D,C	52.56-57.25	10–15	0.047–0.054	Chen and Zhu,(2003)
		Lunnan	LG11	O	1.25	−2.07	0.022	This paper
			LN2-2-3	T	5.26	4.53	0.042	
		Hadexun	HD10-3-3H	C	47.64	—	0.021	
—	Sanshui	Sanshui	SS3	E	10.97	−1.6	4.11	Du et al. (1996)
			SS12	E	15.26	6.8	4.86	

of coal-derived gas and oil-typed gas are obviously overlapped from −8 to 8‰ in their distribution range with the dominant frequency distributed from −8 to 4‰.

From the relationship between nitrogen isotope $\delta^{15}N$ and ethane isotope$\delta^{13}C_2$ of coal-derived gas and oil-typed gas in China, it can be obviously seen that the distribution values of the nitrogen isotopes in coal-derived gas are relatively heavier than these of oil-typed gas. Oil-typed gas generally has relatively lighter nitrogen isotope from −11 to 5‰ with most ethane isotope $\delta^{13}C_2$ generally from −38 to -29‰, while coal-derived gas has relatively heavier nitrogen isotope from −4 to 20‰ with most ethane isotope $\delta^{13}C_2$ generally from −26 to −17.5‰ (**Figure 5**). From **Figure 5**, it can also be concluded that there is an overlap of nitrogen isotopic composition that exists in coal-derived gas and oil-typed gas, and the overlapped area is generally from −4 to 5‰ with limited data distribution points. The reason for this phenomenon will be discussed and given in the following section.

In general, from the relationship between nitrogen content and isotope of coal-derived gas and oil-typed gas in China, the content of nitrogen is relatively low and the $\delta^{15}N$ is relatively heavy in the coal-derived gas, while the content of nitrogen is relatively high and the $\delta^{15}N$ is relatively light in oil-typed gas (**Figure 6**).

Discussions on Nitrogen Genesis and Reasons for Geochemical Characteristics Differences in Coal-Derived Gas and Oil-typed Gas in China

Nitrogen, as a very important and common non-hydrocarbon gas component in natural gas, has closer physical properties with hydrocarbon gas than other non-hydrocarbon gas components and has similar reservoir forming conditions with hydrocarbon gas reservoir. Therefore, studying the geochemical characteristic and origin of nitrogen in natural gases is helpful to find out the

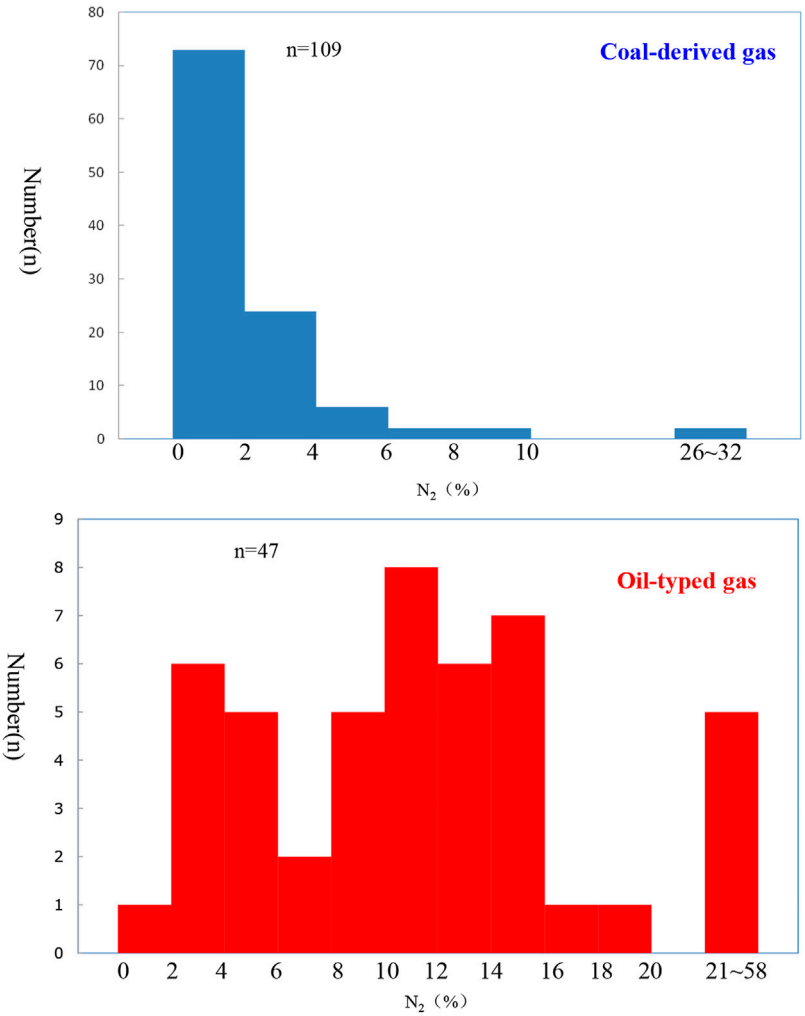


FIGURE 2 | Nitrogen content distributions in coal-derived gas and oil-typed gas in China.

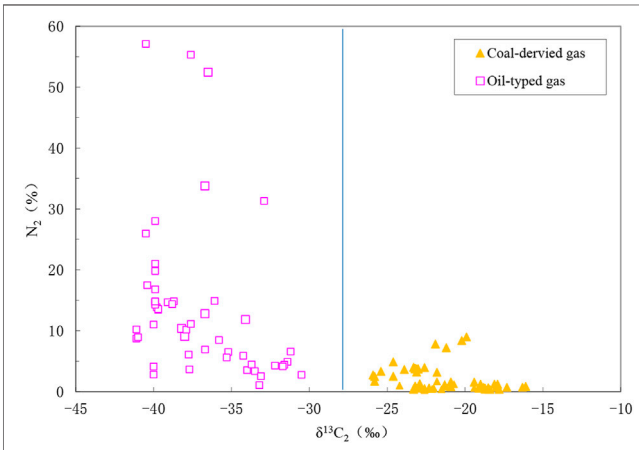


FIGURE 3 | Relationship between nitrogen content and ethane isotope$\delta^{13}C_2$ of coal-derived gas and oil-typed gas in China.

origin of formation, preservation, and enrichment of hydrocarbon gases. By exploring the geochemical characteristics and source of nitrogen in natural gases, great value will be added to the study of hydrocarbon generation, migration, and accumulation in the basin, forecasting favorable gas exploration areas.

The atmosphere is the largest nitrogen reservoir on the earth. About 99% of the nitrogen in the near surface environment exists in the atmosphere or is dissolved in seawater in the form of nitrogen. There is little nitrogen in the biosphere, but it is one of the most indispensable elements in the process of life. The origins and sources of nitrogen in gas reservoirs are diverse, and many scholars have carried out a lot of research on nitrogen in natural gases. The total variation range of $\delta^{15}N$ is 100‰, from about −50 to +50‰, and most of them fall in the range of −10 to +20‰. Nitrogen from igneous rocks ranges from -16 to +31‰; nitrogen in the hydrosphere is represented by that in the ocean water, ranging from -8‰ to+10‰; nitrogen in plants ranges from −10 to+22‰; oil and coal fall within the range of modern biology,

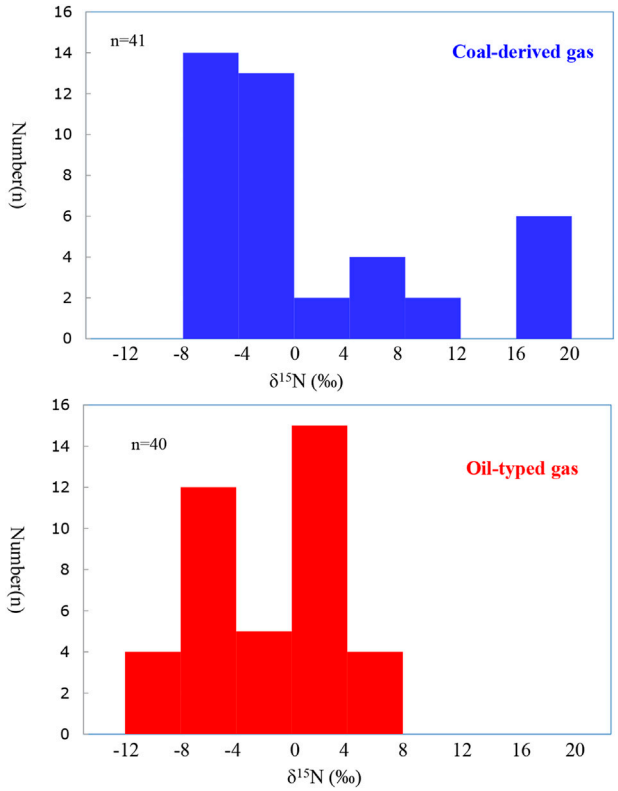


FIGURE 4 | Nitrogen isotope distributions of coal-derived gas and oil-typed gas in China.

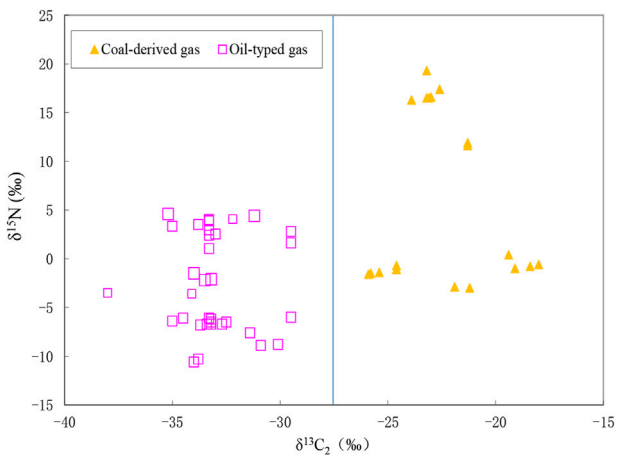


FIGURE 5 | Relationship between nitrogen isotope $\delta^{15}N$ and ethane isotope $\delta^{13}C_2$ of coal-derived gas and oil-typed gas in China.

ranging from 0 to +15‰; $\delta^{15}N$ of natural gas varies greatly ranging from −45 to+45‰; $\delta^{15}N$ of extraterrestrial matter varies the most, ranging from −40 to+100‰, while the value of Martian atmosphere is as high as 700‰ (Hoefs, 1972; Heaton, 1986; Owens, 1987; Peterson and Fry, 1987; Kendall, 1998). According

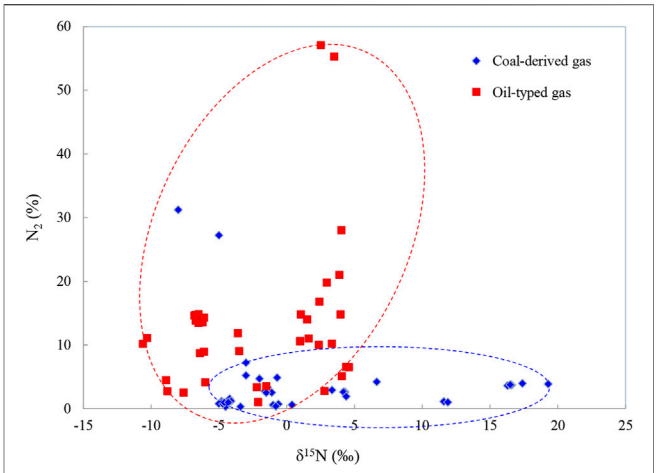


FIGURE 6 | Relationship between nitrogen content and isotope in coal-derived gas and oil-typed gas in China.

to the origins and sources, nitrogen in natural gas may be from a number of sources: the atmosphere, microbial ammoniation or denitrification, thermal ammoniation and thermal pyrolysis of organic matters in source rocks, high temperature metamorphism of nitrogenous minerals in sedimentary rocks, or the deep crust and upper mantle. There are certain differences in geochemical characteristics of nitrogen from different sources. Because of the overlapping distribution of $\delta^{15}N$ in different types of nitrogen (nitrogen isotope value in natural gas is similar to or overlaps with the isotope value of many kinds of nitrogen-bearing materials in nature), it is difficult to identify the origin and source of nitrogen in natural gas only by using nitrogen isotope value and nitrogen content. To solve this problem, it is necessary to combine geological information with other gas geochemical data for comprehensive identification. The isotope value of associated helium is an important indirect indicator for assisted identification of the organic and inorganic origin of nitrogen in natural gas. There are also reports on the use of associated helium to determine the origin of mantle-derived magma nitrogen globally. For example, the nitrogen in some high nitrogen natural gas in the Grand Canyon of California in the United States belongs to magma source (Jenden et al., 1988), the nitrogen in some hot spring gas in China is derived from magma (Dai et al., 1988), and the gas in Sanshui Basin of Guangdong also has magma-sourced nitrogen (Du et al., 1996).

Based on the above studies, R/R_a-$\delta^{15}N$ indexes and charts to identify organic and inorganic nitrogen have been established by using R/R_a (R and R_a denote $^3He/^4He$ of helium in natural gas and air respectively) and nitrogen isotope of $\delta^{15}N$ (**Figure 7**): ① When $R/R_a \leq 0.2$, the nitrogen in natural gas is generally organic in genesis and probably originated from biogenic chemical affection (such as microbial ammoniation or denitrification) or thermal pyrolysis of organic matters in source rocks during diagenetic stage (such as thermal ammoniation in mature and high mature stage or cracking action in over-mature stage); ② When $R/R_a \geq 1$ and nitrogen isotope of $\delta^{15}N$ range from -16 to 31‰, the nitrogen is usually inorganic in genesis from volcano-

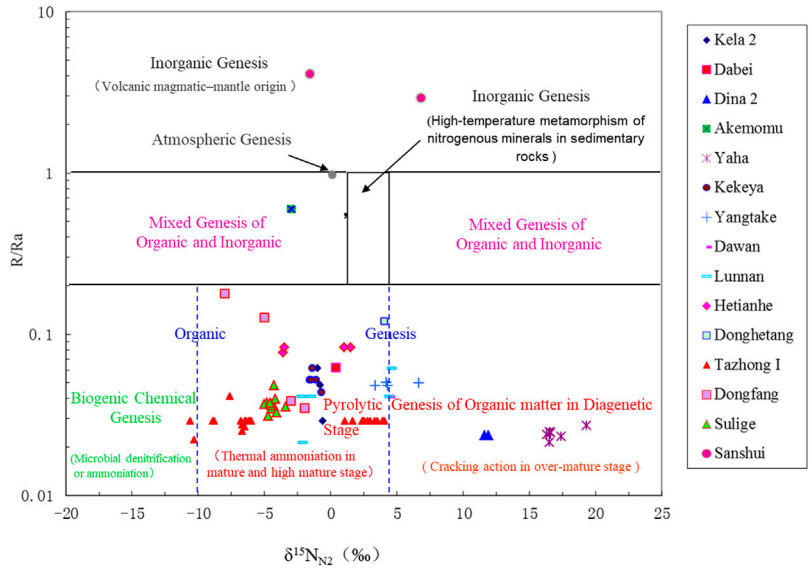


FIGURE 7 | Genesis identification chart of R/Ra-$\delta^{15}N$ for organic and inorganic nitrogen in natural gases in China.

mantle origin; ③When $0.2<R/R_a<1$ and $1‰<\delta^{15}N<4‰$, the nitrogen in natural gas is probably inorganic in genesis and originated from high-temperature metamorphism of nitrogenous minerals in sedimentary rocks; ④ When $0.2<R/R_a<1$ and $\delta^{15}N \geq 4‰$ or $\leq 1‰$, the nitrogen is usually of mixed genesis of organic and inorganic; and ⑤ When $R/R_a \approx 1$ and $\delta^{15}N \sim 0$, the nitrogen in natural gas is of atmospheric genesis.

The genesis identification chart of R/Ra-$\delta^{15}N$ for organic and inorganic nitrogen has been used to identify the genesis of nitrogen in natural gases from these selected gas fields in the Tarim, Ordos, and Ying-Qiong basin. The $^3He/^4He$ value of helium on natural gases in the gas fields of Kela 2, Dabei, Dina 2, Kekeya, Yaha, Sulige, Tazhong I, Hetianhe, Donghetang, Lunnan, and Hadexun are basically at the order of 10^{-8}, and R/Ra<0.1; the helium is typically from the crust. So, according to the R/Ra-$\delta^{15}N$ chart (**Figure 7**), the nitrogen in natural gases of these gas fields are identified from crustal organic origin.

In coal-derived gas, the content of nitrogen is relatively low and the $\delta^{15}N$ is relatively heavy, while in oil-typed gas the content of nitrogen is relatively high and the $\delta^{15}N$ is relatively light. The geochemical characteristic differences of coal-derived gas and oil-typed gas are mainly due to the fact that the sapropel parent material is relatively rich in nitrogen element and rich in light $\delta^{14}N$, while the humic parent material is relatively poor in nitrogen element and rich in heavy $\delta^{15}N$. Sapropel organic matter is mainly originated from aquatic organisms (having an average protein content of 10.3%) and contains a large amount of protein and nucleic acid which provides a sufficient source for the production of N_2; humic organic matter is mainly originated from terrestrial plants (having an average protein content of 2.0%) and is poor in protein and acid and rich in carbon with a limited source of N_2 (Chen et al., 2001; Zhu and Shi, 1998). Therefore, the nitrogen content of sapropelic natural gas is much higher than that of humic natural gas. The nitrogen isotope values of source rocks in a marine sedimentary environment are generally lighter than those source rocks in a continental sedimentary environment. The nitrogen isotope analysis results of some hydrocarbons and kerogen in different sedimentary environments in China show that (Chen and Mei, 2001) the $\delta^{15}N$ of hydrocarbons in a freshwater environment is about 3–6‰. The nitrogen isotope of sedimentary organic matter formed in saline and brackish water environment is the heaviest, and the $\delta^{15}N$ is generally more than 10‰. The $\delta^{15}N$ of organic matter in Paleozoic marine carbonate rocks and generated hydrocarbons is close to 0 or less than 0. In addition, the release of nitrogen is closely related to the thermal evolution of source rocks. In the immature stage, the protein of deposited organic matter will be hydrolyzed to produce amino acids. Amino acids will produce NH_3 through microbial ammoniation, and NH_3 will be further decomposed into N_2. After entering the mature stage, some nitrogen-containing compounds begin to ammoniate under thermal catalysis to produce ammonia until nitrogen is formed. Since the heat received by the organic matter in the mature stage has not yet reached the activation energy required for the pyrolysis and denitrification of nitrogen-containing organic compounds, a considerable amount of nitrogen still exists in the deposited organic matter. In the over mature stage of Ro>2.0%, especially when Ro>3.0%, the thermal energy received by the deposited organic matter begins to fully reach the activation energy required for the pyrolysis and denitrification of nitrogen-containing organic matter, and then produces a large number of nitrogen. Littke et al. (1995) and Kroos et al. (1995) considered that nitrogen formed by the pyrolysis of sedimentary organic matter in high to over mature stage is the main source of high nitrogen gas in petroliferous basins. Therefore, the thermal maturity of source rock has great influences on nitrogen content in natural gas. In addition, the redox conditions of source rock sedimentary environment and the salinity of water

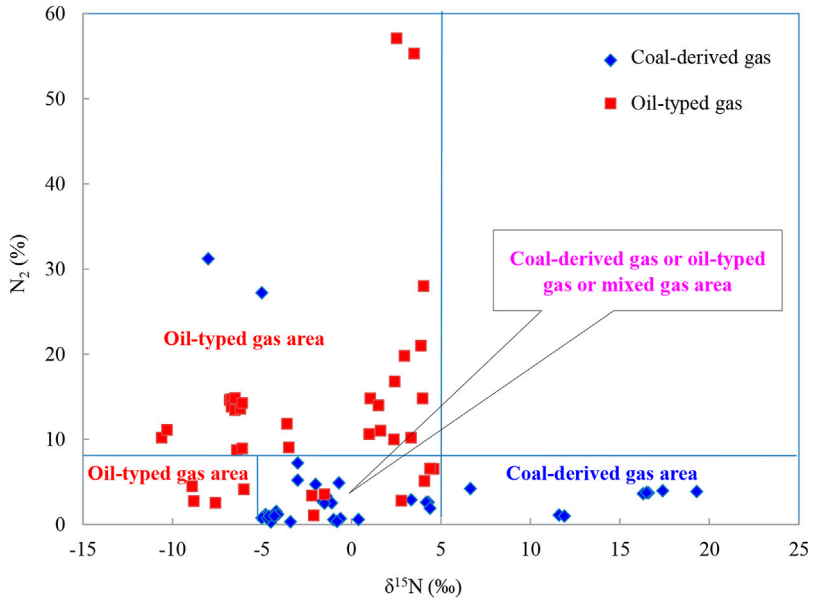


FIGURE 8 | Chart of R/Ra-δ^{15}N for identifying sources of nitrogen in natural gases.

body have different heterogeneity and are also important effective factors (Chen et al., 2015).

Discussions on the Tracing Implication of Geochemical Characteristics Differences of Nitrogen in Coal-Derived Gas and Oil-typed Gas

China's natural gas is mainly coal-derived gas, supplemented by oil-typed gas. Coal-derived gas is the main body of China's natural gas reserves and production growth, and plays an important role in promoting the development of China's natural gas industry. At present, about 28 comprehensive identification indexes and charts have been formed for the identification of coal-derived gas and oil-typed gas in three categories: carbon isotope and component of natural gas, light hydrocarbon, and biomarker. Non-hydrocarbon gas nitrogen and helium are important components of natural gas and are closely related to hydrocarbon gas. The components and isotopes of non-hydrocarbon gas contain very rich geological information, so they are important tracers and indicators for identifying the origins and sources of natural gas. However, there are few reports on genetic identification charts and methods on coal-derived gas and oil-typed gas by using nitrogen and helium jointly. This study has clarified the differences in the geochemical characteristics of nitrogen in coal-derived gas and oil-typed gas and considered the R/Ra ratio of helium isotope from crust and mantle sources. Finally, this paper established the comprehensive charts of R/Ra-δ^{15}N-N_2 for identifying coal-derived gas and oil-typed gas. Geological applications have achieved good results and are of great significance for deepening the research on the origins and sources of natural gas and guiding natural gas exploration. It is of great significance to optimize the related indexes of nitrogen and helium to identify coal-derived gas and oil-typed gas, which is helpful to enrich the existing identification index system of coal-derived gas and oil-typed gas.

Based on the differences in nitrogen content and δ^{15}N value in coal-formed gas and oil-typed gas, combined with the R/Ra value of helium isotope, the R/Ra-δ^{15}N-N_2 identification indexes and charts of coal-formed gas and oil-typed gas jointly identified by nitrogen and helium are established (**Figure 7**, **Figure 8**). For the methods process, the R/Ra-δ^{15}N chart was used to identify the organic and inorganic origin of nitrogen in natural gas (**Figure 7**). When the nitrogen in natural gas was identified as an organic origin, then the δ^{15}N-N_2 chart and indexes of nitrogen was used to judge the associated hydrocarbon gas to be coal-derived gas or oil-typed gas subsequently (**Figure 8**). The specific identification index values of this method are as follows (**Figure 8**). When the R/Ra value of helium isotope in natural gas is less than 0.2 or $^3He/^4He$ value is less than 2.8×10^{-7} (to ensure that the hydrocarbon gas associated with helium and nitrogen in natural gas is crustal organic origin): ① Because the humic parent material from higher plants is poor in nitrogen and relatively heavy in δ^{15}N, when the content of nitrogen is less than or equal to 9% and the δ^{15}N value is greater than or equal to 5%, it is generally coal-derived gas; ② Because the Sapropel parent material from lower zooplankton is rich in nitrogen and relatively light in δ^{15}N, when the content of nitrogen is greater than or equal to 9% and the value of δ^{15}N is less than or equal to 5‰, or the content of nitrogen is less than 9% and the value of δ^{15}N is less than or equal to −5‰, it is usually oil-typed gas; ③When the content of nitrogen is less than or equal to 9%, and δ^{15}N is from−5 to 5‰, it may be coal-formed gas or oil-typed gas or a mixture of the two, which can be further distinguished according to alkane value of δ^{15}C.

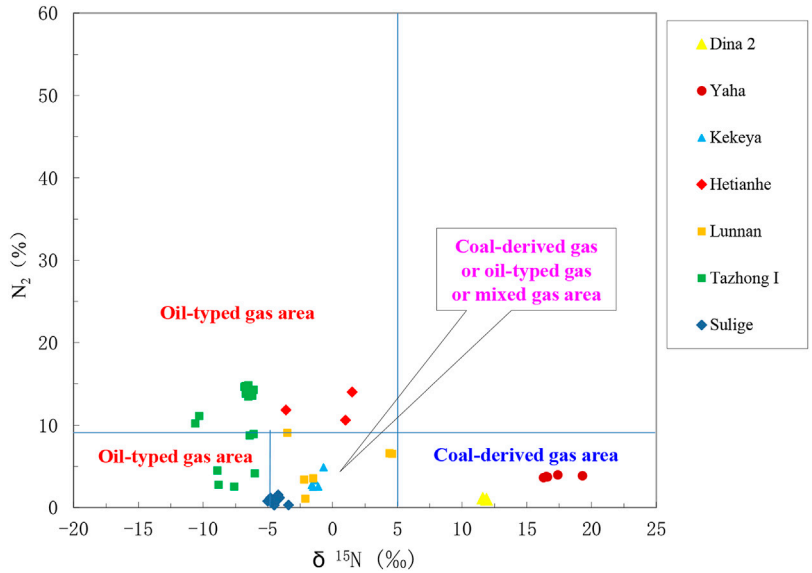


FIGURE 9 | Comprehensive genesis identification application of R/Ra-δ^{15}N-N_2 for some natural gases in the Tarim and Ordos basin.

The comprehensive charts and indicators of R/Ra-δ^{15}N-N_2 have been used to identify coal-derived gas and oil-typed gas from some gas fields in the Tarim and Ordos Basins. The ^{3}He/^{4}He value of helium on natural gases in the Tarim and Ordos Basin is basically at the order of 10^{-8}, and R/Ra<0.1; the helium is typically from the crust. So, according to the R/Ra-δ^{15}N chart (**Figure 7**), the nitrogen of selected natural gases can be identified as originating from organic materials in the crust. Then, the established δ^{15}N-N_2 chart (**Figure 8**) can be used for coal-derived gas and oil-typed gas identification according to geochemical indexes of accompanied nitrogen, and the final genetic identification is shown in **Figure 9** and the detailed results are as follows: ①the Tazhong I and the Hetianhe gas fields fall onto the oil-typed gas zone, so the natural gases are oil-typed gases; ②Dina 2 and Yaha gas fields completely fall onto the coal-derived gas zone, so the natural gases are coal-derived gases; ③Sulige gas field, Kekeya gas field, and Lunnan oil and gas field fall onto the mixture zone, and the oil-typed gas of Lunnan oil and gas field was distinguished from the coal-derived gas of Sulige and Kekeya gas fields by the alkane carbon isotope (**Figure 9**). The results obtained by this method are consistent with those obtained by the carbon isotope of conventional hydrocarbon gas.

CONCLUSIONS

1) Coal-derived gas generally has relatively lower nitrogen abundances, mainly distributed from 0 to 31.2% with main frequency from 0 to 2%. Oil-typed gas usually has relatively higher nitrogen abundances, mainly distributed from 1.1 to 57.1% with main frequency from 2 to 16%.
2) Coal-derived gas generally has relatively heavier nitrogen isotope values mainly distributed from −8 to 19.3‰ with main frequency from −8 to 8‰. Oil-typed gas, meanwhile, usually has relatively lower nitrogen isotope values, mainly distributed from -10.6 to 4.6‰ with main frequency from −8 to 4‰.
3) Coal-derived gas has a relatively low nitrogen content and heavy δ^{15}N value, while oil-typed gas has a relatively high nitrogen content and light δ^{15}N value. The geochemical characteristic differences of coal-derived gas and oil-typed gas are mainly due to the fact that the sapropel parent material is relatively rich in nitrogen element and rich in light δ^{14}N, while the humic parent material is relatively poor in nitrogen element and rich in heavy δ^{15}N, as well as the differences on thermal maturity of the source rocks. In addition, the redox conditions of source rock sedimentary environment and the salinity of water body are also important effective factors.
4) The differences in the geochemical characteristics of nitrogen abundances and isotopes in coal-derived gas and oil-typed gas are of great significance for genetic identification. The genetic identification chart of R/Ra-δ^{15}N for organic and inorganic nitrogen in natural gas and the comprehensive joint identification charts of R/Ra-δ^{15}N-N_2 of nitrogen and helium for coal-derived gas and oil-typed gas have been established, and are of great importance in investigating the origins and sources of natural gas and guiding natural gas exploration in China.

DATA AVAILABILITY STATEMENT

The original contributions presented in the study are included in the article/Supplementary Material, further inquiries can be directed to the corresponding authors.

AUTHOR CONTRIBUTIONS

All authors listed have made a substantial, direct, and intellectual contribution to the work and approved it for publication.

FUNDING

This paper was sponsored by the Major Project of National Special Science and Technology (2016ZX05007-003), the Strategic Priority Research Program of the Chinese Academy of Sciences (XDA14010403), and the Program of PetroChina Company Limited (2018D-500802, 2019B-0604, and 2016ycq03).

ACKNOWLEDGMENTS

Thanks to anonymous reviewers for their constructive suggestions.

REFERENCES

Chen, C. P., Mei, B. W., and Chao, Y. C. (2004). Nitrogen Isotope Geochemistry of Crude Oils in Some of Chinese Basins. *Sci. China:Series D* 34 (8), 721–727. doi:10.3321/j.issn:1006-9267.2004.08.004

Chen, C. P., and Mei, B. W. (2001). Charaterisitcs of Nitrogen Isotope in Different Depositional Enviroments in Chin. *Oil Geology.* 22 (3), 207–209. (In Chinese). doi:10.3321/j.issn:0253-9985.2001.03.003

Chen, C. P., Mei, B. W., and Zhu, C. S. (2001). Nitrogen Isotopic Compostion and Distribution of Natural Gases in Tarim basin. *Geology. Geochem.* 29 (4), 46–49. (In Chinese). doi:10.3969/j.issn.1672-9250.2002.01.008

Chen, C., Zhao, F. H., Ren, D. Y., and Miao, X. N. (2018). Preliminary Study on the Characteristics of Nitrogen Isotopic Composition in Chinese Coals. *Acta Geol. Sinica* 92 (9), 1959–1969. (In Chinese). doi:10.3969/j.issn.0001-5717.2018.09.014

Chen, J. F., Xu, X. M., and Shi, S. B. (2015). Geochemical Characteristics of Crude Oil Nitrogen Isotopes in Different Sedimentary Environments. *J. China Univ. Pet. (Edition Nat. Science)* 39 (5), 1–6. (In Chinese). doi:10.3969/j.issn.1673-5005.2015.05.001

Chen, J. F., and Zhu, Y. N. (2003). The Origin of Meolecular Nitrogen in Natural Gas and Geochemical Characters of Melecular Nitrogen in Natural Gas from East Part of Tarim basin. *Nat. Gas Geosci.* 14 (3), 172–176. (In Chinese). doi:10.3969/j.issn.1672-1926.2003.03.003

Dai, J. X., Song, Y., Dai, C. S., Chen, A. F., Sun, M. L., Liao, Y. S., et al. (1995). *Forming Conditions of Inorganic Natural Gas in east China*. Beijing: Science Press, 195–202. (In Chinese).

Dai, J. X. (1988). Carbon Isotopic Composition Characteristics and Genesis of Liuhuangtang Natural Gas in Tengchong County,Yunan Province. *Chin. Sci. Bull.* 33 (15), 1168–1170. doi:10.1360/csb1988-33-15-1168

Dai, J. X. (1993). Coal-derived Gas and Oil-Typed Gas Identification by Utilizing Light Hydrocarbon. *Pet. Exploration Development* 5, 26–32. (In Chinese).

Dai, J. X. (2014). *Coal-derived Large Gas Fields and Their Gas Sources in China*. Beijing: Science Press, 212–233.

Dai, J. X., Hu, G. Y., Ni, Y. Y., Li, J., Luo, X., Yang, C., et al. (2009). The Distribution Characteristics of Natural Gases in Eastern China. *Nat. gas Geosciences* 20 (4), 471–487. (In Chinese).

Dai, J. X. (1992). Identification of Different Alkane Gas. *Sci. China Ser. B: Chem.* 22 (2), 185–193.

Dai, J. X., Yang, S. F., Chen, H. L., and Shen, X. H. (2005). Geochemistry and Occurrence of Inorganic Gas Accumulations inChinese Sedimentary Basins. *Org. Geochem.* 36 (12), 1664–1688. doi:10.1016/j.orggeochem.2005.08.007

Dai, J. X., and Qi, H. F. (1989). Relationship of $\delta^{13}C$ and Ro of Coal-Derived Gas in China. *Chin. Sci. Bull.* 34 (9), 690–692. doi:10.1360/csb1989-34-9-690

Dai, J. X., Song, Y., and Zhang, H. F. (1994). *Gas Accumulation Zones in China*. Beijing: Sciences Press, 194–198. (In Chinese).

Dai, J. X. (1999). Twenty Year's Important Progress on Coal-Derived Gas Researches in China. *Pet. Exploration Development* 26 (3), 1–10. (In Chinese).

Dai, J. X., Zou, C. N., Zhang, S. C., Li, J, Ni, Y. Y., Hu, G. Y., et al. (2008). Identification of Organic and Inorganic Alkane Gases. *Sci. China Ser. D: Earth Sci.* 38 (11), 1329–1341. doi:10.3321/j.issn:1006-9267.2008.11.001

Dai, J. X., Song, Y., and Dai, C. S. (1996). Geochemistry and Accumulation of Carbon Dioxide Gases in China. *AAPG Bull.* 80 (10), 1615–1626. doi:10.1306/64eda0d2-1724-11d7-8645000102c1865d

Du, J. G., Liu, W. H., Shao, B., and Eckhard, B. (1996). Geochemical Characteristics of Nitrogen in Natural Gases. *Acta Sedimentologica Sinica* 14 (1), 143–148. (In Chinese). doi:10.3321/j.issn:1006-9267.2004.08.004

Du, J. G. (1992). Research Situation of Nitrogen in Natural Gases. *Nat. gas Geosciences* 3 (2), 36–40. (In Chinese).

He, J. X., Li, M. X., Chen, W. H., and Chen, S. H. (2001). Origin of Carbon Dioxide in Natural Gas in Ying-Qiong Basin and its Comprehensive Gas Source Discrimination. *China Offshore Oil and Gas (Geology)* 21 (3), 15–21. (In Chinese). doi:10.3321/j.issn:1000-0976.2001.03.005

He, J. X., Ma, W. H., Zhu, H. Y., and Gong, X. F. (2011). Integrated Identification and Determination of Genetic Types and Accumulation Time in the Marginal basin of Northern South China Sea. *Geology. China* 38 (1), 15–21. (In Chinese). doi:10.3969/j.issn.1000-3657.2011.01.016

Heaton, T. H., Vogel, J. C., Gertrud, V. L. C., and Collett, G. (1986). Climatic Influence on the Isotopic Composition of Bone Nitrogen. *Nature* 322 (6082), 822–823. doi:10.1038/322822a0

Hoefs, J. (1972). *Stable Isotope Geochemistry*. Berlin: J. Springer-Verlag, 140.

Hoering, T. C., and Moore, H. E. (1958). The Isotopic Composition of the Nitrogen in Natural Gases and Associated Crude Oils. *Geochimica et Cosmochimica Acta* 13, 225–232. doi:10.1016/0016-7037(58)90024-3

Hu, G. Y., Li, J., Li, Z. S., Luo, X., Sun, Q. W., and Ma, C. H. (2007). Discussion on Light Hydrocarbon Indexs of Natural Gas Identification. *Sci. China Ser. D: Earth Sci.* 37 (Suppl. p), 111–117. (In Chinese).

Jenden, P. D., Kaplan, I. R., Poreda, R., and Craig, H. (1988). Origin of Nitrogen-Rich Natural Gases in the California Great Valley: Evidence from Helium, Carbon and Nitrogen Isotope Ratios. *Geochimica et Cosmochimica Acta* 52 (4), 851–861. doi:10.1016/0016-7037(88)90356-0

Kendall, C. (1998). in *Isotope Tracers in Catchement Hydrology*. Editors C. Kendall and J. J. Mcdonnell (Elsevier Sci.), 519–576. doi:10.1016/b978-0-444-81546-0.50023-9

Krooss, B. M., Littke, R., Müllera, B., Frielingsdorf, J., Schwochau, K., and Idiz, E. F. (1995). Generation of Nitrogen and Methane from Sedimentary Organic Matter :implication on the Dynamics of Natural Gases Accumulations. *Chem. Geology.* 126 (3/4), 291–318. doi:10.1016/0009-2541(95)00124-7

Li, J., Li, Z. S., Wang, D. L., Li, J., Chen, H. Z., Xie, Z. Y., et al. (2013). Geochemical Characteristics and N_2 Source of Nigtrogen Riched Natural Gas in Tarim basin. *Acta Petrolei Sinica* 34 (S.1), 102–111. (In Chinese). doi:10.7623/syxb2013S1012

Li, J., Luo, X., Shan, X. Q., Ma, C. H., Hu, G. Y., Yan, Q. T., et al. (2005). Resevoir Forming Characteristics of Upper Palezoic Gases in Ordos basin. *Pet. Exploration Development* 32 (4), 54–59. (In Chinese).

Li, J., Xie, Z. Y., Li, Z. S., Luo, X., Hu, G. Y., and Gong, S. (2001). A Gas Source Study for Kuqa Depression of Tarim Basin. *Pet. Exploration Development* 28 (5), 29–32. (In Chinese).

Littke, R., Krooss, B. M., Idiz, E., and Frielingsdorf, J. (1995). Molecular Nitrogen in Natural Gas Accumulations:generation from Sedimentary Orgaric Matter at High Temperatures. *AAPG* 79 (3), 410–430. doi:10.1306/8d2b1548-171e-11d7-8645000102c1865d

Liu, Q. Y., Dai, J. X., Liu, W. H., Qin, S. F., and Zhang, D. W. (2007). Geochemical Characteristics and Genesis of Nitrogen in Natural Gas from Tarim basin. *Oil Gas Geology.* 28 (1), 12–17. (In Chinese). doi:10.11743/ogg20070102

Liu, Q. Y., Liu, W. H., Krooss , B. M., Wang , W. C., and Dai, J. X. (2006). Advances in Nitrogen Geochemistry of Natural Gas. *Natural Gas Geoscience* 17 (1), 119–124. doi:10.3969/j.issn.1672-1926.2006.01.025

Liu, Z. L., and Xia, B. (2005). The Genesis of Molecular Nitrogen of Natural Gases and its Exploratioin Ris Coefficient in Tarim basin. *Nat. Gas Geosci.* 16 (2), 224–228. (In Chinese). doi:10.3969/j.issn.1672-1926.2005.02.020

Owens, N. J. P. (1987). Natural Variations in 15N in the marine Environment. *Adv. Mar. Biol.* 24, 390–451. (In Chinese). doi:10.1016/S0065-2881(08)60077-2

Peterson, B. J., and Fry, B. (1987). Stable Isotopes in Ecosystem Studies. *Annu. Rev. Ecol. Syst.* 18, 293–320. doi:10.1146/annurev.es.18.110187.001453

Prisolov, Z. M., Subbotin, E. S., Tifomirov, B. B., and Sun, Y. X. (1991). Isotopic Composition of Molecular Nitrogen of Natural Gas in Soviet. *Nat. gas Geosciences* 2 (4), 162–167. (In Chinese).

Qin, S., Dai, J., and Liu, X. (2007). The Controlling Factors of Oil and Gas Generation from Coal in the Kuqa Depression of Tarim Basin, China. *Int. J. Coal Geology.* 70, 255–263. doi:10.1016/j.coal.2006.04.011

Rosman, K. J. R., and Taylor, P. D. P. (1998). Isotopic Compositions of the Elements 1997 (Technical Report). *Pur. Appl. Chem.* 70, 217–235. doi:10.1351/pac199870010217

Shi, J. N., Zeng, Z. P., Zhou, L. Y., and Liao, C. J. (2003). Research on Genetic Mechanism of Non-hydrocarbon Gas in Chinese Sedimental Basins. *Spec. oil gas reservoir* 10 (2), 5–9. (In Chinese). doi:10.3969/j.issn.1006-6535.2003.02.002

Xu, X. M., Chen, J. F., Shi, S. B., Wang, S. Q., Sun, W. L., and Shen, B. (2017). Nitrogen Isotope Distribution Characteristics of Different Polar Nitrogen Compounds in Crude Oil. *Bull. Mineralogy Petrology Geochem.* 36 (1), 150–154. (In Chinese). doi:10.3969/j.issn.1007-2802.2017.01.017

Zeng, Z. P. (2002). Analysis on Nitrogen Genesis of Sedimental Basins in China. *Nat. gas Geosciences* 13 (Z1), 29–33. (In Chinese). doi:10.3969/j.issn.1672-1926.2002.03.006

Zhang, L., Hu, G. Y., Xie, Z. Y., Liu, G. D., Wang, X. B., and Xiang, J. (2008). Pyrrole Nitrogen Compound for Tracing the Natural Gas Migration: A Case from the Second Section of Xujiahe Formation in Pingluoba-Qiongxi Area. *Nat. Gas Geosicence* 19 (2), 250–254. (In Chinese).

Zhang, Z. S. (1988). Geological Geochemistry of Nitrogen in Gas Reservoir. *Geology. Geochem.* 2, 51–56. (In Chinese).

Zhu, Y. N. (1994). Developments in Geochemistry of Non-hydrocarbon Constituents of Natural Gas. *Adv. Earth Sci.* 9 (4), 50–57. (In Chinese).

Zhu, Y. N. (1999). Genesis and Identification of Molecular Nitrogen in Natural Gases. *J. China Univ. Pet. (Edition Nat. Sciences)* 23 (2), 22–26. (In Chinese). doi:10.3321/j.issn:1000-5870.1999.02.006

Zhu, Y. N., and Shi, B. Q. (1998). Analysis on Origins of Meolecular Nitrogen in Natural Gas and Their Geochemical Features. *Geology. Geochemisry* 26 (4), 50–57. (In Chinese).

Conflict of Interest: Authors WX, LJ, YC, LZ, WY, LJ, YC, HA and GS were employed by RIPED/PetroChina. The remaining authors declare that the research was conducted in the absence of any commercial or financial relationships that could be construed as a potential conflict of interest.

The authors declare that this study received funding from PetroChina Company Limited. The funder was involved in the study design, collection, analysis, interpretation of data, the writing of this article or the decision to submit it for publication.

Publisher's Note: All claims expressed in this article are solely those of the authors and do not necessarily represent those of their affiliated organizations, or those of the publisher, the editors and the reviewers. Any product that may be evaluated in this article, or claim that may be made by its manufacturer, is not guaranteed or endorsed by the publisher.

Copyright © 2021 Xiaobo, Jian, Chunxia, Zhisheng, Jianfa, Yue, Yifeng, Jin, Chunlong, Aisheng and Shouguo. This is an open-access article distributed under the terms of the Creative Commons Attribution License (CC BY). The use, distribution or reproduction in other forums is permitted, provided the original author(s) and the copyright owner(s) are credited and that the original publication in this journal is cited, in accordance with accepted academic practice. No use, distribution or reproduction is permitted which does not comply with these terms.

frontiers in Earth Science

ORIGINAL RESEARCH
published: 01 February 2022
doi: 10.3389/feart.2022.648337

The Characteristics of Organic Carbon in the Offshore Sediments Surrounding the Leizhou Peninsula, China

Jia Xia[1,2], *Yongqiang Han*[1], *Jingqian Tan*[1], *Grace Awinmalsim Abarike*[1] *and Zhiguang Song*[1]*

[1]Faculty of Chemistry and Environmental Science, Guangdong Ocean University, Zhanjiang, China, [2]Southern Marine Science and Engineering Guangdong Laboratory (Zhanjiang), Zhanjiang, China

A total of 43 seafloor surface sediment samples collected from the offshore region surrounding the Leizhou Peninsula were analyzed in terms of the total organic carbon content (TOC), total nitrogen (TN), organic carbon isotope ($\delta^{13}C_{org}$) and sediment grain size. Our results showed that the organic carbon content in the samples ranged from 0.12 to 0.79%, with an average of 0.42% which was lower compared with other offshore regions of China, whereas the $\delta^{13}C_{org}$ was in the range of –22.47‰ to –19.18‰. The total nitrogen content ranged from 0.011 to 0.100% which was also low. The combination of $\delta^{13}C_{org}$ and TOC/TN ratio (5.1–14.3) suggested that the organic matter is dominant by marine authigenic source input, as marine sourced organic matter accounts for 71%, 82%, and 75% in the sediments from the offshore areas of the east side, west side and the south (Qiongzhou Strait) of the Leizhou Peninsula, respectively. The weak/poor correlations between the organic carbon and clay, silt content, the pH and Eh value suggested that organic matter abundance and distribution were influenced by the source input of organic matter, the seafloor sediments' redox status, and seawater's hydrodynamic condition.

Keywords: seafloor sediments, TOC, organic carbon isotope, TN, offshore of the Leizhou Peninsula

OPEN ACCESS

Edited by:
Giovanni Martinelli,
National Institute of Geophysics and Volcanology, Italy

Reviewed by:
Jiwei Li,
Institute of Deep-Sea Science and Engineering (CAS), China
Venkatramanan Senapathi,
Ton Duc Thang University, Vietnam

***Correspondence:**
Zhiguang Song
zgsong_ocean@163.com

Specialty section:
This article was submitted to Geochemistry, a section of the journal Frontiers in Earth Science

Received: *31 December 2020*
Accepted: *03 January 2022*
Published: *01 February 2022*

Citation:
Xia J, Han Y, Tan J, Abarike GA and Song Z (2022) The Characteristics of Organic Carbon in the Offshore Sediments Surrounding the Leizhou Peninsula, China. Front. Earth Sci. 10:648337. doi: 10.3389/feart.2022.648337

1 INTRODUCTION

The ocean is the most important carbon pool on the earth's surface and a vital system of the global carbon cycle (Gao et al., 2008; Larowe et al., 2020; Yu et al., 2021). The total carbon storage in the ocean is about 50 times that of carbon in the atmosphere (Falkowski et al., 2000), and plays an important role in regulating atmospheric CO_2 concentration. Al thought accounting for just 7.6% of the total global ocean area, the marginal sea plays a major role in the global carbon cycle (Bianchi et al., 2018), as the coastal zone and shelf marginal sea sediments account to more than 96% of yearly buried carbon of the whole ocean (Burdige, 2005; Burdige, 2007). While the buried marine organic matter (OM) also plays a key role in controlling atmospheric carbon dioxide and oxygen concentrations in addition to the fossil fuel formation over the past 500 million years (Berner et al., 2003). Therefore, the study of the organic carbon abundance and its distribution in the offshore seafloor sediments is of scientific significance for understanding and predicting future marine ecological environments and changes (Borges et al., 2005).

Many studies have been carried out on the organic matter abundance and distribution of the seafloor surface sediments in China's offshore areas, such as the Bohai sea (Gao et al., 2016; Wang et al., 2020; Yang et al., 2021), the Yellow Sea (Xiong et al., 2013; Zhang et al., 2014; Liu et al., 2020),

the Yangtze River Estuary (Kang et al., 2014; Fan et al., 2017; Zhang et al., 2020), the East China Sea (Guo et al., 2001), and the Pearl River Estuary in the northern South China Sea (Lian et al., 2019; Yuan et al., 2019; Liu et al., 2018). Guangzhou Marine Geological Survey had conducted a comprehensive research project of "Holocene Environmental Evolution and Anthropogenic impact of the Beibu Gulf, South China" since 2009. In this project, two joint expeditions with the Leibniz Institute for Baltic Sea Research of Germany were carried out in 2009 and 2011, respectively. The objectives of this project were focused on the acquisition of new data such as ocean graphic data, bathymetric measurements, high-resolution seismic data on the structure of Quaternary sediments (Cui et al., 2017). For the first time, a map of Holocene stratigraphic thickness distribution in the eastern Beibu Gulf has been created, with two depositional centers and six provenance areas delineated (Cui et al., 2017). After establishing a long-term topography evolution model for the Beibu Gulf and inverting paleotopographic changes since 6,000 BP, the sedimentary environment evolution history of Beibu Gulf was investigated (Cui et al., 2017). The outcome of this project and other previous studies had also provided some new information on the organic carbon contents, some specific molecular compounds and heavy metal pollutants (Zhang et al., 2011; Zhang et al., 2012; Chen et al., 2014; Cui et al., 2015; Jin et al., 2019; Liu and Chao, 2019). However, the expedition and sampling area of this project-were mainly in the far offshore and relatively deep-water areas, and there is a lack of investigation on sedimentary organic matter in the near coastal region surrounding the Leizhou Peninsula.

Being the important low latitude marine continental transition zone, the offshore surrounding the Leizhou Peninsula is a typical region which influenced by the East Asian monsoon. The coastal area of the Leizhou Peninsula is also the most important region of the mangrove ecosystem in China and it may have significant effects on the carbon pool of marine sediments in the offshore region (Yang et al., 2012). Furthermore, there is intense aquaculture in the shallow coastal water and bay region along the Leizhou Peninsula offshore. These offshore aquaculture industries would consume a large amounts of fish food. Therefore, the metabolic activities of the cultured organisms will impact the abundance of organic matter in the offshore sediments. In general, the abundance and preservation of organic matter in the seafloor surface sediments are controlled by the primary productivity and sedimentary environment, and influenced by human activities in this region. In this study, we aimed to investigate the total organic carbon content in the seafloor sediments and its distribution, origin and controlling factors in the offshore region surrounding the Leizhou Peninsula and study the carbon preservation in the nearshore seafloor sediments and their environmental significance.

2 SAMPLES AND EXPERIMENTS

2.1 Geological and Geographical Background of the Study Area

Being the third-largest peninsula in China, the Leizhou Peninsulalocates at the southern tip of the Chinese mainland (**Figure 1**). The peninsula is about 140 km long from north to south and 60–70 km wide from east to west which covers more than 13,000 km^2, and is surrounded by the Zhanjiang Bay (formerly known as Guangzhou Bay), the Qiongzhou Strait and the Beibu Gulf with a coastline about 1,180 km. A few small rivers enter the surrounding sea area including the Nandu River, the Xixi River, the Yingli River, the Tongming River, and the Jianjiang River. Although these rivers have small flows, their influence on organic carbon input and preservation in the seafloor sediments could not be ignored. They could carry terrestrial organic matter into the offshore area. The coastline of the peninsula is quite twisty, and there are many harbors and islands. The great variation in the geomorphologic condition of the coastline could also cause significant changes in the sedimentary condition of the offshore region. The eastern part of the Leizhou Peninsula is a kind of coast consisting of platform submerged bay, the southern part is a kind of volcanic platform coast, and the west is the coast consisting of sea terrace and platform submerged bay. The type of tide and its impact on the east and west coastlines of the peninsula are significantly different. An irregular semi-diurnal tide affects the east coast and the west coast is affected by a regular diurnal tide. The tidal conditions in the Qiongzhou Strait are more complicated, as the flood tide runs from the west to the east and the ebb tide runs from the east to the west. The eastward currents flow fast than the westward currents (Liu et al., 2015). From previous studies based on the trajectory of the drifting bottle in the offshore region of the western Guangdong and the fixed-point observation of the currents, the coastal currents in western Guangdong generally flow to the southwest all the year round, and goes south along the east coast of the Leizhou Peninsula (Yang et al., 2003). In addition, the direction of the waves in the Beibu Gulf area depends on the wind direction, and the waves are mostly northeast direction during winter and the southwest direction during summer (EBCBS, 1993). Therefore, the sedimentary environments in the offshore region of the Leizhou Peninsula are complicated. The marine survey and sampling region are in the offshore area of the Leizhou Peninsula, within a geographical range between 20°15′~21°30′N north latitude and 109°30′~111°45′E east longitude (**Figure 1**).

2.2 Sample Collection and Analytical Methods

The seafloor sediment samples were collected using a gravity box sampler during the Guangdong Ocean University's comprehensive marine environmental and ecological survey surrounding the Leizhou Peninsula in autumn 2017 (September 29 ~ October 7). A total of 43 seafloor surface sediment samples were obtained from 57 pre-determined sampling sites as shown in **Figure 1**. The water depth of the sampling sites ranges from 8 to 50 m and is listed in **Table 1**. It should be pointed out that about 13 locations among the 57 sampling sites were sandy seabed where the sandy samples were not collected. The on-site measurement of the samples' redox potential (Eh) and pH values were immediately carried out when the sediments were taken to the rear deck of the vessel. However, these on-site measurements were only performed on the sampling sites where the sampled sediment column was in

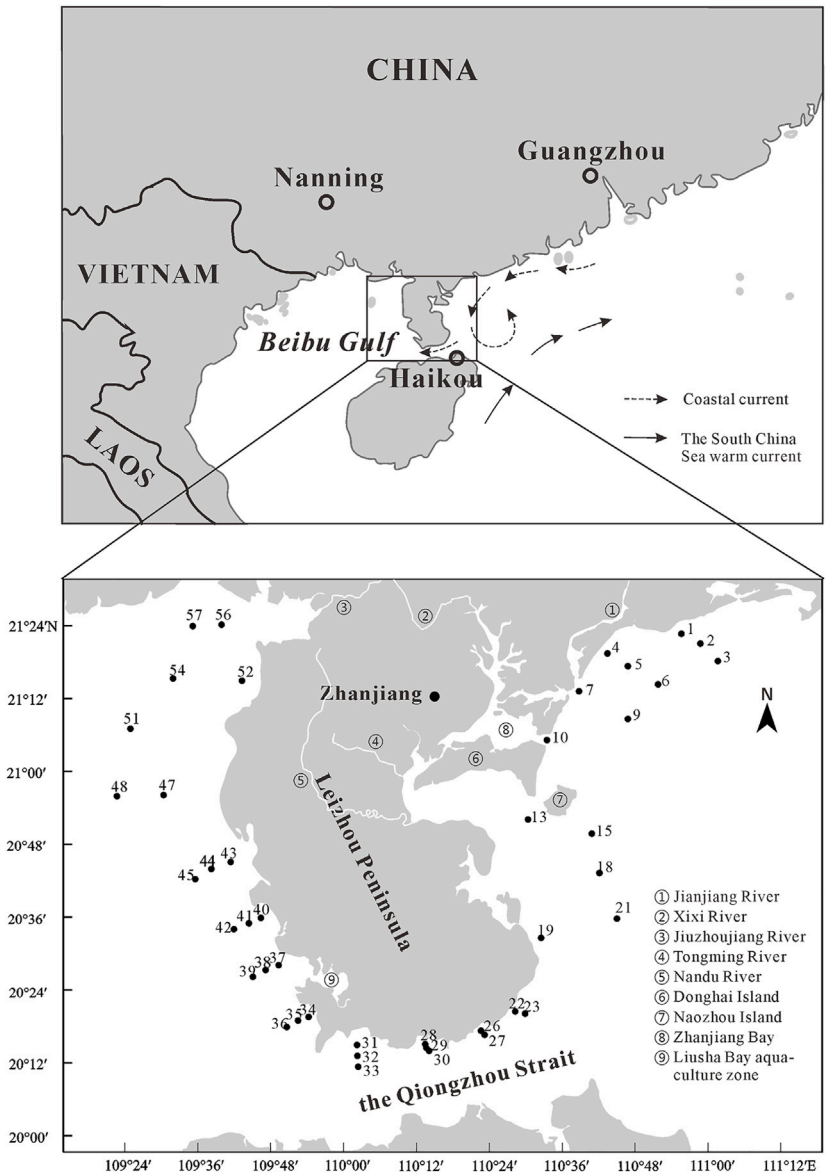


FIGURE 1 | Map of the near offshore region and sampling locations surrounding the Leizhou Peninsula.

good shape and not severely disturbed by the sampling process from the seafloor. A DZB-718L portable multi-parameter analyzer coupled with an oxidation-reduction potential (ORP) platinum electrode and pH glass electrode (with an accuracy of 0.1 mV and 0.1, respectively) was used for measuring Eh and pH values. The electrodes were rinsed with ultra-pure water before use, then Eh and pH electrodes were calibrated with ORP standard solution and standard buffer solutions (pH = 4.01, 7.00, 10.01), respectively. The calibrations satisfy the requirement that the values of three consecutive measurements were the same, and the values were rapidly stable within 1 min of each measurement. The sediment samples were collected on-site by taking the undisturbed 0–10 cm thickness of top layer sediments from the sediment block taken by the box sampler and packed into the PE (TWIRL"EM) sterile sample bag. After removing air from the sample bag, the sealed sample bags were frozen and stored in the refrigerator. The samples were carried back to the laboratory and freeze-dried for further treatment and following experimental analysis.

2.3 Sediment Grain Size Analysis

The particle size analysis was performed on a Malvern Mastersizer 2000 laser particle size analyzer. Before measuring particle size, a small amount of the original wet sediments was treated with 30% H_2O_2 solution to remove organic matter. Precisely 1 mol/L hydrochloric acid was added to remove carbonate, followed by washing with ultra-pure water. The final sediment residue was added with sodium hexametaphosphate as a dispersant with full shaking and then ready for particle size analysis. Instrumental measurement's size

TABLE 1 | TOC content and related measurement data in the offshore samples of the Leizhou Peninsula.

Sample site	Water depth (m)	Sediment types	TOC (%)	TN (%)	TOC/TN	$\delta^{13}C_{org}$ (‰)	pH	Eh (mV)	Clay (%)	Silt (%)	Sand (%)	Median particle size (Φ)
P1	12.0	Mud	0.28	0.055	5.1	−20.95	7.63	−123.6	23.9	55.9	20.3	6.43
P2	10.0	Mud	0.30	0.058	5.2	−21.50	7.59	−183.8	21.8	59.9	18.4	6.48
P3	15.0	Mud	0.59	0.078	7.6	−21.27	7.63	−145.3	26.3	55.6	18.1	6.64
P4	10.0	Mud	0.35	0.042	8.3	−21.02	7.55	−101.3	25.4	62.5	12.2	6.42
P5	14.0	Mud	0.31	0.039	7.9	−20.80	7.89	−172.5	28.7	57.8	13.6	6.86
P6	17.0	Mud	0.51	0.067	7.6	−21.15	7.73	−146.9	24.5	63.9	11.6	6.55
P7	11.0	Mud	0.55	0.054	10.2	−21.54	7.51	−168.0	30.0	65.6	4.4	6.91
P9	17.0	Mud	0.43	0.050	8.6	−21.27	7.78	−109.3	29.4	62.1	8.5	6.91
P10	13.0	Silty	0.36	0.036	10.0	−21.66	7.76	−121.7	31.0	64.1	4.9	6.99
P13	25.0	Sandy	0.19	0.021	9.0	−19.95	7.74	−128.5	31.5	49.1	19.4	6.88
P15	18.0	Mud	0.52	0.059	8.8	−21.52	—	−133.8	29.2	63.5	7.3	6.90
P18	16.1	Mud	0.34	0.028	12.1	−20.13	—	−71.0	32.1	56.2	11.7	6.91
P19	8.0	Mud	0.34	0.045	7.6	−20.16	7.71	−101.7	20.8	48.3	30.9	4.90
P21	16.5	Silty	0.12	0.011	10.9	−21.16	—	10.5	13.6	26.9	59.5	3.55
P22	15.0	Sandy mud	0.36	0.038	9.5	−22.47	7.71	−71.2	19.1	66.2	14.7	5.75
P23	19.0	Sandy mud	0.33	0.040	8.3	−20.38	7.73	9.5	27.4	62.7	9.9	6.79
P26	20.0	Mud	0.45	0.046	9.8	−20.78	—	−51.2	20.7	50.4	28.9	5.23
P27	20.0	Mud	0.59	0.070	8.4	−21.24	7.5	−129.5	30.1	59.9	10.0	6.90
P28	11.0	Mud	0.49	0.050	9.8	−21.05	—	−146.7	22.5	52.7	24.8	5.71
P29	10.8	Mud	0.51	0.058	8.8	−20.95	7.56	−64.7	29.6	62.3	8.1	6.95
P30	43.0	Mud	0.29	0.036	8.1	−20.03	7.25	−137.0	18.5	53.4	28.1	5.45
P31	10.0	Mud	0.33	0.037	8.9	−20.32	7.45	−122.3	25.5	43.4	31.1	6.17
P32	23.0	Mud	0.50	0.041	12.2	−20.90	7.7	−52.0	22.7	62.7	14.6	5.91
P33	50.0	Gritty	0.34	0.036	9.5	−20.47	—	−132.5	21.0	55.7	23.4	5.30
P34	12.0	Mud	0.43	0.044	9.8	−19.39	7.63	−176.0	31.1	47.2	21.7	7.00
P35	14.0	Mud	0.71	0.084	8.45	−20.54	7.53	−125.0	30.0	66.6	3.4	6.94
P36	19.0	Mud	0.52	0.063	8.3	−20.81	7.67	-85.3	30.2	61.9	7.9	6.93
P37	11.5	Mud	0.79	0.100	7.9	−20.65	7.4	−121.4	36.8	61.6	1.6	7.43
P38	17.0	Mud	0.57	0.064	8.9	−20.57	7.62	−255.1	32.4	58.2	9.4	7.07
P39	19.0	Mud	0.70	0.070	10.0	−20.66	7.75	−130.9	32.9	56.4	10.8	7.04
P40	9.0	Mud	0.75	0.093	8.1	−20.61	7.46	−121.5	34.2	60.1	5.8	7.24
P41	11.0	Mud	0.63	0.068	9.3	−20.38	7.57	−109.5	36.1	53.2	10.7	7.31
P42	16.0	Mud	0.50	0.062	8.1	−20.37	7.66	−100.0	31.9	58.6	9.5	7.01
P43	10.0	Mud	0.23	0.016	14.4	−19.45	7.66	−120.3	39.6	47.1	13.3	7.48
P44	12.0	Mud	0.54	0.062	8.7	−19.18	7.48	−83.6	37.6	54.9	7.5	7.39
P45	17.0	Mud	0.55	0.058	9.5	−19.70	—	−107.8	30.7	59.5	9.8	7.13
P47	17.0	Sand	0.20	0.017	11.8	−20.14	7.68	−93.4	29.0	51.7	19.3	7.09
P48	17.0	Mud	0.26	0.024	10.8	−19.73	7.84	−190.4	24.0	34.2	41.9	6.24
P51	19.0	Mud	0.48	0.062	7.7	−20.00	7.39	−181.2	36.7	54.5	8.8	7.37
P52	8.5	Mud	0.23	0.026	8.8	−19.96	7.61	−83.1	33.5	34.4	32.1	6.82
P54	13.0	Sand	0.19	0.021	9.0	−20.06	7.46	−76.7	21.0	19.8	59.2	3.38
P56	10.0	Coarse sand	0.13	0.011	11.8	−21.37	7.55	−97.5	9.4	14.6	76.1	1.57
P57	9.0	Mud	0.53	0.054	9.8	−20.52	7.5	−151.1	36.0	50.7	13.3	7.18

range was 0.2~1,000 μm with a granularity resolution of less than 0.01 Φ. Particle size distributions were accounted as an incremental percentage as particles smaller than 4 μm were considered as clays, 4~63 μm as silts and particle size larger than 63 μm as sand (Folk et al., 1970). The relative error of repeated measurements was <1%.

2.4 TOC, TN and Organic Carbon Isotope Analysis

The freeze-dried sediments were initially ground to 100 mesh powder for instrumental analysis or further treatments. For TOC analysis, the powder samples were treated with 10% hydrochloric acid to remove the inorganic carbon (Schubert and Calvert, 2001; Liu et al., 2015). The dry powder sediments were initially soaked with 10% hydrochloric acid under heating of 60°C for 24 h, and then using a centrifuge to remove the supernatant. They were treated with 10% hydrochloric acid again for 4 h to remove the residue carbonate. The solid residues were washed with ultra-pure water to neutrality and dried at a temperature of 60°C. And then take about 20~30 mg of the treated residue powder sample for instrumental analysis of TOC. According to the weight difference before and after pickling, the final content of total organic carbon in the sample was obtained by adjusting measured data to the sample weight before acid treatment. While the total nitrogen (TN) was measured using the initial powder samples

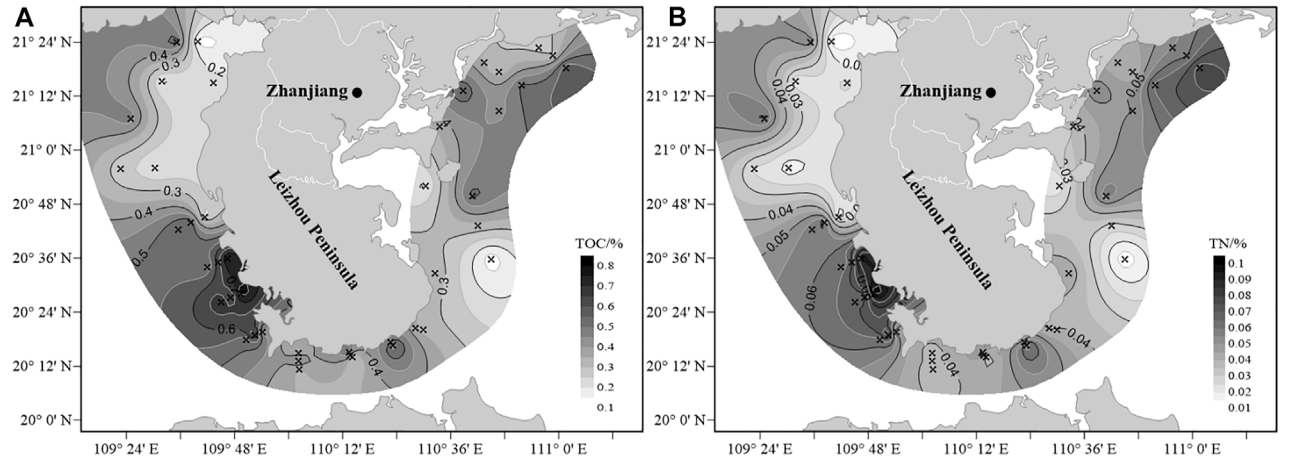


FIGURE 2 | Distributions of TOC **(A)** and TN **(B)** in the near offshore seafloor sediments surrounding the Leizhou Peninsula.

without any further treatment. Both TOC and TN measurement was performed on a German Elementar vario MACRO Organic Element Analyzer. The analysis errors of TOC and TN were ±0.02% and ±0.005%, respectively.

The organic carbon isotopic ($\delta^{13}C_{org}$) analysis was performed on the carbonate-free samples by a Sercon 20-22 isotope ratio mass spectrometer at the Marine and Environmental Monitoring Center of Guangdong Ocean University. The results were expressed in δ notation in parts per mil (‰):

$$\delta^{13}C_{org}\,(‰) = \left(R_{sample}/R_{reference} - 1\right) \times 1000$$

where R_{sample} and $R_{reference}$ are the isotopic $^{13}C/^{12}C$ ratios of the sample and reference, respectively. The carbon isotopic reference was PeeDee Belemnite (PDB). The samples were run in duplicate with an error of ±0.2‰.

3 RESULTS AND DISCUSSIONS

3.1 The TOC, TN Contents and Their Distribution

The TOC content of 43 seafloor surface sediment samples is in the range of 0.12–0.79%, with an average of 0.42% (**Table 1**). **Figure 2A** is the isogram of TOC content of the 43 seafloor sediment samples from the Leizhou Peninsula offshore. It shows that the offshore area of the Liusha Bay is the high TOC content area, and the northwest part of the Beibu Gulf in the west of the Leizhou Peninsula and southeast offshore areas in the east of the Leizhou Peninsula are two low TOC content areas. Except for sediments with high organic carbon content in the Liusha Bay, the TOC content in these offshore sediments is generally low. The TOC contents in the samples of the Leizhou Peninsula offshore fall within the range of that from the vast far offshore region of the Beibu Gulf which is 0.02~0.95% (Cui et al., 2017). This further demonstrated that the whole Beibu Gulf area of the South China Sea is a lower TOC content region.

Table 2 shows that the TOC content of the samples in this study is generally low compared with other offshore areas, and the TOC content from the shallow bay sea area near the coastline is relatively high, such as the Liusha Bay of the Leizhou Peninsula and the western Guangdong Coasts. The difference reflects that the variations in the sedimentary environment between the restricted coastal areas with significant human impact and the open seas in the offshore coastal areas. As mentioned above, the east coastal offshore of the Leizhou Peninsula is greatly affected by irregular semi-diurnal tides. The strong currents with high oxygen content in the shallow region along the east coast of the Leizhou Peninsula resulted in an oxide sedimentary environment that is not favorable for the preservation and accumulation of organic matter in the seafloor sediments (Gao et al., 2016). The Qiongzhou Strait is constantly affected by the strong currents with high energy (Chen and Shi, 2019) and the seafloor sediments are dominated by sand, silty sand and sandy silt (Chen et al., 2014), so it is not favorable for the deposition and preserves of organic matter. On the other hand, the flow direction of the currents in the Qiongzhou Strait varies with the seasons, leading to a complex, oxides marine sedimentary environment, where sediments are frequently disturbed and result in organic-poor sediments (Ma et al., 2012; Chen and Shi, 2019). The Beibu Gulf is situated in the tropical-subtropical monsoon climate zone where the marine primary productivity is significantly high (Wu, 2008; Yao et al., 2021). However, due to the general shallow water depth and strong diurnal tide and currents influence, most areas of the seafloor are oxide condition which is not favorable for organic matter preservation, only in some restricted areas such as the Liusha Bay where the sea current flow rate is lower than 0.3 m/s even at high tide time (Luo et al., 2013). Under this near quiescent flow condition, the water would be depleted of oxygen and favorable for the organic matter to be deposited and preserved, resulting in a relatively high TOC content in the sea floor sediments. On the other hand, according to the on-site observation of the seafloor sediments and benthic organism sampling, it was noticed that the seafloor sediments are generally lacking benthic animals, especially in the low TOC content sites.

TABLE 2 | Comparison of the TOC and TN contents in the offshore surface sediments of China.

Research sea area	TOC (%)	TN (%)	Sampling time	Data sources
Leizhou Peninsula offshore	0.12~0.79 (0.42)	0.01~0.10 (0.05)	October 2017	This study
Bohai Sea	0.19~0.81 (0.46)	0.02~0.12 (0.07)	May 2012	Gao et al. (2016)
Yellow Sea	0.10~1.38 (0.50)	0.01~0.20 (–)	October 2010	Zhang et al. (2014)
Yellow Sea, East China Sea	0.05~1.64 (0.88)	—	2006	Cai et al. (2014)
Western Taiwan Strait	0.01~1.79 (0.37)	0.00~0.11 (–)	April 2005	Ye et al. (2011)
Pearl River Estuary	0.36~1.40 (0.66)	0.02~0.10 (0.04)	July 2013	Lian et al. (2019)
Zhanjiang Port	0.12~1.32 (0.54)	—	February 2009	Zhang et al. (2012)
Liusha Bay	0.06~3.06 (1.43)	—	February 2009	Zhang et al. (2012)
Western Guangdong Coasts	0.01~8.34 (0.9)	0.18~0.37 (0.27)	July 2006	Gu et al. (2010)

This phenomenon indicates that most areas of the Leizhou Peninsula offshore are in a status of severe desertification. Bioturbation and biodeposition of benthic organisms are some of the factors affecting the organic matter in sediments. Bioturbation destroys organic matter by prolonging its exposure to dissolved oxygen, while the biodeposition causes suspended particles in the water column to be deposited into the sediment as fecal pellets (Graf and Rosenberg, 1997). Muschenheim. (1987) has calculated that about 32.5 kg particles are deposited to the seafloor by biodeposition per square meter every year in Kiel Bay of the North Sea. Desertification also is more likely related to intensive fishing activities (Thompson, 1978; Chen et al., 2008; Yue et al., 2017). It has also been reported that bottom trawling and illegal electric fishing could result in massive depletion of benthic fauna in the offshore areas and inevitable desertification of seafloor (Wang and Yuan, 2008), and consequently affect the organic matter content of the seafloor sediments. Therefore, the low organic carbon content in the surrounding offshore seafloor sediments of the Leizhou Peninsula is related to a shallow oxidizing sedimentary condition and limited terrestrial organic matter input, and influenced by intensive fishing activities.

The total nitrogen content (TN) in the sediment samples of the 43 sampling sites is in the range of 0.011–0.100%, with an average of 0.050% (**Figure 2B**; **Table 1**). Among these samples, the P37 site shows the highest TN content, which is consistent with its highest TOC content. However, the TN contents in these near coastal seafloor sediments are significantly lower than the TN contents in the seafloor sediments from the vast far offshore area of the Beibu Gulf obtained from 2009 to 2011 (Cui et al., 2017). The reason for this could be partly attributed to the geographical difference of sampling area and partly to the anthropogenic impact of fishing on the near coastal area. But it needs further investigation as the TOC content show agreement for these studies. **Figure 2** shows that the spatial distribution of TOC content highly coincides with that of TN content in the seafloor surface sediments from the Leizhou Peninsula offshore. The spatial distribution of TOC and TN content in the sediments is consistent. Even the highest TN area is identical to that of the highest TOC region situated outside Liusha Bay of the southwest coast of the Leizhou Peninsula (**Figure 2**). Furthermore, the TOC and TN contents display a good positive linear correlation (**Figure 3**) with a coefficient of 0.8637. The linear correlation between TOC and TN has no intercept indicating that nitrogen in the sediment mainly exists in the form of organic compounds (Goni et al., 1998; Schubert and Calvert, 2001).

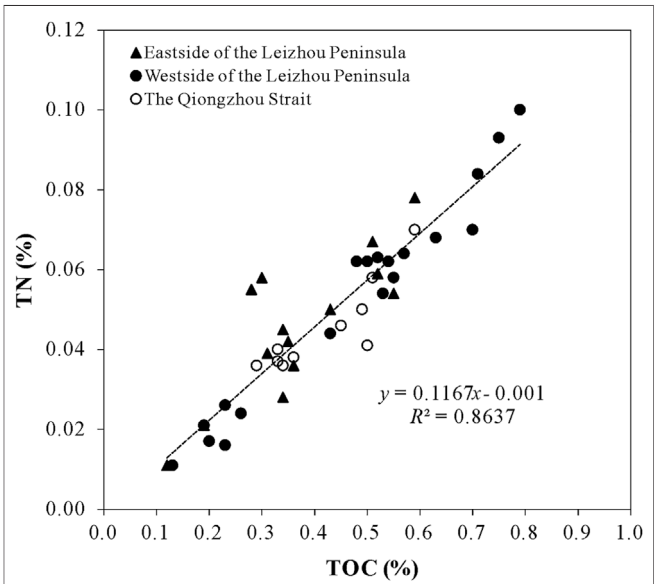


FIGURE 3 | Correlation between TOC and TN content in the near offshore seafloor sediments surrounding the Leizhou Peninsula.

3.2 Source of the Organic Matter

The organic matter in the seafloor sediments is mainly derived from the input of marine organisms and terrestrial organic detritus, and the proportion of these two sources varies significantly in different areas of the ocean depending on many conditions (Bianchi and Allison, 2009; Blair and Aller, 2012). The mass ratio of TOC/TN could be used to identify the input source of organic matter in marine sediments. The TOC/TN less than 8 indicates the marine authigenic sourced organic matter and TOC/TN higher than 12 points the terrestrial source input, whereas the value between 8 and 12 suggests a mixed origin of marine and terrestrial input (Liu et al., 1998; Goslin et al., 2017). The TOC/TN of the samples from the Leizhou Peninsula offshore ranged from 5.1 to 14.3, with an average of 9.1. The results indicate that most of the sedimentary organic matter in the study area has mixed input of marine and terrestrial sources, including three sediment samples with a TOC/TN ratio >12

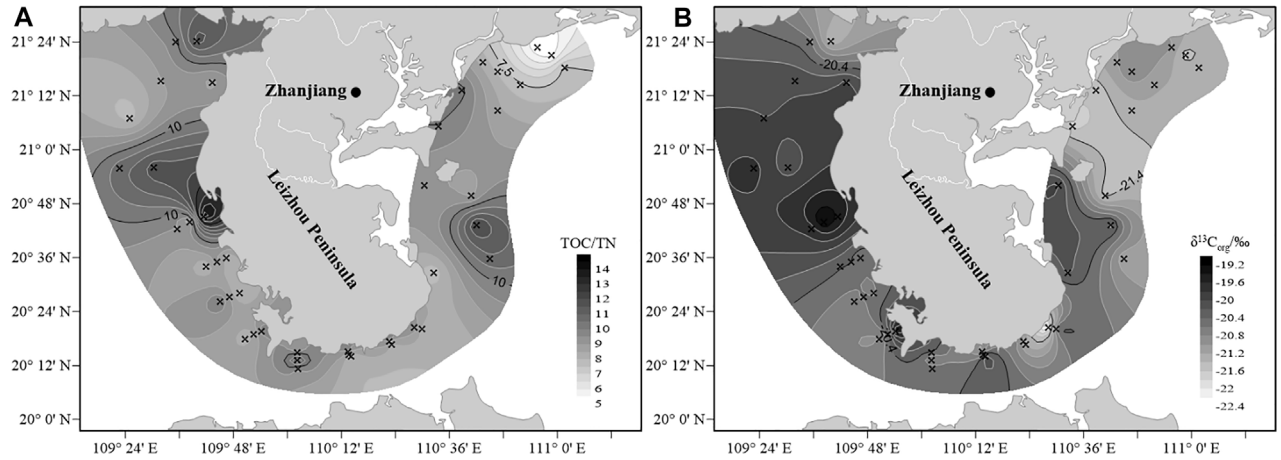


FIGURE 4 | Distribution of TOC/TN ratio **(A)** and organic carbon isotope ($\delta^{13}C_{org}$) **(B)** in the near offshore seafloor sediments surrounding the Leizhou Peninsula.

which suggests that they are affected by terrestrial organic matter. **Figure 4A** shows the TOC/TN ratio distribution in the seafloor samples of the Leizhou Peninsula offshore. The samples with TOC/TN ratio <8 are only distributed in a small area at the northeast Leizhou Peninsula offshore. This area is characterized by mud sediments and higher organic carbon content. Due to the influence of Pearl River material input under the coastal current in western Guangdong (Cao et al., 2017; Huang et al., 2020), higher primary productivity could consequently result in a higher amount of organic matter deposition, while the muddy sediments would be favorable for better organic matter preservation. The samples with TOC/TN ratio >12, which is dominated by terrestrial organic matter, are mainly distributed in the middle area of the westside offshore. This area is a major seawater pearl production base in China and a vital shellfish culture area in Guangdong Province. Therefore, the organic matter content of the seafloor sediments could be affected by aquaculture and intensified biological metabolic activities. Most parts of the Leizhou Peninsula offshore show a mixed sedimentary organic matter input as their TOC/TN ratios of samples are in the range of 8–12. The TOC/TN ratio in the seafloor samples also reveals that terrestrial organic input may significantly impact the carbon deposition and cycling in the most near offshore area of the Leizhou Peninsula region. Because the coastal area of the Leizhou Peninsula is one of the main distribution areas of mangroves (Yang et al., 2017), it is assumed that the coastal mangrove ecosystem and agriculture activities could have a significant effect on the sedimentary organic matter composition in the Leizhou Peninsula offshore. However, there is a paucity of information regarding the contribution or effect of mangroves on sedimentary organic matter in the offshore sediments.

Organic carbon isotopic composition ($\delta^{13}C_{org}$) has been widely used to distinguish the organic matter of marine source inputs (Schubert and Calvert, 2001). For example, C_3 vascular plants are typically characterized by isotopic compositions that are relatively depleted in ^{13}C (−22‰~−33‰, with an average of −27‰; Fry and Sherr, 1984; Ramaswamy et al., 2008), while C_4 plants display significant more enriched ^{13}C value (−9‰~−16‰, with an average of −13‰; Pancost and Boot, 2004). For the typical marine phytoplankton, it exhibits intermediate $\delta^{13}C$ values (−18‰~−21‰, Goni et al., 1998). The values of $\delta^{13}C_{org}$ in the surface sediments from the coastal Leizhou Peninsula range from −22.47‰ to −19.18‰, with an average of −20.61 ± 0.71‰ (**Figure 4B**; **Table 1**), is similar to that of marine organic matter. The distribution features of $\delta^{13}C_{org}$ suggest that the sedimentary organic matter from the coastal Leizhou Peninsula is primarily marine originated with limited terrestrial source input. In addition, the most depleted $\delta^{13}C_{org}$ values of organic matter were observed at the northeast coast of the Leizhou Peninsula which could be attributed to a riverine input by the Jianjiang river (**Figure 4B**).

In order to assess the relative proportions of terrigenous and marine autogenous organic carbon in the sediment samples, a two end-member mixing model based on $\delta^{13}C_{org}$ was employed to distinguish the relative proportion of terrigenous and marine organic carbon in these sediments (Calder and Parker, 1968; Chen et al., 2012). The proportion of terrigenous and marine sourced organic carbon (Ogrinc et al., 2005) was calculated using the following equations:

$$\delta^{13}C_{org} = f_T \times \delta^{13}C_T + f_M \times \delta^{13}C_M$$
$$f_T + f_M = 1$$

where f_T and f_M represent the terrestrial and marine organic matter fractions in the samples; $\delta^{13}C_T$ and $\delta^{13}C_M$ are the carbon isotopic compositions of the terrestrial and marine end-members, respectively. Based on the previous study in the adjacent area Daya Bay, the end-member values of $\delta^{13}C_T$ and $\delta^{13}C_M$ were −26‰ and −19‰, respectively (Qu et al., 2018). The estimated proportion of the terrestrial and marine organic matter in the Leizhou Peninsula offshore sediment samples are displayed in **Figure 5**. The seafloor sediments are dominated by marine sourced organic matter, which accounts for 77 ± 10% on average. Although the lowest proportion of marine organic matter is recorded at station 22, the sediments from the east offshore area of the Leizhou Peninsula has less marine-derived

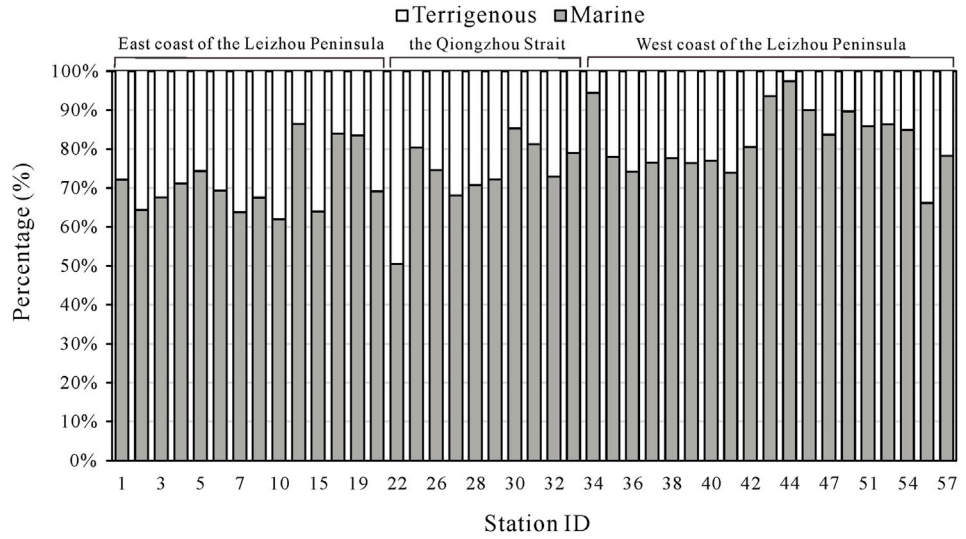


FIGURE 5 | The relative contribution of terrestrial and marine organic carbon in surface sediments.

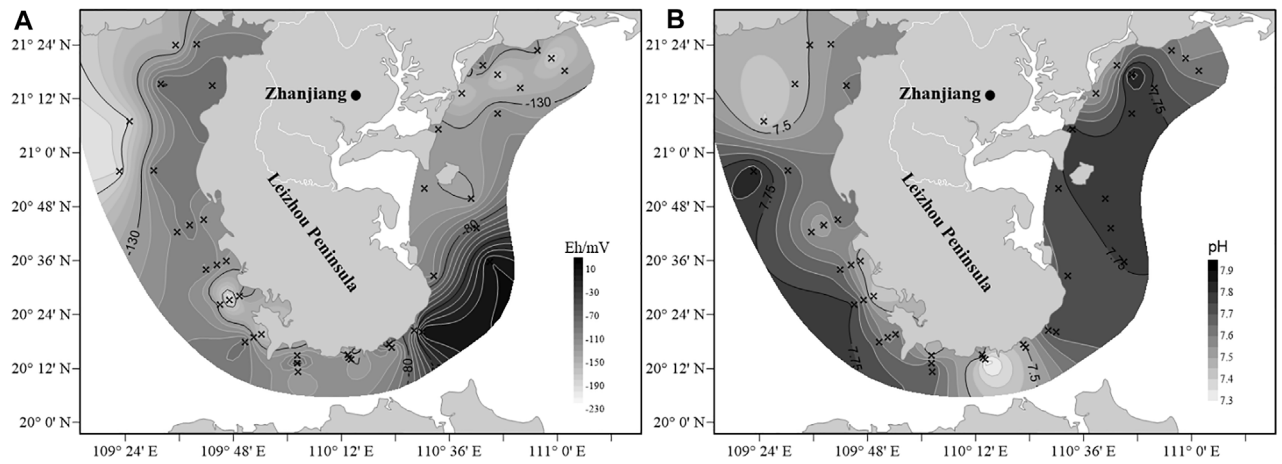


FIGURE 6 | Distributions of Eh **(A)** and pH **(B)** in the near offshore seafloor sediments surrounding the Leizhou Peninsula.

organic matter (71% on average) compared with that of the Qiongzhou Strait (75% on average) and the west offshore area (82% on average). The composition of organic matter in sediments is the combination of multiple processes (primary production, hydrodynamics, preservation condition, source input, etc.) that determine organic carbon's biogeochemical cycle (Schubert and Calvert, 2001; Ogrinc et al., 2005).

3.3 The Eh and pH Values of Sediments and Their Correlations With TOC

The samples' Eh and pH values and their distribution are listed in **Table 1** and shown in **Figure 6**. The Eh values of seafloor sediment samples surrounding the Leizhou Peninsula vary from −255.1 to 10.5 mv. According to the classification of redox potential and status of sediments proposed by Song Jinming and others, these sediments are in a weak reduction to reducing status (Song et al., 1990). **Figure 6A** shows that the higher Eh value areas generally coincide with the low organic carbon content areas. In contrast, the low Eh value areas are overlapped with the high organic carbon content areas. This is in agreement with that the Eh value of marine sediments is largely controlled by the abundance of organic matter (Wu et al., 2012). The various complex chemical and biochemical reactions occur in the seafloor sediments and would affect the geochemical behavior of various substances in the sediments, including the formation and transformation of authigenic minerals and the process of diagenesis (Zhu and Wang, 1980). The organic matter in the seafloor sediments is initially degraded by aerobic bacteria and fungi associated with the consumption of dissolved oxygen

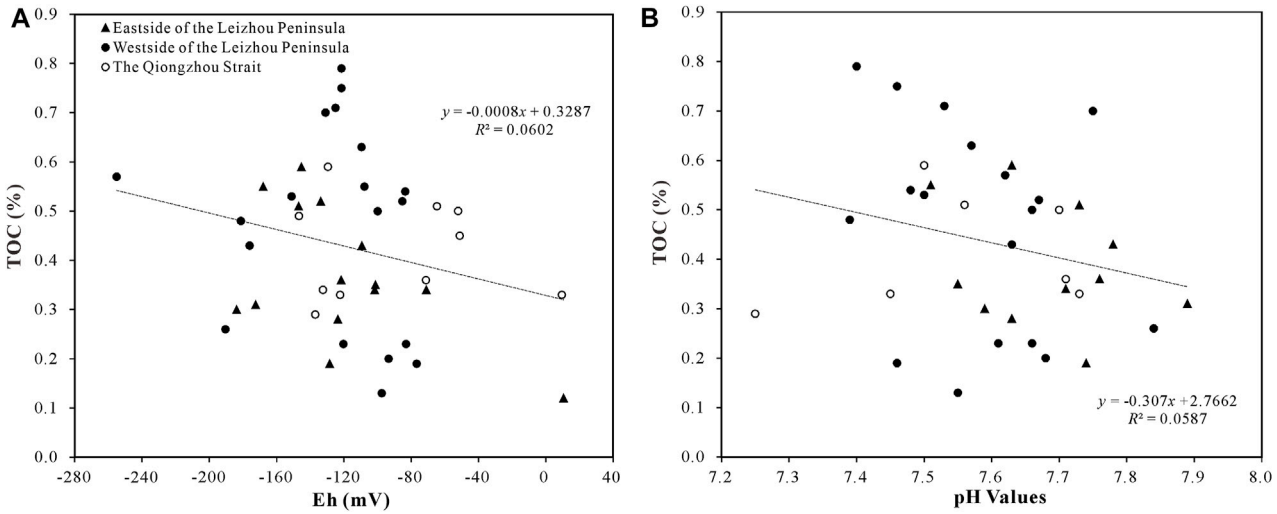


FIGURE 7 | Correlation between TOC and Eh potential **(A)**, pH value **(B)** in the near offshore seafloor sediments surrounding the Leizhou Peninsula.

which leads to the decrease of Eh value in sediments (Wang et al., 2009; Feng et al., 2016). When oxygen is depleted, the organic matter would then be degraded by nitrate, manganese oxide, and sulfate-reducing bacteria, and associated with a continuous decrease of Eh value (Wu et al., 2012). In general, the high TOC content is often associated with strong activities of reducing bacteria, and the higher the TOC content, the lower the Eh value. Therefore, there is a negative correlation between TOC content and Eh value in the sediments. However, the TOC content displays a very weak correlation with Eh values with a coefficient of 0.0602 for the studied samples due to the narrow range of TOC distributions and similar Eh conditions. (**Figure 7A**). It has been proposed that the Eh value could be significantly influenced by the sulfur reduction when the Eh value is in the range of −200~0 mV (Vershinin and Rozanov, 1983; Song et al., 1990). On the other hand, the extraction of soluble organic matter in these seafloor samples shows that they contain a high abundance of elemental sulfur as the fresh copper sheets have been completed blacked during the solvent extraction (Jin et al., 2007; Rogowska et al., 2016). While the high content of elemental sulfur indicates strong evidence that the sulfate reduction process prevailed in these seafloor sediments. The free oxygen has been exhausted in the sediments due to the oxidation of organic matter and the oxidation reaction has turned to use the sulfate as oxidant. So, the oxidation of organic matter is related to the redox condition in the sediments. However, since the offshore sampling area is near the offshore region, the sedimentary environment could be complicated and influenced by various factors, weakening the negative correlation between TOC and Eh values.

The pH value of the Leizhou Peninsula offshore sediment samples ranges from 7.25 to 7.89 and indicates a weak alkaline depositional condition. **Figure 6B** shows that the pH value distribution in the offshore seafloor sediments displays a clear regional variation. The low pH values mainly occur in the near offshore areas of the Qiongzhou Strait, the northwest Beibu Gulf and near the coastal area of the Liusha Bay. The pH value of the offshore seafloor samples from the Beibu Gulf of the westside of the Leizhou Peninsula shows an increasing trend from the near coast to the far offshore area. The seafloor sediments in the eastside of the Leizhou Peninsula generally display a higher pH value of >7.6 with high value area located in the northeast offshore region. The pH value of the seafloor sediments is largely determined by the chemical property of the overlying seawater due to the interaction between the seafloor sediments and the bottom seawater (Qi et al., 2008). At the same time, carbonate and shellfish shells in the seafloor sediments would discharge carbonate ions, which would react with hydrogen ions in the bottom seawater, and could result in excessive hydroxide ions, which makes the seafloor water more alkaline, so the seafloor surface sediments are in a weakly alkaline status (Krumins et al., 2013). **Figure 7B** shows a weak negative correlation between TOC content and pH values with a coefficient of 0.0587, which suggests that the pH value of seafloor sediments has little influence on the abundance of sedimentary organic matter.

3.4 Effects of Sedimentary Grain Size

The seafloor samples are mainly composed of silt, clay and sand with a content of 14.6–66.6% (averaged at 53.6%) for silt, a range of 9.4–39.6% (averaged at 27.9%) for clay and a range of 3.4–76.1% for sand. The granularity of sediments is an important factor in controlling the abundance of organic matter in the seafloor sediments as it reflects the seafloor hydrodynamic conditions. According to the correlation between the TOC content and the contents of clay, silt and sand (**Figure 8**), the TOC content shows a slightly positive correlation with the clay, silt and mean size with a Pearson correlations coefficient (r) of 0.593, 0.617 and 0.548 ($p < 0.01$), respectively. But a clear negative correlation with the sand content (r = −0.684, $p < 0.01$; **Figure 8C**). The clay content of the seafloor samples from the west side of the Leizhou Peninsula

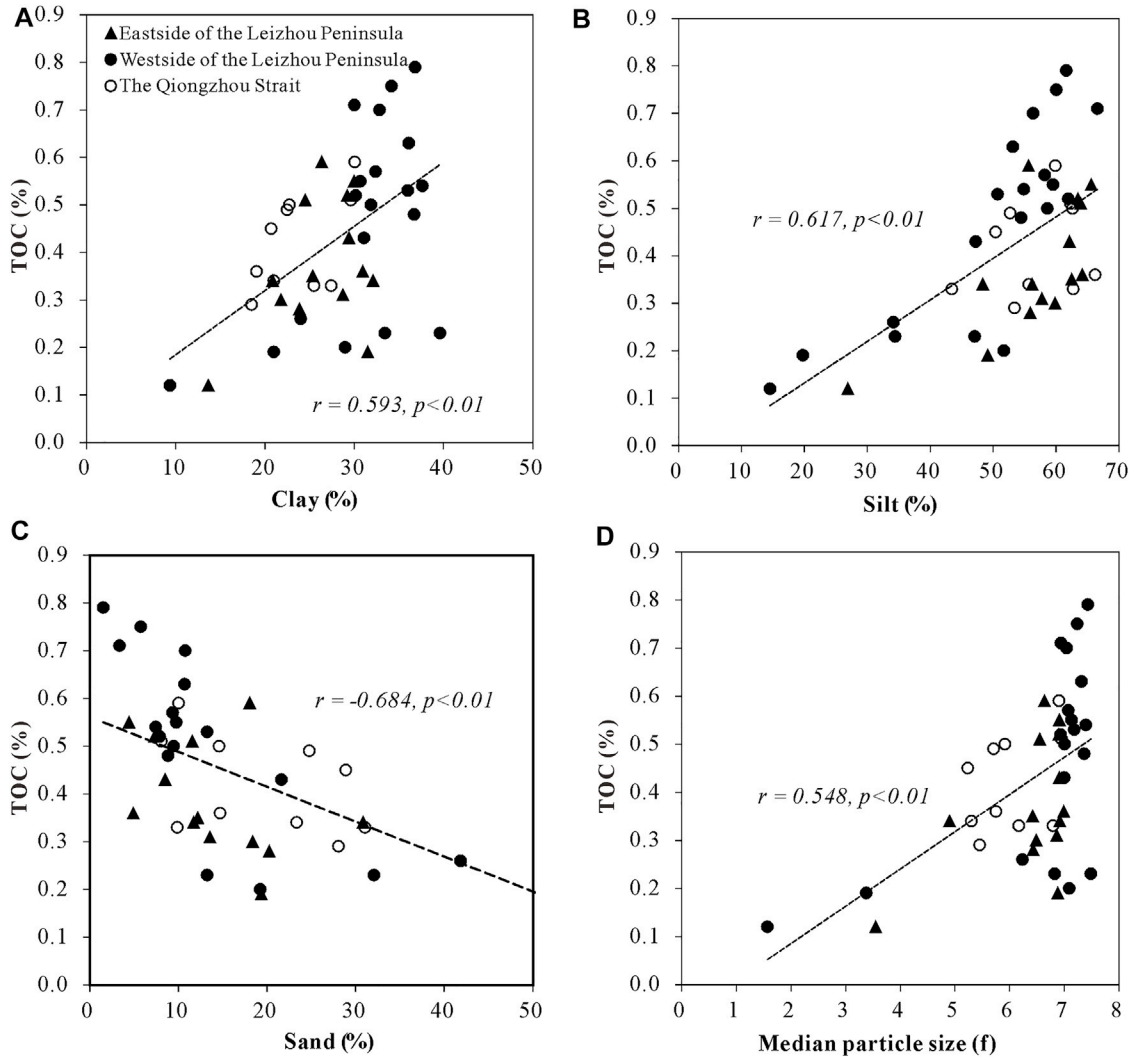


FIGURE 8 | Correlations between TOC content and Clay **(A)**, Silt **(B)**, Sand **(C)**, Median particle size **(D)** in the near offshore seafloor sediments surrounding the Leizhou Peninsula.

is generally higher than that of the samples from the eastern side of the Leizhou Peninsula and the Qiongzhou Strait. **Figure 9** shows the distribution of clay content in the seafloor samples of the near offshore region surrounding the Leizhou Peninsula. This contour plot of the clay content shows that the high content area overlaps with the high TOC content area in the seafloor sediments surrounding the Leizhou Peninsula. The northeastern offshore area of the Beibu Gulf is a low TOC content area and this is related to the high content of sand in the seafloor sediments as the coastal area experienced strong tide erosion (Xia et al., 2001; Xu et al., 2012). The seafloor of the Qiongzhou Strait is a strong eroded area, where the strong currents are not favorable for the fine particle deposits and the organic matter preservation due to the high oxygen content of seawater (Shi and Chen, 1998; Chen et al., 2015). Consequently, the TOC contents in these high hydrodynamic seafloor sediments are often lower and this is common in shallow offshore areas of

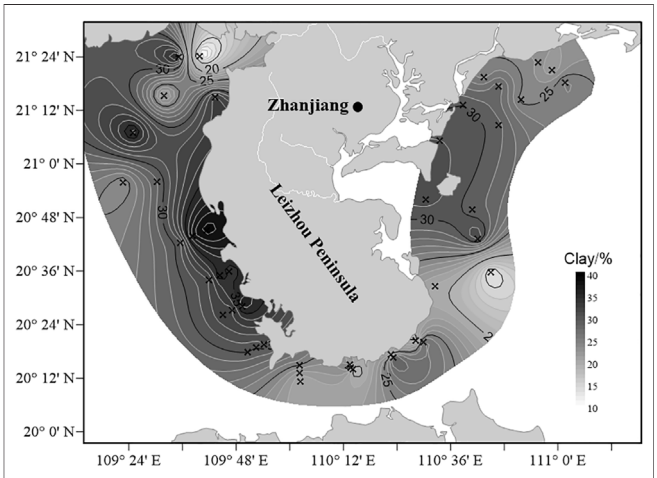


FIGURE 9 | The distribution of clay content in the near offshore seafloor sediments surrounding the Leizhou Peninsula.

Bohai, the Yellow Sea and the Yangtze River estuary (Hu et al., 2013; Yao et al., 2014; Gao et al., 2016).

4 CONCLUSION

The investigation of the TOC, TN contents, organic carbon isotopic composition and their distributions in the offshore seafloor sediment samples surrounding the Leizhou Peninsula could be concluded into following points: 1) both TOC and TN contents in these seafloor sediment samples is significantly lower compared with that of seafloor sediments from other offshore areas of China. The low TOC and TN contents and a lack of benthic organisms observed in the sediment could be suggestive of a desertification status or trend in the offshore seafloor region surrounding the Leizhou Peninsula; 2) The organic carbon isotopic composition and TOC/TN ratio suggest that the sedimentary organic matter is mixed sourced from both terrestrial input and marine input but dominated by the marine sourced organic matter. 3) The seafloor sediments from the offshore region surrounding the Leizhou Peninsula are generally in a weak reduction to reduction status. A weak negative linear correlation between the TOC contents and Eh values suggests that the redox potential of sediments is largely controlled by the abundance of organic matter. On the other hand, pH values seem to have no effect on the TOC content and its distribution in these offshore seafloor sediments surrounding the Leizhou Peninsula; 4) The positive correlation between TOC and clay, silt content, and median particle size (Φ) of the sediments indicates that the clay and silt sedimentary condition is favorable for the organic matter preservation.

DATA AVAILABILITY STATEMENT

The original contributions presented in the study are included in the article/supplementary material, further inquiries can be directed to the corresponding author.

AUTHOR CONTRIBUTIONS

XJ and SZ contributed to conception of the study. Samples were collected by XJ, HY, and TJ. XJ, HY, and AA performed the experimental analysis. XJ wrote the first draft of the manuscript. SZ revised the manuscript.

FUNDING

This study was funded by the Special Talent Support Program of Guangdong Ocean University (No. R17001), the Project of Enhancing School with Innovation of Guangdong Ocean University (GDOUQ18301), the First-class special Funds of Guangdong Ocean University (231419029), the Project of Marine geochemistry and climate change of Guangdong Ocean University (No. 002026002004) and the Fund of Southern Marine Science and Engineering Guangdong Laboratory (Zhanjiang) (Grant No. ZJW-2019-08).

REFERENCES

Berner, R. A., Beerling, D. J., Dudley, R., Robinson, J. M., and Wildman, R. A., Jr (2003). Phanerozoic Atmospheric Oxygen. *Annu. Rev. Earth Planet. Sci.* 31 (1), 105–134. doi:10.1146/annurev.earth.31.100901.141329

Bianchi, T. S., and Allison, M. A. (2009). Large-river delta-front Estuaries as Natural "recorders" of Global Environmental Change. *Proc. Natl. Acad. Sci.* 106 (20), 8085–8092. doi:10.1073/pnas.0812878106

Bianchi, T. S., Cui, X., Blair, N. E., Burdige, D. J., Eglinton, T. I., and Galy, V. (2018). Centers of Organic Carbon Burial and Oxidation at the Land-Ocean Interface. *Org. Geochem.* 115, 138–155. doi:10.1016/j.orggeochem.2017.09.008

Blair, N. E., and Aller, R. C. (2012). The Fate of Terrestrial Organic Carbon in the Marine Environment. *Annu. Rev. Mar. Sci.* 4 (1), 401–423. doi:10.1146/annurev-marine-120709-142717

Borges, A. V., Delille, B., and Frankignoulle, M. (2005). Budgeting Sinks and Sources of CO_2 in the Coastal Ocean: Diversity of Ecosystems Counts. *Geophys. Res. Lett.* 32 (14), L14601. doi:10.1029/2005gl023053

Burdige, D. J. (2005). Burial of Terrestrial Organic Matter in marine Sediments: A Re-assessment. *Glob. Biogeochem. Cycles* 19 (4). doi:10.1029/2004GB002368

Burdige, D. J. (2007). Preservation of Organic Matter in marine Sediments: Controls, Mechanisms, and an Imbalance in Sediment Organic Carbon Budgets? *Chem. Rev.* 107, 467–485. doi:10.1021/cr050347q

Cai, D., Sun, Y., Zhang, X., Su, Y., Wu, Y., Chen, Z., et al. (2014). Reconstructing a Primary Productivity History Over the Past 200a Using Sediment Organic Carbon Content and the Stable Isotope Composition in the East China Sea and the Yellow Sea. *Acta Oceanologica Sinica* 36 (2), 40–50. doi:10.3969/j.issn.0253-4193.2014.02.005

Calder, J. A., and Parker, P. L. (1968). Stable Carbon Isotope Ratios as Indexes of Petrochemical Pollution of Aquatic Systems. *Environ. Sci. Technol.* 2, 535–539. doi:10.1021/es60019a001

Cao, M., Ma, Q., Wu, Y., and Zhang, J. (2017). Difference in Organic Matter Distribution and Degradation in Surface Sediment between Northern South China Sea and Hainan Island. *Oceanologia et Limnologia Sinica* 48 (2), 258–265. doi:10.11693/hyhz20160900188

Chen, B., and Shi, M. (2019). Advances in Study of Beibu Gulf Circulation. *Guangxi Sci.* 26 (06), 595–603. doi:10.13656/j.cnki.gxkx.20200103.001

Chen, F. J., Chen, J., Jin, H., Li, H., Zheng, L., and Zhang, H. (2012). Correlation of $\delta^{13}C_{org}$ in Surface Sediments with Sinking Particulate Matter in South China Sea and Implication for Reconstructing Paleo-Environment. *Acta Sedimentologica Sinica* 30 (2), 340–345. doi:10.14027/j.cnki.cjxb.2012.02.013

Chen, L., Yan, J., and Ma, D. (2015). Comprehensive Analysis of Hydrodynamic Characteristics Simulation of Haikou Port Construction Plan of Qiongzhou Strait Automobile Ferry. *China Water Transport (the second half of the month)* 15 (09), 273–275.

Chen, L., Zhang, Y., Li, T., Yang, W., and Chen, J. (2014). Sedimentary Environment in the Qiongzhou Strait and its Surrounding Waters and Sedimentary Evolution in the Past 10,000 Years. *Earth Sci. (Journal China Univ. Geosciences)* 39 (06), 696–704. doi:10.3799/dqkx.2014.065

Chen, Z. Z., Qiu, Y. S., Jia, X. P., and Zhong, Z. H. (2008). Effects of Fishing on the marine Ecosystem of Beibu Gulf. *Ying Yong Sheng Tai Xue Bao* 19 (07), 1604–1610. doi:10.13287/j.1001-9332.2008.0292

Cui, Z., Lin, J., Gan, H., Liu, W., and Zhang, L. (2015). Geochemical Characteristics of Surface Sediments in the Eastern Waters of the Beibu Gulf of the South China Sea. *Mar. Sci.* 39 (07), 103–111.

Cui, Z., Xia, Z., Lin, J., and Shi, Y. (2017). *Holocene Environmental Evolution and Anthropogenic Impact of Beibu Gulf, South China Sea*. Beijing, China: Ocean Press, 189–191.

EBCBS (1993). *Survey of China Bays*, 12. Beijing: Ocean Press, 73.

Falkowski, P., Scholes, R. J., Boyle, E., Canadell, J., Canfield, D., Elser, J., et al. (2000). The Global Carbon Cycle: a Test of Our Knowledge of Earth as a

System: A Test of Our Knowledge of Earth as a System. *Science* 290 (5490), 291–296. doi:10.1126/science.290.5490.291

Fan, X., Cheng, F., Yu, Z., and Song, X. (2017). The Distribution Characteristics of Sediment Particle Size and Biogenic Factors in the Yangtze Estuary and its Adjacent Waters. *Mar. Sci.* 41 (07), 105–112. doi:10.11759/hykx20170109001

Feng, W., Wang, Z., Zhang, R., Zhang, D., Ye, M., Chen, D., et al. (2016). The Environment Characteristics of Redox in the Surface Sediments of Ningde Coastal Sea Area in Relation to Influence Factors. *Mar. Environ. Sci.* 35 (6), 882–887. doi:10.13634/j.cnki.mes.2016.06.013

Folk, R. L., Andrews, P. B., and Lewis, D. W. (1970). Detrital Sedimentary Rock Classification and Nomenclature for Use in New Zealand. *New Zealand J. Geology. Geophys.* 13 (4), 937–968. doi:10.1080/00288306.1970.10418211

Fry, B., and Sherr, E. B. (1984). $\delta^{13}C$ Measurements as Indicators of Carbon Flow in marine and Fresh-Water Ecosystems. *Contrib. Mar. Sci.* 27, 13–14.

Gao, L., Yao, P., Wang, J., and Zhao, B. (2016). Distribution and Sources of Organic Carbon in Surface Sediments from the Bohai Sea. *Acta Oceanologica Sinica* 38 (6), 8–20. doi:10.3969/j.issn.0253-4193.2016.06.002

Gao, X., Song, J., Li, X., Long, A., and Chen, S. (2008). Analysis on the Main Progress and Key Influencing Factors of China's Offshore Carbon Cycle Research. *Mar. Sci.* 32 (3), 83–90.

Goni, M. A., Ruttenberg, K. C., and Eglinton, T. I. (1998). A Reassessment of the Sources and Importance of Land-Derived Organic Matter in Surface Sediments from the Gulf of Mexico. *Geochimica Et Cosmochimica Acta* 62 (18), 3055–3075. doi:10.1016/s0016-7037(98)00217-8

Goslin, J., Sansjofre, P., Van Vliet-Lanoe, B. V., and Denmark, C. (2017). Carbon Stable Isotope and Elemental (TOC, TN)geochemistry in Salymarsh Surface sediments(Western Brittany, France): a Useful Tool for reconstructingHolocene Relative Sea-Level. *J. Quat. Sci.* 32 (7), 987–1007. doi:10.1002/jqs.2971

Graf, G., and Rosenberg, R. (1997). Bioresuspension and Biodeposition: a Review. *J. Mar. Syst.* 11 (3–4), 269–278. doi:10.1016/s0924-7963(96)00126-1

Gu, Y., Wang, C., Lǚ, S., Yang, Y., Feng, J., Fang, J., et al. (2010). Distribution and Pollution Assessment of Biogenic Sediments in Surface Sediments in Western Guangdong. *J. Shenzhen Univ. (science technology)* 27 (03), 347–353. doi:10.3969/j.issn.1000-2618.2010.03.018

Guo, Z., Yang, Z., Chen, Z., and Deng, Mao. (2001). Provenance Analysis of Sedimentary Organic Matter in the Mud Area of the East China Sea Continental Shelf. *Geochemistry* 30 (5), 416–424. doi:10.19700/j.0379-1726.2001.05.002

Hu, L., Shi, X., Guo, Z., Wang, H., and Yang, Z. (2013). Sources, Dispersal and Preservation of Sedimentary Organic Matter in the Yellow Sea: The Importance of Depositional Hydrodynamic Forcing. *Mar. Geology.* 335 (1), 52–63. doi:10.1016/j.margeo.2012.10.008

Huang, C., Chen, F., Zhang, S., Chen, C., Meng, Y., Zhu, Q., et al. (2020). Carbon and Nitrogen Isotopic Composition of Particulate Organic Matter in the Pearl River Estuary and the Adjacent Shelf. *Estuarine, Coastal Shelf Sci.* 246, 107003. doi:10.1016/j.ecss.2020.107003

Jin, H., Wan, S., Zhang, J., Song, Z., Zhao, D., Huang, J., et al. (2019). Distribution Characteristics and Provenance of Surface Clay Minerals in Beibu Gulf. *Mar. Sci.* 43 (01), 75–84. doi:10.11759/hykx20180423001

Jin, M., Xia, Y., Lei, T., Ma, S., Qiu, J., and Zhang, R. (2007). Note on Sulfur Removal with Metallic Copper. *Geochem. Int.* 45 (6), 620–623. doi:10.1134/s0016702907060109

Kang, Z., Yu, R., Kong, F., Gao Yan, W. Y., Guo, Wei., Chen, J., et al. (2014). Composition, Content and Distribution of Pigment in spring Surface Sediments in Red Tide Area South of Changjiang Estuary. *Mar. Sci.* 38 (10), 30–39. doi:10.11759/hykx20130423001

Krumins, V., Gehlen, M., Arndt, S., Van Cappellen, P., and Regnier, P. (2013). Dissolved Inorganic Carbon and Alkalinity Fluxes from Coastal marine Sediments: Model Estimates for Different Shelf Environments and Sensitivity to Global Change. *Biogeosciences* 10 (1), 371–398. doi:10.5194/bg-10-371-2013

Larowe, D. E., Arndt, S., Bradley, J. A., Estes, E. R., Hoarfrost, A., Lang, S. Q., et al. (2020). The Fate of Organic Carbon in marine Sediments - New Insights from Recent Data and Analysis. *Earth-Science Rev.* 204, 103146. doi:10.1016/j.earscirev.2020.103146

Lian, Z., Jiang, Z., Huang, X., Zhang, L., Wu, Y., and Liu, S. (2019). Spatial Distribution Characteristics of Different Extracts of Organic Carbon in Surface Sediments from the Pearl River Estuary. *Mar. Environ. Sci.* 38 (3), 391–398. doi:10.13634/j.cnki.mes.2019.03.011

Liu, D., and Chao, Q. (2019). Study on the Spatial and Temporal Distribution Oc Chlorophyll a Concentration in Beibu Gulf. *J. Mar. Sci.* 37 (2), 95–102. doi:10.3969/j.issn.1001-909X.2019.02.010

Liu, D., Li, X., Emeis, K.-C., Wang, Y., and Richard, P. (2015). Distribution and Sources of Organic Matter in Surface Sediments of Bohai Sea Near the Yellow River Estuary, China. *Estuarine, Coastal Shelf Sci.* 165 (NOV.5), 128–136. doi:10.1016/j.ecss.2015.09.007

Liu, F., Yang, C., Chang, X., and Liao, Z. (2018). Provenance Discrimination of the Last Glacial Sediments from the Northeastern South China Sea and its Paleoenvironmental Indications. *Terr. Atmos. Ocean. Sci.* 29 (2), 131–148. doi:10.3319/tao.2017.07.31.01

Liu, W., Wang, R., and Li, C. (1998). Carbon to Nitrogen Ratio in the East China Sea Particulate Organic Matter. *Oceanologia Et Limnologia Sinica* 29 (5), 467–470.

Liu, X., Tang, D., and Ge, C. (2020). Distribution and Sources of Organic Carbon, Nitrogen and Their Isotopic Composition in Surface Sediments from the Southern Yellow Sea, China. *Mar. Pollut. Bull.* 150, 110716. doi:10.1016/j.marpolbul.2019.110716

Luo, Z., Zhu, C., Guo, Y., Su, L., Li, J., and Ou, Y. (2013). Distribution Characteristics of C, N and P in Liusha Bay Surface Sediments and Their Pollution Assessment. *South China Fish. Sci.* 10 (3), 1–8. doi:10.3969/j.issn.2095-0780.2014.03.001

Ma, R., He, Y., Yang, Y., Xia, N., Guo, Y., Zhang, G., et al. (2012). Geochemical Characteristic of Surface Sediments from the Qiongzhou Strait. *Mar. Sci. Bull.* 31 (2), 131–135. doi:10.11840/j.issn.1001-6392.2012.2.002

Muschenheim, D. K. (1987). The Dynamics of Near-Bed Seston Flux and Suspension-Feeding Benthos. *J. Mar. Res.* 45 (2), 473–496. doi:10.1357/002224087788401098

Ogrinc, N., Fontolan, G., Faganeli, J., and Covelli, S. (2005). Carbon and Nitrogen Isotope Compositions of Organic Matter in Coastal marine Sediments (The Gulf of Trieste, N Adriatic Sea): Indicators of Sources and Preservation. *Mar. Chem.* 95 (3-4), 163–181. doi:10.1016/j.marchem.2004.09.003

Pancost, R. D., and Boot, C. S. (2004). The Palaeoclimatic Utility of Terrestrial Biomarkers in marine Sediments. *Mar. Chem.* 92, 239e261. doi:10.1016/j.marchem.2004.06.029

Qi, H. (2008). pH and Eh Distribution and Constraints of Surface Sediments in the Changjiang Estuary and Adjacent Waters. *Acta Sedimentologica Sinica* 26 (5), 820–827. doi:10.14027/j.cnki.cjxb.2008.05.022

Qu, B. X., Song, J. M., and Yuan, M. H. (2018). Sediment Records and Responses for Anthropogenic Activities of Organic Matter in the Daya Bay during Recent One Hundred Years. *Haiyang Xuebao* 40 (10), 119–130. doi:10.3969/j.issn.0253-4193.2018.10.012

Ramaswamy, V., Birgit, G., Shirodkar, P. V., Rao, P. S., Chivas, A. R., Wheeler, D., et al. (2008). Distribution and Sources of Organic Carbon, Nitrogen and Their Isotopic Signatures in Sediments from the Ayeyarwady (Irrawaddy) continental Shelf, Northern Andaman Sea. *Mar. Chem.* 111 (3–4), 137–150. doi:10.1016/j.marchem.2008.04.006

Rogowska, J., Sychowska, J., Cieszynska-Semenowicz, M., and Wolska, L. (2016). Elemental Sulfur in Sediments: Analytical Problems. *Environ. Sci. Pollut. Res.* 23 (24), 24871–24879. doi:10.1007/s11356-016-7739-1

Schubert, C. J., and Calvert, S. E. (2001). Nitrogen and Carbon Isotopic Composition of Marine and Terrestrial Organic Matter in Arctic Ocean Sediments: Nitrogen and Carbon Isotopic Composition of Marine and Terrestrial Organic Matter in Arctic Ocean Sediments:: Implications for Nutrient Utilization and Organic Matter Composition. *Deep Sea Res. Oceanographic Res. Pap.* 48 (3), 789–810. doi:10.1016/S0967-0637(00)00069-8

Shi, M., and Chen, C. (1998). Characteristics of the Tidal Residual Flow Field in the Late winter and Early spring of Qiongzhou Strait. *Acta Sedimentologica Sinica* 20 (1), 1–10.

Song, J., Li, Y., and Zhu, Z. (1990). Relationship between Eh and Redox Environment of marine Sediments. *Mar. Sci. Bull.* 9 (4), 33–39.

Thompson, J. D. (1978). Ocean Deserts and Ocean Oases. *Climatic Change* 1 (3), 205–230. doi:10.1007/bf00166175

Vershinin, A. V., and Rozanov, A. G. (1983). The Platinum Electrode as an Indicator of Redox Environment in marine Sediments. *Mar. Chem.* 14 (1), 1–15. doi:10.1016/0304-4203(83)90065-8

Wang, J., Qi, H., Li, N., and Tan, L. (2009). The Sediment Redox Environment of the Shandong Coast. *Periodical Ocean Univ. China* 39 (Sup), 184–188. doi:10.16441/j.cnki.hdxb.2009.s1.035

Wang, X., Yu, J., and Fan, H. (2020). Spatial and Seasonal Variability of Surface Particulate Inorganic Carbon and Relationship with Particulate Organic Carbon in the Yellow-Bohai Sea. *J. Oceanogr* 76 (5), 327–339. doi:10.1007/s10872-020-00547-5

Wang, Y., and Yuan, W. (2008). Changes of Demersal Trawl Fishery Resources in Northern South China Sea as Revealed by Demersal Trawling. *South China Fish. Sci.* 4 (2), 26–33. doi:10.3969/j.issn.2095-0780.2008.02.005

Wu, J., Liu, G., Wang, N., Xu, X., and Song, L. (2012). Oxidation-reduction Potential of Surface Sediments in the Northern Part of Liaodong Bay and its Main Influencing Factors. *Acta Sedimentologica Sinica* 30 (2), 333–339. doi:10.14027/j.cnki.cjxb.2012.02.012

Wu, Y. (2008). *The Temporal and Spatial Patterns and Size-Fractioned Structure of Primary Productivity in Beibu Gulf*. Xiamen: Xiamen University.

Xia, H., Li, S., and Shi, M. (2001). Three-dimensional Wind Flow and Density Flow Simulation in Beibu Gulf. *Acta Oceanologica Sinica* 23 (06), 11–23. doi:10.3321/j.issn:0253-4193.2001.06.002

Xiong, L., Shi, X., Deng, Y., and Bai, Y. (2013). Distribution Characteristics of the Organic Matter in the Surficial Sediments on the Shelf of the Southern Yellow Sea and the Northern East China Sea. *Mar. Sci. Bull.* 32 (3), 281–286. doi:10.11840/j.issn.1001-6392.2013.03.007

Xu, D., Chu, F., Yang, H., Chen, L., and Li, T. (2012). Modern Deposition Rate in the Beibu Gulf. *Mar. Geology. Quat. Geology.* 32 (6), 17–26. doi:10.3724/sp.j.1140.2012.02127

Yang, J., Jay, G., Liu, B., and Alan, C. (2012). Mangrove Edge Effect in Leizhou Peninsula and its Impact on Coastal Organic Carbon Pool. *Acta Oceanologica Sinica* 34 (5), 161–168. doi:10.3724/sp.j.1095.2012.00134

Yang, Q., Qu, K., Yang, S., Sun, Y., Zhang, Y., and Zhou, M. (2021). Environmental Factors Affecting Regional Differences and Decadal Variations in the Buried Flux of marine Organic Carbon in Eastern Shelf Sea Areas of China. *Acta Oceanol. Sin.* 40 (6), 26–34. doi:10.1007/s13131-020-1601-5

Yang, S., Bao, X., Chen, C., and Chen, F. (2003). Characteristics of the Coastal Stream in Western Guangdong in Summer and its Production Mechanism. *Acta Oceanologica Sinica* 25 (06), 1–8. doi:10.3321/j.issn:0253-4193.2003.06.001

Yang, S., Lu, W., Zou, Z., and Li, S. (2017). Mangrove Wetlands: Distribution, Species Composition and Protection in China. *Subtropical Plant Sci.* 46 (4), 301–310. doi:10.3969/j.issn.1009-7791.2017.04.001

Yao, H., Gong, Z., Zhong, W., Na, Z., and Wei, Y. (2021). A Study on the Correlation Between Primary Productivity and Environmental Factors in Guangxi Beibu Gulf. *Mar. Environ. Sci.* 40 (2), 242–249. doi:10.13634/j.cnki.mes.2021.02.012

Yao, P., Zhao, B., Bianchi, T. S., Guo, Z., Zhao, M., Li, D., et al. (2014). Remineralization of Sedimentary Organic Carbon in Mud Deposits of the Changjiang Estuary and Adjacent Shelf: Implications for Carbon Preservation and Authigenic mineral Formation. *Continental Shelf Res.* 91, 1–11. doi:10.1016/j.csr.2014.08.010

Ye, X., Chen, J., Wang, A., Huang, C., Wang, W., and Li, D. (2011). Sources and Burial of Carbon in Sediments from the Western Taiwan Strait. *Acta Oceanologica Sinica* 33 (05), 73–82.

Yu, M., Eglinton, T. I., Haghipour, N., Montluçon, D. B., Wacker, L., Hou, P., et al. (2021). Contrasting Fates of Terrestrial Organic Carbon Pools in Marginal Sea Sediments. *Geochimica et Cosmochimica Acta* 309, 16–30. doi:10.1016/j.gca.2021.06.018

Yuan, X., Yang, Q., Luo, X., Yu, F., Liu, F., Li, J., et al. (2019). Distribution of Grain Size and Organic Elemental Composition of the Surficial Sediments in Lingding Bay in the Pearl River Delta, China: A Record of Recent Human Activity. *Ocean Coastal Manage.* 178, 104849. doi:10.1016/j.ocecoaman.2019.104849

Yue, D., Wang, L., and Zhu, X. (2017). Problems and Countermeasures in the Supply Side of marine Capture Fishery in China. *J. Agric. Sci. Tech.* 19 (7), 17–26. doi:10.13304/j.nykjdb.2016.687

Zhang, C., Lin, H., and Sun, X. (2012). Sources and Distribution of Sedimentary Organic Matter in Typical Bays of Guangdong Province. *J. Trop. Oceanography* 31 (06), 62–68. doi:10.3969/j.issn.1009-5470.2012.06.010

Zhang, J., Xie, Q., Shi, Y., Li, X., and Sun, X. (2011). Redox Characteristics of Surface Sediments in Zhanjiang Harbor and its Influencing Factors. *Mar. Environ. Sci.* 30 (06), 823–826. doi:10.3969/j.issn.1007-6336.2011.06.014

Zhang, S., Liang, C., and Xian, W. (2020). Spatial and Temporal Distributions of Terrestrial and marine Organic Matter in the Surface Sediments of the Yangtze River Estuary. *Continental Shelf Res.* 203, 104158. doi:10.1016/j.csr.2020.104158

Zhang, T., Li, X., Lan, H., Sun, S., and Jiang, Z. (2014). Distribution Characteristics and Influencing Factors of Lignin in Surface Sediments of the Yellow Sea. *Mar. Environ. Sci.* 33 (06), 822–829. doi:10.13634/j.cnki.mes.2014.06.002

Zhu, E., and Wang, Q. (1980). *Marine Authigenic mineral*. Beijing: Ocean Press, 12–17.

Conflict of Interest: The authors declare that the research was conducted in the absence of any commercial or financial relationships that could be construed as a potential conflict of interest.

Publisher's Note: All claims expressed in this article are solely those of the authors and do not necessarily represent those of their affiliated organizations, or those of the publisher, the editors and the reviewers. Any product that may be evaluated in this article, or claim that may be made by its manufacturer, is not guaranteed or endorsed by the publisher.

Copyright © 2022 Xia, Han, Tan, Abarike and Song. This is an open-access article distributed under the terms of the Creative Commons Attribution License (CC BY). The use, distribution or reproduction in other forums is permitted, provided the original author(s) and the copyright owner(s) are credited and that the original publication in this journal is cited, in accordance with accepted academic practice. No use, distribution or reproduction is permitted which does not comply with these terms.

frontiers in Earth Science

ORIGINAL RESEARCH
published: 24 March 2022
doi: 10.3389/feart.2022.675109

Genetic Types, Distribution Patterns and Enrichment Mechanisms of Helium in China's Petroliferous Basins

Shengfei Qin[1]*, *Dan Xu*[2], *Jiyuan Li*[2] and *Zheng Zhou*[3]

[1]Research Institute of Petroleum Exploration and Development (RIPED), Beijing, China, [2]Xi'an Center, China Geological Survey, Xi'an, China, [3]China University of Mining and Technology, Beijing, China, [4]Lancaster Environment Centre, Lancaster University, Lancaster, United Kingdom

Helium is a strategic resource with many scientific, technical and industrial applications. However, despite its importance and scarcity, there is a lack of understanding on its origin, migration and accumulation processes. In view of this, the distribution patterns and enrichment mechanisms of helium are studied based on systematic analysis of the genetic types of helium in petroliferous basins in China. The helium in the petroliferous basins in China is mainly radiogenic, which involves the decay of U and Th. As expected, we found that, in one gas field, the helium content in natural gas increases with the age of reservoir rock, and in the same layer of the same structure within one reservoir, the helium content in natural gas in high altitude part of the structure is higher than that in the lower part. Enrichment of helium is closely related to old deep groundwater. The helium produced by radioactive decay in old strata is dissolved in water and transported and enriched through water migration. Due to large uplift of the structure during the Himalayan period, the helium dissolved in water was exsolved and accumulated with natural gas in the trap above the water. And thus, the helium-rich natural gas reservoirs formed. So, the helium contents in natural gas fields increase gradually along the flow direction of groundwater. The area with large range of uplift often shows higher helium content. This study not only provides a basis for the study of helium enrichment research, but also provides a new idea for industrial helium resource exploration.

Keywords: petroliferous basin, helium, genetic type, distribution pattern, enrichment mechanism, water-soluble gas

OPEN ACCESS

Edited by:
Giovanni Martinelli, National Institute of Geophysics and Volcanology, Section of Palermo, Italy

Reviewed by:
Guodong Zheng, Northwest Institute of Eco-Environment and Resources (CAS), China
Dongya Zhu, SINOPEC Petroleum Exploration and Production Research Institute, China

***Correspondence:**
Shengfei Qin
qsf@petrochina.com.cn

Specialty section:
This article was submitted to Geochemistry, a section of the journal Frontiers in Earth Science

Received: *02 March 2021*
Accepted: *03 March 2022*
Published: *24 March 2022*

Citation:
Qin S, Xu D, Li J and Zhou Z (2022) Genetic Types, Distribution Patterns and Enrichment Mechanisms of Helium in China's Petroliferous Basins. Front. Earth Sci. 10:675109. doi: 10.3389/feart.2022.675109

INTRODUCTION

Helium is an inert gas with the lowest melting and boiling point which has been found in nature so far. It demonstrates extremely strong permeability and thermal conductivity. Because of these characteristics of helium, it is widely used in aerospace, medical application (cooling of NMR magnets) and nuclear industry, as well as scientific research, high-tech and other fields. The global helium resources mainly come from natural gas, and the supply is scarce. According to the report by the United States Geological Survey (U.S. Geological Survey, 2021), the total global helium resources are about 519×10^8 m^3. China's helium resources account for only 2% of the total inventory. In 2020, the global annual production of helium is 1.44×10^8 m^3, and China's production of helium is almost zero. Although researchers in China have carried out helium studies since the 1980s, the studies mainly focused on using helium isotopes as an indicator for the sources of natural gas (Xu et al., 1979; Wang, 1989; Xu et al., 1990a; Wang et al., 1992; Dai et al., 1995; Xu, 1996) and the tectonic environment of basins (Xu et al., 1990a; Xu et al., 1990b; Sun, 1994; Xu et al., 1994; Xu, 1997). There is a lack of helium resource evaluation and potential estimation in China.

Helium in some helium-rich natural gas reservoirs has been released into the atmosphere with the production and utilization of natural gas. Although potential helium resources have been found in central and western superimposed petroliferous basins and eastern rift basins in China, research on the enrichment mechanisms and distribution patterns of helium has not been sufficiently carried out. Our unknown about the enrichment mechanism of helium seriously affects the evaluation and exploration of helium resources in China, and at the same time, hinders the development of helium industry.

This article will summarize the content, origin and distribution of helium in natural gas in 11 major petroliferous basins on land in China. Based on this research, a preliminary discussion will be made on the distribution and enrichment mechanism of helium for future helium exploration.

ANALYTICAL METHODS

Samples from Hetianhe gas field were analyzed in the Key laboratory of the Research Institute of Exploration and Development of PetroChina. Natural gas compositions were determined using an Agilent 6890N gas chromatograph (GC) with He and N_2 as the carrier gases. Double thermal conductivity detectors (TCD) and a 30 m × 0.25 mm × 0.25 μm quartz capillary column were used. The inlet temperature was 150°C, and the TCD temperature was 200°C. The initial oven temperature was maintained at 40°C for 7.5 min isothermally, then rose from 40 to 90°C at 15°C/min, and finally rose from 90 to 180°C at 6°C/min.

The on-line analysis was conducted for the measurement of carbon isotopic compositions with a MAT 253 gas isotopic mass spectrometer. Natural gas samples were separated to methane, ethane, propane, butane and CO_2 through the chromatography column of a SRI 8610C gas chromatograph. They were then transferred into combustion furnace by carrier gas (He) and oxidized into CO_2 by CuO at 850°C. All of the converted species were transferred by carrier gas (He) into MS to measure the isotopic compositions. Dual inlet analysis was performed with international measurement standard of NBS-19 CO_2 ($\delta^{13}C$, VPDB = 1.95 ± 0.04‰, International Atomic Energy Agency, 1995) and the stable carbon isotopic values were reported in the δ notation in per mil (‰) relative to the Peedee belemnite standard (VPDB). Reproducibility and accuracy were estimated to be ± 0.2‰ with respect to VPDB standard.

Data on helium content, helium and argon isotopes are collected from published articles. The early published data was mainly measured using the VG5400 mass spectrometer, and the data from papers published in recent years using the Noblesse SFT noble gas mass spectrometry.

HELIUM CONTENTS AND GENETIC TYPES

Helium Content

According to the proportion of mantle-derived helium to the helium in natural gas, China's petroliferous basins can be divided into three types: western basins which the helium is crust-derived with trace amount of mantle derived; central basins which the helium is only crust-derived; eastern basins which the helium is mixed of crust and mantle (**Figure 1**). The helium contents (by volume) in natural gases from these basins vary greatly, ranging from 0.0002 to 2.085% (**Figure 2**). Some natural gas samples with high helium content can be found sporadically in almost every basin (**Table 1**). At present, helium-rich gas fields include Weiyuan gas field in Sichuan Basin, Hetianhe gas field in Tarim Basin, and Dongping gas field in Qaidam Basin (**Figure 1**). The helium contents in samples from these gas fields are usually over 0.1%.

Helium Genetic Types

The genetic type of helium can be determined using the $^3He/^4He$ ratio. Helium in natural gas samples is mainly from 3 sources: crust source, mantle source and atmospheric source (Lupton, 1983; Ballentine and Burnard, 2002; Ballentine et al., 2002). Helium in the atmosphere can be brought into the underground environment and released into gas reservoir through dissolution into surface meteoric water. Because the content of helium in the atmosphere is very low, helium brought into the gas reservoir through surface water can be ignored. Therefore, the sources of helium in a gas reservoir should be mainly derived from the crust and mantle. Crust-derived helium comes from the decay of radioactive elements of U and Th in crustal rocks, while mantle-derived helium comes from the mantle, which is brought into the crust through magmatic activity. Helium has two isotopes, which are ^3He and ^4He. ^3He is predominantly primordial, while both mantle-sourced and crust-sourced ^4He are mainly radiogenic. Helium derived from different sources have different ratios of $^3He/^4He$. The $^3He/^4He$ ratio has been used for years to determine the origin and source of helium. According to previous studies, the values of $^3He/^4He$ ratios in the atmosphere and crust are 1.4×10^{-6} and 2×10^{-8} respectively (Mamyrin and Tolstikhin, 1984). The $^3He/^4He$ ratio of 1.1×10^{-5} is usually used as the endmember of mantle-sourced helium (Kaneoka and Takaoka, 1985). The $^3He/^4He$ ratio of sample (R) normalized to the atmospheric $^3He/^4He$ value (Ra) is often used to show the helium isotope characteristics of the sample, that is $R/Ra = (^3He/^4He)_{sample}/(^3He/^4He)_{atmosphere}$. On average, the $^3He/^4He$ ratio in the sub-lithospheric mantle can be taken as 6Ra (Dunai and Baur, 1995; Ballentine et al., 2002). In this study, we consider samples with >0.1% (vol) helium concentrations as helium rich samples, because they exceed the atmospheric helium abundance by a factor of 200. As no natural processes are known to concentrate atmospheric helium in such concentrations, we assume that atmospheric helium does not play a significant role during helium enrichment, and hence, no atmospheric correction (e.g. by using ^{20}Ne, ^{36}Ar or N_2) was applied to the helium isotopic ratios. Binary method can be used to calculate the proportion of mantle-derived helium in natural gas samples, following the equation below (Xu, 1997):

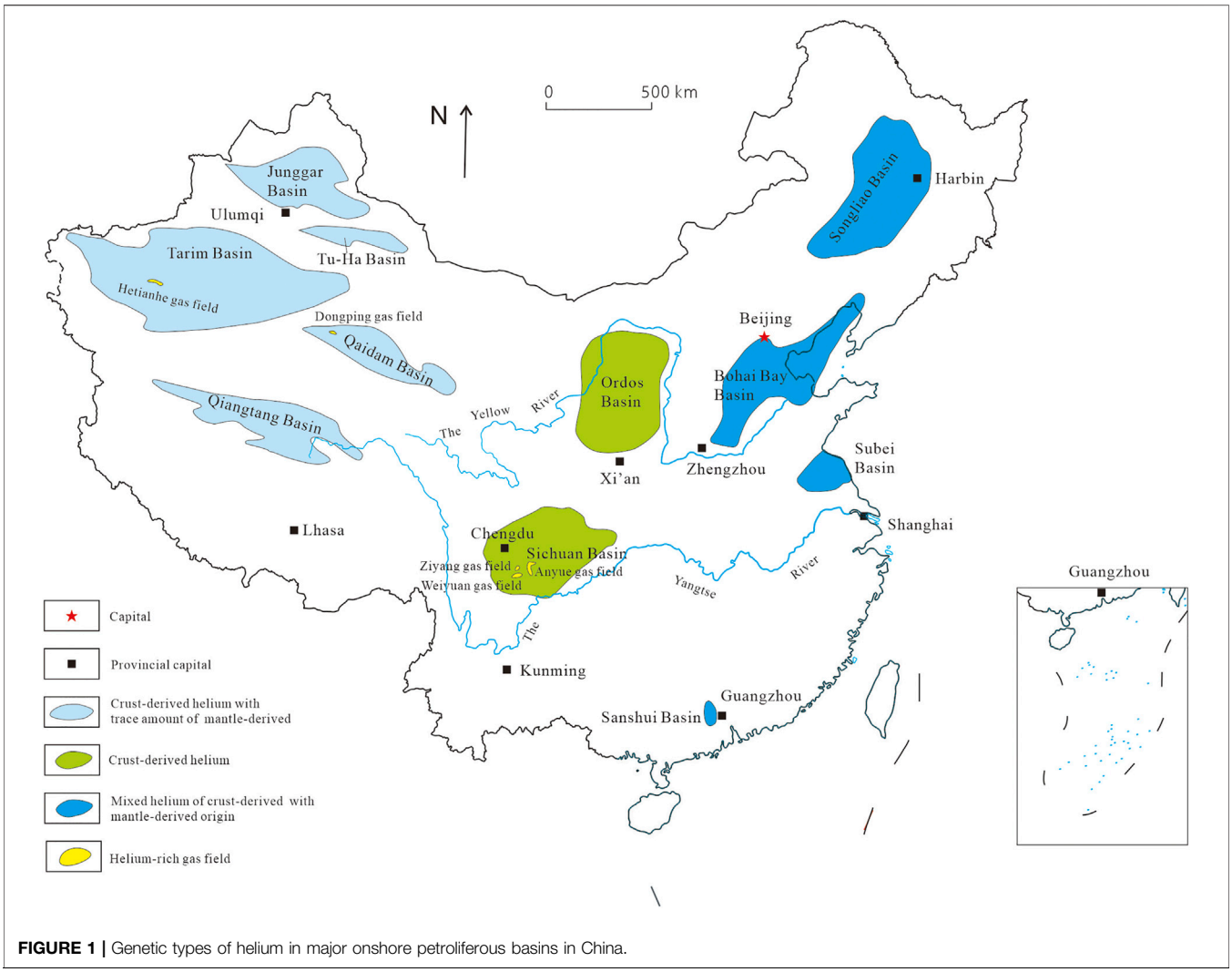


FIGURE 1 | Genetic types of helium in major onshore petroliferous basins in China.

$$\textbf{Ratio of mantle} - \textbf{derived helium}\ (\%) = \frac{\left(\frac{^3He}{^4He}\right)_{sample} - \left(\frac{^3He}{^4He}\right)_{crust}}{\left(\frac{^3He}{^4He}\right)_{mantle} - \left(\frac{^3He}{^4He}\right)_{crust}} \times \mathbf{100}$$

According to the equation, when R/Ra > 3.94, mantle-derived helium in natural gas is more than 50% of the total helium in the gas; when R/Ra > 1, the share of mantle-derived helium is more than 12%; when R/Ra > 0.1, the share of mantle-derived helium is more than 1.1%. Therefore, when R/Ra < 0.1, it is considered that the helium in natural gas mainly comes from the crust.

Helium isotopic ratios vary in a large range in petroliferous basins in China. R/Ra range from 0.002 to 4.99. However, distribution of helium isotopes shows a strong regular pattern. Relatively high ^{3}He content is found in the eastern basins and lower ^{3}He content is found in the central and western basins in China. According to analytical data from references of more than 350 samples, the R/Ra values in samples from petroliferous basins in Eastern China, such as Songliao Basin, Bohai Bay Basin, Sanshui Basin and Subei Basin, are between 0.01 and 4.99, with an average of 1.64 (Xu et al., 1995; Xu et al., 1996; Guo et al., 1999; Cao et al., 2001; Wang et al., 2006; Dai et al., 2017). Most samples show clear mantle-derived helium, and the genetic type of helium in these basins is a mixed crust-mantle type. The R/Ra values in samples from Sichuan and Ordos basins in Central China are between 0.002 and 0.097, with an average of 0.024 (Xu et al., 1989; Dai, 2003; Wu et al., 2013; Ni et al., 2014). It is clear that there is no addition of mantle-derived helium in these basins and all helium is of crustal origin. The R/Ra values in natural gases from Tarim Basin, Junggar Basin, Qaidam Basin and Turpan-Hami Basin in Western China are between 0.01 and 0.55, with an average of 0.06 (Xu et al., 1998; Liu et al., 2009; Liu et al., 2012; Xu et al., 2017; Tao et al., 2019; Zhang et al., 2019). Some samples show trace amount of helium from mantle source, and helium is also of crustal origin in general (**Figure 2**). It can be seen that the genetic types of helium in China have obvious characteristics of east-west zoning, which is related to the tectonic pattern in China. The petroliferous basins in Eastern China are extensional basins, and their development is related to the uplift of the upper mantle (Li, 1982). Therefore, mantle-derived helium

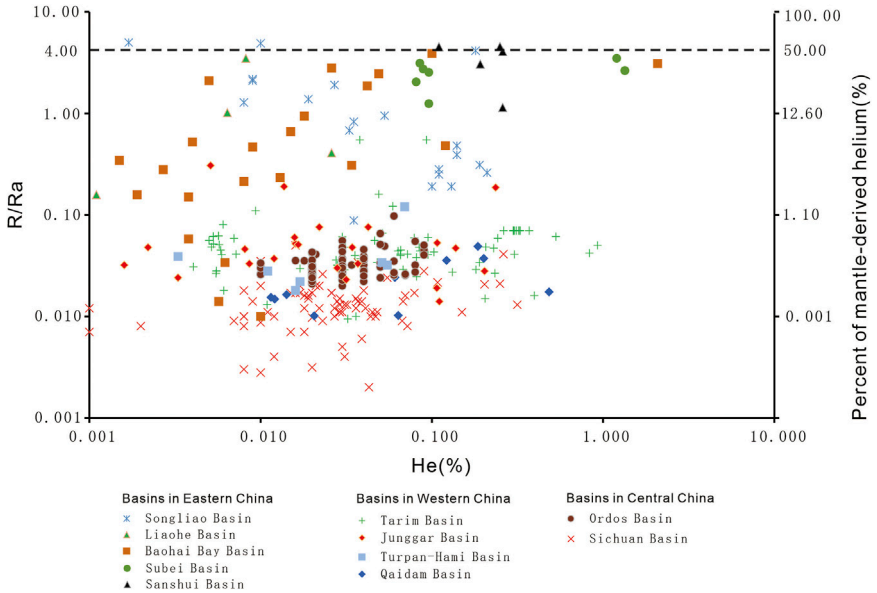


FIGURE 2 | Relationship between helium contents and R/Ra rations in major petroliferous basins in China.

is present. The petroliferous basins in Central China are intra-plate polycyclic depression basins, which are the most stable craton basins. The petroliferous basins in Western China are compressional basins, and the tectonic activity in this area is slightly stronger than that in Central China and much weaker than that in Eastern China (Li, 1982).

Although there is more mantle-derived helium mixed into the natural gases in the eastern basins, according to our calculation, for the samples with helium contents higher than 0.1% in the natural gases of the eastern basin, the majority of helium in the samples still comes from the radioactive decay of U and Th in the crust. A few samples with more than 50% of helium derived from mantle are mainly from non-hydrocarbon gas reservoirs with high N_2 or CO_2, which may be related to local volcanic activity. Volcanic activity brought a large amount of mantle fluid, and the fluid contains not only helium but also a large amount of non-hydrocarbon gases. The proportion of mantle-derived helium in gas reservoirs dominated by hydrocarbon gases is generally less than 50% (**Table 1**).

HELIUM DISTRIBUTION PATTERNS

Previous studies have shown that helium contents in natural gases are related to geological ages of the storage reservoirs. In general, it follows a pattern that the older the geological age, the higher the helium content (Kong, 1997) (**Figure 3**). Some researchers suggested that the older the reservoir was, the earlier the helium would migrate to the reservoir, therefor, the more helium would be accumulated and the higher content of helium (Brown, 2010). However, by analyzing the relationship between helium content and reservoir age in China's petroliferous basins, the above-mentioned helium distribution pattern is not obvious (**Figure 4**). The oldest Sinian gas reservoir is about 700–800 million years old. The samples with helium content greater than 0.1% are mainly from the Weiyuan gas field in the Sichuan Basin. In Paleozoic reservoirs, samples with a helium content of more than 0.1% only come from the Hetianhe gas field in the Tarim Basin. In the Paleozoic, Mesozoic, and Tertiary reservoirs, helium content distribution patterns are relatively consistent, and do not show a trend that the helium contents increase with the increasing ages of the reservoirs. In addition, according to the cumulative effect of argon isotope ^{40}Ar, which is generated by radioactive decay of K, the older the geological formation is, the higher the $^{40}Ar/^{36}Ar$ ratio in the samples from the formation should be. However, the helium contents in samples from various petroliferous basins in China do not increase with the increase of $^{40}Ar/^{36}Ar$ ratios in samples (**Figure 5**). This demonstrates the complexity of helium-rich gas accumulation in China's petroliferous basins. The degree of helium enrichment cannot be determined solely from the age of the geological strata where gas reservoirs are situated.

In this paper, the Weiyuan gas field, Anyue gas field and Hetianhe gas field, which have sufficient amount of analytical data for helium contents in gas samples (Dai et al., 1999; Dai, 2003; Zhu et al., 2007; Wei et al., 2014; Tao et al., 2019), are selected as case studies for the horizontal and vertical distribution of helium to reveal certain patterns of helium distribution and enrichment mechanisms.

The Weiyuan and Anyue gas fields are located on the Leshan-Longnüsi paleo-uplift in the Sichuan Basin, which is a large nose-like paleo-uplift that dips to the east (**Figure 6A**). In 1964, industrial gas flow was obtained from the Sinian Dengying Formation in the Weiyuan structure, and the Weiyuan gas field, the largest and oldest gas field in China at that time, was discovered. Subsequently, 7 exploratory wells were made in the

TABLE 1 | Table of samples with helium content in some natural gas from petroliferous basins in China.

Basin location	Basins	Well No.	Era	Main component (%)				$^3He/^4He$ (10^{-8})	R/R_a	$^{40}Ar/^{36}Ar$	Proportion of mantle-derived helium (%)	Reference
				CH_4	CO_2	N_2	He					
Basins in Eastern China	Songliao	Wu 102	K	94.80	0.45		0.10	26.1	0.19	562	2.2	Wang et al. (2006)
	Songliao	Wushen 1	K	93.70	0.43		0.13	26.1	0.19	585	2.2	
	Songliao	Wu 101	K	94.80	0.51		0.11	35.5	0.25	569	3.1	
	Songliao	Wu 106	K	92.20	0.55		0.21	36.2	0.26	581	3.1	
	Songliao	Wu 109	K	94.80	0.30		0.11	39.9	0.28	542	3.5	
	Songliao	Shuang 17	K	86.90	0.27		0.19	42.9	0.31	396	3.7	
	Songliao	Zhuangshen1	K	89.30	0.26		0.14	54.7	0.39	448	4.8	
	Songliao	Wan 11	K	82.10	0.22		0.14	67.8	0.48	716	6.0	
	Songliao	Qian7 -9	K				0.18	582.4	4.16		52.9	Xu et al. (1995)
	Bohaibay	Hua 501	N		34.27	61.86	2.08	434	3.10		39.3	Cao et al. (2001)
	Subei	Min 7	E		0.55	23.12	0.10	176	1.25	573	15.8	Xu et al. (1998)
	Subei	Tianshen 33	E		7.56		0.09	439	3.13	1805	39.8	Tao et al. (1997)
	Subei	Tianshen 45	E		0.41	2.73	0.08	287	2.05	518	26.0	
	Subei	Huangqian14	N	27.44	4.26	63.26	1.34	371	2.65	716	33.6	Xu et al. (1996)
	Subei	Huangqian 2	N	27.39	8.80	57.87	1.20	489	3.49	717	44.4	
	Subei		N	28.34	4.67	63	1.34	371	2.65		33.6	Guo et al. (1999)
	Sanshui	Nan 35	E	76.81		9.76	0.19	429	3.06	1,124	38.9	Xu et al. (1996)
	Sanshui	Shuishen 3	E	65.23	15.59	13.62	0.26	572	4.09	793	51.9	
	Sanshui	Shuishen 44	E	12.29	83.09	1.79	0.11	636	4.54		57.7	
	Sanshui	Shuishen 24	E	0.25	99.48	0.25	0.25	639	4.56	1,360	58.0	
	Sanshui	Bao 1	E				0.26	160	1.14		14.4	Du and Liu, (1991)
Basins in Central China	Sichuan	Wei 2	Z			6.67	0.20	2.9	0.02	9,255	0.1	Xu et al. (1989)
	Sichuan	Wei 5	P			3.36	0.11	3.03	0.02	2,855	0.1	Dai, (2003)
	Sichuan	Wei 23	Z				0.26	5.74	0.04		0.3	Ni et al. (2014)
	Sichuan	Wei 106	Z				0.32	1.82	0.01		0.0	
	Sichuan	Wei 12	Z				0.25	2.94	0.02		0.1	
	Sichuan	Yuanba 223	T	45.75	33.29	19.93	0.01	1.22	0.01	355	0.0	Wu et al. (2017)
	Sichuan	Yuanba 223	P	86.17	4.55	1.96	0.01	0.39	0.00	458	0.0	
	Sichuan	Yuanba 273	P	89.36	5.83	3.54	0.02	0.44	0.00	475	0.0	
	Sichuan	Yuanlu 10	T	96.43	0.66	1.50	0.02	1.36	0.01	411	0.0	
	Sichuan	Shuang 15	P				0.15	1.54	0.01		0.0	Wu et al. (2013)
	Ordos	Fugu 4	O		9.30	0.76	0.05	5.28	0.04	293	0.3	Ni et al. (2010)
	Ordos	Su 38–16	P	89.96	2.01	1.27	0.02	3.34	0.02	413	0.1	Liu et al. (2007)
	Ordos	Su 35–17	P	90.44	1.14	1.94	0.02	3.65	0.03	526	0.2	
	Ordos	Su 33–18	P	72.72	0.75	16.94	0.02	3.62	0.03	312	0.1	
	Ordos	Su 6	P	88.81	2.64	0.80	0.03	2.94	0.02	528	0.1	
Basins in Western China	Qaidam	Mabei 801		76.64	0.53	8.87	0.19	6.85	0.05	2019	0.4	Zhang et al. (2019)
	Qaidam	Mabei 1					0.12	4.98	0.04	1835	0.3	
	Qaidam	Maxi 1		87.63	0.30	8.54	0.06	3.39	0.02	1726	0.1	
	Qaidam	Maba 2–23		78.83	0.10	7.41	0.20	5.21	0.04	1817	0.3	
	Qaidam	DP 171	Bed rock	95.18	0.10	1.15	0.02	1.41	0.01	883	0.0	
	Qaidam	DP 1	Bed rock	89.99	0.21	6.87	0.06	1.43	0.01	1,350	0.0	
	Qaidam	DP 3	E				0.48	2.44	0.02	2,862	0.0	
	Qaidam	Niu 1	J	89.04	0.19	1.41	0.01	2.07	0.01	410	0.0	
	Qaidam	Niu 1-2-10	J	86.97	0.25	1.54	0.01	2.16	0.02	432	0.0	
	Qaidam	Niu 1-2-11	J	86.47	0.25	2.08	0.01	2.30	0.02	393	0.0	
	Tarim	Luosi 2	O				0.26	9.8	0.07		0.7	Tao et al. (2019)
	Tarim	Ma 5–8H	C, O				0.30	9.8	0.07		0.7	
	Tarim	Ma 5–6H	C, O				0.33	9.8	0.07		0.7	
	Tarim	Ma 5-1H	C				0.32	9.8	0.07		0.7	
	Tarim	Ma 5-4H	C, O				0.31	9.8	0.07		0.7	
	Tarim	Ma 4–10H	C, O				0.30	9.8	0.07		0.7	
	Tarim	Ma 4-3H	C				0.37	9.8	0.07		0.7	
	Tarim	Ma 4–8H	C, O				0.30	9.8	0.07		0.7	
	Tarim	Ma 4-1H	C				0.33	9.8	0.07		0.7	

(Continued on following page)

TABLE 1 | (*Continued*) Table of samples with helium content in some natural gas from petroliferous basins in China.

Basin location	Basins	Well No.	Era	Main component (%)				$^3He/^4He$ (10^{-8})	R/R_a	$^{40}Ar/^{36}Ar$	Proportion of mantle-derived helium (%)	Reference
				CH_4	CO_2	N_2	He					
	Tarim	Ma 4–12H	C, O				0.30	9.8	0.07		0.7	
	Tarim	Ma 4	C, O				0.30	9.8	0.07		0.7	
	Tarim	YK 17	K				0.06	17	0.12		1.4	Tao et al. (2018)
	Tarim	T 813-1H	O				0.04	1.4	0.01	661	0.0	
	Tarim	T 814-1H	O				0.03	1.32	0.01	646	0.0	
	Tarim	T 820(K)	C				0.03	4.03	0.03	493	0.2	
	Tarim	TP 37	T				0.05	4.77	0.03	499	0.3	
	Tarim	TP 313H	O				0.01	1.82	0.01	363	0.0	
	Tarim	YH 1	E				0.13	3.81	0.03		0.2	Liu et al. (2012)
	Tarim	LN 2–25-H1	T				0.30	5.71	0.04		0.3	
	Tarim	DB 201	K				0.01	6.31	0.05	858	0.4	Wang et al. (2016)
	Tarim	DB 302	K				0.01	8.73	0.06	504	0.6	
	Tarim	DB 202	K				0.01	7.14	0.05	521	0.5	
	Tarim	DB 102	K				0.01	8.68	0.06	390	0.6	
	Tarim	DB 103	K				0.01	11.24	0.08	485	0.8	
	Tarim	KL 2–7	E				0.01	3.93	0.03	1,211	0.2	Wang et al. (2018)
	Tarim	KL 2–1	K, E				0.00	4.31	0.03	1,323	0.2	
	Tarim	KL 2–4	K, E				0.01	6.77	0.05	589	0.4	
	Tarim	KL 2–10	K, E				0.01	8.58	0.06	719	0.6	
	Tarim	KL 2–14	K, E				0.01	5.68	0.04	720	0.3	
	Tarim	KL 2–11	K, E				0.01	7.24	0.05	462	0.5	
	Tarim	DH 1	C				0.23	6.58	0.05	549	0.4	Xu et al. (1998)
	Tarim	DH 4	C				0.40	2.24	0.02	482	0.0	
	Tarim	JF 100	T				0.09	6.16	0.04	766	0.4	
	Tarim	JF 123	O				0.18	4.06	0.03	945	0.2	
	Tarim	JF 131	T				0.07	6.3	0.05	595	0.4	
	Tarim	YM 7	E				0.06	6.16	0.04	513	0.4	
	Tarim	LN 14	C				0.10	6.02	0.04		0.4	
	Tarim	LN 10	O				0.24	8.26	0.06		0.6	
	Tarim	LN 17	C, O				0.19	4.76	0.03	756	0.3	
	Tarim	LN 5	J				0.05	7.84	0.06	1,273	0.5	
	Tarim	LN 26	T				0.53	8.54	0.06	753	0.6	
	Tarim	LN 55	T				0.93	7	0.05		0.5	
	Tarim	LN 204	T				0.04	5.18	0.04	801	0.3	
	Tarim	LN 2–2	T				0.83	5.88	0.04	689	0.4	
	Tarim	LN 33–1	J				0.02	10.64	0.08	930	0.8	
	Tarim	LN 22	T				0.07	5.6	0.04	503	0.3	
	Tarim	JL 107	C				0.20	2.1	0.02	820	0.0	
	Tarim	TZ 1	O				0.05	4.62	0.03	923	0.2	
	Tarim	DW 105–25	N-K				0.01	5.74	0.04	1,120	0.3	Zheng et al. (2005)
	Tarim	Jiefang 138	T				0.08	6.72	0.05	343	0.4	
	Tarim	Yangtake 5	E				0.03	6.72	0.05	655	0.4	
	Tarim	LN 10–2	T				0.08	5.32	0.04	624	0.3	
	Tarim	LN 3-H5	T				0.09	8.4	0.06	959	0.6	
	Tarim	LN 2–25-H1	T				0.07	5.74	0.04	862	0.3	
	Junggar	Cai 156	J				0.04	4.62	0.03	1,042	0.2	Xu et al. (2017)
	Junggar	Ca i27	J				0.03	6.72	0.05	1,099	0.4	
	Junggar	Cai 514	J				0.14	6.58	0.05	472	0.4	
	Junggar	Cai 201	J				0.04	10.64	0.08	929	0.8	
	Junggar	Cai 401	J				0.02	7.14	0.05	648	0.5	
	Junggar	Cai 140	J				0.02	8.4	0.06	297	0.6	
	Junggar	Cai 506	J				0.01	6.44	0.05	310	0.4	
	Junggar	Cai 508	J				0.20	3.92	0.03	777	0.2	
	Junggar	Cai 137	J				0.03	4.2	0.03	765	0.2	
	Junggar	Cai 510	J				0.11	2.66	0.02	686	0.1	
	Junggar	Quan 6	J				0.11	1.96	0.01	508	0.0	
	Junggar	C 121	J				0.01	4.62	0.03	311	0.2	
	Junggar	C 3150	J				0.02	7.28	0.05	1,356	0.5	
	Junggar	Dixi 12	J				0.03	3.22	0.02	334	0.1	
	Junggar	Di 20	J				0.11	7.42	0.05	353	0.5	
	Junggar	Sha 1955	J				0.24	26.04	0.19	329	2.2	

Note: N-Neogene; E-Paleogene; K-Cretaceous; J-Jurassic; T-Triassic; P-Permian; C-Carboniferous; O-Ordovician; Z-Sinian.

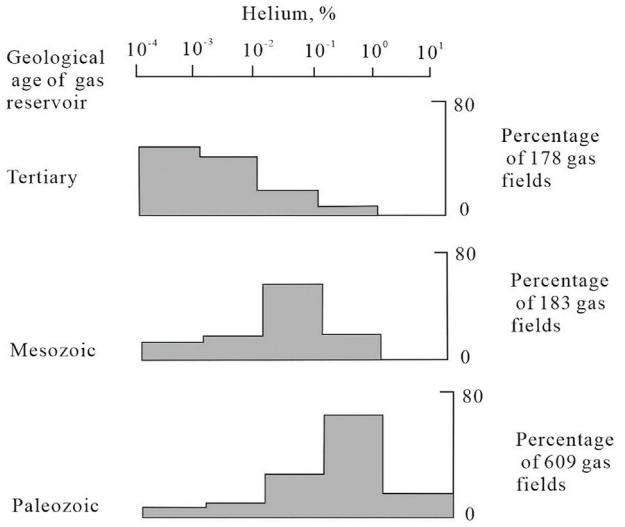


FIGURE 3 | Helium contents in gas fields formed in different geological eras around the world.

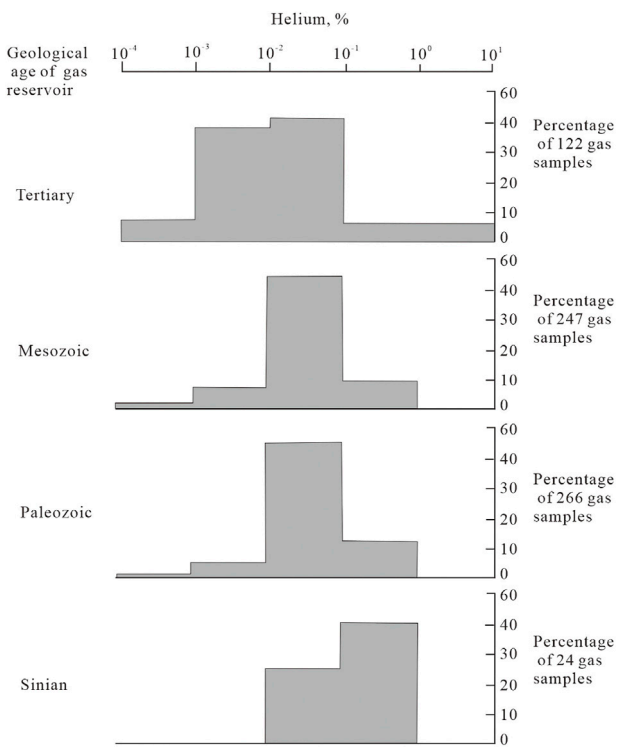


FIGURE 4 | Helium contents in gas fields formed in different geological area in China.

Ziyang area to the north of the Weiyuan gas field, 3 industrial gas wells were obtained, and a small gas field in Ziyang was then discovered (**Figure 6B**). In 2011, the Anyue gas field with reservoirs of the Sinian Dengying Formation and Cambrian

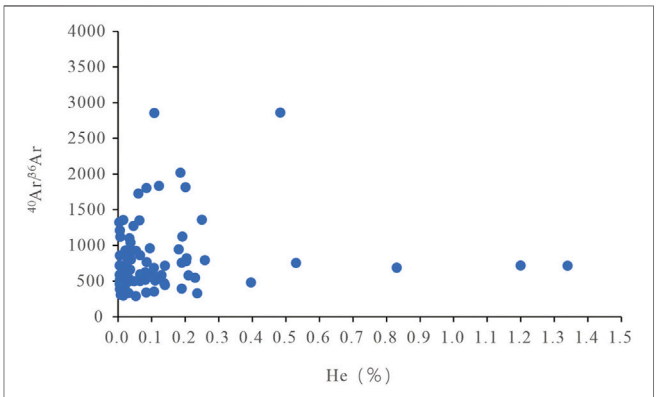


FIGURE 5 | Relationship between helium contents and argon isotopic ratios in China's petroliferous basins.

Longwangmiao Formation was discovered on the Gaoshi-Moxi structure to the northeast of the Weiyuan gas field. This discovery achieved a major breakthrough in natural gas exploration in the Sinian-Cambrian strata in the Leshan-Longnüsi paleo-uplift in Sichuan Basin. The scale of its reserves has exceeded one trillion cubic meters (Wei et al., 2015).

The main gas reservoirs of the Weiyuan gas field are located in the Sinian Dengying Formation (Z_2d) and the Cambrian Xixiangchi Formation (ϵ_2x). Small gas reservoirs are also developed in the Lower Permian (P_1). The main gas reservoirs of the Anyue gas field are developed in the Dengying Formation and the Cambrian Longwangmiao Formation (ϵ_1l). Natural gas is dominated by hydrocarbon gases, and non-hydrocarbon gases are mainly CO_2, N_2 and H_2S, as well as a small amount of noble gases. Natural gas mainly comes from the high-over-mature argillaceous source rocks of the Lower Cambrian Qiongzhusi Formation (ϵ_1q), as indicated by $\delta^{13}C$ values of methane between -37 and -32 per mil (**Figure 6C**, **Figure 9**) (Dai et al., 1999; Zheng et al., 2014).

Increase of Helium Contents With Reservoir Ages

Both in the Weiyuan gas field and Anyue gas field, the helium content is related to the age of the reservoir. It is observed that the older the reservoir age, the higher the helium content (**Figure 7**). The average helium content in the samples from the Sinian Dengying Formation in the Weiyuan gas field is 0.28%. The average content of helium in the samples from the Cambrian Xixiangchi Formation is 0.18%. The average content of helium in the samples from the Lower Permian is only 0.056%. The average helium content of the samples from the lower gas reservoir (Z_2d^2) of the Dengying Formation in Anyue gas field is 0.05%. The average helium content in samples from the upper gas reservoir (Z_2d^4) of the Dengying Formation is 0.017%. The average helium content in the samples from the gas reservoir of the Cambrian Longwangmiao Formation is 0.0078%.

The gas reservoirs of the Hetianhe gas field in the Tarim Basin are mainly Ordovician and Carboniferous. The gas layers are thin and adjacent to each other. There is no obvious change in helium

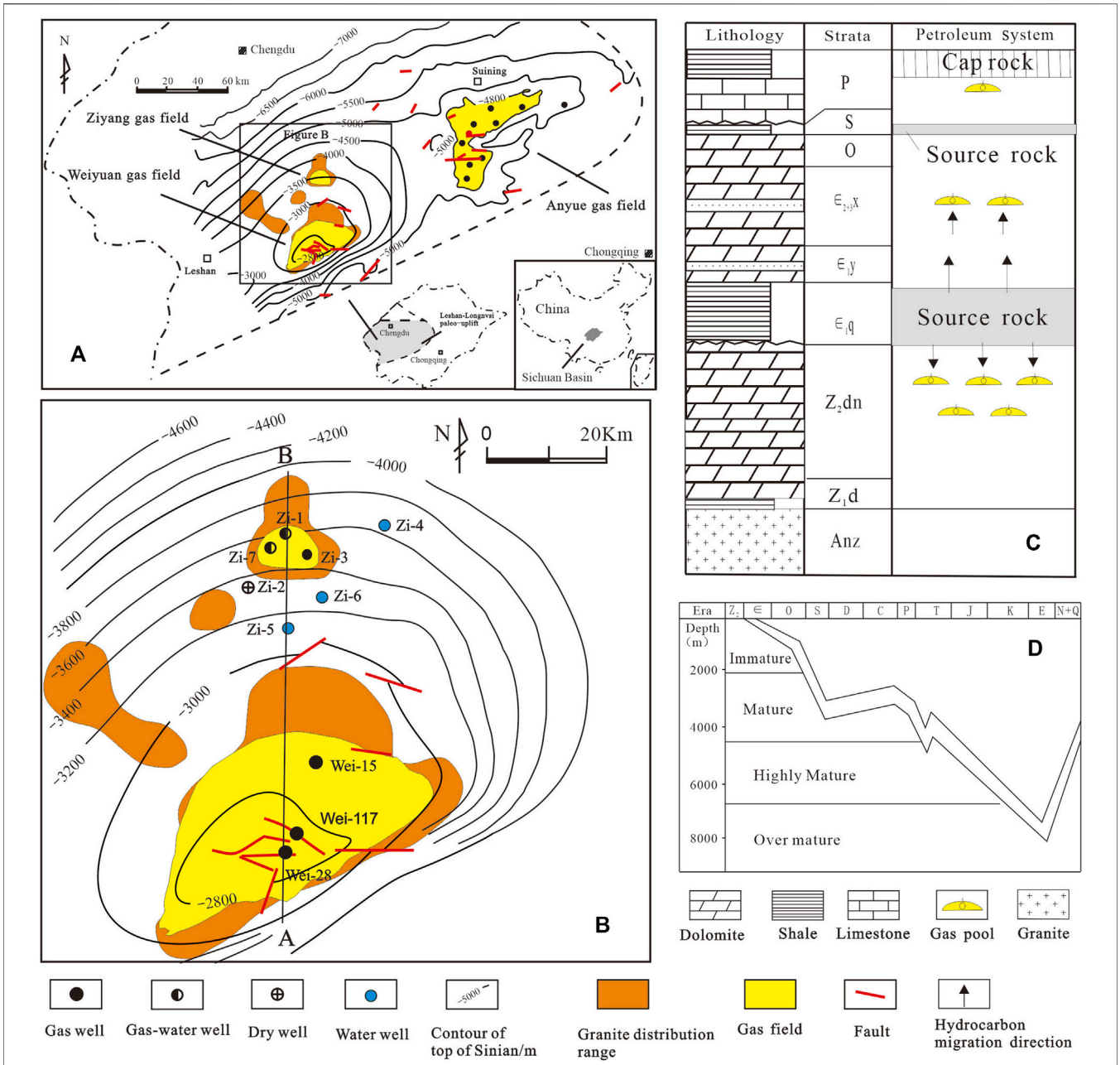


FIGURE 6 | Gas field and granite distribution map of Leshan-Longnüsi paleo-uplift in Sichuan Basin, China (The location of Weiyuan gas field is shown in **Figure 1**). **(A)** Gas fields and granite distribution on Leshan-Longnüsi paleo-uplift. **(B)** More details of Weiyuan and Ziyan gas fields. **(C)** Petroleum system of Leshan-Longnüsi paleo-uplift. **(D)** Tectonic evolution of Leshan-Longnüsi paleo-uplift.

content in the vertical successive geological formations (**Figure 8**).

Concentration of Helium in the Structural High Parts of the Same Horizon

The Anyue gas field has a relatively gentle structural slope, and the helium content does not vary significantly within the structure. However, in the Weiyuan structure, the helium content is closely related to the structural altitude. Both Weiyuan and Ziyang gas fields have been discovered on the Weiyuan structural belt, and tectonic movement that occurred after the Late Cretaceous caused the Weiyuan gas field rising much more than the Ziyang gas field (Huang and Chen, 1993; Dai, 2003), which made Weiyuan gas field a new high point on the Weiyuan structural belt (**Figure 6D**). A huge ascending slope formed from the Ziyang gas field to the Weiyuan gas field. The helium contents in samples from the Dengying Formation gas

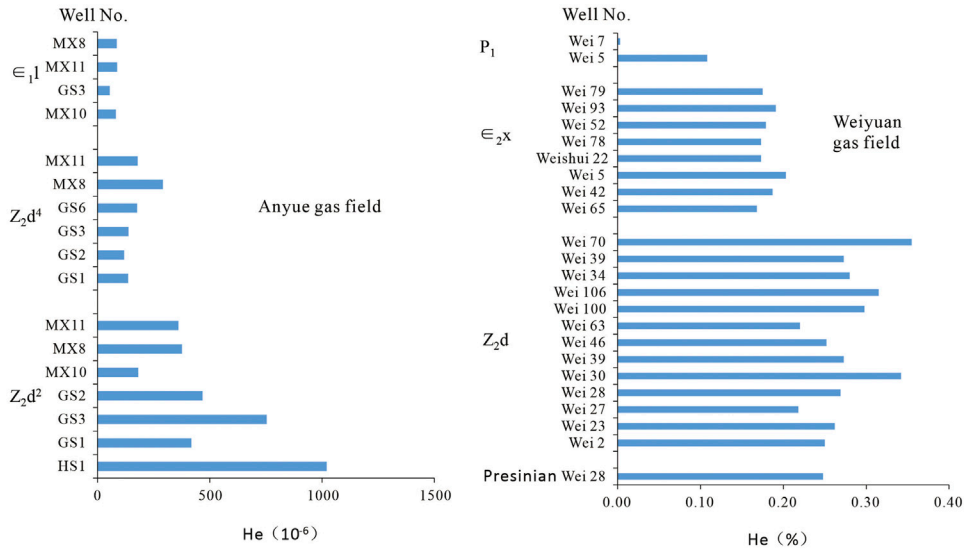


FIGURE 7 | Helium contents in natural gases in different layers in the Anyue and Weiyuan gas fields (Data sited from Zhu et al., 2007; Wei et al., 2014; Zheng et al., 2014; Zhang et al., 2015).

reservoirs gradually increased from the Ziyang gas field to the Weiyuan gas field. The average helium content in samples from the Ziyang gas field is 0.027%, while the helium content in the samples from the Weiyuan gas field is 0.277%, and the average content of helium in the transition zone between the two reservoirs is 0.205% (Dai et al., 1999; Dai, 2003; Zhu et al., 2007) (**Figure 9**).

The phenomenon that helium in samples from the same geological formation is often enriched in high structural parts also occurs in the Hetianhe gas field in the Tarim Basin. The Hetianhe gas field is located on the Mazatag fault structural belt in the Bachu bulge in the eastern part of the central uplift of the Tarim Basin. The gas field is generally a long strip extending east-west (**Figure 8**). The gas field is composed of a series of structural high points. Among them, the wells on the high points of Ma 8 and Ma 3 in the west constitute of western well area, and the wells on high points of Ma 5 and Ma 4 constitute of eastern well area. The high point of Ma 2 is between the eastern and western wells. In general, the western structure of the gas field is higher than the eastern one, and the gas-water interface in the western well area is higher than those in the eastern well area. The contents of helium in the western wells are significantly higher than those in the wells in the eastern area (**Figure 8**). The helium content of wells Ma 8 and Ma 3 are 0.53 and 0.4%, respectively. The Ma 4 and Ma 5 well areas is between 0.298–0.328%, which is lower than the western well area.

Helium in helium-rich reservoirs mainly comes from deep basement rocks. The helium produced by the long-term decay of U and Th in the rock is dissolved in water and preserved. With the tectonic movement of Himalayan, the formation was uplifted, and some deep and large faults connecting the deep formation water and the overlying gas reservoir were generated. Driven by tectonic movement, the deep formation water with dissolved helium migrated up along the fault, and the released helium was mixed into the gas reservoir to form a helium-rich gas reservoir. Since the deep fluids tend to migrate to the high point of the structure, more helium was released from the formation water at the position of the high point of the structure.

HELIUM ENRICHMENT MECHANISM—DEGASSING OF DISSOLVED GAS

Although U and Th concentrations are enriched in the crust relative to the mantle, they are still very low in the crust and their half-lives are extremely long. The helium produced by radioactive decay of U and Th is extremely dispersed in the crust. Due to these facts, helium gas reservoirs cannot be formed independently. It needs to be transported by other fluids in order to enrich and reach an industrial production level. The carrier phases may be other types of gases, or formation water. The study of the Weiyuan and Hetianhe gas fields has shown that the carrier phase is likely to be formation water other than other natural gases.

Weiyuan Gas Field

Previous studies have suggested that the helium in the Weiyuan gas field is of crustal origin *via* radioactive decay of U and Th in the Earth's crust (Dai, 2003). However, the specific source of helium is difficult to determine. The helium may come from the source rocks in the Qiongzhusi Formation, which have high U and Th concentrations, or from the basement granite below the gas field. The U and Th concentrations of the Qiongzhusi Formation increased with the increase of TOC. The average concentrations of U and Th are 29 ppm (Zhao et al., 2019) and 11 ppm (Wang et al., 2021), respectively. The U and Th concentrations of the underlying granites are 6.7 and 32.5 ppm,

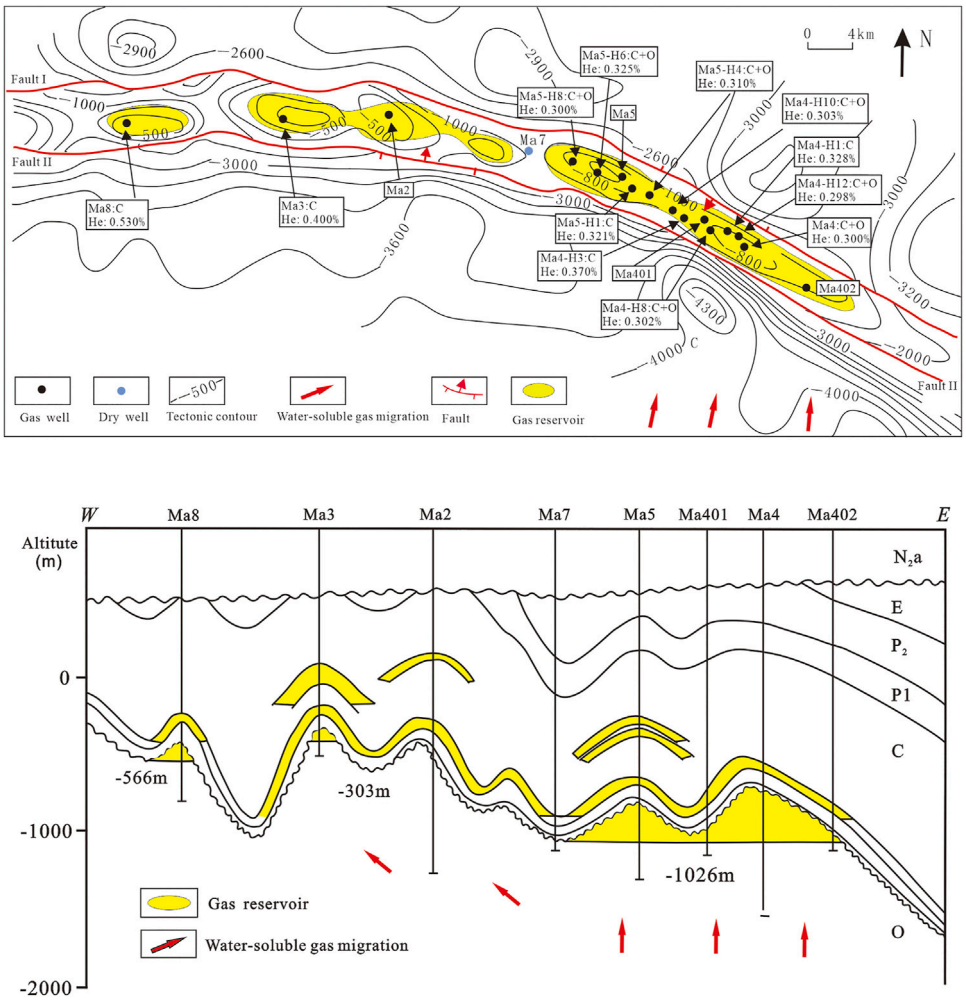


FIGURE 8 | Schematic diagram of water-soluble gas accumulation in Hetianhe Gas Field (The location of Hetianhe gas field is shown in **Figure 1**; The helium data are cited from Tao et al., 2019).

respectively, (Gu et al., 2013). In view of the natural gas accumulation conditions, such as the source rocks, reservoirs, cap rocks, etc., the natural gas reservoirs in the Dengying and Longwangmiao formations in the Anyue gas field are similar to those in the Weiyuan gas field. The natural gases in both reservoirs dominantly come from Qiongzhusi Formation, which are the same source rocks in the Lower Cambrian (Dai, 2003; Wei et al., 2015). However, the helium content in the Weiyuan gas field is much higher than that in the Anyue gas field. This suggests that helium is unlikely originated from the hydrocarbon source rocks or the reservoirs themselves.

There is large granite body under the Sinian in the Weiyuan structural belt (Zhang et al., 2015), but there is no granite body beneath the Anyue gas field (**Figure 6**). Granite is considered by some researchers to be the main contributor to the helium in helium-rich gas reservoirs (Brown, 2010). This may be the main reason why natural gas in the Weiyuan gas field is rich in helium. Helium is likely coming from the pre-Sinian granite basement, where radioactive uranium and thorium are present. Radioactive decay of uranium and thorium can produce helium which is accumulated in the Weiyuan gas field afterwards. However, although both the Weiyuan gas field and Ziyang gas field are located in the area of the granite basement, they demonstrate different helium contents in the samples, where helium content in the natural gas in the Ziyang field is lower than that in the Weiyuan gas field. This can be explained by the special gas forming process of the Weiyuan gas field, which is the degassing of water-soluble gas during the gas pool formation. We ruled out the possibility that in the over-mature stage of the source rock, due to the small amount of gas generated, the degree of dilution of helium by natural gas was low, resulting in a higher content of helium in natural gas, because the natural gas generated before the source rock reaching the over-mature stage would migrate away with the helium generated by the decay of U and Th in the source rock during a long geological period. In the over-mature stage of the source rock, the time of U and Th decay is

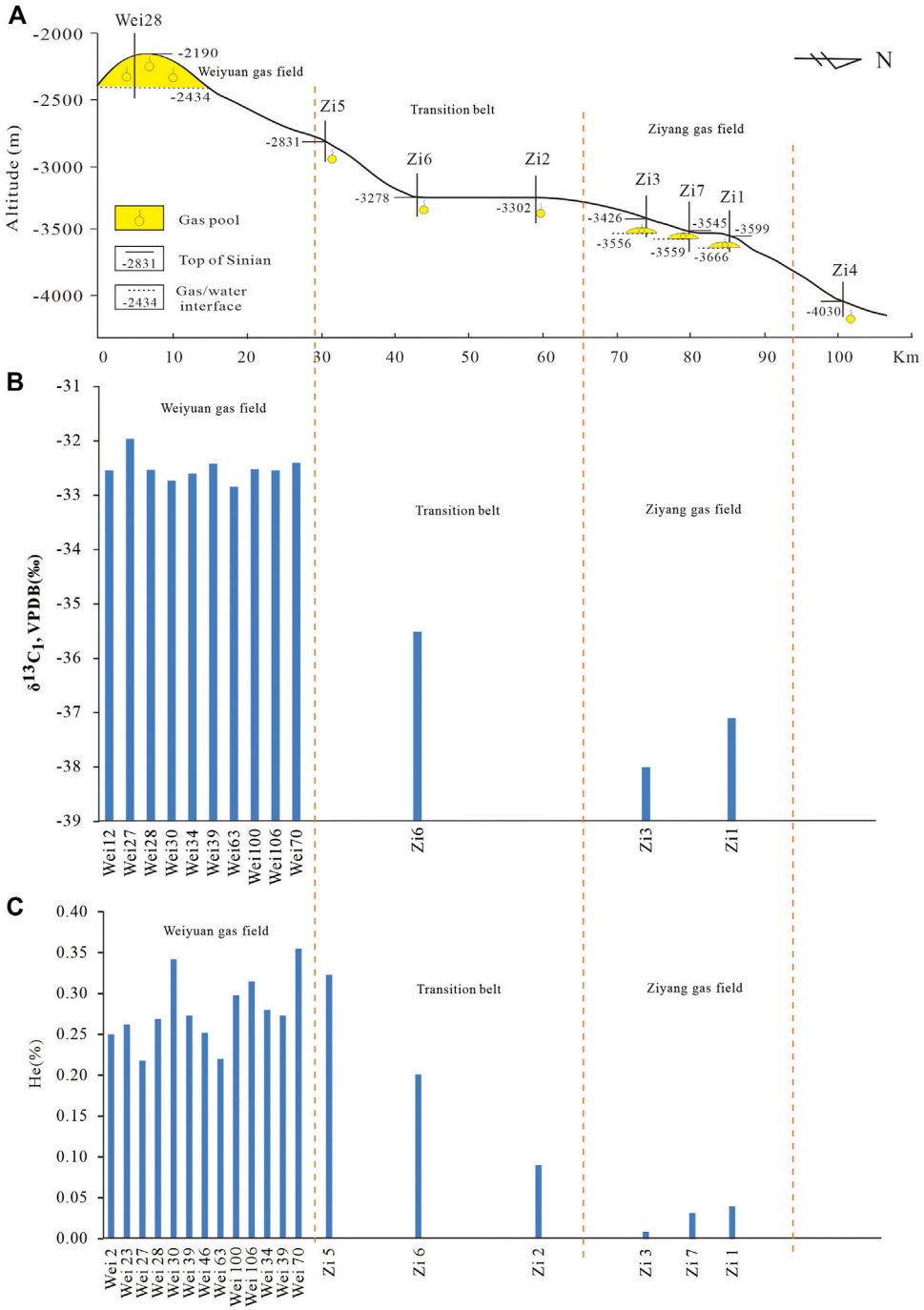


FIGURE 9 | Helium content of natural gases in the Sinian Dengying Formation in the Weiyuan gas field and its adjacent areas. (The location of profile AB is shown in **Figure 7**. The helium data cited from Dai et al., 1999; Dai, 2003; Zhu et al., 2007). **(A)** Section of Weiyuan gas field and adjacent area. **(B)** The $\delta^{13}C_1$ of Weiyuan gas field and adjacent area. **(C)** The helium content of Weiyuan gas field and adjacent area.

very short, and the amount of helium generated is fairly small, therefore, it was unlikely to be enriched in the over-mature natural gas.

The gas generation period of the source rocks in the Weiyuan gas field is before the Himalayan tectonic movement, then the trap is formed and shaped afterwards. Since the trap is formed later than the hydrocarbon generation period of the source rock, the natural gas generated by the source rock cannot be captured effectively. Therefore, gas accumulated in the reservoir is not directly from the source rock in the area. It is proposed that the

natural gas in the Weiyuan gas field is migrated laterally from the Ziyang paleo-uplift. Before the Himalayan period, Ziyang was a structural high of the paleo-uplift, and oil and gas were migrated to and accumulated in the Ziyang area. After the Himalayan period, the new structural trap in the Weiyuan formed by tectonic uplift was higher than the trap in the Ziyang area, which led to the reverse migration of natural gas originally accumulated in the Ziyang Sinian paleo-gas reservoir. The gas was then re-accumulated in the present Weiyuan anticline trap (Yin et al., 2000; Wang et al., 2001).

The geochemical characteristics of the natural gas in the Weiyuan and Ziyang gas fields should be relatively similar, if the natural gas in the Weiyuan gas field had migrated laterally from the Ziyang gas field in the form of free gas. In addition, due to fractionation during migration, the carbon isotope signature of methane in the Weiyuan gas field should be a little more negative than that in the Ziyang gas field. However, the actual situation is opposite. The carbon isotope composition of methane in gas samples from the Weiyuan gas field is significantly less negative than that of the gas from the Ziyang gas field (**Figure 9**). The average $\delta^{13}C_1$ in Weiyuan is −32.5‰, and Ziyang is −36.9‰. This does not explain the lateral movement of natural gas.

In fact, geological conditions at the Weiyuan gas field are favorable for the gases (including helium) to be stored in groundwater, then degas and accumulate in the current reservoir. In the area where the reservoir is located, there is abundant groundwater, which can dissolve large amount of natural gas, forming a considerable reserve of water-soluble gas. The formation water in the Weiyuan gas field is ancient connate water, which provides favorable condition for the preservation of water-soluble gas. The Himalayan structural movement uplifted the formation and caused degassing of the water-soluble gas and migration of the gas into the current traps (Qin, et al., 2016). Previous studies have shown that the carbon isotopic values of methane degassed from water is significantly less negative than that of the samples collected at the wellhead at the same time (Qin, 2012). Therefore, the less negative carbon isotopic values in samples from the Weiyuan gas field support the argument that natural gas in this field mainly comes from gas previously dissolved in formation water. At the same time, the helium produced by the radioactive decay of U and Th from the granite in the basement of the Weiyuan gas field is migrated out of the mineral lattice and dissolved into the pore water. Due to the uplift of geological formations during Himalayan structural movement in the Sichuan basin, the helium dissolved in the formation water was exsolved due to the decrease of pressure and temperature. In addition, near the gas-water interface, the partial pressure of helium in the gas reservoir is extremely low, while the partial pressure of helium in water is relatively high. Helium can easily enter the gas reservoir from water and accumulate with natural gas in the trap to form helium-rich natural gas reservoir. This can explain the formation of a helium-rich gas reservoir in the Weiyuan gas field. The tectonic movement in the Himalayan period lifted the Weiyuan gas field by 4,000 m, and the structural high point was transferred from Ziyang to Weiyuan. As a consequence, groundwater migrated to the Weiyuan gas field, causing dissolved-methane in groundwater to exsolve in the Weiyuan gas reservoir. The groundwater from deep granite also migrated to the Weiyuan gas field, where the dissolved helium gas is released to form a helium-rich gas field. In the Ziyang gas field, which is at the north of the Weiyuan gas field, due to the small uplift during the Himalayan period, the groundwater in the deep granite was migrated to the Weiyuan gas field, but did not move upwards, resulting in a lower helium content in the Ziyang gas field. (**Figure 10**).

Hetianhe Gas Field

The helium accumulation mechanism at the Hetianhe gas field is similar to that at the Weiyuan gas field. It is also related to the water-soluble gas. The natural gas in the Hetianhe gas field mainly comes from the high-over-mature Cambrian marine source rocks in the Southwest Depression to the field (Zhao, 2000; Cai et al., 2002; Qin et al., 2002). Carbon isotopic values of methane in the western part of the field are significantly less negative than those in the gas in the eastern part of the field. (**Table 2**, **Figure 8**). The helium content in the western area is also significantly higher than those in the eastern area (**Figure 8**). Obviously, the less negative of $\delta^{13}C_1$, the higher the helium content. It shows that the formation water is more fully degassed in the western region than in the eastern region. This can also be seen from the trends in CO_2 content. Gas reservoirs in the west of the field have higher CO_2 content than in the east. CO_2 is more soluble in water, and it will be released later from the formation water. The formation water of the gas field migrates from the east to the west of the gas field.

Gas traps in the Hetianhe field were formed mainly during the late Himalayan movement. Large amount of natural gas was generated in the over-mature stage of Cambrian source rocks in the Southwest Depression. They were strip-shaped traps sandwiched by two reverse faults in the south and north, which were formed under the compression stress of the Himalayan movement (**Figure 8**). These two large faults are 90 km in length, and they cut the geological stratum from Cambrian to Neogene. At the same time, the Bachu bulge continued to uplift, causing FaultⅠand FaultⅡto move and open again. It is during this time, the natural gas produced by the deep Cambrian high and overmature source rocks was dissolved into formation water under the abnormally high pressure. Then gas and water migrated upward along the effective migration channel in the eastern part of the gas field to the trap in the lower eastern part of the Hetianhe gas field. Then part of the released free gas accumulated in the eastern trap of the gas field. The water below the gas-water interface in the eastern well area continued to migrate laterally along the unconformity for a long distance from the eastern high-pressure area to the western low-pressure area. The continuous decrease in pressure during the migration of the water body caused the continuous release of water-soluble gas to form free natural gas phase, which accumulated along the migration path, forming the Hetianhe gas field in a strip-like reservoir (Qin et al., 2006). The long distance gas migration has caused the difference in the geochemical characteristics of natural

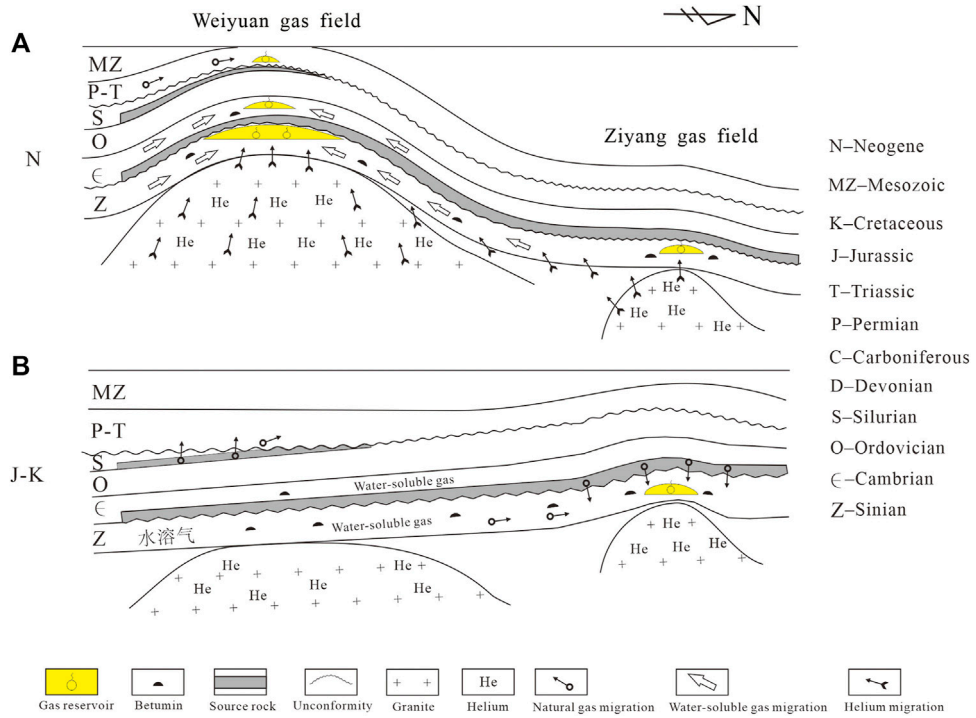


FIGURE 10 | The helium Enrichment mechanism of Weiyuan gas field. **(A)** Structure map after the Himalayan period. **(B)** Structure map before the Himalayan period.

TABLE 2 | Abundance and stable carbon isotopic values in natural gases from Hetianhe gas field.

Well	Sample depth (m)	Era	Main molecular composition (%)					$\delta^{13}C$, VPDB (‰)			
			CH_4	C_2H_6	C_3H_8	CO_2	N_2	CH_4	C_2H_6	C_3H_8	CO_2
Ma 8	1700–1710	O	75.72	0.51	0.00	14.03	9.75	-34.57	-38.09	-35.41	
Ma 8	1790–1800	O	72.84	0.50	0.02	14.39	12.24	-34.39	-37.96	-35.52	
Ma 3	1,045–1,052	C	69.62	0.54		8.22	21.61	-35.60	-35.10	-31.10	-13.60
Ma 3	1,196–1,207	C	79.95	0.34		9.06	10.65	-35.80	-36.60	-32.20	-7.90
Ma 3	1,414–1,424	C	77.40	0.69	0.09	12.20	9.63	-35.80	-35.50	-32.10	-7.80
Ma 3	1,508–1,518	O	74.20	0.65	0.01	11.06	14.08	-35.60	-36.70	-31.80	-8.60
Ma 2	1,462–1,501	C	84.85	0.53	0.17	1.88	12.57	-36.20	-35.70	-33.30	-8.60
Ma 2	1,605–1,607	C	81.78	0.81	0.22	1.94	15.25	-37.20	-37.10	-32.00	-19.30
Ma 2	1,609–1,670	O	86.27	1.02	0.36		12.25	-36.60	-37.20	-33.40	
Ma 5	2073–2,105	C	74.23	1.07	0.29	11.25	13.00	-37.00	-36.70	-32.20	-15.30
Ma 401	2,126–2,165	C	79.00	1.92	1.59	3.75	13.08	-37.60	-37.00	-32.90	-12.10
Ma 401	2,275–2,284	O	80.88	0.97	0.33	1.60	16.03	-37.80	-37.30	-33.50	-5.70
Ma 401	2,350–2,382	O	81.28	1.26	0.48	1.86	14.40	-37.60	-37.20	-33.10	-16.40
Ma 4	1800–2041	C + O	83.22	2.05	0.65	1.55	12.11	-37.60	-37.30	-33.30	
Ma 4	2044–2,140	O	81.43	2.29	0.91	1.95	12.80	-37.70	-37.20	-33.10	
Ma 4	2,235–2,355	O	82.94	1.31	0.49	1.19	13.63	-37.90	-35.50	-33.20	-8.60
Ma 4	2,380–2,395	O	82.58	1.31	0.50	1.51	13.70	-37.80	-37.20	-33.10	-8.30

Note: C-Carboniferous; O-Ordovician.

gas in the east and west areas of the gas field (Qin et al., 2002). Although research is ongoing on whether there is an ancient granite basement in the Southwest Depression of Tarim Basin, U and Th in the ancient basement strata and Cambrian source rocks have produced considerable amount of helium gas through radioactive decay over a long period of time. The helium has been dissolved in the formation water and released into the upper trap along with the uplift during the Himalayan movement. Helium is accumulated together with natural gas in the Hetianhe gas field.

Helium-Rich Gas Fields in Eastern Basins

Although the features of helium-rich gas fields in eastern basins of China are remarkably different from those in Sichuan and Tarim basins, however, the helium is mainly from deep water in most of the helium-rich gas fields in eastern basins. Despite that the helium is crust-mantle mixed origin, the proportion of mantle-derived helium is much less than 50% in most of the fields, except a few non-hydrocarbon gas fields. The helium is still manly from crust. The natural gas produced by source rock diluted the helium produced by itself. Therefore, an additional main source of helium is required to form a helium-rich gas field. This additional source came from deep crust. Helium produced in the deep crust dissolved in water and migrated into the gas fields along fractures created by subsequent magmatic activity, releasing helium.

The helium in many large helium-rich gas fields in the world also comes from water-soluble gas. For instance, the Panhandle-Hugoton gas field. Correlated research of Hugoton-Panhandle giant gas field has showed the association collection, transport, and focusing mechanism for the ^{4}He. The N_2*/^{20}Ne ratio study in this area also indicated that the migration mechanism of the gas field must be carried out in geofluid (Ballentine, et al., 2002; Ballentine and Lollar, 2002).

CONCLUSION

This study suggests that helium in China's petroliferous basins is mainly produced by radioactive decay of U and Th in the crust and mantle. Due to the existence of deep and large faults in the basins in eastern China, although some mantle-derived helium is mixed in natural gas reservoirs, helium in the basins in eastern China is still mainly composed of radiogenic helium. The distribution of helium-rich natural gas is closely related to ancient granite or ancient basement. Helium gas produced by U and Th decay in the ancient rock formations during a long geological period was dissolved and preserved in the formation water. Tectonic uplift of the geological formations can release the helium gas dissolved in the water together with the dissolved natural gas. They accumulate in the traps to form helium-rich natural gas reservoirs. Along the direction of groundwater flow, the helium contents in natural gas gradually increase, while the carbon isotopic values of methane become heavier. We found that reservoirs with large uplift in geological history tend to have gases with high helium concentrations.

DATA AVAILABILITY STATEMENT

The original contributions presented in the study are included in the article/Supplementary Material, further inquiries can be directed to the corresponding author.

AUTHOR CONTRIBUTIONS

SQ: work concept or design, drafting papers. DX: data collection. JL: Drawing. ZZ: Make important revisions to the paper.

FUNDING

This study was jointly sponsored by National Natural Science Foundation of China (Grant No. 41872162, 42141022) and PetroChina Science and Technology Project (Grant No. 2019D-5010-27).

ACKNOWLEDGMENTS

We thank the editor for handling this manuscript and reviewers for helpful comments and suggestions that have improved the manuscript.

SUPPLEMENTARY MATERIAL

The Supplementary Material for this article can be found online at: https://www.frontiersin.org/articles/10.3389/feart.2022.675109/full#supplementary-material

REFERENCES

Ballentine, C. J., Burgess, R., and Marty, B. (2002). Tracing Fluid Origin, Transport and Interaction in the Crust. *Rev. Mineralogy Geochem.* 47 (1), 539–614. doi:10.2138/rmg.2002.47.13

Ballentine, C. J., and Burnard, P. G. (2002). Production, Release and Transport of noble Gases in the continental Crust. *Rev. Mineralogy Geochem.* 47 (1), 481–538. doi:10.2138/rmg.2002.47.12

Ballentine, C. J., and Lollar, S. B. (2002). Regional Groundwater Focusing of Nitrogen and noble Gases into the Hugoton-Panhandle Giant Gas Field, USA. *Geochimica et Cosmochimica Acta* 66 (14), 2483–2497. doi:10.1016/S0016-7037(02)00850-5

Brown, A. (2010). *Formation of High Helium Gases: A Guide for Explorationists 2010. AAPG Conference*. New Oleans, Louisiana, USA: AAPG Convention, 11–14.

Cai, C., Worden, R. H., Wang, Q., Xiang, T., Zhu, J., and Chu, X. (2002). Chemical and Isotopic Evidence for Secondary Alteration of Natural Gases in the Hetianhe Field, Bachu Uplift of the Tarim Basin. *Org. Geochem.* 33, 1415–1427. doi:10.1016/S0146-6380(02)00111-0

Cao, Z., Che, Y., Li, J., and Li, H. (2001). Accumulation Analysis on a Helium-Enriched Gas Reservoir in Huagou Area, the Jiyang Depression. *Pet. Geology. Exp.* 23 (4), 395–399.

Dai, H., Wang, S., Wang, H., and Huang, Q. (1999). Formation Characteristics of Natural Gas Reservoirs and Favorable Exploration Areas in Sinian -Cambrian Petroleum System of Sichuan basin. *Pet. Exploration Development* 26 (5), 16–20.

Dai, J., Ni, Y., Qin, S., Huang, S., Gong, D., Liu, D., et al. (2017). Geochemical Characteristics of He and CO 2 from the Ordos (Cratonic) and Bohaibay (Rift) Basins in China. *Chem. Geology.* 469, 192–213. doi:10.1016/j.chemgeo.2017.02.011

Dai, J. (2003). Pool-forming Periods and Gas Sources of Weiyuan Gas Field. *Pet. Geology. Exp.* 25 (5), 473–480. doi:10.1007/BF02974893

Dai, J., Song, Y., Dai, C., Chen, A., Sun, M., and Liao, Y. (1995). *Inorganic Gas and its Gas Reservoir Forming Conditions in Eastern China*. Beijing: Science Press.

Du, J., and Liu, W. (1991). Helium and Argon Isotopes in Natural Gas in Sanshui Basin. *Nat. Gas Geosci.* 2 (6), 283–285.

Dunai, T. J., and Baur, H. (1995). Helium, Neon, and Argon Systematics of the European Subcontinental Mantle: Implications for its Geochemical Evolution.

Geochimica et Cosmochimica Acta 59 (13), 2767–2783. doi:10.1016/0016-7037(95)00172-V

Gu, Z., Zhai, X., Jiang, X., Huang, P., Qian, H., and Qiao, L. (2013). Geoichemical Characteristics and Tectonic Environment of Basal Granite in Weiyuan Structure, Sichuan Basin. *Earth Science-Journal China Univ. Geosci.* 38 (Suppl. 1), 31–42. doi:10.3799/dqkx.2013.S1.004

Guo, N., You, X., and Xu, J. (1999). Geological Character of Xiqiao Helium-Bearing Gas Field and Prospecting of Helium-Bearing Natural Gas in North Jiangsu Basin. *Pet. Exploration Development* 26 (5), 24–26.

Huang, J., and Chen, S. (1993). Hydrocarbon Source Analysis of Sinian Gas Reservoir Forming Conditions of Sichuan Basin:a Case History of Weiyuan Gas Field. *Nat. Gas Geosci.* 4 (4), 16–20.

International Atomic Energy Agency (1995). *Reference and Intercomparison Materials for Stable Isotopes of Light Elements*.

Kaneoka, I., and Takaoka, N. (1985). Noble-gas State in the Earth's interior - Some Constraints on the Present State. *Chem. Geology. Isotope Geosci. section* 52, 75–95. doi:10.1016/0168-9622(85)90008-9

Kong, L. (1997). *Helium Isotopes in Nature*, 3. Beijing: Patent Literature Press.

Li, D. (1982). Tectonic Types of Oil and Gas Basins in China. *Acta Petrolei Sinica* 3 (3), 1–12. doi:10.7623/syxb198203001

Liu, Q., Dai, J., Jin, Z., and Li, J. (2009). Geochemistry and Genesis of Natural Gas in the Foreland and Platform of the Tarim Basin. *Acta Geologic Sinica* 83 (1), 107–114. doi:10.1016/S1874-8651(10)60080-4

Liu, Q., Liu, W., Xu, Y., Li, J., and Chen, M. (2007). Analysis of Natural Gas Migration and Gas Source in Sulige Gas Field. *Nat. Gas Geosci.* 18 (5), 697–702. doi:10.3969/j.issn.1672-1926.2007.05.014

Liu, Q., Zhijun, J., Jianfa, C., Krooss, B. M., and Qin, S. (2012). Origin of Nitrogen Molecules in Natural Gas and Implications for the High Risk of N2 Exploration in Tarim Basin, NW China. *J. Pet. Sci. Eng.* 81, 112–121. doi:10.1016/j.petrol.2011.12.013

Lupton, J. E. (1983). Terrestrial Inert Gases: Isotope Tracer Studies And Clues to Primordial Components in the Mantle. *Annu. Rev. Earth Planet. Sci.* 11, 371–414. doi:10.1146/annurev.ea.11.050183.002103

Mamyrin, B. A., and Tolstikhin, I. N. (1984). *Helium Isotopes in Nature*. Amsterdam: Elsevier.

Ni, C., Zhou, X., Wang, G., and Wang, Y. (2010). Geochemistry Characteristics and Genesis of Natural Gas in Fuxian Area, Ordos Basin. *J. Xi'an Shiyou Univ. (Natural Sci. Edition)* 25 (5), 20–24. doi:10.3969/j.issn.1673-064X.2010.05.005

Ni, Y., Dai, J., Tao, S., Wu, X., Liao, F., Wu, W., et al. (2014). Helium Signatures of Gases from the Sichuan Basin, China. *Org. Geochem.* 74, 33–43. doi:10.1016/j.orggeochem.2014.03.007

Qin, S. (2012). Carbon Isotopic Composition of Water-Soluble Gases and Their Geological Significance in the Sichuan Basin. *Pet. Exploration Development* 39 (3), 335–342. doi:10.1016/S1876-3804(12)60049-4

Qin, S., Jia, C., and Li, M. (2002). The Difference on Geochemical Characteristics of Natural Gases between East and West Part in Hetianhe Gas Field of Tarim Basin and its Origin. *Pet. Exploration Development* 28 (5), 16–18. doi:10.3321/j.issn:1000-0747.2002.05.005

Qin, S., Zhou, G., Li, W., Hou, Y., and Lü, F. (2016). Geochemical Evidence of Water-Soluble Gas Accumulation in the Weiyuan Gas Field, Sichuan Basin. *Nat. Gas Industry B* 3, 37–44. doi:10.1016/j.ngib.2016.02.004

Qin, S., Zou, C., Dai, J., Li, M., Hu, J., Zhang, Q., et al. (2006). Water-soluble Gas Accumulation Process of Hetianhe Gas Field in Tarim Basin, NW China. *Pet. Exploration Development* 33 (3), 280–288. doi:10.3321/j.issn:1000-0747.2006.03.005

Sun, M. (1994). The Role of Helium Isotopes in Natural Gas Geology. *Nat. Gas Geosci.* 5 (5), 1–5. doi:10.11764/j.issn.1672-1926.1994.05.1

Tao, C., Liu, W., Yang, H., Luo, H., Wang, J., and Wang, P. (2018). Analysis of Concentration and Isotope Ratio of noble Gases in Natural Gas. *J. Chin. Mass Spectrom. Soc.*, 201–208. doi:10.7538/zpxb.2017.0039

Tao, M., Shen, P., Xu, Y., Fei, F., and Luo, J. (1997). Characteristics and Formation Conditions of Mantle-Derived Helium Gas Reservoirs in Subei Basin. *Nat. Gas Geosci.* 8 (3), 1–8.

Tao, X., Li, J., Zhao, L., Li, L., Zhu, W., Xing, L., et al. (2019). Helium Resources and Discovery of First Supergiant Helium reserve in China: Hetianhe Gas Field. *Earth Sci.* 44 (3), 1024–1041. doi:10.3799/dqkx.2018.381

U.S. Geological Survey (2021). Mineral Commodity Summaries. Available at: https://www.usgs.gov/centers/nmic/helium-statistics-and-information.

Wang, J., Chen, J., Wang, T., Feng, Z., Lin, T., and Wang, X. (2006). Gas Source Rocks and Gas Genetic Type in Shuangcheng-Taipingchuan Area of Songliao Basin. *Acta Petrolei Sinica* 27 (3), 16–21.

Wang, P., Zou, C., Li, X., Ma, L., Jiang, L., Jia, D., et al. (2021). Geochemical Characteristics of Element Qiongzhusi Group in Dianqianbei Area and Paleoenvironmental Signification. *Joural China Univ. Pet. (Edition Nat. Science)* 45 (2), 51–62. doi:10.3969/j.issn.1673-5005.2021.02.006

Wang, X., Chen, J., Li, Z., Li, J., Wang, D., Wang, Y., et al. (2016). Rare Gases Geochemical Characteristics and Gas Source Correlation for Dabei Gas Field in Kuche Depression, Tarim Basin. *Energy Exploration & Exploitation* 34 (1), 113–128. doi:10.1177/0144598715623673

Wang, X., Chen, J., Xu, S., Yang, H., Xue, X., and Wang, W. (1992). Geochemistry Characteristics of Hot spring Gases in Earthquake Zone. *Sci. China (Series B)* 22 (8), 849–854. doi:10.1360/zb1992-22-8-849

Wang, X. (1989). *Noble Gas Isotope Geochemistry and Cosmochemistry*. Beijing: Science Press.

Wang, X., Wei, G., Li, J., Chen, J., Gong, S., Li, Z., et al. (2018). Geochemical Characteristics and Origins of noble Gases of the Kela 2 Gas Field in the Tarim Basin, China. *Mar. Pet. Geology.* 89, 155–163. doi:10.1016/j.marpetgeo.2017.02.013

Wang, Y., Chen, S., and Xu, S. (2001). *Natural Gas Accumulation Conditions and Exploration Technology of Upper Proterozoic-Paleozoic in Sichuan Basin*. Beijing: Petroleum Industry Press, 166–168.

Wei, G., Du, J., Xu, C., Zou, C., Yang, W., Shen, P., et al. (2015). Characteristics and Accumulation Modes of Large Gas Reservoirs in Sinian-Cambrian of Gaoshiti-Moxi Region, Sichuan Basin. *Acta Petrolei Sinica* 36 (1), 1–12. doi:10.7623/syxb201501001

Wei, G., Wang, D., Wang, X., Li, J., Li, Z., Xie, Z., et al. (2014). Characteristics of noble Gases in the Large Gaoshiti-Moxi Gas Field in Sichuan Basin. *Pet. Exploration Development* 41 (5), 533–538. doi:10.1016/S1876-3804(14)60069-0

Wu, X., Dai, J., Liao, F., and Huang, S. (2013). Origin and Source of CO2 in Natural Gas from the Eastern Sichuan Basin. *Sci. China Earth Sci.* 56, 1308–1317. doi:10.1007/s11430-013-4601-x

Wu, Z., Liu, X., Li, X., Wang, X., and Zheng, J. (2017). The Application of noble Gas Isotope in Gas-Source Correlation of Yuanba Reservoir, Sichuan Basin. *Nat. Gas Geosci.* 28 (7), 1072–1077. doi:10.11764/j.issn.1672-1926.2017.06.005

Xu, S., Nakai, S., Wakita, H., Xu, Y., and Wang, X. (1995). Helium Isotope Compositions in Sedimentary Basins in China. *Appl. Geochem.* 10 (18), 643–656. doi:10.1016/0883-2927(95)00033-X

Xu, S., Zheng, G., Zheng, J., Zhou, S., and Shi, P. (2017). Mantle-derived Helium in Foreland Basins in Xinjiang, Northwest China. *Tectonophysics* 694, 319–331. doi:10.1016/j.tecto.2016.11.015

Xu, Y. (1997). Helium Isotope Distribution of Natural Gasses and its Structural Setting. *Earth Sci. Front.*, 4. 185–190.

Xu, Y., Shen, P., and Li, Y. (1989). The Oldest Gas Pool of China:Weiyuan Sinian Gas Pool, Sichuan Province. *Acta Sedimentologica Sinica* 7 (4), 3–13. doi:10.1007/s00376-010-1000-5

Xu, Y., Shen, P., Liu, W., Tao, M., Sun, M., and Du, J. (1998). *Noble Gas Geochemistry in Natural Gases*. Beijing: Science Press.

Xu, Y., Shen, P., Tao, M., and Liu, W. (1997). Geochemistry on Mantle-Derived Volatiles in Natural Gases from Eastern China Oil/gas Provinces (II). *Sci. China Ser. D-earth Sci.* 40 (2), 315–321. doi:10.1007/BF02877541

Xu, Y., Shen, P., Tao, M., and Sun, M. (1994). Distribution of Helium Isotopes in Natural Gas of Petroliferous Basins in China. *Chin. Sci. Bull.* 9 (16), 1505–1508.

Xu, Y., Sun, M., Shen, P., and Wang, X. (1990a). Isotopic Measurements of Helium and Their Application in Natural Gas. *Exp. Pet. Geology.* 12 (3), 316–325.

Xu, Y., Shen, P., Tao, M., and Sun, M. (1990b). Industrial Accumulation of Mantle Source Helium and the Tancheng-Lujiang Fracture Zone. *Chin. Sci. Bull.* 12, 932–935.

Xu, Y. (1996). The Mantle noble Gas of Natural Gases. *Earth Sci. Front.* 3 (3-4), 63–71.

Xu, Y., Wang, X., Wu, R., Shen, P., Wang, Y., and He, Y. (1979). Rare Gas Isotopic Composition of Natural Gases. *Geochemica* 8 (4), 271–282. doi:10.19700/j.0379-1726.1979.04.001

Yin, C., Wang, T., Wang, S., and Lin, F. (2000). Natural Gas and Petroleum Generation, Migration and Accumulation in Sinian Reservoirs of Weiyuan

Area, Sichuan. *Geology-Geochemistry* 28 (1), 78–82. doi:10.3969/j.issn.1672-9250.2000.01.014

Zhang, J., Yang, W., Yi, H., Xie, W., Xie, Z., Zeng, F., et al. (2015). Feasibility of High-Helium Natural Gas Exploration in the Presinian Strata, Sichuan Basin. *Nat. Gas Industry B* 2, 88–94. doi:10.1016/j.ngib.2015.02.007

Zhang, W., Li, Y., Zhao, F., Han, W., Zhou, J., Holland, G., et al. (2019). Quantifying the Helium and Hydrocarbon Accumulation Processes Using noble Gases in the North Qaidam Basin, China. *Chem. Geology.* 525, 368–379. doi:10.1016/j.chemgeo.2019.07.020

Zhao, J., Jin, Z., Lin, C., Liu, G., Liu, K., Liu, Z., et al. (2019). Sedimenrary Environment of the Lower Cambrian Qiongzhusi Formation Shale in the Upper Yangtze Region. *Oil Gas Geology.* 40 (4), 701–715. doi:10.11743/ogg20190402

Zhao, M. (2000). Special Source of the Natural Gases of the Hotan River Gas Field and the Origin of its Non-hydrocarbon Gases. *Geol. Rev.* 48 (5), 480–486. doi:10.1080/12265080208422884

Zheng, J., Liu, W., Sun, G., et al. (2005). Characteristics of helium isotopes in natural gas and their tectonic significances in stable and sub-stable basins. *Progress in Natural Science*, 15(8), 951–957.

Zheng, P., Shi, Y., Zou, C., Kong, L., Wang, L., and Liu, J. (2014). Natural Gas Sources in the Dengying and Longwangmiao Fms in the Gaoshiti Maoxi Area, Sichuan Basin. *Nat. Gas Industry* 34 (3), 50–54. doi:10.3787/j.issn.1000-0976.2014.03.008

Zhu, G., Zhang, S., Liang, Y., and Li, Q. (2007). The Genesis of H2S in the Weiyuan Gas Field, Sichuan Basin and its Evidence. *Chin. Sci Bull* 52 (10), 1394–1404. doi:10.1007/s11434-007-0185-1

Conflict of Interest: The authors declare that the research was conducted in the absence of any commercial or financial relationships that could be construed as a potential conflict of interest.

Publisher's Note: All claims expressed in this article are solely those of the authors and do not necessarily represent those of their affiliated organizations, or those of the publisher, the editors and the reviewers. Any product that may be evaluated in this article, or claim that may be made by its manufacturer, is not guaranteed or endorsed by the publisher.

Copyright © 2022 Qin, Xu, Li and Zhou. This is an open-access article distributed under the terms of the Creative Commons Attribution License (CC BY). The use, distribution or reproduction in other forums is permitted, provided the original author(s) and the copyright owner(s) are credited and that the original publication in this journal is cited, in accordance with accepted academic practice. No use, distribution or reproduction is permitted which does not comply with these terms.

Advantages of publishing in Frontiers

OPEN ACCESS
Articles are free to read for greatest visibility and readership

FAST PUBLICATION
Around 90 days from submission to decision

HIGH QUALITY PEER-REVIEW
Rigorous, collaborative, and constructive peer-review

TRANSPARENT PEER-REVIEW
Editors and reviewers acknowledged by name on published articles

Frontiers
Avenue du Tribunal-Fédéral 34
1005 Lausanne | Switzerland

Visit us: www.frontiersin.org
Contact us: frontiersin.org/about/contact

REPRODUCIBILITY OF RESEARCH
Support open data and methods to enhance research reproducibility

DIGITAL PUBLISHING
Articles designed for optimal readership across devices

FOLLOW US
@frontiersin

IMPACT METRICS
Advanced article metrics track visibility across digital media

EXTENSIVE PROMOTION
Marketing and promotion of impactful research

LOOP RESEARCH NETWORK
Our network increases your article's readership